

Lecture Notes in Mechanical Engineering

Ranganath M. Singari  
Prashant Kumar Jain  
Harish Kumar *Editors*


# Advances in Manufacturing Technology and Management

Proceedings of 6th International  
Conference on Advanced Production and  
Industrial Engineering (ICAPIE)—2021

 Springer


# Lecture Notes in Mechanical Engineering

## Series Editors

Francisco Cavas-Martínez , Departamento de Estructuras, Construcción y Expresión Gráfica Universidad Politécnica de Cartagena, Cartagena, Murcia, Spain

Fakher Chaari, National School of Engineers, University of Sfax, Sfax, Tunisia

Francesca di Mare, Institute of Energy Technology, Ruhr-Universität Bochum, Bochum, Nordrhein-Westfalen, Germany

Francesco Gherardini , Dipartimento di Ingegneria “Enzo Ferrari”, Università di Modena e Reggio Emilia, Modena, Italy

Mohamed Haddar, National School of Engineers of Sfax (ENIS), Sfax, Tunisia

Vitalii Ivanov, Department of Manufacturing Engineering, Machines and Tools, Sumy State University, Sumy, Ukraine

Young W. Kwon, Department of Manufacturing Engineering and Aerospace Engineering, Graduate School of Engineering and Applied Science, Monterey, CA, USA

Justyna Trojanowska, Poznan University of Technology, Poznan, Poland

**Lecture Notes in Mechanical Engineering (LNME)** publishes the latest developments in Mechanical Engineering—quickly, informally and with high quality. Original research reported in proceedings and post-proceedings represents the core of LNME. Volumes published in LNME embrace all aspects, subfields and new challenges of mechanical engineering. Topics in the series include:

- Engineering Design
- Machinery and Machine Elements
- Mechanical Structures and Stress Analysis
- Automotive Engineering
- Engine Technology
- Aerospace Technology and Astronautics
- Nanotechnology and Microengineering
- Control, Robotics, Mechatronics
- MEMS
- Theoretical and Applied Mechanics
- Dynamical Systems, Control
- Fluid Mechanics
- Engineering Thermodynamics, Heat and Mass Transfer
- Manufacturing
- Precision Engineering, Instrumentation, Measurement
- Materials Engineering
- Tribology and Surface Technology

To submit a proposal or request further information, please contact the Springer Editor of your location:

**China:** Ms. Ella Zhang at [ella.zhang@springer.com](mailto:ella.zhang@springer.com)

**India:** Priya Vyas at [priya.vyas@springer.com](mailto:priya.vyas@springer.com)

**Rest of Asia, Australia, New Zealand:** Swati Meherishi at [swati.meherishi@springer.com](mailto:swati.meherishi@springer.com)

**All other countries:** Dr. Leontina Di Cecco at [Leontina.dicecco@springer.com](mailto:Leontina.dicecco@springer.com)

To submit a proposal for a monograph, please check our Springer Tracts in Mechanical Engineering at <https://link.springer.com/bookseries/11693> or contact [Leontina.dicecco@springer.com](mailto:Leontina.dicecco@springer.com)

**Indexed by SCOPUS. All books published in the series are submitted for consideration in Web of Science.**

More information about this series at <https://link.springer.com/bookseries/11236>

Ranganath M. Singari · Prashant Kumar Jain ·  
Harish Kumar  
Editors

# Advances in Manufacturing Technology and Management

Proceedings of 6th International Conference  
on Advanced Production and Industrial  
Engineering (ICAPIE)—2021

 Springer



*Editors*

Ranganath M. Singari  
Delhi Technological University  
New Delhi, India

Harish Kumar  
Department of Mechanical Engineering  
National Institute of Technology Delhi  
Delhi, India

Prashant Kumar Jain  
Department of Mechanical Engineering  
Indian Institute of Information Technology  
Design and Manufacturing  
Jabalpur, India

ISSN 2195-4356

ISSN 2195-4364 (electronic)

Lecture Notes in Mechanical Engineering

ISBN 978-981-16-9522-3

ISBN 978-981-16-9523-0 (eBook)

<https://doi.org/10.1007/978-981-16-9523-0>

© The Editor(s) (if applicable) and The Author(s), under exclusive license to Springer Nature Singapore Pte Ltd. 2023

This work is subject to copyright. All rights are solely and exclusively licensed by the Publisher, whether the whole or part of the material is concerned, specifically the rights of translation, reprinting, reuse of illustrations, recitation, broadcasting, reproduction on microfilms or in any other physical way, and transmission or information storage and retrieval, electronic adaptation, computer software, or by similar or dissimilar methodology now known or hereafter developed.

The use of general descriptive names, registered names, trademarks, service marks, etc. in this publication does not imply, even in the absence of a specific statement, that such names are exempt from the relevant protective laws and regulations and therefore free for general use.

The publisher, the authors, and the editors are safe to assume that the advice and information in this book are believed to be true and accurate at the date of publication. Neither the publisher nor the authors or the editors give a warranty, expressed or implied, with respect to the material contained herein or for any errors or omissions that may have been made. The publisher remains neutral with regard to jurisdictional claims in published maps and institutional affiliations.

This Springer imprint is published by the registered company Springer Nature Singapore Pte Ltd.

The registered company address is: 152 Beach Road, #21-01/04 Gateway East, Singapore 189721, Singapore

# Contents

<b>Comparison of Wear Behaviour of Al–12.5Si Alloy Reinforced with ZrO<sub>2</sub> Using Spray Deposition and Stir Casting Technique</b> . . . . .	1
Ishwargouda S. Patil, Shrikantha S. Rao, and Mervin A. Herbert	
<b>Performance Analysis of Microstrip Patch Antenna for Future Millimeter Wave Wireless Communication System</b> . . . . .	10
S. Kannadhasan and R. Nagarajan	
<b>Tool Wear Detection Using Computer Vision System in Machining</b> . . . . .	19
P. J. Bagga, M. A. Makhesana, A. B. Mishra, A. R. Marvaniya, and K. M. Patel	
<b>Hybrid Refrigeration System Hypothesis Using Vapour Compression and Metal Hydride Refrigeration systems—A Review</b> . . . . .	28
Narayan Singh	
<b>Study on Thermal Conductivity and Thermogravimetric Analysis of Glass Fibre Epoxy Resin Composites Modified with Silicon Carbide and Copper Nanoparticles</b> . . . . .	38
Gurushanth B. Vaggar, S. C. Kamate, S. L. Nadaf, and Pramod V. Badyankal	
<b>Processes Required for Certification of an Engineering Equipment</b> . . . . .	48
Manmeet Singh, Nilesh Ware, and Ranjit Singh	
<b>Effects of Mixing Two Non-edible Biodiesels on Performance and Emission of CI Engine</b> . . . . .	55
H. R. Amriya Tasneem, K. P. Ravikumar, and H. V. Ramakrishna	
<b>The Value Research of Communication and Information Sharing in Supply Chain Management (SCM) for Enhancing the Supply Chain Performance (SCP)—A SSI Case Study</b> . . . . .	65
Mahesh R. Latte and Channappa M. Javalagi	

<b>Implementing Mahalanobis Taguchi System in Classification of Air Quality Data</b> .....	73
Dattaraj Gawas and Suraj Rane	
<b>Antimicrobial Adhesive Prepared by Incorporation of <i>Arnebia nobilis</i> into Silicone-Acrylate Copolymer for Potential Wound Care Application</b> .....	85
Kartik Jindal, Chaitanya Chibber, Radha Sachan, and Roli Purwar	
<b>Corrugated Sandwich Structure Modeling Under Low Velocity Impact</b> .....	94
Vikrant Sen and Shivdayal Patel	
<b>High-Velocity Impact Analysis of CFRP Composite</b> .....	108
Sajal Soni, Roopendra Kumar Pathak, and Shivdayal Patel	
<b>Ballistic Performance of 3D Hybrid Composite Laminates</b> .....	115
Roopendra Kumar Pathak, Shivdayal Patel, and Vijay Kumar Gupta	
<b>Experimental and Statistical Analysis of the Jute Fabric Composites Under Tensile Loading</b> .....	124
Kumar Maharshi and Shivdayal Patel	
<b>Development of Predictive Model for Surface Roughness Using Artificial Neural Networks</b> .....	133
Nikhil Rai, M. S. Niranjana, Prateek Verma, and Prince Tyagi	
<b>Design of Pineapple Eye-Removing Device</b> .....	142
Prakash Kumar	
<b>Implementation of Boost Converter for High Step-Up DC/DC for Thermoelectric Generator</b> .....	149
Melisa Miranda, Shivalingesh S. Dhaded, S. M. Akash, and Prithviraj Misra	
<b>Investigation on Geopolymer Concrete Reinforced with Steel and Hybrid Fibre</b> .....	165
Harsh Singh, Shilpa Pal, and Shivam Kasana	
<b>A Critical Analysis of Design, Development, and Failure of Existing Stents</b> .....	173
Jannatul Bashir and K. Jayabal	
<b>Study of Effect of Leading-Edge Tubercles on NACA 4412 Airfoil</b> .....	182
Ishwar Mukesh, Aakash Kaushik, Naushad Ahmad Ansari, and M. Zunaid	
<b>Design of a Wheel Assembly with a Double Bearing System for Formula Student Cars</b> .....	192
N. Rakshith	

**Modeling of Factors Impacting Remote Workforce During COVID-19** ..... 199  
 Kushagra Shukla, Harsh Kumar Singh, Lokesh Yadav, Mohd. Shuaib, and Urfi Khan

**Design of the Automated System for the Acquisition, Recording and Analysis of Data in the Development of Indicators of Consumption and Production Energy** ..... 209  
 Saldaña Enderica Carlos, Chuquimarca Jiménez Luis, Torres Guin Washington, Bustos Gaibor Samuel, and Flores Tomalá Daniel

**An Overview of the Properties of Aluminium Alloys with the Help of Equal Channel Angular Pressing** ..... 218  
 Vishwesh Mishra, Piyush Signal, and Akashdeep Yadav

**Comparison of P&O and Proposed Fuzzy Logic Algorithm for MPPT-Based Charger** ..... 225  
 Parth Malhotra, Prabhav Kumar Yadav, Samyak Jain, and Dheeraj Joshi

**Applications of Friction-Based Processes in Manufacturing** ..... 236  
 Raghavendra Darji, Gaurang Joshi, Vishvesh Badheka, and Dhiren Patel

**Simulating Percentage of Workers Opting to Work from Home During the COVID-19 Pandemic Using N-Player Iterative Game Theory** ..... 244  
 Ayan J. Malhotra, Bhupender Singh, Dev Surya, and Anjana Gupta

**Selection of Ride Frequency for an ATV based on a Full Car Vehicle Model** ..... 253  
 Atul Singh, Ayush Venkat Vats, Sahil Sharma, and Vikas Rastogi

**Design, Fabrication, and Testing of a Solar Powered Air Purifier with UV Sterilization Capability** ..... 261  
 Akhilesh Arora, Kanish Bhardwaj, Naved Esmail, and Pushkar Dhar Dubey

**Double Zone Thermal CVD and Plasma Enhanced CVD Systems for Deposition of Films/Coatings with Eminent Conformal Coverage** ..... 273  
 Shreya, Anukool Yadav, Ritika Khatri, Nikita Jain, Anurag Bhandari, and Nitin K. Puri

**Friction Stir Welding of Two Dissimilar Metal Alloy: A Survey** ..... 284  
 Shantanu Madhukar Kadam and Netra Pal Singh

**Social Intelligence as a Tool for Human Performance Optimization During Post COVID 19: A Review** ..... 292  
 Tanushree Sanwal and Puja Sareen

<b>Modeling and Simulation of Solar-Powered Remote-Operated Floating Trash Harvesting Boat</b> .....	302
Purnyatre Gaur, Aniket, Subhesh Kumar, and J. P. Kesari	
<b>Process Parameters Optimization of Stainless Steel Turning: A Survey</b> .....	313
Tanpure Sandesh Popat and Netra Pal Singh	
<b>Integrated Real Time Database for Supermarkets</b> .....	321
Archit Jain and Nitin K. Puri	
<b>Greywater Reuse and Treatment Methods for Quality Improvement: A Review</b> .....	328
Deepak Narayan Paithankar and Shashi Ranjan Kumar	
<b>Employment of Blockchain Technology in Supply Chain Management</b> .....	339
Aman Pandey, M. S. Niranjana, Amey Jha, and Aneesh Kamal	
<b>An Approach Toward Lean Manufacturing Through Application of SMED as a Lean Tool</b> .....	348
Mahantesh M. Ganganallimath, Sachin Chavaraddi, V. S. Puranik, K. Vizayakumar, Umesh M. Bhushi, Roopa B. Math, and C. M. Veerendrakumar	
<b>Design and Optimization of an Evaporative Condenser: A Detailed Review</b> .....	360
Vivek M. Korde, Shivam N. Dekate, Yash A. Bais, and Chirag P. Raut	
<b>The Numerical Examination for Mixing Characteristics of Modified T Micromixer with Offset and Triangular Obstructions</b> ....	372
Sachin Kaushik and M. Zunaid	
<b>Simulation of Erosion in Abrasive Water-Jet Nozzle to Study Wear Behavior</b> .....	382
Abhijeet Kumar, Abhishek Meghwal, Aakash Sharma, and R. C. Singh	
<b>Artificial Neural Network-Based Modeling of Membrane Contractors for Industrial Gas Treatment</b> .....	391
Harshit Gupta, Arnav Gosain, Akhil Batra, and Manish Jain	
<b>Effect of Process Parameters on CNTFET</b> .....	398
Abhinav Sharma, Adarsh Kumar, and Suresh C. Sharma	
<b>Design and Simulation Study of High-Speed Slab Track</b> .....	404
Priti Rani, Kiran Chholak, and Yamika Patel	
<b>Utilization of Residual Heat Energy Using Pyro Electricity Energy Harvesting</b> .....	419
Ashish Kumar, Ashish Mishra, and Manoj Kumar Shukla	

**Conceptual Design and Computational Analysis of Power Generating Shoes Using Plantar Flexion** ..... 425  
 Naman Goel, Abhishek Jain, Tanishq Arora, and Vikas Rastogi

**Design Optimization of Clutch Plate Using ANSYS** ..... 433  
 Shivam, Rupanshu Singh, and Priyansh Singh

**Estimation of Flyer Velocity for Titan 12 (Grade 1) Plates by Pin Contact Velocity Measurement Method** ..... 441  
 Lavepreet Singh, Rishabh kumar, Yuvraj Bhardwaj, Manish singh, and Rajneesh Kumarr

**Automobile Sales Forecasting and Correlation with Economic Indicators: A Comprehensive Intra-Region Case Study** ..... 452  
 Waquar Shoaib and J. Sanjog

**A Study on Potential and Economic Viability for Developing Infrastructure of Electric Vehicles and Solar Powered Charging Stations in Delhi** ..... 460  
 Durgesh Kumar, Chetan Raj Chauhan, Vidhu Bhardwaj, and Sarita Baghel

**Development and Characterization of Stir Cast Aluminum-Brick Powder Metal Matrix Composites** ..... 469  
 Shubham Kumar Singh, Aniruddha Jaiswal, Manvandra Kumar Singh, Ashwini Kumar, Sunil Mohan, R. K. Gautam, Sudhanshu Shekhar Singh, Gopal Ji, and Rajiv Prakash

**Development of SCADA and PLC-Based Monitoring and Control of Metro Rail System** ..... 479  
 Jetwadee Phanthanachai, Rachana Garg, and Narendra Kumar

**Detection of Tampering in Multimedia Using Blockchain Technology** ..... 492  
 Abhishek Singh, Adarsh Kumar, and Jamkhongam Touthang

**Effect of Vortex Generators and Rear Spoiler on a Low-End Sedan Passenger Car** ..... 501  
 Nikhil Pasricha, Sartaj Anwer Khan, and Faisal Shameem

**Capacitance and Speed Required for Rated Generation by a Self-excited Induction Generator** ..... 511  
 D. C. Meena, Suraj Bhan Yadav, Pawan Yadav, and Sumit

**Design and Analysis of Wheel Rim Using Composite Materials and Carbon Fibres** ..... 519  
 Ashish, Anas Khan, P. Suresh, and Shrikant Vidya

**Attendance Management System Using Modern Face Recognition and Gesture Recognition Using Deep Learning** ..... 527  
 Mahaba Ullas Ekka, Omar ALi Mze, Tarun Singh, and N. S. Raghava

**Plan and Running of a Program Logic Regulator by Using PIC18F4580** ..... 536  
 Tareq AL-hamzah, P. Suresh, and Sheetla Prasad

**Preliminary Observations of Synthesized WS<sub>2</sub> and Various Synthesis Techniques for Preparation of Nanomaterials** ..... 546  
 Anukool Yadav, Shreya, and Nitin K. Puri

**Design of GSM-Based Fire Detection System Using Microcontroller and Sensors** ..... 557  
 Aditya Rana, Tarun Kumar, and Nitin K. Puri

**Investigation of Thermal Battery Management Pack Using Liquid Cooling Systems in 3-D Li-Ion Battery Model** ..... 569  
 Vanshaj Mittal, Bhumika Mathur, Shivam Beniwal, and Amrish K. Panwar

**Short-Term Electricity Demand Forecast Using Deep RNN and Stacked LSTM** ..... 578  
 Surbhi Singh and Madan Mohan Tripathi

**CFD Analysis to Enhance the Heat Transfer Coefficient in Micro-Channels** ..... 589  
 Sauraj Kumar Sharma, Shrikant Vidya, and K. S. Srikanth

**Optimization of Design Parameters for a Quadcopter Using Taguchi Design Methodology** ..... 598  
 Siddharth Sharma, Pratham Khurana, Manan Sharma, and Aditya Kumar

**Comparative Analysis of Different Dye-Sensitizer and Their Impact on a Solar Cell by Using SCAPS-1D Simulator** ..... 610  
 Sushmita Kumari and Cherry Bhargava

**Numerical Analysis of Low GWP Blends of R290 as an Alternative to R410A** ..... 621  
 Subham Mukhopadhyay, Hardik Gupta, Ajay Kumar, and Akhilesh Arora

**Mortality Assessment Due to Fine-PM Exposure During 2019 Stubble Burning Season in Punjab, Haryana, and Delhi Using WHO AirQ+ model** ..... 630  
 Raghav Sharma, Vasu Singla, Aman Kaushik, and Lovleen Gupta

**Design and Analysis of Spur Gear, Helical Gear, and Bevel Gear by Using ANSYS** ..... 641  
Anuj Kumar Singh, Swapnil Kumar, Brahma Nand Agrawal, and Pawan Kumar Singh Nain

**Detection of Counterfeit Drugs in Medical Supply Chain Using Blockchain Technology** ..... 651  
Abhinav Sanghi, Aayush, and Ashutosh Katakwar

**Recognizing Energy Wasting Households Using Data Mining and Incorporating the Cybersecurity Concept** ..... 660  
Rahul Balout, Aarohi Kumari, and Mayank Panchal

**Design, Development, and Manufacturing of Cost-Effective Face Shields for COVID-19** ..... 676  
Mohan Aditya Pabolu, Venkata Nori, and Jayaprakash Sharma Panchagnula



## About the Editors

**Dr. Ranganath M. Singari** is a Professor in the Department of Mechanical, Production and Industrial Engineering and heads the Department of Design, Delhi Technological University, India. He is a graduate in Industrial Production Engineering from Karnataka University. He completed his M.Tech. in Computer Technology and Applications and Ph.D. from the Department of Production Engineering from University of Delhi, India. He has more than 60 international publications in conference and reputed journals. He is also a reviewer for reputed journals. Dr. Singari has organised several international conferences, seminars/workshops, industry-institute interactions and 6 FDP/SDP/STTP. He also serves as Chairman, Production Engineering, Skill India Programme, DTTE, Delhi. He is an expert member of several selection committees for technical, teaching and administrative positions. His research interest is materials, manufacturing, industrial management, production management, CAD/CAM, supply chain management, multi-criteria decision making and sustainable lean manufacturing. He has 25 years of research and teaching experience.

**Dr. Prashant Kumar Jain** is currently Associate Professor at Department of Mechanical Engineering, Indian Institute of Information Technology, Design and Manufacturing, Jabalpur. He obtained his B.E. (Mechanical Engineering) from Dr. H. S. Gour University, Sagar, M.E. (Advanced Production Systems) from SATI, Vidisha and Ph.D. from Indian Institute of Technology Delhi, Delhi. He also has served at IIT Delhi as Project Scientist and at Delhi College of Engineering, Delhi (now Delhi Technological University, Delhi) as Lecturer. His major research interests include rapid prototyping/additive manufacturing, geometric modelling, CAD/CAM integration, computational geometry, rapid prototyping and tooling. He has more than 85 publications to his credit, published in international peer reviewed journals, national and international conferences in India and abroad.

**Dr. Harish Kumar** is currently Assistant Professor at Department of Mechanical Engineering, National Institute of Technology Delhi. He obtained his B.Tech. (Mechanical and Automation Engineering) and Ph.D. from GGS Indraprastha University, Delhi. His major research interests include mechanical measurement and

metrology and composites. He has more than 35 publications to his credit, published in international peer reviewed journals. He has served as Scientist in CSIR-National Physical Laboratory, New Delhi during 2007–2017 and as a guest researcher at National Institute of Standards and Technology, USA in 2016. He has been serving as editor of several peer reviewed journals.



# Comparison of Wear Behaviour of Al–12.5Si Alloy Reinforced with ZrO<sub>2</sub> Using Spray Deposition and Stir Casting Technique

Ishwargouda S. Patil<sup>1,2</sup>(✉), Shrikantha S. Rao<sup>2</sup>, and Mervin A. Herbert<sup>2</sup>

<sup>1</sup> Tontadarya College of Engineering, Gadag, India  
ishwargoudanitik@gmail.com

<sup>2</sup> National Institute of Technology, Surathkal, India

## 1 Introduction

Aluminium is a chemical element with the atomic number 13. The worldwide applications of Al–Si castings constitute  $\approx 80$ – $90\%$  of total production of Al castings. Typically, Al–Si castings found their applications in automotive (engine blocks, cylinder heads, transmission housing, wheel rims, powertrain and suspension components,) and aerospace (aluminium crankcase, Embraer Phenom Winglet, tail rotor gear box, bracket, overwing emergency exit door) industries. The metal matrix composites have become the hot research spot in the field of material science [1]. The strategic link between a material's behaviour and its processing is to investigate its microstructure [2]. This lead the way of development using aluminium silicon alloys using rapid solidification methods following melt atomization. These methods result in modification and substantial refinement of the constituent stages with natural homogeneity of the microstructure [3–6]. Daound et al. [7], however, conventional processing of Al–Si alloys results in coarse and segregated microstructures with inferior mechanical and wear properties [8–13]. These metal matrix composites can be manufactured by many methods including spray deposition [14], reactive processing [15], self-propagating high temperature synthesis [16], stir casting [17], reactive slag process [18], direct metal laser sintering [19], applied load [20] and vacuum pressure infiltration [21]. In this context, zirconium oxides have been used as reinforced material in aluminium silicon alloys because of its outstanding mechanical, wear and chemical properties [22–24]. However, studies on these composites are very limited. One such type was reported by Karthikeyan et al. [25]. The study found that the processing of Al–ZrO<sub>2</sub> composites using stir casting technique resulted in non-uniform distribution of ZrO<sub>2</sub> particles and low wettability. The Taguchi's design of experiments has been used by most of the engineers to optimize the effect of parameters on the engineering problems [26]. In the same vein as the previous studies, James et al. (2018) produced a composite consisting of 5% ZrO<sub>2</sub>, 90% aluminium 6061 and 5% Al<sub>2</sub>O<sub>3</sub> that was restricted to a 10% weight to avoid the formation of cluster and decrease in weight. Ramchandra et al. [27] investigated the Al/ZrO<sub>2</sub> composite fabricated using powder metallurgy method. The deformation of the plastic behaviour during mushy state rolling differs from that of dislocation movement during hot or cold working. As a

result, in the former, relative sliding and rotation across the grains are possible. Therefore, improving the wear properties is by increasing the nanoparticles and decreasing the concentration of microparticles in a synergistic arrangement. Sahin [28] investigated the wear rate by larger flight distances, abrasive size and applied load for SiC paper. The authors found that the wear rate increases to abrasive particle size and applied load and decreases to the flight distance for  $\text{Al}_2\text{O}_3$ . It was to note that the effect of interaction between the variables exhibited a mixed behaviour towards the wear properties.

From the survey, it can be noted that a use of zirconium oxide as a reinforced material in Al–Si metal matrix results in improving wear resistance. It is worthy to note that the works on zirconium oxide as reinforcement material are very limited [29–31]. This paper aims at developing aluminium silicon alloy reinforced with the  $\text{ZrO}_2$  powder particles (15.0 wt %) composites by stir casting and spray deposition processing techniques. Also, there is no comparison between spray deposition and stir casting methods. However, the reduction in density is a greater benefit for automotive industries. The work on the effect of wear properties on stir casting and spray-formed Al–Si and  $\text{ZrO}_2$  is not reported in the literature. Therefore, the current study is to observe the mechanical properties of prepared composite, which can garb its suitability to be used in automotive, aerospace and industrial works.

## 2 Dry Sliding Wear and Hardness

The type of metal matrix composite used in the present study is Al–12.5Si with 15% of zirconium oxide as reinforced material. The composition was chosen based on our previous works. It is to be noted that the sliding between two solid surfaces under pressures causes adhesive wear. The experiments were performed out by using a pin-on-disc wear testing machine according to ASTM G99-95 standard. The test samples were prepared using stir casting and spray deposition methods.

The track diameter was kept constant throughout the tests. The nominal load and the sliding distance were varied from 10 to 50 N and 1000 to 4300 m, respectively. It is noted that for every trail run, the test specimens were removed from the machine and weighted precisely to calculate the weight loss. To obtain accurate results with the surface finish, the specimens were initially polished to 0.25  $\mu\text{m}$ . The specimens were cleaned with isopropyl alcohol before and after wear tests. The specimens are fabricated at different combinations of stir casting, and hot-pressing condition was used as pin material. The experiments were performed out without any lubrication at room temperature under different applied loads of 10, 20, 30, 40 and 50 N, respectively. In this study, the flight distance and sliding velocity are kept as 2300 m and 1.9 m/s. The operating conditions of the test are tabulated in Table 1. Wear debris and surfaces of the tested specimens were investigated using scanning electron microscopy (Model: S-3400 N Hitachi Model).

The hardness testing of Al–12.5Si + 15 $\text{ZrO}_2$  was determined using LECO LV700AT Vickers hardness tester. Every tested sample was polished before starting the new trail. All the tests were conducted in ambient temperature. In order to ensure repeatability during the experiments, each test was repeated at least five times, and the average values of hardness are reported.

**Table 1** Operating conditions of wear test

Parameters	Value	Unit
Rotational speed of the disc	300	rpm
Ambient temperature	31	°C
Number of revolutions	1100	rpm
Track diameter	120	mm

### 3 Results and Discussion

#### 3.1 Microstructural Investigation of Stir Casting and Spray Deposition for Al–12.5Si with 15% ZrO<sub>2</sub> as Reinforced Material

The microstructural images of the developed metal matrix composite for spray deposition and stir casting methods are shown in Fig. 1. It was observed that the presence of precipitates evenly distributed along the grain boundaries, resulting in very clear grain boundaries. For the test specimen, in both cases (spray deposition and stir casting). The mark of an adhesive wear with deformation of the plastic is clearly visible as shown in Fig. 1 and clearly indicates the mark of an adhesive wear with plastic deformation. The edge cracking and metallic fracture of ridges were seen on the surface of the stir-casted composite material. The primary silicon particles easily separate from the Al matrix, and the silicon particle debris becomes embedded in the matrix. This results in non-uniform and deep grooves. Interestingly, the worn surface of spray-deposited composite (refer Fig. 1b) shows smooth appearance and marks with smaller grooves and few small dimples. This can be explained by the fact of oxidation of asperities and deformation of the plastic on the surface indicating the abrasive wear and existence mixed metallic. In general, the increase in the hardness of the material decreases the wear rate of the composite. The lesser wear rate of the spray-formed metal matrix composite as compared with stir-casted composite material is attributed to the refinement of microstructure. This is due to the uniformly distributed Si particles of  $\alpha$ -Al matrix and large amount of fine particles. In both the cases, the grains in the examined specimens are distended in the same as the sliding wear direction. This demonstrates that during the wear process, zirconium oxide particles tend to align themselves in the rolling direction [32].

It is worth noting that the sliding between the two surfaces exerts a tangential force on the particles during the wear process. This leads to localized shear stress which results in particle pull out or fracture, as defined by [33].

#### 3.2 Wear and Hardness Characteristics for Stir Casting and Spray Forming

The wear loss pattern of the developed metal matrix composites by increasing the applied nominal load is shown in Fig. 2. From the plot, it can be noticed that the wear loss is significant at higher loads for both the methods. However, the wear loss is small in spray-formed composite compared to stir casting composite. The reason is the uniform distribution of reinforcing zirconium oxide material in aluminium silicon matrix which

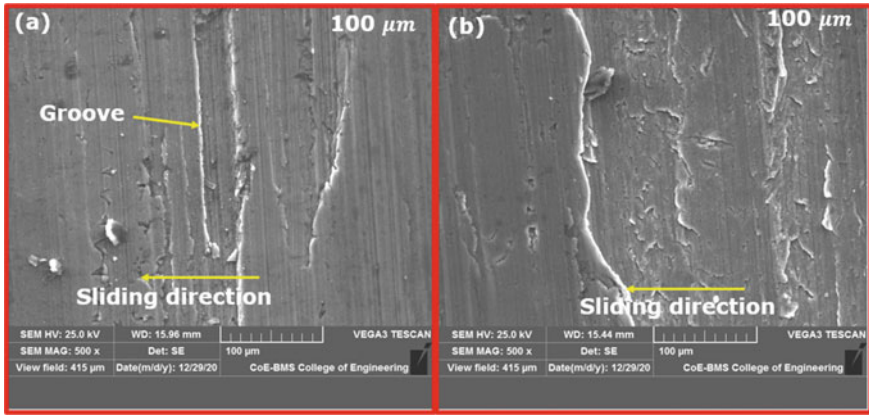


**Fig. 1** SEM microstructure images of wear surfaces of the composite in: **a** Stir casting and tested under 40 N Al12.5Si-ZrO<sub>2</sub> wt 15%; **b** Spray forming and tested under 40 N for Al12.5Si-ZrO<sub>2</sub> wt 15%

is released during sliding condition and forming a shielding tribolayer between counter disc surface and pin [8, 34]. It can be observed that the slope of the wear loss rises in stir casting composites increases by larger amount at the load of 25 N. This is due to the delamination and higher amount of deformation of the plastic occurred on the mating surface.

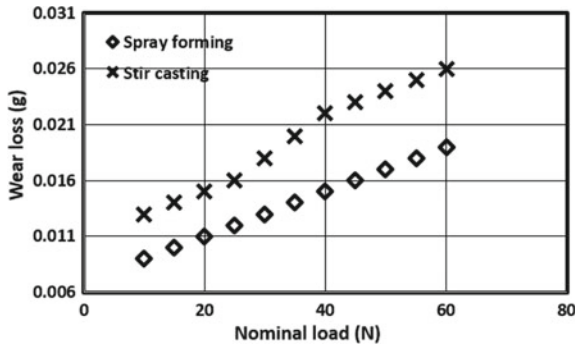


**Fig. 2** Variations of nominal applied load with respect to wear loss

Figure 3 shows the behaviour of wear loss with respect to the applied nominal load for developed metal matrix composite at a flight distance of 2300 mm and sliding velocity of 1.9 m/s. It can be observed from Fig. 3, for both the methods, it is obvious that the wear rate is directly proportional to the applied loads. Comparative study on these two methods revealed that spray-formed composite has got improved wear resistance than the stir casting composite under identical sliding conditions. The wear resistance is larger in stir casting and lowest for spray-formed composite. At larger applied loads, the difference between wear rates of stir casting and spray formed is more significant,

which implies that much of the larger loads is utilized in wear rather than in plastic deformation of the samples. It was to note that there was decrease in wear rate of 18% using spray deposition technique.

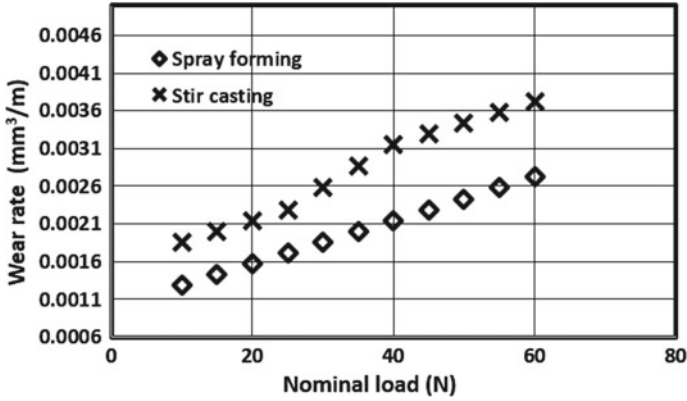


Fig. 3 Variations of applied load with respect to wear rate

Figure 4 depicts the variation of the coefficient of friction (COF) with applied nominal load for the wear of the composite subjected to stir casting and spray forming process. It can be observed in both the cases (stir casting and spray forming) that the COF decreases in the entire range of nominal load applied. One may expect that the coefficient of friction is inversely proportional to the applied load. The asperities deformation does not occur, and the actual area of contact remains unchanged. For both the cases, the COF decreases till 40 N. It is worthy to note that decreasing the hardness on the surface or increasing nominal load, the actual area of contact increases. This leads to increase in COF. The microstructure of the metal matrix composites also influences the friction and wear properties.

The hardness of Al + 12.5Si + 15% ZrO<sub>2</sub> metal matrix composites for stir casting and spray forming composite is shown in Fig. 5. It can be inferred from Fig. 5 that the hardness value of the Al + 12.5Si + 15% ZrO<sub>2</sub> hybrid composite is increased in spray forming method because of considerable uniform distribution of zirconium oxide in the aluminium silicon alloy which can be also seen in the microstructure (refer Fig. 1). Another possibility is due to the addition of zirconium oxide powder that is normally harder.

It is worth noting that the surface layers are much denser than the inner core. However, after wear testing, the surface hardness layer is much higher than after the stir casting process. Another possibility is that the deformation of the plastic at surface layers during wear tests is accompanied by work hardening. In spray forming process, the average hardness 79 is 14.5% larger than the average hardness of stir casting composite.

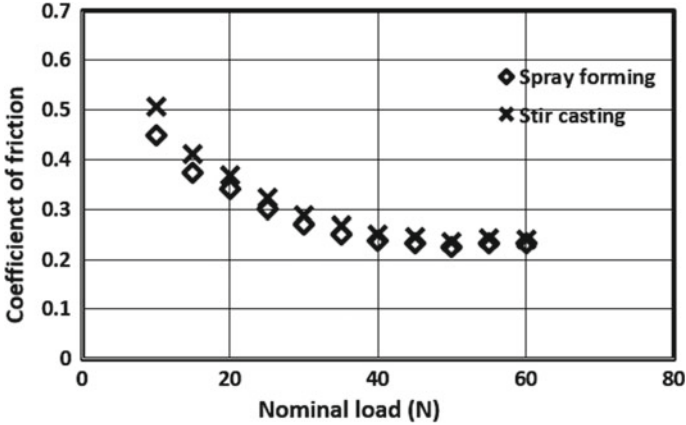


Fig. 4 Influence of nominal applied load on friction plot of metal matrix composites

### 4 Conclusion

Aluminium silicon alloy reinforced with  $ZrO_2$  was developed using spray deposition and stir casting methods. The experiments were performed using pin-on-disc wear machine on the developed metal matrix composite. The following conclusions are drawn from this study:

1. The increase in weight loss was observed at higher applied load for all the composite samples.
2. The maximum friction coefficient was observed in spray deposition composite of 0.45, when compared with stir casting composite of 0.52.
3. As the abrasive particle size expanded, weight reduction increased at a quicker rate until a certain particle size was reached, after which it increased at a slower rate.
4. In both spray deposition and stir casting methods, microstructural images revealed that  $ZrO_2$  particles were evenly distributed along grain boundaries. The microstructure refinement resulted in improved properties in the spray-formed metal matrix

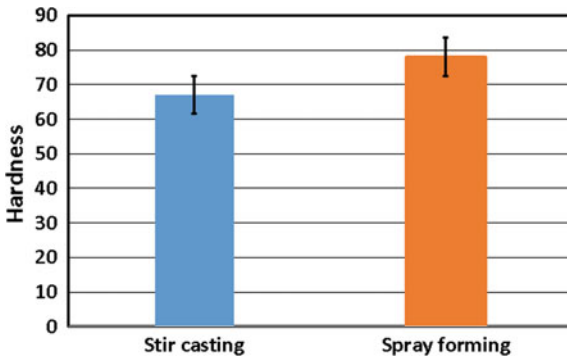


Fig. 5 Variation of hardness with spray forming and stir casting method



composite. It was found that the nominal average size of formed  $ZrO_2$  particles was observed to be less than  $5 \mu m$ .

5. The wear properties and friction factor are lower in stir casting composite compared to spray-formed composite.

In future, the effect of flight distance, sliding velocity and wet wear characteristics will be investigated for the composites. In addition, the variation of reinforced zirconium oxide percentage on the aluminium silicon alloy will be studied, and the results will be present.

## References

1. Lloyd DJ (1994) Particle reinforced aluminium and magnesium matrix composite. *Int Mater Rev* 39(1):1–23. <https://doi.org/10.1179/imr.1994.39.1.1>
2. Botettinger WJ, Coriell SR, Greer AL, Karma A, Kurz W, Rappaz M, Trivedi R (2000) Solidification microstructure: recent developments, future directions. *Acta Mater* 48(1):43–70. [https://doi.org/10.1016/S1359-6454\(99\)00287-6](https://doi.org/10.1016/S1359-6454(99)00287-6)
3. Adachi M (1984) Modification of hyper-eutectic Al-Si system casting alloys. *J Japan Inst Light Metals* 34(7):430–436. <https://doi.org/10.2464/jilm.34.430>
4. Lavernia E, Ayers JD, Srivatsan TS (1992) Rapid solidification processing with specific application of aluminium alloys. *Int Mater Rev* 37(1):1–44. <https://doi.org/10.1179/imr.1992.37.1.1>
5. Srivastava RK, Mandal SN, Ojha SN (2001) Proceedings of the international conference on solidification science and processing, pp 1–8
6. Arif S, Tanwir M, Ansari AH, Siddiqui MA, Mohsin M (2017) Study of mechanical and tribological behaviour of Al/SiC/ZrO<sub>2</sub> hybrid composites fabricated through powder metallurgy technique. *Mater Res Express* 4:076511. <https://doi.org/10.1088/2053-1591/aa7b5f>
7. Daoud A, Abo-Elkhar M (2002) Influence of Al<sub>2</sub>O<sub>3</sub> or ZrO<sub>2</sub> particulate addition on the microstructure aspects of AlNi and AlSi alloys. *J Mater Process Technol* 120(1–3). [https://doi.org/10.1016/S0924-0136\(01\)01067-6](https://doi.org/10.1016/S0924-0136(01)01067-6)
8. Akhlaghi F, Mahdavi S (2011) Effect of the SiC content on the tribological properties of hybrid Al/Gr/SiC composites processed by in-situ powder metallurgy (IPM) method. *Adv Mater Res* 264–265:1878–1886. <https://doi.org/10.4028/www.scientific.net/AMR.264-265.1878>
9. Thema FT, Beukes P, Ngom BD, Manikandan E, Maaza M (2015) Free standing diamond-like carbon thin films by PLD for laser based electrons/protons acceleration. *J Alloys Compd* 648:326–331. <https://doi.org/10.1016/j.jallcom.2015.06.277>
10. Sathyaseelan B, Manikandan E, Baskaran I, Senthilnathan K, Sivakumar K, Moodle MK, Sivam RK, Maaza M (2017) *Compounds* 694:556–559. <https://doi.org/10.1016/j.jallcom.2016.10.002>
11. Selvaraj SK, Nagarajan MK, Kumaraswamidhas LA (2017) An investigation of abrasive and erosion behavior of AA 2618 reinforced with Si<sub>3</sub>N<sub>4</sub>, AlN and ZrB<sub>2</sub> in situ composites by using optimization techniques. *Arch Civil Mech Eng* 17(1):43–54. <https://doi.org/10.1016/j.acme.2016.08.003>
12. Safri S, Sultan M, Jawaid M, Jayakrishna K (2018) Impact behaviour of hybrid composites for structural applications: a review. *Compos Struct B Eng* 133:112–121. <https://doi.org/10.1016/j.compositesb.2017.09.008>

13. Zhao ZY, Misra RDK, Bai PK, Gao JF, Li YJ, Guan RJ, Guo ZH, Liu H (2018) Novel process of coating Al on graphene involving organic aluminium accompanying microstructure evolution. *Mater Lett* 232:202–205. <https://doi.org/10.1016/j.matlet.2018.08.036>
14. Wang F, Liu H, Yang B (2005) Effect of in situ TiC particulate on the wear resistance of spray-deposited 7075 Al matrix composite. *Mater Charact* 54:446–450. <https://doi.org/10.1016/j.matchar.2005.01.011>
15. Ramesh CS, Pramod S, Keshavamurthy RA (2011) Study on microstructure and mechanical properties of Al 6061–TiB<sub>2</sub> in situ composites. *Mater Sci Eng A* 528:4125–4132. <https://doi.org/10.1016/j.msea.2011.02.024>
16. Li P, Kandalova EG, Nikitin VI (2005) In situ synthesis of Al–TiC in aluminum melt. *Mater Lett* 59:2545–2548. <https://doi.org/10.1016/j.matlet.2005.03.043>
17. Shorowordi KM, Haseeb A, Celis JP (2006) Tribo-surface characteristics of Al–B<sub>4</sub>C and Al–SiC composites worn under different contact pressures. *Wear* 261:634–641. <https://doi.org/10.1016/j.wear.2006.01.023>
18. Sheibani S, Najafabadi MF (2007) In situ fabrication of Al–TiC metal matrix composites by reactive slag process. *Mater Sci Des* 28:2373–2378. <https://doi.org/10.1016/j.matdes.2006.08.004>
19. Ghosh SK, Saha P (2011) Crack and wear behavior of SiC particulate reinforced aluminium based metal matrix composite fabricated by direct metal laser sintering process. *Mater Sci Des* 32:139–145. <https://doi.org/10.1016/j.matdes.2010.06.020>
20. Umasankar V, Xavier MA, Karthikeyan S (2014) Experimental evaluation of the influence of processing parameters on the mechanical properties of SiC particle reinforced AA6061 aluminium alloy matrix composite by powder processing. *J Alloy Compd* 582:380–386. <https://doi.org/10.1016/j.jallcom.2013.07.129>
21. Liu L, Li W, Tang Y, Shen B, Hu W (2009) Friction and wear properties of short carbon fiber reinforced aluminium matrix composites. *Wear* 266(7–8):733–738. <https://doi.org/10.1016/j.wear.2008.08.009>
22. Zeher M, Minti H, Reisfield R, Tenne R (1997) Preparation and characterization of Cds films synthesized in situ in Zirconia Sol-Gel Matrix. *Chem Mater* 9(11):2541–2543. <https://doi.org/10.1021/cm970245j>
23. Ray K, Patra H, Swain AP, Parida B, Mahapatra S, Sahu A, Rana S (2020) Glass/jue/sisal fibre reinforced hybrid polypropylene polymer composites: fabrication and analysis of mechanical and water absorption properties. *Mater Today Proc* 1–8. <https://doi.org/10.1016/j.matpr.2020.02.964>
24. Govindan K, Jinu G (2020) Experimental investigation on mechanical and wear behaviour of aluminium LM6/ZrO<sub>2</sub> composites fabricated by stir casting method. *J Balkan Tribol Assoc* 21:539–556. <https://doi.org/10.1080/09534962.1990.11819044>
25. Karthikeyan G, Jinu GR (2015) Experimental investigation on mechanical and wear behaviour of aluminium LM6/ZrO<sub>2</sub> composites fabricated by stir casting method. *J Balkan Tribol Assoc* 21(3):539–566
26. Shetty R, Pai R, Rao S (2008) Tribological studies on discontinuously reinforced aluminium composited based on orthogonal arrays. *ARNP J Eng Appl Sci* 3(1):84–92. ISSN 1819-6608
27. Ramachandra M, Abhishek A, Siddeshwar P, Bharathi V (2015) Hardness and wear resistance of ZrO<sub>2</sub> nano particle reinforced Al nano composites produced by powder metallurgy. *Procedia Mater Sci* 10:212–219. <https://doi.org/10.1016/j.mspro.2015.06.043>
28. Sahin Y (2003) Wear behaviour of aluminium alloy and its composites reinforced by SiC particles using statistical analysis. *Mater Sci Des* 24:95–103. [https://doi.org/10.1016/S0261-3069\(02\)00143-7](https://doi.org/10.1016/S0261-3069(02)00143-7)
29. Smitha VS, Syamili SS, Mohamed P, Balagopal NN, Hareesh US (2018) ORMOSIL–ZrO<sub>2</sub> hybrid nanocomposites and coatings on aluminium alloys for corrosion resistance; a sol gel approach. *New J Chem* 42:10337–10347. <https://doi.org/10.1039/C7NJ05174C>

30. Raju K, Ojha SN, Harsha AP (2008) Spray forming of aluminium alloy and its composites: an overview. *J Mater Sci* 43:2509–2521. <https://doi.org/10.1007/s10853-008-2464-x>
31. James SJ, Ganesan M, Santhamoorthy P, Kuppan P (2018) Development of hybrid aluminium metal matrix composite and study of property. *Mater Today Proc* 5(5):13048–13054. <https://doi.org/10.1016/j.matpr.2018.02.291>
32. Arif S, Jamil B, Shaikh MB, Aziz T, Ansari AH, Khan M (2020) Characterization of surface morphology, wear performance and modelling of graphite reinforced aluminium hybrid composites. *Eng Sci Technol Int J* 23(3):67–690. <https://doi.org/10.1016/j.jestch.2019.07.001>
33. Rosenfield AR (1987) A shear instability model of sliding wear. *Wear* 116(3):317–328. [https://doi.org/10.1016/0043-1648\(87\)90180-3](https://doi.org/10.1016/0043-1648(87)90180-3)
34. Ravindran P, Manisekar K, Rathika P, Narayanasamy P (2013) Tribological properties of powder metallurgy—processed aluminium self-lubricating hybrid composites with SiC additions. *Mater Sci Des* 45:561–570. <https://doi.org/10.1016/j.matdes.2012.09.015>



# Performance Analysis of Microstrip Patch Antenna for Future Millimeter Wave Wireless Communication System

S. Kannadhasan<sup>1</sup>(✉) and R. Nagarajan<sup>2</sup>

<sup>1</sup> Department of Electronics and Communication Engineering, Cheran College of Engineering, Aravakuruchi, Tamil Nadu, India  
kannadhasan.ece@gmail.com

<sup>2</sup> Department of Electrical and Electronics Engineering, Gnanamani College of Technology, Namakkal, Tamil Nadu, India

## 1 Introduction

Microstrip antennas have been a field of research and development which is increasing rapidly. Thanks to their light weight, lightweight scale, and ease of manufacturing, their future uses are endless. Their inherently narrow bandwidth is one restriction. Latest research and trials, though, have identified avenues to resolve this barrier. A number of methods have been taken, including patch form adjustment, substrate parameter experimentation. We built a patch antenna that is easy and low-cost. With the proposed double notch E-shaped patch antenna, satisfactory findings were obtained that demonstrated a substantial increase in terms of bandwidth and VSWR parameters with respect to the basic inset fed patch antenna [1–5].

While there are many benefits to the patch antenna, it still has certain disadvantages, such as small bandwidth and low gain. In order to enhance these criteria, several antenna engineers have created new strategies, but the efficiency of these antennas must be further enhanced. This paper compares the results of utilizing notches in the geometry to improve the gain of the rectangular slotted patch antenna at 2.0675 GHz. The antenna is supplied by the Inset feeding method, which is simple and suits well with impedance. Using the CST studio suite unit, the antenna configuration was simulated. The microstrip patch antenna is a one-layer design that typically consists of four components: the patch, the ground plane, the substrate and the feeding component. A microstrip antenna's physical scale is tiny, but the wavelength-measured electrical size is not so small. A rectangular patch is the most widely used microstrip antenna. The patch antenna is made up of half-wavelength rectangular microstrip transmission lines. If the antenna substrate is air, the size of the rectangular antenna is nearly one-half of the free space wavelengths. If the antenna is packed with a dielectric as its substrate, the antenna's length reduces as the substrate's relative dielectric constant increases. An early development of the microstrip antenna is a segment of microstrip transmission line with equivalent loads on both ends to reflect radiation loss [6–10].

Over the past decade, further contact innovations have advanced constantly, typically after the order of the systems becomes more common and sometime lately, they would not be allowed to be met. This is why the progression of the versatile contact system is regarded as 5G toward anything at this time. A parcel of the electromagnetic spectrum defined as the mm band can be used for more development in the fifth cycle and this is also agreed through transmigrating amount of supply data by few gigabits as minute, cessation of approximately 1 ms and decreasing power usage for more broad-band arrangements. This will accomplish along the needs of this invention this will be practically necessary for planning a radio wire system about new portable gadgets and repairing receiving wire has proved to be a very good applicant without a doubt, really dedicated to its moo profile, light weight calculation, quick to produce and its excellent execution inside the mm range. The unique clusters can resolve the impediments of mimicking and maximizing these proliferations using the high frequency organized simulator. In the area of remote communications, radio wires perform an awfully vital function. Illustrative reflectors, radio cables, space antennas and collapsed dipole radio wires are only a couple of them. The spine and almost all inside remote contact without which the term could not have entered at this age of invention are receiving wires. In today's remote contact frameworks, repairing receiving wires plays a very visible function. Under the development of a standard microstrip construction technique, a microstrip repair receiving wire is incredibly straight forward. The solution may take any type, but the most widely used configurations are rectangular and circular arrangements. These receiving wires for corrections are seen as basic and for the most detailed and most challenging applications. Various feeding methods are used in the construction of dual-band microstrip antennas. Other settings, such as aperture, U-shape and pine shorting, are still used, however. Techniques used to maximize bandwidth are often applicable in order to obtain a dual-band operation. Therefore, for multilayer setups, electromagnetic coupling or crack coupling, with air gap modification, may be used to control the double band antenna [11–15]. Hybrid configurations were conceived for double band service by linking a circular antenna to a waveguide. In addition, for this form of purpose, novel microstrip antennas are defined.

## 2 Microstrip Patch Antenna

Devices covering two or more frequency bands simultaneously have recently been used in modern telecommunications. Indeed, microstrip antennas that enable this request to be guaranteed must have configurations that are more or less complex. The antenna arrays, however, offer a significant interest in improving and modifying the performance of the single antenna. The antenna, based on the configuration of the corner fed rectangular antenna, proposed new configurations to operate on more frequencies. These antennas are miniature and compact, making it easier and more important to integrate them into satellite communication systems. Each setup has its own function and its advantages over others. Through the addition of another radiating element, more can be achieved. Figure 1 depicts the geometry of the antenna under consideration.

Using the conventional formulas provided in literature surveys, each of the antenna dimensions of the proposed model is calculated. The layout rectangular structure length

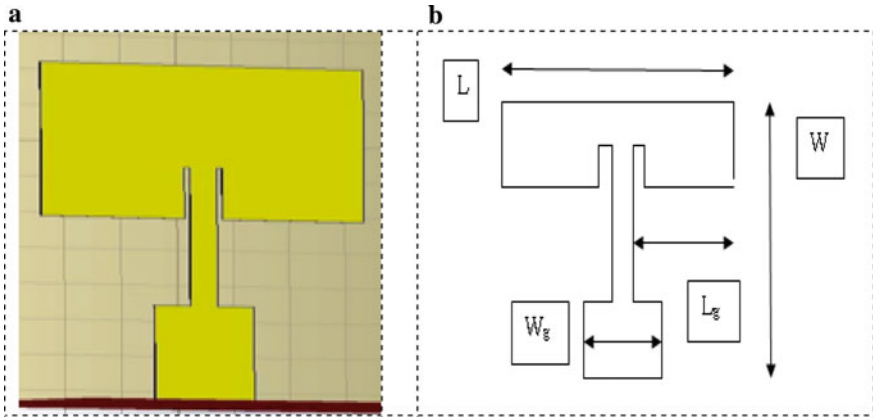


**Fig. 1 a, b** MPA of the geometry

and breadth (width) are taken into consideration. Similarly, the effective size of the loop used at the patch center and the ground plane is formulated using the equations.

$$W = \frac{V_o}{2f_r} \sqrt{\frac{2}{\epsilon_r + 1}} \tag{1}$$

$$L = \frac{V_o}{2f_r \sqrt{\epsilon_{reff}}} - 2\Delta L \tag{2}$$

where

- $V_o$  Speed of Light
- $\Delta_{reff}$  Effective Permittivity
- $2\Delta L$  Extension in Length.

$$f_c = \frac{c}{2L\sqrt{\epsilon_r}} = \frac{1}{2L\sqrt{\epsilon_0\epsilon_r\mu_0}} \tag{3}$$

where

- $\epsilon_0$  Permittivity of free space
- $\epsilon_r$  the dielectric substrate permittivity
- $\mu_0$  Free space permeability.

The operating frequency of a patch antenna considering  $L$  and  $W$  is given by

$$f_r = \frac{c}{2\sqrt{\epsilon_{reff}}} \left[ \left( \frac{n}{L + 2\Delta L} \right)^2 + \left( \frac{m}{w + 2\Delta w} \right)^2 \right]^{1/2} \tag{4}$$

where  $n = 1, m = 0$ .

$$f_r \text{ (nm)} = c/2(L + 2\Delta L)\sqrt{\epsilon_{\text{reff}}} \quad (5)$$

$$\epsilon_{\text{reff}} = \frac{\epsilon_{r+1}}{2} + \frac{\epsilon_{r-1}}{2} \left[ 1 + 12 \frac{h}{w} \right]^{-1/2} \quad (6)$$

$$\Delta L = 0.412h \frac{(\epsilon_{\text{reff}} + 0.3) \left( \frac{w}{h} + 0.264 \right)}{(\epsilon_{\text{reff}} - 0.258) \left( \frac{w}{h} + 0.8 \right)} \quad (7)$$

$$W = \frac{(W_L - W_H)}{2} * \frac{(W_L + W_H)}{2} \quad (8)$$

A single patch on top, one sheet of dielectric (air), and a vertical probe attached from ground to the upper patch make up the antenna. Table 1 shows the basic antenna part, which is a strip conductor of length  $L$  and width  $W$  on a dielectric substrate with constant  $r$ , thickness or height of the patch being  $h$  with a height which thickness  $t$  and assisted by a ground plane. The patch antenna is constructed in such a way that it may run at the resonance frequency. The patch duration is determined by the patch's height, distance and the dielectric substrate.

**Table 1** Design of antenna parameters

Sl. No.	Parameters	Value
1	$L$	3.078 mm
2	$W$	4.823 mm
3	$Lg$	8.678 mm
4	$Wg$	10.423 mm
5	Substrate dielectric material	FR-4 epoxy
6	Substrate dielectric constant	$\epsilon_r = 4.4$
7	Ground plane	35 mm * 35 mm
8	Thickness or height	1.6 mm
9	Loss tangent ( $\delta$ )	0.02
10	Operating frequencies	7, 8.4, 10 and 11.5 GHz

The patch is usually made of conductive metals like copper or gold and can be made into any form. On the dielectric substrate, the radiating patch and feed lines is normally photo engraved. The antenna radiating patch antenna will transmit at high frequencies which can increase the efficiency of current systems by providing more bandwidth.

### 3 Results and Discussion

The substrate between the radiating patch and the ground plane. On parameters such as gain, return loss, radiation efficiency, antenna quality, the impact of adjusting the slot

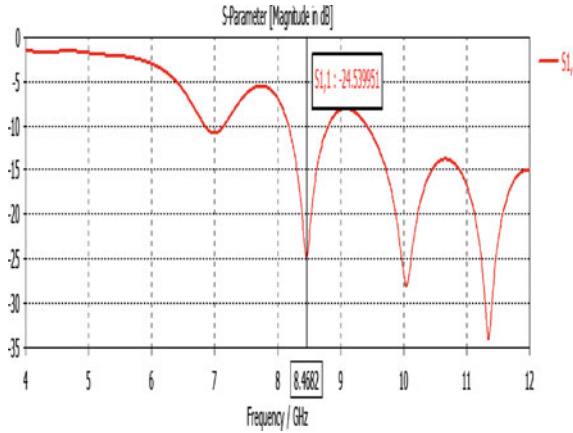


**Fig. 2** Return loss of the antenna

length and width is examined. By adjusting the feed positions, a coaxial probe feed is used at various points and its effect on the above parameters is shown. Moreover, most implementations that use microstrip antennas in communication systems, such as mobile handheld communication units, need smaller antenna sizes. Over the last few years, numerous specialized techniques have been developed to design very light weight microstrip patch antennas. DGS is designed to inject any defective form into the patch antenna ground plane, causing the shielded current distribution to be interrupted due to the defect varying dimensions, form and size. The antenna input impedance and current flow disrupted due to disturbances in the shielded current distribution.

The corresponding return loss at operating frequencies of 7 GHz, 8.4 GHz, 10 GHz and 11.5 GHz as seen in Fig. 2 at  $-10$  dB,  $-24.53$  dB,  $-28.68$  dB and  $-34.82$  dB, respectively. It may also regulate the excitation and electromagnetic waves that travel through the layer of the substrate. The designed patch is etched with a low-cost FR4 substrate with a dielectric constant of 4.4 and a thickness of 1.6 mm. For feeding the antenna, a  $50 \Omega$  microstrip line with a width of 4.823 mm and a length of 3.078 mm is used. A new resonant mode at 7, 8.4, 10 and 11.5 GHz can be conveniently induced to achieve the required activity due to the existence of the slot. The whole antenna scale is just  $35 \text{ mm} \times 35 \text{ mm}$ . To achieve two wide bandwidths sufficient for 6.2/6.8 GHz WLAN operations, the parameters were modified.

Figure 3 displays the VSWR at 7 GHz, 8.4 GHz, 10 GHz and 11.5 GHz operating rates, where the values are 1.8, 1.2, 1.2 and 1.1, respectively. The effects of the simulated current distributions at the operating frequencies of 7, 8.4, 10 and 11.5 GHz is illustrated in Fig. 4, in order to easily see the proposed antenna behavior in generating operations in a conventional microstrip antenna.

Multi band strategies in order to get the optimal resonance at more than one frequency. Cutting slots in the patch is one of the successful ways of achieving multi band operation. In order to receive microstrip patch antennas resonating at more than one frequency, the duration and location of the slots may be modified. In addition to being compact, low profile and wide band, the design also has a large gain of 10.8 dBi in center frequency,



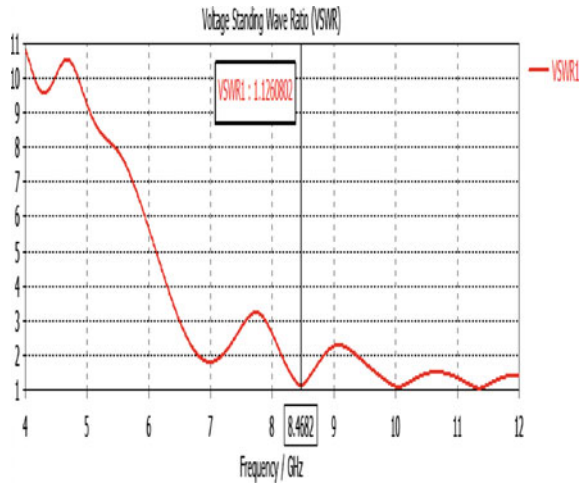


Fig. 3 VSWR of the antenna

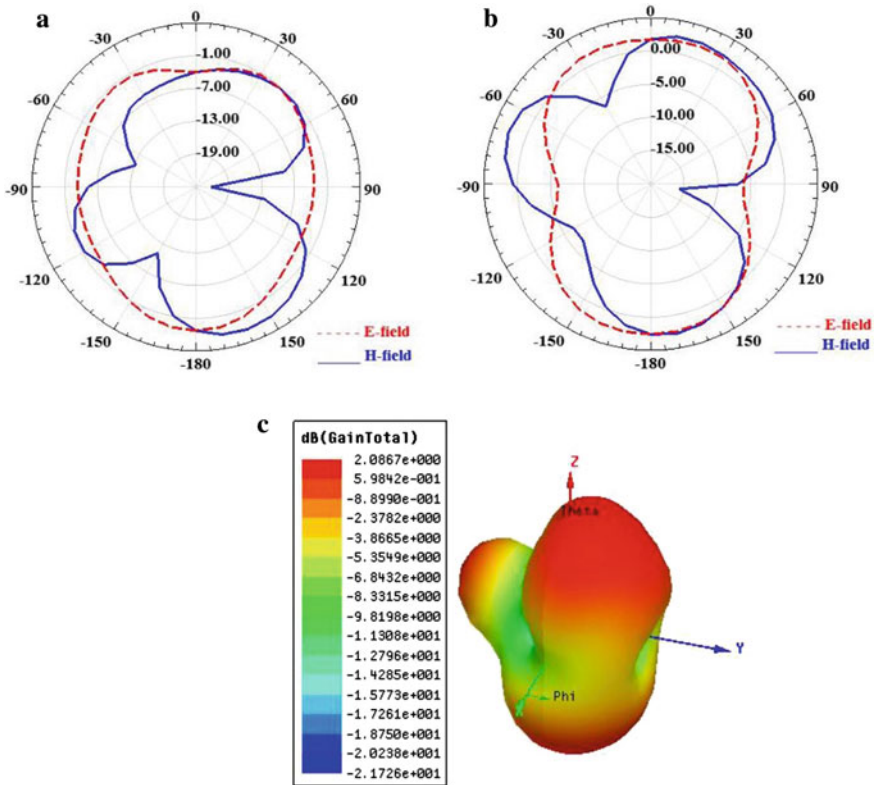


Fig. 4 a–c Radiation pattern of the antenna

making it suitable for usage on a variety of wireless apps such as WLAN and WiMAX, and Fig. 5 displays the X-band. The separate parameter study of the patch antenna in the microstrip is addressed in Table 2.

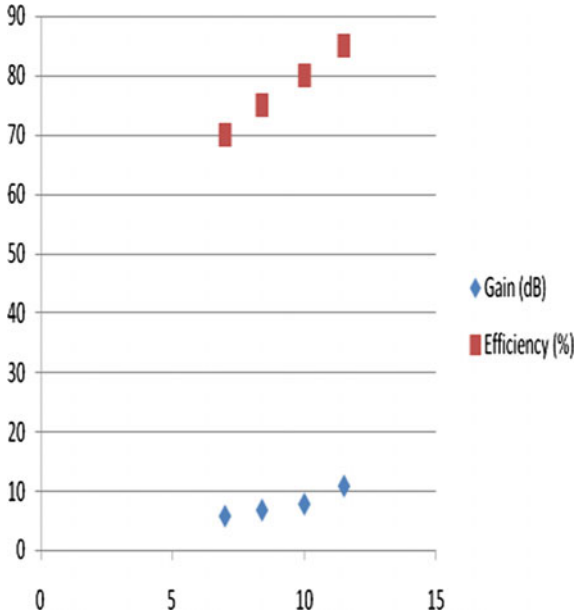


Fig. 5 Gain and efficiency of the antenna

Table 2 Parameter analysis of microstrip patch antenna

Sl. No.	Operating frequencies (GHz)	Return loss (dB)	VSWR	Gain (dB)	Efficiency (%)
1	7	-10	1.8	5.8	70
2	8.4	-24.53	1.2	6.8	75
3	10	-28.68	1.2	7.8	80
4	11.5	-34.82	1.1	10.8	85

### 4 Conclusion

Good return loss  $S_{11}$  operating frequencies at 7 GHz, 8.4 GHz, 10 GHz and 11.5 GHz is achieved by the built antenna with results obtained at -10 dB, -24.53 dB, -28.68 dB and -34.82 dB, respectively. The VSWR findings were recorded at the operating frequencies of 7 GHz, 8.4 GHz, 10 GHz and 11.5 GHz, respectively, at 1.8, 1.2, 1.2 and 1.1 and

achieved a circularly polarized gain of 10.8 dB. The built antenna has a large return loss, VSWR and gain range. So the planned wireless contact can be used with the mmWave. In order to further increase benefit, the planned meta-material and substrate should be used. For the upcoming short range 5G mmWave wireless networking, the recommended antenna would be ideal.

## References

1. Salokhe BT, Mali SN (2014) Analysis of substrate material variation on circular, rectangular and non linear microstrip patch antenna. *Int J Curr Eng Technol* 4(3)
2. Varshney HK et al (2014) A survey on different feeding techniques of rectangular microstrip patch antenna. *Int J Curr Eng Technol* 4(3)
3. Sayeed Z, Sajal et al (2015) "A Microstrip patch antenna manufactured with flexible Graphene-Based conducting material. *IEEE, AP-S* 415–2416
4. Naik KK, Manikanta MHV (2018) Design of circular slot on rectangular patch with meander line antenna for satellite communications 2018. In: *Proceedings of the 2nd international conference on electronics, communication and aerospace technology, ICECA, 2018*, pp 1548–1551
5. Prasad KV, Prasad MVS, Kumar MS, Alekhya B (2018) Surface wave suppression in patch arrays using EBG structures. *Indian J Public Health Res Dev* 9(6):311–316
6. Kumar Naik K, Amala Vijaya Sri P (2018) Design of hexadecagon circular patch antenna with DGS at Ku band for satellite communications. *J Adv Res Dyn Control Syst* 10(2):569–578. ISSN:1943023X
7. Saleem Akram P, Madhav BTP, Jeevana Sravya G, Sudhakar V, Lakshmi Sirisha G, Mounika C, Venkateswara Rao M (2018) Design and analysis of square shaped serrated patch antenna for ultra-wideband applications with single rejection band. *J Adv Res Dyn Control Syst* 10(6):670–676. ISSN:1943023X
8. Ajay Babu M, Madhav BTP, Bhargavi G, Sai Krishna V, Hemanth Kumar Reddy Y, Kalyan GVS, Venkateswara Rao M (2018) Design and analysis of stepped reconfigurable rectangular patch antenna for LTE, vehicular and ultra wideband applications. *J Adv Res*
9. Choudhury S, Kalyani V, Sai Teja R, Sreenivasan P, Kotamraju SK, Sri Kavya KC (2018) A comparative analysis of rectangular cut edge patch antenna on various substrate. *J Adv Res Dyn Control Syst* 10(11):313–320. ISSN: 1943023X
10. Ramakrishna TV, Madhav BTP, Venkateswara Rao M, Babu Rao A, Sunaina A, Avinash A, Shivani B (2018) SRR loaded half-mode substrate integrated waveguide monopole slot antenna for multiband applications (*J King Saud Univ Comput Inf Sci.*) Low complex adaptive algorithm for antenna beam steering. In: *IEEE 2011 international conference on signal processing, communications, computing and networking technology (ICSCCN 2011)*, pp 317–321
11. Kannadhasan S, Nagarajan R (2021) Performance analysis of circular shape microstrip antenna for wireless communication system. In: *AICTE sponsored international E-conference on computing and communication systems for a fourth industrial revolution (AICERA 2020)*, Amal Jyothi College of Engineering, Kerala, 14–16 December 2020, Published for IOP conference series: materials science and engineering, vol 1085. <https://doi.org/10.1088/1757-899X/1085/1/012013>
12. Raman R, Shanmuganantham T (2017) Frequency reconfiguration of microstrip patch antenna with serpentine spring shaped RF MEMS switch. *Int J Adv Microwave Technol (IJAMT)* 2(1)
13. Islam MT, Mobashsher AT, Misran N (2010) Design of microstrip patch antenna using novel U-shaped feeding strip with unequal arm. *Electron Lett* 46(14)

14. Anguera J, Borja C, Puente C (1999) A procedure to design wide-band electromagnetically-coupled stacked microstrip antennas based on a simple network model. *IEEE Antennas Propag Soc Int Symp* 2:944–947
15. Katyal A, Basu A (2017) Compact and broadband stacked microstrip patch antenna for target scanning applications. *IEEE Antennas Wireless Propag Lett* 16



# Tool Wear Detection Using Computer Vision System in Machining

P. J. Bagga , M. A. Makhesana  , A. B. Mishra, A. R. Marvaniya,  
and K. M. Patel 

Mechanical Engineering Department, Institute of Technology, Nirma University, Ahmedabad,  
Gujarat 382481, India

mayur.makhesana@nirmauni.ac.in

## 1 Introduction

Computers are an integral part of automation. The twenty-first century is the age of computers, and every human wishes to automate almost every task by the use of a computer. The application of computers provides us with some advantages over humans which cannot be overlooked. Computers can work continuously, increase accuracy, decrease overall time, decreases labor force and cost, etc. The sudden rise in technological advancement has made it possible for us to use computers in the manufacturing sector as well. The use of automation in the field of production has enabled systems to integrate the computer and machine. Computer vision is one such technique of automation. Computer vision is a field of science wherein computer system are used to stimulate functions similar to human vision. The computer vision system is used to gather and study data from an image or a video. It studies various properties of the image such as image brightness, color, pixels, contrast, and resolution and gathers data from the image. Computer vision systems are employed to teach a computer to detect an object about some specific properties such as color, dimension, and brightness. There are various applications of the computer vision system, and one such important application is the finding the tool wear. Tool wear detection is the process of calculating the amount of wear on the tool. Tool wear is the progressive failure and breakdown of the tool due to its continuous operation. A worn-out tool does not give the expected surface quality and geometry. The geometry of the tool gets distorted as it nears its end of life. So, tool wear detection becomes an important part of the manufacturing process. Computer vision tool wear detection is not prone to human error but also it is not entirely self-efficient. The tool wear detection can be in-process or post-process. In-process tool wear measurement is done while the tool is in motion or is machining. In post-process tool wear measurement, the measurement is done after the tool is stationary. In both the cases, utmost care needs to be taken to employ a proper system which can take the image of the tool and its area of interest, i.e., the worn-out region.

The first step of any computer vision program is to obtain the required image or video of the object. The worn-out region of the tool has a rough surface, and so it has a high reflectivity. The use of optimum lighting condition while taking the image, clearly

sort out worn and the unworn region. The worn region of the tool will appear brighter than the unworn region. After taking the image, it is input into the computer system. The image always has some element of noise. Image noise is random variation of brightness, uneven color information, blurring, etc. Noise can be in the form of random bright spots, fluctuations in color level, etc. An image with noise tends to show false results which is worked upon with computer vision. Image segmentation separates the image into various components based on similarity within a region and difference between adjoining regions. Discontinuity and similarity are two fundamentally used approaches for the segmentation of an image. Similarity within a region is due to a pixel intensity, brightness level, color homogeneity, etc. After extraction of pixels of a worn part in step-3, various operations can be performed on the image part to calculate tool wear. The number of pixels obtained can be compared with the count of pixels on the tool image to obtain the ratio of worn tool area to unworn tool area.

Kurada and Bradley [1] described a combination of the operator to obtain the amount of tool wear. The formulation of vector is done using Frei-Chen operator to detect the point, line, or edge. Tool wear is determined based on the maximum wear land width. Yu et al. [2] utilized the properties of the morphological component analysis (MCA) algorithm and traditional edge detection methods. Different components in the image are separated by MCA. Zhu and Yu [3] utilized an algorithm based on MCA points with varying image brightness. The tool images were processed by identifying the discontinuities. Thresholding is applied to extract the seed points in the target tool image. An online tool wear detection and estimation system were proposed [4]. A strain gauge was used to detect the deflection caused by cutting force in both feed and tangential direction. A statistical approach was used to analyze the signal data. Progressive tool flank wear has been described using eight useful features extracted information from turned surface images. Linear support vector machine-based regression has been used by using these eight features as predictors. The maximum prediction error obtained is 4.9% [5].

Fernández-Robles et al. [6] used a machine vision solution for automatic detection of wear of tool inserts. The program can be run online while the insert is stationary which does not delay the machining. Geometrical properties of the edges were analyzed to measure the wear. Szydłowski et al. [7] proposed a machine vision solution for tool wear estimation in micro-milling. Wavelet-based extended depth of field image reconstruction is proposed which enables geometrical measurement required for determining the location of the cutting edges of the micro-tool. Lee et al. [8] used the workpiece profile signature to identify the amount of wear in ceramic cutting tool inserts. Fast Fourier transform (FFT) was used to convert the profiles into frequency domain from the spatial domain. A Wiener filter was used to remove image noise. Castejon et al. [9] reported tool wear estimation approach for cutting inserts by using computer vision and statistical learning. A total of 1383 flank images were obtained from CNC parallel lathe and a computer vision system. Wang et al. [10] described a system for interrupted measurement of milling tool based on successive image analysis. A high-quality image with minimum blur was ensured with low spindle speed. Multiple image enhancement and image segmentation operations are used to obtain the final image. Li and An [11] described a computer vision system for tool wear monitoring. Watershed transform is used to divide

the tool wear area into regions, and then each region is subjected to automatic focusing and segmentation. The iterated conditional mode (ICM) is used to calculate the minimum potential function, and after calculating the minimum of potential functions, the image is segmented. Riego et al. [12] utilized a machine vision approach to describe the outer and inner surface textures of a workpiece with a cylindrical hole. Images are pre-processed, and the Otsu method is used to find a binary image from the enhanced image. A total of 589 RGB images were used. Loizou et al. [13] reported a method to measure the broaching tool wear. The region of interest is extracted first from the original image by using rough and advanced cropping operations. Alegre-Gutiérrez et al. [14] suggested a method to divide the cutting edge image into several regions called wear patches. The texture descriptors describe the WP-based on local binary pattern. Lim and Ratnam [15] presented the study to find the optimum lighting condition for scanning cutting tool images and carry out nose radius measurements. Best results are obtained by both controlled and open scanning when done with a black internal opaque condition. An edge detection algorithm is used to determine the nose radius. Lins et al. [16] used cyber physical system to monitor the tool wear. The integration between the machine and computer vision algorithm for tool wear measurement was validated by petri net. Ong et al. [17] proposed the method of TCM in CNC end milling using a wavelet neural network (WNN). The performance of WNN was found satisfactory. Kong et al. [18] discussed the application of a tool wear predictive model based on the relevance vector machine (RVM). It was reported that the prediction accuracy of RVM is comparable to SVM. Hou et al. [19] used machine vision approach for the identification of tool wear. Segreto et al. [20] reported the use of vibration signals to estimate the tool wear during machining of Ni–Ti alloys. Wavelet packet transform (WPT) was used to process the collected vibration data. High detection accuracy with the proposed approach was obtained in the results. In similar work, WPT was applied to detect the tool wear during machining of Inconel 718 [21]. Improved performance with ANN was obtained with WPT. A method with high detection accuracy and speed with the use of an algorithm based on image processing technique was proposed by Hou et al. [22]. Swain et al. [23] concluded that the proper selection of TCM is of much importance to reduce the processing time in review presented. Based on the available literature, it is understood that the use of computer vision techniques can be the approach to automate the detection of tool wear during machining which can provide more accurate results with less time-consumed.

## 1.1 Brief Description

The program is designed to compute the quantity of pixels in the wear region of the tool. First, an image is captured with the camera. The image is to be captured such that the tool image can be seen clearly. The lighting condition should be optimum. The reflectivity of the worn-out region is more, and so it appears to be brighter than the rest of the tool image. This feature of the worn-out region helps the program distinguish the area of interest. Now, the image is input into the program. The program applies canny edge operator, dilation operation, erosion operation to determine the edges based on the difference in properties of the image such as brightness and color in different regions. Canny edge operator gives the various lines in the image. Threshold values are applied

to this operator based on the brightness value of pixels in the image. Dilation operation thickens these lines, and erosion operations reduce the thickness of these lines. This gives the pixels of the worn-out region because they appear brighter than the rest of the image. Now the pixels within the obtained region in the image are calculated. To make it easy for anyone to understand, the number of pixels in the wear region is divided by a random number to give out a ratio. A lower ratio indicates a lower amount of tool wear. Also, the region of tool wear is highlighted in a copy of the original image and shown with this ratio.

### 1.1.1 Pre-processing

In this step, the image is cropped such that the region of interest is visible clearly. The image is cropped from the rest of the image such that the background part in the cropped image is minimum, and the entire tool image is there.

### 1.1.2 Blurring

The transition of color and brightness in an actual image can be very sudden from pixel to pixel. Blurring is used to smoothen out an image. The variation of intensity of a pixel is reduced concerning its surrounding by taking the effect of a pixel and its surrounding pixel properties. In blurring operation, a low-pass filter is applied which removes the noise from the image. This removes the noise while keeping the rest intact. The program uses a Gaussian blurring operation to give the necessary blurring effect. Gaussian blurring is generally used before an edge detection operation so that clear edges can be produced. A Gaussian function is used in Gaussian blurring. A normal distribution is shown by a Gaussian function. The transformation that is to be applied to each pixel to smoothen out the image is determined by the Gaussian function. The formula for Gaussian function in one dimension, i.e., in  $X$ -direction, can be shown as:

$$G(x) = \frac{1}{\sqrt{2\pi\sigma^2}} e^{-\frac{x^2}{2\sigma^2}} \quad (1)$$

A two-dimensional Gaussian function can be represented as the product of two one-dimensional where one is an  $X$ -directional Gaussian function and the second is a  $Y$ -directional Gaussian function.

$$G(x, y) = \frac{1}{2\pi\sigma^2} e^{-\frac{x^2+y^2}{2\sigma^2}} \quad (2)$$

Here,  $x$  is the distance from the origin along  $X$ -direction, i.e., along the horizontal direction.  $y$  is the distance from the origin along  $Y$ -direction, i.e., vertical direction, and  $\sigma$  is the standard deviation. When the two one-dimensional functions are applied, a Gaussian two-dimensional surface is formed. A convolution matrix is formed from the values of this Gaussian distribution. This convolution/mask is then applied on the captured image. The convolution matrix is called a kernel. The value of a kernel matrix is always equal to 1. A Gaussian kernel is a square array of the pixel where the pixel value corresponds to the value to the Gaussian curve in two-dimension. A weighted average is applied to the neighborhood pixels to set a pixel's value. The original pixel



receives the highest weightage, and the remaining neighboring pixels receive a smaller weightage which is proportional to their distance from the original pixel. This operation homogenizes the pixel value based on its neighboring value. The operation is performed on each such original pixel in the image supplied to create a blurred image.

### 1.1.3 Edge Detection

The edge detection algorithm used herewith is the Canny edge algorithm. The Canny edge algorithm works in several steps to detect the edges. First, the noise is removed by the application of a Gaussian filter to smoothen the image. Edge detection algorithm works by detecting the difference of properties on either side of an edge thereby detecting it. Due to noise in the image, false regions will be detected and multiple unwanted edges will be formed. So, a Gaussian filter is applied first. The same is given by the following formula:

$$H_{i,j} = \frac{1}{2\pi\sigma^2} \exp\left(-\frac{(i - (k + 1))^2 - (j - (k + 1))^2}{2\pi\sigma^2}\right) \quad (3)$$

The next step is to find the intensity gradient of the image. The Canny edge algorithm uses a Sobel filter to detect the edges in a blurred image where the edge can be two diagonal, horizontal, or vertical. The edge gradient and direction of the edge are determined from the two values along the X- and Y-directions. The formulas are given as below:

$$G = \sqrt{G_x^2 + G_y^2}$$

$$\theta = \arctan\left(\frac{G_y}{G_x}\right) \quad (4)$$

The angles represent a line in horizontal, vertical, or diagonal. The next step is the non-maximum suppression which is an edge-thinning technique, and it is used to find the locations with the sharpest intensity changes. The high threshold value and low threshold values are selected to carry out double thresholding. The fifth step is edge tracking by hysteresis, wherein the weak pixels removed in step four are further checked if they should be included or not. In this step, a region or blob of 8 connected pixels is defined and the weak pixels are merged to the edges if a strong edge pixel is present inside the region/blob. After performing these five operations, all the edges within the image are identified and made visible as output. Out of all the edge detection algorithms, the Canny edge detection algorithm yields the best result. So, it has been incorporated into the program.

### 1.1.4 Dilation and Erosion

It is the addition and deletion of the pixels to the boundary of an object in the image. The shape size of the structuring element used to process the image defines the number of pixels to be removed or added from the boundary of the object in the image.

### 1.1.5 Contours

The image is modified by placing a set of the contour around an object. Here, in the final image, a contour is placed around the worn region which is also the region of interest. The worn region is surrounded by a blue color region. By contour algorithm, the active wear region is measured, and by adding all the active wear regions, the total wear region is determined. Binary images produce better accuracy. In OpenCV, the contours are produced by finding white objects out of black objects or in this case black background.

### 1.1.6 Tool Wear Estimation

The region of tool wear is identified by knowing the number of pixels in the wear area. Then the comparison is done with an arbitrary value in the program to obtain a ratio. The ratio is constantly increasing when multiple images with increasing and progressive tool wear are input (Fig. 1).

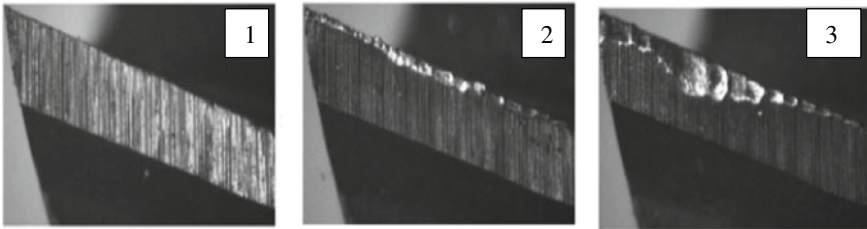


**Fig. 1** Original image showing progressive tool wear

## 2 Results and Discussion

An image has been selected which shows progressive tool wear. The program has been run on each of these images. The output image for each input image shows the region of tool wear and the ratio of current wear to maximum wear. The output of various operations is clubbed in a single image for a particular input image to show the output of the various operation. In each combined image, 1—shows the input image, 2—canny edge operation output, 3—dilation output, 4—final program output. The program works as expected and shows higher pixels in the wear region as several images with increasing tool wear are inserted. Figure 2 (4) shows the lowest amount of tool wear, and Fig. 4 (4) shows the highest amount of tool wear. To make it easy for a layman to understand, the ratio indicates the magnitude of tool wear. The higher the ratio, the higher is the tool

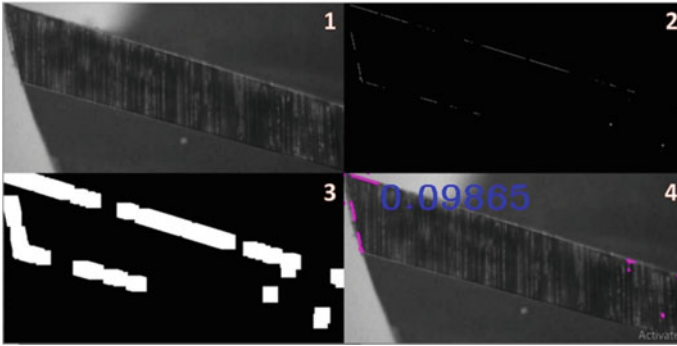


**Fig. 2** Output image—1

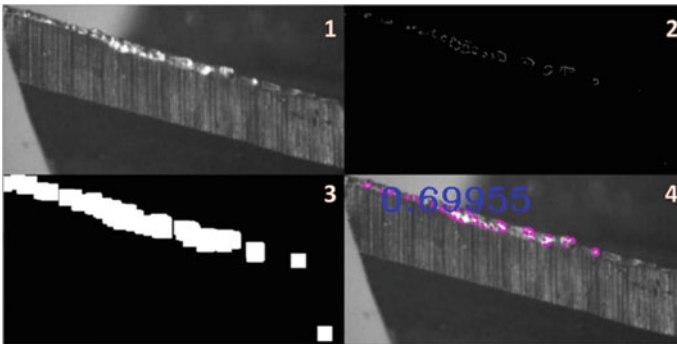


**Fig. 3** Output image—2

wear. Figures 2 (2), 3 (2), and 4 (2) show the output of the canny edge operator. Figures 2 (3), 3 (3), and 4 (3) show the output of the dilation operator. Figures 2 (4), 3 (4), and 4 (4) show the output of the program. The blue region indicates the region calculated by the program. The blue region, i.e., the area of interest, is increasing, it is maximum for Fig. 4 and minimum for Fig. 2. The ratio for Fig. 2 is 0.098, the ratio for Fig. 3 is 0.699, and the ratio for Fig. 4 is 1.109. The threshold value selected to obtain the region of interest has been decided based on the value of brightness of the pixels in the image. In an 8-bit gray image, 0 represents the black color and 255 represents a white color. The worn region pixels will have a value somewhat close to the white region compared to the rest of the area. This threshold selection can also be done automatically as seen from various papers mentioned in the literature review.

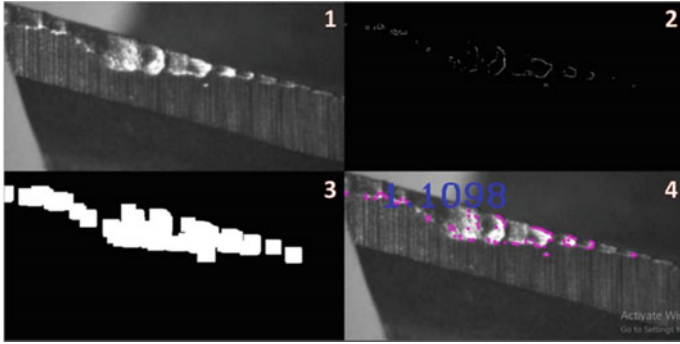


**Fig. 4** Output image—3

The value by which the number of pixels has been divided to obtain the ratio has been selected based on the maximum wear the tool can undergo. Suppose, the maximum tool wear image had about 2500 pixels in the wear zone then comparing the rest of the tool wear images with 2500 gives the tool wear relative to the maximum tool wear. The ratio signifies that when the ratio gets more than 1, then the tool is no longer efficient and needs to be replaced or re-grinded. Currently, this value has been taken arbitrarily.

### 3 Conclusions

The methodology presented within this paper is capable of determining the tool wear region under specific lighting conditions. In conclusion, the proposed program can extract the tool image using canny edge operation, dilation operation, and erosion operation. After extraction of the wear region, the worn-out region is marked and the ratio is presented on a copy of the original image fed to the system. The ratio signifies the amount of tool wear. The ratio equal to or greater than 1 signifies that the tool needs to be replaced or re-grinded. The blue region in the final image indicates the wear area. The program works as expected and shows the increase in the blue region when multiple images of tool wear are input showing the progress of tool wear. The program can be used for images, and the tool wear region can be identified. The program may be modified to automatically detect the region of tool wear and process necessary segmentation steps to extract the final wear region.

### References

1. Kurada S, Bradley C (1997) A machine vision system for tool wear assessment. *Tribol Int* 30(4):295–304
2. Yu X, Lin X, Dai Y, Zhu K (2017) Image edge detection based tool condition monitoring with morphological component analysis. *ISA Trans* 69:315–322
3. Zhu K, Yu X (2017) The monitoring of micro milling tool wear conditions by wear area estimation. *Mech Syst Signal Process* 93:80–91
4. Ghani JA, Rizal M, Nuawi MZ, Ghazali MJ, Haron CHC (2011) Monitoring online cutting tool wear using low-cost technique and user-friendly GUI. *Wear* 271(9–10):2619–2624

5. Dutta S, Pal SK, Sen R (2016) On-machine tool prediction of flank wear from machined surface images using texture analyses and support vector regression. *Precis Eng* 43:34–42
6. Fernández-Robles L, Azzopardi G, Alegre E, Petkov N (2017) Machine-vision-based identification of broken inserts in edge profile milling heads. *Robot Comput Integr Manuf* 44:276–283
7. Szydłowski M, Powalka B, Matuszak M, Kochmański P (2016) Machine vision micro-milling tool wear inspection by image reconstruction and light reflectance. *Precis Eng* 44:236–244
8. Lee WK, Ratnam MM, Ahmad ZA (2016) Detection of fracture in ceramic cutting tools from workpiece profile signature using image processing and fast Fourier transform. *Precis Eng* 44:131–142
9. Castejón M, Alegre E, Barreiro J, Hernández LK (2007) On-line tool wear monitoring using geometric descriptors from digital images. *Int J Mach Tools Manuf* 47(12–13):1847–1853
10. Wang W, Wong YS, Hong GS (2005) Flank wear measurement by successive image analysis. *Comput Ind* 56(8–9):816–830
11. Li L, An Q (2016) An in-depth study of tool wear monitoring technique based on image segmentation and texture analysis. *Measurement* 79:44–52
12. Riego V, Castejón-Limas M, Sánchez-González L, Fernández-Robles L, Perez H, Diez-Gonzalez J, Guerrero-Higueras AM (2020) Strong classification system for wear identification on milling processes using computer vision and ensemble learning. *Neurocomputing*
13. Loizou J, Tian W, Robertson J, Camelio J (2015) Automated wear characterization for broaching tools based on machine vision systems. *J Manuf Syst* 37:558–563
14. García-Ordás MT, Alegre-Gutiérrez E, Alaiz-Rodríguez R, González-Castro V (2018) Tool wear monitoring using an online, automatic and low cost system based on local texture. *Mech Syst Signal Process* 112:98–112
15. Lim TY, Ratnam MM (2012) Edge detection and measurement of nose radii of cutting tool inserts from scanned 2-D images. *Opt Lasers Eng* 50(11):1628–1642
16. Lins RG, de Araujo PRM, Corazzim M (2020) In-process machine vision monitoring of tool wear for cyber-physical production systems. *Robot Comput Integr Manuf* 61:101859
17. Ong P, Lee WK, Lau RJH (2019) Tool condition monitoring in CNC end milling using wavelet neural network based on machine vision. *Int J Adv Manuf Technol* 104(1):1369–1379
18. Kong D, Chen Y, Li N, Duan C, Lu L, Chen D (2019) Relevance vector machine for tool wear prediction. *Mech Syst Signal Process* 127:573–594
19. Hou Q, Sun J, Huang P (2019) A novel algorithm for tool wear online inspection based on machine vision. *Int J Adv Manuf Technol* 101(9):2415–2423
20. Segreto T, Caggiano A, Karam S, Teti R (2017) Vibration sensor monitoring of nickel-titanium alloy turning for machinability evaluation. *Sensors* 17(12):2885
21. Segreto T, D’Addona D, Teti R (2020) Tool wear estimation in turning of Inconel 718 based on wavelet sensor signal analysis and machine learning paradigms. *Prod Eng Res Devel* 14(5):693–705
22. Hou Q, Sun J, Huang P (2019) A novel algorithm for tool wear online inspection based on machine vision. *Int J Adv Manuf Technol* 101(9–12):2415–2423
23. Swain S, Panigrahi I, Sahoo AK, Panda A (2020) Adaptive tool condition monitoring system: a brief review. *Mater Today Proc* 23:474–478



# Hybrid Refrigeration System Hypothesis Using Vapour Compression and Metal Hydride Refrigeration systems—A Review

Narayan Singh<sup>(✉)</sup>

Vellore Institute of Technology University, Vellore 632014, India  
narayan.singh5098@gmail.com

## 1 Introduction

Conventional energy sources are not long-lasting such as nuclear, natural gas, coal, and petroleum are not long-lasting. These are depleting due to continuous and unsustainable exploitation. The constant energy demand and global warming, and environmental health are the primary concern nowadays, and refrigeration systems are one of the machines that we use in our daily lives, which affect all three of the concerns mentioned above.

Refrigeration systems are requisite and indispensable for mankind, but they are also very much under-appreciated on the myriad of harmful footprints on the environment's sustainability. The components used in its conventional manufacturing follow most of the sensitive nature harming aspects. The mechanical VCRS siphons large amounts of electrical energy produced by fossil fuels. These processes cause global warming and many other irreversible effects on the environment by the nature of its function. Due to no other alternatives in the market, it becomes even more imperative to research other technologies that may produce similar cooling effects. Electrical energy and the harmful chemicals, which continuously misuse the environmental resources and ozone layer, need to pursue redundancy by hypothesizing new model configurations.

The amount of refrigerant chemicals used only for commercial refrigeration systems is approximately 1,40,000 tonnes/year worldwide. This quantity suggests the amount of misuse of environmental resources is, unfortunately, being done because of the non-availability of alternate cooling technology in the market. The new configurations of a refrigeration system or new type of techniques can be studied through various current research done, which may be related to each other or independently developed. Similarly, multiple feasible modifications can be done on the VCRS. These modifications include altering the single-stage compression of VCRS, replacing the working fluid (refrigerant) with a combination of less harmful chemicals, having lower GWP and ODP, using hybrid systems to siphon more efficient forms of energy such as solar and metal hydride thermal reaction.

MHRS<sup>1</sup> brings a new light of alternate technology, which is not rising much of the horizon nowadays in terms of practical usage. Although it is not yet commercialized, a metal hydride refrigeration system's capabilities and potential to help us cross a

<sup>1</sup> Metal Hydride Refrigeration System.

toxic chemical and un-efficient energy threshold is not much high. Not only in terms of environment-friendliness but also a simplification of the complex refrigeration process. MHRS is a SSRS<sup>2</sup> that works by employing hydrogen as a non-condensable working fluid (not refrigerant), unlike other SSRS models. By introducing a pair of metal hydride cells in the refrigeration system, we tend to replace the two most energy-consuming devices from two different refrigeration systems: condenser and evaporator from VCRS, generator and absorber from conventional SSRS. It can provide both cooling and heating effects along with 80% credit of electricity bill.

In this paper, several aspects of the operation and design of refrigeration systems and their improved models are discussed, such as (i) heat and mass transfer and recovery, (ii) variants of refrigerants, (iii) compact design, (iv) use of nanoparticles, (v) Envi-hybrid developmental status of proposed hypothesis, (vi) use of atmospheric water generator, (vii) use of a combination of different alloys of metal hydride cells for the best outcome.

## 2 Operating Principle

In the literature regarding the atmospheric water generation system, a simple arrangement of a pump various filters like a carbon filter, sediment filter, ultraviolet radiation light bulb, antioxidant cartridge, mechanical filters, and a purified water tank is given [1]. The water precipitates on the cooled coils, like dew settles on leaves, which is blown into a collection tank by a fan for purification. The amount of water to be generated depends on the air's humidity and cooling effect of coils. This cooling effect can be produced from a conventional refrigeration system as well as an MHRS.

A conventional refrigeration system, i.e. the VCRS, follows the process of maintaining temperatures lower than the surrounding by removing heat from the same area to provide a cooling effect. This process is done by compression, condensation, expansion, and evaporation of the working fluid. Figure 1 shows the cyclic process and phase change of a refrigerant in a vapour compression cycle.

While VCRS systems use refrigerants that are still potentially harmful to the environment, MHRS uses hydrogen and water as working fluid. The usage of these working fluids is itself beneficial for the environment, including their functioning. Hydrogen and water have zero GWP<sup>3</sup> and ODP,<sup>4</sup> unlike R12, R22, R410A, and R134. Its working principle is entirely different from the VCRS system and functions devoid of any high energy consumption devices like compressor, condenser, or expansion device. As shown in Fig. 2, an MH refrigeration system contains two pairs of MH cells A and B which are coupled with the H<sub>2</sub><sup>5</sup> gas in respective pair. One is at high pressure (A1-B1), while the other at low pressure (A2-B2) [3].

---

<sup>2</sup> Solid Sorption Refrigeration System.

<sup>3</sup> Global Warming Potential.

<sup>4</sup> Ozone Depleting Potential.

<sup>5</sup> Hydrogen.

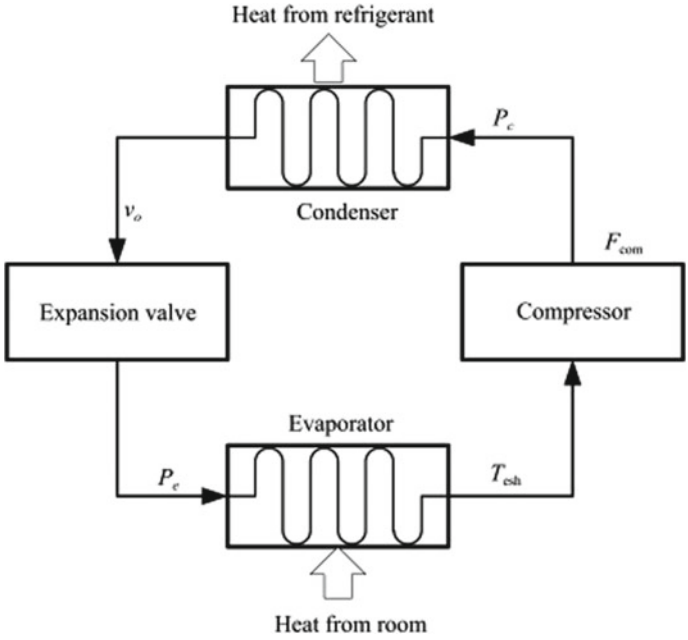


Fig. 1 VCERS process flow [2]

### 3 Literature Review

#### 3.1 Atmospheric Water Generator

Pavithra et al. demonstrated a study of water generation from humid air. The entire procedure of obtaining 99.99% pure drinking water from the atmosphere was explained and

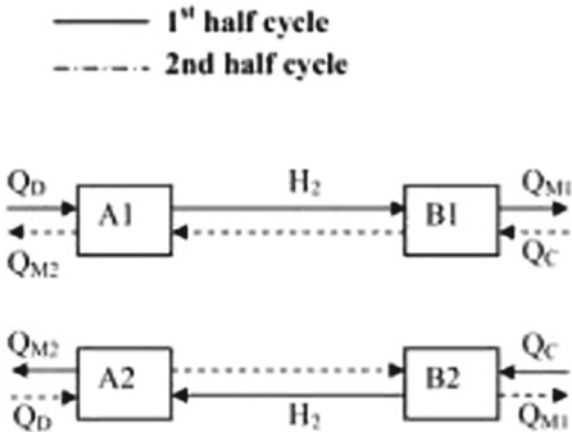


Fig. 2 Metal hydride reaction cell [3]



developed into a working laboratory working model. The water generator was observed to generate enough quantity of water that could support regular household drinking requirements by producing 600 ml/h at 60% RH. It directs the requirement of safe water in isolated areas and answers the imminent shortage of clean water in several regions. It proposes replacing or improving the presently available water production and purification systems in the market to get to the more isolated areas. A further study is proposed to reduce this system's production cost on manufacturing ceramic filters [1].

### 3.2 Performance and Design Improvement of Conventional Cooling Systems

Papade et al. analysed the matrix heat exchanger used in the VCRS. In this study, a VCRS cycle is proposed to use a counter flow matrix heat exchanger which is positioned subsequent to the condenser. The central theme here was to study the COP of a VCRS with and without matrix heat exchanger. This proposed system's COP<sup>6</sup> was observed to be improved by using a matrix heat exchanger through an analytical analysis [4]. Improving the working component function of the conventional refrigeration systems is as essential as using the best possible working fluids iterations to increase the coefficient of performance, which is what Srinivasa et al. had done in his research by studying new variants of environmentally friendly working fluids to reduce the use of harmful refrigerants. HCFCs<sup>7</sup> and CFCs<sup>8</sup> are substituted by HFCs<sup>9</sup> and HFOs,<sup>10</sup> with an assortment of other mixtures. Several issues associated with this substitution of refrigerants being used in VCRS are discussed [5].

Similarly, Barode et al. studied the performances of four less ozone-harming HFC refrigerants (R134a, R143a, R125, and R152a). These are proposed to substitute R12 in a VCRS after an ample number of experiments and compared results. The coefficient of performance of R152a was observed to be greater than those of R12, R143a, R125, R134a refrigerants. Also, it was found that R152a offers the best desired environmentally friendly refrigerant requirements, i.e. lesser GWP and ODP [6]. Coming back to design improvements, in another study, Barbosa et al. presented a critical evaluation of the theory on design, fundamentals, and application features of compacted and miniature mechanical VCRS. For every important application of the VCRS components, this study explains the cooling cycle's thermodynamic and thermal aspects in detail. Also, it sheds light on the recent progress concerning its members, such as compressors, heat exchangers, and expansion devices [7].

Further, design changes were proposed by Leardkun et al. Their study consisted of a miniature version of VCRS using R134a chemical refrigerant, focusing on electronics cooling. This system comprises four important parts: evaporator, compressor, capillary tube, and a condenser. This version of VCRS is proposed to be used for electronics cooling on threshold values of compressor speed around 3000 RPM<sup>11</sup> and heating power

<sup>6</sup> Coefficient of Performance.

<sup>7</sup> Hydrochlorofluorocarbons.

<sup>8</sup> Chlorofluorocarbons.

<sup>9</sup> Hydrofluorocarbons.

<sup>10</sup> Hydrofluoroolefins.

<sup>11</sup> Rotation per minute.

of approximately 199 W. It is appropriate for electronics cooling and has a heating power of 100–150 W since the heater's surface temperature is less than 104 °F [8].

As the design of working components is improved, there is only a limited amount of iterations we can use for refrigerants. This problem of exhausted refrigerant variants for performance enhancement is proposed to be solved by Dongare et al. by enhancing the conventional refrigerants used in VCRS by adding nanoparticles. By doing experiments with different kinds of refrigerants and nanoparticle mixture, the coefficient of performance, heat transfer rate, and thermal conductivity were significantly increased [9].

As we study the latest improvements in the main components and the working fluids of VCRS, it becomes necessary to find the latest analysis models to bring out the study's best results. Nunes et al. describe a dimensionless and simplified mathematical model for VCRS. Key objective was to optimize the dynamic system response. The model proposed here chains the characteristics of heat, thermodynamics, and mass transfer functional to the system components with empirical correlations. Thermodynamic control volumes were also assigned to individual component, improving the functioning of VCRS drastically [10].

Tarrad et al. propose the latest prediction analytics for performance enhancement of air conditioning units. A thorough experimental and theoretical study was done to simulate the performance of VCRS by utilizing R-22 as the refrigerant. This study also carried out the development of a finned tube evaporator heat exchanger coil in an air-conditioner with a thorough design template [11].

### 3.3 Development and Design Improvement of SSRS

There is only a limited scope of improvement for conventional refrigeration systems dating back to the nineteenth century. In the twenty-first century, more efficient cooling systems would make the conventional model redundant if proper research is done in the field. Many laboratory demonstrations of the working model and industrial working models of SSRS are done successfully in the past. Some of the SSRS variants in the field are distinguished based on their solid sorption element used, i.e. ammonia, hydrogen, lithium bromide, and others.

Rao et al. describes the thermodynamic analysis of an SSRS with and without internal heat recovery. NH<sub>3</sub> was used as refrigerant in this system. Results show that the four combinations used in this study, CaCl<sub>2</sub>/CaCl<sub>2</sub> cycle gives the highest COP and specific cooling output per kilogram of salt [12].

Zhong et al. carried out porosity tests on carbon dioxide as a working fluid refrigerant with carbon, zeolite, and silica gel as adsorbents. The Dubinin equation results were used, and models of cycles based on this study are presented. It was suggested in this study that carbon dioxide may be used where ammonia and copper toxicity are fatal [13].

Another SSRS class is defined by the use of metal hydride cells which function on the adsorption and desorption of hydrogen by providing heat. Sharma et al. used lanthanum-nickel alloys as a metal hydride and hydrogen as the sorption gas. In this research, the MH pairs consisting of La<sub>0.9</sub>Ce<sub>0.1</sub>Ni<sub>5</sub>, La<sub>0.8</sub>Ce<sub>0.2</sub>Ni<sub>5</sub>, LaNi<sub>4.7</sub>Al<sub>0.3</sub>, and LaNi<sub>4.6</sub>Al<sub>0.4</sub> were studied, and the reaction kinetics of these cell pairs was recorded. The experiment was carried out at incremental values of temperatures to

determine their adequacy for MH systems. These experiments were also focused on estimating the activation energy from different hydride-pair models [14]. Another study by Sharma V et al. evaluates the efficiency of metal hydrides based on concurrent cooling and heat transformation system (MHCHT) using a combination of La<sub>0.9</sub>Ce<sub>0.1</sub>Ni<sub>5</sub>MmNi<sub>4.4</sub>Al<sub>0.6</sub>MmNi<sub>3.7</sub>Co<sub>0.7</sub>Mn<sub>0.3</sub>Al<sub>0.3</sub> cells was done. For further thermal analyses, the slope and hysteresis factors are also determined. In addition to that, the thermodynamic cycle was analysed in view of the variations in pressure during the H<sub>2</sub> transfer process among the metal hydride cells [15].

Sharma and Kumar also measured the LaNi<sub>5</sub>xAl<sub>x</sub> ( $x = \frac{1}{4}, 0.3$  and  $0.4$ ) hydride pressure concentration isotherms (PCIs) using a volumetric method. Aluminium's properties on the plateau pressure, hydrogen storage capacity and thermodynamic properties were done in this research. The result of the temperature array on the assessment of the enthalpy of formation was done. It was observed that DH largely depends on the experimental temperature range [16]. The La<sub>0.9</sub>Ce<sub>0.1</sub>Ni<sub>5</sub>, La<sub>0.8</sub>Ce<sub>0.2</sub>Ni<sub>5</sub>, LaNi<sub>4.7</sub>Al<sub>0.3</sub>, and LaNi<sub>4.6</sub>Al<sub>0.4</sub> intermetallic hydrides were characterized to evaluate their use in MH-based cooling system. Compared to other conceivable MH pairs, the La<sub>0.9</sub>Ce<sub>0.1</sub>Ni<sub>5</sub> and LaNi<sub>4.7</sub>Al<sub>0.3</sub> hydride pair revealed the high driving potential and transferrable amount of H<sub>2</sub> throughout the cooling and regeneration processes [17].

The pair of La<sub>0.9</sub>Ce<sub>0.1</sub>Ni<sub>5</sub> e LaNi<sub>4.7</sub>Al<sub>0.3</sub> MH appropriate for solid sorption cooling systems were studied using dynamic and static approaches, and it was established that the PCT characteristics; the resulting enthalpy (DH) and entropy (DS) values were suggestively dissimilar to the dynamic and static procedure of measurements [18]. Furthermore, a thorough study of four alloys based on heat pumping, thermodynamic cycle concerning simultaneous cooling and heat transformation was done by Sharma V et al. The performance of the thermodynamic processes was studied using different combinations of AB<sub>5</sub> (La- and Mm-based) MH [19].

Pressure concentration isotherms (PCIs) of LaNi<sub>4.7</sub>Al<sub>0.3</sub> hydride were measured by means of the volumetric method at different temperatures. Reaction enthalpy values were observed to decrease as the hydrogen concentration increases during both absorptions and desorption. Few important physical parameters such as heat of solution, activity coefficient, variation rate '*k*', ' $\Delta H$ ', ' $\Delta S$ ', partial molar volume, and slope factor '*fs*' were calculated. At the end of this study, the simulation and experimental PCI data were found to be similar [20].

The application and importance of metal hydrides are not limited to refrigeration and water generation. It plays an important part in stoichiometric and catalytic transformation processes. This technique enables researchers to understand and predict chemical reactivity, i.e. bond breaking and bond forming that happens in a catalytic reaction [21]. Another example of MH's diverse application is its use in a 2018 research on rehabilitating systems. Pneumatic actuators with a restricted volume and space do not abet compressors for pressurizing air for pneumatic operations. In this case, hydrogen adsorbing alloy-based metal hydride can be used for performing required amount of pressurization of air. This MH pneumatic device only consists of the mechanical component, pneumatic actuator, Peltier element and adsorbing/desorbing hydrogen MH module. 3D models and simulation through LabVIEW (National Instruments) were done to simulate rehabilitative system [22].

## 4 Hybrid Refrigeration System Discussion and Hypothesis

Since the twentieth century a lot of attention is being given to metal hydrides and their uses in different applications. Research like that of Magonetto et al. [23] has been promoting this field of study by demonstrating COP well over 2.5, which is equivalent and better than conventionally used VCRS [24]. In the twenty-first century, there are sufficient research, laboratory experiments, and industrial applications that justify the use of the MH refrigeration system as conventionally as a lesser efficient and environmentally harmful VCRS.

Hybrid refrigeration systems are those which utilize different systems to produce a single fabrication of all, which benefit the user in their mutual working. Such is the configuration suggested through this study that atmospheric water generation (AWG) can be used to generate free water from the air. A metal hydride system can provide enough cooling effect to bring AWG filaments up to the dew point of atmospheric air to produce water. Sharma et al. [17] explained that the metal hydride reaction of adsorption and desorption process requires a very small quantity of external heat. The working fluid (water) requires comparably less electric power to pump cooled liquid throughout the cooling area. According to Vijaykumar et al. [3], the total amount of energy required to run the devices mentioned above can be almost completely driven by solar power. The study suggests various designs of such mechanisms have already been successfully demonstrated as laboratory models as well as prototyping scales. These types of hybrid systems are termed as Envi-hybrid as they deliver a performance which aims to aid the solution of multiple environmental issues.

## 5 Conclusion

The use of metal hydrides in refrigeration is very promising for using a purer form of energy such as thermal to drive solid sorption refrigeration systems using hydrogen. It is also favourable for manufacturing environment-friendly cooling systems. These can insure a wide range of applications ranging from sub-zero temperatures to conventional air cooling. Current VCRS system usage can be justified by using new researched modifications to its refrigerant by using nanoparticles to increase the coefficient of performance. CO<sub>2</sub> can also be used in proper storage as it shows better results where ammonia and copper become toxic and fatal in the long run.

The research has proposed the significance of enhancing the mass and heat transfer characteristics of a VCRS or a metal hydride reactor cell to enhance performance. For performance enhancement, La and Mn alloys are usually used to set the best thermodynamic conditions in MH reactor cells for heat transfer [14].

Envi-hybrid systems suggest a greener approach to modern technology focused on developing similar conventionally usable machines. Using different relevant systems such as atmospheric water generators and MH hydride systems justifies its use as a replacement for conventional refrigeration systems. It promotes the fabrication of environment-friendly technology as, in recent years, several individual designs have been successfully demonstrated in laboratories. They are aiding the conventional refrigeration technology simplification and making refrigeration appropriately portable for small and mobile cooling applications.

## References

1. Pavithra S, Anbarasu T (2011) Vapour compression refrigeration system generating fresh water from humidity in the air. In: Chennai and Dr. MGR University Second international conference on sustainable energy and intelligent system, pp 20–22
2. Yin X, Li S (2018) Energy efficient predictive control for vapor compression refrigeration cycle systems. *IEEE/CAA J Automatica Sinica* 5(5):953–960
3. Vijaykumar GT, Girish KG, Keerthan GU, Shamanth M (2016) Metal hydride based cooling systems with hydrogen as working fluid—a review. *Int J Emer Technol (Special Issue on ICRIET-2016)* 7(2):70–75
4. Papade C, Solankar B (2016) A review on analysis of vapour compression refrigeration system using matrix heat exchanger, *IJLTET*, vol 6, issue 3
5. Srinivasa S, Venkatarathnam G (2012) Refrigerants for vapour compression refrigeration systems. *Indian Acad Sci* 139–162
6. Barode S, Tiwari A (2012) Performance analysis of vapour compression refrigeration systems using hydrofluorocarbon refrigerants. *Int J Sci Eng Res* 3(12)
7. Barbosa R, Oliveira P, Ribeiro G (2015) A state-of-the-art review of compact vapor compression refrigeration systems and their applications. *Heat Transf Eng* 37–41
8. Leardkun R, Poachaiyapoom A, Wongwises S (2018) Miniature vapor compression refrigeration system for electronics cooling. *Case Stud Therm Eng.* <https://doi.org/10.1016/j.csite.2018.100365>
9. Dongare V, Kadam V, Samel A, Pawar R, Sarvankar S (2017) Enhancement of vapour compression refrigeration system using nanofluids. *Int Res J Eng Technol* 2218–2225
10. Nunes T, Vargas J, Ordonez J, Shah J, Martinho L (2015) Modeling, simulation and optimization of a vapor compression refrigeration system dynamic and steady-state response. *Appl Energy* 540–555
11. Tarrad A, Shehhab U (2007) The prediction of environment effect on the performance of a vapor compression refrigeration system in air conditioning application. *J Eng Dev* 169–189
12. Rao K, Gopal M, Bhattacharyya S (2012) Thermodynamic analysis of a sorption refrigeration system with and without internal heat recovery. *Int J Low Carbon Technol* 124–133
13. Zhong Y, Critoph R, Thorpe R (2005) Evaluation of the performance of solid sorption refrigeration systems using carbon dioxide as refrigerant. *Appl Therm Eng* 1807–1811
14. Sharma V, Kumar E (2014) Measurement and analysis of reaction kinetics of La e based hydride pairs suitable for metal hydride e based cooling systems. *Int J Hydrogen Energy* 19156–19168
15. Mohan M, Sharma M, Sharma V, Kumar E, Satheesh E, Muthu Kumar P (2019) Performance analysis of metal hydride based simultaneous cooling and heat transformation system. *Int J Hydrogen Energy* 10906–10915
16. Sharma V, Kumar E (2013) Effect of measurement parameters on thermodynamic properties of La-based metal hydrides. *Int J Hydrogen Energy* 5888–5898
17. Sharma V, Kumar E (2014) Studies on La based intermetallic hydrides to determine their suitability in metal hydride based cooling systems. *Intermetallics* 60–67
18. Sharma V, Kumar E, Murthy S (2014) Influence of dynamic operating conditions on the performance of metal hydride based solid sorption cooling systems. *Int J Hydrogen Energy* 1108–1115
19. Sharma V, Kumar E (2016) Thermodynamic analysis of novel multi-stage multi-effect metal hydride based thermodynamic system for simultaneous cooling, heat pumping, and heat transformation. *Int J Hydrogen Energy* 1–11
20. Sharma V, Kumar E (2014) Measurement and simulation of hydrogen storage and thermodynamic properties of LaNi<sub>4.7</sub>Al<sub>0.3</sub> hydride. *Int J Appl Eng Res* 985–994

21. Wiedner ES, Chambers MB, Pitman CL, Bullock RM, Miller AJ, Appel AM (2016) Thermodynamic hydricity of transition metal hydrides. *Chem Rev* 10:116(15):8655-92. <https://doi.org/10.1021/acs.chemrev.6b00168> (Epub 2016 Aug 2. PMID: 27483171)
22. Kim K, Kim SH, Kim SH, Yu CH (2018) Hydrogen-absorbing alloy-based metal-hydride actuation for application in rehabilitative systems. *Technol Health Care* 26(S1):43–53. <https://doi.org/10.3233/THC-174063> (PMID: 29689754; PMCID: PMC6004936)
23. Magnetto D, Mola S, DaCosta DH, Golben M, Rosso M (2006) A metal hydride mobile air conditioning system. *SAE Int* [2006–01–1235]
24. Delhomme B, Rango P, Marty P, Bacia M, Zawilski B, Raufast C, Miraglia S, Fruchart D (2012) Large scale magnesium hydride tank coupled with an external heat source. *Int J Hydrogen Energy* 37:9103–9111
25. Choudhari M, Ahuja K, Thakkur S, Bardhan S, Sharma V (2019) Performance investigation of metal-hydride based heat transformer. *Energy Storage*. <https://doi.org/10.1002/est2.56>
26. Kumar A, Mishra D, Sharma V (2018) Estimation of enthalpy of formation of metal hydrides—effect of different measurement parameters. *Adv Energy Res* 1271–276
27. Sharma V (2017) Static and dynamic measurement-based thermodynamic analysis of solid sorption refrigeration system. *Int J Energy Res* 553–564
28. Groll M, Klein HP, Srinivasa Murthy S. Metal hydride based thermal systems: a review. In: *World renewable energy congress-VII, Cologne, Germany*
29. Groll M, Klein HP (2002) Metal hydride technology with special emphasis on thermodynamic machines, In: *5th ISHMT-ASME heat & mass transfer conference, Calcutta*
30. Srinivasa Murthy S (1997) Heat and mass transfer in metal hydride reactors: influence on design and performance of heating and cooling systems. In: *3rd ISHMT-ASME heat & mass transfer conference, Kanpur*
31. Sally (2013) A synthesis matrix as a tool for analyzing and synthesizing prior research. Retrieved from <http://www.academiccoachingandwriting.org/dissertation-doctor/dissertation-doctor-blogiii-a-synthesis-matrix-as-a-tool-for-analyzing-and-synthesizing-prior-research>
32. Ram Gopal M, Srinivasa Murthy S (1992) Prediction of heat and mass transfer in annular cylindrical metal hydride beds. *Int J Hydrogen Energy* 17:795805
33. Upadhyay N (2014) Analytical study of vapour compression refrigeration system using diffuser and subcooling. *J Mech Civil Eng* 11(3):92–97
34. She X, Yonggao XZ (2014) A proposed subcooling method for vapour compression refrigeration cycle based on expansion power recovery. *Int J Refrig* 43:50–61
35. Christian JLH (2014) Refrigerant charge reduction in vapour compression refrigeration cycle via liquid-to-suction heat exchanger. *Int J Refrig* 52:93–99
36. Muthukumar P, Ramana SV. Numerical simulation of coupled heat and mass transfer in metal hydride-based hydrogen storage reactor. *J Alloys Compd*
37. Mayer U, Groll M, Supper W (1987) Heat and mass transfer in metal hydride reaction beds: experimental and theoretical results. *J Less Common Metals* 131:235–244
38. Dreepaul RK (2017) A study of alternative refrigerants for the refrigeration and air conditioning sector in Mauritius, earth and environmental science. In: *International conference on new energy and future energy system (NEFES 2017), 22–25 September 2017, Kunming, China, vol 93*
39. Chopra K, Jain D, Chandana T (2012) Evaluation of existing cooling systems for reducing cooling power consumption. *Int J Mech Eng Technol* 3(2):210–216
40. Yang FS, Wang GX, Zhang ZX, Meng XY, Rudolph V (2010) design of the metal hydride reactors—a review on the key technical issue. *Int J Hydrogen Energy* 35:3832–3840
41. Muthukumar P, Groll M (2010) Metal hydride based heating and cooling systems: a review. *Int J Hydrogen Energy* 35:3817–3831

42. Paya J, Linder M, Laurien E, Corberan JM (2009) Dynamic model and experimental results of a thermally driven metal hydride cooling system. *Int J Hydrogen Energy* 34:3173–3184
43. Kemal A, Abdurrazzak A (2011) An experimental investigation of the effect of refrigerant charge level on an automotive air conditioning system. *J Therm Sci Technol (TIBTD Printed in Turkey)*. ISSN 1300-3615
44. Smyth S, Finn DP, Brophy B (2010) Performance evaluation of an economised indirect multi-temperature transport refrigeration system. In: *International refrigeration and air conditioning conference paper 1095*
45. Kim M-H, Pettersen J, Bullard CW (2004) Fundamental process and system design issues in CO<sub>2</sub> vapour compression systems. *Prog Energy Combust Sci* 30(2):119–174
46. Aidoun Z, Ouzzane M (2008) A numerical study of an evaporator coil for a refrigeration secondary loop with CO<sub>2</sub>T. In: *Fifth international conference on transport phenomena in multiphase systems*, June 30–July 3, 2008, Bialystok, Poland
47. Zimmerman PAJ, Maciel RA (2006) Discharge pressure optimization for CO<sub>2</sub> transcritical cycle using a capillary tube. In: *International refrigeration and air conditioning, conference paper 763*
48. Yamasaki H, Yamanaka M, Matsumoto K, Shimada G (2004) Introduction of trans-critical refrigeration cycle utilizing CO<sub>2</sub> as working fluid. In: *International compressor engineering conference paper 1632*
49. Ni J, Liu H (2007) Experimental research on refrigeration characteristics of a metal hydride heat pump in auto air conditioning. *Int J Hydrogen Energy* 32:2567
50. Isselhorst A, Groll M (1995) Two-stage metal hydride heat transformer laboratory model. *J Alloy Comp* 231:888e94
51. Friedlmeier G, Schaaf M, Groll M (1994) How to measure pressure concentration-isotherms representative for technical applications. *Z Phys Chem* 183:185
52. Dehouche Z, de Jong W, Willers E, Isselhorst A, Groll M (1998) Modelling and simulation of heating/air conditioning systems using the multi-hydride-thermal-wave concept. *Appl Therm Eng* 18:457e80
53. Güther V, Otto A (1999) Recent developments in hydrogen storage applications based on metal hydrides. *J Alloys Compd* 293–295
54. Nakamura H, Nakamura Y, Fujitani S (1996) Cycle performance of a hydrogen absorbing La<sub>0.8</sub>Y<sub>0.2</sub>Ni<sub>4.8</sub>Mn<sub>0.2</sub> alloy. *Int J Hydrogen Energy* 21(6):457–460
55. Nakamura H, Nakamura Y, Fujitani S (1997) A method for designing a hydrogen absorbing LaNi<sub>5-x-y</sub>Mn<sub>x</sub>Al<sub>y</sub> alloy for a chemical refrigeration system. *J Alloy Compd* 252(1–2):83–87
56. Kang BH, Park CW, Lee CS (1996) Dynamic behavior of heat and hydrogen transfer in a metal hydride cooling system. *Int Hydrogen Energy* 21:769e74
57. Lototskyy M, Tolj I, Davids MW, Bujło P, Smith F, Pollet BG (2015) “Distributed hybrid” MH–CGH<sub>2</sub> system for hydrogen storage and its supply to LT PEMFC power modules. *J Alloys Compd* 645:S329–S333
58. Sekhar BS, Muthukumar P (2013) Performance tests on a double-stage metal hydride based heat transformer. *Int J Hydrogen Energy* 38:15428–15437
59. Bjurström H, Suda S (1989) The metal hydride heat pump: dynamics of hydrogen transfer. *Int J Hydrogen Energy* 14:19
60. Kim KJ, Feldman KT Jr, Lloyd G, Razani A (1997) Compressor-driven metal-hydride heat pumps. *Appl Thermal Eng* 17:551–560
61. Paya J, Linder M, Laurien E, Corbera JM (2009) Dynamic model and experimental results of a thermally driven metal hydride cooling system. *Int J Hydrogen Energy* 34:3173–3184





# Study on Thermal Conductivity and Thermogravimetric Analysis of Glass Fibre Epoxy Resin Composites Modified with Silicon Carbide and Copper Nanoparticles

Gurushanth B. Vaggar<sup>1</sup>(✉), S. C. Kamate<sup>2</sup>, S. L. Nadaf<sup>3</sup>, and Pramod V. Badyankal<sup>1</sup>

<sup>1</sup> Alva's Institute of Engineering and Technology, Visvesvaraya Technological University, Mijar, Moodbidri 574225, India

gvgr.aiet@gmail.com

<sup>2</sup> Hirasugar Institute of Technology, Visvesvaraya Technological University, Nidasoshi, India

<sup>3</sup> Government Engineering College, Visvesvaraya Technological University, Haveri, India

## 1 Introduction

Composite materials are made with more than two or two components which are variance in shape and chemically non-similar composition. Most of the composite materials are made to obtain properties better than individual constituents. Manufacturing of polymer matrix composites is the reason for high strength low density in nature as compared to that of metals and their alloys. More temperature variable conditions polymer composites are failed to exhibit good thermal properties in different fields like automobile sectors, military weapons, aerospace parts and medical instruments. The solution to this kind of problem, try to use micro- or nano-sized filler particles in the polymer composites, to make them hybrid and are called hybrid polymer composites (HPCs). Adding filler materials in a small percentage to regular polymer composites vary the thermal properties overall and hybrid polymer matrix composites much stable under varied temperature conditions without changing the base strength of polymer matrix composite materials.

For different applications, a predefined desired properties and novel kind of materials are manufactured using fillers in polymer composites and are called hybrid composites. By varying the weight fraction proportion of fillers in epoxy resin glass fibres improve the mechanical, physical and thermal properties of composites. Due to high strength low density and economic compared to metals and metal alloys, hybrid polymer composites are used in various fields of applications like aerospace, marine, military weapons, automotive parts and windmill turbine blades. Requirement and use of hybrid composites have increased in many fields, communication sectors and electronics devices, where high thermal resistance low-density factors are predominant [1].

For many application fields like military, aerospace, wind power mills, automotive and construction, glass fibres are the most used fibres because of easy processing technique, low density, good resistance to corrosion, high strength sustainability, toughness and recyclable [2]. From several study approaches, it is noticed that the toughness and strength of polymer composites are closely associated with interface property improvement [3].



Plane polymer materials have certain disadvantages like poor thermal stability, low-grade environmental and chemical stability, and low thermal conductivity. To overcome such problems, composites need to be redesigned with various filler particles [4]. Polymers start degrade before 200 °C. Some classy polymer composites are thermally stable in air and in inert gases without changing their structures or strength loss, at 300–500 °C temperature range, analysed through TGA test. The GFRP composite has a good heat conduction compared to CFC and HFC composites [5].

In TGA, sample specimens undergone a loss of weight and percentage loss of weight was continuously monitored when the specimen was uniformly heated under specific environs. At specific temperatures, weight loss of specimens was observed which highlights the thermal stability and volatile inert filler. Thus, TGA test is the best to analyse the weight loss of composites with reference to temperatures [6]. The study of thermal properties of composites determines the degradation level of fibres with temperature. Fibres are thoroughly examined for robustness from thermal stability and heat resistance to make sure fibres can withstand high temperatures during operating conditions [7]. Thermal stability of a composite material can be evaluated by thermogravimetric analysis. The higher operating temperature of a composite material can be assessed and obtained by TGA, beyond higher operating temperature the composites will begin to degrade. Hence, TGA has an ability to identify the polymer composite materials which are thermally stable [8]. Thermal degradation temperature improves the addition of silicon carbide particles to polymethyl methacrylate epoxy resin composites [9]. Adding small composition of multi-walled carbon nanotubes in polyurethane polymer matrix thermal degradation temperature of polyurethane composites was improved from 409 to 421 °C [10].

The current global world advances towards the smart and advanced materials, the use of polymer fibre reinforced composites occupies around 50–60% of total materials. High strength, stiffness and low-density properties are encouraging the use of composite materials in many fields instead of metals. The current polymer fibre composites are having very low thermal properties and low thermal resistance against high-temperature applications, and hence, after improvising the thermal properties the polymer fibre reinforced composite materials can be effectively usable in wide applications.

Polymers are low thermal conductivity materials in the range 0.1–0.5 W/mK. By developing the chain alignments and internal chain coupling in polymer matrix blends, the core thermal conductivity can be enhanced. Moreover, the enhancement of thermal conductivity is observed along the unidirectional, but an isotropic material with high thermal conductivity is generally required, which causes the application limits of polymer composites. Slight enhancement in thermal conductivity is shown in blended polymers [11]. Enhancement of thermal conductivity can be made by increasing the nanoparticle weight fraction content in the epoxy hybrid nanocomposites. The design optimization of hybrid nanocomposites can be done based on thermal conductivity results of micro-filler/nanoparticle filler polymer hybrid composites [12]. Adding graphene nanoparticles to epoxy resin carbon fibre composites increases the thermal conductivity [13]. The decomposition temperature improves by adding silicon carbides to epoxy resin carbon fibre composites [14].

## 2 Specimen Preparation

Polymer matrix composite specimens are developed by using the following materials. (1) LY556 Epoxy Resin, (2) E-Glass Fibre, (3) Hardener, (4) Silicon Nanoparticles, (5) Copper Nanoparticles. Silicon Carbide Nanopowder procured from Ultrananotech private limited, Bangalore-560048. Silicon carbide nanoparticles have purity 99.9% and particle size (APS) 30–50 nm. Copper nanoparticles brought from SERENA INC metal powder, Bangalore-560076, India. Copper nanoparticles have purity 99.9% and particle size 100 nm. E Glass fibre (300 GSM), LY556 epoxy resin and hardener purchased from Zenith Industrial Supplies, 174/2, City Market, SadarPatrappa Road, City Market, Bangalore-560002, Karnataka, India.

Initially, glass fibres are cut as per the dimensions (Fig. 1a); after cutting glass fibre weigh, it (Fig. 1b), then take the epoxy resin, hardener and fillers as per the standard (Tables 1 and 2) calculations (Fig. 1c) add hardener and filler particles to epoxy resin (Fig. 1d), mix them thoroughly till it attains thick paste. Apply non-sticky material to mould box, then apply an epoxy resin filler particle paste, place one sheet glass fibre. Similarly, after placing one-by-one glass fibre apply epoxy resin filler particle paste (Fig. 1e), by placing all the glass fibre sheets then keep the mould box in compression moulding machine by applying 20 bar pressure non-heating, for minimum 24 h and allow for solidification (Fig. 1f).

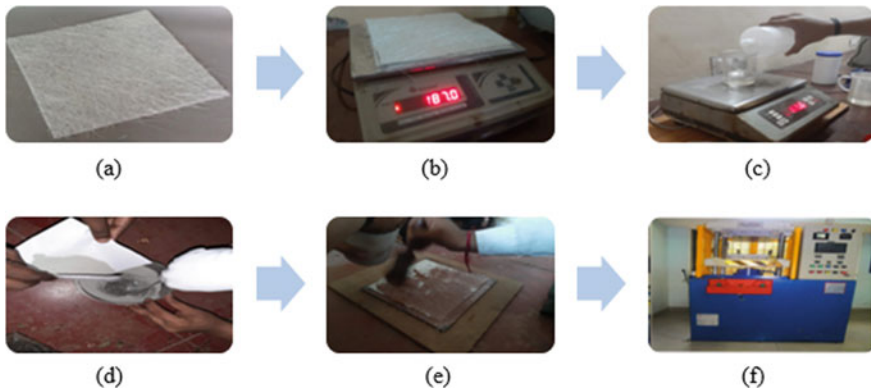


**Fig. 1** a–f Steps involved in development of polymer composites

The above procedure repeated for preparing the specimens with various weight fractions of filler nanoparticles. All specimens are prepared at RTP conditions with machine pressure loading (20 bar), after removing specimens from mould box, kept open to dry atmospheric conditions for another 24 h to check free from moisture observations. Then specimens are ready to cut as per standard dimensions. The method used to develop polymer composites is hand layup with machine moulding technique.

Each constituent of individual materials is considered based on weight ratio, and compositions of each specimens are shown in Tables 1 and 2.

**Table 1** Composition of Cu nanoparticle polymer composites

Designation	Each constituent in grams			
	Cu-NPs	E-GF	ER	Hardener
ERGF	0	179	268.5	26.85
ERGFCu-NPs5	8.89	118.5	168.86	16.89
ERGFCu-NPs10	17.25	115	155.25	15.53
ERGFCu-NPs15	25.313	112.5	143.44	14.34
ERGFCu-NPs20	32.4	108	129.6	12.96

**Table 2** Composition of SiC nanoparticle polymer composites

Designation	Each constituent in grams			
	SiC-NPs	E-GF	ER	Hardener
ERGF	0	179	268.5	26.85
ERGFSiC-NPs5	14.1	188	267.9	26.79
ERGFSiC-NPs10	28.05	187	252.45	25.245
ERGFSiC-NPs15	41.625	185	235.879	23.59
ERGFSiC-NPs20	54.9	183	219.6	21.96

### 3 Experimental Set-ups

#### 3.1 Thermogravimetric Analysis (TGA) Experiment

Thermogravimetric tests performed at CIPET: School for Advanced research in polymers, Bengaluru-562149. About 5–10 g weight square or rectangular specimens used for thermogravimetric analysis test. Equipment used for thermogravimetric analysis test are: (1) Make: M/s. Hitachi, Japan, Model: STA 7300, (2) Make: Perkin Elmer, Model: TGA 8000. In thermogravimetric analysis (TGA) test, the (5 g) cut specimens are exposed to the high-temperature region, the behaviour of specimens observed at various temperature ranges with respect to time. The temperature increases rate of 20 °C/min, and supply of nitrogen and oxygen is maintained 50 ml/min.

#### 3.2 Fox 50 Heat Flow Metre (HFM) Thermal Conductivity Experiment

The FOX 50 is used for testing materials whose thermal conductivity lies in the range of 0.1–10 W/mK. It is an easy and accurate thermal conductivity measuring device in a quick time with fast results. Thickness of the specimen measured digitally by optical encoders operates under wide range of temperatures, FOX 50 (Fig. 2) is most suitable to measure low and medium thermal conductivity materials. Precise temperature control with solid-state heating/cooling, to measure heat flow thin film heat flux transducers are used, WinTherm–50 software is used for operating FOX 50 device.



**Fig. 2** FOX 50 heat flow metre experimental setup to measure thermal conductivity

Thermal conductivity of a specimen can be determined by measuring the steady-state heat flux, temperature difference across the specimen, and its thickness. In each component of the thermal conductivity equation, the FOX50 instrument provides extremely precise readings. Thermal conductivity is measured as per ASTM C518-17. Specimens of 50 mm diameter are placed in between two (upper and lower) plates and allow the heat to flow through specimen (Fig. 3), thermal resistance is generated between the contact surfaces of specimen and upper plate and lower plate. Thermal resistance of a contact layer is equal to its thickness  $\Delta X$  (m) divided by its thermal conductivity  $K$  (W/mK).

$$R_{\text{solid}} = \Delta X_{\text{solid}}/K_{\text{solid}} \left( \text{m}^2\text{K/W} \right) \quad (1)$$

$$R_{\text{liquid}} = \Delta X_{\text{liquid}}/K_{\text{liquid}} \left( \text{m}^2\text{K/W} \right) \quad (2)$$

Thermal contact resistance  $R$  is equal to temperature difference  $\delta T$  between two contacting surfaces divided by heat flux  $q$  ( $\text{W/m}^2$ ) and depends on the types of adjoining materials, their surface roughness, and the interface pressure.

$$R = \delta T/q \left( \text{m}^2\text{K/W} \right) \quad (3)$$

Heat flow metre instruments measure only the total thermal resistance—sum of the cell's thermal resistance of specimen and sample/instrument's thermal contact resistances  $2R$  of both surfaces

$$R_{\text{total}} = R_{\text{specimen}} + 2R_{\text{contact plates}} \quad (4)$$

Thermal conductivity  $K$  is equal to thickness of the specimen divided by the specimen thermal resistance minus the upper and lower plates thermal contact resistances

$$K = (\Delta X_{\text{specimen}}/R_{\text{specimen}}) = \Delta X_{\text{specimen}}/(R_{\text{total}} - 2R_{\text{contact plates}}) \quad (5)$$

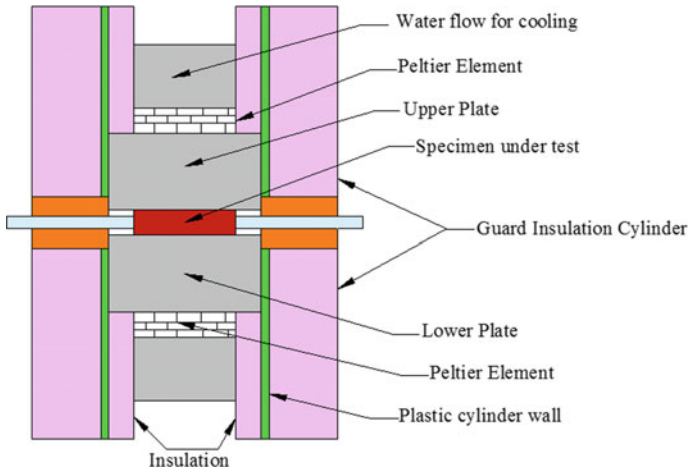


**Fig. 3** FOX 50 heat flow metre cross-sectional view

High-output heat flow metres (HFMs) are bonded to the surfaces of both copper plates. The HFMs are made of dozens of small thermocouples, so they provide high sensitivity and integration of the signals. Type E thermocouples are bonded in the centre of each transducer. The thermocouples provide accurate readings of the both plates temperatures. Each plate has a powerful thermoelectric (Peltier) element, which is controlled independently. Back sides of the elements are cooled down by water flow.

## 4 Results and Discussion

The thermal degradation temperature variation and percentage weight loss of silicon carbide nanoparticles ERGF composites are shown in Fig. 4. It is observed that in the first stage of TGA test there is 3–5% of weight loss occurs at temperature 30 °C due to the removal of moisture and dust particles from the specimen. In second stage, the specimens are heated from 30 to 450 °C at the rate 20 °C/min, weight loss noticed 55.5% in 5% SiC nanoparticles filled composites, 58% in 10% SiC nanoparticles filled composites, 35% in 15% SiC nanoparticles filled composites, 33.5% in 20% SiC nanoparticles filled composites. In the third stage, TGA degradation of specimens was found to be stable from 450 to 600 °C that indicates there is no much reduction in weight loss in this stage. In the fourth stage of TGA, further heating of specimens continues more than 650 °C, and the degradation and further decomposition of specimen take place and maximum weight loss found in this stage which was 72.3% in 5% SiC nanoparticles composites, 76.8% in 10% SiC nanoparticles composites, 50.3% in 15% SiC nanoparticles composites, 44.2% in 20% SiC nanoparticles composites. The TGA of neat epoxy glass fibre composites exhibits 52.7% weight loss in the fourth stage. The SiC-NPs composition of 15 and 20% composites has shown better TGA results than neat composites. More thermal stability observed in 15 and 20% SiC nanoparticles composites, and there is no significant improvement in thermal stability at less percentage SiC Nanoparticles composites when compared neat ERGF composites. Thermal degradation temperature ( $T_g$ ) improves the

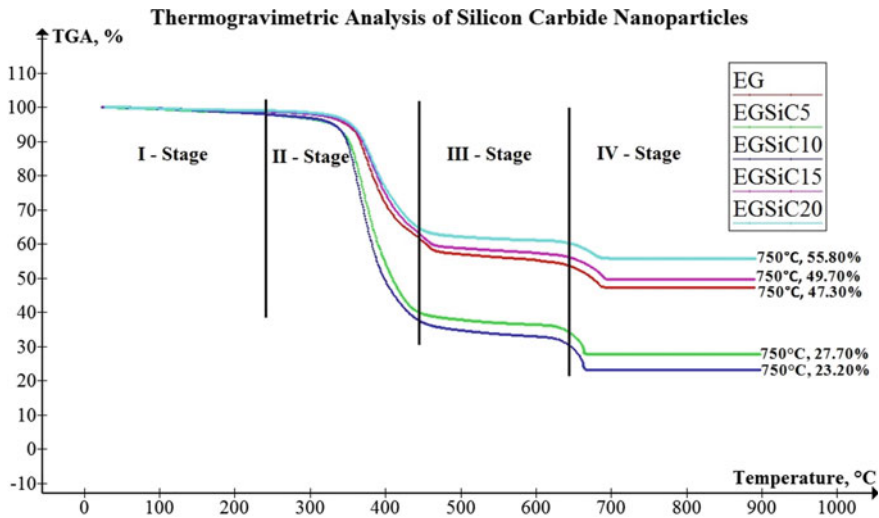


**Fig. 4** TGA (%) versus temperature of SiC-NPs composites

addition of silicon carbide particles (SiC) to epoxy resin composites. Improvement of  $T_g$  occurs due to higher specific heat value of silicon carbide particles absorbs the more heat from heated composites. The addition SiC nanoparticles to ERGF composites causes the increase in thermal stability.

The thermal degradation temperature variation and percentage weight loss of copper nanoparticles ERGF composites are shown in Fig. 5. In the first stage of TGA test of copper nanoparticles (Cu-NPs) composites 1–2% of weight loss occurs at temperature 30 °C due to the removal of moisture and dust particles from the specimens. In second stage, the specimens are heated from 30 to 460 °C at the rate 20 °C/min, weight loss noticed 78.7% in 5% Cu-NPs, 66.85% in 10% Cu-NPs, 52.9% in 15% Cu-NPs, 75.35% in 20% Cu-NPs. In third stage of TGA, degradation of specimens found to be stable from 460 to 610 °C and there is no much reduction in weight loss in this stage. In the fourth stage of TGA, further heating of specimens continues more than 610 °C, the degradation of specimen materials takes place, and maximum weight loss found in this stage was 94.5% in 5% Cu-NPs, 84.8% in 10% Cu-NPs, 64.5% in 15% Cu-NPs, 94.2% in 20% Cu-NPs. The TGA neat epoxy glass fibre composites exhibit 52.7% weight loss after fourth stage. By TGA results, the Cu-NPs have found higher weight loss compared to neat ERGF composites.

Thermal conductivity of silicon carbide and copper nanoparticle hybrid polymer composites are measured by using FOX 50 heat flow metre (HFM). The test has been carried out for three trials for each specimen at temperature difference of 10 °C ( $\Delta T$ ) with top plate heating 65 °C and bottom plate heating at 55 °C, average of three trials results are shown in Table 3.

From the above results, it is clearly indicated that the thermal conductivity values obtained from FOX 50 HFM almost same for both silicon carbide nanoparticle and copper nanoparticle hybrid polymer composites. SiC nanoparticle composites thermal

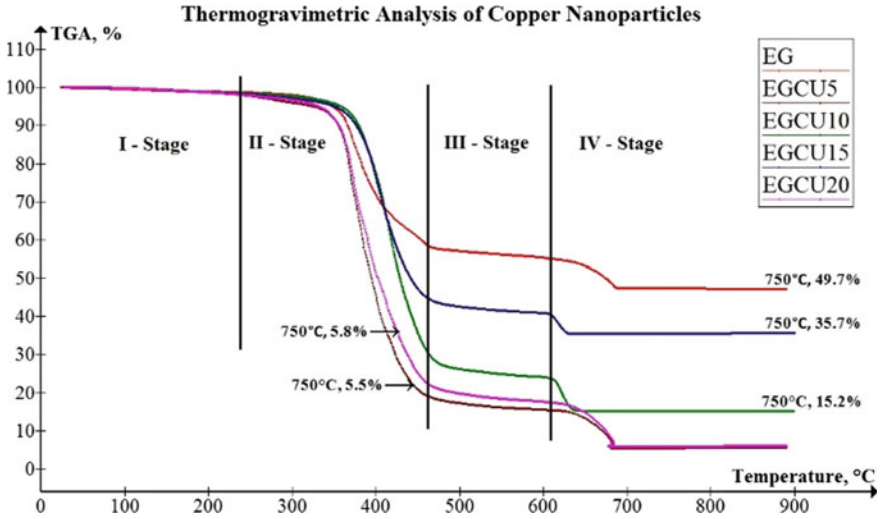


**Fig. 5** TGA (%) versus temperature of Cu-NPs composites

**Table 3** Thermal conductivity results of SiC-NPs and Cu-NPs composites

Sl. No.	Test method	Specimen sample	Thermal conductivity in W/mK
1	ASTM C 518-17	ERGF	0.28
2	ASTM C 518-17	ERGFSiC-NPs5	0.29
3	ASTM C 518-17	ERGFSiC-NPs10	0.29
4	ASTM C 518-17	ERGFSiC-NPs15	0.30
5	ASTM C 518-17	ERGFSiC-NPs20	0.33
6	ASTM C 518-17	ERGFCu-NPs5	0.28
7	ASTM C 518-17	ERGFCu-NPs10	0.28
8	ASTM C 518-17	ERGFCu-NPs15	0.29
9	ASTM C 518-17	ERGFCu-NPs20	0.32

conductivity slightly is higher than that of copper nanoparticle composites; various experimental results are compared with the FOX 50 HFM and are found satisfactory with all specimens. The increase in thermal conductivity observed in 15 and 20% SiC nanoparticles composites and copper nanoparticle composites, and there is no significant improvement in thermal conductivity at low percentage (5 and 10%) SiC and Cu nanoparticles composites when compared neat ERGF composites. The variation of thermal conductivity with percentage of nanoparticle fillers is shown in Fig. 6.

Both SiC and Cu nanoparticles have high thermal conductivity and high specific heat values and can be easily imposed in epoxy resin glass fibre composites. SiC nanoparticles absorb heat and increase the glass transition temperature of polymers, which increases the

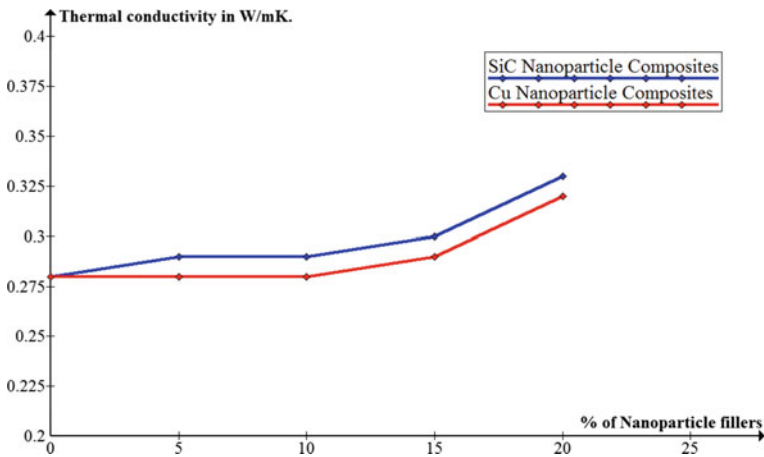


**Fig. 6** Thermal conductivity versus percentage of nanoparticle fillers

thermal conductivity and thermal stability of hybrid polymer composites. High thermal conductivity Cu nanoparticles separates the polymer chain links and decomposes the polymers quickly, and hence, the thermal conductivity of Cu nanoparticle composites obtained is less than that of SiC nanoparticle composites.

## 5 Conclusions

From thermogravimetric analysis, copper nanoparticle composites have shown poor thermal stability and silicon nanoparticles composites shown improved thermal stability at 15 and 20% filler content compared to pure ERGF composites. Mixing of silicon carbide nanoparticles to polymer matrix enhances the thermal degradation temperature, GTT and thermal stability of polymer composites. Due to high bonding strength and good interfacial molecule interactions between silicon nanoparticles and polymer matrix, silicon carbide nanoparticle composites are shown better results as compared to copper nanoparticle composites. Thermogravimetric analysis results have shown that percentage of weight loss occurs more in Cu nanoparticles composites as compared to SiC nanoparticle composites. Thermal conductivity of both SiC and Cu nanoparticle composites increases with increase of fillers. SiC-NPs composites have shown higher thermal conductivity values compared to Cu-NPs composites. This study helps in developing high thermal conductivity polymer composites using various fillers according to the applications and requirements in various fields. In industry applications, the use of materials decided based on weight, strength, stiffness and thermal resistivity. Hence, low-density high strength thermally stable materials are the future advanced materials for all kinds of applications.





## References

1. Devendra K, Rangaswamy T (2013) Thermal conductivity and thermal expansion coefficient of GFRP composite laminates with fillers. *Mech Confab* 2(5). ISSN: 2320-2491
2. Gupta MK (2018) Investigations on properties of glass fibre reinforced polymer composite. *Am J Polym Sci Eng* 6(1). ISSN: 2572-5734
3. Samsur Rahman AKM, Rangari V, Jeelani S (2015) Thermal and mechanical properties of woven glass fiber reinforced epoxy composites with carbon nanotubes grown in-situ. *Int J Eng Sci (IJES)* 4(12):54–61
4. Mittal G, Rhee KY, Mišković-Stanković V, Hui D (2018) Reinforcements in multi-scale polymer composites: processing, properties, and applications. *Compos Part B (Science Direct, Elsevier)* 138:122–139
5. Bhasker B, Devaiah M, Laxmi Reddy P, Ravindra Gandhi M (2019) Thermal characterization of fibre reinforced polymer composites and hybrid composites. *Int J Mech Eng Technol* 10(03):1055–1066
6. Chinnasamy V, Subramani SP, Palaniappan SK, Mysamy B, Aruchamy K (2020) Characterization on thermal properties of glass fiber and kevlar fiber with modified epoxy hybrid composites. *J Mater Res Technol* 9(3):3158–3167
7. Radzi AM, Sapuan SM, Jawaid M, Mansor MR (2019) Water absorption, thickness swelling and thermal properties of roselle/sugar palm fibre reinforced thermoplastic polyurethane hybrid composites. *J Mater Res Technol (Elsevier)* 8(5):3988–3994
8. Bommara B, Devaiah M, Laxmi Reddy P, Ravindra Gandhi M (2019) Thermal characterization of fibre reinforced polymer composites and hybrid composites. *Int J Mech Eng Technol* 10(03):1055–1066
9. Ravi Raj V, Vijaya Ramnath B (2020) Mechanical, thermal and wear behavior of SiC particle strengthening of PMMA-toughened glass-epoxy hybrid composite. *Springer Nature B.V.*, 12 July 2020
10. Kumar D, Jindal P (2019) Effect of multi-walled carbon nanotubes on thermal stability of polyurethane nanocomposites. *Mater Res Express* 6:105336
11. Huang C, Qian X, Yang R (2018) Thermal conductivity of polymers and polymer nanocomposites. *Mater Sci Eng R (Elsevier)* 132:1–22
12. Mahmoodi MJ, Hassanzadeh-Aghdam MK, Ansari R (2018) Overall thermal conductivity of unidirectional hybrid polymer nanocomposites containing SiO<sub>2</sub> nanoparticles. *Int J Mech Mater Des*. <https://doi.org/10.1007/s10999-018-9428-3>
13. Liu F, Wang D, Li S, Wei H, Chen Y, Liu J (2020) Study on thermal conductivity of carbon fiber/resin composite modified with graphene nanoplatelets. *J Phys Conf Ser* 1605(2020):012137
14. Kareem AA (2020) Enhanced thermal and electrical properties of epoxy/carbon fiber–silicon carbide composites. *Adv Compos Lett* 29:1–6. <https://doi.org/10.1177/2633366X19894598>



# Processes Required for Certification of an Engineering Equipment

Manmeet Singh<sup>1,2</sup> , Nilesh Ware<sup>2</sup> , and Ranjit Singh<sup>1</sup>

<sup>1</sup> DRDO, Delhi 110011, India

manmeet.hqr@gov.in

<sup>2</sup> Department of Technology Management, DIAT, Pune 411025, India

## 1 Introduction

Certification for an engineering system is required to attest that the system has been designed to fulfill the parameters required by the customer, and the system has been tested to demonstrate the whole range of the design parameters. The customer requires a robust product when the equipment is designed for rough terrain or when the system has to be airborne. If the equipment required is designed for lower design limits, then it will come out in certification process and the customer is informed about the limiting design parameters of the product before purchase of the product. In this way, the certification ensures that the customer is not resentful of the purchase and helps in building good relationship between the developer firm and the customer.

Design quality [1] is of paramount importance for the success of the product realization. Proving all aspects of design through extensive field testing takes additional time and larger amount of resources. The independent certification can enforce design changes to address the understanding and anticipation of the environment of use, strict adherence to FMEA/FMECA techniques [2], superior workmanship, and use of screened quality components. The independent certification will emphasize and enforce the right design practices with thorough quality assurance process. Independent certification requirements which address the design adequacy and test adequacy are performance, design for testability and maintainability, system failure analysis and failure mode analysis, design for production, design for environmental harshness, rigs and test simulators for testing, test requirement for traceability matrix, concept of operations, process control, and validation and verification. Certification results in considerable quality improvements in products resulting in much less rework and failure. It will involve initial additional efforts for planning, analysis, and testing requirements, but will lead to considerable cost and effort benefits in terms of reduced rework during trial and production stages.

Presently in India, the Design Certification Agency is CEMILAC [3, 4] and the Product Certification Agency is DGCA, CE certification, ISI, and Hallmark.

## 2 Methodology

To identify the processes of certification, a focus group discussion [5, 6] study was planned. The focus group consisted of 09 highly qualified professionals working in the field of quality management and certification. The average experience of focus group participants was 20 years. It was done in a semi-structured way and the focus group discussion lasted for 70 min. In first 10 min, the broad list of activities was presented to the group in the form of questionnaire. Then there was discussion within the group for 50 min. Finally in the last 10 min, the agreement points of the group were debriefed by the moderator. It was done in a controlled manner with targeted questions related to the certification of the product. The result is presented in Sects. 3 and 4.

## 3 Certification Processes and Involvement

Focus group had a consensus that design certification of a product can be done in two ways. One way is to start the certification process from the design stage [7] of the product. Second way is to certify the product after the design process has been completed.

### 3.1 Design Certification

Process of certification of the product by involving the certification body from the design stage is called as design certification [8]. It is an involved process. Design cycle of engineering process consists of verification of quantified qualitative requirements (QR) into system and sub-system specifications, hardware and software design, FMEA analysis, quality assurance plan, system realization, system testing and evaluation, software and testbed assessment [9]. In this, the role of certification agency is to assess robustness of design and to ensure that the design is done to meet the specification parameters.

During the conceptual design stage, the design activities to be performed by the developer are finalization of systems requirement specifications and technical specifications, preparation of system design plan and quality assurance plan, and performing quality and reliability activities like criticality analysis, quality function deployment, FMEA/FMECA, reliability apportionment, etc. Certification organization involvement is to approve all plans, approve Q&R activities, and participate in design review.

During embodiment design stage, the design activities to be performed by the developer are finalization of detailed configuration design, preparation of certification plan, preparation of qualification test plan and acceptance test plan, performing of qualification tests, identification of manufacturing agency and its Q&R assurance audit. Certification organization involvement is to approve certification plan, ascertain design adequacy and test adequacy, clearance for tests, and participation in design review.

During detailed design stage, the design activities to be performed by the developer are realization of the product, integration of subsystems, stage-wise inspection, qualification tests, and performing of Q&R activities like FRACAS and maintenance aspects. Certification organization involvement is to give clearance for tests and conduct trial readiness review, participate in design review and obtain data required for certification. Finally, certification organization approves design certification (Fig. 1).

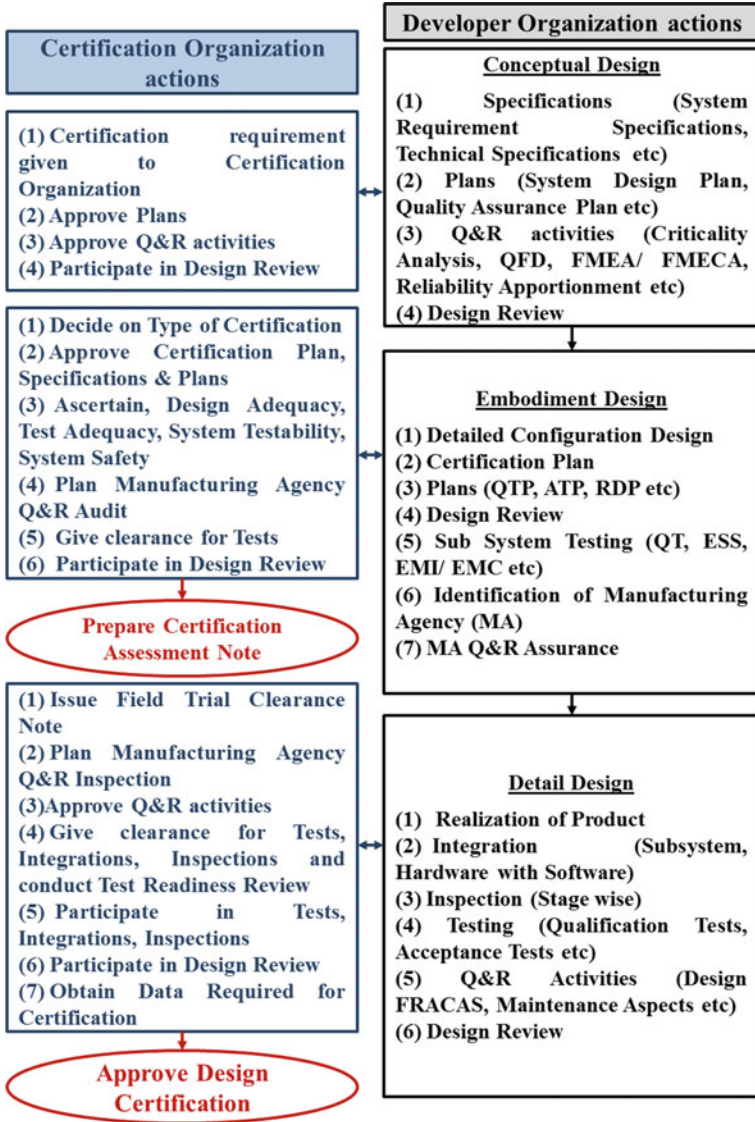


Fig. 1 Processes of design certification

### 3.2 Product Certification

Process of certification of the product after the completion of design process and after the production of first prototype is called as product certification [10]. Product certification is limited to system design validation based on scenario simulation and assessment of system robustness. The certification requisite for system validation involves the activity of testing to verify all the system requirements [11] (Fig. 2).

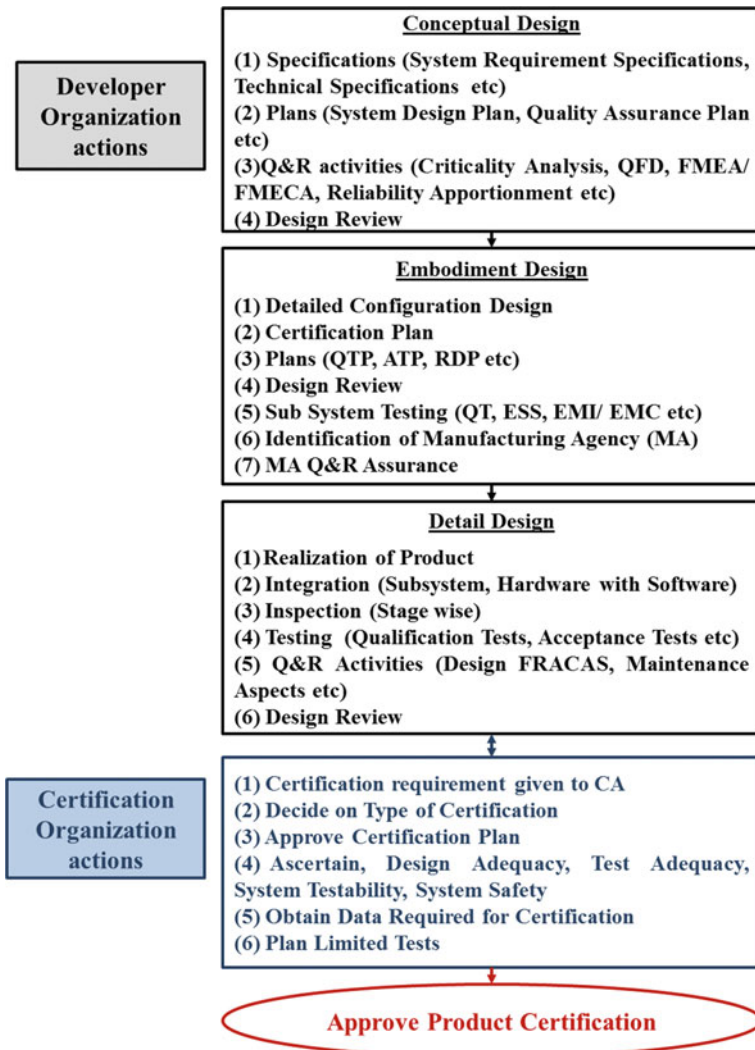


Fig. 2 Processes of product certification

## 4 Benefits

Focus group listed out the following benefits of having certification (design certification or product certification) of the product:

- (i) By certification the processes related to QR quantification, quality assurance, testing, and evaluation of product will be clearly defined and will set a benchmark for the evaluation of product.
- (ii) All relevant design standards, material standards, process standards and management standards are expected to be followed by the product during certification [12, 13].
- (iii) The quality and reliability of the product are improved by ensuring the product for design adequacy, test adequacy, system testability, and system safety.
- (iv) The investment of time and money during initial stages of the product to improve the reliability of the product will help in reducing the failure cost during the trial stage and the maintenance or product support/design improvement costs after the product have been released in market.
- (v) The economic worth of the product is increased due to certification [14].
- (vi) Certification of products will make the product more reliable and increase the acceptance of product in international market. This will encourage the industry to develop quality products and make the country self-reliant.
- (vii) The listing out of the defined procedures to be performed during different stages of the product will bring uniformity among all design centers and ensure the implementation of necessary processes like system safety analysis, QR matching, reliability improvement, FMEA, and FRACAS.
- (viii) For meeting the requirements of certification, the additional time has to be devoted during design and development of the product. This time is required to ascertain and ensure adequacies and robustness in the product. However, it will reduce the overall project completion time as the time lost in subsequent reiteration of design after non-compliance during trials will be reduced.
- (ix) The design adequacy and test adequacy of the product will improve the rate of successful performance of the products during trials and minimize the trial observations. This will result in improving brand of the product/company [15].

## 5 Conclusion

The focus group discussion of highly qualified professional has been performed in semi-structured way to gather the qualitative data. Certification increases the quality of the product to boost the customer's confidence. It helps in improving the process of the development organization and results in the design and production of a robust product. Certification ensures design adequacy and test adequacy of the product. The independent certification will emphasize and enforce the right design practices and their verification with thorough quality assurance process.

In design certification, the involvement of certification organization starts from the initial stage of the design, and the actions of certification organization are concurrently defined. In this, the developer organization can change the design based on the

inputs from the analysis of the certification organization. During conceptual stage, the potential flaws which can happen in the design of the product are addressed through important quality and reliability activities of quality function deployment (QFD) and FMEA/FMECA. QFD ensures that all the qualitative requirements of customer are converted into technical requirements and then into product specifications. FMEA/FMECA identifies all potential failures that can happen in the product and then investigates these potential failures through analysis and implementation of a corrective or preventive action. During the embodiment design and critical design, the important activities are the design adequacy and test adequacy assessment of the product by the certification organization. Design adequacy assesses the relevance of all the design parameters to the customer requirements and technical requirements. Test adequacy assesses the relevance of test data to the technical design parameters. Both test adequacy and design adequacy have important role to play to make the final product compliant to the customer requirements. The initial involvement of certification agency ensures less expenditure on design changes in case the product needs improvement in design adequacy and test adequacy.

In product certification, the involvement of certification organization begins once the prototype of the product is manufactured. The final product is evaluated through qualification and acceptance testing. Qualification testing ensures that the product will be able to withstand the environmental stresses during the actual operating environmental conditions. In this, the product is either certified or some design changes are suggested. The design changes at this stage are costly since the design has already been finalized by the developer organization and the product is in manufacturing stage. Here the scope of improvement is less unless the developer organization decides to go for redesign of the product. However, the quality rating can be provided to the product for the benefit of the customer. This will make the customer aware about the value of the product in terms of performance as well as the final cost of the product.

Certification organization has essential part to perform in ensuring the quality of the product. Benefits of certification of product are standardization of required processes, improved product quality, reduced trial cycles, reduction in life cycle cost of the product, increase in customer's confidence, enhancement of export potential, and encouragement of industry to come with quality products toward Atmanirbhar Bharat. In conclusion, it can be said that certification of all the products made in India will help the Indian Industry in capturing markets abroad and at the same time improve the experience and confidence of Indian customer in local products.

## References


1. Silvestrini RT, Burke SE (2018) The certified quality engineer handbook, 4th edn. ASQ Quality Press
2. Durivage MA (2017) The certified reliability engineer handbook, 3rd edn. ASQ Quality Press
3. Subir D, Atre VK (2002) Procedure for design, development and production of military aircraft and airborne stores DDPMAS-2002. CEMILAC
4. Prasad APVS (2021) Framework and procedure for design, development and production of military air systems and airborne stores, DDPMAS Version 1.0. CEMILAC
5. Patton MQ (2002) Qualitative research and evaluation methods. Sage Publications

6. Gill P, Stewart K, Treasure E, Chadwick B (2008) Methods of data collection in qualitative research-interviews and focus groups. *Br Dent J* 204(6)
7. Kaspar J, Vielhaber M (2018) Integrated cross-component lightweight and material-oriented development methodology—the embodiment design cycle. In: 28th CIRP design conference, May 2018, Nantes, France, *Procedia CIRP*, vol 70, pp 481–486
8. da Silva Andrade LPC, da Silva RC, Mascarenhas LAB, de Oliveira Gomes J, de Souza Marinho F (2016) Proposal of an innovative environment for supporting production scale-up, including design, prototyping, manufacturing, assembly, testing, and certification of products that require special conditions. In: 48th CIRP conference on manufacturing systems—CIRP CMS 2015. *Procedia CIRP*, vol 41, pp 177–182
9. Singh M, Nandula S (2019) Reliability improvement of single-shot device. In: Reliability, safety and hazard assessment for risk-based technologies, proceedings of ICRESH 2019, LNME, reliability, safety and hazard assessment for risk-based technologies, vol 1. Springer, pp 153–158
10. Nederlof AJ (1994) Product certification of the future. *Flow Meas Instrum* 5(2)
11. Arunachaleswaran A, Kabadwal A, Joshi R, Singh S, Prabhu M, Singh AP, Elangovan S, Sundararaj M (2020) Innovative method for the estimation of closure velocity between RAT driven drogue and IFR probe: air-to-air refueling flight trials. *Defence Sci J* 70(2):140–144
12. Terziovski M, Guerrero J-L (2014) ISO 9000 quality system certification and its impact on product and Process innovation performance. *Int J Prod Econ* 158:197–207
13. O’Neill C, Largey A (1998) The role of quality standards—accreditation in redressing asymmetry of information in healthcare markets. *Health Policy* 45:33–45
14. Ticona JM, Frota MN (2008) Assessment of the economic impact of product certification: a significant area of application of measurement. *Measurement* 41:88–104
15. Bhushan G, Madhusudan M (2019) DRDO and expectations of stakeholders. *Defence Sci J* 69(6):613–618





# Effects of Mixing Two Non-edible Biodiesels on Performance and Emission of CI Engine

H. R. Amriya Tasneem<sup>(✉)</sup> , K. P. Ravikumar, and H. V. Ramakrishna

MCE, Visveswaraya Technological University, Hassan 573202, India  
amriya.tasneem@gmail.com

## 1 Introduction

As a species, humanity has adapted remarkably well to the whims of the environment. We have been fortunate enough to inherit a world containing a ready source of fuel in the form of fossilized organic matter [1]. This buried treasure has enabled humankind to survive harsh environments and drastic climate changes. It has helped us prosper on the tide of cheap energy powering our lives [2]. Consumption of fossil fuels and their derived products is ruinous to the environment, economy, and therefore, every living being's health [3].

The supply chain dynamics of crude oil hold many countries hostage to the petroleum market's whims [4]. For example, at the time of this writing, we face a pandemic that prevents the free movement of products due to restrictions to slow the spread of infection in communities. The covid-19 pandemic currently affecting most of the world has revealed the fragile supply chains that most countries are dependent on [5]. Plant-based biodiesel is a better option among all available alternative fuels since it is renewable, biodegradable, environmentally friendly, and domestically available [6]. Hence, biodiesel is an excellent candidate for the same. Locally produced biodiesel can provide a fillip to agriculture, employment, and the local economy [7].

### 1.1 Non-edible Plant Seed Oil

Non-edible oils are considered second-generation feedstocks for the production of biodiesel [8]. An investigation regarding single biodiesel with diesel has been carried out and reported their potential to be alternative diesel fuel. Some of the non-edible seed oil sources explored by researchers are Karanja [9], Neem [10], Jatropha [11], Bilva, Cottonseed [12], Moha, Saemuruba [12]. There is minimal literature about mixing two biodiesels with diesel as a fuel blend in the CI engine. Inadequate investigations on dual biodiesel as an alternate fuel to diesel are worth reconnoitering.

The FFA content in non-edible seed oil is higher than in edible seed oil due to triglyceride molecules presence in a large percentage. Triglycerides are chemically treated to separate fatty acid esters (biodiesel) and glycerin using a two-phase catalytic reaction. The fatty acid compositions of biodiesel derived from these feedstocks presage desirable variations in their physicochemical properties. The percentage of FFA affects the fuel

properties, considerably influencing engine performance and emission characteristics [10].  $\text{NO}_x$  and  $\text{CO}_2$  in biodiesel emissions appear in higher percentages than in diesel, but the more toxic HC, CO, and smoke were lower [13]. The utilization of biodiesel in an engine is reported to reduce engine wear by 30% because of their additional lubricity [14]. Based on the literature survey, the CI engine performance with biodiesel is on the negative side compared with diesel when used in the existing engine [8].

In the present investigation, the domestically available *Pongamia pinnata* (Karanja) and Neem seed oil extracts respective methyl esters. The physicochemical properties of vegetable oil-derived biodiesels are examined, and their suitability as fuels in a diesel engine is determined. The standard test procedures are followed for testing biodiesel and validated based on the values of the ASTM D6751 standard for biodiesel [15]. The results indicated that the mixture of two biodiesel exhibited favorable improvement in their properties like calorific value and density regarding single biodiesel [16]. Fuel blends B00, B10, B20, B30, B40, and B100, are prepared for experimentation, and their composition is as listed in Table 1. Engine performance is gauged based on the amount of fuel consumed by the engine at different loading conditions while maintaining a constant speed. Furthermore, the engine performance is justified by heat generation after air-fuel combustion. Engine exhaust analyzer is used to detect emissions like  $\text{NO}_x$ , CO and HC in the exhaust gas.

**Table 1** Dual biodiesel fuel blends

Blends	Blend composition (% volume)		
	<i>Pongamia pinnata</i> biodiesel	Neem biodiesel	Diesel
B00	0	0	100
B10	5	5	90
B20	10	10	80
B30	15	15	70
B40	20	20	60
B100	50	50	0

## 2 Experimental Setup and Procedure

The production procedure of biodiesel and the properties of biodiesel blends produced are estimated to check their feasibility as fuel in an engine according to ASTM Standard testing method are discussed in this section. And the experimental setup of the CI engine test rig used for the present investigation.

### 2.1 Production of Biodiesel and Properties of Biodiesel

Oil extracted from the *Pongamia pinnata* and Neem seeds is dense as it has an FFA content of more than 4%. A two-step catalytic reaction can reduce the density of crude

seed oil [17]. The first step is to treat the crude seed oil with methanol and an acid catalyst. This pretreatment of seed oil with an acid catalyst is called esterification. Step two involves chemical modification of pretreated oil by transesterification to produce fatty acid methyl esters (FAME) or biodiesel. The FAME extracted from Pongamia Pinnata seed oil is called Pongamia methyl esters or Pongamia biodiesel. Furthermore, the esters extracted from Neem seed oil are called Neem methyl esters or Neem biodiesel.

After the transesterification process, FAME derived from plant seed oil has a much lower viscosity, making it capable of replacing petroleum [18]. The triglyceride present in oil reacts with alcohols like methanol to produce FAME, called transesterification. A base catalyst like sodium hydroxide is used to speed up the reaction to form fatty esters and glycerin [19]. Figure 1 represents a triglyceride composed of three long-chain fatty acids with a glycerin base. The number of these FFA determines the characteristics of the produced biodiesel.

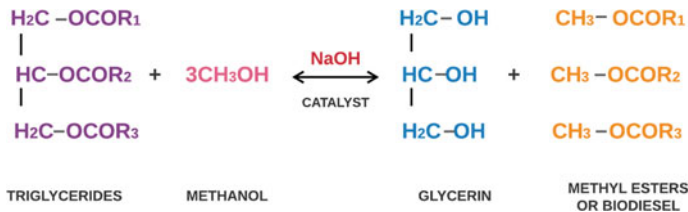


**Fig. 1** Representing chemical reaction in the transesterification process

The estimated properties of biodiesels and diesel with the help of the test methods approved by ASTM standards are listed in Table 2. The blends are prepared with different compositions of Neem biodiesel and Pongamia pinnata biodiesel with diesel. The properties of dual biodiesel blends like the flashpoint and calorific value are improved, as shown in Table 2.

## 2.2 Engine Specification

It consists of a single-cylinder CI engine, cooled using water, and computerized to capture data. An eddy current dynamometer is employed to vary the torque and achieve different loading conditions.

The test rig used for this experiment is represented in Fig. 2, and its specification is listed in Table 3. The engine was kept in running condition for around 20 min before taking the readings with every fuel blend. The exhaust gas analyzer indicates the different engine exhaust emissions.

## 3 Results and Discussion

### 3.1 Engine Performance Analysis

The analysis of the subject engine's performance is characterized based on a speed of 1500 rpm is maintained at different load conditions. A variety of fuel blends are used

**Table 2** Physiochemical properties of diesel and biodiesel with ASTM D6751 fuel standard

Fuel name	Density (kg/m <sup>3</sup> )	Flashpoint (°C)	Kinematic viscosity cSt at 40 °C	Calorific value (kJ/kg)
Pongamia biodiesel	876	178	6.72	37,000
Neem biodiesel	870	76	5.64	35,010
B00 or pure diesel	824	50	2.30	42,850
B10	828	53	2.85	41,500
B20	833	56	3.22	41,880
B30	837	58	4.37	41,120
B40	842	60	5.35	39,400
B100	873	110	6.24	36,100

to collect data relating to performance and efficiency. Fuel consumption and thermal efficiency of prepared blends were compared with diesel as a benchmark. There were three iterations of this experiment for all fuel modes to ensure accuracy, and the error bars are included while plotting the results.

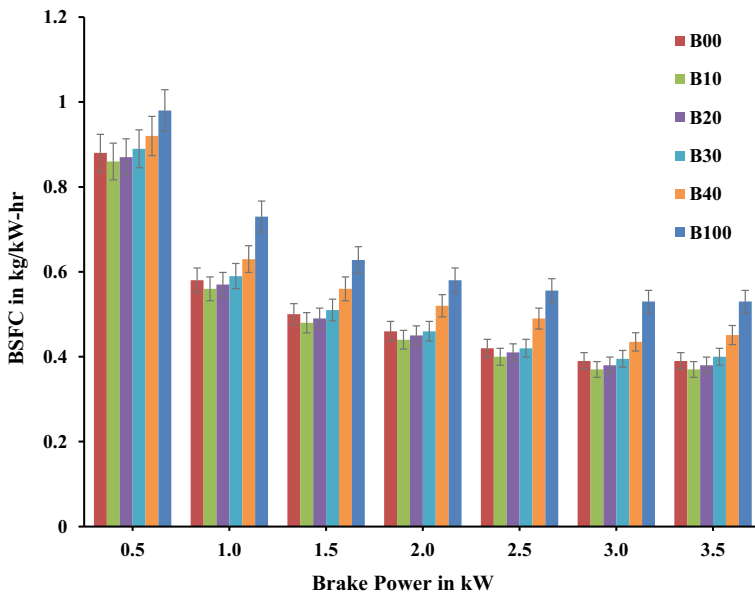
**Brake-Specific Fuel Consumption (BSFC).** Figure 3 demonstrates the impact on BSFC for the six fuel modes at all load conditions. The BSFC is higher at a lower engine load due to high engine speed and lower in-cylinder temperatures [20]. The higher in-cylinder temperature results in increased atomization of fuel and a better air-fuel mixture, thereby decreasing BSFC.

**Fig. 2** Photographic view of the test engine's rig

**Table 3** Test engine specifications

Particulars	Specifications
Make	Kirloskar
No. of cylinder	1
Bore	80 mm
Stroke	110 mm
Injection pressure	190 bars
Compression ratio	16.5:1
Dynamometer	Eddy current
Type of cooling	Water-cooled
Rated speed	1500 rpm
Rated power	3.75 kW

From Fig. 3, the BSFC decreases with an increase in engine loading and tends to stabilize for all fuel modes at maximum load. The BSFC of the CI engine for fuel blend B00 (100% diesel) was observed to be 0.39 kg/kW-hr at full load condition. The BSFC with dual biodiesel blends B10 and B20 was 0.37 kg/kW-hr and 0.36 kg/kW-hr, lower than diesel. The higher cetane number and fire point of dual biodiesel blends reduce the physical ignition delay during the combustion phase [21]. The BSFC with blend B30

**Fig. 3** BSFC for all the prepared blends versus brake power

was observed to be 0.40 kg/kW-hr, marginally higher than diesel. This might be due to the lower calorific value of the B30 blend when compared with diesel [22]. The lower energy content of the esters in biodiesel increases the BSFC of the engine.

Further, with the increase of biodiesel percentage in the fuel blends, the BSFC increases. BSFC for blends B40 and B100 was 0.45 kg/kW-hr and 0.58 kg/kW-hr, higher than diesel due to the ester's lower energy content. The dual biodiesel blend can be used in CI engine for up to 30% of diesel without any engine modifications.

**Brake Thermal Efficiency (BTE).** The impact of brake power on the BTE of an engine under all load conditions is represented Fig. 4. BTE is lower at lower loads due to higher engine speed and BSFC [23]. BTE is higher at higher loads because of the increased temperature inside the combustion chamber.

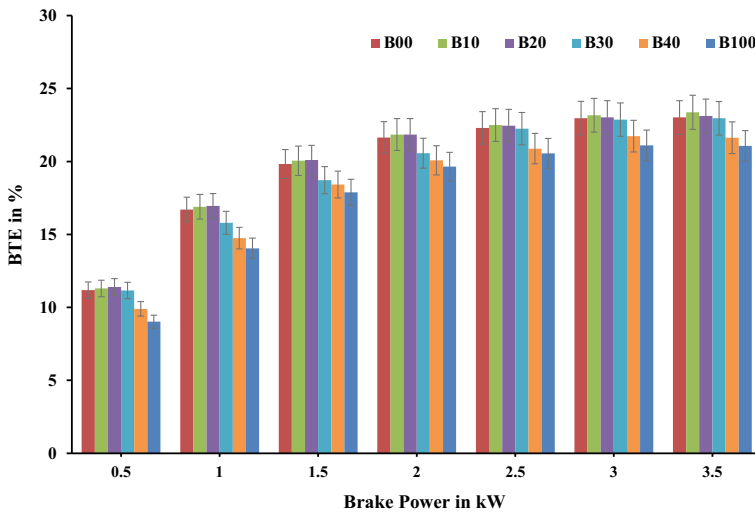


**Fig. 4** BTE for the prepared fuel blends

The BTE was 23.02% with blend B00 or diesel at full load condition. The BTE of blends B10 and B20 is 23.21% and 23.17%, marginally higher than diesel due to oxygenated biodiesel in the fuel blend. When blended with diesel, the oxygenated biodiesel enhances the fuel's complete combustion ability and increases the BTE with a drop in BSFC. The BTE of blend B30 was 22.56%, slightly lower than diesel. The BTE of blends B40 and B100 was 21.63% and 20.07%, respectively. The diesel dilution in the higher biodiesel blends results in lower energy release due to the burning of low energy biodiesel esters. Lowering the energy released after combustion will lower the in-cylinder temperature and peak pressure, causing reduced BTE [24].

### 3.2 Engine Emissions

The significant components of emissions from diesel engines such as  $\text{NO}_x$ , CO, and unburnt HC that have exited out of the combustion chamber are graphically represented for different fuel modes at various load conditions.

**$\text{NO}_x$  Emission.** The influence of brake power on the emissions of oxides of nitrogen with dual biodiesel blends is represented in Fig. 5. The graph demonstrates the presence of  $\text{NO}_x$  in the engine exhaust at different loads. The  $\text{NO}_x$  emission increases with increasing load for each dual biodiesel blend [20]. It is clear from the graph that the dual biodiesel blends tend to emit higher levels of  $\text{NO}_x$ . Higher exhaust gas temperature and oxygen in fuel with dwelling time at higher load conditions contribute to higher  $\text{NO}_x$  emissions in the blends.

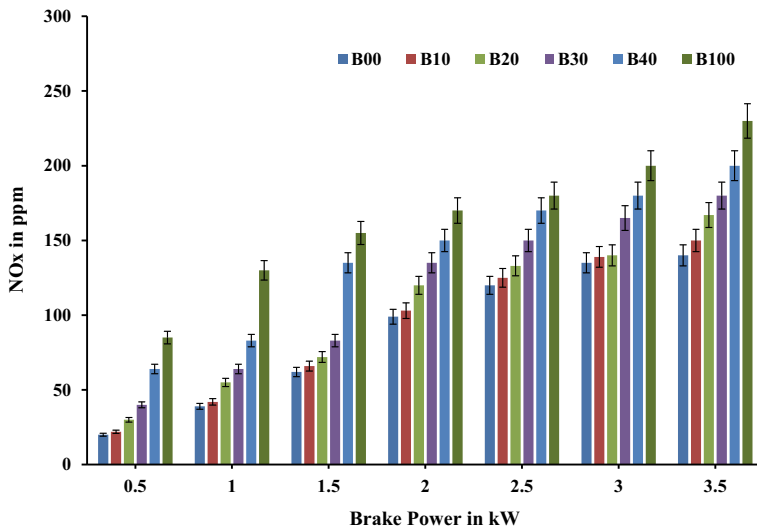


Fig. 5  $\text{NO}_x$  emissions in exhaust versus brake power

**CO Emission.** The effect of brake power deviation on carbon monoxide emission at all load condition is shown in Fig. 6. CO content present in engine exhaust increases with an increase in load conditions. An increase in engine load leads to a corresponding rise in combustion temperature and increases CO emissions. A paucity of oxygen and lowered cooling time leads to partial combustion and generates CO.

**HC Emission.** The variant brake power effect on unburnt hydrocarbon emission is as shown in Fig. 7. HC emission is directly proportional to load, brake power, and indirectly proportional to temperature and oxygen availability [16]. Longer ignition delays mean that fuel combustion time is lowered, and HC emissions display an uptick. At part-load condition, HC emissions are 55 ppm for B00 or diesel, 45 ppm for B10, 40 ppm for B20, 38 ppm for B30, 35 ppm for B40, and 37 ppm for B100. HC emission in comparison to diesel is dropped in 18.18% with B10, 27.27% with B20, 30.9% with B30, 36.36% with

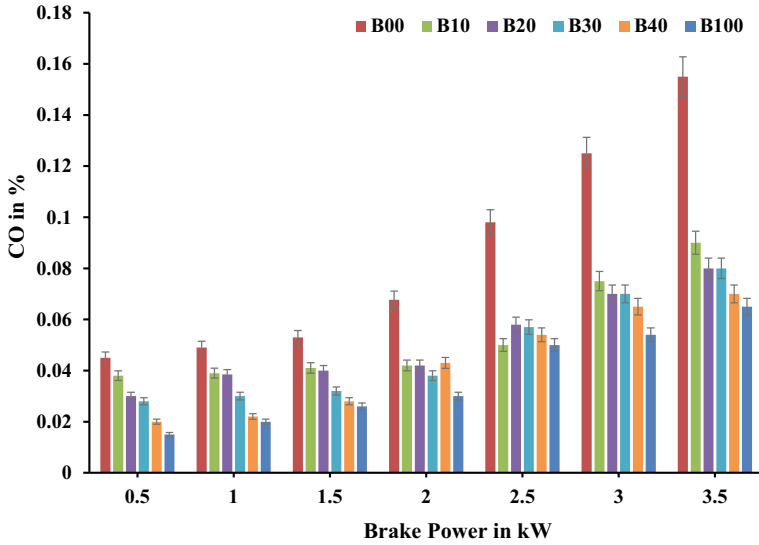


Fig. 6 Impact of CO emission with brake power

B40, 32.7% with B100. When compared with biodiesel blends, a diesel fuel exhibits a longer ignition delay.

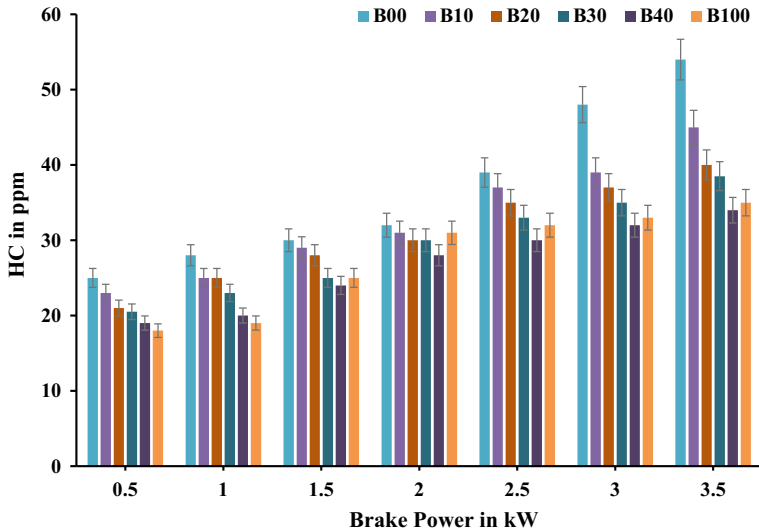


Fig. 7 Variant brake power effect on unburnt HC emission at different fuel modes



## 4 Conclusions

Dual biodiesel blends of *Pongamia pinnata*, Neem and regular diesel are used as fuel in a single-cylinder diesel engine. The results obtained are subject to analysis for their performance and emission characteristics.

- No modifications to the diesel engine were necessary to accommodate the utilization of a dual biodiesel blend.
- Properties of *Pongamia pinnata* and Neem biodiesel after chemically modified with transesterification are in the range of ASTM standards and can be used as an alternative to replacing fossil fuel.
- From the experimental analysis, dual biodiesel blends B10, B20, and B30 have BSFC and BTE values strikingly close to those of the diesel.
- The dual biodiesel blends have lesser CO and HC emissions than that diesel at all load conditions.
- The emission of NO<sub>x</sub> from dual biodiesel blends was higher than that of diesel.

From this investigation, it could be summarized that biodiesel derived from *Pongamia pinnata* and Neem oil blended with diesel has the potential to be fuel in a conventional diesel engine. Dual biodiesel can be used as a substitute to diesel in the ratio of up to thirty by volume, which is B30 could be used without significant compromise to the engine performance and emissions. It also provides the opportunity to combine the biodiesels and not limit ourselves to one feedstock of biodiesel.

## References

1. Shafiee S, Topal E (2009) When will fossil fuel reserves be diminished- Energy Policy 37:181–189
2. Asif M, Muneer T (2007) Energy supply, its demand and security issues for developed and emerging economies. *Renew Sustain Energy Rev* 11:1388–1413
3. Perera F (2017) Pollution from fossil-fuel combustion is the leading environmental threat to global pediatric health and equity: solutions exist. *Int J Environ Res Public Health* 15:16
4. Olson C, Lenzmann F (2016) The social and economic consequences of the fossil fuel supply chain. *MRS Energy Sustain* 3:E6
5. Kumar A, Luthra S, Mangla SK, Kazançoğlu Y (2020) COVID-19 impact on sustainable production and operations management. *Sustain Oper Comput* 1:1–7
6. Jeswani HK, Chilvers A, Azapagic A (2020) Environmental sustainability of biofuels: a review: environmental sustainability of biofuels. *Proc R Soc A Math Phys Eng Sci* 476
7. Biofuels S (2010) Sustainable production of. *Renew Energy* 35:1027–1032
8. Tasneem HRA, Ravikumar KP, Ramakrishna HV (2022) Performance and wear debris characteristics of karanja biodiesel and biolubricant as a substitute in a compression ignition engine. *Fuel* 319:123870. <https://doi.org/10.1016/j.fuel.2022.123870>
9. Prasada R, Suresh KV (2014) *Pongamia Pinnata* (karanja) biodiesel as an alternative fuel for diesel engine: a review. *Adv Eng Appl Sci* 4:52–61
10. Ali MH, Mashud M, Rubel MR, Ahmad RH (2013) Biodiesel from neem oil as an alternative fuel for diesel engine. *Procedia Eng* 56:625–630

11. Kawade GH, Satpute ST (2013) Jatropha biodiesel blending with diesel fuel suitable for diesel engine. In: 2013 international conference on energy efficient technologies for sustainability, ICEETS 2013:508–511. <https://doi.org/10.1109/ICEETS.2013.6533437>
12. Bobade SN, Khyade VB (2012) Detail study on the properties of Pongamia Pinnata (Karanja) for the production of biofuel. Res J Chem Sci 2. [www.isca.in](http://www.isca.in)
13. Monyem A, Van Gerpen JH (2001) The effect of biodiesel oxidation on engine performance and emissions. Biomass Bioenergy 20:317–325
14. Agarwal AK, Bijwe J, Das LM (2003) Effect of biodiesel utilization of wear of vital parts in compression ignition engine. J Eng Gas Turbines Power 125:604–611
15. Knothe G, Jürgen K, Gerpen JV (2010) The biodiesel handbook (2nd ed). Urbana, Illinois: AOCS Press. <https://doi.org/10.1201/b17510-1>
16. Srithar K, Arun Balasubramanian K, Pavendan V, Ashok Kumar B (2017) Experimental investigations on mixing of two biodiesels blended with diesel as alternative fuel for diesel engines. J King Saud Univ Eng Sci 29:50–56
17. Hassani M, Amini G, Najafpour GD, Rabiee M (2013) A two-step catalytic production of biodiesel from waste cooking oil. Int J Eng 26:563–569
18. Ramírez-Verduzco LF, Rodríguez-Rodríguez JE, del Jaramillo-Jacob AR (2012) Predicting cetane number, kinematic viscosity, density and higher heating value of biodiesel from its fatty acid methyl ester composition. Fuel 91:102–111
19. Efavi JK et al (2018) The effect of NaOH catalyst concentration and extraction time on the yield and properties of Citrullus vulgaris seed oil as a potential biodiesel feed stock. S Afr J Chem Eng 25:98–102
20. Sivakumar M, Shanmugasundaram N, Rameshkumar R, Syed Thasthagir M (2017) Effects of pongamia methyl esters and its blends on a diesel engine performance, combustion, and emission characteristics. Environ Prog Sustain Energy 36:269–276
21. Lahane DSV, Subramanian K (2012) Analysis of physical and chemical ignition delay of a diesel engine for biodiesel-diesel blend (B20) using combustion characteristics
22. Adaileh WM, Alqdah KS (2012) Performance of diesel engine fuelled by a biodiesel extracted from a waste cooking oil. Energy Procedia 18:1317–1334
23. Dhanamurugan A, Subramanian R (2013) Performance of single cylinder diesel engine with bael seed biodiesel. J Sci Ind Res 72
24. Amriya Tasneem HR, Ravikumar KP, Ramakrishna HV, Kuldeep B (2021) Ceramic materials for thermal barrier coatings in compression ignition engine for its performance evaluation with biodiesel. Mater Today Proc 46:7745–7751. <https://doi.org/10.1016/j.matpr.2021.02.274>



# The Value Research of Communication and Information Sharing in Supply Chain Management (SCM) for Enhancing the Supply Chain Performance (SCP)—A SSI Case Study

Mahesh R. Latte<sup>1</sup> and Channappa M. Javalagi<sup>2</sup>(✉)

<sup>1</sup> K.L.E. College of Engineering and Technology, Chikodi, Belgavi, India  
latthemahesh@gmail.com

<sup>2</sup> Basaveshwar Engineering College (A), Bagalkot, India  
cmjavalagi@gmail.com

## 1 Introduction to Importance of Communication and Information Sharing

An information and good communication can help to improve the consumption of the supply chain assets and the synchronization of supply chain flows to increase sensitivity and diminish cost. Even though the sharing of data can help a supply chain more, it is better to satisfy customer needs at lower cost; there is a threat in the assumption that additional data is always better. As extra information is shared across the supply chain, the complicity and expenditure of the both required infrastructure and the follow-up analysis rise exponentially. The trivial value provided by the information share, however, lessens as more and more information become obtainable. It is thus important to assess the minimum data required to complete the desired objective. Advances in information technology have transformed present business practices, communication, and information sharing is the main recourses for implementing the strategic supply chain response and making effective supply chain management (SCM).

Many companies are investing heavily in information technologies for building stronger supply chain relationships and to create value for the stakeholders. Valuable two-way communication between selling and buying firms could be differentiated as recurrent, genuine, and agreeable. The present study or value research is mainly focusing on the small-scale industries (SSIs). An effort is made to understand the gap with respect to the information sharing methods and communication channels practiced by the selected SSIs. Theoretical analysis was done, and to support it statistical analysis is also been done to understand the gaps and find out the remedies to make the maximum benefit of the available resources with respect to communication and information sharing.

## 2 Survey of Different Industries and Its Description

For our study, we have actually approached 15 small-scale industries in Gokul-Shirgoan MIDC area and Shirol MIDC industrial estate in Kolhapur, Maharashtra. Out of 15, we

have got permission in 7 SSI, namely Akhilesh industries, Kalakruti steel furniture's Pvt. Ltd., Mahalaxmi Tubes, Kamla Plastics, Mogn Machine Works (MMW), Ratnaprabha Industries (RI), and Saraswati Machine Works (SMW). The questionnaire is prepared with respect to communication, and information sharing and the meeting is fixed with the key persons in these companies for the survey. The glimpse of the survey is described below company-wise.

### **2.1 Name of the Industry: Akhilesh Industries**

Information and communication technology has been used in supply chain in progressive phase. The collaboration between companies and their supply chains achieves higher productivity. Telephone is used for orders and instructions about product and raw material procurement with local foundries. Vector flow software and B2-B software are used to communicate with customer regarding order specification, and confirmation of dispatch and inspection report is used. Personal meetings are preferred for important deals and negotiation. Nature of information shared with supplier is based on component drawings and machining specifications, material composition of castings and on the spot demands of products. As software technology is implemented, the communication becomes very easy and convenient. Within the organization, nature of information shared is CNC programs of components, raw material slip and quality assurance chart. Applied innovations for information sharing are used inside the organization. Paper tags and barcodes are used to identification of the goods.

### **2.2 Name of the Industry: Kalakruti Steel Furniture's Pvt. Ltd. (KSFPL)**

Information system and communication makes positive impact over the supply chain. As we increase level of information sharing and communication makes it easier to reach toward customer needs and make supply chain efficient. Telephones are used for taking orders and placing orders of raw material or machining-related parts or tools, E-mail is used for online business, and personal meetings are preferred for important orders or business-related activities. Nature of information shared with supplier is based on component drawings and design of the product and raw material slip and quality assurance chart is provided for giving information about the product. Nature of information shared with the organization is drawings and manufacturing instructions. Industry is not using use any new technology for communication and information sharing. For packaging and delivery, they use barcode for easy identification and handling of products.

### **2.3 Name of the Industry: Mahalaxmi Tubes**

Communication plays important responsibility in supply chain activity. The effectiveness of supply chain is dependent on co-ordination between various departments inside the firm. Telephone is used for most of the communication, and sometimes internet is used for online orders and procurement of material. Personal meetings are preferred for major orders and deals. Nature of information shared with suppliers is weight of the metal strips and their size and shape. Nature of information shared within the organization is

drawings for special designs of the pipes for furniture as per requirement. There are no applied innovations, and coding facility is used for communication. They adopted TIG welding process for welding of rolled metal strips which increases their productivity.

#### **2.4 Name of the Industry: Kamla Plastics**

Information system and communication makes positive impact over the supply chain. As we increase level of information sharing and communication makes it easier to reach toward customer needs and make supply chain efficient. Company uses telephone for collecting orders and internet to carry out online business. Important information is conveyed by personal meeting with customer regarding product and with dealers regarding material. There are no special statistical tools like X-bar, R-bar chart for analysis are used by industry. The nature of information shared with supplier is design of the product and number of quantities to be produced. The nature of information shared within the organization is design parameters and scheduling of order. They have used applied innovations for online business and coding system for shipments.

#### **2.5 Name of the Industry: Mogne Machine Works (MMW)**

Communication plays important function in supply chain activity. The competence of supply chain is dependent on co-ordination between various departments inside the firm. The major communication is done over phone. For important aspects, personal meetings are preferred for better communication and information exchange. There are no statistical tools used by organization like R-bar X-bar charts. Nature of information shared with suppliers is component drawings, raw material slips, and quality assurance chart for better co-ordination in manufacturing while process plans and manufacturing instructions are given to workers for efficient manufacturing. There are no applied innovations for business for information sharing.

#### **2.6 Name of the Industry: Ratnaprabha Industries (RI)**

Communication plays important position in supply chain activity. The effectiveness of supply chain is dependent on co-ordination between various departments inside the firm. Ratnaprabha industry uses Internet for checking the rates of the standard parts and components required for production. All the major information is conveyed via telephone. Company is not implementing any statistical tools like X-bar, R-bar charts. The nature of information shared with suppliers mainly consists component drawings, raw material slips, and quality assurance charts for better co-ordination for manufacturing. Within the industry process sheets instruction charts and CNC, VMC programs are shared with workers. For packaging of finished goods, barcodes and stickers are used to convey transportation information of batch.

#### **2.7 Name of the Industry: Saraswati Machine Works (SMW)**

In supply chain management, you will come across that communication is one of the important parts of your job. If you are communicating with your co-workers, consumers,

or customer, you will need to be a successful communicator as well. There are many advantages in having good communication skills in supply chain management. All the important information is conveyed via telephone. Personal meetings are preferred for effective communication. Company is not using any statistical tools for analysis purpose. The nature of information shared with supplier is component drawings, raw material slips and quality assurance chart. Within the industry process plans, CNC programs and machining instructions are provided to workers this prevents mistakes in machining and increases overall functionality of supply chain. CNC software like FANUC and SIEMENS is used.

### **3 Overall Analysis of the Communication and Sharing**

This value research is a work carried out for effectiveness of information sharing and communication in supply chain management, in order to increase the supply chain performance and efficiency of the organizational. A firm follows basic communication regarding orders within and outside the firm. Telephones for basic communication and digital platforms such as Internet for seeking out of materials and specifications, to make communication with long-distance vendors/customers. Personal meetings are also preferred for discussing important deals and inspection. Most of the industries are not using any statistical tools like X-bar and R-bar chart to evaluate their performance but some of the firms are using applied innovations for statistical tools like vector flow software, B2-B software which allows communication smoothly. Within the industry, there are various ways to convey information regarding orders like drawings of the component, machining specification, CNC programs, raw material slip, and quality assurance chart to communicate with the workers. Nature of information shared with the suppliers is in the form of drawings, material composition, machining specifications, and on-the-spot demands of the orders. Paper tags and barcodes are placed on the shipments to convey information regarding the product which is in bulk quantity. After theoretical analysis and brainstorming session were done with the owners of the firms, some suggestions were drawn from analysis and they are as there should be proper communication for the purchase of raw material inside the firm so that production stoppages due to the lack of raw material can be avoided. There should be proper information sharing done during the material handling of the materials to avoid excess time during logistic operations. Firms should use applied innovation for communication like B2-B software so that on-the-spot demands of the delivery can be tackled efficiently. Information of delivery dates and purchase orders should convey which promotes the business. Communication of manager with the workers plays very important in small-scale firms, it boosts the morale of the workers and increases the productivity of the firm so manager-worker communication should be there.

### **4 Industry-Wise Performance**

Sr. No.	Factors	Akhilesh industries	KSPFL	Mahalaxmi tubes	Kamla plastics	MMW	RI	SMW
1	Information sharing and methods	Telephone, internet, software, personal meetings	Telephone, internet, personal meetings	Telephone, internet, personal meetings	Telephone, internet, personal meetings	Telephone, personal meetings	Drawing, internet, telephone	Drawing, telephone
2	Statistical tools used by organization	Vector flow software, B2- B software	No	No	No	No	No	No
3	Nature of information shared with supplier	Drawing, material composition, machining specification, and on the spot demands	Drawings, raw material, slip, quality assurance chart	Weight, size, and shape of material	Design and quantity	Drawings, raw material slip, quality assurance chart	Drawings, raw material slip, quality assurance chart	Drawings, raw material slip, quality assurance chart
4	Nature of information shared within the organization	CNC programs, raw material slip, quality assurance chart	Drawings, manufacturing instructions	Drawings and designs as per requirement	Design	Drawing, instruction chart	Drawing, instruction chart, CNC-VMC programs	CNC programs, machining instruction
5	Applied innovation used for business	Yes	No	No	Online business	No	CNC, VMC	CNC
6	Information technology and coding methods	Paper tags, barcode	Barcodes	No	Yes	No	Barcode method	Box Tagging

## 5 Statistical Analysis

Descriptive statistics			
	Mean (M)	Standard deviation	Analysis “N”
IS methods	3.7143	0.69864	7
Advance tools	3.4286	0.78680	7
Communication with supplier	4.0714	0.44987	7
IS within organization	3.7857	0.63621	7
Applied innovation	3.5000	0.64550	7

Here as you observe that by the above descriptive analysis factors such as IS methods, i.e., information sharing methods plays vital role in our study.

### 5.1 Communalities

Communalities statistics		
	Initial	Extraction
IS methods	1.0000	0.860
Advance tools	1.0000	0.965
Communication with supplier	1.0000	0.656
IS within organization	1.0000	0.582
Applied innovation	1.0000	0.704

For communality, the value should be above 0.5, and through the factor analysis, you can observe that all the factors are having values above 0.5 so the factors are agreeable.

### 5.2 Total Variance Explained



Total variance explained						
Components	Initial Eigen values			Extraction sums of squared loadings		
	Total ( <i>T</i> )	Percentage (%) of variance	Cumulative percentage (%)	Total ( <i>T</i> )	Percentage (%) of variance	Cumulative percentage (%)
1	3.767	75.331	75.331	3.767	75.331	75.331
2	0.786	15.717	91.048			
3	0.370	7.393	98.441			
4	0.076	1.529	99.970			
5	0.001	0.030	100.000			

The percentage (%) variance obtained after the analysis are the equivalent factors which are important in our factor analysis (Fig. 1).

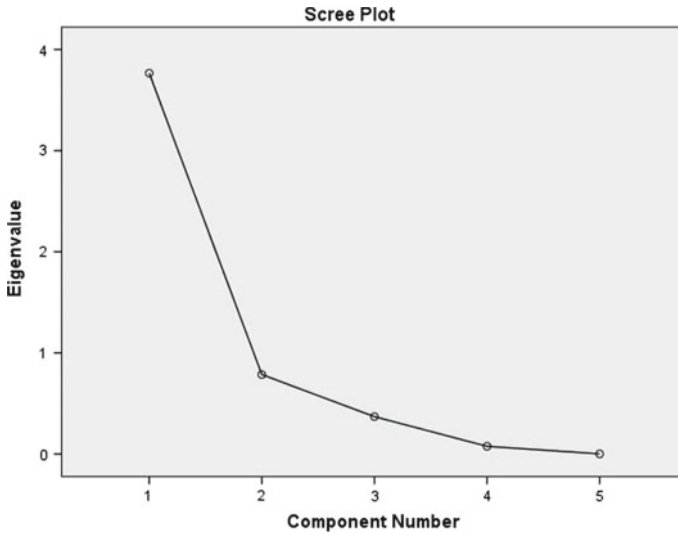


**Fig. 1** Screen plot of factors

A screen plot demonstrates the eigenvalues associated with factors. Here we can visually make out the factors variability in the data. The eigenvalues below 1.0 are insignificant, and above 1.0 is the most significant factor to be considered for improvements.

## 6 Conclusion

The current value research is carried out with a view to improve the supply chain performance (SCP) in small-scale industries (SSI) with respect to information sharing and communication. Here the theoretical and statistical analyses about communication and information sharing in small-scale industries in Kolhapur area is done as a case study, and from the study, it is evident that proper implementation of informing sharing (IS) methods will enhance the supply chain performance (SCP) in small-scale industries (SSI).



# Implementing Mahalanobis Taguchi System in Classification of Air Quality Data

Dattaraj Gawas<sup>(✉)</sup> and Suraj Rane

Department of Mechanical Engineering, Goa College of Engineering, Farmagudi, Goa 403401,  
India

dattarajgawas88@gmail.com

## 1 Introduction

Air pollution has been a long-term consequential health hazard. Air pollution is a significant risk factor to human health. Authors in [1, 2] give insights into the detrimental effects of air pollution on the environment as well as on human health. In the 1970s, air pollution began to be looked upon as the primary cause of respiratory diseases. World Health Organization (WHO) (1999) emphasized the need to monitor air quality for gauging the influence of air pollution on human well-being [3]. Over the years, technology and research advancement have developed public awareness and public health concern which has compelled individual countries to take substantial steps in controlling air pollution to safeguard the population against the probable health implications.

The prerequisite to oversee the quality of air of a region is the collection of air quality data for which stations are set up for measuring the ambient concentrations of various pollutants. However, just the provision of raw data would make it difficult for the general public to recognize the air quality in their surroundings. There is a need to put up information regarding air quality in simple terms so that it is easily understood. Air quality standards are thus laid down by individual countries, and a term Air Quality Index (AQI) is introduced.

AQI communicates a value that determines the quality of air. In general, AQI classifies air quality depending on the severity of pollution. Lower AQI represents cleaner air. The ambient concentrations of individual pollutants are measured, and corresponding AQI is calculated. Various methods have been proposed for the calculation of AQI universally. However, a globally accepted method ceases to exist which will consider the combined effect of all the pollutants in determining the air quality for a place. This paves a way for multivariate methodologies which would consider the contribution of all the necessary pollutants and provide a better result.

The Mahalanobis Taguchi System (MTS) is one such method which may be used. MTS uses the concept of distinguishing one group from another. The first group is the healthy or the normal group for which MTS carries out pattern recognition by studying its parameters. For the second group which is the unhealthy or the abnormal group, the veering of these parameters is identified and learning from it, a scale can be generated to distinguish the healthy and the unhealthy items with a certain threshold value. MTS

also uses the concept of orthogonal arrays and signal-to-noise ratio (S/N Ratio) for the selection of the handiest parameters that would significantly contribute to pattern recognition. S/N ratio also proves useful in measuring the accuracy of the method. A new item can now be accordingly classified as healthy or unhealthy elicited from its parameter values. The concept of MTS has been explained by authors in [4, 5]. The peculiar feature of MTS is the selection of the most significant variables contributing to the result. This would reduce the time as well as the cost of analysis. In this paper, in furtherance of the air quality data collection, the classification of air quality was done using MTS.

## 2 Air Quality Index (AQI)

The AQI has turned out to be an important tool for the dissemination of information regarding air quality. It generally exhibits a value between 1 and 500. Also, there are AQI categories demarcated to set forth a clear picture of air quality. The fundamental objective of AQI was to convert the ambient pollutant concentrations into a single number that would elucidate the air quality in a region. Several techniques were developed all over the world to determine AQI. Authors in [6] have reviewed the major air quality indices globally. In 1999, the USEPA proposed a method to calculate the AQI [7]. Bishoi et al. [8] presented a study of AQI based on factor analysis in comparison with the US EPA method. Each method makes use of its aggregation function in calculating AQI by involving a variety of pollutant combinations.

The most sought-after method is the one by US EPA [7]. The AQI has been defined considering five common pollutants. The ambient concentrations of individual pollutants are measured, and corresponding sub-indices are calculated for each of these pollutants. A linear interpolation Eq. (1) was used to calculate the sub-indices for individual pollutants [7].

$$I_p = \frac{I_{hi} - I_{lo}}{BP_{hi} - BP_{lo}} \times (C_p - BP_{lo}) + I_{lo} \quad (1)$$

where

- $I_p$  Sub-index for a pollutant.
- $C_p$  Pollutant concentration.
- $BP_{hi}$  Higher breakpoint concentration.
- $BP_{lo}$  Lower breakpoint concentration.
- $I_{hi}$  AQI for  $BP_{hi}$ .
- $I_{lo}$  AQI for  $BP_{lo}$ .

The breakpoints have been established per the guidelines set by National Ambient Air Quality Standards (NAAQS). The worst sub-indices of a pollutant would reflect the overall AQI which can be expressed using Eq. (2) for  $p$  pollutants [7].

$$AQI = \text{Max}(I_p) \quad (2)$$

A similar method was floated by the Indian Government in the form of the National Air Quality Index (NAQI) in 2014 [9]. The proposed AQI considers eight pollutants. Sub-indices are calculated for each of these pollutants depending on the ambient concentration of each pollutant again by using the linear segmented principle demonstrated in Eq. (1). The categorization of AQI is made based on the values of sub-indices for each pollutant. Authors in [10] have contributed in defining Air Quality Index for India and the scientific evaluation of air quality standards. The ambient concentration breakpoints for each pollutant required for the calculation of sub-indices have been presented in the NAQI report [9].

In furtherance to the calculation of sub-indices for individual pollutants, they need to be aggregated in a simple or weighted form for which various methods can be used. However, two characteristics of the index (ambiguity and eclipsing) pose a challenge in the case of additive and multiplicative indices. To avoid this, a maximum operator method is employed as it eliminates ambiguity and eclipsing. The AQI for the region is determined using Eq. (2) as used in the US EPA method.

The above method infers that while determining the AQI for a particular place only the contribution of the most prominent pollutant will be considered and will rule out the synergistic effect of other pollutants in the same region. This motivates other multivariate methodologies to be applied in the calculation of AQI.

### 3 Mahalanobis Taguchi System (MTS)

The MTS is a methodology used for the diagnosis of multivariate data. It helps to make a decision based on multivariate input characteristics. The basic concept of MTS is that it distinguishes one group from another. It requires two known groups of data, namely the normal and the abnormal. For example, a person's health can be classified into healthy and ill. The reference group with healthy data set forms the normal group. We can expect that most of the input characteristics for all the persons in the healthy group would be similar, whereas the input characteristics for the unhealthy group would largely vary if compared to the healthy group. MTS calculates the Mahalanobis distance (MD) using the data and averages the pattern distance for the healthy group. MD is then calculated for the unhealthy group and is expected to be higher than that for the healthy group. Using the Mahalanobis distance, MTS generates a measurement scale for the multivariate data based on the degree of abnormality. It is important to note that the items in the healthy, as well as the unhealthy group, are a part of the same population, and the variation in pattern is the only aspect by which they are separated. Using the generated scale, a decision can hence be taken for a new entry and it may be appropriately grouped. The scale is considered to be good if the variation of MD for the unhealthy items is large in comparison with the MD of the healthy group. MTS uses the concept of orthogonal arrays and S/N ratios to select only the useful variables, hence reducing the time and cost of the analysis. MTS has an advantage in that the correlation between the variables is considered during the measurement. For example, the illness of a patient may be due to several factors which are interdependent of each other. This interdependency between the variables is removed by MTS.

MTS has been widely used in cases where a decision needs to be taken based on some input signals given to the system. Several applications in business process forecasting, health care, medical treatment, mechanical industry, electrical industry, chemical industry, space industry, software industry, and government department along with case-studies related to the same have been discussed by Taguchi and Rajesh [4] and Taguchi, Chowdhury, and Wu [5]. Other listed applications include patient monitoring, manufacturing, fire detection, earthquake forecasting, weather forecasting, automotive collision prevention system, and business applications. MTS has widely been used in quality [11, 12], inspection [13, 14], data mining [15], failure prediction [16], prediction of financial crises [17], optimal feature selection [18–20], optimization [21, 22], process control [23–25], fault classification [26, 27] and diagnosis [28–32]. In the next section, the detailed methodology of the application of the MTS in determining the air quality has been discussed.

## 4 MTS Applied to Air Quality Data

To apply MTS to air quality, there is a requirement of data that will form the normal or the healthy group. In this case, the normal group would comprise the data of a clean environment. The data will include the ambient pollution concentration of various pollutants which are responsible for the air quality in a particular region. Similarly, data needs to be collected to form the abnormal or the unhealthy group. The unhealthy group will comprise data collected from polluted cities for the same pollutants considered in the healthy group. MTS will create a reference multidimensional measurement scale by calculating the Mahalanobis distance (MD) for the normal group. This will be considered as the reference for the measurement and is termed as Mahalanobis space (MS). MTS would now measure the variation in the pattern of the unhealthy group with respect to the MS. Subsequently, the use of orthogonal arrays and S/N ratios would help in the selection of the most critical pollutants.

### 4.1 Data Collection

In this work, air quality data at various stations in India is obtained from the public repository [33]. Data consists of the ambient concentrations of seven pollutants at each station. The seven pollutants include PM<sub>10</sub>, PM<sub>2.5</sub>, NO<sub>2</sub>, SO<sub>2</sub>, CO, O<sub>3</sub>, and NH<sub>3</sub>. Initially, four clean stations were chosen. For each station, fifty data sets were collected comprising of the ambient pollutant concentrations of each of the seven pollutants for the year 2020. A total of two hundred data sets formed the healthy or the normal group. Data from five different polluted stations for the same seven pollutants was also collected during the year 2020. Three data sets for each polluted station adding up to a total of fifteen data sets formed the unhealthy or the abnormal group. Table 1 lists the various stations whose data was used for analysis.

### 4.2 Methodology

The MTS which is a methodology for diagnosis and forecasting of multivariate data can be seen as an amalgam of Mahalanobis distance (MD) and Taguchi's design of

**Table 1** List of clean and polluted stations used for data collection

Clean stations	Polluted stations
Lumpyngngad, Shillong—Meghalaya PCB	Indirapuram, Ghaziabad—UPPCB
Model Town, Patiala—PPCB	Alipur, Delhi—DPCC
Vidayagiri, Bagalkot—KSPCB	Anand Vihar, Delhi—DPCC
Plammoodu, Thiruvananthapuram—Kerala PCB	Ashok Vihar, Delhi—DPCC
	Loni, Ghaziabad—UPPCB

experiments. MTS can be applied to a multidimensional system consisting of identified variables that exhibit information about the healthiness of a system. A healthy or normal group is identified, and MD is calculated for this group. This becomes the reference and is termed Mahalanobis space (MS). A measurement scale now needs to be generated to segregate any items falling outside the MS. This is accomplished by identifying a known set of abnormal and calculating MD for the unhealthy group. The unhealthy group comprises abnormal data or the data that falls outside the MS. The scale can be validated if values of severity in the abnormalities are known. The scale is considered adequate if the value of MD is higher for unhealthy conditions. The next phase introduces the utilization of orthogonal array (OA) and signal-to-noise ratios (S/N ratios) for the selection of critical variables. OA helps in recognizing the effect of each variable in the overall response by reducing the number of runs. OA uses the presence and absence of each variable, thereby helping to understand the effect of individual variables. S/N ratios play an important role in the selection of the most useful variables. A new item can accordingly be grouped by calculating its MD for the selected variables. The application of MTS to air quality data has been discussed in four stages namely, Construction of Mahalanobis space, (MS), validation of MS, selection of useful variables, and forecasting and future processing. Figure 1 schematically depicts the various steps involved in each stage.

**Construction of Mahalanobis Space.** The Mahalanobis space (MS) is the reference group containing mean, standard deviation, and correlation structures of the normal group. The construction of MS includes identification of variables and data collection of the normal group, standardization of the data, and calculation of MDs for the normal group. In this study, seven pollutants defining the quality of air were identified and data for these pollutants at four clean stations listed in Table 1 were collected. Fifty data points were collected at each station totaling two hundred data points in the normal group. The data was then standardized using Eq. (3).

$$X_{ij} = \frac{X_{ij} - \mu_j}{\sigma_j} \tag{3}$$

where

- $i = 1, 2, \dots, 200$  denotes the number of data points.
- $j = 1, 2, \dots, 7$  denotes the various pollutants.

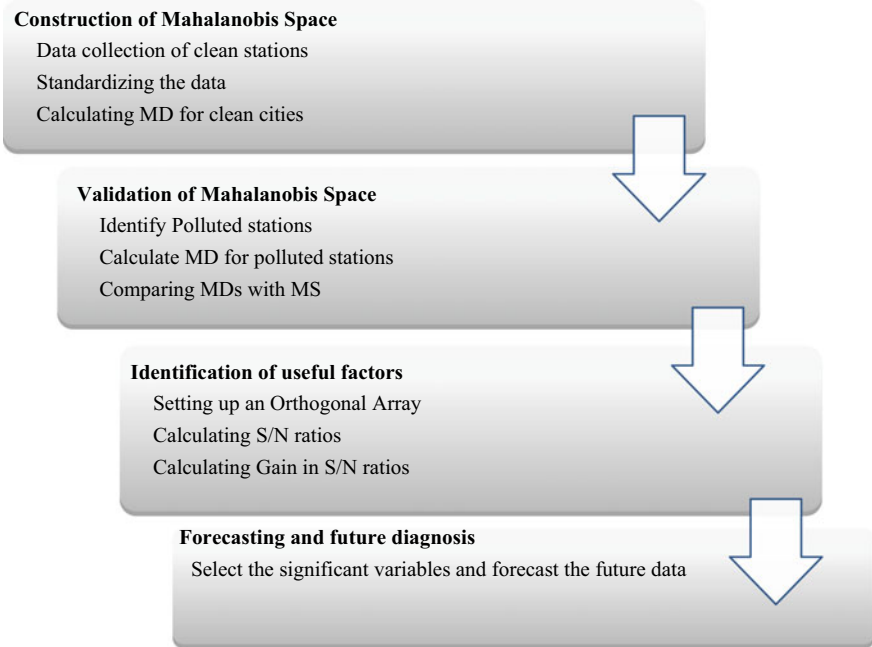


**Fig. 1** Methodology for MTS applied to air quality data

$\mu_i$  mean of the  $j$ th pollutant.  
 $\sigma_i$  standard deviation of the  $j$ th pollutant.

Next, the MDs for the items in the normal group are then calculated using Eq. (4).

$$MD = \left(\frac{1}{k}\right) X_{ij}^T C^{-1} X_{ij} \tag{4}$$

where

- $X_{ij}$  Standardized vector obtained by Eq. (3).
- $X_{ij}^T$   $X_{ij}$  Transpose.
- $C^{-1}$  Inverse correlation matrix.
- $k$  number of pollutants.

The average  $MD_i$  value for all the two hundred data points was obtained as 0.9953. Authors in [34] explicated that the marginal distribution of MD is associated with beta distribution and has an average value given by  $(m - 1)/m$ , where  $m$  corresponds to the number of normal items in the MS. As two hundred data points were considered, the expected value of average MD would be 0.995 and not unity. MS is, however, called unit space as it averages the pattern of the normal group and is expected to have zero points and unit distance.



**Validation of Mahalanobis Space.** To validate the MS, the unhealthy data is identified. In this paper, the unhealthy data comprised of fifteen data points collected from five polluted stations listed in Table 1. The MDs for abnormal items are computed using Eqs. (3) and (4). It is important to note that during this calculation, reference parameters of the normal group are used. This is because the abnormality of the unhealthy data is measured keeping the normal group as reference. It may also be noted that the unhealthy group is a part of the same population and differs only with respect to the values of variables. The Mahalanobis scale is justified and considered to be good if the MDs for the unhealthy items are much higher than the MDs for healthy items. Figure 2 confirms the considerable variation of the MDs for healthy and unhealthy items, and the MS is therefore validated. The maximum and minimum values of the MD for the healthy group were found to be 2.832 and 0.378, respectively, while that of the unhealthy data was 9.17 and 3.55, respectively. The same can also be seen in Fig. 2, and it is worth noting that there is a disassociation between the MDs of the healthy and the unhealthy groups; however, this may not be the case every time and overlap can be expected between the two groups.

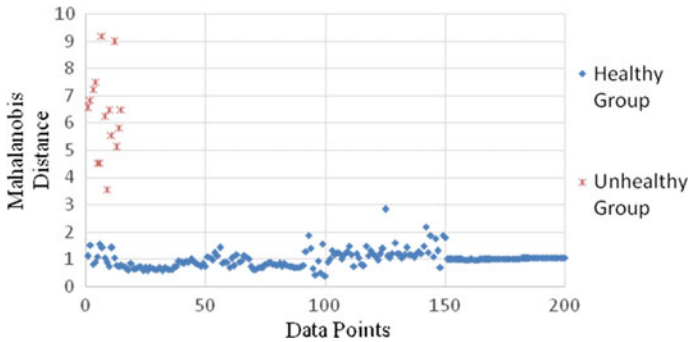


**Fig. 2** Validation of Mahalanobis space

**Identification of Useful Variables.** In this stage, OA and S/N ratios are used to identify and select the most useful variables. An OA provides various combinations of the variables to explore the effect of each variable in the response by minimizing the experimental runs. In MTS, the columns of the OA comprise the variables while each row of the matrix corresponds to each experimental run. A two-level OA is selected, the lower level signifying the exclusion of a particular variable while the higher level corresponding to the inclusion of the variable in the experimental run. In this paper, there were seven pollutants, and therefore, the L8 (27) orthogonal array was used. MD values are then calculated for all the combinations of the L8 OA. S/N ratios for each run of the OA are also computed. Taguchi and Rajesh [10] have discussed the various types of S/N ratios which can be used for the selection of useful variables. In this study, it was noticed in Fig. 2 that higher levels of abnormality resulted in higher MD, and therefore, larger the better S/N ratios were calculated for each run of the orthogonal array using Eq. (5). Table 2 presents the L8 orthogonal array along with S/N ratio associated with each run.

Level 1 for a pollutant represents the absence of the pollutant in the run while level 2 represents its presence.

$$S/N \text{ Ratio} = -10 \log_{10} \left[ \left( \frac{1}{t} \right) \sum_{i=1}^t \frac{1}{MD_i} \right] \tag{5}$$

**Table 2** L<sub>8</sub> orthogonal array with S/N ratios corresponding to each run

L <sub>8</sub> orthogonal array								S/N ratio
Run	PM 10	PM 2.5	NO <sub>2</sub>	O <sub>3</sub>	CO	SO <sub>2</sub>	NH <sub>3</sub>	
1	1	1	1	1	1	1	1	N.A.*
2	1	1	1	2	2	2	2	13.69263
3	1	2	2	1	1	2	2	17.07332
4	1	2	2	2	2	1	1	14.60914
5	2	1	2	1	2	1	2	13.91696
6	2	1	2	2	1	2	1	16.18289
7	2	2	1	1	2	2	1	16.68571
8	2	2	1	2	1	1	2	13.84592

\* The levels of all the variables in this run are 1, and therefore, the S/N ratio for the run was not calculated

where  $t$  = number of unhealthy conditions.

For every pollutant, the mean S/N ratio is computed at both levels. The S/N ratio for a higher level for a particular pollutant would comprise the average S/N ratio of all experimental runs of the OA, wherein the pollutant has been included. Similarly, the S/N ratio for a lower level of a pollutant will represent the average S/N ratio for all runs of the OA, wherein the particular pollutant has been excluded. The ‘gain’ in the S/N ratio for a pollutant is the difference between the average S/N ratio for the high level of the pollutant and that for the low level of the pollutant. The gain in the S/N ratio is used to identify the most critical pollutants. A positive gain indicates that the particular pollutant is useful while a negative gain would indicate that it is not. Figure 3 depicts the mean S/N ratio for both levels of the pollutants.

A negative slope of the curve would mean a greater S/N ratio for the high level of a pollutant. This represents positive gain. The gain would be negative if the case is the opposite. The variable demonstrating negative gain will contribute negatively to the pattern recognition in MTS, and these variables are not considered for analysis. It can be seen in Fig. 3 that four pollutants contributed positively to the recognition. This signifies that these pollutants play a better role in the classification of air quality as compared to the others. Therefore, the negatively contributing variables can be removed for better pattern recognition in the future.

**Forecasting and Future Diagnosis.** The measurement scale will have to be reconstructed using only the selected variables in the previous stage. Any new entry can now

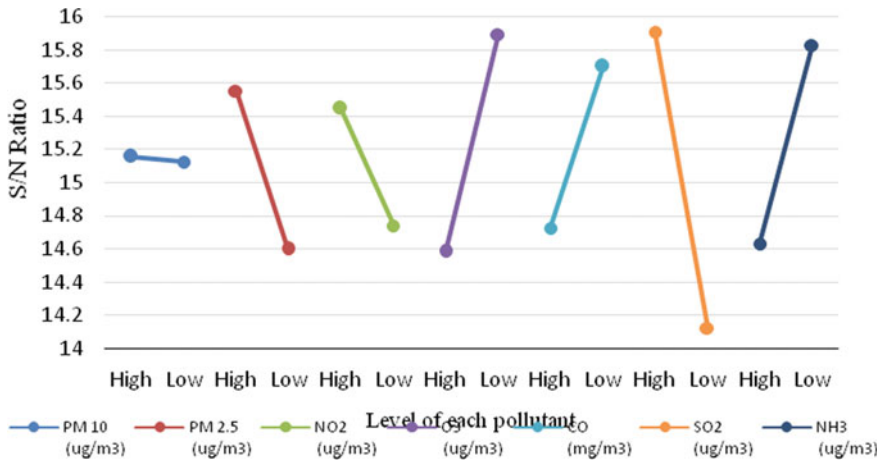


**Fig. 3** Mean S/N ratio for both levels of each pollutant

be grouped into either clean or polluted based on its computed MD. However, there may be an overlap in the MDs calculated for the clean and polluted stations. A threshold, therefore, needs to be determined to classify the new entry. Taguchi and Rajesh [4] recommended the use of a quadratic loss function to determine the threshold. The threshold can also be seen as an error rectifier for the classification as there may be a few data outliers involved. However, Taguchi et al. [5] have proposed other methods such as the bisection algorithm to determine the threshold. An MD higher than the threshold for the new entry would mean the item is abnormal and vice-versa.

### 4.3 Result Discussion

The above-made calculations imply that MTS can successfully be applied in the classification of air quality data. The average  $MD_i$  value for the normal group obtained was 0.9953 and very close to the expected value which is 0.995. This infers that MTS has been successful in being able to average the pattern of the normal group. The separation between the MDs of the healthy and the unhealthy group validates the use of MTS in the classification of air quality data. From the calculations of SN ratios, it can be concluded that the prominent pollutants resulting in pollution at the studied region are P10, PM<sub>2.5</sub>, NO<sub>2</sub>, and SO<sub>2</sub>. The highest gain can be seen in SO<sub>2</sub> and PM<sub>2.5</sub>. This indicates that the levels of these pollutants are quite low in clean areas and drastically increase in polluted areas. It is important to note that the pollutants selected by MTS may not be the only ones critically affecting the environment but controlling these pollutants would help in improving the air quality drastically in comparison with the clean stations selected. The variables O<sub>3</sub>, CO, and NH<sub>3</sub> contribute negatively to the pattern recognition which implies that the values of the ambient concentrations of these pollutants do not exhibit significant changes in clean or polluted areas.

## 5 Conclusion

This paper presents the effective application of MTS in determining the air quality for a particular region. MTS also has scope in continuous monitoring of the air quality data. The MTS methodology provides a more logical interpretation in determining the air quality in comparison with the methodologies presently adopted as MTS considers the contribution of all the prominent pollutants in that particular area rather than determining the air quality based on just the single largest pollutant.

The useful feature selection aspect of MTS can help in figuring out the most critical pollutants, and focusing on the control of these specific pollutants can help the improvement of the quality of air more effectively which can turn out to be beneficial to society.

Each geographical area is subjected to varying conditions and therefore having a solitary standard for all would not be ideal. MTS can play an important role in such a situation, wherein the air quality for a particular region can be classified in comparison with the areas in and around the same geographical location. The pollution levels of the region can be determined in comparison to the clean areas in its vicinity. In the future, MTS may be thought of being applied in a smaller region for the classification of air quality locally. This would nullify the effect of change in conditions with respect to the geographical location.

**Acknowledgements.** The contributions of the agencies Central Pollution Control Board, Delhi Pollution Control Committee, State Pollution Control Boards of the States, System of Air Quality and Weather Forecasting and Research in providing the data are greatly appreciated.

## References

1. Manisalidis I, Stavropoulou E, Stavropoulos A, Bezirtzoglou E (2020) Environmental and health impacts of air pollution: a review. *Front Public Health* 8(14)
2. Bernstein J, Alexis N, Barnes C, Bernstein L, Nel A, Peden D, Diaz-Sanchez D, Tarlo S, Williams P (2004) Health effects of air pollution. *J Allergy Clin Immunol* 114(5):1116–1123
3. World Health Organization (1999) Regional Office for Europe. Monitoring ambient air quality for health impact assessment. <https://apps.who.int/iris/handle/10665/107332>
4. Taguchi G, Rajesh J (2000) new trends in multivariate diagnosis. *Sankhyā Indian J Stat Ser B* (1960–2002) 62(2):233–248
5. Taguchi G, Chowdhury S, Wu Y (2002) *The Mahalanobis—Taguchi system*, International Edition. McGraw-Hill, Asia
6. Kanchan K, Gorai A, Goyal P (2015) A review on air quality indexing system. *Asian J Atmospheric Environ* 9(2):101–113
7. United States Environment Protection Agency (1999) Guideline for reporting of daily air quality—air quality index (AQI) EPA-454/R-99-010. <https://www.epa.gov/>
8. Bishoi B, Amit Prakash A, Jain V (2009) A comparative study of air quality index based on factor analysis and US-EPA methods for an urban environment. *Aerosol Air Qual Res* 9(1):1–17
9. National Air Quality Index Report, Central Pollution Control Board Homepage. <https://cpcb.nic.in>. Last accessed 02 Nov 2021

10. BeigG (2010) Scientific evaluation of air quality standards and defining air quality index for India, research report number RR-127 Indian Institute of Tropical Meteorology, Pune, India Ministry of Earth Sciences, Govt. of India
11. Wang H, Huo N, Li J, Wang K, Wang Z (2018) A Road quality detection method based on the Mahalanobis-Taguchi system. *IEEE Access* 6:29078–29087
12. Khanzode V, Maiti J (2008) Implementing Mahalanobis-Taguchi system to improve casting quality in grey iron foundry. *Int J Prod Qual Manag (IJPQM)* 3(4)
13. Yang T, Cheng Y (2010) The use of Mahalanobis-Taguchi system to improve flip-chip bumping height inspection efficiency. *Microelectron Reliab* 50(3):407–414
14. Huang JCY (2010) Reducing solder paste inspection in surface-mount assembly through Mahalanobis-Taguchi analysis. *IEEE Trans Electron Packag Manuf* 33(4):265–274
15. Huang C, Hsu T, Liu C (2009) The Mahalanobis-Taguchi system—neural network algorithm for data-mining in dynamic environments. *Expert Syst Appl* 36(3)Part 1:5475–5480
16. Rai B, Chinnam R, Singh N (2008) Prediction of drill-bit breakage from degradation signals using Mahalanobis-Taguchi system analysis. *Int J Ind Syst Eng* 3(2):134–148
17. Lee Y, Teng H (2009) Predicting the financial crisis by Mahalanobis-Taguchi system—examples of Taiwan’s electronic sector. *Expert Syst Appl* 36(4):7469–7478
18. Reséndiz-Flores EO, Navarro-Acosta JA, Hernández-Martínez A (2020) Optimal feature selection in industrial foam injection processes using hybrid binary particle swarm optimization and gravitational search algorithm in the Mahalanobis-Taguchi system. *Soft Comput* 24:341–349
19. Reséndiz E, Rull-Flores C (2013) Mahalanobis-Taguchi system applied to variable selection in automotive pedals components using Gompertz binary particle swarm optimization. *Expert Syst Appl* 40(7):2361–2365
20. Cudney EA, Paryani K, Ragsdell KM (2008) Identifying useful variables for vehicle braking using the adjoint matrix approach to the Mahalanobis-Taguchi system. *J Ind Syst Eng (JISE)* 1(4):281–292
21. Reséndiz E, Moncayo-Martínez L, Solís G (2013) Binary ant colony optimization applied to variable screening in the Mahalanobis-Taguchi system. *Expert Syst Appl* 40(2):634–637
22. Pan JN, Pan J, Lee C (2009) Finding and optimizing the key factors for the multiple-response manufacturing process. *Int J Prod Res* 47(9):2327–2344
23. Sikder S, Panja SC, Mukherjee I (2017) An integrated approach for multivariate statistical process control using Mahalanobis-Taguchi system and Andrews function. *Int J Qual Reliab Manag* 34(8):1186–1208
24. Sikder S, Mukherjee I, Panja SC (2020) A synergistic Mahalanobis-Taguchi system and support vector regression based predictive multivariate manufacturing process quality control approach. *J Manuf Syst* 57:323–337
25. Dasgupta T (2009) Integrating the improvement and the control phase of six sigma for categorical responses through application of Mahalanobis-Taguchi system (MTS). *Int J Ind Syst Eng* 4
26. Taiwo A, Cudney E (2015) Mahalanobis-Taguchi system for multiclass classification of steel plates fault. *Int J Qual Eng Technol* 5(1):25–39
27. Jin X, Chow T (2013) Anomaly detection of cooling fan and fault classification of induction motor using Mahalanobis-Taguchi system. *Expert Syst Appl* 40(15):5787–5795
28. Shakya P, Kulkarni M, Darpe A (2015) Bearing diagnosis based on Mahalanobis-Taguchi-Gram-Schmidt method. *J Sound Vib* 337:342–362
29. John B (2014) Application of Mahalanobis-Taguchi system and design of experiments to reduce the field failures of splined shafts. *Int J Qual Reliab Manag* 31(6):681–697
30. Soylemezoglu A, Jagannathan S, Saygin C (2010) Mahalanobis Taguchi system (MTS) as a prognostics tool for rolling element bearing failures. *ASME J Manuf Sci Eng* 132(5)

31. Soylemezoglu A, Jagannathan S, Saygin C (2011) Mahalanobis-taguchi system as a multi-sensor based decision making prognostics tool for centrifugal pump failures. *IEEE Trans Reliab* 60(4):864–878
32. Wang Z, Lu C, Wang Z, Liu H, Fan H (2013) Fault diagnosis and health assessment for bearings using the Mahalanobis-Taguchi system based on EMD-SVD. *Trans Inst Meas Control* 35:798–807
33. Central Pollution Control Board. <https://app.cpcbcr.com/ccr/#/caaqm-dashboard-all/caaqm-landing>
34. Tracy N, Young J, Mason R (1992) Multivariate control charts for individual observations. *J Qual Technol* 24(2):88–95



# Antimicrobial Adhesive Prepared by Incorporation of *Arnebia nobilis* into Silicone-Acrylate Copolymer for Potential Wound Care Application

Kartik Jindal, Chaitanya Chibber, Radha Sachan, and Roli Purwar<sup>(✉)</sup>

Discipline of Polymer Science and Chemical Technology, Department of Applied Chemistry,  
Delhi Technological University, New Delhi 110042, India  
roli.purwar@gmail.com, roli.purwar@dtu.ac.in

## 1 Introduction

The healthcare sector utilizes a plethora of dressings for wound care purposes in its day-to-day functioning. A vast majority of these make use of adhesives to hold the dressing firmly in position. Prevalent adhesive systems are either external systems like tapes or an inherent part of the dressing ecosystem itself in the form of ‘bordered’ dressings (adhesives over complete surface or around central padding). Throughout history, wound dressings have been of several types (adherent, low-adherent, non-adherent). This classification is targeted at showing their contact with the wound bed and the skin. However, there is a fallacy behind this classification, that it does not factor in trauma to sensitive skin surrounding the wound when the rather tenacious adhesives used are removed during/after the process of healing [1].

A perfect adhesive is an adhesive that keeps dressings in their place for a predefined length of time commonly known as the wear period, thus diminishing the ever-present danger of wound bed trauma. Dressings in an ideal scenario should be easily removable without posing any danger or causing any harm to the wound and surrounding skin, be healthy (i.e., non-irritating), allow for residue-free transfer from the skin, provide sufficient instant tack and constant prolonged adhesion such that dressings can be moved from one place to another without losing their shielding capabilities [2].

Acrylics are a common type of adhesive used in wound care traditionally due to their high tackiness, cohesion, and adhesion; UV, solvent, and temperature stability [3]. Adhesives made from acrylics are often used in pressure-sensitive tapes, bandages for injuries, and for throwaway short-term use. Polyacrylic pressure-sensitive adhesives (PSA) find use in several industries including the automotive, electronic, aerospace, and medical sector [4]. Acrylate formulations created are versatile and appropriate for dry as well as wet usage. Both solvent-based and hot-melt acrylics find various uses. In the medical industry, curing or hardening happens through atmospheric moisture or UV light [5]. A significant reason behind the use of acrylic adhesives is that they secure dressings in place with ease. On the flipside, they can be hard to remove prematurely

and tend to cause stripping of wounded skin. They also tend to leave residues on the skin after removal and have been known to cause skin irritation [2].

Dressings that do not damage the wound bed or the surrounding skin when removed are called a traumatic in nature [1]. Traumatic removal of dressings has been such a widespread menace that many practitioners have started avoiding using dressings with traditional acrylic adhesives on certain risky patients with sensitive skin like elderly patients, young children and people with dermatological conditions. This is because the possibility of allergy and trauma is higher in these groups than usual, and hence, potential pitfalls need to be circumvented. In addition, the wound bed is often fragile and demands extra care and attention. There is a high chance of tissue damage and medical adhesive-related skin injury (MARS) if more tenacious adhesives are used [6]. That is why, in research on wound care adhesives, there are no challenges more formidable than to ensure an optimum level of adhesion to the human skin. The adhesive should hold the two adherents together while simultaneously allowing removal at an appropriate time without damage to the healing skin.

Silicone adhesives unlike acrylic adhesives are categorized as an advanced adhesive. Silicone adhesives are soft and tend to form several contacts over the uneven disordered surface of human skin and thus show the property of being 'micro-adherent' [2]. Silicones are synthetic in nature and contain Si–O–Si bonds. They find use in many industries including the medical sector because of their water repellence, tendency to completely wet surfaces, permeability to gases, property of being stable in extreme temperatures, and resistance to thermal and chemical degradation. Silicone adhesives are almost always in a tacky state and provide a safe level of adhesion that does not increase on contact with the skin over time. Silicones are also inert and non-toxic in nature. Furthermore, it has been suggested that certain drugs diffuse through silicone adhesives with ease which has prompted newer applications in transdermal patches too apart from wound care adhesives [7]. However, silicone adhesives have some problems of their own including lower adhesion in moderate temperatures (between 0 and 100 °C) as compared to acrylic adhesives [8].

Wound sites are extremely susceptible to bacterial infections because in most cases the protective layer of skin has been breached. That is why it is essential to provide a certain degree of antimicrobial protection to the wound bed. Plant extracts are an exceedingly common source of antimicrobial medicine worldwide. *Arnebia nobilis* (also known as Ratanjot) is a perennial plant found in Afghanistan which is known to exhibit antimicrobial properties. A red dye is extracted from its roots, which is used to make medicine for healing wounds, burns, and even stomach ulcers [9]. *Alkannin and Shikonin* (compounds found in root of *Arnebia nobilis*) also show anti-inflammatory properties and help in reducing swelling [10]. *Arnebia nobilis* has been extensively researched and been found to exhibit considerable antibacterial activity against multi-drug-resistant bacteria including *E. coli* and *S. aureus* among others [11].

Recently, there have been instances of people exploiting benefits provided by acrylic and silicone adhesives and combining them to make a hybrid adhesive with better overall properties [7]. However, not many such adhesives are created specifically to cater to wound care needs and none with inherent antimicrobial properties. The main motivation behind this research was to create such an adhesive which circumvents all known flaws of



existing individual source compound-based adhesives and provides suitable properties to find application in the wound care sector while simultaneously tapping previously unexploited benefits by the addition of a natural antimicrobial agent.

In the present work, an antimicrobial silicone-acrylate adhesive was prepared with an intended use in wound care. Emulsion polymerization of butyl acrylate and acrylic acid was conducted. The resulting stabilized copolymer was mixed with Bis-3-aminopropyl terminated polydimethylsiloxane. *Arnebia nobilis* (Ratanjot) was then added to the adhesive to incorporate antimicrobial properties. Fourier transform infrared spectroscopy (FTIR) was conducted in order to characterize the adhesive emulsion and map the presence of different compounds by analyzing their spectra. Rheology analysis was done to check viscosity of prepared adhesive over a wide range of varying shear rates. Antimicrobial activity of adhesive was calculated via antimicrobial testing and measurement of zone of inhibition created against *E. coli* bacteria (gram negative) 180-degree peel strength testing was performed to fathom the degree of adhesion or tensile strength of the adhesive.

## 2 Experimental

### 2.1 Materials

Butyl acrylate (BA) 99% purity was purchased from Otto Chemie Pvt. Ltd. Acrylic acid (AA) 99% purity and sodium lauryl sulfate 86% purity were procured from Central Drug House Pvt. Ltd. (CDH). Bis-3-aminopropyl terminated polydimethylsiloxane (Mol. Wt. = 2500) was supplied by Sigma Aldrich Chemicals. *Arnebia nobilis* (or Ratanjot) was procured from Khari Baoli. Ammonium persulfate 98% purity and liquid ammonia 25% purity were obtained from Fisher Scientific. Sodium hydroxide pellets were procured from Qualigens. Milli-Q water was used during experimentation. Methanol was obtained from Finar Limited.

### 2.2 Preparation of the Antimicrobial Silicone-Acrylate Adhesive

Emulsion polymerization was performed between the two acrylic monomers—butyl acrylate (BA) and acrylic acid (AA). Emulsifier sodium lauryl sulfate (0.16 g) was mixed with 40 ml of distilled water in round bottom flask. Butyl acrylate (24 ml) and 16 ml of acrylic acid were added. 50 ml liquid ammonia (NH<sub>3</sub>) was added to make the mixture basic, and magnetic stirrer was used to perform agitation for 20 min. Sodium hydroxide pellets were added during mixing as and when necessary to shift the pH from 4 to between 7 and 8. Initiator ammonium per sulfate (0.16 g) was added to the flask as it forms free radicals on heating to begin the polymerization. The flask was covered with a lid and heated for 30–40 min until its temperature reached 80 °C. Emulsion polymerization was carried out for 45 min, and a thick white sticky liquid (copolymer emulsion of butyl acrylate and acrylic acid) was obtained.

The amount of solid adhesive formed in the copolymer emulsion was calculated by gravimetric method. The percentage of solid weight adhesive in the emulsion was found to be close to 30%. The ratio of PDMS to be mixed following the Flory-Fox calculations

was found to be 1:20 (5% of solid weight content). So, in accordance with calculations, 5% of solid adhesive content (19.5 g) or about 1 g of PDMS was added to the 65 g of BA-co-AA copolymer emulsion. After addition, stirring of the blend was carried out for 30 min on a magnetic stirrer in order to make a continuous homogenous mixture of acrylic copolymer and PDMS giving rise to the final silicone-acrylate adhesive.

Extract of *Arnebia nobilis* was extracted by solvent extracted method using methanol. Four samples with different concentrations (Control Samples 1, 5, and 10% w/w of *Arnebia nobilis*) were prepared with 15 g of silicone-acrylate adhesive emulsion each. Mixing was carried out at 500 RPM for 24 h to produce a homogenous mixture. Films were prepared (solvent casting method) by pouring this emulsion into polypropylene petri plates and drying them under ambient conditions.

### 2.3 Characterization of the Silicone-Acrylate Adhesive

To confirm copolymerization between monomers and the presence of PDMS in the adhesive prepared, sample was analyzed with a Fourier Transform spectrophotometer (Thermo Scientific Nicolet 380 spectrophotometer). This was done in the transmission mode with wavenumbers ranging between 4000 and 650  $\text{cm}^{-1}$ .

Rheological properties of the adhesive were measured using the Anton Paar Modular Compact Rheometer (MCR) 302 at 25 °C. The shear rate test was performed in a range from 1 to 1000  $\text{s}^{-1}$ . Viscosity readings were then plotted against varying shear rate values to obtain viscosity profile of the adhesive.

Antimicrobial activity of the prepared adhesive blended with *Arnebia nobilis* was determined using agar diffusion assay (AATCC 30) against *E. coli* (gram negative) bacteria. Prepared adhesive film samples were cut in the form of circular disks of 10 mm diameter. These sample adhesive disks were then carefully put on *E. coli* cultured agar gel plates. These agar plates were then sealed with tape and incubated at 37 °C for 24 h in a vacuum incubator. After 24 h of incubation, the antimicrobial activity of samples was estimated. The diameter of zone of inhibition produced was measured to map the efficacy of samples against *E. coli* bacteria.

Peel strength of the adhesive sample was measured using the 180-degree peel adhesion test as per ASTM D903. The test was conducted on the Instron Precision Ltd. Universal Testing Machine Series 5900 using standard testing fixtures. For testing purposes, pure cotton fabric was chosen for the backing layers between which the adhesive was applied uniformly. The dimension of the cotton fabric taken was 25 mm  $\times$  250 mm, and the value calculated for grams per square meter (GSM) was 70. All the tests were carried out at room temperature with a machine speed of 150 mm/min, and a total of three samples were tested to ascertain the average values. The test samples were conditioned at 25 °C for 72 h before testing.

## 3 Results and Discussion

### 3.1 Fourier Transform Infrared Spectroscopy (FTIR) Analysis

The FTIR spectra of blend of BA-co-AA/PDMS recorded in transmission mode is shown in Fig. 1. The  $-\text{CH}$  stretching of  $-\text{CH}_2$  and  $-\text{CH}_3$  is recorded at 2950  $\text{cm}^{-1}$  while the peak

at  $1725\text{ cm}^{-1}$  is assigned to  $\text{C}=\text{O}$  stretching vibration. The stretching vibrations of  $-\text{C}=\text{C}$  were observed at  $1625\text{ cm}^{-1}$ , and vibrations observed at  $1174\text{ cm}^{-1}$  can be assigned to the  $-\text{O}-\text{CH}_3$  group [12, 13]. Furthermore, the peak at  $3425\text{ cm}^{-1}$  is clearly visible which shows  $-\text{N}-\text{H}$  stretching. The carboxylic peak expected around  $1700\text{ cm}^{-1}$  was not observed indicating neutralization by liquid ammonia which in turn got converted into amide group. In the adhesive preparation stage, PDMS was blended with acrylic copolymer and its characteristic peak is clearly visible in the spectra at  $802\text{ cm}^{-1}$  and  $1058\text{ cm}^{-1}$  of  $\text{Si}-\text{O}-\text{Si}$  [14]. By virtue of these inferences, it can be concluded that copolymerization between butyl acrylate and acrylic acid has successfully occurred and addition of  $\text{NH}_3$  and PDMS has also been determined.

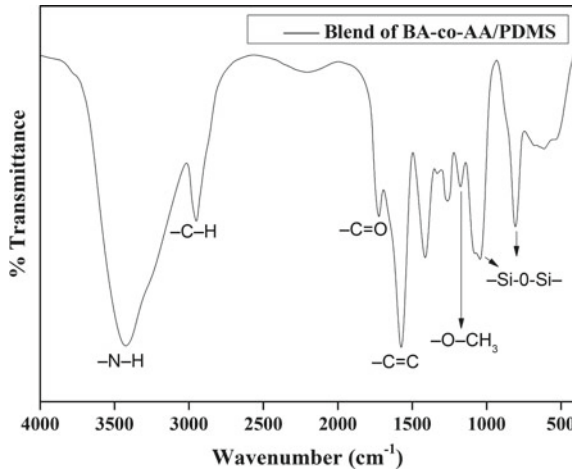


**Fig. 1** FTIR spectra of blend of BA-co-AA/PDMS adhesive

### 3.2 Rheological Property

Viscosity profile of adhesive with varying shear rate is shown in Table 1 and Fig. 2. From the graph, it is evident that the behavior of the emulsion formed is shear thinning as the value of the viscosity is reduced with increase in shear rate. At lower shear rates (0.1–0.3)1/s, the difference in viscosity values was huge. Addition of PDMS increased the flexibility of the polymer chains and simultaneously bonded the polymeric chains more rigidly. As the value of shear increased, the differences between the viscosities reduced and approximately equaled at shear value between (4–12)1/s. This is somewhat the region of application of prepared pressure sensitive adhesive (PSA) where the change in viscosity is not significant. On further increase in the shear rate, at higher values, viscosity values again showed decline as observed in the beginning. But this decline was more uniform as compared to earlier reduction. It reached the value of 305 mPa s at shear rate of 1000. Therefore, from rheology study we can conclude that the adhesive formed by the copolymerization shows non-Newtonian and shear thinning behavior. As the shear rate was increased, the viscosity of the adhesive decreased since entanglement

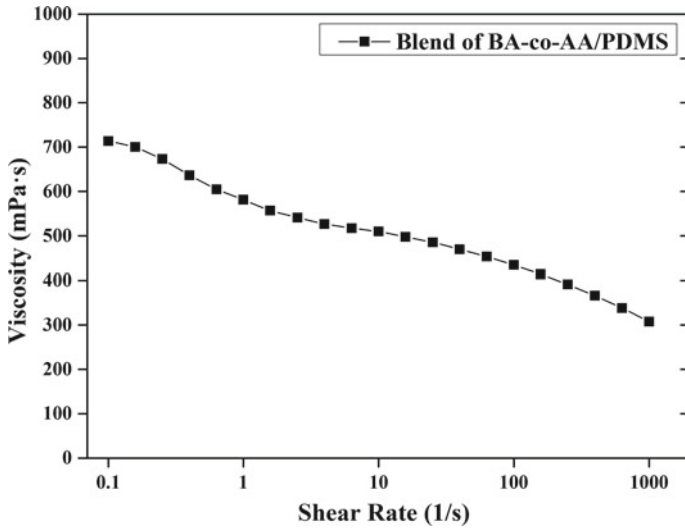


**Fig. 2** Viscosity profile of blend of BA-co-AA/PDMS adhesive with varying shear rate

and minor forces such as Van der Waals forces among polymer chains got destroyed. Furthermore, within the shear rate range of (8–30)1/s, the adhesive is highly stable and can be used for medical applications.

**Table 1** Shear values and viscosity of blend of BA-co-AA/PDMS

S. No.	Shear values (1/s)	Viscosity (mPa s)
1	0.1	713
2	1	584
3	10	509
4	100	429
5	1000	305

### 3.3 Antimicrobial Activity Analysis

Antimicrobial potential of *Arnebia nobilis* blended BA-co-AA/PDMS was ascertained by disk diffusion assay against *E. coli* (gram negative) bacteria. *E. coli* was chosen because it is a preferred host in gene cloning due to its high-efficiency establishment of DNA molecules into blood cells and power to grow on chemically established media [15, 16]. *Arnebia nobilis* incorporated into BA-co-AA/PDMS showed a prominent zone of inhibition against *E. coli* bacteria. Mean diameter of zone of inhibition was 28.32, 30.60, 31.63, and 34.63 mm, respectively, for control sample, 1, 5, and 10% concentrations of *Arnebia nobilis* against *E. coli* (gram negative) bacteria as shown in Fig. 3. From the

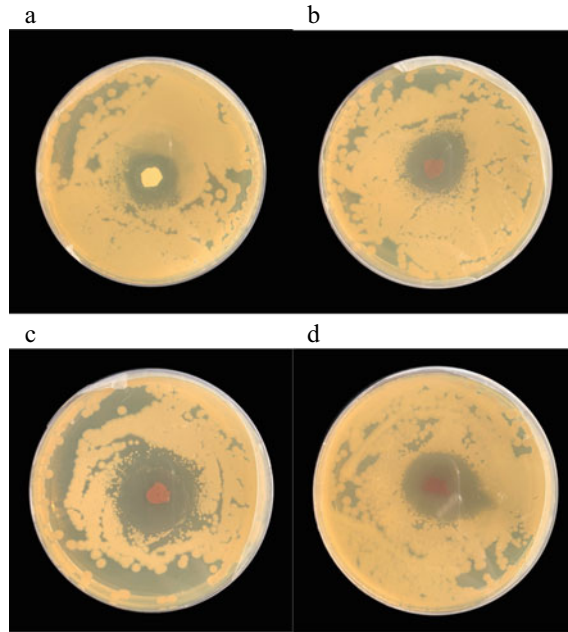


**Fig. 3** Antimicrobial testing samples **a** control **b** 1% **c** 5% **d** 10% *Arnebia nobilis*

data recorded in Table 2, it was observed that there is a significant increase in the zone of inhibition as the concentration is increased. At 10% concentration, the mean diameter of inhibition rose to 34.63 mm which is very significant for an antimicrobial agent. These findings make a strong case for the efficacy of this adhesive as a potential antimicrobial adhesive to find use in wound care.

**Table 2** Change in zone of inhibition with increasing *Arnebia nobilis* concentration

S. No.	<i>Arnebia nobilis</i> concentration (in w/w % of polymer content)	Zone of inhibition (mean diameter in mm)
1	Control sample	28.32
2	1%	30.60
3	5%	31.63
4	10%	34.63

### 3.4 Peel Strength Testing Analysis

Peel adhesion testing is used to determine the bond strength of any material and is computed as the average bond line load per unit area required to separate the bonded

material where the separation angle is 180 degrees. Adhesive strength is calculated on the adhesion between the cotton fabric and the value of the peel force came out to be 2.637 N/mm. The range of values calculated by Tanveer et al. in his formulation of silicone acrylic adhesive is (1.88–3.82) N/mm [17]. Also, the adhesive peel strength made by *Wacker Chemie AG* for medical and skin care applications is between (1.1–5.5) N/mm [18]. The adhesive formed by our experimentation has peel strength values well between the desired range, and therefore, we can conclusively say that this adhesive can be easily peeled off from the skin after application.

## 4 Conclusion

Adhesive formulation involved copolymerization of butyl acrylate and acrylic acid via emulsion polymerization followed by blending of PDMS and incorporation of *Arnebia nobilis* (antimicrobial agent). Fourier transform infrared spectroscopy (FTIR) indicated successful copolymerization between butyl acrylate and acrylic acid and showed the presence of PDMS. Rheology testing of adhesive showed non-Newtonian and shear thinning behavior proving that the adhesive is highly stable and suitable for medical application. Antimicrobial testing indicated a marked increase in zone of inhibition against *E. coli* (gram negative) bacteria on increasing *Arnebia nobilis* concentration in adhesive. Peel strength test results confirmed that the value of peel force of adhesive prepared (2.637 N/mm) is well in line with industry standards (1.1–5.5) N/mm and can create an optimum level of adhesion with the skin. All test results obtained reveal that the adhesive prepared has appropriate properties and is suited for potential use in the wound care sector.


## References

1. Steve T (2020) Atraumatic dressings. <http://www.worldwidewounds.com/2003/january/Thomas/Atraumatic-Dressings.html>. Accessed 19 Dec 2020
2. White R, Davies P, Manager MM, Words K skin adhesives and their role in wound dressings
3. Krzysztof Antosik A (2017) Acrylic-silicone pressure-sensitive adhesives. *OMCIJ* 4(5). <https://doi.org/10.19080/OMCIJ.2018.05.555648>
4. Zhu M et al (2020) Preparation of environmentally friendly acrylic pressure-sensitive adhesives by bulk photopolymerization and their performance. *RSC Adv* 10(17):10277–10284. <https://doi.org/10.1039/C9RA10514J>
5. Types of medical adhesives—a ThomasNet buying guide. <https://www.thomasnet.com/articles/adhesives-sealants/types-of-medical-adhesives>. Accessed 19 Dec 2020
6. Medical Adhesives Matter (2020) Elite learning, Sep 07, 2015. <https://www.elitecme.com/resource-center/nursing/medical-adhesives-matter>. Accessed 19 Dec 2020
7. Ii GKS, Bobenrieth A, Huber RO, Nartker LS, Thomas X (2017) Silicone adhesives in medical applications. *Appl Adhes Bond Sci Technol*. <https://doi.org/10.5772/intechopen.71817>
8. Silicone vs acrylic adhesive—a comparison, silicon adhesives, acrylic adhesives. <http://www.industrialrubbergoods.com/articles/silicone-acrylic-adhesive.html>. Accessed 05 Feb 2021
9. Hosseini A, Mirzaee F, Davoodi A, Bakhshi Jouybari H, Azadbakht M (2018) The traditional medicine aspects, biological activity and phytochemistry of *Arnebia* spp. *Medicinski glasnik: official publication of the Medical Association of Zenica-Doboj Canton, Bosnia and Herzegovina*, vol 15, pp 1–9. <https://doi.org/10.17392/926-18>

10. PubChem, "Shikonin." <https://pubchem.ncbi.nlm.nih.gov/compound/479503>. Accessed 05 Feb 2021
11. Arora A, Gupta D, Rastogi D, Gulrajani M (2012) Antimicrobial activity of naphthoquinones extracted from. *J Nat Prod* 5:11
12. Yılmaz O, Özkan ÇK, Yılmaz CN, Yorgancıoğlu A, Özgünay H, Karavana HA (2017) Synthesis and characterization of functional acrylic copolymers via RAFT mini-emulsion polymerization. *AIP Conf Proc* 1918(1):020006. <https://doi.org/10.1063/1.5018501>
13. Çetin M, Sarac A (2013) Transparent poly(methyl methacrylate-co-butyl acrylate) Nanofibers. *J Appl Polym Sci* 130. <https://doi.org/10.1002/app.39705>
14. Hofmann J (2021) IR spectroscopic method for determination of silicone cross-linking, 2016. /paper/IR-SPECTROSCOPIC-METHOD-FOR-DETERMINATION-OF-Hofmann/485334873c8e4551f510bfdc83ac5369e5567310. Accessed 13 Feb 2021
15. Srivastava CM, Purwar R, Gupta AP (2019) Enhanced potential of biomimetic, silver nanoparticles functionalized *Antheraea mylitta* (tasar) silk fibroin nanofibrous mats for skin tissue engineering. *Int J Biol Macromol* 130:437–453. <https://doi.org/10.1016/j.ijbiomac.2018.12.255>
16. Cronan JE (2014) *Escherichia coli* as an experimental organism. In: eLS. American Cancer Society
17. Tanveer W, Chotprasert N, Wonglamsam A, Shrestha B (2018) Evaluation of peel bond strength between plexiglas acrylic (pmma) and maxillofacial silicone using three different primers, vol 37, pp 263–272
18. 7843-EN.pdf (Online). Available: <https://www.wacker.com/h/medias/7843-EN.pdf>. Accessed 17 Feb 2021



# Corrugated Sandwich Structure Modeling Under Low Velocity Impact

Vikrant Sen and Shivdayal Patel<sup>(✉)</sup> 

Department of Mechanical Engineering, PDPM Indian Institute of Information Technology  
Design and Manufacturing, Jabalpur, Madhya Pradesh 482005, India  
vikrantsagar13@gmail.com, shivdayal@iiitdmj.ac.in

## 1 Introduction

The CFRP composite materials are mostly used in several applications such as automobile, wind turbine, and rail transport industry. Sandwich structure consists of mainly face sheets and core material [1, 2]. In sandwich, we use different kind of materials for face sheets and core. There are different types of sandwich are available, for example metallic sandwich (both face sheet and core are of metallic structure), pure composite sandwich (both face sheet and core material are of composite), and hybrid sandwich (both face sheet and core of composite and metallic). The advantage of using the sandwich structure is that we get the higher stiffness and strength for the same weight of structures as compared to the solid structure [1–6]. The sandwich consists of CFRP face sheets and a lightweight core material aluminum used between the face sheets. The hybrid CFRP sandwich structure provides an excellent property such as high specific stiffness and strength and also excellent corrosive resistance properties, with it the core we are using, i.e., aluminum foam is lightweight and having excellent energy absorbing capacity [1–8].

Žmindák et al. [9] presented the perforation of steel and aluminum sandwich structure under impact load with using the eight layers of carbon reinforced with core aluminum. The Johnson–cook material model and Hashin damage were used to determine the failure behavior of the core aluminum and composite plate, respectively. It was observed that the ply orientation provided the significant effect of the sandwich structure under high velocity impact. Tang et al. [10] studied the CFRP sandwich panel behavior subjected to the high velocity impact to determine the residual velocity, impactor velocity, and energy absorption for the different impactor shape. Hua et al. [9] performed the LVI analysis of the sandwich panel to determine the ballistic limit of the sandwich structure using different shape of impactor. Force and displacement curves were showed the flat and conical shape impactor showed the higher and minimum energy, respectively. Zhu et al. [11] determined the numerical result of the circular sandwich structure subjected to the LVI. The contact force versus displacement showed that the different stage of failure behavior. Zhang et al. [12] performed the quasi-static and LVI test by experimental method on hybrid sandwich panel. By varying the thickness of the upper and lower face sheet but keeping the total thickness constant. In this work, they explained the various failure modes due to varying the thickness and how the impact load vary



with the deflection of various sandwich beam with varying thickness. He et al. [13] presented an extensive work on the sandwich panel with CFRP as it faces sheet and a corrugated Al sheet as its core member. In this work, they performed the LVI test of various energy levels by varying the thickness of the core member only and obtained the impact load and energy curve with respect to time. In this work, they also explained the failure mechanism in detailed. Shi et al. [14] studied the CFRP composite plate under LVI performs the experimental and numerical analysis to determine different modes of failure, displacement, various failure mechanism, and energy absorption.

The above literature showed that some literature available on the LVI response on composite panels but the limited work available on the different core design of the sandwich panels under LVI. So, in this paper, developed the different corrugated core's structure design such as trapezoidal, rectangular, and circular shape with the CFRP composite face sheet under LVI to determine the failure behavior of the sandwich structure, energy absorption, and force time history. Numerical simulation results validated with experimental results [13] for the trapezoidal core with CFRP composite faces under LVI. In this study, the progressive damage modeling is used for the CFRP composite plate under LVI to determine the composite failure such as fiber mode tensile and compressive, matrix modes tensile, and compression as well as delamination failure using the thickness of the various core structures are constants.

## 2 Numerical Simulation

The corrugated sandwich structure is made up of metal core structure and composite face plates. The aluminum core and composite face sheet damage modeling are used for the Johnson–Cook and Donaldson criteria, respectively. The Johnson–Cook ductile damage models are given in below.

### 2.1 Ductile Damage Initiation Model

The finite element analysis (FEA) is performed for the different shapes of core structure to predict the plastic deformation of the core structure using the ductile damage initiation and propagation model based on Johnson–Cook and tabular form criteria, respectively.

$$\omega_d = \int \frac{d\varepsilon_{pl}}{\dot{\varepsilon}_{pl}^d(\eta, \dot{\varepsilon}_{pl})} = 1 \quad (1)$$

Here,  $\omega_d$  is state variable,  $\dot{\varepsilon}_{pl}^d(\eta, \dot{\varepsilon}_{pl})$  equivalent plastic strain,  $\eta$  is the stress triaxiality, and  $\dot{\varepsilon}_{pl}$  is the equivalent plastic strain-rate [13].

### 2.2 Damage Propagation Criteria for Metal

Damage propagation model is used for the plastic deformation of the structure to calculate the plastic deformation of the aluminum core. If the damage initiation criterion  $\omega_d \geq 1$  is satisfied, then propagation-based failure model as shown in Eq. (2) is used to predict the plastic failure. The damage variables are calculated based on the relative plastic

displacement is specified by the tabular form plastic stress and strain curve. Ductile damage propagation is defined as

$$\dot{\bar{u}}_{pl} = L\dot{\bar{\epsilon}}_{pl} \tag{2}$$

Here,  $L$  is the characteristics length of the element,  $\bar{u}_{pl}$  is the effective plastic displacement. The damage variable directly based as a tabular function of equivalent plastic displacement,  $d = d(\bar{u}_{pl})$  as shown in Fig. 1.

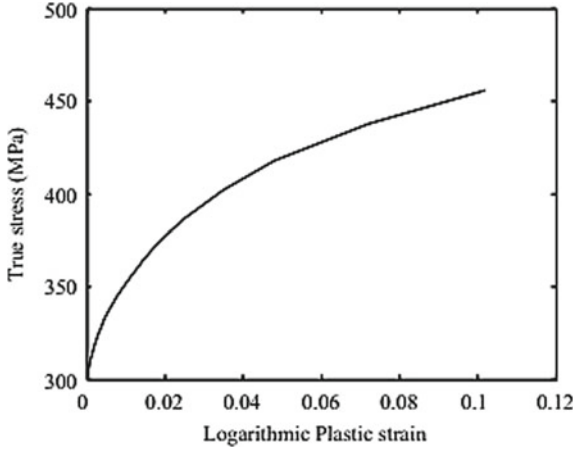


Fig. 1 Compression test curve of Al sheet [13]

### 2.3 Composite Damage Modeling:

The continuum damage modeling is included the damage initiation and the propagation-based model using the Hashin [14] and Donaldson criteria [14], respectively, to determine the different modes of failure for the composites structure such fiber failure, matrix failure, and delamination failure. Hashin-based damage initiation criteria are used for the matrix tension mode, fiber tension, and compression modes. The matrix compression-based criterion did not provide the accurate results for the prediction of the matrix cracking [3–6]. Hence, the Puck and Shurman-based matrix compression criterion is used for the present study to determine realistic failure behavior for the matrix compression.

## 3 Sandwich Structure Modeling under Impact Load

The sandwich structure is made up of the CFRP composite face sheets with aluminum core material. The Al core was modeled as shown in Fig. 2. Dimensions of core are taken as  $L_1 = 7$  mm,  $L_2 = 25$  mm, and  $\omega = 55^\circ$ . The composite top and bottom face sheets were modeled as the deformable solid having dimensions of  $96 \times 96 \times 1$  mm (Fig. 3) with stacking sequence  $[0/90/0/90]_s$ . The impactor was modeled as the discrete rigid

cylindrical shell with hemispherical end, and the mass was assigned on the reference point. Impact tests were performed on the sandwich panels with a hemispherical shape of impactor having diameter of 12 mm and total weight of 13.2 kg. In boundary condition, the edges were fixed of the face sheets. The energy level of impactor was obtained by the initial velocity, i.e., for 10 J, the velocity was given as the 1.23 m/s. The panel was modeled 8-node quadrilateral (SC8R) in-plane general purpose continuum shell element. The element assigned to the impactor is R3D4 which is a 4-node-3D bilinear rigid quadrilateral. Mesh density of the impactor region was chosen dense as compared the other region. The impactor zone was divided into 50 elements by number, and the global size of the element was assigned as the 1 \* 1 mm. The same impactor zone was also crated on the core part. The degradation parameter was set to 0.98–0.99 for panel, and the failed elements were removed from the FE model once the failure criterion was satisfied.

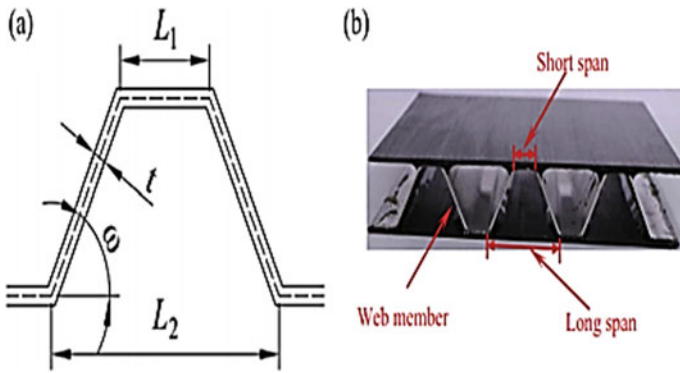


Fig. 2 Geometrical shape of trapezoidal core [13]

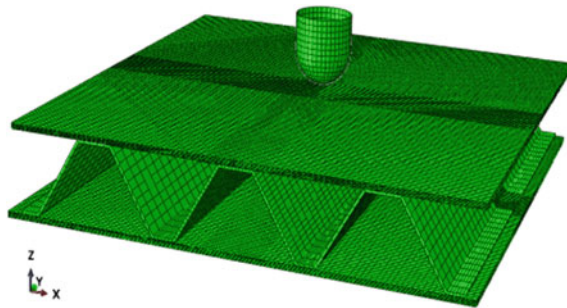


Fig. 3 Mesh model of sandwich panel

The different shapes of aluminum core structures are modeled using the ductile damage initiation and propagation model based on Johnson–Cook and tabular form criteria, respectively, to predict the plastic deformation of the core structure. The Hashin failure model was applied for the CFRP face sheets to determine the different model of

failure of composite faces. The property was used as the input for the ductile damage model and Hashin model in literature [13].

## 4 Hybrid Sandwich Structure Modeling of Different Cores

In the present study, the three different types of hybrid sandwich core structures modeling are performed using the FEA under the LVI.

### 4.1 Hybrid Sandwich Structure with Trapezoidal Core

Hybrid sandwich structure most commonly is used for the impact energy absorption. In this section, all the dimension of the trapezoidal core and top and bottom faces of the composites are considered the experimental literature [13]. The complete sandwich structure assembly and the FE mesh of the complete assembly is shown in Fig. 3. The trapezoidal sandwich structure subjected to the LVI considering the mass of impactor 13.2 kg and velocity impactor is 1.23 m/s (Fig. 4). The different modes of failure for the trapezoidal core structure and composite face sheet are shown in Figs. 5 and 6, respectively.

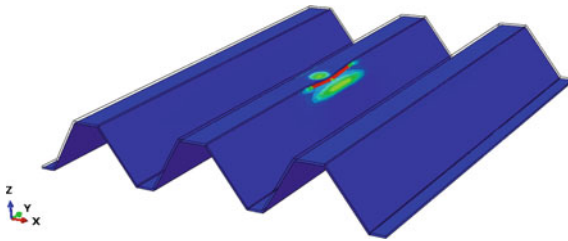


**Fig. 4** Plastic deformation of the trapezoidal AL sheet core

### 4.2 Validation Study of the Hybrid Sandwich Structure with Trapezoidal Core

Hybrid sandwich structure with trapezoidal core numerical results is validated with the experimental result [13] for the same core structure with the CFRP face sheets. Numerical result for the impact load versus time and energy versus time is validated with the experimental published results [13]. The impact force versus time (Fig. 7) and energy versus time (Fig. 8) results showed the very close to experimental result. It is observed that the most of the energy are dissipated by the CFRP composite face sheets.

### 4.3 Rectangular Shell Core

The hybrid sandwich structure with rectangular core and CFRP face sheets are showed in Fig. 9 to determine the impact energy absorption. The rectangular core structure area is considered to be same as the trapezoidal section. The top and bottom faces are used for

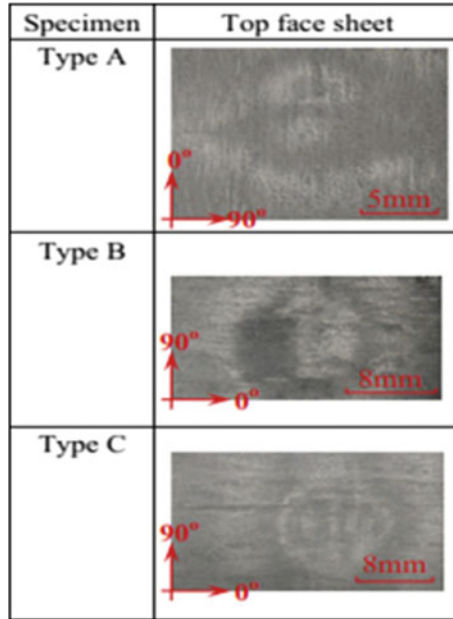


**Fig. 5** Damage of top face sheet in testing [13]

the same as for the trapezoidal sandwich structure of the composites [13]. The complete sandwich structure assembly and the finite element mesh of the complete assembly are shown in Fig. 9. The rectangular sandwich structure subjected to the low velocity impact considering the mass of impactor 13.2 kg and velocity impactor is 1.23 m/s. We designed the rectangular shell member (Fig. 10) for core by choosing the dimension such that the thickness and the total volume of core remain constant as used in the previous corrugated core which is shown in the Fig. 2. The different modes of failure for the rectangular sandwich structure face sheets are the fiber failure in tension and compression, as well as matrix failure in tension and compression are shown in Figs. 11 and 12, respectively. The rectangular corrugated sandwich structure showed the impact force versus time and energy versus time Figs. 13 and 14, respectively.

#### 4.4 Circular Shell Core

The hybrid sandwich structure with circular core and CFRP face sheets are showed in Fig. 15 to determine the impact energy absorption. The circular core structure volume and thickness are considered to be same as the trapezoidal section. The top and bottom faces are used for the same as the trapezoidal sandwich structure of the composites [13]. The complete sandwich structure assembly and the FE mesh of the complete assembly are shown in Fig. 15. The circular sandwich structure subjected to the LVI considering the mass of impactor 13.2 kg and velocity impactor is 1.23 m/s. The different modes of failure for the circular sandwich structure face sheets are the fiber failure in tension and

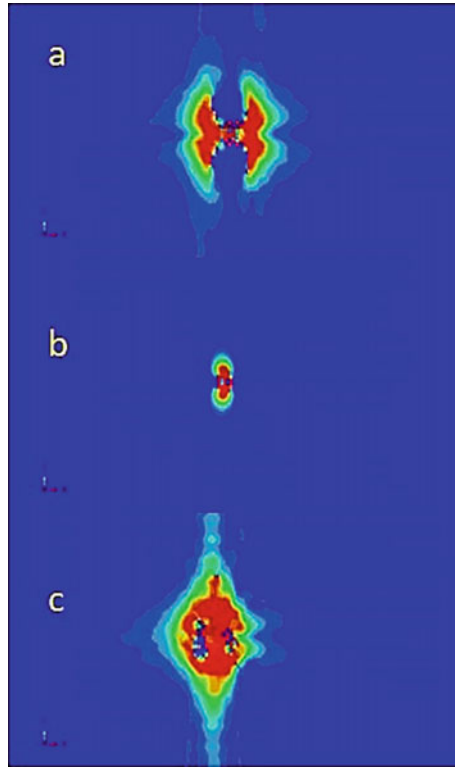


**Fig. 6** Damage behavior of the trapezoidal corrugated structure (a) fiber tension (b) fiber compression (c) matrix tensile failure

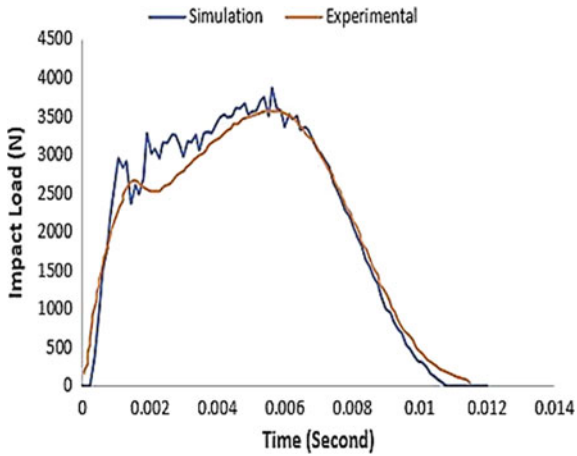


**Fig. 7** Validation results of impact load versus time

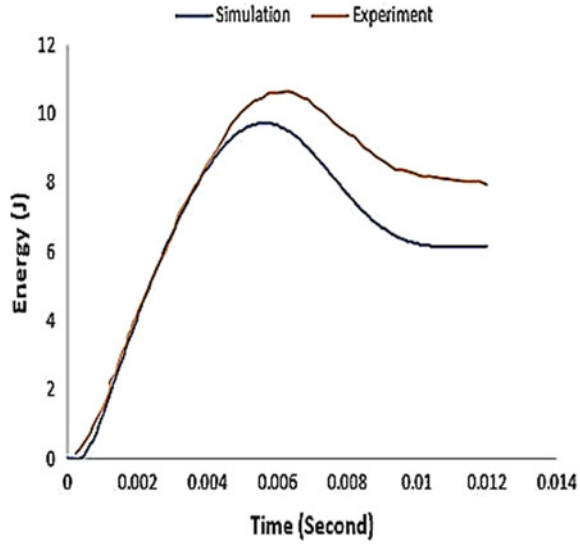


Fig. 8 Validation results of energy versus time

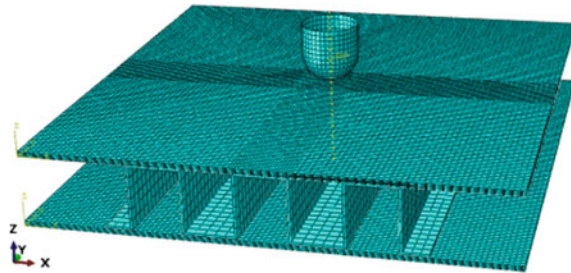


Fig. 9 FE mesh model of the rectangular corrugated structure

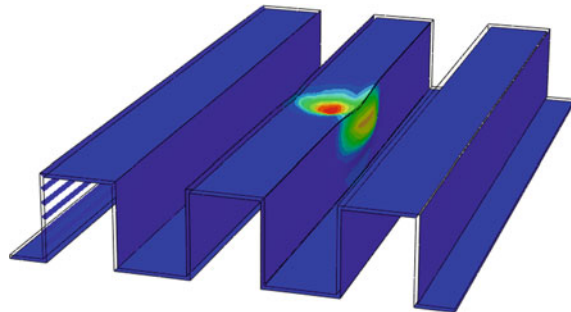
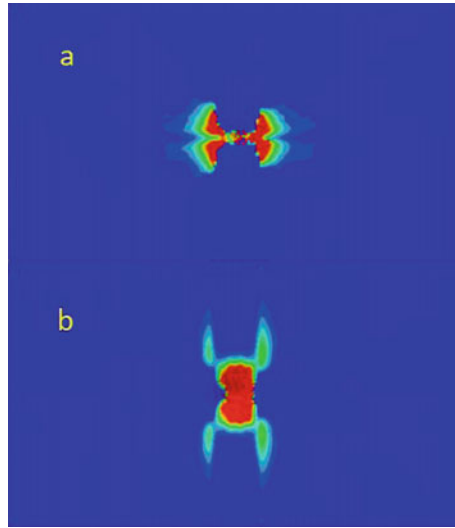
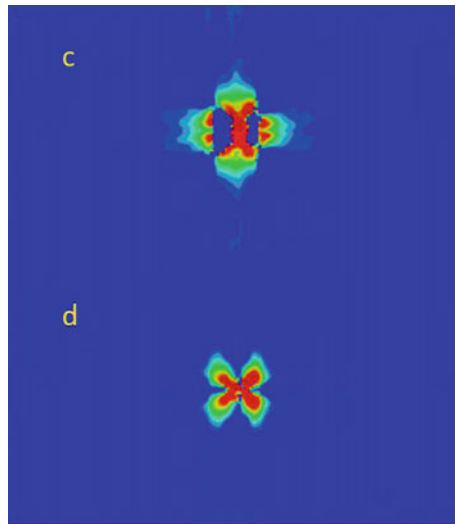


Fig. 10 Plastic deformation of the square AL sheet core



**Fig. 11** Damage behavior of the rectangular corrugated structure (a) fiber tension (b) fiber compression

compression, matrix failure in tension and comparison are shown in Figs. 16, 17 and 18, respectively.



**Fig. 12** Damage behavior of the rectangular corrugated structure (c) matrix tension (d) matrix compression failure



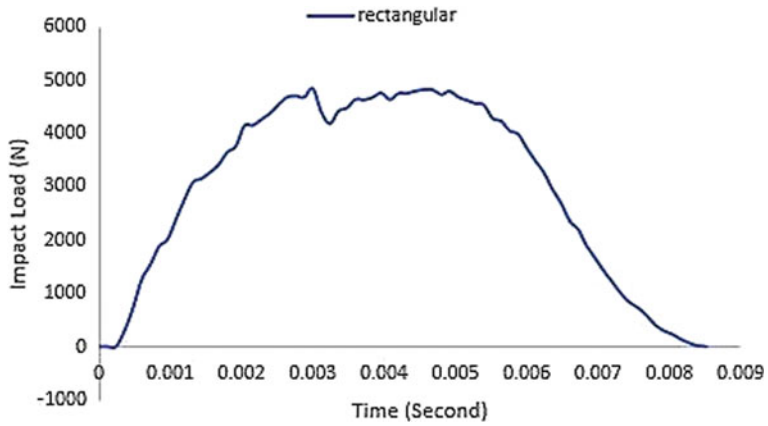


**Fig. 13** Simulation results of impact load of rectangular core of 10 J impact energy level

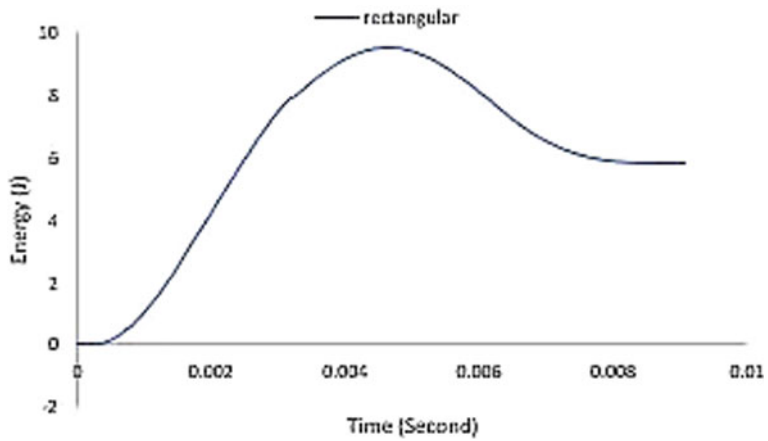


**Fig. 14** Simulation results of impact energy absorption rectangular core for 10 J energy level

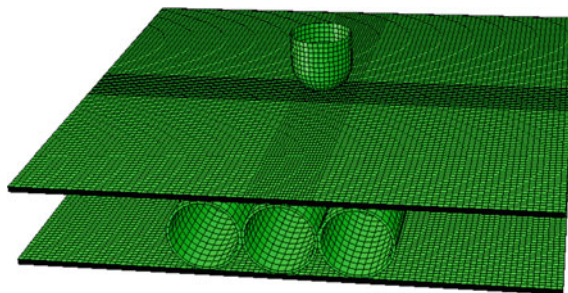


**Fig. 15** FE mesh model of the circular corrugated structure

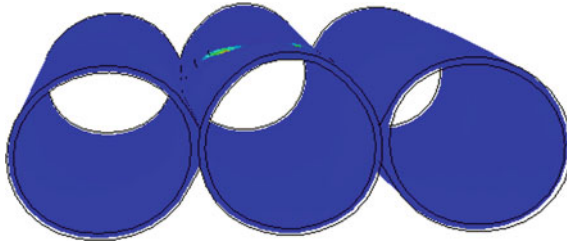


**Fig. 16** Al damage of circular tube as core

## 5 Results and Discussion

In the current study, the three different types of corrugated cores such as trapezoidal, rectangular, and circular shapes are modeled using the FE analysis subjected to the LVI. The impactor transfers its kinetic energy to the panels. Initially, the impact load increases and reaches its first peak value. There is slight drop in the impact load for short time this is due to the fact that there may be little buckling occur in the core part and then increases the value of load again and reaches its maximum value. After reaching the maximum value, the load value again decreases as the impactor rebound back. The initial oscillation occurs in the impact load value due to the elastic vibration in the panel.

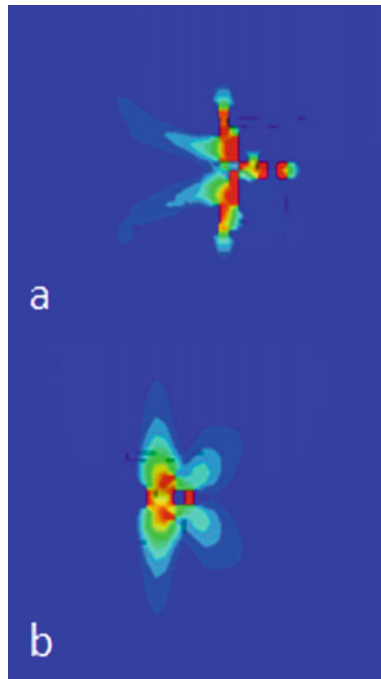


**Fig. 17** Damage behavior of the circular corrugated structure (a) fiber tension (b) fiber compression failure

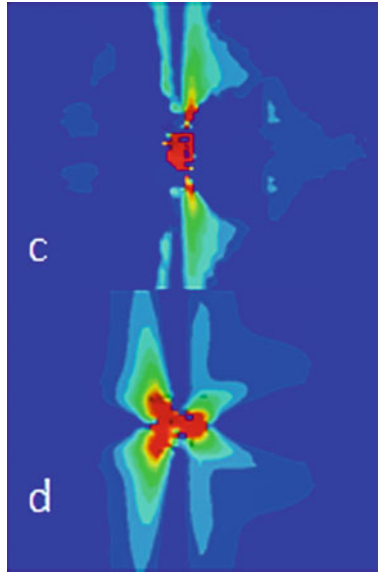


**Fig. 18** Damage behavior of the circular corrugated structure (c) matrix tension (d) matrix compression failure

### 5.1 Contact Force Time History

As shown in the Fig. 7, initially, load increases with time and reaches the maximum value of 2.6 kN. Due to the very slight buckling of the core, the load values drop and increase again at the maximum value of 3.56 kN in the experiment. There is barely visible indentation occurs on the core surface. At this peak load, their damage initiation starts. However, during the unloading phase, the specimen returns to its original state more slowly and less completely. As shown in Fig. 8, the relation of impact energy and the time curve shows that as the impactor transfer its kinetic energy to the panel and the internal energy of the panel increases reaches its maximum absorption, i.e., near 10.6 J, and then during the unloading phase, it releases its elastic energy to the impactor. So, the energy drops to some value, i.e., near 6 J and then constant. Ideally, the whole elastic energy does not recovers because some part of energy losses due to the friction between the impactor and plate or damage of the fiber-matrix.

### 5.2 Comparison Study of Rectangular Shell Core and Circular Core Design

In this paper, studied the effect of impact loading and energy absorption by varying the core design and keeping all other same. Various simulations were performed on different core design, and the effect of impact on panel and results is shown in Figs. 3, 9, and 15 on various core geometries (i.e., rectangular shell and circular tubes). After impact on rectangular core, the initiation of damage take time as compared to the trapezoidal one and also the damage initiated at higher load, i.e., near 4.8 kN as against 2.6 kN. Also, the maximum energy absorption capacity in it is 9.4 J which is slightly less as

compared to trapezoidal but with it also recover faster than the trapezoidal core (Fig. 7). Overall comparing impact load, it was observed that the rectangular shell could wear the maximum load and also it returns to its original state fast as compared to other cores. In circular tubes of core, the initiation damage occurs at long as compared to the previous one but there is no buckling observed in the core. Also, the maximum energy absorption is same but its elastic recovery takes long time as compared to the previous trapezoidal core.

## 6 Conclusion

The continuum damage mechanics approach is developed and implemented the ABAQUS software to determine the realistic failure behavior. Impact force versus time and energy versus time were validated with experimental results, and it is showed the good agreements. The rectangular core sandwich structure investigated the initiation of damage take time as compared to the trapezoidal core structure. Rectangular core structure damage initiated at higher load, i.e., near 4.8 kN as against 2.6 kN in trapezoidal sandwich structure. The maximum energy absorption capacity in it is 9.4 J which is slightly less as compared to trapezoidal but with it also recover faster than the trapezoidal core. In next work, the effect of core geometry (rectangular, circular tubes) was studied on impact load and energy absorption capacity of sandwich panel and the result were compared. It was observed that the rectangular core has more impact wearing load capacity, i.e., nearly 20% and 25% greater than the trapezoidal and circular core, respectively. Similar behavior is also observed for the displacement and energy absorption for the rectangular and circular core structure. The rectangular corrugated sandwich structure showed the maximum energy absorption and maximum impact force as compared to the other core structure designs (trapezoidal and circular).

## References

1. Patel S, Vusa VR, Soares C (2019) Guedes crashworthiness analysis of polymer composites under axial and oblique impact loading. *Int J Mech Sci* 156:221–234
2. Gen LI, Tan KH, Fung TC (2021) A rate-dependent continuum damage model for dynamic shear debonding of CFRP-concrete interface. *Int J Impact Eng* 152:103844
3. Bandaru AK, Patel S, Sachan Y, Alagirusamy R, Bhatnagar N, Ahmad S (2016) Low velocity impact response of 3D angle-interlock Kevlar/basalt reinforced polypropylene composites. *Mater Des* 105:323–332
4. Patel S, Ahmad S, Mahajan P (2014) Reliability analysis of a composite plate under low-velocity impact using the Gaussian response surface method. *Int J Comput Methods Eng Sci Mech* 15(3):218–226
5. Patel S, Guedes Soares C (2018) Reliability assessment of glass epoxy composite plates due to low velocity impact. *Compos Struct* 200:659–668
6. Bandaru AK, Patel S, Ahmad S, Bhatnagar N (2017) An experimental and numerical investigation on the low velocity impact response of thermoplastic hybrid composites. *J Compos Mater* 52(7):877–889
7. Patel S, Ahmad S (2017) Probabilistic failure of graphite epoxy composite plates due to low velocity impact. *J Mech Des* 139(4):044501

8. Patel S, Ahmad S, Mahajan P (2018) Safety assessment of composite beam under ballistic impact. *J Thin Walled Struct* 126:162–170
9. Huo X, Liu H, Luo Q, Sun G, Li Q (2020) On low-velocity impact response of foam-core sandwich panels. *Int J Mech Sci* 181:105681
10. Tang E, Yin H, Chen C, Han Y, Feng M (2020) Simulation of CFRP/aluminum foam sandwich structure under high velocity impact. *J Market Res* 9(4):7273–7287
11. Zhu S, Chai GB (2015) Low-velocity impact response of composite sandwich panels. *Proc Inst Mech Eng, Part L: J Mater: Des Appl* 230(2):388–399
12. Zhang W, Qin Q, Li J, Li K, Poh LH, Li Y, ... Zhao J (2020) Deformation and failure of hybrid composite sandwich beams with a metal foam core under quasi-static load and low-velocity impact. *Compos Struct* 242:112175
13. He W, Liu J, Tao B, Xie D, Liu J, Zhang M (2016) Experimental and numerical research on the low velocity impact behavior of hybrid corrugated core sandwich structures. *Compos Struct* 158:30–43
14. Shi Y, Swait T, Soutis C (2012) Modelling damage evolution in composite laminates subjected to low velocity impact. *Compos Struct* 94(9):2902–2913



# High-Velocity Impact Analysis of CFRP Composite

Sajal Soni, Roopendra Kumar Pathak, and Shivdayal Patel<sup>(✉)</sup> 

Discipline of Mechanical Engineering, PDPM, Indian Institute of Information Technology  
Design and Manufacturing, Jabalpur, India  
shivdayal@iiitdmj.ac.in

## 1 Introduction

Nowadays, a bulletproof vest or bullet armour vest has become an essential element for the defence industry to protect the projectile and dissipate the energy [1–8]. Advanced composite materials such as carbon fibre-reinforced polymer, Kevlar-29, Kevlar-49 and Kevlar-149 are most commonly used for the bulletproof vest due to the superior mechanical properties of composite materials [5–9]. Sudhir et al. [10] studied the variation of impactor velocity of the composite laminate using the woven fibre of carbon/epoxy and Kevlar/epoxy composite to determine ballistic limit and residual velocity. Hazell and Appleby-Thomas [11] performed a woven laminate of CFRP to determine the dissipation energy and ballistic limit of the composite panel. Wang et al. [12] and Manes et al. [13] performed a numerical study of the Kevlar-29 plates under ballistic impact load using the armour-piercing projectile. Bandaru et al. [14] developed the numerical model of hybrid lamina made of Kevlar and Basalt having 2D planer and 3D interlock architecture. The hybrid laminates made up of 16 plies and having the different stacking sequence and the plate dimensions is  $150 \times 150$  mm and impactor diameter of 9 mm for full metal jacket bullet in the velocity ranging from 150 to 450 m/s. The residual velocities due to impact at different velocities have been determined for the Kevlar/basalt hybrid laminate. Tanabe and Aoki [15] determined the residual resistance of the Kevlar material subjected to finite simulating projectile under HVI analysis of a Kevlar helmet experimentally and through AUTODYN simulations. But it has been observed that the CFRP panels of practical thickness are resistant to perforation only up to a range of velocity, 100–150 m/s. To work in a higher velocity range, we have to go with Kevlar fibres or basalt fibres.

Oblique impact analysis of the CFRP composite plate did not perform enormously. Hence, in the current study, numerical modelling of the CFRP composite laminate was developed to investigate the realistic failure behaviour, ballistic impact, residual velocity and energy balance under the normal and oblique impact load. The modified Hashin damage criteria was developed to determine the failure behaviour of the CFRP composites. But the biggest drawback of Hashin damage criteria is that it is formulated for unidirectional laminated and, thus, does not consider the effect of transverse compressive stress and shear stress on direct longitudinal tensile stress. Hence, the progressive

damage-based model are used in user-defined subroutine ABAQUS to determine the realistic failure behaviour of the subjected to the normal impact and oblique impact. Nowadays, the advanced CFRP composite material has gained importance in the field of defence due to its wide range of properties like high strength and low weight. They have been widely used for making bulletproof vests and helmets.

## 2 Composite Damage Modelling

The continuum damage modelling was carried out to determine the failure initiation and failure propagation of the CFRP laminate subjected to the HVI. The Hashin damage criteria are most commonly used to calculate the failure initiation and propagation of the fibre-reinforced composite, but in the matrix, the failure criterion does not include the transverse compressive stress on the shear strength of the matrix. Several modifications in the Hashin damage criteria have been made over the last two decades. Hence, the modified Hashin damage criteria are performed to calculate the failure behaviour of the CFRP composites. Implicit and explicit solvers are available for FE software to calculate the non-linear behaviour of structure under loading conditions. In implicit solver, displacement is calculated by inverting the stiffness matrix; no time limit is there and calculates the time step through iterations. Nodal forces are calculated directly at the time step 't' by doing the inversion of the mass matrix, and it gives acceleration value in the explicit solver. In short duration time, the explicit solver is efficient to calculate the non-linear dynamic behaviour of impact problem for the small time steps for large model compared to the implicit solver as well as the inverse of the stiffness matrix in implicit analysis depends on mesh elements of the model for that numerical solver needed but not in case of explicit analysis.

### 2.1 Damage Propagation Criteria

The CFRP composite material under the impact load determined the different modes of failure such as the fibre, matrix and delamination failure between the plies. Damage initiation and propagation criteria are investigated to determine the failure behavior of the CFRP laminate [3–6].

### 2.2 Modelling of CFRP Laminate and Impactor

The CFRP laminate is made up of ten plies, and each ply thickness is 2.2 mm and the dimension of the plate 80 mm × 80 mm × 2 mm [13]. The plate and spherical projectile are considered as deformable and rigid projectile, respectively. The composite plate is having a 2D planer structure with all fibres having 0° orientation. The spherical bullet diameter is 7.5 mm and impactor velocity varied 100–150 m/s. The general contact modelling was applied between the plate and the spherical projectile with the friction coefficient value of 0.3. The composite ply and spherical projectile are meshed by the eight-noded brick element and shell element, respectively (Fig. 1). The composite plate and projectile are meshed with converged value of 45,560 and 1653 elements, respectively. Cohesive surface modelling is employed between the plies using the interlaminar properties of the stiffness, strength and fracture energy.

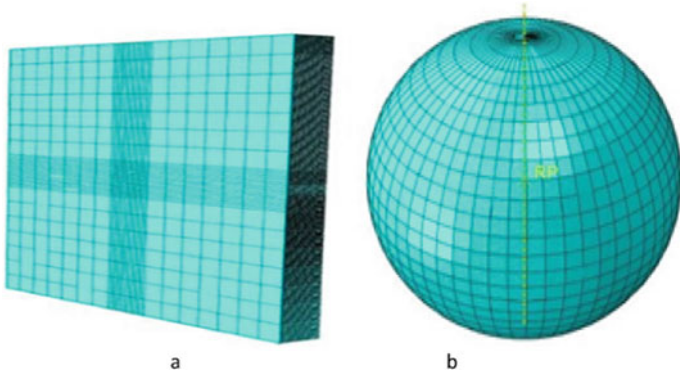


**Fig. 1** Finite element modelling of (a) composite laminate (b) spherical projectile

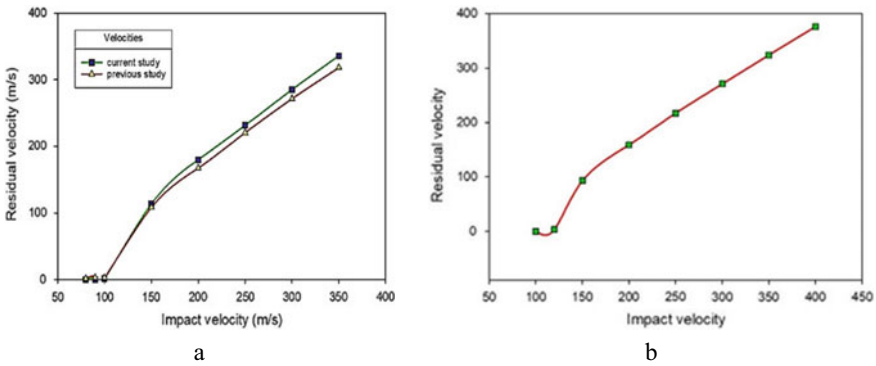


**Fig. 2** a Ballistic limit of the for normal impact b ballistic limit for oblique impact

### 3 Numerical Results and Discussion

The CFRP composite consists of eight plies of laminate is subjected to the rigid spherical projectile for the normal and oblique impact (Fig. 2a, b). The progressive damage modelling was developed based on the failure initiation and propagation model. The numerical response of CFRP composite plate under normal impact results are validated from the literature Puente et al. [16] for the residual velocity versus impactor velocity. The normal and oblique impact results are also showed that the non-linear behavior of the residual velocity. The CFRP composite plate showed that the ballistic limit of the normal and oblique impact are 100 m/s and 120 m/s, respectively. Similar non-linear behaviour for the residual velocity and impactor velocity also observed that for the oblique impact at 45° of CFRP composite plate. The oblique impact at 45° clearly showed that the ballistic impact velocity increases 16.66% as compared to normal impact.



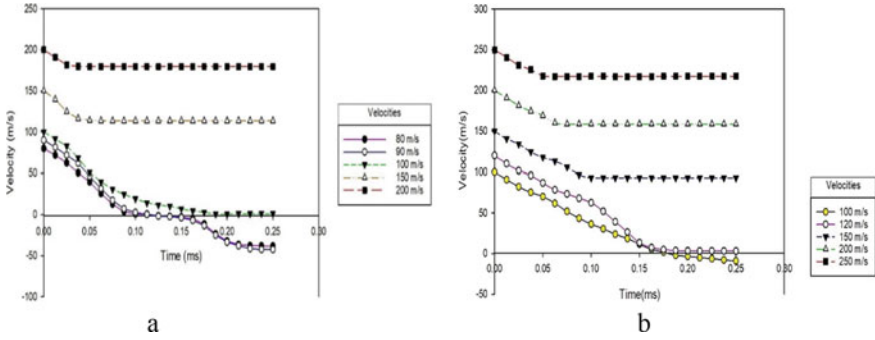


**Fig. 3** a Impactor velocity versus time for normal impact b impactor velocity versus time for oblique impact

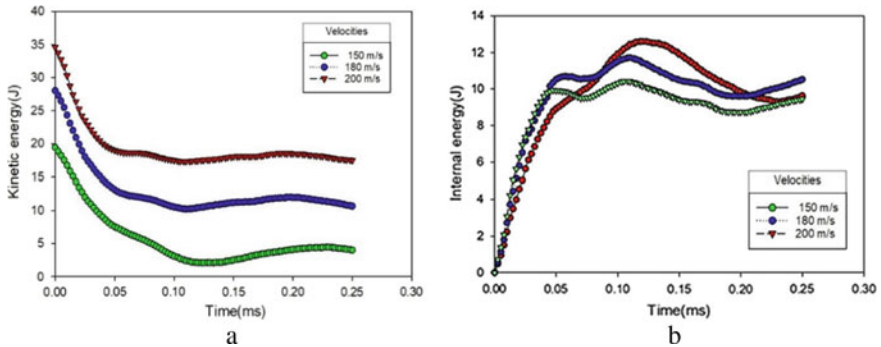


**Fig. 4** Kinetic energy and internal energy time history for normal impact

The impactor velocity of the last ply is nearly equal to zero for the composite laminate; the impactor velocity is known as the ballistic limit of the CFRP composite. The present study considered the eight different impactor velocities for the normal and oblique impact (Fig. 3). It is also found that the resistance of the CFRP plate to the perforation in case of oblique impact is more as compared to normal impact because the oblique impact loads; load is distributed partially in the longitudinal direction and partially in the transverse direction. Hence, the CFRP composite showed that the oblique impact offers more ballistic velocity, more energy absorption and resistance to the perforation in comparison to the normal impact. The impactor velocity versus time graphs also found that the limiting velocity of the normal impact is 100 m/s (Fig. 3). The CFRP laminate subjected to the oblique impact 45° angle showed the ballistic limit of 120 m/s.

The kinetic energy and internal energy dissipation of the CFRP plate under normal impact are showed in Fig. 4. CFRP plate is showed that the maximum energy absorption approximate 20 J for the normal impact at velocity 100 m/s.

Similar results for the kinetic energy (KE) and internal energy (IE) of the CFRP composite panel for the oblique impact showed in Fig. 5. Energy balanced models are shown in Fig. 6. The results showed that the total KE is dissipated from the IE of the

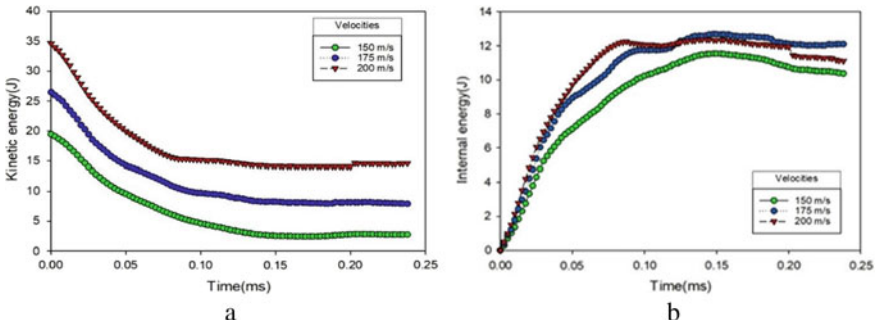


Fig. 5 Kinetic energy and internal energy time history for oblique impact

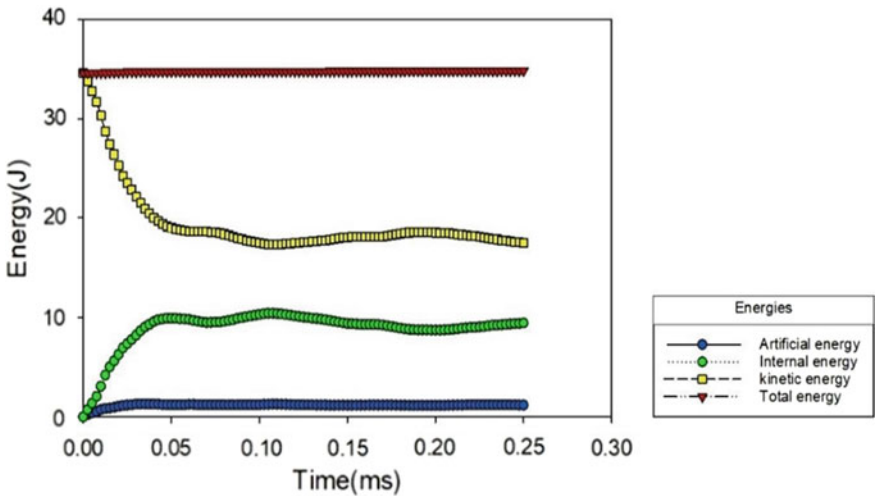


Fig. 6 Energy time history for normal impact at 200 m/s

plate, KE of the plate and artificial energy of the plate. The artificial energy result also showed that the very less in comparison to the internal energy (<5%) of the plate.

The cohesive surface modelling is considered in between the laminates; a certain amount of energy is dissipated at the cohesive zone to model the delamination failure. The delamination failure behaviour of the CFRP laminates is subjected to the normal impact showed (Fig. 7) in between the plies for the different time intervals at impactor velocity 200 m/s.

#### 4 Conclusion

The continuum damage modelling is used to determine the realistic behaviour of the CFRP panel subjected to normal and oblique impacts. Residual velocity versus impactor velocity results are verified with the published results in normal impact. Numerical results that showed are very close to the experimental results. The ballistic limit for the CFRP

composite under normal impact and oblique impact are investigated at 100 m/s and 120 m/s, respectively. Hence, the present results observed that the CFRP composite laminate subjected to oblique impact provides more resistance in comparison to the normal impact. Residual velocity versus impactor velocity showed the non-linear behaviour for the CFRP composite plate under the normal impact and oblique impact. The eight plies of the CFRP composite laminate showed that the maximum energy absorption approximate 20 J for the normal impact at velocity 100 m/s. Energy balanced model showed that the artificial energy is less than 5% of the internal energy. The CFRP composite laminate also observed that fibre matrix and delamination modes of failure under normal and oblique impact loading.

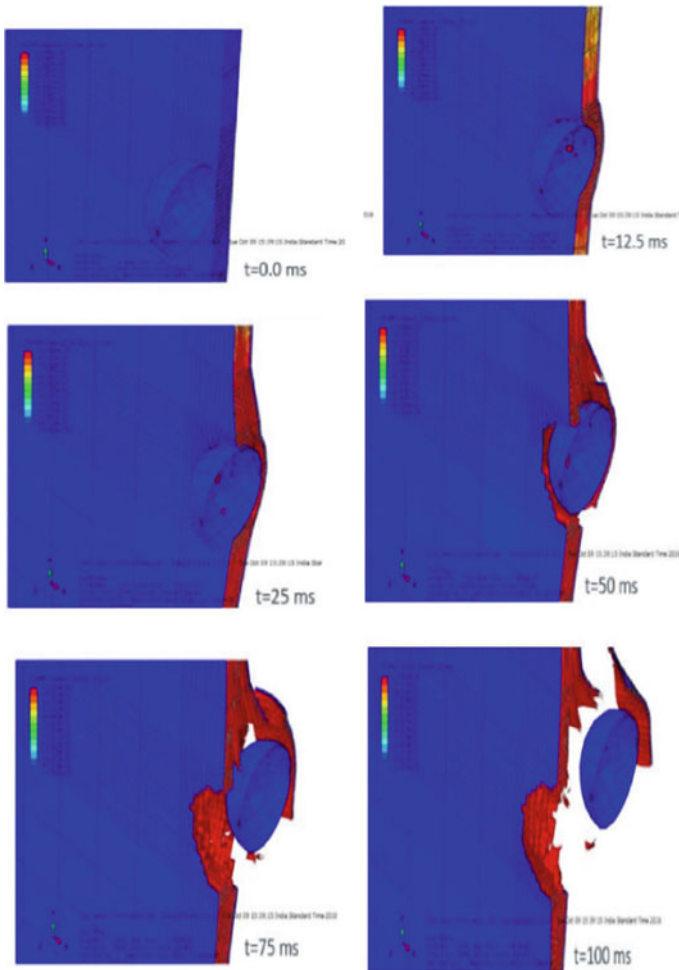


**Fig. 7** Delamination analysis of plate due to impact at 200 m/s, normal direction

## References

1. Patel S, Vusa VR, Soares CG (2019) Crashworthiness analysis of polymer composites under axial and oblique impact loading. *Int J Mech Sci* 156:221–234
2. Li G, Tan KH, Fung TC (2021) A rate-dependent continuum damage model for dynamic shear debonding of CFRP-concrete interface. *Int J Impact Eng* 152:103844
3. Yan J, Lia Y, Xua Z, Li Z, Huang F (2020) Experimental and numerical analysis of CFRP strengthened RC columns subjected to close-in blast loading. *Int J Impact Eng* 146:103720
4. Patel S, Ahmad S (2016) Probabilistic failure of graphite epoxy composite plates due to low velocity impact. *ASME: J Mech Des* 139(4):044501–044501-4
5. Bandaru AK, Patel S, Sachan Y, Ahmad S, Alagirusamy R, Bhatnagar N (2016) Low velocity impact response of 3D angle-interlock Kevlar/basalt reinforced polypropylene composites. *Mater Des* 105:323–332
6. Bandaru AK, Patel S, Sachan Y, Ahmad S, Alagirusamy R, Bhatnagar N (2016) Mechanical behavior of Kevlar/basalt reinforced polypropylene composites. *Compos A Appl Sci Manuf* 90:642–652
7. Patel S, Ahmad S, Mahajan P (2018) Safety assessment of composite beam under ballistic impact. *J Thinwalled Struct* 126:162–170
8. Patel S, Guedes Soares C (2017) System probability of failure and sensitivity analyses of composite plates under low velocity impact. *Compos Struct* 180:1022–1103
9. Patel S, Ahmad S, Mahajan P (2016) Probabilistic finite element analysis of S2-glass epoxy composite beams under damage initiation due to high velocity impact. *ASCE-ASME J Risk Uncertain Eng Syst Part B: Mech Eng* 2(4):044504–044504-3
10. Sudhir Sastry YB, Budarapu PR, Krishna Y, Devaraj S (2014) Studies on ballistic impact of the composite panels. *Theoret Appl Fract Mech* 72:2–12
11. Hazell PJ, Appleby-Thomas G (2009) A study on the energy dissipation of several different CFRP-based targets completely penetrated by a high velocity projectile. *Compos Struct* 91(1):103–109
12. Wang B, Xiong J, Wang X, Ma L, Zhang GQ, Wu LZ, Feng JC (2013) Energy absorption efficiency of carbon fiber reinforced polymer laminates under high velocity impact. *Mater Des* 50:140–148
13. Manes A, Bresciani LM, Giglio M (2014) Ballistic performance of multi-layered fabric composite plates impacted by different 7.62 mm caliber projectiles. *Proc Eng* 88:208–215
14. Bandaru AK, Ahmad S, Bhatnagar N (2017) Ballistic performance of hybrid thermoplastic composite armors reinforced with Kevlar and basalt fabrics. *Compos A* 97:151–165
15. Tanabe Y, Aoki M (2003) Stress and strain measurements in carbon-related materials impacted by a high-velocity steel sphere. *Int J Impact Eng* 28(10):1045–1059
16. Puente JL, Zaera R, Navarro C (2008) Experimental and numerical analysis of normal and oblique ballistic impacts on thin carbon/epoxy woven laminates. *Compos Part A* 39:374–387



# Ballistic Performance of 3D Hybrid Composite Laminates

Roopendra Kumar Pathak, Shivdayal Patel<sup>(✉)</sup>, and Vijay Kumar Gupta

Discipline of Mechanical Engineering, PDPM, Indian Institute of Information Technology  
Design and Manufacturing, Jabalpur, India  
shivdayal@iiitdmj.ac.in

## 1 Introduction

Recently, polymer composite materials under impact loading have grown over the years due to the superior properties they exhibit over metals. Polymer composites are commonly used for various applications such as military, aerospace, and engineering field because of their high specific strength, high specific stiffness, and impact resistance. Wei et al. [1] reported 3D woven fiber ballistic performance was evaluated in the form of residual velocity, damage distribution area, and energy absorption mechanisms. Liu et al. [2] compared deformation and energy absorption of multi-phase of STF with graphene oxide, carbon nanotubes and found that graphene oxide additives gave better results. Gilson et al. [2] studied the kinetic energy of projectile after impact, displacement of laminas, and failure phenomena of fibers were influenced by projectile geometry and material. Liu et al. [3], Zhu et al. [4] investigated the failure parameters of fiber metal composites under high-velocity impact based on continuum damage. Nunes et al. [5] proposed an experimental and numerical approach for Kevlar fiber composites impacted by projectiles of various geometrical parameters. Abtey et al. [6] discussed the effect of the thickness of the laminate, density of laminate, and projectile are the key parameters for defining the ballistic impact. Contact time, damage area, and displacement for hemispherical, flat, and conical punches on the laminated plate have been discussed [7]. Considerable work has been carried out in the field of ballistic impact on composite panels is evaluated by modeling, simulation, and experiments [8]. Impact velocities of different ranges are considered for normal and oblique impacts [9]. Palta et al. [10, 11] worked with the advanced combat helmet (ACH) using the NIJ-0106.01 standard for 1.1 g FSP, 9-mm FMJ bullet, and 0.223 FMJ rifle projectiles. Patel et al. [12] suggested that antisymmetric cross-ply is more reliable than the symmetric cross, symmetric angle, and antisymmetric angle plies. Soutis and Shi [13] investigated of dynamic and static properties of carbon/basalt composite in intercalated. Bandaru et al. [14, 15] compared non-symmetric and symmetric hybrid armors with polypropylene (PP) as a matrix adding maleic anhydride grafted (MAg) and found a 26.27% increment in the ballistic limit of symmetric stacking sequence panel compared to the non-symmetric panel. It has been concluded that ballistic performance increased by 16.44% and 20% for 3D orthogonal and 3D angular architecture fabric armor panels compared to 2D plain-woven fabric armor panels [14]. Chakrabarti and Ansari [16] studied the damage dominating area in

the panel and impactor, failure in the thickness direction, deflection, front and back surface damaged area, effects of length, and thickness of lamina on the ballistic limit. The behavior of damage propagation and erosion of impactor analyzed under high-velocity impact for spherical projectile, FSP, and FMJ impactor strikes the Kevlar composite helmet with different impact velocities [17, 18]. Rahman et al. [19] compared the FE models for 7.62 mm armor-piercing projectile for the ballistic limit velocity of different layered configurations. Ahmad and Bandaru [20] have been carried out the results in the field of simulation with cohesive elements exhibit better delamination progression in reduced and full integration hexahedra elements. Yen [21] introduced failure-initiation criteria and damage evolution laws for differentiating the fiber and matrix modes of damages.

The lightweight hybrid composite panels were developed to investigate the ballistic behavior of the different laminates that offer high impact resistance. Progressive damage modeling is developed for different hybrid composite panels to investigate the ballistic velocity, residual velocity, and failure behavior of the hybrid composite material. Damage initiation and propagation failure model implemented in the user-defined subroutine to investigate the different modes of failure such as fiber tension and compression, matrix tension and compression, and delamination failure. Validation study of the hybrid composite panel performed with experimental results is available for the literature [17]. In the present study, the strain-based Yen failure criteria are used to predict the failure initiation and propagation failure behavior of the hybrid composites. Presently, 3D fiber damage analysis of hybrid laminates with deformable impactors has been done.

## 2 Numerical and Material Modeling

See Table 1.

**Table 1** Composite laminates with stacking sequences

Laminate	Number of layers
K3B3	8 layers of Kevlar and 8 layers of basalt
B3K3	8 layers of basalt and 8 layers of Kevlar
K3-16	16 layers of Kevlar
B3-16	16 layers of basalt

### 2.1 Numerical Modeling of Composite Laminate and Projectile

K3B3 and B3K3 are hybrid configurations and B3-16 and K3-16 are non-hybrid configurations (Table 1). Laminates for each configuration were impacted by the FMJ projectile. Dimensions of 150 mm × 150 mm × 32 mm with fixed boundary conditions along their edges. Target plates meshed with SC8R (8 node quadrilateral) elements. The FE model

of the plates is simplified to just 16 layers. The finite element mesh of a 9 mm FMJ bullet (Mass = 8.2 g) has two components: a copper jacket and a lead core [20]. Meshing for brass Jacket (Shell thickness = 0.25 mm) and lead core (diameter of core = 8.5 mm) are S4R (0.001 m) and C3D8R (0.001 m), respectively (Fig. 1).

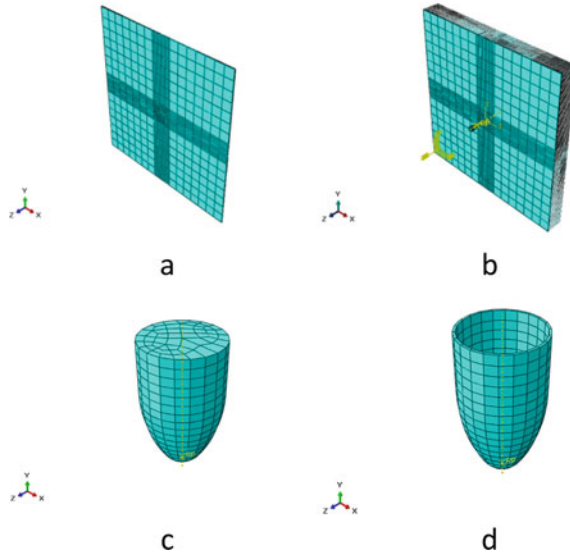


**Fig. 1** Numerical model of (a) composite lamina (b) composite laminate (c) brass jacket (d) lead core

## 2.2 Material Damage Constitutive Models for Composite Laminate and Projectile

Constitutive equations and appropriate failure criteria are the important factors for simulating the high-velocity impact phenomenon for composite panels. The copper jacket material is modeled by the Johnson–Cook (J–C) model while the lead material is assumed as elastic using Steinberg–Guinan [14, 17]. Mie-Gruneisen EOS can be used for modeling high strain rates. Thermal stresses and strain rates are the effective parameters of this model which are applicable in a wide range of engineering and industrial fields. Yen criteria were used with considering the high strain rate effects to analyze which is generally a modified form of Hashin’s damage criteria. The fiber failure modes are considered due to combined transverse shear and uniaxial tension, uniaxial compression, transverse compressive loading while matrix damages are considered due to shear stresses and in-plane tensile and delamination. Hashin’s damage initiation for fiber composites has been modified in several forms. Yen [19] derived the following equations for different damage mechanisms (Table 2).

**Table 2** Cohesive properties of laminate

Properties	Mode I	Mode II	Mode III
Normalized elastic modulus (Pa/m)	1.03346E+013	4.672E+012	4.672E+012
Interlaminar strength (Pa)	2.1176E+008	3.4049E+008	3.4049E+008
Interlaminar fracture toughness ( $J/m^2$ )	1500	4500	4500

### 3 Numerical Results and Discussion

The dynamic explicit analysis is performed for the high-velocity impact problem to investigate the modes of failure for the composite laminate. Finite element analysis is carried out for the different laminates subjected to the high-velocity impact of the FMJ projectile. The hybrid composite laminates are made up of Kevlar and basalt fabric plies to determine the ballistic behavior of the FMJ projectile. The panel and bullet stored 100% of the total internal energy because both of them had large plastic deformations. Another important observation is that the K3-16 panel absorbed the maximum internal energy which is 78.75% of the total internal energy at its ballistic limit velocity, while K3B3, B3K3, and B3-16 absorbed 78.37%, 78.39%, 77.31%, respectively, of the total internal energy at their ballistic limit velocity. The round nose of the FMJ impactor of its geometry gives a better result to absorb the internal energy of the laminates. During the ballistic impact, composite laminate absorbed kinetic energy also from the bullet and spread to all areas failing the laminate. It is observed that among the four different composite panels with deformable FMJ projectile, K3-16 absorbed the maximum kinetic energy because of its high ballistic limit velocity. Several numerical analyses on hybrid panels are carried out to normal impact of FMJ projectile. The impact velocity of the impactor is varied from 320 to 520 m/s, and the numerical simulation is also carried out in the same velocity range (Fig. 2).

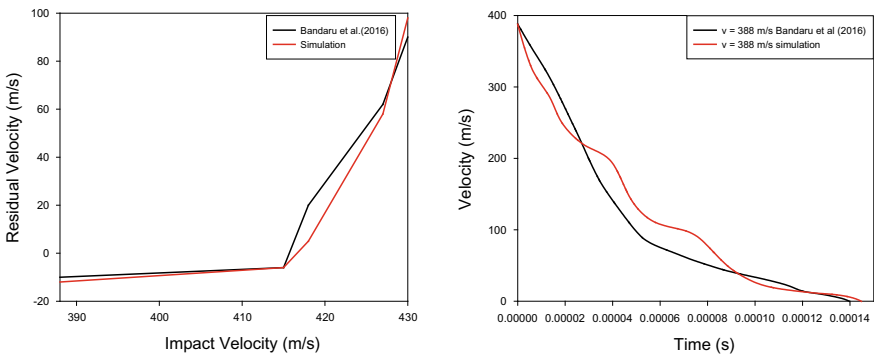


**Fig. 2** The response of composite panel [B3D/BPL2/H3D/HPL2/K3D/KPL]<sub>s</sub> impacting with FMJ projectile (a) impact velocity versus residual velocity (b) velocity versus time



Figure 3 shows velocity–time histories of FMJ impactors with strike velocity 410 m/s, 430 m/s, 400 m/s, 450 m/s impacting K3B3, B3K3, B3-16, K3-16, respectively, the respective residual velocity approaches to zero. The ballistic limit velocity of K3-16 obtained 450 m/s which is more than 8.88%, 4.44%, 11.11% of K3B3, B3K3, B3-16, respectively. The ballistic limit velocity of K3-16 among different laminates for FMJ projectile is found high. Thick laminates absorbed the maximum amount of energy due to delamination. Crushing of fibers at local region after impact also occurred. Delamination has been occurred due to tensile wave reflection after the generation of compressive wave formation through thickness.

Four composite laminates with a different arrangement of lamina have been impacted by FMJ impactor to study the impact resistance. The numerical model predicts perforation of laminate and residual velocity. When strike velocity reaches the ballistic limit velocity, the effect of impact becomes very sensitive to impact speed, material defects, and angle. Basalt laminate promotes natural fibers backing with Kevlar fibers and shows good agreement of damage tolerance compared to other laminates. Numerical simulation results of the ballistic limit velocity of K3B3, B3K3, B3-16, and K3-16 are shown in Fig. 4. The projectile impacts the front surface of the laminate and initiates damages. Erosion of the materials starts at the projectile front face and progresses to the laminas. Energy from the projectile passes to the next ply in the form of back face deflection on the rear side of the last plate. Stretching of fibers on the backside of laminate absorbed a large amount of kinetic energy of the impactor. The flattened and mushroomed shape of the impactor after the impact occurred due to the dissipation of kinetic energy (Table 3).

When the projectile left the laminate contact, the laminate still deforms. Damage failure phenomena of the laminates in terms of damage area on front and back surface, deformation of the lamina near the impact zone, delamination, and bending of laminate were more pronounced in the numerical simulation results. When the material is pulled back after the impact of the conical flat bottom as it penetrates, showing the sinking of material at the front face and the spreading of laminas near the back surface. As the projectile perforates, the damaging effect in the composite panel changes. Initially, compression phenomena are dominant. At later stages, fiber stretching and shearing are dominant. Delamination, in-plane failure, and erosion of material are the three modes in the case of partial perforation. The detachment of fibers is also a failure mode due to tensile force near the contact point. The detachment of fiber longitudinal and transverse direction is observed as the projectile penetrates. Different failure modes such as matrix cracking, delamination, fiber failure, and fiber crushing are shown in Table 4.

## 4 Conclusion

The ballistic impact has been investigated for basalt hybridization with Kevlar fibers and polypropylene. The nonlinearity of 3D composite laminates was seen more than 2D composite laminates. Arrangements of laminas were found to affect the ballistic velocity with K3-16 and B3K3 configuration in numerical results. Basalt has good toughness property; the effect of higher toughness at the interfaces of laminas gives more resistance and efficient response to ballistic impact. Front face basalt fiber has a higher ballistic

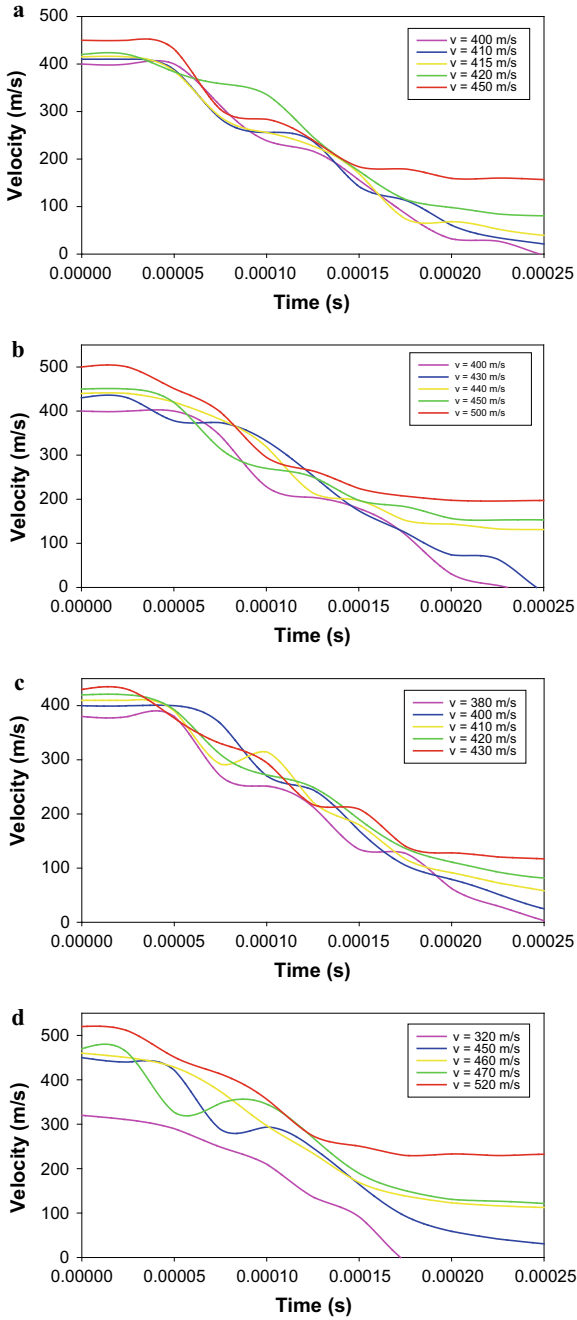


**Fig. 3** Velocity versus time plots for (a) K3B3 (b) B3K3 (c) B3-16 (d) K3-16

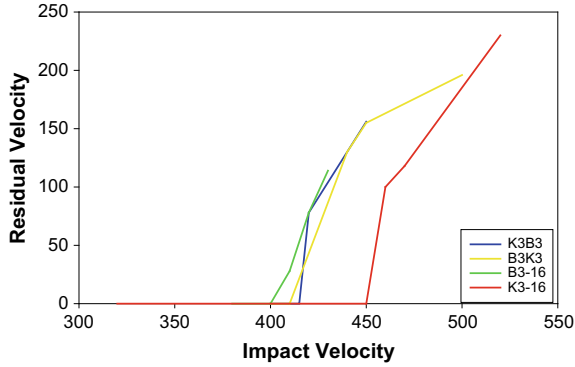


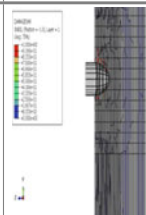
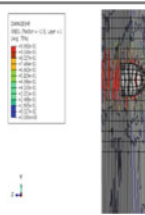
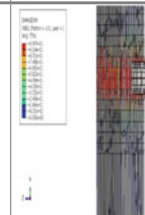
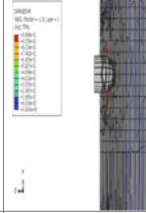
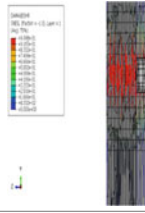
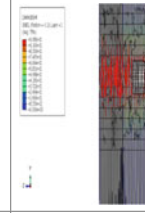
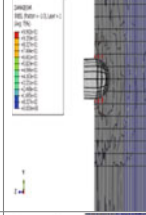
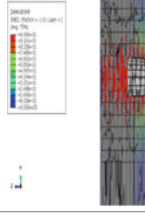
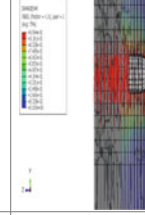
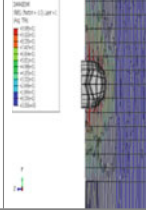
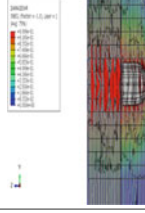
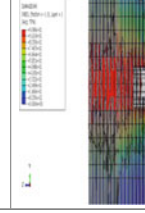
Fig. 4 Impact velocity versus residual velocity for different panels

Table 3 Ballistic impact performance for different eight composite laminates

S. No.	Type of laminate	$V_i$ (m/s)	$V_r$ (m/s)	IE of whole model (J)	IE of bullet (J)	IE of panel (J)
1	K3B3	400	0	400	90	310
		410	0	411	93	318
		415	28	420	96	324
		420	78	430	98	332
		450	156	447	107	340
2	B3K3	400	0	420	90	330
		430	0	435	94	341
		440	110	450	98	352
		450	165	455	100	355
		500	196	510	118	392
3	B3-16	380	0	375	88	287
		400	0	410	93	317
		410	38	434	95	339
		420	78	440	97	343
		430	114	437	100	337
4	K3-16	320	0	270	72	198
		450	0	480	102	378
		460	118	490	104	386
		470	145	490	109	381
		520	230	520	117	403

velocity compared to front Kevlar face. B3K3 and K3-16 are found as the best laminates for ballistic performance. Delamination and fiber stretchings were observed as the important damage mechanisms accompanied by laminate failures. A significant amount of energy has also been absorbed in the form of plastic deformation of the projectile which also increases the ballistic performance of any composite laminate. There has not been found much difference in ballistic velocity of K3-16 and B3K3. The K3-16 finds a suitable combination of dynamic and static properties, but the highest fraction of expensive Kevlar reinforcement while basalt promotes the natural fibers with approximately the same impact resistance.

**Table 4** Shear failure mechanisms of different laminates for spherical impactor


Laminate	$t = 7.5e-5$ s	$t = 1.5e-4$ s	$t = 5e-4$ s
K3B3 ( $v = 410$ m/s)			
B3K3 ( $v = 430$ m/s)			
B3-16 ( $v = 400$ m/s)			
K3-16 ( $v = 450$ m/s)			

## References

1. Wei Q, Yang D, Gu B, Sun B (2021) Numerical and experimental investigation on 3D angle interlock woven fabric under ballistic impact. *Compos Struct*
2. Liu L, Cai M, Liu X, Zhao Z, Chen W (2020) Ballistic impact performance of multi-phase STF-impregnated Kevlar fabrics in aero-engine containment. *Thin-Walled Struct* 157:107103
3. Liu YJ, Jiang Z, Wen HM (2020) Predicting impact induced delamination of FRP laminates. *Int J Impact Eng* 137:103436
4. Zhu Q, Zhang C, Curiel-Sos J, Bui TQ, Xu X (2019) Finite element simulation of damage in fiber metal laminates under high velocity impact by projectiles with different shapes. *Compos Struct* 214:73–82
5. Nunes SG, Scazzosi R, Manes A, Amico SC, Junior WFA, Giglio M (2019) Influence of projectile and thickness on the ballistic behavior of aramid composites: experimental and numerical study. *Int J Impact Eng* 132:103307
6. Abteaw MA, Boussu F, Bruniaux P, Loghini A, Cristian I (2019) Ballistic impact mechanisms—a review on textiles and fibre-reinforced composites impact responses. *Compos Struct* 223:110966
7. He J, He L, Yang B (2019) Analysis on the impact response of fiber-reinforced composite laminates: an emphasis on the FEM simulation. *Sci Eng Compos Mater*:1–11
8. Okhawilal M, Hizirolu S, Rimdusit S (2018) Measurement of ballistic impact performance of fiber reinforced polybenzoxazine/polyurethane composites. *Measurement* 130:210
9. Schwaba M, Todta M, Tauchner J, Schlie D, Pettermann HE (2018) Modeling, simulation, and experiments of high velocity impact on laminated composites. *Compos Struct* 205:42–48
10. Palta E, Fang H, Weggel DC (2017) Finite element analysis of the advanced combat helmet under various ballistic impacts. *Int J Impact Eng*
11. Yen CF (2012) A ballistic material model for continuous-fiber reinforced composites. *Int J Impact Eng* 46:11–22
12. Patel S, Ahmad S, Mahajan P (2017) Safety assessment of composite armor under ballistic impact. *Proc Eng* 173:1901–1908
13. Shi Y, Soutis C (2017) Modelling low velocity impact induced damage in composite laminates. *Mech Adv Mater Modern Process* 3:14
14. Bandaru AK, Chavan VV, Ahmad S, Alagirusamy R, Bhatnagar N (2016) Ballistic impact response of Kevlar® reinforced thermoplastic composite armors. *Int J Impact Eng* 89:1–13
15. Bandaru AK, Patel S, Sachan Y, Ahma S, Alagirusamy R, Bhatnagar N (2016) Mechanical behavior of Kevlar/basalt reinforced polypropylene composites. *Compos Part A*, 90:642–652
16. Ansari MM, Chakrabarti A (2016) Impact behavior of FRP composite plate under low to hyper velocity impact. *Compos B* 95:462–474
17. Rodríguez-Millán M, Olmedo A, Romualdo G, Feito N, Loya JA, Miguélez MH (2015) Behavior of a new combat helmet design against ballistic impact. *Exp Num Anal*
18. Silva MAG, Cisma-siu C, Chiorean CG (2005) Numerical simulation of ballistic impact on composite laminates. *Int J Impact Eng* 31:289–306
19. Rahman NA, Abdullah S, Zamri WFH, Abdullah MF, Omar MZ, Sajuri Z (2016) Ballistic limit of high-strength steel and Al7075-T6 multi-layered plates under 7.62-mm armour piercing projectile impact. *Latin Am J Solids Struct*
20. Bandaru AK, Ahmad S (2016) Modeling of progressive damage for composites under ballistic impact. *Compos B* 93:75–87
21. Tham CY, Tan VBC, Lee HP (2008) Ballistic impact of a KEVLARs helmet: experiment and simulation. *Int J Impact Eng* 35:304–318



# Experimental and Statistical Analysis of the Jute Fabric Composites Under Tensile Loading

Kumar Maharshi and Shivdayal Patel<sup>(✉)</sup> 

PDPM Indian Institute of Information Technology, Design and Manufacturing, Jabalpur,  
Madhya Pradesh, India  
shivdayal@iiitdmj.ac.in

## 1 Introduction

Jute fiber composite is most commonly demanded due to the superior mechanical characteristics for structural applications in aerospace and automobile industries. There have been a constant strive for better materials which encompass the lightweight and high strength to density ratio capabilities along with low cost. Composite materials, especially the synthetic fiber composites pose these properties and have been under use for decades. But now, the demand for more eco-friendly and low-cost materials that could help sustain environment have been driven by various regulatory bodies throughout the industries. The natural fiber composites serve the purpose like those of jute, flax, hemp and other fibers [1–3]. Jute fiber composites offer the biodegradability, recyclability, lightweight, low energy consumption advantages and low cost. However, these composites have been needed to determine the variability of the composite material to determine the realistic failure behavior of the composite [4–10].

Despite having many better properties compared to the conventional materials, they have always shown poor reliability in strength and failure properties. To compensate for such issues, more and more testing has to be done to establish a reliable database, but that ultimately defeat the purpose by increasing the cost. This has led many scientists to perform statistical analysis to predict the properties for the desired applications. Basu et al. [11] performed the strength reliability analysis on monolithic  $ZrO_2$  and  $ZrO_2-TiB_2$  composites and found that Weibull model was more appropriate for the strength-based data of composites. Torres et al. [12] presented the detailed study of long natural fiber composites for elastic modulus, strength and failure strain where they observed that elastic modulus followed normal distribution and other parameters to Weibull distributions. Many authors reported similar study for the fracture properties of natural fiber composites as well [11, 13–17].

The main objective of this paper was to study the probabilistic behavior of the tensile properties of jute fabric composite under tension test due to very limited study in this area of research. The author fabricated the samples using VIM technique where 38% fiber volume fraction (FVF) was achieved, and the specimen was machined using Abrasive water jet machine (AWJM) as per the GOST 25.061-80 standard. The experimental data was extrapolated and was curve fitted to normal, log-normal and two-parameter

Weibull distribution to calculate the parameters, and then goodness of fit test was done to check the feasibility of the distribution functions. The analysis showed that tensile Young's modulus and strength followed log-normal and Weibull distributions, respectively, which could help determine the variability and actual failure behavior of the jute fiber composites.

## 2 Experimental Study of Jute Fabric Composite

In the present study, the commercially available 240 GSM jute fiber fabric with plain weave ( $1 \times 1$  twill) was used as the reinforcement, and a general purpose epoxy and hardener were used as matrix due to its affordability and easy availability. The fabrication of the composite panels for tensile testing was done using vacuum infusion method (VIM). This method eliminates gases and air from the composite and distribute the matrix evenly, minimizing the flaws and helps achieve higher fiber volume fraction. The woven jute fabric composite was considered as transversely isotropic material because of its balanced and similar properties in 1- and 2-directions.

The composite was made in panel form for the tensile testing, and abrasive water jet machining (AWJM) was employed for cutting the sample as per the standard to achieve higher accuracy on the dimensions and low surface roughness on the edges to minimize the stress concentration. A total of four layers of jute fabric was taken for the fabrication process. After the successful fabrication of the sample, the composite obtained had 38% fiber volume fraction.

## 3 Tensile Testing

The use of natural fiber composite materials has grown many folds as they pose specific properties compared to conventional materials. Their ability to showcase combination of high strength, toughness and hardness has been very useful in many engineering applications such as in aerospace and automobile industries. These significant properties still lack reliability due to the variations and flaws that come during their fabrication. The present study was focused to study the reliability of the tensile properties of jute composite as it is the most important mechanical property that highlights the strength, modulus and failure aspects of any material. The tension test was performed using the Russian GOST 25.601-80 standard on state-of-the-art universal testing machine (UTM) of Russian make, and properties like longitudinal tensile strength, modulus, Poisson's ratio and failure strain were obtained during the test. The details of the specimen as per the standard is shown in Fig. 1. The crosshead speed was 1 mm/min, and a total of 4 samples were tested.

Bonded strain gauges were used for measuring the longitudinal and transverse strains to calculate Poisson's ratio. The foil type strain gauges were preferred for strain measurement, and gauge specification was  $350 \Omega$  resistance and 2.0 gauge factor. All the data collected by the strain gauges were recorded in the form of load–deflection curves in the data acquisition system (DAQ).

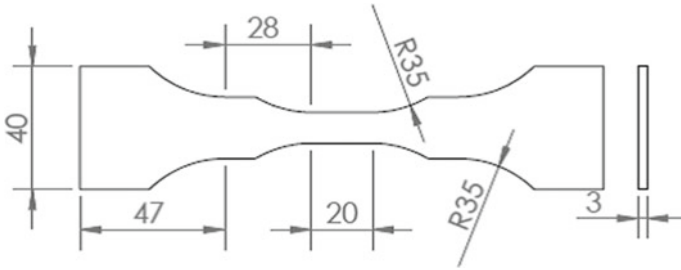


**Fig. 1** Schematic of the tension test sample as per standard GOST 25.601 (dimensions are in mm)

## 4 Statistical Analysis of Jute Composite

The use of natural fiber composites has been limited not only due to their par inferior properties compared to synthetic ones in some aspects but also due to the reliability in their properties. The reliability in strength and fracture failure have been the important deciding factors for any natural fiber composites because various factors such as chemical compositions, plant species, location of fiber in the plant, environmental conditions in cultivation area, fiber processing methods, inherent shape and cross-section irregularity cause variations in the properties. Thus, it becomes difficult to rely only on the experimental/deterministic data to evaluate the reliability of the composite especially related to engineering applications. The probabilistic approach for such composites lays groundwork for the experimental data by realizing the behavior of the material under the given set of conditions.

In the present study, the experimental data have been extrapolated to 100 data points based on mean and standard deviation of the tested data as the basis. The data points for tensile strength and modulus have been studied under normal, log-normal and two-parameter Weibull distribution, where the distribution parameters such as location, scale and shape were evaluated. Based on these parameters, maximum likelihood estimation, chi-squared and Kolmogorov–Smirnov fit tests were performed to check which model best fitted the dataset.

### 4.1 Normal Distribution

A normal distribution function is a continuous probability distribution for real-valued random variable whose distribution function in general form is given below

$$f(x) = \frac{1}{\sigma\sqrt{2\pi}} e^{-\frac{1}{2}\left(\frac{x-\mu}{\sigma}\right)^2} \quad (1)$$

Here,  $\mu$  and  $\sigma$  represents location and scale parameters, respectively.

### 4.2 Log-Normal Distribution

A log-normal distribution is a continuous probability distribution of random variable whose logarithm is normally distributed. The distribution function in general form is



given below.

$$f(x) = \frac{1}{x\sigma\sqrt{2\pi}} e^{\left(-\frac{(\ln x - \mu)^2}{2\sigma^2}\right)} \tag{2}$$

The unique property about this distribution is that it takes only positive real values and is convenient to model for measurement purpose in engineering sciences.

**4.3 Weibull Distribution**

A two-parameter Weibull probability function is given as

$$f(x; \lambda, \beta) = \begin{cases} \frac{\beta}{\lambda} \left(\frac{x}{\lambda}\right)^{\beta-1} e^{-(x/\lambda)^\beta}, & x \geq 0 \\ 0, & x < 0 \end{cases} \tag{3}$$

where  $\beta > 0$  is shape parameter, and  $\lambda > 0$  is scale parameter of the distribution. It is a widely used function for reliability analysis and uses shape parameter and scale parameter to define the characteristics of the given dataset of the population.

All the above equations were formulated to linear equations by inverting them, and the data points were fitted to get the curve fitting parameters [11].

To evaluate which model best fitted the dataset, different model discrimination methods were implemented including maximum likelihood estimation, chi-squared and Kolmogorov–Smirnov goodness of fit tests.

**4.4 Log-Likelihood Estimation**

The maximum likelihood estimators of the unknown parameters can be obtained by maximizing the log-likelihood function of the observed data

$$\ln(\theta; x) = \sum_{i=1}^N \ln[f_x(x_i; \theta)] \tag{4}$$

and differentiating to obtain the maximum of the function.

**4.5 Chi-squared Test**

A chi-squared test is a non-parametric test that is used to find out how the observed value of a given phenomenon is significantly different from the expected value. It determines how well theoretical distribution (such as normal, log-normal or Weibull) fits the empirical distribution.

$$\chi^2 = \left[ \frac{(O - E)^2}{E} \right] \tag{5}$$

where  $O$  is the observed frequency, and  $E$  is the expected frequency.

#### 4.6 Kolmogorov–Smirnov Test

The Kolmogorov–Smirnov test is a non-parametric test of the equality of continuous or discontinuous, on-dimensional probability distribution that can be used to compare the distance between empirical distribution function of the sample and the cumulative distribution function of the reference distribution

$$D = \max_{1 \leq i \leq N} \left( F(Y_i) - \frac{i-1}{N}, \frac{i}{N} - F(Y_i) \right) \quad (6)$$

### 5 Results and Discussion

To study the probabilistic behavior of jute composite, the experimental evaluation of the composite for tensile test was performed. A total of four samples were tested for various properties whose data have been tabulated in Table 1.

**Table 1** Experimental data of the tensile test for Jute composite

Sample No.	Young's modulus, $E_1 = E_2$ (GPa)	Ultimate tensile strength, $\sigma_1$ (MPa)	Poisson's ratio, $\nu_{12} = \nu_{13}$	Strain to failure, $\varepsilon_1$
1	7.822	53.65	0.144	0.01
2	6.835	65.2	0.169	0.014
3	7.114	53.7	0.149	0.021
4	8.04	64.6	0.152	0.022
Mean (SD)	7.45 (0.5708)	59.3 (6.4854)	0.153 (0.0108)	0.0167 (0.0057)

The load carrying ability of fibers in a composite is calculated by the fiber volume fraction (FVF). In the present study, higher FVF of 38% was achieved. During the test, the initial load was taken up by the matrix which was evident as linearly elastic in Fig. 2. The transfer of load was marked by smooth curve which also indicated the damage initiation in the composite. The load carrying behavior of jute fiber during the test showed nonlinearity. This could be attributed to several reasons such as non-uniformity in fiber, presence of air bubbles and void during fabrication or resin pockets near the interlacing fibers. These factors contributed to the variations in the properties of composite as also evident in the present work. To analyze such behavior, statistical approach was taken, and the properties obtained during the test were assessed.

To compensate for the limited experimental data available, these were extrapolated to 100 data points using the mean and standard deviation as the basis. The dataset was fitted to normal, log-normal and two-parameter Weibull distribution functions as shown in Figs. 3 and 4, and corresponding distribution parameters were obtained.

From the extrapolated dataset, the distribution parameters, log-likelihood values, chi-squared and Kolmogorov–Smirnov values were evaluated for tensile strength and modulus. The values are reported in Tables 2 and 3.

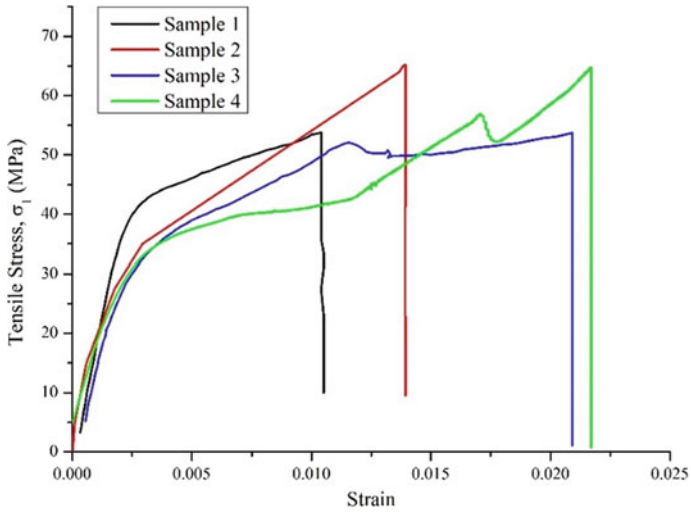


Fig. 2 Stress versus strain graph of the tension test

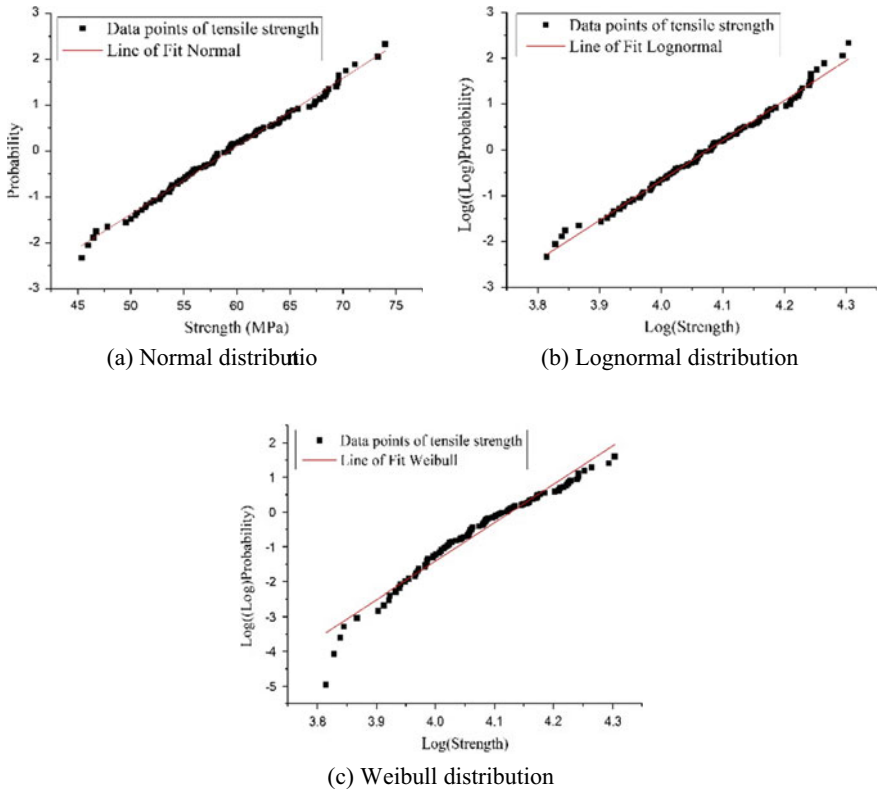
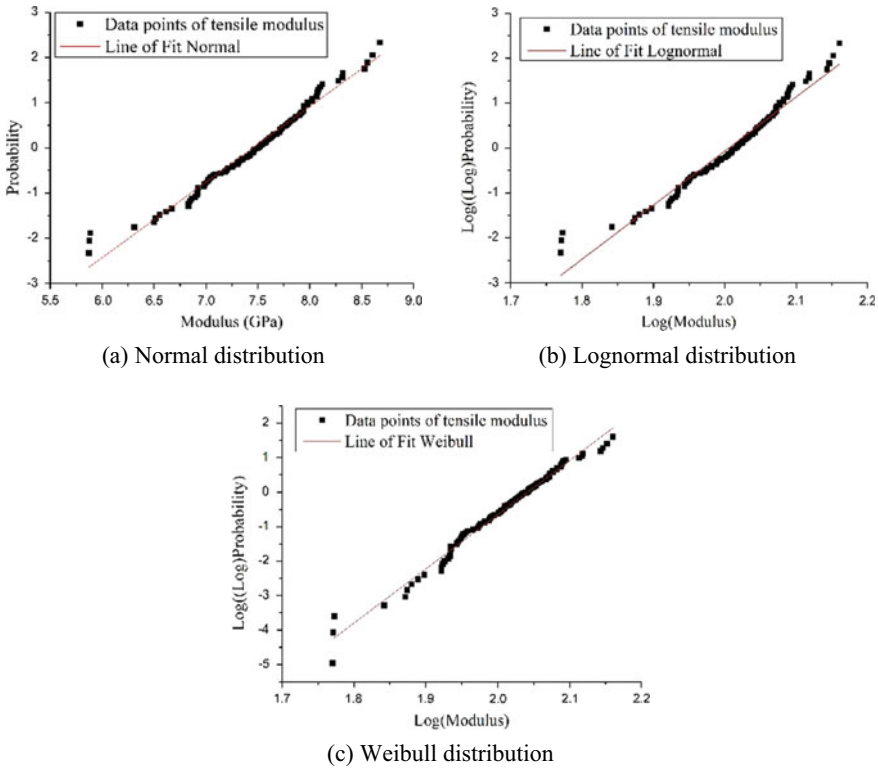


Fig. 3 Curve fitting plots of distribution functions for extrapolated data points of tensile strength



**Fig. 4** Curve fitting plots of distribution functions for extrapolated data points of tensile modulus

**Table 2** Estimated parameters, log-likelihood values and fitted chi-square and *K-S* values for different distribution functions of tensile strength

Distribution	Location	Scale	Shape	Log-likelihood	Chi-square	Kolmogorov–Smirnov
Normal	59.287	6.485	–	–328.349	–	–
Log-normal	4.076	0.1146	–	–328.551	7.1385	0.25096
Weibull	–	62.039	11.052	–331.571	13.9389	0.1887

**Table 3** Estimated parameters, log-likelihood values and fitted chi-square and *K-S* values for different distribution functions of tensile modulus

Distribution	Location	Scale	Shape	Log-likelihood	Chi-square	Kolmogorov–Smirnov
Normal	7.453	0.3258	–	–85.3292	–	–
Log-normal	2.0058	0.0786	–	–87.5685	5.8028	0.109
Weibull	–	14.9645	7.70786	–84.8461	1.7837	0.144

From Table 2, it is clear that for tensile strength, Weibull distribution best fit the dataset based on maximum likelihood criteria and goodness of fit test. It is a known fact that chi-square fit test may not be reliable, so the fitness based on  $K-S$  criteria was accepted. On the contrary, the tensile modulus showcased the opposite behavior where, it best fit the log-normal distribution. Higher likelihood and better chi-square value compared to Weibull was apparent from Table 3, and  $K-S$  value confirmed the fit.

The results clearly showed that the strength values strongly followed Weibull distribution, and modulus followed Log-normal distribution. The nature of Weibull distribution for strength values indicates that the experimental values obtained would have distributed symmetrically around the mean if the number of samples were more. Also, the skewed behavior of other parameter indicated the flaws in fabrication technique, presence of voids and unevenness of the fiber alignment which resulted in more divergent values from the theoretical approach and varying strength values, though the samples were machined from the same panel for experiment.

## 6 Conclusion

In the present study, the tensile properties were evaluated based on Russian GOST 25.601-80 standard, and the reliability of the experimentally obtained data was statistically studied and assessed to predict the behavior of each property. Jute fabric was chosen as the reinforcement, and epoxy-based resin and hardener was taken as the matrix for the fabrication of the composite using VIM and testing. The experiment showed the nonlinear behavior of the composite which was then assessed by fitting the data to normal, log-normal and two-parameter Weibull distributions. The strength values best fitted the Weibull distribution, indicating that higher probability of the data around the mean, whereas other parameter fitted to log-normal distribution.

The implication of such study is to define the reliability of the composite for engineering applications when fiber misalignment, air voids and resin pockets are some of the major defects that could drastically alters the strength properties of the materials. This study helps in understanding the composite behavior using the standard distribution models for jute fabric composite and help engineers analyze for its typical usage in automobile and aerospace load bearing applications.

**Acknowledgements.** The authors would like to thanks to Dr. Atul R. Bhagat, Head of the composite lab at DRDL Imarat, Hyderabad for their support in allowing us to perform the tests.

## References

1. Tsai SW, Hahn HT (1980) Introduction to composite materials. Technomic Pub., West Post
2. Li M, Pu Y, Thomas VM, Yoo CG, Ozcan S, Deng Y, Nelson K, Ragauskas AJ (2020) Recent advancements of plant-based natural fiber-reinforced composites and their applications. *Compos Part B: Eng* 200:108254
3. Pickering KL, Efendy MGA, Le TM (2016) A review of recent developments in natural fibre composites and their mechanical performance. *Compos: Part A*, 83:98–112

4. Patel S, Ahmad S, Mahajan P (2016) Probabilistic finite element analysis of S2-glass epoxy composite beams for damage initiation due to high velocity impact. *ASME J Risk Uncertainty Part B, Mech Eng* 2(4):044504–044504-3
5. Kumar BA, Patel S, Sachan Y, Ahmad S, Alagirusamy R, Bhatnagar N (2016) Low velocity impact response of 3D angle-interlock Kevlar/basalt reinforced polypropylene composites. *Mater Des* 105:323–332
6. Kumar BA, Patel S, Sachan Y, Ahmad S, Alagirusamy R, Bhatnagar N (2016) Mechanical behavior of Kevlar/basalt reinforced polypropylene composites. *Compos A* 90:642–652
7. Patel S, Soares CG (2018) Reliability assessment of glass epoxy composite plates due to low velocity impact. *Compos Struct* 200:659–668
8. Patel S, Ahmad S, Mahajan P (2018) Safety assessment of composite beam under ballistic impact. *J Thin-walled Struct* 126:162–170
9. Bandaru AK, Patel S, Bhatnagar N, Ahmad S (2018) An experimental and numerical investigation on the low velocity impact response of thermoplastic hybrid composites. *J Compos Mater* 52(7):877–889
10. Patel S, Ahmad S (2017) Probabilistic failure of graphite epoxy composite plates due to low velocity Impact. *ASME: J Mech Des* 139(4):044501–044501-4
11. Basu B, Tiwari D, Kundu D, Prasad R (2009) Is Weibull distribution the most appropriate statistical strength distribution for brittle materials? *Ceram Int* 35(1):237–246
12. Torres JP, Vandi LJ, Veidt M, Heitzmann MT (2017) The mechanical properties of natural fibre composite laminates: a statistical study. *Compos A Appl Sci Manuf* 98:99–104
13. Baley C (2002) Analysis of the flax fibres tensile behaviour and analysis of the tensile stiffness increase. *Compos A Appl Sci Manuf* 33(7):939–948
14. Trujillo E, Moesen M, Osorio L, Van Vuure AW, Ivens J, Verpoest I (2019) Bamboo fibres for reinforcement in composite materials: strength Weibull analysis. *Compos Part A* 61:115–125
15. Xia ZP, Yu JY, Cheng LD, Liu LF, Wang WM (2009) Study on the breaking strength of jute fibres using modified Weibull distribution. *Compos Part A* 40:54–59
16. Dirikolu HM, Aktas A (2002) Statistical analysis of fracture strength of composite materials using Weibull distribution. *Turkish J Eng Env Sci* 26:45–48
17. Djeghader D, Redjel B (2020) Weibull analysis of fatigue test in jute reinforced polyester composite material. *Compos Commun* 17:123–128



# Development of Predictive Model for Surface Roughness Using Artificial Neural Networks

Nikhil Rai<sup>(✉)</sup>, M. S. Niranjana, Prateek Verma, and Prince Tyagi

Department of Mechanical Engineering, Delhi Technological University, Delhi, India  
nikhilrai637@gmail.com

## 1 Introduction

Engineering application utility of metallic components depends heavily on their surface roughness values. In the present scenario of heavy industrialisation and emerging automation techniques, the importance of surface properties has increased manifold making it a determining factor of product quality. Good surface finish is appreciable for improved tribological properties and enhanced resistance to corrosion. Machining and finishing operations on the automated CNC lathes render components variable surface roughness values depending on the process parameters like speed of cutting, feed rate and depth of cut. Researchers have created various prediction models for proper planning and control of cutting conditions and figuring out the optimal parameters for machining.

The consideration of machining parameters becomes crucial so as to perform economical machining with the desired characteristics in the product. The surface integrity produced after machining is recognised to have a great impact on the lifecycle of the product. It represents the nature of the surface condition of the workpiece after machining. In today's dynamically changing world, manufacturing industries are relying more and more on application of optimisation methods in the metal cutting process so that production units can perform optimally under the rigorous competition pressure in the market and produce products of superior quality.

This research paper is focussed on figuring out the optimal combination of speed of cutting, feed rate and depth of cut to minimise the surface roughness in a CNC lathe turning operation using the ANN technique.

In this work, we have tried to compute the influence of speed of cutting, feed rate and depth of cut on surface roughness, and an optimisation model has been created using the artificial neural network technique. Data have been collected from various published papers to train the model and validate the results.

## 2 Literature Review

A lot of work has been done to optimise the input variable parameters of machining. Residual stress developed during machining impacts the life time and quality of machined components. Neural network-based prediction models are used to predict the accuracy of residual stress development. ANN-FPA models prediction had the accuracy of 99.8%

and 99.7%, respectively [1]. Surface roughness prediction is done using convolution neural networks directly from the digital image of surface texture of the machined component instead of doing feature extraction and image segmentation by the virtue of image segmentation [2]. Good material removal rate enhances productivity of machining. Tool chatter degrades MRR [3]. Optimal cutting parameters are predicted using ANN for the stable machining operation in turn increasing the productivity. Accurate prediction of tool life prevents the catastrophic stoppage of machining processes due to tool wear. ANN models are used for the prediction of tool life and cutting-edge wear to make it industry ready [4]. Experiments were performed that are designed on the basis of Taguchi's methodology for optimal result. The study demonstrates that the surface roughness increases when the feed rate is increased, the influence of cutting speed was found to be less than that of feed followed by the effect of change in depth of cut [5]. Another researcher has studied the influence of tool overhang along with other parameters on residual stress and surface roughness developed during the turning of aluminium alloy by designing the experiments based on Taguchi's technique. The results obtained reveal that the most optimal result for surface roughness could be obtained by using tool overhang in the medium or lower range [6]. Regression models were developed for predicting the surface roughness and an artificial neural network to account the combined influences of the tool vibration amplitudes and cutting force which provides a model with higher accuracies of prediction [7]. A comparative study has been established with aluminium alloys and brass machining on computer numerical control machine and analysed by the help of prediction techniques. It was found that surface properties are dependent on cutting force which is ultimately decided by speed of cutting, feed rate and depth of cut [8]. Some other researchers have also used the Taguchi technique. Experiments were conducted by taking feed rate, speed of cutting and depth of the cut as cutting process parameters. Experiments are designed on the basis of Taguchi's technique for optimisation using orthogonal arrays. In hindsight, it was inferred that speed of cutting highly influences the surface roughness than feed and in case of MRR, depth of cut is the primary parameter and then the speed of cutting [9]. Artificial neural networks are being developed for the prediction of tool life, failure-mode on the basis data obtained by recording different experiments based on multiple values of speed of cutting and feed rate and constant depth of cut. The neural network best predicted the failure-mode prediction. The network training could be improved using the real-time datasets [10].

An artificial neural network is developed for predicting so as to control the surface roughness in a computer numerically controlled lathe. Experiments were conducted, and the cutting parameters were the speed of cutting, feed rate and depth of cut. It is found that we can predetermine optimised parameters of cutting for surface roughness of machining operation using the control algorithm and artificial neural network [11]. An on-line fuzzy neural network (FNN) model [12] to estimate the flank and crater wear on the basis of modified least square backpropagation [13]. It has been found that an on-line FNN model has great accuracy for the estimation of progressive flank and crater wear with very less time for computation [14]. A linear model was generated for three responses, i.e. material removal rate, surface roughness and chip thickness ratio (CTR), and experiments were conducted based upon the Taguchi's technique of optimised response using orthogonal array. ANOVA was used to find out the main



influences of S/N ratio, and graphs are plotted. The resulting optimised value for depth of cut, time and the speed of cutting are best fit for the optimised metal cutting to extract the competitive results from commercial mild steel [15]. Mathematical models were also developed for predicting surface roughness [16] on the basis of parameters for cutting and tool vibrations. Tool vibrations were measured using an FFT analyser. It is inferred that tool vibrations and cutting parameters based prediction models are more accurate [17, 18]. Multiple attribute decision making methods [19] had been used for investigating multiple parameters and their impacts on surface roughness. The investigation is done to devise an optimised procedure for selection of tool insert for improved surface finish in turning operation whilst working on different materials. After analysing the previous research works, it was observed that enormous work had been done on optimising cutting parameters using statistical tools and techniques for better surface finish but this is felt that a lot better predictions can be done by the virtue of neural networks. Here, an attempt is made to train an artificial neural network for the prediction of surface roughness of the mild steel whilst being machined on CNC lathe. In order to train the model well, experimental readings from other prediction and optimisation-based research work are used. In the end, the neural network was validated with two unseen datasets to gauge the efficiency of the model.

### 3 Methodology

Artificial neural network (ANN) algorithms are modern information processing models used to make approximations from real objective functions. The algorithm has taken the inspiration from working of neural cells in the human brain. Artificial neural networks have the scope of modelling linear and non-linear systems. A trained neural network depicts a quick mapping of the given input with the expected output quantities. We have incorporated this modern technique to quantify the effect of process parameters on surface properties of the material during turning operations on CNC lathe machine tools.

An artificial neural network is represented as an acyclic graph. Different sets of nodes comprise different layers.

Mainly, there are three categories of layers.

#### *Input layer*

Different formats of inputs provided by the programmer.

#### *Hidden layer*

It is responsible for the calculations to figure out the hidden features and patterns in the data.

#### *Output layer*

Sequential transformation is done on the input received in accordance with the functions of hidden layers, and the finally obtained result is conveyed by the virtue of the output layer (Fig. 1).

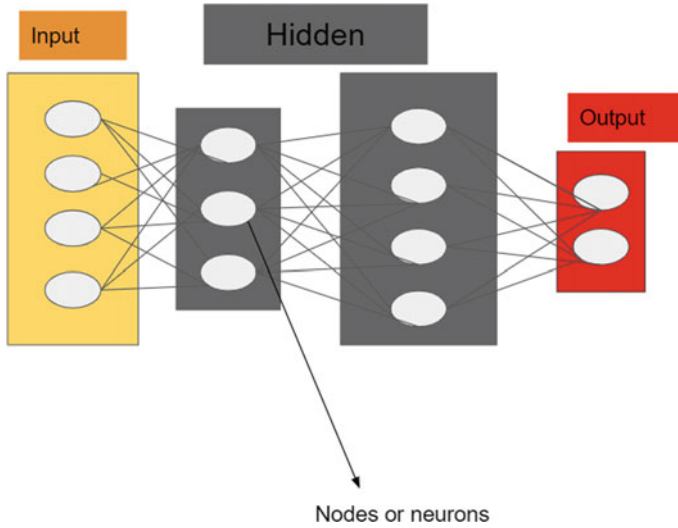


**Fig. 1** Perceptron in the form of acyclic graph

ANN calculates the weighted sum of the inputs and adds the bias effect. The following is the representation of the transfer function.

$$\sum W_i * X_i + b \quad (1)$$

The determined weighted sum is passed to an activation function. Activation functions decide whether a node should fire or not. Only those who are fired reach the output layer. Ample activation functions are available that can be applied to the tasks that we perform.

ANN is significantly powerful computer modelling techniques which is being used these days in multiple engineering fields for modelling of complicated relationships which are difficult to optimise using traditional techniques. Neural networks gain information by detection of patterns in the data and are trained for futuristic predictions. The proposed system is based on the ANN training technology to optimise the machining parameters.

## 4 Dataset

See Tables 1, 2 and 3.

## 5 Results and Discussion

Table 1 is used for training the neural network whilst Tables 2 and 3 are the unseen datasets for validating the neural networks. The neural network architecture is made of three dense layers each containing 250,100,100 neurons and the finally an output layer.

ReLU activation [20] was applied in each layer. The network was trained using SGD and was validated on 10% of this data during training time. The feed rate, speed of cutting and depth of cut were provided as input to the neural network, whilst surface roughness was predicted on the basis of these inputs (Fig. 2). The network was evaluated on the basis of MSE, MAE, MAPE error and was trained on 2000 epochs during which the model finally converged. Final training errors are listed in Table 4 as shown.

**Table 1** Experimental data from for depth of cut (DOC), feed rate (FR), cutting speed (CS) and resulting surface roughness on machining of mild steel on CNC lathe [5]

S. No.	CS (mm/min)	FR (mm/rev)	DOC (mm)	SR ( $\mu\text{m}$ )	S/N ratio (dB)
1	60	0.25	0.2	5.6	-14.96
2	60	0.25	0.3	7.1	-17.02
3	60	0.25	0.4	7.4	-17.38
4	60	0.35	0.2	7.1	-17.02
5	60	0.35	0.3	6.03	-15.6
6	60	0.35	0.4	6.98	-16.87
7	60	0.45	0.2	4.85	-13.71
8	60	0.45	0.3	5.55	-14.88
9	60	0.45	0.4	6.31	-16
10	80	0.25	0.2	4.23	-12.52
11	80	0.25	0.3	4.44	-12.94
12	80	0.25	0.4	5.14	-14.21
13	80	0.35	0.2	3.84	-11.68
14	80	0.35	0.3	5.57	-14.91
15	80	0.35	0.4	5.73	-15.16
16	80	0.45	0.2	4.06	-12.17
17	80	0.45	0.3	4.85	-13.71
18	80	0.45	0.4	6.28	-15.95
19	100	0.25	0.2	4.12	-12.29
20	100	0.25	0.3	3.57	-11.05
21	100	0.25	0.4	3.3	-10.37
22	100	0.35	0.2	3.41	-10.65
23	100	0.35	0.3	3.12	-9.88
24	100	0.35	0.4	3.42	-10.68
25	100	0.45	0.2	2.63	-8.39
26	100	0.45	0.3	4.33	-12.72
27	100	0.45	0.4	4.1	-12.25

**Table 2** Experimental data from for depth of cut (DOC), feed rate (FR), cutting speed (CS) and resulting surface roughness on machining of mild steel on CNC lathe [9]

Exp	FR (mm/rev)	DOC (mm)	CS (mm/min)	SR ( $\mu\text{m}$ )
1	0.1	0.5	75	1.464
2	0.1	0.75	125	2.062
3	0.1	1	175	2.972
4	0.2	0.5	125	3.284
5	0.2	0.75	175	4.264
6	0.2	1	75	2.22
7	0.3	0.5	175	3.662
8	0.3	0.75	75	2.549
9	0.3	1	125	3.586

**Table 3** Experimental data from for depth of cut (DOC), speed and resulting surface roughness on machining of mild steel on CNC lathe [15]

Speed (revolutions/min)	Time	DOC (mm)	SR ( $\mu\text{m}$ )	Chip thickness ratio	MRR
2000	8	1	0.86	1.08	30
2000	8.2	1.3	0.02	1.12	38.05
2000	8.3	1.5	1.5	1.15	43.37
1500	8	1	1.6	1.09	30
1500	8.2	1.3	0.42	1.1	34.67
1500	8.3	1.5	0.47	1.14	45
900	8	1	0.38	1.09	21.81
900	8.2	1.3	6.18	1.13	28.36
900	8.3	1.5	2.72	1.15	30

The network was tested on two unseen datasets each containing 10 data points. The errors during testing training and validation are quite close to each other, hence the model is able to learn patterns in the data really well during training period.

The loss for network is defined as squared difference summation of predicted and truth values of surface roughness over all data points divided by total number of data points.

During training period, we have received MSE, MAE, MAPE loss as 0.3415, 0.5293, 20.2629, respectively, whilst during testing, it is 0.5654, 0.6178, 38.5695 and 1.0916, 1.1089, 97.7567, respectively, for unseen dataset 1 and 2. From these results, we can clearly see that neural network is capable of predicting surface roughness on the basis of feed rate, speed of cutting, depth of cut.

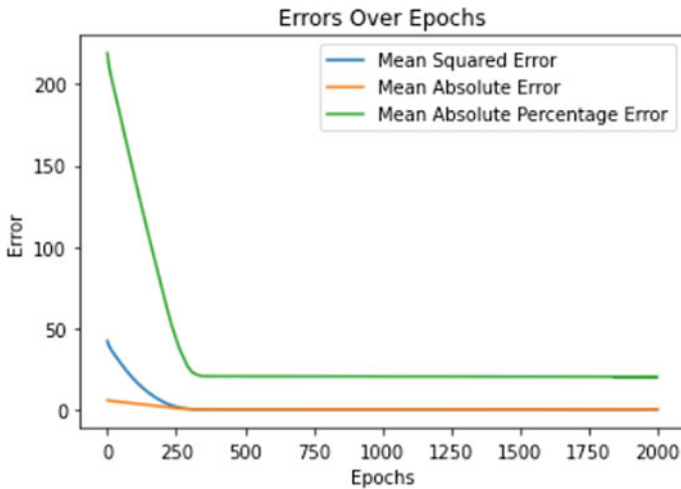


**Fig. 2** Error versus epochs curve during training time

## 6 Conclusion

In this study, we have used the ANN model for CNC turning. The artificial neural network was trained upon 27 data points with parameters feed rate, speed of cutting, depth of cut for the corresponding surface roughness. Further, the dataset is validated upon 18 unseen data points. It is been found that unseen data values of surface roughness and predicted values of surface roughness are significantly close. The predicted values give us a mean absolute error of 0.86. In conclusion, there is very close agreement between predicted and actual surface roughness value. The prediction of surface roughness as done using the ANN algorithm has shown comparatively better results than the existing models and hence can be relied upon for further prediction for industrial standards application.

We can know about the surface roughness on a mild steel upon selecting feed rate, speed of cutting, depth of cut which in turn will help tremendously in the decision-making for getting a high standard surface finish. Further, the study can be integrated with optimisation algorithms like genetic modelling for optimisation of the multiple

**Table 4** Errors during training, validation and testing period

	MSE	MAE	MAPE
Training	0.3415	0.5293	20.2629
Validation	0.7040	0.8391	23.3986
<i>Test</i>			
On dataset-1	0.5654	0.6178	38.5695
On dataset-2	1.0916	1.1089	97.7567

turning parameters to enable better parameter selection on the CNC lathe to produce quality products in the competitive market landscape.

## References

1. Khoshaim AB et al (2021) Prediction of residual stresses in turning of pure iron using artificial intelligence-based methods. *J Mater Res Technol* (2021)
2. Rifai AP, Aoyama H, Tho NH, Dawal SZM, Masruroh NA (2020) Evaluation of turned and milled surfaces roughness using convolutional neural network. *Measurement* 161:107860
3. Gupta P, Singh B (2020) Local mean decomposition and artificial neural network approach to mitigate tool chatter and improve material removal rate in turning operation. *Appl Soft Comput* 96(2020):106714
4. Mikołajczyk T, Nowicki K, Bustillo A, Pimenov DY (2018) Predicting tool life in turning operations using neural networks and image processing. *Mech Syst Signal Process* 104:503–513
5. Sharma SK, Kumar ES (2014) Optimization of surface roughness in CNC turning of mild steel (1018) using Taguchi method. *Carbon* 100(2014):0–26
6. El-Axir MH, Elkhabeery MM, Okasha MM (2017) Modeling and parameter optimization for surface roughness and residual stress in the dry turning process. *Eng Technol Appl Sci Res* 7(5):2047–2055
7. Vasanth XA, Paul PS, Varadarajan AS (2020) A neural network model to predict surface roughness during turning of hardened SS410 steel. *Int J Syst Assur Eng Manage* 11(3):704–715
8. Bharilya RK, Malgaya R, Patidar L, Gurjar RK, Jha AK (2015) Study of optimised process parameters in turning operation through force dynamometer on CNC machine. *Mater Today: Proc* 2(4–5):2300–2305
9. Ezugwu EO, Arthur SJ, Hines EL (1995) Tool-wear prediction using artificial neural networks. *J Mater Process Technol* 49(3–4):255–326
10. Goyal S, Kandra VS, Yadav P (2016) Experimental study of turning operation and optimization of MRR and surface roughness using Taguchi method. *Int J Innov Res Adv Eng*
11. Karayel D (2009) Prediction and control of surface roughness in CNC lathe using artificial neural network. *J Mater Process Technol* 209(7):3125–3137
12. Wang N, Er MJ, Meng X (2009) A fast and accurate online self-organizing scheme for parsimonious fuzzy neural networks. *Neurocomputing* 72(16–18):3818–3829
13. LeCun Y, Touresky D, Hinton G, Sejnowski T (1988) A theoretical framework for back-propagation. In: *Proceedings of the 1988 connectionist models summer school*, vol 1, pp 21–28
14. Chungchoo C, Saini D (2002) On-line tool wear estimation in CNC turning operations using fuzzy neural network model. *Int J Mach Tools Manuf* 42(1):29–40
15. Jaiganesh V, Yokesh Kumar B, Sevel P, Balaji AJ (2018) Optimization of process parameters on commercial mild steel using Taguchi technique. *Int J Eng Technol* 7(11):138–142
16. Tse R, Cruden DM (1979) Estimating joint roughness coefficients. *Int J Rock Mech Min Sci Geomech Abs* 16(5)
17. Abouelatta OB, Madl J (2001) Surface roughness prediction based on cutting parameters and tool vibrations in turning operations. *J Mater Process Technol* 118(1–3):269–277
18. Rahman MZ, Das AK, Chattopadhyaya S, Reyaz M, Raza MT, Farzeen S (2020) Regression modeling and comparative analysis on CNC wet-turning of AISI-1055 & AISI-4340 steels. *Mater Today: Proc* 24:841–850

19. Tzeng G-H, Huang J-J (2011) Multiple attribute decision making: methods and applications. CRC Press
20. Li Y, Yuan Y (2017) Convergence analysis of two-layer neural networks with relu activation. arXiv preprint [arXiv:1705.09886](https://arxiv.org/abs/1705.09886)
21. Taka M, Raygor SP, Purohit R, Parashar V (2017) Selection of tool and work piece combination using multiple attribute decision making methods for computer numerical control turning operation. Mater Today: Proc 4(2):1199–1208
22. Kumar MV, Kumar BJK, Rudresha N (2018) Optimization of machining parameters in CNC turning of stainless steel (EN19) by Taguchi's orthogonal array experiments. Mater Today: Proc 5(5):11395–11407



# Design of Pineapple Eye-Removing Device

Prakash Kumar<sup>(✉)</sup>

Shiv Nadar University, Dadri, Uttar Pradesh 201314, India

Prakash.kumar@snu.edu.in

## 1 Introduction

Fruits are an important part of the Indian diet due to their high nutritional value and taste. However, due to varying structure and properties, many fruits are difficult to be processed for consumption. There have been efforts to study the ergonomics issues related to their processing tasks and design solutions for addressing them. Equipments have been developed for de-husking coconut shells, peeling and slicing apples, extracting walnut kernels, cashew nuts and deseeding pomegranates [1–6]. There also have been studies reported on the design of machines for easing the tasks related to elephant apple coring, garlic peeling, *Makhana* processing as well as pineapple peeling and slicing [7–11]. The literature also shows significant works in similar fields related to meat processing [12] and fish processing [13]. However, most of such research, reported in the literature, has been from point of view of the larger industry and not much has been reported with respect to the development of equipment for small vendors and domestic users. Also, though studies have been reported from the field of design equipment for different fruits, not much has been reported as far as the development of the device, especially for removing pineapple eyes. Pineapple is a juicy, nutritious and tasty fruit that is cultivated abundantly in different parts of India [14]. There are different varieties of processed pineapple items like jam, jellies, squash, juice, pulp, etc., but it is largely consumed fresh during the harvest season. One general method is to peel off the cover, remove the eyes, cut the fruits in slices, remove the core and consume it. The whole operation is done by the knife. Pineapple peeling and eye removing are generally done manually with a knife at the domestic level and for consumption at the fruit and juice centers, canteen, fruit hawker stalls, etc. It is a time-taking and cumbersome task. Also, it often leads to finger cuts and injuries too. There are some pineapple eye-removing devices available too. But, most of such tools dig deep into the pineapple which leads to excessive wastage (see Fig. 1).

In order to understand the various aspects of the problem related to pineapple eye-removing task at domestic and small commercial level, a study has been conducted among the housewives and small fruit vendors. Based on this study, an initiative was taken to design an aid that could reduce the overall effort required for the task.





**Fig. 1** Material wastage while using the present tools

## 2 Method

### 2.1 Subjects and Location of Study

Thirty-three female subjects, all housewives, and eighteen male subjects, consisting of the local street hawkers and workers in the fruit juice shops, have been contacted to understand the problem related to eye-removing task in the fresh and ripe pineapple.

### 2.2 Demographic Data

All the female subjects were housewives and between the age group 20 and 40 years. The males were of age group 18–35 years. Most of the female subjects hailed from different parts of the country. The male respondents were all vendors working in the fruit juice counters and hawker stalls and were all local people.

### 2.3 Unstructured Interview, Video Study and Survey and the Findings

An unstructured interviews and survey was conducted among the subjects to understand the discomforts and problems faced by the housewives and fruit vendors in general. Some video study was also done to ascertain how the task carried out presently with the knife. The observations were also taken to see how the performance is enhanced with the new device. The digital camera of FUJIFILM, FinePix S5700 (7.1 mp, 10× optical zoom) was used for this purpose. Some of the findings of these studies have been as following:

- Pineapple processing takes place in number of steps which are generally in sequence peeling the cover, removing the eye, slicing, coring, etc.
- Process is very time-taking and cumbersome as compared to the other fruits.
- Pineapple eye removing is the most time-taking, repetitive and monotonous task.
- Generally, the tool used for all the operations are knife.
- Due to the difficulties faced in processing the fruit, many housewives avoid buying the unprocessed pineapple. Instead, they prefer buying peeled and sliced fruit.

- Consumption of pineapples at domestic level is less as compared to the other seasonal fruits owing to difficulties faced in removing the pineapple lies.
- The housewives feel that there should be some tool that reduce their effort and be simple and easy to learn, use and maintain keeping constrains of cost and required space.
- For fruit and juice center, sliced pineapple is one of highest selling commodities during the season with a consumption of almost 30–40 pineapples per day. Since pineapple processing is time-consuming, it leads to increased waiting time. The vendor also aspired for faster processing of the pineapple in order to reduce the waiting time of the customer.

### 3 Design and Development of the Device

#### 3.1 Design Brief

On the basis of the above findings, specifications were made to design a handheld eye-removing device mainly for the domestic and small commercial use that would

- Reduce the time of removing pineapple eyes
- Ease the process
- Reduce the wastage
- Convenient to clean
- Less space occupying
- Cost effective
- Manufacture able locally
- Safe to use.

Design process is mainly grouped into three steps, i.e., analysis, synthesis and evaluation [15]. In the analysis phase, we diverge to various information for better understanding of the problem and the present solutions to tackle it. This consists of literature survey, exploring various practices used in the field or the similar fields, study of present technologies, etc. Synthesis is conceptualization; different concepts are generated keeping in mind the function, ergonomic principles, available resources and feasibility. In the evaluation process, different concepts are compared on the basis of the initial specifications, and the best concept is chosen for the realization.

#### 3.2 Conceptualization

Considering the design specifications, many concepts were generated which were further filtered on the basis of the ergonomic principles for designing handheld tool [16] and the feasibility analysis. The rough prototypes of the potential solutions were made for further testing and analysis (see Fig. 2).



**Fig. 2** Sketches and rough prototypes of the different concepts

### 3.3 Evaluation: Video Analysis

For evaluation of the product, ten subjects were chosen consisting of six females and four males. They were observed cutting the pineapple with the normal knife, and the time as well as task was video captured. Each subject was given three peeled pineapples for removing eyes to be peeled with and without the aid. The time required for removing the eyes was also observed for both the processes, i.e., using the knife and the new device. The amount of wastage occurring was also determined when the fruit was cut with the knife and with the device. The general process of eye removal is that the pineapple was put in the plate or held in one hand and the knife is moved diagonally on the surface, and then the knife is moved at almost equally opposite axial angle along the same diagonal, thereby removing a V-shaped strip along with the eyes. There are generally ten to twelve spiral grooves are to be made to remove all the eyes. Eventually the same procedure was followed for capturing the performance using newly made tool. The material was also ascertained weighing the leftover material after removing pineapple eyes from both the processes.

## 4 Results

With the help of the device, the subjects were able to remove the pineapple eyes neatly with a bit of small brown spots of the pineapple visible at some places. However, these brown parts were also visible when the task was done with the knife.

#### 4.1 Quantitative Results

Each respondent was given three pineapples to remove eyes with the knife as well with the new device. The average time of the eye removing, with the normal knife and the new device, were determined by each participant (see Fig. 3).



**Fig. 3** Video recording of the subjects using the aid for removing pineapple eyes

The mean time required for the task using the knife (method-1) varied between 163 and 251 s. Whereas, the mean time needed for the task using the new device (method-2) varied between 110.7 s and 177.1 s. For every individual subject, the time required for completing the task using the new device was less than that by using knife (see Fig. 4).

Also, the material removed by weight during the task, using knife and the new device, was measured. The result showed a reduction in material removed while removing pineapple eyes in the case of the new device. The mean material removed using method-1, varied between 70 and 100 gm. Whereas, the mean material, removed using method-2, varied between 60 and 80 gm. For every individual subject, the material removed using method 2 was less than that using Method 1 (Fig. 5).

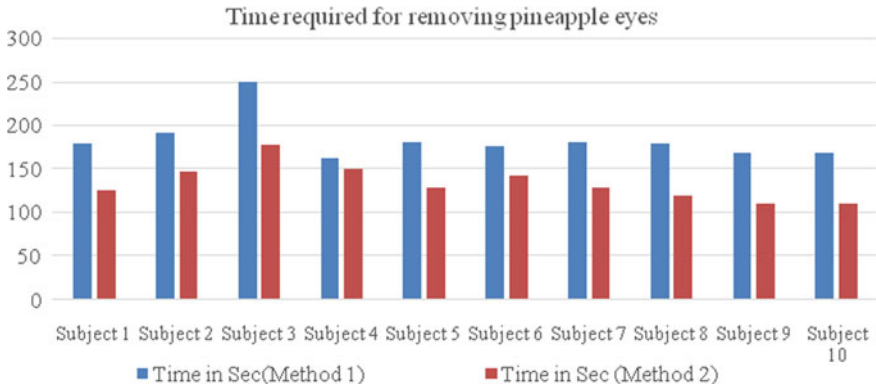


**Fig. 4** Comparative results of time required for eye removing using knife (method 1) and new device (method 2)

## 4.2 Subjective Responses

After peeling the pineapple with the new device, the respondents were also asked about their opinion about the device. A positive feedback was recorded with salient points as following:

- It is safer as compared to knife.
- It enables faster eye removing from the pineapple.
- The handle can be further improved for better grip.

## 5 Conclusion

The test conducted to assess the performance of the new device showed clear reduction in time and wastage, and it also got good feedback from the subjects. But still refinement was required in the design so that the time of peeling could be further reduced. The device has to be further worked upon so as to ensure a better grip. The manufacturing

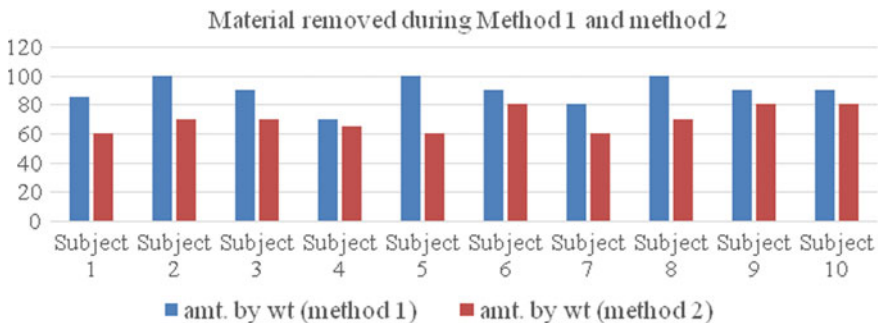


**Fig. 5** Comparative results of total material removed during the eye-removing task using knife (method 1) and new device (method 2)

aspects are to be further looked into, in order to make it easy and cheap to manufacture with the help of the local manufacturers.

The product has significant ergonomic relevance due to difficulty related to pineapple eye-removing task. The design of a handheld device will reduce the effort and time of the manual operations at domestic and small commercial level. The various product features like its electricity free operation, ease in making the product with help of local artisans and by local material makes it more relevant and sustainable in present times. The effort also opens scope for developing low-cost devices for other fruits and vegetables that are difficult to process for consumption.

## References

1. Samuel Ratna Kumar PS (2018) Design and fabrication of an economical coconut dehusking machine. *Int J Eng Technol* 7(2.8):588–591
2. Krishnan RN, Ganesh S (2017) Design and fabrication of apple peeler/slicer-green engineering. *Int J Inno Sci Res Technol* 2(5):723–727
3. Makarichian A, Chegini GR (2014) Design and construction a walnut peeler. *J Nuts* 5(1):19–29
4. Ojolo SJ, Damisa O, Orisaley J, Ogbonnaya C (2010) Design and development of cashew nut shelling machine. *J Eng Des Technol* 8(2):146–157
5. Patole PP, Badi AJ, Gotkhindi RR, Nadkarni VS, Shinde R, Kharade S (2018) Design and development of pomegranate deseeding machine. *Int J Adv Res Sci Eng* 7(1):727–731
6. Khatra V (2010) Pomegranate seed remover. *The Hindu*, June 10, Punjab
7. Nayak PK, Rayaguru K (2017) Design, development and performance evaluation of elephant apple core cutter. *J Food Sci Technol* 54(12):4061–4066
8. Rajesh K, Reddy MK, Anusha Y, Haritha P, Narendra D, Srujana S (2018) Design and fabrication of garlic peeler. *Int J Adv Eng Res Sci* 5(7):165–170
9. Manjunatha M, Samuel DVK, Anurag RK, Gaikwad N (2012) Development and performance evaluation of a garlic peeler. *J Food Sci Technol*
10. Mahawar HK (2016) Technologies for *Makhana* processing, report on *Makhana* (Foxnut) production, processing and supply chain. Centre for technology alternatives for rural areas, IIT Bombay, Mumbai, 17
11. Singh V, Verma DK (2014) Development of pineapple peeler-cum-slicer. *Popular Kheti* 1(2):21–24
12. Sormunen E, Oksa J, Pienimäki T, Rissanen S, Rintamäki H (2006) Muscular and cold strain of female workers in meatpacking work. *Int J Indus Ergon* 36(8):713–720
13. Nag PK, Nag A (2007) Hazards and health complaints associated with fish processing activities in India—evaluation of a low-cost intervention. *Int J Indus Ergon* 37:125–132
14. Kumar B (2008) Indian horticulture database. NHB Publication, New Delhi, pp 130–131
15. Cross N (1982) Engineering design methods: strategies for product design, 3rd edn. John Wiley & Sons Ltd., UK
16. Waly SM, Aghazadeh F (1998) A design and selection guide for hand held tools, ergonomics in manufacturing, Dearborn. *Soc Manufact Eng*:65–81



# Implementation of Boost Converter for High Step-Up DC/DC for Thermoelectric Generator

Melisa Miranda, Shivalingesh S. Dhaded<sup>(✉)</sup>, S. M. Akash, and Prithviraj Misra

Department of Electronics and Communication Engineering, PES University, Bengaluru, India  
slingesh2000@gmail.com

## 1 Introduction

The surging need of energy requirement integrated coupled with the probability of decreased supply of conventional fuels, indicated by petroleum catastrophe, along with increasing concern about the environmental conservation, has forced to navigate research and development of substitute energy sources that are more efficient, renewable, and produce less effect on the environment. Harvesting imperishable, harmless pollution-free electricity is a very important part of ensuring that the world's energy supply increases applications are met without harming the environment.

The idea of having an electric energy source which is both sustainable and non-polluting is an intriguing prospect. Because of harmful effects on the biosphere by the use of natural gas, gasoline, and coal, to produce energy from these has become pernicious for human beings. At 28% in 2014, 35% in 2018, and 36% in 2019, electricity produced from power plants using natural gas increased annually [1]. It was therefore time to find other areas for alternatives. Thermal energy is among the few available energy sources that can be used in many places, such as the activity of electronic devices, cars, buildings, and even the human body. Throughout history, scientists and researchers have sort very hard to find a fair solution for converting thermal energy into useable electric energy. Thermoelectric generators (TEGs) in recent times have become a frontrunner in doing so. TEGs are semiconductor devices that are mechanically and electrically stable and can transform heat energy into electrical energy if a temperature gradient is maintained through them, taking advantage of the influence of the Seebeck effect [2]. The fascinating thing about TEGs are that there are no mobile parts, they are impressively durable, and they are less likely to produce noise pollution because of their subdued working sound. Moreover, they are not harmful to the atmosphere and do not release any kind of pollutants.

There are always certain disadvantages while dealing with energy conversions, TEGs, in this case, are very expensive and less efficient. For these reasons, the usage is limited. However, as mentioned above, the increasing demands have bound researchers to find ways to use it in a feasible manner [3]. The performance of TEGs, on the other hand, has been increased, and the cost of the unit has decreased. As a consequence, TEGs can now be effectively engaged in extracting heat energy from other processes [4].

The initial devices that were developed experimentally had power ranges of 5 kW [5] and also the ones that went downhill to microwatt systems [6]. Companies that produce TEGs in huge quantities have power levels currently between 0.5 and 20 W [7]. The  $V-I$  characteristics of the device are linear with the slope of the curve being shallow, which depicts a low-voltage and high-current analogy. Applications of commercially serviceable devices have been particular to niche products; nonetheless, a tenacious amount of research have paved the way for it being utilized in small-scale applications for solar energy. The fundamental goal of these projects is to develop thermoelectrics at the same stage as photovoltaic (PV's) systems, which are now a core component of the microgrid-based DC system. The operating voltage of the dc microgrid varies from 120 to 400 V [8].

A step-up converter is required to concur the TEG module into the DC microgrid-based system. In principle, traditional step-up converters can provide a high step-up conversion for a high duty cycle ratio. However, in reality, there are many imperfections in circuitry, loss of power switches, and rectifier diodes limiting conversion efficiency and profit. This leads to serious problems with reverse recovery and very low efficiency [9, 10]. Lowering the duty ratio will not only help overcome the gain issue but also dodging the risk of a large electromagnetic interference emission, which would have occurred due to a rapid fall in the diode conduction period in a high duty ratio converter. Also, it would mean the output diodes with larger peak currents. It is therefore advantageous to move forward with an obvious low duty ratio to produce a high voltage gain.

A converter is an electrical circuit that takes DC input and produces a variable voltage DC output, typically accomplished by the use of inductive and capacitive filters in a high-frequency operation. Boost converters are being used to enhance the snagging in the step-up voltage gain and conversion efficiency. In fact, the maximum gain is restricted by various circuit deformities such as passive elements and periods of shift commutation. Various high DC-DC converters are developed using the coupled inductor with low-current ripple [11–13]. However, problems related to leakage inductance increased voltage spike, and efficiency remain notable.

Liang et al. suggested a very simple topology for a high-performance high-voltage gain DC-DC converter. Although the switching frequency can only be increased by the use of fast switching elements, the predicted gain can be accomplished with a very compact duty ratio by applying a different topology [14]. In addition, the use of lower duty cycles has brought advantages to this. Usually, coupling inductors are used to optimize the voltage gain of converters. Additionally, the combination of capacitors with coupled inductor windings in the device are referred to as voltage multipliers, as unveiled in [15–18].

Apart from these, there are additional problems such as voltage multiplier that affects gain while adding small components and leakage of coupled inductors. Due to additional components, there will be an increase in heat which in consequence, the power loss will rise. Hence, now, it is time for a better idea to look for the less to average efficient TEGs. Moreover, as a result, new topologies based on the voltage multiplier-based converter arrangement with coupled inductor will be introduced in this paper.



## 2 Proposed Converter and Principle of Operation

The circuit proposed by Laird and Lu [19] for high DC/DC conversion is taken into consideration. By using the principle of coupled inductor and voltage multiplier [20], the gain of the circuit can be increased comparatively by making considerable changes in the circuit.

A boosting DC–DC converter circuit consists of the basic coupled inductor and voltage multiplier technology [21]. Switching capacitors and coupled inductors make up the voltage multiplier device. It requires reasonably fast step-up transfer with large proficiency to design a high boost-up converter. However, owing to part resistance and leakage inductance, boost converters, and flyback converters do not attain high step-up with elevated proficiency.

To understand the working of the proposed topology, it is necessary to have a basic understanding of coupled inductors. The coupling between the inductors can be signified by applying the voltage at one inductor results in inducing the voltage at another inductor [22]. Generally, concerning reducing the size of the components, two distinct inductors with two different interleaving channels can be mounted on a single core [23].

### 2.1 Review of Coupled Inductor Model

Figure 1 shows the basic coupled inductor model that can be used to design the converters for high step-up gain. To find the inductor parameter, mathematical modeling can be used with dot convention.

$$V_{L1} = L_1 \frac{di_1}{dt} - M \frac{di_2}{dt} \quad (1)$$

$$V_{L2} = -M \frac{di_1}{dt} + L_2 \frac{di_2}{dt} \quad (2)$$

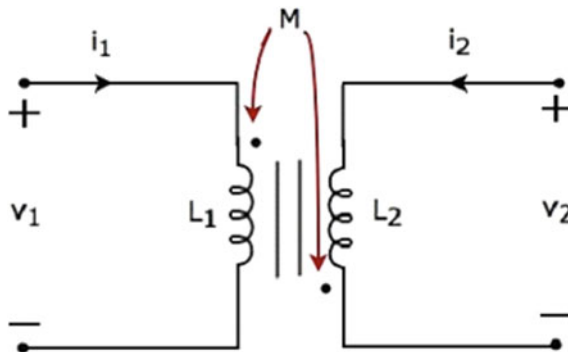


Fig. 1 Two inversely coupled inductors

where  $L_1$  is self-inductance primary winding, and  $M$  is mutual inductance.

Rearranging expression (1) and (2) [24],

$$V_{L1} = L_1 \left( 1 - \frac{M^2}{L_1 L_2} \right) \frac{di_1}{dt} - \frac{M}{L_2} V_{L2} \tag{3}$$

$$V_{L2} = -\frac{M}{L_1} V_{L1} + L_2 \left( 1 - \frac{M^2}{L_1 L_2} \right) \frac{di_2}{dt} \tag{4}$$

where it can be seen that coupling coefficients can be defined as  $K = \frac{M}{\sqrt{L_1 L_2}}$ . This can be further simplified as,

$$V_{L1} = L_1 (1 - K^2) \frac{di_1}{dt} - \frac{M}{L_2} V_{L2} \tag{5}$$

$$V_{L2} = -\frac{M}{L_1} V_{L1} + L_2 (1 - K^2) \frac{di_2}{dt} \tag{6}$$

Hence, it can be seen that a coupled inductor can be modeled as a transformer by using parallel magnetic inductance and series leakage inductance.

An analogous circuit can be built out of (5) and (6), as seen in Fig. 2 where terminologies  $(1 - K^2) \times L$  and  $K^2 \times L$  are referred to as leakage inductance and magnetizing inductance in general.

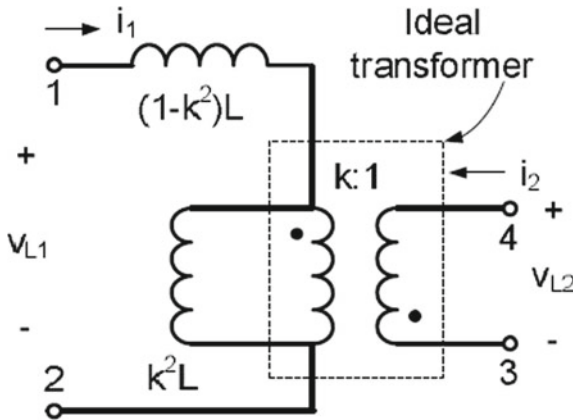


Fig. 2 Coupled inductor as equivalent transformer model

To get the linear relationship between inductors, leakage inductance can be considered as  $(1 - K) \times L$ , and magnetizing inductance as  $K \times L$ .

## 2.2 Converter Design

While the above model is mathematically exact, studying the power converter operations is not quite pleasant as both primary and secondary winding are asymmetrical to each

other due to the presence of magnetizing inductance and leakage inductance only on one winding. Hence, to ensure symmetry, a transformer model is developed in such a way that it has a primary magnetizing inductor  $L_m$ , an ideal transformer with a turns ratio of  $N = N_s : N_p$ , and secondary leakage inductor  $L_k$ .

To regulate the energy transfer between input and transformer switching, MOSFET is used. The principal operating theory is that the primary inductor is parallel to the voltage input and the secondary inductor when the switch turns ON. Due to this, the capacitor gets charged along with the inductors. The primary inductor, capacitor, and secondary inductor are modeled to be such that capacitor along with inductor discharge to load. All three modules are then integrated to increase the load output voltage. During the OFF-state, circuit holds the charge.

The interleaved conversion can be seen, mainly, in implementing a coupled-inductor voltage multiplier principle, which involves, through windings of a coupled inductor, the capacitor gets charged when the switch is ON, and then to boost the voltage, discharging takes place with both windings into the load such that all voltage sums up together. This concept can be outstretched by utilizing multiple capacitors in such a way that they discharge at a time during the ON stage and charge independently during the switch-OFF stage (Fig. 3).

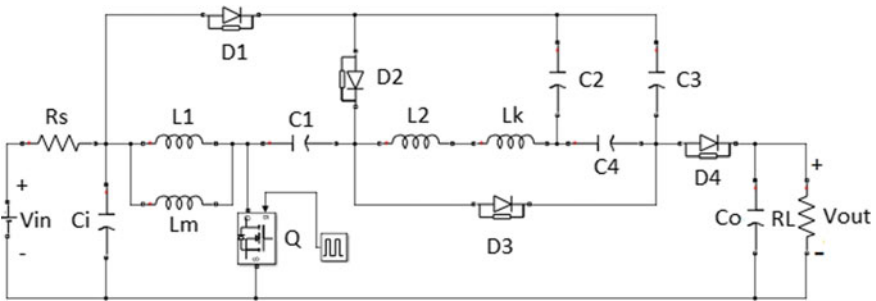


Fig. 3 Proposed circuit for high step-up converter

However, the rearrangements can be made so that during both stages, the discharge takes place in one energy storage element to the other energy storage element along with the windings. Because of which the voltage is boosted.

As passive elements can store energy or dissipate energy, by using passive elements such as capacitors and inductors, the power can either be conserved or transferred. The change of voltage is resisted by the capacitor, and an inductor opposes the change in current. In the DC circuits, use of capacitors and inductors will involve the transient response. During the transient response, capacitors build up a charge which stops the flow of current, and inductors build up energy in the form of magnetic fields. But energy dissipation through heat must be taken into consideration [25]. Hence, including capacitors and inductors in the circuit and positioning them would chip in energy loss of the circuit.

The fundamental symbolic representation used are summarized as follows.  $V_{in}$  and  $R_s$  designate DC input voltage applied and input resistance in series with the voltage

input, and  $C_i$  is input capacitor filter in the input circuit. The primary and secondary coils of the coupled inductor are represented by  $L_1$  and  $L_2$ .  $Q$  is a switch on the primary side of the circuit, and  $T_q$  is a square pulse trigger signal. Diodes with regenerative resistor–capacitor (RC) snubber circuit are denoted by  $D_1$ ,  $D_2$ , and  $D_3$ . The capacitor with high voltage on the secondary side of the circuit is  $C_1$ ,  $C_2$ ,  $C_3$ , and  $C_4$  are capacitors employed for energy boosting. Diode  $D_4$  is employed to transfer the energy stored in capacitors and inductors to the output circuit. Capacitor  $C_0$  and  $D_4$  both form the output filter circuit.  $V_{out}$  is referred as the voltage output of the circuit. Resistance  $R_L$  is used to drive all the voltage stored by energy-storing components also referred to as load resistance.

The voltage drop across the switch is indicated as  $V_q$ , and similarly, the drop across the primary winding and secondary winding of the ideal transformer associated with a coupled inductor is described as  $V_p$ , and  $V_s$ , respectively. The current due to the magnetizing effect by the primary coil is  $i_{L_m}$ , and the current that is induced at the primary coil is  $i_p$ . The combined effect of turns ratio  $N$  and current induced by a primary coil through an ideal transformer result in generating current in the secondary coil ( $i_s$ ). As the circuit starts conducting the voltage drop across, the current passing through the diode  $D_1$  is given as  $V_{D1}$  and  $i_{D1}$ , respectively. Similarly,  $V_{D2}$ ,  $V_{D3}$ , and  $V_{D4}$  represent voltage drop across  $D_2$ ,  $D_3$ , and  $D_4$ , respectively.  $i_{D2}$ ,  $i_{D3}$ , and  $i_{D4}$  denote current through them accordingly.

In order to make the study of the circuit simpler, the following conditions are assumed,

1. All the capacitors are high enough so that the voltage is constant for one switching cycle.
2. It is considered to be ideal condition for all semiconductor components such as diodes and metal–oxide–semiconductor field-effect transistor (MOSFET).
3. The coupling inductor's turns ratio is equal to  $N_s/N_p$ , and the coupling coefficient  $k$  is equivalent to  $L_m/(L_m + L_k)$  [18].
4. The analysis and simulation of the converter done in the discrete mode with the sampling time,  $T_s = 5 \times 10^{-9}$  s.

The characteristic waveforms of the proposed high step-up converter are demonstrated in Figs. 4, 5, and 6. Moreover, Fig. 3 demonstrates the topological model of the proposed converter. The switching cycle and the detailed modes of operation across different time intervals are described in Sect. 2.3.

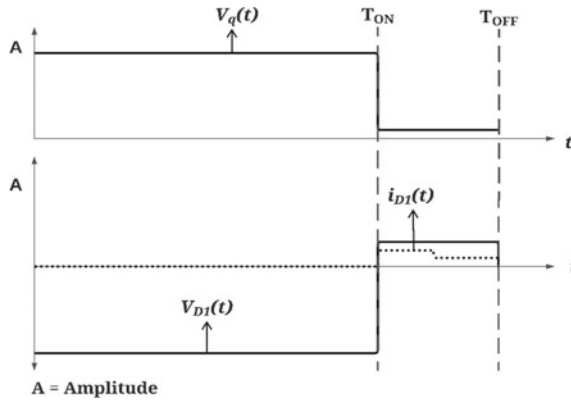


**Fig. 4** Switching waveforms of switch  $Q$  and diode  $D_1$

### 2.3 Converter Analysis

#### State Analysis during Switch ON [ $T_{ON}$ ]

*Diode 1.*  $D_1$  is OFF if the  $Q$  is ON. Therefore,  $D_1$  is reverse biased over this interval. There is a negative voltage drop around the diode. Because of the high reverse-bias voltage, the reverse leakage current will pass through it.

*Diode 2.*  $D_2$  is forward biased. Figure 5 corresponds to a progressive rise of the forward voltage over the diode at interval  $T_1$ . There will be a steady forward voltage through  $D_2$

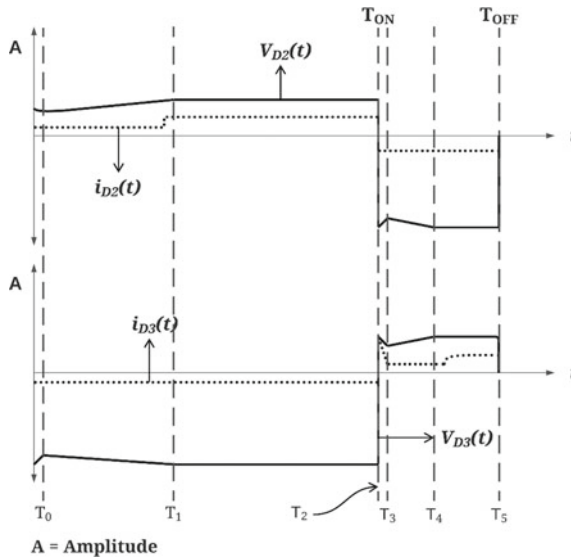


**Fig. 5** Switching waveforms of diodes  $D_2$  and  $D_3$

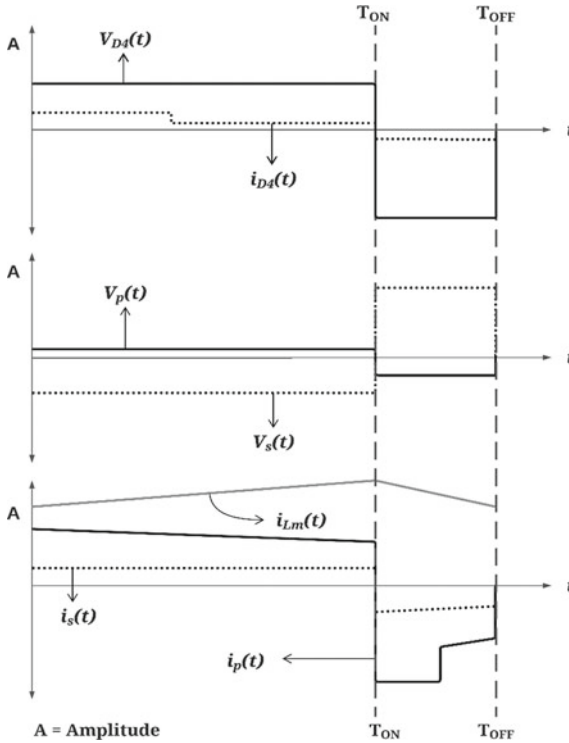


**Fig. 6** Switching waveforms of diode  $D_4$ , the primary and secondary coil

over the  $T_2$  interval. As can be seen, by the fact that the voltage drop in  $T_2$  is higher than  $T_1$ , the forward current rises in  $T_2$  relative to  $T_1$ .

*Diode 3.*  $D_3$  will be reverse biased. Referring to Fig. 5, in interval  $T_0$ , the reverse-bias voltage drop will gradually decrease, while in  $T_1$ , it will gradually increase. During  $T_2$ , it almost remains constant. Due to the high reverse-bias voltage, there will be a small amount of reverse leakage current through  $D_3$ .

*Diode 4.*  $D_4$  is ON, and it is possible to see forward voltage through it. The diode is biased forward, so the current passes through the diode and allows capacitor  $C_o$  to charge.

*Primary Inductor.* The voltage is positive around the primary inductance, which means that the primary inductor charges during the  $T_{ON}$ . The energy is stored in magnetic inductance  $L_m$ . When the switch is ON, the current through the  $L_m$  raises, signaling that it is charging.

*Secondary Inductor.* The voltage appearing around the secondary inductance is “N” times of that the primary inductance due to the coupling between the primary and secondary inductance. There is going to be a negative voltage drop around the inductor. The dot convention across primary and secondary inductors should be carefully taken into account.

### State Analysis during Switch OFF [ $T_{OFF}$ ]

*Diode 1.*  $D_1$  is biased forward, and the forward voltage happens around the  $D_1$ . As a consequence, the forward power flows over the  $D_1$ . However, after some time, the current flow decreases. The internal resistance of the diode resulting in a drop in the forward voltage will be around 0.8 V.

*Diode 2.* Referring to Fig. 5, the reverse-bias voltage across  $D_2$  decreases during  $T_3$ , increases during  $T_4$ , and remains constant till  $T_5$ . However, due to a large reverse-bias voltage, reverse leakage current flow can be observed (As in the case of  $D_3$  during switch  $T_{ON}$  state analysis).

*Diode 3.* During the interval  $T_3$ , the forward voltage decrease, and hence, current through  $D_3$  decreases. However, during the time interval  $T_5$ , voltage drop increases slightly due to which current also increases at the end of  $T_5$ .

*Diode 4.* The  $D_4$  is reverse biased, flow of reverse leakage current can be observed.

*Primary Inductor.* The drop in voltage around the primary inductance is negative since it results in the inductor losing electricity. The current through the  $L_m$  decreases as the voltage across it decreases, indicating discharging.

*Secondary Inductor.* With secondary inductance, the voltage falls through the inductor is positive, which results in charging the inductor (Table 1).

**Table 1** Proposed converter components and parameters

Component/Parameters	Values
Turns ratio ( $N$ )	10
Diodes	MBR40250
Capacitors ( $C_1, C_2, C_3, C_4$ )	22 $\mu$ F
Input capacitor ( $C_i$ )	1000 $\mu$ F
Output capacitor ( $C_o$ )	22 $\mu$ F
Magnetizing inductor ( $L_m$ )	25 $\mu$ H
Switching frequency ( $f$ )	100 kHz
Load resistance ( $R_L$ )	2698 $\Omega$

## 3 Simulation Results

The model is applied using the MATLAB/Simulink tool to achieve the stated goals in the abstract and validate the performance of the proposed converter.

The converter in Fig. 3 is planned and simulated for the 100 kHz switching frequency and 4.5 V input voltage. The voltage output of the circuit is 218.2 V with a gain of 48,487. Figures 7, 8, 9, and 10 show the switching waveforms of diodes  $D_1, D_2, D_3, D_4$ ; Figs. 11 and 12 provide the voltage waveforms at primary and secondary inductors. Figure 13 shows the output voltage waveform attaining the steady-state from the transient state with an increase in time.

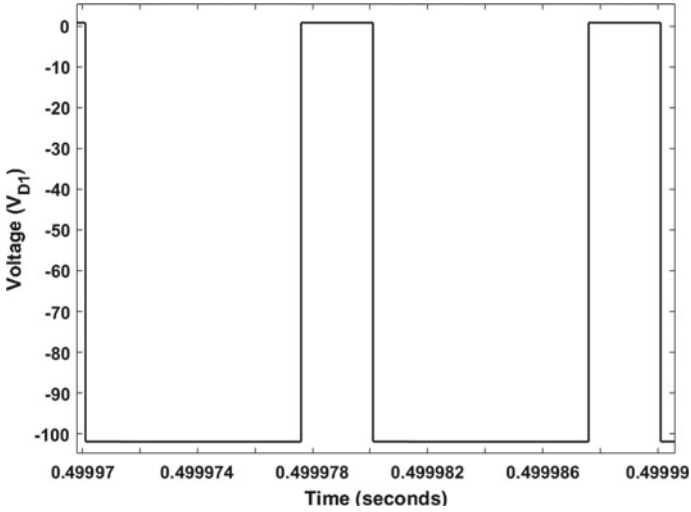


Fig. 7 Switching waveform of diode  $D_1$

Figure 14 compares the gain versus duty cycle ratio. Initially, the gain increases with the duty cycle. It can be noticed that as the duty cycle crosses the value of 90, the gain decreases.

As the duty cycle increases, there will be a minute increase in the AC ripple of the output voltage. Transient time also increases with the surging in the duty cycle. Hence, the output voltage takes additional time to reach the steady-state. As  $L_m$  is decreased, the gain decreases. The energy contained in the inductor is expressed as (7). As the  $L_m$  value decreases, the energy storage in the capacitor decreases accordingly. Hence, the

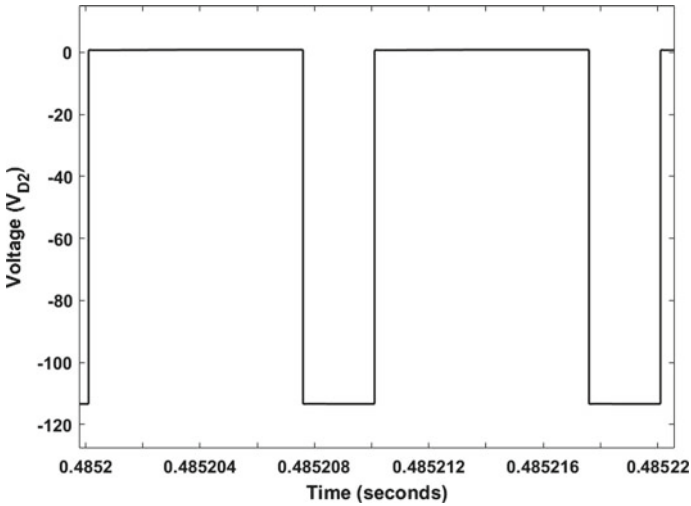
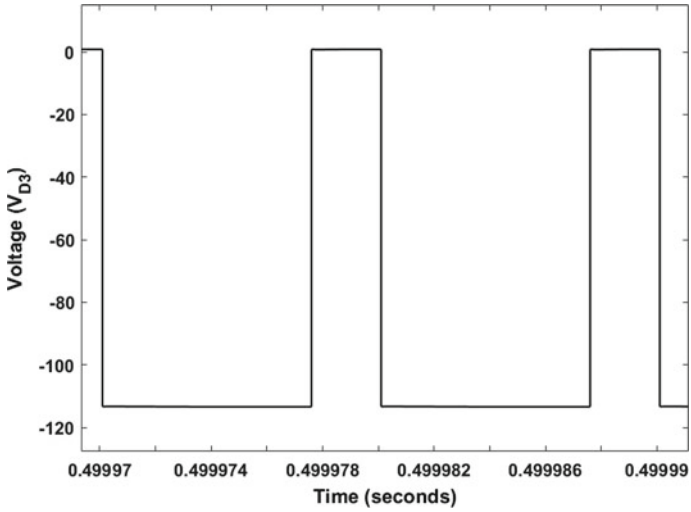
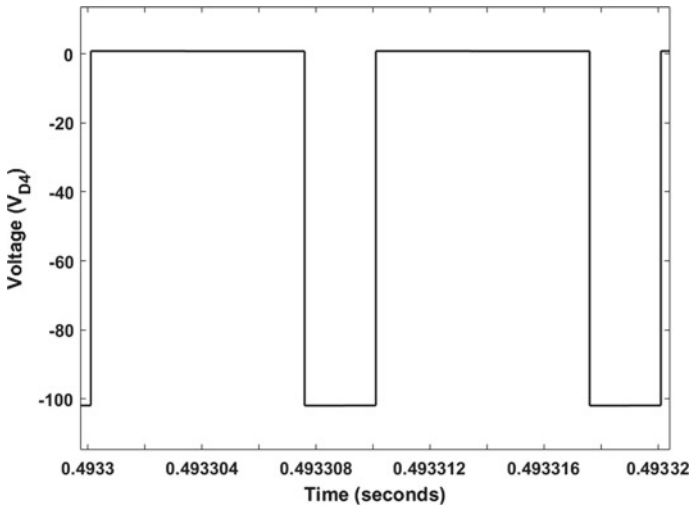


Fig. 8 Switching waveform of diode  $D_2$





**Fig. 9** Switching waveform of diode  $D_3$



**Fig. 10** Switching waveform of diode  $D_4$

gain gets reduced significantly.

$$E = \frac{1}{2}Li^2. \quad (7)$$

Figure 15 compares the gain versus load resistance. The gain increases to a certain value as the value of load resistance increases. This is because the highest power in the load can be dissipated when the load resistance is equal to the source resistance from its

output terminals. Hence, we can nearly get a maximum gain of around  $20,000 \Omega$  load resistance.

Another pattern that is evident here is that the rise in load resistance value raises the transient time of the output voltage.

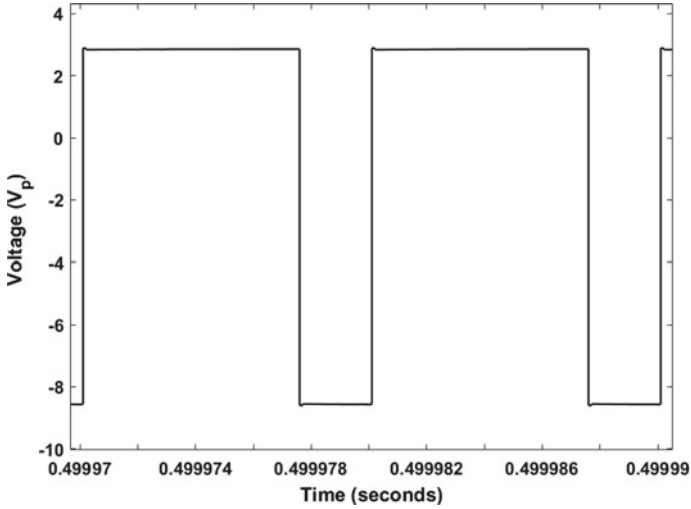


**Fig. 11** Switching waveform of primary inductor

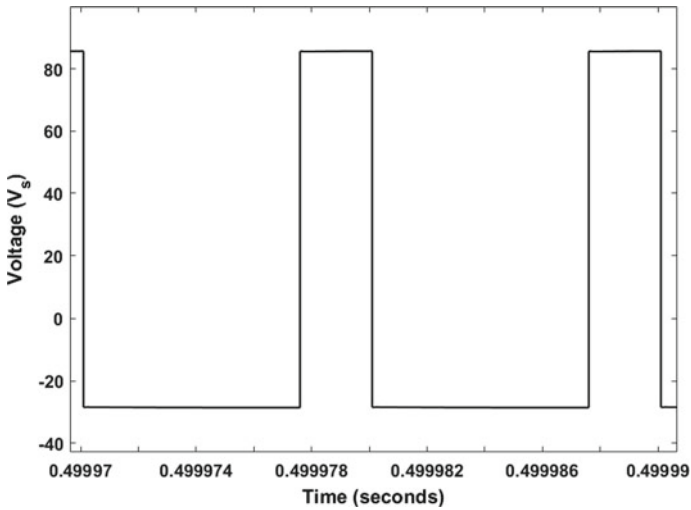


**Fig. 12** Switching waveform of secondary inductor

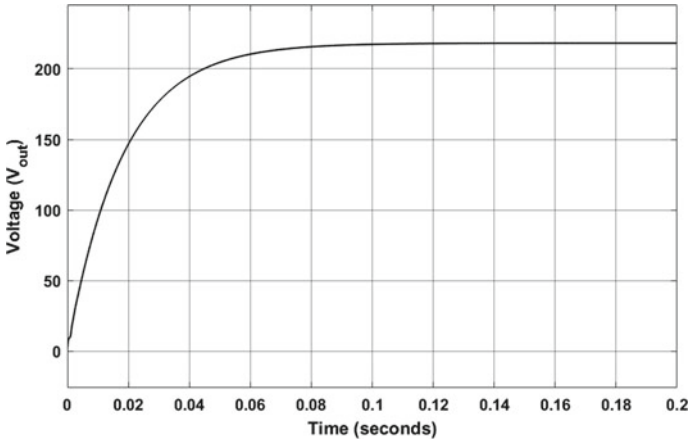


Fig. 13 The output waveform of voltage across resistor  $R_L$

## 4 Result

The gain is the average capacity of a two-port circuit (usually an amplifier) in increase power. Since the paper aims to boost up the voltage from input to output, the gain parameter should be taken into consideration.

$$\text{Gain} = \frac{V_{\text{out}}}{V_{\text{in}}} \quad (8)$$

Thus, the gain of the converter proposed has been enhanced by using voltage multiplier using coupled inductor topology and making the changes in the circuit by adding the respective capacitances ( $C_3$ ,  $C_4$ ) helps in storing the charge during switch-OFF state and inductors ( $L_m$  in with inductor  $L_1$ ) boosts the charging during switch ON state.

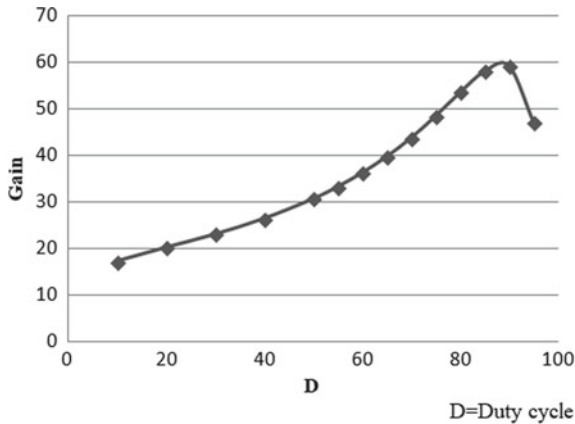
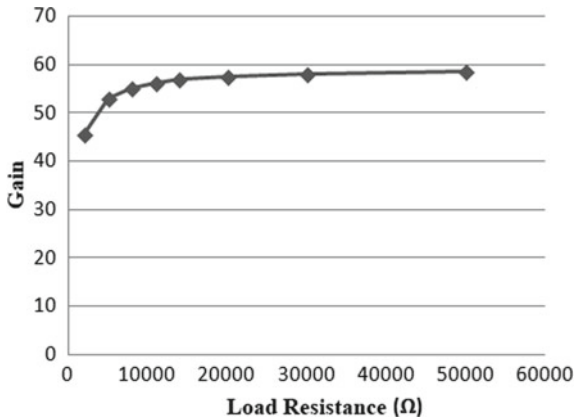


Fig. 14 The waveform for the gain versus duty cycle



**Fig. 15** The waveform for the gain versus load resistance

## 5 Conclusion

A high-gain DC/DC boost converter was put forward in this article. The presented converter simulation model was modeled in MATLAB/Simulink. It can produce a high increase in gain and also reduce the power loss factor (which is a significant concern when dealing with traditional voltage amplifiers). The coupled inductor was modeled as a transformer by using parallel magnetic inductance and series leakage inductance. To increase the energy storage, a switching MOSFET was used. The proposal of adding additional capacitors and diode to an already successful coupled inductor model proved to be tremendously vital. The energy dissipated solely through a couple of inductor model was quite an area of concern, but the addition of the inductor–capacitor circuit chipped in very efficiently dealing with the energy loss of the circuit. The plus point of having capacitors in the circuit was that it stored energy throughout the switch ON the state and assisted transfer to the in-series inductors while loading off the energy during the switch-off state thus providing a high-voltage output. It can also be shown that the output ripple is much lower and is around 0.03258 V. The proposed converter, engineered and set up for TEG service, is capable of generating 218.2 V for a 4.5 V supply.

Hence, by still using the voltage multiplier concept, adding inductors and capacitors, the gain of the circuit can be enhanced, but the area of concern to be considered simultaneously is heat generated by including the passive components which lead to power loss. As the new generation will be looking for generators with very less power loss and high gain with better efficiency, the concept of maximum power point tracking (MPPT) algorithm comes into play by which the converter can be proposed such that it accomplishes all the problems mentioned above and make the circuit to work efficiently with less loss and high gain.

## References

1. Publication of “Energy Statistics—2018” is the financial year 2016–17 and the previous financial years since 2007–08. Available: [http://mospi.nic.in/sites/default/files/publication\\_reports/Energy\\_Statistics\\_2018.pdf](http://mospi.nic.in/sites/default/files/publication_reports/Energy_Statistics_2018.pdf)
2. Rowe D (2005) *Thermoelectrics handbook: macro to nano*. CRC Press, Boca Raton, FL, USA
3. Rowe D (1999) Thermoelectrics, an environmentally-friendly source of electrical power. *Renew Energy* 16:1251–1256
4. Biswas K, He J, Blum ID, Wu C-I, Hogan TP, Seidman DN, Dravid VP, Kanatzidis MG (2012) High-performance bulk thermoelectrics with all-scale hierarchical architectures
5. Fisher M, Kastovich J, Moreland W, Corry T (1962) Experimental 5-kW thermoelectric generator. *Adv Energy Convers* 2:275–279
6. Lu C, Park SP, Raghunathan V, Roy K (2010) Analysis and design of ultra-low power thermoelectric energy harvesting systems. In: *Proceedings ACM/IEEE international symposium low-power electronics and design*, pp 183–188
7. Kryotherm. Thermoelectric cooling and power generating solutions [Online]. Available: <http://www.kryotherm.ru/dir2attz/Kryotherm%20catalog.pdf>, product catalog
8. S. Maneewan, J. Khedari, B. Zeghami, J. Hirunlabh, and J. Eakburanawat, “Investigation on generated power of thermoelectric roof solar collector;”
9. Erickson RW, Maksimovic D (2001) *Fundamentals of power electronics*, 2nd edn. Kluwer Academic Publishers, MA, USA, pp 39–55
10. Mohan N, Undeland TM, Robbins WP (1995) *Power electronic, converters, applications and design*, 2nd edn. Wiley, New York, USA, pp 172–178
11. Wang J, Dunford WG, Mauch K (1996) A comparison of modified boost converters with continuous inductor current mode and ripple free input current with conventional converters. In: *Proceedings IEEE industry applications conference*, pp 878–885, New York, NY, USA
12. Cheng DKW, Liu XC, Lee YS (1998) A new improved boost converter with ripple free input current using coupled inductors. In: *Proceedings of IEEE international conference on power electronics and variable speed drives*, pp 592–599, London, UK
13. Wang J, Dunford WG, Monrad K (1997) Analysis of a ripplefree input-current boost converter with discontinuous conduction characteristics. *IEEE Trans Power Electron* 12(4):684–694
14. Tseng KC, Liang TJ (2004) Novel high-efficiency step-up converter. *IEEE Proc Inst Elect Eng Electr Power Appl* 151(2):182–190
15. Wai R-J, Duan R-Y (2005) High step-up converter with coupled-inductor. *IEEE Trans Power Electron* 20(5):1025–1035
16. Changchien S-K, Liang T-J, Chen J-F, Yang L-S (2010) Step-up dc/dc converter by coupled inductor and voltage-lift technique. *IET Power Electron*. 3(3):369–378
17. Li W, Zhao Y, Deng Y, He X (2010) Interleaved converter with voltage multiplier cell for high step-up and high-efficiency conversion. *IEEE Trans Power Electron* 25(9):2397–2408
18. Hsieh Y-P, Chen J-F, Liang T-J, Yang L-S (2011) A novel high step-up DC–DC converter for a microgrid system. *IEEE Trans Power Electron* 26(4):1127–1136
19. Laird I, Lu DD (2013) High step-up DC/DC topology and MPPT algorithm for use with a thermoelectric generator. *IEEE Trans Power Electron* 28(7):3147–3157. <https://doi.org/10.1109/TPEL.2012.2219393>
20. Liu X, Zhang X, Hu X, Chen H, Chen L, Zhang Y (2019) Interleaved high step-up converter with coupled inductor and voltage multiplier for renewable energy system. *CPSS Trans Power Electron Appl* 4(4):299–309. <https://doi.org/10.24295/CPSS TPEA.2019.00028>
21. Reaungpattawanawat C, Kanthaphayao Y (2015) Voltage multiplier circuits with coupled inductor applied to a high step-up DC–DC converter. In: *Applied mechanics and materials*. Trans Tech Publications, Switzerland. <https://doi.org/10.4028/www.scientific.net/AMM.781.418>

22. Wikipedia contributors (2020, June 19). Inductive coupling. In: Wikipedia, The Free Encyclopedia. Retrieved 28 Oct 2020, from [https://en.wikipedia.org/w/index.php?title=Inductive\\_coupling&oldid=963445998](https://en.wikipedia.org/w/index.php?title=Inductive_coupling&oldid=963445998)
23. Kroics K, Sirmelis U, Brazis V. Institute of physical energetics (1), Riga Technical University (2) Design of coupled inductor for interleaved boost converter
24. Zhu G, McDonald B, Wang K (2009) Modeling and analysis of coupled inductors in power converters. In: 2009 Twenty-fourth annual IEEE applied power electronics conference and exposition, pp 83–89, Washington, DC
25. Chang Y, Lin J (2018) Modeling and implementation of high-gain coupled-inductor switched-capacitor step-up DC–DC converter. In: 2018 3rd International conference on control and robotics engineering (ICCRE), Nagoya, pp 135–138. <https://doi.org/10.1109/ICCRE.2018.8376449>



# Investigation on Geopolymer Concrete Reinforced with Steel and Hybrid Fibre

Harsh Singh<sup>1</sup>, Shilpa Pal<sup>2</sup>(✉), and Shivam Kasana<sup>2</sup>

<sup>1</sup> GBU, Greater Noida, India

<sup>2</sup> Delhi Technological University, Delhi, India  
shilpapal@dtu.ac.in

## 1 Introduction

The geopolymer concrete is manufactured by metakaolin which is thermally active in nature and by-products of thermal power plant such as slag or fly ash. Fly ash acts as a rich source of silicon and aluminium that after dissolving in alkaline active solution polymerizes and becomes the binder. About one tonne CO<sub>2</sub> is produced when one tonne of OPC is manufactured [1]. Also, a huge amount of energy is required for the production of cement. Hence, geopolymer concrete may be an alternative binder. Also, the effect of cracking and low ductility can be overcome by introducing the fibre reinforcement which controls the propagation of cracks and reduces the tendency of brittle material failure [2]. Geopolymer concrete can be manufactured from recycled industrial wastes that made it a greener building material [3].

The common method of reinforcing the tensile strength is steel reinforcement in normal concrete mix. The fibres transmit tensile forces which minimize the tendency to crack. Synthetic fibres such as polyester fibres have gained popularity in for production of concrete not only because of their best characteristics and less price but also because they improve the resistance to cracking and toughness of normal concrete [1]. The price of geopolymer concrete is reduced by 40% as compared to OPC at bulk level [4]. Fibres can be classified into two broad parts such as fibres having high modulus and high strength such as glass, asbestos and steel that increase toughness and strength of concrete and fibres with high elongations and less modulus such as nylon, polyester, polypropylene and polyethylene fibres that have the impact on the energy absorption features of concrete. In this study, the efforts are made to develop the mix proportion for GPC with target strength of M25, the influence of fibres over workability and strength related properties of fly ash and GPC having GGBS and the finest percentage of fibre is determined. The impact of hybrid fibres over the workability and mechanical properties of fly ash and GPC having GGBS is studied too. The durability for the GPC with steel and hybrid fibre at their optimum content is explored in this study.

## 2 Experimental Approach

### 2.1 Mix Designation of Steel Fibre Reinforced with Geopolymer Concrete Mixes (SGPC)

The geopolymer concrete reinforced with steel fibres mixture slightly improves the strength [5]. The fibres transmit tensile forces which minimize the tendency to crack. In the mix proportion for geopolymer concrete with steel fibres were mixed from zero to 1% with gradual increment of 0.25% of total volume of concrete are termed as CGPC or SGPC0, SGPC0.25, SGPC0.5, SGPC0.75, SGPC1.0, respectively. The mix design for SGPC mixes is presented in Table 1.

**Table 1** Mix design of geopolymer concrete reinforced with steel fibre (SGPC)

Mix designation	CGPC or SGPC0	SGPC0.25	SGPC0.5	SGPC0.75	SGPC1.0
Steel fibre (%)	0	0.25	0.5	0.75	1.0
Qty. of steel fibre (kg/m <sup>3</sup> )	0	19.62	39.25	58.87	78.50

### 2.2 Mix Designation of Hybrid Fibre Reinforced with Geopolymer Concrete Mixes (HGPC)

In HGPC, polyester fibre is introduced in excess of steel fibres. After getting the optimum mixture proportion for geopolymer concrete reinforced with steel fibre, polyester fibres were mixed from zero to 1% with gradual increment of 0.25% of total volume of concrete and termed as HGPC0, HGPC0.25, HGPC0.5, HGPC0.75, HGPC1.0, respectively. The mix design for HGPC mixes is presented in Table 2.

**Table 2** Hybrid fibre-reinforced geopolymer concrete mix design (HGPC)

Mix designation	HGPC0	HGPC0.25	HGPC0.5	HGPC0.75	HGPC1.0
Polyester fibre (%)	0	0.25	0.5	0.75	1.0
Qty. of polyester fibre (kg/m <sup>3</sup> )	0	3.48	6.95	10.43	13.90

## 3 Results and Discussion

The in-depth discussion and interpretation of results on the workability, hardened properties and durability of the SGPC and HGPC have been presented in this section. As far as the concentration of NaOH is considered, 12 M geopolymer concrete (GPC) mix



shows highest compressive strength in comparison with the 10 M GPC and 14 M GPC mix. Therefore, 12 M GPC has been taken for final mixture proportion for further study. With the increase in molarity of NaOH, compressive strength rises but beyond a point, it decreases [6].

### 3.1 Workability

The flow per cent increases as the percentage of steel fibre is taken up to 0.5%. Beyond this, no further increase in flow per cent was observed rather the values start decreasing for steel fibre up to 1% volume fraction. Hence as per the workability criteria, the mix obtained by 0.5% steel fibre is selected as the best suited mix for the geopolymer concrete reinforced with steel fibre as the mixes with higher steel percentages does not allow the addition of polyester fibre for the manufacturing of geopolymer concrete reinforced with hybrid fibre at desired workability. Flow per cent values corresponding to each batch mix of SGPC and HGPC are shown in Fig. 1.

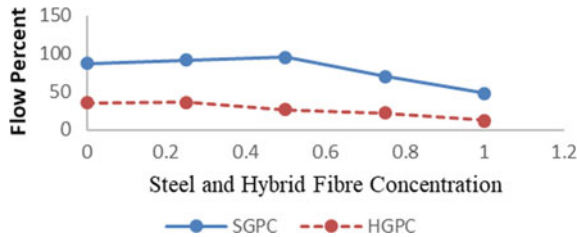


Fig. 1 Flow table curve

For HGPC, it is clearly seen that the flow per cent is maximum for 0.25% of polyester fibre. Beyond this, the values of flow per cent start decreasing for up to 1% volume fraction.

Hence, it is clear that workability of HGPC gradually decreases from volume fraction of 0.25% to 1% of polyester fibre. It may be due to the uneven dispersal of steel and polyester fibres in the mix and increased cohesive forces amongst the fibres. Therefore, HGPC0.25 may be taken as the optimum mix for hybrid fibre-reinforced GPC.

### 3.2 Hardened Properties of Geopolymer Concrete

In this section, hardened properties such as strength in compression, tension and bending are discussed.

#### 3.2.1 Compressive Strength

The strength in compression for SGPC and HGPC when examined at 28 days at different percentage of steel fibre and polyester fibre is shown in Table 3.

From Fig. 2, the growth in compressive strength when tested at 28 days of ambient curing of SGPC0.25, SGPC0.5, SGPC0.75 and SGPC1.0 is 5.82%, 22.68%, 36.03% and

**Table 3** Compressive strength at 28 days

S. No.	SGPC specimen	Average compressive strength (MPa)	% increase in strength	HGPC specimen	Average compressive strength (MPa)	% increase in strength
1	SGPC0	25.00		HGPC0	28.23	22.69
2	SGPC0.25	26.45	5.82	HGPC0.25	34.50	49.93
3	SGPC0.5	28.23	22.68	HGPC0.5	30.70	33.42
4	SGPC0.75	31.30	36.03	HGPC0.75	28.03	21.81
5	SGPC1	33.50	33.50	HGPC1	26.51	15.21

45.58%, respectively, when compared to CGPC. Hence, it is clear that the compressive strength found to be increase when percentage of steel fibre is increased up to 1% volume fraction. This is justified by the high strength and high modulus property of steel fibre. Compressive strength increment may also be due to the increasing frictional resistance between steel fibre and GPC mix. Similarly, the growth in compressive strength when tested at 28 days of ambient curing of HGPC0, HGPC0.25, HGPC0.5, HGPC0.75 and HGPC1.0 is 22.69%, 49.93%, 33.42%, 21.81% and 15.21%, respectively, when compared to CGPC. It can be noted that the strength in compression increases when polyester fibre is taken up to (HGPC0.25) 0.25% volume fraction of polyester fibre (keeping 0.5% of steel fibre constant). Beyond this, compressive strength does not increase rather the values start decreasing on further addition of polyester fibre up to 1%. It may occur because synthetic fibres such polyester fibres have low stiffness to mend the ultimate load. However, the post crack hardening behaviour is found to be better when compared with steel fibre. Also the total aggregate content in the mixture has significant effect on the compressive strength [4].

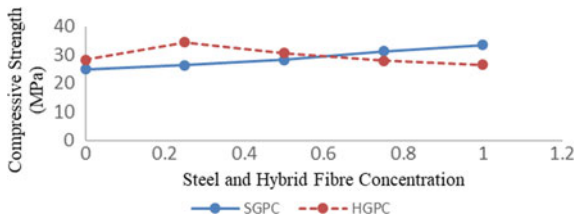


**Fig. 2** Compressive strength of SGPC and HGPC

### 3.2.2 Split Tensile Strength

From Fig. 3, the rise in split tensile strength tested at 28 days of ambient curing of SGPC0.25, SGPC0.5, SGPC0.75 and SGPC1.0 is 18.26%, 22.12%, 34.07% and 58.40%, respectively, when compared to CGPC. Hence, the inference may be made that split

tensile strength enhances as percentage of steel fibre is taken up to 1% volume fraction. Because of the crack joining property of fibres, the rise in split tensile strength is noted, whereby the movements of cracks were deferred and stresses due to tension were shifted across the fibres [4]. Similarly, the increment in split tensile strength when tested at 28 days of ambient curing of HGPC0, HGPC0.25, HGPC0.5, HGPC0.75 and HGPC1.0 is 22.12%, 23.89%, 10.62%, 3.98% and 3.09%, respectively, when compared to CGPC. The inference can be made that the split tensile strength enhances as steel fibre is taken up to (HGPC0.25) 0.25% of polyester fibre (keeping 0.5% of steel fibre constant).

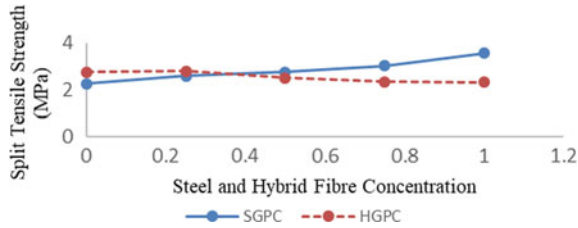


**Fig. 3** SGPC and HGPC split tensile strength

Beyond this, no further increase was noted rather the values start decreasing for addition of polyester fibre up to 1%. This may be because of the low modulus property and tensile strength for polyester fibre.

### 3.2.3 Flexural Strength Test

Flexural strength of SGPC and HGPC at 28 days is determined by performing four point test.

From Fig. 4, the enhancement in modulus of rupture when tested at 28 days of ambient curing of SGPC0.25, SGPC0.5, SGPC0.75 and SGPC1.0 is 2.78%, 26.90%, 56.03% and 76.47%, respectively, when compared to CGPC. Therefore, the flexural strength increases with the volume fraction for steel fibre with 0.25% to 1% as steel fibre effectively takes the tension developed in the specimens. Similarly, for modulus of rupture with ambient curing of HGPC0, HGPC0.25, HGPC0.5, HGPC0.75 and HGPC1.0, the increment is 26.93%, 39.0%, 42.41%, 61.6% and 85.75%, respectively, when compared to CGPC. It can be inferred that the flexural strength rises with volume fraction of polyester fibre. This is because the finer polyester fibre effectively covers the small cracks.

### 3.3 Flexure Cracks on Prismatic Specimens

Flexure cracks were observed during four point bending test on UTM on various specimens. It is clearly visible that the cracking in the specimen subjected to bending starts in the tensile zone, i.e. soffit of the beam or prisms. The cracks with moderate depth can be observed in steel fibre-reinforced GPC and very minute cracks with low depth can be observed in hybrid fibre-reinforced geopolymer concrete when load is applied at

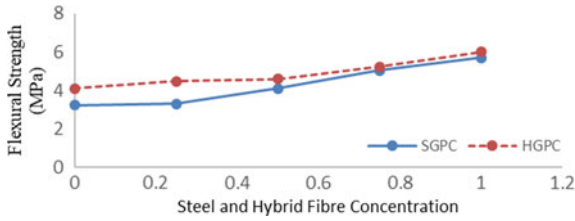


**Fig. 4** SGPC and HGPC flexural strength

initial crack. This is because the finer polyester fibre fills the small cracks better than steel fibres.

### 3.4 Durability Test

The specimens including conventional cement concrete, control geopolymer concrete, optimum steel fibre-reinforced GPC and optimum hybrid fibre-reinforced GPC were tested after immersed in 3% solution of sulphuric acid for acid resistance test for durability test. Changes in percentage of mass and compressive strength were calculated for 1, 2, 3 and 4 weeks.

#### 3.4.1 Change in Weight

The losses in weight for CC, CGPC, SGPC0.5 and HSGPC1.0 after exposure for 1 week were observed to be 3.6%, 1.96%, 1.91% and 0.64%, respectively, and percentage losses in weight after exposure for 2 weeks were 6.59%, 2.83%, 2.53% and 1.29%, respectively. After exposure for 3 weeks, the loss in weight was 7.32%, 3.92%, 2.57% and 1.94%, respectively, and % loss in weight were 11.21%, 4.32%, 2.69% and 2.2%, respectively, after exposure of specimens for 4 weeks. The loss in weight in GPC specimens is very less in comparison with normal concrete specimens, and the reason is geopolymer does not produce lime (CaO) during chemical reaction. Thus, it does not dissolve in acid solution. The variation is presented in Fig. 5.

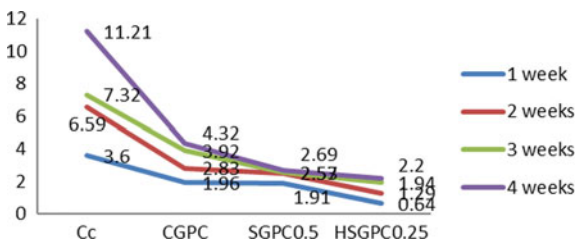


**Fig. 5** Percentage loss in weight

### 3.4.2 Change in Compressive Strength

Figure 6 presented the variation of compressive strength when specimens were exposed to sulphuric acid solution. It can be inferred that the compressive strength diminishes when content of fibre is increased. The percentage losses in strength for CC, CGPC, SGPC0.5 and HGPC1.0 after exposure for 1 week were observed to be 53.72%, 39.76%, 34.24% and 29.43%, respectively, and percentage losses in weight after exposure for 4 weeks were 65.8%, 51.45%, 45.34% and 31.9%, respectively.

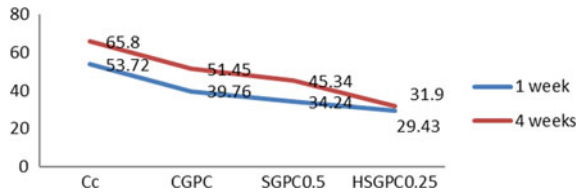


**Fig. 6** Percentage loss in strength

### 3.4.3 Change in Visual Appearance

The appearance of samples shown in Fig. 7, after soaking in the solution of sulphuric acid, shows the GPCs undergoes erosion of the surface. It can be noted that the conventional concrete specimen open to sulphuric acid experiences severe erosion and efflorescence of acid solution on the outer surface when compared to the GPC specimens. There was a sign of cracking, slight erosion on the surface of test specimen of geopolymer concrete. However, amongst all the GPC specimens, damage to the outer surface was severe in CGPC, moderate in SGPC0.5 and less in HSGPC0.25.



**Fig. 7** Visual appearance of specimens after acid attack

## 4 Conclusion

Based on the present experimental investigation on geopolymer concrete, the following remarks and findings have been drawn:

- As per the workability criteria, the SGPC0.5 is selected as the best suited mix for the GPC reinforced with steel fibre as mixes with higher percentage of steel does not

allow the addition of polyester fibre for the production of hybrid fibre-reinforced GPC at desired workability. The hardened properties increase as the fraction of steel fibre changed from zero to 1%.

- For HGPC, as per the workability criteria, the mix obtained by 0.25% polyester fibre and 0.5% steel fibre (HSGPC0.25) is taken as the optimum mix for hybrid fibre-reinforced GPC. When steel fibre is taken from zero to 0.25%, compressive and split tensile strength increase and beyond 0.25%, it gradually decreases up to 1%. However, flexural strength rises when the fraction of polyester fibre is taken from zero to 1% due to effective property of finer polyester fibre bridging the small cracks.
- As far as cracking pattern is considered, the cracking in the specimen subjected to bending starts in the tensile zone, i.e. soffit of the prisms or beam. The cracks with high depth are observed in conventional cement concrete and control GPC, whereas moderate depth cracks are observed in steel fibre-reinforced GPC, and very minute cracks with low depth are observed in hybrid fibre-reinforced geopolymer concrete at the stage of first crack load.
- Based on the visual appearance and percentage loss in mass and strength, it can be established that GPC reinforced with hybrid fibre reinforced is the most durable, and the conventional cement concrete is the least durable amongst all the mixes.

## References

1. Aswani E, Karthi L (2017) A literature review on fibre reinforced geopolymer concrete. *Int J Sci Res (IJSR)* 8(2, Feb)
2. Al-Majidi MH, Lampropoulos A, Cundy AB (2017) Steel fibre reinforced geopolymer concrete (SFRGC) with improved microstructure and enhanced fibre-matrix interfacial properties. *Constr Build Mater* 139:286–307
3. Hassan A, Arif M, Shariq M (2019). A review of properties and behavior of reinforced geopolymer concrete structural elements—a clean technology option for sustainable development. *J Clean Prod* 245
4. Hassan A, Arif M, Shariq M (2020) Age dependent compressive strength and elastic modulus of fly ash based geopolymer concrete. *Struct Concr*:1–15
5. Hassan A, Arif M, Shariq M (2020) Structural performance of ambient-cured reinforced geopolymer concrete beams with steel fibres. *Struct Concr*:1–19
6. Verma M, Dev N (2021) Sodium hydroxide effect on the mechanical properties of flyash-slag based geopolymer concrete. *Struct Concr*:1–12
7. Abdul Aleem MI, Arumairaj PD (2012) Geopolymer concrete—a review. *Int J Eng Sci Emerg Technol* 1(2):118–122
8. Adak D, Sarkar M, Mandal S (2014) Effect of nano-silica on strength and durability of fly ash based geopolymer mortar. *Constr Build Mater* 70:453–459
9. Ahmed SFU, Ronnie Z (2017) Ductile behavior of polyethylene fibre reinforced geopolymer composite. In: MATEC web of conferences, vol. 97. EDP Sciences, p 01047
10. Anuradha R, Sreevidya V, Venkatasubramani R, Rangan BV (2012) Modified guidelines for geopolymer concrete mix design using Indian standard
11. Anusuya R, Chanraleka D, Sarumathi S, Karthikeyam G (2018) Experimental study on concrete by replacement of fine aggregate with copper slag, GGBS and M-Sand. *Int J Inno Sci Res Technol*. ISSN No. 2456-2165



# A Critical Analysis of Design, Development, and Failure of Existing Stents

Jannatul Bashar and K. Jayabal<sup>(✉)</sup>

Mechanical Engineering Department, Indian Institute of Information Technology Design and Manufacturing, Kancheepuram, Tamilnadu, India

jayabal@iiitdm.ac.in

## 1 Introduction

There are two ways to communicate your words related to design selection, the first identity directly on what design characteristics should be taken into consideration and why, it will consist of all properties, characteristics, method, etc., and the next high lighten what design characteristics mainly we should avoid and of course its reason behind it. The intent of this outline was a methodical evaluation of underlying causes for stent collapse, eventually coming toward the decisions for what not to design, especially the geometry of the stent.

Stent geometries are nothing but the periodic organization of a reforming unit cell or defined by the topology of the unit cell. For a better understanding, the stent is a mechanical solution to the biological problem term used by Sigwart [1]. The study by Bashar and Jayabal [2] has quantified various stent structures and their performance based on the mechanical integrity of the stent deployment process and has shown that the stent structure is a major factor in percutaneous coronary intervention (PCI).

In the PCI process, sporadically, a stent does not open its geometry completely during deployment. In further, the major problem is the circumvention of the stent itself formed by the body's therapeutic rejoinder [3]. The blockage can be either partial or total. Once a stent is located in a coronary artery, it cannot be driven out. Therefore, it is extremely desirable to design such a stent that will not lead to failure at deployment or in future.

Traditional methods of producing a stent and its dilating catheter by examining various structures and deciding the most suitable among them cannot get the best accomplishing stent in the design extent [4]. If the designer knows where we should be concerned while producing a life rescuer stent, and hence, it will give a more reliable result.

Using the finite element method, capture the effects on the stent during its deployment inside the cylindrical artery. Considering the method of minimizing the computational time in FEA, take a stent as one-eighth of the whole stent model.

Stent failure is not an unexpected event. This failure can happen due to multiple reasons such as an oversight in the stent geometry, material, design, parameters, deployment process, etc.

Stents are very tiny frames, and their links are created such that it should have uncoiling and coiling geometrical capabilities when applied and release the pressure

inside the balloon catheter to inflate and deflate it, respectively. Five models of the stent are acknowledged which failed due to manifold reasons. Three designs were taken from the previously published literature Prithipaul et al. [5], and two were created to manifest key circumstances of the failure that shows the principal contribution of stent design and its purpose of use.

The aspiration of designing a stent is always to minimize the fundamental mechanical properties. Using these mechanical properties such as stresses, PEEQ, recoil, and foreshortening, the stent demonstrates that either it successfully placed or failed.

## 2 Method

### 2.1 Stent Model

Five stent models are considered and named as H-form, I-form, M-form, O-form, and q-form in the present manuscript. The name assigned to all of the models is based on their geometrical structure shown in Fig. 1. The last two “O” and “q” forms are designed by their ideas only for demonstrating purpose. For an Indian state, the accessible coronary artery measurement fluctuates from 2.6 to 4.52 mm diameters disclosed by Raut et al. [6] and Holzapfel et al. [7]. Therefore, established a 3.5 mm diameter artery structure to illustrate the unbiased results among five stents. The artery thickness is anchored as 0.7 mm, and hence, its inner diameter confines as 2.8 mm. The artery characterizes in three layers known as intima, media, and adventitia that specifies 0.3 mm, 0.25 mm, and 0.15 mm thickness, respectively [7]. The parameter of each unit cell of tubular stent structure is presented in Table 1, and their notations are displayed in Fig. 2a.

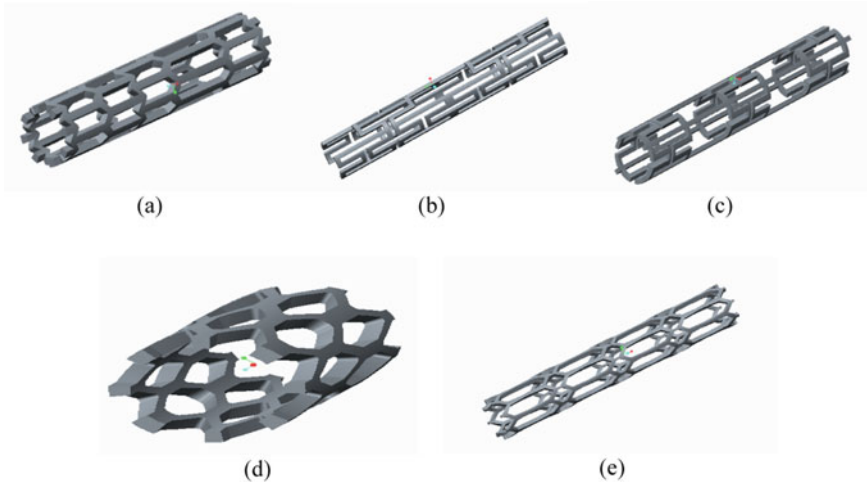


**Fig. 1** Stent CAD models **a** H-form, **b** I-form, **c** M-form, **d** O-form, and **e** q-form



**Table 1** Input parameter of the stent in mm

Stent	Outer diameter $D_o$	Thickness $T$	Length $L_s$	Strut width $W_s$	Centerline space $C_s$	Link width $W_l$
H-form	2.030	0.11	3.86	0.12	0.17	0.14
I-form	2.030	0.20	3.60	0.25	0.68	0.20
M-form	2.030	0.20	5.28	0.24	0.40	0.25
O-form	2.030	0.20	3.21	0.25	0.80	0.16
q-form	2.030	0.20	3.13	0.22	0.40	0.13

**2.2 Material**

All three films of an artery are proper for hyperelastic material holding incompressible isotropic performance. For each zone, the coefficients of reduced polynomial strain energy potential are shown in Table 2 given by Tammareddi et al. [8]. The structure of

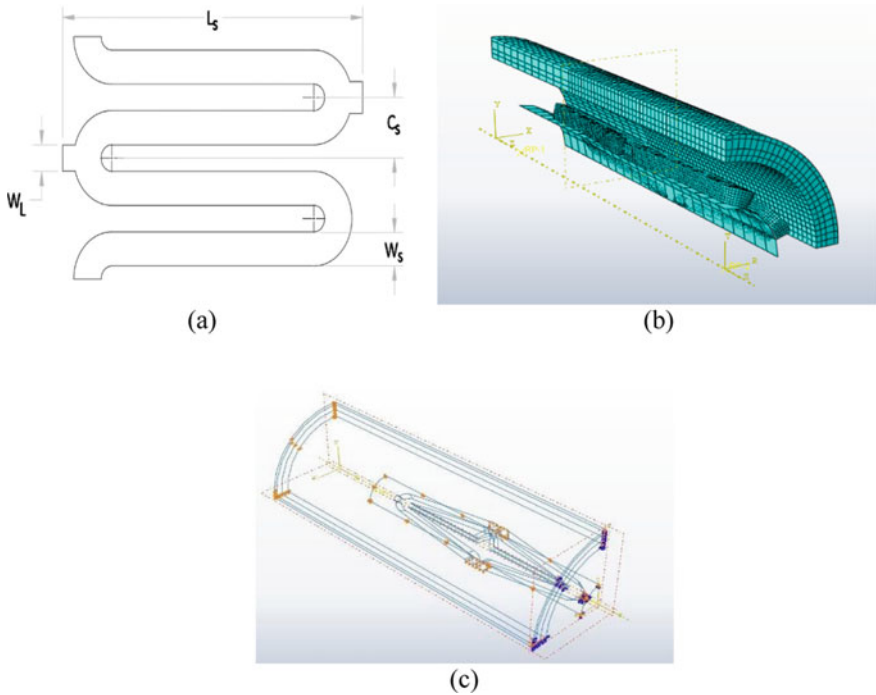


**Fig. 2** a Dimensioning parameters b meshing and c assembly of the artery, stent, and balloon with boundary conditions

the reduced polynomial strain energy potential is expressed as

$$U = \sum_{i+j=1}^N C_{i0} (\bar{I}_1 - 3)^i (\bar{I}_2 - 3)^j + \sum_{i=1}^N \frac{(J_{el} - 1)^{2i}}{D_i}$$

**Table 2** Coefficients for the constitutive model for each layer of the artery [7]

Artery layer	C10	C20	C30	C40	C50	C60
Intima	6.79E-03	0.54	-1.11	10.65	-7.27	1.63
Media	6.52E-03	4.89E-02	9.26E-03	0.76	-0.43	8.69E-02
Adventitia	8.27e-03	1.2e-02	0.52	-5.63	21.44	0.00

where  $N$  is a material parameter for constitutive equations.  $D_i$  and  $C_{i0}$  refer to the temperature-dependent material,  $\bar{I}_1$  is the first deviatoric strain invariant. The material becomes incompressible if the second phrase becomes zero in the preceding equation.

An elastic-plastic material such as the stainless steel 316L (SST) [8] is used to model the stent. Their material properties are shown in Table 3.

**Table 3** Stainless steel 316L mechanical properties

Young’s modulus GPa	Density kg/m <sup>3</sup>	Poisson ratio	Yield strength MPa	Plastic strain
196	8000	0.3	205	0
			515	0.6

### 2.3 Meshing of the Model

It has proved that the exact solution reaches only by defining the finer mesh element and small seed size [9]. To accomplish the above theory and complexity of the solver, refine the mesh elements only at the contact portions of the stent and artery. The elements used for the stent are C3D8R eight-node linear brick elements, for the balloon is SFM3D4 four-node quadrilateral surface element, and for artery is C3D8H eight-node linear brick hybrid element as shown in Fig. 2b.

### 2.4 Boundary Conditions

Practice cylindrical coordinate system as a datum that has  $R$ ,  $T$ , and  $Z$  mutual perpendicular axis. One-eighth of the model is considered, hence the boundary condition is

defined accordingly as follows: longitudinal axis symmetry that is *Z*-symmetry which represents the whole length, cyclic symmetry that represents the cyclic pattern of unit stent geometry in *T* direction, and the stent is allowed to move radially outward in *R* direction as shown in Fig. 2c. The radial displacement is stipulated to the balloon for its inflation rather than using pressure boundary conditions, as per reverse engineering by Jiao et al. [10].

### 3 Result

After the completion of finite element analysis, the mechanical integrity: stress generation on the stent, recoil, PEEQ, foreshortening, arterial stress, and longitudinal stretch of the artery are extracted from the FEA output database (ODB field output) that shows results w.r.t time. The maximum values of mechanical properties are determined at the end step of expansion during deployment. These values at the pick point of the stent element are collected for all the five models shown in Table 4. The negative value of foreshortening shows that its length has slightly increased after deployment.

**Table 4** The stresses on the stent, PEEQ, arterial stress, foreshortening, recoil are listed below for stainless steel stents at the most expansion stage

Design name	Stent stress (MPa)	Artery stress (MPa)	PEEQ	Recoil (mm)	Foreshortening stent (mm)	Longitudinal stretch artery (mm)
H-form	162.301	5.021	0.018	0.735	-0.0789	0
I-form	508.805	24.125	0.293	0.036	0.198	0.741
O-form	620.415	5.297	0.382	0.039	1.336	0.483
M-form	895.000	6.111	1.528	0.050	0.000	-0.001
q-form	825.206	6.308	0.544	-	0.002	-0.001

The mechanical integrity for the stent and artery element is von Mises' stresses. Foreshortening is specified as the variation in length against enlargement. Radial recoil refers to the contraction measure of the stent against a deflation of the balloon, it is also known as the spring-back effect. Radial stiffness is required to prevent a collapse of the stent. All outcomes are shown in Table 4, whereas the corresponding contour plots are displayed in Fig. 3 for all five models.

The function of the stent is to expand and push plaque back against the artery wall. That can inaugurate by uncoiling the designed link of the stent. The above designs of the stent failed due to various reasons such as higher recoil, longer foreshortening, profoundly plasticity, and inadequate uncoiling capability that does not allow the stent to expand.

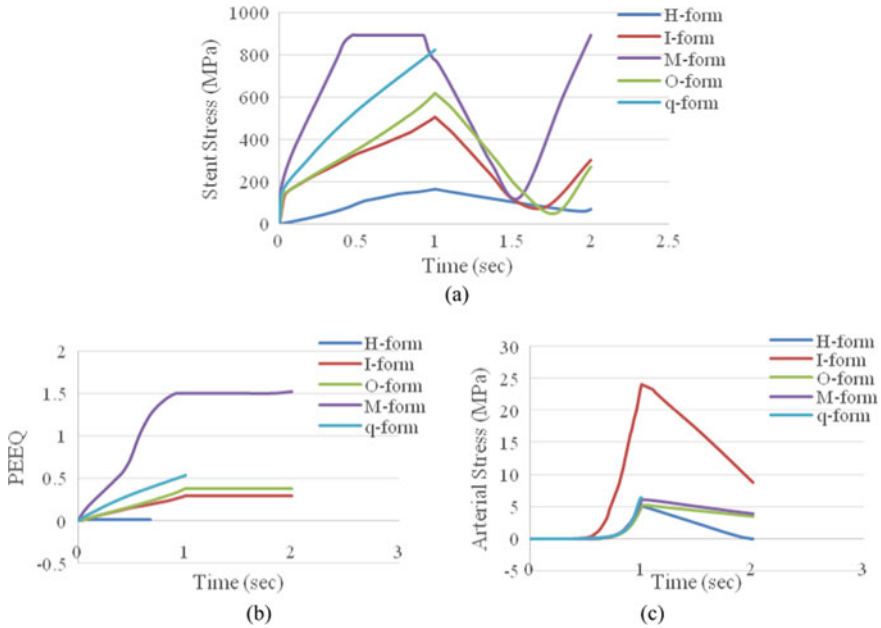


**Fig. 3** Result plots **a** stress on stents, **b** arteria stress, and **c** PEEQ for all models

### 3.1 Models’ Descriptions

The unit cell of each tabular stent geometry before and after deployment of the PCI process is laid out in Fig. 4. Among all five stents structure, it is found from the analysis that H-form is generating high recoil of the link that is unable to hold the artery open competently, hence it may block the artery moreover in future, shown in Fig. 5a, b. This happened because of inappropriate linking geometry. I-form is generating more arterial stress. The geometric area or structure that is requisite to support the artery adequately, but due to the extended length of this form, minimizes the necessity. Hence, it became an irregular inner artery configuration after the deployment as displayed in Fig. 5c. O-form prompts high stent foreshortening, indicated in Fig. 5d. The stent connecting links are bonded to each other such that it is flexible to expand against its length. In M-form, there are two different vertical connecting links with horizontal strut geometry. One is having a smaller width dimension than the other. The outcomes show variation in expansion rate and amount on those two vertical link structures. The more link width with shorter link length leads to reach the plastic stage of the material and further failure of an object manifested in Fig. 5e. There is also a slight contrast to the expanding radius at the two points. At last, the q-form has two design-loops along its longitudinal axis. Where one design-loop has a longer length connection among links that helps in the expansion, and another link has a very compact-loop pattern that opposes expansion as appears in Fig. 5f. The second loop is unable to open its link up to the required level and generates relatively high stress on this loop strut.

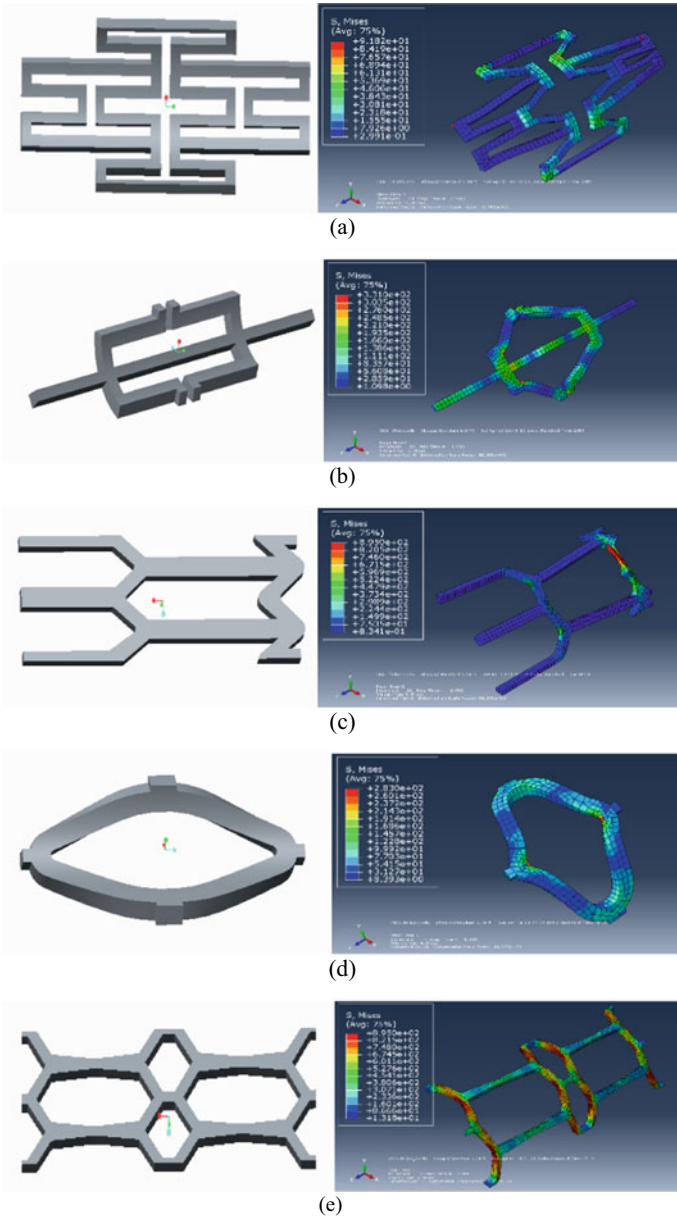


**Fig. 4** Stent models, before (left) and after (right) deployment **a** H-form, **b** I-form, **c** M-form, **d** O-form, **e** q-form

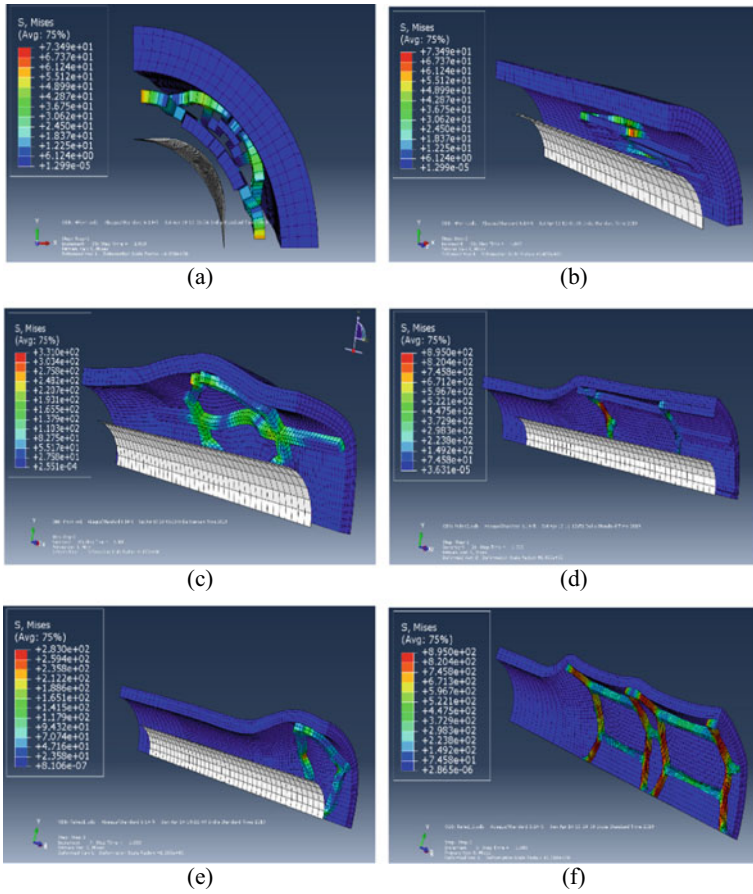


**Fig. 5** Stent models after deployment by FEA analysis **a** and **b** H-form, **c** I-form, **d** M-form, **e** O-form, **f** q-form

### 4 Conclusion

Five tabular structures of the bio-stent designs were considered in this work to demonstrate mistakes that generally happen while generating a stent. In the present work, several parameters are taken into account to suggest the various failure reasons that appear in this critical analysis; stent stress, PEEQ, foreshortening, recoil, arterial stress, and foreshortening. This work may help to provide some additional input for what should be avoided during designing a bio-stent structure. The outcomes manifest that the individual cell topology of the stent has its structural staging and shortcomings. Furthermore, this could be used to compare and discard the stent geometry from the design of a desirable stent. This analysis does not consider blood flow analysis under computational fluid dynamics. The suggestions collected from the outcomes are based on stent failure only during its deployment.

## References

1. Sigwart U (1997) Stents: a mechanical solution for a biological problem? *Eur Heart J* 18(7):1068–1072
2. Bashar J, Jayabal K (2020) Analysis and selection of bio-stents using finite element method. In: *Advances in applied mechanical engineering*, pp 485–493
3. Donelli G, Guaglianone E, Di Rosa R, Fiocca F, Basoli A (2007) Plastic biliary stent occlusion: factors involved and possible preventive approaches. *Clin Med Res* 5(1):53–60
4. Li H, Liu T, Wang M, Zhao D, Qiao A, Wang X, Gu J, Li Z, Zhu B (2017) Design optimization of stent and its dilatation balloon using kriging surrogate model. *Biomed Eng Online* 16(1):13
5. Prithipaul PK, Kokkolaras M, Pasini D (2018) Assessment of structural and hemodynamic performance of vascular stents modelled as periodic lattices. *Med Eng Phys* 57:11–18
6. Raut BK, Patil VN, Cherian G (2017) Coronary artery dimensions in normal Indians. *Indian Heart J* 69(4):512–514
7. Holzapfel GA, Sommer G, Gasser CT, Regitnig P (2005) Determination of layer-specific mechanical properties of human coronary arteries with nonatherosclerotic intimal thickening and related constitutive modeling. *Am J Physiol Heart Circul Physiol* 289(5):H2048–H2058
8. Tammareddi S, Sun G, Li Q (2016) Multiobjective robust optimization of coronary stents. *Mater Des* 90:682–692
9. Ching J, Hu YG (2016) Effect of element size in random finite element analysis for effective Young's modulus. *Math Probl Eng*
10. Jiao GY, Li PP, Zhang RJ (2013) Application of periodic boundary conditions in studying stent expansion. In: *Applied mechanics and materials*, vol 419, pp 286–291



# Study of Effect of Leading-Edge Tubercles on NACA 4412 Airfoil

Ishwar Mukesh<sup>1</sup>(✉), Aakash Kaushik<sup>1</sup>, Naushad Ahmad Ansari<sup>2</sup>, and M. Zunaid<sup>2</sup>

<sup>1</sup> Department of Automobile Engineering, Delhi Technological University, Delhi, India  
ishwarmukesh@gmail.com

<sup>2</sup> Department of Mechanical Engineering, Delhi Technological University, Delhi, India

## 1 Introduction

Biomimicry is a method of imitating the structures, functioning, and core elements of nature for the sole purpose of solving complex problems inclined to the human span base [1]. The features of nature have developed adaptations over the geological period through the fundamental laws of natural selection. The human literati have looked at nature for answers to engineering problems throughout our existence.

The flippers of humpback whales have bumps or protuberances on their leading edges called tubercles. These structures allow whales to take tight turns underwater and swim efficiently. These disproportionate size flippers produce ample aerodynamic load, which can carry a whale weighing close to tons [1]. Despite their large size, they are proficient in translation and can efficiently perform loops and turns underwater. The presence of tubercles on these whales indicated reduced stall and increased lift while reducing noise in the post-stall regime [1].

The purpose of this paper is to evaluate the performance of tubercles under low Reynolds number flow conditions. A performance improvement can be referred equivalent to increased values of lift. A set of 5 tubercle configurations are investigated.

### 1.1 Flow Control

Flow control involves changes introduced in the flow region to obtain a particular objective. However, this study's main motive is to incorporate flow control procedures by introducing variations in the airfoil surface. The effect of Reynolds number also plays a significant role. It determines whether the flow is laminar or turbulent. For a laminar flow regime, it is advantageous to increase the delay of flow separation, increasing the maximum lift. For a turbulent boundary layer, flow separation is somewhat random, and skin friction also plays a significant role in determining the flow region. In the presence of these tubercles, flow separation generally starts at the wingtips and gradually translates inwards, with increasing angle of attack and therefore finally converts into full separation [2].



## 1.2 Research into Tubercles

Various researchers have outlined the effects of leading-edge tubercles when introduced to an airfoil in terms of performance increment [3–6]. It showed how the separation was delayed and led to maximum lift to enhance and produce maximum attainable stall [3]. The introduction of these protuberances also enhanced acoustic performance even led to an increase in propellers' aerodynamic efficiency by 6% [7]. These structures, when incorporated in turbine blades, positioned at 62% and 95% span, led to performance enhancement [8].

Cases were also shown where the introduction of tubercles into airfoil geometry led to a deterioration in performance. However, later it was posited that these tubercles still gave advantages in the form of improved stall characteristics and, therefore, post-stall lift [9, 10].

## 1.3 Effect of Reynolds Number

Reynolds number plays a vital role when three-dimensional effects are brought to study. It was concluded that enhancement in the lift was only achieved for Reynolds number between 500,000 and 631,000 [3, 6]. At low Reynolds number between 44,000 to 120,000, there was a reduction in maximum lift and stall occurred early [11]. However, at a high Reynolds number ( $Re = 270,000$ ), although there was a reduction in lift and drag performances, the ratio of lift to drag improved [12]. Therefore, it can be inferred that Reynolds number plays a vacillating role on performance when it is incorporated in an airfoil.

## 2 Tubercle Geometry Design

We researched the optimum aspect ratio (AR) for the wing to ensure minimal blockage of the accuracy of results. The ratios were needed to be kept large so the effects of sidewalls from the wind tunnel could be neglected. An  $AR = 4.3$  and  $AR = 2.04$  were employed in wind tunnel experiments [3, 13]. The aspect ratio of a humpback whale flipper was found to be  $AR = 6.1$  [14]. We decided to use this same value in our simulations. Furthermore, it was needed to have enough surface area to get accurate results. The full span of the airfoil model has a chord length( $c$ ) of 5 inches and a span( $l$ ) of 30.5 inches.

Similarly, deciding the amplitude (A) and wavelength (W) of tubercles was made in reference to results obtained by previous research. When the airfoil NACA 0021 was tested, it was found that a configuration of the lowest order gave the best results [1].

The configurations tested were A2W7.5 and A4W30, where 'A' stands for amplitude in mm and 'W' stands for wavelength in mm. Of all the configurations tested, it was found that minimum amplitude gave better coefficients, but there was a limit to which the wavelengths were to be reduced. Therefore, considering a good A/W ratio would have been better than studying the variation in parameters.

As a result, based on these researches, we decided the ratio to be  $A/W = 0.27$ . With a hit and trial approach, the configurations to be studied were selected to be started with an amplitude value of 6.34 mm and, therefore, a wavelength value of 54.42 mm. Five

different iterations were analyzed with the successive decrease in amplitude values by 1 mm. As mentioned in Table 1, the following were the decided sinusoidal configurations of tubercle that was chosen to be tested.

**Table 1** Tubercle configuration

S. No.	Amplitude (mm)	Wavelength (mm)	Equation	Notation
1	6.34	54.42	$y = 6.34 * \sin(0.115x)$	A6.34W54.42
2	5.34	23.48	$y = 5.34 * \sin(0.267x)$	A5.34W23.48
3	4.34	19.77	$y = 4.34 * \sin(0.317x)$	A4.34W19.77
4	3.34	12.37	$y = 3.34 * \sin(0.507x)$	A3.34W12.37
5	2.34	8.66	$y = 2.34 * \sin(0.725x)$	A2.34W8.66

### 3 Numerical Analysis

#### 3.1 Numerical Model

The major drawback noticed in the studies of [15] was the use of an unsuitable turbulence model. They considered the one equation Spalart–Allmaras turbulence model. Aftab and Ahmad [15] focused on the use of a physical condition-specific turbulence model. Accordingly, the turbulence model chosen for the analysis was K- $\omega$  SST with default settings. The model has been proved to be very accurate for low Reynolds number studies in various CFD simulations of wings.

#### 3.2 Domain and Mesh

A bullet domain (Fig. 4) was created for validation purposes; this was in reference to [16] and inlet, and outlet face distance was calculated according to it.

The research paper mentioned above used a structured mesh for analysis because it was performed on a wing with only one tubercle tip. On the contrary, this paper focuses on an array of tubercle tips with varying amplitude; i.e., a series of tubercle tips (Figs. 1 and 2) were placed on the wing with a uniform span (distance between each tubercle tip). Since the study is based on a broader array of tubercles, a tetrahedral mesh was preferred. The amplitude variation could not be meshed by the hexahedral mesh settings (Fig. 3).

The blue face in Fig. 4 represents the inlet, the yellow represents the face of symmetry, and the red one is the outlet. The Reynolds number for the flow was taken to be 240,000, and the corresponding velocity of the fluid was calculated as 26.84 m/s using the chord length as the characteristic length. Two different rectangular bodies of influence were also added to efficiently capture the wake region of the airfoil with an element size of 4 mm and 10 mm, respectively.

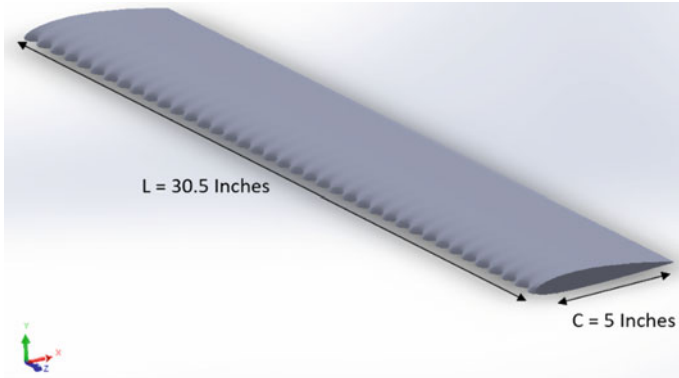


**Fig. 1** Isometric view of the wing with tubercles (4412 A4.34W19.77) with chord length = 5 inches and span = 30.5 inches

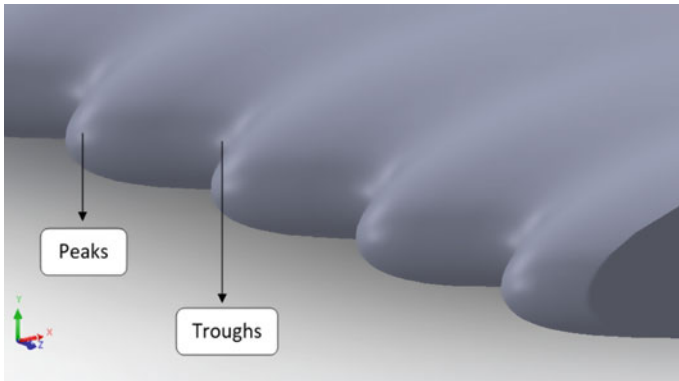


**Fig. 2** Closer look at the peaks and troughs (4412 A4.34W19.77)

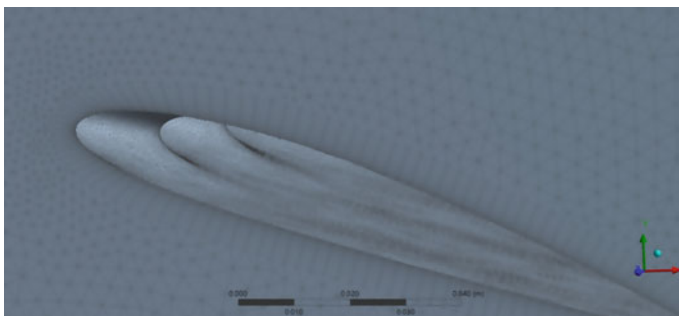


**Fig. 3** Grid representation (A6.34W54.42)

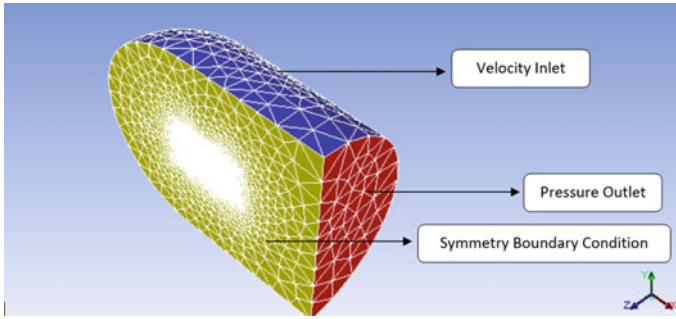


**Fig. 4** Computational domain where the blue section represents the inlet, the red, the outlet and, the yellow, symmetry boundary condition

To capture the geometry of the wing and tubercles precisely, a face sizing of 2.2 mm was incorporated at all the surfaces of the wing in addition to an inflation layer with a first-layer thickness of 60 microns with 15 layers of subsequent inflation layers having a growth rate of 1.15 were also used. A total mesh count of 6.3–8.50 million elements was observed for the different variations of tubercles proposed (Fig. 3).

The solver was initialized with hybrid initialization, and then it ran for over 1000 iterations. The convergence criterion was set to be  $10e-4$  with skewness of less than 0.75 in all cases.

Also, the  $Y^+$  value reached 3.33 for the wing surface.

## 4 Validation

On tabulation of the lift coefficient data at varying angles of attack at Reynolds number = 240,000 (Fig. 5), the contrast between the present computation and the experimental results from [17]. As obtained, the deviations were minimal, and accuracy of 98.6% was achieved, as shown in Fig. 5. This profitable association with the experimental and numerical data proved the reliability of the model and guided us to use it for computations to be carried out on future modified variants of the airfoil.

### 4.1 Grid Independence Test

Mesh independence came at 6.2 million with an error of 1.6%; hence, the model was assumed to be correct for it to be studied with tubercles. Although the mesh independence study was conducted for a 20-degree angle only, the error for all other angle of attacks was under 5%, as shown in Fig. 5. The model was also able to capture how the flow was being separated near the suction surface, as shown in Fig. 6.

## 5 Results and Discussions

### 5.1 Effectiveness of Tubercles

See Fig. 7.

**CHART 1.COMPARISON OF PRESENT COMPUTATION WITH EXPERIMENTAL RESULTS FROM REF.7**

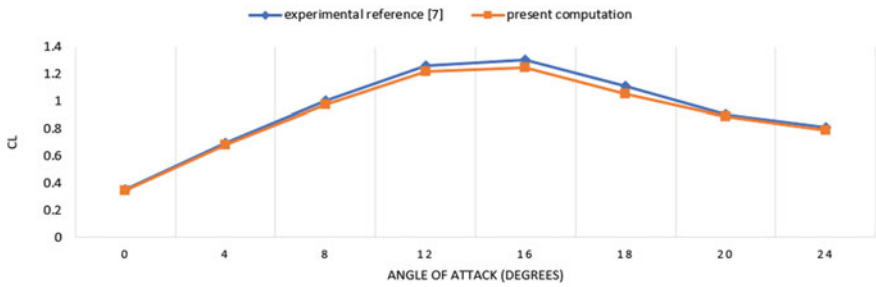


**Fig. 5** Comparison of numerical versus experimental values of Cl for NACA 4412

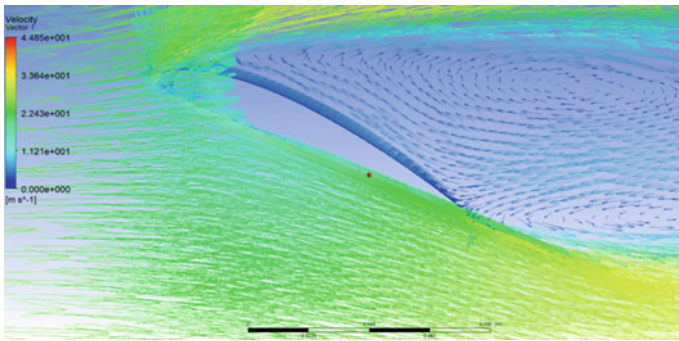


**Fig. 6** Region of flow separation NACA 4412

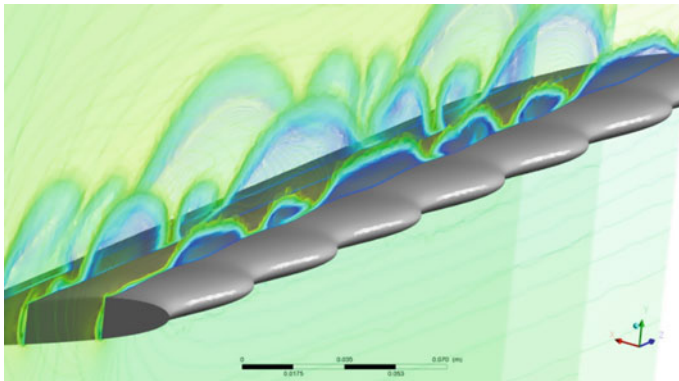


**Fig. 7** Contours of velocity showing the formation of vortices

The implementation of tubercles on the airfoil led to vortices' formation, which in turn helped in smooth exchange of boundary layer momentum and, therefore, delayed flow separation (Figs. 8 and 9). Strong vortices were formed on the aft region of the troughs. However, the simulation results notify that tubercles' introduction and its beneficial effects are predominantly airfoil-dependent. Furthermore, the change in amplitude and wavelength values has a significant impact on lift values.

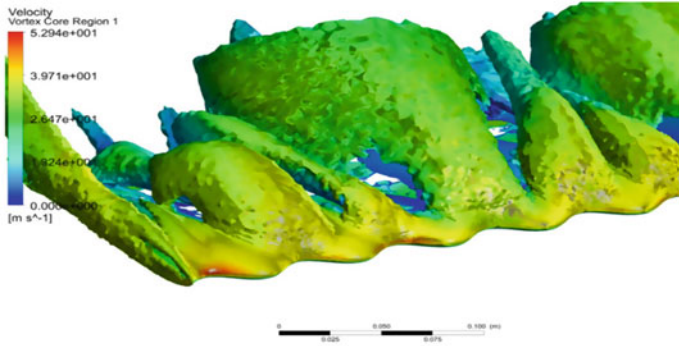


**Fig. 8** Resulting vortex core region for  $Re = 240,000$

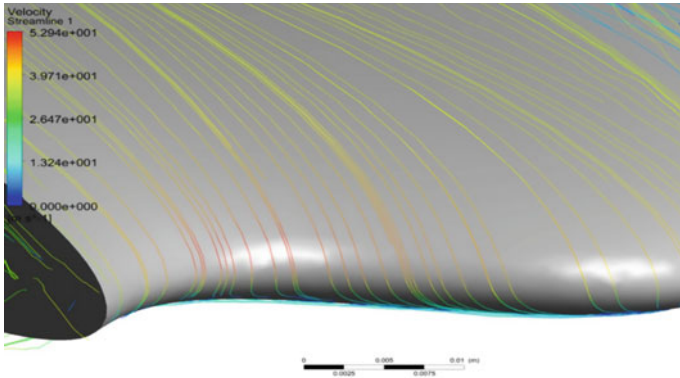


**Fig. 9** Velocity streamlines around the tubercles (A6.34W54.42)

From the study conducted on NACA 4412, the tubercle configuration with the maximum amplitude gave the highest lift coefficient.

It was also found that with the decrease in values of amplitude, the behavior of lift coefficient was erratic, as shown in Fig. 10. Therefore, it is very well expected that there exists a particular tubercle configuration that would lead to an increase or thus produce maximum lift coefficient.

Tubercles at a low Reynolds number of 240,000 showed a decrease in the overall lift of the NACA 4412 airfoil. This can be clearly seen from the significant drop of lift coefficient from 0.886 to 0.7944 at a 20-degree angle of attack in Fig. 10.

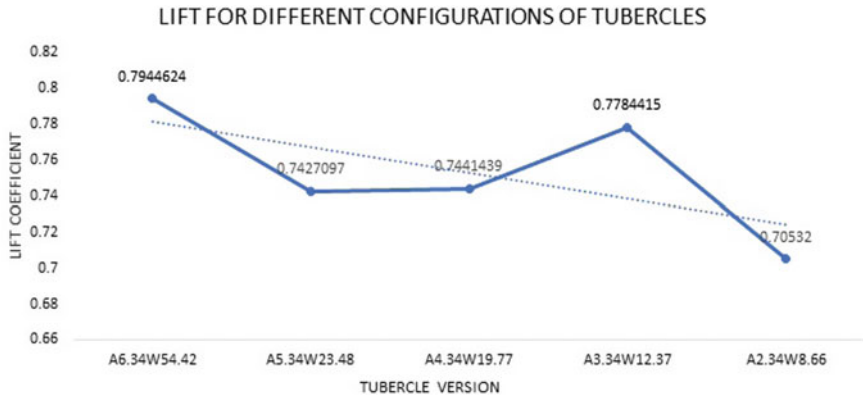


**Fig. 10** Values of  $C_l$  obtained for various lift configurations

Once the optimal tubercle configuration was obtained, that is, A6.34W54.42, the optimum airfoil's post-stall behavior was then studied by increasing the angle of attack beyond 20 degrees at angles 23, 25, and 27.

The results indicate tubercles have reduced the lift significantly at the stall angle of NACA 4412; however, with reference to Fig. 11, it was found that the deviations are not that significant in comparison with the modified NACA 4412. In regions of post-stall, on the addition of tubercles, it was found that the drop in the values of lift coefficient was not abrupt with a simultaneous increase in the angles of attack. Compared to the wing with no tubercles, where the reduction in lift post-stall was around 10%, in the A6.34W54.42, the drop was calculated to be 2.56%.

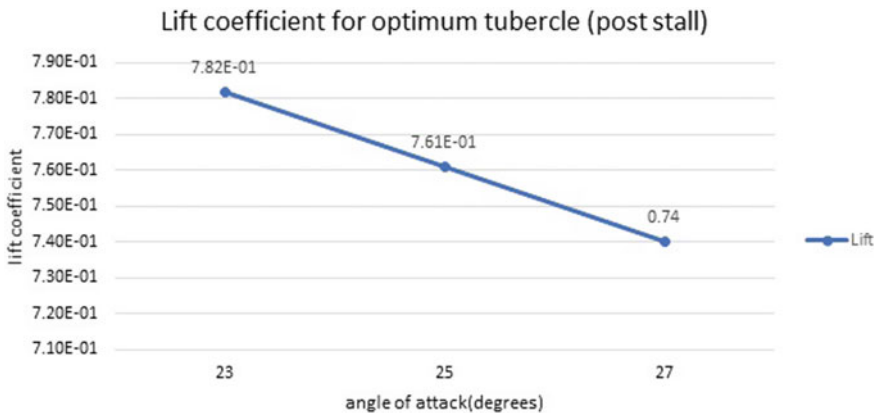


**Fig. 11** Values of  $C_l$  obtained for A6.34W54.42 post-stall

## 6 Conclusion

Flow simulation in ANSYS Fluent is carried out on primary NACA 4412 wing and different tubercle configurations. A fixed ratio of amplitude and wavelength is maintained while carrying out the study. The effects of these configurations on parameters such as lift coefficient and flow separation are discussed. The whole test was performed at  $Re = 240,000$ .

- Introduction of tubercles on the model of NACA 4412 led to the creation of rotating vortices which helped better exchange of boundary layer momentum, thus delaying the flow separation. Besides, it was inferred that the optimization of performance was solely based on the values of amplitude and wavelength being chosen while carrying out the investigation.
- These tubercles, however, led to a significant decrease in the values of lift from the base model for the current Reynolds number. The study of the flow behavior revealed that in the regions of troughs, streamwise vortices were generated and its strength was predominantly dependent upon streamwise location.
- The configuration with the highest amplitude, A6.34W54.42, gave the overall best values of lift.
- At  $Re = 240,000$ , the results for a NACA 4412 airfoil indicated that in terms of maximum lift coefficient and minimum drag, and in the pre-stall regime, it was not preferable to utilize tubercles.
- When the post-stall regime of this configuration was studied, it was found that it was able to sustain the same values of lift, and there was a very gentle drop in these values in comparison with the base model of NACA 4412 had produced.

Thus, the introduction of tubercles to NACA 4412 would lead to a decrease in lift values. Although it can sustain the same value of lift post-stall, it is advised that more variations in amplitude and wavelength must be studied, and thus this parameter must be kept in mind while using tubercles on NACA 4412 for flow control.

**Scope for the Future:** There are many future aspects of this topic since there are many possible applications and a large number of variables to be considered while choosing a tubercle configuration. These aspects outlined below could be the Reynolds' number variation, modification of tubercle configuration, choosing airfoils with different profile shapes, and studying dynamic stall behavior. Another interesting phenomenon associated with these tubercles could be how are they going to affect the flow regime if this waviness was not incorporated on the leading edge, in the spanwise direction.

## References

1. Hansen KL (2012) Effect of leading-edge tubercles on airfoil performance, thesis
2. Kim H, Kim J, Choi H (2018) Flow structure modifications by leading-edge tubercles on a three-dimensional wing. *Bioinspiration Biomimetics*
3. Mikloslovic et al (2004) Experimental evaluation of sinusoidal leading edges. *J Aircraft* 44:1404–1407



4. Watts FE, Fish JM (2002) Scalloped wing leading edge, US patent 6,431,498 B1
5. Watts FE, Fish JM (2006) Scalloped wing leading edge advancements, US patent 2006/0060721 A1
6. Pedro PH, Kobayashi M (2008) Numerical study of stall delay on humpback whale flippers
7. Asghar A, Perez RE, Jansen PW, Allan WDE (2020) Application of leading-edge tubercles to enhance propeller performance. *AIAA J* 1–13
8. Abate G, Mavris DN (2018) Performance analysis of different positions of leading-edge tubercles on a wind turbine blade. 2018 Wind Energy Symp
9. Johari H, Henoch CW, Custodio D, Levshin A (2007) Effects of leading-edge protuberances on airfoil performance. *AIAA J* 45(11):2634–2642
10. Stein B, Murray MM (2005) Stall mechanism analysis of humpback whale flipper models. In: Proceedings of unmanned untethered submersible technologies (UUST), Durham, NH, August
11. Stanway MJ (2008) Hydrodynamic effects of leading edge tubercles on control surfaces and in flapping foil propulsion. Thesis submitted to Massachusetts Institute of Technology, February
12. Sudhakar S, Karthikeyan N, Venkatakrishnan L (2017) Influence of leading-edge tubercles on aerodynamic characteristics of a high aspect-ratio UAV. *Aerosp Sci Technol* 69:281–289
13. Watts P, Fish FE (2001) The influence of passive, leading edge tubercles on wing performance
14. Fish FE, Battle JM (1995) Hydrodynamic design of the humpback whale flipper. *J Morphol* 225:51–60
15. Aftab SMA, Ahmad KA (2017) CFD study on NACA 4415 airfoil implementing spherical and sinusoidal Tubercle Leading Edge. *PLoS ONE* 12(8):e0183456
16. Agarwall S, Kumar P. Numerical investigation of flow field and effect of varying vortex generator location on wing performance
17. Report No. 613—National Advisory Committee for Aeronautics Pressure Distribution over an NACA 4412 Airfoil



# Design of a Wheel Assembly with a Double Bearing System for Formula Student Cars

N. Rakshith<sup>(✉)</sup>

National Institute of Technology Karnataka, Mangalore, India  
rakshith152000@gmail.com

## 1 Introduction

The wheel assembly is the outboard link of the suspension mechanism. Its main function is to hold the wheel in the required position and orientation and allow some adjustment if required. As it constitutes to most of the unsprung mass of the car (not supported by the suspension system), it is important to keep it as light as possible at the same time ensure that it has the required factor of safety. All the forces acting on the car act on it via the tyres as the wheel assembly is connected to the tyre, it is under high loads both in static and dynamic conditions. It experiences the highest loads during braking and cornering. The wheel assembly should be designed to withstand the loads without failure or excessive deformation for the required duration.

The design of any component is controlled by some constraints, the major factors influencing this design are ease of assembly of the finished parts, cost, type and ease of manufacturing process involved and its limitations and the materials used (available).

## 2 Literature Survey

The wheel assembly is generally consisting the knuckle (upright), hub, bearings and brackets.

The knuckle is the outboard link in the suspension mechanism its shape and size are controlled by parameters like camber, caster and KPI. The knuckle is a bearing seat integrated with mounting points to mount the brackets which get mounted on to the out-board points of the A-arms.

The tabs can be integrated into the knuckle but it will drastically increase the time and complexity of machining and also the size of the billet used, this will drastically increase the cost of manufacturing. So, generally the tabs are designed and manufactured separately as brackets and then assembled on the knuckle. Separate tabs provide an option of changing the camber and also the KPI to a certain extent. This plays a big role in optimizing (tuning) the car for a particular event in the competition. The shape and length of the tabs are controlled by the size and shape of the A-arms' outboard points and the suspension travel of the car.

The bearing(s) is press-fit into the bearing seat in the knuckle, the bearings support the hub and allow relative motion between the spindle (hub) and the suspension system (knuckle). The rim of the tyres is mounted on the hub with lug nuts [1, 2]. There is a detailed explanation of the existing model in Sect. 3.1.

As mentioned before the wheel assembly constitutes to most of the unsprung mass and is subjected to high loads. So, it has to as light as possible at the same time have the required factor of safety, the best compromise between the two was got by an iteratively optimizing the design using the results finite element analysis, until desirable values of stresses, deformation was achieved [1, 3].

### 3 Review of the Existing Model

#### 3.1 Basic Construction

The bearing seat in the knuckle has a radially inward projection which will be in contact with the outer raise of the bearing and prevent its axial motion of the bearing. To prevent the axial motion on the other side generally a circlip is used and sometimes a cover plate is used. Using a circlip implies that a groove has to be cut into the bearing seat to mount the circlip. It is ensured that the circlip or the cover plate is in contact only with the outer raise of the bearing to ensure that there is no wear. The radial projection and the circlip or the cover plate is are used as an additional measure to prevent axial motion of the bearings in case of very high loads. Generally, a single bearing is used.

The hubs are then press-fit into the bearing its axial motion can be prevented with circlips or a custom nut and a radially outward projection. The hubs are generally made hollow to increase bending stiffness and torsional rigidity and also reduce weight [1, 4].

The Fig. 1 shows the cross-section view of the existing version of the wheel assembly. The numbered parts are:

- Hub
- Knuckle (integrated with the tabs)
- Custom nut
- Bearing.

#### 3.2 Problems with the Design

The above-mentioned wheel assembly has a lot of limitations, they are as follows:

The load in the single bearing will be very high and the bearing selected to withstand such high loads will be generally big, this will make the bearing seat big making the knuckle and the hub bigger thus making the entire assembly bulky and heavy and as mentioned earlier it is the part of the unsprung mass and it has to be as less as possible. So, this is an important issue to address.

The circlip groove has to be manufactured properly if not it tends to slip out making it possible for the bearings also it slips. This might not be a concern to other teams who can ensure a good quality of machining. Our teams experienced problems with this so a different method had to be adopted.

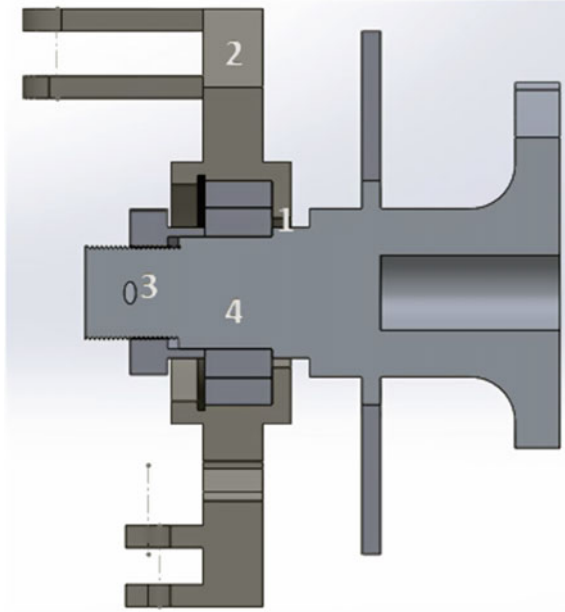


**Fig. 1** Cross sectional view of the existing version of the wheel assembly

The press-fit make the process of assembly very difficult and the disassembling the assembly is almost impossible without damaging the parts. Disassembly is important to facilitate replacement of damaged parts and allow reusability of parts as budget is a big constraint. To solve this problem a modular design is necessary and the use of press-fit has to be minimized.

## 4 Designing the New Model

### 4.1 Conceptual Design

Double bearings instead of one this will reduced the load on the individual bearing and smaller bearings can be selected and reduce the internal diameter of the bearing seat is smaller and because of the double bearings the stresses are more distributed, this reduces the overall size of the bearing seat and thus reduces the weight of the wheel assembly. The bearings have to be as far apart as possible for this to be effective. So, the bearings should be separated by a set of collars [4].

A cover plate is used instead a circlip. The cover plate will be in contact with the outer raise of the second bearing and be bolted on to a tab in the bearing seat, this will ensure that the bearings' axial motion is restricted. The entire assembly is should be assembled from the same side to reduce the possibility of misalignment and pre-loading of the components.

## 4.2 Detailed Design

The bearing seat in the knuckle has a radially inward projection the first bearing is press-fit into the seat and the inward projection is only in contact with the outer raise and restricts the bearings axial motion.

The bearings are separated by a pair of collars. The collars should not touch each other and they should be in contact with either the inner or outer raise of the bearings. The outer collar can be a hollow cylinder with the required height which is equal to the distance between the collars and the other parameters same as the outer raise of the bearing with the required tolerance for a clearance fit. The inner collar is a hollow cylinder with the same inner diameter and two different outer diameters, thus creating a step. The smaller outer diameter will be inserted into the bearing, it ensures that the inner collar is held in the required position.

Then the cover plate is mounted and just like the radial projection in the knuckle it is in contact with the outer raise of the bearing and the cover plate and the bearing seat in the knuckle is equipped with tabs onto which the cover plate is mounted on.

The hub has a radially outward projection which forms a step which is in contact with the inner raise of the bearing. And the end of the shaft part of the hub is threaded it is used to fasten a restraining nut. The retention nut and the radially outward projection in the hub restricts the axial motion of the hub. The assembly of all the components is in the same direction, this is to prevent misalignment of the bearings is the nut is over tightened and unnecessarily preload the cover plate.

The custom nut has to be positively locked, i.e. it should not loosen because of vibrations. So, either cotter pin or a nylon lock nut has to be used. If nylon insert locknut is used the hub has to be anodized to reduce the possibility of wear as the nylon lock nut is an OEM part and is a standard and is made of a high grade of steel which is a lot harder than the aluminium hub.

Solid works was used to model the wheel assembly and Figs. 1 and 2 are screenshots of the design.

## 5 Analysis

Analysis is done to check if the part design can withstand the loads the component will experience during its life without failing. Finite element analysis is used to find the maximum stress and deformation values under the maximum loading condition and validate the reliability of the design.

The worst loading condition was assumed for analysis, i.e. the car is under maximum deceleration and is experiencing maximum lateral acceleration at the same time and front outer tyre is under maximum load due to load transfer. This load from the front outer tyre are considered for analysis. Lap time simulation was done to find the maximum lateral and longitudinal acceleration. The maximum values obtained were around  $12 \text{ m/s}^2$  for lateral acceleration and around  $14 \text{ m/s}^2$  for longitudinal acceleration. The data from the simulation is shown below, it is the elapsed time versus lateral and longitudinal accelerations, respectively [3, 4].

There is a possibility that the values of accelerations can be more so a buffer is given and 1.5 g was considered for analysis.

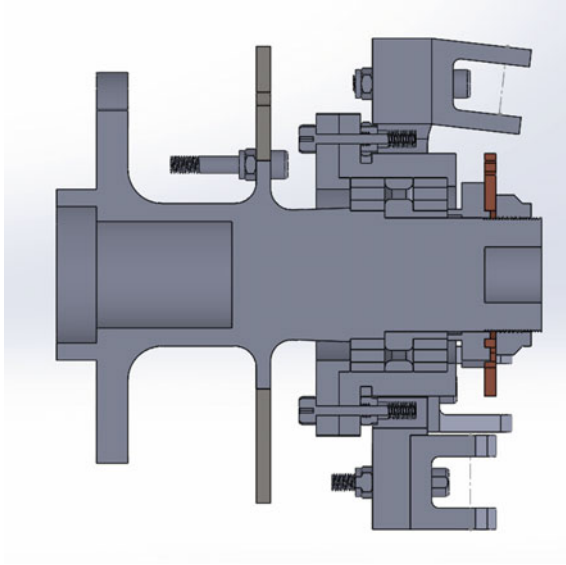


**Fig. 2** Cross sectional view of the new of the wheel assembly

The loads will act on the contact patch, it will be transferred to the hub via the tyre and the rim. A remote load is used to simulate this scenario and the hub is supported by the bearings so cylindrical support is used to depict this scenario and the reaction force from the hub is the bearing load acting on the knuckle and the same is done for the simulation. The analysis of the cover plate is also done, the axial force acting on the bearing will be the load on the cover plate and the mounting point is considered as the support.

A similar process was carried out for the analysis of the entire wheel assembly. The design was iteratively modified to obtain the best combination of factor of safety, weight and manufacturability [3] (Fig. 4).

There will be regions in the component which will have large variations of stresses to get accurate values of stresses in those regions a process called convergence is carried

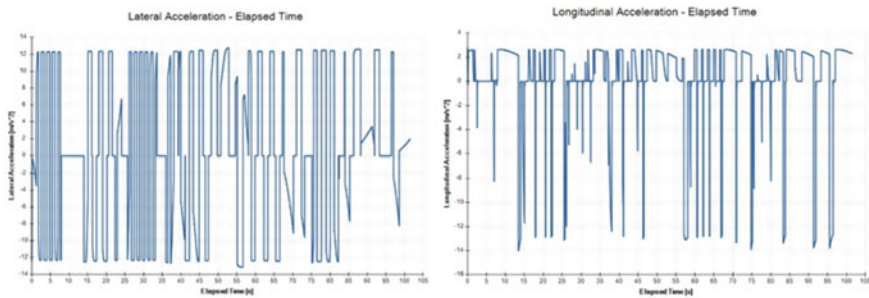


**Fig. 3** Acceleration versus time graphs, results of point mas lap time simulations

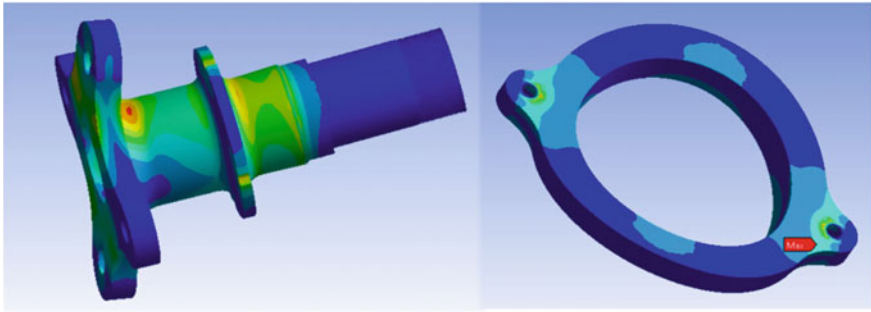


**Fig. 4** Results of finite element analysis of the hub and cover plate are shown

out. The elements in such regions are further broken down into smaller elements and the stresses are calculated, by doing so more accurate results are got. This process is carried out till the values of stresses converge to a particular value this is done to obtain reliable results which are generally experimentally accurate. Ansys a FEM software was used for analysis because it is a widely used software in industries and is well known for its accuracy and has a student version.

## 6 Conclusion

The wheel assembly is an important component of the car and probably the part under maximum load so it is important that its design is reliable and has a good factor safety, the design suggested is more reliable than the previous version and the dimensions were iteratively modified inferring from the results of finite element analysis to get the best compromise between factor of safety and weight.

### 6.1 Future Scope

The present design though it solved all the problems with the previous version of the assembly it slightly complicated to manufacture and has a lot of parts, the next version will aim to make the components simpler to manufacture and use lesser number of components.

With advancements in additive manufacturing technology 3-D printing metal parts is also on option and the cost of 3-D printing is also reducing, so, with this manufacturability will not be a limitation so weight can be further reduced while maintaining a good factor safety.

## References

1. Kaushal R, Chauhan P, Sah K, Chawla VK (2021) Design and analysis of wheel assembly and anti-roll bar for formula SAE vehicle. Mater Today Proc
2. Mahadik SS (2018) Design and ANSYS analysis of components of wheel assembly of SAE car. Int J Curr Eng Technol

3. Dhakar A, Ranjan R (2016) Force calculation in upright of a FSAE race car. Int J Mech Eng Technol (IJMET)
4. Bhandari VB (2017) Design of machine elements. McGraw Hill, 4th edn





# Modeling of Factors Impacting Remote Workforce During COVID-19

Kushagra Shukla<sup>1</sup>(✉), Harsh Kumar Singh<sup>1</sup>, Lokesh Yadav<sup>1</sup>, Mohd. Shuaib<sup>1</sup>,  
and Urfi Khan<sup>2</sup>

<sup>1</sup> Department of Mechanical Engineering, Delhi Technological University, Delhi, India  
kshgrshukla119@gmail.com

<sup>2</sup> Department of Mechanical Engineering, Indira Gandhi Delhi Technical University, Delhi,  
India

## 1 Introduction

A remote workforce used to be a matter of trivial discussion a few years back when the world was busy improving the efficiency of offices. COVID-19 pandemic had a different effect on organizations resulting in changes in operations of companies. The majority of the workforce now have to exercise their professions remotely. This forced transition has resulted in many difficulties and challenges which have led to a loss in productivity and opportunities and in certain cases, it resulted in huge mismanagements and massive layoffs. Today's business organizations depend upon maximizing from limited resources, eliminating redundancy, and automating processes to achieve business goals. But the operations for the same has been a huge challenge after remote working became the new normal. Businesses have researched on improving the efficiency of the traditional office work culture for ages but efforts to improve remote working efficiency and identifying the major factors which affect the employers and employees in an organization has not been focused upon much. This study focuses on identifying such factors in remote working which affect the employers and the employees in an organization. In some cases, remote working is just not possible, such cases have also been considered in this study to have a cumulative analysis in almost all types of professions.

## 2 Problem Definition and Objective of the Study

In this paper, a model of 'remote working' critical factors has been generated in order to analyze the current situation of remote working and building a mathematical model to predict the feasibility of remote working for a profession. These identified factors are an influence to the remote working of any organization.

## 3 Brief Description of Critical Factors of Remote Working

### 3.1 Occupation Type

For our study we have classified employees under three heads on the basis of whether remote working is possible or not [1]:

- Remote working not possible: e.g., Assembly line employees
- Remote working possible but with additional costs: e.g., Sales employees
- Remote working is highly possible: e.g., Coder [2].

### 3.2 Communication Gap

When working remotely, teams will require an approach to articulate with one another easily [1]. Email/Messaging is not generally the better alternative, so far off the teams should go for specialized instruments which offer live streaming options to stay updated about work or targets [2]. The tool should be able to offer constant apprising, video call alternatives, screen sharing and the capacity to sort out discussions or weekly progress meetings [3].

### 3.3 Productivity Deviation

The traditional parameters for assessing the productivity of the employee have to be done away with the changing times [1]. Presently, most distant groups should scrutinize their workforce on the parameter of quantity of assignments finished and whether they are meeting their objectives or not [4], instead of the quantity of hours they clock in every day which has been the norm [5]. If there should arise an occurrence of profitability starts to slip, time-following instruments can be utilized to measure productivity.

### 3.4 Data Management Issues

Appropriate management of information will be key for groups working distantly. It is a smart thought to set up a cloud-based information management tool with the goal that everybody can get to the records and data they need whenever [2]. These instruments help in getting sorted out information between various offices and set cutoff time updates. Also lack of equipment in homes results in difficulties in managing data [3].

### 3.5 Data Security Compromises

Going remote implies colleagues will interface into Wi-Fi networks at home, bistros, collaborating spaces, libraries and other public spaces to manage their job [1]. Hence, it is imperative to have a data security rule set up prior to changing to remote functioning as any digital assault can be a catastrophe for the association [2]. Data security is an important aspect in modern times otherwise there are chances of sensitive data leak which can cause damage to the organization both financially as well as its credibility [3].

### 3.6 Flexibility

It is important to define beforehand whether the team needs to be available at a specific time period or whether they are independent to set their own time schedules as per their convenience [2].

### 3.7 Training Management Difficulties

An effective change to remote working additionally relies vigorously upon very much prepared directors or group pioneers [3]. For some executives, the process can immediately get mind-boggling due to the extent of technology involved, so it is important to have proper training for them in order to become accustomed to the changing times [4].

### 3.8 Business Development Issues

Development of businesses is a key focus for every business house in order to gain maximum market share and maximize profits. Expansion, recruitment, investment, assets management are dependent on human resources and remote working affects significantly in development plants. Processes get delayed more often due to availability and infrastructure issues [1].

### 3.9 Underdeveloped Infrastructure

Infrastructure is an important factor required for remote working. Network requirements like Wi-Fi for communication purposes are an aspect of the desired infrastructure along with cloud-based data storage in order to keep the data safe and accessible to all anytime [2].

### 3.10 Psychological Aspects

Remote workforce may appreciate the opportunity to live and work any place they like [6], yet working through and with others turns out to be more testing in the event of distant working it goes from communications to information sharing [4].

## 4 Interpretive Structural Modeling

### 4.1 Methodology

The different steps associated with ISM displaying are as per the following [7]:

1. Distinguishing the elements which have an influence on the system under investigation, the elements can vary from objectives to actions. Identifying is done through literature review, brainstorming or expert opinion.
2. A contextual connection is generated among the different elements of the system regarding which sets ought to be inspected.
3. A Structural Self-Interpretive Matrix (SSIM) is set up for the components, which means pair-wise association among the components of the framework under scrutiny.
4. An initial reachability matrix is produced from the SSIM created in the above step. This initial reachability matrix is investigated for hidden connections or transitivity which when accommodated gives us the final reachability matrix [8].
5. The final reachability matrix generated in the above step is partitioned in to various steps based on the reachability set, antecedent set and intersection set of each element.
6. Based on the relationships given above in the final reachability matrix a directed graph is generated. The resultant graph in the above step is converted into an ISM, by replacing the element nodes with the statements.

**4.2 Structural Self-Interaction Matrix**

SSIM is made by using the specialist’s assessment dependent on different administration methods [9], for example, conceptualizing. In this paper, the SSIM for ISM was filled with the help of practitioners in the area, who are working at the middle level [10].

Following four characters are utilized to mean the association between the remote working components [11]:

- V: component x impact component y yet component x is not affected by component y.
- A: component x is affected by component y yet component x does not impact component y.
- X: component x and component y impact each other, i.e., commonly identified with one another.
- O: component x and component y do not impact each other, i.e., commonly inconsequential.

Based on context-oriented connection between remote working, the SSIM has been created (Table 1).

**Table 1** SSIM of remote working factors

Serial No.	Factors	10	9	8	7	6	5	4	3	2
1	Occupation type	V	V	V	V	V	V	V	V	V
2	Communication gap	V	A	V	V	V	O	V	V	
3	Productivity deviation	X	A	V	V	A	A	A		
4	Data management issues	O	A	V	O	O	X			
5	Data security	V	A	V	O	O				
6	Flexibility	V	A	O	V					
7	Training management difficulties	O	A	X						
8	Business development issues	A	A							
9	Underdeveloped infrastructure	V								
10	Psychological aspects									

**4.3 Reachability Matrix**

Introductory reachability matrix is created utilizing the structural self-interaction matrix as base [12]. The information in every cell of the structural self-interaction matrix is changed into paired structure, i.e., 0 and 1. This change is completed by replacing V, A, X, O with 0 s and 1 s [13]. If the section in the SSIM relates to:

- V: (x, y) gets 1 and (y, x) gets 0
- A: (x, y) gets 0 and (y, x) gets 1
- X: (x, y) gets 1 and (y, x) gets 1
- O: (x, y) gets 0 and (y, x) gets 0

Utilizing the initial reachability matrix, as shown in Table 2, as base the final reachability matrix is generated by consolidating covered up associations or transitivity among the different components. Transitivity is characterized as ‘if component x impacts component y and component y influences component z, at that point it suggests that component x will likewise impact component z’. It is signified by 1\* in the matrix. Final reachability matrix is as demonstrated in Table 3.

**Table 2** Initial reachability matrix of remote working factors

Factors	1	2	3	4	5	6	7	8	9	10
1	1	1	1	1	1	1	1	1	1	1
2	0	1	1	1	0	1	1	1	0	1
3	0	0	1	0	0	0	1	1	0	1
4	0	0	1	1	1	0	0	1	0	0
5	0	0	1	1	1	0	0	1	0	1
6	0	0	1	0	0	1	1	0	0	1
7	0	0	0	0	0	0	1	1	0	0
8	0	0	0	0	0	0	1	1	0	0
9	0	1	1	1	1	1	1	1	1	1
10	0	0	1	0	0	0	0	1	0	1

#### 4.4 Level Partitioning

From the final reachability matrix, reachability set and predecessor set for every component has been inferred into the even structure as demonstrated in Table 4. The reachability for a component incorporates the components which are driven by it and the actual component. The predecessor set for a component incorporates the components which drive it and the actual component. Besides, the crossing point set for every component is inferred utilizing the reachability and the predecessor set which helps in deciding the level of every component [14]. The component for which the reachability and crossing point set are equivalent possesses the primary level and consequently is situated at the highest point of the chain of importance in the ISM model. Subsequent to distinguishing the top component, it is eliminated from thought of different components. Furthermore, the way toward isolating the components into different level proceeds till every component has been allotted a level. The levels help in creating the ISM model [15].

**Table 3** Final reachability matrix of remote working factors

Factors	1	2	3	4	5	6	7	8	9	10	Driving power
1	1	1	1	1	1	1	1	1	1	1	10
2	0	1	1	1	1*	1	1	1	0	1	8
3	0	0	1	0	0	0	1	1	0	1	4
4	0	0	1	1	1	0	1*	1	0	1*	6
5	0	0	1	1	1	0	1*	1	0	1	6
6	0	0	1	0	0	1	1	1*	0	1	5
7	0	0	0	0	0	0	1	1	0	0	2
8	0	0	0	0	0	0	1	1	0	0	2
9	0	1	1	1	1	1	1	1	1	1	9
10	0	0	1	0	0	0	1*	1	0	1	4
Dependence	1	3	8	5	5	4	10	10	2	8	

**4.5 Formation of ISM Model of Remote Working Factors**

Figure 1 address the ISM model for remote working components. The segments which are put at lower levels in the model have a solid driving force however weak reliance power, then again, components set at the highest point of the model have a solid reliance power and weak driving force [12]. The driving force of every component is dictated by the way that the number of components does it drive or may assist with accomplishing them. Though, the reliance force of the component is controlled by tallying the quantity of components help accomplishing it [13].

**Table 4** Level of factors of remote working factors

Factor	Reachability set	Predecessor set	Intersection set	Level
1	1 2 3 4 5 6 7 8 9 10	1	1	VI
2	2 3 4 5 6 7 8 10	1 2 9	2	IV
3	3 7 8 10	1 2 3 4 5 6 9 10	3 10	II
4	3 4 5 7 8 10	1 2 4 5 9	4 5	III
5	3 4 5 7 8 10	1 2 4 5 9	4 5	III
6	3 6 7 8 10	1 2 6 9	6	III
7	7 8	1 2 3 4 5 6 7 8 9 10	7 8	I
8	7 8	1 2 3 4 5 6 7 8 9 10	7 8	I
9	2 3 4 5 6 7 8 9 10	1 9	9	V
10	3 8 7 10	1 2 3 4 5 6 9 10	3 10	II

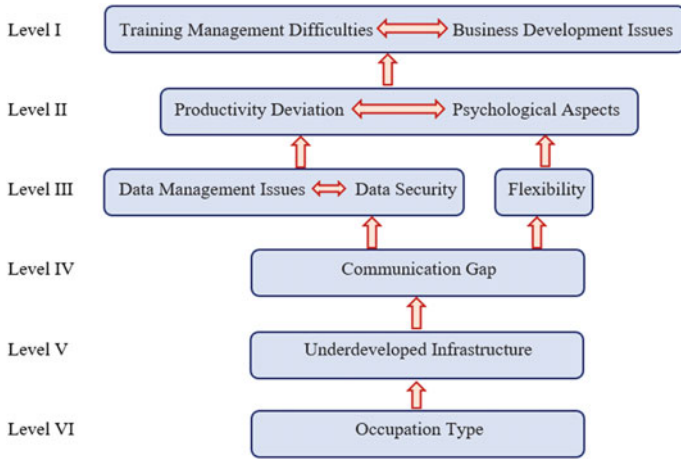


Fig. 1 ISM-based structural model for factors of remote working

### 5 Classification of Remote Working Factors Through Four Clusters of Driving and Dependence

The components are ordered into four classifications as per their driving force and dependence plotted and appeared in Fig. 2 [16].

DRIVING POWER	1					
		IV	2,9		III	
				4,5,6		
					3,10	
		I			II	
						7,8
	DEPENDENCE					

Fig. 2 Driver power and dependence graph

Class I (Autonomous). These are the components with fragile driver and ward powers. They are discovered nearest to the origin and reasonably disengaged from the system. These neither effect the structure much nor are they influenced by the system.

Class II (Dependent). They are mostly needy elements. They are recognized by their feeble driving force. Variables 7 (Training Manager Difficulties), 8 (Business Development Issues), 3 (Productivity Deviation), and 10 (Psychological Aspects) are under this class.

Class III (Linkage). The third class has the linkage elements that have solid driving force and dependence. Components 4 (Data Management Issues), 5 (Data Security), 6 (Flexibility) are under this class.

Class IV (Independent). The fourth class incorporates free elements with solid drivers and powerless dependence. Elements 1 (Occupation Type), 2 (Communication Gap), and 9 (Underdeveloped Infrastructure) are under this class [4] (Table 5).

**Table 5** Viability of various factors

Serial No	Factor	Driving power	Dependence	Viability (driving power—dependence)
1	Occupation type	10	1	9
2	Communication gap	8	3	5
3	Productivity deviation	4	8	−4
4	Data management issues	6	5	1
5	Data security	6	5	1
6	Flexibility	5	4	1
7	Training management difficulties	2	10	−8
8	Business development issues	2	10	−8
9	Underdeveloped infrastructure	9	2	7
10	Psychological aspects	4	8	−4

## 6 Results and Discussion

The mix of different methodologies involves literature review approach, workshop and meetings to generate new ideas have been utilized to comprehend the central idea of remote working. Exploratory examination has been done to recognize the important basic components. ISM strategy has been discovered suitable to display the basic components (ten in number). ‘Occupation Type’ has been distinguished as a base level independent factor driving the effective remote working implementing toward ‘Training Management Difficulties’ and ‘Business Development Issues’ which have been recognized as the top dependent factors in the model. In the current examination of the system, there is no autonomous factor in this arrangement. Dependent factors ought to be basically explored as they have a solid dependence on different variables. Linkage variables are likewise precarious consequently require cautious examination. Independent components ought to be considered for the usage of remote working. In this research, using the ISM examination, a relationship model between the parts has been made. Majority of the research has been based on some or other theories, few assumptions and some data from start-ups and companies. Still this research has to be statistically validated as very limited data from actual organizations has been used. A broader view from a variety of occupations



can also be used to fine tune this model as the research was limited to a few popular professions.

## 7 Conclusion

Remote working has now become the new normal in the corporate world and all business organizations. Through this research, the major factors which affect the employers and the employees in an organization due to remote working were identified and a relationship among the factors was established and analyzed. A mathematical model was also developed which can be helpful for organizations to find the impact factor according to the type of occupation. This research's main work is to help the organizations identify the source of mismanagements and obstacles in carrying out a smooth operation process during remote working and then implement required changes to resolve these problems. The factors can also contribute in structuring the core of operations in the organization to benefit more from remote working and build the required infrastructure around it.






## References

1. Assessing the growth of remote working and its consequences for. Retrieved 6 March 2021, from <https://onlinelibrary.wiley.com/>. <https://doi.org/10.1111/ntwe.12097>
2. Bernick M (2021) Remote work and best practices: the coronavirus workplace series. [online] Forbes. Available at: <<https://www.forbes.com/sites/michaelbernick/2020/03/16/remote-work-and-best-practices-the-coronavirus-workplace-series/?sh=6f2a337f769c>>
3. Reimagining the post-pandemic workforce. McKinsey & Company. Retrieved 6 March 2021, from <https://www.mckinsey.com/business-functions/organization/our-insights/reimagining-the-postpandemic-workforce>
4. Singh R, Kumar MA, Varghese ST (2017) Impact of working remotely on productivity and professionalism
5. The effects of remote working on wellbeing, stress and productivity. Retrieved 6 March 2021, from <https://www.nuffieldhealth.com/article/the-effects-of-remote-working-on-wellbeing-stress-and-productivity>
6. A study of 1100 employees found that remote workers feel. Retrieved 6 March 2021, from <https://hbr.org/2017/11/a-study-of-1100-employees-found-that-remote-workers-feel-shunned-and-left-out>
7. Ravi V, Shankar R (2005) Analysis of interactions among the barriers of reverse logistics. *Technol Forecast Soc Chang* 72:1011–1029
8. Warfield JW (1974) Developing interconnected matrices in structural modelling. *IEEE Trans Syst Men Cybern* 4(1):51–81
9. Barve A, Kanda A, Shankar R (2007) Analysis of interaction among the barriers of third-party logistics. *Int J Agile Syst Manage* 2(1):109–129
10. Hasan MA, Shankar R, Sarkis J (2007) A study of barriers to agile manufacturing. *Int J Agile Syst Manage* 2(1):1–22
11. Ravi V, Shankar R, Tiwari MK (2005) Productivity improvement of a computer hardware supply chain. *Int J Prod Perf Measur* 54(4):239–255
12. Shuaib M, Khan U, Haleem A (2016) Modeling knowledge sharing factors and understanding its linkage to competitiveness. *Int J Global Bus Compet* 11(1):23–36

13. Singh RK, Sharma HO, Garg SK (2010) Interpretive structural modeling for selection of best supply chain practices. *Int J Bus Perf Supply Chain Model* 2(3):237–257
14. Jadhav JR, Mantha SS, Rane SB (2013) Interpretive structural modeling for implementation of integrated green-lean system. Retrieved from <https://research.ijcaonline.org/icgct/number2/icgct1314.pdf>
15. Attri R, Dev N, Sharma V (2013) Interpretive structural modelling (ISM) approach: an overview
16. Sage AP (1977) *Interpretive structural modeling: methodology for large scale systems*. McGraw-Hill, New York, NY
17. Farris DR, Sage AP (1975) On the use of interpretive structural modeling for worth assessment. *Comput Electr Eng* 2:149–174
18. Ortego J, Andara R, Navas, LM, Vásquez CL, Ramírez-Pisco R (2021) Impact of the Covid-19 pandemic on traffic congestion in Latin American cities: an updated five-month study. <https://link.springer.com/chapter>. [https://doi.org/10.1007/978-3-030-69136-3\\_15](https://doi.org/10.1007/978-3-030-69136-3_15)
19. Raj T, Attri R (2011) Identification and modelling of barriers in the implementation of TQM. *Int J Product Quality Manage* 28(2):153–179
20. Raj T, Shankar R, Suhaib M (2007) An ISM approach for modeling the enablers of flexible manufacturing system: the case for India. *Int J Prod Res* 46(24):1–30
21. Singh MD, Shankar R, Narain R, Agarwal A (2003) An interpretive structural modeling of knowledge management in engineering industries. *J Adv Manage Res* 1(1):28–40



# Design of the Automated System for the Acquisition, Recording and Analysis of Data in the Development of Indicators of Consumption and Production Energy

Saldaña Enderica Carlos<sup>(✉)</sup> , Chuquimarca Jiménez Luis ,  
Torres Guin Washington , Bustos Gaibor Samuel , and Flores Tomalá Daniel 

Facultad de Sistemas y Telecomunicaciones, Universidad Estatal Península de Santa Elena,  
Santa Elena, Ecuador

{csaldana, lchuquimarca, wtorres, sbustos}@upse.edu.ec

## 1 Introduction

Energy efficiency indicators are seen as a tool for formulating strategies and designing effective policies to support energy efficiency. The main requirement for all industrial machinery to move is energy, whether chemical, thermal or electrical, without energy it would be impossible to carry out any industrial activity. Therefore, to know the behavior of these variables becomes a topic of discussion, because from here it is possible to evaluate many factors that intervene in the economy of the company [1].

There are international efforts to develop indicators and extract parameters or characteristics of trends in addition to comparative analysis. However, in developing countries the lack of data currently limits the role of energy efficiency indicators [2, 3]. In the Ecuadorian industrial sector, knowledge of the real cost of production of a certain product is a necessity to make decisions in the different areas of the company, such as: financial, commercial, marketing, quality, etc.

This project seeks to near the information of the variables of energy consumption and production of a particular plant to the desktop of manager through energy management indicators, in order to obtain reliable and fast information to plan and implement better mechanisms of efficiency in production and in turn to greater energy efficiency within company.

## 2 Information Processing Tools

Different types of tools are used for the system, from hardware to software development, as well as previous administrative procedures for its implementation. The topics directly related to the development of SAICEP are discussed below.

Firstly, management indicators are studied as an assessment tool for energy efficiency in drinking water supply plants, management indicators have gained relevance as management tool in the water industry over the last decade [4]. Thanks to these it is

possible to observe trends over a period of time, comparisons between units (different but comparable). It is also possible to make a proper planning as well as improve the ability to make decisions, carry out a formulation of strategy and policy changes within the company, allow an instant analysis of the impact, effectiveness and efficiency of a pumping plant by comparing with others [5].

Interrelate the different management areas (human resources, financial management, information systems, maintenance). All this allows the establishment of quality standards within the organization, the set of actions that optimize the relationship between the amounts of energy consumed, the final products and services obtained resulting in the energy efficiency [6].

OPC is a communication standard in the field of industrial process control and monitoring, it offers a common communication interface that allows individual software components to interact and share data with each other. It is an open and flexible solution to the problem of proprietary drivers, as all the major manufacturers of control, instrumentation and process systems have included OPC in their products [7].

The standard mechanism for data access consists of a standard automation interface aimed at allowing visual basic applications as well as other automation applications to be enabled to communicate to data sources, the important is in an architecture open and effective communication that focuses on data access [8].

OPC data access automation: defines a standard by which automation applications access process data, this interface is designed to facilitate application development [9]. An OPC client–server: application is built to access data from a network server using to the OPC data access automation libraries [8].

Database is a set of Microsoft objects and components is used example: the ADO.NET architecture [10]. KEPServerEX flexible and scalable platform to connect, manage, monitor and control different devices and software applications used in industrial automation [11].

For this article, energy costs are examined according to the following categories: general category, medium voltage level group, medium voltage tariffs, medium voltage tariffs with demand, medium voltage tariffs with and without hourly demand recorder for industrialists, billable demand, correction factor and low power factor charges.

### **3 SAICEP Conceptual Design**

For development the system, two areas are basics: administrative and technical. By the technical side, the project is divided the design, the installation of the equipment, and software to be used, which is made up of the client–server application and the application for processing and analyzing the information.

Hosting the SAICEP application on standard PC is one of the objectives of the project, and by means of this application obtain the data through the administrative network from the server (see Fig. 1).

There are some steps that the organization should be taken time of implementation. A survey of information specifically on energy management must first be carried out, this leads to an energy planning which will depend on the efficiency principle. This system

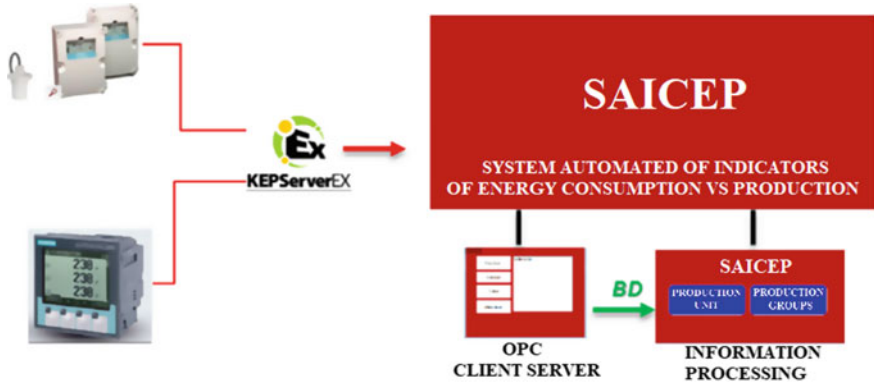


**Fig. 1** Conceptual design SAICEP specifications

is implemented in a drinking water re-pumping plant and the following equipment is used for data acquisition.

In this case, due to the geographic implications of the pumping stations, the lack of connectivity via GPRS [12], the company use radios signals, in the licensed frequency of 436 MHz to integrate their pumping stations to the SCADA [13], the system use serial DNP3 communication protocol, through MR400 equipment [14]. Distributed network protocol, is an industrial protocol for communications between intelligent equipment and control stations [15].

The level of the elevated tank is taken with a level meters, SIEMENS brand of the Multiranger 100 family, which corresponds to an ultrasonic level meter with remote electronics, the measurement range is between 0.3 to 15 m, accuracy is 0.25% of the measurement range, resolution is 0.1%, communication is via Modbus RTU or integrated ASCII via RS-485 or RS232 [16]. The ST-H sensors measure the fill level in storage tanks and containers with liquids [17]. The architecture for the purpose mentioned in this project is described below (see Fig. 2).

The configuration for the communication between the field variables and the OPC is managed by the PLC which has DNP3 communication to transmit the information to the RACOM MR400 radio, which finally sends the data by telemetry to the server located in a remote place. To register the energy variables, it have the SENTRON PAC [18] with Modbus TCP communication through an Ethernet interface, to do this must configure the equipment because by default the communication is SEAbus [19].

The production variable calculates to the physical conditions of drinking water storage and the direct measurement of the level sensor installed in the reservoirs. The programming and management of the destined variables are done from the controller with DNP3 communication, who is charge of communicating with the Radio which sends the data to the server.

The following equipment is used to implement SAICEP: SENTRON PAC 3200 energy meter, level meter and ST-H transducer. The PLC controller the communication between the variables of the field devices and the OPC through the DNP3 communication protocol [20].

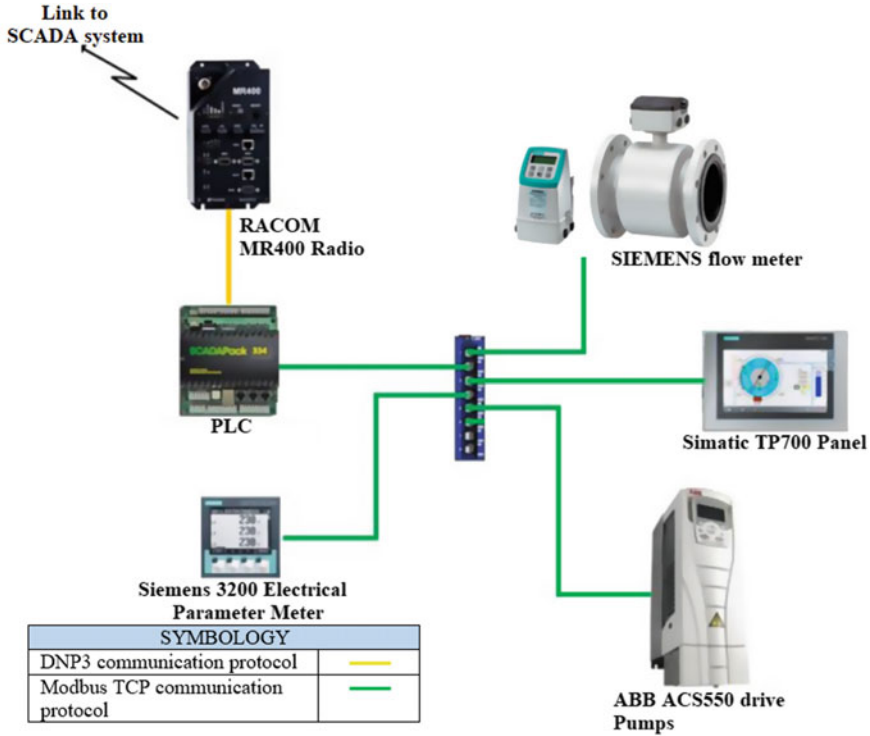


Fig. 2 Network architecture

Data is obtained by to devices connected in the field. The following restrictions are considered in order to obtain data on the production of drinking water:

- The reservoir from which the data are taken has an input and two types of outputs, the input is identified as the flow that enters the reservoir and the outputs, the first is identified as the output flow to the community that feeds from this reservoir, the second output is identified as the pumping by a group of pumps installed in this reservoir to another with a higher level.
- To be able to find the relationship between kWh and m<sup>3</sup>, the data must be taken without intervention of the other two outputs, can close valves for this is obtained 134.28 kWh pumps the amount of 691 m<sup>3</sup> of drinking water:

$$\begin{aligned}
 \text{Total level}_{(t)} = & \text{Measurement level } 1_{(t)} - \text{Caudal output}_{(t)} \\
 & - \text{Pumping output}_{(t)} \text{ in } m^3
 \end{aligned}
 \tag{1}$$

- The tank area is 1596 m<sup>2</sup>.
- The offset margin of the sensor is 1 m, therefore, the volume in question will be 1596 m<sup>3</sup>.

The client–server application is created to achieve the manipulation of the values of the OPC server variables, a desktop application created in visual studio which, in addition to making the respective connections to OPC, generates a database where the data is stored. Information received and finally performs data processing and analysis through a decision tree.

### 3.1 Client-OPC Application

For the communication between the client application and the server, programming is developed with specific libraries for OPC communication such as OPC automation [21], for the database the OLEDB library is used [22]. Datatable type, OleDbDataAdapter and OleDbCommandBuilder variables are created for database management [23], while OPCServer, OPCGroup and OPCItems type variables are created for communication [24].

### 3.2 Data Selection

The variables stored in the database must pass a set of filters before being shown to the user, which are described in the following generalization of the data selection algorithm.

if  $Kw(i + 1) \geq Kw^{esp}$  and  $Ts(i + 1) < h1^{esp}$

or

$Kw(i + 1) \geq Kw^{esp}$  and  $h2^{esp} > Ts(i + 1) < h3^{esp}$

or

$Kw(i + 1) \geq Kw^{esp}$  and  $h1^{esp} > Ts(i + 1) < h2^{esp}$

then

$$Kw' = \sum_{i=j}^n \frac{Kw(i)}{n} \text{ and } Ts' = \sum_{i=j}^n Ts(i) \text{ and}$$

$$m^{3'} = \sum_{i=j}^n m^3(i)$$

else

$$Kw' = 0, Ts' = 0, m^{3'} = 0$$

end if

$$KwT = \sum Kw' \times Ts'$$

$$\$KwT = \left[ \$h^{esp} \times FP \times \sum Kw' \times Ts' \right] \times \left[ 1 + FAP + \frac{0.92}{FP - 1} \right]$$

$$M3 \text{ tot} = m^{3'} \times Ts'$$

$$\$M3 \text{ tot} = M3 \text{ tot} \times \$M3$$

$$\text{Ind} = \sum_{t=t'_i}^{t'_f} \frac{\text{Kw}'(t)}{M3'(t)} \text{ for } t_i < t_f$$

where Kw indicates Kilowatts, Ts indicates the timestamp that is stored in each record.  $H1$ ,  $h2$ ,  $h3$  indicates the different schedules of electricity consumption, the value of  $\text{Kw}^{\text{esp}}$  is related to the setpoint of the measurement,  $\text{Kw}'$  is the accumulator as much as  $\text{Ts}'$  and  $M3$ , of the final averages for the calculations of the subsequent indicators.

The cost per energy and production indicator, the following variable \$KwT, is created, the cost of  $M3'$  is represented by the variable \$M3tot and the energy vs production indicator is represented by the variable 'Ind', for  $t_i < t_f$ .

## 4 System Operation

The user by means of the interface unit of production carries out the consultations of the indicators, to arrive at this one proceeds to the creation of entities, which are a class that contains a set of attributes which contribute to the operation of the program.

This project is developed in two parts, the first is the acquisition of data, this involved the entire process of review, installation and configuration of the equipment to request the variables that are required, then from a server located in the control room where KEPServerEX is installed, the application is configured to manage the variables in question, then the client-server application is executed, and it begins to record the data according to the specifications created within it.

Plant data acquisition: For the plant data acquisition, the equipment is installed and configured on the electrical panel of a re-pumping station. The search for available servers is carried out, for project is use Kepware, and then it connects ensuring the connection of the communication link between the server and the client application and finally the data record in the database.

## 5 Result and Analysis

The group of variables the behavior of energy consumption, production and energy cost over time can be observed. For the production unit is observe the production variable over time, within a range of days, this variable shows the  $\text{m}^3$  of water produced daily or monthly, the following graph shows the daily production of the central re-pumping station, this variable must be linked to energy, because the water levels in the reservoir depend on pumping.

In the same way, can compare the production between two or more stations within the system, in this case has three stations to consider and the following graph shows the monthly production of two pumping stations to perform the respective analysis.

To evaluate the energy indicator, take the SCADA data from a normal working day, on a normal day the pumping works an average of 16 h, if take this example the approximate average kWh is 138.00 kW which is the installed load for 16 h resulting in



an approximate of 2208 kWh per day, the behavior of the energy variable for our central station is observed in the following graphs.

This information is useful to decide whether to implement some control to avoid these peaks within these ranges, one option would be to move the operating point to activate the pumping before entering the time of highest energy cost, so that there is a greater buffer of drinking water. In this way SAICEP shows in a quick, clear and organized way the information related to the energy efficiency of the pumping stations in this case study. Figure 3 shows the results of the energy indicator according to demand.

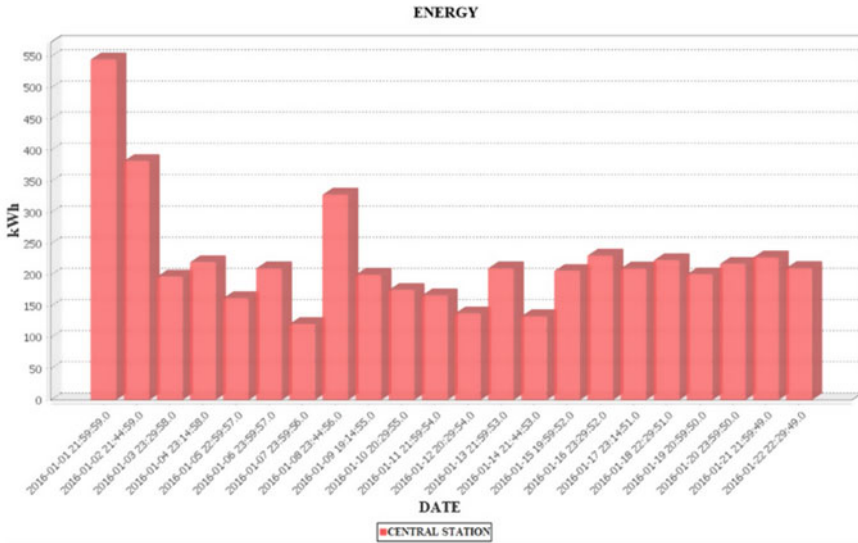
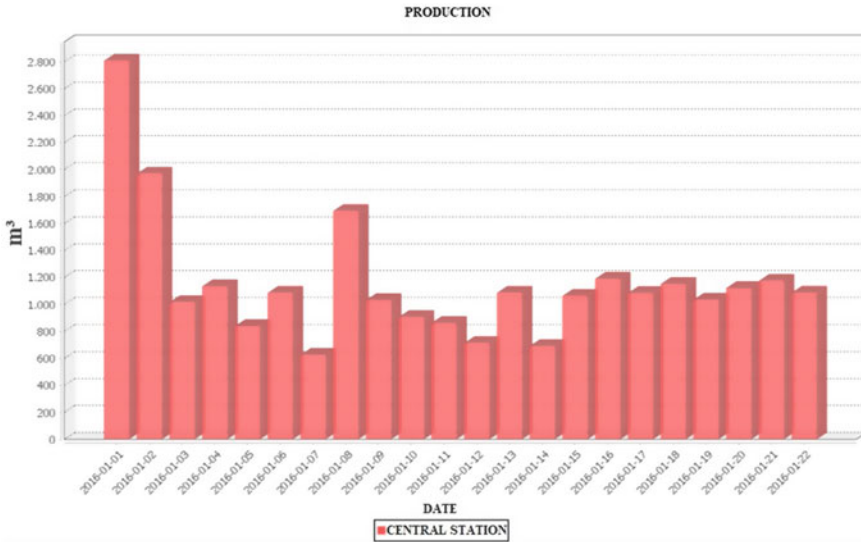


Fig. 3 Power indicator

Figure 4 shows the results of the production indicator.

## 6 Conclusions

This project involved the design of an automated system, hardware and software, for the acquisition, recording and analysis of data, for the development of energy efficiency indicators. An automated information analysis system is established for the Ecuadorian industry that allows to know what is happening in a plant in a fast way. It is possible to adjust the set of indicators in a flexible way, to monitor energy consumption vs production to the reality of each industry. Behaviors of production variables and energy-related variables, which influence positively or negatively the energy efficiency of the plant, are quickly discovered.



**Fig. 4** Production indicator

## References

1. Armaroli N, Balzani V (2016) Solar electricity and solar fuels: status and perspectives in the context of the energy transition. *Chem A European J* 22:32–57
2. Li ML, Tao W-Q (2017) Review of methodologies and polices for evaluation of energy efficiency in high energy-consuming industry. *Appl Energy* 187:203–215
3. Vikhorev K, Greenough R, Brown N (2012) An advanced energy management framework to promote energy awareness. *J Clean Prod* 43:103–112
4. Longo S, Mauricio-Iglesias M, Soares A, Campo P, Fatone F, Eusebi A, Akkersdijk E, Stefani L, Hospido A (2019) ENERWATER—a standard method for assessing and improving the energy efficiency of wastewater treatment plants. *Appl Energy* 242:897–910
5. Evanschitzky H, Eisend M, Calantone RJ, Jiang Y (2012) Success factors of product innovation: an updated meta-analysis. *J Prod Innov Manage* 29:21–37
6. Organización Internacional de Normalización. ISO, [En línea]. Available: <https://www.iso.org/iso-50001-energy-management.html>
7. Cavalieri S, Salafia MG, Scropo MS (2019) Integrating OPC UA with web technologies to enhance interoperability. *Comput Stand Interf* 61:45–64
8. Li Z, Yang L (2021) Pipeline real-time data, pipeline SCADA and OPC. Pipeline real-time data integration and pipeline network virtual reality system, pp 7–20
9. Trunzer E, Lötzerich S, Vogel-Heuser B (2018) Concept and implementation of a software architecture for unifying data transfer in automated production systems. *IMPROVE-innovative modelling approaches for production systems to raise validatable efficiency*, pp 1–17
10. Aithal P, Pai VT (2017) Disconnected data access architecture using ADO.NET framework. *Int J Appl Eng Manage Lett (IJAEML)*, pp 10–17
11. Duymazlar O, Engin D (2019) Design and application of OPC-based SCADA system with multiple controllers: an electro-pneumatic case study. *Innov Intell Syst Appl Conf (ASYU)* 1–6

12. Manoj K (2019) *Industrial automation with SCADA: concepts, communications and security*. Notion Press
13. Pliatsios D, Sarigiannidis P, Lagkas T, Sarigiannidis AG (2020) A survey on SCADA systems: secure protocols, incidents, threats and tactics. *IEEE Commun Surv Tutor* 22(3):1942–1976
14. Nemeč Z, Pidanic J, Tekovic A, Dolecek R (2015) Investigation of UHF system for mobile communication in indoor environments. In: *57th International symposium ELMAR (ELMAR)*, pp 185–188
15. Marian M, Cusman A, Popescu D, Ionica D (2019) A DNP3-based SCADA architecture supporting electronic signatures. In: *20th International carpathian control conference (ICCC)*, pp 1–6
16. Zhang H, Qin J (2017) PLC-based level control system. *Topics in intelligent computing and industry design*, pp 92–94
17. Guayu L, Yuan S, Joel WA, Markus K, Rong X (2019) Research advances towards large-scale solar hydrogen production from water. *Energy Chem* 1
18. Albo Valladares L, Hernandez Baute O (2020) Automation engineering service for corn steeping and wet milling processes, in factory of glucose and corn derivatives (GYDEMA). *ITEGAM-JETIA* 4–10
19. Bautista E, Whitney C, Davis T (2016) Big data behind big data. *Conquering big data with high performance computing*, pp 163–189
20. Chuquimarca Jiménez L, Asencio Gonzabay A, Torres Guin W, Bustos Gaibor S, Sánchez Aquino J (2021) Development of network system for connection PLC to cloud platforms using IIoT. *Adv Dig Sci ICADS 2021* 1352:433–443
21. González I, Calderón AJ, Barragán AJ, Andújar JM (2017) Integration of sensors, controllers and instruments using a novel OPC architecture. *Sensors* 17
22. Alqahtani A, Jaafar N, Alfadda N (2011) Interactive speech based games for autistic children with Asperger syndrome. In: *International conference and workshop on current trends in information technology*, pp 126–131
23. Schmalz M (2012) *C# database basics: moving from visual basic and VBA to C*. O'Reilly Media, Inc.
24. Santosh Kumar P, Majumder M, Wisniewski L, Jasperneite J (2020) Real-time industrial communication by using OPC UA field level communication. In: *25th IEEE international conference on emerging technologies and factory automation (ETFA)*, pp 1143–1146



# An Overview of the Properties of Aluminium Alloys with the Help of Equal Channel Angular Pressing

Vishwesh Mishra<sup>(✉)</sup>, Piyush Signal, and Akashdeep Yadav

Department of Mechanical Engineering, GLA University Mathura, Chaumuhan, India  
vishwesh.mishra@gla.ac.in

## 1 Introduction

Some factor establish the physical and mechanical properties of crystalline materials [1]. In this field the grain size have very important role to establish the some effect of materials on various process. In material reveal improved hardness/toughness and enhanced ductility/strength among them when compare to coarse-grained materials. In the last some years have been seen the big interest for scientific use in generating the refine microstructure and grain size. ECAP is the common process to severe plastic deformation **process to find** ultrafine grained microstructure, micro hardness and some other properties of any alloy like ALUMINIUM, mg, etc. with the help of using some special method. On working equipments using on this process like UTM machine or press machine and heating element. This process have done for different alloys in different condition means in room temperature and below the melting point temperature and find the changes in properties like microstructure, micro hardness, and other mechanical properties. So ECAP is used for industrial application. In ECAP process first prepare samples of alloy and then make samples and using heating element like induced die into the furnace or other heating arrangement for specific temperature and before holding the die at specific temperature put sample into die after this process using press machine pass the sample from the die, three type different dies with using channels intersecting at 120°, 105°, 135° following route A, BA, BC up to 3 or 4 passes [2]. Microstructure and Vickers hardness Tensile strength studied in ECAPed samples [3]. In this learning aluminium was picked for ECAP handling. So serve plastic deformation (SPD) has been established as a valuable advance to generate ultrafine grain (UFG) materials. An Al alloy are an imperative group of materials, broadly use for severe structural applications. In current years, the require to develop the mechanical properties of light alloys has driven the awareness of industry or engineering and research or study efforts towards two different, but equivalent, fields. The primary playing field is the procedure of age hardening of alloys and the next field is the improvement of latest metal processing technique such as ECAP to improve the mechanical strength and refine microstructure and to improve the mechanical strength. A number of researchers have common these two fields to achieve even improved property [3] (Fig. 1).

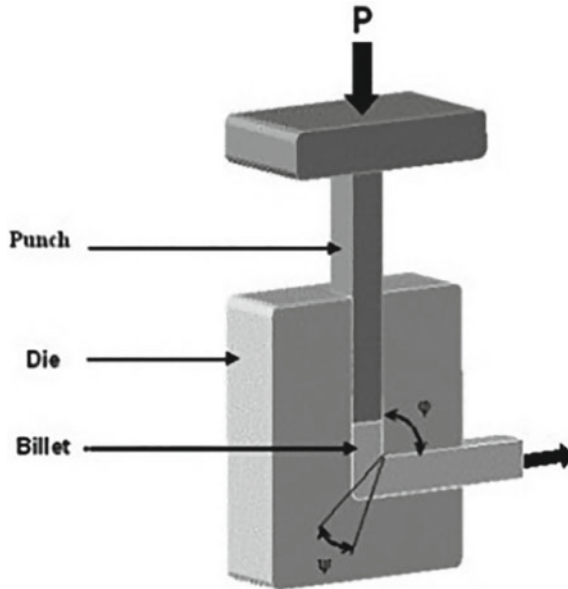


Fig. 1 ECAP study on aluminium and its alloys [3]

## 2 Aluminium Alloy Series

### 2.1 Aluminium-1000 Series and Pure Aluminium

After working on Al and its alloy with the help of ECAP process some fact are prove here like found grain structure is highly refine and improve the hardness of pure Al and its alloy.

And other impact showing on this process like tensile strength and other properties improved of grain materials. ECAP sample subjected to small punch test found the yield strength and ultimate strength decrease after four passes.

AL-1000 series materials considered as a commercially pure in the ECAP working taken route C and BC then observed grain size of 1.1  $\mu\text{m}$  and 2.9  $\mu\text{m}$  [2]. And also observed the hardness and yield strength improvement for both routes.

### 2.2 Aluminium-2000

Alloys of aluminium, have many more applications and are also similarly studied and researched. There is not easy to attain grain size less than 10  $\mu\text{m}$ . So ECAP process is capable to generate size less than 10  $\mu\text{m}$ . This study is based on the grade wise learning [3]. Al and these alloy like Al 2014 mostly used in industry prospects and involve deep loads and high temperatures. So this method result obtain good result and better strength including ECAP. After three passes of this material found or observed the grain size decrease approx. (94% in 3 passes) and its also observed the microhardness increase 27%. The microstructure of Al 2014 showing in the figure after and before the ECAP

process. Observed the effect of various passes the hardness after four to eight pass and tensile strength enhancement in the term increase after three passes at room temperature ECAP process provide elevated ideal ductility and strength before furnace cool sample (Fig. 2).

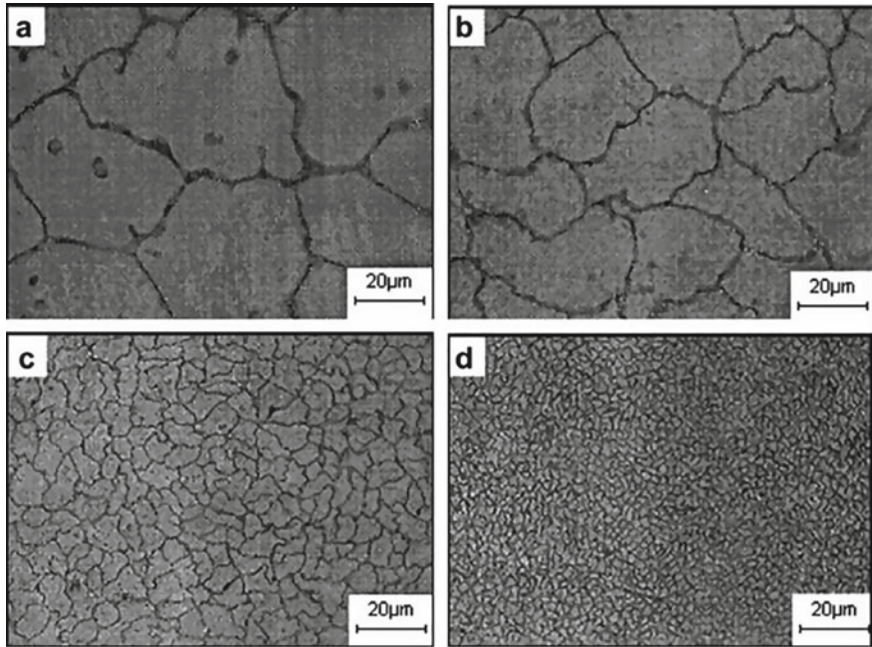


**Fig. 2** Microstructure **a** before ECAP and after ECAP of AL alloy 2014, **b** 6 pass, **c** 3pass, **d** 9 pass [3, 4]

### 2.3 Aluminium-3000 Series

Study about a 3000 series Al alloy where improvement in strength and hardness which become flooded as number of passes increase [5] and establish the major grain refinement (5–10  $\mu\text{m}$ ) it is found that the route BC might generate larger longitudinal strength though route could generate much constant.

### 2.4 Aluminium-4000 Series

This series alloys of aluminium have silicon (Si) is principal element. Many alloys of this category explore are unnamed, though, because of their composition, drop under this category. Some study provided that close into the special effects of the number of passes on the alloy (Al-7%Si alloy) [6]. A steady enhancement about 50–60% in the UTS was experimental in four process routes subsequent to eight passes [2]. Still samples process throughout routes C and BC display smaller ductility as compare to the enduring two routes.

## 2.5 Aluminium-5000 Series

In the 5th series of aluminium alloy have magnesium is the main alloying element. Some types of the series those usable for industry or research purpose are 5050, 5052, 5054, and 5083 and with others. After 4 passes the yield strength in tension too as compare widely improved. AL 5083 is used in the industry aspects as well as study or research purpose because its resist quality of corrosion under to seawater too high and its strength, ductility as well as formability have good. After increasing pass at using route C and A the microhardness and strength improved or increased. Working after 4–8 pass the grain size found near 0.3 [7].

AL 5083 is the alloy of 5th series which is very highly use in the aircraft and ship making and some other industry use. When Al 5083 pass through the specific angle  $120^\circ$  then its observed the specific mechanical and physical properties were changed after 1st pass to 4th pass like microstructure or grain structure were reformed and hardness were also changed. The melting point of Al 5083 is  $570^\circ\text{C}$ .

### Industrial use of Al 5083

1. Al 5083 use to resist extremely environment effect and this material also resist the effect of seawater and other chemical environments.
2. Aluminium 5083 is used in industrial level
  - a. Ship making
  - b. Railways car
  - c. Vehicle area
  - d. Mining skip and cages

So there are diverse discussion about the Al alloys in different series (1000–5000). If ECAP proceed on these alloys then effect discussed.

## 3 Wear Properties After ECAP Process

The wear property of manufacturing material have important effect on the strength and serviceability of their system or components. Therefore, the wear properties required to be in use into relation in the drawing of manufacturing part [8]. It is studied that the wear resistance of alloys and metals is proportional to the hardness. The wear resistance of materials can be improve by surface coating and heat treatment. Another technical trick is using to improve the wear resistance characteristics by the grain refinement. Materials produced in grain sized with the help ECAP. Where include nanometre or micrometre for producing grain structure and the improve the mechanical and physical properties [9] (Fig. 3).

Effect discussed due to ECAP on alloys on wear resistance

Impact of first to 4th to eight pass the wear resistance of Aluminium alloy has been improved because after ECAP passes microhardness increase through grain refinement.

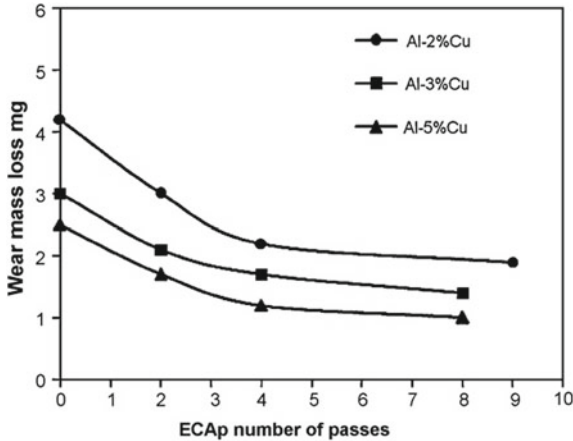


**Fig. 3** The effect of passes on Cu on wear mass loss of Al-2, and 5% Cu alloys under the sliding distance of 268.6 m and applied load of 19.6 N [3, 10]

#### 4 Using Different Dies on ECAP Process at Different Angle at AL 5083 Alloy

The value of microhardness of an escaped sample improve or increased the passes at die. At the ECAP working time its observed when decrease the channel angle and its reached at maximum value 138HV after three to four successive passes using route BC and using die minimum angle of them 105°. Its shown on this process compare to other dies angle at 105° lower channel angle higher effective for yields and higher strength as well as valuable grain refinement [11].

It is fulfilled that process of at diverse ECAP dies improved microstructural and mechanical characteristics of Al alloy 5083. Improvement of these property has been prepared it achievable to utilize the alloy in a variety of technical and engineering applications require high strength (Figs. 4 and 5)

#### 5 Conclusion

Equal channel angular pressing (ECAP) pressing process successfully applied on the Al alloys in different grades and also discussed AA 5083. In this paper also carried various type die in different geometry to increasing the mechanical properties. And also studied about the microhardness which has also increase with increased number of passes and when decrease the die angle then its reached at maximum value 138 HV at 105° using route BC. For AA 5083 at 105° angel all mechanical properties found much better than compare to angle 120° and 135° geometry dies. So its concluded in lower die angle the mechanical and microstructural properties were improved.

So improvement of these mechanical and microstructural properties of Al alloy and AA 5083 possible to use in future for engineering application and technology required high strength.

ECAP effect on Al alloys.



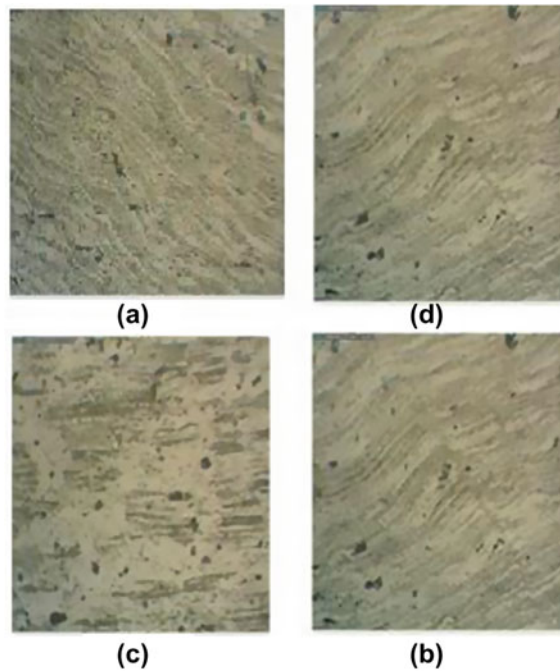


**Fig. 4** ECAP sample images after process through the die at  $105^\circ$  **a** image of raw material, **b** first pass, **c** third pass using route A, **d** BC route, 3rd pass [2]

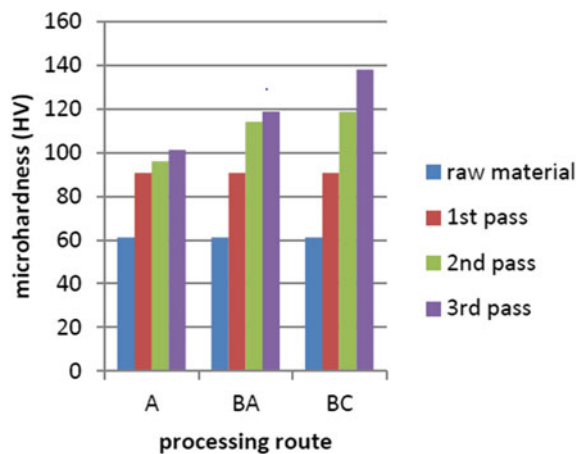


**Fig. 5** At angle  $105^\circ$  the microhardness all value of samples [2]

1. With the help of ECAP have improve the mechanical properties like hardness, yield strength, and UTS.
2. In this present paper studied different die angles impact on the AA alloys.
3. In ECAP process mostly trials have use similar angle  $120^\circ$  through route B using lubricant  $\text{MoS}_2$ .
4. So the ECAP is much future scope as well as it process also helpful for improving the efficiency of process.
5. So its observed in the ECAP effect on the microstructure, microhardness, mechanical and physical properties, and corrosion resistance were discussed or studied.
6. On that process studied the how grain size were reduced, respectively.
7. The impact of ECAP on the Al 5083 were discussed.
8. The industrial use of Al 5083 were discussed very briefly.

## References

1. Brodova I, Shirinkina I, Antonova O, Shorokhov E, Zhgilev I (2009) Formation of a sub-microcrystalline structure upon dynamic deformation of aluminum alloys. *Mater Sci Eng, A* 503(1–2):103–105
2. Bolem K, Varadala A, Swaminaidu G (2017) Equal channel angular pressing of aluminium alloy 5083 using different die geometries. *Int Res J Eng Technol (IRJET)* 4(05)
3. Vishnu P, Mohan RR, Sangeetha EK, Raghuraman S, Venkatraman R (2020) A review on processing of aluminium and its alloys through equal channel angular pressing die. *Mater Today Proc* 21:212–222
4. Gazizov M, Dubina A, Zhemchuzhnikova D, Kaibyshev R (2015) Effect of equal-channel angular pressing and aging on the microstructure and mechanical properties of an Al-Cu-Mg-Si alloy. *Phys Met Metallogr* 116(7):718–729
5. Ferrasse S, Hartwig KT, Goforth RE, Segal VM (1997) Microstructure and properties of copper and aluminum alloy 3003 heavily worked by equal channel angular extrusion. *Metall and Mater Trans A* 28(4):1047–1057
6. Gutierrez-Urrutia I, Munoz-Morris M, Morris DG (2007) Contribution of microstructural parameters to strengthening in an ultrafine-grained Al–7% Si alloy processed by severe deformation. *Acta Mater* 55(4):1319–1330
7. Iwahashi Y, Horita Z, Nemoto M, Langdon TG (1998) Factors influencing the equilibrium grain size in equal-channel angular pressing: role of Mg additions to aluminum. *Metall Mater Trans A* 29(10):2503–2510
8. Nashith A, Sanjid P, Shamsudheen M, Rasheeque R, Ramis M, Shebeer A (2014) Effect of equal channel angular pressing (ECAP) on hardness and microstructure of pure aluminum. *Int J Mater Eng* 4(3):119–122
9. Chegini M, Fallahi A, Shaeri M (2015) Effect of equal channel angular pressing (ECAP) on wear behavior of Al-7075 alloy. *Procedia Mater Sci* 11:95–100
10. Abd El Aal MI, El Mahallawy N, Shehata FA, Abd El Hameed M, Yoon EY, Kim HS (2010) Wear properties of ECAP-processed ultrafine grained Al–Cu alloys. *Mater Sci Eng, A* 527(16–17):3726–3732
11. Van Thuong N, Zuhailawati H, Seman AA, Huy TD, Dhindaw BK (2015) Microstructural evolution and wear characteristics of equal channel angular pressing processed semi-solid-cast hypoeutectic aluminum alloys. *Mater Des* 67:448–456



# Comparison of P&O and Proposed Fuzzy Logic Algorithm for MPPT-Based Charger

Parth Malhotra<sup>(✉)</sup>, Prabhav Kumar Yadav, Samyak Jain, and Dheeraj Joshi

Delhi Technological University, New Delhi, India  
parthmalhotra30@yahoo.com

## 1 Introduction

“Solar energy usage is continuously rising because of rising in energy needs and depletion of the non-renewable source [1].” Sunlight energy is not constant throughout the day and year and its temperature and irradiance level keeps on changing, thus an energy storage device, like battery is always connected between the load and the solar panel to provide energy during night time or in bad weather conditions. “Due to sudden increase in energy need solar energy is among the best source of renewable energy that is present in abundance [2].” With the use of the right technology, it must be utilized to its fullest so that there is a reduction in our dependency on conventional energy sources for the generation of electricity. The charge from the solar panel needs to be stored for which batteries are used along with a battery controller which controls the batteries charging and discharging rate. A solar charge controller is the major component of any PV system which maintains an accurate charging voltage and current of the batteries. Extensive research is being made to improve the efficiency of both the solar panel and the charge controller so that maximum energy can be converted from one form to the other. MPPT involves finding a particular voltage where maximum power can be attained from the solar panel and MPPT is the method to find that voltage value. Various algorithms are used to determine the MPPT point. One such classical method is the P&O method which is easy to implement, low cost, and also gives satisfactory results. Our proposed algorithm is a fuzzy logic-based algorithm that has an improved efficiency than the P&O algorithm. Two variables  $\Delta P$  and  $\Delta V$  are used as input variables and output is the duty cycle ratio ( $\Delta D$ ) which is fed to the buck-boost converter to change its  $R_{TH}$  so that voltage remains constant.

## 2 Solar Cell Model

A solar cell is responsible for converting sunlight to electricity. Series and parallel combination of PV cells form a PV panel and series and parallel arrangement of PV panels form a PV array which is used for commercial use and it used to harvest kilowatts of energy. To compare the efficiency of the solar panels, basic standard conditions are to be followed. The nominal test conditions are as follows:

$$\text{Irradiance } (G_N) = 1000 \text{ W/m}^2$$

$$\text{Temperature}(T_M) = 25^\circ\text{C}$$

The basic mathematical model of the solar cell that is widely used is shown below in Fig. 1.

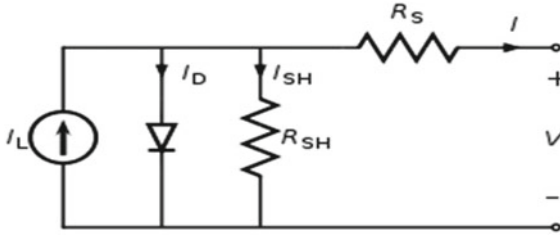


**Fig. 1** Typical single diode solar cell model

In the above model is the single diode, solar cell model. Applying the node equation, we get the following equation of a single solar cell. “The simplicity of the single diode model makes this model perfect for the simulation of PV devices with power converters [3].”

$$I = I_{pv} - I_0 \left[ e^{\left( \frac{V+R_S I}{aV_T} \right)} - 1 \right] - \frac{V + R_S I}{R_P} \tag{1}$$

Here,

- $I_{pv}$ —photo current
- $I_0$ —cell saturation of dark current
- $V_T$ —Thermal voltage
- $Q$ — $1.6 \times 10^{-19}$  C charge of an electron
- $T$ —the cell’s working temperature
- $A$ —Ideality factor
- $R_p$ —Shunt resistance
- $R_s$ —Series resistance.

### 2.1 Solar Panel Parameters

The solar panel is a connection of the solar cells in series and parallel that are modelled as described previously. The solar panel datasheet provided by the manufacturers consists of various parameters conducted using the standard conditions. Below is the parameter detail of the solar panel used for our simulation (Table 1).

### 2.2 MPPT Concept

The MPPT concept requires the load line to be constant irrespective of the load change at the terminal. For this operation, it is necessary to use the power interface whose job

**Table 1** Solar panel parameters

Maximum power ( $P_{max}$ )	213 W
Voltage at maximum power ( $V_{MP}$ )	29 V
Current at maximum power ( $I_{MP}$ )	7.35 A
Open circuit voltage ( $V_{oc}$ )	36.3 V
Short circuit current ( $I_{sc}$ )	7.84 A

is to maintain the  $R_T$  at the operating point whatever may be the value of the R load by changing its duty cycle. The input Thevenin impedance from the solar panel is hence made to be constant. The buck-boost converter here outperforms the other converters. Below is the equation of the input impedance of the buck-boost converter.

$$R_T = R_O(1 - D/D)^2 \tag{2}$$

In buck-boost converter when the duty cycle is zero ( $D = 0$ ),  $R_T$  is equal to the infinity and behaves as the open circuit for the PV panel and the hence the virtual load line is along the x-axis. In other case when  $D = 1$ ,  $R_T$  is equal to zero and behaves as a short circuit to the PV panel and hence the virtual load line is along the y-axis. So, this entire first quadrant portion of the IV characteristic is the operating region for the PV module, and therefore, obviously, the peak power point and the voltage will be reachable by the buck-boost converter by changing the value of the input Thevenin impedance by varying the duty cycle. So, one of the main advantages of the buck-boost converter is that it covers the entire first quadrant and any point on the IV characteristic is reachable by the buck-boost converter interface for any isolation and any type of load.

### 2.3 Li-Ion Cell Modelling

Li-ion cells has several modelling methods. One of the most used methods for mathematical modelling Li-ion cell is done by using a Thevenin RC circuit model (Fig. 2).

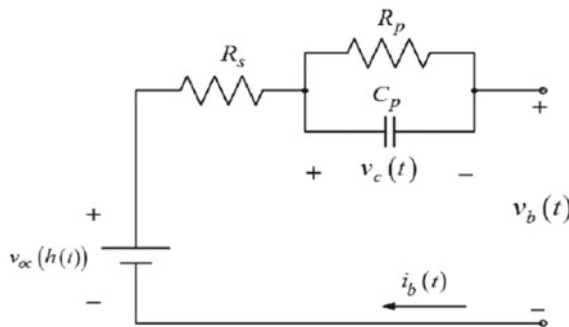


**Fig. 2** Thevenin equivalent model of Li-ion cell

$R_S, R_P, C_P, V_{OC}$  are all function of (SOC, Temp).

Estimating these parameters require experimentation work to determine the parameters using a lookup table [4]. Estimating is a complex task hence SIMULINK model is used.

Parameters of battery used are shown below:

Nominal voltage : 24 V	Rated Capacity : 8 Ah
Initial SOC : 70%	Nominal discharge current : 3.47 A
Fully charged voltage : 27.9 V	

### 3 Maximum Power Point Tracking

#### 3.1 Perturb and Observe (P&O) Method

In this method, the tracking point power is calculated and is compared with the previously calculated power to decide the next movement. It is also called the hill-climbing method. This method works on the derivate change of power with respect to voltage. The output voltage is gradually increased by increasing the duty cycle and power is calculated upon every incrementation value. If the new power calculated is more than the previous power, then the voltage is increased further. This means that the maximum power point is at the right side of the current point and output voltage must be further increased to reach the maximum voltage. If the new power calculated is less than the previous power, then the voltage is decreased by reducing the duty cycle in the corresponding step.

Here, the tracking point is reversed which means that the MPPT point is at the left of the current point and hence the output voltage is to be lowered. Hence it is called Perturb and Observe method [5]. In this method, the point continuously hovers between the MPPT point and does not reach a stable point. However, reading with high precision can be obtained by choosing a proper value of the difference ( $\Delta D$ ). Here the value of the difference ( $\Delta D$ ) is constant. A major drawback of this algorithm can be seen when there is a change in the weather conditions or irradiance level. But this drawback can be neglected as sudden changes in irradiance and weather occur very rarely.

#### 3.2 Proposed Fuzzy Logic Algorithm

“A fuzzy logic controller is used to track the MPPT in the PV module [6]”. Fuzzy logic is another method to calculate the maximum power point. Fuzzy logic compares the change in power ( $\Delta P$ ) and change in the voltage ( $\Delta V$ ) and based upon the amount of change in these quantities, it corresponds to the change in duty cycle which is required to reach maximum power [7, 8, 9]. In the P&O algorithm, the change in duty cycle is done by a fixed constant value ( $\Delta D$ ) as mentioned above, but in fuzzy logic here the incremental and decremental duty cycle value is not fixed but depends on how much change is observed in the power as well as voltage. Based on this observation fuzzy logic rule base is formed which is shown in the Table 2.

**Table 2** Fuzzy logic rule

$\Delta P/\Delta V$	NL	NS	ZE	PS	PL
NL	NL	NL	NS	PL	PL
NS	NS	NS	ZE	PS	PS
ZE	NS	ZE	ZE	ZE	PS
PS	PS	PS	ZE	NS	NS
PL	PL	PL	NS	NL	NL

## 4 MPPT Implementation

For achieving the maximum power output from the panel, the output voltage and the output current of the panel are to be controlled by changing the Thevenin resistance of the DC converter. This is done by varying the gate pulse signal of the MOSFET of the buck-boost converter. The relationship between input impedance and the duty cycle is discussed in Eq. 2. The P&O algorithm is encoded in a MATLAB function of the Simulink model. It generates the value based on the algorithm which is converted into the pulses using the PWM generator technique. Similarly, in the FLC method voltage and power are sensed and are given to the fuzzy block and a variable duty cycle is generated which is then fed to the MOSFET.

### 4.1 Charge Controller

Charging of Li-ion battery plays a crucial role in maintaining the proper functioning and long life of a battery. Here, CCCV charging technique is used. In this methodology, a constant charging current is fed into the battery for a certain range of SOC and beyond that range, a constant voltage is maintained across the terminals of a battery. For controlling the charging of the battery, the output of the buck-boost converter is fed to the battery using a two-quadrant chopper. The gate signals are altered to obtain CCCV charging of the battery. A control system with a PID controlled is used to vary the duty cycle of the gate signal with the help of a PWM generator. “PI controller is used to regulate the output voltage for correct charging of the batteries [10, 11]”. A difference voltage is fed into the controller and the limiting current and final voltage are set as per the predefined nominal discharge current and full charge voltage of the battery, respectively (Fig. 3).

## 5 Results

The system was operated for three stages at 25 °C. The value of input irradiance on the solar panel is given below (Fig. 4):

- Stage 1 : 1000 W/m<sup>2</sup>
- Stage 2 : 800 W/m<sup>2</sup>

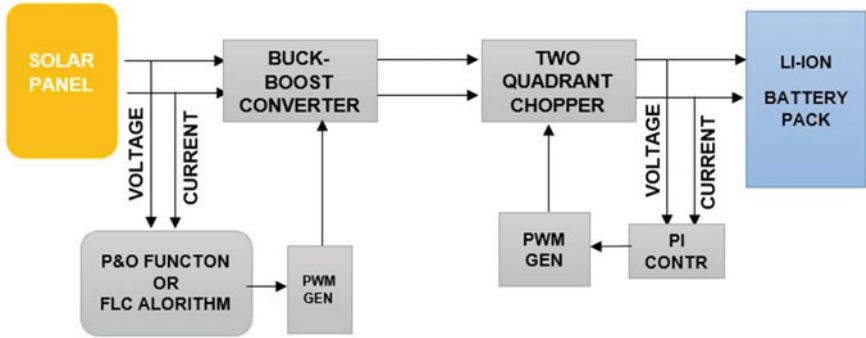


Fig. 3 Block diagram of circuit model

Stage 3 : 500 W/m<sup>2</sup> for 1.5 sec duration each.

Figure 5 shows the PV curves under different input irradiance conditions. Maximum power ( $P_{max}$ ) and  $V_{MP}$  can be seen from the figure. A comparison between the maximum achievable power from the panel ( $P_{max}$ ) and the output solar panel power using the P&O algorithm is shown in Fig. 6. The results show that with the change in irradiance the output power changes according to the input irradiance level and it settles down to a stable value close to the  $P_{max}$  after few oscillations. The efficiency and the power output of the solar panel using the P&O algorithm are tabulated in Table 3. The values show that the P&O has an. The output voltage at the PV panel must be maintained in between 27 and 29 V which is the ( $V_{MP}$  is equal to 29 V as mentioned in Table 1.) MPPT required voltage. Figure 7 shows the successfully obtained voltage using the P&O algorithm but has a lot of oscillations in it. Figure 8 depicts the charging of the Li-ion battery connected with a Constant Current (CC) method and a steady increase in the battery SOC and its voltage, validating the charging of the battery.

A comparison between the maximum achievable power from the panel ( $P_{max}$ ) and the output PV panel power using the proposed FLC algorithm is shown in Fig. 9. The power

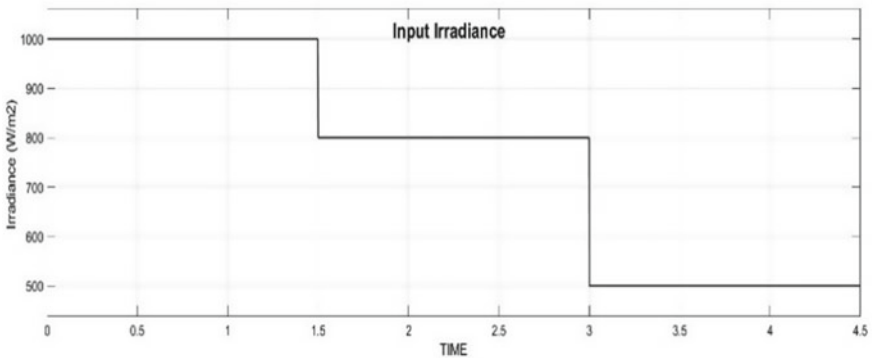
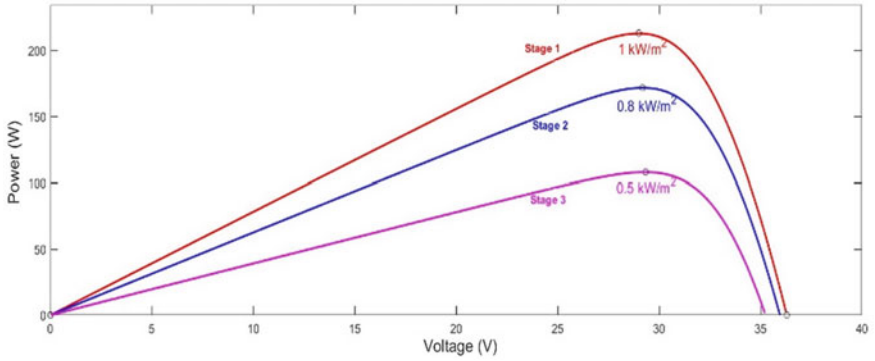
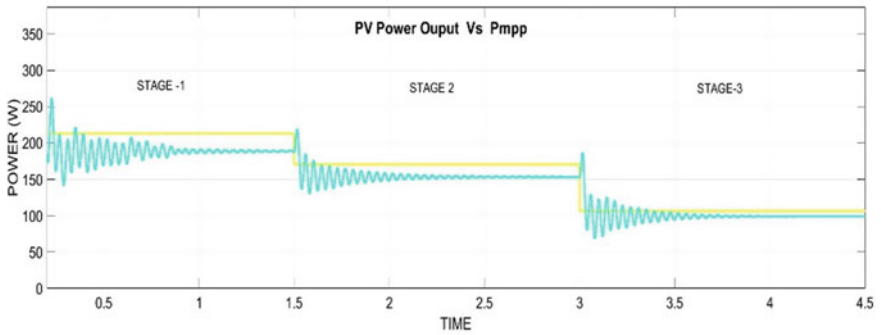


Fig. 4 Input irradiance curve





**Fig. 5** P–V curve in different stages



**Fig. 6** Power of solar panel using P&O algorithm versus  $P_{max}$

**Table 3** Simulation results of P&O algorithm

Stage No.	$P_{max}$ (W)	$P(pv)$ (W)	Efficiency (%)	$V_{bat}$ (V)	$I_{bat}$ (Amp)
1	213.5	189.02	88.53	26.07	3.39
2	170	153.8	90.47	26.09	3.26
3	105	99.0	94.28	26.04	1.20

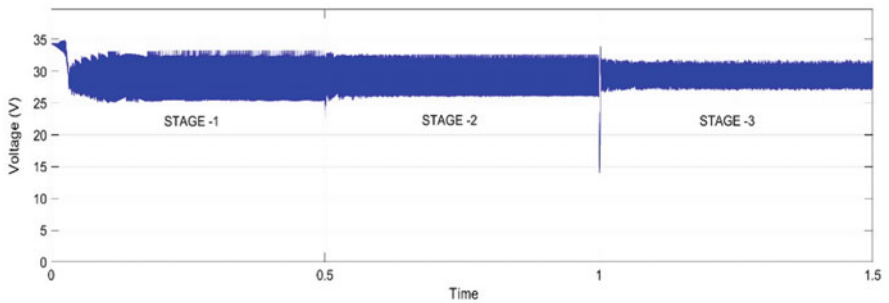


**Fig. 7** Voltage variation of solar panel using P&O algorithm

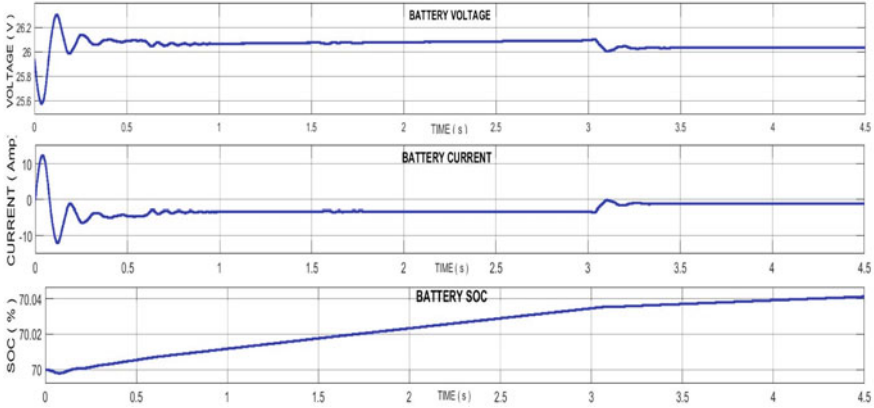


**Fig. 8** Battery voltage, current and SOC graph using P&O algorithm

output from the panel is very close to the ( $P_{max}$ ) at different irradiance level. Results also show a less oscillatory behaviour as compared to P&O and also faster settling time than P&O. The numerical values of power output and efficiency using the proposed FLC algorithm are tabulated in Table 4. From Fig. 10, it is observed that the proposed FLC algorithm successfully attains the panel output voltage of 29 V with negligible oscillations indicating the stable performance of the algorithm as compared to the P&O algorithm which has a highly oscillatory voltage output as shown in Fig. 7. Figure 11 highlights “the charging of the battery with a Constant Current (CC) method” [12] and a steady increase in the battery SOC and its voltage can be observed. The voltage rise is observed more in the fuzzy algorithm as more power is supplied to the battery from the solar panel hence more charging of the battery which means higher efficiency under similar conditions and less energy and power wastage.

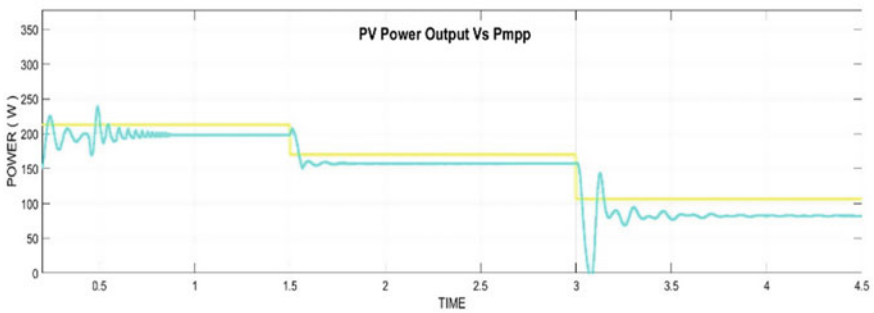


**Fig. 9** The power of PV panel using proposed fuzzy logic algorithm versus  $P_{max}$

**Table 4** Simulation results of proposed fuzzy algorithm

Stage No.	$P_{max}$ (W)	$P(pv)$ (W)	Efficiency (%)	$V_{bat}$ (V)	$I_{bat}$ (Amp)
1	213.5	199.2	93.30	26.07	3.39
2	170	157.1	92.41	26.09	3.40
3	105	81.66	77.77	26.01	0.52

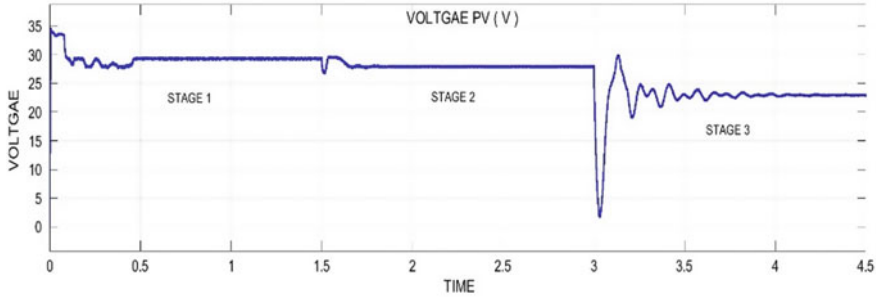


**Fig. 10** Voltage of PV panel using proposed fuzzy logic algorithm

## 6 Conclusion

In this paper, a comparison is being made between the classic P&O method and a proposed fuzzy logic-based algorithm. Fuzzy logic-based solar controller outperforms the P&O type solar charge controllers. Implementation of a MATLAB simulation comparison is done. A buck-boost converter with the solar controller is used because of its

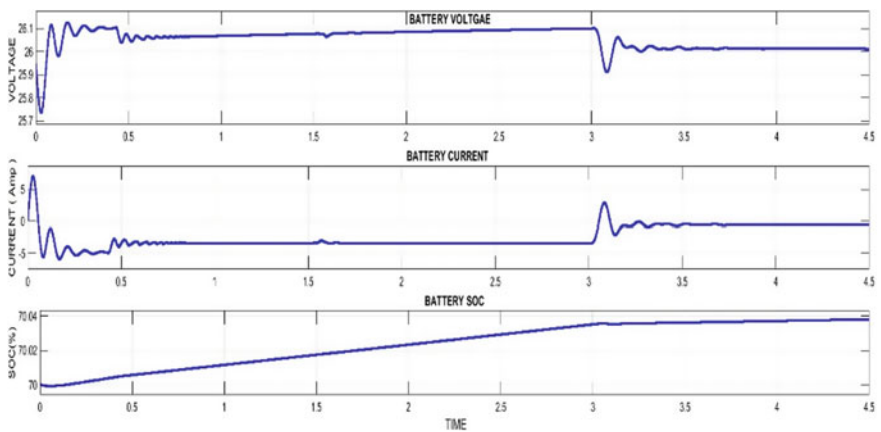


**Fig. 11** Battery voltage, current and SOC graph using proposed fuzzy logic algorithm

advantage of getting an entire first quadrant operation for MPPT tracking. Buck-boost converters can also provide both low and high output voltages as per the requirement.

P&O algorithm has certain advantages like improved efficiency, low cost implementation, and ease to code and compute. The only drawback of this method is that it depends upon the sensitivities of both current and voltage sensors because in this method both current and voltage are used to compute the power from which the maximum power point is tracked. The proposed fuzzy system is complex to implement but the results and efficiency are better than the P&O algorithm along with less settling time and very few oscillations.

Our MATLAB Simulink model shows a good result using the fuzzy algorithm with good efficiency of 93% as compared to the P&O algorithm giving an output of 89%. In cases when irradiance level is very low like  $500 \text{ W/m}^2$ , P&O has a better result but for the majority of the high irradiance day time, the proposed fuzzy logic algorithm outperforms.

A Li-ion battery is used as energy storage to store the energy from the PV panel and act as a backup energy source. A charge controller is a must for the safe charging of the batteries. It is implemented along with the MPPT controller which regulates the charging of batteries. The CCCV charging method adopted with the charge controller ensures that a stable charging current value so that the Li-ion battery does not get heated up or get overcharged which can be dangerous for Li-ion batteries as they are highly volatile in nature.






## References

1. Pathare M, Shetty V, Datta D, Valunekar R, Sawant A, Pai S (2017) Designing and implementation of maximum power point tracking (MPPT) solar charge controller. In: 2017 international conference on nascent technologies in engineering (ICNTE), Navi Mumbai, pp 1–5. <https://doi.org/10.1109/ICNTE.2017.7947928>
2. <https://www.ijser.org/paper/Photovoltaic-Solar-Energy-Review.html>
3. Villalva MG, Gazoli JR, Filho ER (2009) Comprehensive approach to modeling and simulation of photovoltaic arrays. *IEEE Trans Power Electron* 24(5):1198–1208. <https://doi.org/10.1109/TPEL.2009.2013862>
4. Ali D, Mukhopadhyay S, Rehman H, Khurram A (2017) UAS based Li-ion battery model parameters estimation. *Control Eng Pract* 66:126–145
5. Ahmed J, Salam Z (2015) An improved perturb and observe (P&O) maximum power point tracking (MPPT) algorithm for higher efficiency. *Appl Energy* 150:97–108
6. Ali A, Hasan AN, Marwala T (2014) Perturb and observe based on fuzzy logic controller maximum power point tracking (MPPT). In: 2014 international conference on renewable energy research and application (ICRERA), Milwaukee, WI, USA, pp 406–411. <https://doi.org/10.1109/ICRERA.2014.7016418>
7. Kumar A, Chaudhary P, Rizwan M (2015) Development of fuzzy logic based MPPT controller for PV system at varying meteorological parameters. In: 2015 annual IEEE India conference (INDICON), New Delhi, India, pp 1–6
8. Nabipour M, Razaz M, Seifossadat SGH, Mortazavi SS (2017) A new MPPT scheme based on a novel fuzzy approach. *Renew Sustain Energy Rev* 74:1147–1169, ISSN 1364-0321
9. Al-Majidi SD, Abbod MF, Al-Raweshidy HS (2018) A novel maximum power point tracking technique based on fuzzy logic for photovoltaic systems. *Int J Hydrogen Energy* 43(31):14158–14171

10. Yilmaz U, Kircay A, Borekci S (2018) PV system fuzzy logic MPPT method and PI control as a charge controller. *Renew Sustain Energy Rev* 81(Part 1):994–1001
11. Pathak PK, Yadav AK (2019) Design of battery charging circuit through intelligent MPPT using SPV system. *Solar Energy* 178:79–89
12. Selmi T, Abdul-Niby M, Devis L, Davis A (2014) P&O MPPT implementation using MATLAB/Simulink



# Applications of Friction-Based Processes in Manufacturing

Raghavendra Darji<sup>1</sup> , Gaurang Joshi<sup>2</sup> , Vishvesh Badheka<sup>1</sup> ,  
and Dhiren Patel<sup>3</sup>  

<sup>1</sup> Pandit Deendayal Energy University, Gandhinagar, Gujarat 382007, India

<sup>2</sup> Marwadi University, Rajkot, Gujarat 360003, India

<sup>3</sup> Indus University, Ahmedabad, Gujarat 382125, India

dhirenpatel185@gmail.com

## 1 Introduction

Applications of the friction-based processes are increasing day by day for certain specific and critical applications when the conventional processes are not able to satisfy the purpose. Friction-based processes started form the 1940s commercially through the friction welding [1]. However, since then the development of the friction-based processes was found limited till the year 1991, in which TWI developed the process called friction stir welding (FSW) which was initially developed for the welding of various aluminum grades [2]. Further, the FSW process developed for many metals and alloys, at present any metal, alloy, plastic and composite material can be joined using FSW process [3–5]. This shows that the industries as well as the researchers have found too many solutions for their challenges through the FSW which were not possible to resolve using the traditional processes. Along with the FSW [6], friction welding (FW) [7] process also reported extremely useful and applicable for many dissimilar metals and alloys joining. Nevertheless, the friction-based processes not limited to only joining but they are equally useful for certain other applications as well. Friction stir processing (FSP) [8], super plasticity [9, 10], friction stir surfacing (FSR) [4], manufacturing of surface and volume composited using FSW are the very uncommon application of the friction-based process. Note that the first paragraph of a section or subsection is not indented.

The fundamental characteristics of the friction-based processes are very much compatible for the processing of these much applications as mentioned above. The most important feature of the friction-based processes is that the welding or processing takes place in a viscoelastic state which means the material is not melted during the welding or processing instead it remains in solid state only. This phenomenon of keeping material in solid state during the welding or processing eliminates many metallurgical incompatibilities such as low distortion of the work piece, dimensional stability, no loss of alloying elements, easy to obtain fine grains and absence of cracking [11]. All the friction-based processes possess the above-mentioned advantages; grain refinement is of course the most important output of these processes. In this article, various friction-based processes introduced and the applications of the specific friction-based process

imported from the available literature at present. The friction-based processes encompass in this article are as friction stir welding (FSW), friction welding (FW), and friction stir processing (FSP).

Here are the basics of each process and their application one by one, subsequent paragraphs, however, are indented.

## 2 Applications of FSW

Friction stir welding (FSW) was invented by TWI in 1991, the fundamentals of the FSW presented in the Fig. 1. The process consists of the very rigid fixture to hold the specimen during the process and a tool which is to be plunged into the base material in which shoulder generates the major portion of the heat and pin provides the mechanical movement to the material at the faying surfaces, design of a tool and fixture are the two critical parameters one has to consider [12]. FSW was invented to overcome the difficulties such as poor solidification microstructure, porosities in the fusion zone in the welding of 2XXX and 7XXX series alloys, before that these alloys almost considered as a non-weldable despite of having critical applications in the aerospace due to high strength, fatigue and fracture resistance [2, 11].

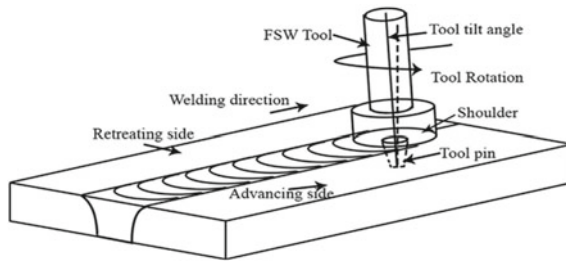


**Fig. 1** Schematic diagram of friction stir welding (FSW) [13]

Since then, FSW is extensively used for joining of aluminum alloys. Al alloys have wide range of application in the field of aerospace, automotive and ship building, cryogenics, vacuum and also in the electronic industries [14]. As mentioned earlier due to the solid state process metallurgical challenges can be easily avoided in fact during the welding grain refinement is possible which results into the fine grain microstructure and better mechanical properties. The metals which are having higher thermal conductivity such as Al and Cu for both FSW was found the excellent process for the joining. In case of Al, around 90% joint efficiency was reported [15]. In fact, the most recent experiments on 0.5 mm thick (ultrathin) Al sheet, higher tensile strength obtained than the base metal with the micro FSW [16]. Welding of pure Cu is also very challenging due to its fluidity and thermal conductivity, the stability of the beam assisted (specially Laser beam welding) processes are still questionable, while on the other hand FSW is an excellent process for Cu welding. Figure 2 shows the joint efficiencies obtained for the Cu welding under different welding processes. Cu having the highest thermal conductivity of 397 W/mK, preheating becomes mandatory along with the higher heat input

which result into the very slow cooling rate and coarse grains microstructure contrary to these conditions of the fusion welding processes, FSW being solid state process only mixes the material between the faying surfaces of the two plates and join them and tool pin deforms the grains as well which results into the fine grains microstructure in the stir zone [12]. Apart from these FSW also used for the welding of SS, Titanium, Ni alloys and LAS [17–19].

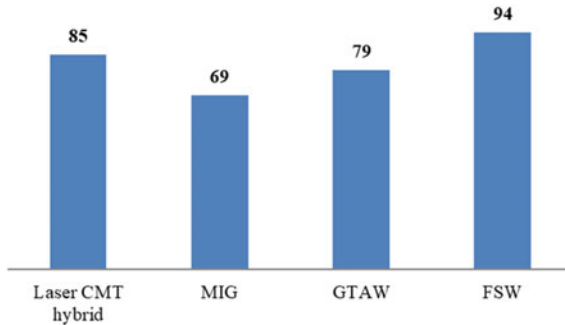


**Fig. 2** Joint efficiencies (%) comparison for Cu welding under different welding processes [12, 20–22]

Not only the similar material joining but the FSW explored to the great extent for the dissimilar welding specifically in case of lacking metallurgical compatibility between the two materials such as Al–Cu [23], SS–Al [24, 25], SS–Ti [17] and many more. Using the conventional fusion welding processes these material combinations are extremely difficult to join, contrary FSW provides the very good solution for these combinations in the absence of metallurgical compatibility. Considering the most non-compatible materials SS and Ti welding, it was reported that increase in temperature during the FSW leads to the diffusion of Ti into SS and diffusion of Fe, Cr and Ni into Ti, Due to this diffusion  $\beta$  Ti stabilizes at room temperature however, the presence of FeTi intermetallic compound were observed. Nonetheless, FeTi layer can be reduced by using the lower tool rotational speed [17]. FSW can also produce the joints between the metal and plastic for the applications in aerospace, automobile and electronic industries for attaining the advantages such as light weight, moderate strength, electrical and thermal insulation with the design flexibility [26].

Hence it can be concluded that the FSW is such a process which has solutions of most of the problems which cannot be taken care by using any conventional fusion welding process. FSW can be considered as a boon for the joining of any dissimilar combination of materials.

### 3 Applications of FW

As mentioned in the introduction that the friction-based processes started with the friction welding only in the year 1940 [1]. Friction welding is a process in which one part remains



stationary and the opposite part to that is rotating with the close contact of the stationary part due to which the two faying surfaces are under the rubbing action which generates the friction due to which the joining obtained in a few seconds [7]. Friction welding process is extensively useful for joining of any ferrous alloy to non-ferrous metal and alloys [7, 27–29]. The most crucial advantage of the friction welding is the absence of any tool as the friction generated by the rubbing action of the two opposite surfaces. As a consequence, the reaction layer thickness can be reduced to the greater extent as that of the friction stir welding, the reaction layer for the SS 304L to Al 6063–T6 in pipe configuration reported by Vyas et al. [29] was from 1.1  $\mu\text{m}$  to 2.0  $\mu\text{m}$  which was considerably thinner and because of that the intermetallic formation region can be reduced. The highest tensile strength secured was around 194  $\text{N}/\text{mm}^2$  which was very good result [29] (Fig. 3).

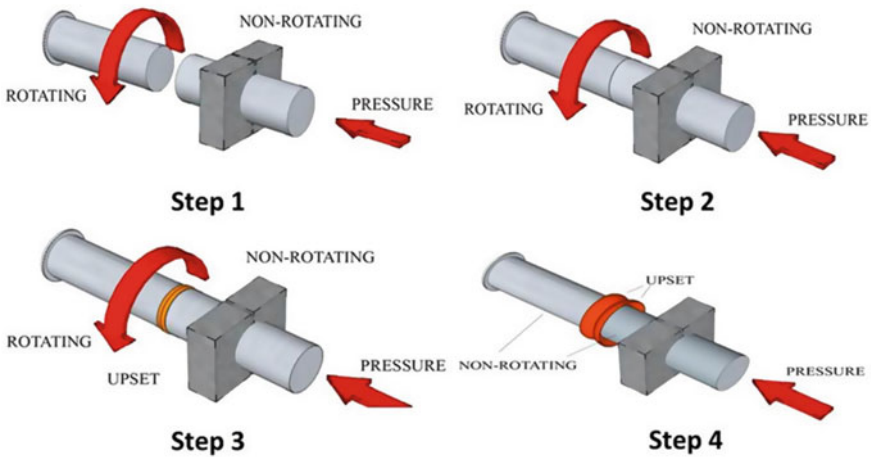


Fig. 3 Friction welding process [30]

In case of SS to CP Ti joining through friction welding, Ni interlayer was used and the joining obtained successfully, these kinds of dissimilar welds are having large applicability in the aerospace, cryogenics, vacuum applications and other application where low cost and optimum strength are required, the difference in corrosion resistance of SS and non-ferrous metal/alloys is very useful in certain applications. The transition joints can be easily produced using the friction welding process. For such applications the friction welding process provides the unique solutions for such applications.

## 4 Applications of FSP

Friction stir processing (FSP) is a variant of FSW in which the same equipment's are used as that of FSW but the motive behind the processing is not joining instead refinement of the grains. The FSP in recent years explored for the various applications such as to obtain the super plasticity which can be define as the ability of a material to exhibit more

than 200% uniform elongation under tension prior to failure [31, 32]. Super plasticity as mentioned earlier is the % of elongation. The grain refinement during the FSP can be obtained very easily; grain size can be received below 15  $\mu\text{m}$  and equiaxed grains obtained [31, 33]. For effective utilization of the fuel in the automobiles super plastic parts used in Europe and USA [32]. Al, Mg and their alloys are widely exposed to FSP due to their low weight [11, 31]. 2xxx, 5xxx, 6xxx and 7xxx series of aluminum alloys are widely used for the FSP for the super plasticity, specific components which can be manufactured using FSP are in the aerospace applications such as wing tips, winglets, engine nacelle skins, lip skins, equipment cover, air intakes, interior furnishings, door skins, lamp drums [31, 34]. These much applications of FSP are due to the capability of modifying the microstructure which is again same as that of FSW [11]. Tool geometry, processing parameters, and joint design are the fundamental parameters which one has to take into consideration while performing the processing for the super plasticity [11]. The effectiveness of the FSP is so high that Patel et al. [35] obtained 572% elongation for AA7075 using hybrid approach by obtaining smallest grain size using  $\text{CO}_2$  cooling.

FSP can also be used to enhance the microstructure of the cast components, for making surface composites, volume composites, additive manufacturing and for many such applications [32]. Surface properties are very important for the applications where wear becomes dominant to degrade the metal. Hard particles are added onto the surface of the plate through the FSP, the mostly used particles are B<sub>4</sub>C, SiC, Al<sub>2</sub>O<sub>3</sub>, TiC and TiN however, many such particles can be introduced [36–38]. By doing this processing and introducing the particles into the subsurface of the metal the surface hardness improved, wear resistance also improved, however, the basis of the introducing particles into the base metal depends upon the application for which the friction stir surfacing is executed [37]. Using multi pass technique of FSP continuous improvement of the tensile strength and the elongation were obtained for aluminum [39]. Surfacing through FSP has two major advantages, (a) the process decreased the grain size by which the mechanical properties improve by inherent characteristics of the process and (b) introduction of the second phase particles/ceramic particles creates the metal matrix composite kind of structure which is having articulated properties of particles and matrix both. Alongside this metal matrix composites are known for their strength to weight ratio [40]. Again, application not limited to mechanical properties but also helpful for the wear resistance, Sharma et al. [38] had found 50% decrement in the wear rate for Al 6061 (Friction stir processed with addition of ceramic particles in the form of surface composites) as that of the unprocessed Al 6061.

One of the latest modifications for FSP is for the formation of the channel (to generate continuous defect in the plate through single pass FSP in monolithic plate) which further can be employed for the heat exchange purpose [41]. Friction stir channeling (FSC) was patented by Mishra et al. [42] for the first time. Aluminum and its alloys were studied on many occasions by the researcher [41, 43]. In this process, the parameters for the FSP are deliberately selected such that a continuous defect can be formed, the size and shape of the channel certainly affected by the parameters of FSP.

## 5 Conclusions

Friction stir welding is the process which is widely applied for many metals and alloys considering the fact that it eliminates all the metallurgical non uniformities. The metals such as aluminum and copper had successfully welded using the FSW and obtaining the very good joint efficiency which cannot be possible with any fusion welding process. Friction welding is the process which can be the most effective process for the dissimilar metal/alloy joining as it reduces the reaction layer thickness by which the layer of the intermetallic reduced significantly. Friction stir processing can be said as modified FSW, FSP has many applications based on the requirement such as super plasticity, channeling, surface composites. Certainly, the friction-based processes can be the solution for many applications.

## References

1. Song J, Field R, Clarke A, Fu Y, Kaufman M (2019) ASM vol 6 welding, brazing, and soldering. *Acta Mater* 165:362–372
2. Friction stir welding—TWI. <https://www.twi-global.com/technical-knowledge/job-knowledge/friction-stir-welding-147>. Accessed on 15 Oct 2020
3. Dressler U, Biallas G, Alfaro Mercado U (2009) Friction stir welding of titanium alloy TiAl6V4 to aluminium alloy AA2024-T3. *Mater Sci Eng A* 526(1–2):113–117. <https://doi.org/10.1016/j.msea.2009.07.006>
4. Salih OS, Ou H, Sun W, McCartney DG (2015) A review of friction stir welding of aluminium matrix composites. *Mater Des* 86:61–71. <https://doi.org/10.1016/j.matdes.2015.07.071>
5. Scialpi A, Troughton M, Andrews S, de Filippis LAC (2009) Viblade™: friction stir welding for plastics. *Weld Int* 23(11):846–855. <https://doi.org/10.1080/09507110902843271>
6. Mehta KP, Badheka VJ (2017) Influence of tool pin design on properties of dissimilar copper to aluminum friction stir welding. *Trans Nonferrous Met Soc China* 27(1):36–54. [https://doi.org/10.1016/S1003-6326\(17\)60005-0](https://doi.org/10.1016/S1003-6326(17)60005-0)
7. Vyas H, Mehta KP, Badheka V, Doshi B (2020) Pipe-to-pipe friction welding of dissimilar Al-SS joints for cryogenic applications. *J Brazilian Soc Mech Sci Eng* 42(2):1–12. <https://doi.org/10.1007/s40430-020-2181-1>
8. Chang CI, Du XH, Huang JC (2007) Achieving ultrafine grain size in Mg-Al-Zn alloy by friction stir processing. *Scr Mater* 57(3):209–212. <https://doi.org/10.1016/j.scriptamat.2007.04.007>
9. Charit I, Mishra RS (2003) High strain rate superplasticity in a commercial 2024 Al alloy via friction stir processing. *Mater Sci Eng A* 359(1–2):290–296. [https://doi.org/10.1016/S0921-5093\(03\)00367-8](https://doi.org/10.1016/S0921-5093(03)00367-8)
10. Patel VV, Badheka V, Kumar A (2017) Effect of polygonal pin profiles on friction stir processed superplasticity of AA7075 alloy. *J Mater Process Technol* 240:68–76. <https://doi.org/10.1016/j.jmatprotec.2016.09.009>
11. Mishra RS, Mahoney MW, Sato Y, Hovanski Y (2016) Friction stir welding and processing VIII 50
12. Nia AA, Shirazi A (2016) Effects of different friction stir welding conditions on the microstructure and mechanical properties of copper plates. *Int J Miner Metall Mater* 23(7):799–809. <https://doi.org/10.1007/s12613-016-1294-0>
13. Friction stir welding schematic—Bing images. <https://www.bing.com/images/search?view=detailV2&ccid=Jo3VD%2BeA&id=5CBEC01DE1FD8D3B1C8E2880BF6347F838F7418B&thid=OIP>

14. Threadgill PL, Leonard AJ, Shercliff HR, Withers PJ (2009) Friction stir welding of aluminium alloys. *Int Mater Rev* 54(2):49–93. <https://doi.org/10.1179/174328009X411136>
15. Liu HJ, Fujii H, Maeda M, Nogi K (2003) Tensile properties and fracture locations of friction-stir-welded joints of 2017–T351 aluminum alloy. *J Mater Process Technol* 142(3):692–696. [https://doi.org/10.1016/S0924-0136\(03\)00806-9](https://doi.org/10.1016/S0924-0136(03)00806-9)
16. Panchal M, Patel D, Vyas H, Mehta K (2019) Ultra-thin friction stir welding on aluminum alloy. *Mater Today Proc* 26(xxxx):2888–2894. <https://doi.org/10.1016/j.matpr.2020.02.597>
17. Gotawala N, Shrivastava A (2020) Microstructural analysis and mechanical behavior of SS 304 and titanium joint from friction stir butt welding. *Mater Sci Eng A* 789(April):139658. <https://doi.org/10.1016/j.msea.2020.139658>
18. Lemos GVB, Hanke S, Dos Santos JF, Bergmann L, Reguly A, Strohaecker TR (2017) Progress in friction stir welding of Ni alloys. *Sci Technol Weld Join* 22(8):643–657. <https://doi.org/10.1080/13621718.2017.1288953>
19. Pradeep A, Muthukumar S (2018) An analysis to optimize the process parameters of friction stir welded low alloy steel plates. *Int J Eng Sci Technol* 5(3):25. <https://doi.org/10.4314/ijest.v5i3.3>
20. Hao K, Gong M, Xie Y, Gao M, Zeng X (2018) Effects of alloying element on weld characterization of laser-arc hybrid welding of pure copper. *Opt Laser Technol* 102:124–129. <https://doi.org/10.1016/j.optlastec.2017.12.029>
21. Zhang LJ et al (2016) A comparative study on the microstructure and properties of copper joint between MIG welding and laser-MIG hybrid welding. *Mater Des* 110:35–50. <https://doi.org/10.1016/j.matdes.2016.07.117>
22. Lin JW, Chang HC, Wu MH (2014) Comparison of mechanical properties of pure copper welded using friction stir welding and tungsten inert gas welding. *J Manuf Process* 16(2):296–304. <https://doi.org/10.1016/j.jmapro.2013.09.006>
23. Mehta KP, Badheka VJ (2015) Materials and manufacturing processes a review on dissimilar friction stir welding of copper to aluminum: process, properties and variants March:37–41. <https://doi.org/10.1080/10426914.2015.1025971>
24. Ghosh M, Kar A, Kumar K, Kailas SV (2012) Structural characterisation of reaction zone for friction stir welded aluminium-stainless steel joint. *Mater Technol* 27(2):169–172. <https://doi.org/10.1179/175355509X12608916825994>
25. Hassan KAA, Norman AF, Price DA, Prangnell PB (2003) Stability of nugget zone grain structures in high strength Al-alloy friction stir welds during solution treatment. *Acta Mater* 51(7):1923–1936. [https://doi.org/10.1016/S1359-6454\(02\)00598-0](https://doi.org/10.1016/S1359-6454(02)00598-0)
26. Liu FC, Liao J, Nakata K (2014) Joining of metal to plastic using friction lap welding. *Mater Des* 54:236–244. <https://doi.org/10.1016/j.matdes.2013.08.056>
27. Muralimohan CH, Muthupandi V (2013) Friction welding of type 304 stainless steel to Cptitanium using nickel interlayer. *Adv Mater Res* 794:351–357. <https://doi.org/10.4028/www.scientific.net/AMR.794.351>
28. Kumar R, Balasubramanian M (2015) Application of response surface methodology to optimize process parameters in friction welding of Ti-6Al-4V and SS304L rods. *Trans Nonferrous Met Soc China* 25(11):3625–3633. [https://doi.org/10.1016/S1003-6326\(15\)63959-0](https://doi.org/10.1016/S1003-6326(15)63959-0)
29. Vyas HD, Mehta KP, Badheka V, Doshi B (2021) Processing and evaluation of dissimilar Al-SS friction welding of pipe configuration: nondestructive inspection, properties, and microstructure. *Meas J Int Meas Confed* 167(June 2020):108305. <https://doi.org/10.1016/j.measurement.2020.108305>
30. Types of Friction Welding—Bing images. <https://www.bing.com/images/search?view=detailV2&ccid=snuoidxJ&id=9237B7A681DE8A2D0A6BACEE33F61B7BFCD821C8&thid=OIP>. Accessed on 23 Oct 2020

31. Patel VV, Badheka V, Kumar A (2016) Friction stir processing as a novel technique to achieve superplasticity in aluminum alloys: process variables, variants, and applications. *Metallogr Microstruct Anal* 5(4):278–293. <https://doi.org/10.1007/s13632-016-0285-x>
32. Wang W et al (2020) Friction stir processing of magnesium alloys: a review. *Acta Metall Sin* 33(1):43–57. <https://doi.org/10.1007/s40195-019-00971-7>
33. Harwani DM, Badheka VJ, Patel VK (2021) Superplasticity: recent approaches and trends. Springer, Singapore, pp 387–397
34. AerospaceSuperform Aluminium. <https://www.superforming.com/aerospace>. Accessed on 23 March 23
35. Patel V, Badheka V, Li W, Akkireddy S (2019) Hybrid friction stir processing with active cooling approach to enhance superplastic behavior of AA7075 aluminum alloy. *Arch Civ Mech Eng* 19(4):1368–1380. <https://doi.org/10.1016/j.acme.2019.08.007>
36. Rana H, Badheka V, Kumar A, Satyaprasad A (2018) Strategic parametric investigation on manufacturing of Al–Mg–Zn–Cu alloy surface composites using FSP. *Mater Manuf Process* 33(5):534–545. <https://doi.org/10.1080/10426914.2017.1364752>
37. Gangil N, Maheshwari S, Siddiquee AN (2018) Multipass FSP on AA6063-T6 Al: strategy to fabricate surface composites. *Mater Manuf Process* 33(7):805–811. <https://doi.org/10.1080/10426914.2017.1415448>
38. Sharma A, Narsimhachary D, Sharma VM, Sahoo B, Paul J (2019) Surface modification of Al6061-SiC surface composite through impregnation of graphene, graphite & carbon nanotubes via FSP: a tribological study. *Surf Coatings Technol* 368:175–191. <https://doi.org/10.1016/j.surfcoat.2019.04.001>
39. Abbasi M, Bagheri B, Dadaei M, Omidvar HR, Rezaei M (2015) The effect of FSP on mechanical, tribological, and corrosion behavior of composite layer developed on magnesium AZ91 alloy surface. *Int J Adv Manuf Technol* 77(9–12):2051–2058. <https://doi.org/10.1007/s00170-014-6577-x>
40. Gdoutos EE (2020) *Composite Materials* 263
41. Rashidi A, Mostafapour A, Salahi S, Rezazadeh V (2013) Modified friction stir channeling: a novel technique for fabrication of friction stir channel. *Appl Mech Mater* 302:365–370. <https://doi.org/10.4028/www.scientific.net/AMM.302.365>
42. Wolf F (2016) (12) United States Patent (10) Patent No.: Primary Examiner—Snigdha Maewall 2(12)
43. Balasubramanian N, Mishra RS, Krishnamurthy K (2011) Process forces during friction stir channeling in an aluminum alloy. *J Mater Process Technol* 211(2):305–311. <https://doi.org/10.1016/j.jmatprotec.2010.10.005>



# Simulating Percentage of Workers Opting to Work from Home During the COVID-19 Pandemic Using N-Player Iterative Game Theory

Ayan J. Malhotra<sup>1</sup>(✉), Bhupender Singh<sup>1</sup>, Dev Surya<sup>1</sup>, and Anjana Gupta<sup>2</sup>

<sup>1</sup> Delhi Technological University, Delhi 110042, India  
ayanmalhotra13@gmail.com

<sup>2</sup> Professor, Department of Applied Mathematics, Delhi Technological University, Delhi 110042, India  
anjanagupta@dce.ac.in

## 1 Introduction

The novel coronavirus has affected the lives of a vast number of human beings as it not only poses a health risk but also a financial one. The decision to work from home during a pandemic can have serious implications. It can have extreme implications such as getting infected by the virus and facing financial difficulties and can even cause mental health issues [1]. Therefore, it is vital to know how a population will behave at a particular time instance of the outbreak. Estimating the percentage of the population following the guidelines is not only beneficial to the governing bodies but also for each individual who may be deliberating over this issue.

Game theory is a fascinating field of study and can be used to model several aspects of life and putting it into use to simulate such a relevant scenario was thus deemed rational. Game theory has vast applications in the field of understanding the behavior of participants in a certain game [2]. In our game, the players involved are the people residing in a certain city affected by the pandemic, and we will simulate their behavior, i.e., if they will work from home or not.

In this paper, we aim to simulate this situation logically and coherently and then implement the model for several cities having their unique infection curves. We hope that our project can help analyze the situation so that the readers can better understand the trade-off between working from home and being safe and working outside in the pursuit of more capital.

Our contributions are consolidated below:

- (1) We propose a novel model based on game theory to predict the behavior of a population affected by the COVID-19 pandemic
- (2) Our unique approach to simulate the environment with a well-structured method leads to results that one expects in the real-life scenario.

## 2 Related Work

Game theory in the past has been used to simulate a wide variety of events and scenarios. Talwariya et al. [3] used game theory to simulate a power tariff model for various industries. Wong et al. [4] used it to create an evacuation model during a disaster situation. Nguyen et al. [5] were able to imitate the behaviors of buyers and sellers in a market. Villar and Rudnick [6] predicted the actions of several players in a hydrothermal power market. Cheng et al. [7] created a multi-agent decision-making model to determine the measures taken by residents to live a sustainable lifestyle. In each of these games, the players involved are either cooperators or defectors where their behaviors and the current state of the system affect the future state of the system. Such a model provides a brilliant platform to incorporate any behavioral changes of the players.

In the previous papers, the utility functions of both cooperators and defectors in n-player iterative games are directly affected by the percentage of cooperators at any given time within a group in the system [8]. Here, the number of people cooperating in a particular scenario will affect the future states of the model and the algorithm should take this into account.

As the COVID-19 pandemic is a recent phenomenon, there is a lack of studies on this topic and whatever predictions we could find were simply based on percentages of workers belonging to a particular profession and how compatible that profession is with working from home. The previous studies are seemingly trivial [9]. Game theory has not been used to predict the given scenario before providing us a great opportunity to research this topic in the hope of finding any significant results.

## 3 Basics Related to Work

### 3.1 Evolving the Situation into a Game Theoretical Scenario

We developed our model for situations of conflict. Such situations and interactions are called games, and the participants in them are called players. In such conflicting games, two or more players may compete among each other for a certain utility or payoff at the expense of the other player [10].

In our model, we have taken our two players as two people living in a particular COVID-19 infected area. The players have the choice of either cooperating or defecting. The cooperators are the ones who follow the work from home guidelines. The defectors are the ones who do not obey the work from home guidelines and hence go outside to work. The payoff in this situation is determined by two factors, namely the financial gains and the other being the risk of getting infected by the coronavirus. In our model, we assume the chances of a certain person to get infected by the coronavirus as directly proportional to the number of persons present outside at any given instance of time [11, 12].

### 3.2 Two Player Game and Payoff Matrix

Let us say, we take our two players as A and B:

- If both A and B work from home, then both the players would have lesser chances of getting infected by COVID-19, however, their payoff would not be maximum as working from home will reduce the monetary gains they can acquire.
- If one out of A and B works from home and the other goes outside, the chances of getting infected by corona would be minimal, in addition to that the financial gains would also be higher for one of the players. Hence, the payoff would be higher.
- If both the players' A and B work from outside, the chances of getting infected by the coronavirus would be quite high and thus the payoff would be minimal, as the risk of being infected with the virus outweighs any financial gains (Table 1).

**Table 1** Sample payoff matrix for 2 player game

	Cooperator	Defector
Cooperator	30: 30	30: 40
Defector	40: 30	10: 10

### 3.3 Extension to N-Players

To extend our game to n-players and simulate a real-world environment, we need to create utility functions for both cooperators and defectors. Utility functions are a great way to model a scenario, where the ratio of cooperators and defectors determines the behavior of the players [13].

The utility function of the defectors is represented by the given equation,

$$u_d = mx + c_1$$

- Here,  $m$  denotes the slope of the graph and  $c_1$  denotes the payoff for the defectors when none of the people are working from their home, that is, when  $x = 0$ .
- When the value of  $x$  is zero, it means none of the people are working from their home and thus the risk of getting infected by the virus would be high and it outweighs any of the financial gains. Thus, the utility would be zero.
- The utility of the defectors would be maximum when  $x$  is 1 which means all the people are working from home. This would mean there would be no risk of any infection, and henceforth, the utility is maximum.

The utility function of cooperators is represented by the equation,

$$u_c = -mx + c_2$$

- Here,  $m$  denotes the slope of the graph and  $c_2$  denotes the payoff for the cooperators when none of the people are working from their home.
- When the value of  $x$  is zero, it means none of the people are working from their home, hence a cooperator would enjoy the maximum payoff as he would be having no risk of getting the virus even though the financial gains might be a little less.



- The utility of the cooperators would be minimum when  $x$  is one because when it is so all the people are working from home, and hence even though, the cooperator has no risk of getting the virus his payoff would be least as his financial gains would be quite low. The initial utility functions can be better visualized through Fig. 1.

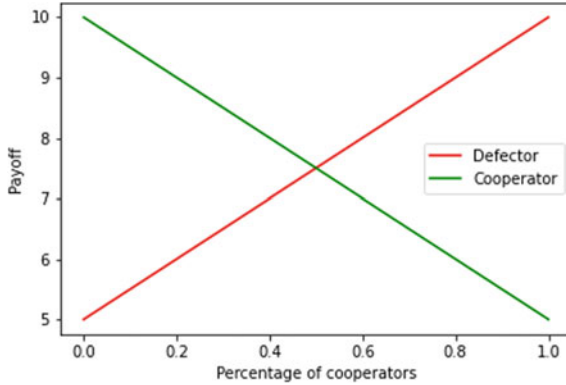


Fig. 1 Initial utility functions

### 3.4 Limitations of Initial Utility Functions

The one major limitation of our equations is that we have made an assumption considering all the factors as constant. However, in a real-world scenario, there are a lot of factors that come into the picture.

When the number of active cases in a given location increases, the workers would not step out of the house because of the imminent fear of getting infected by the virus. However, in the initial equations, we have not considered any such scenarios and assumed the situation to be static. Therefore, a need of adding factors that would account for the dynamic coronavirus scenario arises. These factors should take into account the rise and fall of active cases in a location and affect the utility functions and hence the decision-making of individuals in the area.

## 4 Methodology

### 4.1 Normalized Active Case Factor

The utility function used above fails to incorporate the current coronavirus situation of the state/union territory/city. Therefore, the need for a factor that accounts for the current scenario, for both cooperators and defectors, arises.

The number of active cases in a region highlights the current scenario to a great extent. The dataset for coronavirus cases in India [14] from the period of 9th September 2020 to 16th November 2020 was used to calculate the number of active cases in various

states/union territories for a period of hundred days. The active case data were then normalized by dividing the cases by the maximum number of cases during the given period [15]. This results in the formation of normalized active case factor ( $\alpha$ ), 0 representing the minimum number of active cases and 1 representing the maximum.

## 4.2 Average Growth Factor

Even though the active case factor ( $\alpha$ ) improves our model to a great extent, it mainly takes into account, the sudden changes in the situation. Therefore, we need another parameter that will help account for how fast the current situation is worsening, improving, or stabilizing.

We used the active case data to calculate the growth rate for each day during the given period [16]. While growth rate per day can oscillate often, taking an average growth rate for a period of 3 days, results in a parameter that does not change drastically. The calculated parameter is our average growth factor ( $\gamma$ ). Further, we normalized this factor using, and the range is transformed to [0–1], where 0 represents the lowest growth rate, and 1 represents the maximum growth rate.

## 4.3 Updated Utility Function Equations

Incorporating the factors mentioned above, the utility function equations are changed and represented as follows:

$$\begin{aligned} u'_d &= (mx + c_1) \times (2 - (\alpha + \gamma)) \\ u'_c &= (-mx + c_2) \times (\alpha + \gamma) \end{aligned}$$

These equations are more suitable as they depend not only on the fraction of cooperators and defectors rather also on the situation of the pandemic on any given day. For example, if say a new strain of the virus was introduced [17] into the society and the number of active cases grew rapidly, our modified utility function equations will take this into account and update accordingly.

$\alpha + \gamma$  will range from 0 to 2 and higher its value, higher is the current risk of going out, and hence the utility for defecting will decrease, whereas the utility for cooperating will increase.

## 4.4 Calculating Fraction of Cooperators and Defectors

Using updated utility functions, we will determine the ratio of cooperators and defectors for various cities and thus complete our simulation. The detailed procedure is given below in algorithm 1.

**Algorithm 1.** returns fraction of cooperators and defectors over a period of 100

**Input:** active case factor for a period of 100 days; average growth factor for a period of 100 days

**Output:** calculated percentage of cooperators and defectors for each day

**Parameter Initialization:** Initial percentage of cooperators ( $x$ ) = 0.5, Line constants ( $c1, c2$ ) = (this, this), Line slope ( $m$ ) = (slope)

**for** each  $\alpha, \gamma$  **do**

- 1) Declare  $y_{coopnew}$  and  $y_{defnew}$
- 2) Update  $y_{coopnew}$  and  $y_{defnew}$  using (eq no)
- 3) Declare  $y_{coopfactor}$  and  $y_{defactor}$
- 4) Assign  $y_{coopfactor} = \frac{y_{coopnew}}{y_{coopold}}$  and  $y_{defactor} = \frac{y_{defnew}}{y_{defold}}$
- 5) Declare  $a = x * y_{coopfactor}$
- 6) Declare  $b = (1-x) * y_{defactor}$
- 7) Update  $x = a / a + b$
- 8) Update  $y_{coopold} = y_{coopnew}$
- 9) Update  $y_{defold} = y_{defnew}$

**end for**

## 5 Experiments and Result

In this section, we provide a visual representation of our model through various graph plots. These graphs have been plotted for four Indian states suffering greatly from the COVID-19 pandemic, namely Delhi, Kerala, Karnataka, and Maharashtra. Further, multiple levels of initial cooperation have been considered varying from as low as 30% to as high as 70%. Values of other constants have been taken as presented in Algorithm 1.

Figure 2 depicts the simulation curves for various states while also showing the initial considerations. The simulation for each state is demonstrated by a set of two graphs, one displaying how the cooperators are varying versus the active case factor and the average growth rate on each day while the other pointing out the ratio of cooperators and defectors on each of the 100 recorded days. Hence, these graphs provide a holistic viewpoint of the entire scenario

## 6 Conclusion

The payoff is correctly predicted with the combination of a total number of active cases at a given point, the rate of growth of these cases, and the fraction of workers deciding

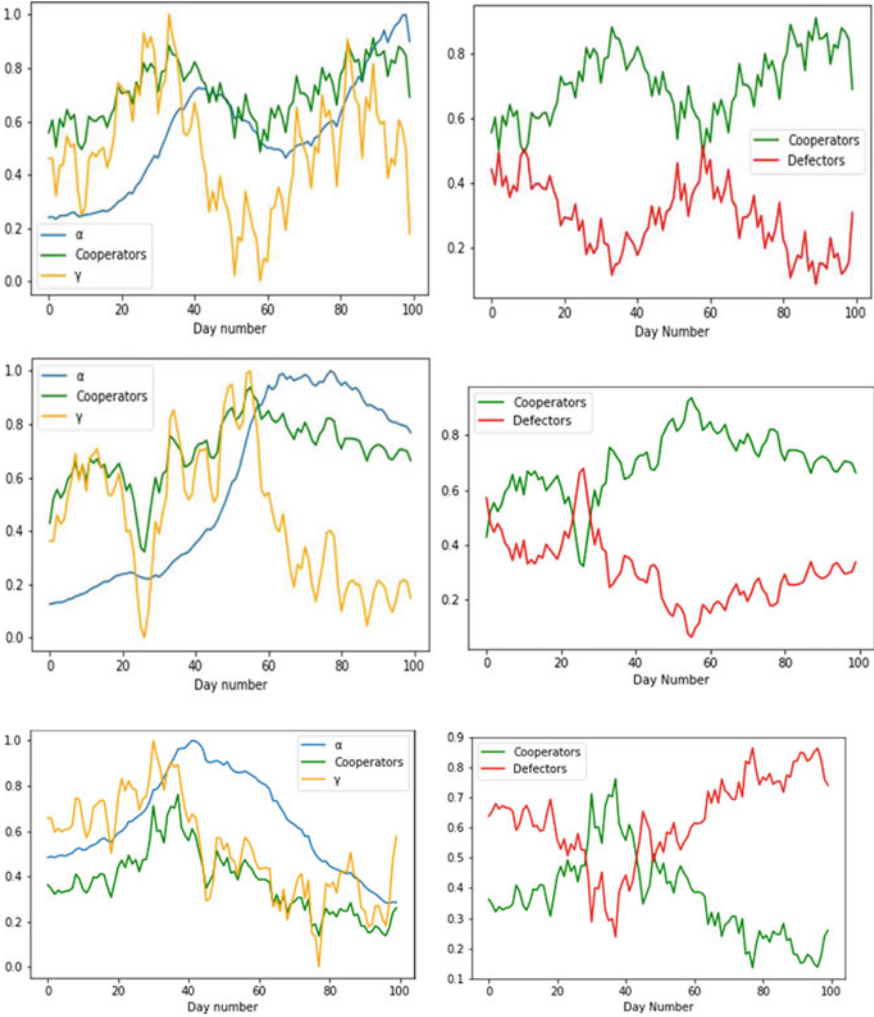


Fig. 2 Simulation curves for various states

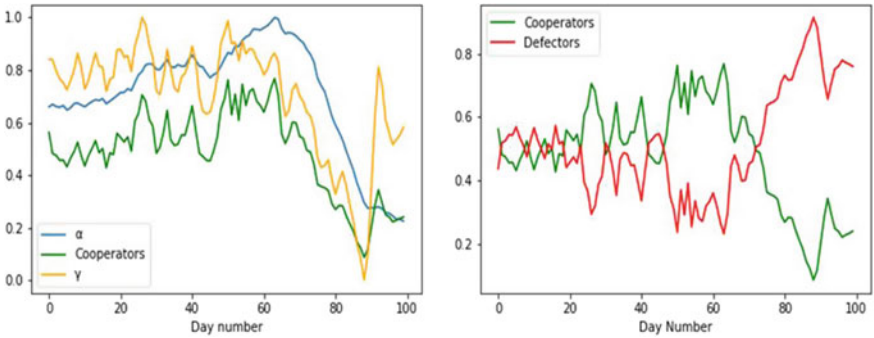


Fig. 2 continued

to cooperate. This trend continues in a cycle where the fraction of cooperators on the next day is dependent on the fraction of cooperators of the previous day.

There is a direct correlation between the total number of active cases and the growth rate with the percentage of players deciding to cooperate. The inclusion of the two factors in the utility equations correctly modifies the equations, and they allow the simulation to be more dynamic and versatile. The model will work smoothly while trying to predict the curves not only for a large population such as a city but also a small one such as a group of office employees.

The results of our simulation seem coherent to what one would expect to happen in a real-life scenario. Hence, our simulation predicts useful outcomes which can assist a governing body or an individual take a well-informed decision. However, our results can be improved/added upon using various techniques as discussed in the next section.

## 7 Future Scope

### 7.1 Creating Optimal Player Using Reinforcement Learning

In future, we plan on creating an optimal player which can maximize their payoff in various scenarios through machine learning. The agent will learn from various active case graphs present in several cities and their corresponding cooperator and defector.

### 7.2 Using Different Utility Functions

Currently, our initial utility functions presented in chapter 4 for both cooperators and defectors vary linearly with the fraction of cooperators. However, we may use functions that follow a polynomial or exponential curve. This may be used to incorporate the effect of several other factors as discussed in the limitations presented in chapter 8.3. To depict the above idea, you can see the equations of one such utility function following logarithmic activity down below:

$$\begin{aligned}
 u'_d &= (\log_2(1 + x) \times (2 - (\alpha + \gamma))) \\
 u'_c &= (\log_2(2 - x) \times (1 + (\alpha + \gamma)))
 \end{aligned}$$

As in the previous scenarios, these equations are dependent on normalized active case factor too. If the value of  $x$  is small, i.e., everyone is defecting, then the utility function value of the defectors will be minimized. In contrast, when  $x$  approaches 1, i.e., when everyone decides to stay at home, then the value of the utility function of defectors is maximized. This is in agreement with the ideas provided in the earlier parts of the paper.

### 7.3 Incorporating Other Factors

The fraction of workers working from home may be impacted by several other factors, and our work has not accounted for such as government policies and organizational policies. For example, if the government imposes a lockdown in a particular area, then

the residents will not have the freedom to make the decision of working from home or not. Other factors such as the presence of a vaccine will also affect the decision-making process of an individual.

We have simulated our model while considering every player similar to one another but in future, we can divide our players into clusters where players within the same cluster have similar features.

## References

1. Nicola M, Alsafi Z, Sohrabi C, Kerwan A, Al-Jabir A, Iosifidis C et al (2020) The socio-economic implications of the coronavirus and COVID-19 pandemic: a review. *Int J Surg* 75:185–193
2. Harsanyi JC (1997) Rational behavior and bargaining equilibrium in games and social situations. Cambridge University Press, Cambridge
3. Talwariya A, Singh P, Kolhe M (2019) A stepwise power tariff model with game theory based on Monte-Carlo simulation and its applications for household, agricultural, commercial and industrial consumers. *Int J Electr Power Energy Syst* 14–24
4. Wong SK, Chou YH, Yang HY (2018) A framework for simulating agent-based cooperative tasks in crowd simulation. In: Proceedings of the ACM SIGGRAPH symposium on interactive 3D graphics and Games, 15–18 May, Montreal, Quebec, Canada, pp 1–10
5. Nguyen HK, Song JB, Han Z (2012) Demand side management to reduce peak-to-average ratio using game theory in smart grid. In: 2012 IEEE Conference on computer communications workshops (INFOCOM WKSHPS). IEEE
6. Villar J, Rudnick H (2003) Hydrothermal market simulator using game theory: assessment of market power. *IEEE Trans Power Syst* 1(18):91–98
7. Cheng X, Long R, Chen H, Yang J (2019) Does social interaction have an impact on residents' sustainable lifestyle decisions? A multi-agent stimulation based on regret and game theory. *Appl Energy* 251
8. Fletcher J, Zwick M (2000) N-player prisoner's dilemma in multiple groups: a model of multilevel selection
9. Van der Lippe T, Lippényi Z (2019) Co-workers working from home and individual and team performance. *N Technol Work Employ* 35(1):60–79. <https://doi.org/10.1111/ntwe.12153>
10. Peters H (2008) Game theory—a multileveled approach. Springer, Berlin
11. Hu H, Nigmatulina K, Eckhoff P (2013) The scaling of contact rates with population density for the infectious disease models. *Math Biosci* 244:125–134
12. Kodera S, Rashed EA, Hirata A (2020) Correlation between COVID-19 morbidity and mortality rates in Japan and local population density, temperature, and absolute humidity. *Int J Environ Res Public Health* 17(15):5477
13. Bell R, Buchner A, Musch J (2010) Enhanced old–new recognition and source memory for faces of cooperators and defectors in a social-dilemma game. *Cognition* 117:261–275. <https://doi.org/10.1016/j.cognition.2010.08.020>
14. SRK and others. March, 2020. Covid 19 in India, Version 215. Retrieved December, 2020 from <https://www.kaggle.com/sudalairajkumar/covid19-in-india>.
15. Vafaei N, Ribeiro RA, Camarinha-Matos LM (2016) Data normalization techniques in decision making: case study with TOPSIS method. *Int J Inf Decis Sci* (in press)
16. de Silva E, Ferguson NM, Fraser C (2012) Inferring pandemic growth rates from sequence data. *J R Soc Interface* 9:1797–1808
17. Iacobucci G (2021) Covid-19: new UK variant may be linked to increased death rate, early data indicate. *BMJ* 372(230). <https://doi.org/10.1136/bmj.n230>, pmid: 33500262



# Selection of Ride Frequency for an ATV based on a Full Car Vehicle Model

Atul Singh<sup>(✉)</sup>, Ayush Venkat Vats, Sahil Sharma, and Vikas Rastogi

Department of Mechanical Engineering, Delhi Technological University, Shahbad Daultapur,  
Main Bawana Road, New Delhi 110042, India  
atul.singh3787@gmail.com

## Mathematical Notations

$k_{sf}$	Stiffness of front spring
$k_{sr}$	Stiffness of rear spring
$m_s$	Sprung mass
$C_{sf}$	Damping stiffness of front suspension
$C_{sr}$	Damping stiffness of rear suspension
$K_t$	Tire stiffness
$Z_{cg}$	Displacement of cg
$Z_r$	Displacement of road
$Z_{fr}$	Displacement of front right wheel
$Z_{fl}$	Displacement of front left wheel
$Z_{rr}$	Displacement of rear right wheel
$Z_{rl}$	Displacement of rear left wheel
$I_x$	Moment of inertia in roll
$I_y$	Moment of inertia in pitch
$a$	Distance between front tire center and CG in longitudinal direction
$b$	Distance between rear tire center and CG in longitudinal direction
$c$	Distance between tire center and CG in lateral direction
$m_f$	Unsprung mass of front right/left wheel
$m_r$	Unsprung mass of rear right/left wheel
MR	Motion ratio
$\Theta$	Roll angle
$\phi$	Pitch angle

## 1 Introduction

Suspension is an arrangement of springs, shock absorbers, and other linkages that connects a vehicle to its wheels and allows relative motion between the two. The suspension system performs the task of reducing the vertical forces and maintaining contact between the wheel and the ground, through an assembly of springs, dampers, and other suspension

linkages. Its configuration maintains a reasonable compromise between ride handling and ride quality. A brief review of past literature shows that a lot of research has been conducted on modeling of suspension systems. Generally, quarter car, half car, and full car models are used for the purpose of modeling suspension dynamics.

Hedrick [1], Gobbi [2] studied the quarter car models of vehicle dynamics. Hedrick [1] used a quarter car model with hydraulic actuator under the effect of Coulomb friction. Gobbi [2] studied dynamic responses of a suspension on a rough road using 2 sensors, one for velocity and the other for displacement. Lin [3] performed a time-domain direct identification for vehicle mass, damping, and stiffness on a half car model. Barbosa [4] studied the frequency response caused by pavement roughness on a half car model. Phalke and Mitra [5] analyzed ride comfort and road holding of a quarter car model by Simulink. Can et al. [6] analyzed chaotic behaviors in a half car model using road surface profile. PSA Singh [7] used fuzzy logic to analyze full car models. Li [8] performed computer simulation studies through multi-body model, identifying twenty degrees of freedom. Puneet et al. [9] used multi-objective genetic algorithm (MOGA) to optimize the input parameters for better ride comfort and road holding.

Generally, the literature on this topic is based on arriving at an appropriate model using different methodologies and subsequent study of various aspects of vehicle dynamics. The present research work in addition to constructing a full car 7-DOF model also describes a methodology for selecting the ride frequency of an all-terrain vehicle. This will prove very useful for people working in the domain of vehicle dynamics and ride frequencies.

## 2 Mathematical Model

The following figure shows a full car model with 7-degree of freedom (DOF) which involves the vertical displacement of the four unsprung masses, motion of the sprung mass, pitch, and roll motion of the vehicle (Fig. 1).

Some important assumptions made in this model are

1. Aerodynamic effects are neglected.
2. The vehicle is assumed to be rigid.
3. Model parameters such as stiffness and damper coefficient are assumed to be invariant with time (Table 1).

### 2.1 Equations

- (1) Vertical equilibrium of sprung mass:

$$\begin{aligned}
 m_s \ddot{Z}_{cg} = & -(2k_{sf} + 2k_{sr})Z_{cg} - (2C_{sf} + 2C_{sr})\dot{Z}_{cg} + (2aK_{sf} - 2bK_{sr})\phi \\
 & - (2aC_{sf} - 2bC_{sr})\dot{\phi} + K_{sf}Z_{fl} + C_{sf}\dot{Z}_{fl} + K_{sr}Z_{rl} + K_{sr}Z_{rr} \\
 & + C_{sr}\dot{Z}_{rr} + k_{sf}Z_{fr} + C_{sf}\dot{Z}_{fr} + C_{sr}\dot{Z}_{rl}
 \end{aligned} \tag{1}$$



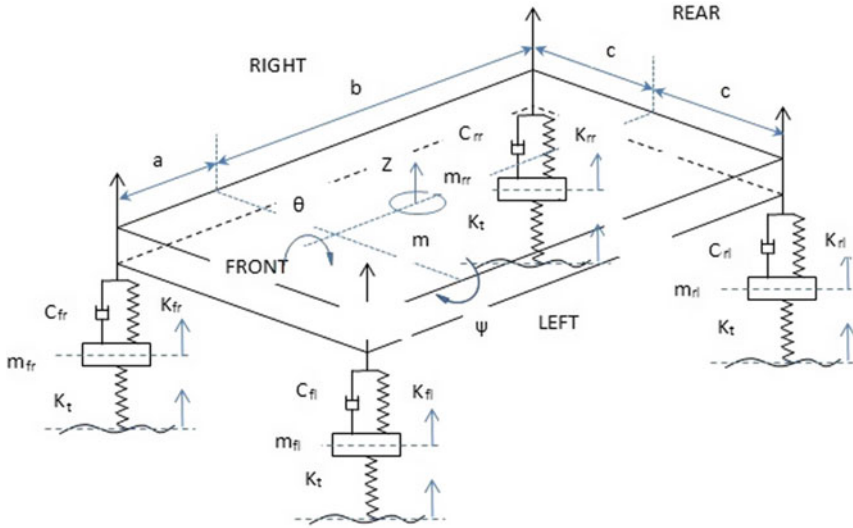


**Fig. 1** Full car model of an ATV

(2) Pitch equilibrium of sprung mass:

$$\begin{aligned}
 I_y \ddot{\phi} = & (2aK_{sf} - 2bK_{sr})Z_{cg} + (2aC_{sf} - 2bC_{sr})\dot{Z}_{cg} - (2a^2K_{sf} + 2b^2K_{sr})\phi \\
 & - (2a^2C_{sf} + 2b^2C_{sr})\dot{\phi} - aK_{sf}Z_{fl} - aC_{sf}\dot{Z}_{fl} - aK_{sf}Z_{fr} - aC_{sf}\dot{Z}_{fr} \\
 & + bK_{sr}Z_{rl} + bC_{sr}\dot{Z}_{rl} + bK_{sr}Z_{rr} + bC_{sr}\dot{Z}_{rr}
 \end{aligned} \tag{2}$$

**Table 1** Parameters of the system

S. No.	Parameters	Value	Units
1	$m_f$	15	kg
2	$m_r$	15	Kg
3	$m_s$	160	kg
4	$C_s$	200	N s/m
5	$I_x$	50	Kg*m <sup>2</sup>
6	$I_y$	60	Kg*m <sup>2</sup>
7	$a$	460	mm
8	$b$	690	mm
9	$c$	550	mm
10	$K_t$	55,000	N/m

(3) Roll equilibrium of sprung mass:

$$I_x \ddot{\theta} = -c^2(2k_{sf} + 2k_{sr})\theta - c^2(2c_{sf} + 2c_{sr})\dot{\theta} + cK_{sf}Z_{fl} - cK_{sf}Z_{fr} - cC_{sf}Z_{fr} + K_{sr}Z_{rl} + cC_{sr}Z_{rl} - cK_{sr}Z_{rr} - cC_{sr}Z_{rr} \quad (3)$$

(4) Vertical equilibrium of unsprung mass 1:

$$m_f \ddot{Z}_{fl} = k_{sf}(Z_{cg} - Z_{fl} - c\theta + a\phi) - C_{sf}(\dot{Z}_{cg} - \dot{Z}_{fl} - c\dot{\theta} + a\dot{\phi}) - k_t(Z_{fl} - Z_{r1}) \quad (4)$$

(5) Vertical equilibrium of unsprung mass 2:

$$m_f \ddot{Z}_{fr} = k_{sf}(Z_{cg} - Z_{fr} + c\theta + a\phi) - C_{sf}(\dot{Z}_{cg} - \dot{Z}_{fr} + c\dot{\theta} + a\dot{\phi}) - k_t(Z_{fr} - Z_{r2}) \quad (5)$$

(6) Vertical equilibrium of unsprung mass 3:

$$m_r \ddot{Z}_{rl} = k_{sr}(Z_{cg} - Z_{rl} - c\theta - b\phi) - C_{sr}(\dot{Z}_{cg} - \dot{Z}_{rl} - c\dot{\theta} - b\dot{\phi}) - k_t(Z_{rl} - Z_{r3}) \quad (6)$$

(7) Vertical equilibrium of unsprung mass 4:

$$m_r \ddot{Z}_{rr} = k_{sr}(Z_{cg} - Z_{rr} + c\theta - b\phi) - C_{sr}(\dot{Z}_{cg} - \dot{Z}_{rr} + c\dot{\theta} - b\dot{\phi}) - k_t(Z_{rr} - Z_{r4}) \quad (7)$$

### 3 Methodology

A full car model was developed using free body diagram for all 5 masses (4 unsprung and 1 for sprung mass). In this way, a system of 7 s order differential equations was developed.

1. Four equations representing the acceleration of the unsprung masses.
2. One equation representing the acceleration of the sprung mass.
3. One equation each representing roll and pitch.

The disturbance generated by the road profile was used as an input in these 7 equations. To solve these second order differential equations, we prepared a Simulink model.

Assuming the system to be at equilibrium at  $t = 0$ , we use the initial values to solve for the output variables. Thus, the solution of these equations gave function of output variables w.r.t. time. For assessing the performance of the model, a frequency range was selected based on the data available for passenger on which the model was to be simulated.

$$f_{(\text{rear})} = 1 \text{ Hz} - 2 \text{ Hz} \quad (8)$$

$$(f_{(\text{rear})} - 0.5) < f_{(\text{front})} < (f_{(\text{rear})} + 0.5) \quad (9)$$

The above scheme gives us a total of 121 combinations of frequency at the front and the rear. Using these frequency combinations, we then calculated the spring stiffness at the front and the rear for substituting in the equations.

$$K_{sf} = (4\pi^2 F_{\text{front}}^2 m_f) / (MR)^2 \tag{10}$$

$$K_{sr} = (4\pi^2 F_{\text{rear}}^2 m_r) / (MR)^2 \tag{11}$$

Substituting the values of  $K_f$  and  $K_r$  as obtained above, a Simulink model was built for each combination (through looping). Disturbances were applied to the model, and the response of the model was studied under all combinations.

To select the frequency combination which gives optimum results, we select the combination which minimized

- (i) roll (20% weightage)
- (ii) pitch (60% weightage)
- (iii) sprung mass displacement (20% weightage).

Of the vehicle body. The final results of mean pitching, mean roll, and mean sprung mass displacement were calculated for each combination. These values were then normalized, and their weighted average was used for comparisons. The frequency combination which gave the minimum weighted average for these variables is finally selected (Fig. 2).

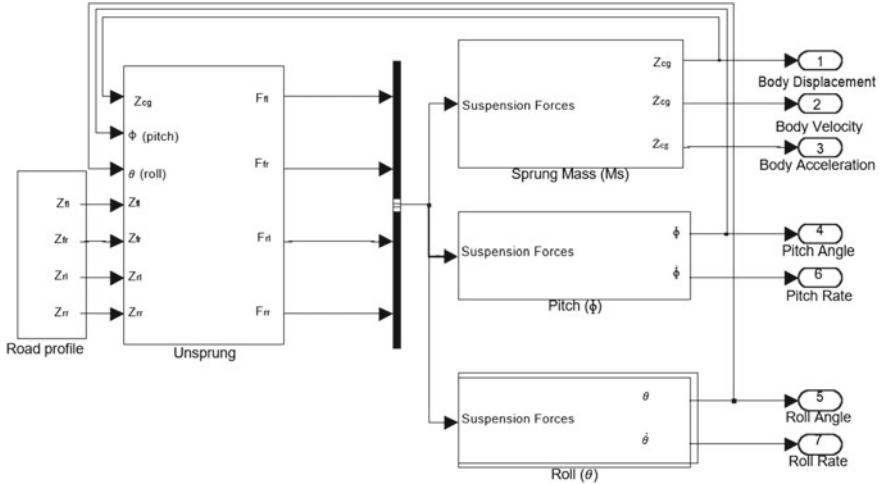
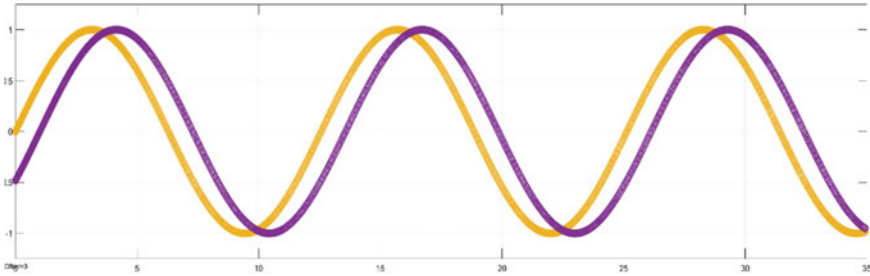


Fig. 2 Simulink block diagram

### 4 Model Validation

Conventionally, it is considered that the frequency of the rear of a vehicle should be kept different from the front. The reason the front and rear have different ride frequencies is

to reduce the pitch of the vehicle over bumps. The rear ride frequency is typically higher than the front so that after encountering a bump, the rear will “catch up” with the front, and the front and rear will move in phase. This assertion is proved valid by the results obtained by our model (Figs. 3 and 4).



**Fig. 3** Phase lag at the front and rear of the vehicle when encountering a bump

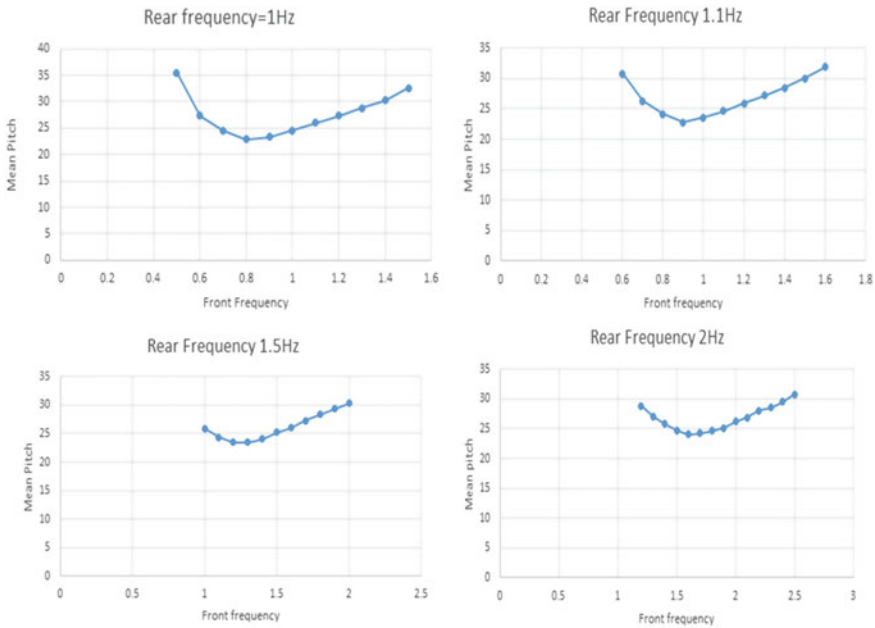


**Fig. 4** Variation of mean pitch w.r.t front frequency for a given rear frequency

In the above graphs, the rear ride frequency of the vehicle has been kept constant, and the front ride frequency (x-axis) is varied. The mean pitch for the simulation is then plotted as a function of front frequency.

Through the results obtained, it is observed that the value of mean pitch (average pitch angle for the whole ride) is minimized when the ride frequency at the front of the

vehicle was about 20% lower than the rear. Thus, the conventional assumption can be validated.

### 5 Results and Discussion

As discussed above, the objective of this paper is to find the ride frequency of an ATV using a full car model, and while doing this, it is found that the simulation results for the values of all the different parameters are consistent with the simulation conditions. They vary in a periodic fashion, similar to the sinusoidal disturbance to which they are subjected to.

The weighted average of mean pitch, mean roll, and mean sprung mass displacement is considered, to select the best combination of ride frequency at the front and rear. The table below shows the set of frequencies for the rear and front of the vehicle and their weighted average. Here in our study, we have given maximum weight to pitch and equal weights to roll and CG displacement (Table 2).

**Table 2** Frequency combinations

Front frequency (Hz)	Rear frequency (Hz)	Weighted average = (60 * pitch) + (20 * roll) + (20 * cg displacement)
0.8	1	54.387
1	1.2	53.606
1.2	1.5	62.199
1.4	1.7	64.842
1.6	2.0	72.219

To arrive at the final result, the frequency combination which has the minimum weighted average should be selected since it maximizes the stability. Accordingly, the combination with 1 Hz as the front frequency and 1.2 Hz as the rear frequency turns out to be the winner in our analysis.

In general, it is observed that combinations with higher frequencies increase the sprung mass displacement and therefore should be avoided.

### 6 Conclusion

The 7-DOF model of a full car vehicle has thus been successfully constructed and validated on Simulink. The results obtained from the model are quite close to established principles of vehicle dynamics. The frequencies obtained this way also provided the car with excellent performance in real-life scenarios. This model can be easily used in future to obtain optimum ride frequency for different configurations of the vehicle. However, there is further scope for validating all the results obtained through this model in many different real-life scenarios in future. Other different modeling techniques such as genetic

algorithm and fuzzy logic can also be used to carry out such simulations. More accurate assumptions about the chassis and tires of the car can also be used in future. Altogether there are many bright avenues for future research work.

## References

1. Hedrick JK (1992) Nonlinear control of a quarter car active suspension. In: Proceedings of the American control conference, Chicago, June 1992
2. Gobbi M, Mastinu G (2001) Analytical description and optimization of the dynamic behaviour of passively suspended road vehicles. *J Sound Vib* 245(3):457–481
3. Lin Y, Kortum W (2007) Identification of system physical parameters for vehicle systems with nonlinear components. *Int J Vehicle Mech Mobil* 46(12):354–365
4. Barbosa RS (2012) Vehicle vibration response subjected to long wave measured pavement roughness. *J Mech Eng Autom* 2(2):17–24
5. Phalke TP, Mitra AC (2017) Analysis of ride comfort and road holding of quarter car model by SIMULINK. *Mater Today Proc* 4(2):2425–2430
6. Can W, Weirui W (2009) Chaotic behaviors of half car model excited by the road surface profile. *Information science and engineering (ICISE)*. In: 2009 1st international conference, pp 3752–3755, Nanjing, China, 18–20 Dec 2009
7. Singh PSA, Darus IZM (2011) Enhancement of SUV roll dynamics using fuzzy logic control. *Informatics and computational intelligence (ICI)*. In: 2011 first international conference, pp 106–111. Bandung, Indonesia, 12–14 Dec 2011
8. Li L, Li Q (2007) Vibration analysis based on full multi-body model for the commercial vehicle suspension system. In: Proceedings of the 6th international conference on signal processing, robotics and automation, Greece, February 2007, pp 203–207
9. Puneet NP, Hegale A, Kumar H, Gangadharan KV (2021) Multi objective optimization for quarter car parameters for better ride comfort and road holding
10. Hajkurami H, Samandari H, Ziaei-Rad S (2009) Analysis of chaotic vibration of nonlinear seven degree of freedom full car model. In: 3rd International conference on integrity, reliability and failure, Portugal, July 2009
11. Al-Ghanim A, Nassar A (2017) Modeling, simulation, and control of half car suspension system using Matlab/Simulink
12. Giaraffa M. *Tech Tip: Springs & Dampers*
13. Kamalakkannan K, Elayperumal A, Managalararamam S (2012) Simulation aspects of a full-car ATV model semi active suspension. *J Sci Res Eng* 4:384–389
14. Wang F-C (2001) Design and synthesis of active and passive vehicle suspensions. University of Cambridge, A PhD dissertation, September 2001
15. Alenezi A (2014) Active suspension control based on a full-vehicle model. *IOSR J Elect Electron Eng (IOSR-JEEE)* 9(2 Ver. VI):6–18, e-ISSN: 2278–1676, p-ISSN: 2320–3331
16. Niresh J, Archana N, Raj G (2019) Optimisation of linear passive suspension system using MOPSO and design of predictive tool with artificial neural network



# Design, Fabrication, and Testing of a Solar Powered Air Purifier with UV Sterilization Capability

Akhilesh Arora, Kanish Bhardwaj<sup>(✉)</sup>, Naved Esmail, and Pushkar Dhar Dubey

Department of Mechanical, Production and Industrial and Automobile Engineering, Delhi Technological University, Delhi, India

kanishbhardwaj\_2k17pe24@dtu.ac.in

## 1 Introduction

Pure air is the most basic need for sustenance of sound lives of human species and its supplementary ecosystems, largely responsible for the human welfare. Extensive industrialization and rational nature of humans have led to the discharge of numerous gaseous emissions and particulate matter (PM). As a result, various kinds of emissions are being pushed into the ambient air (known as primary pollutants) and are contributing to the formation of novel contaminants through biochemical reactions in the ambient air (known as secondary pollutants). Because of all these concerns, atmospheric air pollution has become a pre-eminent worldwide threat to human health to a great extent. For example, “almost all the climate-changing contaminants (barring carbon-dioxide) are toxic for the health, either directly or by adding to the secondary contaminants in the ambient air” (*Fifth Assessment Report, IPCC, 2018*).

Air pollution in the cities is chiefly an outcome of fossil fuel combustions which are essential for goods and people’s transportation, industries, power production, and other activities related to economy. Indoor air pollution (IAP), which was earlier dominant in the rural areas, has now become a greater problem in the urban areas, and it has become imperative to use different methods for air purification. As a result, air purifiers have become a necessity. They can be used in homes, commercial places, offices, outdoors (if their efficiency is high), etc. The use of air purifier is not a very new concept rather it has been in use since 1823, when John Deane was awarded with a patent for his “smoke helmet.” Subsequently, advancements were made in 1860s and 1870s but the biggest breakthrough came in picture in 1950, when the HEPA filters were commercialized. With the ever-rising air pollution post 1980s, this field has gain immense importance and new technological advancements are being made with passing days to effectively curb the air pollution. We are residents of the second most polluted city in the world, Delhi (India). The situation sometimes becomes so challenging, it becomes difficult for us to even step out of our houses. So, while growing up in such a city, a natural query which comes to us is that “who will save us from this problem?” By God’s grace, we got a chance to work on this problem, and we have tried our best in making a contribution

in whatever way possible to fight this problem. Also, most of the purifiers available in the Indian market were either costly or were not very much effective.

The primary objective of making this device is to a low-cost affordable solar powered air purifier that can be installed in each and every house indoor as well as outdoors catering to the air quality indoors and contributing in purifying air of the outside environment. In order to achieve our goal, we pursued the project with the following conditions and constraints in mind:

- Designing an efficient air purifier
- Selection of best design
- Cost effective and easy manufacturing
- Renewable source of power supply
- Combating the harmful microbials
- Low cost of overall device

“According to data in 2019, 1.6 million deaths were reported in India due to air pollution.” So, the use of air purifiers has become very essential nowadays, and during these COVID-19 times, our UV-C sterilized air purifier could be a bane for numerous lives throughout India as well. The paper mainly focuses on the global burden of air pollution (mainly in Indian context) and tries to prove our claims in regard of our air purifier.

**National Air Quality Index:** At the present time, it is extremely important for citizens to be aware about level at which the air is polluted on a daily basis, especially for those suffering from diseases caused due to exposure to polluted air. Indian National Air Quality Standards (INAQS) has devised AQI system in India. The AQI system is based on maximum operator of a function (i.e., selecting the maximum of subindices of individual pollutants as an overall AQI). The primary objective of AQI is to give information regarding air quality at that instant which accounts for pollutants that have short-term impacts. Eight parameters (PM<sub>2.5</sub>, PM<sub>10</sub>, SO<sub>2</sub>, NO<sub>2</sub>, CO, O<sub>3</sub>, NH<sub>3</sub>, and Pb) are considered to calculate the AQI at that very instant. Table 1 provides the AQI, its corresponding remarks, and based on these possible health impacts (Table 2).

**Table 1** Air quality index

AQI	Remarks	Color Scheme	Impact on Health
0-50	Good		Minimal impact
51-100	Satisfactory		Sensitive people face minor discomfort in breathing
101-200	Moderate		Breathing discomfort to the people with lung diseases, asthma and heart diseases.
201-300	Poor		Prolonged Exposure leads to breathing discomfort in most people
301-400	Very poor		Prolonged exposures lead to respiratory track issues
401-500	Severe		Affects healthy people and has serious impacts on those with diseases



**Table 2** Health impacts of pollutants

Pollutants	Sources	Health impacts
Particulate matter	Dust from paved roads, industrial processes, power plants, etc.	Breathlessness, nasopharyngitis, increased infant mortality rate, and longer exposures can cause cardiovascular disease
Nitrogen oxides (NO <sub>x</sub> )	By-product of the combustion in IC engines; predominant in the diesel engines	Coughing, wheezing, dyspnea, bronchospasm, if high concentrations are inhaled, some cases have even reported pulmonary edema
Sulfur oxides (SO <sub>x</sub> )	Product of combustion in the IC engines; predominant in the petrol engines	Irritation in nose, throat and eyes, bronchitis, mucus production, and bronchospasm, it irritates sensory organs and even penetrates deep into the lungs, also cause bronchoconstriction
Carbon monoxide (CO)	Incomplete combustion	CO combines with hemoglobin and decreases oxygen carrying capacity of blood causing dizziness, nausea, hallucinations, paralysis (in severe cases), and even death; greenhouse gas
Lead	Lead smelters, lead-acid battery, piston-engine aircraft operating on leaded aviation fuels, etc.	Severe impact on health of new born babies or fetus, degrades thinking capacity, cognitive skills, and effects mental health in children, carcinogenic
Volatile organic compounds (VOCs)	Generally found in greater quantities indoors due to burning of fuels for cooking and use of edible oils	Carcinogenic, irritates eyes, nose and throat, and other mucosal membranes

The main focus of an air purifier has been on separating the suspended particles from air which are the major contributors in air pollution. Some models use the principle of adhesion to separate the pollutant particles suspended in the air, a liquid is sprayed, and due to adhesion, the pollutants stick to liquid particles which increase in weight, and due to gravity, they settle down, thereby getting separated, leaving behind clean air [1]. Air filtration technique can remove air pollutants and effectively alleviate the deterioration of indoor air quality. Air filtration technologies can be evaluated on parameters such as air quality improvement, filtering performance, energy and economic behavior, thermal comfort, and acoustic impact [2]. UV-C light can inactivate viruses

such as SARS-CoV-2(COVID-19) [3]. The inactivation of bacterial and fungal spores by UV-C irradiation and gaseous iodine treatment can be applied to air handling filters. Bio-defense and indoor air quality communities are paying interest in the assessment and control of exposure to bacterial and fungal spores that are re-aerosolized from air filters and create major health risks. Bacteria and fungi from the air can be inactivated using UV-C radiation [4].

## 2 Methodology

### 2.1 Design

Iterations 1 and 2 of the designing phase were similar, having a cuboidal shape as the main body. The only difference between the two was in order of the filters. In iteration 2 (see Fig. 1), the pre-filter was placed outside the inlet fan, so that the large pollutants which could enter directly into inlet fan and choke it in longer run were trapped. Following this, the air passes through the HEPA filter, then the activated carbon filter and finally the UV-C sterilization.

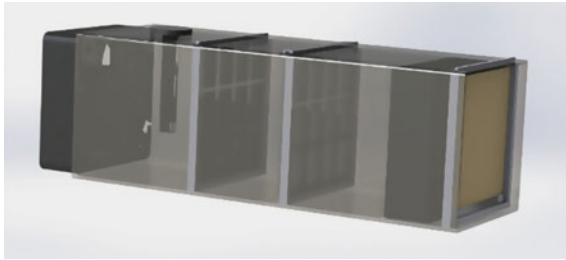


**Fig. 1** Iteration 2

In the 3rd iteration (see Fig. 2), a venturi shaped body was taken which has greater air flow, and it was esthetically more pleasing as well. The important replaceable filters were given in the throat section (for easy replaceability) which was one of our main objectives. Also, the comparative air flow analysis has shown that our proposed design has a higher airflow through the air purifier, which itself is a poof of its higher efficiency.

### 2.2 Components

- **Inlet and Outlet Fan:** To facilitate air flow within the purifier, inlet and outlet fans are used. These fans were equipped with 2600 rpm. For this purpose, we have used the axial fan (exhaust fan) (see Fig. 8d).
- **Pre-filter (Nylon Cloth):** A pre-filter is basically a wall or a guard to stop larger particles before it can enter the main filter. It is important for maintaining long life of the main filter by decreasing the load on the main filter (see Fig. 8f).

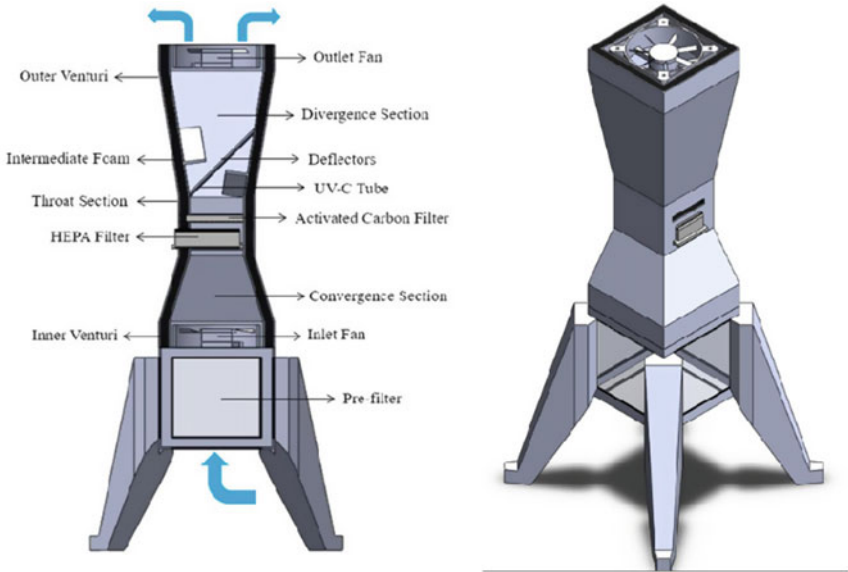
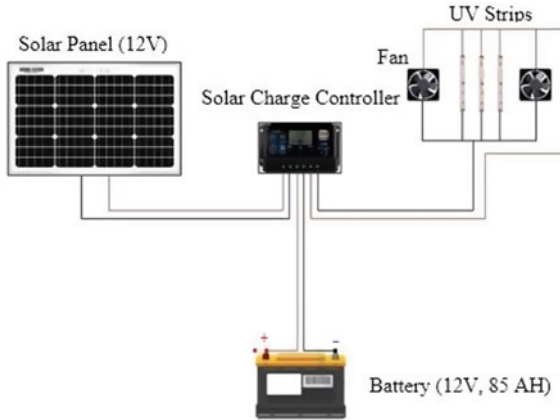


Fig. 2 Final design

- **High-efficiency Particulate Air Filter (HEPA):** This is the filter which removes about 99.97% of the unnecessary air particles having a diameter of 0.3 micron. But for particles having a diameter more or less than this, it has a greater efficiency. It can even reduce odor (see Fig. 8c).
- **Activated Carbon Filter:** In catering the indoor pollutions which we generally think are pollution free, this filter plays major role as it gets rid of are plenty of organic chemicals due to cooking, in furniture PET odor, moisture, and oil paints (see Fig. 8a, b).
- **UV-C Filter:** Recent studies have shown that UV-C light has been effective in neutralizing COVID-19 virus. UV-C light destroys various microbes (bacteria and annihilate viruses, molds, and yeasts). It is used for sterilization and is quite effective in neutralizing chemical fumes, cigarette smoke, and bad odor (see Fig. 8e).
- **Solar Power System:**
  - *Solar Panel:* Using sunlight as a source of energy, solar panels absorb it to generate electricity or heat. The electricity generated by the solar panel is stored in a battery (see Fig. 3).
  - *Battery:* It is the storehouse of energy which can be extracted as per the requirement (see Fig. 3).
  - *Charge Controller:* Overcharging and overvoltage are the problems which are faced in the electrical circuits. Basically, the rate at which electric current is added to or drawn from electric batteries is limited by a charge controller (see Fig. 3).

### Selection of Battery for Power Storage:



**Fig. 3** Solar power system

*Total Wattage/Max. Wattage of system:*  $45 * 2$  (2 Fans) +  $3 * 3$  (3 UV-C Strips) = 99 watts

*Daily Energy Usage:*  $99 * 5 = 495$  watt-hours

*Battery Bank Capacity:*  $495 * 1 * 2 = 990$  watt-hours (To accommodate for battery discharge and a battery backup of 1 day) =  $990/12$ (System Voltage) = 82.5 AH.

### 2.3 Design Analysis

#### Structural Analysis

*Total Deformation:* The maximum deformation that occurred in the structure was of 0.04 mm, and minimum deformation that occurred was of 0 mm (see Fig. 4).

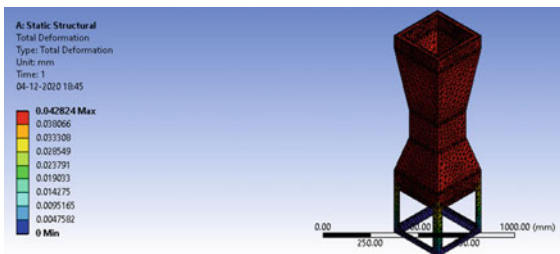


**Fig. 4** Total deformation (mm)

*Equivalent (Von Mises) Stress:* The maximum stress undergone by the structure due to the applied load was of 0.241 MPa, and the minimum stress undergone was of 0.026 MPa (see Fig. 5).

#### Air Flow Analysis

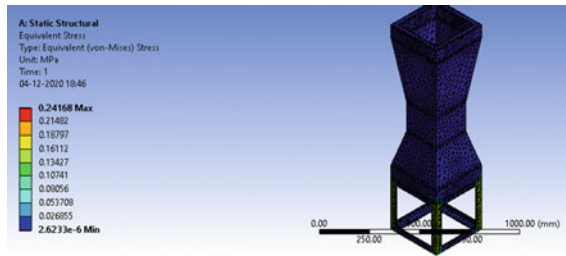


**Fig. 5** Equivalent stress (MPa)

*Velocity Variations:* From the analysis of air flow (inlet velocity was obtained running the inlet fan at 2600 RPM), it is observed that the velocity is found to increase in the throat of the venturi and reaches to a maximum value of 39 m/s compared to the inlet stream velocity of 13 m/s. So, we can observe that by setting the convergence angle at 15 deg. We are able to attain a velocity multiplication of 3x (see Fig. 7) (Fig. 6).

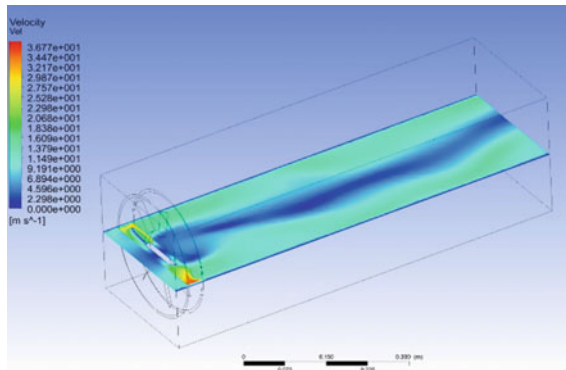


**Fig. 6** Velocity variations (cuboidal design)

The image below depicts the air flow through the venturi. In the divergence cone, it can be observed that deflectors added in the 3rd design iterations come into play as they deflect the air and reduce the air speed so that the UV-C strips can disinfect the viruses in the air (see Fig. 7) (Fig. 8).

## 2.4 Model Fabrication

The body of the purifier prototype was manufactured in the shape of a venturi with an intention of increasing the air flow inside the purifier. The body material was Sunpack Sheets (polypropylene reinforced with glass fiber) with medium density fiber (MDF) sheets at section ends and the exhaust fans. The gap between the outer and inner venturi was decided to be covered with the help of a high-density foam (Thermocole a.k.a polystyrene). All the filters were placed as planned in the design phase (refer Fig. 3).

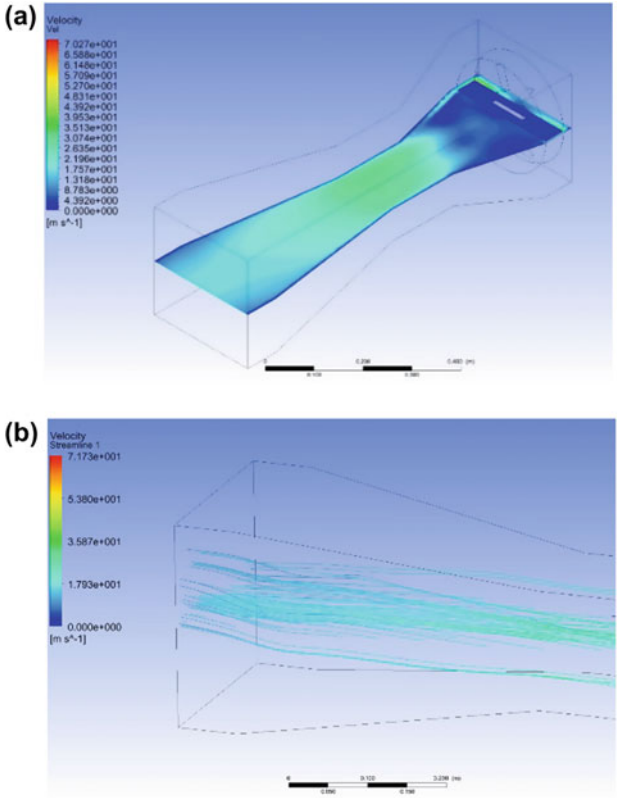


**Fig. 7** Velocity variations (a) and streamlines (b) (venturi design)

The inlet fan creates negative pressure leading to suction of air which passes through the filtrates on the bases of size of dust particles and obstacles will be stopped and absorbed. HEPA and activated carbon filters are placed in the throat section with the facility for easy removal of this section. Other additions to this prototype were of deflectors at outlet portion of the venturi which were added with an intention of keeping the air circulating in this portion so as to gain enough time for the UV-C light to neutralize any air borne virus/bacteria. The convergence, throat, and the divergence sections were manufactured separately and were assembled together with an intention of easy replacement of the throat section. The whole system is being powered using solar energy. This air purifier is economical, compact, contains easily replaceable filters, easy to handle, less power consuming.

### 2.5 Model Testing

**Flue Gas Testing:** Through this testing, the effectiveness of the model in eliminating gas pollutants was observed. The parameters considered for this test were like NO<sub>2</sub>, CO, and SO<sub>2</sub>. The amounts were observed, 10 min after running the model. The test was conducted in a room with dimensions 11 × 10 × 10 ft. The results are shown in Table 3.

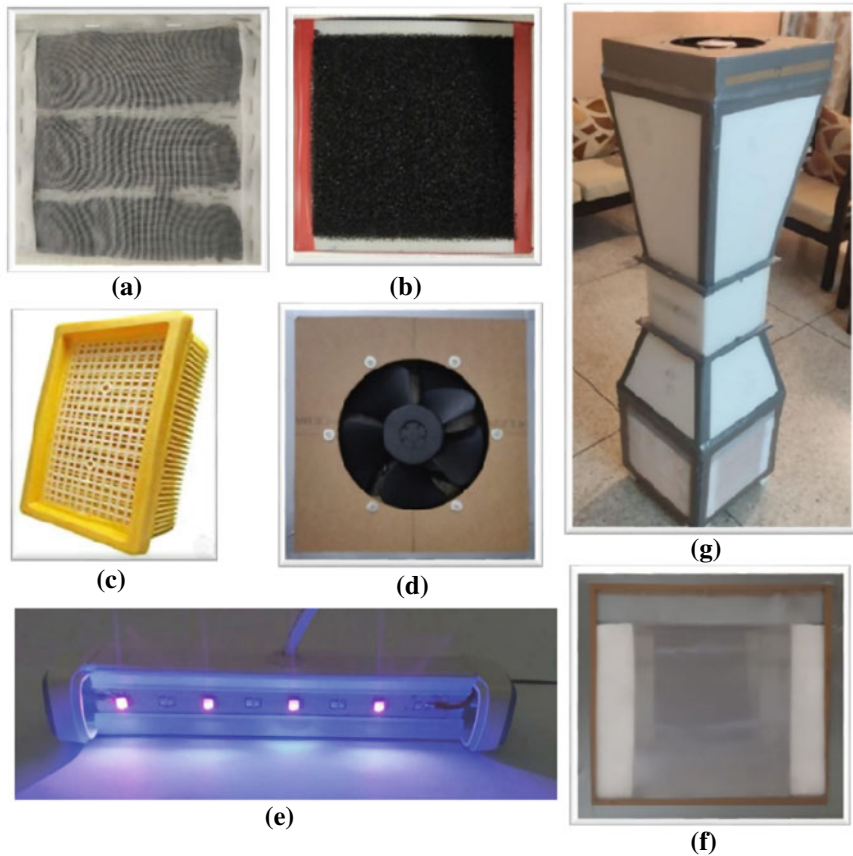


**Fig. 8** **a** Granulated carbon, **b** activated carbon filter, **c** HEPA filter, **d** inlet/outlet fan, **e** UV-C, **f** nylon filter, **g** model prototype

**Table 3** Test results

Parameter	Initial	10 min after activation
CO <sub>2</sub>	7	4.6
NO <sub>2</sub>	0	0
SO <sub>2</sub>	1.7	1.5

**Microbial Testing:** Through this testing, the effectiveness of the model in eliminating microbial pollutants was observed. The parameters considered for this test were total bacterial count, yeast, mold and E. coli. The test was conducted in a room with dimensions 11 × 10 × 10 ft. The test was a two-sample test, the first was collected in the initial room conditions, and the other was taken after letting the model to run for 30 min. The results are shown in Table 4.

**Table 4** Test results

Parameter	Initial	After activation
Total bacteria count	345	230
Yeast	0	0
Mold	172	115
E. coli	0	0

**Particulate Matter Testing:** Through this testing, the effectiveness of the model in eliminating particulate matter pollutants was observed. The parameters considered for this test were air quality index (AQI) level, PM 2.5 level, PM 10 level, particle level, and formaldehyde (HCHO) level. The levels were observed in 15-min intervals after running the model. The test was conducted in a room with dimensions 15 × 12 × 10 ft. The results are shown in Figs. 9, 10, and 11.

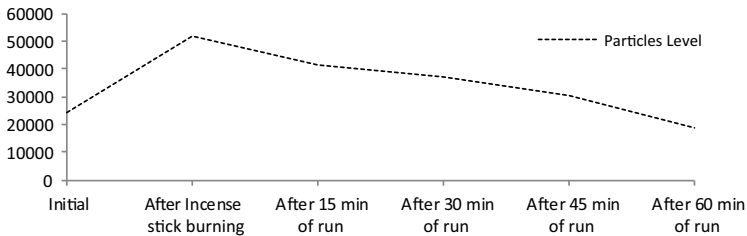


**Fig. 9** Particles level (no. of particle/liter)

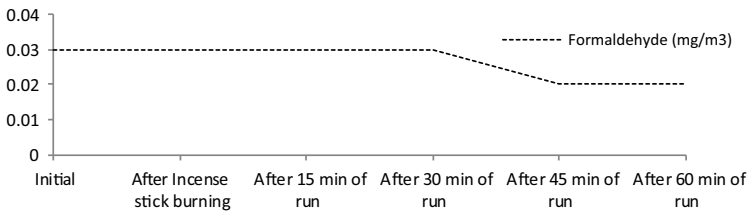


**Fig. 10** Formaldehyde levels

### 3 Conclusion

The project, designed and analyzed, satisfies all the necessary conditions for an efficient and economical air filter. The different filters used are easily available and inexpensive. The different layers of filtration give out a clean, pure, de-odorized, and disinfected air, which is evident from the results obtained. The prototype underwent the following tests:



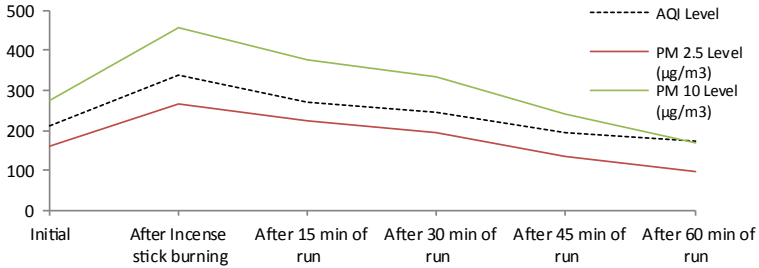


**Fig. 11** AQI, PM 2.5, and PM 10 levels

AQI, PM<sub>2.5</sub>, PM<sub>10</sub>, total particle count (TPC), HCHO, NO<sub>2</sub>, SO<sub>2</sub>, and CO (ambient air testing). Apart from this, the prototype underwent a microbial testing which included total bacterial count (TBC), yeast, mold, E. coli. It was found that the prototype was successful in decreasing the quantity of pollutants to a considerable amount after few minutes of operation (see Table 5). It reduces particulate level to a position where a person does not need to worry about the consequences of pollution. The prototype was successful in neutralizing the bacteria and mold within thirty minutes of operation only. Yeast and mold were not found in either of the samples.

**Table 5** Percentage reductions

Parameter	AQI	PM 2.5	PM 10	HCHO	TPC	CO	SO <sub>2</sub>	TBC	Mold
Reduction (%)	49.41	63.48	62.99	33.33	63.07	34.29	11.76	33.33	33.14
Time taken (min)	60	60	60	60	60	10	10	30	30

Now, we have seen that how efficient this concept is. The biggest USP is that all of this operation would be powered by solar energy, and the entire project is sustainable, generating, and receiving energy from the solar power pack. It is also economical, and one does not need to replace any component quickly. Moreover, the component replacement is easy, and the model is designed in such a way that the component replacement is effortless.

## References

1. Kumar M, Singh SJ, Shukla PK, Singha RV, Dey M, Singh A (2018) Design and fabrication of solar powered air purifier. *Int Res J Eng Technol* 2(4):3528–3534
2. Ciambelli P, Corbo P, Palma V, Russo P, Vaccaro S, Vaglieco B (2001) Study of catalytic filters for soot particulate removal from exhaust gases. *Top Catal* 16(1–4):279–284
3. Doughty DC, Hill SC, Mackowski DW (2021) Viruses such as SARS-CoV-2 can be partially shielded from UV radiation when in particles generated by sneezing or coughing: numerical simulations. *J Quant Spectr Radiative Transf* 262, ISSN 0022–4073

4. Nakpan W, Yermakov M, Indugula R, Reponen T, Grinshpun SA (2019) Inactivation of bacterial and fungal spores by UV-C irradiation and gaseous iodine treatment applied to air handling filters. *Sci Total Environ* 671:59–65
5. Central Pollution Control Board (Ministry of Environment, Forest & Climate Change) (2016) Air pollution in Delhi: an analysis. ENVIS Centre on Control of Pollution (Water, Air, & Noise)
6. Manisalidis I, Stavropoulou E, Stavropoulos A, Bezirtzoglou E (2020) Environmental and health impacts of air pollution: a review. *Front Public Health* 8:14. <https://doi.org/10.3389/fpubh.2020.00014>
7. Chaurasiya V, Tripathi RK, Yadav SK, Kannaujiya RK (2019) Solar powered water purifier. *Int J Res Eng Sci Manage* 2(5):823–825
8. Liu G, Xiao M, Zhang X, Gal C, Chen X, Liu L, Pan S, Wu J, Tang L, Clements-Croome D (2017) A review of air filtration technologies for sustainable and healthy building ventilation. *Sustain Cities Soc* 32:375–396
9. Klun TP, Dunshee WK, Schaffer KR, Andrews JF, Neu DM, Scholz MT (2004) 3M innovative properties Co. Hydrophilic polypropylene fibers having antimicrobial activity. U.S. Patent 6,762,339
10. Verdenelli MC, Cecchini C, Orpianesi C, Dadea GM, Cresci A (2003) Efficacy of antimicrobial filter treatments on microbial colonization of air panel filters. *J Appl Microbiol* 94(1):9–15



# Double Zone Thermal CVD and Plasma Enhanced CVD Systems for Deposition of Films/Coatings with Eminent Conformal Coverage

Shreya, Anukool Yadav, Ritika Khatri, Nikita Jain, Anurag Bhandari,  
and Nitin K. Puri<sup>(✉)</sup>

Nanomaterial Research Laboratory, Department of Applied Physics, Delhi Technological  
University, Main Bawana Road, Delhi 110042, India  
nitinkumarpuri@dtu.ac.in

## 1 Introduction

In the twentieth century, revolutionary advancements were going on in the electronics industry. Silicon (Si) was replacing germanium (Ge) to be used as a basic semiconductor material for all device fabrications due to its remarkable properties like large bandgap and ease in forming the oxide layer on the surface [1, 2]. Soon, the basic requirements of n-, p-doped Si for Si integrated circuit technology were at peak heights to meet the ever-increasing demand for personal computers [3]. It was in the year 1960 that Theurer successfully fabricated good quality Si films which attracted the attention of various industries toward the manufacturing of silicon semiconductor devices [4]. These advancements have created a tremendous urge for highly pure ultra-thin films in the scientific world.

Though various methods like electroplating [5], spin coating [6] vacuum evaporation [7], sputtering [8] and others have been explored at times to meet the early requirements of film deposition/coatings, many drawbacks and complications like deposition of multiple films, coating of large surface area and conformal coverage have been observed with them [9]. This search takes us to the chemical vapor deposition technique which was at an early stage at that time. Since the late 1960s, its usage has gained momentum due to various advantages that it offers and it has emerged as the leading candidate for good quality thin film deposition [10]. It involves the deposition of one or more stable solid films on a heated substrate by a suitable chemical reaction at the surface of the substrate [11].

### 1.1 Double Zone Thermal CVD

Double zone thermal CVD technique is a versatile, non-line of sight deposition technique by which uniform thin films can be deposited at a reasonable processing cost. Highly

---

Shreya and Anukool Yadav—These authors have contributed equally

dense and pure materials can be obtained by this method. Though this method is a little complex, uniform and conformal deposition of films is possible with good reproducibility which is the biggest advantage [12–14]. Since the inception of novel CVD, its market has skyrocketed. The films deposited by CVD technique have found their applications in numerous fields like the communication industry, optoelectronics industry, synthesis of high-temperature superconductors, coatings and many interdisciplinary fields [15–17]. One of the key reasons for the popularity of this technique comes from the fact that a variety of materials can be used as precursors in this method. Some of them are metals, metal hydrides, halides, halo-hydrides and metal–organic compounds and many more [18–22].

## 1.2 PECVD

PECVD is one of the numerous variants of CVD used to deposit thin films. Like double zone thermal CVD, it is also a non-line of sight technique which involves a chemical reaction at a low temperature activated by a high-energy plasma stream. The stream is produced using electrical energy which later transfers the energy of its species to the precursors. This initiates the homogeneous reaction to produce free radicals or active ions followed by radical polymerization resulting in the deposition of thin films. It is a widely used technique to fabricate various thin nanofilms and modify their properties for diverse applications [29].

## 1.3 Variants of CVD

Various variants of CVD including thermal chemical vapor deposition, plasma enhanced chemical vapor deposition (PECVD), metal–organic chemical vapor deposition (MOCVD) and atomic layer chemical vapor deposition (ALCVD) have been introduced at times [23–26]. Every variant has some advantages as well as disadvantages over others. Thermal CVD can be considered more of kind of a growth process rather than a deposition process in which the chemical reaction takes place at the surface of the substrate. In thermal CVD, the reaction is initiated by thermal energy provided by various means, while in PECVD, the electrical energy is used to initiate homogeneous reactions for production of chemically active ions and radicals that can participate in heterogeneous reaction. CVD variants can also be differentiated based on zones such as (a) single zone CVD and (b) multiple zone CVD (two or more zones).

Looking at their significant advantages and future scopes, the double zone thermal CVD system and PECVD systems present in the Nanomaterials Research Laboratory (NRL), Department of Applied Physics of Delhi Technological University (DTU), Delhi, have been studied. Here, in this report, we present the detailed role of their various components, technical specifications and working with labeled diagrams, schematics and relevant flowcharts.

## 2 Instrumentation of Double Zone Thermal CVD and PECVD

The impetus provided to the phenomenal usage of thermal CVD in diverse areas is due to ease in its installation and simple fabrication process. The most basic requirements

for a CVD system are as follows: a gas supplier with a flow controller, some heating mechanism, a reactor chamber and a temperature controller. In the double zone thermal CVD system in NRL, DTU, Delhi (shown in Fig. 1.), there are two independent heating zones with a 31.4-inch chamber size made up of quartz tube that can operate up to 1000 °C which makes it a high-temperature CVD [29]. On one side of the quartz tube, a gage meter is attached to observe the pressure inside it. It can show the pressure in the range 0–1838 mm Hg on the positive side and 0 to –760 mm Hg on the negative side. On the other side, there is a gas outlet valve and a vacuum valve connected to the vacuum pump used for the suction of air inside the tube and creates the desired level of vacuum. There are two load current meters and temperature programmers for both zones, respectively. There are two gas cylinders also, containing inert gases, nitrogen ( $N_2$ ) and argon (Ar) respectively. The one filled with  $N_2$  gas has the capacity of 46.7 liters weighing 51.7 kg, and the other one filled with Ar has the same capacity weighing 52.2 kg. Complete technical details are presented in Table 1. As it is a hot wall reactor, the whole quartz tube is heated uniformly with the precursors, and the substrate is placed inside it. Figure 2 shows the PECVD system in NRL, DTU, Delhi. PECVD has three cylinders of gases containing acetylene, hydrogen and argon gas. A chiller and heater are attached to the system for cooling and heating purposes, respectively. Vacuum pump is also attached for suction of the air and for creating vacuum as per desired conditions.

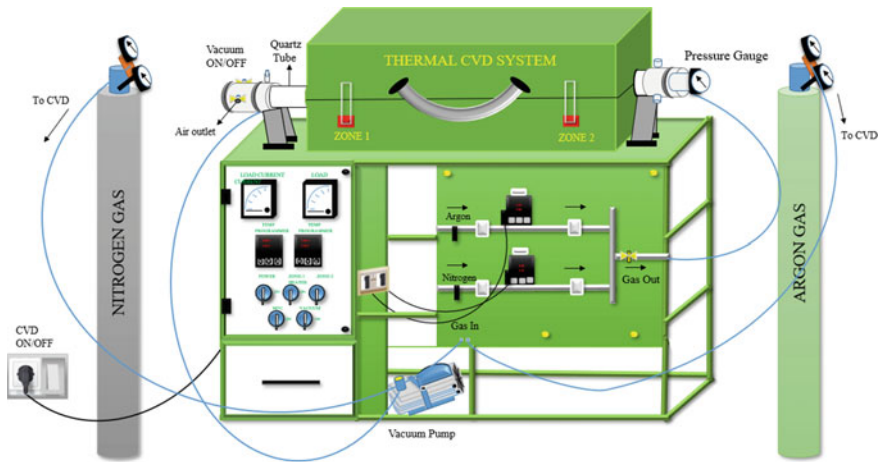


**Fig. 1.** Labeled diagram of typical laboratory double zone thermal chemical vapor deposition (CVD) at NRL, DTU, Delhi, India

### 3 Principle

#### 3.1 Double Zone Thermal CVD

The basic principle of thermal CVD is described in the flowchart as shown in Fig. 3. Here, volatile precursors are provided thermal energy in the presence of an inert gas

**Table 1** Technical details of double zone thermal CVD system

Technical parameters	Values
Zones	2
Chamber size	31.4 inch
Maximum temperature	1000 °C
Pressure range (positive side)	0–1838 mm Hg
Pressure range (negative side)	0 to –760 mm Hg
Volume (cylinder filled with N <sub>2</sub> )	46.7 liters
Volume (cylinder filled with Ar)	46.7 liters
Weight (cylinder filled with N <sub>2</sub> )	51.7 kg
Weight (Cylinder filled with Ar)	52.2 kg

that is used as a carrier gas. At appropriate temperature, when precursors are in the vapor state, they get mixed with the molecules of inert gas and undergo a homogenous vapor phase reaction. These precursors diffuse to the substrate surface, and the gas molecules get adsorbed on the surface of the substrate. The molecules of precursors heterogeneously react with heated substrate forming a thin solid film. After this, the by-products are formed, and the adsorbed gas molecules and other unwanted materials are carried out of the reactor by outlet valve with the flow of gas [28]. The principle of double zone thermal CVD is no different from the above principle. Double zone CVD is better to control the evaporation moment of the precursors. Here, the precursors that require different temperatures to evaporate can be placed in different zones. Thus, the precursor-1 with lower evaporation temperature is placed in zone-1. The precursor-2 with a higher evaporation temperature is placed in zone-2. Both the precursors are placed

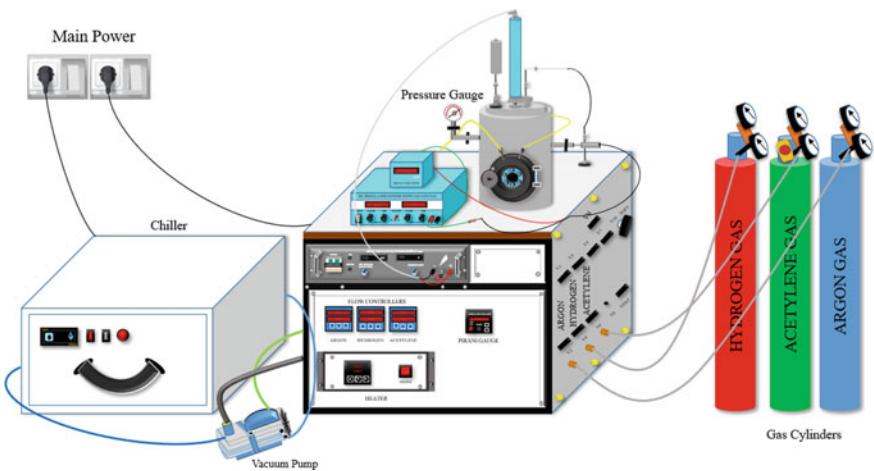


**Fig. 2** Labeled diagram of PECVD in NRL, DTU, Delhi, India

in the center of the respective zones. The substrate is placed downstream at an optimized distance from the precursor-2. Both the precursors and the substrate are placed in boats of appropriate material depending on temperature.

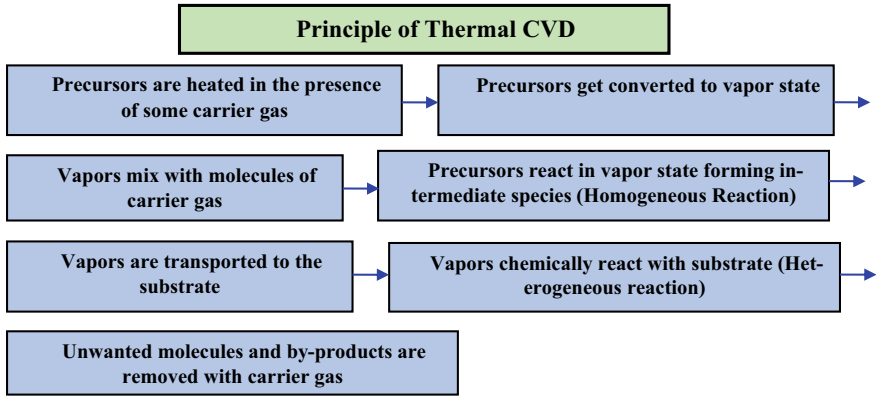


Fig. 3 Principle of thermal CVD

### 3.2 PECVD

The basic principle of the PECVD system is described in Fig. 4. The process starts with the reaction of gases followed by ionization of gases to form the plasma state by DC current. It leads to the dissociation of precursor molecules by energetic electrons of plasma to free radicals which results in the particle movement to the substrates. Finally, the radicals are adsorbed onto the substrate and the reactor walls. Thus, the nano-layers are formed in this way.

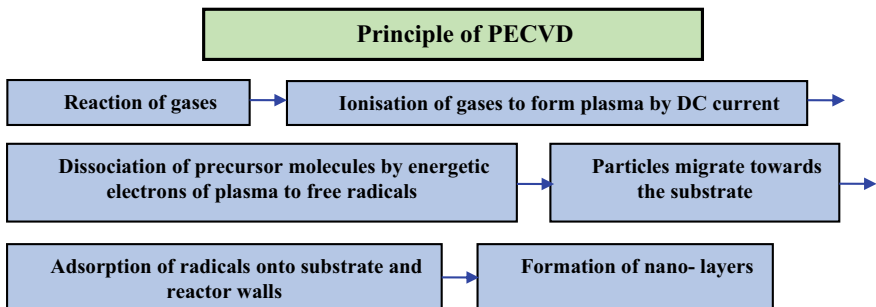
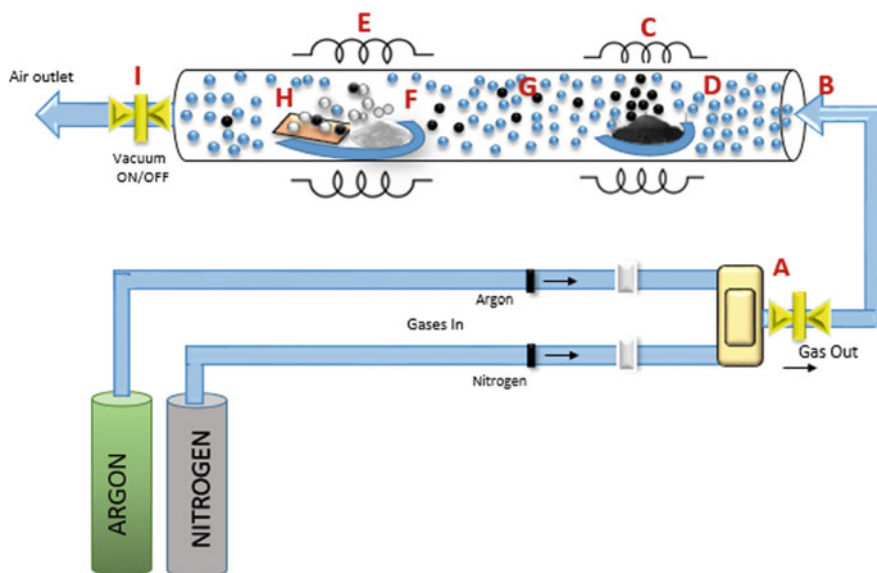


Fig. 4 Principle of PECVD

## 4 Working of Double Zone Thermal CVD

The working of the double zone thermal CVD system is shown in Fig. 5. Here, 'A' denotes the flow of inert gas from cylinders through the gas tubes controlled by flow controllers. 'B' denotes the flow of gas into the quartz tube in the direction shown. 'C' and 'E' denote the heating of volatile precursors by heating elements attached to the CVD. 'D' and 'F' denote the conversion of precursors from solid form to vapor form. 'G' denotes the diffusion of precursors in the vapor phase to the substrate's surface. 'H' denotes the heterogeneous reaction at substrate's surface and formation of a thin solid film. 'I' denotes the removal of by-products and unwanted materials.



**Fig. 5** Schematic diagram of double zone thermal CVD

The complete procedure of depositing the films on the system present in the laboratory is shown in Fig. 6. Initially, the precursors have to be placed inside the boats, and then the boats are positioned at the center of the respective zones. In the second zone, at some distance from the precursors downstream, the substrate has to be placed. Then, CVD has to be switched ON by turning the power ON knob present on the system. After that, the vacuum inlet valve has to be opened, and the vacuum knob has to be turned ON. Then, the pressure gage has to be checked which should have been showing the reading of 0.1 mm Hg. After checking that, the mass air flow controller (MFC) has been switched ON and has to be set as per desired conditions. Then, knobs of gas cylinders have to be turned on to allow the gas to enter CVD.

After all the initial steps, finally, temperature controllers have to be programmed to set the temperature, time and power-consuming unit of both zones. To run the temperature-controlled program, the 'Set' button has to be pressed seven times. After setting the



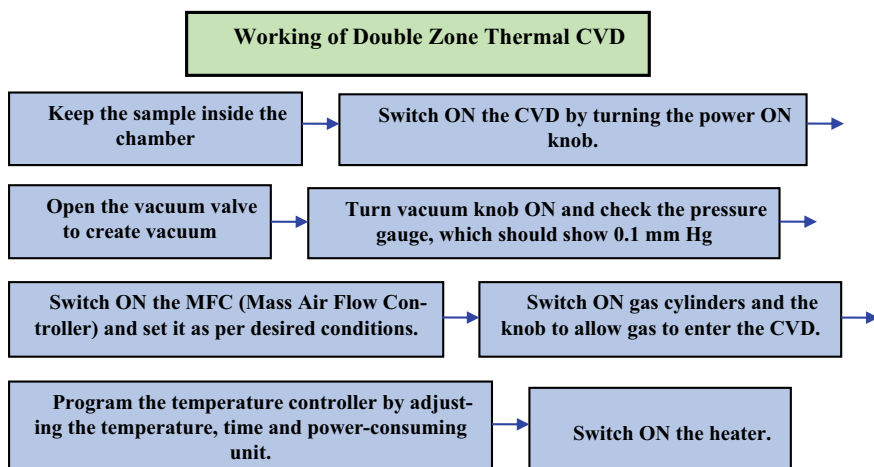


**Fig. 6** Flowchart of working of thermal CVD system at NRL in DTU, Delhi

temperature, time and power consumption unit, the up button, as shown in Fig. 1, has to be pressed to run the program. After looking for all the initial check points and taking all the precautionary measures, the heater has to be switched ON, and it starts functioning. The program can be shut off by pressing the ‘Set’ and ‘Down’ buttons simultaneously.

## 5 Differences Between Double Zone Thermal CVD and PECVD System

In conventional CVD, the temperature ranging from 500 to 1000 °C is taken to thermally decompose the precursor gases. However, in PECVD, much lower temperatures are considered as the energetic electron gas of plasma can highly dissociate the feed gas. Even when the feed gas and the substrate are near room temperature, the PECVD can deposit films on sensitive substrates that are damaged by high temperature or in the case of semiconductor production where dopant redistribution is an important concern, so high temperatures are not needed here. During the deposition process, the consistent ‘ion bombardment’ of the PECVD film by the plasma may also modify the properties of the film. PECVD technique has some limitations too which are listed here: (a) It requires a sophisticated reactor to contain the plasma. (b) It is difficult to deposit high purity films using PECVD. The reason could be the incomplete desorption of by-products and unreacted precursors at low temperatures. (c) Incorporation of impurities like toxic, explosive gases in the plasma stream can be detrimental for many applications. (d) High ion energy plasma (<20eVs) used in PECVD can damage fragile substrates because of ion bombardment. (e) The selection of an appropriate monomer is a challenge. (f) Suitable inlet instruments are needed to be installed separately. (g) Films formed may comprise compressive and residual stresses because of low-frequency requirements in PECVD. (h) If super lattice structures are synthesized using PECVD, it could be time consuming. (i) Instability against humidity and aging are two more disadvantages. (j) Costly parts of equipment and machinery are generally not desirable.

## 6 Precursor Selection

As stated above, one of the key reasons for the popularity of CVD is the variety of precursors used in the technique. The precursors can be inorganic compounds like halides, hydrides and halo-hydrides of metals and metalloids. The precursors used can also be organic compounds like alkoxides, acetylacetonates, alkyl and aryl-derivatives of metal, carbonyls, arenes, etc., as shown in the classification in Fig. 7. Though a large no. of materials can be used as precursor in this technique, some conditions that are applied to the materials to be used as precursor are as follows: (a) At room temperature, the precursor should be stable. (b) It should have a low evaporation temperature such that it has sufficient volatility. (c) Its reaction temperature should be below the melting point of the substrate. (d) It should be available in an adequate amount in pure form at a low cost. (e) It should be non-hazardous. [3, 11, 27]. Above-stated conditions are applicable on all the precursors irrespective of the variant of CVD, while some more conditions may vary depending upon the variant of CVD in which they will be used.

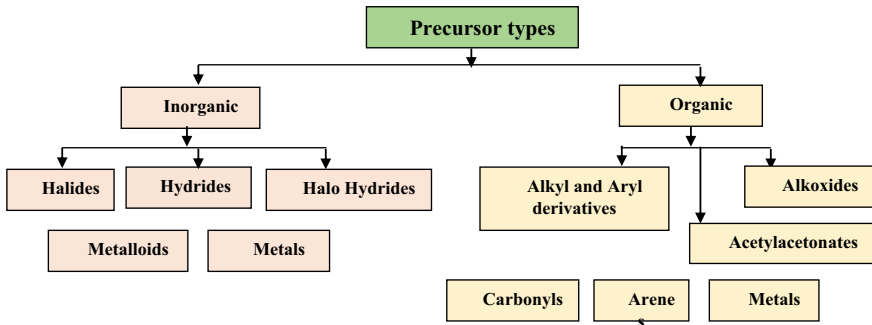


Fig. 7 Classification of precursors used in CVD

## 7 Precautionary Measures

While operating any device, there are always some safety guidelines that must be followed. Failure in doing so may cause trouble to the user and damage to the instrument. Unlike any other device, while operating a double zone thermal CVD system too, there are some safety precautionary measures that must be followed for the safety of the user and the long life of the CVD system. These are listed here: (a) CVD should not be operated at power-consuming unit greater than 60 percent. (b) Heater should be switched ON only after the last step described in the working procedure. It should not be switched ON in between. (c) It should always be ensured that the pressure inside the chamber is 0 psi or 0 mmHg. If it increases, the outlet valve should be opened; otherwise, the quartz tube may get cracked. Some precautions that need to be followed while operating PECVD system are listed as follows: (a) UPS should always be kept on. (b) After starting rotary pump, user should open SOFT valve first, and only after few min of suction, ROUGHING valve should be opened. (c) V11 valve should be opened before injecting gases

into process chamber, and it should be closed before opening VENT valve. (d) Acetone should be avoided for cleaning purposes, especially for o-rings. Apart from these instrumental precautions, there are some other rules too that should be followed as thumb rule. Especially, while handling hazardous chemicals, extra care needs to be taken to avoid accidents. Some of them are listed here: (a) Good ventilation should be ensured while handling the hazardous chemicals or the instrument. (b) Enough equipment should be arranged for the protection of user's safety like face shield, glasses for eyes and others. (c) Fire extinguishers should be installed at various places to ensure people's safety. (d) Arrangement of first aid treatment should have been ensured in case of any emergency [11, 27].

## 8 Conclusion

CVD technique finds potential applications in the deposition of thin films offering many advantages like conformal coverage and coating over the large surface area. There are numerous variants of CVD including thermal CVD, PECVD, MOCVD, ALD and others. Two of the variants of CVD, i.e., double zone thermal CVD and PECVD, were studied, and it is concluded that both have their own advantages and disadvantages. However, achieving control over ultimate film properties like thickness and film composition is a challenge in PECVD which is not the case with the thermal CVD system. Furthermore, these systems can be used to synthesize various types of materials ranging from pure dense materials to thin nanofilms for many industries. They find applications in areas like microelectronics (electrical insulation and conductive films, diffusion masks, capacitors, etc.); optoelectronics; protective, decorative, optical coatings (photovoltaics and photonics, e.g., notch filters and anti-reflective coatings); synthesis of transition metal dichalcogenides, carbon films, graphene-based polymeric nanocomposites, etc.; fabrication of integrated circuits, solar cells, transistors and some others like food packaging, biosensors, device fabrication and various biomedical applications (immobilization of biomolecules, degradation of biopolymers, etc.).

**Acknowledgments.** We are indebted to Prof. Yogesh Singh, Vice-chancellor, Delhi Technological University, Delhi, India, for providing us the research opportunities. Our sincere gratitude to the companies, Nano Tec, Perungudi, Chennai, Tamil Nadu, India, for designing and employing the double zone thermal CVD system and TechnoS Instruments, J-422, RIICO Industrial Area, Sitapur, Jaipur-302022, India, APLab and Crown for assembling the PECVD in NRL.

## References

1. Grimmeiss HG (1999) Silicon-germanium—a promise into the future? *Semiconductors* 33:939–941
2. Wieder AW, Nepl F (1992) Cmos technology trends and economics. *IEEE Micro* 12(4):10–19. <https://doi.org/10.1109/40.149732>
3. Jones AC, Hitchman ML (2009) *Chemical vapour deposition—precursors, processes and applications*. Royal Society of Chemistry, Cambridge

- Riordan M (2007) From bell labs to silicon valley: a saga of semiconductor technology transfer, 1955–61. *Electrochem Soc Interface* 16(3):36–41. <https://doi.org/10.1149/2.f04073if>
- Schlesinger M (2004) Electroplating. In: Kirk-Othmer encyclopedia of chemical technology. Wiley, Hoboken, NJ, USA
- Hall DB, Underhill P, Torkelson JM (1998) Spin coating of thin and ultrathin polymer films. *Polym Eng Sci* 38(12):2039–2045. <https://doi.org/10.1002/pen.10373>
- Safarian J, Engh TA, Vacuum evaporation of pure metals. <https://doi.org/10.1007/s11661-012-1464-2>
- 184 VE, Er NB, Targets P, Sigmundt P (1969) Physical reviews theory of sputtering. I. Sputtering Yield of Amorphous and
- Powell CF, Oxley JH, Blocher JM (1966) Vapour deposition. The Electrochemical Society, Pennington NJ
- Haubner R (2013) The history of hard CVD coatings for tool applications at the University of Technology Vienna. *Int J Refract Metal Hard Mater* 41:22–34. <https://doi.org/10.1016/j.ijrmhm.2013.01.012>
- Morosanu CE (1990) Thin films by chemical vapour deposition, vol 7, 1st edn. Elsevier Science, New York
- Kim MJ et al (2020) Large-Area, conformal, and uniform synthesis of hybrid polymeric film via initiated chemical vapor deposition. *Macromol Mater Eng* 2000608. <https://doi.org/10.1002/mame.202000608>
- Alf ME et al (2010) Chemical vapor deposition of conformal, functional, and responsive polymer films. *Adv Mater* 22(18):1993–2027. <https://doi.org/10.1002/adma.200902765>
- Abelson JR, Girolami GS (2020) New strategies for conformal, superconformal, and ultrasmooth films by low temperature chemical vapor deposition. *J Vac Sci Technol A* 38(3):030802. <https://doi.org/10.1116/6.0000035><https://doi.org/10.1116/6.0000035>
- Kamalakar MV, Groenveld C, Dankert A, Dash SP (2015) Long distance spin communication in chemical vapour deposited graphene. *Nat Commun* 6(1):6766. <https://doi.org/10.1038/ncomms7766>
- Chen K, Shi L, Zhang Y, and Z. Liu, (2018) Scalable chemical-vapour-deposition growth of three-dimensional graphene materials towards energy-related applications. *Chem Soc Rev* 47(9):3018–3036. <https://doi.org/10.1039/c7cs00852j>
- Perrin J, Schmitt J, Hollenstein C, Howling A, Sansonnens L (2000) Physics of plasma-enhanced chemical vapour deposition for large-area coating: industrial application to flat panel displays and solar cells. *Plasma Phys Control Fusion* 42(12 SUPPL. B). <https://doi.org/10.1088/0741-3335/42/12B/326>
- Cheon J, Gozum JE, Girolami GS (1997) Chemical vapor deposition of MoS<sub>2</sub> and TiS<sub>2</sub> films from the metal-organic precursors Mo(S-*t*-Bu)<sub>4</sub> and Ti(S-*t*-Bu)<sub>4</sub>. *Chem Mater* 9(8):1847–1853. <https://doi.org/10.1021/cm970138p>
- Brossard JM, Hierro MP, Sánchez L, Bolívar FJ, Pérez FJ (2006) Thermodynamical analysis of Al and Si halide gaseous precursors in CVD. Review and approximation for deposition at moderate temperature in FBR-CVD process. *Surf Coatings Technol* 201(6):2475–2483. <https://doi.org/10.1016/j.surfcoat.2006.04.018>
- Gordon PG, Kurek A, Barry ST (2015) Trends in copper precursor development for CVD and ALD applications. *ECS J Solid State Sci Technol* 4(1):N3188–N3197. <https://doi.org/10.1149/2.0261501jss>
- Hess DW et al (1991) Advances in chemistry 221. Am Chem Soc. Accessed 07 Mar 2021 (Online). Available: <https://pubs.acs.org/sharingguidelines>
- Kafizas A, Carmalt CJ, Parkin IP (2013) CVD and precursor chemistry of transition metal nitrides. *Coord Chem Rev* 257(13–14):2073–2119. <https://doi.org/10.1016/j.ccr.2012.12.004>

23. Hellegouarc'h F, Arefi-Khonsari F, Planade R, Amouroux J (2001) PECVD prepared SnO<sub>2</sub> thin films for ethanol sensors. *Sens Actuators B Chem* 73(1):27–34. [https://doi.org/10.1016/S0925-4005\(00\)00603-1](https://doi.org/10.1016/S0925-4005(00)00603-1)
24. Crowell JE (2003) Chemical methods of thin film deposition: chemical vapor deposition, atomic layer deposition, and related technologies. *J Vac Sci Technol A Vacuum Surfaces Film* 21(5):S88–S95. <https://doi.org/10.1116/1.1600451>
25. Mathur S, Kuhn P (2006) CVD of titanium oxide coatings: comparative evaluation of thermal and plasma assisted processes. *Surf Coatings Technol* 201(3–4):807–814. <https://doi.org/10.1016/j.surfcoat.2005.12.039>
26. Dorval Dion CA, Tavares JR (2013) Photo-initiated chemical vapor deposition as a scalable particle functionalization technology (a practical review). *Powder Technol* 239:484–491. <https://doi.org/10.1016/j.powtec.2013.02.024>
27. Choy KL (2003) Chemical vapour deposition of coatings. *Progress Mater Sci* 48(2):57–170. [https://doi.org/10.1016/S0079-6425\(01\)00009-3](https://doi.org/10.1016/S0079-6425(01)00009-3)
28. Vahlas C, Caussat B, Serp P, Angelopoulos GN (2006) Principles and applications of CVD powder technology. *Mater Sci Eng R: Reports* 53(1–2):1–72. <https://doi.org/10.1016/j.mser.2006.05.001>
29. Won TK, Choi SY, White JM (2018) Thin-Film PECVD (AKT). In: Flat panel display manufacturing. Wiley, Chichester, UK



# Friction Stir Welding of Two Dissimilar Metal Alloy: A Survey

Shantanu Madhukar Kadam<sup>(✉)</sup> and Netra Pal Singh

Department of Mechanical Engineering, Oriental University, Indore, India  
shantanukadam1981@gmail.com

## 1 Introduction

Friction stir welding (FSW) has become an optimal choice in the joining process for light metals. Within FSW, content binding occurs during integrity. The procedure is approved by including a rotating device that descends on the outer sides of the connecting components. Provides clear, near-flawless welds while reducing fine-grained texture and distortion. However, welding methods or even parametric mixing of the procedure for welding with consistent or reliable results is not clearly developed although FSW offers several advantages over the traditional one. Welding procedures are considered a gradual process from a business point of view. Attempts to gather a good combination of parameters to create excellent welds had generally been limited to reducing linear speeds. In general, there is an ambiguity in persisting in system parameters to create reliable welds during higher welding speed. Attempts to increase the welding speed resulted in defects generated due to improper heating through the weld [1–3].

The initiatives claimed in the field of optimization of the details of the resistance welding procedure have not disappeared toward information on microstructural changes due to differences in parameters. What is not stored within the FSW procedure will be the tool. Research claimed for fine-tuning of details for much better results generally recommended complicated condition features for the device that clearly add to the cost of the procedure. Compiling a good combination of procedure parameters with basic equipment geometry, therefore, could have contributed a lot to research in the FSW procedure region [1].

The FSW procedure is a current strong state combination procedure capable of combining a wide selection of materials. This takes into account the consequences of the rotation speed of the device blades plus the welding speed on the pulling power of different AA2219 and AA7039 hum welded pickers tensile Strength in aggregate strength. Fabricated welded joints exposed to different tooling mixes transverse and rotational speeds are calculated experimentally. An arithmetic element for the attractive power of important combinations is worked out using an external response to the practice detail terminology methodology. The unit is used to know the impact of the rotation speed of the tool blades, as well as the welding speed in the pulling power of all combinations. Much research and investigation have been conducted to analyze the outcome of the FSSW process limitations in bonding by shaking points of resistance of similar or

different materials. Of all process parameters, three important parameters of the friction and stretch spot welding procedure were changed, for example, tool rotation speed, dwell time or immersion depth to observe their impact on automatic (tensile properties, micro-hardness) or metallurgical of the joints. Significant contributions and observations, reported by the various authors, have been reviewed and critically examined in the following sections [4].

## 2 Literature Review

Heidarzadeh et al. [1], this paper explains about FSW as FSW offers particular benefits over traditional combination welding in wording of the materials that can be welded and the level of micro-structural control that can be exercised. As plans gotten more enhanced for weight or execution, there is an expanding need to weld disparate materials. We are probably going to see expanding utilization of FSW to accomplish hybrid structures including various metals and amalgams customarily considered as troublesome or impossible to join.

Kumar Rajak et al. [5], Friction-based welding processes incorporated different types of FRW and FSW techniques, their mechanism, research advancements, and parameters affecting the weld properties have been studied. The basic difference between FRW and FSW is the application of a tool, since in FRW technique, work piece itself undergoes mechanical friction, while FSW uses a rotating tool to provide friction.

Mabuwa et al. [6], the FSW or the grinding mix-welded unique aluminum combination joints were contact mix processed under air (ordinary) and submerged (lowered) with room temperature conditions. The joints delivered through these two particular conditions were concentrated relatively.

Paidara el. [7], In this article, modified grating mix securing (MFSC) measure was utilized to joint different AA2024-T3 and AA6061-T6 Al sheets by exchanging the upper and the lower sheets during the joining measure. The material stream, microstructure, rigidity, and break behaviors of the MFSC joints were contemplated.

Carlone and Astarita [8], the principle focal point of this exceptional issue is to talk about some new advances in the field of holding disparate metals. Chosen utilizations of the fundamental welding and joining measures were featured. Specific consideration was paid to the components basic for the association of unique metals for exceptional applications, examining the reception of customary trial approaches notwithstanding computational displaying, for a more profound assortment of data. The following segment gives an outline of the chose articles.

Kah [2], one of the objectives of utilizing various gaskets is to improve item plan adaptability, so various materials can be utilized proficiently and practically dependent on their particular properties. Metal-polymer congregations consolidate the strength and flexibility of metal with the physico-substance opposition and softness of polymers. Metal is utilized in segments where high solidness and strength are required, while plastic gives remarkable substance properties. Consequently, it is essential to boost the joint commitment of every material to guarantee ideal operational execution while keeping an efficient and burden bearing methodology. Be that as it may, joining disparate materials is frequently hard to accomplish. The conduct of such bonds is once in a while completely saw, especially when holding and warming strategies are utilized.

Kundu et al. [9], Friction welding (FSW) is one of the most important joining processes used for aluminum and its alloys. This new bonding process binds materials below the melting point before any other bonding process. This study aims to investigate the quality of the weld produced using GMAW and GTAW and FSW. Several advantages of FSW over other joining techniques have been discussed in this article. This study also examines the different types of test methods used to determine the performance of welded joints. Characterization of the material through microstructure analysis is important for comparing the performance of the weld produced using FSW and other processes. FSW has been found to be more beneficial and beneficial than other welding techniques for joining aluminum and its alloys.

Kaha and Martikainen [3], the welding of divergent materials tracks down a wide assortment of uses in the development and mechanical assembling areas, where the qualities of the various materials are upgraded for the ideal application to accomplish cost-viability and added esteem. This article presents an expansive grouping of the most ordinarily utilized welding measures for various materials, talks about a portion of the usually utilized welding measures with instances of some normal material blends, basic factors for great welding, and down to earth troubles experienced properties of materials.

Krishnaa et al. [10] presented the best value of the procedure parameters, for example, rotational speed, cruising speed, or axial power are set at 1300 rpm (stage 2), 1.3 mm / s (stage 2) or 7000N (stage 3) correspondingly, the ideal factors are evaluated with the level of compromise of the factors of the welding process with stretch friction has been evaluated. It was found that to facilitate the speed of rotation of the device a compromise of 68.35% was captured; the speed of navigation had a compromise of 14.5%, and the power of rotation had a compromise of 15.7% at the point yield strength of welded joints.

Winczenko et al [11], the resulting model for the FW procedure clarifies the 97% variance ( $R^2 = 0.97$ ) for the tensile strength, the 99% incongruence ( $R^2 = 0.99$ ) to obtain an iron flash width, or 94% ( $R^2 = 0.94$ ) for a smaller carbon steel flash width. The optimization was performed using more of the inherent multipurpose algorithm of the RSM model.

Quadri et al. [12], the present work uses AHP and TOPSIS multi-lens techniques to optimize the parameters related to friction welding. AHP was used to find the relative importance of forging pressure, friction time, forging time, temperature, and RPM. By using TOPSIS, relative proximity was achieved. Relative proximity is also used to decide the best parameter for FW.

Reddy et al. [13], under conditions of fluctuating TRS and WS, the divergent aluminum alloys AA 2024 and AA 7075 were FSW and the TS of the joint was calculated. RSM compared to TRS and WS, and the model was used to study the effect of TRS, and WS on the TS set was used to develop a mathematical model for TS.

Magudeeswaran and Rajapndiyan [14] demonstrated that LFW offers several interesting advantages over traditional fusion welding strategies, including excellent mechanical properties that prevent fusion, considering the scope of the different materials to be joined. LFW is a much better process for manufacturing butt joints other than DSS and MS.



Shubhvardhan and Surndran [15] presented austenitic stainless steel (AISI 304) and aluminum materials were welded effectively. The welding procedure was investigated using elastic tests, roll tests, Vickers small-scale hardness tests, exhaustion tests, microbasic perception, and EDS estimates with corresponding results. Ramesh et al. [16], presented the following which are the research examinations considered as of the literature review:

- Friction pressure,
- Friction time,
- Rotational speed.

Ambrziak et al. [17] showed the various research problems that can occur throughout the FW of unique materials that have been described in this research. Auxiliary impacts were disrupted by automatic welding of joint properties or various process projects to acquire premium welds.

Chepu and Che [18] revealed that mixtures of carbon steel with stainless steel are effectively connected by friction welding. Tang et al. (1988) showed that the development of FSW at high temperatures is mainly due to two sources: friction between the device and the surfaces of the moving part and also a clear plastic deformation in the stressed materials. The high temperature produced is conducted toward the stressed part, the support plates, and the tool. The amount of heating performed toward the stressed part establishes good results in metal marking, weld quality, weld microstructure, and defect development.

Lakshminarayanan et al. [19], the friction-stirred zone bonding procedure was used to bond 0.8 mm thick very low CO<sub>2</sub> thick automotive sheet. The non-consumable device was manufactured using a cylinder-shaped (flat) geometry having an eight mm diameter for the pin and shoulder with a 3.2-mm to 1.6-mm cone. As the keyhole was evident within each joint produced, the tensile strength of the important joints was related to the tensile strength (TSFL) values of the FSSW bones which were subjected to tensile assessments using a team of common assessment. With a main compound design and a style version, the rotation speed of the device ranged from 1200 to 1600 rpm, with five quantities. Sun et al. [20] observed the variation in the division of the hardness in the whole welding zone for smooth FSSW bones other than aluminum Al 6061 on soft metal. During the initial action, for a non-consumable tool with probe, 700 rpm of tool speed was used, and when using the tool without a probe, 600 rpm was used as tool speed. Already in the second sanding procedure by smooth application without FSSW probe, the dimensions of the micro-hardness were taken.

Lin et al. [21] analyzed the application rotation speed result on the FSSW bone user interface hardness of Al 6061 plates using traditional pinning and off-target application. The relationships between UI micro-hardness and back shear disaster modes were evaluated.

Bilici [22] performed FSSW tests on 4-mm-thick-polypropylene pieces using four kits of different length and width. The rotational speed of the instrument and the amount of immersion were kept regular for 900 rpm and 0.33 mm/second, and the dwell period was indicated as one hundred and five seconds at the beginning. Subsequently, a delay

time period of nearly fifty seconds was provided before the device was removed from the nugget area. The TSFL values of the important joints were ranged from 3305 to 4032 N.

Podrzaj et al. [23] demonstrated that the temperature of the process affects the grain size, re-precipitation, and dissolution, as well as the division of fortifying precipitates that determine the traction qualities of the welds. Flow of components from agitation and filling conditions is detrimental to the development of defects. Friction-welded joints are susceptible to imperfections such as pin hole, tunnel imperfection, pipe imperfection connection, and zigzag type, as well as cracks due to improper metal flow and improper consolidation of the metal within the FSP (friction processing area or also weld nugget area).

### 3 Concept of Friction Stir Welding

FSW has appeared as a replacement for conventional FW over the past decade. FSW was created at TWI [21]. FSW has proven to be a popular choice for welding non-ferrous metals, especially high-power aluminum alloys. It is a very good state welding system where the metal becoming member requires positions well below the melt in the main metals; as there is absolutely no melting or melting of the main metal, it provides transparent welds with almost imperfections due to the excellent mechanical qualities shown in Fig. 1 [22]. Since there are no light hazards or perhaps toxins, friction welding is either safe or environmentally sensitive. Since the working temperature is lower for the purpose of dissolving base metals, it eliminates the natural imperfections of fusion welding procedures, such as shrinkage, sensitivity, and distortion to crack. Friction welding is fascinatingly reintegrated into a number of uses, as the former provides greater burnout resistance, greater structural rigidity, and better fat burning [23]. It has become a common choice for welding non-ferrous metals, especially high-strength aluminum alloys.

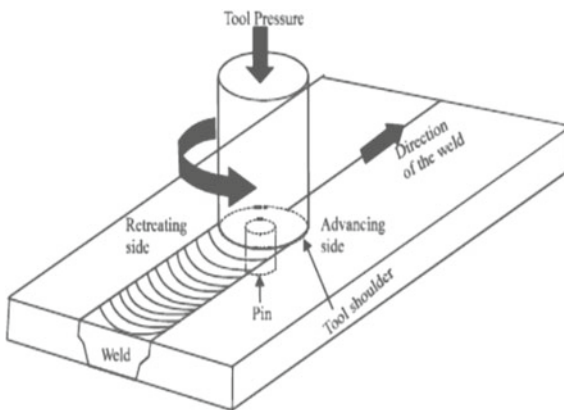


**Fig. 1** Schematic of FSW process by ref

## 4 Process Parameters of FSW

Within the friction stir welding tool, accept will be the main part intended for the development of high temperatures, as well as the one that contains the plasticized content within the welding zone. The pin joins the elements to be forged thus producing an audio articulation. The activity of the shoulder strap is guided by the speed and quality of the instrument. Based on the above, the details of the main practice in FSW are labeled as uses, rotational speed on the device (N).

- Linear velocity on the device (S)
- Tool shoulder area geometry as well as length and width
- Pin profile as well as length and width
- Axial pressure (F).

The production associated with a good joint with planned hardness, efficiency, reliability, and without defects depends on the appropriate number of parameters [10, 21, 22].

## 5 Limitations of FSW

Despite the advantages mentioned above, the FSW is related to specific flaws, in case it is not completed correctly. Apart from that particular sequence of FSW activities, it is inevitably linked to particular drawbacks as indicated below.

- The job piece must be nicely supported as well as clamped securely in an effort to have the utilized forces and also in order to keep the probe by approaching the task part textiles separately.
- Superiority of FSW weld is resolute with the number of weld details, and they are dependent upon base metal information, tool, and thickness. The number of weld parameters is a compound procedure.

## 6 Conclusion

FSW is a rapidly growing method of joining materials, especially in substances that are difficult to weld with other welding substances. The way it is not marketed properly in response to production demand. Despite the functional particularity, the visible obstacle during FSW disclosure could be a problem within the appropriate number of welding details. Each different material requires various blends of parameters. A common method for choosing welding variables has yet to be completed.

## References

1. Heidarzadeh A, Mironov S, Kaibyshev R, Çam G, Simar A, Gerlich A, Khodabakhshi F, Mostafaei A, Field DP, Robson JD, Deschamps A, Withers PJ (2020) Friction stir welding/processing of metals and alloys: a comprehensive review on microstructural evolution. *Progress Mater Sci.* <https://doi.org/10.1016/j.pmatsci.2020.100752>

2. Kah P (2017) Overview of techniques for joining dissimilar materials. *Metal Finish Solutions*
3. Kaha P, Martikainen MSJ (2014) Trends in joining dissimilar metals by welding. *Trans Tech Publ Switzerland Appl Mech Mater* 440:269–276
4. Venkateswarlu D, Nageswararao P, Mahapatra MM, Harsha SP, Mandal NR (2015) Processing and optimization of dissimilar friction stir welding of AA 2219 and AA 7039 Alloys. *J Mater Eng Perform* 24(12):4809–4824
5. Kumar Rajak D, Pagar DD, Menezes PL, Eyvazian A (2020) Friction-based welding processes: friction welding and friction stir welding. *J Adhes Sci Technol*. <https://doi.org/10.1080/01694243.2020.1780716>
6. Mabuwa S, Msomi V, Comparative analysis between normal and submerged friction stir processed friction stir welded dissimilar aluminum alloy joints. Cape Peninsula University of Technology, Mechanical Engineering Department, Cape Town, 7535, South Africa
7. Paidara M, Vigneshb RV, Khorramc A, Ojod OO, Rasoulpouraghdame A, Pustokhinaf I (2020) Dissimilar modified friction stir clinching of AA2024-AA6061 aluminum alloys: effects of materials positioning. Elsevier, *JMR&T*
8. Carlone P, Astarita A (2019) Dissimilar metal welding. *MDPI, Metals* 9:1206. <https://doi.org/10.3390/met9111206>
9. Kundu J, Ghangas G, Rattan N, Kumar M (2017) Friction stir welding: merits over other joining processes. *Int J Current Eng Technol* 7(3). E-ISSN 2277-4106, P-ISSN 2347-5161
10. Krishnaa PM, Ramaniahb N, Raoc KP, Optimization of processes parameters for friction stir welding of dissimilar aluminum alloys (Aa2024 -T6 And Aa 6351-T6) by using taguchi method. *IJIEC AA:2024–2030*
11. Winiczenko R, Sibicki A, Skoczylas P, Trajer J (2019) Multi-objective optimization of the process parameters for friction welding of dissimilar metals. In: *E3S Web of conferences*, vol 132, no 010
12. Quadri SSH, Ahmed GMS, Mohuddin MS (2017) Optimization of the processes parameters in friction welding of dissimilar combination of metals using topsis methodology. *Indian J Sci Res* 17(2):91–96
13. Reddy AG, Saketh Ch, Padmanaban R, Balusamy V (2013) Process parameter optimization for friction stir welding of dissimilar aluminum alloys. *IJERT* 2(10)
14. Magudeeswaran G, Rajapndiyan P (2019) Establishing the process parameters of linear friction welding process for dissimilar joints. *IJMET* 10(06):01–10
15. Shubhvardhan RN, Surndran S (2012) Friction welding to join stainless steel and aluminum materials. *IJMMSE* 2(3):53–73. ISSN 2278-2516
16. Ramesh AP, Subramaniyan M, Eswaran P (2019) Review on friction welding of similar/dissimilar metals. In: *ICPPNS-2019*, p 1362
17. Ambrziak A, Korzeniowski M, Kustron P, Winicki M, Bowski PS, Nska EH (2014) Friction welding of aluminium and aluminium alloys with steel. *Adv Mater Sci Eng*. Article ID 981653
18. Cheepu M, Che WS, Effect of burn-off length on the properties of friction welded dissimilar steel bars. ISSN 2466–2232, Online ISSN 2466–2100
19. Lakshminarayanan AK, Annamalai VE, Elangovan K (2015) Identification of optimum friction stir spot welding process parameters controlling the properties of low carbon automotive steel joints. *JMRT* 4(3):262–272
20. Sun P, Gerlich A, North TH, Bendzszak GJ (2007) Intermixing in dissimilar friction stir spot welds. *Metall Mater Trans* 38(A):584–595
21. Lin YC, Liu JJ, Lin BY (2012) Effect of tool. Geometry on strength of friction stir spot welded. *Adv Mater Res* 579:109–117
22. Bilici MK (2012) Effect of tool geometry on friction stir spot welding of polypropylene sheets. *Express Polym Lett* 6(10):805–813
23. Podrzaj P, Jerman P, Klobcar D (2015) Welding defects at friction stir welding. *Metalurgija* 54(2):387–389

24. Squeo EA, Bruno G, Guglielmotti A, Quadrini F (2009) Friction stir welding of polyethylene sheets (Fascicle V. Technologies in Machine Building)
25. Jeong-Won C, Huihong L, Hidetoshi F (2018) Dissimilar friction stir welding of pure Ti and pure Al. *Mater Sci Eng A* 730:168–176
26. Boccarusso L, Astarita A, Carlone P, Scherillo F, Rubino F, Squillace A (2019) Dissimilar friction stir lapwelding of AA 6082-Mg AZ31: force analysis and microstructure evolution. *J Manuf Processes* 44:376–388
27. Kah P, Suoranta R, Martikainen J, Magnus C (2013) Techniques for joining dissimilar materials: metals and polymers, Lappeenranta University of Technology, PO Box 20, 53851 Lappeenranta, Finland Received: 12 Aug 2013
28. Patel V, Li W, Wang G, Wang F, Vairis A, Niu P (2019) Review-Friction stir welding of dissimilar aluminum alloy combinations: state-of-the-art. *Metals* 9:270
29. Shinde G, Gajghate S, Dabeer PS, Seemikeri CY (2017) Low cost friction stir welding: a review. *Mater Today Proc* 4:8901–8910



# Social Intelligence as a Tool for Human Performance Optimization During Post COVID

## 19: A Review

Tanushree Sanwal<sup>(✉)</sup> and Puja Sareen

Amity University, Noida 201313, India  
tanushreesanwal112@gmail.com

### 1 Introduction

Today in India, societies are constantly facing pressures of social transformation and change. There are forces of industrialization, urbanization, modernization, and migration operating with intends to provide a deliberate and clearer direction of social transformation. In the context of widespread poverty, unemployment, destruction of natural resources, displacement, dislocation, and galloping population, our society entails a creation of framework of equity and justice along with economic growth and progress, and in all this, our organizations are playing a lead and commendable role. Today, many organizations are operating in developed as well as developing countries. These recognized organizations which have business and profit objectives are also concerned with social and humanitarian aims. The significant characteristics of many organizations are their position, their purposeful charitable character, and promotion of welfare for the needy [1].

Organizations work for the people and by the people. Human resource is the most vital resource for any good organization. The accomplishment of any work place is the result of its employees and managers who are committed to their work and are versatile in nature. Employees who are working in organizations are creative and social beings. Their intelligence and performance are a framework for high organizational growth and maximum optimization. Hence, they should be managed properly. The non profit sectors also needs good employees like the multinational corporations and other private sectors. Moreover organizations, that are working for the needy and catering to the large masses of the society, require good human resource because it not only has to look into the social issues but also has to arrange finances for its survival. Unlike big MNCs earlier, which only focused on profit, organizations today during pandemic has to do much more commendable job of solving societal problems for the welfare of the masses, along with growth in GDP.

### 2 Purpose of the Study

Today, the work sector in India is plagued with problems of their own. The efficient and competent manpower is shifting from small organizations to multinational companies

where the salaries and perks are high. The employment in the former sector is usually on a contractual basis, and receiving funds from international and local aid organizations is not very reliable. There are also related problems like lack of career progression, absence of HR policies, and an employment based on shifting project priorities. The youngsters today are not keen to join this sector, and those who join often lack the ability and characteristics to survive in the sector. Further, they show lack of social skills needed to perform better. Hence, they require more intelligence, especially social intelligence to handle these issues. Further, they must also have proper work performance and motivation for the sustenance, survival, and growth of the organization, especially during the time of pandemic where the economy growth and profit are in a pitfall. They must also have proper work-life satisfaction so that they can serve the organization in a better way than before the times of pandemic. Besides, steps should also be taken up by the organizations to build up social intelligence in employees through better training as it may be a key factor in human performance optimization, motivation, and work-life satisfaction [2–5].

Thus, the following review is carried out with an aim to investigate the relationships between social intelligence and human performance optimization. Further, secondary data were also studied to see if social intelligence has any relationship with values and motivation of employees in the time of pandemic.

### 3 Literature Review

Organizations are a vital place for economic growth. Today, they are doing a mammoth task in increasing the GDP of the country and sustaining its employee during the time of pandemic. These organizations are today creating networks, doing innovation, and interacting with people on global platform. Today, post-covid-19 organizations have to play a key role in survival. Following characteristics can be seen in organizations involved in human performance optimization:

- They bring people nationally and internationally together.
- They focus on only key issues for sustenance.
- They involve in discussions and deliberations of international matters.
- They also focus on the problems of communities and voice their needs.

Further, studies have also revealed that human performance can be achieved and enhanced when its employees have intelligence, especially social intelligence [3, 6].

#### 3.1 Intelligence

Intelligence is the capability found universally in a person. It helps us to think logically and rationally, act in a purposeful manner and effectively deal with the environment. Intelligence is required in our daily life for accomplishing various tasks. It is required for success, accomplishment, and growth of an individual. David Wechsler [7, 8] defined intelligence as the universal capability of a man to think logically, to act in a purposeful manner and deal commendably with the environment. The earliest proponent of

viewing intelligence as a set of specific factors was Spearman [9]. This was called a two-factor theory of intelligence. He believed that intelligence consists of a general factor (g) and a specific factor(s). Spearman believed that these two factors could account for performance of a human being on an intelligence test. The 'g' factor is conceived of as 'general fund of mental energy', identified as general intelligence, 's' factor and 'specific factor' are the individual's specific ability for a particular trait. Thurston [10] propounded the multiple factor theory of intelligence. The view stressed that a number of specific factors rather than one general factor makes up intelligence. Further, Guilford [11] developed what has been called the 'structure of intellect' model of intelligence. He conceived of intelligence as having three major dimensions, each with several sub-dimensions. Although Guilford's model of mental abilities is the most comprehensive available, other researchers have not obtained clear factor analytic support for it. Consequently, they question whether such an extensive list of factors accurately represents human intelligence. Recently, Guilford suggested that his 180 factors could be reduced to a smaller number of higher-order mental abilities [12].

Robert Sternberg's [13] in his triarchic theory views intelligence as a product of both external and internal forces. The theory is further sub-divided into three interacting theories. Componential sub-theory tells us about information processing skills needed for an intelligent behavior. The second sub-theory of experiential intelligence focuses on more intelligent people who can deal with any kind novel situation. The last contextual theory speaks about intelligent people who adapt to their everyday situations using their processing skills.

Howard Gardner's [14, 15] theory of multiple intelligence tells us more about the information skills that are required for intelligent behavior. He distinguished seven important sets of processing operations like intrapersonal, interpersonal, linguistic, logico-mathematical, spatial, musical, and bodily-kinesthetic for doing meaningful activities.

Intelligence has emphasized on the universal psychometric notions like testing and intelligent quotients. Intelligence also has to deal with society and its people. They must have the ability to deal with their social circles in home as well as in organizations. Hence, they must have social intelligence to deal effectively and act purposefully.

### 3.2 Social Intelligence

The term was given by Thorndike [16], which mean the person's ability to manage and understand other people in their surroundings. In 1930, he said that social intelligence is not the academic capability but an important element for successful life.

Vernon [17], said that social intelligence is the person's 'ability to get along with people in general, social technique or case in society, knowledge of social matters of a group, as well as insight into the temporary moods or underlying personality traits of strangers'. This kind of intelligence is defined as representing the 'ability to judge people' with respect to their thought process, motives, attitudes, or other psychological temper which may change a person's behavior in social surroundings. Sometimes, the knowledge a person has about their social world is also termed as social intelligence.

Social intelligence is the wisdom that a person has traditionally. It is not the current idea of 'smartness'. In this, a person understands his social surrounding and acts in an



effective and clever manner. Social intelligence not only deals with academic or financial smartness, but it let people know how to live a life in a better manner.

A major aspect of social intelligence is the capability to see through the social myths in their prevailing life. Karl Albrecht [18] has defined social intelligence as the capability to get along with others in a cooperative manner. He said that social intelligence is the social radar or an attitude of generosity and consideration. People having social intelligence are sensitive to others needs and interests. They have practical skills in a social setting which help them to get along well. According to Chadha and Ganesan [19], a socially intelligent person has patience and confidence. He is highly cooperative and sensitive. Further, he has tactfulness, sense of humor, and has a sharp memory.

Social intelligence has also been defined as the skill to assess other's feelings and dispositions. It is the intrapersonal knowledge a person have and the ability to understanding other's gestures. People having social intelligence can sympathize well with others as well as control their own emotions. Further, this kind of intelligence also helps in various kinds of mental activities and decision-making. Goleman findings in 1998 reveal that socially intelligent people can control their and others feelings.

Social intelligence indicates the capabilities like social skills, social information processing, social awareness, and social desirability [3].

- Social skills are the skills that help us to recognize strength and weakness of people. The employees who have this ability are constantly seeking feedback for their activities, and they try to enhance their performance by scrutinizing their failures.
- Processing social information skills help a person to cope up with distress situations and nervousness.
- Social awareness means that an employee is aware of other's feelings, tastes, and needs. He or she can easily identify the situations which are illogical and use this information to make better social relationships. Goleman [20] believes that while making judgments and taking ethical decisions, we must understand others' feelings as this is of high value, but not showing kindness and empathy is a parameter of low social intelligence [21].
- Social desirability denotes how to get along and cooperate with people in the emotional situations. Only through having superior social skills, the individuals know how to react in an emotional situation [22].

Social intelligence is required in many fields. Advancement and growth in organization are also prerequisites of social intelligence in employees. Human performance optimization can be achieved when human beings are fully functional and dedicated in an organization. This dedication-optimized performance can also be achieved when employees along with their managers are socially intelligent.

There are many things needed for enhanced performance of employees in a job. Variables, like employee's ability in establishing relationship with people, their ability in recognizing personal and social skills in their colleagues, their high social intelligence (social skills, social information processing, social awareness, and social desirability), and societal values, are taken as a viable advantage for the growth of the organization. They are the key factors in enhancing employee performance, motivation, and work-life satisfaction [2-5].

A positive correlation between psychological health and social intelligence has been observed [23]. It was found that persons with enhanced social intelligence possess positive psychological health which in turn has a positive effect on organizational performance and job satisfaction [24, 25]. Further, work stress and illness have negative effect on organizational commitment [26]. So, one can enhance one's performance by improving social intelligence. Hence, training should be provided in social intelligence in employees for enhanced organizational performance.

The employees having higher social values are also highly required by the organizations. This is because higher values lead to higher organizational growth, higher employee motivation, higher organizational citizenship behavior, and organizational support [27].

The word value has an important role in every organization. Hofstede [28] has described the term value as 'a broad tendency to prefer certain states of affairs over others'. The term value has an important place in business ethics and in organizational theory. Goals, roles, and behavior of a person can be identified with the help of value [29]. Further, studies have also confirmed that values notably affect behaviors and attitudes of a person working in an organization [30]. They link the members or employees in ways that can facilitate the accomplishment of goals [31].

### 3.3 Social Intelligence and Societal Values in Organization

Social intelligence and societal values are required in any kind of organization be it profit or nonprofit type. Today organizations are working hard and collecting revenues not only from the government sector but also from the private organizations for the welfare of the society as well as to earn profit for its future missions. They are continuously working for the deprived, destitute, and the underprivileged along with making profit. New plans, schemes, and projects are continuously being implemented for the growth of the company; the prime motive of the country of increasing GDP post-covid is also being targeted. In all these, components of social intelligence and societal values are playing an important role and are being utilized variedly in various tasks by the employees. Values and intelligence both help in establishing a mutually beneficial relationship with other people and industries. A person working in an organization in covid-19 has to be sensitive, tactful, and must be able to recognize his social environment. He or she must have social skills, social awareness, and social desirability. This would help the organization to increase its funds, tackle situations, and develop schemes and sensitization programs for increasing GDP. Social information processing is a component of social intelligence which helps to get things done by people. The component also helps in crisis situations by bringing people together and focusing their mind on important issues.

Social intelligence and societal values in a business also help a person to be goal oriented. It also provides historical, current, and predictive views of various operations in a tactful manner. Further, those who possess social intelligence and societal values can develop a set of processes that help organizations optimize their performance, develop a framework for organizing, automating and analyzing their methodologies, processes and systems that drive the organizations performance. Further, social intelligence also helps to collaborate successfully with other organizations to implement schemes and programs for the welfare of people. Performance in organization represents a value that

is expected from its employees over a period of time. Behavior and performance are two different indicators and concepts. Behavior is the act performed by an employee, and performance is the value of their behavior for the organization [32].

Today, in India, we have a very few good worker. Young graduates never turn up toward a small organization because they are paying less than the MNCs. Former is asking for hard work in an atmosphere without the luxuries of modern life. Retention of smart employees is big challenge companies are facing today [33]. Today, the youngsters in organizations are wanting very different things from work than their senior counterparts [34]. Findings suggest that the preferences have changed for different age groups [35]. Those organizations are successful in retaining employees and optimizing their performance, which meet the individual's need and their preferences in a better manner [36].

However, the youth today do not find the small sectors impressive because it does not have a proper business model and pay well. Moreover, the youths in this sector were paid less and many lost their job due to pandemic. Now, as the things are stabilizing, they want to join big sectors with handsome salary. Moreover, these young employees working in various organizations often lack social intelligence and societal values needed for optimize work performance, work motivation, and work-life satisfaction. These parameters are necessary for the welfare of the society, its prime mission and for the welfare of the organization, and its necessary sustenance. Hence, the job sector needs to reinvent their business model and develop work performance optimization model, create work motivation, and work-life satisfaction in its employees through better HR policies, training program, and compensation management, especially post-covid-19.

### 3.4 Work Performance Optimization

Work performance is the comparative strength of involvement of a person employed in a company. Organizational performance is important because employees with high and optimize performance are less likely to leave for another job and are more likely to execute at higher levels. Work performance refers to quality of functions or operations performed in organizations [37]. Work performance is also a parameter or indicator which shows the achievement level and growth of an organization [38]. Post-pandemic, effective work performance has become an essential requirement for achieving better outcomes in an organization. Work performance optimization helps organization in achieving its target and gaining profit. According to balance score card model, work performance can be measured in terms of finance, customer, internal processes, learning, and growth. This model helps in creating a strategy for human performance optimization in organizations by achieving the set objectives framed by senior managers and by evaluating past performance of employees [39]. Further, social intelligence has also worked as a tool for enhanced human performance. Socially intelligent people in an organization perform better and excel more. They help in achieving the set objectives and targets of an organization [40–44].

### 3.5 Work Motivation

The word motivation has been derived from the word ‘movere’ which means to move. Motivated employee is an essential requirement of any organization who wants to excel in performance optimization. Generally, motivation is effected by various intrapersonal and environmental factors [45]. Today, many organizations are framing different policies for motivating employees in their organizations [46]. Post-pandemic has become an essential requirement as people are in a distress situation. They need to be motivated for enhanced performance and blooming economic growth. According to Manzoor [47], motivating employees has always been a difficult task for the senior counterparts in an organization. Managers, post-covid-19, are really working hard to boost their economy. Hence, for sustenance growth and profit, managers have to motivate their employees through different strategies. Motivated employees have always helped in optimization of performance in an organization as their talent is only directed toward achieving organizational goals and objectives [47, 48]. Further, managers who are socially intelligent can motivate their employees in a better manner. These managers can even handle generational differences in a company [4].

Moreover, companies that are not providing better facilities for its employees’ are unknowingly enhancing the numbers of dissatisfied and unproductive employees and hence increasing attrition rates [49]. Just making or creating a framework for work-life balance is not enough for the senior counterparts. Loui [50] further found that commitment was also important to develop involvement, trust, and satisfaction in employees which in turn enhanced work performance optimization [51, 52].

## 4 Discussion

The value that organizations are creating has to be spread in a proper manner. The organizations and the society have to come up with true employees who have social intelligence and societal values. This will invent the business model and will bring new innovation in the job sector. If a person has social intelligence and social values in a job, he or she can perform better, build relationships, and develop trust. Today, post-covid-19, organizations need to develop their resources, spread their influence, and generate awareness. They need to design new management structures which would help in the decision-making process. They need to batten down the hatches and grid themselves against attacks from hostile critics and develop as supporting partners. As the company’s work is targeted toward the profit making, it becomes all the more important for the human resource department to be strong and actively engage in reading the mindset of the people in the company on whom the project is allocated. Steps must be taken to prepare them to accept the change after the pandemic and be motivated for their own betterment. There should be motivation through rewards, which is not quite prevalent in the job sectors today post-pandemic. Even if the rewards are not administered on a regular basis, there should be system of rewards on an intermittent basis, and standards should be established in advance. There should be proper feedback system within all the companies by which all the projects being undertaken are properly judged [53]. So, as the organizations move into a journey with strategic purpose, the requirement for social

intelligence and societal value is seen to be paramount, especially post-pandemic. This will in turn help in work performance optimization.

Thus, with review of literature, it becomes evident that social intelligence and societal values might be important factors in obtaining motivation and work performance optimization in organizations.

## 5 Conclusion

From the above review of literature, we can say that social intelligence has a positive effect on human performance in an organization. Further, secondary data reveal that motivation and values are also key parameters in enhancing performance of an employee as they affect social intelligence in a positive manner. Hence, a following conceptual model was framed for enhanced human performance optimization in an organization.



## References

1. Green A, Matthias A (1997) Non-Governmental organizations and health in developing countries. Macmillan Press Ltd., London
2. Liao C-W, Chien-Yu Lu, Huang C-K, Chiang T-L (2012) Work values, work attitude and job performance of green energy industry employees in Taiwan. *Afr J Bus Manage* 6(15):5299–5318
3. Ebrahimipour H, Zahed A, Elyasi A (2013) The study of relationship between social intelligence and organizational performance (case study: Ardabil regional water company's managers). *Int J Organ Leadersh* 2(1):1–10
4. Njoroge CN, Yazdanifard R (2014) The impact of social and emotional intelligence on employee motivation in a multigenerational workplace. *Glob J Manage Bus Res* 14(3):31–36
5. Rezaei A, Khalizadeh A (2009) The relationship between social intelligence managers with job satisfaction of teachers in schools. *J Instr Eval J Educ Sci* 2(7):121–145
6. Korauš A, Kaščáková Z, Parová V, Veselovská S (2017) Sustainable economic development through human resource management: social intelligence of managers and performance. *J Secur Sustain Issues* 6(3)
7. Wechsler D (1939) The measurement and appraisal of adult intelligence. Williams & Wilkins, Baltimore
8. Wechsler D (1958) The measurement and appraisal of adult intelligence, 4th edn. Williams & Wilkins, Baltimore

9. Spearman C (1927) *The abilities of man*. Macmillan, New York
10. Thurstone LL (1938) *Primary mental abilities*. University of Chicago Press, Chicago
11. Guilford JP (1967) *The nature of intelligence*. McGraw-Hill, New York
12. Guilford JP (1981) Higher-order structure-of-intellect abilities. *Multivar Behav Res* 16:411–435
13. Sternberg RJ, Smith C (1985) Social intelligence and decoding skills in nonverbal communication. *Soc Cogn* 3:168–192
14. Gardner H (1983) *Frames of mind: the theory of multiple intelligences*. Basic Books, New York
15. Gardner H (1993) *Multiple intelligences: the theory in practice*. Basic Books, New York
16. Thorndike EL (1920) Intelligence and its use. *Harper's Mag* 140:227–235
17. Vernon PE (1933) Some characteristics of the good judge of personality. *J Soc Psychol* 4:42–57
18. Albrecht K (2006) *Social intelligence: the new science of success*. Wiley Imprint, San Francisco, CA
19. Chadha NK, Ganesan U (1986) Social intelligence scale
20. Goleman D (1998) What makes a leader? *Harvard Bus Rev* 77:93–102
21. Aristu AL, Tello FPH, Ortiz MA, Gandarn M (2008) The structure of bryants empathy index for children: acroo-validation study. *J Psychol* 11(2):670–677
22. Nwkah NG, Ahiauzu AL (2009) Emotional intelligence and marketing effectiveness. *Mark Intell Planning* 27:867–881
23. Hooda D, Sharma NR, Amrita Y (2009) Social intelligence as predictor of positive psychological health. *J Indian Acad Appl Psychol* 35:143–150
24. Garg P, Rastogi R (2009) Effect of psychological wellbeing on organizational commitment of employees, ICFAI Univ *J Organ Behav* 7(2):42–51
25. Rathi N, Rastogi R (2008) Job satisfaction and psychological wellbeing. ICFAI Univ *J Org Behav* 7(4):47–57
26. Tiwari S, Mishra PC (2008) Work stress and health as predictors of organizational commitment. *J Indian Acad Appl Psychol* 34(2):267–277
27. Kwon IG, Banks DW (2004) Factors related to the organizational and professional commitment of internal auditors. *Manage Auditing J* 19:606–622
28. Hofstede G (1980) *Culture's consequences*. Sage, London
29. Schwartz SH, Bilsky H (1987) Toward a universal psychological structure of human values. *J Pers Soc Psychol* 53:550–562
30. Gamble PR, Gibson DA (1999) Executive values and decision making: the relationship of culture and information flows. *J Manage Stud* 36:217–240
31. Meglino BM, Ravlin, E.e. (1998) Individual values in organizations: concepts, controversies, and research. *J Manage* 24:351–390
32. Motowidlo SJ (2003) Job performance. In: Borman WC, Ilgen DR, Klimoski RJ (eds) *Handbook of psychology*, vol 12. Industrial and organizational psychology. Wiley, Hoboken, NJ, pp 39–53
33. Davenport T (1999) *Human capital*. Jossey-Bass, San Francisco, CA
34. Conger JA (1998) How 'Gen X' managers manage. *Bus Strategy* 10:21–31
35. Sparrow PR (1996) Transitions in the psychological contract: some evidence from the banking sector. *Hum Resour Manag J* 6:75–92
36. Guest DE (1998) Is the psychological contract worth taking seriously? *J Organ Behav* 19:649–664
37. Neely AD, Adams C, Kennerly M (2002) *The performance primes: the scorecard for measuring and managing stakeholder relationship*. Financial Times/Prentice Hall, London
38. Ho L (2008) What affects organizational performance? *Ind Manage Data Syst* 108–118

39. Llivisaca J, Jadan D, Guamán R, Arcentales-Carrión R, Peña M, Siguenza-Guzma L (2020) Key Performance indicators for the supply chain in small and medium-sized enterprises based on balance score card. *Test Eng Manage* 83:25933–25945
40. Albrecht K (2009) Social intelligence: the new science of success. *Pers Excellence* 10(12):5
41. Emmerling RJ, Boyatzis RE (2012) Emotional and social intelligence competencies: cross cultural implications. *Cross Cult Manage Int J* 19(1):4–18
42. Goleman D, Boyatzis R (2008) Social intelligence and the biology of leadership. *Growth: J Manage Training Inst* 36(2):52–55. 12
43. Goleman D (2006) *Social intelligence: the new science of social relationships*. Bantam Books, New York
44. Riggio RE, Reichard RJ (2008) The emotional and social intelligences of effective leadership: an emotional and social skill approach. *J Manag Psychol* 23(2):169–185
45. Devadass R (2011) Employees motivation in organizations: an integrative literature review. *Int Proc Econ Dev Res* 10
46. Guillen L, Saris WE (2009) Making sense of managerial competencies: a motive-based approach. *INSEAD Working Paper*
47. Manzoor Q (2011) Impact of employees motivation on organizational effectiveness. *Eur J Bus Manage* 3(3):36–44
48. Ningsih LK, Prastiwi NLPEY, Gorda AES (2020) The optimization of employee performance improvement reviewed from the perspectives of performance allowances, work motivation, and work discipline in the Lpd Banyuning, Lpd Lumbanan, Lpd Padang Bulia, Lpd Sari Mekar. *J Bus Hospitality Tourism* 6(1):94–103
49. Gupta S (2014) Research paper on emotional intelligence and work life balance of employees in the information technology industry
50. Loui K (1995) Understanding employee commitment in the public organization: a study of the juvenile detention center. *Int J Public Adm* 18(8):1269–1295
51. Angle H, Perry J (1981) An empirical assessment of organizational commitment and organizational effectiveness. *Adm Sci Q* 26:1–14
52. Wiener Y, Vardi Y (1980) Relationships between job, organization, and career commitments and work outcomes: an integrative approach. *Organ Behav Hum Perform* 26:81–96
53. Chakraborty S (2008) A study of the Hrd practices in an Ngo-bodh Siksha Samiti. In: Sahay BS, Tojo Thatchenkery, GD Sardana (ed) *Handbook on Management Cases*, Allied Publishers, New Delhi



# Modeling and Simulation of Solar-Powered Remote-Operated Floating Trash Harvesting Boat

Purnyatre Gaur<sup>(✉)</sup>, Aniket, Subhesh Kumar, and J. P. Kesari

Mechanical Engineering Department, Delhi Technological University, Delhi, India  
pgaur151998@gmail.com

## 1 Introduction

For sustainable future development, solar-powered boats are evolved in various parts of the world; the particular reason for this is their environment-friendly nature. The solar-powered ferry is developed in Bangladesh for inland rural navigation [1]. In large solar-powered boats, generally, a Karvin 2700 engine is used, but for small boats or AUVs, small thrusters can perform the required tasks with excellent efficiency [2, 3]. Using solar energy with required efficiency is a cumbersome task, and another issue is PV system cost; thus, optimization can be performed [4].

In this paper, “Remotely operated solar-powered surface vehicle” has been developed. The purpose of designing this vehicle is to tackle increasing plastic waste in the water bodies. The vehicle comprises a catamaran type of hull, and it is equipped with a solar panel to power it using solar energy. The remotely operated vehicle’s behavior in actual conditions has been analyzed on various simulation software while subjecting it to nearly the same operating conditions as that of actual ones.

## 2 Mechanical System

### 2.1 Design Methodology

The vehicle consists of a structural frame, wire mesh, waste collecting mechanism, electrical components, and propellers. Each of the component and subsystem has been planned and situated in a manner, keeping the required relative positions of the COG and COB such that metacentric height is well enough to provide adequate torque to arrange itself if there is any disturbance along the roll axis because of little waves. The vehicle is designed and assembled in the *SolidWorks*, and simulation is carried out in *ANSYS*.

The vehicle uses a catamaran-type hull, so that there is plenty of room for the component and has better stability than a monohull, and capable of spurring a relatively high speed (Figs. 1 and 2).



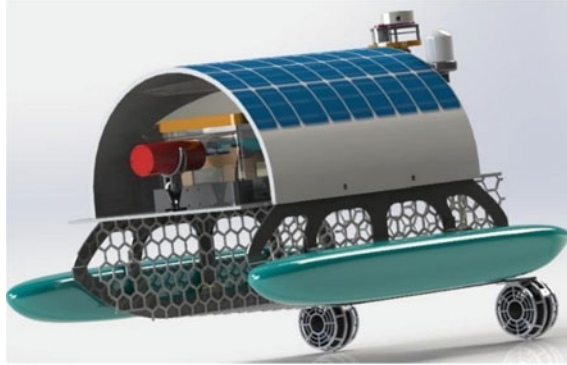


**Fig. 1** Rendered CAD file of the boat

## 2.2 Outer Frame

The frame is particularly designed by thinking about the stability (both dynamic and static), structural support, weight optimization, along with the simplicity of dismantling and accessibility.

As opposed to utilizing a solitary material for the structural frame, clear virgin cast acrylic, aluminum, and polycarbonate are used for the base plate, side plates, and curved surface for the solar panel, respectively. The frame has been changed depending upon strength, stiffness, weight, machinability, safety, and esthetics. Outer frame parts were topologically optimized while keeping up adequate strength to meet the requirements, as a result weight can be optimized.

## 3 Subsystem

### 3.1 Electronic Box

The discreet box encases all the sensitive electronic components while guaranteeing the greatest use of the accessible volume. The electronic components are placed on the

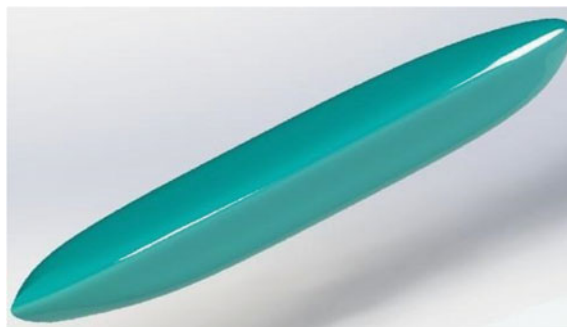


**Fig. 2** Hull

electronic tray made up of wood for quick removal of these components and enough spacing for the wires and connectors (Fig. 3).

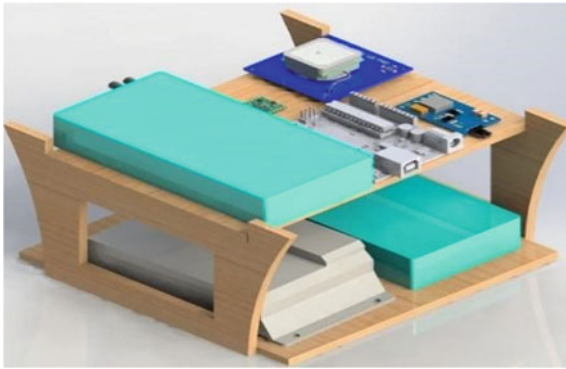


**Fig. 3** Electronic stack CAD

### 3.2 Waste Collecting Mechanism

Different mechanisms are investigated for waste collection, e.g., conveyor belts, bilge pumps, after considering various parameters like the location of the center of gravity, cost, and the weight of the vehicle. To collect the floating waste from the stagnant water bodies centrifugal pump, placed above the water surface, is used of required suction pressure, which is connected to the PVC pipe system, from which pump sucks the water from the drain as well as dispose the water into the drain itself and collects the waste material in the wire mesh.

### 3.3 Solar Panel, LiDAR, and Camera

For generation of power, a solar panel is placed on a curved section fabricated using polycarbonate and connected to the side plates. The solar panel is then connected to the electronic box for further connections.

A custom-made LiDAR is placed at the rear end at the vehicle's highest point, enabling the vehicle to avoid collision with any obstacle that may come in the predefined range and not appear in the camera view.

A battery level indicator pole is also placed to always keep an eye on the battery percentage during operation. The camera is placed in a cylindrical hull having a transparent end cap at one side and connected to the electronic box on the other.

## 4 Propeller Analysis

A ducted propeller has been used to improve the propeller's efficiency by taking advantage of the hydrodynamic design shaped like a foil. While it increases efficiency at

lower speeds producing greater thrust in a smaller package, it also reduces bottom suction while operating in shallow depths and provides better course stability. Nevertheless, on the contrary, it increases cavitation and drag due to additional shrouding.

The propeller calculations are simply based on the momentum theory. Talking about the math, the thrust  $F$  generated by the propeller disk is equal to the product of disk area of propeller ( $A$ ) and change in pressure:

$$F = \Delta p \times A \quad (1)$$

Bernoulli's equation is used to relate the front and back side pressure and velocity of the propeller disk but not through the disk. At the front of disk, the summation of static pressure  $p_o$  and the dynamic pressure  $0.5 * \rho * V$  is equal to the total pressure  $p_{to}$ .

$$p_{to} = p_o + 0.5 \times \rho \times V_o^2 \quad (2)$$

Here,  $\rho$  is density of water, and  $V_o$  is the vehicle's velocity. Downstream of the disk,

$$p_{te} = p_o + 0.5 \times \rho \times V_e^2 \quad (3)$$

Here,  $V_e$  is velocity at exit, and  $p_{te}$  is the total pressure at downstream. Pressure jumps at the disk:

$$\Delta p = p_{te} - p_{to} \quad (4)$$

Therefore, at the disk,

$$\Delta p = 0.5 \times \rho \times [V_e^2 - V_o^2] \quad (5)$$

Putting the values obtained by Bernoulli's equation in the equation of thrust, we get

$$F = 0.5 \times \rho \times A \times [V_e^2 - V_o^2] \quad (6)$$

Momentum equation based on propeller analysis is used to obtain the exit velocity magnitude. The thrust force relies upon the mass flow rate of propeller and the change of velocity through the propulsion system from primary thrust equation. The thrust  $F$  is equivalent to the rate of mass flow, i.e.,  $m_o$  times the distinction in velocity  $V$ :

$$F = [m_o \times V_e] - [m_o \times V_o] \quad (7)$$

As exit pressure is the same as the free stream pressure, thus, there is no pressure-area term. The value of mass flow through propulsion system can be obtained at propeller's plane and is a constant. Since the propeller rotates, an area  $A$  can be characterized as the propeller having length of blade  $L$  sweeps that out. The mass flow rate through this area is the product of density  $\rho$ , velocity  $V_p$ , and area  $A$ .

$$m_o = \rho \times V_p \times A \quad (8)$$

To obtain the thrust in the terms of  $V_e$ ,  $V_o$ ,  $V_p$ , i.e., exit velocity, entrance velocity, velocity through propeller, substituting the above value of mass flow rate in the equation of thrust:

$$F = \rho \times V_p \times A \times [V_e - V_o] \tag{9}$$

Bernoulli’s equation at upstream and downstream of the propeller:

$$F = 0.5 \times \rho \times A \times [V_e^2 - V_o^2] \tag{10}$$

Solving the Eqs. 9 and 10 of thrust  $F$  for  $V_p$ ;

$$V_p = 0.5 \times [V_e + V_o] \tag{11}$$

Average of free stream and exit velocities gives the velocity of water through the propeller disk. When going at a steady speed, the thrust delivered by the motors is same as the vehicle’s friction or drag, i.e.,

$$\text{Thrust} = \text{Drag} = 0.5 \times \rho v^2 \times A \times C_d \tag{12}$$

Here,  $\rho$  is the density of water;  $C_d$  is coefficient of drag;  $v$  is the speed, and  $A$  is the effective surface area. As thrust power is equal to the product of thrust and the speed, i.e., power is the speed cube’s function. Therefore, for the propulsion system, with the increment of the speed, the power consumption increases dramatically.

Further, using ANSYS Fluent, a graph was plotted between the thrust and the battery current (Fig. 4).

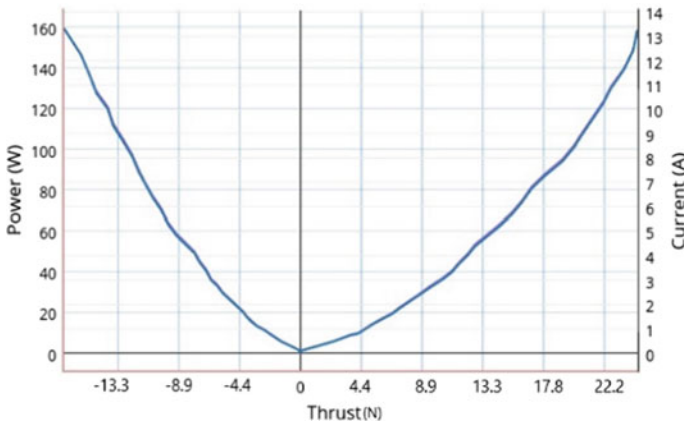


Fig. 4 Thruster performance curve

## 5 Drag Analysis of Hull

*Viscous Drag:* It is the resistance offered to the body by the liquid due to its viscosity, and it depends on the velocity with which the body moves inside the medium, density of the medium, and the frontal area of the body.

$$\text{Drag} = 0.5 \times \rho v^2 \times A \times C_d \quad (14)$$

*Wave making resistance:* It is a sort of drag that influences surface watercraft, e.g., boats and ships; it also shows the energy needed to remove the water from the way of the structure. Moreover, this energy is utilized into the creation of the wave.

$$R_s = fSV^m \quad (15)$$

where  $S$  is the wetted surface,  $V$  the speed,  $f$  a frictional coefficient, and “ $m$ ” an index whose value is about 1.83.

To simplify our problem statement and lack of appropriate testing software, the surface vehicle was analyzed for a viscous drag only. For the calculation of viscous drag force, the coefficient of drag was found out by simulating the model of the vehicle through a range of velocities on ANSYS Fluent, which gave us an average value of drag as,  $C_d = 0.029$  (Fig. 5).

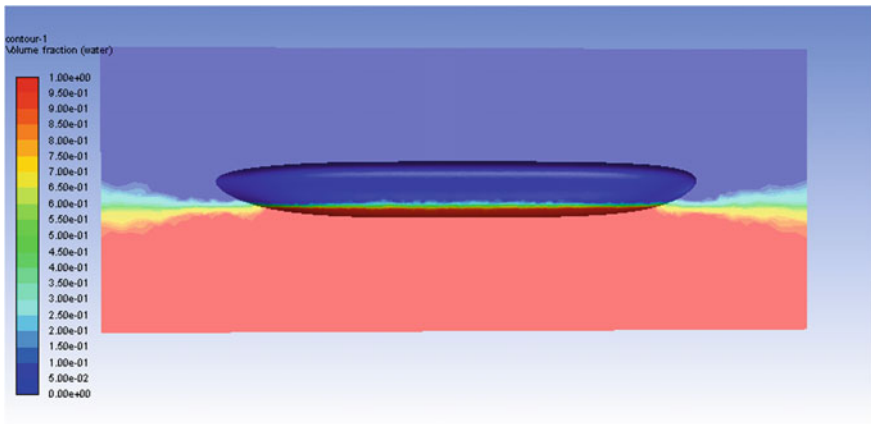


**Fig. 5** Volume fraction of water

Further, this drag coefficient was utilized to calculate the value of the viscous drag force experienced by the catamaran when operated at different velocities (Table 1; Fig. 6).

## 6 Electrical and Electronic Subsystem

The vehicle's electrical and electronic subsystem will be divided mainly into four main segments: power unit, sensors, control unit, and actuators.

**Table 1** Vehicle velocity and corresponding drag force values

Velocity (m/s)	Drag force (Newton)
0.15	0.01
0.2	0.02
0.25	0.032
0.3	0.042
0.35	0.051
0.4	0.061

### 6.1 Power System

The vehicle is entirely solar powered and uses 100 W, 12 V monocrystalline solar panels with 36(4 × 9) cells for the charging of batteries. The solar panels are connected to a suitable charge controlling unit that will handle the nominal amount of current and voltage input to the battery when charging.

#### Photocurrent

$$I_{ph} = [I_{sc} + K_i \times (T - 298)] \times \frac{G}{1000} \tag{16}$$

#### Saturation Current

$$I_o = I_{rs}(T/T_n)^3 \times \exp\left(q \times E \times \frac{\frac{1}{T_n} - \frac{1}{T}}{n.k}\right) \tag{17}$$

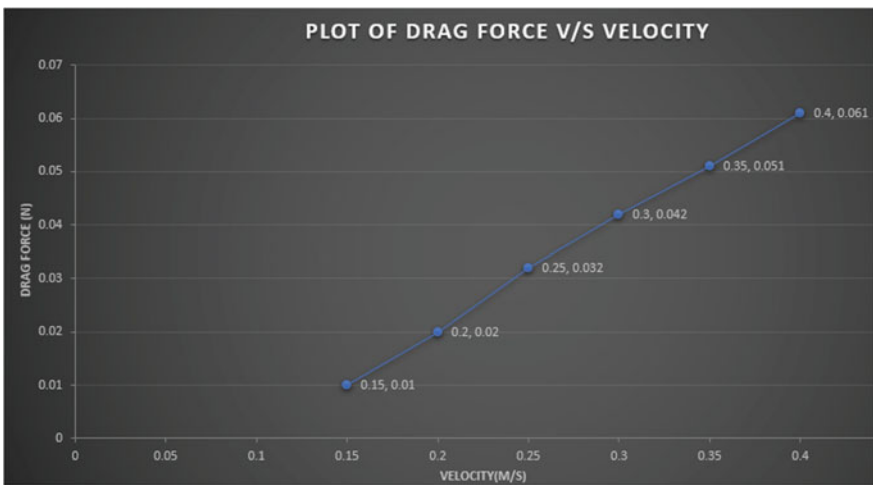


**Fig. 6** Drag versus velocity plot

**Reverse Saturation Current**

$$I_{rs} = I_{sc} / \{e^{(q \times V_{oc}) / (n \times N_s \times K \times T)}\} \tag{18}$$

**Current Through shunt resistor**

$$I_{sh} = (V + I.R_s) / R_{sh} \tag{19}$$

**Output current**

$$I = I_{ph} - I_o \cdot \left[ \exp\left(\frac{q \cdot (V + I \cdot R_s)}{n \cdot K \cdot N_s \cdot T}\right) - 1 \right] - I_{sh} \tag{20}$$

Total power consumed at all time (Fig. 7; Table 2).

$$(120 + 66.5 + 5.1 + 36 + 3)W = 230.6 W$$

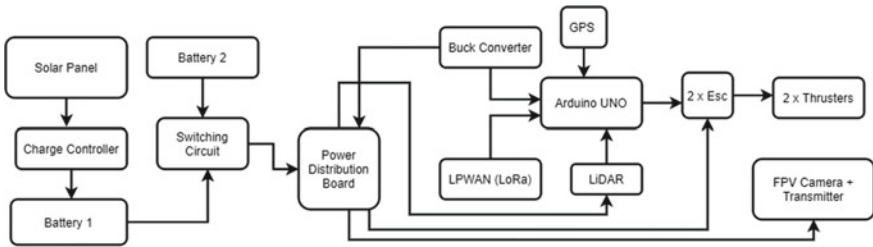


**Fig. 7** Block diagram of electronic subsystem

**Table 2** Power usage table

S. No.	Component	Operating voltage (V)	Current ratings (A)	Drawn power (W)
1	Pump	12	3	36
2	Arduino UNO	5	0.6	3
3	FPV camera	19	3.5	66.5
4	LiDAR	3	1.7	5.1
5	Thruster	12	5	60

Nominal capacity of two main batteries (Total):

$$8 \times 14.8 Wh = 118.4 Wh$$

Runtime of the vehicle with a single battery

$$118.4 \div 230.6 = 0.513 hrs = 30.8 min$$

Runtime of the vehicle with the backup battery.

$$30.8 \text{ min} * 2 = 61.61 \text{ min}$$

The vehicle is equipped with two 14.8 V, 8000 mAh lithium-ion batteries. One of the two batteries runs the whole system and acts as the primary powering unit, while the other acts as a backup.

The batteries have an inbuilt battery management system (BMS). In case of battery failure or its voltage dropping below the threshold value, the inbuilt charge protection circuit cuts off the battery's power supply. A power relay based on a switching circuit has been designed so that it can switch the power supply to the backup battery. Additionally, an inrush circuitry has been implemented to protect the system against inrush current and smooth and interruption-free operation.

For transmission of power to different sensors and actuators, a parallel output power distribution board is designed considering the power requirements and high-performance efficiency. As the voltage demanded by each of these may vary, the buck and boost converter converters are used.

## 6.2 Control Subsystem Sensors and Actuators

**Control Subsystem:** The vehicle's central embedded system uses an ATmega328 Arduino UNO (16 MHz) microcontroller as the main interfacing unit between various sensors and commanding the actuators. The vehicle uses long range wide area network (LoRa WAN) for wireless control of the vehicle and transmitting the data from sensors like GPS and LiDAR to and fro the vehicle and the controller.

**Sensors:** The sensor subsystem consists of GPS, LiDAR, IMU sensor, and FPV camera. GPS provides location and time synchronization and helps in tracking the location of our vehicle during operation and makes it easier to retrieve in case of loss of communication.

LiDAR is exceptionally cost-effective and is designed to map the distances of the surroundings in a plane by using a time-of-flight distance sensor placed on a spinning cylindrical surface, which in turn is moved by a stepper motor using the L293D motor driver. It gives the vehicle a complete 360° dynamic view.

First-person view (FPV) camera transmitter is used to transmit a continuous live video feed wirelessly to the control station. The AV transmitter works in the range of 5.725–5.850 GHz that makes it suitable for use (Figs. 8 and 9).

**Actuators:** The vehicle will use two Blue Robotics T100 thrusters, especially designed for marine applications. The thrusters will operate at the voltage of 12 V, 5A to give a thrust output of 3.5Kgf each. The thrusters will be connected to electronic speed controllers (ESCs) that will receive PWM values from the Arduino UNO and thus can be operated at different speeds.

## 7 Result and Conclusion

- Appropriate materials were chosen as operating conditions harsh on the structure. It is made lightweight for easy deployment of the vehicle without compromising the waste collection capacity and performance.



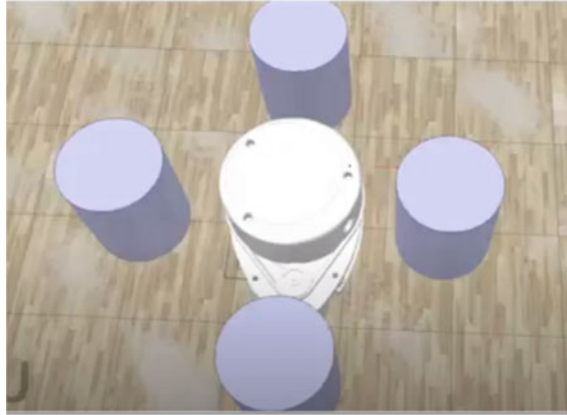


**Fig. 8** LiDAR simulation environment setup

- The catamaran hull was chosen to achieve better controls and stability, and all the simulations were performed considering the steady water assuming the laminar flow conditions,
- The boat would run for approx. 60 min to 75 min (as the boat would always not run-on full throttle) on a single charge.
- Custom LiDAR is built as an economical alternative. It is placed as a safety precaution to avoid collision with any obstacle that may have been missed from the camera view or any human error.
- The controller has a range of up to 8 km, and the FPV transmitter has a range of 5 km. If the vehicle is lost, it can be found with the help of the last known GPS and IMU readings.

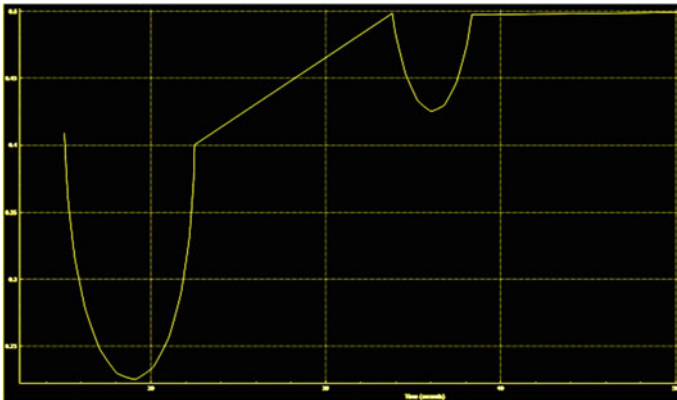


**Fig. 9** LiDAR time versus distance plot

If someone investigates the project's applications and capabilities, it can be concluded that this concept vehicle can be scaled to different sizes for different environments, and various manipulators can be added considering task complexity.

## References

1. Chao R-M, Lin HK, Wu C-H (2018) Solar-powered boat design using standalone distributed PV system. In: 2018 IEEE International Conference on Applied System Invention (ICASI). IEEE, pp 31–34
2. Natu A, Badhwar A, Garg V, Biswas U, Bansal D, Kumar A, Modeling and development of an autonomous underwater vehicle ARYA for object recognition
3. Natu A, Garg V, Gaur P, Dhruv PR, Sain S, Biswas U, Bansal D et al, Design and development of an autonomous underwater vehicle VARUNA 2.0
4. Kabir SL, Alam I, Khan MR, Hossain MS, Rahman KS, Amin N (2016) Solar powered ferry boat for the rural area of Bangladesh. In: 2016 International conference on advances in electrical, electronic and systems engineering (ICAEES). IEEE, pp 38–42



# Process Parameters Optimization of Stainless Steel Turning: A Survey

Tanpure Sandesh Papat<sup>(✉)</sup> and Netra Pal Singh

Department of Mechanical Engineering, Oriental University, Indore, India  
sani20048@gmail.com

## 1 Introduction

Milling and turning are the cutting processes which are an essential part of manufacturing processes of any industry. Tool wear affects the turning process by changing the contact conditions between the cutting tool and the work piece. The effects of tool wear are particularly important for hard steel machining applications where the cut size is comparable to the size of the resulting wear scars. Instrument wear causes bothersome impacts like loss of dimensional exactness of the completed item, conceivable harm to the work piece, diminished surface respectability, remaining pressure and unpleasantness, and enhancement of vibrations during the cutting interaction. Therefore, it is vital to assess instrument wear and anticipate apparatus life. The present study consists of reducing wear by providing coating on the surface of the cutting tool, optimizing machining parameters using the TAGUCHI technique, and developing the tool failure prediction model [1, 2].

## 2 Literature Review

Sousa and Silva [1] goes on being the biggest section of the machining business, featuring the proceeded with interest for turned parts and generally speaking cycle improvement. The turning interaction has gone through a significant development, from fundamental machines with strong instruments to complex multi-measure computer numerical control (CNC) machines, which use, generally, covered embeds and covered devices. This article is a presentation of the various kinds of coatings that have actually been used in the turning cycle, the turning of hard-to-machine materials, for instance, titanium and Inconel composites, similarly as the correspondence of these coatings with turned surfaces, the wear plans that cover these coatings during material turning and relate these wear instruments to the fate of the covered device.

Qehaja et al. [3], This article portrays the different boundaries that impact the surface unpleasantness in dry turning of covered carbide embeds. At the point when instrument wear arrives at a specific worth, cutting power, vibration and cutting temperature increment, bringing about helpless surface completion and size blunder surpassing resistance. This article gives surface harshness models  $R_a$  to different mixes of feed rate ( $f$ ), nose range ( $r$ ), and cutting time ( $T$ ). Expanding the tip range with lower feed rates and slicing

time has been found to prompt abatement in surface unpleasantness. The examination in this investigation shows that rate of feed has the main prevalence on surface harshness, trailed by nose span, and time for cutting.

Saini and Ali [4], From this research article, it could be concluded that turning operations generally involve high stresses, high interface temperatures (tool chip, tool part) ranging between 700–1250 °C. Coatings have been observed to reduce cutting forces and provide tool life, resulting in increased productivity. The author noted that the thickness of the coatings affects the adhesion of the coating as well as the tool life at high turning speeds. Among the various coatings examined in the research, the TiC coating was found to provide the longest tool life, and the Ti/TiN/TiCN/TiC multilayer composite coating showed great promise for high-speed turning operations. However, it requires further development to improve and optimize tool life at high cutting speeds.

Derflinger et al. [5], in this article, the author discussed the benefits of coolants in machining processes. In any case, the utilization, support, and removal of coolants involve huge expenses. Examination shows that occasionally, the expenses of utilizing a coolant are ordinarily higher than the expenses of instruments. In this way, the testimony of a hard covering/ointment on slicing instruments seems, by all accounts, to be an exceptionally appealing choice to decrease the immense measures of cooling emulsion in metal slicing and to work with practically no grease in various applications. Potential fields of utilization can incorporate the machining of combination prepares aluminum amalgams and cast iron.

Zheng et al. [6], this record centers around TiN/TiAlN-covered carbide device material. The rubbing and wear conduct of the covered instrument contrasted with steel of high strength were concentrated to uncover the components wear. The surface unpleasantness of the covered apparatus likewise influences its wear obstruction. It is presumed that between cycles of sliding which is dry, the sliding grating goes through the underlying stage and the steady-stage wear with the time of sliding. At the most noteworthy applied burden, the disagreement time was decreased, and the little variance in the coefficient of grating happened. As the sliding velocity and applied burden expanded, the wear volume of the circle test improved; however, the wear rate was diminished. The aggregation layer shaped on the well-used surface of the covered material of the apparatus can forestall direct contact of the rubbing force, which has assumed a positive part in oil and against grinding. During the dry turning measure, the joined activity of stripping, chipping, grip, mechanical scratching, component dispersion, and oxidation was the primary wear instrument of the TiAlN/TiN-covered apparatus. Above all, on the substance of the rake, titanium oxide (for example  $\text{TiO}_2$ ) has framed and can improve cutting execution.

Rajaguru et al. [7], in this investigation, the presentation of various covered apparatuses while machining overly duplex tempered steel (SDSS) was analyzed. The instrument study for wear presented that the “MT-TiCN”– $\text{Al}_2\text{O}_3$ -covered apparatus gave great wear opposition in all different type of coatings. The larger hardness of “MT-TiCN” and the oxidation security of  $\text{Al}_2\text{O}_3$  at the connection gave more noteworthy wear obstruction in all different coatings. The AlTiN covering created a more temperature because of the great rubbing and low warm conductivity. The leftover weight on the machined surface showed that the burdens were elastic for all coatings examined, which can prompt

disappointment. The surface machined with TiN-“MT-TiCN”-Al<sub>2</sub>O<sub>3</sub> covering showed lower leftover tractable pressure among different surfaces because of the overall prevalence of plastic twisting from mechanical burdens on the impacts of high temperatures. The surface harshness profile showed that the “MT-TiCN”-Al<sub>2</sub>O<sub>3</sub> covering displayed lower unpleasantness (X<sub>a</sub>) values because of its higher scraped spot obstruction along the front lines, and the surface had less buildup than different surfaces. The investigation recommends that the “MT-TiCN”-Al<sub>2</sub>O<sub>3</sub> covering gave moderately better execution as far as instrument wear, cutting power, cutting temperature, and surface respectability.

Ramana and Aditya [8], in this exploration article, dry investigations are directed on the ACE Designer Super Jobber 500 CNC machine. The material to be machined is a Grade 5 alpha-beta titanium compound (Ti-6Al-4 V). Investigation of fluctuation (ANOVA) uncovered that the impact of individual elements and connection factors on surface unpleasantness is huge for the uncoated instrument. Feed rate is accepted to offer more than cutting pace and profundity of slice to limit surface unpleasantness for both covered and uncoated devices. It was additionally seen that the uncoated device performed better at lower cutting rates, and the PVD covered apparatus performed better at higher cutting paces.

Narasimha [9], in this paper, the creator examined that when machining solidified M42 instrument steel, TiAlCrYN coatings are compelling in diminishing apparatus wear because of chipping and will in general improve device life. In this article, the writer attempts to show the significance of improving cutting instrument execution by utilizing PVD or CVD coatings. It endeavors to apply the overall model of a quality administration framework dependent on “shut circle quality circles” in the turn of events and useful presentation of covered slicing instruments and to decide the machinability system in getting done with machining, where the “dimensional exactness, surface unpleasantness, and device life are the primary concerns. It very well may be reasoned that the outside of the cutting apparatus and the portrayal of surface coatings, just as quality affirmation, are vital pieces of the powerful improvement of cutting instruments.

Siraj [10], In this exploration, we attempted to examine the impact of cutting boundaries (feed, rate of cutting, and profundity of cut) on the presentation attributes of surface harshness in turning hard of AISI 52,100 bearing solidified steel to 60 HRC with boron nitrate cubic (CBN) utilizing the apparatus tip with a range of 0.4 mm, 0.8 mm, and 1.2 mm. The instrument tip sweep assumes a significant part and tribological boundaries like feed, speed, and profundity of cut assume a similarly significant part in the machining cycle; however, in investigation, feed and profundity of cut showed superb holding impact in forecast of the unpleasantness esteem. As indicated by the introduced results analysis, the surface harshness is unequivocally impacted by the rate of feed, while the cutting pace has a negative impact and the profundity of cut an insignificant impact.

### 3 Optimization Methods for Process Parameters

Following are some methods used for finding optimum process parameters.

### 3.1 Taguchi Method

Dr. Taguchi of Nippon Telephones and Telegraph Company, Japan, has constructed a method structured on “Symmetrical Arrangement” assessments that offers an rather diminished “fluctuation” for the evaluation with “best fit” of the manipulate boundaries. In this way, the marriage of the design of experiments with the streamlining of the manage boundaries to gather the BEST results is performed in the Taguchi method. The “symmetrical arrangement” (OA) supplies a development of even (negligible) investigations and Dr. Taguchi’s signal-to-clamor (S/N) proportions, which are logarithmic factors of the perfect yield, fill in as goal capacities for development, assist in investigating statistics, and foreseeing perfect results. Taguchi traces use symmetrical groups, what separate the outcomes of elements on the response MRR and surface. A symmetrical bunch drives the association is modified with the goal that variable tiers are weighted comparably [11, 12].

#### 3.1.1 Taguchi Optimization Methods

(A) Static Problems:

By and large, an interaction to be advanced has a few control factors that straightforwardly choose the objective or wanted estimation of the yield. Improvement at that point includes deciding the best factor control levels, so the yield is at the objective worth. This issue is known as the “STATIC PROBLEM.” This is best clarified utilizing a P chart appeared underneath in Fig. 1 (“P” represents process or product). The commotion is appeared during the interaction yet it shouldn’t have any impact on the yield. This is the principle objective of the Taguchi tests: to limit varieties in the yield regardless of whether there is commotion all the while. So, the interaction is said to have gotten hearty [12, 13].

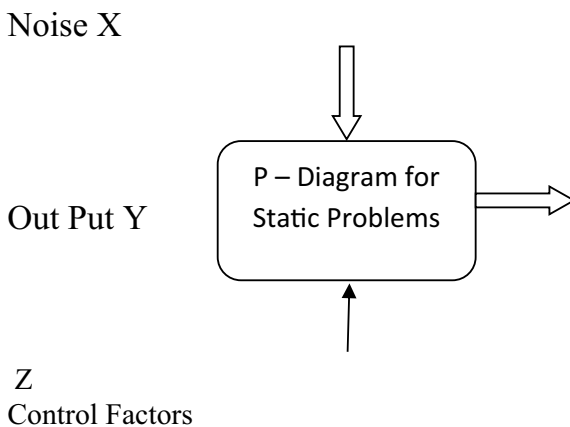


Fig. 1 Static problem optimization

(B) Dynamic Problems:

In the event that the item to be improved has a sign information that straightforwardly chooses the yield, enhancement includes deciding the best factor for control levels, so the “input/yield signal” proportion is the nearest to the ideal proportion. This issue is known as a “powerful issue.” This is best clarified by a P chart appeared underneath in Fig. 2. Once more, the primary goal of the Taguchi tests, to limit yield varieties regardless of whether there is commotion all the while, is accomplished by accomplishing better linearity in the information/yield proportion [12–14].

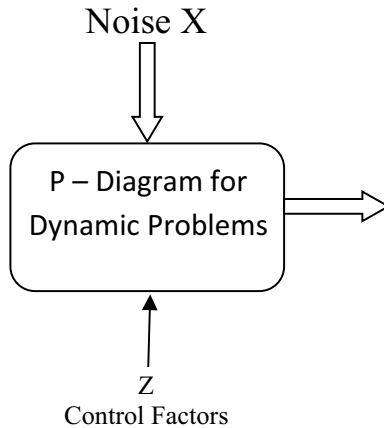


Fig. 2 Dynamic problem optimization

3.2 Support Vector Machines

SVM is a highly beneficial tender computerized analysis approach dependent totally on the statistical gaining knowledge of principle introduced by way of Vladimir Vapnik. SVM tries to assemble a separation hyperplane by way of maximizing the margin between two records units based totally on their instructions that have before been mapped into a large dimensional space. To decide the area, two parallel hyperplanes are developed on every facet of the setting apart hyperplane. Optimal or best separation is accomplished by using the hyperplane that has the best distance from neighboring records factors of each classes, due to the fact the large the margin, the higher the classifier’s generalization error. SVM has been used in many mannequin cognizance and regression estimation issues and has been utilized to dependency estimation, prediction, and clever computer constructing problems. SVM has classification issues; SVMs have the manageable to deal with very giant function spaces; due to the fact, SVM coaching is accomplished in such a way that the dimension of labeled vectors does no longer have as clear an effect on SVM overall performance as it does.

In traditional SVM, overall performance classifiers are there; this is why it is mentioned that it is in particular tremendous in massive classification problems. Furthermore, it is noted that SVM-based classifiers have right of generalization homes in contrast to traditional classifiers; due to the fact with the aid of education, the SVM classification which is also called constructive misclassification chance needs to be minimized, while regular classifiers are commonly used risk. The expression which is in the mathematical form of the SVM classification is shown as proven beneath [15, 16].

$$f(x) = w^T x + b = \sum_{j=1}^n w_j x_j + b = 0$$

### 3.3 Artificial neural networks

ANNs are productive in adjusting and learning, and therefore, they are utilized as displaying devices in various applications. An ANN is comprised of three kinds of levels: an info level that acknowledges input factors. The secret layers have various neurons and a yield layer comprising of a neuron which, for the situation analyzed here, gives the surface unpleasantness Ra. The covered up and yield layers are comprised of various neurons that play out a particular non-direct capacity. Neurons in a single layer are interconnected with neurons in the front and back layers ineffaceable weighted connections. Every neuron in the covered up and yield layers is made up for by a limit esteem. The numerical model of fake neuron conduct is the disentanglement of the organic cerebrum neuron, as demonstrated in Fig. 3. A few information sources  $x(n)$  to the organization duplicated by the loads  $y(n)$  are shipped off a neuron. While gathering and thresholding, the neuron adds the weighted information sources, goes the outcome through a non-direct exchange capacity, and gives a yield  $Y_i$  [15].

$$Y_i = f\left(\sum_{i=0}^{n-1} w_i x_i - \theta\right)$$

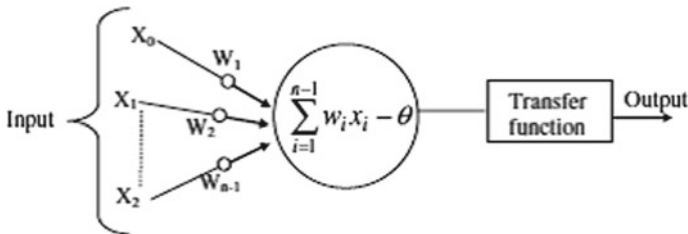


Fig. 3 Analysis of an artificial neuron

The average value for the error of complete system is calculated by [15]



### 3.4 ANOVA (Analysis of Variance)

“ANOVA” (Analysis of variance)—the fundamental target of “ANOVA” is to research the plan boundaries and show which boundaries altogether influence the yield boundaries. The amount of squares and change is determined in the investigation. ANOVA can be valuable for deciding the impact of a given information boundary from a bunch of trial results by planning tests for the assembling cycle and can be utilized to decipher test information. Examination of fluctuation (ANOVA) is an assortment of measurable models and related systems, wherein the noticed change in a specific variable is separated into parts inferable from various wellsprings of variety. In its easiest structure, “ANOVA” gives factual data to choose ideal qualities for the material evacuation rate “MRR.” “ANOVA” is a specific type of factual speculation testing broadly utilized in the examination of trial information. A factual theory test is a strategy for settling on choices utilizing information [2, 17, 18].

A test outcome (determined from the invalid speculation and the example) is supposed to be genuinely huge on the off chance that it is viewed as improbable that it happened by some coincidence, expecting the reality of the invalid theory. A genuinely critical outcome, when a likelihood (p-esteem) is not exactly an edge (importance level), legitimizes the dismissal of the invalid theory, however just if the deduced likelihood of the invalid speculation isn’t high. In the commonplace ANOVA application, the invalid theory is that all gatherings are basically irregular examples from a similar populace. For instance, when contemplating the impact of various medicines on comparable patient examples, the invalid theory would be that all medicines have a similar impact (potentially none). Dismissing the invalid theory would infer that various medicines produce adjusted impacts. By development, speculation testing limits the pace of type I blunders (bogus positives prompting bogus logical cases) to a degree of importance. Experimenters likewise need to restrict type-II mistakes (bogus negatives that bring about lost logical forward leaps). The sort-II mistake rate is an element of a few components, including the example size (emphatically corresponded to the expense of the analysis), the degree of importance (if the norm of confirmation is large, the odds of missing a revelation are likewise high), and the impact size is clear to the easygoing eyewitness, type-2 blunder rates are low. The phrasing for “ANOVA” generally gets from the measurable plan of the tests. The experimenter changes factors and measures reactions trying to decide an impact. Components are allotted to exploratory units utilizing a mix of randomization and hindering to guarantee legitimacy of results. Visual deficiency keeps on weighing accurately. The reactions show fluctuation that is incompletely the consequence of the impact and is a somewhat arbitrary mistake [2, 17, 18].

## 4 Conclusion

In the Taguchi method, “improvement” suggests “deciding the BEST degrees of control factors.” Thus, the BEST degrees of factors for control are those that augment signal-to-commotion proportions. The sign-to-noise proportions are logarithmic elements of the ideal yield qualities. The trials, which are directed to decide the best levels, depend on “symmetrical networks,” are offset as for all the control factors yet they are insignificant in number. All SVM expectations utilized were superior to ANN results. The ANN

model takes more time to process than SVMs, lastly, change examination can be utilized to depict complex connections between factors.

## References

1. Sousa VFC, Silva FJG (2020) Recent advances in turning processes using coated tools—a comprehensive review. *MDPI, Metals* 10:170. <https://doi.org/10.3390/met10020170>
2. Shivade AS, Bhagat S, Jagdale S, Nikam A, Londhe P (2014) Optimization of machining parameters for turning using Taguchi approach. *Int J Recent Technol Eng (JRTE)* 3(1). ISSN: 2277-3878
3. Qehaja N, Jakupi K, Bunjaku A, Bruci M, Osmani H (2014) Effect of machining parameters and machining time on surface roughness in dry turning process. Elsevier
4. Saini DP, Ali M (2003) New generation coating for high speed cutting tools. University of Wollongong, Australia
5. Derflinger V, Brandle H, Zimmermann H (1998) New hard/lubricant coating for dry machining. Elsevier
6. Zheng G, Zhao G, Cheng X, Xu R, Zhao J, Zhang H (2018) Frictional and wear performance of TiAlN/TiN coated tool against high strength steel. Elsevier
7. Rajaguru J, Arunachalam N (2017) Coated tool performance in dry turning of super duplex stainless steel. Elsevier
8. Ramana MV, Aditya YS (2017) Optimization and influence of process parameters on surface roughness in turning of titanium alloy
9. Narasimha M, Patel M, Rejikumar R (2014) Application of coating on carbide insert. *Int J Eng Sc (IJES)*
10. Siraj S, Dharmadhikari HM, Gore N (2018) Modeling of roughness value from tribological parameters in hard turning of AISI 52100 steel. Elsevier
11. Venkatesan K, Ramanujam R, Saxena V, Chawdhury N, Choudhary V (2014) Influence of cutting parameters on dry machining of inconel 625 alloy with coated carbide insert—a statistical approach. *ARPN J Eng Appl Sci* 9(3)
12. [https://www.ee.iitb.ac.in/~apte/CV\\_PRA\\_TAGUCHI\\_INTRO.htm](https://www.ee.iitb.ac.in/~apte/CV_PRA_TAGUCHI_INTRO.htm)
13. Vijay Kumar M, Kiran Kumar BJ, Rudresha N (2018) Optimization of machining parameters in CNC turning of stainlesssteel (EN19) by Taguchi's orthogonal array experiments. *Sci Dir Mater Today Proc* 5:11395–11407
14. Gopalsamy BM, Mondal B (2009) Taguchi method and ANOVA: an approach for process parameter optimization of hard machining while machining hardened steel. *J Sci Ind Res* 68
15. Çayda U, Ekici S (2012) Support vector machines models for surface roughness prediction in CNC turning of AISI 304 austenitic stainless steel. *J Intell Manuf* 23:639–650
16. Quazi T, More PG (2014) Optimization of turning parameters such as speed rate, feed rate, depth of cut for surface roughness by Taguchi method. *Asian J Eng Technol Innovation* 02(02):05–24
17. Mohan Kumar S, Kiran Kumar K (2017) Optimization techniques in turning operation by using Taguchi method. *Int J Eng Adv Technol (IJEAT)* 6(6). ISSN: 2249-8958
18. Gopalsamy BM, Mondal B, Ghosh S (2009) Taguchi method and ANOVA: an approach for process parameters optimization of hard machining while machining hardened steel. *J Sci Ind Res* 68:686–695



# Integrated Real Time Database for Supermarkets

Archit Jain and Nitin K. Puri<sup>(✉)</sup>

Delhi Technological University, Delhi, India  
nitinkumarpuri@dtu.ac.in

## 1 Introduction

### 1.1 Improvements in the Grocery Shopping Experience

To aid in the task of grocery shopping, the first shopping trolley was introduced in 1937, increasing the customers comfort and efficiency while they shop. But the possibilities of improving comfort afforded to the customers do not end at the shopping trolley. Since then, there have been improvements in the design of the shopping trolley including the invention of the Nested cart. Even after latest upgrades as shown by the robotic trolley [1–4] that can follow the customer or even keep a track of the total cost of the products that have been added to the cart and automatically bill them such as the Amazon Dash Cart [5], we feel that there is still a lot of scope for improvement and innovation. Current upgrades to shopping infrastructure are focused on the shopping trolley and checkout system, where trolleys using a wide range of sensors such as infra-red, ultrasonic, etc. are enabled to follow customers to give them a hands free approach to shopping. The trolleys are also equipped with RFID scanners so that they can directly bill items with RFID tags attached to them [6, 7]. This is impractical as this raises cost of fitting each product in the inventory with RFID tags. The Amazon Dash Cart instead is pushed by customers themselves while items are billed by cameras and fusion sensors to scan barcodes of each item as it is put in the cart. In [8], it has been found that customers spend minimal time on making decisions and instead opt to buy products that they are directly habituated to. This is due to the vast amounts of data that needs to be processed so that customers can make better and informed decisions, regarding their health and the overall cost of their items.

The aim of any project or innovation is to improve the functionality or increase comfort and safety of any user, along with making it easier for them to process the vast amounts of information that needs to be processed at a supermarket. In day-to-day grocery shopping, there are still many inconveniences faced by customers that can be resolved to immensely improve the customer experience. With the innovations suggested, we have tried to remove few inconveniences faced by the customers, to enable some comfort and delight in the shopping experience.

## 1.2 Issues Faced in Shopping

Some of the major inconveniences or issues faced by customers while shopping are:

1. **Product Availability:** While shopping at the supermarket visited for your urgent and essential needs, the biggest issue faced is of the product stock-out. To buy this essential need now you need to visit another supermarket to get the required product, leading to wastage of time and spending more on commute cost.
2. **Cost:** The customer cannot reliably compare the total cost or expenditure at any supermarket, as there are many promotional offers or alternatives that are found only when they go to the supermarket.
3. **Navigation:** When customers go to a supermarket, they spend a lot of time searching for products, repeatedly ask for directions to the supermarket staff or search around by trial and error, the aisle/shelf of the item they need. This leads to wastage of time and increases the hassles in shopping. Furthermore, to help customers, shopping marts are required to employ more staff to guide customers to the products they need.
4. **Congestion:** Supermarkets are very congested especially during rush hours. Aisles are blocked by multiple carts and customers and there is generally very little space to move in. To manage the traffic inside the supermarket, more staff is employed during rush hours. This is an issue made more prominent due to COVID-19, where it is essential to maintain social distancing.

## 2 Resolving the Inconveniences

### 2.1 Real Time Online Database of Product Inventory

For a customer to make better informed decision of the supermarket from where to buy their groceries from, they need to be able to easily compare:

1. **Product Availability:** To ensure they can buy all the essential groceries they need without making multiple trips to various supermarkets.
2. **Product Prices and Promotional Offers:** To get their groceries at the best price available, thereby minimizing total cost.

To help the customers with this, we have designed an Online Database that will store the real time Product Inventories of all supermarkets. This means that database will reflect changes in product inventory immediately as they are checked out from supermarkets. This database can be accessed from Mobile app and thus a customer can search the real time inventory of nearby shopping markets.

This is beneficial to the customer as this reduces the number of trips they need to make or the number of supermarkets they visit. For e.g., they can confirm using the database, that Shop A has 90% of the immediate need and essential products they need to buy (Example: Salt/Flour they need to cook their dinner) and 95% of the products that they can do without at the moment (Example: Ice-cream) but is on their shopping list. While Shop B has 100% of the immediate needs and essential products but only

75% of the products they can do without at the moment. Thus, the customer can directly go to Shop B and get all their essential needs and buy the remaining products at a later date. This is advantageous over the present trial and error, where the customer would first visit Shop A, and then Shop B to get all their essential products. This may even lead to over expenditure on the customer's part, as they waste fuel on traveling between multiple supermarkets. Also, the customer would invariably end up buying extra items (not in the shopping list) on impulse (a natural trait), as he keeps on visiting multiple supermarkets, whereas the extra shopping would be very limited, if the customer visits only a single supermarket for his essential needs.

## 2.2 Navigation Inside the Supermarket

Current advancements in technology in supermarkets include the Amazon Go Store. Inside the Amazon Go Store to help with navigation, kiosks have been installed, where a customer can interact with Alexa and ask which shelf a product can be found. But what if the customer had the directions shown to them via their smartphones, leading them directly to the shelf that contains their product. This will lead to saving time and effort for the customer and cost of installing kiosks for the supermarket. Through the database, the supermarkets can store the aisles/shelves the products are stocked on. Using the shelf id's, and a digital map of the store (using Indoor Mapping services such as Mapwize), the customer can navigate through the supermarket easily. To accurately detect the position of the user inside the supermarket, there are various methods such as Simultaneous Localization and Mapping, BLE beacons, RFID Tags and WI-FI, and Magnetic Positioning [9]. From these indoor positioning methods, the best overall that offers precise positioning with least installation and cost is the Magnetic Positioning as it can use the sensors inside the phone itself and the store mapped easily [10]. Magnetic Positioning relies on the fact that Buildings have unique magnetic fields or fingerprints. Using mapped out magnetic readings, the position of the user can be determined by reading the magnetic field near the user.

Furthermore, creating and updating the Magnetic Field Data are very easy and can be done with little technical expertise provided by using the app Indoor Atlas. And the main support for using Magnetic Positioning lies in the accuracy provided by it compared to the other methods as in a supermarket shelves are very close and a discrepancy of 6 feet can lead the customer to a different shelf than the required one.

## 2.3 Maintaining Distance/Avoiding Congestion in Aisles

During rush hours, the entire supermarket is crowded as people search for their products through the maze of other shoppers, trolleys, and shelves inside the supermarket. The mapping aspect of the project resolves the issue of searching for products and allows customers to directly go to the shelf they need. But another issue is that they may end up, taking rounds of the entire supermarket to get all of the items in their shopping list. This would be a hassle to the customer and tire them out, decreasing customer comfort. To resolve this, the shelves id's can be sorted by 'nearest to Entrance' to 'farthest from entrance.' The customer can then search for all the items they need and the app will store all the shelves they need to visit, along with the product they will buy from it.

The app can then show directions for the shortest path throughout the supermarket, to get all the products they need. This will allow customers to buy their products in a more organized manner, spend less time in the supermarket, increase efficiency and comfort, leading to less congestion in the supermarket and overall increase in customer delight. Customers would naturally prefer to spend less time in the supermarket and have more time available for leisure activities. Furthermore, the organized manner and increased efficiency of shopping will lead to an increase of customers during the weekday’s as currently the time required for shopping is not available during the weekdays due to time constraints such as jobs, schools, etc. But shorter shopping times can be afforded during the weekdays while returning from work and hence free up weekends for customers. This would further improve the weekend shopping experience, due to decrease in the flow of customers that is concentrated on weekends will spread out into the weekdays.

### 3 Architecture and General Design of the System

#### 3.1 Architecture

Figure 1 shows the architecture of the system designed and tested with arrows showing the flow of data from one node of the system to another (node being the Smartphone App, Database, and the checkout counter). The Inputs for the Smartphone App are information that is entered by the user and the outputs are information and messages displayed to the users.

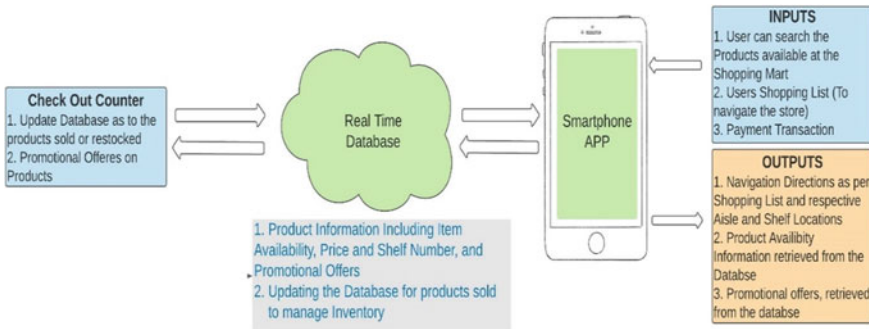


Fig. 1 Architecture of the system

#### 3.2 Software Design

The Database was built using PostgreSQL. The server API’s were created using Python and Flask. The database was hosted locally for testing purposes and can be migrated to online Database Management services like Amazon Web Services or MongoDB Atlas. The database consists of two types of tables, one is the Super Market table and the other is the Product Inventory table.

The Super Market Table has the list of supermarkets, their location, and the link to their corresponding Product Inventory table. This will allow the user to use one common app to access the Product Inventory for all supermarkets that will share their data to the App. The location will also allow the user to search for supermarkets at a specific location (Table 1).

**Table 1** Super market table sample

S. No.	Name	Location	Link
1	A	Rohini	http/...
2	B	Prashant Vihar	http/...
3	C	Pitumpura	http/...
4	D	Undri	http/...
5	E	Kundli	http/...

*Note* The data shown is random and not real. Links will be replaced by links to the actual data set

The Product Inventory Table has all the information regarding the products as mentioned below:

1. Barcode: To identify the product when scanned
2. Name: Name of the Product
3. Price: The price of the product
4. Promotional Offer: That is the details on the promotional offer available on the product.
5. Area: The identification used to show which shelf or area the product is stocked in. (Shelves can be numbered or divided into areas depending upon the supermarket)
6. Inventory: The number available in stock (Table 2).

**Table 2** Product inventory table

Barcode	Name	Price (INR)	Promotional Offer	Area	Inventory
890105885129	Noodles	1512.62	10%	12	35
620514000121	Vermicelli	200	5%	13	45
234378624568	Paprika Seasonings	100	Buy 2 get 1	1	100
378905687846	Mayonnaise	255	–	6	200
375879665305	Chocolate Ice-cream	500		15	15

*Note* The Table shown above does not reflect real data and the barcodes and prices are random while the Product names may exist

### 3.3 Functioning of the App

The user will first select the supermarket they want to check the real time inventory for. They can then paste their entire shopping list or individually search for each item. The App will then search the Product inventory of the selected supermarket and return the Inventory for each item and keep a check on it in real time. Upon arrival to the supermarket, the user can then click the button Navigate, which will then show the user directions to the shelves and guide the Customer through the supermarket in the least time.

## 4 Applications and Future Endeavors

### 4.1 Applications

- The supermarkets can use the searches sent to the database by customers to individualize promotional offers and directly send it to them using machine learning.
- Supermarkets can also use the searches, to better analyze market trends and hence stock their inventory accordingly, boosting sales and margins.
- Supply Chain Management can be improved as customer demand can be better analyzed through the searches.
- Manufacturers have access to real time data of the demand of their product and the prices it is sold at, allowing them to better their product and marketing strategy.

### 4.2 Future Endeavors

- Add a Third table to the Database that contains only the number of items on the shelves. This will be updated in real time with the checkout of items. The Database will then be used to trigger warnings to the staff when the stock on shelves fall below certain levels allowing them to restock it as soon as possible.
- Use the trolley to bill items automatically and update the Database so that checkout counters can be eliminated or reduced and save time for customers.
- Provide Nutritional Information on Products depending on user choice so that they can make healthier decisions and create an assistant that can offer better alternatives to the products that they buy both health wise and cost wise.

## 5 Conclusion

There is lot of scope in the supermarket industry to increase comfort to the customers and hence boost sales and margins. The App and database designed and developed by us resolve some of the most common inconveniences faced by customers. The customer is able to better plan their shopping trip at the minimum cost with the help of the online inventory and promotional offers provided by the app. They will spend less time at the supermarkets with the help of the navigation system. These comforts will push customers for weekday shopping, thereby leaving their weekends free for recreational activities, giving them option to work in the improvement of their health. The



supermarkets will benefit by better inventory management and reducing the stocks of the unpopular products, reducing costs for them. The supermarket will also be able to offer better promotions, based on the customers need and choices. The stress on supermarket staff will also reduce as they will be saved from frequent queries on product inventory and directions to the shelves. An additional advantage from the database created will help the manufacturers plan their product and marketing strategies.

Furthermore, the database provides all relevant information to the customer in a clear and concise manner, making it easier for the customer to process all the data and therefore actually make decisions instead of opting to just buy according to habits.

## References

1. Engineering C, Kumar Sultania S, Jaiswal G, Jain P (2011) RFID based automatic shopping cart Ankit Anil Agarwal (corresponding author). 1(1). Accessed: 22 Mar 2021. (Online). Available: [www.iiste.org](http://www.iiste.org)
2. Wani M, Keswani N, Neel S, Chopade S (2021) Automatic billing trolley. Accessed 22 Mar 2021. (Online). Available: [www.irjet.net](http://www.irjet.net)
3. Developing a multitasking shopping trolley based on RFID technology 180
4. Soni A, Singhai A, Poras AS, Namdev K, Trivedi P, Bluetooth remote controlled shopping cart using arduino. Int Res J Modernization Eng Technol Sci 02(04)
5. "Amazon.com: Amazon dash cart: grocery & gourmet food. <https://www.amazon.com/b?ie=UTF8&node=21289116011>. Accessed 22 Mar 2021
6. Naveenprabu T, Mahalakshmi B, Nagaraj T, Kumar SPN, Jagadesh M (2020) IoT based smart billing and direction controlled trolley. In: 2020 6th International conference on advanced computing and communication systems (ICACCS), Coimbatore, India, 2020, pp 426–429. <https://doi.org/10.1109/ICACCS48705.2020.9074173>
7. Akshatha NA, Nikshitha N, Jyothi S, Aishwarya K, Design of an embedded high efficiency intelligent smart trolley
8. Machín L, Curutchet MR, Gugliucci V, Vitola A, Otterbring T, de Alcantara M, Ares G (2020) The habitual nature of food purchases at the supermarket: implications for policy making. *Appetite* 155:104844
9. Indoor Positioning: what do you do in a building when your GPS stops working. <https://www.geospatialworld.net/blogs/indoor-positioning-indoors-gps-stops-working/>. Accessed 22 Mar 2021
10. Senior GS (2021) Technologies for indoor location and offline analytics differ substantially in their magnetic positioning. Accessed 22 Mar 2021. (Online). Available: [www.opusresearch.net](http://www.opusresearch.net)



# Greywater Reuse and Treatment Methods for Quality Improvement: A Review

Deepak Narayan Paithankar<sup>(✉)</sup> and Shashi Ranjan Kumar

Department of Civil Engineering, Oriental University, Indore, India  
deepakpaithankar@msn.com

## 1 Introduction

Water plays an important and varied role for human activity, industries and irrigation. It works as a reagent, solvent, cleaning and washing agent [1]. Life without water is scary. But, this natural source is continuously reducing due to rising population and human activities, and the water available per capita/year has already reduced indicating the condition of severe water shortage [2]. Drinking water is emerging as one of the most valuable needs worldwide [3] and its shortage has already forced the Australian water industry and its population to search for alternate source of water [4]. The shortage in natural water resources and a rising population have become an alarming situation [5].

It is estimated that 50–75% of domestic water consumption is related to wastewater due to human activities such as washing, cleaning, bathing, gardening, etc. [1]. The actual requirement of tap water for cooking and drinking is low. Population growth and their activities have led to an increase in the amount of domestic wastewater load discharged into water bodies, thereby, affecting the aquatic life and the environment [2]. To overcome the problem of water shortage and pollution, some countries have already adopted the practice of desalination of sea and brackish water and reuse wastewater [3].

In the recent years, smart practices of saving water due to the use of a greywater treatment system are gaining popularity [6]. In literatures, greywater is defined as domestic wastewater except the water from toilet flushes [7]. Greywater originating from bath and laundry contains remains of soaps, detergents, hairs, lints, etc. while the greywater emerging from kitchen contains oils, fats, salts and food particles. The pathogenic microorganisms like bacteria, protozoa, viruses and parasites are also found in greywater. Concentrations of these pathogens may be high in untreated greywater, therefore, it is necessary to take precautions in greywater reuse. Some countries have strict guidelines for handling greywater, and direct human contact is forbidden [8]. Treated greywater should be safe, hygienic, eco-friendly, economical and esthetic [9].

Treatment and reuse of greywater can be a useful non-potable source of water for toilet flushing, gardening, washing of cars and floors, etc., [10, 11]. There are many psychological issues related to use of greywater which sometimes presents a barrier in its recycling. Areas of rural India facing drought/short supply have already started recycling greywater. Wastewater from food processing is reused in cattle rearing [12].

Methods used for greywater treatment may include physical systems such as sedimentation filters, screening and ultra-filtration (UF) membranes; chemical processes

such as ion exchange resins, coagulation/flocculation for removal of effluents and biological processes such as constructed wetlands, RBC, MBR and SBR to reduce pathogenic concentration. Physical treatment systems cannot reduce the desired microbial concentration, they are used along with some disinfection steps like chlorination or addition of activated charcoal or in combination with chemical or biological process [13]. Bark and charcoal are gaining attention as filter media in addition to soil and sand because of their high porosity and high carbon content [14, 15]. The aim of this paper is to review the works carried out in different parts of the world for greywater treatment.

## 2 Literature Review

Barzegar et al. [1] collected greywater samples from a dormitory in Iran. The sample water was kept at 4 °C to avoid biological reactions. 750 mL of greywater sample was inserted into an electrocoagulation reactor consisting of 2 electrodes, and the system was powered with a D.C supply of 20 V. The sample water was subjected to electrolysis and magnetically stirred. The researchers added the pH of the sample by adding sulfuric acid and Sodium Peroxide. An ozone generator and UV lamp were also used for treatment. The researchers measured the COD and TOC removal rate with samples of different pH values and concluded that the removal rate reached a maximum of 85% and 70% with pH = 7.0 and was related to the current density and ozone dosage. The removal efficiency of the system is not very good and also practical implementation of the project on site would be unfeasible due to cost and complexity requirements.

Liberman et al. [3] constructed a pilot system in Ben-Gurion university sports center. Two tanks were used for filtration of greywater. The shower water of the sports center was pumped from the sewage into the feed tank which served as a sedimentation filter. For removal of hair and other impurities, three filters with reducing pore size were connected at the outlet of the feed tank. The water was inlet to an MBR which contained a submerged ultra-filtration module. To start the system, the researchers obtained 160 L of activated sludge from a local wastewater treatment plant as a starting biomass which had a mixed liquor suspended solid (MLSS) concentration of 500 mg/L. The MLSS concentration increased to a value of 5000 mg/L over a period of 9 months and no sludge was wasted during the process. High MLSS concentration and no sludge wastage indicated the development of biomass needed for biological reaction. The system produced very low levels of COD, TSS, BOD<sub>5</sub> and TOC levels. The authors have reported that the cost of effluent production by the system is less than the cost of domestic water in Israel.

Al-Ismaili et al. [6] performed the treatment on wastewater collected from a house in Oman. The treatment system involved a storage tank to preserve raw greywater which was later pumped into a polyethylene tank consisting of layers of natural filters i.e., dune sand followed by fine gravel and medium and large stones. The water was subjected to Chlorination to purify the water. The treated water met the required standards for irrigation of trees and garden crops. The system automatically pumps water from storage tank to the filter tank as soon as the water level in the storage tank reaches 0.4 m<sup>3</sup>/d. The system requires cleaning and replacement maintenance only in case of upper layer of dune sand in order to clean debris every 6–8 weeks. The system needs a maintenance cost of nearly 60 US \$ every 3 years where the sand dunes have to be completely replaced whereas other materials of the filter can be thoroughly washed and reused.

Bani et al. [16] evaluated the performance of an SMBR system in terms of effluent quality and membrane fouling. The team operated the SMBR for a period of 42 days with constant pressure of 13 kPa in six consecutive stages. The system produced the following values for COD, NH<sub>3</sub>-N, turbidity and color: 45 mg/L, 0.26 mg/L, 3 FTU and 18 PtCo in the effluent, respectively. Furthermore, TSS was completely eliminated and fecal coliform count was below the required value. The researchers concluded that the treated greywater could be used for most of the non-potable applications—in arid areas.

Ramprasad et al. [17] describe the operation of a GROW (Green Roof Top Water) Recycling system which was installed and monitored in a student hostel at IIT Madras for a period of 2 years. The system consists of 12 trapezoidal shaped troughs placed in 4 rows one above the other over a steel scaffolding frame which gives the appearance of a staircase. Each trough had the capacity to hold 125 L of water. Troughs in a row were serially connected whereas rows one above the other were laterally interconnected. The GROW treatment system is a novel approach with a shallow horizontal subsurface flow with 8 varieties of local plants, and the treatment was carried out in two different phases by replacing the filter media and the species of plants. The greywater was inlet to trough 1 through an overhead tank which moved from trough 1–12 and finally appeared at the output of trough 12. The system produced a high removal efficiency for BOD, COD, TSS, Fecal coliform as 90.8%, 92.5%, 91.6% and 91.4% respectively. The removal rate was found to increase during the summer and also with high loading rate.

Couto et al. [18] constructed a greywater treatment unit in a Brazilian airport. The unit consisted of two 500 L of polyethylene tanks, one for controlling the flow rate of the greywater to the filter bed and second to store treated greywater. The unit included two hydraulic pumps to operate the inlet and outlet flows of the tank. An anaerobic filter and UV disinfectant device working at 36 W was placed between the two tanks. pH average was 7.7 with BOD<sub>5</sub>, COD, Turbidity and TSS efficiencies as 73%, 71%, 88% and 77% respectively. The *E. coli* removal rate was 80%. The reuse of treated greywater did not pose any health threats. However, the installation and maintenance cost of the cost ran into thousands of US\$.

Cui et al. [19] constructed a pool to study the removal efficiency of constructed wetlands. The researchers divided the pool into 4 cells, with each cell measuring 2 m × 1 m. All 4 cells were constructed to work as independent constructed wetlands. The first 3 cells were further divided to hold 5 compartments each. The first cell was designed to work as a horizontal baffle flow constructed wetland where the water horizontally moved from one compartment to the other. The second cell was a vertical baffle flow constructed wetland where holes were made in the compartment to enable vertical flow from one compartment to other. The third cell was a hybrid baffle flow constructed wetland where water flow among the compartment was vertical as well as horizontal. The 4th cell was a subsurface horizontal baffle flow constructed wetland. All the cells were filled with limestones and gravel. The first compartment of all the first 3 cells was filled with cinder, rubble and blast furnace slag, whereas the remaining 4 compartments were filled with blast furnace slag. The 4th cell was only filled with blast furnace slag above the gravel layer. Finally a layer of fine sand was spread over all the 4 cells. Finally yellow flower canna was planted in all the 4 cells. The vertical baffle flow constructed wetland showed higher nitrogen and phosphorous removal efficiency among the 4 methods. The

removal efficiency of TP, COD, BOD<sub>5</sub>, pollutants was highest in the hybrid baffle flow constructed wetland.

Ghaitidak et al. [20] carried out a treatment study on the greywater originating from students hostel located at (SVNIT), Surat. The researchers examined four treatment options on site, namely a two-stage sand filtration and three coagulation/flocculation options with alum, polyaluminium chloride (PAC) and ferric chloride (FeCl<sub>3</sub>) treatment. Treated GW from all four options was found to be safe for restricted access area irrigation, construction and industrial cooling as per USEPA [21], WHO [22] and CPCB [23] standards. Treated greywater from all 4 options was compared on the basis of (i) effluent quality and (ii) removal of parameters. The researchers found that results with two-stage sand filtration technique outperformed the other methods of treatment but the major limitation in the implementation of a two-stage sand filtration system is that it needs close monitoring, addition of coagulant, cleaning of screening mesh and mini coarse sand filter on a daily basis. Also the filters have to be regenerated after 30–40 days.

Masi et al. [24] demonstrated a pilot installation of green wall located at the main entrance of an office building in Pune. The experiment was carried out in two phases. In the first phase, the green wall was filled with LECA (lightweight expanded clay aggregate) and the treated greywater was analyzed for the removal rate. Chemical oxygen demand, COD removal rate varied between 16% and 20% in the first phase. In the second phase, the green wall was filled with two different mixtures (i) LECA and sand (ii) LECA and coconut fibers as both are porous in nature and can increase the treatment time. The removal rate observed in the second phase was 7–80% and 14–86% with LECA-sand and LECA-coconut fiber respectively. Researchers found that the treated greywater was suitable for irrigational use as per Indian regional and National regulation. In one sample they found that treated greywater could even be used for toilet flushing after UV treatment.

Kariuki et al. [25] made a 5 barrel greywater system using recycled polyethylene plastic barrels. First tank was used to collect greywater. The other 3 tanks were used to perform flocculation, sedimentation and disinfection and the last tank was used as the storage tank. A case study was performed by collecting sample water from Kenyatta University. The low-cost technology was found to be effective in reducing pollutants and turbidity and it reduced the *E. coli* and total coliform concentration. Researchers found that the treated greywater met the required standards for surface irrigation.

Gorky [26] studied the vertical subsurface flow constructed wetland system for treatment of greywater. Two miniature size tanks were separately constructed in a lab with volume less than 5 m<sup>3</sup>. Both tanks were used as independent filters. The first tank consisted of graded stone filters. The second tank was filled with coarse aggregate gravel followed by layers of fine sand and coarse aggregate. *Colocasia esculenta* was planted in this bed and allowed to grow for some days. The greywater was then inlet into the bed through the graded stone filter. The treated greywater was collected through the down flow filter and tested. The average pH, BOD, COD, TDS, TSS values obtained were 7.28 mg/L, 142 mg/L, 0.3 mg/L and 16 mg/L respectively. The root zone treatment improved the quality of greywater either for reuse or safe disposal into water bodies. The results achieved in the first stage of the research were not satisfactory owing to the small size of the plants, but improvement in efficiency was observed later with their growth.

Katuliza et al. [27] performed a case study in slum area of Kampala city (Uganda). The researchers made a two step filter unit mounted on a hollow steel frame to treat greywater. Both filtration tanks were made of plastic and first filled with gravel which was followed by a layer of crushed lava rock. The size of crushed lava rocks differed in both the tanks and it was smaller in the second tank. Both tanks were fitted with an outlet valve in addition to the exit valve, so that 200 mL of sample could be collected from either of them at any time without disturbing the filtration process. The sedimentation process was carried out by first collecting the greywater originating from kitchen, laundry and bathing in a 20 L bucket and the water was allowed to settle for an hour. Oil and grease floating over the water were manually removed while other impurities settled at the bottom of the bucket were carefully discharged. The sediment water was then poured into the first tank for filtration. The filter achieved an efficiency of 85–88% for COD and TSS while *E. coli* was almost eliminated. As lava rocks are easily found in the Kampala city (Uganda) therefore maintenance of the system was not a cost issue.

Fountoulakis et al. [28] performed a study to evaluate the efficiency of a compact Submerged Membrane Bioreactor (SMBR) system. The SMBR system was supplied with greywater generated from bathtub, shower and washing machine through a single house in Greece. The system achieved a mean removal rate of more than 80% for both COD and anionic surfactants. TSS before and after treatment was found to be 95 mg/L and 8 mg/L respectively. Total coliform and *E. coli* removal was almost 100%. The system was also analyzed for the level of nitrogen as it is beneficial for plant growth. The researchers found that in case of nitrogen, removal rate of SMBR fluctuated from 19% in winter to 45% during other seasons of the year. The treated greywater quality was compared with the defined standards for its reuse and the researchers found that it was suitable for indoor use i.e., toilet flushing.

Poyyamoli et al. [29] performed a case study on the greywater originating from a single house in Puducherry. The greywater treatment unit was designed to filter 350 L of water daily. The greywater produced in kitchen, bath and laundry was fed to a filtration and sedimentation tank where most of the dissolved solids were filtered and settled. Then the filtered water was supplied to a vertical subsurface flow constructed wetland in which *Arundo donax* was planted. Two 500 L tanks were used to manage the treated water. After filtration through the constructed wetland, treated water was first collected in the collection tank and then pumped to the storage tank from where it was utilized for toilet flushing and gardening. The system helped to reduce the municipal water intake by 47%. The removal efficiency for BOD<sub>5</sub>, COD, alkalinity, coliform bacteria was 95.2%, 81.1%, 74% and 99.1% respectively.

Singh et al. [30] used an inexpensive laboratory treatment method to purify 5 L of greywater collected as a sample from kitchen, bathroom and laundry by using primary, secondary and tertiary treatment. The greywater was first treated using filter bed made up of natural materials such as coconut shell, wood, sand, etc. In the secondary stage, the greywater was further treated by microbial cultures of *Aspergillus niger*, *Pseudomonas* sp. and *Penicillium* sp. In the tertiary stage, activated charcoal was used to remove the dissolved solids. They used the treated greywater to find if could be helpful in irrigation. The researchers performed two independent trials, where the seeds of *V. radiata* and *V. mungo* were fed with treated and untreated greywater for 30 days. The seeds fed

with treated greywater showed 100% germination and they attained a higher length than the other pair which was supplied with untreated greywater. The researchers concluded that there are many rural settlements which lack an access to water and the greywater treated by such inexpensive methods can be used by these settlements for the purpose of irrigation and cultivation of crops.

Tee et al. [31] created experimental set-up to compare the performance of conventional horizontal subsurface flow (HSF) constructed wetland with an up-down flow baffled constructed wetland. Two tanks were independently designed and divided into 6 compartments such that in the conventional HSF the greywater horizontally moves between the compartments and in the second tank the greywater movement from one compartment to another was in an up-down manner. First 4 compartments of both the tanks were filled with Rice husk followed by gravel in the other two outermost compartments. Both tanks were planted with cattails. Better removal efficiency was observed with the up-down flow constructed wetland as the greywater traveled through the filter media for a longer time.

The study undertaken by Vakil et al. [32] made use of the electrocoagulation technology for treatment of greywater by collecting greywater generated from a single Indian household. Results reveal that nearly 70% of the total COD and more than 99.9% pathogens were removed in the experiment by using energy of 0.3 kW h/m<sup>3</sup> of wastewater. Removal of COD could not exceed 70% despite repeated attempts due to discharge of aluminum anode in greywater during the process of treatment. The system used in this research required 12 V source for its operation which according to the researchers can be made available by using a 12 V battery that can be charged using a solar cell.

In addition to the above review, case studies carried out by different researchers and their findings are shown in Table 1. The use of Living walls and green roofs has been found in some of the literatures. Greywater treatment through green walls is gaining popularity in urban areas. Green walls not only help to recycle wastewater, they also help to provide a cooler air circulation and act as filters to reduce noise levels. The concept of green walls is being used in many offices and hospitals as its effect on health has also shown good results. However, proper plant and media selection are important in green wall design [33, 34].

## 2.1 Research Gap

Techniques involved in literatures indicate that there is wide scope to work on cost effectiveness of greywater treatment which gives a scope to develop a low-cost greywater filter which may include use of different low-cost materials as a filter media along with other cost effective accessories.

The potential use of greywater can be studied for regenerative purposes, say irrigating the agricultural lands, toilet flushing's, home garden watering, etc.

Proper management and utilization of treated greywater for a locality can be taken up for the study to extend the results for probable use of treated greywater on a mass scale.

Nawatech Project [40] is an Indian-European based research and development project to treat and reuse greywater in urban parts of India. Various projects undertaken by this joint venture in Maharashtra are shown in Table 2.



**Table 1** Few case studies around the world

Location	GWT system	Pollutant removed	Advantage	References
Nigeria (Residential quarters)	Gravity system by sedimentation unit. Filtration unit	BOD (85.68%) COD (57.09%) TSS (70.74%) FC (100%)	Handling of graywater. Possesses no risk of health	Nnaji et al. [35]
Malaysia (Kitchen water)	Filtration system using sand, peat, charcoal and gravel	BOD <sub>5</sub> 40%, COD 37%, SS 72%, NH <sup>+</sup> <sub>4</sub> N 87% pH 6.6–6.7	Peat is an effective and inexpensive filter media. Low cost system	Mohamed et al. [36, 37]
Jordan (Village Houses)	Filter system using volcanic ash and white gravel	BOD (73%) COD (65%) TSS (84%) FC (15.67%)	No effect on soil and plants. Local water is saved	Mohamed et al. [36–38]
Cairo, Egypt (Mosque)	Physical and chemical treatment system	BOD (71%) COD (67%) SS (87%) Turbidity (90%) TC (100%)	Applicable for multiple occupancy building	Mohamed and Ali [39]

Source Wurochekke et al. [2]

### 3 Greywater Reuse Standards

Globally, there are no specific rules and regulations for treatment and reuse standards of greywater. WHO [41], published the safety manual for reuse and disposal of greywater. In addition to WHO guidelines, each country has defined its own standards for reuse of greywater in different applications. In India, central Pollution control board has set some standards to reuse greywater for certain applications. However direct contact with treated greywater is restricted in many countries concerning health risk. The quality standards of treated waste water by CPCB and US EPA are given in Table 3 [10].

### 4 Conclusion

Greywater reuse can help us to reduce our dependencies on freshwater supplies for non-potable uses such as toilet flushing, irrigation, watering of lawns, backyards kitchen gardens, floor washing, etc. Many countries have adopted the practice of recycling greywater. The importance to reutilize wastewater can be understood by looking at the scenario in drought prone areas. This paper reviewed the reuse applications of greywater and the treatment process adopted by various researchers. It was found that in addition to the filter media, design process also played an important role in the removal efficiency of greywater treatment system. Many researchers have designed their systems by making use of locally available filter media, and they achieved good results which meet



**Table 2** Nawah Tech case studies in Maharashtra

Location	GWT system	Volume Treated	Parameters of treated greywater
Amanora Park, Pune	SBR and MBR	40 m <sup>3</sup> /d	BOD: 25 COD: 125
MJP, Pune	Green Wall	0.24 m <sup>3</sup> /d	BOD: 6.7 ± 2.7 COD: 21.0.4 ± 15.3
COEP, Pune	Anaerobic treatment with constructed wetlands	180 m <sup>3</sup> /d	pH: 6.93 BOD: 65 COD: 175 TSS: 66
Indradhanush Environ. Education & Citizenship center, Pune	Filter beds	40 m <sup>3</sup> /d	BOD: <30 COD: <80 TSS: <30
Ordnancefactory, Nagpur	Constructed wetlands with reed beds	100 m <sup>3</sup> /d	pH:6.8–7.0 BOD: <5 COD: <10 TSS: Nil
Dayanand Park, Nagpur	Constructed wetlands with different configurations	100 m <sup>3</sup> /d	pH: 6.8–7.2 BOD: <30 COD: 50–60 TSS: 20–30

Source Nawah Tech Project, Issue 25, 2016 [40]

**Table 3** Quality standards of treated greywater

Stds	Use	pH	BOD	Turbidity	TSS	FC	RC	References
CPCB (India)	Irrigation	5.5–9	100	–	200	–	–	CPCB (2008)
	Inland surface water	5.5–9	30	–	100	–	1	
	Public sewer	5.5–9	350	–	600	-	–	
USEPA	Toilet flushing, Irrigation of lawns, home gardens	6–9	10	2	–	–	1	USEPA (2012)
	Agriculture use, Industrial cooling, Construction	6–9	30	–	30	200	1	

Source Sonali [10]

the required standards for reuse in certain applications. Greywater treatment systems should be eco-friendly, economical and low maintenance systems. Low-cost treatment system opens the opportunity for large scale implementation of such systems in urban and drought prone areas to utilize greywater.

**Acknowledgements.** Authors express their sincere thanks to Dean, Oriental University, Indore, India and Management of Sanjivani Group of Institutes, Kopargaon, Maharashtra, India for availability of resources all the time.

**Author Contributions.** Deepak Paithankar (Research Scholar) done writing of the manuscript. Dr. Shashi Ranjan Kumar (Professor) participated in editing and done corrections in the manuscript.

## References

1. Barzegar G, Wu J, Ghanbari F (2019) Enhanced treatment of greywater using electrocoagulation/ozonation: investigation of process parameters. *Process Saf Environ Prot* 12:125–132
2. Wurochekke A, Mohamed R, Al-Gheethi A et al (2016) Household greywater treatment methods using natural materials and their hybrid system. *J Water Health* 427–434
3. Liberman N, Shandalov S, Forgacs C et al (2016) Use of MBR to sustain active biomass for treatment of low organic grey water. *Clean Technol Environ Policy* 1219–1224
4. Toole J, Sinclair J, Malawaraarachchi M et al (2012) Microbial quality assessment of household greywater. *Water Res* 46:4301–4313
5. Blanky M, Rodríguez MS, Halpern M et al (2015) *Legionella pneumophila*: from potable water to treated greywater; quantification and removal during treatment. *Sci Total Environ* 533:557–565
6. Al-Ismaïli M et al (2017) Extended use of grey water for irrigating home gardens in an arid environment. *Environ Sci Pollut Res* 24:13650–13658
7. Boano F, Caruso A, Costamagn E et al (2020) A review of nature-based solutions for greywater treatment: applications, hydraulic design, and environmental benefits. *Sci Total Environ* 711:134–141
8. Oron G, Adel M, Agmon V et al (2014) Greywater use in Israel and worldwide: standards and prospects. *Water Res* 58:92–101
9. Comino E, Riggio V, Rosso M (2013) Grey water treated by an hybrid constructed wetland pilot plant under several stress conditions. *Ecol Eng* 53:120–125
10. Manna S (2018) Treatment of gray water for reusing in non-potable purpose to conserve water in India. *Int J Environ Sci* 13(8):703–716
11. Sushmitha M, Chanakya H, Khuntia H (2019) Efficient grey water treatment and reuse options for india—a review. Springer, pp 225–232
12. Chanakya H, Khuntia H (2014) Treatment of gray water using anaerobic biofilms created on synthetic and natural fibers. *Process Saf Environ Prot* 92(2):186–192
13. Baris S, Turkyay O (2016) Domestic greywater treatment by electrocoagulation using hybrid electrode combinations. *J Water Process Eng* 10:56–66
14. Dalahmeh S, Pell M, Hylander L et al (2014) Effects of changing hydraulic and organic loading rates on pollutant reduction in bark, charcoal and sand filters treating greywater. *J Environ Manage* 132:338–345

15. Dalahmeh S, Pell M, Vinnerås B et al (2013) Efficiency of bark, activated charcoal, foam and sand filters in reducing pollutants from greywater. *Water Air Soil Pollut* 223(7):3657–3671
16. Bani M, Al-Qodah Z, Al-Shannag M et al (2015) On the performance of real grey water treatment using a submerged membrane bioreactor system. *J Membr Sci* 476:40–49
17. Ramprasad C, Smith C, Fayyaz M, Philip L (2017) Removal of chemical and microbial contaminants from greywater using a novel constructed wetland: GROW. *Ecol Eng* 106:55–65(2017)
18. Couto E, Calijuri M, Assemany P et al (2015) Greywater treatment in airports using anaerobic filter followed by UV disinfection: an efficient and low cost alternative. *J Clean Prod* 106:372–379
19. Cui L, Ouyang Y, Yang W et al (2015) Removal of nutrients from septic tank effluent with baffle subsurface-flow constructed wetlands. *J Environ Manage* 153:33–39
20. Ghaitidak D, Yadav K (2016) Greywater treatment for reuse: comparison of reuse options using analytic hierarchy process. *J Water Health* 873–881
21. USEPA (2012) Water reuse guidance manual factsheet. Report EPA/600/R-12/618, USEPA, Washington
22. WHO-guidelines (2006) Guidelines for safe use of waste water, excreta and graywater – Excreta and graywater use in agriculture. World Health Organization
23. CPCB (2008) Performance of sewage treatment plants – coliform reduction. Central Pollution Control Board, Ministry of Environment and Forests, New Delhi, India
24. Masi F, Bresciani R, Rizzo A et al (2014) Short communication green walls for greywater treatment and recycling in dense urban areas: a case-study in Pune. *J Water Sanit Dev* 153–163
25. Kariuki F, Kotut K, Ngángá V (2011) The potential of a low cost technology for the greywater treatment. *Open Environ Eng J* 4:32–39
26. Gorky S (2015) Treatment of gray water using constructed wetlands. *Int Res J Eng Tech* 2:62–68
27. Katukiza Y, Ronteltap M, Niwagaba C et al (2014) A two-step crushed lava rock filter unit for grey water treatment at household level in an urban slum. *J Environ Manage* 133:258–267
28. Fountoulakis M, Markakis N, Petousi I et al (2016) Single house on-site grey water treatment using a submerged membrane bioreactor for toilet flushing. *Sci Total Environ* 551–552:706–711
29. Poyyamoli G, Golda A, Nandhivarman M (2013) Constructed wetlands for the treatment of domestic gray water: an instrument of the green economy to realize the millennium development goals. *The Economy of Green Cities*. Springer, Netherlands, pp 313–321
30. Singh S, Pradhan N, Ojha N et al (2016) Grey water treatment and its application in cultivation of plants. *Asian J Microbiol Biotechnol Environ Sci* 18(4):1043–1053
31. Tee H, Lim P, Seng C et al (2012) Newly developed baffled subsurface-flow constructed wetland for the enhancement of nitrogen removal. *Bioresour Technol* 104:235–242
32. Wakil K, Sharma M, Bhatia A et al (2014) Characterization of greywater in an Indian middle-class household and investigation of physicochemical treatment using electrocoagulation. *Sep Purif Technol* 130:160–166
33. Prodanovic V, Hatt B, McCarthy D et al (2017) Green walls for greywater reuse: understanding the role of media on pollutant removal. *Ecol Eng* 102:625–635
34. Snigdhendubala P, Al-Ghamdi S, Mackey H (2019) Greywater recycling in buildings using living walls and green roofs: a review of the applicability and challenges. *Sci Total Environ* 652:330–344
35. Nnaji CC, Mama CN, Ekwueme A, Utsev T (2013) Feasibility of a filtration/adsorption grey water treatment system for developing countries. *Hydrol Curr Res* S1:006
36. Mohamed B, Abeer A, Theib O (2013a) Assessing the efficiency of grey-water reuse at household level and its suitability for sustainable rural and human development. *J Appl Sci Technol* 3(4):962–972

37. Mohamed RM, Amir HMK, Martin A, Stewart D (2013b) A monitoring of environmental effects from household greywater reuse for garden irrigation. *Environ Monit Assess* 185:8473–8488
38. Mohamed RM, Martin A, Stewart D (2013c) A monitoring of environmental effects from kitchen greywater reuse for garden irrigation. *Environ Monit Assess* 185:8473–8488
39. Mohamed NM, Ali SS (2012) Economical study for greywater reuse to achieve the sustainability in Egypt. *Aus J Basic Appl Sci* 6(3):655–665
40. Meinhold K et al (2016) Sustainable sanitization practice. *Nawah Tech* (2016)
41. Sanitation safety planning (2015) manual for safe use and disposal of waste water, gray water and excreta. World Health Organization, WHO



# Employment of Blockchain Technology in Supply Chain Management

Aman Pandey<sup>1,2(✉)</sup>, M. S. Niranjana<sup>1,2(✉)</sup>, Amey Jha<sup>1,2</sup>, and Aneesh Kamal<sup>1,2</sup>

<sup>1</sup> Department of Mechanical Engineering, Delhi Technological University, New Delhi 110042, India

aman\_2k17me30@dtu.ac.in, mahendraitr2002@gmail.com

<sup>2</sup> Production & Industrial Engineering, Delhi Technological University, New Delhi 110042, India

## 1 Introduction

Blockchain technology, a novel technology developed in recent times, is a deeply regarded tool owing to its excellent features of security, immutability and decentralisation of data among many more. Traditionally, data manipulation has been possible, as CRUD (Create-Read-Update-Delete) methodology is followed and data is stored centrally. Alternatively, in blockchain technology, the data stored is decentralised which guarantees enhanced security. Also, centralised systems are sensitive to a single point of breakdown, causing an entire system failure [1]. The data is stored across peer-to-peer networks and is made up of nodes on the network. Any changes to previously stored data are not possible and new data can only be appended, or added in the end, and in order to add a transaction, every node needs to check the validity and the data is appended only in the case where majority nodes deem it is valid [2]. Blockchain technology sees its applications in various fields, disrupting the ongoing methods and practices and giving a boost to sectors by providing the useful characteristic features it is equipped with. Supply chain management, one such field, which includes everything from collection of raw materials for a product right to the final stage where the finished product is delivered to the customer [3], can be revolutionised, when employed with the salient features of blockchain technology. It is a topic of discussion gaining much popularity in recent times and the true potential of this amalgamation is yet to be realised. This research focuses on the same and studies how introducing one technology to the other can improve the efficiencies of the processes involved.

The paper attempts to address a relatively new application of blockchain technology, i.e. in a cooperative, that too an FMCG cooperative, illustrating at a small level how applying the technology in one of the processes can make a difference hoping to encourage discussion and practical implementation on the same.

## **2 Basic Concepts**

### **2.1 Supply Chain Management**

Supply chain management is the detailed analysis and science behind each step involved in producing the final product from its raw materials and delivering it to the place intended. SCM is the constant drive made by managers and officials to make the supply chains involved in any process as economical and efficient as possible [4]. Orderly management of the supply chain results in cutting off excess costs and delivery of end products to the intended user sooner. Although supply chains have existed since forever, they have received the due attention they required only recently and continuous and persistent endeavours to improve the quality and productivity of operations have followed ever since.

### **2.2 Blockchain Technology**

Blockchain, sometimes referred to as Distributed Ledger Technology (DLT), is used for creating an unalterable history of any digital asset by using decentralisation of the data network and cryptographic hashing. It is a distributed ledger or a distributed database across numerous interconnected nodes within a single organisation or multiple organisations which are using a single network. It contains various characteristics like communication channels, smart contracts and hashing systems. Blockchain transforms the data to be stored into hashes and saves it into numerous blocks, which are linked to each other, at different locations instead of a single database. It is a relatively new technology and is already becoming popular and has even found moving applications in various industries like Healthcare [5], Banking, Cyber Security, Transportation [6] along with the Supply Chain industry.

### **2.3 Smart Contracts**

The idea for Smart contracts was originally put forward by Szabo and resembles the nature of legal contracts [7]. It is a self-operating or automated contract [8], wherein the conditions involved with the contract are entered into a digital platform (Blockchain). The basic motive behind the use of smart contracts is that these will be automatically ended if any infringement is revealed. Also, no involvement of a third party is necessary for the contract connecting the buyer and the seller and the whole process of carrying out transactions is implemented using electronic algorithms and is automated resulting in an efficient completion of the agreement.

### **2.4 Blockchain Technology in Supply Chain Management**

The application of Blockchain Technology was limited to the Finance Industry [9] for some time but with the rising popularity of Cryptocurrency, it has made its way to become an integral part of many industries and some are finding it even superior to the current setup [10]. In the management of supply chains, it can be used to eliminate the problems of tracking the products, distrust between the parties involved as well as the middlemen,

reduce time delays, maintain proper records of transactions at all the steps involved, among many more features while providing a high degree of security at the same time, owing to its decentralised peer-to-peer network and bring about higher efficiency and reduction of excess costs.

Multiple industries and organisations have implemented various features of BCT in their supply chains and have realised the virtues of the novel technology. One such is the Oil industry. Abu Dhabi National Oil Company has launched a blockchain supply chain pilot programme along with IBM intending to track oil from the source, that is wells, to the customers and maintaining a record of each transaction on every step of the way. The current plan is to incorporate customers and investors in the chain alike and bring about more transparency to the operation. Including features of blockchain technology in their supply chain will not only help in clarity and credibility but also reducing process times, hence increasing efficiency and reducing costs.

The food industry is another one where the applications of blockchain are being reported in the supply chains and suitably so, as transparency and shipment efficiency are essential to this industry. Walmart has been employing blockchain technology in its processes and harvesting the benefits that come with. Walmart, with IBM, joined forces with the ecommerce company JD.com from China along with Tsinghua University to form a Blockchain Food Safety Alliance to handle security problems faced by the various food supply chains of China [11]. Following the trend, other larger corporations are expected to get in the race and reap the benefits that come with this technology.

### 3 Research Methodology

The purpose of the study is to determine the limitations in the supply chain management system employed in industries and find possible solutions for the same with the implementation of blockchain technology. To get the process started and in order to get acquainted with the technology, processes and identify the limitations in the literature in the field of implementation of blockchain technology in supply chain management. A study was carried out in an Amul warehouse, catering to the distribution of products to distributors around the southern portion of Delhi, where the process of goods incoming from the production sites was broken down into various steps and studied individually and as a whole. On identifying bottlenecks in the process, solutions using blockchain technology were discussed for the same. This study vividly brought to light what potential blockchain technology contains to bring an impact to the supply chain industry when executed appropriately.

### 4 Case Study

The case study is focused on the incoming carriers from the production site to the Amul warehouse and their unloading of goods. It was carried out in the month of November and December 2020.

Amul is a cooperative society in the dairy sector, which was founded in 1946. It has its headquarter in Gujarat in the municipality of Anand. It is operated by the GCMMF (*Gujarat Cooperative Milk Marketing Federation Limited*). It is currently owned by 36

lakh dairy farmers based in Gujarat together. It was founded by Verghese Kurien, also known as the “Father of the White Revolution”, and Tribhuvandas Kishibhai Patel. Amul generated revenue of ₹ 38,550 crores in the year 2020. The Amul warehouse where we conducted our study is situated in Asola near Chhatarpur in South Delhi. It caters to distributors around the south and east Delhi.

#### 4.1 Existing System of Unloading of Goods

The process flow at Amul can be described by the following steps.

**Carrier Arrives At The Gate.** The carriers arrive at the Amul warehouse from the production site for which they have a period of five working days (excluding Sundays and national holidays), crossing which can entice levying a fine called delay charge. Products brought to the warehouse can belong to either of the three categories: Dry, Wet and Frozen, each having a different storage area in the warehouse. If the carrier is not freed up to leave within 48 h, a detention charge is levied on the warehouse.

**Submission And Checking Of Goods Receipt/Lorry Receipt At The Main Gate.** After the arrival of the carrier, a security check takes place at the entry gate and the goods receipt/lorry receipt is submitted by the driver at the entry gate. This document contains information regarding the shipment like vehicle number, driver details, material name, quantity, owner info, etc., and is verified during the security check. These details are noted down manually at the gate in a register.

**Truck Proceeds To The Bay Area (Waiting Point) And Waits There.** After clearance at the main gate, the carrier proceeds to the bay area which is in front of the unloading spot. The truck waits until the designated unloading spot is cleared. There are multiple spots for unloading depending on the type of the product and size of the shipment.

**Truck Queues Up At The Unloading Point When Its Turn Comes.** After the previous shipment is unloaded, the carrier proceeds to the designated unloading spot and inspection of the shipment takes place. The actual conditions of the products are noted down and the temperature is checked using a thermometer, and preparation for unloading is carried out which involves setting up of wheeled pallets in front of the carrier gate. Upon recording the quality of the shipment, finally unloading of products starts which are then carried to their allocated storage spots in the warehouse either using pallets or carried manually.

**Delivery Report Provided To And Signed By The Driver.** After the goods are unloaded, a delivery report is created by officials in the warehouse summarising the quality and quantity of goods, temperature, time of entry, unloading and completion. This report is provided to the driver and is required to be signed on by him as a mutual agreement on the details mentioned.

**Exit From The Main Gate.** Finally, after fulfilment of all the aforementioned steps, the carrier exits the facility. If more than 48 h are consumed for these steps, a fine called detention charge can be levied on the warehouse.



### 4.2 Time Recorded and Analysis

By analysing the data regarding the carriers (1st November 2020–5th December 2020), the following graph was created showing the distribution of the unloading time as shown in Fig. 1.

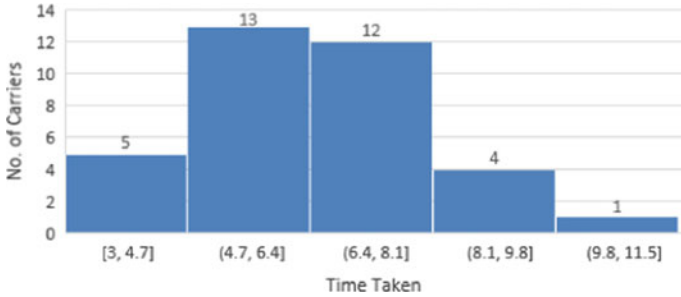


Fig. 1 Distribution of time taken

The cycle time should not exceed 6 h ideally. But it can be inferred that most vehicles have a cycle time more than that from the above chart. The scope for improvement is depicted by the red bars in Fig. 2.

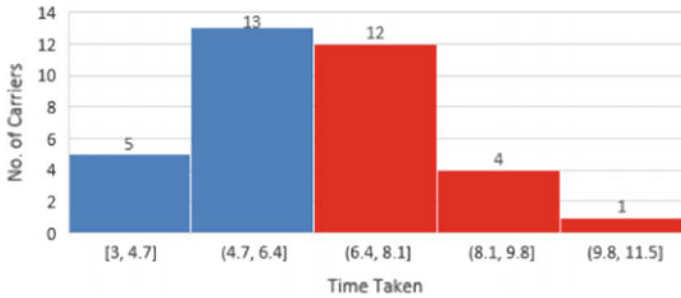


Fig. 2 Section of improvement

Thus, to minimise the overall cycle time, emphasis should be laid on reducing the vehicles in between the time bracket of 6–10.5 h. Further analysis of time taken per procedure and areas of possible optimization has been given in the following pages. Time taken per activity is given in Table 1.

1. MGT-GRV (Main gate entry to submission of Goods Receipt)
2. GRV-NTD (Recording of Consignment Details)
3. NTD-BAY (Proceeding to Bay Area and waiting for turn)
4. BAY-QTC (Queuing up at unloading point when turn comes)
5. QTC-UNL (Inspection and unloading)
6. UNL-DRS (Delivery Report provided to driver)
7. DRS-EXT (Exit from main gate).

**Table 1** Time recorded for the following activities at the Amul warehouse

Process	Time taken (in minutes)
MGT-GRV	5
GRV-NTD	15
NTD-BAY	100
BAY-QTC	10
QTC-UNL	120
UNL-DRS	30
DRS-EXT	10
Total time	290

**4.2.1 X Bar Charts and Analysis**

Further analysis of data has been done using  $\bar{x}$  bar charts. The control limits for an  $\bar{x}$  bar chart are as follows and the chart is depicted in Fig. 3.

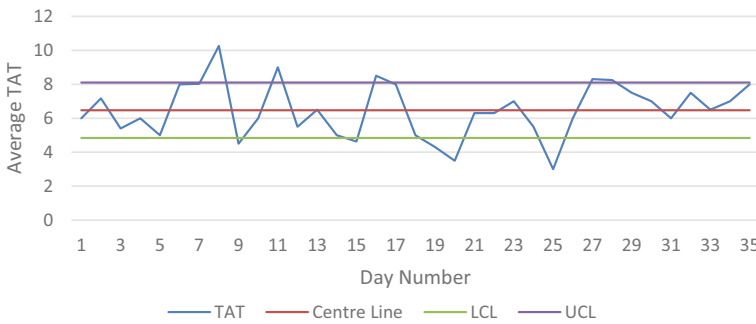


**Fig. 3** Control chart

It is evident that there is scope for improvement, for which we will identify and tackle bottlenecks in the unloading process. The identified bottlenecks are:

1. Manual recording of data on entry leading to consumption of extra time.
2. Preparation for unloading is not started till the truck is parked and queued properly at the designated unloading spot.
3. Sharing, updating and reacting on information of activities is not automated
4. Same gate used for entering as well as exiting for carriers.
5. Significant dependency on paper medium for communication.

## 5 Results, Discussion and Conclusion

After identifying the bottlenecks in the current Supply Chain scenario at the Amul warehouse, a theoretical implementation of Blockchain Technology resulted in addressing the same as follows and the changes are quantified in Table 2.

**Table 2** Updated time required for activities after theoretical implementation of BCT

Process	Time taken (in minutes)	Updated time taken (in minutes)
MGT–GRV	5	5
GRV–NTD	15	1
NTD–BAY	100	70
BAY–QTC	10	10
QTC–UNL	120	110
UNL–DRS	30	5
DRS–EXT	10	10
Total Time	290	211

1. There was substantial decrease in the time taken for recording of consignment details at the main gate which could be replaced by a simple QR scanner.
2. The time required to record the data and then generate the Delivery Report to the driver is also reduced as this will be completed in real time.
3. Due to the time saved in generating the report the next carrier would also have to wait for less time for its proceeding to the unloading spot.

Finally, after the theoretical employment of Blockchain Technology, there was a total decrease of 79 min in the whole cycle. Thus, reducing cycle time by 27.2%. Apart from these results, various other advantages of incorporating BCT in Supply Chain Management are discussed further.

### 5.1 Immutability

Unlike using a centralised data system, in Blockchain it is almost impossible to manipulate the original content in the ledger due to the hashing algorithm used [12]. Once a cryptographic hash is generated, any slight change in the input would reflect in the hash sharply.

### 5.2 Traceability

Blockchain can be used to improve traceability and identify predictable delays in the process. Amalgamated with the Internet of Things (IoT), it can not only track the shipment but also the actual conditions of the products (like temperature) using units of GPS capabilities and sensors [13].

### 5.3 Trust

The visibility of any change in the data (input) at all the nodes ensures transparency in the process. Also, this enables trust among the stakeholders as they are guaranteed that no manipulation is taking place at any step. The trust is brought about by the infrastructure itself, by providing a local copy for all [14].

### 5.4 Security

A non-centralised data system combined with a cryptographic hashing system means a high degree of security and non-vulnerability to a malware attack. Blockchain Technology is itself encrypted in nature and furthermore, smart contracts thus enforce validation and establish a secure data network.

The motive behind this study was to find the potential of blockchain technology in the current scenario of supply chain management in India and realise how wide the scope of improvement actually is, in revolutionising the whole structure using this relatively new technology.

The paper brings forth the following conclusions.

1. The theoretical employment of Blockchain Technology in the existing Supply Chain at the Amul warehouse resulted in reduction of the cycle time by 27.2%.
2. Blockchain Technology also eliminated the bottlenecks and some of the delays (like time taken at Main Gate Entry, Generation of Delivery Report and the overall waiting time for each carrier) in the current system, thus increasing efficiency of the whole process.
3. BCT improved the overall supply chain by enhancing the system's security and trust. It holds huge potential in supply chain management and is relatively an unexplored option.

Every study is subjected to limitations, and likewise this study must have been affected by the sample size we used to draw inferences which was not a big one. This study concluded in 35 days and the limited expertise of the researchers would have contributed to the limits of this paper.

## References

1. Perboli G, Musso S, Rosano M (2018) Blockchain in logistics and supply chain: a lean approach for designing real-world use cases. *IEEE J Mag* 6:62018–62028
2. E. Tijan, S. Aksentijević, K. Ivanić, and M. Jardas, "Blockchain Technology Implementation in Logistics", *Sustainability*, vol. 11, no. 4, 2019. <https://doi.org/10.3390/su11041185>
3. Mentzer JT (2001) Defining supply chain management. *J Bus Logist* 22(2):1–25. <https://doi.org/10.1002/j.2158-1592.2001.tb00001.x>.
4. Stock JR, Boyer SL (2009) Developing a consensus definition of supply chain management: a qualitative study. *Int J Phys Distrib Logist Manag* 39(8):690–711. <https://doi.org/10.1108/09600030910996323>

5. Mettler M (2016) Blockchain technology in healthcare: the revolution starts here. In: IEEE 18th international conference on e-health networking, applications and services (Healthcom), pp 1–3. <https://doi.org/10.1109/HealthCom.2016.7749510>
6. Astarita V, Giofrè VP, Mirabelli G, Solina V (2020) A review of blockchain-based systems in transportation. *Information* 11(1). <https://doi.org/10.3390/info11010021>
7. Wang S, Yuan Y, Wang X, Li J, Qin R, Wang F (2018) An overview of smart contract: architecture, applications, and future trends. In: 2018, IEEE intelligent vehicles symposium (IV), pp 108–113. <https://doi.org/10.1109/IVS.2018.8500488>
8. Cong LW, He Z (2019) Blockchain disruption and smart contracts. *Rev Financ Stud* 32(5):1754–1797. <https://doi.org/10.1093/rfs/hhz007>
9. Treleaven P, Brown RG, Yang D (2017) Blockchain technology in finance. *Computer* 50(9):14–17. <https://doi.org/10.1109/MC.2017.3571047>
10. Treiblmaier H (2018) The impact of the blockchain on the supply chain: a theory-based research framework and a call for action. *Supply Chain Manag Int J* 23(6):545–559. <https://doi.org/10.1108/SCM-01-2018-0029>
11. Tan B, Yan J, Chen S, Liu X (2018) The impact of blockchain on food supply chain: the case of Walmart. *Smart Blockchain*, pp 167–177. [https://doi.org/10.1007/978-3-030-05764-0\\_18](https://doi.org/10.1007/978-3-030-05764-0_18)
12. Hofmann F, Wurster S, Ron E, Böhmecke-Schwafert M (2017) The immutability concept of blockchains and benefits of early standardization. In: *ITU Kaleidoscope: challenges for a data-driven society (ITU K)*, pp 1–8. <https://doi.org/10.23919/ITU-WT.2017.8247004>
13. Sunny J, Undralla N, Madhusudanan Pillai V (2020) Supply chain transparency through blockchain-based traceability: an overview with demonstration. *Comput Ind Eng* 150. <https://doi.org/10.1016/j.cie.2020.106895>
14. Gurtu A, Johny J (2019) Potential of blockchain technology in supply chain management: a literature review. *Int J Phys Distrib Logist Manag* 49(9):881–900. <https://doi.org/10.1108/IJP-DLM-11-2018-0371>



# An Approach Toward Lean Manufacturing Through Application of SMED as a Lean Tool

Mahantesh M. Ganganallimath<sup>1</sup>(✉), Sachin Chavaraddi<sup>1</sup>, V. S. Puranik<sup>1</sup>, K. Vizayakumar<sup>2</sup>, Umesh M. Bhushi<sup>3</sup>, Roopa B. Math<sup>1</sup>, and C. M. Veerendrakumar<sup>1</sup>

<sup>1</sup> Basaveshwar Engineering College, Bagalkot, Karnataka 587102, India  
mmgmath@gmail.com

<sup>2</sup> Bapatla Engineering College (Autonomous), Bapatla, Andhra Pradesh 522102, India

<sup>3</sup> Sahyadri College of Engineering and Management, Mangalore, Karnataka 575009, India

## 1 Introduction

Many industries in the market are leading toward competition for the satisfaction of market demands. Customer's demand for a variety of products in a shorter delivery span made the industries to have an optimized production planning toward the satisfaction of their customers. Changing the production planning in the existing industry setup may be the best economic solution to the problem of demand satisfaction. Instead of this, if the industry needs to increase its productivity by increasing plant capacity by increasing the number of machines, labor, and assets, it drags plenty of economies and increases the economic liabilities of the industry. A different approach should be made to overcome this problem. Today market demands have shifted toward more product variants and also customization. This is not limited to certain types of industries. Short delivery times and high delivery reliability are the customer's requirements. The best way to overcome this problem is to produce small lot sizes in the most economic and efficient way. It can be shown that there is a direct relationship between lot sizes and setup times.

## 2 Literature Survey

Palanisamy and Siddiqui [1], Setup time reduction through SMED with MES (planning system interface) was focused in the work. After implementing the methodology the changeover time of the crimping assembly process was reduced by 69% which resulted in an increase of production by 18.86%.

Ali [2] investigated the methodology of reducing setup time and the importance of applying SMED methodology in print house. Implementing SMED has enabled the reduction of the number of operations carried out by about 73%. Increase productivity by increasing the number of operations at the same time of operation by up to about 220%.

Kumar and Bajaj [3], explained the implementation of SMED in the machining processes with 5S's principle. The total setup time of three mechanical press machines

before SMED implemented was 265 min. Thus SMED technique has been helpful for setup time reduction.

Khusaini et al. [4], Sample study on Lean Tools (LT) implementation in the Malaysian Food and Beverages Industry. Kaizen was the most preferable LT along with Single Minute Exchange of Die (SMED).

Winatie et al. [5], implement the SMED methodology to a pharmaceutical company to overcome the problem of long time changeover and to meet consumer demand. With SMED the maximum change over time was observed to be 120 min which was lesser than the previous.

Mulla et al. [6], focus on the importance of change over time reduction in manufacturing industries. On-time delivery is increased from 65 to 77% after the implementation of the SMED methodology. Thus, on-time delivery is increased up to 12% than previous on-time deliveries, after Lean implementation.

Trovinger and Setup (2005) [7], SMED was applied to setups of high-speed circuit board assembly tools. A reduction of key setup times by more than 80% was found as estimated, and benefits of \$1.8 million per year.

Ulutas [8], worked on implementing SMED to a manufacturing industry of Machine parts. Work mainly focused on the recognition of internal and external activities. Particularly transferring internal activities into external was mainly concerned in as many numbers as possible, by also minimizing the internal ones.

Mali and Inamdar [9], have mainly focused on low volume and high variety product manufacturing with fast changeover time. The technique of Lean manufacturing SMED was used for changeover time reduction. Machines were chosen for SMED, which were having a utilization of less than 80%. SMED can significantly reduce the changeover time this was shown in the result after implication of SMED.

## 2.1 Observations from Literature Survey

1. By implementing changeover time of crimping assembly process, there was a reduction of 69% and resulted in an increase of production by 18.86%.
2. The application of this methodology to all machines at all operational stages, greatest effect in raising the capacity of machines.
3. The total setup time of three mechanical press machines before SMED implemented was 265 min and after SMED implemented it was 196 min.
4. Kaizen and SMED are the most preferable Lean Tools. Lean Manufacturing (LM) implementers are still at the infancy level.

## 3 Methodology

The raw material required for the industry is “Nonwoven Fabric” for manufacturing D-cut and W-cut bags (Ref. Figs. 1 and 2). The colors, sizes, and the weight required for the raw materials are pre-ordered according to the orders of customers or the regular market demand. As per the requirement of the customers, the fabric vending companies provide the raw materials. Raw material feeding is the first step in the manufacturing of these nonwoven bags. Feeding of raw material takes nearly about “10 min” every time.

It includes material movement from raw material storage to machine (Ref. Fig. 3). The selection of raw material is done according to the required size of the bag and the model of the bag. In D-Cut bags, the height of the bag is considered for the selection of raw material width. That is the height of the bag is doubled and the top folding part is doubled and added up. This gives the total width of the raw material required for production. Raw materials will be in the form of rolls.



**Fig. 1** W-Cut bag



**Fig. 2** D-Cut bag

### **3.1 Process of Set-Ups During Manufacturing**

There are different processes (Refer Figs. 4 and 5) are identified in this machine for manufacturing the nonwoven fabric bags. But all the twelve processes are not implacable to all variety of bags (Fig. 6).

There are mainly two varieties called D-Cut and W-cut bags. The complete process in the selected industry is studied. Plant layout, processes, movement of materials, and





**Fig. 3** Nonwoven fabric machine



**Fig. 4** Inserting feeding rod



**Fig. 5** Feed roll aligning



**Fig. 6** Feed control unit

the timings of each changeover are keenly observed and studied. In this selected industry two varieties of bags are produced. The study is concentrated on these two types. All the processes that are applicable for the manufacturing of these bags are listed below (Tables 1 and 2).

**Table 1** Processes of manufacturing

S. No.	Processes	D Cut	W Cut
1	Raw material feeding	Yes	Yes
2	Top folding and sealing	Yes	No
3	Fabric alignment	Yes	Yes
4	Fabric folding (center folding)	Yes	Yes
5	Folded fabric alignment	Yes	Yes
6	Gazette fixing	No	Yes
7	Side sealing and folding	No	Yes
8	D-Cut punching positioning	Yes	No
9	Main sealing	Yes	Yes
10	Cutting setting	Yes	Yes
11	W-Cut handle punching	No	Yes
12	Packaging and Storage	Yes	Yes

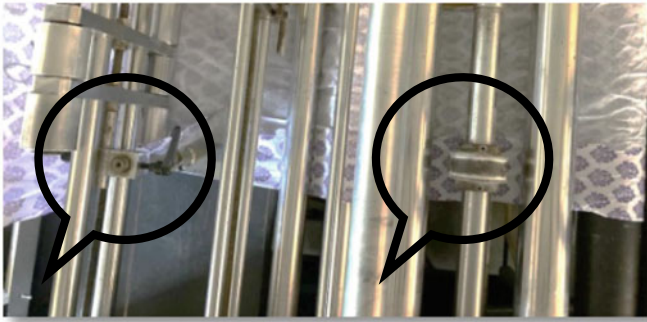
The machine used is from Taiwan. As per the requirement of the customers, the fabric vending companies provide the raw materials. The top folding and sealing process is applicable only for D-Cut bags. During this stage, the required top folding for the bag will be folded along the sideways of the roll. Using a side folding plate the fabric is folded and then folded part is measured for the accuracy of required measurement. The process is continued until the required measurement is attained. In the fabric aligning process the fabric is set to a required path to move into the complete machine.

**Table 2** Gazette size Selection

S. No	Bag size (W-Cut)	Width (Inches)	Side folding (Inches)	Gazette selection	Distance between two gazette plates (Inches)
1	10 × 14	10	2	Small	6
2	13 × 16	13	2.5	Medium	8
3	16 × 20	16	3	Medium	10
4	17 × 20	17	3	Large	11
5	20 × 26	20	4	Large	12

### 3.2 Fabric Alignment

After the feeding part, center folding and aligning of the unit will be done. In the fabric aligning process (Refer Figs. 7 and 8), the fabric is set to a required path to move into the complete machine. The aligning process is done with the help of a threaded long screw with a handle.

**Fig. 7** Top folding and sealing

The alignment process takes 6 min to set perfectly while changing one size of roll with another, if the same sized roll is to be processed then takes nearly 1 min if any mismatches are found. The folding process doesn't require any settings it just gets folded naturally with the movement of fabric above the triangle. The triangle part is located in the path of the fabric. After the folding process of fabric top ends of the fabric is to be aligned one over the other. This setting takes approximately about 3 min while changing one size of roll with another, if the same sized roll is to be processed then takes nearly 1 min if any mismatches are found.



Fig. 8 Fabric aligning screw

### 3.3 Gazette Fixing

Gazette fixing process (Ref. Figs. 9 and 10) is required for the W-Cut bag only. The required sizes of gazette plates are selected and according to the size of the bag, the plates are distantly fixed onto the gazette holder. The selection of gazette plates depends upon the size of the bag and the size of the side-folding required for the bag.



Fig. 9 PLC panel

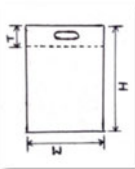
This setting takes about 15 min for setting up while changing one size of roll with another, if the same sized roll is to be processed then minor errors can be neglected for this process setting. Even if a minor error like folded fabric misalignment is present then in this process error is covered by side sealing where there is an extra fabric available for the side sealing. This is the main setting for the W-Cut Bags which defines the shape of the W-Cut Bags. Gazette setting is the high time-consuming setup in the process of W-Cut bag manufacturing.



Fig. 10 Gazette set-up

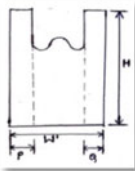
### 3.4 Side and Main Sealing

The D Cut punching process results in the handle formation for the D-Cut bags. A small portion of the bag is punched out pneumatically with the help of a small punching unit. But the punching should be exactly at the center of the D-Cut bag. Trial and error methods are used to fix it. The cutting size required for the bags is fed into PLC in mm. For D-Cut cutting size will be the width of the bag in the same way, for W-Cut cutting size will be the height of the bag. After feeding these values in mm, the machine starts cutting the fabric exactly. The supportive roller has to be adjusted by moving it up and down. By roller adjustment, the cutting will come to an exact position between the two sealed lines. For roller adjustment, there is no measurement available hence trial and error method is used. This setting takes nearly 5 min to set while changing one size of roll with another, if the same sized roll is to be processed then takes nearly 1 min if any mismatches are found.



H	Height	18
W	Width	12
T	Top Fold	3
12X18 Bag		Inches
D-Cut Bag		

$$\begin{aligned}
 \text{Roll size} &= [2 \times H] + [2 \times T] \\
 \text{required} &= [2 \times 18] + [2 \times 3] \\
 &= 36 + 6 \\
 &= 42 \text{ Inches}
 \end{aligned}$$



H	Height	14
W	Width	10
T	Top Fold	2
10X14 Bag		Inches
W-Cut Bag		

$$\begin{aligned}
 \text{Roll size} &= [2 \times W] + S \\
 \text{required} &= [2 \times 10] + 2 \\
 &= 20 + 2 \\
 &= 22 \text{ Inches}
 \end{aligned}$$

## 4 Results and Discussion

Observations after implication of SMED as a lean tool (Tables 3, 4, 5, and 6):

1. Two process setups are identified as internal and external setups.
2. All the process setup timings have been reduced to single-digit timings.
3. Overall time reduced to single-digit or lesser than the 10 min.
4. After the implication of changeover, the overall setup time for W-Cut bags is observed to be 14 min.
5. For D-Cut Bags, production process setup time is reduced to a single digit.
6. Reduced time to change different bag sizes and W-Cut to D-Cut bags.
7. Reduction of Gazette fixing time in W-Cut setup.
8. Improved side sealing and folding time in the W-Cut process setup.
9. W-Cut handle punching, Storage and packaging are not considered in the changeover setups because of no machine intervention, and all the work is carried out manually in these two processes and non-time consuming.

**Table 3** Processes on basis of SMED for D-Cut before and after implication of SMED

S. No.	Processes	Type of setup before SMED Implication	Type of setup after SMED implication
1	Raw material feeding	Internal	Internal
2	Top folding and sealing	Internal	Internal
3	Fabric alignment	Internal	External
4	Fabric folding (center folding)	Neither (non time consuming)	Neither (non time consuming)
5	Folded fabric alignment	Internal	External
6	D-Cut punching positioning	Internal	Internal
7	Main sealing	Neither (non time consuming)	Neither (non time consuming)
8	Cutting setting	Internal	Internal
9	Packaging and Storage	Neither (non time consuming)	Neither (non time consuming)

## 5 Conclusion

Setup times have been reduced due to the implication of SMED by 70%. Wastage of fabrics due to inappropriate setups or due to human error in setups has been reduced by

**Table 4** Processes on basis of SMED for W-Cut before and after Implication of SMED

S. No.	Processes	Type of setup before SMED implication	Type of setup after SMED implication
1	Raw Material Feeding	Internal	Internal
2	Fabric alignment	Internal	External
3	Fabric folding (center folding)	Neither (non time consuming)	Neither (non time consuming)
4	Folded fabric alignment	Internal	External
5	Gazette fixing	Internal	Internal
6	Side sealing and folding	Internal	Internal
7	Main sealing	Neither (non time consuming)	Neither (non time consuming)
8	Cutting setting	Internal	Internal
9	W-Cut handle punching	Neither (non time Consuming)	Neither (non time consuming)
10	Packaging and Storage	Neither (non time consuming)	Neither (non time consuming)

nearly 4 to 5%. Increased productivity compared to before the implication of SMED average of 5Tons/Month increase in the productivity. Verity of production can be approached due to the decreased setup times. Means small lot orders with different models of bags can also be produced. Changing between the sizes and changing between the models like D Cut and W Cut is made easy because of decreased setup times and perfect setups with references.

1. Overall setup time for D-Cut was 36 min and after implication, it is 8 min. There is a nearly 78% reduction of setup time is observed.
2. Overall setup time for W-Cut before the implication of SMED was 41 min and after implication, it is 14 min. Nearly 66% reduction in setup time.
3. The wastage produced due to improper setups before implication SMED was high, after SMED implication wastage has been reduced from 21 to 13% in W-Cut and 7% to 3% in D-Cut.

**Table 5** Setup timings of each process for D-Cut before and after Implication of SMED

S. No	Process	Before SMED implication		After SMED implication	
		Changing of size (Minutes)	Continuing same size (Minutes)	Changing of size (Minutes)	Continuing Same size (Minutes)
1	Raw material feeding	10	10	4	4
2	Top folding and sealing	7	1 (If any mismatch)	2	1 (If any mismatch)
3	Fabric alignment	6	1 (If any mismatch)	0 (Converted as external)	0 (Converted as external)
4	Fabric folding (center folding)	0 (Inline process)	0 (Inline process)	0 (Inline process)	0 (Inline process)
5	Folded fabric alignment	3	1 (If any mismatch)	0 (Converted as external)	0 (Converted as external)
6	D-Cut punching positioning	5	1 (If any mismatch)	1	1 (If any mismatch)
7	Main sealing and folding	0 (Inline process)	0 (Inline process)	0 (Inline process)	0 (Inline process)
8	Cutting setting	5	1 (If any mismatch)	1	1 (If any mismatch)
Total Timings for full setup		36	15	8	7

**Table 6** Setup timings of each process for W-Cut before and after Implication of SMED

Sr No	Process	Before SMED implication		After SMED implication	
		Changing of size (Minutes)	Continuing same size (Minutes)	Changing of size (Minutes)	Continuing same size (Minutes)
1	Raw material feeding	10	10	4	4
2	Fabric Alignment	6	1 (If any mismatch)	0 (Converted as external)	0 (Converted as external)
3	Fabric folding (center folding)	0 (Inline process)	0 (Inline process)	0 (Inline process)	0 (Inline process)
4	Folded fabric alignment	3	1 (If any mismatch)	0 (Converted as external)	0 (Converted as external)

*(continued)*



**Table 6** (continued)

Sr No	Process	Before SMED implication		After SMED implication	
		Changing of size (Minutes)	Continuing same size (Minutes)	Changing of size (Minutes)	Continuing same size (Minutes)
5	Gazette fixing	15	–	7	–
6	Side sealing and folding	2	1 (If any mismatch)	2	1 (If any mismatch)
7	Main sealing and folding	0 (Inline process)	0 (Inline process)	0 (Inline process)	0 (Inline process)
8	Cutting setting	5	1 (If any mismatch)	1	1 (If any mismatch)
Total timings for full setup		41	14	14	6

## References

1. Palanisamy S, Siddiqui S (2013) Changeover time reduction and productivity improvement by integrating conventional SMED method with implementation of MES for better production planning and control. *Int J Innovative Res Sci Eng Technol* 2(12). ISSN: 2319-8753
2. Ali ARRH (2017) Enhancing the productivity of printing houses by implementation of SMED (single minute exchange of dies). *Int Des J* 7(3):205–206
3. Kumar V, Bajaj A (2015) The implementation of single minute exchange of die with 5'S in machining processes for reduction of setup time. *Int J Recent Technol Mech Electr Eng (IJRMEE)* 2(2). ISSN: 2349-7947
4. Khusaini NS, Jaffar A, Yusoff N (2013) A survey on lean manufacturing tools implementation in malaysian food and beverages industry using rasch model. *J Adv Mater Res* 845(2014):642–646
5. Winatie A, Maharani BP, Riksa VH, Hasibuan S (2019) Increasing time efficiency of change over process on solid product using SMED (single minute exchange of dies) method in pharmaceutical industry. *Int J Innovative Sci Res Technol* 4(6). ISSN No: 2456-2165
6. Mulla ML, Bhatwadekar SG, Pandit SV (2014) Implementation of lean manufacturing through the technique of single minute exchange of die (SMED) to reduce change over time. *Int J Innovative Res Sci Eng Technol* 3(6). ISSN: 2319-8753
7. Trovinger SCB, Setup RE (2005) Time reduction for electronics assembly: combining simple (SMED) and IT-based Methods. *Int J Prod Oper Manage* 14(2). ISSN: 1059-1478
8. Ulutas B (2011) An application of SMED methodology. *Int J Mech Aerosp Ind Mechatron Manufact Eng* 5(7)
9. Mali YR, Inamdar KH (2012) *Int J Eng Res Appl (IJERA)* 2(3):2441–2445. ISSN: 2248-9622



# Design and Optimization of an Evaporative Condenser: A Detailed Review

Vivek M. Korde, Shivam N. Dekate<sup>(✉)</sup>, Yash A. Bais, and Chirag P. Raut

Department of Mechanical Engineering, Yeshwantrao Chavan College of Engineering, Nagpur  
441110, India

shivamdekate90@gmail.com

## Abbreviations

$h_w$	Film water heat transfer coefficient, (W/m <sup>2</sup> K)
$h_d$	Air water mass transfer coefficient, (W/m <sup>2</sup> K)
$G_w$	Water mass velocity, (Kg/m <sup>2</sup> s)
$G_a$	Air mass velocity, (Kg/m <sup>2</sup> s)
$T_{wm}$	Mean deluge water temperature, (°C)
$T_w$	Water Temperature, (°C)
$\alpha_m$	Mass transfer coefficient for water vapor, (W/m <sup>2</sup> K)
$\alpha_{\text{spray}}$	Heat transfer coefficient between tube surface and water film, (W/m <sup>2</sup> K)
$m$	Mass flow rate, (Kg/s)
$m_{\text{max}}$	Maximum mass flow rates, (Kg/s)
$\varepsilon_e$	Efficiency of evaporative condenser
$L$	Flow rate of liquid, (Kg/s)
$G$	Flow rate of air, (Kg/s)
$T_s$	Temperature of heating steam, (°C)
$T_w$	Wet-bulb temperature, (°C)
$\varepsilon_a$	Efficiency of air condenser.
$h_o$	Outer heat transfer coefficient, (W/m <sup>2</sup> °C)
$E$	Percentage of evaporated water
$b$	Empirical constant.
$\dot{m}_p$	Mass flow rate of fluid used, (kg/s)
$\Delta t_p$	Cooling temperature range, (°C)
$\dot{m}_{w,i}$	Mass flow rate of water at inlet, (kg/s)

## 1 Introduction

Energy saving, water usage and effluent management are crucial parameters under consideration for a cooling system. Thus, the potential of implementing water uniformity source with a fine dispersion of water and minimum utilization should be put into reality. One of the industrial units that follow all these methods is an evaporative condenser.

Technically, evaporative condenser is a device that extracts the heat from working refrigerant and transfers it to the surrounding by application of cooling tubes bounded system with water supply sprinkles. Condenser works with air circulation over the surface, which is regulated by an axial or centrifugal arrangement of the exhaust fan.

These condensers are used in water coolers, air conditioning plants and industries. For its working, some general values of parameters are taken as, air velocity from 1.5 to 4 m/s for economic design consideration. Usually, evaporative condensers using a forced type of flow model is used, as it is very important for cooling purpose with the required efficiency. But, the efficiency of condenser unit is still under consideration for improvement.

In this review, the performance improving parameters are first classified as passive and active types for the analysis. Passive techniques generally refer to the characteristic design, tube modification, extended surface area, etc. whereas; Active techniques refer to the change in any external agent that is used like the attachments and adding's. The experimental investigations require a special emphasis and hence they are separately studied along with the condenser losses.

## 2 Passive Technique

The techniques where main focus is given on the design problems for the evaporative condenser based on of numerical simulation and by the application of software simulations without any external modifications is referred to as passive techniques.

### 2.1 Numerical Simulation

Working on mathematical simulations [1–3], used different design models with different modification in sizes for increasing the performance and they have put some parameters like heat and mass transfer in calculated technique using empirical formulae. Rana and Haran [4] mainly focused on the heat transfer coefficient for water side without air flow, mass transfer coefficient, evaporative Effectiveness. It was found that heat transfer coefficient for water side deprived of air flow increases along with increase in the coolant and product flow rates, also the calculation was carried out with 20% accuracy of range,  $13 < Re_w < 1.7 \times 10^2$ . In addition to it, the mass transfer coefficient also increases with increase in flow rates of fluids. Eventually, the effect of flow rate decreases evaporative effectiveness for the flow of cooling water and increases the effectiveness for flow of air. Hsu et al. [5] investigated on the enhancement of system design work for three different wet surface heat exchanger structures. It was found that the air can be cooled below the wet-bulb temperature range by evaporation. Moreover, satisfying the range it can also cooled very close to dew-point temperature. His main focus was on water wetting techniques on heat exchanger which is also another type of evaporative condenser. Zalewski et al. [6] proposed a mathematical simulated model for forced air flow type of evaporative condenser and have shown that it agrees with the empirical data. The computer program, based on this model, for simulation of bare tube condenser may be used to improve the design. Zalewski et al. [7] optimized the operating and geometrical parameters for fluid type evaporative coolers. Besides, mathematical model for the transfer of mass and heat

in evaporative coolers, model of evaporative heat exchanger for production costs along with evaluations of air pressure drop have also examined. More attention was on design of heat exchanger for maximum heat capacity with low cost. Searching for economical results, Manske et al. [8] studied on the optimization of industrial based refrigeration system using evaporative condenser for cold storage distribution. The system consists of single screw, an evaporative condenser, reciprocating compressor, evaporators, developing a mathematical model. It was observed that the pressure head, condenser fan and condenser sizing were the key elements that affect the total power expenditure of the refrigeration system. Hasan and Siren [9] performed experiments on two different evaporative coolers to analyze the effect of circular and oval tubes under same operating conditions. Moreover, it was shown that the combined thermal-hydraulic characteristic for the oval tube was found better than the circular tube. Min and Webb [10] worked for the effect of tube geometry on performance of heat exchangers. It was found that the pressure drop and heat transfer coefficient decreases on air side and increases on water side as the aspect ratio of oval tube increases. Qureshi and Zubair [11] have proposed the mathematical model to investigate the scenario for the effective design and rating analysis of an evaporative condensers and coolers, which was validated using numerical and experimental data reported in literature. Risk based thermal performance characteristics were evaluated using the fouling model for these heat exchangers. It was shown that there were about 50% decrease in the effectiveness for both types of heat exchanger and also 5% increment of the fluid outlet temperature. In addition, the effectiveness rose with mass flow ratio for both heat exchangers. While investigating the thermal-flow characteristics Heyns and Kröger [12] evaluated the methodology for the evaporative cooler analysis and derived the governing equations. Performance trials were steered on evaporative cooler with 15 tube rows in 76.2 mm triangular pitch pattern made of galvanized steel having outer diameter of 38.1 mm. The following correlations were developed from the experimental data that is revived,

‘Air mass flow rate and deluge water temperature’ is

$$h_w = 470G_a^{0.1}G_w^{0.35} \quad (1)$$

Here,  $0.7 < G_a < 3.6 \frac{\text{Kg}}{\text{m}^2\text{s}}$ ,  $1.8 < G_w < 4.7 \text{Kg}/(\text{m}^2\text{s})$  and  $35 < T_{wm} < 53^\circ\text{C}$ .

‘Air mass velocity and deluge water mass velocity’ is

$$h_d = 0.038G_a^{0.73}G_w^{0.2} \quad (2)$$

Here,  $0.7 < G_a < 3.6 \text{Kg}/(\text{m}^2\text{s})$  and  $1.8 < G_w < 4.7 \text{Kg}/(\text{m}^2\text{s})$ .

‘Air side pressure drop’ is

$$\Delta p = 10.2G_a^{1.8}G_w^{0.22} \quad (3)$$

Here,  $0.7 < G_a < 3.6 \text{Kg}/(\text{m}^2\text{s})$  and  $1.8 < G_w < 4.7 \text{Kg}/(\text{m}^2\text{s})$ .

A similar study, Jahangeer et al. [13] have demonstrated extensively on the numerical study of coefficient of heat transfer for an evaporative cooling condenser working with aspects near tropical climatic region. Very high combined heat transfer coefficients were observed for various film thicknesses over the condenser tubes in the evaporative cooled

condenser. It was noticed that the performance increased by decreasing temperature lift with the help of water droplets inclusion. By modifying the design slightly, Sun et al. [14] concluded that, by using these all method air pressure drop in elliptical tube bundle decreases by an average of 20–30%. In addition, heat transfer rates found to be increased by an average of 8.3–30.9%. Moreover, by giving the attention on capacity and COP they found to be increased by 21.3–27.5% and an average of 3–7% respectively. Harbyn et al. [15] reviewed the domestic evaporative condensers and presented innovative designs intending to reduce the power consumption and improve the COP. It is reported that the use of evaporative condenser instead of air cooled one may increase the COP by 113.4% and decrease the power consumption by 58%. Xu et al. [16] made some innovative developments in structure of the evaporative condenser to improve the efficiency and other benefits such as reduced wind resistance, expedient cleaning operation and greater energy-efficient fan. The noise level was reduced by changing the spray direction, inorganic fillers were arranged to reduce the cooling water temperature with enhancement of heat transfer, elliptical finned tubes were used in bottom evaporative coils, inlet air temperature was reduced all of which resulted in more efficient and compact device. Anicalliea et al. [17] have proposed the comprehensive experimental thermal investigation with effect of key parameter on condensation heat transfer in ammonia evaporative condensers. It was revealed for the evaporative condensers using ammonia, that the correlations presently accessible in literature describe the processes of heat as well as mass transfer appropriately. Liu et al. [18] have conducted the tentative examination of high efficiency dew-point evaporative operational cooler by modified and effectively optimizing the water and air flow arrangements. It was found that corrugated plates enhance the efficiency of cooling by 10%. The counter flow arrangement also improves the efficiency by more than 30%. The cooling efficiency is enhanced within a practical range by the increase in lengths of channel and air entrance and also by reducing the width and gap of channel. Experiments were performed by Zhu et al. [19] on evaporative condenser with an elliptical tube bundle to study the effect of various parameters, such as inlet wet-bulb temperature, relative humidity, spray density and frontal air velocity on heat and mass transfer performance. Using the experimental data the accurate empirical correlations were obtained for predicting the mean condensation coefficient of heat transfer, wall-film coefficient of convective heat transfer and the film-air coefficient of convective mass transfer.

## 2.2 Software Simulation

Abbassi and Bahar [20] predicted outcomes of their thermal design on the basis of software. They concluded that PID controller can appropriately replace by the neural network controller to model the thermal behavior of an evaporative condenser with advantage of reduced time for generation of model and minimizing the process error. In search of best satisfactory operating conditions to guarantee the complete wet ability of the heat transfer geometry with minimum pumping cost, Fiorentino and Starace [21] have conducted the pervasive numerical and investigational performance examination of evaporative type condensers. Novel relations were presented for engineers to quantify thermal performance depending on actual working conditions. Fiorentino et al. [22] conducted experiments on a test rig to analyze the combined effect of DBT and RH on

performance of evaporative condenser. It was found that the heat transfer rate reduces by 30% with 6% increase in relative humidity at highest DBT. The air process was shown on psychometric chart revealing that the ratio of latent heat to sensible heat decreases with increase in RH.

### 3 Active Techniques

The techniques where in main focus is given on the attachments, additions, modifications externally rather than focusing on modifying the model itself.

Bykov et al. [23], have defined different heat and mass transfer spaces in evaporative condensers. They have presented a procedure to optimize such spaces, the effect of fins and spray-filled spaces which will result in optimizing the thermal efficiency characteristics and obtaining a better design of evaporative condensers. Goswami et al. [24], retrofitted media pads to the condenser of a 2.5 ton air conditioner as an additive technique to improve the performance which resulted in 20% savings with a remuneration period of two years. Hwang et al. [25] introduced by modifying the normal pump into split heat pump, by putting the tubes immersed down in the water, where the disks fitted near tubes rotate with the help of pump and simultaneously the air is also blown over them. Rejection of heat from tubes takes place in water whereas, heat from the film is extracted in the surrounding. This resulted in increase in capacity of condenser by 1.5–8.3% and also increases COP by 11.1–21.6%. The setup introduced by him consists of copper serpentine laid wrapped by cloth placed in rectangular shaped duct. This cloth soaks the water and reduces the heat inside the tubes and helps in effective transfer of heat. Horacek et al. [26] investigated on the spacing of nozzles, so that every area must come under its dispersing shower. When spray height is nearly 11–14 mm then spray of water will satisfy this situation. Experiment with 2-spray nozzles was performed to improve heat transfer performance. Moreover, attention was provided toward distribution of heat transfer beneath two spray nozzles with revelation of the liquid to solid contact area. For a nozzle, higher transfer of heat was achieved when nozzles were situated directly over the surface area. Also, the heat flux becomes uniform as the distance from nozzle to surface goes on increasing. Hence, it concludes that the heat flux is directly connected to contact length and not the wet area. Royne [27] worked on key factor affecting the performance of cooling device i.e., nozzle configuration. Instead of considering the transfer of heat and the drop in pressure, he investigated various types of nozzle consisting of short (straight), long (straight), sharp edging, contoured, countersunk nozzles. After this experiment it was concluded that:

1. Countersunk nozzles are having average heat transfer at higher rates, preferring them over others.
2. Longer nozzles are having lower pressure drop as compared to smaller nozzles. This makes longer nozzles beneficial than the smaller, on the basis of pumping power.
3. Sharp edging and contoured shape nozzles yield similar results for pump power requirement when compared with straight nozzles but still sharp-edged nozzle is used as it decree lower flow rate.

Nozzles spacing and inclination also matters, this is because all the tubes area must be covered with water spray to shun the expenditure over buying unrequited number of nozzles. Silk et al. [28] investigated on spray cooling methods on various types of enhanced surfaces, nozzle angle and the type of nozzles. Basically, this experiment was performed on cubic pin fin, pyramids and straight fins with working fluid as PF-5060. Moreover, comparison between flat surface and enhanced surfaces was done with inclination angle in the range of 0–45° at highest CHF. It was concluded that straight fins are the best option for increasing performance, multiphase efficiencies, heat flux and also for cost effectiveness. Camargo et al. [29] proposed three methods that can be used as reference for efficient use of evaporative cooling systems. Idrissi et al. [30] mentioned that the implementation of water spraying over condenser will increase the efficiency. The experimental validation was none for the semi numerical model but it was observed that the COP can be increased averagely up to 55%. Vrachopoulos et al. [31] proposed a novel evaporative condenser where his work anticipated on very unique additions like electrical circuit pump and drop clouding computer engaged system for water spraying. It was observed that by using such novel condenser the COP can be enhanced up to 21.1% which is result of reduction in the operating temperature difference of compressor. Tissot et al. [32] investigated the performance improvement of a refrigerator by employing water spray in air near the condenser inlet. The numerical analysis found a rise of 22.4% in COP for the machine with this spraying technique, which was validated experimentally. A detailed study was given by Ndukaife et al. [33] on performance and proposed the mathematical research relevant to the enhancement in performance and diminution in energy consumption of air conditioning system by using evaporative cooling condenser. Contact of the hot air with water on porous medium can yield a result in immediate heat as well as mass transfer. Reduction in the air temperature results in rise in relative humidity interpreted for being a function of thickness of pad. It was accomplished,

1. The lower mass flow rate was obtained by 15 cm pad which ultimately reduces the work of compression up to 20%. Also this thickness of pad increases COP by 44% as compared to other thicknesses.
2. The fall in air temperature of 1 °C causes the fall in condensing temperature by 0.6 °C. In addition to this, it was predicted that about 4% raised in COP occurred due to the drop in condensing temperature by 1 °C.

Wang et al. [34] have reviewed the research status of evaporative condensers and have suggested the use of nano-technology and nano-materials to enhance the performance. Chien et al. [35], carried out the investigational study using various flow rates, spacing of nozzles and its geometric designs to investigate the uniformity of the water spray and collection ratio of sprinkler in an evaporative cooled condenser. It was observed that the uniformity depends upon the flow rate, nozzle opening and properly adjusted flow rate that can prevent the impact and loss of droplet. A smaller spacing of nearly 17 cm and larger opening size of nozzles are preferable to accomplish the task.

## 4 Experimental Investigations in Evaporative Condenser as a Comparison

This section describes various experiments that result in the formation of new model.

Facao and Oliveira [36] conducted thermal investigation for a new closed wet cooling tower to use with chilled ceiling through different thermal models. Experimental correlations were presented in order to predict augmentation in thermal performance. Better results were obtained using these new correlations by the models, for small towers. The new correlations were,

$$\alpha_m = 0.1703 \left( \frac{m}{m_{\max}} \right) 0.8099 \quad \text{air} \quad (4)$$

$$\alpha_{\text{spray}} = 700.3 \left( \frac{m}{m_{\max}} \right) 0.6584 \quad \text{spray} \quad (5)$$

Ettouney et al. [37] conducted experiments with two different finned-tube heat exchangers which can be arranged in parallel, series and stand alone with water or air cooling. Steam temperature and the water to air mass flow rate ratio ( $L/G$ ) were under consideration for the analysis. The efficiency was highest for arrangement in series, followed by parallel and then single condenser. It was also shown that the system efficiency increases when  $L/G$  ratio is low and steam temperatures are high. Simple correlations were presented for the evaluation of external heat transfer coefficient and efficiency in terms of  $L/G$  ratio and temperature of steam.

The efficiency correlation for the evaporative condenser is:

$$\begin{aligned} \varepsilon_e = 98.57 - 1.76 \left( \frac{L}{G} \right) - 2.09 \times 10^{-2} (T_s) \\ + 0.27A + 4.83 \times 10^{-2} (T_w) \end{aligned} \quad (6)$$

Similarly, the efficiency correlation for the air condenser is

$$\varepsilon_a = 223.03 + 1.81 \times 10^{-2} (T_s) - 0.31A - 5.29(T_w) \quad (7)$$

The correlation for wet heat transfer coefficient is

$$h_o = 0.16(L/G)^{0.23} (T_s)^{2.13} \quad (8)$$

Hosoz and Kilicarslan [38] conducted a comparative analysis for three types of condensers; viz air cooled, water cooled and evaporative type condenser and revealed that water cooled condensers were superior whereas the air cooled exhibits lower performance. However, in various cases, outcomes of the evaporative type condenser were found equivalent with water cooled type condenser system. To improve chiller efficiency, Yu and Chan [39], installed direct evaporative coolers in front of air cooled condensers so that the outdoor air gets cooled prior to entering the condensers. It was observed that



the refrigeration was increased for all operating conditions. Wolfgang, Leidenfrost and Korenic [40] have emphasized that air side heat transfer augmentation can be achieved best with evaporative cooling as heat can be rejected to ambient even when the ambient temperature is greater than the condenser temperature. Complete wetting of the heat transfer surface is sufficient to get maximum performance of the condenser thus amount of water sprayed should be just sufficient rather than deluging the surface which not only saves the power but also reduces the water loss. The air flow rates should be appropriately adjusted to have air water-film interaction just sufficient to remove water film partially by drag force which results in low blower power. Nasr and Salah Hassan [41] suggested an innovative condenser for a small refrigerating system, which was cooled with the help of wick wrapped over the condenser tubes, sucking water from the basin by capillary action and providing the evaporative cooling. The evaporative cooling condenser has 13 times more capacity to reject heat as compared to air cooled type condenser. Eghtedari and Hajidavalloo [42] performed experiments by retrofitting the air cooled condenser with evaporative cooling. They found 20% decrease in the power consumption and 50% increase in the overall performance with this adaption. It was also observed that the increasing ambient temperature has hardly any effect on COP while using evaporative cooling condensers. Patel and Shah [43] optimized the evaporative condenser in two different ways, first by reducing condenser pressure and second, using VFD for fan and pump. It was also observed that for same rate of heat rejection total specific power consumption is less for optimal reduction in condenser pressure comparatively with using VFD for fan and pump. Shen et al. [44] studied the peak power reduction and saving of energy of evaporative condenser cooling. It was found that the energy saving was much higher for HVAC systems, with R-410A as a refrigerant than R-22 refrigerant.

## 5 Evaporative Condenser Losses and Water Treatment

The very factor that affects the performance of evaporative condenser at greater extent but occurs stagnantly as evaporation losses are generally neglected in thermal design of cooling tower. Nahavandi et al. [45] developed a new technique, including the evaporation losses in the energy balance, leading to conservative design of a cooling tower where accurate results are needed. The Merkel's method, ignoring these losses, introduces up to 12% of error on design conditions. Khan and Zubair [46] developed a fouling model to predict the decrease in the tower performance characteristics and validated it with experimental data. It was found that fouling decreases the NTU, which in turn decreases the effectiveness of the cooling tower and increases the exit water temperature. Fouling allowance factor should be considered in the design procedure of cooling towers for adequately compensating the fouling loss. Qureshi and Zubair [47] developed an empirical relation, considering the thumb rule by Baltimore Air Coil which was a patent based on increasing the uniformity with increased efficiency related to water flow. Calculation of evaporation losses which causes increases in the concentration of dissolved solids and other impurities. The values predicted were in good concurrence with the numerical standards obtained from the calibrated model.

$$E = \left( \frac{b\dot{m}_p \Delta t_p}{\dot{m}_{w,i}} \right) \cdot 100 \quad (9)$$

Mehrabi and Yuill [48] studied on research about the effects of fouling along air side on the performance of air cooled condensers. They examined nine fouled condensers from field, seven plate fin coils along with that two spine fin coils. On the basis of this, they concluded that the performance of the system was negligible affected by fouling on air side even though it substantially decreases the coil's air side pressure drop. Also, in some cases fouling improved the performance. For cleaning the coil, water was found to be used in most of the cases as compared to detergents that causes reduction in performance. Browning et al. [49] discussed the problems in evaporative condensers related to the water and its treatment. They mentioned that water deposits on condenser tubes not only reduce the heat transfer effectiveness and increase the operating cost but also lead to potential failure. Hence the treatment of water should be an essential operational program.

## 6 Conclusion

The intent of writing this review paper was to recognize the adaptation workings performed on evaporative condenser as,

- Water cooled type condenser is more effective till now, but the water scarcity and ground space management problem makes evaporative condenser as a better option. However, in some cases, outcomes of the evaporative type condenser are found equivalent with water cooled type condenser system which again justifies their use. Evaporative type condenser has compact structure, small footprint, low investment, easy maintenance, stable performance, clear water saving, low operating pressure which makes it more preferable over others.
- If more than one condenser is used then the efficiency is highest for arrangement in series, followed by parallel and then single condenser.
- Maximum amount of inlet vapor can be processed in parallel configuration whereas, largest degree of sub-cooling is offered by arrangement in series.
- The use of evaporative condenser instead of air cooled one may increase the COP by 113.4% and decrease the power consumption by 58%. At high inlet vapor temperatures and lower L/G ratios the evaporative condenser efficiency increases.
- Elliptical tubes should be preferred over circular tubes as it lowers the pressure drop on air side and increases the heat transfer because of increased surface area.
- Countersunk nozzles and sharp edging nozzles should be used for higher and lower flow rates respectively.
- Allowance data should be added in thermal calculations, as evaporation loss is significantly important for condenser. Also, fouling should be considered.
- Adding techniques, such as media pads and water pads, should be adopted for optimum cooling of the refrigerant and to reduce the power consumption.
- PID controller can be appropriately replaced by the neural network controller to model the thermal behavior of an evaporative condenser with advantage of reduced time for generation of model and minimizing the process error.
- The noise level can be reduced by changing the spray direction, inorganic fillers can be arranged to reduce the cooling water temperature which leads for enhancement of

heat transfer, elliptical finned tubes can be used in bottom evaporative coils all these can result in more efficient and compact device. Additionally, corrugated plates will enhance the performance.

- Novel relations are presented with strong predictive potential for engineers to quantify various parameters against the specific conditions in evaporative condensers which can be used for improving the design and performance.
- The heat exchanger performance of the evaporative condenser is affected by both the inlet relative humidity and the inlet wet-bulb temperature of air. But the effect of change in the inlet WBT is quite larger than that of relative humidity. For each 1 °C increase in the wet-bulb temperature, the total heat exchange decreases by an average of 1.445% whereas, the same decreases by about 12.8% as the relative humidity increases from 0 to 90%.
- The total vapor-to-liquid film heat transfer performance increases with increase in frontal air velocity and spray density.
- The water treatment program for an evaporative condenser system is integral to the operation of an energy, water and resource efficient facility.
- For getting enhanced effect over evaporative condenser performance, nano-material and nano-particles should be added to coil of condenser and working refrigerant respectively.

## References

1. Parker RO, Treybal RE (1965) The heat, mass transfer characteristics of evaporative coolers. *AIChE Chem Eng Prog Symp Ser* 32(57):138–149
2. Mizushima T, Ito R, Miyasita H (1967) Experimental study of an evaporative cooler. *Int Chem Eng* 7 (4):727–732
3. Niitsu Y, Naito K, Anzai T (1969) Studies on characteristics and design procedure of evaporative coolers. *J Shase* 43
4. Rana RS, Haran V (1983) Heat and mass transfer from a single horizontal tube of an evaporative tubular heat exchanger. *Int Comm Heat Mass Transfer* 0735-1933/83 10:403–412. @Pergamon Press Ltd. Printed in the United States
5. Hsu ST, Lavan Z, Worek WM (1989) Optimization of wet-surface heat exchangers. *Energy* 11:757–770
6. Zalewski W (1991) Mathematical model of heat and mass transfer processes in evaporative condensers. *Int J Refrig* 16(1). Technical University of Cracow, ul. Warszawska 24:31–155
7. Zalewski W, Niezgodna-Zelasko B, Litwin M (2000) Optimization of evaporative fluid coolers. *Int J Refrig* 23:553–565
8. Manske KA, Reindl DT, Klein SA (2001) Evaporative condenser control in industrial refrigeration systems. *Int J Refrig* 24:676–691
9. Hasan A, Sirén K (2003) Performance investigation of plain and finned tube evaporatively cooled heat exchangers. *Appl Therm Eng* 23:325–340
10. Min JC, Webb RI (2004) Numerical analyses of effects of tube shape on performance of a finned tube heat exchanger. *J Enhanced Heat Transfer* 11:61–73
11. Qureshi BA, Zubair SM (2006) A comprehensive design and rating study of evaporative coolers and condensers Part I. Performance evaluation. *Int J Refrig* 29:645–665
12. Heyns JA, Kröger DG (2010) Experimental investigation into the thermal-flow performance characteristics of an evaporative cooler. *Appl Therm Eng* 30:492–498

13. Jahangeer KA, Tay AAO, Islam MR (2011) Numerical investigation of transfer coefficients of an evaporatively-cooled condenser. 1359–4311 (2011)
14. Sun L, Yang L, Shao L-L, Zhan C-L (2015) Overall thermal performance oriented numerical comparison between elliptical and circular finned-tube condensers. *Int J Therm Sci* 89:234–244
15. Harbyn K, Gebaly DR, Koura NS, Hassan MS (2016) Performance improvement of vapor compression cooling systems using evaporative condenser: an overview. *Renew Sustain Energy Rev* 58:347–360
16. Xu G-F, Zhang N-N, Yu H-F, Zheng D-Y (2016) The structure optimization design of evaporative condenser. In: International conference on energy and environmental protection (ICEEP)
17. Iliea A, Dumitrescu R, Drugheana L, Calotă R, Giripa A (2017) Experimental investigation of condensation heat transfer in ammonia evaporative condensers. *Energy Procedia* 112:150–157
18. Liu Y, Akhlaghi YG, Zhao X, Li J (2019) Experimental and numerical investigation of a high-efficiency dew-point evaporative cooler. *Journal* 0378–7788
19. Zhu X, Chen S, Shen S, Shuangquan Ni, Xu Shi, Qinggang Qiu (2020) Experimental study on the heat and mass transfer characteristics of air-water two-phase flow in an evaporative condenser with a horizontal elliptical tube Bundle. *Appl Therm Eng* 168:114825
20. Abbassi A, Bahar L (2005) Application of neural network for the modelling and control of evaporative condenser cooling load. *Appl Therm Eng* 25:3176–3186
21. Fiorentino M, Starace G (2016) Numerical and experimental performance analysis of evaporative condensers. *Energy Procedia* 101:26–33
22. Fiorentino M, Starace G (2017) Experimental Investigations on evaporative condensers performance. 1876–6102
23. Bykov AV, Gogolin VA, Tovaras NV (1984) Investigation of heat, mass transfer and fluid flow characteristics in evaporative condensers. *Int J Refrig* 7:342–347
24. Goswami DY, Mathur DS, Kulkarni SM (1993) Experimental investigation of performance of a residential air conditioning system with an evaporatively cooled condenser. *J Solar Energy Eng* 115:206–211
25. Hwang Y, Radermacher R, Kopko W (2001) An experimental evaluation of a residential-sized evaporatively cooled condenser. *Int J Refrig* 24:238–49
26. Horacek B, Kim J, Kiger KT (2004) Spray cooling using multiple nozzles: visualization and wall heat transfer measurements. In: IEEE transactions on device and materials reliability, vol 4, no 4
27. Royne A, Dey CJ (2006) Effect of nozzle geometry on pressure drop and heat transfer in submerged jet arrays. *Int J Heat Mass Transfer* 49:800–804
28. Silk EA, Kim J, Kiger K (2006) Spray cooling of enhanced surfaces: impact of structured surface geometry and spray axis inclination. *Int J Heat Mass Transfer* 49:4910–4920
29. Camargo JR, Ebinuma CD, Cardoso S (2006) Three methods to evaluate the use of evaporative cooling for human thermal comfort. *Engenharia Térmica (Therm Eng* 5:09–15
30. Youbi-Idrissi M, Macchi-Tejeda H, Fournaison L, Guilpart J, McGraw-Hill (2007) Numerical model of sprayed air-cooled condenser coupled to refrigerating system. *Energy Convers Manage* 48:1943–1951
31. Vrachopoulos MG, Filios AE, Kotsiovelos GT, Kravvaritis ED (2007) Incorporated evaporative condenser. *Appl Therm Eng* 27:823–828
32. Boulet TJ (2014) Improved energy performance of a refrigerating machine using water spray upstream of the condenser. *Int J Refrig* 38:93–105
33. Ndukaife TA, Nnanna AGA (2018) Enhancement of performance and energy efficiency of air conditioning system using evaporatively cooled condensers. *Heat Transfer Eng.* <https://doi.org/10.1080/01457632.2018.1429063>

34. Wang F, Yang Y (2018) Research status of evaporative condenser. In: ICAESEE 2017, IOP conference series: earth and environmental science, vol 113, p 012102
35. Chien L-H, Xu J-J, Yang T-F, Yan W-M (2019) Experimental study on water spray uniformity in an evaporative condenser of a water chiller. *Case Stud Therm Eng* 15:100512
36. Facao J, Oliveira AC (2000) Thermal behaviour of closed wet cooling towers for use with chilled ceilings. *Appl Therm Eng* 20:1225–1236
37. Ettouney HM, El-Dessouky HT, Bouhamra W, Al-Azmi B (2001) Performance of evaporative condensers. *Heat Transfer Eng* 22(4):41–55
38. Hosoz M, Kilicarslan A (2004) Performance evaluations of refrigeration systems with air-cooled, water-cooled and evaporative condensers. *Int J Energy Res* 28:683–696
39. Yu FW, Chan KT (2005) Application of direct evaporative coolers for improving the energy efficiency of air-cooled chillers. *J SolEnergy Eng* 127:430–433
40. Leidenfrost W, Korenic B (2007) Evaporative cooling and heat transfer augmentation related to reduced condenser temperatures. *Heat Transfer Eng* 3:3–4
41. Nasr MM, Salah Hassan M (2009) Experimental and theoretical investigation of an innovative evaporative condenser for residential refrigerator. *Renew Energy* 34:2447–2454
42. Eghtedari H, Hajidavalloo E (2010) Performance improvement of air-cooled refrigeration system by using evaporatively cooled air condenser. *Int J Refrig* 33:92–988
43. Patel MC, Shah BA (2014) Performance optimization of the evaporative condenser design. *IJERT* 3(5)
44. Shen B, New J, Ally M (2019) Energy and economics analyses of condenser evaporative precooling for various climates, buildings and refrigerants. *Energies*
45. Nahavandi AN, Kershah RM, Serico BJ (1975) The effect of evaporation losses in the analysis of counter flow cooling towers. *Nucl Eng Des* 32:29–36
46. Khan JUR, Zubair SM (2004) A study of fouling and its effects on the performance of counter ow wet cooling towers. *Proc Instn Mech Eng* 218. Part E: J. Process Mech Eng
47. Qureshi BA, Zubair SM (2007) Prediction of evaporation losses in evaporative fluid coolers. *Appl Therm Eng* 27:520–527
48. Mehrabi M, Yuill D (2019) Fouling and it's effects on air cooled condensers in split system air conditioners (RP-1705). *Sci Technol Built Environ* 25:784–793. Taylor & Francis, 2374–4731
49. Browning A, Sanders M, Weimar D (2010) Effective water treatment for evaporative condensers. In: 32nd Annual meeting international institute of ammonia refrigeration, industrial refrigeration conference & exhibition 1417



# The Numerical Examination for Mixing Characteristics of Modified T Micromixer with Offset and Triangular Obstructions

Sachin Kaushik<sup>(✉)</sup> and M. Zunaid

Department of Mechanical Engineering, Delhi Technological University, New Delhi 110042,  
India

sachink181@gmail.com

## 1 Introduction

Micromixers are a type of concentrated mixing device for different phases existing in different forms such as solids, liquids, and gases. The arrangement of a micromixer is put together in a whole or partial form, using precision engineering or microtechnology. There are many key characteristics of micromixers but two lays the foundation of microfluid dynamics. First, the design phase of the micromixers is predicated on manipulating the flow using external disturbances or channel geometry. Second, although micromixers being several vital advantages in various fields of mechanical engineering, molecular-level processes remain almost constant. Micromixer deals with the study of microfluidics. When fluid is studied on the small microscale of the order of micrometer that study is termed microfluidics [1–4].

In the past few years, miniature devices have gained a lot of interest because of their versatile applications in various fields of thermal engineering [5–8]. But being small in size, i.e., in the order of micrometers, these devices only have laminar flow through them and no turbulent flow is experienced. This also limits the mixing and heat transfer rate in them. Increased mixing should be done in the smallest possible length at the crossroads of a small channel [9–11]. Over time, many new approaches are provided to increase the integration, and geometry modification has proved to be the best. Mixing methods often rely on chaotic production advection, in which the movement of the fluid varies abnormally, and thus it causes the same value as pressure and velocity to vary randomly in space and time [9].

Micromixers can be divided into common types: active and passive [6–8]. Inactive micromixers, mixing is performed by external forces such as electric or magnetic fields which interact with the fluid without coming in their direct contact. In the other kind, i.e., passive micromixers no external source other than a pumping device is needed for the mixing of fluids. The fluid is made to flow in a certain manner so that the streamlines of incoming fluids cross each other and mixing can take place. This is done by altering the geometry of the channel and also by installing barriers and ridges in the microchannel [5, 8]. Passive micromixers (also known as lamination [4] micromixers) can be very useful in biomedical fields and have applications in chemical engineering [1]. Despite

being simple devices in terms of geometry and construction, passive micromixers offer a wide range of mixing performance. Their mixing is mostly based on the phenomenon of molecular diffusion and advection [13]. In micromixers with laminar flow, i.e., at values of low Reynolds number, mixing is mostly due to advection and time of fluid in the micromixer only [12–15].

Many experimental works have been performed on both of these types of micromixers. Mohammad et al. [3] worked on the mixing of two fluids. The two fluids he took were having the same physical properties but different concentrations. He used sinusoidal electrical fields on four electrodes to enhance the mixing. Also, he varied various electrical parameters to increase the mixing. Stroock et al. [10] developed a method using ridges implanted in the microchannel which caused the flow to become chaotic and hence increased the mixing index. Bottauski et al. [11] in their study made a new design having three channels. These three channels were secondary and placed crossed stream to the mainstream. The results obtained were having better mixing performance and proved that high Mixing can be achieved with disconcertion of the main flow through the secondary channels using sinusoidal oscillating sinusoidal jet flow.

Dundi et al. performed the numerical methods using CFD to calculate the Mixing Performance of Simple T Micromixer. In our study, the work performed by Dundi et al. is taken forward by providing some obstacles for the flowing fluid [1]. An attempt to increase the mixing index is made by installing triangular obstructions and offset of the inlet.

## 1.1 Mathematical Modeling

Both the inlets are provided with water. For the study, two different species Water\_A and Water\_B are considered. Since the density of the water remains the same throughout the study, it is considered an incompressible fluid. The following two equations are involved in the solving of the model numerically.

1. Continuity equation:  $\Delta \cdot V = 0$
2. Navier–Stokes equation:  $V \cdot \Delta V = -\frac{1}{\rho} \Delta P + \nu \Delta^2 V$

where

$V$ —Velocity Vector.

The governing equation for the process of mixing is given by the equation:

where  $(V \cdot \Delta)c = D\Delta^2 c$ .

$c$  represent Concentration.

$D$  represents Coefficient of Diffusion.

The average concentration of a species at any section is given by:

$$\bar{c} = \frac{\int_A c dA}{A}$$

where

$A$  represent Area of the section ( $\text{m}^2$ ).

For any cross-section the value of the mixing index for a species is calculated as follow:

$$MI = 1 - \sqrt{\frac{\int_A (c - \bar{c})^2 dA}{A \cdot \bar{c}(1 - \bar{c})}}$$

The extent of the mixing of fluids in the micromixer is governed by the value of the mixing index. Higher MI corresponds to better mixing (Fig. 1).

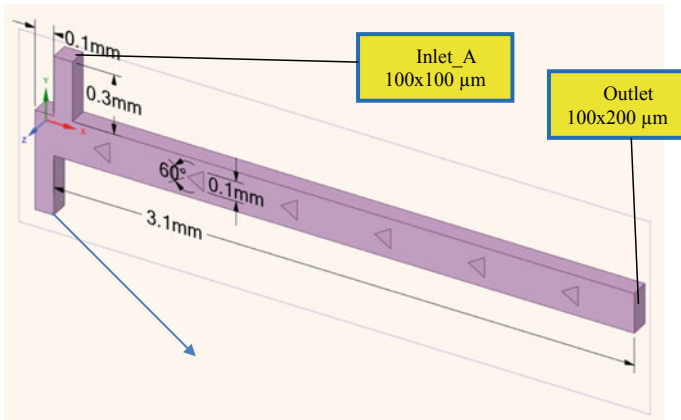


**Fig. 1** Modified T micromixer with triangular obstructions and offset (MTMO)

The meshing is done with an element size of  $2.68\text{E}-6$  m. Since for hexahedral elements the number of elements required to get an accurate result is less, hexahedral elements are chosen. This also reduced the computational time considerably. The mesh generated is shown in Fig. 2. A very fine and uniform mesh with an average skewness of  $9.5919\text{E}-003$  is generated. Figure 2 represents the mesh obtained in the mesh. It is clear from the mesh diagram that the meshing is uniform.

Water\_A and Water\_B are provided from Inlet\_A and Inlet\_B, respectively. The Water\_A and Water\_B are considered as two species of water having similar properties. The temperature of both the species is taken as  $20^\circ\text{C}$ ; hence, all the properties of water at  $20^\circ\text{C}$  are considered. While solving in the solver 1 and 0 is taken as species concentration for Water\_A and Water\_B, respectively. For verification of the result to be correct, the species concentration at the outlet must be 0.5 if the same velocity is given at both the inlets. Properties of the working fluid, i.e., water at  $20^\circ\text{C}$  are summarized in Table 1.

The model was chosen for the study of steady-state laminar flow. The species transport model is also turned ON with two species being Water\_A and Water\_B. The residuals chosen are very small for better accuracy and are mentioned in Table 2.

Pressure velocity coupling is done with the help of SIMPLEC solution method keeping Pressure as Standard. For momentum, the solution method taken is Second-Order Upwind. For species also Second-Order Upwind is chosen. Table 3 summarizes



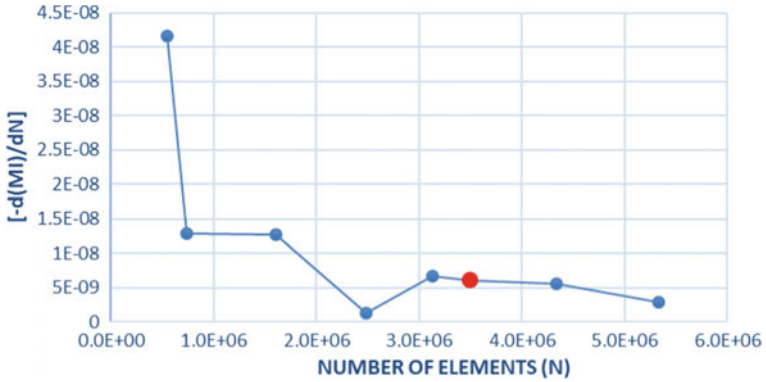


**Fig. 2** Change in the slope of MI versus N for MTMO

**Table 1** Liquid water (20 °C)

Coefficient of diffusion ( $D$ )	$20 \times 10^{-9} \text{ m}^2/\text{s}$
Dynamic viscosity ( $\mu$ )	0.001 Pa-s
Density ( $\rho$ )	998.2 kg/m <sup>3</sup>

the value of Reynolds number for which the calculations are done in the micromixer, i.e., for which the mixing index at the outlet is calculated.

**Table 2** Residuals

Momentum	$10^{-5}$
Species equation	$10^{-5}$
Continuity	$10^{-6}$

**Table 3** Boundary conditions

S. No.	Axial velocity (m/s) perpendicular to surface	Reynolds number
1	0.30	40
2	0.60	80
3	0.90	120
4	1.20	160
5	1.50	200
6	2.00	266

### 1.2 Grid Independence Test

To get a valid result independent of the number of elements taken in meshing, appropriate mesh size is considered, which is obtained with the help of a grid independence test. The value for mixing indices for a various number of elements is calculated. The value where we get negligible change in mixing index for different element sizes, that is considered to be optimum element size. More are the number of elements taken for simulations, higher will be the accuracy of the result. However, taking a large number of elements require more time for computational result and high system requirement are needed. So, a balance between the number of elements, the time required for calculations, and desired accuracy is needed to be maintained.

From the graph obtained in grid independence test, it can be concluded that the value of the MI is improving even when a large number of elements are taken for study, i.e., at 6,465,613 elements. After analyzing the graph obtained by grid independence test for Reynolds number 16 mesh element size of  $2.68E-6$  (3,313,239 elements) is chosen for this study. The sole purpose of taking this number of elements is to maintain a good accuracy to the results and reduce the time required for computing the results. While deciding the number of elements that we should take for our study, the graph of the slope of MI with variation in several elements plays an important role. Wherever the slope of this graph is almost constant, a value of that range for several elements must be chosen.

## 2 Validation

See Figs. 3 and 4.

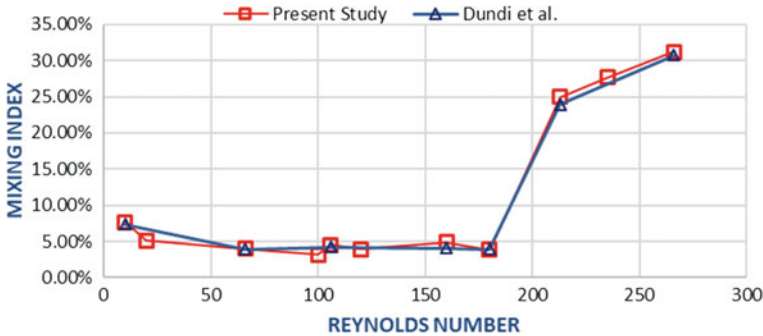


Fig. 3 Comparison of MI for STM between our study and existing results

The result for STM is compared with the results published in Cortes-Quiroz et al. and Manoj [1, 12]. Figure 5 shows the relative performance of STM with existing literature and the present study. Table 4 represents the data comparison of this study and the existing study. From Fig. 5, it can easily be depicted that the results obtained are almost identical to actual values and hence the study is accurate.

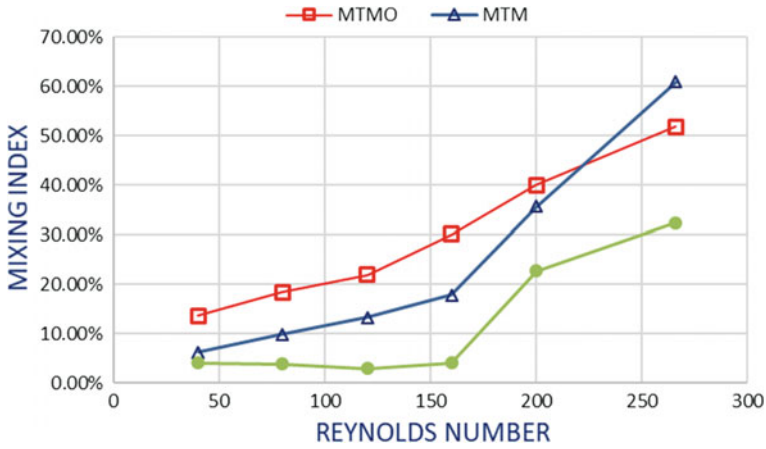


Fig. 4 MI comparison for MTMO, MTM, and STM

### 3 Results

The results for Modified T Micromixer (MTM) and Modified T micromixer with Offset (MTMO) are simulated and then their comparison to STM with the same dimensions is made. Also, the results for STM are calculated for some other values of Reynolds number for properly studying the relative performance of STM, MTM, and MTMO.

Table 5 represents the values of MI for STM, MTM, and MTMO at various Reynolds number ranging from 40 to 266. For both MTM and MTMO, there is a considerable increase of mixing characteristics at all values of Reynolds number. This increase of mixing index is more for values at higher Reynolds number, especially for values above 160. For MTMO there is a good increase in mixing index even at low Reynolds number,

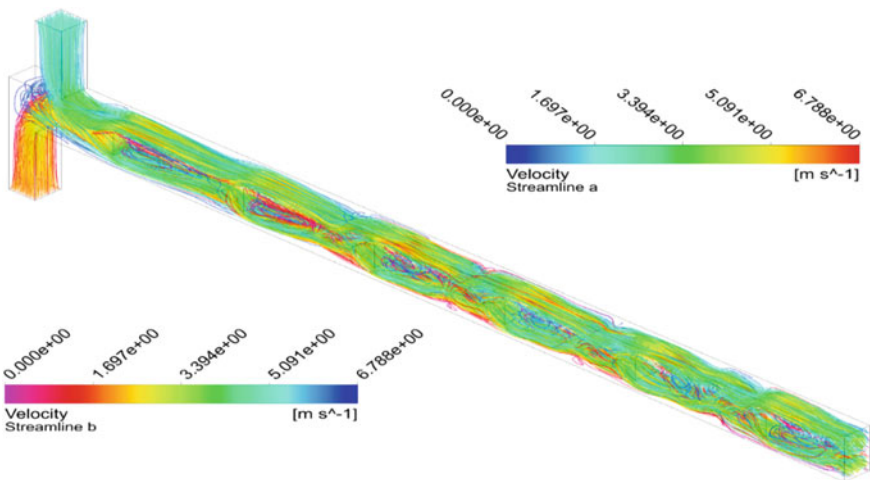


Fig. 5 Streamline for MTMO at RE 266

**Table 4** Comparison for MI between Existing and Present literature

Inlet velocity (m/s)	Reynolds number (outlet channel)	Mixing index (MI)	
		Simple T micromixer (existing literature) (%)	Simple T micromixer (present study) (%)
0.075	10	7.4	7.68
0.15	20	–	5.11
0.495	66	3.9	3.97
0.75	100	–	3.17
0.795	106	4.2	4.49
0.90	120	–	2.95
1.2	160	4.1	4.88
1.35	180	3.9	3.88
1.5975	213	23.9	24.94
1.7362	235	–	27.64
1.995	266	30.7	32.20

i.e., at 40 also, although MI for most micromixers at low Reynolds number is less (Figs. 6, 7, and 8).

**Table 5** Mixing indices at different Reynolds numbers

Inlet velocity (m/s)	Reynolds number (outlet channel)	Mixing index (MI)		
		STM (%)	MTM (%)	MTMO (%)
0.30	40	4.08	6.20	13.62
0.60	80	3.81	9.86	18.45
0.90	120	2.95	13.34	21.92
1.20	160	4.12	17.88	30.07
1.50	200	22.73	35.71	39.91
2.00	266	32.32	60.91	51.82

The increase in the mixing index for MTM and MTMO is due to the presence of triangular obstructions. The triangular obstructions disperse the fluid flow which can easily be depicted with the help of streamline diagrams. As the value of Reynolds number is increased, the streamline is getting more deviated from a straight path and hence more mixing is taking place. Also, more the number of obstructions more is the dispersion of fluid particles and hence more will be the MI. Also, if we look closely, it can be observed that the introduction of triangular obstructions is leading to the merging of streamlines of both the fluids entering the micromixer. This is resulting in an increase

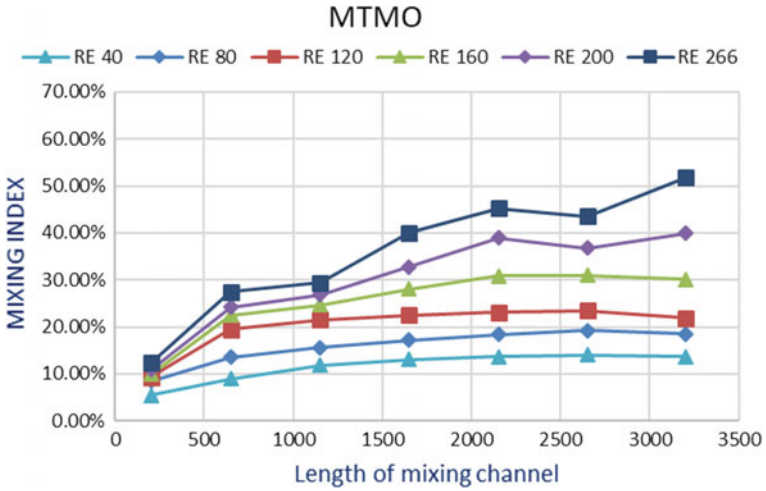


Fig. 6 Variation on MI along with channel length of MTMO

of MI for micromixers. Due to the merging of streamlines more diffusion opportunities are provided to the flowing fluid.

### 4 Conclusions

The study for the simulation of working of Modified T micromixer is done using computational fluid dynamics. A simple T micromixer was modified into new micromixers with 6 triangular obstructions, one of them having offset of an inlet and the other with no offset. The performance of micromixers is then compared and validated with the results obtained by Dundi et al. [1]. The results obtained depict that the Mixing performance

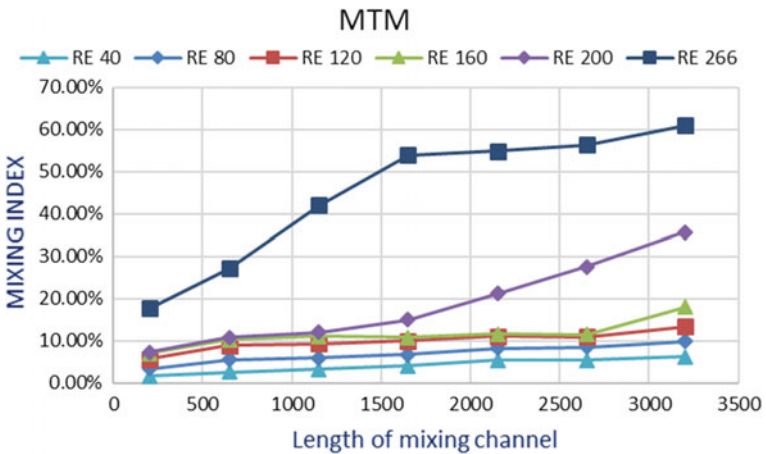
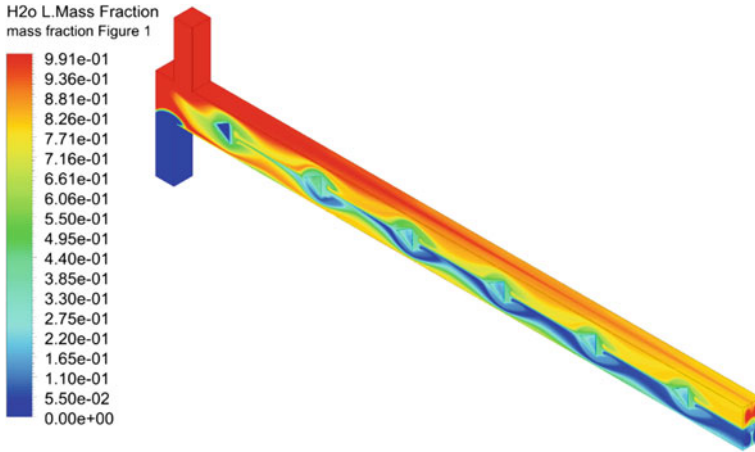


Fig. 7 Variation on MI along with channel length of MTM



**Fig. 8** Mass fraction contour for MTMO at RE 120

of MTM and MTMO was significantly better than that of STM. The triangular obstructions were installed for disturbing the linear path of streamlines which resulted in better Mixing performance of the micromixers. The length of all the micromixers was kept  $3000\ \mu\text{m}$  for better comparison with each other. The MTM and MTMO are better from STM as they provide better mixing than STM. Also, the performance of MTMO is better even at a low value of the Reynolds number.

The work in the present study can be further increased by varying the number of obstacles in the micromixer. A variation for the value of offset and change in the shape of the offset can also be done. The mixing performance can also be varied by trying various values and ranges of Reynolds number. This work can be carried further by selecting a different number of twists and different aspect ratios for the outlet channel. By increasing the MI after adopting the mentioned methods, new micromixers can be made which will be helpful in various applications.

## References

1. Manoj DT, Raju VRK, Chandramohan VP (2019) Numerical evaluation of swirl effect on liquid mixing in a passive T-micromixer. *Austr J Mech Eng*
2. Bahiraei M et al (2017) CFD simulation of irreversibilities for laminar flow of a power-law nanofluid within a minichannel with chaotic perturbations. An innovative energy-efficient approach. *Energy Convers Manage* 144:374–387
3. Jeong GS et al (2010) Applications of micromixing technology. *Analyst* 135(3):460–473
4. Afzal A, Kim K-Y (2015) Convergent–divergent micromixer coupled with pulsatile flow. *Sens Actuators B Chem* 211:198–205
5. Shakhawat H, Kim K-Y (2010) Numerical study on mixing performance of straight groove micromixers. *Int J Fluid Mach Syst* 3(3):227–234
6. Lin W (2008) A passive grooved micromixer generating enhanced transverse rotations for microfluids. *Chem Eng Technol Ind Chem Plant Equip Process Eng Biotechnol* 31(8):1210–1215

7. Salman, M.: Fluid micro-mixing in a passive microchannel: comparison of 2D and 3D numerical simulations. *Int J Heat and Mass Transfer* 139:907–916
8. Lee C-Y, Fu L-M (2018) Recent advances and applications of micromixers. *Sens Actuators B Chem* 259:677–702
9. Stroock AD et al (2002) Chaotic mixer for microchannels *Science* 295:647–651
10. Bottausci F et al (2007) An ultrashort mixing length micromixer the shear superposition micromixer. *Lab Chip* 7(3):396–398 (2007)
11. Cortes-Quiroz CA, Azarbadegan A, Zangeneh M (2017) Effect of channel aspect ratio of 3-D T-mixer on flow patterns and convective mixing for a wide range of Reynolds number. *Sens Actuators, B Chem* 239:1153–1176
12. Raza W, Hossain S, Kim K-Y (2020) A review of passive micromixers with a comparative analysis. *Micromachines* 11(5):455
13. Okuducu MB, Aral MM (2021) Toward the next generation of passive micromixers: a novel 3-D design approach. *Micromachines* 12(4):372
14. Tokas S, Zunaid M, Ansari MA (2021) Numerical investigation of the performance of 3D-helical passive micromixer with Newtonian fluid and non-Newtonian fluid blood. *Asia-Pacific J Chem Eng* 16(1):e2570
15. Javed SF (2020) Numerical analysis of mixing performance in a spiral passive micromixer, Dissertation



# Simulation of Erosion in Abrasive Water-Jet Nozzle to Study Wear Behavior

Abhijeet Kumar<sup>(✉)</sup>, Abhishek Meghwal, Aakash Sharma, and R. C. Singh

Department of Mechanical Engineering, Delhi Technological University, Shahbad Daultapur,  
New Delhi, India

abhijeetkumar9791@gmail.com

## 1 Introduction

Abrasive water jet cutting (AWJ) is a machine which comes under the machining category and is used in various industries for various applications. Some applications include cutting, drilling, deburring, cleaning, peening, forming, etc. In an AWJ cutting abrasive particles entered in a pressurized water jet medium, affecting the inner wall of the nozzle by causing erosion of particles from wall material. The speed of an abrasive entrained water jet is good enough to impact any material whether it is hardened steel or any soft material. Because of this high speed of the mixture, shear stresses get to develop on the wall of nozzle that ultimately leads to nozzle erosion. Nozzle erosion is a series of actions in which particles of the material leave the inside walls of the AWJ nozzle at a slow. Such type of surface wear is more specifically called solid particle erosion. Nozzle erosion causes jet divergence and decreases the quality of being exact, and it becomes necessary to replace the nozzle but frequent changing of nozzle not only minimizes the overall process efficiency but also increases the cost. Thus the nozzle erosion has become one of the prime reasons to put a limit on the development of AWJ as a piece of equipment needed for industries [1].

Process parameters can be determined by the speed at which material removal takes place, surface roughness, nozzle wear rate, and abrasive. Since the nozzle is constantly in contact with the abrasive particles flowing at high speeds, therefore it becomes one of the important parameter among above-mentioned parameters. To avoid any significant wear, the nozzle material must be hard. Normally tungsten carbide or sapphire is used [2]. This erosion can cause the AWJ machine to not work properly or we can say due to erosion it fails without any prior warning and resulted in very high-cost repairs and loss in production time. Therefore, precisely prediction of the speed at which erosion occurs and recognition of the place or position that is at most risk is very necessary.

Inner surface wear characteristics are very difficult to determine due to its long pore structure. We can visualize wear characteristics by cutting the nozzle along the longitudinal axis. So, without damaging the nozzle, visualization of erosion is not easy. To avoid this difficulty, a numerical simulation method has been adopted for knowing and understanding a picture of nozzle erosion in our mind.



So, we have adopted a structured methodology to simulate the erosion process in the nozzle. The methodology includes determining essential process parameters, understanding different wear mechanisms, theoretical formulation, 3D model creation, simulation model selection, simulation results analysis. We have used  $k-\varepsilon$  turbulence model and discrete phase model as simulation model. We have used SOLIDWORK as 3D modeling software and ANSYS FLUENT as simulation software.

## 1.1 Wear Characterization Background

The mechanism or the way by which particles of material get removed from the inner wall of the Nozzle is rather very complicated. The main reason for the removal of particles of the nozzle material is due to the impact between abrasives and the inner surface of the nozzle that leads to plowing and micro-cutting. It is assumed that in AWJ, the speed at which particles of material erode has direct relationship with speed of water jet.

Nozzle erosion influenced by various nozzle and system parameters. System parameters that are supposed to have a direct effect on nozzle erosion include pressure of water jet, the diameter of hole or opening, abrasives (its type, its shape and size, and speed of flow), and the dimension of closed space in the body where mixing takes place. Nozzle shape parameters that affect erosion include the length of the nozzle, the diameter of the bore, the inlet angle of the cone, and its depth [2].

Nozzle erosion is checked regularly through opening bore measurement at exit using gauge pins. This opening bore measurement type descriptions are used to study the progression of nozzle erosion. There are several methods are utilized in the measurement of the bore profile. Sectioning the nozzle longitudinally is one of method to get direct measurement of the bore profile with the help of a co-ordinate measuring machine but this technique being a tedious and destructive one. Therefore, it cannot be used for progressive erosion observation. Another way for studying erosion profiles can be achieved by making replica of the bore that helps in the visualizing of the profile easily. Silicon resin is generally used form making replica. Another way of examining the bore profile is by utilizing progressively larger gauge pins that are inserted through opening of the nozzle at entrance. By measuring the gauge pin penetration, the profile plot of erosion can be produced or created [3].

## 2 Methodology

### 2.1 Theoretical Formulations

The abrasive water mixture flow is presumed to be a multiphase flow. It is considered to be an incompressible flow. The discrete particle velocity is presumed to be same as of the flowing fluid. Discrete particle model is utilized to simulate the complex flow of discrete particle and water. The theory used by Mostofa et al. [4] is utilized to corroborate the erosion model for the present work. The following theoretical water jet speed is obtained using the Bernoulli equation.

The theoretical velocity of the jet was calculated from the equation.

$$V_{th} = \sqrt{\frac{2p}{\rho}} \quad (1)$$

where  $p$  is operating pressure and  $\rho$  is the density of water.

$$V_J = C_d V_{th} \tag{2}$$

where  $C_d$  is the Coefficient of discharge. Water jet velocity ( $V_J$ ) was calculated from the above equation where the value of  $C_d$  is based on the function of the jet size taken from past research [4].

The turbulence can be described by percentage intensity ( $I$ ) which is described at water pressure inlet boundary conditions. Formula to calculate the percentage intensity is

$$I = \frac{u'}{u_{avg}} = 0.16 Re_{Dh}^{-\frac{1}{8}}$$

$$Re_{Dh} = \frac{\rho u D_h}{\mu}$$

where  $\mu$  is the viscosity of water,  $Re$  is Reynolds number for the given size of hydraulic diameter ( $D_h$ ),  $u'$  is fluctuating component of velocity; and  $u_{avg}$  is average velocity.

### 2.2 Geometric Parameters and Meshing

The geometric parameters for the construction of the model of the nozzle are taken from Mostofa et al. [4]. The geometric parameters are shown in Fig. 1 and Table 1. We have used SOLIDWORKS 2016 software to model the nozzle. SOILDWORKS file is saved as a step file so that it can be attached in the ANSYS File during simulation. We have selected ANSYS FLUENT solver to simulate the turbulent flow of the mixture.

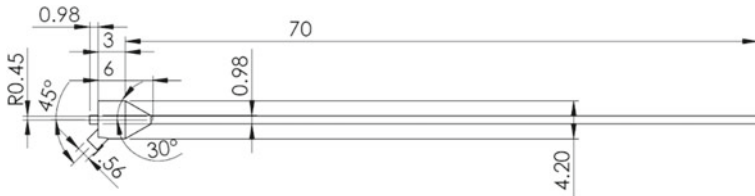


Fig. 1 Geometry of the nozzle

Nozzle erosion simulation requires considerable wall interaction to accurately predict the erosion occurring at the walls. A mesh was created having an inflation layer at the walls with smooth transition function ON. Curvature and proximity function were switched on to capture the curvature and proximity in the nozzle geometry. Figure 2 shows the final mesh created.

### 2.3 Model Selection

We have selected  $k-\epsilon$  turbulence model for our simulation study. It is commonly used turbulence model to simulate the turbulent flow. It is a two-equation model that gives a

**Table 1** Geometrical parameters

Parameters	Value
Orifice diameter	0.96 mm
Coefficient of discharge	0.8
Mixing chamber diameter	4.2 mm
Mixing chamber length	3 mm
Focus tube diameter	0.98 mm
Focus tube length	70 mm
Abrasive inlet diameter	1.56 mm

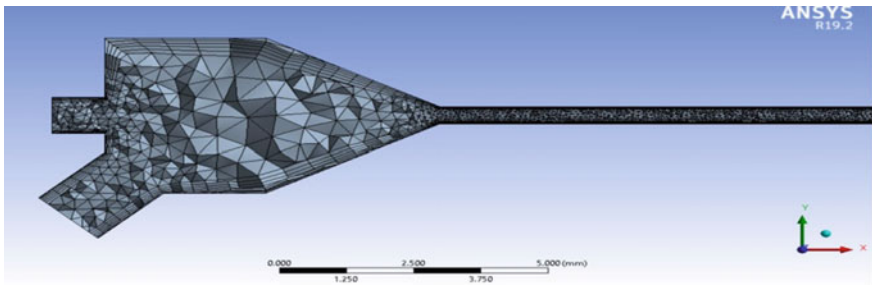
general idea of turbulence. It can be used in medium to high complexity flows. In the equation, it has two transport variables: kinetic energy ( $k$ ) and rate of loss of kinetic energy ( $\epsilon$ ). It only requires initial and final boundary conditions to work.

We have also selected a discrete phase model to simulate the flow of the abrasive particles and water. The model is used when we have to simulate a flow between a continuum such as water and a discrete phase particle such as an abrasive particle. DPM is used in the Lagrangian frame of reference to track the motion of the particles and the Eulerian frame is simultaneously used for the continuous phase. We have used the DPM which is available in ANSYS FLUENT solver.

## 2.4 Process Parameters

Boundary conditions like speed of water jet, initial gauge pressure, and intensity of turbulence are specified at the inlet and outlet of the nozzle. The discrete particles or abrasives were injected perpendicular to the face of the abrasive inlet with speed equal to the speed of water jet.

We have performed simulation of erosion on a combination of varying parameters such as water pressure, abrasives (its type, its shape and size, and speed of flow), and diameter of nozzle opening. Abrasive shape factor is associated with the sharpness or irregularity in the abrasive particles. It lies between 0 and 1, as it approaches 1 shape

**Fig. 2** Sectional view of meshed nozzle

becomes spherical and vice versa. The detailed information combination of parameters is given in Table 2.

**Table 2** Combination of boundary conditions

I	Velocity of Jet (m/s)	Pressure (MPa)	Mass flow rate (g/s)	Abrasive particle size ( $\mu\text{m}$ )	Nozzle diameter (mm)	Abrasive shape factor
1	537	200	8	80	0.46	1
2	601	250	8	80	0.46	
3	658	300	8	80	0.46	
II	Velocity of jet (m/s)	Pressure (MPa)	Mass flow rate (g/s)	Abrasive particle size ( $\mu\text{m}$ )	Nozzle diameter (mm)	Abrasive shape factor
1	711	350	8	80	0.46	1
2	711	350	20	80	0.46	
3	711	350	30	80	0.46	
III	Velocity of jet (m/s)	Pressure (MPa)	Mass flow rate (g/s)	Abrasive particle size ( $\mu\text{m}$ )	Nozzle diameter (mm)	Abrasive shape factor
1	711	350	20	20	0.46	1
2	711	350	20	70	0.46	
3	711	350	20	145	0.46	
IV	Velocity of jet (m/s)	Pressure (MPa)	Mass flow rate (g/s)	Abrasive particle size ( $\mu\text{m}$ )	Nozzle diameter (mm)	Abrasive shape factor
1	711	350	20	80	0.24	1
2	711	350	20	80	0.46	
3	711	350	20	80	0.9	
V	Velocity of jet (m/s)	Pressure (MPa)	Mass flow rate (g/s)	Abrasive particle size ( $\mu\text{m}$ )	Nozzle diameter (mm)	Abrasive shape factor
1	711	350	20	80	0.46	1
2	711	350	20	80	0.46	0.9
3	711	350	20	80	0.46	0.7

The variation in process parameters is kept in such a way that it lies in the application range for the abrasive water jet manufacturing process. By varying any one process factor and keeping other factors constant we can analyze the effect of a particular parameter on erosion rate and its behavior.

It is very important to note that the value of speed at which erosion occurs does not represent the actual erosion rate. It only gives the idea of erosion behavior and erosion dependence on different parameters.

### 3 Result and Discussion

Results of the simulations are compiled in Table 3. In the results, we have specifically focused on the generic erosion rate. From the results, we can see that as the pressure of the water increases, the rate of erosion of the nozzle increases because increasing the pressure results in an increase in the velocity of the abrasive particles and thus there is an increase in their erosion capability. When the rate of mass flow is increased, initially the erosion rate increases then it decreases as water has to carry a greater number of particles so that the effective momentum transfer to the individual particle is decreased and thus the erosion rate decreased.

When the size of the particles is increased, the erosion gets increased as now larger size abrasive particles contribute to erosion. Nozzle diameter also has a significant effect on nozzle erosion as the nozzle diameter is decreased erosion rate is increased as now the abrasive mixture has to flow through a narrower path. Lastly, the abrasive shape factor has a significant role in the erosion process. As we decrease the abrasive shape factor erosion rate is increased as a sharper abrasive particle would contribute to the erosion process more than the spherical abrasive particle.

The visual simulation of the nozzle erosion for the variation in pressure is shown in Figs. 3, 4, 5. It shows the erosion behavior.

### 4 Conclusion

The main objective of our research work was to study nozzle wear mechanisms and finding essential parameters that affect nozzle erosion, then performing simulation of the erosion process in ANSYS FLUENT. The results of the simulation are in co-relation with a previous research study conducted by Mostofa [4]. The combination of varying process parameters reveals the influence of each process parameters on the nozzle erosion. These results do not represent actual erosion rate it only gives the idea of the erosion and flow characteristics.

### 5 Further Scope

As part of our further work in our research, we could develop a formula for erosion rate based on the knowledge of the dependence of parameters on erosion. By considering essential parameters and defining their limit up to which the formula is considered to be true. We can use the approach of linear regression to find the expression to capture the dependence of the particular parameter on erosion.

**Table 3** Nozzle erosion simulation results

I	Pressure (MPa)	Maximum erosion rate (kg/m <sup>2</sup> s)
1	200	4.17E-05
2	250	2.35E-05
3	300	2.85E-05
II	Mass flow rate (g/s)	Maximum erosion rate (kg/m <sup>2</sup> s)
1	8	3.36E-05
2	20	1.31E-04
3	30	7.62E-05
III	Abrasive particle size (μm)	Maximum erosion rate (kg/m <sup>2</sup> s)
1	20	2.11E-05
2	70	6.81E-05
3	145	1.62E-04
IV	Nozzle diameter (mm)	Maximum erosion rate (kg/m <sup>2</sup> s)
1	0.24	7.06E-04
2	0.46	1.31E-04
3	0.9	5.96E-05
V	Abrasive shape factor	Maximum erosion rate (kg/m <sup>2</sup> s)
1	1	4.97E-05
2	0.9	2.00E-04
3	0.7	7.21E-05

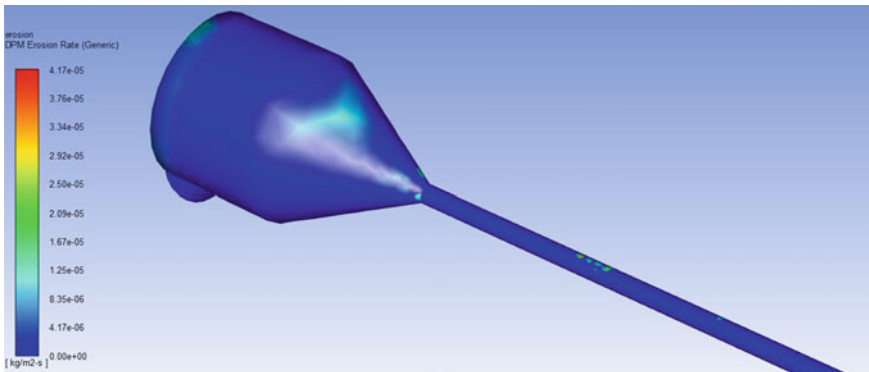


**Fig. 3** Nozzle erosion for pressure 200 MPa

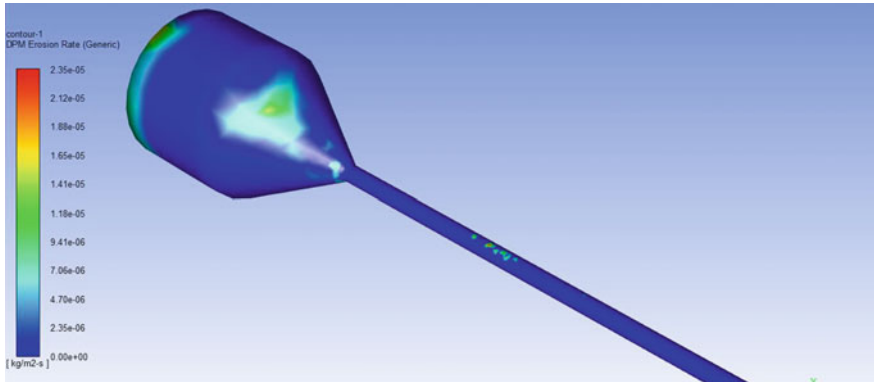


**Fig. 4** Nozzle erosion for pressure 250 MPa

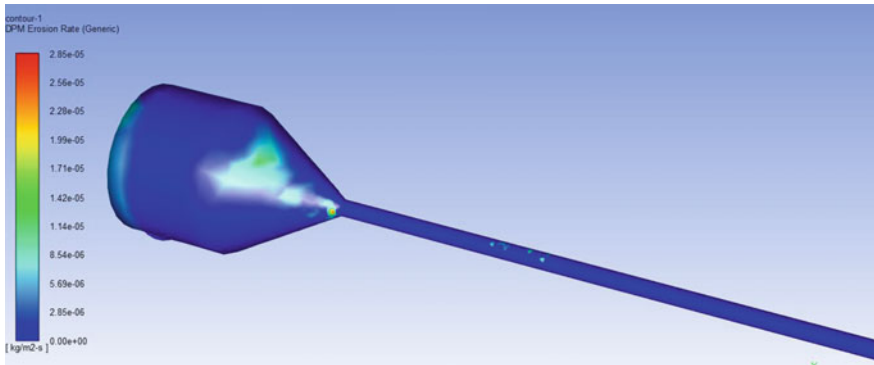


**Fig. 5** Nozzle erosion for pressure 300 MPa

## References

1. Momber AW, Kovacevic R (2012) Principles of abrasive water jet machining. Springer Science & Business Media, Berlin
2. Soyama H (2012) Effect of nozzle geometry on a standard cavitation erosion testing cavitating jet. *Wear* (2012)
3. Mansouri N, Arabnejad H, Shirazi SA, McLaury BS (2014) A combined CFD/experimental methodology for erosion prediction A. Elsevier, Amsterdam (2014)
4. Nanduri M, Taggart DG, Kim TJ (2000) A study of nozzle wear in abrasive entrained water jetting environment. *J Tribol* 122:465–471
5. Laniel R, Bouchareb O, Brient A, Miroir M (2017) Discrete elements model of an abrasive water-jet through the focal canon to the work-piece. *Procedia CIRP* (2017)
6. Deshmukh YK, Mishra SK (2020) Wear analysis of single step nozzle in abrasive water suspension jet machining through CFD. *i-Manager's J Mech Eng* 10(4)
7. Chen X, Deng S, Guan J et al (2017) Experiment and simulation research on abrasive water jet nozzle wear behavior and anti-wear structural improvement. *J Braz Soc Mech Sci Eng* 39:2023–2033
8. Mostofa MdG, Kil KY, Hwan AJ (2010) *J Mech Sci Technology* 24(2010)249–252





# Artificial Neural Network-Based Modeling of Membrane Contractors for Industrial Gas Treatment

Harshit Gupta, Arnav Gosain, Akhil Batra, and Manish Jain<sup>(✉)</sup>

Department of Applied Chemistry, Delhi Technological University, Delhi, India  
manishjain@dtu.ac.in

## 1 Introduction

Emissions of harmful gases from different chemical processes are a grave area of concern for environmentalists and scientists worldwide. Two main components of the flue gases emitted from the industrial furnaces are hydrogen sulfide ( $H_2S$ ) and carbon dioxide ( $CO_2$ ), while the chemical and physical properties of both the gases are pretty similar,  $CO_2$  is a significant contributor to global warming and  $H_2S$  is a very lethal and corrosive gas leading to several respiratory diseases, especially in children and in older people [1]. Therefore, removing these compounds from flue gases is essential to limit their adverse effects on the environment. One such process is the chemical/physical absorption of these gases on the alkaline solvents. Physical absorption has several advantages over other processes. This process is more economical, consuming less energy than reactive processes, and solvents can be easily regenerated by applying higher temperature and lower pressure [1].

One of the critical factors in the industrial scale absorption process is the liquid/gas contractors [1]. Efficient liquid gas contractors enhance liquid/gas interfacial area per unit volume of the separator and improve the amount of gas absorbed. Most traditional contractors such as regular or random packaging and different types of trays have several limitations such as low interfacial area, high-pressure drop along the length of the tower, channeling, and flooding [1, 2]. One of the solutions to these problems is membrane contractors. Membrane contractors are micro-porous membranes. These micro-pours present in the membranes acts as the interphase between liquid phase and gaseous phase [2]. When organizing in membrane modules, the flat sheets or hollow-fibers membranes have a very high surface area per unit of reactor volume, which provides exceptionally high interfacial density for liquid gas mass transfer [1, 2]. Moreover, these membranes are organized in a systematic geometry inside the membrane modules, which reduce the pressure drop along the length of the reactor and solve the problem of channeling and flooding in the reactor [1, 2].

At a local level, liquids gas interphase may present in three different forms. First, micro-pours are filled with a gas called non-wetted membranes; second, micro-pours are filled with a liquid called wetted membranes; and third, micro-pours are partially filled with both liquid and gas called partially wetted membranes. Since the diffusivity

of molecules is different in liquid and gaseous phases, the mass transfer rate hugely depends on these three conditions of the membrane [2]. The prediction of the wetting condition of a membrane is a challenging task as it may depend on several different factors such as pressure, temperature, viscosity, and other physical properties of gas and liquid streams, the physical properties of the membrane, and size and size distribution of micro-pours. [2]. Different phenomena may be observed at different points due to varying operating parameters along the length of the column, even in a single unit. Thus, mathematical modeling of mass transfer in membrane contractors is a very tricky task.

Artificial neural network (ANN)-based modeling is an empirical method to predict the system performance and does not require the physics behind the process [3, 4]. Thus, the ANN-based method may be beneficial to model the performance of membrane contractors. ANN is an artificial intelligence-based model that works on the neurons found in the brain that process information and recognize patterns using those [5].

In this study, an ANN-based approach simulates the H<sub>2</sub>S gas separation process using HF membrane contractors. Simulation results are validated using the already known experimental results. Later, the effects of operating parameters on gas separation efficiency are compared with experimental results.

## 2 Theory

Artificial neural network (ANN) mimics the working of the human mind for problem solving. ANN uses the experimental data to identify the underlying correlations among input and output parameters. This process is known as the training of the ANN. Identified correlations are then validated by comparing them with a different set of experimental results, known as the validation step. Different processes related to ANN are also optimized for minimizing the processing power and maximizing prediction efficiency. Finally, the trained ANN is used to predict the performance of the system at given sets of input parameters.

## 3 Procedure

In this study, MATLAB deep learning toolbox is used to simulate the ANN. Experimental results of PVDF membrane contractors to remove H<sub>2</sub>S from flue gases [6] were taken to train the ANN. Na<sub>2</sub>CO<sub>3</sub> two molar solutions were taken as a solvent in this study [6]. ANN was trained, validated, and tested by using individual sets of experimental results. ANN is trained, tested, and validated for each output parameter separately for better results.

The trained ANN was then used to determine the performance of the membrane contractor for percent CO<sub>2</sub> removal, H<sub>2</sub>S outlet concentration, and H<sub>2</sub>S selectivity at different values of gas to liquid ratio and CO<sub>2</sub> inlet concentrations. Here, H<sub>2</sub>S selectivity is a dimensionless number defined as the ratio of mass transfer coefficients of H<sub>2</sub>S and CO<sub>2</sub> across the membrane.

A total of 12 experimental points were taken from [6] to train the ANN. Details of the experimental points may be found in [6]. In this study, gas–liquid ratio and CO<sub>2</sub> concentration in the feed. The gas to liquid ratio represents the amount of solvent required

to absorb the given amount of CO<sub>2</sub>. Therefore, it is an important parameter to reduce the chemical footprint of the solvent.

Moreover, the amount of solvent required is also directly linked with the energy consumption in heating/cooling of solvent during the absorption/desorption cycle and pumping of solvent in different units. Thus, the gas to liquid ratio is also an important parameter to minimize the operational cost of the operation. Most of the industrial gases and flue gases contain a significant amount of CO<sub>2</sub>, which has similar acidic properties as H<sub>2</sub>S. Since, H<sub>2</sub>S is significantly more harmful than CO<sub>2</sub>, H<sub>2</sub>S should be selectively absorbed in the solvent. Different industrial gases or flue gases contain significantly different amounts of CO<sub>2</sub>. Thus, the efficiency of the process for different feed systems can be evaluated by varying the CO<sub>2</sub> concentration in the feed. In this study, gas to liquid ratio was varied from 280 to 1630 (volume/volume), and CO<sub>2</sub> concentration was varied from 5.38 to 22.87 (vol.%), while values of other parameters such as gas flow rate and gas pressure were kept constant at 2600 ml/min and 0.4 bar (gage pressure). The range of operating parameters was taken from the experimental study [6] as predictions of the trained ANN were applicable in this range only.

## 4 Results and Discussion

### 4.1 ANN Training and Model Validation

Initially, simulations were performed with different nodes in the hidden layer, and mean square errors were compared (Table 1). Results showed that minimum values of mean square errors were found at three, ten, and four nodes for H<sub>2</sub>S selectivity, H<sub>2</sub>S outlet concentration, and CO<sub>2</sub> outlet concentration, respectively. The exact numbers of nodes were used in all simulations.

**Table 1** Mean square errors at different number of nodes

Number of nodes	Mean square error		
	H <sub>2</sub> S selectivity	H <sub>2</sub> S outlet concentration	CO <sub>2</sub> outlet concentration
2	0.3732	0.1663	0.1928
3	0.3001	0.1896	0.4416
4	0.658	0.3112	0.0712
5	0.7554	0.1106	0.1595
10	0.4505	0.0047	0.2921
20	0.5857	1.7508	1.5424

Experimental results and model predictions are compared in Fig. 1. Model predictions were consistent with experimental results with  $R^2$  values of more than 0.89 in all cases. These results validate the trained ANN for all cases.

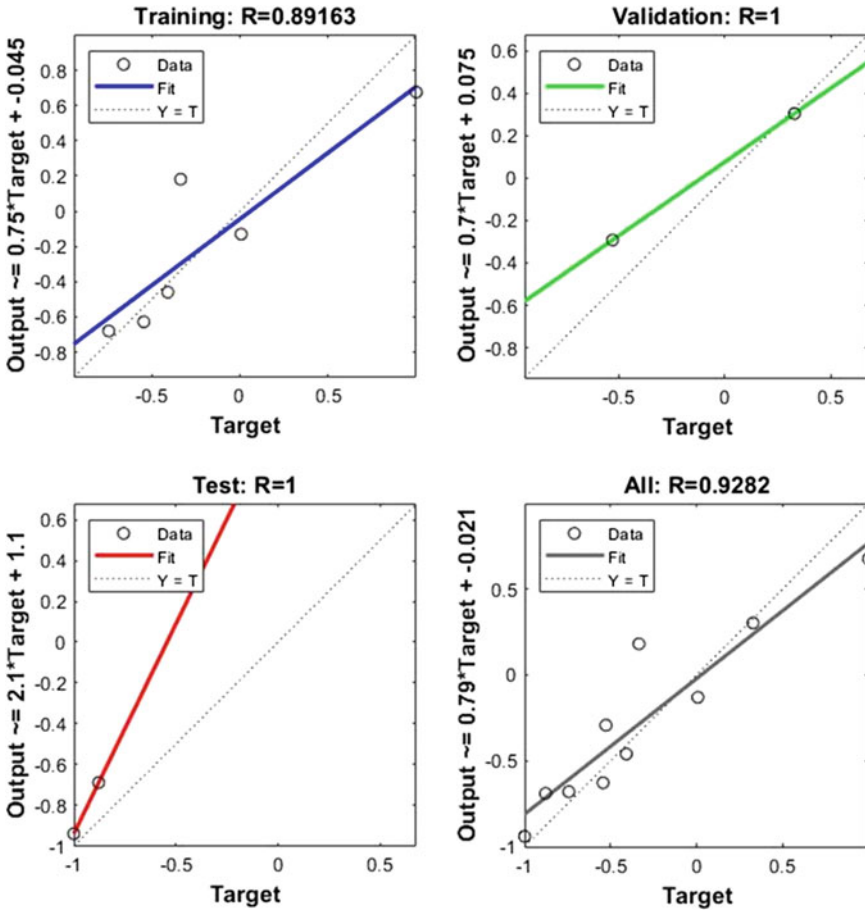
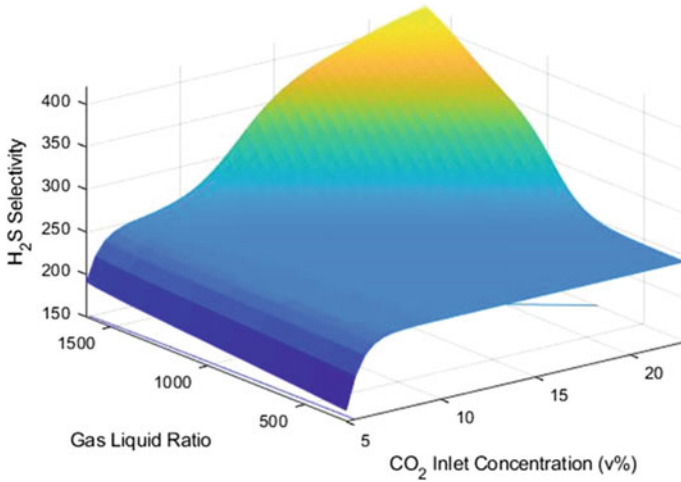


Fig. 1 Comparison of experimental results and model predictions

#### 4.2 Effects of Gas–Liquid Ratio and CO<sub>2</sub> Concentration in Feed on H<sub>2</sub>S Selectivity

Figure 2 depicts the effects of gas–liquid ratio and CO<sub>2</sub> concentration on H<sub>2</sub>S selectivity. Here, H<sub>2</sub>S selectivity is defined as the ratio of mass transfer coefficients of H<sub>2</sub>S and CO<sub>2</sub> gases. Results show that H<sub>2</sub>S selectivity was less at lower CO<sub>2</sub> concentration and improves as CO<sub>2</sub> concentration increased in feed. These results indicated that higher CO<sub>2</sub> concentration facilitates the transport of H<sub>2</sub>S across the membrane. CO<sub>2</sub> molecules have a smaller molecular size than H<sub>2</sub>S; thus, the higher concentration of CO<sub>2</sub> may increase the convective diffusion of H<sub>2</sub>S gas across the membrane. On the other hand, H<sub>2</sub>S gas is acidic than CO<sub>2</sub> gas. Thus, once the H<sub>2</sub>S molecules are transported across the membrane, they absorbed selectivity in liquid.

Results also showed that selectivity of H<sub>2</sub>S was found higher at high gas to liquid ratio. At lower gas to liquid ratio, boundary layer resistance at the feed side may start the dominant mass transport resistance, which may hinder the transport of H<sub>2</sub>S molecules



**Fig. 2** Effects of gas–liquid ratio and CO<sub>2</sub> concentration in feed on H<sub>2</sub>S selectivity

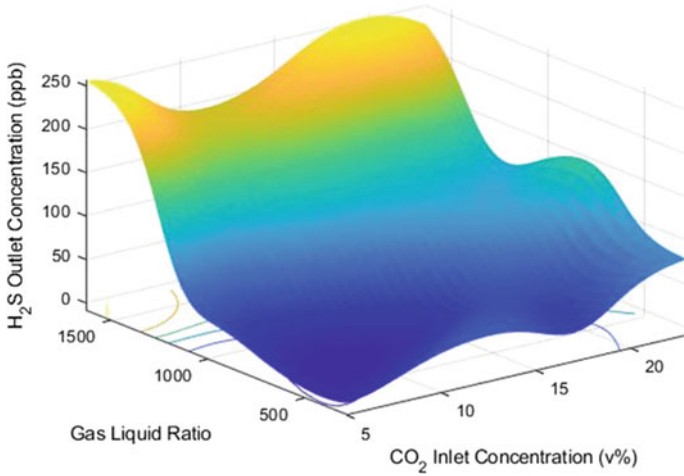
across the membrane. On the other hand, at higher gas flow rates, the effects of boundary layer resistance would be substantially reduced as a consequence of the H<sub>2</sub>S selectivity increased.

#### 4.3 Effects of Gas–Liquid Ratio and CO<sub>2</sub> Concentration in Feed on H<sub>2</sub>S Concentration in the Outlet

Figure 3 showed the effects of gas–liquid ratio and CO<sub>2</sub> concentration on H<sub>2</sub>S concentration in the outlet stream. Results showed that H<sub>2</sub>S concentration in the outlet stream increased with increasing gas to liquid ratio, which is exactly opposite trained for H<sub>2</sub>S selectivity with increasing gas to liquid ratio. These results suggest that though the higher gas flow rate improves the H<sub>2</sub>S selectivity, overall absorption of H<sub>2</sub>S per unit volume of feed may be reduced due to the more H<sub>2</sub>S available per unit time in feed, which leads to the observed results. Effects of CO<sub>2</sub> concentration in feed on H<sub>2</sub>S concentration in feed did not show a particular trained as H<sub>2</sub>S concentration fluctuated significantly in both directions.

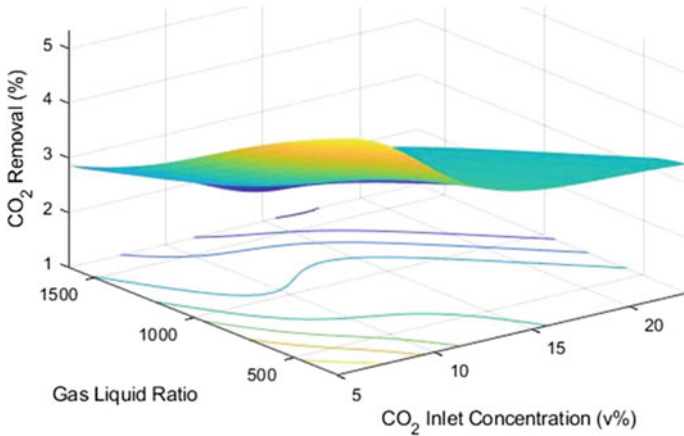
#### 4.4 Effects of Gas–Liquid Ratio and CO<sub>2</sub> Concentration in Feed on CO<sub>2</sub> Removal

Figure 4 shows the effects of gas–liquid ratio and CO<sub>2</sub> concentration in feed on CO<sub>2</sub> removal. Values of percent CO<sub>2</sub> removal were found nearly constant at all gas and liquid ratio values and CO<sub>2</sub> concentration in the feed. This may be due to a higher concentration of CO<sub>2</sub> in feed (up to 20%). Moreover, the values of CO<sub>2</sub> removal were also found significantly low (<4.5%) as CO<sub>2</sub> has a comparatively lower solubility in Na<sub>2</sub>CO<sub>3</sub> than H<sub>2</sub>S. These results indicate that solvent selectively absorbs the H<sub>2</sub>S over CO<sub>2</sub>, which confirms the results shown in Fig. 2. However, removal of CO<sub>2</sub> was found



**Fig. 3** Effects of gas–liquid ratio and CO<sub>2</sub> concentration in feed on H<sub>2</sub>S concentration in the outlet

slightly higher at lower gas to liquid ratio and low CO<sub>2</sub> concentration in the feed. It was slightly lower at high gas to liquid ratio and high CO<sub>2</sub> concentration in the feed.



**Fig. 4** Effects of gas–liquid ratio and CO<sub>2</sub> concentration in feed on CO<sub>2</sub> removal

## 5 Conclusion

In this study, artificial neural networks were successfully used to model the performance of membrane contractors for the removal of H<sub>2</sub>S gas from flue gas mixture. Initially, the number of nodes was optimized for minimizing the mean square errors. The optimum

number of nodes was found at three, ten, and four nodes for H<sub>2</sub>S selectivity, H<sub>2</sub>S outlet concentration and CO<sub>2</sub> outlet concentration. Later, the performance of trained ANNs was successfully validated with the experimental results.

Higher CO<sub>2</sub> concentration in feed and higher gas to liquid ratio were found to better operating conditions for high selectivity of H<sub>2</sub>S. Therefore, the efficiency of the unit to absorb H<sub>2</sub>S over other acidic gases present in the system will improve with higher gas to liquid ratio and higher CO<sub>2</sub> concentration in the feed. This result also suggests that the process is more efficient for the gases containing a higher concentration of CO<sub>2</sub>.

However, H<sub>2</sub>S concentration in the product increased with increasing gas to liquid ratio due to the high mass flow rate of H<sub>2</sub>S in feed. Thus, gas to liquid ratio values should be optimized for high H<sub>2</sub>S selectivity and lower H<sub>2</sub>S concentration in the feed.

Both input parameters (gas to liquid ratio and CO<sub>2</sub> concentration) did not affect the CO<sub>2</sub> absorption as the CO<sub>2</sub> absorption in Na<sub>2</sub>CO<sub>3</sub> is lower than H<sub>2</sub>S absorption.

Overall, this study proves that the artificial neural networks can be used to analyze the absorption operation using membrane contractors to achieve higher H<sub>2</sub>S selectivity and separation.

## References

1. Xu Y, Goh K, Wang R, Bae T-H (2019) A review on polymer-based membranes for gas-liquid membrane contacting processes: current challenges and future direction. *Sep Purif Technol* 229:115791
2. Mosadegh-Sedghi S, Rodrigue D, Brisson J, Iliuta MC (2014) Wetting phenomenon in membrane contactors – Causes and prevention. *J Membr Sci* 452:332–353
3. Asghari M, Dashti A, Rezakazemi M, Jokar E, Halakoei H (2018) Application of neural networks in membrane separation. *Rev Chem Eng* 36(2):265–310
4. Mittal S, Gupta A, Srivastava S, Jain M (2021) Artificial Neural Network based modeling of the vacuum membrane distillation process: effects of operating parameters on membrane fouling. *Chem Eng Process—Process Intensification* 164:108403
5. Himmelblau DM (2008) Accounts of experiences in the application of artificial neural networks in chemical engineering. *Ind Eng Chem Res* 47(16):5782–5796
6. Wang D, Teo WK, Li K (2004) Selective removal of trace H<sub>2</sub>S from gas streams containing CO<sub>2</sub> using hollow fibre membrane modules/contractors. *Sep Purif Technol* 35:125–131



# Effect of Process Parameters on CNTFET

Abhinav Sharma, Adarsh Kumar, and Suresh C. Sharma<sup>(✉)</sup>

Department of Applied Physics, Delhi Technological University, Shahbad Daultapur, Bawana Road, Delhi 110042, India  
prof\_sureshsharma@dtu.ac.in

## 1 Introduction

### 1.1 CNTFET

The high demand of the semiconductor industry has encouraged the downward scaling of MOSFET-based electronic devices to strive for smaller size, minimal power consumption and superior performance. It is suggested that continuous shrinking of Si-MOSFET is not viable below 10 nm because of the physical limitations caused by short channel effects like leakage current and industry demand of low power consumption would not be met. CNTFET has been suggested as a promising nanoelectronic device to replace the existing MOSFET as it offers better performance due to the higher quality of conducting and structural characteristics of carbon nanotube (CNT). CNT exhibits nearly ballistic transport and the carrier mobility does not degrade even after high-k gate insulators are deposited. CNT is compatible with complementary applications because the valence band and the conduction band in CNT are symmetric and finally, CNT is highly resistant to electromigration. All features confirm that CNT is suitable for device applications [1–6]. In [7] Bala and Khosla proposed an electrostatic doped tunnel CNTFET and benchmarked its performance using Nano-ViDES simulator, whilst tuning various performance parameters. Various methods exist to testify CNTFET, one such method is used in [8] where they perform process validation test to check the device's response to change in various operational parameters. This method also helps us in the noise characterization of the device. The reliance of current–voltage properties of CNTFET on carbon nanotubes diameter has been observed in this paper. The VS-CNTFET Stanford Model has been leveraged to illustrate the simulation work [9].

### 1.2 CNT Growth Technique

Multi-walled carbon nanotubes (MWCNTs) are mainly produced by plasma enhanced chemical vapour deposition (PECVD) techniques. PECVD produced nanotubes are vertically aligned. PECVD-based CNTs have relatively lower growth temperatures than the CNT produced by the CVD method. When the feedstock gas gets dissociated due to plasma, it leads to the availability of more carbon radicals and highly stable hydrocarbons which further contributes to carbon nanotube growth.

Tewari and Sharma [10] have shown the procedure of carbon nanotube growth in plasma medium which is corroborated by the interface of catalyst–substrate. The effect



of substrate temperatures on the CNT growth in an atmosphere like reactive plasma is evident from the work of Tewari and Sharma [11].

The nanotubes which possess semiconducting characteristics are mainly grown by the PECVD method because the drain current can be controlled by gate voltage which furthermore leads to little non-depletable drain current. This is evident from the work of Mizutani et al. [12].

## 2 Device Structure

### 2.1 Design

In the case of a MOSFET, the charge–voltage and the current–voltage properties are delineated by the Stanford virtual source (VS) CNTFET model. Essentially, it is an experimental model which covers the entire spectrum of possibility ranging from short channel effects to tunnelling and the contact mode is taken into consideration. The virtual source (VS) model forms the basis of the terminal charges and the intrinsic drain current. The experimental data provides information regarding the virtual source velocity ranging from 3- $\mu\text{m}$  down to 15-nm of channel length [9].

VS-CNTFET consists of a gate-all-around device having a cylindrical geometry. Source/drain extensions are heavily doped to ensure the adequate density of carriers. The CNTs are placed on a bulky insulator such as  $\text{HfO}_2$  so that the body terminal does not get affected. Henceforth, the VS-CNTFET is a model which is basically a three-phase transistor prototype.  $V_{\text{gs}}$  and  $V_{\text{ds}}$  have been used to point out the voltages across the gate to the (internal) source and the (internal) drain. Since the p-CNTFETs and n-CNTFETs are fully symmetric because the valance and conduction band of CNT are symmetric, this results in the same V-I and V-C characteristics for both types for the same  $|V_{\text{gs}}|$  and  $|V_{\text{ds}}|$  [13–17].

### 2.2 Parameters

In this experimental analysis, the parameters that have been used are shown in Table 1. Other than these parameters, this device model has different features like geometry, tunnelling properties, etc. to experiment with. Device geometry is taken as cylindrical gate-all-around, contact mode is taken as diameter-dependent power line model, tunnelling of the source to drain has been used without inter-band tunnelling and band to band tunnelling is included. This model operates at room temperature and the series resistance is taken as zero.

As shown in Table 1, the diameter of CNT is varied to experimentally analyse the relation between CNT diameter and the performance of CNTFET which reflects the effectiveness of the PECVD process to provide better quality CNT. CNT diameter is varied from 1 to 4 nm in this case for study and other parameters is constant as shown in Table 1 for the whole experiment.

## 3 Simulations and Observation

See Figs. 1, 2, 3 and 4.

**Table 1** CNTFET device parameters [9]

Name	Value	Description
$W$	10	Transistor width [micrometre]
$L_g$	5	Length of gate [nm]
$L_c$	12.9	Length of contact[nm]
$L_{ext}$	3.2	Extension length of source/drain [nm] (or spacer length)
$D$	[1–4]	CNT diameter [nm]
$T_{ox}$	3	Thickness of gate oxide [nm]
$k_{ox}$	23	Dielectric constant of (HfO <sub>2</sub> ) gate oxide
$k_{cnt}$	1	Dielectric constant of CNT
$H_g$	20	Height of the gate [nm]
$E_{fsd}$	0.258	Fermi level to the band edge [eV] at the source/drain
$V_{fb}$	0.015	Flat band voltage [V]
$V_{dd}$	0.71	Supply voltage [V]

### 4 Results

The effect of CNT diameter on  $I_{DS}-V_{DS}$  characteristics has been shown in Fig. 5. The saturation current, as well as the output conductance, has been observed which shows a clear increment with the increase in the CNT diameter. As the diameter increases from 1 to 4 nm saturation current increases from 0.1 to 9 mA/ $\mu$ m which is a very significant increase. As a result, the performance of CNTFET has improved significantly. Performance is better also compared to MOSFET because 1-D confinement results in minimum scattering compared to MOSFET which in turn results in ballistic transport.

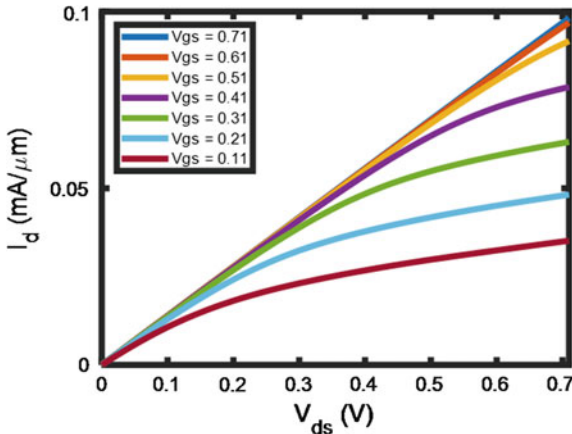


**Fig. 1** Impact on  $I_d$  versus  $V_{ds}$  at CNT diameter of 1 nm due to gate source voltage ( $V_{gs}$ )

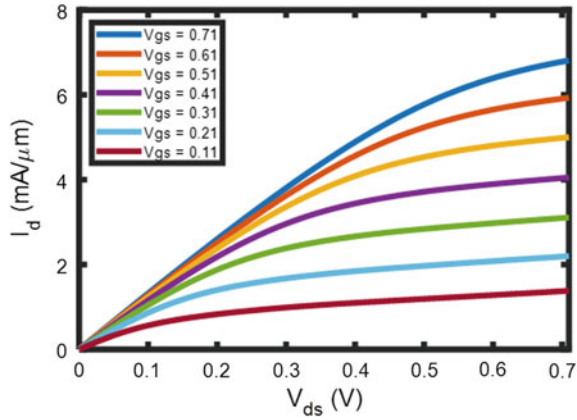


**Fig. 2** Impact on  $I_d$  versus  $V_{ds}$  at CNT diameter of 2 nm due to gate source voltage ( $V_{gs}$ )

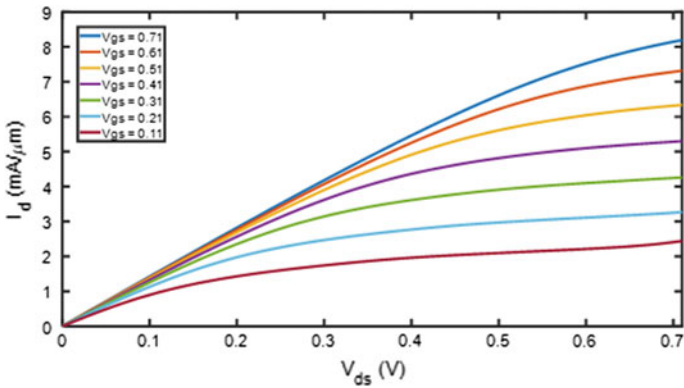


**Fig. 3** Impact on  $I_d$  versus  $V_{ds}$  at CNT diameter of 3 nm due to gate source voltage ( $V_{gs}$ )

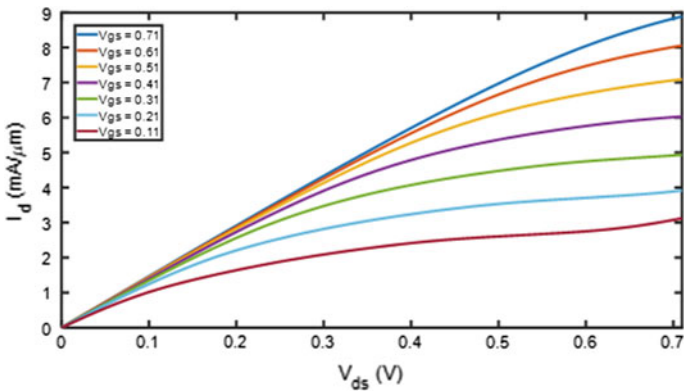


**Fig. 4** Impact on  $I_d$  versus  $V_{ds}$  at CNT diameter of 4 nm due to gate source voltage ( $V_{gs}$ )

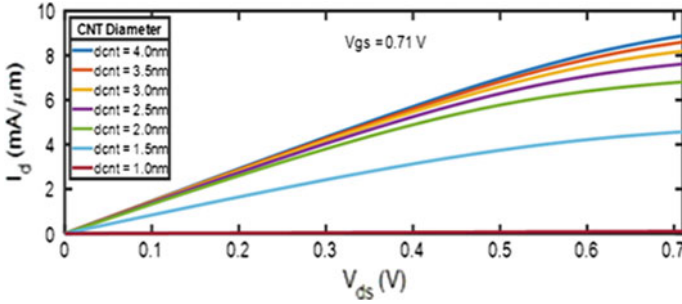


**Fig. 5** Impact on  $I_d$  versus  $V_{ds}$  due to CNT diameter ( $d_{cnt}$ )

The effect of process parameter (i.e. Substrate Temperature) on CNT diameter, mobility and carrier density is shown in Table 2. The relation of CNT diameter with substrate temperature in Table 2 which has been taken from Tewari and Sharma [11] suggests that increase in substrate temperature results in an increase in CNT diameter. It has been observed that with the increase in diameter, there is a significant increase in mobility (from  $12.6$  to  $60.3e-3$   $m^2/V$  s which is approx.. 4 times higher) and carrier density (from  $3.80e+5$   $m^{-1}$  to  $7.97e+8$   $m^{-1}$  which is approx. 2097 times higher) which in turn increases the performance and the efficiency of CNTFET.

**Table 2** Effect of process parameter on device metrics

Diameter ( $d$ ) [nm]	Mobility ( $\mu$ ) [ $m^2/V$ s]	Carrier density ( $n$ ) [ $1/m$ ]	Substrate temperature (eV)
1.0	0.0126	$3.80E+05$	0.068
1.5	0.0199	$6.83E+07$	0.089
2.0	0.0276	$3.12E+08$	0.111
2.5	0.0355	$4.25E+08$	0.120
3.0	0.0436	$5.23E+08$	0.138
3.5	0.0519	$6.75E+08$	0.160
4.0	0.0603	$7.97E+08$	0.173

## 5 Conclusion

It has been established that with the increase in the CNT diameter, the performance of CNTFET has improved significantly which comes because of the increase in density and substrate temperature of the acetylene ions used in the PECVD method. An increase in the mobility and current density of the CNTFET device has been observed basis the corresponding increase in the diameter of the CNT that clearly reflects the performance

enhancement. Similarly, the effect of variations in other parameters of the carbon nanotube can be observed on the performance of CNTFET. Our results are in accordance with those obtained in [7] which solidify the position of CNTFET as a forthcoming candidate for low power applications and circuits based on memory. Further studies will entail noise characterization of CNTFET devices and study of any possible correlation with changing operational parameters and noise.

## References

1. Dass D, Prasher R, Vaid R (2014) Characterization of carbon nanotube field effect transistor using simulation approach. In: Physics of semiconductor devices. Springer, Cham, pp 585–588
2. Almodéver CG (2014) Variability and reliability analysis of carbon nanotube technology in the presence of manufacturing imperfections
3. Lundstrom M, Antoniadis D (2014) Compact models and the physics of nanoscale FETs. *IEEE Trans Electron Devices* 61(2):225–233
4. Franklin AD, Chen Z (2010) Length scaling of carbon nanotube transistors. *Nat Nanotechnol* 6:858–863
5. Zhang J, Lin A, Patil N, Wei H, Wei L, Wong H-SP, Mitra S (2012) Robust Digital VLSI using carbon nanotubes. *IEEE Trans Comput Aided Des. Integr Circ Syst* 31(4):453–471
6. Oh S-H, Monroe D, Hergenrother JM (2000) Analytic Description of Short-Channel Effects in Fully-Depleted Double-Gate and Cylindrical, surrounding-gate MOSFETs. *IEEE Electron Device Lett* 21(9):445–447
7. Bala S, Khosla M (2018) Design and analysis of electrostatic doped tunnel CNTFET for various process parameters variation. *Superlattices Microstruct* 124:160–167
8. Sarbazi H, Sabbaghi-Nadooshan R, Hassanzadeh A (2021) Process validation test of CNTFET using Stanford model. *Int J Electron* 1–22
9. <https://nano.stanford.edu/stanford-cnfet2-model>
10. Tewari A, Sharma S (2014) Modeling carbon nanotube growth on the catalyst-substrate surface subjected to reactive plasma. *Phys Plasmas* 21(6):063512
11. Tewari A, Sharma SC (2015) Theoretical modeling of temperature dependent catalyst-assisted growth of conical carbon nanotube tip by plasma enhanced chemical vapor deposition process. *Phys Plasmas* 22(2):023505
12. Mizutani T, Ohno Y, Kishimoto S (2008) Electrical properties of carbon nanotube FETs. In: 2008 international conference on advanced semiconductor devices and microsystems, Smolenice, Slovakia. *IEEE*, pp 1–8
13. Khakifirooz A, Nayfeh OM, Antoniadis D (2009) A simple semi-empirical short-channel MOSFET current-voltage model continuous across all regions of operation and employing only physical parameters. *IEEE Trans Electron Devices* 56(8):1674–1680
14. Rakheja S, Antoniadis D (2013) MVS 1.1.1 nanotransistor model (Silicon). nanoHUB.org. MVS Nanotransistor Model (Silicon)
15. Lee C, Pop E, Franklin AD, Haensch W, Wong H-P (2015) A compact virtual-source model for carbon nanotube FETs in the sub-10-nm regime—Part I: intrinsic elements. *IEEE Trans Electron Devices* 62(9):3061–3069
16. Lee C, Pop E, Franklin AD, Haensch W, Wong HP (2015) A compact virtual-source model for carbon nanotube FETs in the Sub-10-nm Regime—Part II: extrinsic elements, performance assessment, and design optimization. *IEEE Trans Electron Devices* 62(9):3070–3078
17. Bu2010diman GE, Gao Y, Wang X, Koswatta S, Lundstrom M (2010) Cylindrical CNT MOSFET simulator. <https://nanohub.org/resources/moscntr>



# Design and Simulation Study of High-Speed Slab Track

Priti Rani<sup>(✉)</sup>, Kiran Chholak, and Yamika Patel

Delhi Technological University, New Delhi 110089, India  
priti.annu24@gmail.com

## Nomenclature

HBL Hydraulic bearing layer  
CBL Concrete bearing layer  
ASL Asphalt supporting layer

## 1 Introduction

Due to high structural stability and low maintenance cost, the ballastless track has become a more popular worldwide for high-speed railways over the past 30 years. Japan is the first country which developed ballastless track for high-speed application and further adopted by Netherlands, Germany, China, and Spain. Earlier use of slab track is limited to bridge and tunnel areas. But slab track technology evolved in the last three decades and it is performing well for high-speed passenger train application but still limited for freight trains [1]. Apart from developed country, many developing countries like India and other are planning to build high-speed railway network [17]. Climate change and the effects of the COVID-19 pandemic would almost certainly encourage greater use of public transportation and a transition to high-speed train for short to medium distance travel (around 100–1000 km), which is the most environmentally friendly mode of transportation” [18].

Ballasted track has several advantages like relatively lower construction cost, high elasticity, and higher noise absorption capacity, but its floating nature in lateral and longitudinal direction due to nonlinear behavior of ballast, lower lateral resistance, and permeability value limited its high-speed application. The ballastless/slab track is a concrete or asphalt surfaces comprises of five different layers which are classified as sub-structure and super-structure as shown in Fig. 1. The ballastless track developed all over the world has been categorized as discrete rail support (continuous rail supported by sleeper through fasteners on discrete points) and continuous rail support (continuous rail supported by concrete bearing either embedded or clamped on it), which further divided into subcategory as shown in Fig. 2.

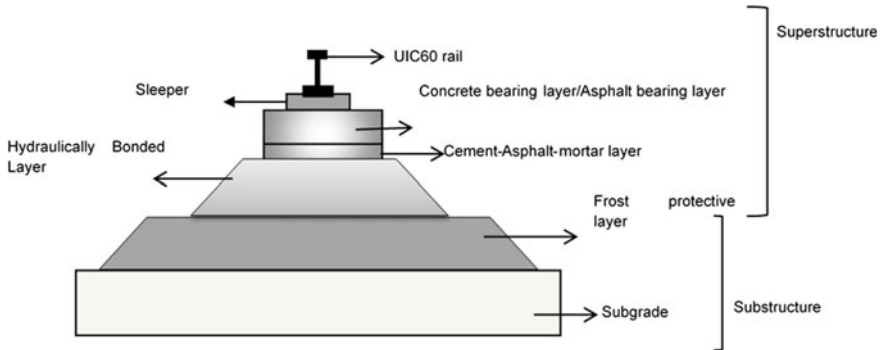


Fig. 1 Schematic diagram of ballastless track

## 2 Development of Slab Track Technology

Since the ballastless track is popular because of its stability, high load bearing capacity and its bearing capacity depend on supporting layer properties and homogeneity of subgrade which should be free of settlement. Hence, a proper preparation of subgrade/subsoil is necessary before the construction of slab track. There is no single slab track which is suitable for all the cases. Hence, a comprehensive study is required to find out which slab track is most suited for a given condition (Table 1).

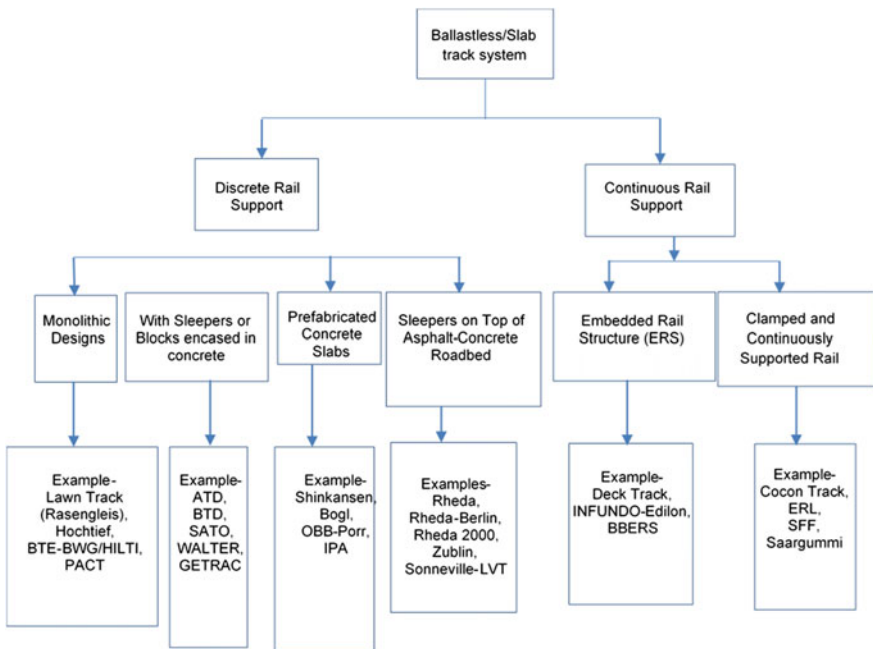


Fig. 2 Classification of Ballastless/Slab track [2, 13–15]

**Table 1** Key features of slab track

Slab track design	Country	Speed (km/h)	Total Construction (km)	Key features
Bögl	Germany		4391	Steel fiber concrete slab (B55 or C45/55) 6.45 m × 2.55(2.80 m) × 20 cm, slabs are laterally prestressed and longitudinally reinforced by GEWI bars
Shinkansen	Japan	> 300	3044	Prefabricated concrete slab 4.95 m × 2.34 m × 0.19 m and 0.16 m (in tunnels), 4 cm thick CAM layer beneath slab, supported on HBL
Rheda	Germany	300	2205	Concrete slab quality C30/37, sleeper length 2.6 m, HBL 30 cm thick, FPL 50 cm thick, very flexible system
Rheda 2000	Germany, China, Spain, Netherland	300–350	Approx. 1500	Modified twin-block sleepers (B 355 W60M SBS), Highly elastic rail fastenings system (vossloh 300)
Sonneville-LVT	Swiss		1031	High flexibility and good vibration absorption due to resilient pad encased in rubber boot placed under sleeper, easy to construct, possible erosion of rubber boot by water, fastner-VosslohW14, Pandrol e-clip
Zublin	Germany	300	606	Concrete twin-block or monoblock sleeper, CBL 2.25 m × 2.8 m × 0.28 m, HBL 30 cm thick, FPL 50 cm thick, Longitudinal and lateral steel reinforcement in the bottom of CBL

*(continued)*



**Table 1** (continued)

Slab track design	Country	Speed (km/h)	Total Construction (km)	Key features
Stedef	France		334	Similar key feature as Sonnevile-LVT, polyurethane waterproof seal to prevent rubber boot erosion from water
Infundo-Edilon	Netherland	160	211	Low noise emission, fast construction, rail supported by elastic component in Groove, CSL 2.4 m wide and 40 cm thick
OBB-Porr	Austria		122	
Sato	Germany		36	Y-steel sleeper anchored on asphalt supporting layer through welding
WALTER	Germany		9.4	Monoblock sleeper, asphalt supporting layer, clamp fastening with a clip glove at the sleeper midpoint of every second sleeper
PACT TRACK				Developed by British rail, PACT TRACK surface slab 229 mm thick and 2.43 m wide, Pandrol clips used for direct fixation of rail on slab
SFF				Also known as vibration damped slab track, rubber provide continuous support to rail, limited to tunnel and urban rail system
CRTSIII	China			

The Japanese National Railways has developed A type slab track and then RA type slab track in the 1970s [3]. With the evolution of technology, a current version of reinforced prefabricated concrete slab has been developed with the key features mentioned in Table 2. The first slab track developed in Germany at Rheda-Wiedenbruck station is named as Rheda system. During construction, tracks, consisting of rail, ties, and fastenings, are assembled on the base slab. After laying and lining of the slab panels, concrete is placed into cribs and spaces below the ties. It is required that the slab track be constructed over load-bearing frost-protected subgrade and that the groundwater be greater than 1.5 m below the slab [2]. With time significant changes have been done in Rheda system mentioned in reference [4]. Latest version of slab track used in Germany is Rheda 2000.

**Table 2** Track model properties of track with railpad and CAM layer

	Dimension	Young's modulus (MPa)	Poisson's ratio ( $\nu$ )	Density (kg/m <sup>3</sup> )
Rail	I section	205,800	0.3	7872
Rail pad	stiffness = 70kN/mm Thickness = 9 mm	1100	0.42	950
Slab	Length = 6.45 m Width = 2550 mm Thickness = 300 mm	38,000	0.2	2400
Concrete Asphalt Mortar Layer	Length = 6.45 m Width = 2550 mm Thickness = 40 mm	8000	0.25	1800
Hydraulic bearing layer	Length = 6.45 m Width = 2950 mm Thickness = 200 mm	23,000	0.25	2400
Subgrade	Length = 6.45 m Width = 7.5 m Thickness = 4 m	100	0.3	1800

A variety of ballastless track has been developed in Netherland based on Embedded Rail system providing a continuous support of the rail by means of cork/polyurethane mixture shown in Fig. 1. Various test track has also been developed to simulate the tunnel, bridge, and heavy traffic freight line condition. Albert Canyon, Mount MacDonalad, and Mount Shaughnessy are the few test sections that have been developed to investigate the use of PACT TRACK system [1] (mentioned in Table 2). Different types of slab track system developed all over the world have been mentioned in Table 1. And few of them are shown in Figs. 3, 4, 5, 6, and 7.

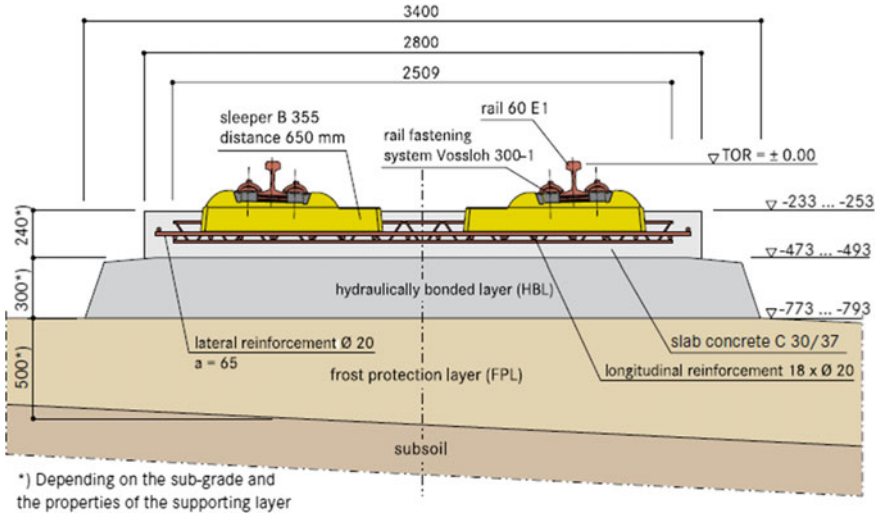


Fig. 3 Rheda 2000 [13]

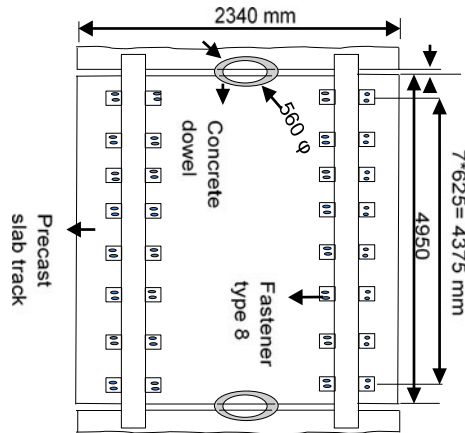


Fig. 4 Shinkansen [13]

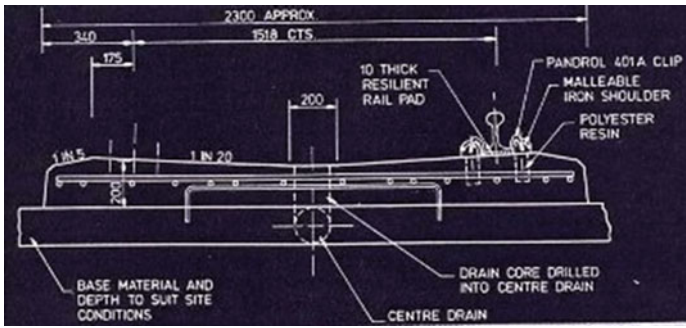


Fig. 5 PACT TRACK [13]

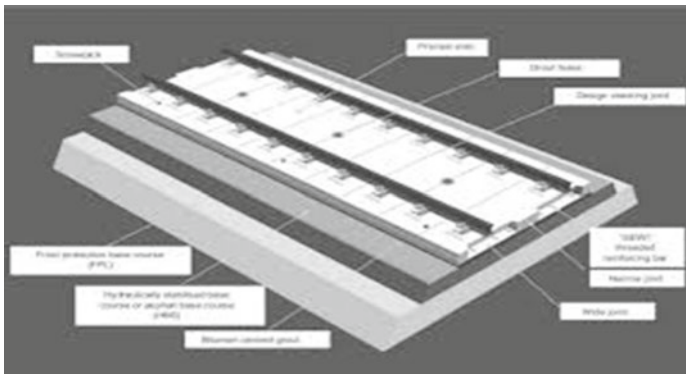


Fig. 6 Max Bogl slab track [13]

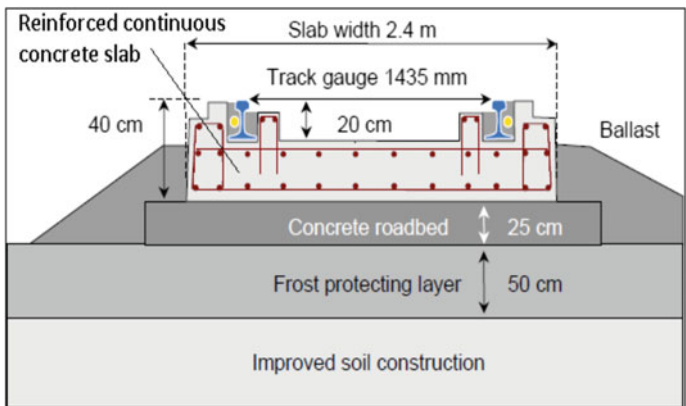


Fig. 7 Max Bogl slab track [13]

### **3 Ballastless Track Over Ballasted Track**

Ballastless track scheme benefits the slab track layout by considerably decreasing maintenance requirements and providing greater stability of the structural track and greater service life. Better high-speed operation is achieved in comparison with conventional ballasted track as it offers higher degree of stability to track bed. It has been observed that due to high speed the fine ballast particles move out of track and deposit on the rail surface which causes severe damage when wheel passes by it. The research examined the assessment of the environmental life cycle throughout the life of the track, including material source, production, design, and maintenance, decommissioning and recycling and discovered that it was the most sustainable choice over a 60-year and 120-year life-cycle owing to the lengthy design life and low maintenance requirements of concrete slab track.

### **4 Design Issue with High Slab Track**

Before replacing the ballasted track with slab track, it is important to understand the basic mechanics of ballast track and nature of problem associated with it. High mechanical stress, poor load distribution, and churning of ballast at high speed are the main cause of track degradation. Higher track modulus is necessary for track stability and a minimum ballast height must be calculated to ensure bearing stress should not exceed the allowable value. Design consideration recommended by American Railway Engineering and Maintenance of Way Association is mentioned in Ref. [5]. To overcome the problem of ballasted track, design criteria which need to be considered in the design of slab track are allowable rail bending stress and deflection, allowable subgrade and concrete slab stress and allowable concrete slab deflection. Cracks in ballastless track are inevitable in the construction and during operation of high-speed railway. So, the factor responsible for the development and propagation of crack should also considered during design of slab track [6]. In addition to this dynamic analysis of slab track must also be taken care to analyze the effect of noise and vibration. Due to uncoupling of rail fastening system and poor vibration absorption capacity of concrete slab, it produces higher noise compare to ballasted track at higher speed [2]. Parametric investigation of high-speed slab track has been done in the next section.

### **5 Parametric Studies of Ballastless Track**

A comprehensive study on the behavior of ballastless track structure for high-speed train under stationary load condition is carried out. Finite element analysis is used for analysis. A standard ballastless track has been developed for the analysis under stationary wheel load. Stresses have been calculated in various section of ballastless track to analyze the performance of track system. Parametric investigation has been carried out to study the behavior of track structure for the variation in material properties.

### 5.1 Geometric Model

A standard track model consists of rail, rail pad, concrete bearing layer, CAM layer, HBL layer, and foundation has been developed using SOLIDWORKS. Dimensions of the track component are mentioned in Table 2. Figure 8 shows the standard model of ballastless track.

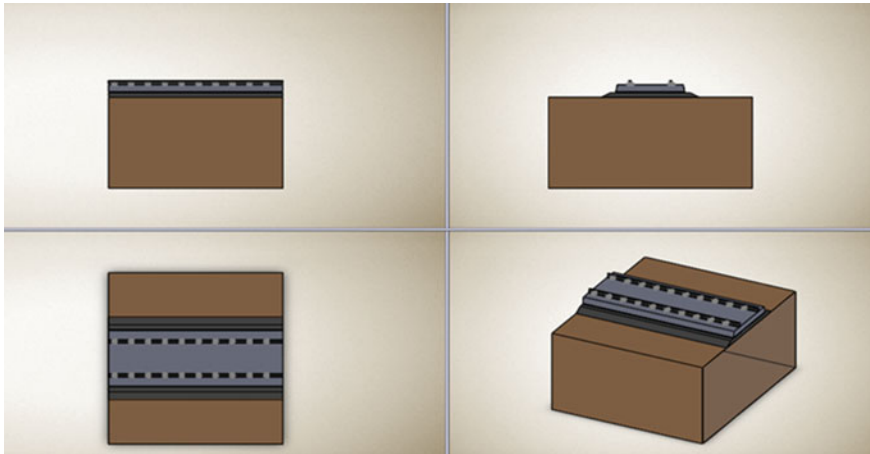


**Fig. 8** A standard model of ballastless track

*Loading condition:* A high-speed train is operated for 22 tons per axle load. When wheel and rail come in contact with each other, a contact patch shown in Fig. 9a has been developed at their contact point which is of elliptical shape. So, to replicate the real condition, pressure has been applied in that contact patch only. Two patches on each rail are made at a distance of 2800 mm showing the distance between wheels of Boggie as defined by RDSO as shown in Fig. 9b.

Area of elliptical patch =  $8.905 \times 10^{-4} \text{ m}^2$

$22/2 = 11 \text{ tons} = 11 \times 9.81 = 107.91 \text{ kN}$

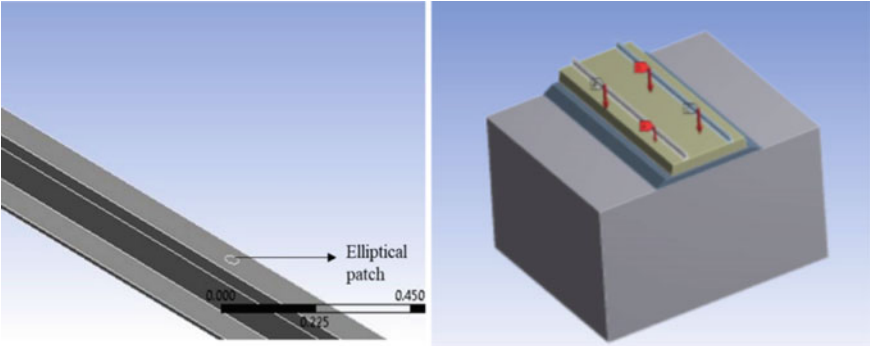
Therefore, applied pressure force = 121184556.3 Pa

### 5.2 Simulation

Flow chart in Fig. 11 shows the three-consecutive step in simulation of the model. The whole model has been discretized using mesh features shown in Fig. 10 and mesh details are mentioned in Table 3. For the loading conditions stationary multiple vertical wheel loads in terms of pressure are applied for the present study.

### 5.3 Parametric Studies

The influence of various parameters on the behavior of ballastless track structure under stationary wheel load (22t/axle) condition is investigated as under. The track with rail,



(a) (b)  
**Fig. 9 a** Elliptical patch, **b** loading conditions

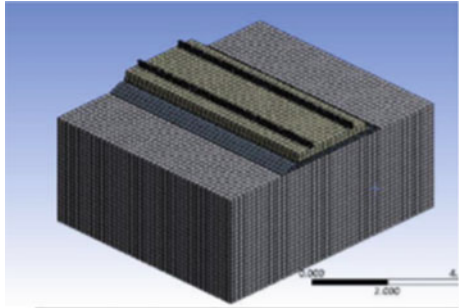


**Fig. 10** Meshing diagram

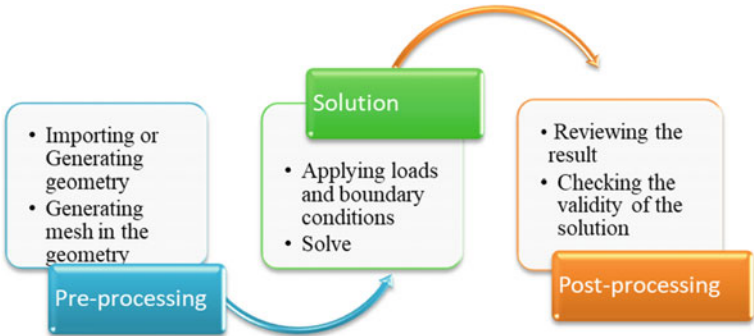


**Fig. 11** Flow chart of process of analysis in ANSYS Workbench

**Table 3** Mesh details

Mesh size	Fine
Mesh type	Quadrilateral
Edge length	0.00216 m
No. of Elements	60,394

railpad, concrete slab, cement asphalt layer, concrete treated hydraulic bounded layer and subgrade is considered for analysis. Variations in the parameters were made and comparison is done based on deformations and stresses produced in the rail and the concrete slab. Stiffness is directly proportional to modulus of elasticity, so the stiffness is induced using this relation by changing the modulus of elasticity. The track structure has been analyzed for varying modulus of elasticity of rail pad, CBL layer, and CAM layer. The variation in properties has been shown in Table 4 and equivalent stress has been calculated.

**Table 4** Variation in values of parameters used in the analysis

Stiffness of rail pad (kN/mm)	50	60	70	80	90	100
Modulus of CAM layer (MPa)	4000	6000	7000	8000	9000	10,000
Modulus of CBL (MPa)	25,000	30,000	34,000	38,000	40,000	42,000
Modulus of subgrade (MPa)	50	70	100	120	150	200

## 6 Results and Discussion

Simulation results show that the maximum stress occurs in the track structure is at contact path where wheel load is applied. This has been proved by Hertz Theory that maximum stress in the track is at contact surface of rail and wheel. In the analysis, an elliptical patch is formed on the rail representing contact area between rail and wheel (Ashofteh, R.S., 2013). Due to CAM layer present in track structure shows the rapid mitigation of stress for the subgrade part. Figures 12, 13, 14, and 15 show the stresses in rail and concrete slab by varying the properties of different components. With increase in all the parameters the contact stress in the rail decreases. But in concrete slab increase in stiffness of rail pad and modulus of elasticity of concrete slab increases the equivalent stress.

A comparison of equivalent stress induced in various track components due to percentage variation in material properties shown in Figs. 16 and 17. It has been observed from Fig. 16 that increasing the rail pad stiffness and modulus of elasticity other track component always results in increasing the equivalent stress in the rail section. Elasticity of CAM layer and subgrade does not make bigger difference in stress value in concrete slab.



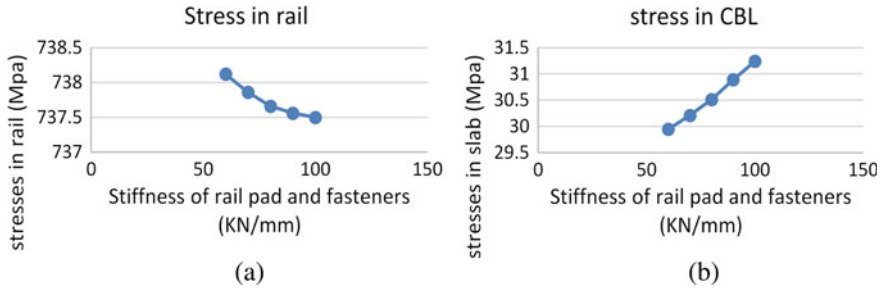


**Fig. 12** **a** Stresses in rail due to variation in stiffness of railpad. **b** Stresses in concrete slab due to variation in stiffness of railpad

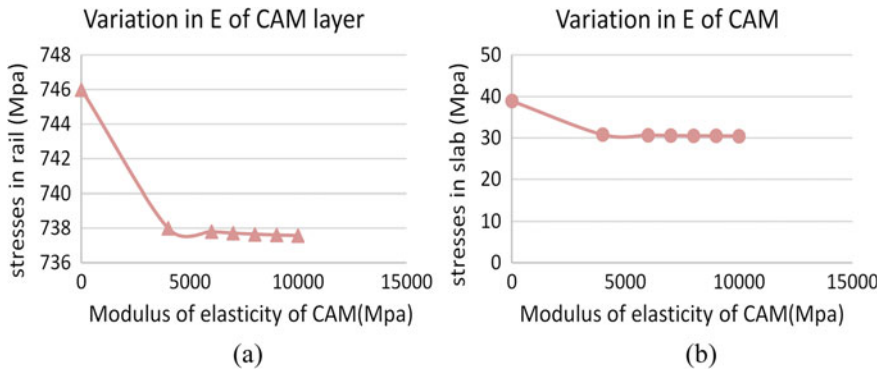


**Fig. 13** Stresses in **a** rail and **b** due to variation in modulus of elasticity of CAM layer

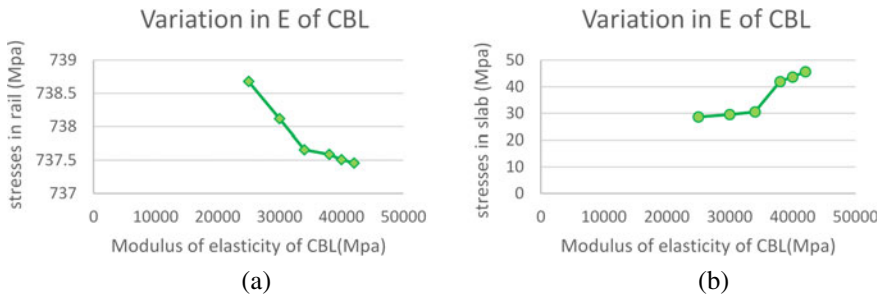


**Fig. 14** Stresses in **a** rail and **b** concrete slab due to variation in modulus of elasticity of concrete slab

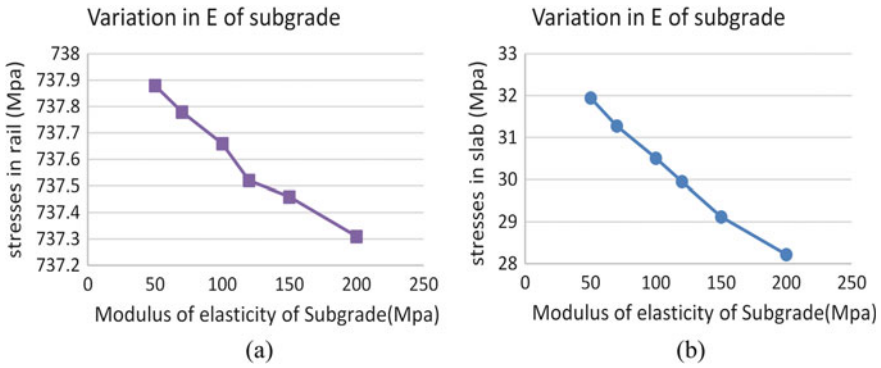


**Fig. 15** Stresses in **a** rail and **b** concrete slab due to variation in modulus of elasticity of subgrade

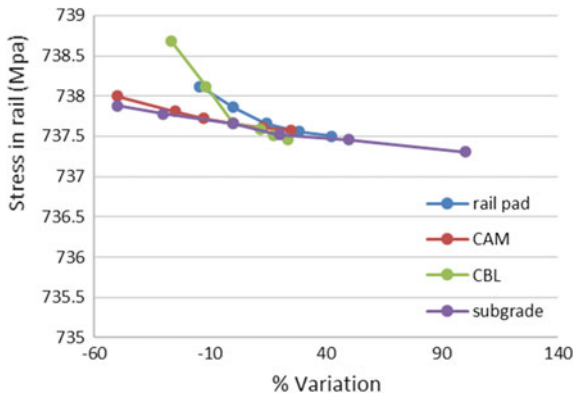


**Fig. 16** Effect on equivalent stress in rail due to % variation in parameters

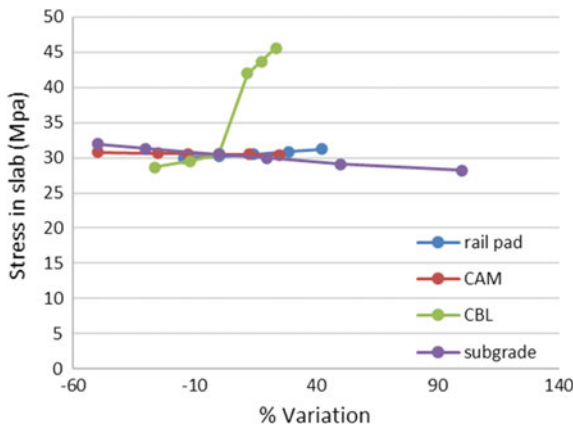


**Fig. 17** Effect on equivalent stress in concrete slab due to % variation in parameters

## 7 Conclusions

With increasing vehicle speed, axle load, and traffic density, a variety of slab track has been developed throughout the world and description of most commonly used slab track and their construction principle are given in this paper. A variety of ballastless track developed all over the world has been discussed in this report will be at the forefront of the solutions to construct the improved track structures that will be demanded in future years. Cost and vibration absorption capacity is the limitation of slab track. A variety of computational and experimental approach has been done to reduce the vibration and noise emission of the system. It is seen from the parametric studies performed in ANSYS workbench, that with increase in all the parameters the contact stress in the rail decreases. In concrete slab with an increase in stiffness of rail pad equivalent stress in CBL increases. From the study, it has been observed that modulus of elasticity of CBL has major influence on the equivalent stress in the concrete slab. Stress increases with increases in the parameter and decreases with decreasing the parameter in concrete slab. Modulus of elasticity of CAM layer and subgrade layer has negligible influence on equivalent stress in the concrete slab. Though these parameters have greater influence on displacement in the concrete slab. Parametric investigation can show the nonlinear behavior of railway track under different operating condition. Extensive research still needs to be carried out in this area.

## References

1. Tayabji S, Bilow D (2001) Concrete slab track state of the practice. *Transp Res Rec J Transport Res Board* 1742:87–96
2. Michas G (2012) Slab track systems for high-speed railways. master degree project. Royal Institute of Technology, Stockholm, Sweden
3. Ando K, Sunaga M, Aoki H (2001) Development of slab tracks for Hokuriku Shinkasen line. *QR of RTRI*. 42:35–41
4. Rail One. Rheda 2000 Ballastless Track System
5. Manual for Railway Engineering (1999) Volume 1, American Railway Engineering and Maintenance of Way Association, Landover, MD, USA
6. Xiangmin L, Suoyan Z, Zun L (2014) Research on CRTSIII ballastless track slab cracks of high-speed railway. *Appl Mech Mater* 443:69–73
7. Jee S, Nguyen H, Jang Y, Lee S (2018) Key characteristics of a floating slab track based on longitudinal interaction analysis. *Mathemat Probl Eng* 1–16
8. Lei X, Zhang B (2011) Analysis of dynamic behavior for slab track of high-speed railway based on vehicle and track elements. *J Transp Eng* 137(4):227–240
9. Lorenzo B, Santamaria, J., Vadillo, E.G.: Dynamic comparison of different types of slab tracks and ballasted track using a flexible track model. *Proc IMechE Part F: J Rail and Rapid Transit*. 225, 574–592 (2011)
10. Vale C, Ribeiro N, Calcada R, Delgado R (2011) Dynamics of a precast system for high-speed railway tracks. *Comput Methods Struct Dyn Earthquake Eng* (2011)
11. Hu J, Bian X, Xu W, Thompson D (2019) Investigation into the critical speed of ballastless track. *Transport Geotechnics* 18:142–148
12. Wang P, Chen R, Chen PX (2010) Dynamic assessment of ballastless track stiffness and settlement in high-speed railway. In: Proceedings of the joint rail conference

13. Lichtberger B (2005) Track compendium, 1st edn. Eurail Press
14. Esveld C (2003) Recent developments in slab track. Delft University of Technology
15. Esveld C (1999) Recent developments in slab track application. Delft University of Technology, Netherlands
16. Steenbergen M, Metrikine V, Esveld V (2007) Assessment of design parameters of a slab track railway system from a dynamic viewpoint. *J Sound Vibr*
17. Bharule S, Kidokoro T, Seta F (2019) Evolution of high-speed rail and its development effects: stylized facts and review of relationships. ADBI Working Paper 1040. Tokyo: Asian Development Bank Institute
18. <https://www.globalrailwayreview.com/article/112553/perpetual-growth-high-speed-rail/2020/11/03>



# Utilization of Residual Heat Energy Using Pyro Electricity Energy Harvesting

Ashish Kumar, Ashish Mishra, and Manoj Kumar Shukla<sup>(✉)</sup>

School of Mechanical Engineering, Galgotias University, Greater Noida, Uttar Pradesh, India  
manoj.shukla@galgotiasuniversity.edu.in

## 1 Introduction

Electricity production processes are inefficient and approximately two-third of energy was released into residual in the form of residual heat [1]. Force age measures are tormented by shortcomings, what's more, reject around 66% of the total energy was released as a residual heat or excess heat. Almost all the part of this heat is second rate heat (by and large under 95–235 °C), that is released in the environment and not utilized properly. The reutilization of this residual warmth for energy increment, notwithstanding, was restricted because of poor people's productivity of energy collecting frameworks work with few heat differentials which are far below the main limit of Carnot. The state's strong resources to manage the collection of this energy, such as thermoelectricity [2], are generally limited by their weak legitimacy for energy transformation beneath 95 °C. Natural smoke-Rankine Cycles (ORC) have been shown to be financially savvy to an enormous reach but have become restrictive of low power costs because of turbine inefficiency [3]. Hence this article is motivated in the need to create strategies which convert secondary residual heat with high parts of Carnot [4, 5] effectiveness. Hence, we examine a way to deal with doing exactly that—pyro electricity energy change (PEC).

## 2 Experimental Studies

Pyro electricity consists of a class of polar gems that are not centrosymmetric and that have an internal pairing between electric polarizing  $P$  and heat dependent  $T$ , like in improvement in heat causes a change in the timing of the electrical dipole or a pyro electricity (PE) effect (Fig. 1a), that is quantitative explained using pyro electricity coefficient,  $\pi - \left(\frac{\partial P}{\partial T}\right)$ . Therefor PE is manifested by a heat -reliant change in plane load density, PE can also be produced by heat dependency of insulator permeability, thermally induced deformation piezoelectric materials [6], and flexoelectricity [7] effects because of heat gradient into all substances. Can reverse polarizing using application of electric field and some EPs close to their phase transition heat  $s$ , therefore often forming PEC devices.

Unlike the thermoelectric that uses a spatiotemporal heat slope, EEC needs a fleeting variety. In heat  $\left(\frac{\partial P}{\partial T}\right)$ , making PEC extraordinarily attractive in certain situation in which heat changes are hard to accumulate or heat of the warm heating source is deflecting.

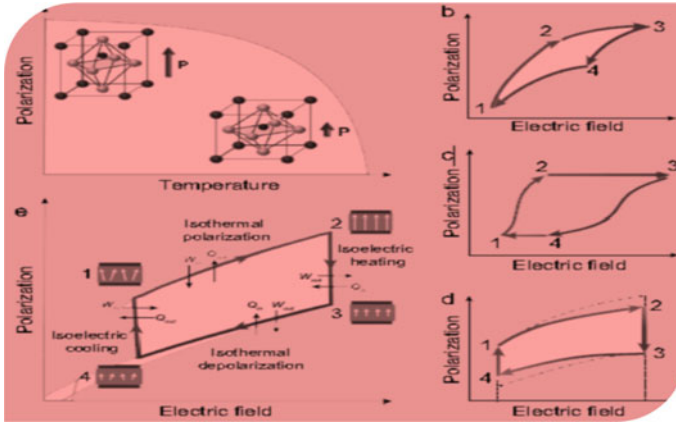


**Fig. 1** Pyroelectric results and pyroelectricity cycles. **a** Diagram depicts the change in polarization when the temperature changes. Polarizing versus electric field tracks for, **b** Carnot, **c** Sterling, **d** Joule and **e** First Brayton (Olsen)

These heat deflections result in a pyroelectricity waft  $i_p = \pi A \frac{dT}{dt}$ , in which  $A$  is the execution scales with the place, now not the volume, of a fabric. These truth activates numerous likely focal points for slender movie-based devices and for this reason spurs our emphasis on substances as calculations shown here. To truly gain waste heat, a percent gadget imitates a thermodynamic warmth motor.

### 3 Results and Discussion

The polarizing is corresponding to the extent, and the electrified area is much like the important element of the operating liquid. A verities of thermodynamic variations [8] had been proposed for present and are diagnosed with the aid of their polarizing as opposed to electrified pathways (P-E). Even it can be conceivable to imagine a Carnot Cycle (i.e., no heat transfer process  $3 \leftarrow 2, 1 \leftarrow 4$ ) and temperature constant process  $2 \leftarrow 1, 4 \leftarrow 3$  measures, Fig. 1b), the acknowledgment of no temperature change process getting ready in a ferroelectricity is troublesome, results in unfeasibility of these cycles. Sterling (2 elimination  $2 \leftarrow 1, 4 \leftarrow 3$ ) and 2 temperature constant process  $3 \leftarrow 2, 1 \leftarrow 4$  measures, Fig. 1c), Joule (isoelectric  $2 \leftarrow 1, 4 \leftarrow 3$ ), and two no temperature change process  $3 \leftarrow 2, 1 \leftarrow 4$  measures, Fig. 1d), and First Brayton (or Olsen) cycles (there are two temperature constant process and isoelectric measures, Fig. 1e), are utilized in distinctive instances depends upon the example math and heat source [8, 9]. Also, the Olsen cycle has utilized and has exhibits to supply probably the most improved p.c efficiencies characterized as [10]:

$$\eta = \frac{\oint E dP}{\int_{T_L}^{T_H} c(t) dT + Q_{ECE}} \tag{1}$$

where in  $c(t)$  is the warmth restrict,  $(T_H$  and  $T_L)$  is the heat for warmth supply (warmth sink),  $\oint E dP$  is the Internet electrical paintings executed  $W$ , and  $Q_{ECE}$  is the electro

caloric work done because change in harmonic entropy (related with the warm heat restrict) is in the main plenty bigger than the bipolar entropy exchange, electro caloric work can be unnoticed in the denominator of Eq. (1), which speaks to the warmth enter. The FOM for PEC [11] is sooner or later FOMPEC— $(\pi^2 T)/(C\varepsilon_{\text{zero}} \varepsilon_r)$ ; thusly, a massive % effectiveness requires freely upgrading  $\pi$  and lowering insulator permittivity  $\varepsilon_r$ . the second-request subordinates of the loose electricity often wander in the location of level adjustments; ultimately, situating the material near the precarious edge of ferroelectric-to Para electric degree development (Curie heat, TC) fills in as a route to improve the natural  $\pi$ . therefore, impressive exertion has zeroed in on fining TC through the chemistry [12], hydrostatic pressure [13], or epitaxial strain [14] due to tiny films. Moreover, advances between special ferroelectric stages can result in polarizing flip (e.g., inside the location to a morph tropic level restrict) that could result in the distinction in the floor fee thickness. The request for these stage adjustments is giant. First-order transitions, regardless of getting a precarious change in the polarizing as for heat (huge  $\pi$ ), are linked with a system which restricts the operating heat system inside hysteresis loop. 2d-request modifications (in most cases the case beneath a giant electric-powered-area and for clasped meager movies) skip heat hysteresis but are related with a generally more modest size of  $\pi$ , leaving a definitive selection of fabric (first- vs. second-request) to be together upgraded with the running heat range. The enlargement inside the insulator consistent and specific warm heat around the degree progress can decrease the general advantage if there is an increment in herbal  $\pi$ , as located within the circumstance for the FOMPEC. As the pressure increases the thickness of the devices often requires the utilization of high instance electric field that additionally will in widespread hose first-request adjustments. Direct estimations of the PE have likewise validated a lower in the p.c at low electric fields for polynomial meager movies and that no intrinsic effects will have a similar considerable diploma as inherent effects [15, 16].

The polar structure changed by the structure of heat irritations and request now for not just at a single-cellular stage (i.e., the function response) but in addition also at a mesoscopic level (e.g., space systems). Earlier these works on polynomial ferroelectrics slight moves has indicated that the heat-subordinate motion of Ferro elastic regions can bring about increment to the PE through alleged outward contributions [17]. Thusly, studies are targeted at distinguishing frameworks with great underlying level dangers and designing novel area systems that react substantially to heat. As an example, the heat-incited rivalry between exclusive conventional ferroelectrics and toroidal polar vortex degrees in  $\frac{\text{PbTiO}_3}{\text{SrTiO}_3}$  super lattices [18] and blended stage modern vicinity systems in structure which is tetragonal  $\text{PbZr}_{1-x}\text{Ti}_x\text{O}_3$  [19] offer energizing activities to enhance outward commitments. Mild movies are likewise precisely clipped to their substrate and the nice and cozy improvement mismatch among the film and the substrate brings about non-obligatory commitments to the PE, which is intervened by piezoelectricity. An evaluation of the inborn commitment, the optional dedication might be both bad and tremendous, improving the PE inside the preceding or stifling it inside the last case [17]. Accurately, the utilization of “unclamped” micro fabricated or unattached structures may want to offer additional ways for a big  $\pi$  and p.c. As stated, % requires the usage of thermodynamic cycles utilizing a strong kingdom gadget. These devices are for

the maximum element organized around a pyro electricity capacitor with helper structures devoted to heat/electrical administration. The dynamic material in a plc. Gadget is coupled to electrical and warm waveforms, bringing about price  $\rightarrow$  warmth  $\rightarrow$  launch  $\rightarrow$  cool cycles that produce electric-powered work. For any cycle (Fig. 1b–e), electric-powered discipline biking with massive greatness is directly done in slim movie devices and is essentially restricted through the rate-launch electrical misfortunes, which scale with the cycle recurrence, misfortune digression, insulator consistent, and DC electrical losses [20]. Developing heat motions, notwithstanding, provides all of the greater charming tests. This outcome in % gadgets falling extensively into two classifications depending on the idea of the nice and cozy property accessible: those who initiate occasional warming from two static heat repositories (Fig. 2a, b) and those that couple to a solitary, time-fluctuating warmth source (Fig. 2c). Inside the two cases, the percent machine may be advanced for maximal effectiveness, strength thickness, or pressure thickness. The usage of significant electric-powered fields activates high-energy densities and efficiencies [21] that are constantly constrained through  $\eta$  Carnot. The force thickness, be that as it may, is represented by the joined electric and heat time consistent,  $\tau$ , of the percent machine, in which the maximum excessive force  $P_{max} - WE_{fmax} - WE/\tau$  and  $f_{max}$  is the finest cycling recurrence. The warm time constant may be plenty larger than the electrical-time steady what is more, is, therefore, the limiting detail in carrying out a full-size pressure thickness. Disregarding touch obstruction between the warmth source and the p.c system,  $\tau_{thermal} = L^2/\alpha$ , wherein  $L$  and  $\alpha$  are the thickness and heat diffusivity of the gadget, in my opinion. It follows that  $P_{max} - WE/\tau_{thermal} \propto 1/L^2$  and along those traces mild movie devices [21] innately have a preferred pressure thickness over mass devices [22]. This became exhibited as of past due, where dainty film relax or ferroelectrics [21] completed a pressure thickness that is 3 extensive stages bigger than that of mass versions [22] however a strength thickness having this is just one great diploma larger. Searching forward, it creates the influence that slim film calculations are promising for future percent machine plans.

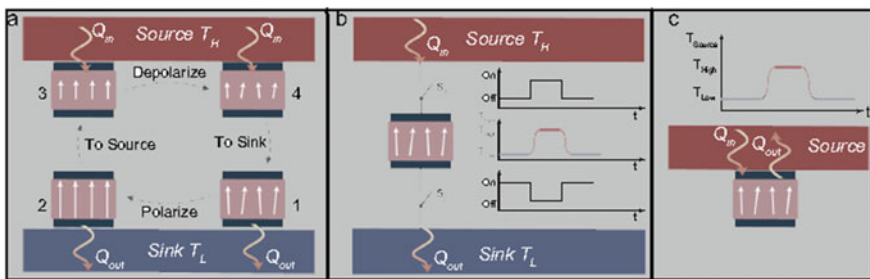


**Fig. 2** One-of-a-kind techniques for biking a pyro electricity strength conversion (percent) device among thermal sources. **a** A % tool automatically cycles b/w the sink and the heat source to enforce an Ericsson cycle. **b** The identical thermodynamics process can be done using switches which pump/discharge heat to the percent tool. **c** A percent tool coupled with an unmarried-sided warmth source with a periodically various heat



No matter advances within the power and force densities, much need to be finished to improve the effectiveness of the percent cycle. The excessive express warmth of pyro electricity materials brings approximately greater warmth strength retained than electrical dipolar power received. Despite the fact that the go-section constantly regulations plc. Exchange fabric technology, regenerative plans making use of multi-arranged warmth repositories were proposed to decrease absolutely the warm heat data and alongside these traces increment efficiency [10].

This device, anyhow, should work quasistatically; ultimately, the force thickness (and utility) endures. in place of looking for reversible cycles, examiners have, in this manner, zeroed in on diverse electricity gathering cycles (e.g., First Brayton and Brayton) to expand execution. Past due endeavors have, anyways, moved considerably in addition through thinking about, for instance, crossover cycles. In this soul, joined piezo/pyro electricity devices have shown larger most severe yield voltages [23], and others have even created slim films equipped for gathering sun primarily based, heat, and mechanical energies. Consolidated Ferro-/antiferroelectric cycles have been stated in a solitary system, exploiting the bidirectional concept of the pyro electricity coefficient in these substances is 20. Those crossover generators plan to build machine execution by means of coordinating frameworks to enhance the extractable power between two heat extrema. Within the everyday % technique, there are a few chances for improving execution. At an absolute minimum, there may be a requirement for a focused plan of substances custom-suited to a specific residual-warmness supply. Beyond this, it is miles workable to restrict warmth misfortunes to assistant systems (e.g., the usage of unsupported movies) or to join evaluating effects rising from paramagnetic (by multiferroic and magneto electric materials) to enhance usually talking execution.

## 4 Conclusion

At remaining, the development of contemporary percent substances and gadgets is ready for a renaissance. Advances in our potential to exactly gage materials, center across the plan of elite pyroelectrics, and the creation of nanoscale system systems offer tremendous admittance to development. Those upgrades empower further hobby in a blossoming field, the association of a powerful examination of the nearby area, and a supported exploration exertion like that visible in thermoelectric. Nowadays denotes the start of a duration of splendid advancement for pyro electricity substances and their utility in the field of p.c.

## References

1. Vining CB (2009) An inconvenient truth about thermoelectrics. *Nat Mater* 8:83–85
2. Tchanche BF, Lambrinos G, Frangoudakis A, Papadakis G (2011) Low-grade heat conversion into power using organic Rankine cycles—a review of various applications. *Renew Sustain Energy Rev* 15:3963–3979
3. Lee SW et al (2014) An electrochemical system for efficiently harvesting low-grade heat energy. *Nat Commun* 5:3942
4. Straub AP, Yip NY, Lin S, Lee J, Elimelech M (2016) Harvesting low-grade heat energy using thermo-osmotic vapour transport through nanoporous membranes. *Nat Energy* 1:16090

5. Zook JD, Liu ST (1978) Pyroelectricity effects in thin film. *J Appl Phys* 49:4604–4606
6. Zubko P, Catalan G, Tagantsev AK (2013) Flexoelectric effect in solids. *Annu Rev Mater Res* 43:387–421
7. Olsen RB, Bruno DA, Briscoe JM (1985) Pyroelectricity conversion cycles. *J Appl Phys* 58:4709–4716
8. Hanrahan BM, Sze F, Smith AN, Jankowski NR (2017) Thermodynamic cycle optimization for pyroelectricity energy conversion in the thin film regime. *Int J Energy Res* 41:1880–1890
9. Olsen RB, Brown DD (1982) High efficiency direct conversion of pyroelectricity measurements heat to electrical energy-related. *Ferroelectrics* 40:17–27
10. Sebald G, Lefeuvre E, Guyomar D (2008) Pyroelectricity energy conversion: optimization principles. *IEEE Trans Ultrason Ferroelectr Freq Control* 55:538–551
11. Zhang N et al (2014) The missing boundary in the phase diagram of  $\text{PbZr}_{1-x}\text{Ti}_x\text{O}_3$ . *Nat Commun* 5:5231
12. Merz WJ (1950) The effect of hydrostatic pressure on the curie point of barium titanate single. *Cryst. Phys. Rev.* 77:52–54
13. Martin LW, Rappe AM (2016) Thin-film ferroelectric materials and their applications. *Nat Rev Mater* 2:16087
14. Hanrahan B et al (2018) Accounting for the various contributions to pyroelectricity in lead zirconate titanate thin films. *J Appl Phys* 123:124104
15. Pandya S et al (2019) Understanding the role of ferroelastic domains on the pyroelectricity and electrocaloric effects in ferroelectric thin films. *Adv Mater* 31:1803312
16. Karthik J, Agar JC, Damodaran AR, Martin LW (2012) Effect of  $90^\circ$  domain walls and thermal expansion mismatch on the pyroelectricity properties of epitaxial  $\text{PbZr}_{0.2}\text{Ti}_{0.8}\text{O}_3$  thin films. *Phys Rev Lett* 109:257602
17. Damodaran AR et al (2017) Phase coexistence and electric-field control of toroidal order in oxide superlattices. *Nat Mater* 16:1003–1009
18. Damodaran AR et al (2017) Three-state ferroelastic switching and large electromechanical responses in  $\text{PbTiO}_3$  thin films. *Adv Mater* 29:1–9
19. Hanrahan BM et al (2018) Combining inverse and conventional pyroelectricity in antiferroelectric thin films for energy conversion. *J Mater Chem C* 6:9828–9834
20. Pandya S et al (2018) Pyroelectricity energy conversion with large energy and power density in relaxor ferroelectric thin films. *Nat Mater* 17:432–438
21. Sebald G, Pruvost S, Guyomar D (2007) Energy harvesting based on First brayton pyroelectricity cycles in a relaxor ferroelectric ceramic. *Smart Mater Struct* 17:015012
22. Zakharov D et al (2013) Combined pyroelectric, piezoelectric and shape memory effects for thermal energy harvesting. *J Phys Conf Ser* 476:012021 (2013)
23. McKinley IM, Lee FY, Pilon L (2014) A novel thermomechanical energy conversion cycle. *Appl Energy* 126:78–89



# Conceptual Design and Computational Analysis of Power Generating Shoes Using Plantar Flexion

Naman Goel<sup>(✉)</sup>, Abhishek Jain, Tanishq Arora, and Vikas Rastogi

Delhi Technological University, New Delhi, India  
naman.goel142@gmail.com

## Nomenclature

- $\alpha$  Electromechanical efficiency
- $\beta$  Pivot angle
- $p$  Pitch (rotations/length)
- $x$  Length differential
- $r$  Foot height

## 1 Introduction

Use of gadgets to complement our daily life is increasing day by day, whether it is the use of fitness tracking devices or health-related devices such as a hearing aid. One thing that is common across this spectrum of utilities is their energy capacity. These devices come under the capacity of low-power electronics which are designed for long-term usage. Another trait of these devices is that they must not compromise on its portability yet have a longer charge cycle. To obtain a longer charge cycle, we need a larger battery which compromises the portability of such devices which is not at all feasible. Fast charging is one solution. It requires redesigning these devices for a fast-charging compliant battery. It will not affect the charge cycle directly by increasing the operating time but will significantly reduce it by decreasing its recharge time. But, it is not possible to redesign every possible device for a fast-charging solution. The availability of a charger and a wall socket is another requirement. GPS trackers are another set of low-power electronics which demand a longer life and cannot be taken out for charging. GPS trackers, in vehicles, are constantly powered by the vehicle's energy source. But wearable tracking devices need a solution. This is where our concept comes in. It will provide a larger recharge cycle to such devices by constantly powering them up without redesigning them for a larger battery and not compromising on their portability. With the use of our device, energy will be generated in each step and will be stored simultaneously.

Most of the research in this field uses either the pressure conversion or electromagnetic conversion to generate power. Pressure conversion is done by placing piezoelectric

sensors at the pressure points of our foot [1, 2], while the latter uses relative movement of the magnet with respect to coil to induce electricity. [3] This has a high electromagnetic efficiency but interferes with the gait cycle, whereas the former generates miniscule amounts of energy [4]. The concept we propose will be purely based on mechanical design and will generate electricity by a periodic length differential in our foot using a linear actuator onto a rack and pinion mechanism to rotate the dynamo. Also, it will not compromise the gait cycle as the actuation is purely dependent on our foot movement [5].

## 2 Principle

Walking is an indispensable part of our daily routine. Be it for moving from one place to another or a simple morning walk. One cannot get rid of it. Still, this movement is the one least utilized. While walking or running, the sequential movement of the foot which one follows is called a gait cycle [6]. Underneath mentioned is a pictorial representation of the same. When we walk, our foot goes through various oblique movements which create a length differential in our foot. Plantar flexion refers to this movement of the foot muscle which is stretched during push off which generates length differential in skin; we utilized this differential using our actuating mechanism to generate clean sustainable electricity. Unlike other forms of conventional energy sources, electricity generated by this process could be immediately utilized in mobile gadgets (Fig. 1).

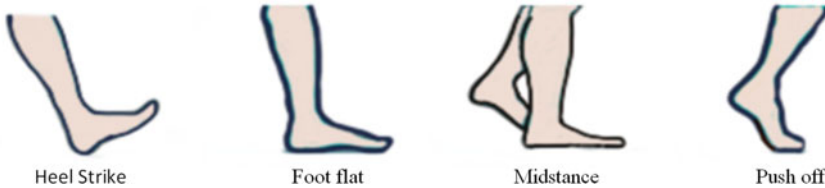


**Fig. 1** Position of foot and its terminology during a typical gait cycle

## 3 Working

From the heel strike to push off of the right toe. A similar range of motion of the left foot in succession to it will comprise a complete stride. If we take a look carefully at the position of the foot in midstance and push off, there is a presence of a length differential. To observe it more clearly, let us take a look at the following diagram (Figs. 2 and 3).

Here let us assume that rectangle  $A E F D$  is our foot.  $A B C D$  is the forefoot. When we move our foot from the midstance to push off, the forefoot remains in contact with the ground, and the remaining part of the foot propels as it is shown in the figure aforementioned.  $C-C''$  is the length differential which would be converted into rotary motion with the help of rack–pinion mechanism.

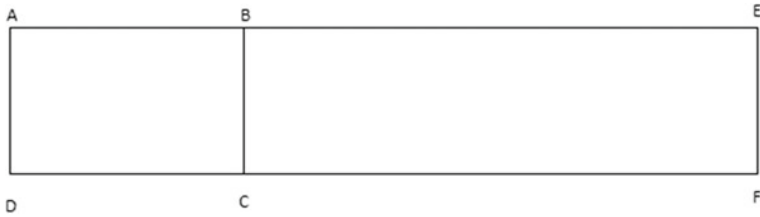


**Fig. 2** Forefoot and back foot in foot flat position

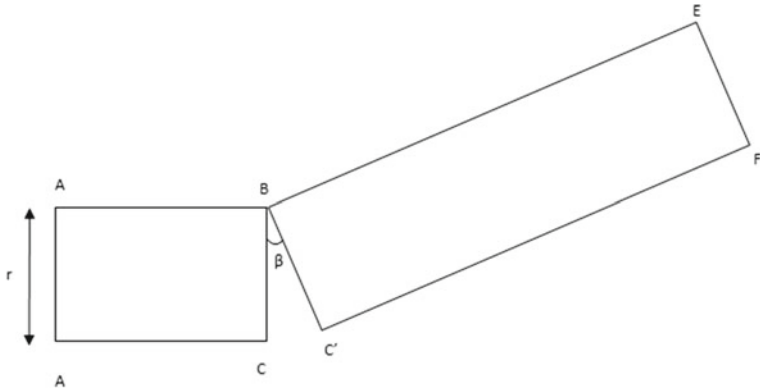


**Fig. 3** Forefoot and back foot in push off position

### 3.1 Components and Their Functions

**Spring:** A spring is a device that is used to store the energy while our foot is in push off position and makes our rack come back to original position when in foot flat position (Fig. 4).

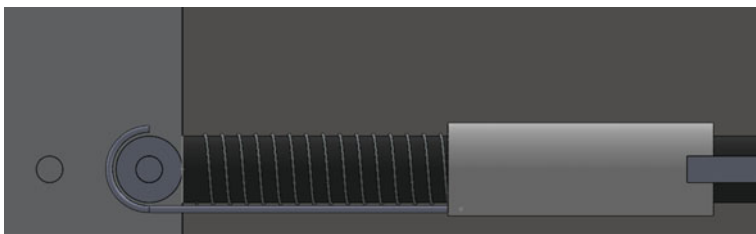


**Fig. 4** CAD model of spring

**Rack and Pinion:** A rack and pinion mechanism is a type of actuating machine which converts actuating motion to rotary motion. These mechanisms are mainly used to generate electricity from linear motion. In our device, we have connected our rack to the

front part of our foot. When the foot is in a relaxed position, the rack is in a position as shown by our diagram (Fig. 5).

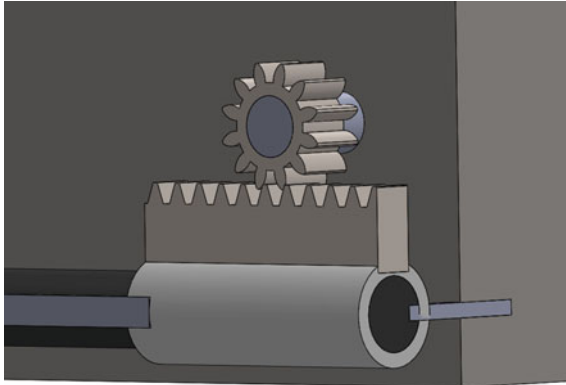


**Fig. 5** CAD model of rack and pinion mechanism

When our foot is in midstance position, our rack slides towards the right position as shown in the figure, hence causing rotatory motion in the pinion (Fig. 6).



**Fig. 6** CAD model of mechanism when foot is in relaxed position

When our foot comes in the push off position, the rack comes at the extreme right position as shown in the diagram. Due to this movement, there is rotation in the pinion as shown in the subsequent figures (Figs. 7 and 8).

**Dynamo:** Dynamo is a device which uses rotatory motion to generate electricity. Here dynamo is connected to the pinion of our assembly which will rotate the shaft of the dynamo and hence generate electricity. Electric current in dynamo is produced by rotating a wire within a magnetic field or rotating a permanent magnet around coils of wire. Both processes produce alternating current because the wire passes between two magnetic poles every half turn. The principal concept used behind this is the Lorentz force.

#### 4 Mathematical Model

The mathematical model involves calculation of voltage per rotation.

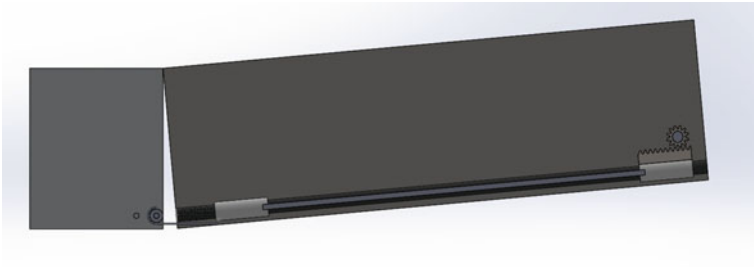


**Fig. 7** CAD model of mechanism when foot is in midstance position

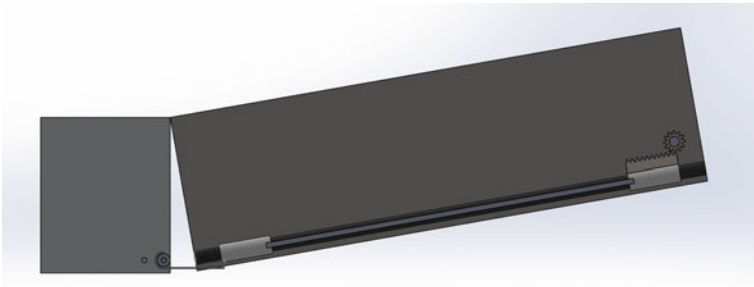


**Fig. 8** CAD model of mechanism when foot is in push off position

$\alpha$  (Electromechanical Efficiency)—We have taken this to be 80% as a standard.

$\beta$  (Pivot Angle)—The maximum angle obtained came out to be  $10^\circ$  by considering practical usage.

$p$  {Pitch (rotations/length)}—The pitch is calculated by rotation obtained per movement of rack. This came out to be 1.39 revolution per cm.

$r$  (Foot Height)—The average foot height was found to be 2 cm.

$x$  (Length Differential)—The length differential is given by

$$x = \beta * r \quad (1)$$

[Since EF remains constant, we could apply the formula. From here, we get our arc length which would be used to harness energy]

$$\text{Rotation/step} = p * x \quad (2)$$

Thus, the relation between volts and step is given by

$$\text{Volts} = (\alpha * p * x) * (\text{Steps}) \quad (3)$$

Therefore, volts per steps is given by

$$\text{Volts} = (\alpha * p * r * \beta) * (\text{Steps}) \quad (4)$$

## 5 Simulation Study

### 5.1 Displacement Versus Time

When we walk or run, we often follow periodic motion; hence, it is quite intuitive to expect a periodic response from our rack and pinion mechanism also, and this is quite evident from our computer simulation graph which shows an approximately sinusoidal periodic pattern with maximum displacement at 10 degrees which is the maximum limit that we have assumed for our plantar flexion motion (Fig. 9).

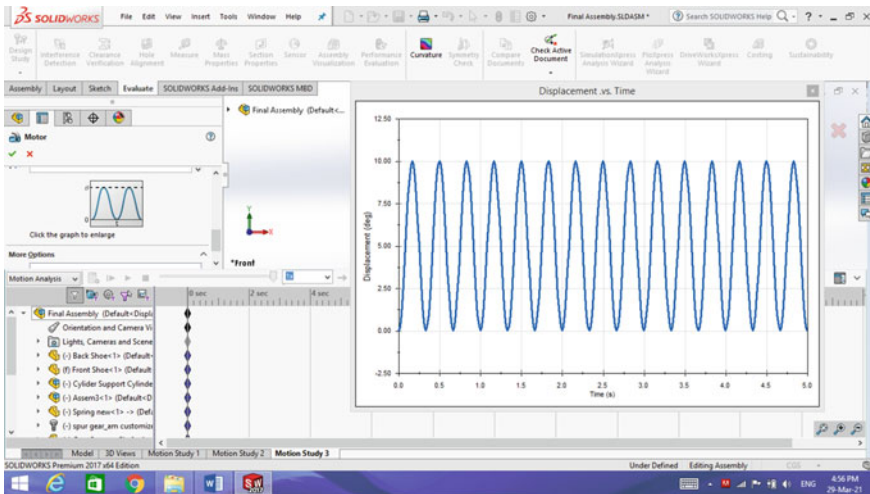


Fig. 9 Displacement versus time plot

We used motion study in SOLIDWORKS to plot displacement versus time graph.

### 5.2 Voltage Versus Steps Taken

We utilized plotting features of Python matplotlib.pyplot to plot voltage versus steps graph (Fig. 10).

When plotted voltage versus step graph, we obtained a cyclic graph that gives a maximum possible value of 0.3891 V/step with an average output of 0.2141 V/step.

### 5.3 Kinetic Energy Versus Time

Figure 11 shows the result of computer simulation of our CAD model. We have plotted kinetic energy of the pinion against time to simulate real-world energy output. We have placed the pivot on the upper edge of the cube which, in real world, would mean the pivot of our foot. Intuition says that since our motion is periodic, energy should also be periodic, which is validated by our simulation study which shows peak kinetic energy at 0.024 J per step, which could be easily converted into potential difference using



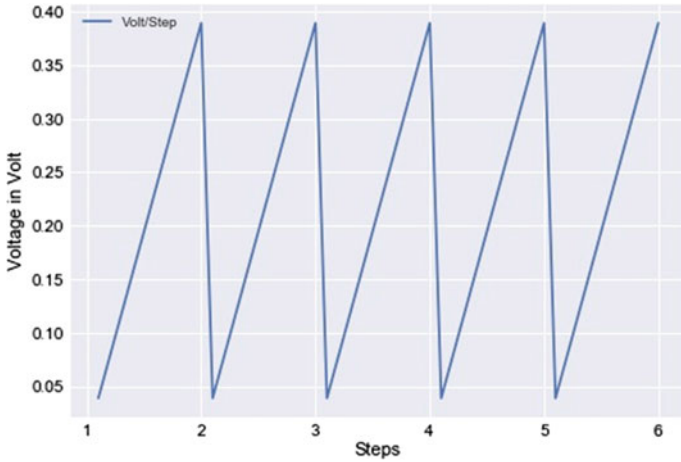


**Fig. 10** Voltage generated versus steps taken

appropriate motor generators. It is generally expected that since motion is periodic, energy generated should also be present in reverse plantar flexion also. The software has already incorporated the energy change in our kinetic energy graph, but we have not shown it exclusively unlike in voltage versus time graph.

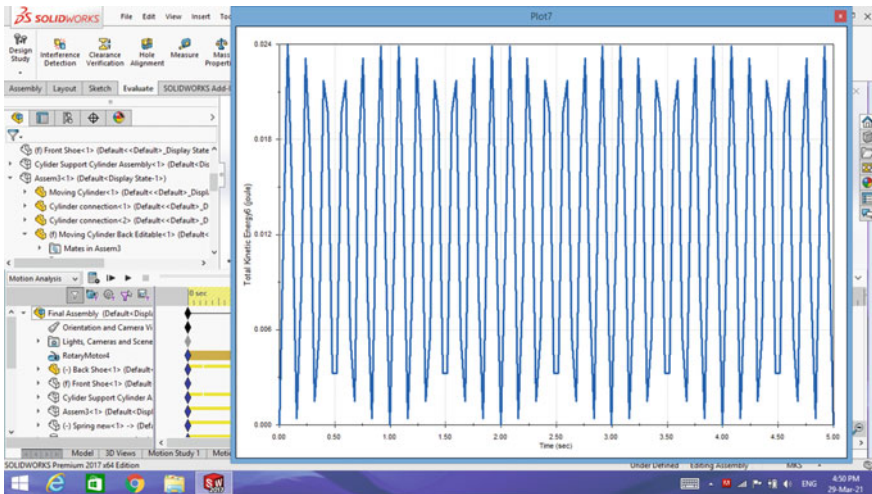


**Fig. 11** Kinetic energy versus time plot

## 6 Conclusion

Our design of utilizing plantar flexion for electricity generation has a potential of generating sustainable and pollution-free power which could be used to power small mobile

devices. Our research provides alternative mechanism for electricity generation using foot movements, which was previously limited to only piezoelectric crystals. From computer simulations, it could be concluded that at most 0.3891 V/step could be generated from our device with peak kinetic energy of 0.024 J/step, our speculations of a cyclic graph are also verified by the graphs of voltage and kinetic energy. Since a substantial amount of energy is generated, hence, our device would be having many cross-domain applications.

## References

1. Zhu G, Baia P, Chena J, Wanga ZL. Power-generating shoe insole based on triboelectric nanogenerators for self-powered consumer electronics
2. Asry A, Mustafa F, Yi S, Sim Y, Ishak M, Mohamad A (2019). Study on footstep power generation using piezoelectric tile. *Indon J Electr Eng Computer Sci* 15:593. <https://doi.org/10.11591/ijeecs.v15.i2.pp593-599>
3. Beeby SP, Tudor MJ, White NM (2006) *Measure Sci Eng* 17:175
4. Li T, Zhang X, Jiang C, Hou L (2009) Analysis of the characteristics of piezoelectric sensor and research of its application. In: 2009 18th IEEE International Symposium on the Applications of Ferroelectrics, Xi'an, China, pp 1–4. <https://doi.org/10.1109/ISAF.2009.5307537>
5. Kutnjak-Mravlinčić S, Akalović J, Bischof S (2019) Merging footwear design and functionality. *Autex Res J* 20. <https://doi.org/10.2478/aut-2019-0023>
6. Shahid S, Nandy A, Mondal S, Ahamad M, Chakraborty P, Nandi G (2012) A study on human gait analysis. <https://doi.org/10.1145/2393216.2393277>



# Design Optimization of Clutch Plate Using ANSYS

Shivam<sup>(✉)</sup>, Rupanshu Singh, and Priyansh Singh

Department of Mechanical Engineering, Delhi Technological University, New Delhi 110042,  
India

shivam27777@gmail.com

## 1 Introduction

An automobile generates power in the engine, which is transmitted through the transmission system to the wheels for mobility. The engine and transmission system is connected with a clutch, which engage or disengage the two systems for smooth and consistent power transmission in the vehicle. A clutch has a wide range of applications in helicopters, ships and automobiles [1]. It comprises of separator and frictional plates. The total friction offered by the plates contributes to the variation in the overall torque transmitted [2]. Bezzazi et al. [3] experimentally found difference between the pin-on-disc wear test as compared to conventional SAE J661 clutch test. Several equations were developed for the plate toward morphology, observed the temperature on the other side of the plate in pin-on-disc testing which obtained correlation between coefficient of friction with respect to sliding velocity and temperature. The experiment was performed on composite clutch plate under dry conditions to evaluate effects on tribological behavior. The experiment showed that there is a lot of difference in temperature generation between pin-on-disc testing and conventional testing system. Results showed that the friction coefficient behavior as function of temperature was well characterized by the pin-on-disk test. When a clutch is engaged, it is subjected to high pressure generated between the connection parts. A rise in temperature near the clutch is observed due to the generation of heat due to friction. So, thermal deformities and instabilities are observed on the plate's surface at a higher relative sliding velocity [4, 5]. At the friction interface of a clutch the temperature is reported to be around 370 °C. This non uniform pressure application and thermal stresses can lead to the wearing and failure of the clutch plate. The heat affected zone and area increases with the increase in time of clutching process [6]. When clutch is disengaged, drag torque is developed between the plates due to viscous shearing of fluid film, which contributes to power loss [7].

For obtaining a smooth transmission and reducing overheating, transmission fluid is added over the clutch. In the process of disengagement of clutch, the transmission fluid accumulates between the plates and produces a loss in power by generating viscous drag. Thus to promote aeration grooves are provided over the plate, to make a passage for lubricating fluid to pass [8, 9]. Moreover, materials like ceramic (with reinforced organic material) can be used for clutch, to minimize the heat generation effect [10, 11].

Scott and Suntiawattana, [12] determined the performance of wet friction clutch on addition of oil additives. The properties related to pressure, anti-wear, corrosion of the clutch were analyzed, while adding lubricating oil. The results showed that addition of oil had a beneficial effect on the wear and frictional characteristics.

Yu et al. [13] developed a mathematical model to investigate the multi disc clutch's failure. The pressure, temperature and buckling variation were considered and wear, frictional properties were analyzed by conducting the pin-on-disc test. Different wear characteristics were observed when temperature varied between 15 and 400 °C.

There are many researches on finite element analysis of clutch. Purohit et al. [14] designed a model of clutch and conducted the static structural analysis on ANSYS. The stresses and deformation occurrence in the clutch plate, pressure plate and diaphragm spring were reported. Karna and Rao [15] observed the temperature distribution and stress variation in the clutch plate by setting up a model of given dimensions on the pro-e software and conducted analysis on the ANSYS software, the material considered for analysis were aluminum and steel for wet clutch plates.

Zhu et al. [16] conducted the temperature analysis of a dry dual clutch. CFD analysis was conducted to determine heat flux, heat distribution factor and temperature field. The results of the two clutches were obtained and compared. The major usage of friction clutch is for transmitting power between shafts, in delivering power to fully or partially loaded machines and as a connection between an automobile's driveshaft and engine [4]. It can be further classified into disc or plate, centrifugal and cone clutch.

Iqbal et al. [17] developed a reset-integrator friction model-based SAE-2 setup for analyzing vibrational and dynamic characteristics in the engagement dynamics of friction clutch. The results showed that stick–slip mechanisms caused the post-lockup vibrations, while the pre-lockup torsional vibrations were caused by oscillating sliders.

In this research, structural analysis is conducted on ANSYS software to determine the stress generation and deformation occurrence in the frictional clutch plate. Different shapes of clutch plates are analyzed and compared. The optimal design having lowest stress and deformation will be proposed.

## 2 Material and Design of Clutch Plate

The basic requirement of clutch plate is that it should be able to generate sufficient amount of friction force. The force depends on the surface area of the plate therefore all the clutch plate were designed in such a way that there surface area and thickness is same. The size of the central holes was kept same only the shape of the vent were varied which can be seen in Fig. 1.

The clutch plate is subjected to high pressure and temperature variation, the surface should show decent tribological behavior. Structural steel is chosen for the simulation analysis [2, 18].

The various types of clutches used in the automobile depend upon the type and use of vehicle. The clutch plate is designed on the Solidworks software, according to the given dimensions. The commercially used clutch plate comprises several rectangular holes.

Rectangular (positioned parallel to radius), this has rectangular holes such that the longer side of rectangle is perpendicular to the radius whereas in rectangular (positioned

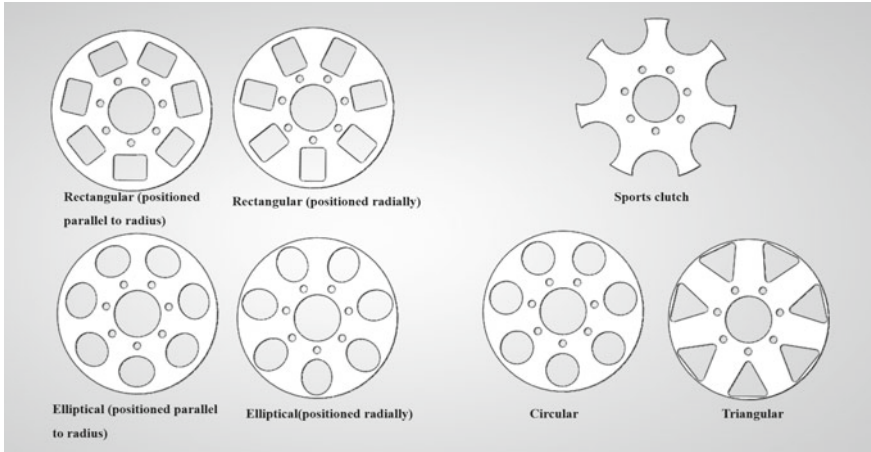


**Fig. 1** Different shaped holes were designed on the clutch plate

radially), the longer side of rectangle is parallel to the radius vector of clutch plate. Sports clutch has semicircular cuts at the periphery of the plate. Circular plate comprises of circular cuts and the triangular plate consists of triangular cuts. Elliptical (positioned parallel to the radius) plate is such that the minor axis of the elliptical holes are kept parallel to the radius of clutch plate whereas in the elliptical (positioned radially) plate it is kept perpendicular to the radius vector of plate.

While designing all the sharp corners of hole were avoided in every plate by giving same value of fillet at corners (Table 1).

**Table 1** Dimensional parameters of clutch plate

Name of property	Symbol	Value
Outer radius	$R_1$	55 mm
Inner radius	$R_2$	16 mm
Clamping hole radius	$R_3$	2.5 mm
Surface area of clutch plate	$A$	$m^2$

### 3 Simulation

#### 3.1 Methodology

ANSYS software develops a mathematical model based on the given governing equations and input boundary conditions and generates the numerical solution at different specified nodes and elements. The clutch plate models were imported from Solidworks into Ansys workbench.

Structural analysis is conducted on the models and von-mises stress and deformation is analyzed. It involves the study and prediction of behavior of structures using the set of physical laws and mathematics [19].

### 3.2 Meshing

ANSYS software generates a mesh of nodes and elements for calculating governing equations and determining results [20]. Meshing on all the plates was kept same and was made more refined. No compromise was done with the size of mesh although it affects the calculation time. For obtaining accurate and constructive results, a fine mesh with 46,998 nodes and 23,296 elements is generated with a tetrahedral shape. At further reducing the size of mesh elements, there was no effect on the end results therefore this mesh properties were finalized.

### 3.3 Boundary Conditions

To simulate the results and compare the stress generation and deformation occurrence in different shaped clutches keeping the surface area the same, an appropriate set of boundary conditions are required to be applied. The ANSYS solver applies the boundary conditions at the specified nodes and results are produced.

A moment of magnitude 29,208.75 N mm was applied on one face of the clutch plate and all the seven holes which are used for clamping the clutch plate are made fixed (Fig. 2).

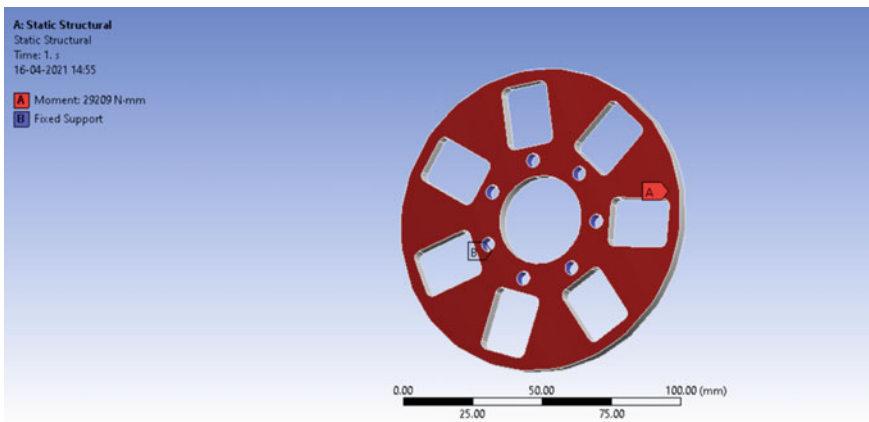


**Fig.2** Boundary conditions on a rectangular (positioned radially) clutch plate

Calculation for moment:

Surface area of rectangular clutch plate

$$\begin{aligned}
 &= \pi(R_1^2 - R_2^2) - 7(L \times B) - 7 \times \pi \times R_3^2 \\
 &= \pi(55^2 - 16^2) - 7(23 \times 17.66) - 7 \times \pi \times 2.5^2
 \end{aligned}$$

$$= 6094.68 \text{ mm}^2$$

Torque = Friction force  $\times$  Distance =  $\mu \times P \times A \times (R1 + R2) \div 2$ .  
(friction coefficient ( $\mu$ ) for structural steel = 0.45)

$$= 0.45 \times 0.3 \times 6094.68 \times (55 + 16) \div 2$$

$$= 29208.75 \text{ KN mm}$$

For the analysis, static structural software from Ansys was chosen for calculation of stress and deformation as it is best suited for structural analysis of those models in which induced inertia and damping do not have significant effect.

After loading the boundary conditions in the static structural solver in Ansys, the results were calculated for all the seven friction clutch plate designs.

## 4 Results and Discussion

The results show high stress concentration near the holes and edges. Grid independence test was conducted before comparing the results from simulation. The stress and deformation contours were developed.

The result obtained from the contours (Fig. 3) were compared and plotted on a graph (Fig. 4) shown. The results shows that highest stress and deformation was developed in rectangularly shaped holes while lowest was developed in elliptical ones, while an average stress and deformation occurred in rest of the clutch plates.

Both the rectangular plates performed poorly in the analysis carried out, they had the maximum amount of stress generation and total deformation which makes them the worst choice in all the seven clutch plates.

## 5 Conclusion

A comparative study for determining the stress variation and deformation occurrence in different shaped holes on a clutch plate was carried out. A brief methodology was presented and ANSYS software was used. The results showed that the sports clutch has the minimum induced stress. Usually, friction clutch plates with rectangular vents are used in commercial vehicles but on performing the analysis, it is concluded that clutch plates with elliptical vents positioned radially have optimum values of stress and deformation. Between both the elliptical plates, elliptical (positioned parallel to the radius) performed better in both tests, Von-mises stress and total deformation analysis. The triangular plate has minimum value of deformation but the induced stress is higher than the other plates except both the rectangular ones.

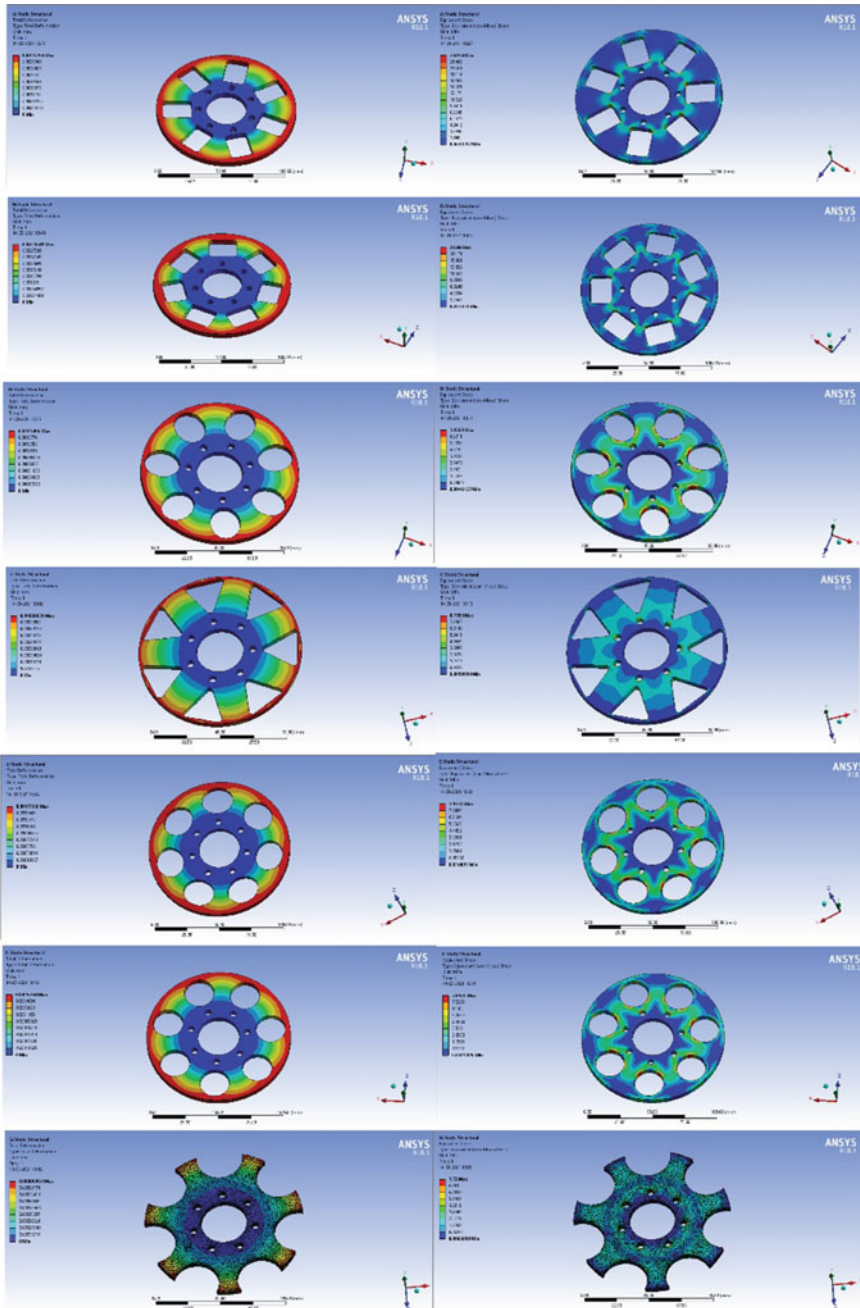


**Fig. 3** Stress and deformation contours of **a** rectangular-radial, **b** rectangular-parallel to radius, **c** elliptical-radial, **d** triangular, **e** elliptical-parallel to radius, **f** circular, **g** sports clutch



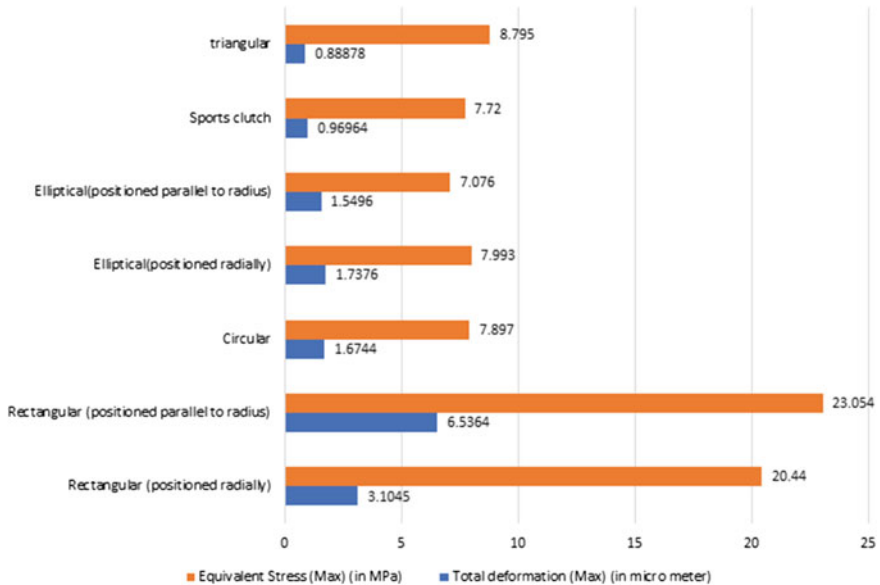


Fig. 4 Comparative stress strain results for different types of clutches

## References

1. He-yun B, Wei H, Feng-xia L (2021) Investigation of engagement characteristics of a multi-disc wet friction clutch. *Tribol Int* 159:106940.
2. Zou Q, Rao C, Barber G, Zhou B, Wang Y (2013) Investigation of surface characteristics and tribological behavior of clutch plate materials. *Wear* 302(1–2):1378–1383
3. Bezzazi M, Khamlichi A, Jabbouri A, Reis P, Davim JP (2007) Experimental characterization of frictional behavior of clutch facings using pin-on-disk machine. *Mater Design* 28(7):2148–2153
4. Abdullah O, Schlattmann J (2013) Contact Analysis of a dry friction clutch system. *ISRN Mech Eng* 2013:1–9
5. Kong J, Jang S (2020) Temperature analysis of wet clutch surfaces during clutch engagement processes based on friction pad patterns. *Int J Automot Technol* 21(4):813–822
6. Fu H, Fu L, Liu A, Zhang G (2010) finite element analysis of temperature field of clutch in tunnel boring machine. In: 2010 WASE International conference on information engineering
7. Pan H, Zhou X (2019) Simulation research on the drag torque of disengaged wet clutches. In: 2019 IEEE 5th International conference on mechatronics system and robots (ICMSR)
8. Aphale C, Schultz W, Ceccio S (2009) The influence of grooves on the fully wetted and aerated flow between open clutch plates. *J Tribol* 132(1)
9. Rohan Ramesh M, Atharva Ravindra K, Ashok B, Kannan C (2021) Optimizing thermal performance of a dry rigid clutch by varying groove pattern and friction material. *Mater Today Proc*
10. Virmani K, Madhogaria T, Baskar P (2021) Design optimization of friction lining of a clutch plate. *Mater Today Proc*
11. Vakili Rad C, Thomas F, Seay B, van Tooren M, Sockalingam S (2019) Manufacturing and characterization of novel clutch non-conventional fiber-reinforced composite laminates. *Compos Struct* 215:454–470

12. Scott W, Suntiawattana P (1995) Effect of oil additives on the performance of a wet friction clutch material. *Wear* 181–183:850–855
13. Yu L, Ma B, Chen M, Li H, Liu J, Li M (2019) Investigation on the failure mechanism and safety mechanical-thermal boundary of a multi-disc clutch. *Eng Fail Anal* 103:319–334
14. Purohit R, Khitoliya P, Koli D (2014) Design and finite element analysis of an automotive clutch assembly. *Procedia Mater Sci* 6:490–502
15. Karna P, Rao TB (2013). Analysis of friction clutch plate using FEA. *Int J Eng Res Develop.* e-ISSN: 2278-067X.
16. Zhu M, Yao P, Pu Y, Liu T (2019) Comparative study on the temperature rise of a dry dual clutch under different starting conditions. *Autom Innov* 2(1):35–44
17. Iqbal S, Al-Bender F, Ompusunggu A, Pluymers B, Desmet W (2015) Modeling and analysis of wet friction clutch engagement dynamics. *Mech Syst Signal Process* 60–61:420–436
18. Kishor Patil K, Randiv V, Mulla S, Parit R, Mane S, Kadam S (2020) Design and analysis of single plate clutch using ANSYS. *Mob Vehicle Mech* 46(2):19–31
19. Jayaraj M, Kumar S, Uppalapati S (2020) Computational modeling and analysis of multi plate clutch. *Mater Today Proc*
20. Abdullah O, Schlattmann J (2016) Thermal behavior of friction clutch disc based on uniform pressure and uniform wear assumptions. *Friction* 4(3):228–237



# Estimation of Flyer Velocity for Titan 12 (Grade 1) Plates by Pin Contact Velocity Measurement Method

Lavepreet Singh<sup>(✉)</sup>, Rishabh kumar, Yuvraj Bhardwaj, Manish singh,  
and Rajneesh Kumarr

Department of Mechanical Engineering, Galgotias University, Greater Noida, India  
punstu@gmail.com

## 1 Introduction

There are several methods available for measuring the detonation velocity of condensed explosives, which involve various degrees of sophistication. The best electrical method for the measurement of detonation velocity with sophisticated recording system is pin contactor method [1]. The pins are connected to a pulse network where the electrocontact method was used to study the initial stage of plate acceleration. While in flight, the plate successively closed contacts at fixed points in space such as that described by Crossland [1], which produces a series of positive and negative pulses and these are recorded on a recording oscillograph. The shock wave, which is ionized, shorts the pairs of pins as it reaches them, and this triggers the pulse network. Podder et al. [11] applied the photogrammetry method for measurement of distortion in welding plates and found the results close to laser measurement. Photographic method can also be employed to measure the detonation velocity, which has the advantage of continuous recording. This technique is usually employed to take a streak photograph; the third experiment was conducted by this method along with pin contact velocity measurement method.

Although there was sufficient analytical and experimental evidence to conclude the flyer plate velocity for other materials [2], the authors intended to find out the velocity of thick titanium plates. The propulsion of metal plates by layers of explosives in the sliding detonation regime is widely used in the processing of materials by explosion, as well as in conducting various types of experiments. The velocity of the flyer plate from the initial position of the detonator is the determining factor in this process through dynamic bend angle (Figs. 1 and 2).

There was a slight change from the strategy used to record profile of the plate with skewed opposition rooftop wire method was embraced and depicted by Vaidyanathan et al. [3] in which a tensioned nichrome wire was put in the arrangement, rather than utilizing nichrome wire, a bunch of metal needles were embedded in machined openings of PMMA plate at that point set under the flyer plate, and associated them with sections of nichrome wire as clarified by Kiselev [4] and appeared in Fig. 3. Vidya et al. [12] reviewed the medical applications of same with micromachining and fabrication of microstructures. The needles worked as resistors in an electric circuit. The needles were

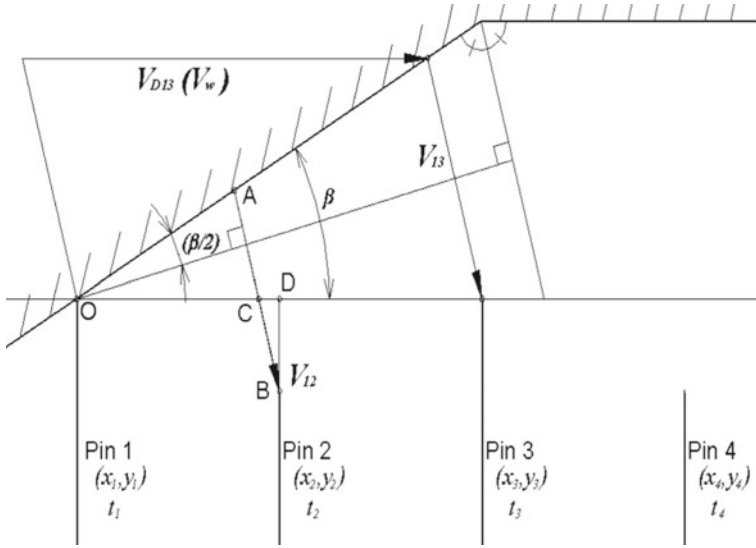


**Fig. 1** Representation of vector diagram

situated vertically on one straight line along with the longitudinal hub of the plate. While in flight, the plate progressively short-circuited the top finishes of the needles, subsequently diminishing the complete obstruction of the circuit. The voltage at the yield of the oscillograph diminished step by step for a steady estimation of current going through the circuit. It was feasible to situate the short-circuited finishes of the needles along any predetermined bend with the utilization of uniquely made layouts. The situating of the

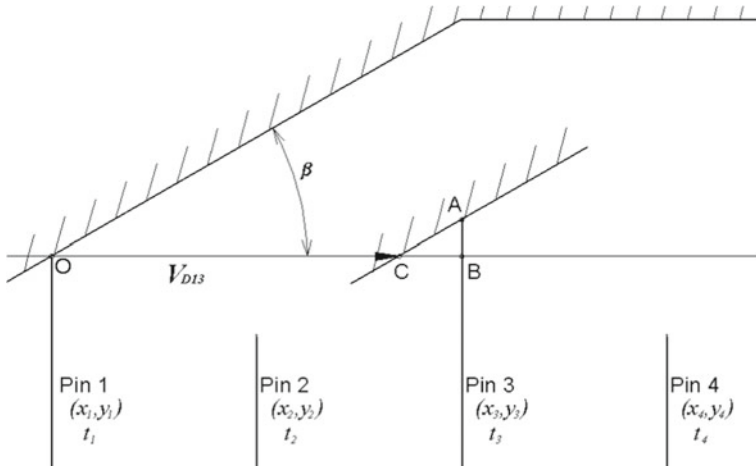


**Fig. 2** Representing the vector diagram for the pin 1 and 3 or 2 and 4 having different height when measured from the bottom surface of the flyer plate

finishes of the needles along the straight line was done cautiously. Utilizing the oscillogram to decide the hour of short-circuiting of each needle and knowing the type of the bend depicted by the short-circuited finishes of the various needles, the profile of the plane in flight was directed, and it is expected that the drive interaction was consistent. The exploratory plan is portrayed in Fig. 3.

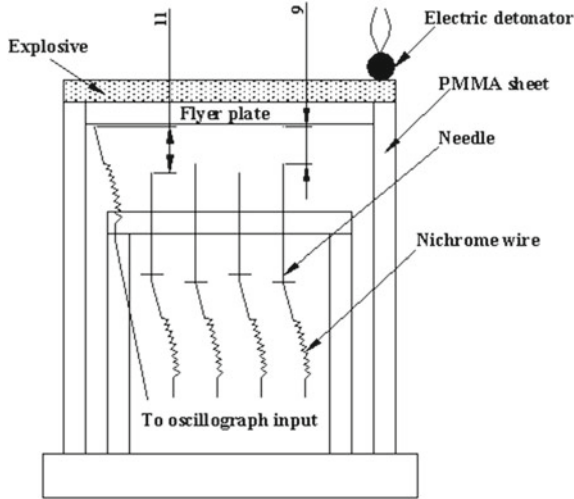


Fig. 3 Pin contact velocity measurement technique

### 1.1 The formulae's

The vector diagram of pin contact velocity measurement technique for pins 1, 2, 3, and 4 was given in Fig. 1 for the pins 1 and 3 or 2 and 4 having equal height when measured from the bottom surface of the flyer plate. If the pins 1 and 3 or 2 and 4 were arranged in different heights, then the formula for finding the detonation velocity with velocity diagram was given in Fig. 2.

Flyer (collision) velocity and collision angle (using pin 1, pin 2, pin 3)

$$\begin{aligned} \Delta t_{12} &= |t_2 - t_1|, & \Delta x_{12} &= |x_2 - x_1|, & \Delta y_{12} &= |y_2 - y_1| \\ \Delta t_{13} &= |t_3 - t_1|, & \Delta x_{13} &= |x_3 - x_1|, & \Delta y_{13} &= |y_3 - y_1| \end{aligned}$$

$$\therefore V_{12} = \frac{\Delta x_{12} \sin \beta + \Delta y_{12} \cos \beta}{\Delta t_{12} \cos(\beta/2)} \tag{1}$$

For relation between pin 1 and pin 3,

$$V_{13} = \frac{\Delta x_{13} \sin \beta + \Delta y_{13} \cos \beta}{\Delta t_{13} \cos(\beta/2)} \tag{2}$$

$$\therefore \beta = \tan^{-1} \left\{ \frac{\Delta t_{13} \Delta y_{12} - \Delta t_{12} \Delta y_{13}}{\Delta t_{12} \Delta x_{13} - \Delta t_{13} \Delta x_{12}} \right\} \quad (3)$$

Similarly, the flyer (collision) velocity and collision angle (using pin 2, pin 3, pin 4)

$$\beta = \tan^{-1} \left\{ \frac{\Delta t_{24} \Delta y_{23} - \Delta t_{23} \Delta y_{24}}{\Delta t_{23} \Delta x_{24} - \Delta t_{24} \Delta x_{23}} \right\} \quad (4)$$

$$V_{23} = \frac{\Delta x_{23} \sin \beta + \Delta y_{23} \cos \beta}{\Delta t_{23} \cos(\beta/2)} \quad (5)$$

$$V_{24} = \frac{\Delta x_{24} \sin \beta + \Delta y_{24} \cos \beta}{\Delta t_{24} \cos(\beta/2)} \quad (6)$$

Detonation (welding) velocity (using pin 1 and pin 3 or pin 2 and pin 4).

When the height of pin 3 is taller than the one of pin 1, the detonation velocity between pin 1 and pin 3,  $V_{D13}$  represents the following equation;

$$V_{D13} = \frac{\overline{OC}}{\Delta t_{13}} \quad (7)$$

where  $\Delta t_{13} = t_3 - t_1$ ,  $\Delta x_{13} = x_3 - x_1$ ,  $\Delta y_{13} = y_3 - y_1$ ,  $\overline{OC} = \overline{OB} - \overline{BC} = \Delta x_{13} - \Delta y_{13} / \tan \beta$

$$\therefore V_{D13} = \frac{\Delta x_{13} - \Delta y_{13} / \tan \beta}{\Delta t_{13}} \quad (8)$$

Therefore,  $V_{D13} = \frac{\Delta x_{13}}{\Delta t_{13}}$  when  $y_1 = y_3$ .

## 2 Experimental Procedure

Figure 3 shows the schematic representation of the pin contact velocity measurement technique. The photographs of the entire setup taken just before the explosion were shown in Fig. 4. The specimen photographs of 6 mm flyer after the explosion were shown in Fig. 5. Commercially, pure grade titanium (supplied by MIDHANI, Hyderabad, India) as per the given composition in Table.1 measuring 80 mm × 60 mm was used as flyer (thickness 6 mm and 9 mm) and was propelled by a charge of PAVEX (provided by ASAHI KASEI Chemicals Corp., Japan), with density 550 kg/m<sup>3</sup> was selected to conduct the experiments.

The parallel plate configuration method was employed with detonation velocity of 2350 and 2600 m/s for minimum and maximum thickness of explosive te, 30 mm and 60 mm, respectively. For all the experiments, the first pin was arranged at a distance of 25 mm from the point of initiation of detonator. A careful attention was given while positioning the ends of the needles along the straight line, where the distance between the first needle and the bottom surface of flyer was set as 9 mm, and the second needle was set as 11 mm alternatively from the surface below the flyer plate [8]. The space between the pins was measured as 10 mm apart for the first experiment, 10.3 mm apart

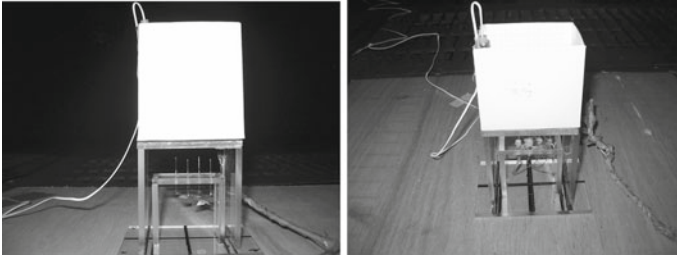


**Fig. 4** Pin contact velocity measurement setup

for the second and third experiments. For the fourth experiment, the space between the pin 1 to 2 and 3 to 4 was measured as 10.2 mm and between 2 and 3, it was 10.6 mm apart.

During the experiments, the time taken by the flyer plate to reach the pins 1, 2, 3, and 4 was recorded using a storage oscilloscope which registers the voltage signal as the flyer sweeps over the needles, on detonation, in the first experiment, the time taken for the flyer to reach the pins 1 to 2, 2 to 3 and 3 to 4 was recorded as 8.750, 9.425, and 10.000  $\mu\text{s}$ , respectively; in second experiment, it was recorded as 4.900, 6.800, and 7.600  $\mu\text{s}$  [9]. During the third experiment, a high-speed photo recorder technique was also incorporated for the measurement of velocity of the flyer plate along with pin contact velocity measurement technique. For the fourth experiment, the time taken from the pins 1 to 2, 2 to 3, and 3 to 4 was 2.710  $\mu\text{s}$ , 3.690  $\mu\text{s}$ , and 5.340  $\mu\text{s}$ , respectively (Fig. 6).

The recorded results of oscillograph were shown in Figs. 7 and 8. The details of oscillograph results as per the given figures for 1, 2, 3, and 4th experiments were reported.

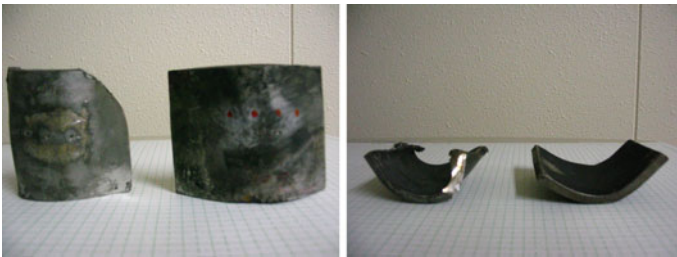


**Fig. 5** Specimen photographs of 6 mm flyer after the explosion

**Table 1** Chemical compositions of material (mass %)

Materials	C	O <sub>2</sub>	N	Fe	Ti
Titan 12 Spl. ASTM 1	–	0.1	0.05	0.2	99.8

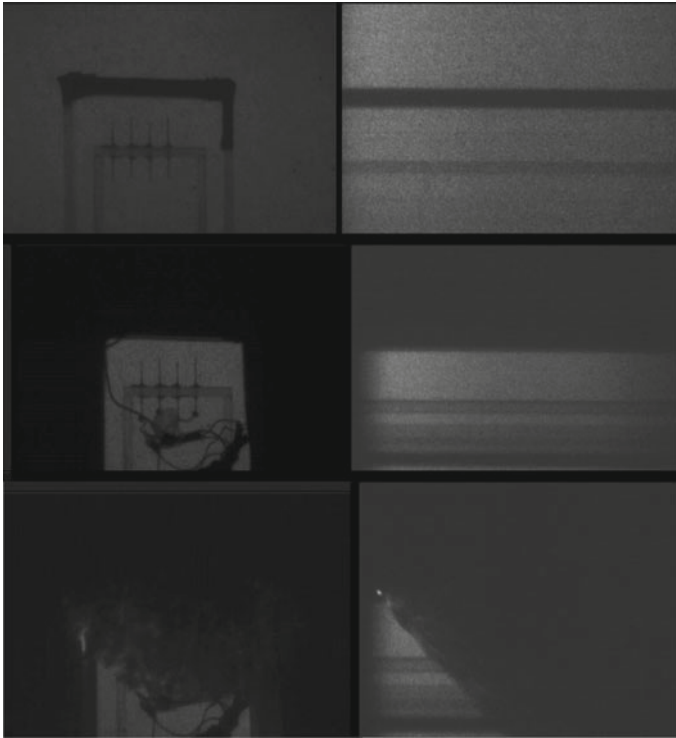


**Fig. 6** Streak photograph taken during the third experiment

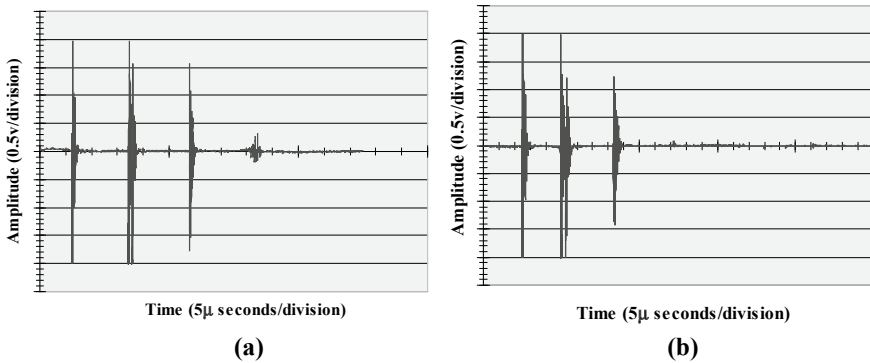


**Fig. 7 a, b** Recorded oscillograph of first and second experiment

The experimental conditions and the results were shown in Table 2. The experimental value for first experiment with  $t_f = 6$  mm and  $t_e = 30$  mm, the analysis of the signals showed that at a distance of 25 mm from the initial position, the angle of the plate rotation  $\beta$ , during the propulsion, was obtained as  $79^\circ$  at  $VCE = 1062$  m/s, but the expected theoretical value [6] was  $VCT = 2350$  m/s with  $r = 0.6$ , and the experimental



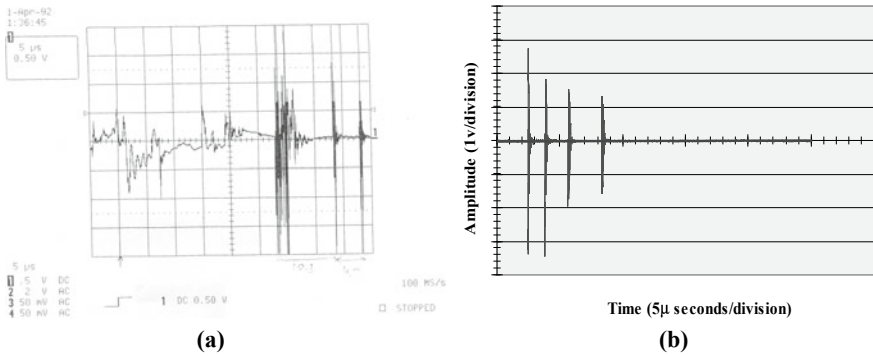


**Fig. 8 a** Recorded oscillograph of collapsed geometry of third experiment, **b** recorded oscillograph of successful fourth experiment

and theoretical value of flyer plate velocity were  $VPE = 140 \text{ m/s}$  and  $VPT = 366 \text{ m/s}$ , respectively.

### 3 Result

Similarly, for second experiment with  $t_f = 6 \text{ mm}$  and  $t_e = 60 \text{ mm}$ , the result was obtained as  $\beta = 50^\circ$  at  $VCE = 1595 \text{ m/s}$ , theoretical value calculated as  $VCT = 2600 \text{ m/s}$  with  $r = 1.21$ , and the experimental value of  $VPE = 149 \text{ m/s}$  and  $VPT = 492 \text{ m/s}$ . It was found that the error (difference between theoretical and experimental) due to wrong positioning of flyer plate over the support of PMMA plate, then which was corrected during the velocity measurement of 9 mm thick titanium flyer plates, in which the flyer plate was kept in between the PMMA plate instead of keeping it over the PMMA plate.

During the third experiment with  $t_f = 9 \text{ mm}$  and  $t_e = 30 \text{ mm}$ , a streak photograph was also taken using high-speed photo recorder for the measurement of velocity of the flyer plate along with pin contact measurement method. The gas expansion was completely arrested while taking streak photographs, hence a recorded series of streak photographs as given in Fig. 6 show the complete collapse of entire geometry, due to which the data could not be able to measured using pin contact method (Fig. 8a) for the calculation of  $\beta$  and other parameters from the initial position of the detonation. A satisfactory results were obtained while conducting fourth experiment, the result shows for the flyer plate with  $t_f = 9 \text{ mm}$  and  $t_e = 60 \text{ mm}$ , the angle of rotation of the plate as  $\beta = 55^\circ$  at  $VCE = 2776 \text{ m/s}$ , the theoretical value was  $VCT = 2600 \text{ m/s}$  with  $r = 0.81$ , and the experimental value of flyer plate velocity  $VPE = 300 \text{ m/s}$  was near by the theoretical value of  $VPT = 357 \text{ m/s}$  [10].

### 4 Discussion

Literally, few papers were available for the flyer plate velocity measurements by using explosive welding technique. Particularly, for 6 and 9 mm thickness titanium flyer plates,

**Table 2** Experimental conditions and results

Ex. No.	Flyer plate thickness, mm	Thickness of explosive, mm	Loading ratio, R	Theoretical flyer plate velocity, VPT, m/s	Experimental flyer plate velocity, VPE, m/s	Theoretical collision velocity, VCT, m/s	Experimental collision velocity, VCE, m/s	Experimental dynamic bend angle, $\beta$ , degrees
1	6	30	0.60	366.72	140	2350	1062	79.48
2	6	60	1.21	492.86	149	2600	1595	50.09
3	9	30	0.40	258.12	–	2350	Collapsed	–
4	9	60	0.81	357.62	300	2600	2776	55.9

no such papers were available. Hence, a series of experiments with minimum and maximum thickness of explosives as 30 mm and 60 mm, respectively, were selected and conducted, and for both the thickness of plates and parallel plate technique along with pin contact velocity measurement, method was adopted to find out the required velocity.

The results obtained were shown in Table 2. In first experiment, the value of  $\beta$  calculated from the Eq. (3) was  $79^\circ$ . While comparing the experimental collision velocity of 1062 with the theoretical value of 2350 m/s, the result shows 50% less value for  $r = 0.6$ , and the experimental flyer plate velocity calculated from the Eq. (1) was 140 m/s, which was also less when compared with theoretical value of 366 m/s. Similarly, for second experiment, the value of  $\beta$  was  $50^\circ$  with experimental collision velocity of 1595 m/s, it was also concluded to be very less when compared with theoretical value of 2600 m/s for  $r = 1.21$ , and the experimental value of flyer velocity was calculated as 149 m/s, when compared with theoretical value of 492 m/s. After conducting the first two experiments by 6 mm flyer plate, the results were not reached its required level, hence a small change was made in the experimental setup as shown in Fig. 1, and in third and fourth experiments for the velocity measurement for 9 mm thick flyer plates, the plates were kept in between the PMMA plate instead of keeping it over the PMMA plate.

While comparing the Fig. 7a with Fig. 8b, there was a less response of the fourth pin after the explosion, also when comparing Fig. 7b with Fig. 8b, it was clearly evident that during sliding of flyer plate after detonation of charges, fourth pin does not get any contact. Hence, from the first two experiments due to the wrong positioning of the flyer plate, the pins does not reaches its estimated value of collision velocity VCE and flyer plate velocity VPE. For the first experiment from Fig. 7a, the components of the flyer velocity and dynamic bend angle of Eqs. (1) and (3) were

$$\begin{aligned} \Delta t_{12} &= |t_2 - t_1| = 8.750 \mu\text{s}, & \Delta x_{12} &= |x_2 - x_1| = 10 \text{ mm}, \\ \Delta y_{12} &= |y_2 - y_1| = 9 - 11 = -2 \text{ mm} \\ \Delta t_{13} &= |t_3 - t_1| = 8.750 + 9.425 = 18.175 \mu\text{s}, \\ \Delta x_{13} &= |x_3 - x_1| = 10 + 10 = 20 \text{ mm}, \\ \text{and } \Delta y_{13} &= |y_3 - y_1| = 9 - 9 = 0. \end{aligned}$$

For the second experiment from Fig. 7b, the components for the Eqs. (1) and (3) were

$$\begin{aligned} \Delta t_{12} &= |t_2 - t_1| = 4.900 \mu\text{s}, & \Delta x_{12} &= |x_2 - x_1| = 10.3 \text{ mm}, \\ \Delta y_{12} &= |y_2 - y_1| = 9 - 11 = -2 \text{ mm} \\ \Delta t_{13} &= |t_3 - t_1| = 4.900 + 6.800 = 11.700 \mu\text{s}, \\ \Delta x_{13} &= |x_3 - x_1| = 10.3 + 10.3 = 20.6 \text{ mm}, \\ \text{and } \Delta y_{13} &= |y_3 - y_1| = 9 - 9 = 0. \end{aligned}$$

While conducting fourth experiment for finding the velocity of 9 mm thick titanium flyer plate by pin contact velocity measurement technique shows the successful result as in Fig. 8b, the recorded oscillograph showing the complete contact with all the four pins when flyer sweeps over it due to the exact positioning of the flyer kept in between the PMMA plates and reaches with the collision velocity of 2776 m/s and flyer velocity of

300 m/s, when compared with theoretical value of 2600 m/s and 357 m/s, respectively, with dynamic bend angle of  $55^\circ$  for the  $r$  value of 0.81. From Fig. 8b, the components for the Eqs. (1) and (3) were given in the following.

Model calculation of flyer (collision) velocity and collision angle fourth experiment (using pin 1, pin 2, pin 3)

$$\Delta t_{12} = |t_2 - t_1| = |2.710 - 0| = 2.710 \mu\text{s}$$

$$\Delta x_{12} = |x_2 - x_1| = |10.2 - 0| = 10.2$$

$$\Delta y_{12} = |y_2 - y_1| = |9 - 11| = -2 \text{ mm}$$

$$\Delta t_{13} = |t_3 - t_1| = |(2.710 + 3.690) - 0| = 6.400 \mu\text{s}$$

$$\Delta x_{13} = |x_3 - x_1| = |(10.2 + 10.6) - 0| = 20.8 \text{ mm}$$

and

$$\Delta y_{13} = |y_3 - y_1| = |9 - 9| = 0$$

$$\begin{aligned} \beta &= \tan^{-1} \left\{ \frac{\Delta t_{13} \Delta y_{12} - \Delta t_{12} \Delta y_{13}}{\Delta t_{12} \Delta x_{13} - \Delta t_{13} \Delta x_{12}} \right\} \\ &= \tan^{-1} \left\{ \frac{(6.400)(-2) - (2.710)(0)}{(2.710)(20.8) - (6.400)(10.2)} \right\} = 55.9^\circ \end{aligned}$$

$$\therefore V_{12} = \frac{\Delta x_{12} \sin \beta + \Delta y_{12} \cos \beta}{\Delta t_{12} \cos(\beta/2)} = \frac{(10.2)(\sin 55^\circ) + (-2)(\cos 55^\circ)}{(2.710) \cos(55^\circ/2)} = 300.9 \text{ m/s}$$

Similarly for relation between pin 1 and pin 3,

$$V_{13} = \frac{\Delta x_{13} \sin \beta + \Delta y_{13} \cos \beta}{\Delta t_{13} \cos(\beta/2)} = 300.9 \text{ m/s}$$

$$V_{C1} = \frac{\Delta x_1 + \Delta x_2}{\Delta t_1 + \Delta t_2} = \frac{10.2 + 10.6}{2.710 + 3.690} = 3.25 \text{ mm}/\mu\text{s} = 3250 \text{ m/s}$$

$$V_{C2} = \frac{\Delta x_2 + \Delta x_3}{\Delta t_2 + \Delta t_3} = \frac{10.6 + 10.2}{3.690 + 5.340} = 2.303 \text{ mm}/\mu\text{s} = 2303 \text{ m/s}$$

$$\therefore V_C = \frac{V_{C1} + V_{C2}}{2} = \frac{3250 + 2303}{2} = 2776 \text{ m/s}$$

Similarly, the flyer (collision) velocity and collision angle (using pin 2, pin 3, pin 4)

$$\beta = \tan^{-1} \left\{ \frac{\Delta t_{24} \Delta y_{23} - \Delta t_{23} \Delta y_{24}}{\Delta t_{23} \Delta x_{24} - \Delta t_{24} \Delta x_{23}} \right\} = 43.35^\circ$$

$$V_{23} = \frac{\Delta x_{23} \sin \beta + \Delta y_{23} \cos \beta}{\Delta t_{23} \cos(\beta/2)} = 1710 \text{ m/s}$$

$$V_{24} = \frac{\Delta x_{24} \sin \beta + \Delta y_{24} \cos \beta}{\Delta t_{24} \cos(\beta/2)} = 1710 \text{ m/s}$$

## 5 Conclusion

From the sequence of experiments conducted above, it was concluded that for the titanium flyer of 6 and 9 mm thickness plates, and the experimental flyer plate velocity (VPE) could be fixed as 300 m/s or more with dynamic bend angle  $55^\circ$ , loading ratio of 0.81, and detonation velocity of 2600 m/s by using PAVEX explosives with parallel plate configuration technique.

There is a vast scope for determining the flyer plate velocity of various thickness plates by pin contact velocity measurement technique with parallel plate configuration using powder explosives.

**Acknowledgements.** All these experiments were performed, and the facilities were sponsored by Shock Wave and Condensed Matter Research Center of the 21st Century COE program on Pulsed Power Science, Kumamoto University, Japan.

## References

1. Crossland B (1982) Explosive welding of metals and its application. Oxford University Press, pp 46–47 (1982)
2. Manikandan P, Hokamoto K, Raghukandan K, Chiba A, Deribas AA (2005) The effect of experimental parameters on the explosive welding of Ti and stainless steel. *Sci Tech. Energy Matter* 66:370–374
3. Vaidyanathan PV, Rathinasabapathi M, Ramanathan AR (1989) A note on the flyer-plate velocity in explosive cladding. *J Mech Work Tech* 18:343–350
4. Kiselev V (1995) Estimation of the parameters of metal plates propelled by the sliding detonation of charges of condensed explosives in the initial phase of the process. *Comb Exp Shock Waves* 31(1):134–137
5. Kuroda T (1991) A study for explosive welding of the difficult-to-weld materials. Ph.D. thesis, Kumamoto University, Kumamoto, Japan, pp 27–29
6. Hokamoto K, Izuma T, Fujita M (1993) New explosive welding technique to weld aluminum alloy and stainless steel plates using a stainless steel intermediate plate. *Metall Trans* 24(A):2289–2297
7. Deribas A (2001) Impact engineering and application. In: Chiba A, Tanimura S, Hokamoto K (eds) Elsevier, London, pp 527–534
8. Crossland B, Williams JD (1970) Explosive welding. *Metall Rev* 15(1):79–100
9. Daehn GS (2006) High-velocity metal forming. In: *Metalworking: sheet forming (ASM Handbook Volume 14 B)*, pp 405–418
10. Hopler Jr RB (1961) An investigation of the factors influencing the design of a dense prilled ammonium nitrate-fuel oil mixture
11. Podder D, Gadagi A, Mandal NR, Kumar S, Singh L, Das S (2017) Numerical investigation on the effect of thermo-mechanical tensioning on the residual stresses in thin stiffened panels. *J Ship Prod Design* 33(1)
12. Vidya S, Wattal R, Singh L, Mathiyalagan P (2021) CO<sub>2</sub> Laser micromachining of polymethyl methacrylate (PMMA): a review. *Adv Manuf Ind Eng* 939–945



# Automobile Sales Forecasting and Correlation with Economic Indicators: A Comprehensive Intra-Region Case Study

Waquar Shoaib and J. Sanjog<sup>(✉)</sup>

Department of Mechanical Engineering, Vaugh Institute of Agricultural Engineering and Technology (VIAET), Sam Higginbottom University of Agriculture, Technology and Sciences (SHUATS), Prayagraj, Uttar Pradesh, India  
sanjog.j@shuats.edu.in

## 1 Introduction

Production normally commences before the actual demand from customers is known. Therefore, the production should be started based on the expected demand which is known as forecasted demand. Forecasting is defined as “A technique for using past experiences to project expectation for the future” [1]. Here, it is observed from the definition that forecasting is not a prediction but the knowledge based on the projection obtained from the past data. Forecasting can be used for demand planning, purchasing decisions, strategic plans, scheduling, etc. in the manufacturing sector.

The two major categories of forecasting are qualitative forecasting and quantitative forecasting. The forecast for a product with no previous sales history will be based on personal judgment or experience. The advantage of this method is that fast results may be obtained. Sometimes qualitative forecasts are very important because they are the only method available and feasible. The common methods of qualitative forecasting are market surveys, Delphi or panel consensus, life cycle analogy, and informed judgment. The concept of quantitative forecasting method is based on the relationship between variables. Quantitative forecasting can be done using past data. The most commonly used quantitative forecasting [1] methods are time series, simple moving averages, weighted moving averages, simple exponential smoothing, and regression. Efficient forecasting method is very important for successful management [2]. Rothe [2] discussed the importance of forecasting for companies, users and preparers of forecasts, forecasting techniques employed, and use of macroeconomic data, forecasting error, and management of forecasting systems. Exponential smoothing relies on three basic methods: simple exponential smoothing, trend corrected exponential smoothing, and seasonal variation [3]. Johnston et al. [4] analyzed the combination of two simple moving averages. Simple moving averages are generally used to forecast future value and estimate the current level of the process. The linear combination of two simple moving averages can be more accurate [4]. Robb and Silver [5] presented the all possible combination of moving averages up to a given number of periods. Combining of moving averages can improve sales

forecasting. The composite moving average should be considered a relatively robust, simple, and effective alternative to other simple forecasting methods [5]. Each forecasting technique is unique and can be applied accurately for certain situations [6].

Correlation analysis is one of the most widely used statistical methods for summarizing scientific research data [7]. Correlation analysis is very convenient to determine the type of relationship between two variables. The correlation coefficient is generally referred to as Pearson's correlation coefficient ( $r$ ) [7]. The correlation coefficient considers both the magnitude and direction to analyze the relationship between variables. The value of ( $r$ ) lies between  $-1$  to  $+1$ . The value of  $r$  closer to  $\pm 1$  indicates that there is a linear relationship between the variables [7]. If the value of  $r$  is found to be zero it means that there is no correlation between variables [7]. The strength of the correlation is independent of the sign as it shows the proportionality between the variables [7].

The various macroeconomic factors such as consumer price index, gross domestic product, exchange rate, interest rate, and unemployment rate influence the sales of passenger cars in Malaysia [8]. Using data from the year 1981 to 2010, it was observed that there is a positive correlation between GDP and passenger car sales, while on the other hand, there was an inverse relationship between the car sales and other macroeconomic factors [8]. Small car sales in America were nearly constant from 1970 to 1973 but with the sudden rise in gasoline price, the small car sales increased dramatically [9]. However, there was no effect on overall car sales, but the distribution of big and small automobile sales was directly affected by the price of the gasoline [8]. Oil price changes influences the economic activity of a country [10]. The macroeconomic variables such as gross domestic product, inflation, unemployment rate, and load rate have a long term correlation with automobile sales for Malaysia, Singapore, Thailand, and the Philippines [11]. The GDP has a positive relationship with the sales of the car on the other hand increase in inflation, unemployment rate, and interest rate have a negative influence on car sales [11]. The relationship between macroeconomic factors and car sales in Malaysia was examined [12]. The considered macroeconomic factors were interest rate, inflation rate, and unemployment rate, and gross domestic product. It was found that gross domestic product had a positive relation with the number of car sales [12]. The interest rate, inflation rate and unemployment rate had a negative relationship with the number of car sales [12]. A study in Indonesia showed that GDP and the growth of GDP significantly influenced car and motorcycle sales [13]. Another study comprising of first four (China, USA, Japan, and Germany) largest automobile manufacturing nations showed that the real GDP, car production, gasoline price had positive effect while change in per capita GDP, inflation and exchange rate caused negative influence on the car sales [14].

Investigations aimed at finding the appropriate forecasting for automobile sales and the correlation between actual automobile sales volume and the selected economic indicators (industrial production, consumer price index, exchange rate, unemployment rate, and crude oil production) within a particular region needs to be performed for better understanding the behavior of the selected variables in each country. Further, there is a need to understand the existence of a common trend if any regarding the ease of doing business score, foreign direct investment as a percentage of gross domestic product and gross domestic product on the results of correlation analysis between the actual sales and the selected macroeconomic variables. Therefore, the present descriptive investigation

aims to find out the appropriate traditional forecasting technique applicable within a particular region as an individual company case study. The investigation also aims to find the correlation between the actual automobile sales volume and the certain economic indicators within a particular region and also attempts to group the countries based on correlation results using the available information for a leading automobile manufacturing company and draw suitable inferences. The objectives of the investigations are to find the best traditional forecasting technique applicable within a region and to investigate the correlation between vehicle sales and the selected economic indicators.

## 2 Results

### 2.1 Mean Absolute Percentage Error (MAPE)

Using the actual automobiles sales data [15] for a particular company, the forecasting was performed using four different traditional forecasting (simple moving averages, weighted moving averages, simple exponential smoothing method, and regression forecasting) methods for the selected countries. The simple moving averages and weighted moving averages are calculated for different moving periods (2-months moving average, 3-months moving average, 4-months moving average, 5-months moving average, and 7-months moving average). Additionally, the Mean Absolute Percentage Error (MAPE) for each method is also tabulated as shown in Table 1. The MAPE is calculated for simple and weighted moving average methods considering multiple periods. The MAPE is also obtained for simple exponential smoothing and regression forecasting.

### 2.2 Correlation Analysis

Five macroeconomics variables (industrial production, consumer price index, exchange rate, unemployment rate, and crude oil production) were considered. Pearson's correlation coefficient was calculated between actual sales volume and the corresponding data [16] for various macroeconomic variables of the selected countries in Asia. Some correlations could not be performed due to lack of availability of reliable data. The summary of the correlation analysis is presented in Table 2.

### 2.3 Comparison of Correlation Results with FDI, Ease of Doing Business Score and GDP for Identifying Similarities Among the Countries

The factors, namely, ease of doing business, FDI as a percentage of GDP, and GDP for the selected countries [16] were compared with the correlation results for identifying any similarities among the countries. It is considered normal for any country to receive 2–3% of the GDP as FDI [17]. Indonesia, Malaysia, and Philippines received 2–3% FDI as a percent of their GDP during the years 2017, 2018, and 2019. It was observed that Indonesia and Malaysia showed positive, weak and Philippines exhibited negative, weak correlation between actual sales volume for the industrial production. The correlation between the actual sales volume and the consumer price index indicated that Indonesia, Malaysia, and Philippines had negative, weak correlation. The correlation



**Table 1** Average MAPE using different forecasting methods

Forecasting method	Average MAPE (%)									
	China	Indonesia	Malaysia	Philippines	Pakistan	Republic of Korea	Thailand	Taiwan	Vietnam	
2 MMA	10.22	11.94	29.03	12.41	15.83	23.18	11.86	27.41	26.55	
2 MWMA	9.96	11.84	27.25	11.53	15.61	18.44	11.00	27.36	26.29	
3 MMA	10.30	10.48	32.56	14.06	15.48	26.76	11.35	27.09	26.41	
3 MWMA	9.65	10.43	27.45	11.45	14.87	18.43	10.73	26.70	25.58	
4 MMA	10.42	10.20	31.70	13.63	18.49	28.57	11.80	26.36	27.37	
4 MWMA	9.54	9.98	26.33	10.59	15.19	18.75	10.60	25.40	26.27	
5 MMA	10.76	9.89	33.94	13.07	19.94	29.82	11.78	25.01	27.18	
5 MWMA	9.72	9.72	27.06	9.96	15.44	18.89	10.54	21.89	25.60	
7 MMA	9.94	9.83	35.95	13.68	22.16	30.20	11.35	22.22	26.17	
7 MWMA	10.17	8.77	27.70	10.08	14.29	19.43	10.49	14.96	24.02	
SES	10.59	9.15	27.02	11.41	15.50	18.44	11.47	23.53	24.35	
Regression	8.27	8.15	27.56	12.71	20.92	26.45	12.14	21.40	24.93	

MAPE—Mean Absolute Percentage Error, MMA—Month Moving Average, MWMA— Month Weighted Moving Average, SES— Simple Exponential Smoothing

**Table 2** Summary of the correlation analysis

Countries	Macroeconomic variables														
	Industrial production			Consumer price index			Exchange rate			Unemployment rate			Crude oil production		
	Correlation coefficient	Strength of correlation coefficient	Correlation coefficient	Strength of correlation coefficient	Correlation coefficient	Strength of correlation coefficient	Correlation coefficient	Strength of correlation coefficient	Correlation coefficient	Strength of correlation coefficient	Correlation coefficient	Strength of correlation coefficient	Correlation coefficient	Strength of correlation coefficient	
China	Positive	Medium	Positive	Strong	Positive	Weak	Positive	Weak	Negative	Strong	Negative	Strong	Negative	Weak	
Indonesia	Positive	Weak	Negative	Weak	Negative	Weak	Negative	Weak	-	-	Positive	-	Positive	Weak	
Malaysia	Positive	Weak	Negative	Weak	Negative	Weak	Positive	Weak	-	-	Negative	-	Negative	Medium	
Pakistan	Positive	Medium	Negative	Strong	Negative	Medium	Negative	Medium	-	-	Positive	-	Positive	Strong	
Philippines	Negative	Weak	Negative	Weak	Negative	Medium	Negative	Medium	Positive	Weak	Negative	Weak	Negative	Weak	
Republic of Korea	Negative	Weak	Positive	Weak	Negative	Medium	Negative	Medium	Positive	Weak	-	Weak	-	-	
Taiwan	-	-	Positive	Weak	Positive	Weak	Positive	Weak	Positive	Weak	-	Weak	-	-	
Thailand	Positive	Weak	Positive	Strong	Negative	Medium	Negative	Medium	Positive	Weak	Negative	Weak	Negative	Weak	
Vietnam	Positive	Weak	Positive	Medium	Positive	Medium	Positive	Medium	Negative	Weak	Negative	Weak	Negative	Medium	

analysis between the actual sales volume and the exchange rate for Indonesia, Malaysia, and Philippines revealed negative weak, positive weak, and negative medium correlation, respectively. The crude oil production and actual sales volume correlation analysis for Indonesia, Malaysia, and Philippines showed positive weak, negative medium, and negative weak correlation, respectively.

Malaysia, Republic of Korea and Taiwan showed score of above 75 regarding the ease of doing business during the years 2017, 2018, and 2019. It was observed that Republic of Korea and showed positive correlation whereas Malaysia shows negative correlation between the actual sales volume and the industrial production. Malaysia showed negative correlation whereas Republic of Korea and Taiwan showed positive correlation for consumer price index. Republic of Korea showed negative correlation whereas Malaysia and Taiwan showed positive correlation between actual sales volume and exchange rate. The correlation between actual sales volume and unemployment rate is positive for the Republic of Korea and Taiwan. The correlation analysis between crude oil production and actual sales volume for Malaysia showed negative correlation.

The Gross Domestic Product (GDP) of China, Republic of Korea and Indonesia were significantly much higher for the years 2017, 2018, and 2019, when compared to Taiwan, Thailand, Philippines, Malaysia, Pakistan, and Vietnam. It was observed that China and Indonesia showed positive correlation while Republic of Korea showed negative correlation between actual sales volume and the industrial production. For consumer price index China and Republic of Korea showed positive correlation and Indonesia showed negative correlation. For exchange rate Republic of Korea and Indonesia showed negative correlation and China showed positive correlation. For unemployment rate China showed negative result and Republic of Korea showed positive correlation. For crude oil production China and Indonesia showed negative correlation.

Taiwan, Thailand, Philippines, Malaysia, Pakistan, and Vietnam have comparatively lower GDP when compared with China, Republic of Korea and Indonesia for the years of 2017, 2018, and 2019. For the industrial production Thailand, Malaysia, Pakistan, and Vietnam showed positive correlation whereas Philippines showed negative correlation. For consumer price index, Taiwan, Thailand, and Vietnam showed positive correlation while Philippines, Pakistan, and Malaysia showed negative correlation. For exchange rate Thailand, Philippines, and Pakistan showed negative correlation on the other hand Taiwan, Malaysia, and Vietnam shows positive correlation. Regarding the unemployment rate, Taiwan, Thailand, and Philippines showed positive correlation whereas Vietnam showed negative correlation. The correlation analysis between crude oil production and actual sales volume for Thailand, Philippines, Malaysia, and Vietnam showed negative correlation and Pakistan showed positive correlation.

### **3 Summary, Conclusion, and Scope for Future Work**

#### **3.1 Summary**

The forecasting analysis of automobile sales is a very crucial factor for any automobile company. The automobile industry in general will suffer financial loss without proper identification of the most accurate method for forecasting automobile sales. There are different methods of forecasting. For the present study, the chosen methods were simple

moving averages, weighted moving averages, simple exponential smoothing method, and regression forecasting method. The different periods considered for simple and weighted moving averages were two months, three months, four months, five months, and seven months. Forecasting was done for nine countries of Asia using all the four different methods. The forecasting error was calculated by Mean Absolute Percentage Error (MAPE). It was found that the regression forecasting method showed good results for China and Indonesia. On the other hand, the weighted moving average showed minimum error for Philippines, Pakistan, Republic of Korea, Thailand, Taiwan, and Vietnam.

The macroeconomic factors have a tendency to influence the sales of automobiles. The macroeconomic factors considered in the present case study were industrial production, consumer price index, exchange rate, unemployment rate, and crude oil production. To find out the type of relationship between the macroeconomic factors and automobile sales, Pearson's correlation coefficient methodology was utilized. Regarding the industrial production, six countries out of eight countries considered showed a weak positive correlation. The consumer price index five countries showed a positive correlation when compared with their automobile sales, while the other four countries were found to have a negative correlation. The relationship between the vehicle sales and the exchange rate of the four countries showed a positive but weak correlation. However, the relationship between the vehicle sales and the exchange rate for the five other countries exhibited a negative correlation signifying the presence of a negative linear correlation between exchange rate and actual car sales. A weak positive correlation between automobile sales and the unemployment rate was observed for most of the countries but not necessarily a linear correlation. Crude oil production and actual automobile sales indicated a negative linear correlation for five countries out of the seven countries considered.

### **3.2 Conclusion**

The weighted moving average forecasting method exhibited more accurate sales forecasting for most but not all of the selected countries when compared with the other methods considered in the present case study. Hence, it is concluded that any one sales forecasting method may not accurately capture the sales trend of an individual company for all the countries. An individual firm needs to find out the best forecasting technique applicable for analyzing future demand for each of the countries in any given region. The macroeconomic variables considered for the present study does not always positively influence the automobile sales for all the countries. The countries which had similar characteristics with respect to the scores for ease of doing business, foreign direct investment as a percentage of GDP, and gross domestic product did not show similar results on the basis of the correlation analysis between actual sales and the selected macroeconomic indicators.

### **3.3 Future Scope**

Non-traditional or hybrid forecasting methods can be used for investigating the region wise sales forecast. Other regions (North America, South America, Europe, etc.) may be considered for investigations to find the performance of the forecasting methods. Region

wise comparisons of the results obtained by the various forecasting methods may also be studied. Investigations for studying the correlation of various other macroeconomic variables with the automobile sales may be considered in future.

## References

1. Chapman SN (2006) The fundamentals of production planning and control. 2nd Edn. Pearson/Prentice Hall, Upper Saddle River
2. Rothe JT (1978) Effectiveness of sales forecasting methods. *Ind Mark Manage* 7(2):114–118
3. Billah B, King ML, Snyder RD, Koehler AB (2006) Exponential smoothing model selection for forecasting. *Int J Forecast* 22(2):239–247
4. Johnston FR, Boylan JE, Shale E, Meadows M (1999) A robust forecasting system, based on the combination of two simple moving averages. *J Oper Res Soc* 50(12):1199–1204
5. Robb DJ, Silver EA (2002) Using composite moving averages to forecast sales. *J Oper Res Soc* 53(11):1281–1285
6. Shahabuddin S (2009) Forecasting automobile sales. *Manage Res News* 32(7):670–682
7. Taylor R (1990) Interpretation of the correlation coefficient: a basic review. *J Diagn Med Sonography* 6(1):35–39
8. Nawi AS, Ahmad SB, Mahmood WMW, Nair GKS, Nurathirah AS, Hamid BA (2013) Determinants of passenger car sales in Malaysia. *World Appl Sci J* 23:67–73
9. Duncan RS (1980) The effect of gasoline prices on automobile sales. *Am Econ* 24(1):62–66
10. Fukunaga I, Hirakata N, Sudo N (2010) The effects of oil price changes on the industry-level production and prices in the US and Japan (No. w15791). National Bureau of Economic Research
11. Muhammad F, Hussin MYM, Razak AA (2012) Automobile sales and macroeconomic variables: a pooled mean group analysis for ASEAN countries. *IOSR J Bus Manag* 2(1):15–21
12. Islam R, Ghani ABA, Kusuma B, Ho ETY (2016) An analysis of factors that affecting the number of car sales in Malaysia. *Int Rev Manage Market* 6(4)
13. Johan S (2019) Macroeconomic determinants of automobile sales in Indonesia: an empirical study in 1986–2016. *Binus Business Rev* 10(3):159–166
14. Pehlivanoglu F, Riyanti R (2018) Macroeconomic effect on the automobile sales in top four automobile production countries. *Kocaeli Üniversitesi Sosyal Bilimler Dergisi* 35:139–161
15. Toyota Motor Corporation (2021) Toyota's global sales and production up year-on-year in January for Fifth Consecutive Month. Available from: [https://global.toyota/en/company/profile/production-sales-figures/202101.html?\\_ga=2.20719931.2085423268.1615786013-1969085341.1615786013](https://global.toyota/en/company/profile/production-sales-figures/202101.html?_ga=2.20719931.2085423268.1615786013-1969085341.1615786013). Accessed on 20 Feb 2021
16. Knoema (2021) World Bank Global Economic Monitor. Available from: <https://knoema.com/WBGEM2020Mar/world-bank-global-economic-monitor>. Accessed on 15 Mar 2021
17. Anonymous (2021) India: foreign direct investment, percent of GDP. Available from: [https://www.theglobaleconomy.com/India/Foreign\\_Direct\\_Investment/#:~:text=FDI%20is%20reported%20on%20an,by%20its%20gross%20domestic%20product](https://www.theglobaleconomy.com/India/Foreign_Direct_Investment/#:~:text=FDI%20is%20reported%20on%20an,by%20its%20gross%20domestic%20product). Accessed on 20 Mar 2021



# A Study on Potential and Economic Viability for Developing Infrastructure of Electric Vehicles and Solar Powered Charging Stations in Delhi

Durgesh Kumar, Chetan Raj Chauhan<sup>(✉)</sup>, Vidhu Bhardwaj, and Sarita Baghel

Delhi Technological University, New Delhi, India  
cchauhan1206@gmail.com

## 1 Introduction

As the world's dependence on oil becomes highly unreliable, countries worldwide are calling for the development of natural alternatives. India is also the world's fourth-largest contributor to greenhouse gas emissions (GHG). The transportation industry is responsible for 1/10th of India's CO<sub>2</sub> emissions (INCCA, 2010). To move toward sustainable development, the National Action Plan for Climate Change (NAPCC) of India acknowledges that Green House Gas pollution from transportation can be minimized by integrating steps such as expanded usage of public transportation, improved energy efficiency of transportation vehicles and adoption of Electric vehicles [1]. Adopting electric vehicles would simply not mitigate the fossil fuels usage as electricity is still derived from non-renewable and polluting resources. As resources get exhausted, a paradigm shift in how we charge power our vehicles is needed. Currently solar contributes as less as 4% of India's electricity supply, while coal accounts for nearly 70%. By 2040, it is estimated that power generation will converge in the low 30% (see Fig. 1) [2]. India's policy aspirations, especially the goal of 450 GW of green energy by 2030, and the remarkable cost-competitiveness of solar, which outdo existing coal-fired electricity by 2030 even when combined with battery storage, are driving this drastic transformation [3].

To reach this goal, the Delhi Government believes that solar power is the most viable source of renewable energy in Delhi. It can reduce the state's electricity costs, improve energy security, and reduce reliance on outdated fossil fuels [4]. Rapid photovoltaic capacity expansion is required to realize this potential. To address these problems Delhi Electric Vehicle policy, 2020 has been adopted. The primary aim of the policy is to create Delhi as India's EV capital and increase the adoption of electric vehicles across all vehicle categories (see Fig. 2), especially in the category of 2 wheelers, Light Vehicles, public transport vehicles, and goods carriers [5]. The policy aims to accelerate the introduction of Battery Electric Vehicles (BEVs) and make a significant difference in Delhi's climate by reducing pollution from the transportation sector. While there is large investment from the government as well as the private sector, a comprehensive policy is yet to be implemented to benefit small scale agencies and individuals.

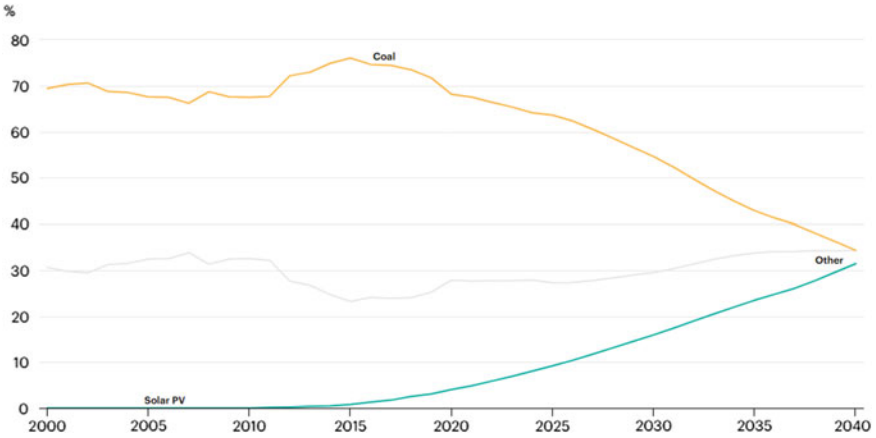


Fig. 1 Power generation share in India, 2010–2040

## 2 Potential for Solar Energy in Delhi

### 2.1 Solar Potential

Delhi has an Average Global Horizontal Irradiance of  $5.1 \text{ W m}^{-2}$  [6]. Delhi has nearly 260–300 sunshine days a year and nearly  $31^2 \text{ km}^2$  of possible rooftop area. Delhi has a solar energy capacity of 2500 MWp per year, which translates to approximately 3,500 million kWh of annual electricity production. The government/public sector accounts for 26% of this potential, followed by the commercial/industrial sector at 25% and the domestic sector at 49% [7].

Delhi projects to increase solar energy generation up to 2 GW by 2025. India has agreed to generate 40% of its energy from renewable sources by 2030 as part of the Paris

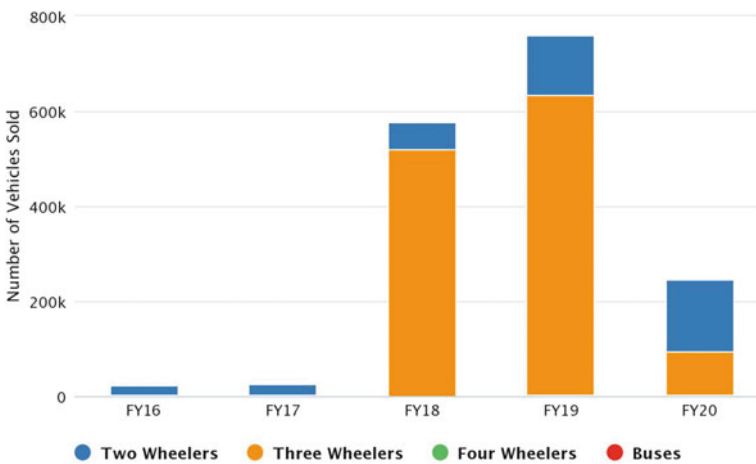


Fig. 2 India electric vehicle market size by segments

Climate Change Agreement. By 2022, the nation intends to add 100 GW of solar power to a 175 GW sustainable energy fleet, bringing total renewable capacity to 450 GW by 2030 [8]. Therefore Delhi would have approximately 1–2% of the countries share in the renewable sector in the coming 5 years.

## 2.2 Electric Vehicle Potential

The goal of the Delhi Electric Vehicle Policy is to increase the share of BEVs to 25% by 2024. Before the launch of the policy, the share of these environment-friendly vehicles in the capital was merely 0.2% of the total registered vehicles. This percentage has risen to 2.2% of all licensed vehicles since the program was implemented [9]. With incentives like up to ₹1.5 lakhs on EV purchase, Scraping incentives, Interest subvention on loans, waiver on road tax and registration fees [6].

Total EV sales reached 365,920 units in 2018, according to ISEA, and are projected to rise at a 36% annual pace until 2026. The battery industry, on the other hand, is forecast to hit USD 520 million in 2018 and rise at a rate of 30% annually over the next 5 years [10]. There are currently 72 chargers [11] on the road of Delhi working towards installing as many as 500 charging points. Delhi road length of urban roads 14,336 km. Delhi has the highest road density of 2103 km/100 km<sup>2</sup> in India [12]. The Policy aims to install charging stations every 3 km which roughly estimated to 6000 chargers to be installed to remove any charging anxiety that is the foremost problem associated with driving an EV.

## 3 Charging Infrastructure

Electric Vehicles (EVs) are powered by batteries using only 25–30 moving parts in comparison to over 2000 moving parts in any Internal Combustion Vehicle (ICV). The vehicle's range is determined by the battery's power capacity which universally is expressed in Kilowatt Hours (kWh), and the vehicle's energy consumption, measured in Watt Hours per Kilometers (Wh/km) [13]. These battery packs perform best when slowly charged (typically overnight) to their full capacity, ensuring they are ready to be used for their full range. This becomes a problem for consumers when the vehicle is required to go more than its capacity and at such instances, slow charging is highly undesirable and unacceptable for the consumer as it can take up to 6–7 h to completely charge the e-vehicle [13]. To tackle these problems we can either provide fast-charging stations throughout the nation (see Fig. 3) for an extended range or provide the users with swappable battery stations.

### 3.1 Public Charging Infrastructure

Charging an electric vehicle is an effortless task and only requires the user to plug in the charger from the Electric Vehicle Charging Station (also known as electric vehicle supply equipment, or EVSE) which is a wall-mounted electric supply box for the charging of EVs, having safety lock features which do not allow the flow of current till the car is plugged in. Below listed are the standard charging infrastructure and terminology accepted throughout the country [14].



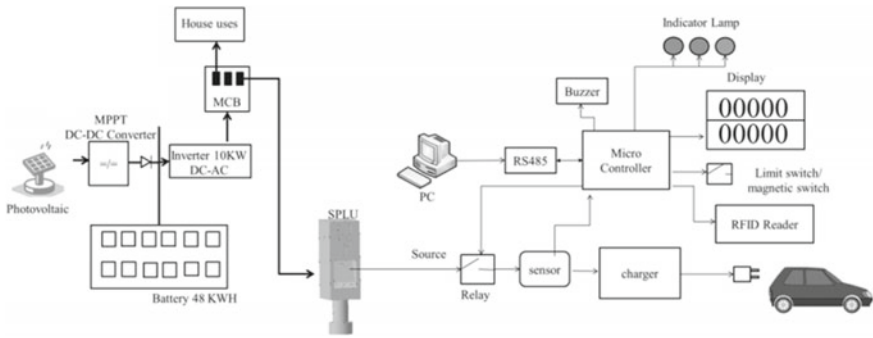


**Fig. 3** Electric vehicle charging system using fast DC charging

### 3.1.1 Public Charging Standards for EVs

In addition to home charging it is important to provide users of EVs with outside home charging stations for emergency/fast charging of their vehicle, for this the Department of Heavy Industries (DHI) formed a committee to issue Bharat Charger Specifications for AC and DC chargers (see Table 1), which are based on the Chinese standards GB/T having output voltages below 120 V and are mentioned as follows:

**Table 1** Types of chargers available for EVs in Indian Market [14]

Type of charger	Charger connectors	Specified voltage (kV)	No. of charging points/no. of connector guns (CG)
Fast	CCS2 (minimum 50 kW)	0.2–1	1/1 CG
	CHAdEMO (minimum 50 kW)	0.2–1	
	Type 2 AC (minimum 22 kW)	0.38–0.48	
Slow and moderate	Bharat standard DC-001 (15 kW)	0.072–0.2	3/3 CG of 3.3 kW each
	Bharat standard AC-001 (15 kW)	0.23	

- (a) For AC: Bharat EV Charger AC001
- (b) For DC: Bharat EV Charger DC001

Vehicles with higher battery capacity and requirement for fast charging generally have batteries with a DC output of 400 V or more and require CCS2 or CHAdEMO which will coexist with above mentioned Bharat charger [15].

*Proposed Solar Powered Charging Station (SPCS) Design.* For commercial parking spaces and open areas, a SPCS is proposed to reduce the energy demand on the grid. This carport would consist of 5 panels and would produce 1.8 kW of energy per day. The carport would be connected with Grid for giving back unutilized energy (see Fig. 4). A smart meter system consisting of RFID tags would also be installed for easy payments and bill generation.



**Fig. 4** Solar powered charging station design

### 3.2 Home Charging Infrastructure

A single-phase 230 V/15A plug is used in home chargers which is capable of drawing 2.5 KWh power. The AC supplied by EVSE is converted to DC by the vehicle's onboard charger to charge the battery pack of the EV [14].

## 4 Economic Viability

The government considers the shortage of charging stations to be a significant issue. As a result, the establishment of Public Charging Stations (PCS) has been delicensed, and any person or agency is free to create PCS as long as they follow the technological and performance requirements defined. When opposed to a comparable traditional vehicle, the high cost of EVs is a barrier to adoption. According to studies, the benefits given encourage people to buy electric vehicles. Lower operating and maintenance costs, it is said, stimulate BEV adoption [16]. ICE vehicles' energy costs were eight times higher than EVs. Lower operating costs benefit from lower electricity use and power tariffs. As a result, the average cost of ownership is smaller, which offsets the higher cost of an EV [17, 18].

### 4.1 Public Charging Infrastructure

Setting a public charging station by an agency or individual is found to be a profitable investment. Below is estimation with minimum infrastructure needed as per the GoI notification.

### 4.1.1 Cost Estimation

To study the cost (Table 2 gives a summary of estimated construction cost for a SPCS) and revenue of commercial parking space after being converted to SPCS a case study is performed on the parking space available at Akshardham temple which comprises of 1600 parking lots available for public. Here we consider that an average, a 330 W solar panel generates 44–58 kWh of energy per month, supplying us with a minimum of 1.8 kWh of energy on a daily basis. Since we used 5 of these 330 W panels in our carport layout (see Fig. 5), we can confidently estimate that each carport would generate about 9 kWh of energy per day.

**Table 2** Estimated cost for construction of SPCS

Item	Specification	Quantity	Approx. price including GST
CCS 2	50 kW	1	₹ 7,25,000
CHAdEMO	50 kW	1	₹ 7,25,000
Type 2 AC	22 kW	1	₹ 1,25,000
Luminous solar panel 330 W/24 V poly	Dimension: 6.48 × 3.25 feet Power: 330 W/24 V	5	₹49,495 (₹9,899.00 each)
Luminous hybrid inverter	MPPT inverter 2 kW	1	₹ 32,000
Luminous solar battery	150 Ah tall tubular battery	4	₹ 70,000 (₹17,500 each)
New electricity connection (250 KVA)	–	–	₹ 7,50,000
Civil construction work	–	–	₹ 2,25,000
Estimated total cost of construction of a SPCS			₹ 27,01,495

The parking lot at Akshardham Temple handles a maximum of around 1600 vehicles at any given time; converting half of these parking spaces, or 800 lots, to solar harvesting carports will produce 7200 kW of energy per day. It would be better if half of these solar harvesting carports, or 400 carports, were converted to EV charging carports with EVSEs so that electric vehicles could be charged without difficulty (refer to Table 3. For revenue estimation), as number of EVs are considerably lower than ICE vehicles.

## 4.2 Cost of Ownership of an Electric Vehicle

Residential places will charge their electric vehicles directly from Grid as setting up a carport is not economically viable in most cases. The average Indian driver travels 35 kms per day, which translates to about kWh of electricity.

The total cost of ownership of electric vehicles compared to their ICE equivalents is seen (see Table 4).

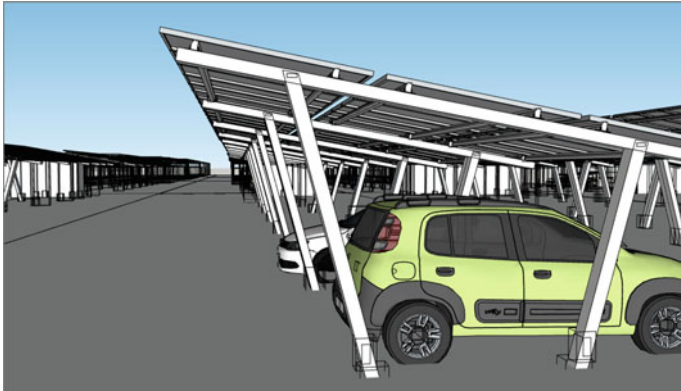


**Fig. 5** SPCS design for Akshardham parking lot

**Table 3** Estimated revenue generated through SPCS at akshardham parking lot

Revenue head	Description	Quantity (in a year)	Revenue generated
Electricity generated through solar carport	Electricity sold to customer @ ₹7.5/kW	7200 kW * 300 (no. of sunny days in Delhi)	₹ 1,62,00,000
Electricity from grid sold to customer	Margin on electricity tariff- ₹2.5/KW	380 kW (per carport/day) 400 (no of charging stations)	₹ 1,36,00,000
Net revenue generated in a year			₹2,98,00,000

**Table 4** Five year cost of similarly priced vehicles

Description	EV	Petrol	Diesel
Cost of vehicle	10 lac	10 lac	10 lac
Mileage	120 km/charge	16 km/ltr	18 km/ltr
Maintenance cost	15,000	40,000	50,000
Cost of battery	1.5 lac	0	0
Cost of units of power consumed	0.45 lac	0	0
Fuel consumption	0	3,800 l	3,400 l
Fuel expenditure	0	3 lac	2.3 lac
Total cost	12,10,000	13,40,000	13,83,000

At the normal average daily consumption of the vehicles in Indian cities, it is discovered that the cost per km of electric two-wheelers and electric three-wheelers is less than that of their ICE equivalents [16]. According to recent notification from Delhi government, electricity rates are slashed to Rs. 4.5 to further promote Electric vehicles [17]. Generally it takes about 4–8 h for an Electric Vehicle (EV) to get fully charged with Slow Charge. In sum, having an EV raises the monthly electricity bill by 1200 in New Delhi.

## 5 Conclusion

With increase in investment in infrastructure EV prices are bound to go down. As many firms like Tesla, Tata, Mahindra invest more in EV technology, research and development need to focus on Indian conditions. As things stand now Electric vehicles are still on the higher end of costs compared to ICE. By increasing the charging network, driver range anxiety will be reduced leading to increase in sales due to reliability factor. As Delhi is a heavily congested city, models like Akshardham SPCS hub as presented in this paper can be imitated in Delhi as well as other parts of the country. In the long term electric vehicles give a positive return on investment as found in the paper and can be a potential source for revenue for the Government in the long run.

## References

1. Shukla PR, Dhar S, Pathak M, Bhaskar K (2014) Electric vehicles scenarios and a roadmap for India. UNEP DTU Partnership
2. IEA, Changes in share of power generation in India in the stated policies scenario, 2010–2040. IEA, Paris. <https://www.iea.org/data-and-statistics/charts/changes-in-share-of-power-generation-in-india-in-the-stated-policies-scenario-2010-2040>
3. Sudarshan Varadhan (2021) Institute for energy economics and financial analysis. <https://ieefa.org/solar-will-equal-coal-generation-in-india-by-2040-iea/>. Last accessed 07 Apr 2021
4. Delhi Solar Policy (2016) [http://www.cbip.org/Policies2019/PD\\_07\\_Dec\\_2018\\_Policies/Delhi/1%20Summary%20Delhi%20Solar%20Policy%202016.pdf](http://www.cbip.org/Policies2019/PD_07_Dec_2018_Policies/Delhi/1%20Summary%20Delhi%20Solar%20Policy%202016.pdf). Last Accessed 07 Apr 2021
5. Delhi EV Policy 2020 [https://transport.delhi.gov.in/sites/default/files/All-PDF/Delhi%20Electric%20Vehicles%20Policy%2C%202020\\_0.pdf](https://transport.delhi.gov.in/sites/default/files/All-PDF/Delhi%20Electric%20Vehicles%20Policy%2C%202020_0.pdf). Last Accessed 07 Apr 2021
6. Average estimated Irradiance from Solcast.com
7. Uma Gupta (2021) Making Delhi a solar city. <https://www.pv-magazine-india.com/2019/11/29/making-delhi-a-solar-city/>. Last Accessed 07 Apr 2021
8. Uma Gupta (2021) Solar module to face 40 customs duty cells 25 from Apr next year. <https://www.pv-magazine-india.com/2021/03/10/solar-modules-to-face-40-customs-duty-cells-25-from-april-next-year/>. Last Accessed 07 Apr 2021
9. Delhi to cut auto emission govt will focus on electric vehicles. <https://www.hindustantimes.com/cities/delhi-news/to-cut-auto-emissions-govt-will-focus-on-electric-vehicle-infra-says-sisodia-in-budget-speech-101615315043606.html>. Last Accessed 07 Apr 2021
10. Hemant Karichrla (2019) Growth of EV in India 2018–2026. <https://electricvehicles.in/growth-of-ev-india-from-2018-2026/>. Last Accessed 07 Apr 2021
11. List of Charging Stations. [https://ev.delhi.gov.in/ui/images/List\\_of\\_Charging\\_Stations.pdf](https://ev.delhi.gov.in/ui/images/List_of_Charging_Stations.pdf). Last Accessed 07 Apr 2021

12. Basic Road Statistics India. <https://www.morth.nic.in/basic-road-statistics-india>. Last Accessed 07 Apr 2021
13. Electric Vehicle in India homepage. <http://electric-vehicles-in-india.blogspot.com/>. Last accessed 07 Apr 2021
14. Ministry of Housing and Urban Affairs homepage. <http://mohua.gov.in/>. Last Accessed 07 Apr 2021
15. Nimesh Shah (2019) Cost estimation and revenue models for a public charging stations. <https://www.pluginindia.com/blogs/cost-estimates-and-revenue-model-for-a-public-charging-station-pcs>. Last Accessed 07 Apr 2021
16. Aasness MA, Odeck J (2015) The increase of electric vehicle usage in Norway—Incentives and adverse effects. *Eur Trans Res Rev*
17. Adepetu A, Keshav S (2015) The relative importance of price and driving range on electric vehicle adoption: Los Angeles case study. *Transportation*
18. Barth M, Jugert P, Fritsche I (2016) Still underdetected: social norms and collective efficacy predict the acceptance of electric vehicles in Germany. *Transportation Research Part F: Traffic Psychology and Behaviour*
19. Kumar P, Chakrabarty S (2020) Total cost of ownership analysis of the impact of vehicle usage on the economic viability of electric vehicles in India. *Transp Res Rec* 2674(11):563–572. <https://doi.org/10.1177/0361198120947089>
20. Ramya Ranganath (2019) Delhi tariffs ev charging electric mobility. <https://mercomindia.com/delhi-tariffs-ev-charging-electric-mobility/>. Last accessed 07 Apr 2021



# Development and Characterization of Stir Cast Aluminum-Brick Powder Metal Matrix Composites

Shubham Kumar Singh<sup>1</sup>, Aniruddha Jaiswal<sup>2</sup>, Manvandra Kumar Singh<sup>3</sup>,  
Ashwini Kumar<sup>4</sup>, Sunil Mohan<sup>5</sup>, R. K. Gautam<sup>6</sup>, Sudhanshu Shekhar Singh<sup>4</sup>,  
Gopal Ji<sup>1</sup>(✉), and Rajiv Prakash<sup>2</sup>

- <sup>1</sup> Mechatronics, Centre for Advanced Studies, Dr APJAKTU Lucknow, Lucknow, UP 226031, India  
gopalji@cas.res.in
- <sup>2</sup> School of Materials Science and Technology, IIT BHU Varanasi, Varanasi, UP 221005, India
- <sup>3</sup> Department of Mechanical Engineering, Amity School of Engineering and Technology, Amity University Madhya Pradesh, Gwalior 474005, India
- <sup>4</sup> Department of Materials Science and Engineering, IIT Kanpur, Kanpur, UP 208016, India
- <sup>5</sup> Department of Metallurgical Engineering, IIT BHU Varanasi, Varanasi, UP 221005, India
- <sup>6</sup> Department of Mechanical Engineering, IIT BHU Varanasi, Varanasi, UP 221005, India

## 1 Introduction

Aluminum is a lightweight material and owner of good mechanical properties. The mechanical and other useful properties of Al can be improved by alloying with other materials. Al 6061 is an alloy of Mg, Si, and Al, and possesses better functional properties than pure aluminum [1]. In some cases, Al 6061 is not enough to deal with the requirements alone and further improvement in the properties is needed. This can be achieved by developing Al-based MMCs (AMMC). Due to excellent functional properties, AMMC are frequently used in the automotive industries to develop various automobile parts like piston, crank, rings, and cylinders [2]. Due to high strength to weight ratio, high hardness, low density, better wear, and corrosion resistance, AMMC are also used in the aircraft industries in making of aircraft frame and other parts [3, 4]. Thus, it is evident that AMMC are well known for its excellent functional properties. However, these properties of AMMCs greatly depend on the reinforcement material. Several reinforcement materials have been tried to develop MMCs with desirable properties. Kok [5] have investigated the tensile strength and hardness of Aluminum 2024 reinforced with  $Al_2O_3$  particles. Wear and corrosion behavior of Al-Si matrix reinforced with Alumina is studied by El Aziz et al. [6]. Seleman et al. [7] have studied the hot extruded Aluminum 6016 alloy reinforced with graphite particles for mechanical properties and microstructures. Senapati et al. [8] have investigated the Al-Si-based MMC reinforced with industrial waste (fly ash) material and tested for tribological properties. Kumar et al. [9] have studied for wear properties of Aluminum-based MMCs reinforced with silicon carbide and granite powder. Study of Mechanical and wear properties of Al LM6 MMCs reinforced

with nano SiC, fly ash, and red mud is done by Ahemad et al. [10]. Thus, it is evident that selection of reinforcement material is an important step to achieve the desirable properties according to the working environment.

The aim of the present work is to develop AMMC by stir casting using brick powder as reinforcement material. Stir casting technique is selected because it is easy, fast, economic, and widely used technique for development of MMCs [11]. Several researchers have developed MMCs using stir casting method. Tamilanban et al. [12] have studied the Al(6061)-based MMCs developed by stir casting and reinforced with SiC, Mg, Cu according to different weight percentage. Bhowmik et al. [13] have investigated the tribological properties of Al7075 MMCs developed by stir casting and reinforced with Titanium diboride according to different weight percentages. Kumar et al. [14] have investigated the Al7075 MMCs developed by friction stir processing and reinforced with SiC in micro- and nano-grain forms. Arunachalam et al. [15] discussed about the stir casting techniques in detail in his review paper. In present work, brick powder has been chosen as reinforcement material because it is a hot hard ceramic material, can increase hardness of AMMC to sufficient high level and never used as reinforcement material till date as per the best of our knowledge. Four MMCs, namely MMC1, MMC2, MMC3, and MMC4, have been developed by varying concentration and size of brick powder. The sizes of powder are varied using ball milling for different times (2–4 h). The concentration of brick powder is kept as 1–7% (by weight of pure aluminum) to study the concentration effect on the functional properties. The developed MMCs have been examined by SEM, EDAX, and XRD, which indicate that MMCs have been successfully formed. In the next part of this work, tribological properties and corrosion resistance of the developed MMCs will be investigated.

## 2 Experiment Methods and Materials

### 2.1 Metal Matrix Material

In this work, Al 6061 is used as a matrix material. Al 6061 is procured from the metal market of Lucknow, India. The purchased material is also checked by FESEM, and details are shown in the results section of the manuscript.

### 2.2 Ball Milling of Brick Material

The ball milling of the brick powder is performed by Fritch P6 machine. A 30 g of the brick powder was individually ball milled for 2–4 h at 300 rpm. The camera images of brick powder and ball milled powders are shown in Fig. 1. The FESEM images of the powders are shown in the results section of the manuscript.

### 2.3 Development of MMCs

First, Al 6061 (300 g) was put in a graphite crucible in a muffle furnace at 750 °C for melting. A graphite rod was used for stirring of molten metal at 220 rpm for 10 min. During stirring, reinforcement materials were added according to the concentration (1–7%) and size (2–4 h ball milled). Afterward, the molten metal with reinforcement was



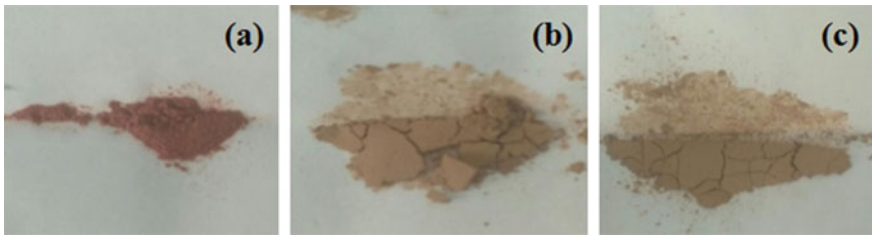


**Fig. 1** Showing camera images of brick powder **a** without ball milled, **b** 2 h ball milled and **c** four hours ball milled

poured in a rectangular mold of  $12 \times 3 \times 2 \text{ cm}^3$  and left for solidification. The whole process was performed according to Singh et al. [16]. The set up used for stir casting and cast product is shown in Figs. 2 and 3. For reference, Al 6061 is recast by stir casting.

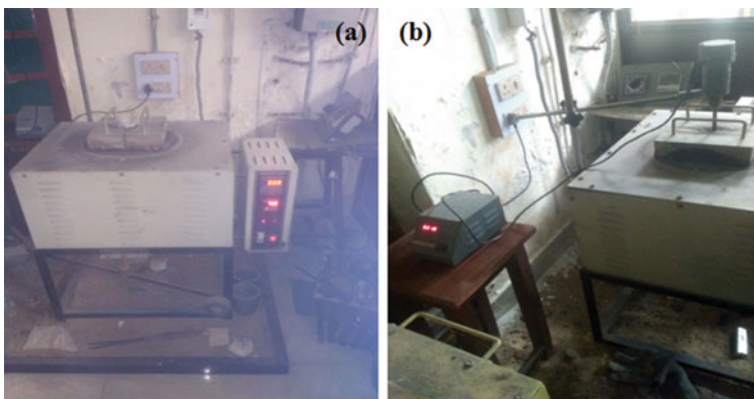


**Fig. 2** Stir casting setup **a** muffle furnace without stirrer and **b** muffle furnace with stirrer

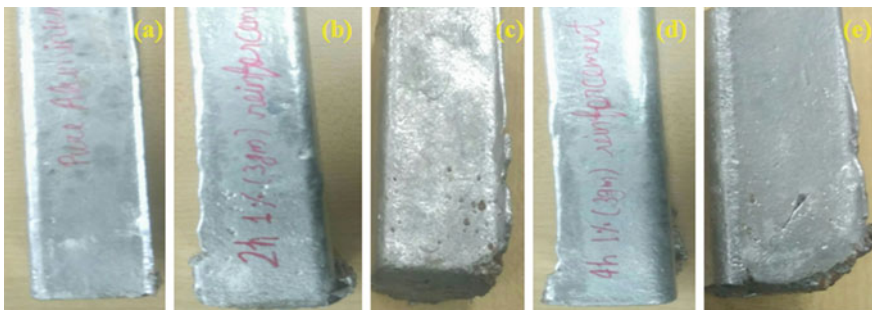


**Fig. 3** Showing cast **a** Al 6061 **b** MMC1, **c** MMC2, **d** MMC3, and **e** MMC4

## 2.4 Surface Morphology Analysis

The cast Al 6061 and MMCs were cut into suitable sizes from the middle by power hacksaw. These samples were abraded by emery paper, cleaned with ethanol, and then put in a vacuum desiccator for one day. Afterward, the surface of the developed MMCs and Al was examined by Carl Zeiss Gemini FESEM and EDAX.

## 2.5 XRD Analysis of MMCs

The XRD patterns for the cast MMCs were obtained by Rigaku Miniflex 600. The powders of Al6061 and MMCs were collected during their cutting for making samples for SEM analysis. These powders were examined, and XRD patterns were recorded.

# 3 Result and Discussion

## 3.1 Analysis of Ball Milled Brick Powder

The ball milling of the brick powder was done to obtain different size of the powders. The powder was ball milled for 2–4 h. It was expected that 4 h ball milling could produce finer particles than 2 h ball milling. The FESEM images of brick powder are shown in Fig. 4. It was evident through images at both magnifications that size of the powder was reduced after ball milling. The 4 h ball milled powder was looking finer than 2 h ball milled powder. The average sizes of 0, 2 and 4 h ball milled powders were approximately 5, 1.5, and 408 nm. Thus, it was found based on FESEM analysis that 2–4 h ball milled powder could be used to study the effect of size on reinforcement quality.

## 3.2 FESEM and EDX Analysis of Cast MMCs

The cast MMCs were analyzed through FESEM to check successful formation of the composites. Figure 5 shows their images at 500 magnifications. It was evident that Al6061 surface changed due to addition of brick powders in MMCs; however, this change was more prominently observed for MMC2 and MMC4 (more amount of powders). These changes indicated that MMCs were formed.

The changes due to addition of brick powders of Al 6061 could be more clearly observed through Fig. 6. A drastic change in Al 6061 surface was observed. Also, surface change due to size decrease (micro to nano) and concentration increase (1–7%) was evidently noticed through analysis of Fig. 6b–e. These changes in surface were self-indicators of MMC formation.

To do further confirmation, a comparison of elemental composition of MMCs is done based on EDAX and presented in Table 1. According to the analysis, brick powders were having three major elements: Be, O, and Si. On the other side, Al 6061 was having Al, O, and Si. Table 1 indicated that Be was not present in Al 6061, while Be was present in all the composites along with Al, C, O, and Si. This confirmed the Al-brick powder MMCs. It was also noticed that the wt.% of elements (especially Be) were changed due to size and concentration of brick powders, which indicated compositional differences among developed MMCs. These differences could affect functional properties.

### 3.3 XRD Analysis

Figures 7 and 8 show XRD patterns of MMC1, MMC2, MMC3, and MMC4 for observing size and concentration effects. There were five peaks in XRD patterns of Al 6061 and MMCs. The positions of the peaks ( $2\theta$ ) in XRD patterns of Al 6061 were  $38.5^\circ$ ,  $44.8^\circ$ ,  $65.1^\circ$ ,  $78.2^\circ$ ,  $38.5^\circ$ , and  $82.3^\circ$ . The intensity of the peaks was found decreased coming from left to right in XRD patterns. The similar XRD patterns of Al 6061 were reported elsewhere [17], which confirmed the matrix material was Al 6061.

The MMCs were presented in two figures to analyze size and concentration effect on the XRD peaks as well as to confirm formation of composites. Figure 7 shows the XRD peaks for all MMCs. The peaks were same in numbers (5) and same in positions.

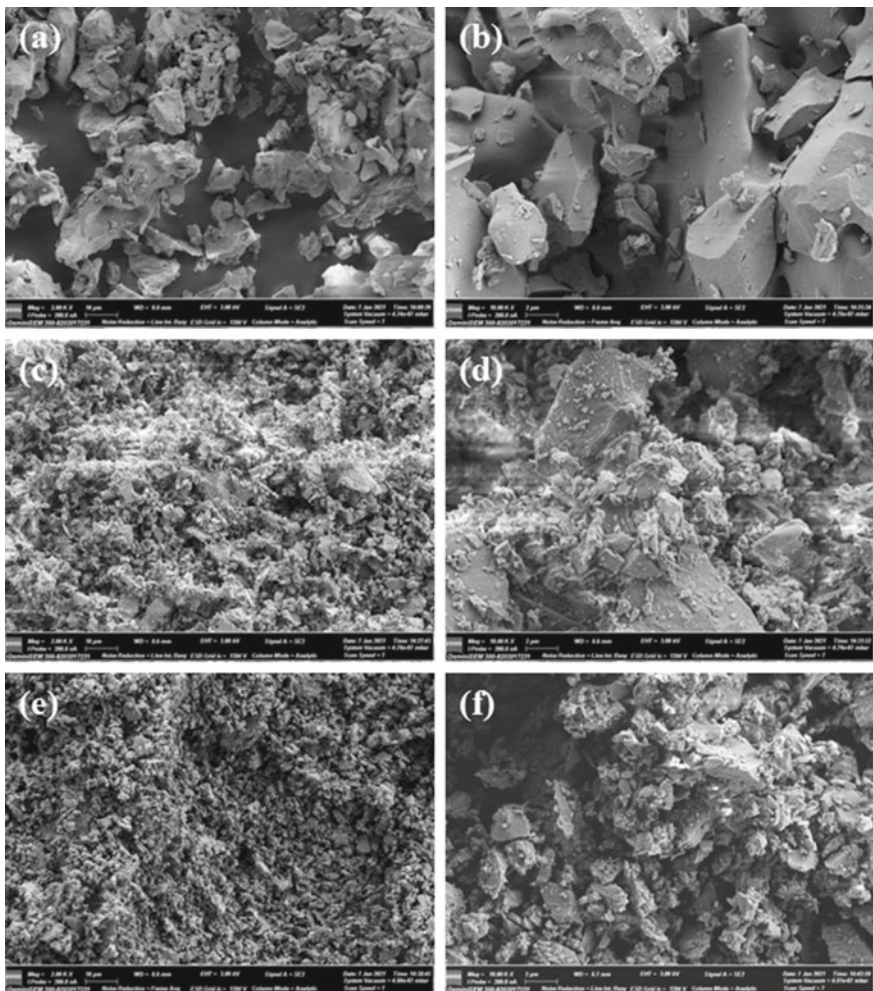


**Fig. 4** FESEM images of brick powder after 0, 2, and 4 h ball milling at 2 K (a, c, and e) and 10 K (b, d, and f) magnifications

However, the most intense peaks (characteristic peaks) showed slight differences in peak intensity and peak positions in magnified view (Fig. 7b, d). Due to increase in concentrations, similar shifts in peak positions as well as increase in peak intensities were observed for both 2–4 h ball milled powder reinforced composites. These changes represented that composites were formed. Furthermore, the size effects (different time of ball milling) on XRD peaks were analyzed and it was observed that changes were occurring (Fig. 8). In magnified view of the XRD peaks (Fig. 8b, d), it was noticed that increase in intensity and shifting in peaks positions were occurring in accordance with the size. However, these changes were more prominent in the composites having 7%

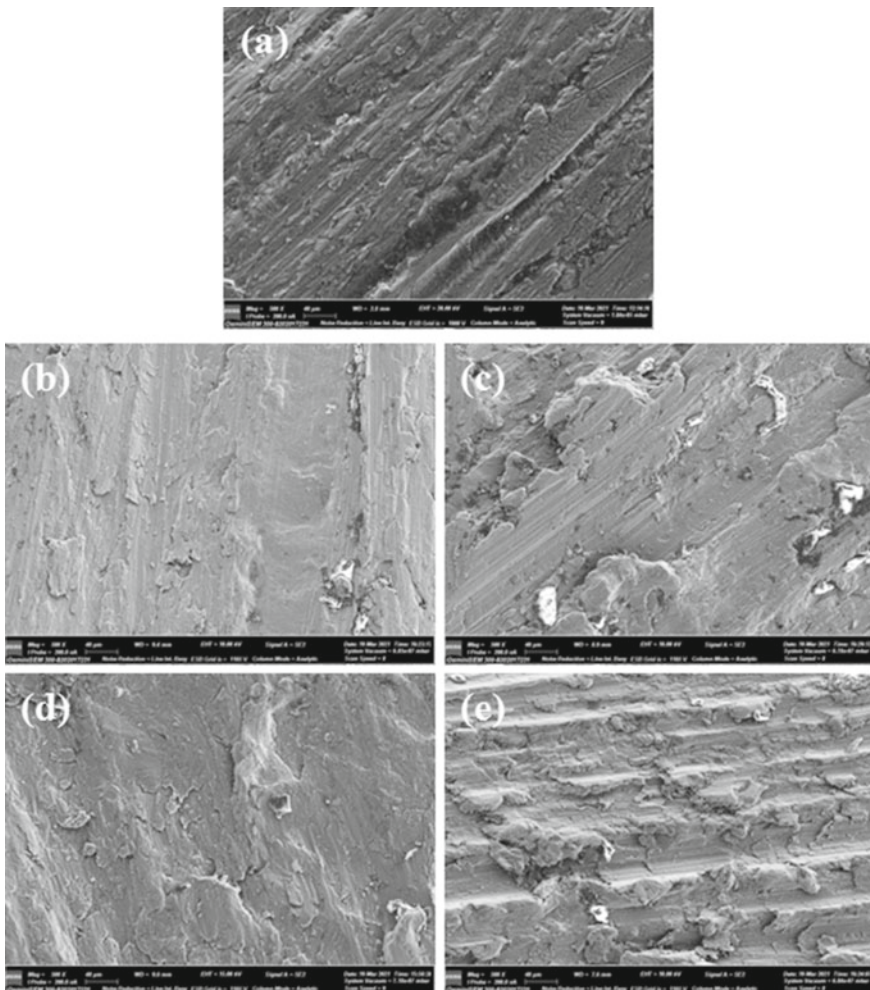


**Fig. 5** FESEM images **a** Al 6061, **b** MMC1, **c** MMC2, **d** MMC3, and **e** MMC 4 at 500 magnification



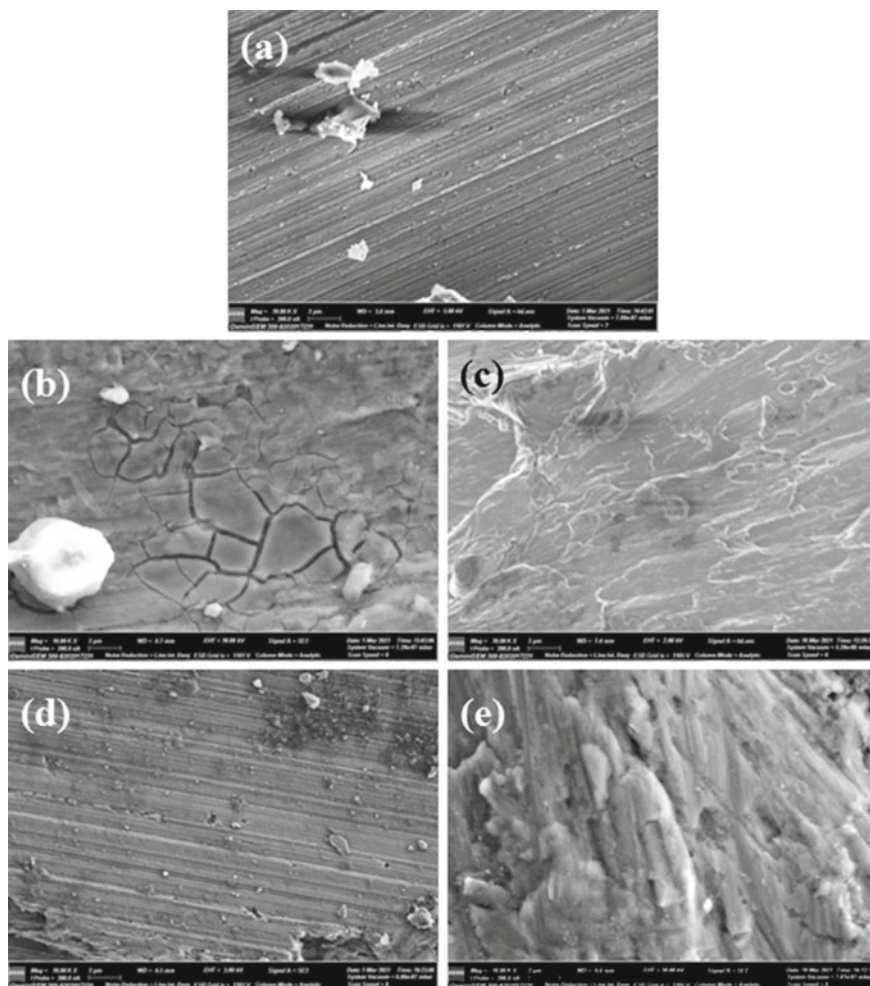


**Fig. 6** FESEM images **a** Al 6061, **b** MMC1, **c** MMC2, **d** MMC3, and **e** MMC4 at 10,000 magnifications

**Table 1** Elemental analysis (wt.%) of Al 6061 and developed MMCs by EDAX

Elements	Al 6061	Brick powder	Composite-2 h and 1%	Composite-2 h and 7%	Composite-4 h and 1%	Composite-4 h and 7%
Be	–	39.72	2.30	43.08	3.05	48.5
C	–	2.69	33.17	13.68	4.14	11.16
O	7.10	33.95	16.41	1.42	5.26	1.50
Al	92.55	6.04	44.33	41.68	87.49	38.55
Si	2.05	11.55	0.08	0.14	0.06	0.29

brick powders (both 2–4 h ball milled) as reinforcements. This observation indicated that composites were successfully formed.

As an overall conclusion of XRD analysis, it was stated that formation of composites was confirmed through the changes in peak intensity and peak positions. The changes were shown here only for the most intense peak (characteristic peaks); however, the change in other peaks was also observed (not shown).

## 4 Conclusions

The Al 6061-brick powder MMCs were developed by stir casting in this work. The brick powder was never used as reinforcement material for Al 6061-based MMCs. The brick powders were ball milled for 2–4 h for obtaining different size of the powders and added in MMCs in different weight concentrations (1 and 7%). Thus total four composites were developed: MMC1, MMC2, MMC3, and MMC4. The FESEM analysis of ball milled powders revealed that they were different in sizes (2 h ball milled > 4 h ball milled). The FESEM images of MMCs surfaces were recorded at 500–10,000 magnifications, which

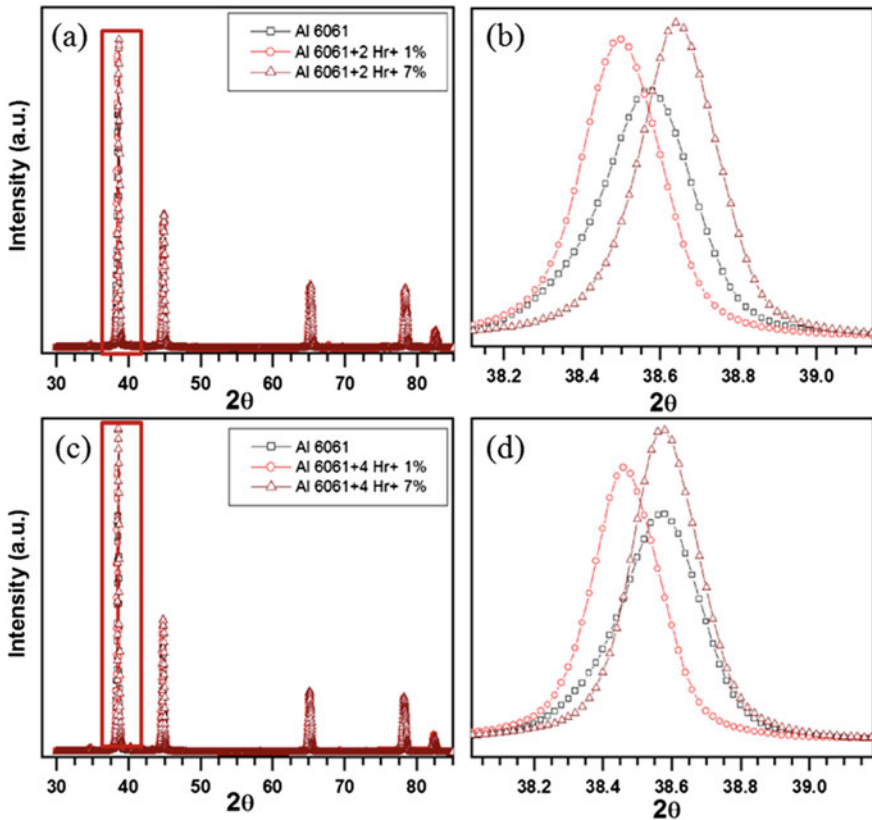


**Fig. 7** XRD patterns of **a, b** Al 6061, MMC1, MMC2 and **c, d** MMC3 and MMC4 for observing concentration effect

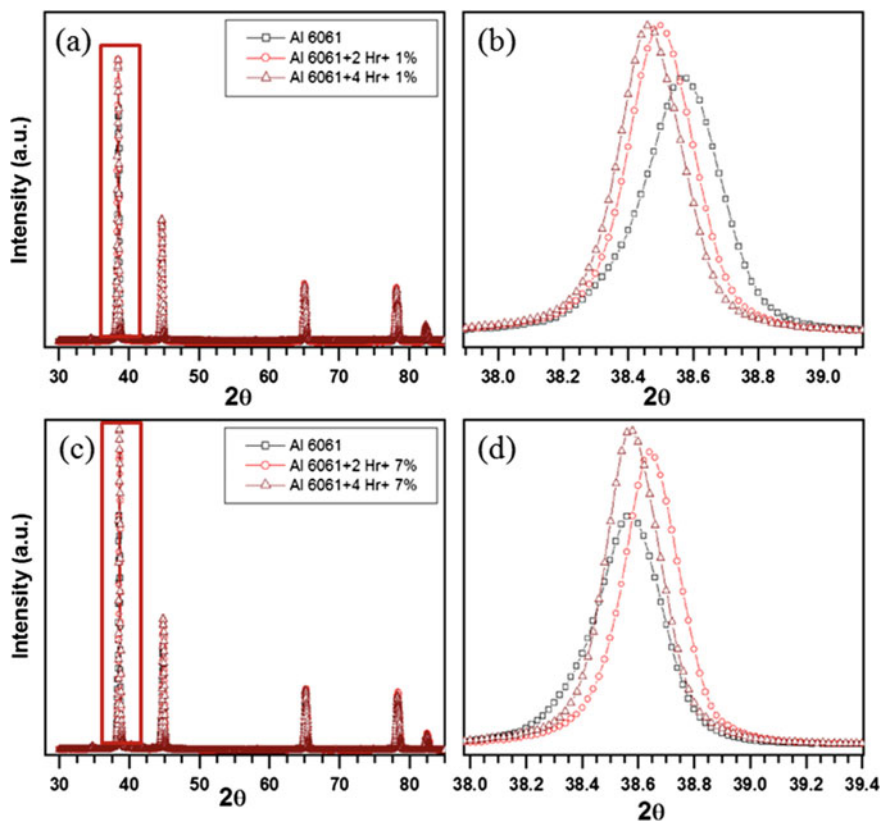


**Fig. 8** XRD patterns of **a, b** Al 6061, MMC1, MMC2 and **c, d** MMC3 and MMC4 for observing size effect

suggested that composites were formed. Additionally EDAX analysis were performed on MMCs and it was noticed that Be (major element in brick powder) was present in all the composites, while it was absent in Al 6061. Thus EDAX analysis confirmed that the composites were formed. Further, XRD analysis was performed on MMCs. The XRD analysis evident showed size and concentration effects on XRD peaks, which confirmed that the composites were formed. Thus, it was stated based on analysis in this work that Al 6061-brick powder composites were successfully developed by stir casting.

**Acknowledgements.** Shubham Kumar Singh wants to acknowledge Mr. Ankit Kumar Singh of IIT BHU Varanasi for his help during casting of MMCs and Dr. Piyush Jaiswal (CAS Lucknow) for SEM analysis.

**Conflict of Interests.** Authors declare no conflict of interest.

## References

1. Mallikarjuna C, Shashidhara SM, Mallik US, Parashivamurthy KI (2011) Grain refinement and wear properties evaluation of aluminium alloy 2014 matrix TiB<sub>2</sub> in situ composites. *Mater Design* 32:3554–3558
2. Rohatgi P (1991) Cast aluminum-matrix composites for automotive applications. *JOM* 43:10–15
3. Dursun T, Soutis C (2014) Recent developments in advanced aircraft aluminium alloys. *Mater Des* 56:862–871
4. Pragathi P, Elansehian R (2021) Wear and corrosion behaviour on pure aluminium matrix reinforced with SiC and spent catalyst by using the stir casting method. In: Gupta M, Davim P, Reddy UMP (eds) ICE3MT 2020, *Mater Today Proc* 38:3246–3252. Elsevier, Netherlands
5. Kok M (2005) Production and mechanical properties of Al<sub>2</sub>O<sub>3</sub> particle-reinforced 2024 aluminium alloy composites. *J Mater Process Technol* 161:381–387
6. El-Aziz KA, Saber D, Sallam HEDM (2015) Wear and corrosion behavior of Al–Si matrix composite reinforced with alumina. *J Bio Tribo Corrosion* 1:1–10
7. Seleman M, El-Sayed M, Ahmed MMZ, Ataya S (2018) Microstructure and mechanical properties of hot extruded 6016 aluminum alloy/graphite composites. *J Mater Sci Technol* 34:1580–1591
8. Senapati AK (2015) Experimental investigation on tribological properties of Al–Si alloy based MMC developed from an industrial waste material 3:13–16
9. Kumar KS, Karthikeyan S, Rahesh RG (2020) Experimental investigation of wear characteristics of aluminium metal matrix composites. In: Sakhtivel S, Karthikeyan S, Palani A (eds) ICNIDII 2020. *Mater Today Proc* 33:3139–3142. Elsevier, Netherlands
10. Ahmed SA, Motgi BS (2015) A study on mechanical and tribological properties of Al LM6 MMCs reinforced with nano SiC, fly ash and red mud. *Int J Sci Res Dev* 3:91–96
11. Reddy PV, Kumar GS, Krishnudu DM, Rao HR (2020) Mechanical and wear performances of aluminium-based metal matrix composites: a review. *J Bio Tribo Corrosion* 6:1–16
12. Tamilanban T, Ravikumar TS (2020) Influence of stirring speed on stir casting of SiC reinforced Al Mg Cu composite. *Mater Today Proc*, in press. <https://doi.org/10.1016/j.matpr.2020.08.633>
13. Bhowmik A, Dey D, Biswas A (2020) Tribological behaviour of aluminium-titanium diboride (Al7075-TiB<sub>2</sub>) metal matrix composites prepared by stir casting process. In: Singh SK, Akinlabi ET, Kumar K, Davim JP, Saxena KK (eds) ICMPC 2020. *Mater Today Proc* 26:2000–2004
14. Kumar A, Pal K, Mula S (2017) Simultaneous improvement of mechanical strength, ductility and corrosion resistance of stir cast Al7075-2% SiC micro- and nanocomposites by friction stir processing. *J Manuf Process* 30:1–13
15. Arunachalam R, Kumar P, Muraliraja R (2019) A review on the production of metal matrix composites through stir casting—furnace design, properties, challenges, and research opportunities. *J Manuf Process* 42:213–245
16. Singh MK, Gautam RK, Ji G (2019) Mechanical properties and corrosion behavior of copper based hybrid composites synthesized by stir casting. *Results Phys* 13:102319
17. Suresh S, Moorthi NSV, Selvakumar N, Vettivel SC (2014) Tribological, tensile and hardness behavior of TiB<sub>2</sub> reinforced aluminium metal matrix composite. *J Balkan Trib* 20:380–394





# Development of SCADA and PLC-Based Monitoring and Control of Metro Rail System

Jetwadee Phanthanachai<sup>(✉)</sup>, Rachana Garg, and Narendra Kumar

Department of Electrical Engineering, Delhi Technological University, Delhi, 110042, India  
rachanagarg@dce.ac.in

## 1 Introduction

Automation means controlling and handling any manufacturing or running process using automatic equipment and other facilities with minimal human interference. Thus, industries exploit the primitive process with automatized processes, which provides flexibility and cost-effectiveness in operations and improved efficiency. Previously, the industries having such problems are now being enhanced with automation. Automation has also reduced the probability of errors, thus improving the low power consumption and energy resources [1].

In the scope of industrialization, automation is being developed to draw some advantages. The advantages are mainly process decentralization, interpolation, visualization and monitoring, real-time data acquisition, and essential mechanization, which is provided the human operator with machinery to assist them with the muscular requirement of work; automation significantly decreases power consumption, high industrial efficiency, and security. In order to prevent failure, methods such as SCADA and PLC are used to achieve automation. Automation (automatic control) helps numerous process control systems for operating metro rail system equipment such as a machine AC, DC motor, control switching in electrical transmission lines, computer systems to monitor and control process, and the railway's electrical system station [2]-[3].

SCADA system incorporates input-output modules, software, database, human-machine interface (HMI), signal processing hardware controller, networking, and communication protocols. These modules are interfaced in general via the PLC program [4]. The PLC is programmable in automation, machine, and capable of adjusting or modifying the operation series according to the configurations to avoid failure and crucial to help you understand how real-world stuff works and thus help the user test if PLC code is working.

The Wonderware Intouch SCADA software is used to monitor the operation and running of metro rail systems and the power supply flowing to the utility load through various transformers and their standby. The procedure is regulated and controlled OMRON PLC (NX1P2-9024DT1) with ladder logic programming. The software used for PLC programming is OMRON's Sysmac Studio Programming software [5, 6].

The research paper is distributed amount six sections having basic Introduction, Prototype of automated metro rail system operator, Operation, Simulation result, Appendix, and Conclusion.

## 2 Prototype of Automated Metro Rail System Operator

Metro rail system has two components used for automation which are PLC and SCADA. The correspondence between the SCADA and the PLC is achieved through a PC, wired, or wireless. A PLC is a programmable memory to implement a specific function for internal storage by continuously scanning the program [7, 8]. The purpose of PLC is to adjust process operations accordingly and monitor crucial process parameters. As a result, the automation of metro rail systems in Fig. 1 demonstrates that the PLC is at the core of it. Signals or input data from input devices like a sensor or push button switch or contact limit switch are sent into PLC. The information will be feed first to the input module then the info will be processed by the processor to get the outcome on the output module such as a motor, valve, or alarm.

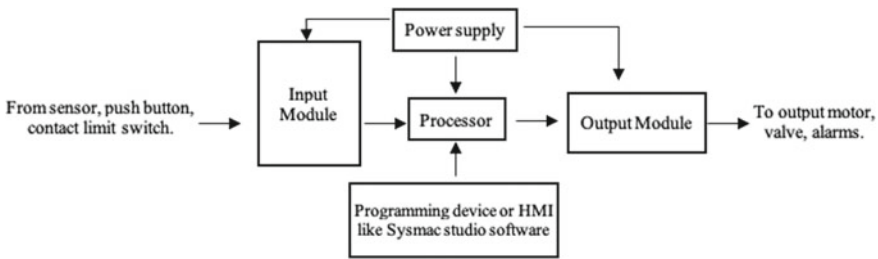


**Fig. 1** PLC block diagram

SCADA is a control and industrial measurement system comprising of a single master terminal unit (MTU), and one or many control and field data gathering units or remote terminal unit (RTU), and a set of customized or standard software which is being used to control and monitor remotely placed field data elements by centralized OCC or HMI will be located at the central depot to control traction system equipment and entire power supply through SCADA. Figure 2 shows that the PLC has eight inputs, and it requires a 24 V DC supply to perform its functions which are provided by a switch mode power supply (SMPS), infrared (IR) sensor, station, and emergency feed into PLC and get six output signals such as signal/alarm, the train is running or stopping, door open or close. The output module from PLC will transfer command from SCADA to the train. An important part is that if we have an emergency, the alarm will send digital status (emergency alarm status).

The prototype of the automated metro rail system operator including four applications as following as.

- The main application is OCC. It is used to control the metro rail system by an operator sitting in front of the HMI. Each station is remotely connected to the OCC. It has control over every station and processes the highest command priority. The various modes of operation such as emergency and congestion are controlled by this only. This process can be connected with automatic train supervision (ATS) to manage train operations automatically.

- Sub-application has CCTV function, metro stations view (metro rail system), metro platform view, and electrical control (traction power control and power supply system).

The flowchart below illustrates the functioning of the main application also including sub-application. The main application represents the OCC runtime window in SCADA Wonderware InTouch software from Fig. 3. The operator can command and monitor through the window. RTU is used to scan the programs by the sensor (IR sensors and reflective sensors). If any fault occurs at the process, RTU sent a message to MTU, and then, MTU sent signals or alarms to the operator on screen.

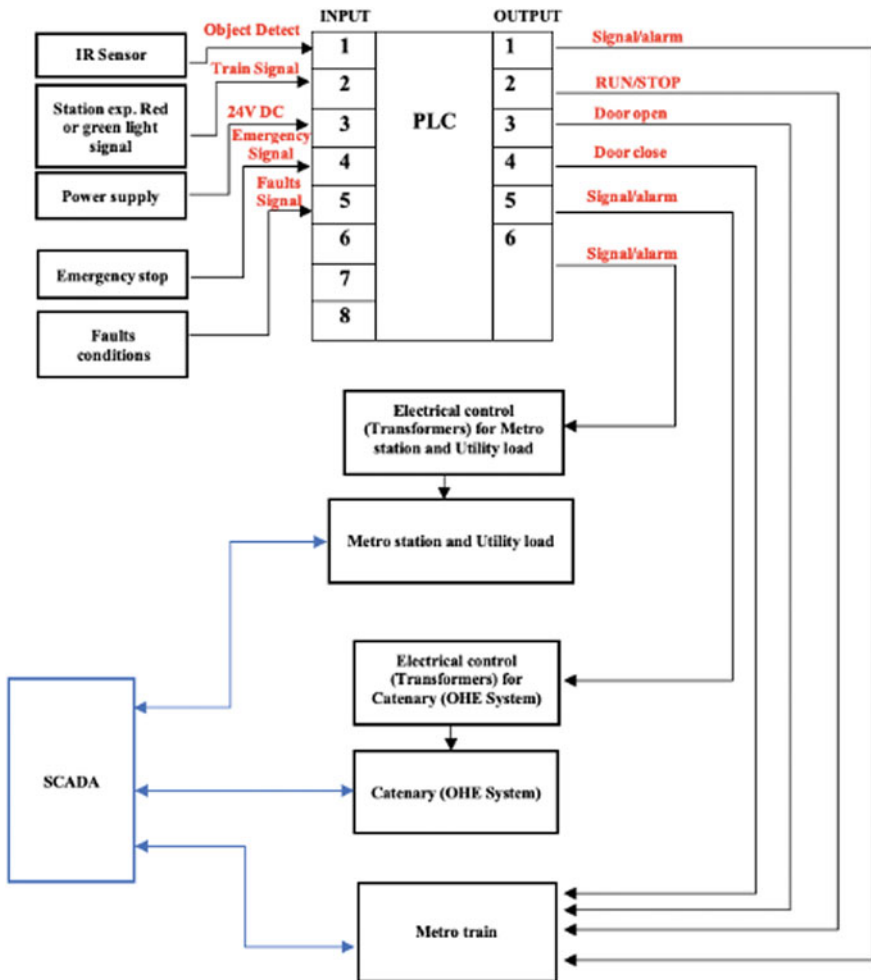


Fig. 2 Functional block diagram of metro rail using PLC and SCADA

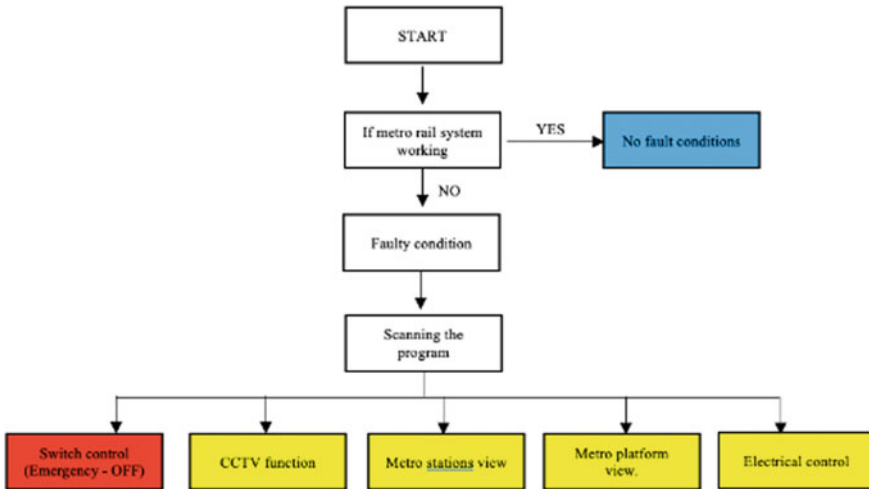


Fig. 3 Functional block diagram of main application

### 3 Operation

The project has a main application and four sub-application. This operation part is a brief four sub-application representation of the system which is demonstrated with the help of the figure and tables discussed below:

#### 1. Metro platforms view sub-application

Metro platforms control by the driver in the trains and the operator in any platforms can control the metro station’s traffic. In this flowchart, when the traffic light is red, the train stops, the door opens, and the passenger can get into the coach as shown in Fig. 5. The operator starts the process by pushing the switch button, as shown in Table 1

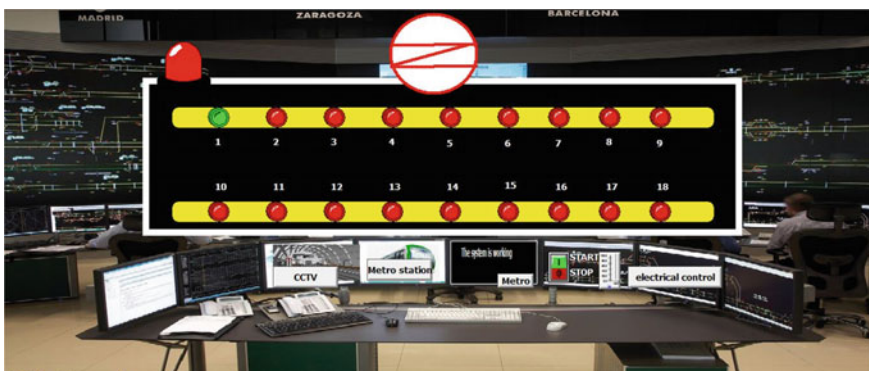


Fig. 4 Operational control center runtime window in SCADA Wonderware InTouch software

is the description of the timing of the process metro platforms view. After some time, the traffic light is still red, the train is stopped, and the door is closed, passengers can get into the coach after few minutes. After that, the train is ready to move. When the traffic light is green, the trains start moving, and the pantograph will collect the power from the contact wire.

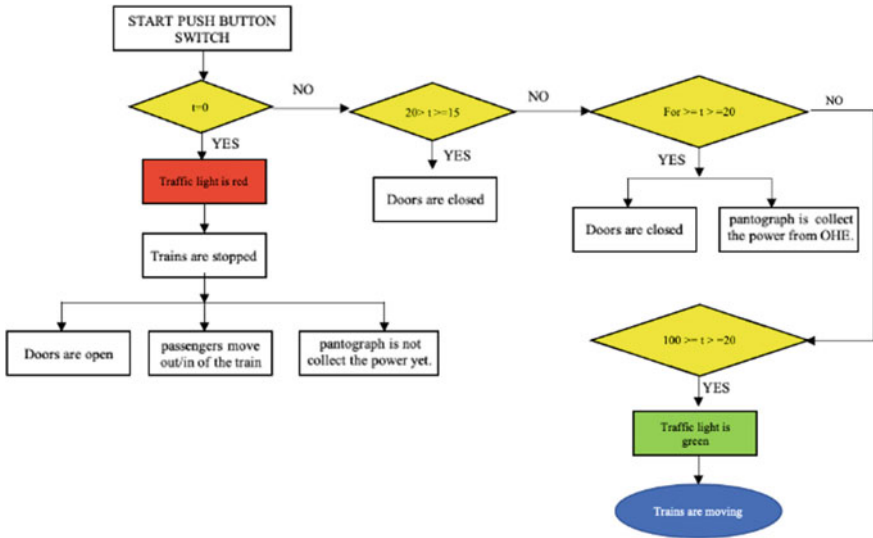


Fig. 5 Functional block diagram of metro platforms views sub-application

Table 1 Metro platform view description

Label	Description
1. $t = 0$	The traffic train light is red, the trains are stopped, the passengers move out/in the train, and the pantograph is not collecting the power yet
2. $20 > t \geq 15$	The doors are closed
3. For $\geq t \geq 20$	The doors are closed, and the pantograph is collecting the power, and the electrical signal on an overhead system is ON. Train starts running
4. $100 \geq t \geq 20$	The traffic light is green. The train starts moving forward
5. $t = 0$	The traffic train light is red, the trains are stopped, the passengers move out/in the train, and the pantograph is not collecting the power yet

From Table 1,  $t$  is the timing tag of the process or the tag of a slider.

## 2. Metro stations (traction SCADA system) views sub-application

When the switch is ON, metro train stations moving and the LED will indicate the correct position of the metro train in the control panel view, and the operation can see

the display where it will show the proper process condition of the train. Train locations can be identified and controlled after interruption of power supply or any failure.

From Fig. 6, if there is any fault that occurs at any station, the emergency light will turn on, and operation control shows the alert in the particular metro station on HMI or operation display.

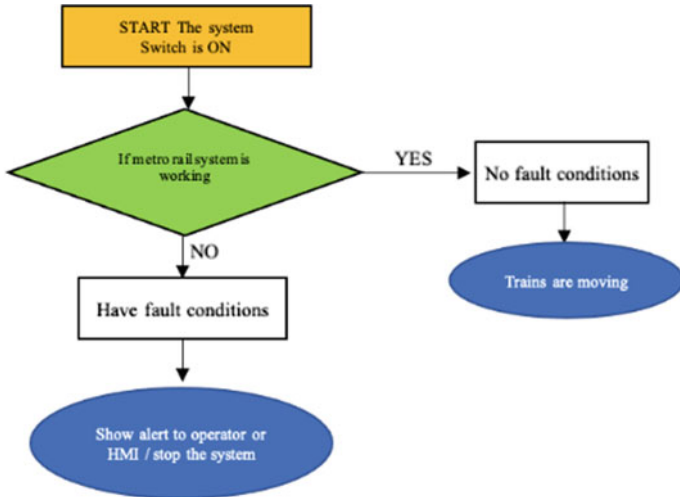


Fig. 6 Functional block diagram of metro stations (traction SCADA) views sub-application

### 3. Electrical control

For overhead equipment to transfer electrical energy to electric trains or railways for driving the motor, traction power control, and power supply systems must be powered at 25 kV, single phase, and 50 Hz. The power supply system consists of the substation, feeding post, and miscellaneous equipment at the control center and switching stations. Traction systems for metro rail are a catenary (OHE: overhead equipment) to supply electricity to a metro train equipped with a pantograph. 132 kV incoming line from generating station, after that transfer to busbar and transformer1 ( $T_1$ ) is a stepdown transformer (feeding post) for metro stations, and utility load, transformer2 ( $T_2$ ) is a stepdown transformer (feeding post) for catenary (OHE system), and transformer3 ( $T_3$ ) is a step-up transformer (feeding post). The system is started by switch ON  $S_0$  as following in Fig. 7.

Switch ON  $S_0$  and  $S_1$  means the system is working. 132 kV incoming lines from generating station to transformer1 ( $T_1$ ) is a stepdown transformer from 132 to 33 kV. Transformer3 ( $T_3$ ) is a step-up transformer from 33 to 415 kV for metro stations and utility load. The alarm tells the operator transformer1 is damage.

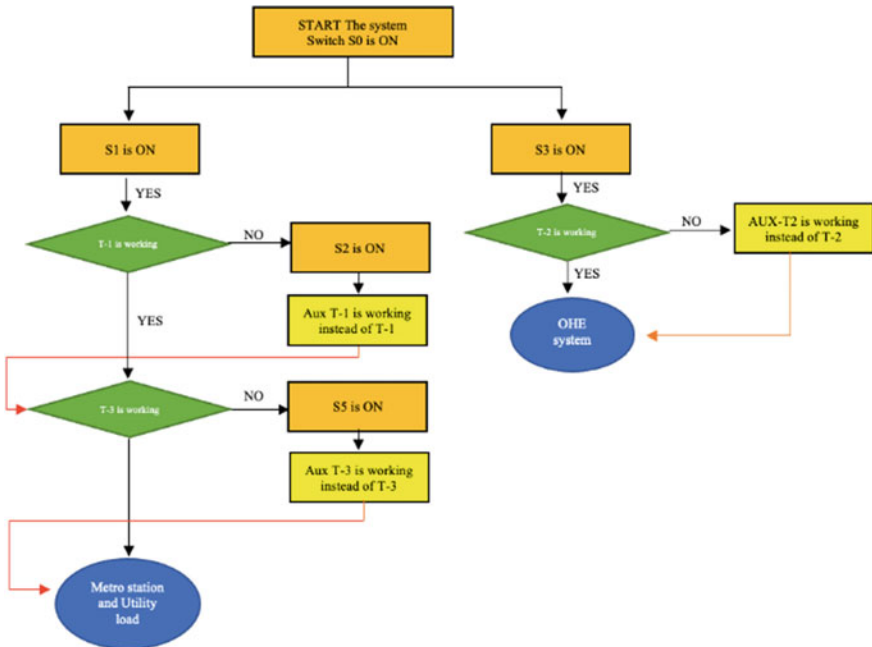


Fig. 7 Functional block diagram of electrical control views sub-application

Switch ON  $S_0$  and  $S_2$  means the system is working. The auxiliary transformer1 ( $T_1$ ) provides the power in case of transformer1 ( $T_1$ ) miscellaneous.

Switch ON  $S_0$ ,  $S_2$ , and  $S_3$  means the system is working. The transformer2 ( $T_2$ ) is provided the power to the catenary system (OHE). After some time, transformer2 ( $T_2$ ) gets damaged.

The auxiliary transformer2 (Aux- $T_2$ ) provides the power in case of transformer2 ( $T_2$ ) miscellaneous. Switch ON  $S_0$ ,  $S_2$ , and  $S_4$  means the system is working.

After some time, transformer3 ( $T_3$ ) gets damaged. The auxiliary transformer2 (Aux- $T_2$ ) provides the power incase transformer2 ( $T_2$ ) miscellaneous. Switch ON  $S_0$ ,  $S_2$ , and  $S_4$  means the system is working.

After some time, transformer3 ( $T_3$ ) gets damaged. The auxiliary transformer3 (Aux- $T_3$ ) provides the power in case of transformer3 ( $T_3$ ) miscellaneous. Switch ON  $S_0$ ,  $S_4$ , and  $S_5$  means the system is working. From Table 2,  $t$  is the timing tag of the process or the tag of a slider.

#### 4. CCTV

In the national capital region, the metro train has become the most convenient mechanism of urban transportation. The metro rail system’s intrinsic features make it a perfect target for terrorists and criminals because it is accessible and diverse, transporting millions of passengers every day, and high infrastructure cost. The metro rail system, including

**Table 2** Electrical control view description

Label	Description
1. $S_0$ is ON	The power supply is ON
2. $T_1$ and $S_1$ are ON	Power supply(132/33 kV) is fed to the stepdown transformer ( $T_1$ ), then fed to the step-up transformer ( $T_3$ ), and then provided to metro stations and utility load
3. For $50 \leq t_1 < 100$	Transformer ( $T_1$ ) is damaged
4. $S_2$ is ON	When transformer1 ( $T_1$ ) is damaged, the auxiliary transformer1 (Aux- $T_1$ ) is operated, and the power supply is fed to the stepdown transformer on standby (132/33 kV). If transformer3 ( $T_3$ ) is also not working, the power supply runs through the auxiliary transformer3 (Aux- $T_3$ step-up transformer 33/415 kV) and then fed to metro stations and utility load
5. $S_3$ is ON	Stepdown transformer2 ( $T_2$ , 132/25 kV) is ON, and the power supply is fed to catenary overhead electrical lines (OHE) through which the metro train is connected

its economic importance as the city's lifeline, presents a security risk of mass casualties. In the field of public transportation, security is a relatively new challenge. People whose activities are intended to weaken or interrupt the public transportation system to impact passengers or the country's economy cause security concerns or threats. Security concerns such as daily operations issues, vandalism, cyber-attacks, and possibility of terrorist groups are just a few of the challenges. There would be extensive close-circuit television (CCTV) or video surveillance coverage of stations, parking, and public areas. A sophisticated intrusion detection system (IDS) will be installed on the platform. Automatic train supervision (ATS) system, SCADA, passenger information system (PIS), and public address system (PA) can be installed for internal security monitoring to reduce response time from the personals. These systems can be used as risk assessment code (RAC) systems [9, 10]. This CCTV definition provides the control room operator an intelligent interface that facilitates making more effective decisions on operating the metro system and delivering the necessary services. Figure 8 describes this.

## 4 Simulation Results

## 5 Conclusion

PLC has a wide array of applications from industrial use to the metro rail system (Figs. 9, 10, 11, 12 and 13). PLC has also been incorporated in a real-time application that helps and makes life easier for human beings. PLC also supports SCADA systems such as automatic train supervision (ATS). The servers used in SCADA are known to have a similar interface as the ATS servers, allowing the operators in the control center to access any required information from the servers. The HMI provides a dedicated interface for each of the previous section functions, enabling the operators to implement



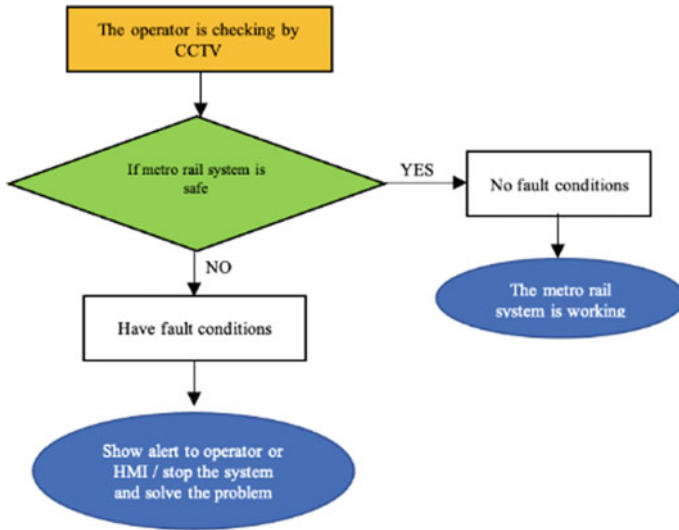


**Fig. 8** Functional block diagram of CCTV view sub-application

the necessary controls and monitor it. Therefore, SCADA functionality can control and monitor the infrastructure to track the train's location so that the sensors can reduce speed to avoid any accidents. Hence, the inter-passage door will get locked for the safety of all the passengers. These capacities also give the operator a dashboard to highlight the system status and send a warning to the operator. If the system can perform the necessary tasks or any part of the metro rail system requires regular maintenance. The HMI provides dedicated interfaces for each of the previous functions that allow the operator to implement the necessary controls and monitor the information. The emphasis on PLC and SCADA's future scope can be implemented by cybersecurity considering measuring it and network security, providing access to the local controls and firewall protection for regular threat assessment. These also provide an audit capability for both internal and external IT security professionals.



Fig. 9 Operational control center of main application

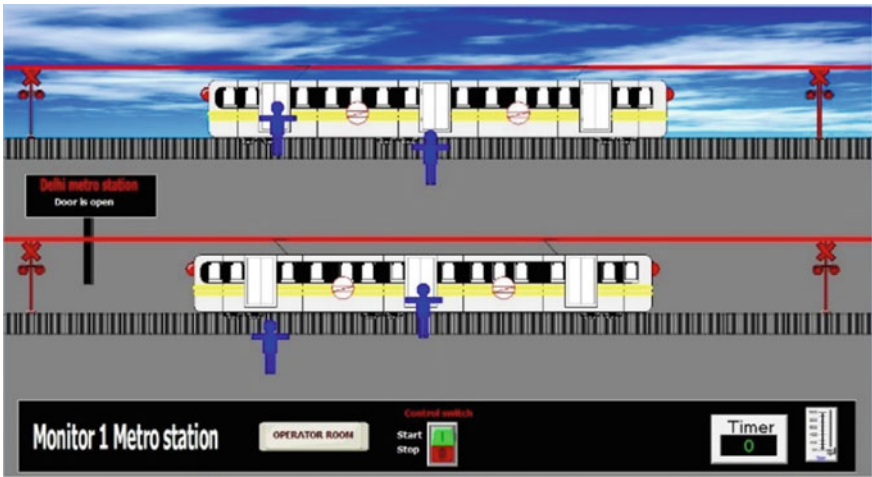


Fig. 10 Metro platforms of sub-application

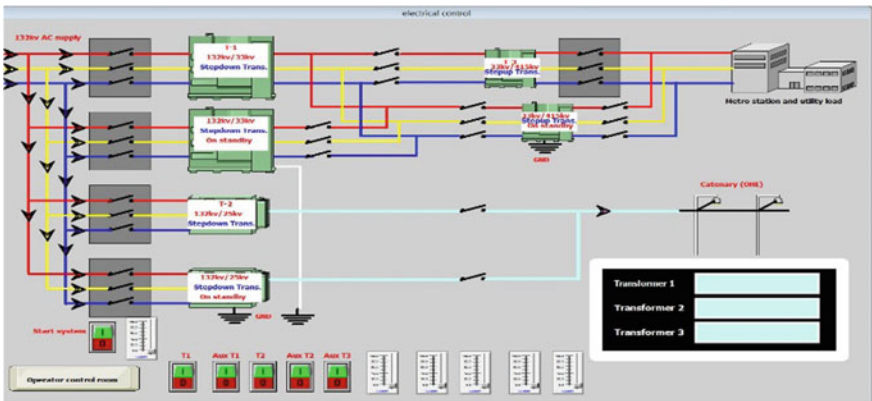


Fig. 11 Electrical control view sub-application

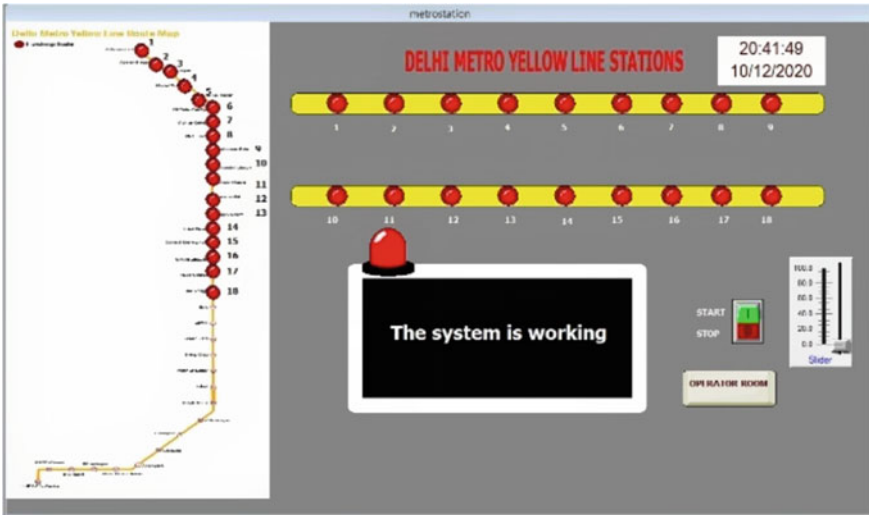


Fig. 12 Metro stations (traction SCADA) of sub-application

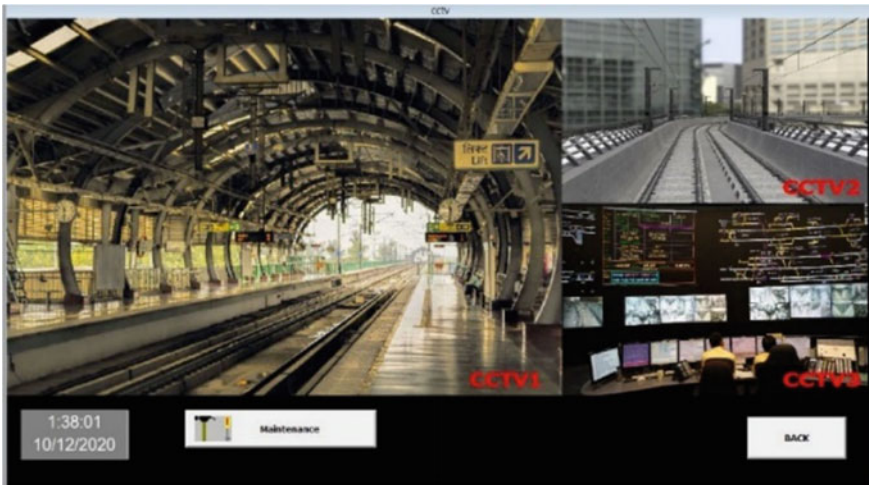
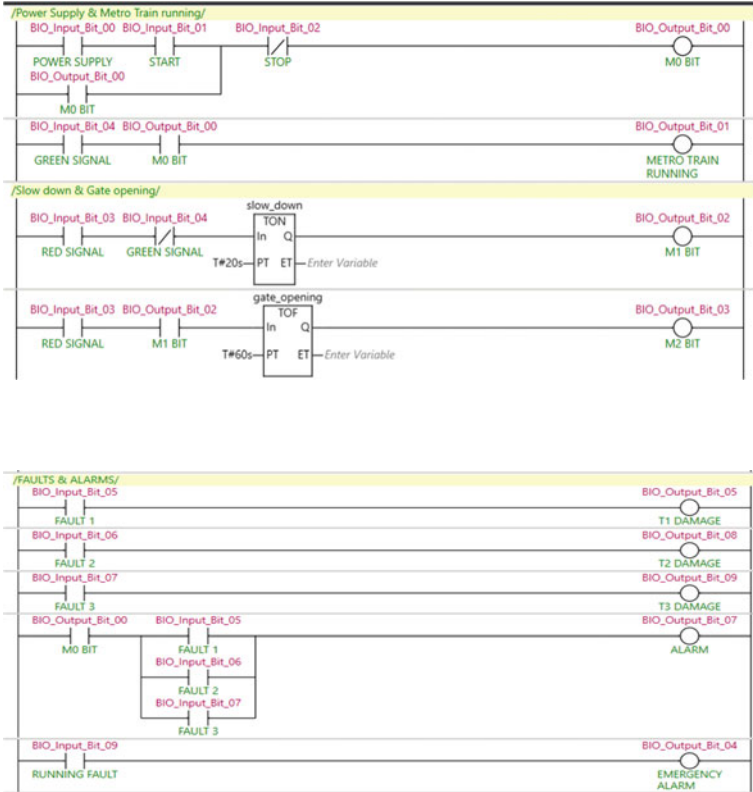


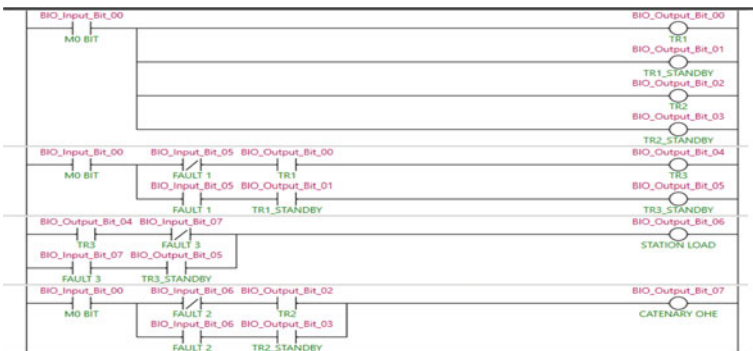
Fig. 13 CCTV of sub-application

# Appendix

## Appendix 1



## Appendix 2



## References

1. Gaurav K, Chawla MPS (2019) Railway signaling and interlocking with enhance safety system using PLC and SCADA. *J Electr Power Syst Eng (MAT Journals 2019)* 5(1):17–34
2. Sonia KK, Wang Z (2019) An industry 4.0 approach to develop auto parameter configuration of a bottling process in a small to medium scale industry using PLC and SCADA. *Procedia Manufacturing* 35: 725–730
3. Tomar B, Kumar N (2020) PLC and SCADA based industrial automated system. *International conference for innovation in technology (INOCON-2020)*
4. Aung HH, Ei Aung TT (2019) Simulation and implementation of PLC based for nonstop filling process using PLCSIM and HMI. *Renew Sustain*, 693–702
5. Sreejeth M, Chouhan S (2016) PLC based automated liquid mixing and bottle filling system. *1st IEEE international conference on power electronics. Intelligent control and energy systems (ICPEICES-2016)*
6. Rahul EK, Ramachandra CG, Srinivas TR (2016) Automated railway signaling and interlocking system design using PLC and SCADA. *National conference on advances in mechanical engineering science (NCAMES), Issue 2016*
7. Anandhan P, Logeswaran V, Lakshmakumar PS, Rajkumar G Kalpanadevi S (2014) A novel approach in railway system protection using PLC/SCADA. *Int J Innov Res Technol (IJIRT)*, 1(2014). ISSN: 2349–6002
8. Gopinathan R, Sivasankar B (2014) PLC based railway level crossing gate control. *Int J Emerg Technol Comput Sci Electron. (IJETCSE)* 8(1), April 2014. ISSN:0976–1353
9. Li Y, Chen B, Zheng VW, Temple WG, Kalbarczyk Z, Yue Wu (2017) Enhancing anomaly diagnosis of automatic train supervision system based on operation log. *Int Conf Dependable Syst Netw Workshops (IFIP) 2017*:133–136
10. Kanso K, Moller F, Setzer A (2009) Automated verification of signalling principles in railway interlocking systems. *Electron Notes Theoretical Comp Sci* 250(2009):19–31



# Detection of Tampering in Multimedia Using Blockchain Technology

Abhishek Singh, Adarsh Kumar<sup>(✉)</sup>, and Jamkhongam Touthang

Department of Mathematics, Delhi Technological University, New Delhi, India  
adarshkumar\_2k17mc09@dtu.ac.in

## 1 Introduction

In this advanced age, we are heavily and rapidly relying on media sources, especially computerized pictures and recordings, for information regarding the happenings in different parts of the world. However, the accuracy of such information received through these media platforms has become highly questionable mainly because of the presence of content altering tools.

Controlled movies, sound, and photos have been around for quite a long time now, yet the approach of man-made brainpower and modern altering innovations has made them substantially more hard to spot. We live in a world which is highly vulnerable to media manipulation to such an extent that it is very hard to spot differences in a real picture and that produced by algorithms. Political elections and campaigns are also affected by the fake media and news. For example, a few recordings and photos were shared during the US official race for president election that ended up being doctored. However, fraud goes much further than that.

Over the most recent couple of years, consequently, visual media and legal sciences have arisen as a key region of examination that basically manages the formation of devices and strategies that help to decide if computerized content being referred to is legitimate or not, in other words, a genuine, unaltered portrayal of truth. Throughout the most recent twenty years, this exploration area has seen impressive turn of events and innovativeness.

## 2 Background

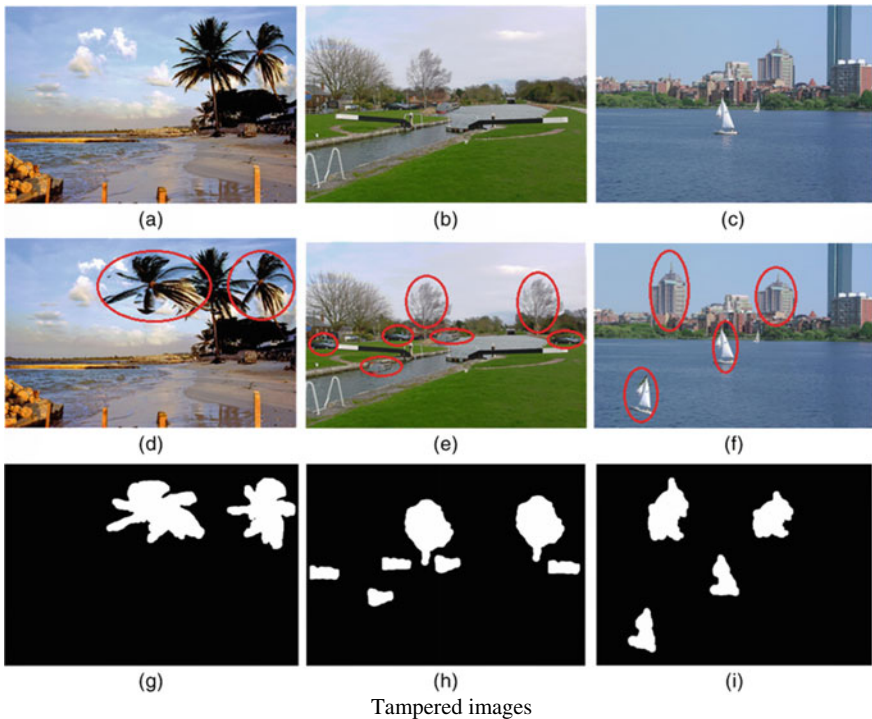
### 2.1 Video Tampering/Modification

Video control is a pristine variety of media control that targets altering unique computerized media with the utilization of a combination of traditional video preparing and video adjusting procedures and assistant methods from manufactured knowledge like face acknowledgment. In typical video control, the facial structure, outline developments, and voice of the worry are reproduced as a decent method to make a recorded recording of the worry. The bundles of those strategies fluctuate from instructional movies to films focused on (mass) control and promulgation, a true augmentation of the long status

chances of picture control. This state of PC created inaccurate data has added to false news, and there were times while this age got utilized over the span of political missions. Different applications are less vile; delight and harmless tricks give buyers film-quality imaginative conceivable outcomes.

Handmade films, sound, and photography have been around for years, but the proliferation of artificial intelligence and sophisticated editing tools has made them extremely difficult to detect. We live in a dangerous new world, where our sense of truth can be put into question. Often, when it comes to political tactics, we think of this as deception. Several fake videos and photos were shared during the US presidential election. But this problem goes further than that, and these distorted bits of content will appear in surprising ways.

In conclusion, we can say that video tampering is a threat to human society. It can cause harm at various levels in various forms. Propaganda and mass manipulation are one of those. Also, there has been a major concern of piracy in the media industry. Every artist gets some amount of time whenever there is a sale of his/her work. But, due to illegal replication and distribution of the content, artist’s income gets impacted. Hence, leading to deteriorate the value of the artist’s work as the majority of the population participates in this awful activity. Additionally, due to the wide availability of content online, anybody can copy the work and claim the ownership. When this happens, it becomes highly difficult to find the origin of the work. The digital media is insufficient in providing transparency in its ecosystem.



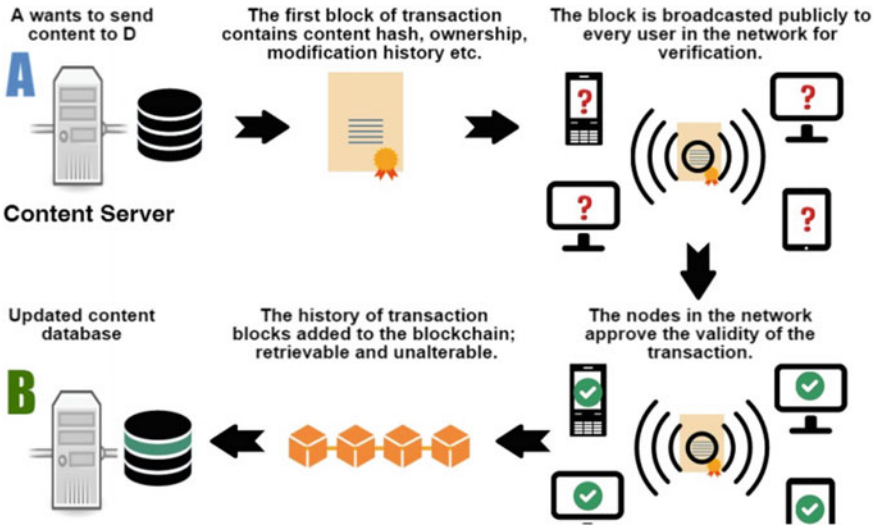


So, what can we do about it? Is it investing money in innovation that outsmarts deep fakes and AI? That is an exceptionally ill-conceived notion as we would see it. As AI is growing at a tremendous rate, so is the deep fake. What if, rather than investing money in finding solutions to detect media modification or tampering, we can eliminate the problem in the first place and never let it come into existence.

### 2.2 Blockchain Technology

Blockchain advancement is a design that stores esteem-based records, in any case called the node, of everybody in a couple of databases, known as the “chain,” in an association related through dispersed centers. Ordinarily, this amassing is insinuated as an “electronic record.” Each trade in this record is affirmed by the mechanized sign of the owner, which affirms the trade and safeguards it from changing. Thus, the information the mechanized record contains is outstandingly secure. In more direct words, the modernized record looks like a Google accounting page divided between different PCs in an association, in which the worth-based records are taken care of subject to genuine purchases. The intriguing point is that anybody can see the data, anyway they cannot deteriorate it.

Each trade in this record is affirmed by the high-level sign of the owner, which affirms the trade and guards it from modifying. Therefore, the information the mechanized record contains is astoundingly secure. The means by which information is what differentiates information on blockchain from typical information. A blockchain collects information and stores them conjointly called blocks that hold sets of knowledge. Blocks have limited storage capacities and, once a chain of the blocks is formed, that series of information is called the “blockchain.”



Working of Blockchain



### 3 Methodology

In this section, we briefly describe the method we have used to achieve the results, that is “a contextual framework” based on our research, a method to detect tampering in media. The whole process is purely based on how similar the given two images are. For finding the similarity, we will perform two steps which are briefly described below: First, “difference hash value” of two images is calculated, and then using the difference hash value, Hamming distance will be calculated. Using that we will decide how similar the given images are.

#### Similar Image Detection Steps:

- Calculate the difference hash value of the two images separately.
- Calculate the Hamming distance of the two images by difference hash value, and judge the similarity of the two images by the size of the Hamming distance.

#### 3.1 Difference Hash Calculation

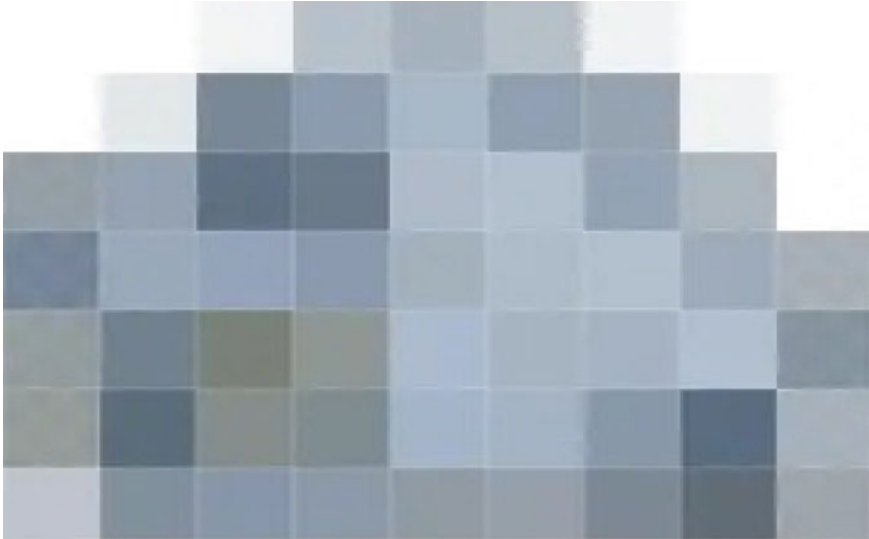


The picture that needs to calculate the dHash value

##### 3.1.1 Zoom Picture

On the off chance that we need to ascertain the dHash esteem in the figure over, the initial step is proportional to an adequately little size. For what reason do you have to zoom? Since the goal of the first picture is by and large extremely high. A 200\*200 picture has an entire 40,000 pixels, and every pixel holds a RGB esteem. 40,000 RGB is an enormous measure of data, and numerous subtleties should be handled. Along these lines, we need to zoom the image to a minuscule size, conceal its subtleties, and just see the woodland yet not the trees. That is we need to zoom the image/picture enough to the pixel level so that each and every pixel and its adjacent pixel will be clearly visible,

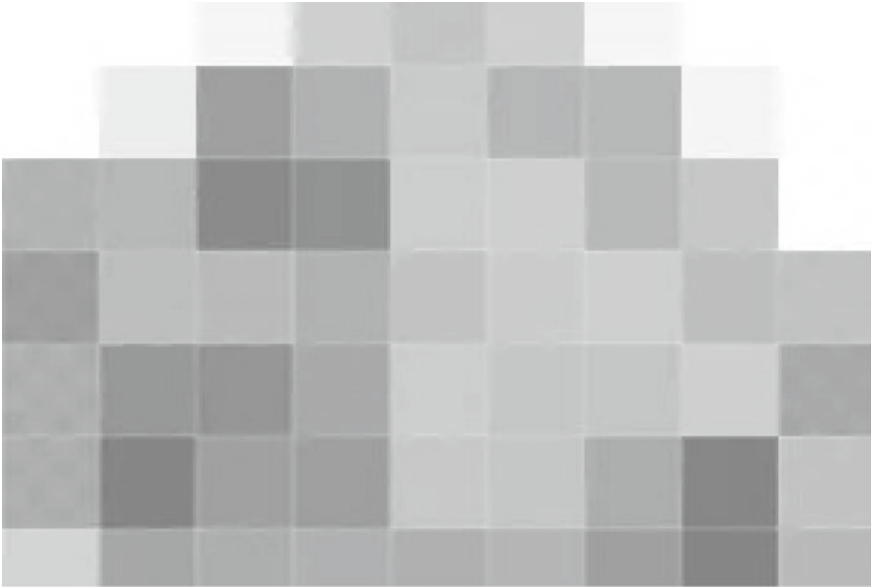
their size and color. The suggested scaling is  $9 \times 8$ . In spite of the fact that it very well may be scaled to any estimate, this worth is generally sensible. What is more, the width is 9, which is useful for us to change over to the hash esteem, look beneath you will comprehend.



After scaling to  $9 \times 8$  resolution

### 3.1.2 Graying

The full name of dHash is the distinction esteem hash, which is calculated by getting the shading power contrast between two contiguous pixels. The subtleties of our zoomed picture have been covered up, and the measure of data has gotten less. Yet, it is not sufficient, on the grounds that it is huge and comprises RGB esteems. White is addressed as  $(255, 255, 255)$ , and dark is addressed as  $(0,0,0)$ . The bigger the worth, the more brilliant the tone, and the more modest the hazier. Each tone is made out of three qualities, in particular the red, green, and blue qualities. In the event that you straightforwardly utilize the RGB worth to think about the shading force distinction, it is very confounded, so we convert it into a dim value just a number from 0 to 255 addresses the dim. For this situation, the three-dimensional correlation is streamlined to a one-dimensional examination.



After graying

### 3.1.3 Difference Calculation

The distinction esteem is calculated by computing the force correlation of adjoining pixels present in each line. Our image has a goal of  $9 \times 8$ , so there are eight columns, each with nine pixels. The distinction esteem is completed for each line independently, which is to ensure that the principal pixel in the following line will not be in contrast to any pixel in the primary column. There are nine pixels in each column, at that point eight contrast esteems will be created, which is the reason we pick 9 as the width, in light of the fact that 8 bit can simply shape a byte, which is advantageous to change over to hexadecimal worth.

On the contrary if the shading force of the past pixel is more recognized than the subsequent pixel, at that instant the distinction esteem is set to True (i.e., 1), while in case when it is not distinguishable than the subsequent pixel, it is put to False (i.e., 0).

### 3.1.4 Convert to Hash Value

We treat each worth in the distinction esteem cluster as a piece, and every eight pieces structure a hexadecimal worth, and link the hexadecimal qualities, and convert them into a string to get the last difference hash esteem.

## 3.2 Calculate Hamming Distance

The idea of Hamming distance is not just utilized in the field of picture correlation, yet in addition in numerous fields. For a particular presentation, kindly allude to Wikipedia. The Hamming distance demonstrates that the number of steps is expected to adjust A

to B. For instance, for the strings “abx” and “ab3”, the Hamming distance is 1, since you just need to change “x” to “3”. The Hamming distance in “difference hash” is the quantity of changed pieces by figuring the distinction esteem. Our distinction of esteem is addressed by 0 and 1, which can be viewed as twofold. The Hamming distance between two fold 0110 and 0111 is 1.

We convert the difference hash estimation of the two pictures into a twofold contrast and take a XOR. The quantity of digits of “1” in the computation of the XOR result, that is, the quantity of various digits, is the Hamming distance. On the off chance that the info boundary is not the difference, Hash estimation of the two pictures, yet straightforwardly, analyzes the two pictures, at that point there is no compelling reason to create the difference hash esteem and straightforwardly utilizes the distinction exhibited in Step3 to check the various digits, which is the Hamming distance. As a rule, the Hamming distance is under 5, which is essentially a similar picture. You can pass judgment on the basic benefit of Hamming distance dependent on your genuine circumstance.

## 4 Results

For solving the problem of media tampering, we have used our model which is based on blockchain infrastructure. The proposed system heavily relies on a “difference hash” algorithm for detecting the tampered image. We calculate the difference hash value for the two pictures separately. To calculate the same, we zoom in the image enough so that pixel color and size are clear. The color picture will be transformed to grayscale, and the color intensity will be green (0 to 255). Now, we compare the intensity of adjacent pixels in each row to get the difference values for each row separately. Finally, we use these differences to generate hexadecimal values which in turn is used to calculate the Hamming distance. Using this Hamming distance, we conclude if the image is tampered or not. The picture is unaltered if the Hamming distance is less than five.

## 5 Conclusion

In this paper, we proposed another dispersed and altered conformation media exchange structure dependent on the blockchain model. The proposed multimedia blockchain structure is based on a difference hash calculation that employs hash to distinguish any altering and to recover the first substance. We have effectively shown the confirmation of this idea.

We have successfully recognized tampering of images so far. This work of field can be extended for identifying tampering of videos on social media. A video is defined as the collection of many images. Let us say that a video consists of  $n$  images. We create an array of size  $n$  starting from 0 to  $n-1$  storing images. Next, we store the hash created for each of these images stored in another array  $A$ . Eventually, we create the hash of the video at a later stage of time after it has been shared to multiple places, which might or might not be tampered. We store these hashes in an array called  $B$ . Next we compare the hashes stored in  $A[t]$  with  $B[t]$ , where  $t$  ranging from 0 to  $n-1$ . If any of the hashes does not match, we can easily say that the video is tampered.

At present, we have been using a different hash algorithm. In the future, we plan to work on developing other algorithms which will provide better efficiency and accuracy.

**Acknowledgements.** We wish to express our sincere gratitude to Jamkhongam Touthang for providing us with the golden opportunity to do this wonderful project on the topic “detection of tampering in multimedia using blockchain technology to ensure security, privacy, confidentiality and decentralization”. We sincerely thank him for his guidance and encouragement in carrying out this project. We also wish to express our gratitude to the Delhi Technological University.




## References

1. The impact of counterfeit drugs in south and south-east Asia, Available Online. “<https://www.europeanpharmaceuticalreview.com/article/92194/the-impact-of-counterfeit-drugs-in-south-and-south-east-asia/>”
2. Hasan et al (2020) A Blockchain-Based Approach for the Creation of Digital Twins. *IEEE Access* 8:34113–34126
3. Lin C, He D, Kumar N, Huang X, Vijayakumar P, Choo KR (2020) HomeChain: A Blockchain-Based Secure Mutual Authentication System for Smart Homes. *IEEE Internet Things J* 7(2):818–829
4. Zhang C et al (2020) BSFP: Blockchain-Enabled Smart Parking With Fairness, Reliability and Privacy Protection. *IEEE Trans Veh Technol* 69(6):6578–6591
5. Liu X, Sun SX, Huang G (2020) Decentralized Services Computing Paradigm for Blockchain-Based Data Governance: Programmability, Interoperability, and Intelligence. *IEEE Trans Serv Comput* 13(2):343–355
6. S. Seven, G. Yao, A. Soran, A. Onen, and S.M. Muyeen “Peer-toPeer Energy Trading in Virtual Power Plant Based on Blockchain Smart Contracts” *IEEE Access*, vol. 8, pp. 175713–175726, 2020.
7. Jaiman V, Urovi V (2020) A Consent Model for Blockchain-Based Health Data Sharing Platforms. *IEEE Access* 8:143734–143745
8. Guo H, Li W, Nejad M, Shen CC (2020) Proof-of-Event Recording System for Autonomous Vehicles: A Blockchain-Based Solution. *IEEE Access* 8:182776–182786
9. Yang X, Yi X, Nepal S, Kelarev A, Han F (2020) Blockchain voting: Publicly verifiable online voting protocol without trusted tallying authorities. *Future Generation Computer System* 112:859–874
10. Y. Yuan and F. Wang, “Towards blockchain-based intelligent transportation systems,” in *IEEE 19th International Conference on Intelligent Transportation Systems*, pp. 2663–2668, Brazil, 2016.
11. Mengelkamp E, Notheisen B, Beer C, Dauer D, Weinhardt C (2018) A blockchain-based smart grid: towards sustainable local energy markets. *Computer Science-Research and Development* 33:207–214
12. Turkanovic M, Holbl M, Kosic K, Hericko M, Kamisalic A (2018) EduCTX: A Blockchain-Based Higher Education Credit Platform. *IEEE Access* 6:5112–5127
13. J. Kishigami, S. Fujimura, H. Watanabe, A. Nakadaira and A. Akutsu, “The Blockchain-Based Digital Content Distribution System,” *IEEE Fifth International Conference on Big Data and Cloud Computing*, pp. 187–190, China, 2015.
14. M. Mettler, “Blockchain technology in healthcare: The revolution starts here,” *IEEE 18th International Conference on e-Health Networking, Applications and Services*, pp. 1–3, Germany, 2016.
15. McGhin T, Choo KR, Liu CZ, He D (2019) Blockchain in healthcare applications: Research challenges and opportunities. *J Netw Comput Appl* 135:62–75
16. C. C. Agbo , Q. H. Mahmoud and J. M. Eklund, “Blockchain Technology in Healthcare: A Systematic Review”, *Healthcare*, vol. 7, no. 2, article no. 56, 2019.

17. A. A. Siyal et al., “Applications of Blockchain Technology in Medicine and Healthcare: Challenges and Future Perspectives”, *Cryptography*, vol. 3, no.1, article no. 3, 2019.
18. C. Esposito, A. Santis, G. Tortora, H. Chang, and K. R. Choo, “Blockchain: A Panacea for Healthcare Cloud-Based Data Security and Privacy?”, *IEEE Cloud Computing*, vol. 5, 2018.
19. Gordon WJ, Catalini C (2018) Blockchain Technology for Healthcare: Facilitating the Transition to Patient-Driven Interoperability. *Comput Struct Biotechnol J* 16:224–230
20. T. Kumar, V. Ramani, I. Ahmad, A. Braeken, E. Harjula and M. Ylianttila, “Blockchain Utilization in Healthcare: Key Requirements and Challenges,” in *IEEE 20th International Conference on e-Health Networking, Applications and Services*, pp. 1–7, Czech Republic, 2018.
21. L. Bell, W. J. Buchanan, J. Cameron, and O. Lo, “Applications of Blockchain Within Healthcare”, *Blockchain in Healthcare Today*, vol. 1., 2018.



# Effect of Vortex Generators and Rear Spoiler on a Low-End Sedan Passenger Car

Nikhil Pasricha<sup>(✉)</sup> , Sartaj Anwer Khan , and Faisal Shameem 

School of Mechanical Engineering, Galgotias University, Greater Noida, UP, India  
nikhil.pasricha01\_2017@galgotiasuniversity.edu.in

## 1 Introduction

Entering in the industrialization, need for fossil fuels increased drastically. The significant contribution of fossil fuel is to the automobile industry, but the fossil fuel is finite, and thus, automobiles should be designed as efficiently as possible to keep the fuel usage to a minimum and get output as much as possible. Therefore, keeping these conditions in mind, aerodynamic components were introduced. As the twentieth century began, there has been some significant improvements in the aerodynamics of base models. The world also witnessed some of the finest racing cars like Bugatti Veyron achieving top speed up to 253 mph [1]. Improved aerodynamics are the only reason such top speed was achieved. This work briefly shows how the aerodynamics components can help in reducing drag and lift in passenger sedan base models and help increase fuel economy while improving performance.

### 1.1 Aerodynamic Forces

In numerous aerodynamics studies, the important forces are the basic forces, such as lift, drag, thrust and weight of these forces. The lift and drag are aerodynamic forces, i.e. forces due to airflow over the solid body. There are three essential forces to be considered in aerodynamics, and these forces are as follows-

**Thrust**—which assists with pushing an object ahead.

**Drag**—which keeps it down.

**Lift**—which keeps it airborne.

All these properties are measured in aerodynamics having different equations.

1. Conservation of mass
2. Momentum of air
3. Energy in air flows

## 2 Literature Review

The main focus for most of the literature that were studied was minimizing aerodynamic drag, mostly done on higher-end base models and race base models. Some studies modified the Aerodynamics of the Maruti 800 with double spoiler design and concluded that model with both upper and lower spoiler showed minimum  $C_d$  value [3]. Some literature showed work on varying the taper angle or rear underbody angle. Few studies analysed Ahmed model fitted with a rear roof spoiler at different spoiler angles [4]. None of the literature mentioned use of vortex generators or spoilers on passenger base model. Ipilakyaa et al. [5] designed a car model and simulated it with a wing type rear spoiler and reported increased drag coefficient value but decrease in lift coefficient value which is good for stability of cars at higher speed. A passenger car model was studied with different spoiler angle at a particular height, and it was concluded that at angle of  $12^\circ$  minimum,  $C_L$  was observed which is necessary for car stability at higher speeds [6]. Madane et al. [2] analysed a racing car model with different styles of spoiler and concluded that divided rear spoiler gave the best results in reducing drag and lift on the base model. Dickison et al. [7] used various design components like intercooler vent and rear air outlet on a racing car model and observed. The changes in drag and lift values were also recorded with and without added components. The addition of spoiler and other components increased the drag force but the down force helped in decreasing the lift force and stabilizing the base model. A Santro car model stimulation at different velocities showed that with increasing velocity, drag on the base model increased and lift values were higher than usual, and it was concluded that using a base model with rear spoiler improves the overall performance of the base model [8]. In a study of generic car model, it was observed that drag force and lift force decreased with the use of rear spoiler, which shows the effectiveness of rear spoiler at high speeds [9]. In a study on sedan car, different vortex generator shapes was taken, and it was concluded that GOTHIC type of VG was the most efficient of all the other shapes [10]. Yakkundi et al. [11] analysed sedan model with wing type rear spoiler and saw an increase of around 8.2% in  $\Delta C_d$  values at speed of 70 km/hr.

## 3 Governing Equations

Computational fluid dynamics (CFD) model is important to indicate the reasonable arrangement technique. Navier–Stokes expression considered the best technique to tackle the airflow problem and examine the changes in the stream. The Navier–Stokes equation is the conventional technique utilized in all turbulence models and can be considered a “standard” approach. The Navier–Stokes equations can be derived from the three conservation equations, based on the Reynolds transport theorem. The arrangement of conservation equations underneath is autonomous of Navier–Stokes conditions [12].

### (a) Continuity of mass

$$\frac{\partial p}{\partial t} + \frac{\partial y}{\partial x_i}(p u_i) = 0 \quad (1)$$



**(b) Momentum equation**

$$\frac{\partial \rho u_i}{\partial t} + \frac{\partial}{\partial x_j} (\rho u_i u_j) = \frac{\partial p}{\partial x_i} + \frac{\partial \tau_{ij}}{\partial x_j} + \rho g \quad (2)$$

**(c) Energy equation**

$$\frac{\partial \rho c_p T}{\partial t} + \frac{\partial}{\partial x_j} (\rho c_p u_j T) = \frac{\partial p}{\partial x_i} \left( \lambda \frac{\partial T}{\partial x_i} \right) + \frac{\partial}{\partial x_j} (u_i \tau_{ij}) \quad (3)$$

where  $x_i$  stands for a coordinate direction,  $u_i$  denotes a velocity component,  $\tau_{ij}$  denotes components of stress tensor,  $P$  denotes density, and  $g$  denotes gravity.

Eddy viscosity of turbulent heat flux can be modelled as below:

$$q_j^{\text{Re}} = -\bar{\rho} c_p u_j'' T'' = \frac{u_i c_p (T) \partial T}{\rho \nu_i \partial x_j} \quad (4)$$

**3.1 K-ε Turbulence Model**

In the Navier–Stokes condition to yield the Reynolds averaged Navier–Stokes (RANS) equation, Reynolds time averaging procedure was utilized to represent the turbulence effect on the stream field [13], which can be numerically expressed as:

$$\frac{\partial \bar{u}_i}{\partial t} + \bar{u}_j \frac{\partial \bar{u}_i}{\partial x_j} = -\frac{1}{\rho} \frac{\partial \bar{p}}{\partial x_i} + \frac{\partial}{\partial x_j} \left( \nu \frac{\partial \bar{u}_i}{\partial x_j} - \tau_{ij} \right) : i = 1, 2, 4; j = 1, 2, 3; \quad (5)$$

**4 Methodology**

A passenger sedan model with suitable dimensions was designed in CAD software SolidWorks. Various edges were tuned and fined for improving the aerodynamics of the model. The model was the meshed with suitable inputs and simulated at different speeds in Ansys Fluent software [14]. Spoiler and VGs were designed and scaled according to the car model and were then used with model. The final model was then meshed and simulated in same ways as the base model. The results were then recorded and observed for the final conclusion.

- i. Modelling of Base model and mesh it.
- ii. Analyse the Base model at various speed.
- iii. Modelling and Meshing of the base model with Vortex Generator and Rear Spoiler.
- iv. Analyse the final model at the same speed as the base model.

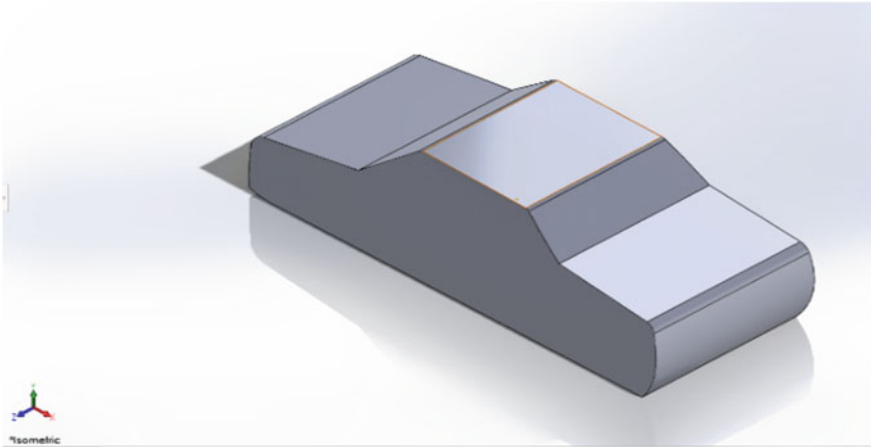


**Fig. 1** Solid model of car

#### **4.1 Base Model Modelling and Meshing**

The base model was designed and drafted in SolidWorks and was converted in solid model (Fig. 1).

The base model was then imported in IGS format in Ansys Fluent 19 R2 and wind tunnel setup enclosure was formed around the model (Fig. 2).

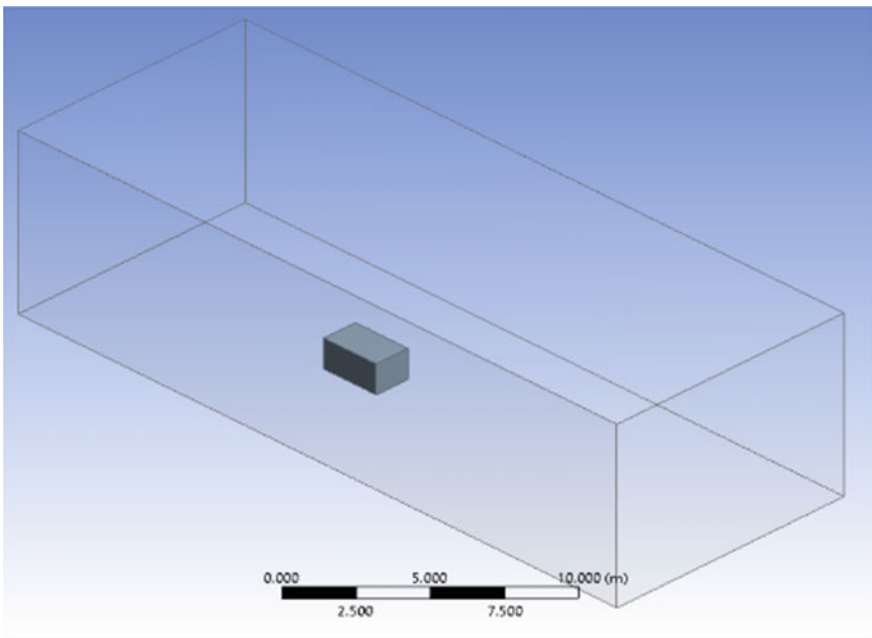


**Fig. 2** Wind tunnel setup in Ansys

The domain size was taken as-

In  $X$  direction:  $+X = 8L$ ,  $-X = 5L$ . In  $Y$  direction:  $+Y = 5L$ ,  $-Y = 0.2L$ . In  $Z$  direction:  $+Z = 2.5L$ ,  $-Z = 2.5L$ ,

where  $L$  is length of the car.

The meshing was done linear with element size 2.5 m (global) and in inflation, first layer thickness was taken as 0.001 m with 30 boundary layers, and growth rate was set at 1.1. Face sizing also was done on base model with element size 0.008 (Fig. 3). The body sizing was also done on a primitive box taken around the base model with type body of influence and element size is 0.05, and the total number of mesh element were 6,006,993, and the total number of nodes formed were 2,751,102.

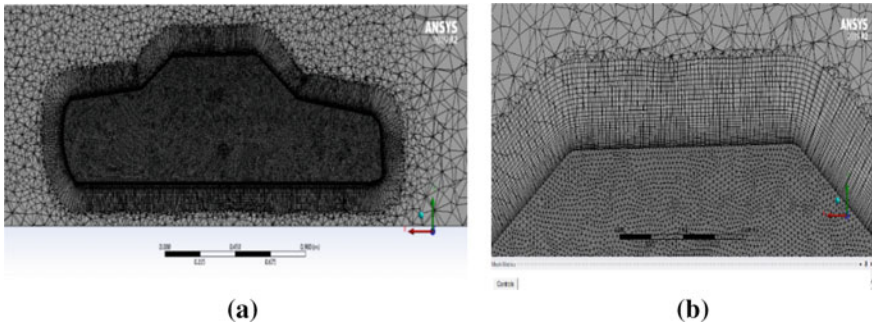


**Fig. 3** Meshing of base model (a) normal view, (b) magnified view

#### 4.2 Analysis of Base Model

The simulation was done at various velocities to get the better results of the base model. The viscous model was taken as standard  $k$ -epsilon, and steady flow was used for the simulation. The solution method scheme used was set as “SIMPLE”, the special discretization “Gradient” was “Least Squares Cell Based”, and the pressure was taken as “Second Order”, whereas momentum was taken as “Second Order Upwind”. After simulating the wind tunnel test, following results were observed (Figs. 4, 5, 6).

#### 4.3 Model and Meshing with VGs and Rear Spoiler

The same settings of base model were used in meshing the final model with the addition of face sizing of each VG and rear spoiler so that better mesh quality could be obtained and better results can be recorded. The values of nodes and elements recorded were 2,001,992 and 4,489,714.

#### 4.4 Analysis of Final Model

See Figs. 7 and 8.

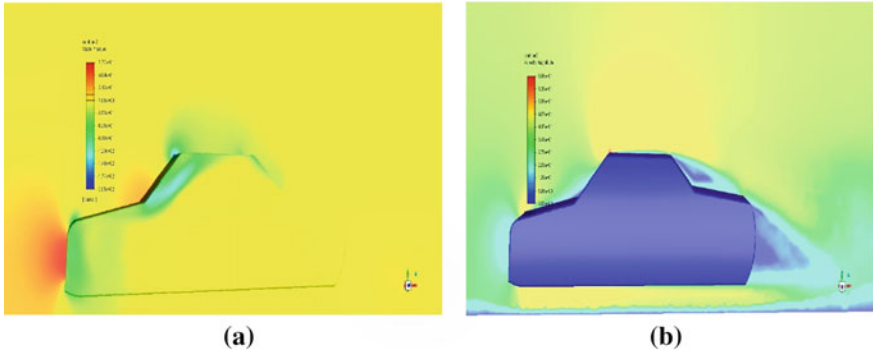


Fig. 4 Pressure (a) and velocity (b) contour of base model (At 120 Km/hr)

### 5 Results and Discussion

In comparing the base model results at changing velocities, it can be seen that the drag and lift coefficients values are increasing steadily with the increase in velocity. At 40 km/h, the base model did not show any significant drag coefficient value because of low speed, and the coefficient value recorded was 0.42, whereas at 80–120 km/h, the values of  $\Delta C_d$  were 0.42 and 0.43. The lift coefficient values also increased steadily with  $\Delta C_l$  (at 40 km/h) 0.055, whereas  $\Delta C_l$  (at 80–120 km/h) was 0.098 and 0.195. These results clearly show that with the increase in vehicle speed, the value of drag and lift coefficients increases steadily with maximum drag and lift coefficient value at 120 km/h. Increased

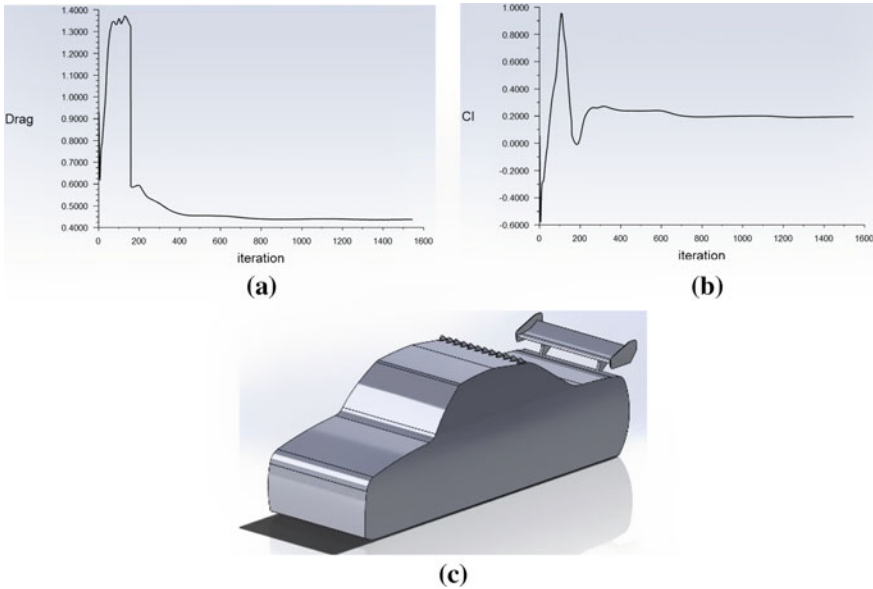
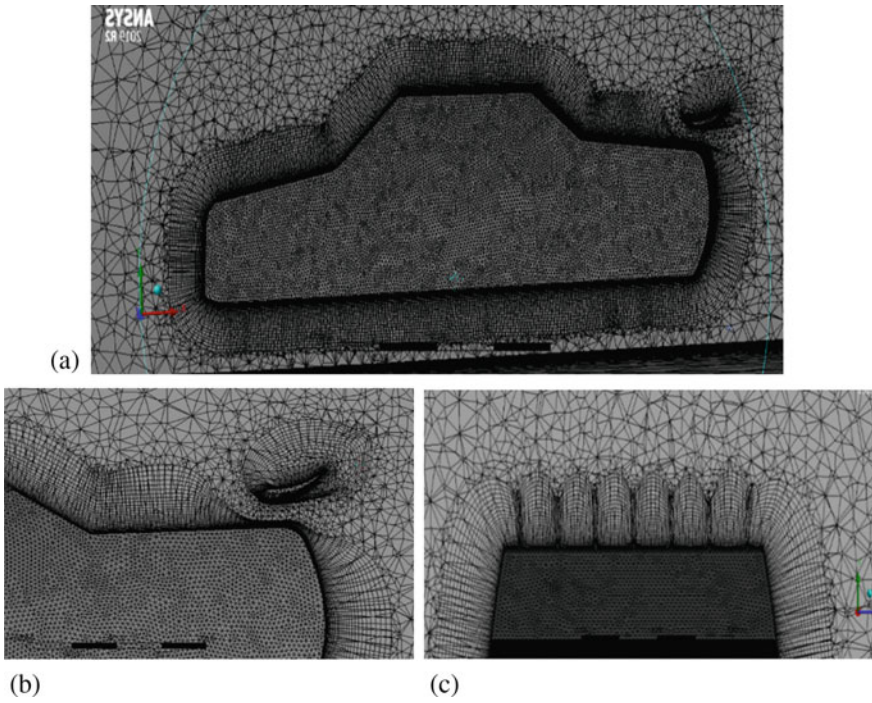
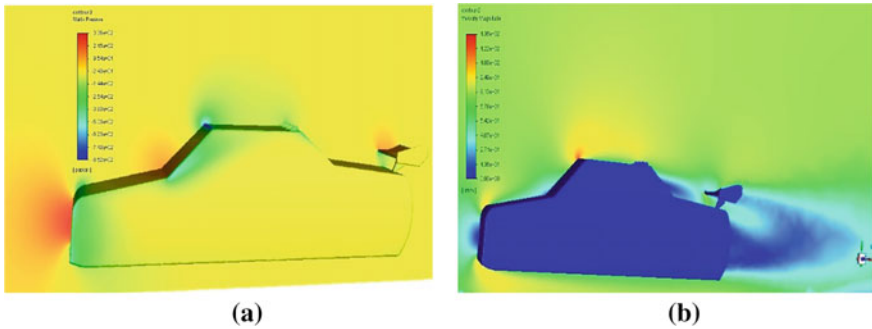


Fig. 5 Coefficient of drag (a) and lift (b) of base model (c) base model with components (solid)



**Fig. 6** Meshing of final model (a) full model, (b) rear spoiler, (c) vortex generators



**Fig. 7** Pressure (a) and velocity (b) contour of final model (At 120 Km/hr)

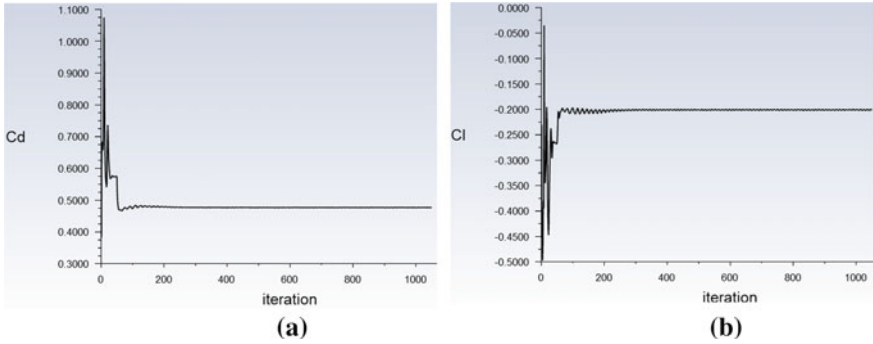


**Fig. 8** Co-efficient of drag (a) and lift (b) of final model

$\Delta C_l$  can make the car unstable at higher speeds; thus, aerodynamic components must be used [15].

Now, with use of aerodynamic components with the base model, the value of  $\Delta C_d$  increased marginally around 9% change with increasing speeds, but  $\Delta C_l$  values decreased around 200% as expected because of aerodynamic components (Figs. 9 and 10). Rear spoiler and VGs helped the car to achieve the negative lift value which will help the car model to generate downforce, which will further be beneficial in maintaining better stability and control at higher speeds [16].

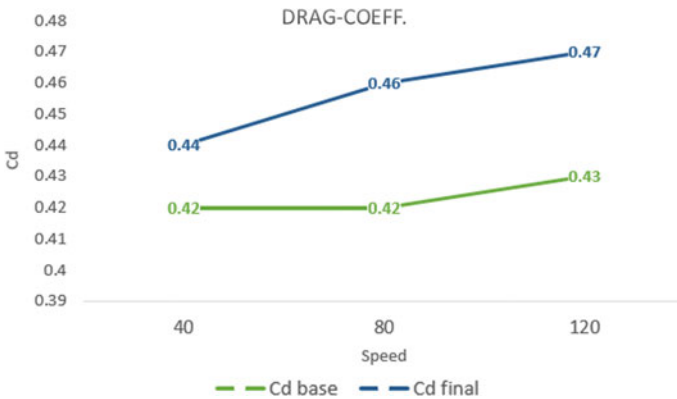


**Fig. 9** Comparison of coefficient of drag of final model to the base model

## 6 Conclusion

This study shows the  $C_d$  observed for the base model was 0.43 at higher speed, whereas with vortex generators and rear spoiler attached, we saw an increase of about 9.3% in  $C_d$  value when compared to the base model at a speed of 120 km/h. Addition of spoiler can be considered as the reason for increased  $\Delta C_d$  value. The  $C_l$  value observed was

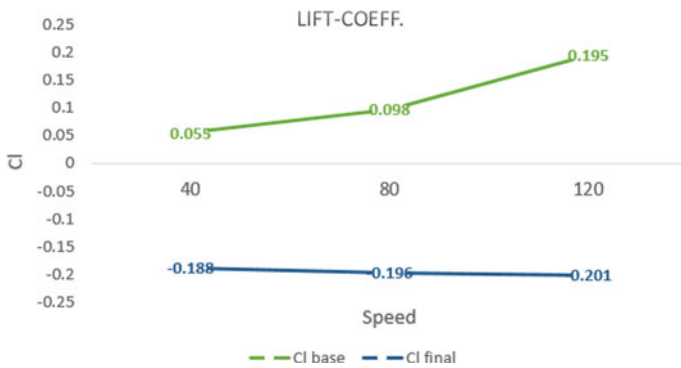


**Fig. 10** Comparison of coefficient of lift of final model to the base model

much lower (around 200% change) which is one of the basic concerns of the model at higher speeds.

Thus, it can be concluded that adding aerodynamic components to the budget sedan cars can help get much better stability and control at higher speeds, which will also help in smooth driving. Increased drag can also be improved by making some design changes in the overall shape of the car, and thus, lower budget sedan cars can also be much stable to drive at higher speeds.

## References

- America E (2010) Showstopper, 1–2
- Madane P, Pande K, Gote P, Dongare P (2020) Study and overview of aerodynamic active rear wing of high speed vehicles, pp 4127–4132
- Guda NT, Suriseti BV, Ram S, Kolla C (2020) Enhancing aerodynamic performance of a hatchback model passenger car using ansys fluent software, Volume IX(V), May 2020, pp. 2593, Issn no, pp. 2347–3150. IX:2593–2605
- Yuan CS, Mansor S, Abdullah MA (2017) Effect of spoiler angle on the aerodynamic performance of hatchback model. *Int J Appl Eng Res* 12:12927–12933
- Pilakyaa TD, Tuleun LT, Kekung MO (2018) Computational fluid dynamics modelling of an aerodynamic rear spoiler on cars. *Niger J Technol* 37:975. <https://doi.org/10.4314/njt.v37i4.17>
- Das RC, Riyad M (2017) CFD analysis of passenger vehicle at various angle of rear end spoiler. *Procedia Eng* 194:160–165. <https://doi.org/10.1016/j.proeng.2017.08.130>
- Dickison M, Ghaleeh M, Milady S et al (2020) Investigation into the aerodynamic performance of a concept sports car. *J Appl Fluid Mech* 13:583–601. <https://doi.org/10.29252/jafm.13.02.30179>
- Patel JR (2017) Fluid dynamics simulation of a car spoiler, pp 0–11. <https://doi.org/10.13140/RG.2.2.18149.91364>
- Prabhu L, Krishnamoorthi S, Gokul P et al (2020) Aerodynamics analysis of the car using solidworks flow simulation with rear spoiler using CFD. *IOP Conf Ser Mater Sci Eng* 993. <https://doi.org/10.1088/1757-899X/993/1/012002>
- Sen W (2020) Experimental and CFD analysis on car with several types of vortex generators

11. Yakkundi V, Mantha SS (2018) Effect of spoilers on aerodynamic properties of car effect of spoilers on aerodynamic properties of a car 7:271–280
12. Elewe AM (2020) Numerical simulation of surface curvature effect on aerodynamic performance of different types of airfoils. IOP Conf Ser Mater Sci Eng 928. <https://doi.org/10.1088/1757-899X/928/3/032003>
13. Tsai CH, Fu LM, Tai CH (2009) Computational aero-acoustic analysis of a passenger car with a rear spoiler. Appl Math Model 33:3661–3673. <https://doi.org/10.1016/j.apm.2008.12.004>
14. ANSYS Fluent 2019 R2 theory guide. <https://ansyshelp.ansys.com/>. Last Accessed 16 April 2021
15. Velagapudi NK, LN K, Rao LNVN, SR Y (2015) Investigation of drag and lift forces over the profile of car with rearspoiler using CFD. Int J Adv Sci Res 1:331. <https://doi.org/10.7439/ijasr.v1i8.2510>
16. Cakir M (2012) Scholar commons CFD study on aerodynamic effects of a rear wing/spoiler on a passenger vehicle, pp 1–72





# Capacitance and Speed Required for Rated Generation by a Self-excited Induction Generator

D. C. Meena, Suraj Bhan Yadav<sup>(✉)</sup>, Pawan Yadav, and Sumit

Delhi Technological University, New Delhi, India

## 1 Introduction

Rising demand for energy is a consequence of rapid development happening all around the world. Proportion of power which is generated through conventional sources, like coal, fuel and gas, is around 70–75% of the total generation, which is very harmful for nature. Thus, in recent years, emphasis has been on looking for non-conventional energy sources for power generation like solar, wind, hydro, bio-gas etc. Amongst these sources, it has been found that wind is one of the most feasible resources for generation [1–3]. Induction generator is popularly employed for harnessing wind energy because of its capability to generate at variable minimal maintenance and repair [4].

Induction generator has an important feature: self-excitation, which requires connecting a capacitor bank across the stator terminal. The self-excitation process in SEIG is similar to that observed in DC generator. Also, there should be some residual magnetism present in machine, which is essential for the voltage build up process. Also, it is to be noted that the residual magnetism must be enough for voltage build up process to occur. RC Bansal [5] has given an overview of SEIG.

Despite its numerous advantages, SEIG finds limited application due to poor voltage and frequency regulation. However, introduction of power electronic controllers has improved the scenario. Venkatesa and Bhim Singh have examined the performance of SEIG using controllers like impedance controller and DSTATCOM [6, 7], and it was demonstrated that these controllers are quite effective in regulating output voltage and frequency.

For studying the power generation and problems associated with SIEG using wind energy, steady-state analysis of SEIG becomes very essential. There are various methods for steady-state analysis, the most common being application of loop impedance and nodal admittance to the equivalent electrical circuit of the system. Steady-state analysis of SEIG has been examined and presented by Murthy [8] and Sharad Rajan [9]. In this paper, nodal admittance method has been used for obtaining the non-linear equations governing the system in steady state. These non-linear equations are used in study and analysis of performance for parameters such as load, excitation capacitance, speed and generated voltage and frequency.

Research work has been carried out previously, wherein magnetizing reactance of machine and frequency of generated voltage has been evaluated for known values of

load, speed and capacitor bank. Jain, Mittal and Bhim Singh [10] developed a new iterative technique for steady-state analysis of a three phase SEIG, thereby determining the frequency and magnetizing reactance. A similar work is presented using linear search and binary search algorithms [11]. Application and result of optimization techniques—GA, APSO, PSO and simulated annealing—to a same problem have also been analyzed [12, 13]. However, in analysis carried out in this paper, value of magnetizing reactance is fixed as rated value and the generated frequency as 50 Hz in the non-linear equations governing the system. Afterwards, these equations are solved for capacitance (to be connected at stator terminal) and the corresponding rotor speed, for different load types and values. Multivariate Newton Raphson technique is used to obtain the solution of these non-linear equations. Once speed and capacitance are known, evaluation of output load voltage, current and power is also done.

## 2 Equivalent Circuit

Figure 1 represents the experimental setup under study. A wind turbine is coupled, via gear, to the rotor of an induction generator. Capacitor bank is used for providing reactive power to generator and load.

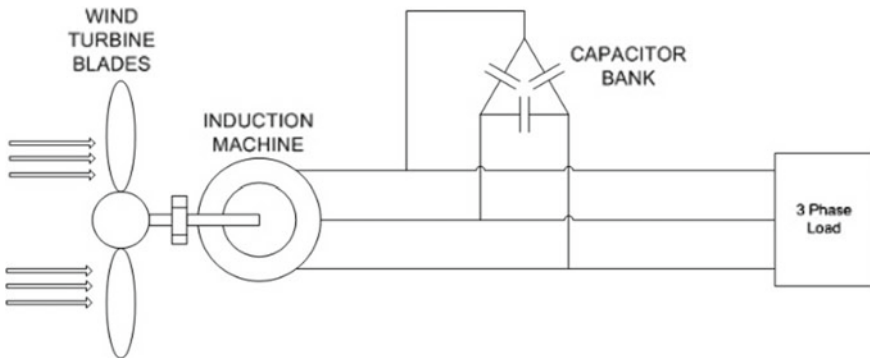


**Fig. 1** SEIG coupled to a wind turbine and delivering to a 3 phase load

Per phase equivalent circuit of this setup is given below, as shown in Fig. 2. Where

$R_1$ : Stator resistance.

$R_2$ : Rotor resistance (referred to stator).

$X_1$ : Stator leakage reactance.

$X_2$ : Rotor leakage reactance (referred to stator).

$X_m$ : Magnetizing reactance.

$X_C$ : Excitation capacitance.

$R_L$ : Load resistance.

$X_L$ : Load reactance.

$F$ : Per unit frequency.

$N$ : Per unit speed.

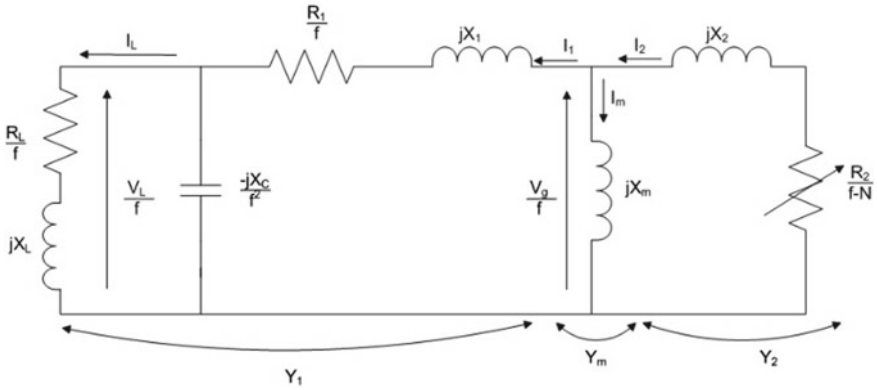


**Fig. 2** Per phase equivalent circuit

Application of KCL in the equivalent circuit yields

$$I_1 + I_m = I_2 \tag{1}$$

$$\frac{V_g}{f} \times Y_1 + \frac{V_g}{f} \times Y_m = -\frac{V_g}{f} \times Y_2 \tag{2}$$

Since air gap voltage must not be zero, i.e.  $V_g \neq 0$ , therefore

$$Y_1 + Y_2 + Y_m = 0 \tag{3}$$

Equating real and imaginary parts of Eq. (3) to zero, real part yields

$$\frac{\left(R + \frac{R_1}{f}\right)}{\left(R + \frac{R_1}{f}\right)^2 + (X_1 - X)^2} + \frac{\left(\frac{R_2}{f-N}\right)}{\left(\frac{R_2}{f-N}\right)^2 + (X_2)^2} = 0 \tag{4}$$

and equating imaginary part

$$\frac{(X_1 - X)}{\left(R + \frac{R_1}{f}\right)^2 + (X_1 - X)^2} + \frac{(X_2)}{\left(\frac{R_2}{f-N}\right)^2 + (X_2)^2} + \frac{1}{X_m} = 0 \tag{5}$$

where

$$R - jX = \left(\frac{R_L}{f} + jX_L\right) \parallel \left(\frac{-jX_C}{f^2}\right) \tag{6}$$

### 3 Solution using Newton Raphson Method

Equations (4) and (5) have been previously solved by authors for known values of speed, load and excitation capacitance. Solution thus yields value of generated frequency and magnetizing reactance. However, in this paper, the aim is to evaluate the speed and capacitance required for rated operation of a SEIG, i.e. at rated value of  $X_m$  and rated frequency which is 50 Hz. Parameters: load voltage, current and power are also evaluated.

Once  $X_m$  and  $f$  are fixed and considering the applied load to be balanced, each of Eqs. (4) and (5) is essentially a two variable function given by

$$F_1(X_C, N) = \frac{\left(R + \frac{R_1}{f}\right)}{\left(R + \frac{R_1}{f}\right)^2 + (X_1 - X)^2} + \frac{\left(\frac{R_2}{f-N}\right)}{\left(\frac{R_2}{f-N}\right)^2 + (X_2)^2} = 0 \tag{7}$$

$$F_2(X_C, N) = \frac{(X_1 - X)}{\left(R + \frac{R_1}{f}\right)^2 + (X_1 - X)^2} + \frac{(X_2)}{\left(\frac{R_2}{f-N}\right)^2 + (X_2)^2} + \frac{1}{X_m} = 0 \tag{8}$$

There are two unknowns and two equations (non-linear). Equations (7) and (8) are solved for  $X_C$  and  $N$  using the multivariate Newton Raphson method given below.

$$X^{i+1} = X^i - [J^i]^{-1} F^i \tag{9}$$

where  $X^i$ ,  $J^i$  and  $F^i$  are given by Eqs. (10), (11) and (12), respectively.

$$X^i = \begin{bmatrix} X_C^i \\ N^i \end{bmatrix} \tag{10}$$

$$J^i = \begin{bmatrix} \left. \frac{\partial F_1(X_C, N)}{\partial X_C} \right|_{(X_C^i, N^i)} & \left. \frac{\partial F_1(X_C, N)}{\partial N} \right|_{(X_C^i, N^i)} \\ \left. \frac{\partial F_2(X_C, N)}{\partial X_C} \right|_{(X_C^i, N^i)} & \left. \frac{\partial F_2(X_C, N)}{\partial N} \right|_{(X_C^i, N^i)} \end{bmatrix} \tag{11}$$

$$F^i = \begin{bmatrix} F_1(X_C^i, N^i) \\ F_2(X_C^i, N^i) \end{bmatrix} \tag{12}$$

Initially,  $i = 0$  and  $X^0$  are the initial solution guess, and thereby  $X^1$  is evaluated with help of Eq. (9). Each iteration of Eq. (9) gives a closer value to the actual solution. Hence, similarly,  $X^2$  is evaluated after having found  $X^1$  and so on  $X^3, X^4 \dots$  are evaluated. Equation (9) is allowed to execute in a loop, and the condition for the termination of loop is when the solution, i.e.  $X_C$  and  $N$ , either starts repeating itself or converges.

Once  $X_C$  and  $N$  are known, capacitance is simply given by Eq. (13)

$$C = \frac{1}{2 \times \pi \times 50 \times X_C} \tag{13}$$

and rotor speed is given by Eq. (14)

$$N_r = N \times \text{synchronous speed} \tag{14}$$

Load voltage and current are obtained using Eqs. (15) and (16), respectively. Equations (17) and (18) are used for calculating power.

$$V_L(\text{line}) = \frac{\sqrt{R^2 + X^2}}{\sqrt{\left(R + \frac{R_1}{f}\right)^2 + (X_1 - X)^2}} \times V_g \quad (15)$$

$$I_L(\text{line}) = \sqrt{3} \times \frac{\frac{V_L}{f}}{\sqrt{\left(\frac{R_L}{f}\right)^2 + (X_L)^2}} \quad (16)$$

$$\text{Power}_{\text{kVA}} = \frac{\sqrt{3} \times V_L \times I_L}{1000} \quad (17)$$

$$\text{Power}_{\text{kW}} = \frac{\sqrt{3} \times V_L \times I_L \times \cos(\theta)}{1000} \quad (18)$$

## 4 Results and Discussion

Induction machine, to be used as a SEIG, is rated as 3.7 kW, 3 phase, 4 pole, 50 Hz, 415 V, 7.6 A, 1420 rpm,  $\Delta$  connected. Also, per phase parameters of the machine are  $R_1 = 0.053$  p.u,  $R_2 = 0.061$  p.u,  $X_1 = 0.087$  p.u,  $X_2 = 0.087$  p.u,  $X_m = 1.853$  p.u.

In Eqs. (7) and (8), values of  $f$  and  $X_m$  are taken as 1 and 1.853, respectively. Multivariate Newton Raphson method is applied, as discussed in Sect. 3, to solve for 'X<sub>c</sub>' and 'N'. This paper considers two types of balanced loads for the study: purely resistive (pf = 1) and inductive (pf = 0.8 lagging).

### 4.1 UPF Load

Balanced resistive loads of per phase value, 1, 1.2, 1.4, 1.6, 1.8 and 2 p.u, are connected at the stator terminals, each at a time. Thus, values of speed and capacitance, for rated operation, are predetermined using Newton Raphson technique for given different loads, as listed in Table 1. Load line voltage, line current and three phase power have also been calculated.

Load voltage outputs for various UPF loads are quite close to each other, as shown in Fig. 3, and are equal for all practical purposes. Also, note that all the computed voltages are at rated frequency, i.e. 50 Hz.

### 4.2 Inductive Load at 0.8 Pf Lagging

The proposed method is also applied to inductive loads at 0.8 lagging pf. Impedance of loads connected at the stator terminal, per phase, is 1.25, 1.375, 1.5, 1.625, 1.75 and 1.875 p.u. Results obtained by application of Newton Raphson technique are listed in Table 2.

Again, the Newton Raphson solution yields nearly similar generated voltage levels (at 50 Hz) for different load values, as observed in Fig. 4.

**Table 1** Results for unity power factor loads

S. no.	$R_L$ (p.u)	Speed (rpm)	Slip (%)	Capacitance/phase (mF)	$V_L$ (V)	$I_L$ (A)	Power (kW)
1	1.0	1601.5	-6.7652	2.4736	417.6335	7.6490	5.530
2	1.2	1584.4	-5.6250	2.2387	419.5780	6.4038	4.654
3	1.4	1572.4	-4.8248	2.0967	421.1734	5.5099	4.019
4	1.6	1563.4	-4.2301	2.0034	422.4807	4.8361	3.539
5	1.8	1556.6	-3.7699	1.9385	423.5628	4.3098	3.162
6	2.0	1551.0	-3.4027	1.8912	424.4696	3.8871	2.858

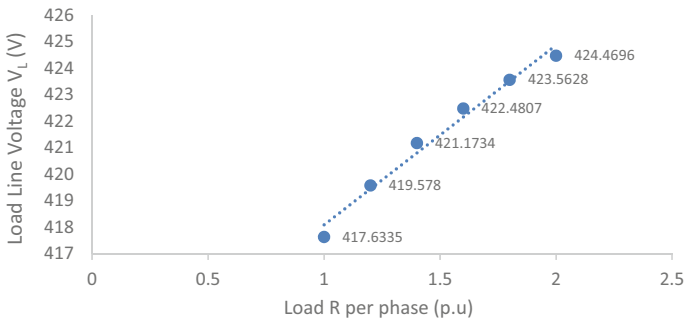


**Fig. 3** Voltage generated for different unity power factor loads

**Table 2** 0.8 pf lagging loads

S. no.	$Z_L$ (p.u)	Speed (rpm)	Slip (%)	Capacitance per phase (mF)	$V_L$ (V)	$I_L$ (A)	Power	
							kVA	kW
1	1.250	1564.947	-4.3298	3.5462	422.2545	6.1869	4.52	3.62
2	1.375	1559.156	-3.9438	3.3510	423.1468	5.6363	4.13	3.30
3	1.500	1554.344	-3.6229	3.1923	423.9211	5.1761	3.80	3.04
4	1.625	1550.279	-3.3519	3.0602	424.5980	4.7856	3.52	2.82
5	1.750	1546.799	-3.1199	2.9488	425.1943	4.4500	3.28	2.62
6	1.875	1543.784	-2.9189	2.8535	425.7230	4.1585	3.07	2.45

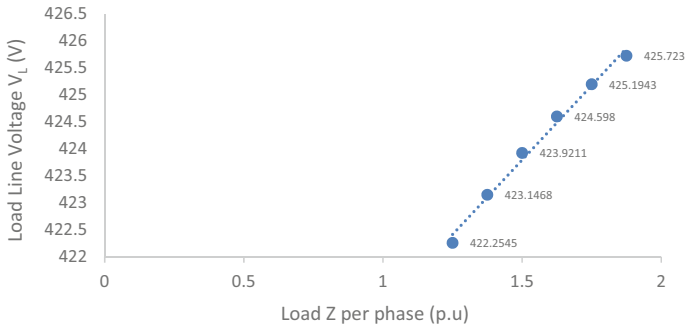


**Fig. 4** Voltage generated for different inductive loads at 0.8 pf lagging

## 5 Conclusion

Given work presents a simple approach to predetermine the capacitance and rotor speed, for different load values, which ensues rated operation of a SEIG. It is inferred that for various resistive loads (UPF) in range of 1–2 p.u, speed and capacitance requirement both decrease with increase in load, however, it is to be noted that it is also accompanied by a decrease in load current and load power (load voltage remains nearly constant). Similar trend is observed when inductive loads (0.8 pf lagging) ranging between 1.250 and 1.875 p.u are considered. Again, with increasing load, there is a decrease in the speed and capacitance requirement, and decrease in the load current and power as well, at almost equal voltage levels. Frequency of generated voltage is 50 Hz in all cases. It is noted that load power is compromised for ensuring rated voltage and frequency generation.

To conclude, this work can find practical application in designing of a control system which constantly monitors the load, and for any change, it automatically controls the speed of rotor and switches on capacitor units of desired value so that the output voltage level and frequency do not fluctuate causing malfunctioning otherwise. It might not be feasible to find practical capacitors with capacitance value equal to what is theoretically desired, hence an approximately equal value of capacitor must be employed.

## References

1. Raina G, Malik OP (1983) Wind energy conversion using a self excited induction generator. In: IEEE Trans Power Apparatus Syst, vol. PAS 102(12):3933–3936, Dec 1983
2. Abdel-Karim AS, Hassan SA, Shakralla SS (1983) Power generation by wind energy systems using induction generators. In: Proc. 2nd national power system conf. Hyderabad, India, Sept. 1983, pp. 43–50
3. Bansal RC, Bhatti TS, Kothari DP (2003) A bibliographical survey on induction generators for application of nonconventional energy systems. In: IEEE Trans Energy Convers 18(3):433–439, Sept 2003
4. Chapallaz JM, Ghali J, Eichenberger P, Fischer G (1992) Manual on induction motors used as generators 10

5. Bansal RC (2005) Three-phase self-excited induction generators: an overview. In: IEEE Trans Energy Convers 20(2):292–299
6. Venkatesa Perumal B, Chatterjee JK (2008) Voltage and frequency control of a stand alone brushless wind electric generation using generalized impedance controller. In: IEEE Trans Energy Convers 23(2), June 2008
7. Chilipi RR, Singh B (2014) Performance of a self-excited induction generator with DSTATCOM-DTC drive-based voltage and frequency controller. In: IEEE Trans Energy Convers 29(3), Sept 2014
8. Murthy SS, Singh BP, Nagamani C, Satyanarayna KVV (1988) Studies on the use of conventional induction motors as selfexcited induction generator. In: IEEE Trans Energy Convers 3:842–848
9. Rajan S (2012) Steady state performance evaluation of self excited induction generator for SHP. Dissertation IIT-Roorkee
10. Jain DK, Mittal AP, Singh B (1998) A new iterative technique for the steady state analysis of three phase self excited induction generator. In: 10th national power systems conference 1998, MS Univerity of Baroda, Vadadora
11. Arthishri K, Anusha K, Kumaresan N, Senthil Kumar S (2017) Simplified methods for the analysis of selfexcited induction generators. In: IET Electric Power Appl, July 2017
12. Saha SK, Sandhu KS (2017) Optimization techniques for the analysis of self-excited induction generator. In: 6th international conference on smart computing and communications, ICSCC Dec 2017
13. Chaturvedi Y, Kumar S, Bansal P, Yadav S (2019) Comparison among APSO, PSO and GA for performance investigation of SEIG with balanced loading. In: IEEE





# Design and Analysis of Wheel Rim Using Composite Materials and Carbon Fibres

Ashish, Anas Khan, P. Suresh, and Shrikant Vidya<sup>(✉)</sup>

Galgotias University, Uttar Pradesh, Greater Noida, India  
shrikant.vidya@galgotiasuniversity.edu.in

## 1 Introduction

In this theory, we have discussed an automotive wheel; the wheels are designed in the earlier time generally with woods and steels; with time, wheels are built with the metal configuration, and rims are made with forged aluminium alloys. Today in modern vehicles, wheels are made for aesthetic and for better durability.

In the year 1970s, numerous innovative techniques of testing which well support the wheel with stress measurement have been introduced. In recent years, a series of steps have been improved by the experiment's quality and an analytical method developed for doing a structural analysis of the wheel. Wheels are the crucial parts of vehicles; it handles all the weight of vehicles. Therefore, the design of the wheel is a prime consideration. For better safety and long life, it is necessary to study the fatigue life cycle of the wheel. Basically, steel, an alloy of aluminium, and magnesium are used in making the wheel. Alloy wheels different from base and steel wheels are the better choice because of their lighter weight, which helps to increase fuel efficiency and also enhances the efficiency of the engine [4, 5]. Alloy wheels are also a good heat conductor than steel, which helps in improving heat dissipation to the surrounding from the brakes. This reduces the risk of brake failure and accident [6, 7]. Further alloy continues to be one of the best choices for manufacturer and customer because of its mechanical and thermal property than steel. After the development of carbon fibres, the aluminium alloy loses its grip in the market. Carbon fibre provides much better quality and results than alloys [8]. However alloy performed better at some places, it becomes very necessary to analyse the fatigue life of both the materials for better understanding and selecting better material for the wheel design. ANSYS provides a better platform for analysing 3D models [9, 10]. It also has a material library which provides many different types of material to do analysis. However, ANSYS is not much capable of finding stress in composite material. There are many softwares which are specifically made to determine stress will perform better than ANSYS when dealing with composite materials. But finite element analysis is the most widely used method [11, 12]. Wheel fatigue or failure happens generally due to notches, welded regions, or any irregularity during manufacturing [13, 14]. The initial stage of fatigue is the development of a small crack in structure, and as time passes, this crack propagates through the body and ultimately results in failure of parts.

- Composite materials: A composite material is also known as composition material or sometimes also called as shortened to composite. They are mainly produced from two or more constituent materials, and the resultant material is developed with high strength and durability. These constituent materials have dissimilar properties from their base material and are merged to create a material with desired properties [15]. Within the resulted structure, the individual elements remain distinct and separate. There are many types of composite materials like UD, woven, wet, Prepreg, etc.
- Carbon fibres: Sometimes it is also written as carbon fibres, which are fibres that size about 5–10  $\mu\text{m}$  in diameter, and the main constituent is the carbon atom. High tensile strength, low weight-to-strength ratio, high stiffness, high temperature, etc., are some of the advantages of carbon fibres. These properties have made carbon fibre very popular in mechanical engineering military, aerospace, along with other fields like sports. However, they are expensive when compared with similar fibres.

Carbon fibres are combined with other materials like polymers, epoxy, etc., to develop the desired composite. To make carbon fibre, it is first permeated with a plastic resin and then baked, after which the resulting material develops a very high strength-to-weight ratio and is extremely rigid but a little bit brittle [16]. When carbon fibres are composited with other materials like graphite, its resultant product reinforced carbon–carbon composites. Carbon–carbon composite has high heat tolerance.

## 2 Methodology

### 2.1 Wheel Rim Design

The design of the rim is modelled in SOLIDWORKS. SOLIDWORKS is an easy and user-friendly CAD software to develop 3D models. It also provides the feature of simulation, but the simulation is done in ANSYS. The model is made into one single part, and then we split the model into two equal halves (Fig. 1).

### 2.2 Material Selection

There are three different materials considered for this analysis whose properties are given below:

#### (A) Aluminium alloy

1. Density:  $2.77 \text{ E-6 kg/mm}^3$
2. Yield tensile strength: 280 MPa
3. Compressive tensile strength: 280 MPa
4. Ultimate tensile strength: 310 MPa
5. Modulus of elasticity: 71,000 MPa.

#### (B) Epoxy\_Carbon\_UD\_230GPa\_Prepreg

The property of composite materials is slightly different from general material. The property table is taken from ANSYS and shown below:

- (1) Orthotropic elasticity

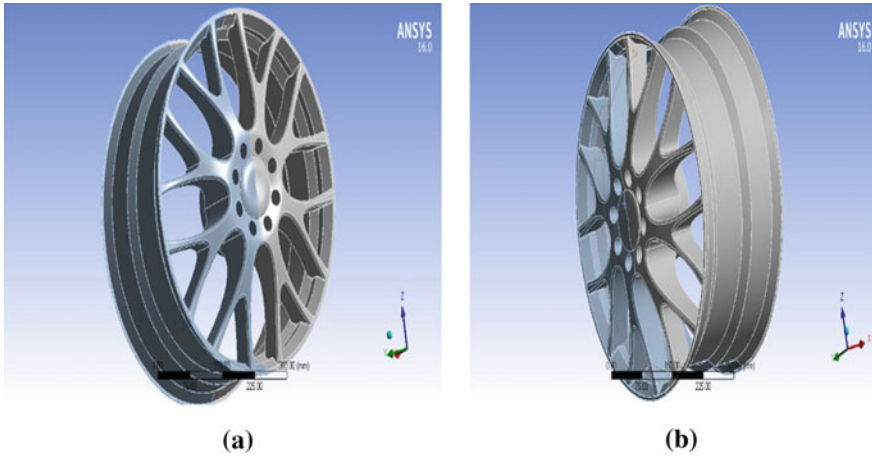


**Fig. 1 a** Model of wheel rim **b** isometric view of the rim in the X, Y, Z plane

Temperature °C	Young's modulus X direction MPa	Young's modulus Y direction MPa	Young's modulus Z direction MPa	Poisson's ratio XY	Poisson's ratio YZ	Poisson's ratio XZ	Shear modulus XY MPa	Shear modulus YZ MPa	Shear modulus ZX MPa
	1.21e+005	8600	8600	0.27	0.4	0.27	4700	3100	4700

(2) Orthotropic strain limits

Temperature °C	Tensile X direction MPa	Tensile Y direction MPa	Tensile Z direction MPa	Compressive X direction MPa	Compressive Y direction MPa	Compressive Z direction MPa	Shear XY MPa	Shear YZ MPa	Shear XZ
	1.67e-002	3.2e003	3.2e003	-1.08e-002	-1.92e-002	-1.92e-002	1.2e-002	1.1e-002	1.2e-002

(3) Orthotropic stress limits

Temperature °C	Tensile X direction MPa	Tensile Y direction MPa	Tensile Z direction MPa	Compressive X direction MPa	Compressive Y direction MPa	Compressive Z direction MPa	Shear XY MPa	Shear YZ MPa	Shear XZ
	2231	29	29	-1082	-100	-100	60	32	60

There are three different materials considered for this analysis whose properties are given below:

**(C) Epoxy\_Carbon\_UD\_395GPa\_Prepeg**

(1) Orthotropic elasticity

Temperature °C	Young's modulus X direction MPa	Young's modulus Y direction MPa	Young's modulus Z direction MPa	Poisson's ratio XY	Poisson's ratio YZ	Poisson's ratio XZ	Shear modulus XY MPa	Shear modulus YZ MPa	Shear modulus ZX MPa
	2.09e+005	9450	9450	0.27	0.4	0.27	5500	3900	5500

(2) Orthotropic strain limits

Temperature °C	Tensile X direction MPa	Tensile Y direction MPa	Tensile Z direction MPa	Compressive X direction MPa	Compressive Y direction MPa	Compressive Z direction MPa	Shear XY MPa	Shear YZ MPa	Shear XZ MPa
	9.2e-00	3.1e-00	0	-5.3e-003	-1.72e-002	0	1.6e-002	0	0

(3) Orthotropic stress limits

Temperature °C	Tensile X direction MPa	Tensile Y direction MPa	Tensile Z direction MPa	Compressive X direction MPa	Compressive Y direction MPa	Compressive Z direction MPa	Shear XY MPa	Shear YZ MPa	Shear XZ MPa
	1979	26	26	-893	-139	-139	100	50	100

2.3 Meshing and Analysis of Wheel Rim

Meshing is an important task in analysis. A high-quality mesh generates a more accurate result. Meshing divides the model into small blocks, and analysis is done in each block. For this paper, we have set meshing type to tetrahedron and sizing to 25 mm. The meshed body is shown below (Fig. 2).

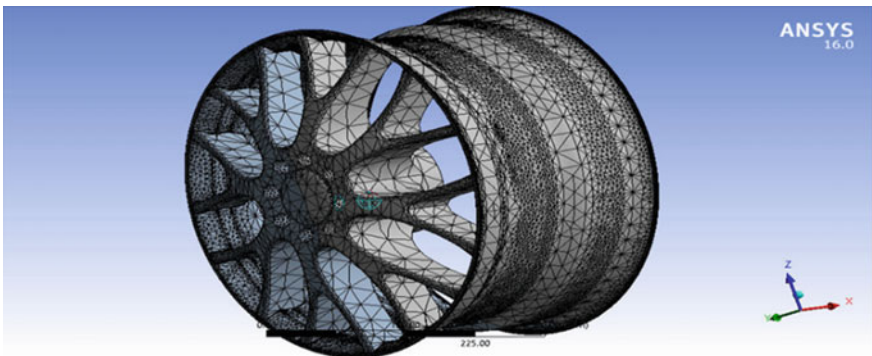


Fig. 2 Meshing of wheel rim using ANSYS

## 2.4 Analysis Parameters

For finite element analysis, a normal pressure of 0.24131 MPa is applied to the circumference of the tyre. Since nominal tyre pressure is approx. 0.24131 MPa. The fixed support is applied to the bolt face. A downward force is applied on the rim face, as an average weight of a car is around 2000 lbs approx. 8853 N, but we have applied 10,000 N for more safety. Also, an angular velocity of 69.7 rad/s is given at the centre (Fig. 3).

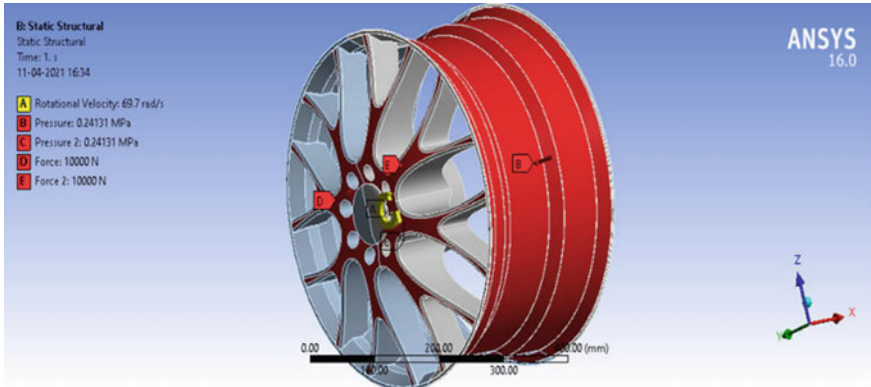


Fig. 3 Applied load and forces to the rim using ANSYS

## 3 Results and Discussion

The result of the analysis shows that the maximum stress and deformation of the rim occur at circular circumference and notches, while the spokes part is not much affected and can withstand the load under given conditions. From the analysis, we can say that every element performs better at some conditions than others. Figure 6b shows that aluminium alloy performs better at case of stress than carbon fibres. On the other hand, Figs. 4a and 5a show that carbon fibre performance is better in the total deformation case. The values of total deformation are as follows:

- I.Epoxy\_Carbon\_230GPa\_UD: 1.3422–23.53 mm
- II.Epoxy\_Carbon\_395GPa\_UD: 0.85261–13.848 mm
- III.Aluminium alloy: 8.3532–56.759 mm.

Figure 4a shows that total deformation in carbon epoxy 230GPa (UD) occurs at the notches. The circumference and the spokes part develop a medium level of deformation approx. 6–21 mm. Overall, all the parts experience a low amount of deformation. While in the case of Epoxy\_Carbon\_395GPa\_UD, it shows the same deformation distribution as seen in Epoxy\_Carbon\_230GPa\_UD, but in this case, the maximum deformation is very less which is 13.848 mm. In Fig. 6a, aluminium alloy shows that the maximum total deformation is 56.756 which is nearly double the carbon fibre. The stress values of materials are as follows:

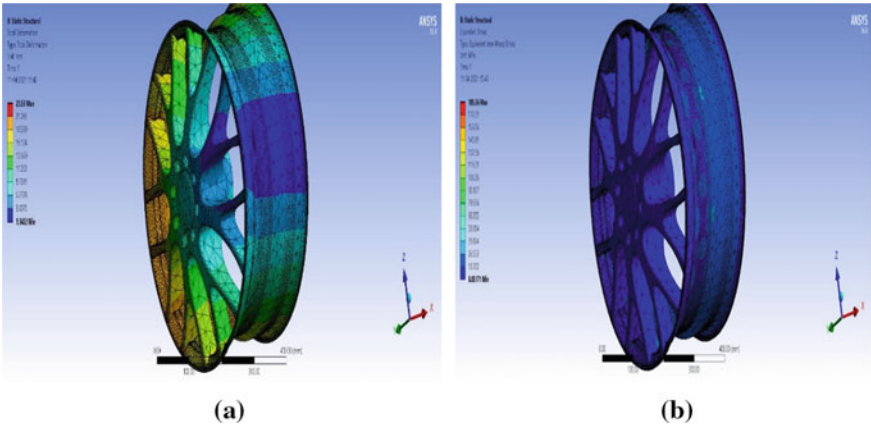


**Fig. 4 a** Total deformation of Epoxy\_carbon\_UD\_230GPa **b** Stress of Epoxy\_carbon\_UD\_230GPa

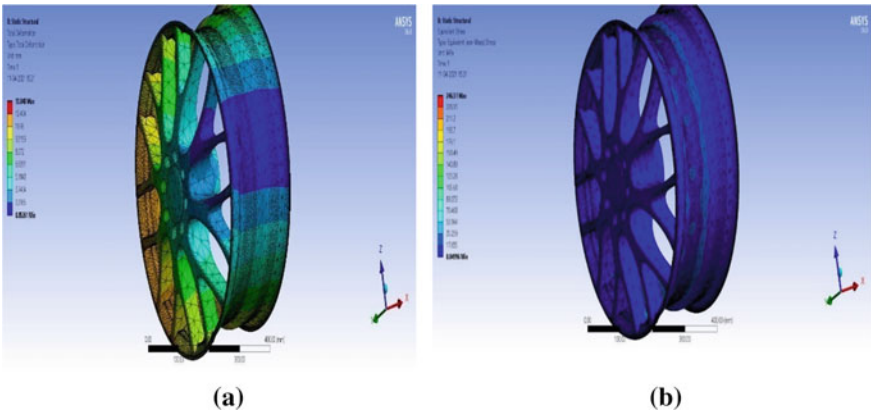


**Fig. 5 a** Total deformation of Epoxy\_carbon\_UD\_395GPa **b** Stress in Epoxy\_carbon\_UD\_395GPa

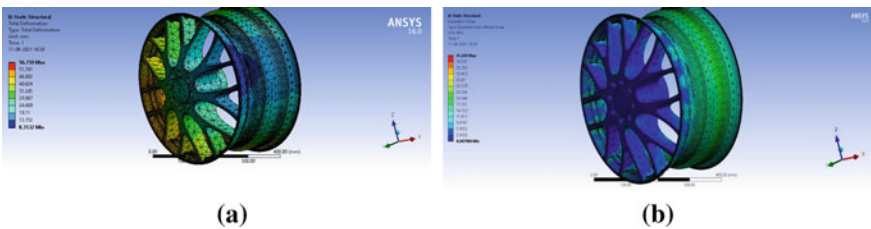


**Fig. 6 a** Total deformation in aluminium alloy **b** Stress in aluminium alloy

- I.Epoxy\_Carbon\_230GPa\_UD: 0.05171–185.56 mm
- II.Epoxy\_Carbon\_395GPa\_UssD: 0.4996–246.51 MPa
- III.Aluminium alloy: 0.0487–41.239 MPa.

The data shows that aluminium has resistance towards stress when compared to Epoxy\_Carbon\_230GPa\_UD and carbon\_epoxy\_395\_ud. On carefully looking at the figures of stress development in carbon fibres, it shows that almost full body experiences a very less amount of stress approx. 0–20 MPa. The main reason for max stress is the area of notches and fillets. This can be reduced by improving the surface finish. So, we can say that carbon fibre is a better choice when compared with aluminium alloy. Among the two carbon fibres, Epoxy\_Carbon\_395GPa\_UD performs poorly in handling stress which can be seen in Fig. 5b as compared to Epoxy\_Carbon\_230GPa\_UD in Fig. 4b, and Epoxy\_Carbon\_230GPa\_UD has more resistance in deformation.

## 4 Conclusion

In this paper, we have successfully analysed the rim design with different types of carbon fibre and compared the result with aluminium. The design is made in SOLIDWORKS and analysed using ANSYS. Finite element analysis is done on the rim to calculate total deformation and stress. The loads are applied by considering average values. Epoxy\_Carbon\_230GPa\_UD, Epoxy\_Carbon\_395GPa\_UD and aluminium alloy are considered as materials under analysis. There are two types of carbon fibres present in ANSYS, namely UD and woven. We have considered UD because these types of materials have more strength than woven. The stress mainly develops in the area of notches or irregularity or fillet sections. The spokes part of the rim does not get much affected by loads. The circumference of the rim shows deformation and stress formation. Carbon fibres perform better in case of total deformation, and aluminium performs better in case of stress formation. Although stress developed in carbon fibres is very high than carbon fibres, in carbon fibres almost 95–99% of the body experience very less stress. The main area where stress concentration is very high is notches and fillet sections. By improving the manufacturing technique such as reducing notches and welded sections, we can reduce max stress in carbon fibres. From the above analysis, we can say that carbon fibres are a better option for making a rim, and by improving its surface finish, its life can be improved. Although ANSYS is not much accurate when it comes to analysing stress in composite material, results are quite satisfactory.

## References

1. Singh J, Saha S (2015) Static analysis of alloy heel using ANSYS15.0. IJRET 04(July 2015). eISSN: 2319–1163 | pISSN: 2321–7308
2. Batl M, Manazir Md, Chitresh N, Kumar A (2016) Finite element analysis on two wheeler alloy wheel. National conference on progresses and research in mechanical engineering. At Dharwad, India, Sept 2016
3. Beardmore P, Johnson CF (2005) The potential for composites in structural automotive applications. J Compos Sci Technol 26(1986):251–281, 3 Sept 2005

4. Dharanikumar V, Mahalingam S, Santhoshkumar A (2014) Review on fatigue analysis of aluminum alloy wheel under radial load for passenger car. *IJEDR* 3(1):2321–9939
5. Gebresilassie A (2012) Design and analysis of composite drive shaft for rear-wheel drive engine. *Int J Sci Eng Res* 3(5), May 2012
6. Salunkhe KR, Pimpale SS (2017) Design, FEM analysis and of alloy wheel rim of a four wheeler. *Int Adv Res J Sci Eng Technol* 4(9), September 2017
7. Ganesh S, Periyasamy P (2014) Design and analysis of spiral wheel rim for four wheeler. *Int J Eng Sci* 3(4), July 2014
8. Sureshkumar M, Tamilselvam P, Kumaravelan R, Dharmalingam R (2014) Design, fabrication, and analysis of a hybrid fiber composite monoleaf spring using carbon and e-glass fibers for automotive suspension applications. *Mech Compos Mater* 50(1):115–122
9. Meghashyam P, Girivardhan Naidu S, Sayed Baba N (2013) Design and analysis of wheel rim using CATIA and ANSYS. *Int J Appl Innov Eng Manage* 2(8):2319–4847
10. Wang L, Chen Y, Wang C, Wang Q (2011) Fatigue life analysis of aluminum wheels by simulation of rotary fatigue test. *Strojniški Vestnik J Mech Eng* 57(1):31–39
11. Akbulut H (2003) On optimization of a car rim using finite element method. *Finite Elem Anal Des* 39(5–6):433–443
12. Raghupathi et al (2014) Design and analysis of car wheel rim using fem technique. *J Int J Comput Sci Inform Eng Technol* . Dec. 2014, Vol. 3, Series 4, Issue. 4.
13. Hamidian H, Lahijani AT, Shahriari S (2017) Fatigue life enhancement of automobile wheel disc considering multi-axial stresses based on critical plane approach. *J Mech Sci Technol* 31:2883–2892
14. Schijve J (2001) Fatigue as a phenomenon in the material. In: Schijve J (eds) *Fatigue of structures and materials*. Springer, Dordrecht, 7–44. ISBN: 978-0-306-48396-7
15. Chang F-K, Scott RA, Springer GS (1982) Strength of mechanically fastened composite joints. *J Compos Mater* 16(6):470–494
16. Wang F, Cai X (2018). Improvement of mechanical properties and thermal conductivity of carbon fiber laminated composites through depositing graphene nanoplatelets on fibers. *J Mater Sci* 3847–3862





# Attendance Management System Using Modern Face Recognition and Gesture Recognition Using Deep Learning

Mahaba Ullas Ekka<sup>✉</sup>, Omar ALi Mze, Tarun Singh, and N. S. Raghava

Delhi Technological University, New Delhi 110042, India

## 1 Introduction

The face is our essential focal point of consideration in public activity assuming a significant part in passing on character and feelings. We can perceive various countenances learned all through our life expectancy and recognize faces initially even following quite a while of division. This expertise is very vigorous not withstanding of enormous varieties in visual boost because of evolving condition, maturing, and interruptions like facial hair, glasses, or changes in haircut [1]. Computational models of face acknowledgment are fascinating on the grounds that they can contribute not exclusively to hypothetical information yet additionally to viable applications. PCs that distinguish and perceive countenances could be applied to a wide assortment of errands including criminal ID, security framework, picture and film handling, character confirmation, labeling purposes, and human-PC communication [2]. In our task, we have contemplated and carried out a lovely basic, however, powerful face discovery calculation which considers human skin tone. Our point, which we accept we have reached, was to build up a strategy for face acknowledgment that is quick, hearty, sensibly straightforward, and precise with a generally basic and straightforward calculations and procedures. After face location and acknowledgment, all subtleties of the identified face such as name, move number, date of birth, date, and time are enrolled naturally on a watch list [3]. Attendance information will be constant sync to our cloud-based time attendance programming. It has numerous adaptable reports which can be effectively fare to Excel, CSV, or continuous sync to different applications. In the interim, similar facial pictures over the audit limit will be given as an alarm to the client. Any remaining facial pictures will be naturally disposed of right away. The models given in this proposal are constant and taken from our own environmental factors [4]. Gesture acknowledgment fundamentally makes the correspondence simple between the instructor and the class. Also, this element is particularly pertinent when we take online classes, gatherings, and so on into play in light of the fact that for, e.g., [5]. In the event that a client has a defective mic and sound framework on their gadget, at that point this component explicitly permits them to pass on anything they desire to say without a mic and a sound framework. Our proposed system will help in eradicating any flaws that have earlier prevailed in smart attendance systems which have not used facial recognition, and it will also be disability friendly.

## 2 Problem Statement

In a world where technology and automation are quickly taking over day to day work, the untouched and unaffected side of this advancement needs to be considered [6]. There have been multiple researches in the field of facial recognition, and today, it is one of the most used and reliable form of technologies known to human beings [7]. In a day and age of online education, it is not equally accessible by everyone, not every technology is disability friendly [8]. It has been observed that not all disabled individuals are equally able to access this technology; this idea is proposed to help provide equal opportunity for the differently abled and in general make the means of online education more fluid between the two sides [9]. Gesture recognition has worked out for many models in various industries, but this approach is to shed light on online education and improving its features and services and making it available to everyone using it. This idea is to establish a more stable and comfortable environment for online education in the coming years where there is no underlying unfairness to anyone using the system.

## 3 Related Work

Over the past few years' various models of attendance systems using facial recognition have evolved in order to improve the status of students and faculty in numerous organizations in order to keep up with the technology in use and to create a more automated environment in order to reduce human effort. In Adam Geitgey [10] has explained a facial recognition system using the histogram of oriented gradients (HOG) method which is a more reliable method than previous models. For the other part where gesture recognition is involved, Bharath [11] has used a different approach involving a VGG-16 architecture to train the model to read and identify hand gestures. Another good approach is proposed by Priyanka Parvathy et al. [12] where they have used the Sebastian Marcel model to train the system and have used a discrete wavelet transform to extricate turn and scale invariant key descriptors. There has been a detailed comparison and study between four major algorithms, namely k-nearest neighbor (k-NN), naive Bayes (NB), artificial neural network (ANN), and support vector machines (SVM) for detecting hand gestures in Paulo Trigueiros et al. [13]. A slightly unique approach on hand gesture recognition was adopted by Abhishek et al. [14], where in relevance to existing systems where majorly spatial modeling had been used to identify hand gestures, they have used a rather different approach, i.e., temporal modeling to detect hand gestures which not only makes the gestures more accurate but it also makes it easier for the system to recognize hand gestures in a temporal environment as compared to the spatial modeling as it does not need input gestures to be fed into the system to recognize the gestures as well as it can be performed in a real-time setting. While gesture recognition involves less complications as compared to facial recognition systems, some research models have found the optimal use of facial recognition techniques to be implemented in various systems that require facial recognition. One such system is discussed in Kaneez Laila Bhatti et al. [15] where they have used the HOG method mentioned above in one of the models and they improved user interaction by implementing a GUI for the user and the server and the user communicate through an interpersonal communication (IPC) bridge. All in all,

there have been major advancements in the field of facial and gesture recognition and via numerous research models the technology has and is being improved.

## 4 Methodology

### 4.1 Facial Recognition

- **Finding every one of the countenances:** To find faces in an image, we will start by making our image profoundly differentiating in light of the fact that we need not waste time with concealing data to find faces, and by then, we will look at every single pixel in our image one by one [10, 21].
- **Posturing and Forecasting Faces:** The essential thought is we will make sixty-eight unequivocal focuses (called accomplishments) that exist on every appearance, the most critical spot of the facial construction, the external edge of each eye, the internal edge of every eyebrow, and so on, and by then, we will set up an AI calculation to have the choice to track down these sixty-eight express bright lights on any face [10, 21].
- **Encoding Faces:** The course of action is to set up a deep convolutional neural network. In any case, as opposed to setting up the association to see pictures objects as we did the previous time, we will set it up to create one hundred and twenty-eight assessments for each face [10, 21].
- **Finding the individual's name from the encoding:** This last development is actually the easiest development in the whole collaboration. We ought to just find the person in our database of known people who have the closest assessments to our test image [10, 21].

### 4.2 Attendance System Using Facial Recognition

- **Data Acquisition:** The first step in setting up our attendance system is data acquisition, and it is done with the help of Kaneez Laila Bhatti et al. [15] image acquisition and data set creation. The pictures of the students are fed to the system, and a database is created with the student's information, and it can be accessed by the system anytime.
- **Face Recognition:** After the data of students is acquired, the system now implements facial recognition process where it uses [10] four major steps to run facial recognition across the system; face detection and extraction, face positioning, face encoding, and finally face matching.
- **Attendance Marking:** When the face is related to the picture put away in the document, Python produces move quantities of present students and return that, and when information is restored, the framework creates a participation table which incorporates the name, move number, date, day, and time with comparing subject ID. And, afterward, it passes the information to Python to store the table into an excel sheet consequently.

### 4.3 Notification System for User

**System Design:** The notification system is designed using the smtp function from the Python library, where the email IDs of students are fed into the system. The framework distinguishes an individual before the camera, and if the individual is perceived, his name appears in the message box. Presently, this data will be shipped off the host's email [19, 20, 22].

### 4.4 Hand Gesture Recognition

- **Skin Detection:** In the given methodology, the HSV concealing space was used with the histogram-driven skin acknowledgment strategy. The HSV concealing space has three channels, hue (H), saturation(S), and value (V). The H and S channels hold the concealing information, while the V channel holds the power information. The data image from the webcam would lie in the RGB concealing space; likewise, it should be changed over to the HSV concealing space using the change formulae. The histogram-driven skin distinguishing proof procedure mentioned uses thirty-two containers of H and S histograms to achieve skin area [16].
- **Hand Contour Removal:** Ensuing to procuring the skin partitioned twofold image, the accompanying stage is to execute edge acknowledgment to get the hand shape in the image. This infers that we can explore each shape in the image autonomously, to choose the hand structure. The Canny and Laplacian edge finders can find the shapes in the image, anyway does not give permission to each individual structure. In this manner, the limit finding edge acknowledgment procedure was used in the proposed plan. In this phase of the interaction, the convex hull and convexity defects are two significant parts that ought to be thought about [17, 18].
- **Gesture Recognition:** The signal affirmation procedure used in the mentioned arrangement is a mix of two methods. The computation for the mentioned motion acknowledgment technique is depicted in the stream framework of figure below. It might be seen from the diagram above that the convexity absconds for the hand shape ought to at first be resolved. The absconds for the hand structure was resolved using the OpenCV inbuilt function “cvConvexityDefects.” The limits above forsake (start point, finish point, and significance point) are taken care of in a gathering of groups. After the absconds are gotten, there are two essential steps for signal affirmation [17, 18].

## 5 Results and Output

The implementation of our proposed system was successful, and the desired model was created where facial recognition and gesture recognition complement each other. The attendance part of the project is safely implemented using facial recognition where the computer recognizes the student and marks his/her attendance and successfully sends an email to the student. The outputs of all these stages can be seen in this paper (Figs. 1, 2, 3, 4, and 5).

The gesture recognition system is designed to prompt the user to place their hand inside the box when the box does not read any object/hand inside it for the system to be

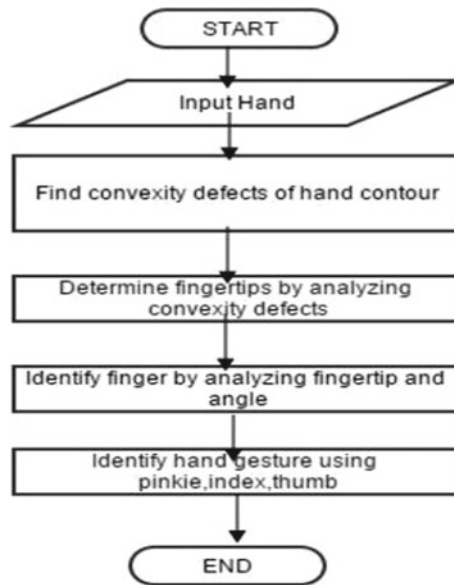


**Fig. 1** Algorithm for gesture recognition process

able to read the gestures signed by them. As the users make gestures with their hands inside the green box, the system reads their gesture and then outputs it on the frame window with red text, and simultaneously, users can see a real-time gray scale image of their hand in the mask window so that they can correct or adjust their gestures accordingly because the system is designed to read the gray scale image of their hand. Along with the shown gestures, the model is trained to identify a total of eight gestures, namely

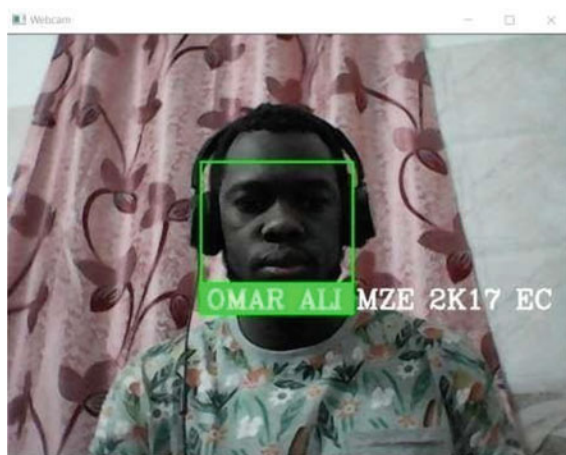


**Fig. 2** Face detected by attendance system

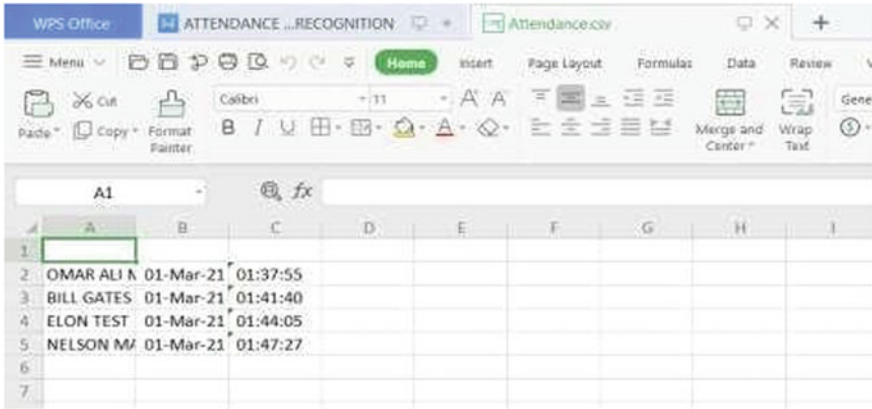


Fig. 3 Attendance is marked on the excel sheet

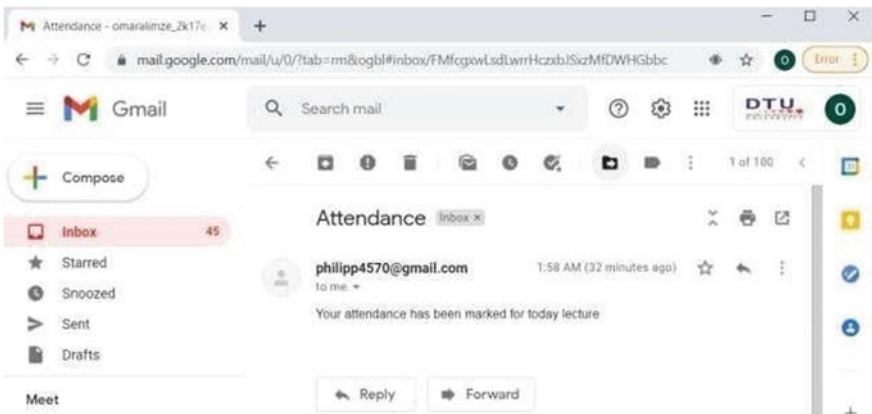


Fig. 4 Email is sent to the student

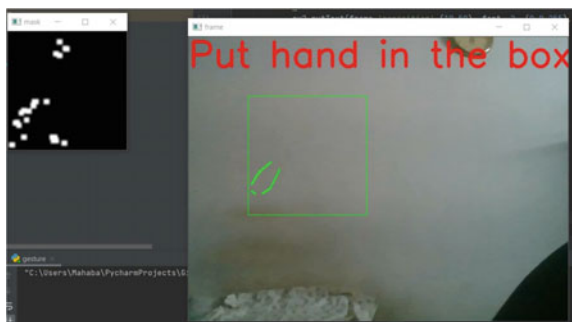
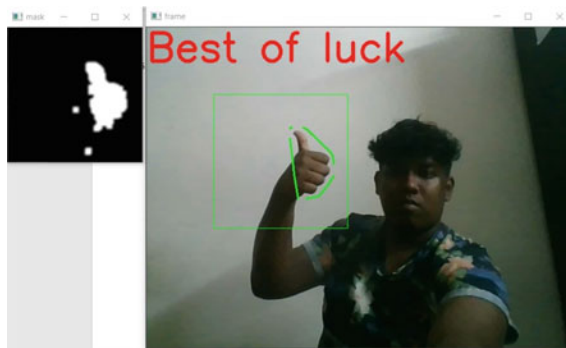
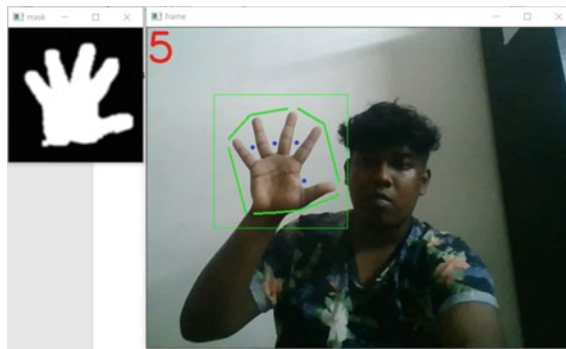


Fig. 5 Overview of the gesture recognition model

zero, one, two, three, four, five, best of luck, and OK. These gestures are successfully recognized by the system, and the model is trained accordingly (Figs. 6, 7, and 8).



**Fig. 6** Best of luck gesture identified by the model



**Fig. 7** Gesture of “five” recognized by the system

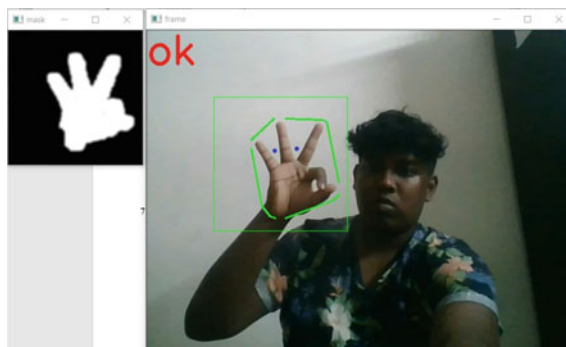


**Fig. 8** Gesture of “OK” recognized by the model

## 6 Conclusion

In the current system, we implemented the facial and hand gesture recognition systems and successfully trained them to identify the faces of the students that were fed into the database of the system and to correctly mark their attendance without failure and on attendance marking send an email to the respective recipients of the attendance that they had been marked present or absent according to the system, and we furthermore designed the system to pick up and identify the given hand gestures that were fed into the system to make interaction more fluid and comfortable for anyone who chooses to avail this service of the system. We can say that we successfully created an attendance system that works on facial recognition and gesture recognition to help the differently abled (individuals with speaking and/or listening disabilities) as well.

## 7 Future Scope

We would improve the presentation of the product particularly hand following soon. What's more, we likewise need to diminish the reaction time of the product for cursor development so it can totally be utilized to supplant our ordinary mouse. We are likewise intending to plan an equipment execution for the equivalent in order to improve exactness and increment the usefulness to different areas like a gaming regulator or as a universally useful PC regulator. Other progressed execution incorporates the hand motion acknowledgment stage to utilize the template matching technique to recognize the hand signals. This technique requires the utilization of an AI classifier, which sets aside a significantly long effort to prepare to create. Another tale execution of this innovation would utilize the PC to prepare the differently abled (with speaking or listening disabilities).

## References

1. Schwaninger A, Wallraven C (2004) Heinrich H Bu'lhoff: computational modeling of face recognition based on psychophysical experiments. *Swiss J Psychol* 63(3):207–215. <https://doi.org/10.1024/1421-0185.63.3.207>
2. Alabbasi HA, Moldoveanu F (2014) Human face detection from images, based on skin color. In: 18th international conference on system theory, control and computing (ICSTCC). IEEE. <https://doi.org/10.1109/ICSTCC.2014.6982471>
3. Yadav V, Bhole GP (2019) Cloud based smart attendance system for educational institutions. In: International conference on machine learning, big data, cloud and parallel computing (COMITCon). IEEE. <https://doi.org/10.1109/COMITCon.2019.8862182>
4. Nguyen QT, Tieu BH, Bui TD, Phuong Dung NT (2019) Student postures and gestures recognition system for adaptive learning improvement. In: 6th NAFOSTED conference on information and computer science (NICS). IEEE. <https://doi.org/10.1109/NICS48868.2019.9023896>
5. Badi H (2016) Recent methods in vision-based hand gesture recognition. *Int J Data Sci Anal* 1:77–87. <https://doi.org/10.1007/s41060-016-0008-z>
6. Castelluccia C, Le Mé'tayer Inria Daniel (2020) Impact analysis of facial recognition: towards a rigorous methodology. PRIVATICS—Privacy models, architectures and tools for the information society, version 1



7. M´arquez-Olivera M, Ju´arez-Gracia A-G, Hern´andez-Herrera V, Argu´elles-Cruz A-J, L´opez-Y´an˜ez I (2019) System for face recognition under different facial expressions using a new associative hybrid model Am-KNN for people with visual impairment or prosopagnosia, sensors (Basel). <https://doi.org/10.3390/s19030578>
8. Przybylo J (2012) Vision based facial action recognition system for people with disabilities, information technologies in biomedicine, lecture notes in computer science, vol 7339. Springer, Berlin
9. Mourad B, Ayaou T, Karim A, Estraillier P (2014) Real-time system of hand detection and gesture recognition in cyber presence interactive system for e-learning. *Int J Eng Res Appl* 4(9):2248–9622
10. Geitgey A (2016) Machine learning is fun! part 4: modern face recognition with deep learning. Blog article
11. Bharath K (2020) ‘Human emotion and gesture detector using deep learning: part-2. Blog article
12. Parvathy P, Subramaniam K, Prasanna Venkatesan GKD, Karthikaikumar P, Varghese J, Jayasankar T (2020) Development of hand gesture recognition system using machine learning. *J Ambient Intell Humaniz Comput*. Springer. <https://doi.org/10.1007/s12652-020-02314-2>
13. Trigueiros P, Ribeiro F, Reis LP A comparison of machine learning algorithms applied to hand gesture recognition. <http://www.csie.ntu.edu.tw/~cjlin/libsvm/>
14. Abhishek B, Krishi K, Meghana M, Daaniyaal M, Anupama H (2020) Hand gesture recognition using machine learning algorithms. *Comput Sci Inform Technol* 1(3):116–120
15. Bhatti KL, Mughal L, Khuhawar FY, Memon SA (2018) Smart attendance management system using face recognition. *J EAI Endorsed Trans Creative Technol* 5(17)
16. McGinty R (2016) Hand gesture recognition. <http://www.github.com>
17. Dhawan A, Honrao V (2013) Implementation of hand detection based techniques for human computer interaction. *Int J Comput Appl* (0975–8887) 72(17)
18. Salian S, Ganorkar P, Serai D (2015) Hand gesture recognition and cursor control. <https://www.researchgate.net/publication/280112512>. <https://doi.org/10.13140/RG.2.1.3185.0082>
19. Al-Bakeri AA, Basuhail AA (2016) Notification system based on face detection and recognition: a novel approach. *Int J Comput Sci Inform Security* 14(4)
20. Riabov V (2006) Handbook of information security, chapter: simple mail transfer protocol (SMTP). John Wiley and Sons
21. Okokpuije K, Noma-Osaghae E, John S, Oput R (2017) Development of a facial recognition system with email identification message relay mechanism. International Conference on Computing Networking Informatics (ICCNI), IEEE. <https://doi.org/10.1109/ICCNI.2017.8123776>
22. PruthviRaj Goud B, Sravan Reddy S, Praveen Kumar K (2020) Smart attendance notification system using SMTP with face recognition. *Int J Innov Technol Explor Eng* 9(5). ISSN: 2278–3075



# Plan and Running of a Program Logic Regulator by Using PIC18F4580

Tareq AL-hamzah<sup>(✉)</sup>, P. Suresh, and Sheetla Prasad

School of Mechanical Engineering, Galgotias University, Greater Noida, India  
tareq\_kareem.scmemtech@galgotiasuniversity.edu.in

## 1 Introduction

In the event that method performs that working of individuals halfway or finished, this method is known as automated frameworks. On the off chance that a method performs the exertion or missions of individuals somewhat or totally, this method is known as automation frameworks. The principle motivations to automat frameworks are limitations of people in strength, information measure ability so that working rate. Besides, items made by people may not generally be of a similar quality in light of the fact that the working group of laborers fluctuates after some time. All the reasons mentioned recently exhibit the essentialness of computerization. Computerization history goes back to antiquated occasions. Albeit mechanical control frameworks are a piece of present day age later eighteenth before there was robotization implementations which that before used by civic establishments in Old Time Arabic and old Greece teams water tickers, oil lights, and boosted water terminals are a few case from the applications. The steam machine, which James Watt boosted it in year of (1788) that opened another epoch, the mechanical epoch. Numerous were of studies and developments identified with machine steam in nineteenth hundred years. Fruitful explores dependent on the (Maxwell) conditions that time had a significant function in developing of modern robotization. So, later than these compelling upgrades, a lot of scientific items designed were particularly in part of moving, assembling, also force plans [1, 2]. To start with, mechanization frameworks are depended on electromechanical frameworks comprising of transfers and contactors. After 1970, other items have been utilized by the assistance of improvements from the semiconductor innovation, PLC which possesses tremendous impact and expansive use in modern creation. The maker of the book “Prologue to programmable logic control Jay Hooper clarifies the motives of ubiquity of programmable logic control with a model. A vehicle maker was drained in view of altering the electromechanical control units for each adjustment underway line. They opted to take aid from a product organization to take action of their framework. It was successful though the organization perceived that they were relied for programming organizations for each change since they didn’t realize programming great enough, for example, Assembler. Consequently, so that chose to buy a framework, because that has ladder-method tic, and the each hardware master in manufacturing is aware also utilizes well. So that is likewise the behind points from the achievement of the programmable logic control: And the diagram ladder is norm of

mechanical computerization. Morley Dick, from who is moreover popularly called as “the dad of programmable logic control,” delivered his first programmable logic control in year of (1968). He gave a name to his organization, Modicon, which indicates “Particular Advanced Controller.” In year of (1988), the brand of SIEMENS created the programmable logic control, and that had a wide extensive use. That turn of events and utilization of programmable logic control invention proceeds, and programmable logic controllers are still extremely famous items in modern robotization territory [2, 3]. A common programmable logic control is a gadget, which includes a CPU, input also, yield interfaces, programming gadget, memory and client program [4]. Moreover, these ones, most programmable logic control gadgets too, have association segments for specialized strategies such as Modbus, ProfiNet, regulator region network (CAN) also Ethernet [5–7]. The remainder group from this paper is based upon the following. In second area, connected works are so that given. Third area presents the recommended strategy also execution of the framework. In fourth part, reproduction of the framework is illustrated. At last, ends and future works are summarized in fifth section.

## 2 Concerning Works

In writing that is a great deal of studies and books [8, 9] identified with programmable logic controllers. Some scholastic examinations about programmable logic controllers are recorded what is more, clarified quickly beneath. A few investigations in writing are centered on plan new instruments for programmable logic control gadgets. For instance, Burhan et al. and new things included to FPI-NAIS C24 programmable logic control in some DC gear, for example, engine, hand-off, and solenoid cylinder chamber, empowering this programmable logic control to be an easy to use gadget [10]. A few investigations are zeroed in on execution and conformance investigation of programmable logic controllers. Wagner et al. [11] considered the droop reaction of the programmable logic control utilized in manufacturing plants for terrible force conditions of quality. Baniyon is et al. [12] concentrated in their endeavors on deciding the errors of mistakes in programmable logic control programming. They additionally proposed another model to decide programming fault better. A different model is the investigation of Darvas et al. [13]. So, they built up another terms for conformity of programmable logic control with various levels of permissibility. Network protection in programmable logic control programming has a significant job since programmable logic controllers delivered as of late accompany Ethernet/IP associations. Wardak et al. [5] exhibited those weaknesses of ongoing programmable logic controllers from attacking the network. In an investigation [6], researchers inspects having the danger of weakness also that methods to conquer it. Gavrilov [7] further clarified the online protection techniques for programmable logic control applications in an incredible recent study. Programmable logic control instruction is of significantly very important. After investigating their understudies, Gavali et al. [14] finished that college understudies that a lot of fruitful in mastering programmable logic control with the help of graphical research center investigations. Programmable logic controllers can be helpfully utilized in a wide range of zones other than the business. For example, Howimanporn et al. [15] used programmable logic control to build up another speed control procedure for transport line utilizing molecule

swarm streamlining based the control of PID. Iqbal et al. [16] developed the level tank control execution utilizing programmable logic control. Further, Akmansayar et al. [17] utilized programmable logic controllers for railroad signalization framework approaches for programmable logic control and the limit of programmable logic controllers without altering equipment of programmable logic control. Petri nets have basic utilization from mechanical purposes to playful the applications of game [18]. Andreu et al. [19] recommended another programming approach for programmable logic control utilizing Petri nets. Moallim et al. [20] boosted remote correspondence limit of programmable logic control for ZigBee correspondence. They announced that their own programmable logic control has greater attainability and adaptability in remote correspondence. Rida et al. [21] planned another programmable logic control device utilizing ATxmega256A3U-AU micro-control, testifying that their framework is a perfect answer for small-scale board applications. Asif et al. [22] planned a programmable logic control model utilizing PIC18F452 micro-control. Their significant objective in this usage is to show inward design of programmable logic control to understudies. They utilized C language for programming the micro-control and C# for user interface. Vasu et al. [23] planned also apply another programmable logic control device dependent on multi-center programmable logic control on the grounds that they accepted that solitary center programmable logic control has not by and large sufficient rapidity for compound uses like same of speed control. Accordingly, those utilized Python language for the programs multicourse gadget. So, this article, an ease programmable logic control, has been planned and actualized utilizing PIC18F4580 microcontroller. Graphical UI programming has been intended for creating programs on the programmable logic control and transferring code information to the gadget. In request to program the programmable logic control, either stepping stool chart or word directions can be utilized.

### 3 Execution and Strategies

The planned and executed programmable logic control includes an information, microcontroller, and yield interfaces, programming device and client program. The square outline of our programmable logic control configuration is shown in Fig. 1.

Resulting areas expound on equipment structure, client [plan] interface, transferring programming of programmable logic control, and association among programmable logic control and UI.

#### A. Hardware Design

Executed hardware of programmable logic control has a few segments. The most important part is the microcontroller of PIC18F4580. The most unmistakable highlights of the microcontroller (PIC1854580) for favoring it in this work are recorded underneath:

- 40 pins in double inline bundles (DIPs),
- Memory streak 32 KB.
- SRAM bytes IS 1536 also EEPROM bytes are 256 information memory.
- Input/output is 36 pins.

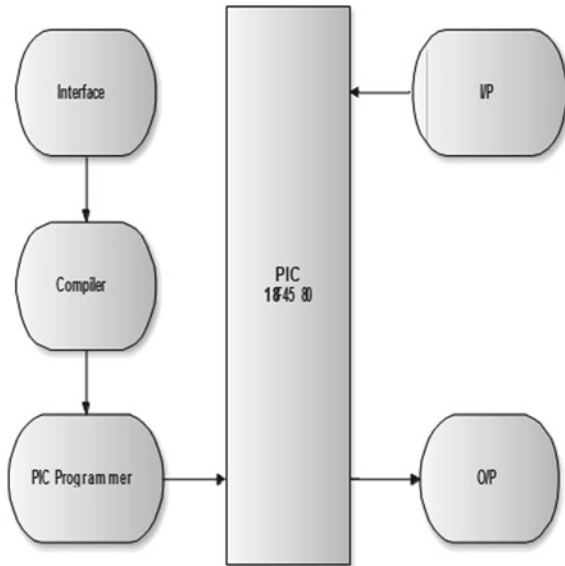


**Fig. 1** PLC design

- Innovation ECAN is 24.

So that planned programmable logic control has equally eight I/O. There are four outputs are utilized for hand-off associations; also, different outputs are utilized for semiconductor associations. All the origins of info and outputs associated with the microcontroller are disengaged utilizing opt couplers. Used for transferring code to the programmable logic control, every gadget which program can be the microcontroller, for instance, biopic, picket, also, microelectronic gadgets. So, the UI already has been constructed in illustration basic stage. Illustration basic stage is a usually utilized stage in explicit finish-client applications [24]. The UI of our planned programmable logic control can be found in Fig. 2.

In this easy to use climate, one can without much of a stretch develops the stepping stool graph utilizing eight interior transfers, eight counters, furthermore, eight clocks, and recently referenced eight information and yields. The unit quantity of these can be expanded when important. The principle routine of the actualized programmable logic control client interface is given that the meanings for counters and clocks are taken from client toward the start. Primary structure squares of programmable logic control framework plan are regularly open, typically lock calling also loops as in the frameworks dependent on transfers also contactors. These building with the circuit squares can likewise be numerically communicated with bitwise activities. The programmable logic control L program makes a code for each single building square also figuring. Later than the plan of a curl, the framework figures the bitwise activity for this curl. Here, the sequential association of calling is bitwise augmentation measure; furthermore, equal association of calling is bitwise adding measure. In the stepping stool graph, each line

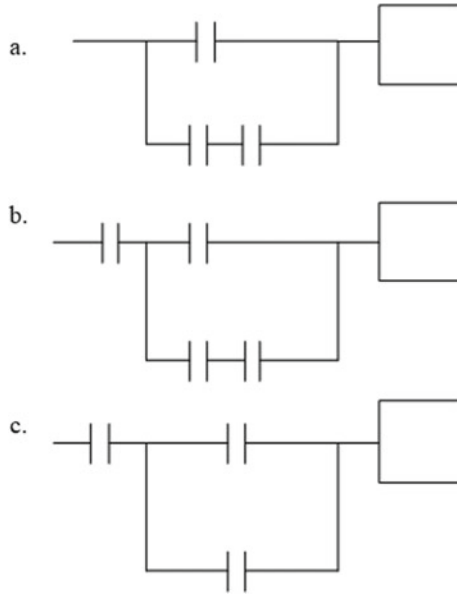


**Fig. 2** PLC user design

composing of some structure blocks closes with a curl. As such, tasks of structure blocks are equivalent to a curl toward the end. A basic case of a stepping stool graph showed that in Fig. 3.

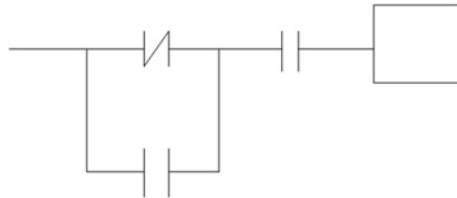


**Fig. 3** Showed ladder diagram of plc

Figure showed that for model [4], “G0,” “G1,” also “G2” represent inputs callings, where “G0” and “G2” are regularly unlock callings, and “G1” is regularly shut contact. “C0” represents the curl of yield. The program makes that code arrangement for the stepping stool plan in. After the stopping point (for the yield loop, “C0”), the programmable logic control program translates this code succession. Every three digit has various implications. The implications of bytes code in this model are clarified in schedule [1].

Code bytes	Meaning
255	Start
253	Sub-branch
150	Normally-open contact of G0
247	End of this sub-branch
251	Serial connected contact means, but here no usage
101	Normally-closed contact of G1
252	End of OR operations
251	Serial connected contact, AND operation
152	Normally-open contact of G2
254	End of the one side of equation
210	The coil output interface, C0

Codes bytes and example ladder bytes. These factors in this condition {of C code} are clarified, while the client builds his extraordinary craft bit by bit in the stepping stool graph; the programmable logic control program readies the C code in the foundation. Subsequent to finishing the stepping stool chart, the client has to push the send button. After squeezing the catch, the programmable logic control program summons MikroC programming consequently. There is no compelling motive to compose any code or doing whatever thing here in MikroC programming C. Transferring the programmable logic control code to gadget, the MikroC programming is used extraordinarily for arranging the programmable logic control code and creating hex document. On the off chance that the client has a programming unit of microelectronics for program logic control, the client be able to insert the programmable logic control code just utilizing one catch as found in Fig. 4.



**Fig. 4** Programmable logic control of embedded system by using microelectronic device

Then again, other PIC developers, for instance, picket also biopic that can be utilized to implant hex documents are made by MikroC programming.

### 3.1 Recreation

The electronic equipment of the actualized programmable logic control is planned first in a famous reenactment program, Proteus (ISIS) of Lab center Electronics. All the equipment segments for this programmable logic control replica are tried in the reproduction program previously collecting the model. In any case, here, least number of segments is utilized in the reenactment stage in order to follow the steps of the client’s custom program. For this reason, as it was catches for information sources, and LEDs for yields are utilized. The client should primarily insert the hex record in microcontroller in recreation programs. In the wake of implanting the code, the client easy can be starting the recreation. The reenactment screenshot of the executed programmable logic control is given in Fig. 5.

## 4 Conclusion and Future Work

Usually, utilized costly business items include relatively more ability that a portion of their highlights are utilized seldom. In this work, a minimal effort programmable logic control utilizing PIC18F4580 microcontroller is planned and actualized (Fig. 6). It is meant to create an essential programmable logic control model which can certainly be adjusted as per the necessities of explicit cycles. Another inspiration to understand this undertaking is to have an instructive device that makes a difference understudies to comprehend the methodic of the programmable logic control gadget and inspire them to make their own ones. The decision of PIC18F4580 micro-control is on the grounds, so the CAN is having correspondence ability. In this exemption, the RS-232 correspondence

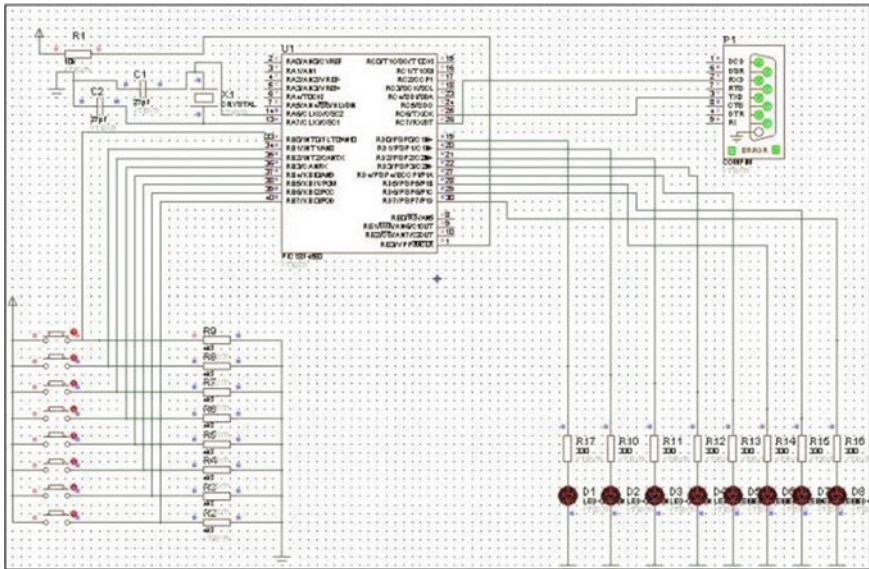
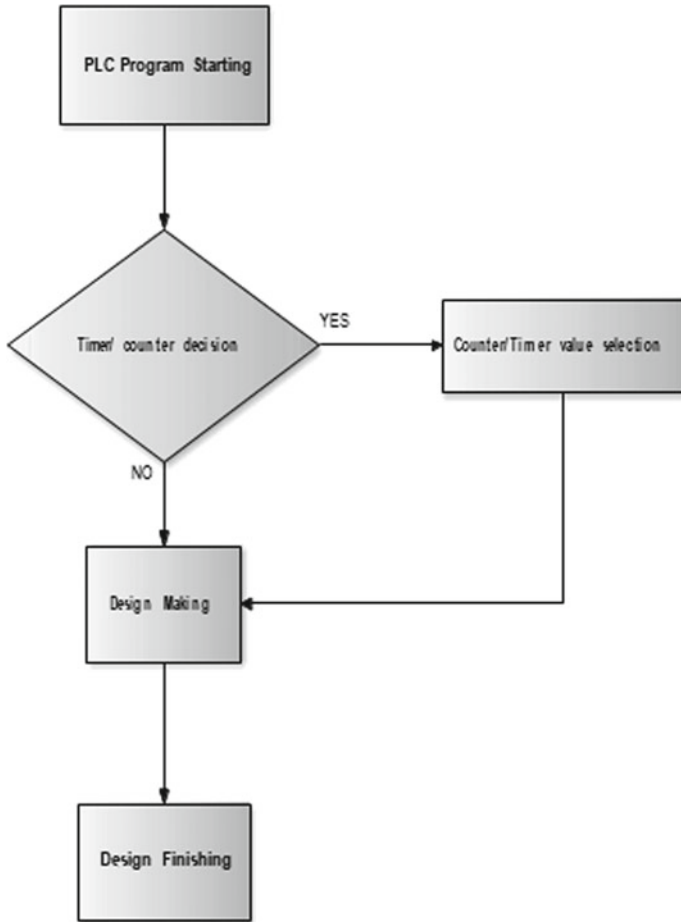


Fig. 5 PLC implementation with number of component



of the micro-control is misused. In the future, it is intended to join CAN correspondence since it is a generally utilized convention in manufacturing. Likewise, it is planned to move this code to MPLAB programming of microchip also, arrange the hex document directly from UI.



**Fig. 6** User interface of programmable logic control

## References

1. Sanver U (2015) Scoreboarding method for table tennis game with using Pic32. Master Thesis, Istanbul Technical University
2. Hayden E, Assante M, Conway T (2014) An abbreviated history of automation and industrial controls methods and cybersecurity. SANS Analyst Whitepaper
3. Hooper JF (2005) Introduction to programmable logic controls. Carolina Academic Press

4. Rahama1 AS, Mahmoud D (2016) Control of induction motors by using programmable logic controllers (programmable logic controls). *Int J Sci Res (IJSR)*, 1923–1926
5. Wardak H, Zhioua S, Almulhem A (2016) Programmable logic controls access control: a security analysis. *IEEE 2016 World Congress on Industrial Control Methods Security (WCICSS)*
6. Ahmed I, Obermeier S, Sudhakaran S, Roussev V (2017) Programmable logic controller forensics. *IEEE Security Privacy* 15:18–24
7. Gavrilov NV (2017) Appliace of WEB-technologies in automation of industrial facilitie. In: 2017 IEEE conference of Russian young researchers in electrical and electronic engineering (EIconRus)
8. Bolton W (2015) *Programmable logic controllers*. Newnes
9. Bryan LA, Bryan EA (1997) *Programmable controllers: theory and implementation*. Industrial Text Company
10. Burhan I, Azman AA, Talib S (2015) Multiple input/outputs programmable logic controller (programmable logic control) module for educational applications. In: 2015 Innovation and commercialization of medical electronic technology conference (ICMET)
11. Wagner VE, Andreshak AA, Staniak JP (1990) Power quality and factory automation. *IEEE Trans Ind Appl* 26:620–626
12. Baniyounis M, Mesmar A. (2017) Diagnosability of programmable logic controllers. In: 14th International multi-conference on methods, signals and devices (SSD)
13. Darvas D, Majzik I, Vinuela EB (201) Conformance checking for programmable logic controller programs and specifications. In: 2016 11th IEEE symposium on industrial embedded methods (SIES)
14. Gavali AB, Patil SA, Koli AR (2016) Technology-based learning method in programmable logic controller education. In: 2016 IEEE eighth international conference on technology for education (T4E)
15. Howimanporn S, Thanok S, Chookaew S, Sootkaneung W (2016) Speed control technique for conveyor using PSO based PID with programmable logic controller. In: 2016 IEEE/SICE international symposium on method integration
16. Iqbal MM, Gupta S, Gurudas C (2017) Overflow protection of level tanks using programmable logic controller. In: International conference on electronics, communication and aerospace technology (ICECA)
17. Akmansayar B, Kurtulan S, Ors SB (2015) Design of core blocks and implementation on a programmable logic controller for a train signalization method. In: 2015 23th signal processing and communications applications conference (SIU)
18. Yavuz E, Sanver U, Kasapbasi MC, Yazici R (2014) An implementation of vibration-based automatic score-keeping method for table tennis game. *Mech Mechatron Eng* 4:725–732
19. Andreu D, Pascal J-C, Valette R (1997) Fuzzy petri net-based programmable logic controller. *IEEE Trans Methods Man Cybern—Part B Cybern* 27:952–961
20. Moallim A, Lee J-M, Kim D-S (2017) Wireless control and monitoring using programmable logic controller (Programmable logic control). In: 2017 17th International conference on control, automation and methods (ICCAS)
21. Rida ME, Liu F, Jadi Y (2014) Design mini programmable logic control based on ATXmega256A3U-AU microcontrol. In: 2014 international conference on information science, electronics and electrical engineering (ISEEE)
22. Asif M, Raza A, Sultan A, Malik F (2016) Design of Mini programmable logic control based on PIC18F452 Microcontrol using concepts of graceful degradation. *Tech J Univ Eng Technol Taxila* 21(1):51–57

23. Vasu P, Chouhan H, Naik N (2017) Design and implementation of optimal soft-programmable logic controller on multicore processor. In: 2017 International conference on microelectronic devices, circuits and methods (ICMDCS)
24. Sanver U, Yavuz E, Kasapbasi MC, Yazici R (2016) Modelling and implementation of an automatic table-tennis score boarding method. In: 2016 IEEE NW Russia young researchers in electrical and electronic engineering conference (EIconRusNW)
25. PIC18F2480/2580/4480/4580 Data sheet, microchip company, 2007



# Preliminary Observations of Synthesized WS<sub>2</sub> and Various Synthesis Techniques for Preparation of Nanomaterials

Anukool Yadav, Shreya, and Nitin K. Puri<sup>(✉)</sup>

Nanomaterials Research Laboratory (NRL), Department of Applied Physics, Delhi Technological University, Main Bawana Road, Delhi 110042, India  
nitinkumarpuri@dtu.ac.in

## 1 Introduction

All the technological advancements of the future that seem impossible right now can indeed become a reality by the discoveries of today. These discoveries in the field of nanotechnology have a very promising future where the arrangement of atoms in the desired way can show some amazing results. There are a large number of pieces of evidence that show how the world's smallest materials are changing our lives including the nano-machines that defeat the cancer cells, tiny computer chips, a few inches long high definition cameras and others. Synthesis of these nanomaterials is in itself a huge topic of research where the change in a single parameter like temperature can also make a difference in the structure and morphology of the product [1]. There are various synthesis techniques with different working principles that give very different products at specific conditions [2]. The hunt for new tiny gadgets creates a need for new and better synthesis techniques to get products of high purity and controlled dimensions. Initially, it was believed that 2-D materials are not stable but after the successful synthesis of graphene as a 2-D material, the search for the other 2-D materials with enhanced properties like wider band-gap began. We got other potential materials in the form of Transition Metal Dichalcogenides (TMDs) with wonderful electronic and optical properties [3]. Amongst these, MoS<sub>2</sub> and WS<sub>2</sub> have attracted considerable attention because of the peculiar layered structure, an impressive rate of electron transfer and layer-dependent band-gap. Various applications of these materials include solid lubrication, optical devices, gas sensing, and others [4, 5]. The schematic structure of WS<sub>2</sub> is shown in Fig. 1.

### 1.1 Hydrothermal and Solvothermal Method

These are two promising inorganic synthesis methods that involve the synthesis via chemical reaction as shown in Fig. 2a. These are the green processes as the reaction takes place in a sealed reactor known as autoclave shown in Fig. 2b. The autoclave is generally made up of metal and is employed with Teflon or alloy lining to protect it from highly corrosive solvent. These processes offer numerous advantages over other techniques apart from being the green processes: (a) these are relatively low-cost processes,

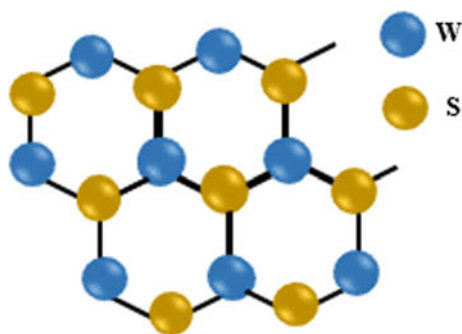


**Fig. 1** The schematic layered structure of WS<sub>2</sub>

(b) an environment-friendly process as it takes place inside a sealed reactor and (c) high purity products are formed [6]. In the hydrothermal method, the solvent used is water while the solvothermal process uses aqueous and non-aqueous organic solvents like ethylenediamine, ethanol, diethylenetriamine [7], polyethylene glycol [8], etc. Furthermore, the solvothermal process has some additional advantages over the hydrothermal process: (a) it requires relatively low temperature and pressure, (b) precursors which are sensitive to water can be used in this process and (c) the crystallinity of products formed is very well controlled in this process.

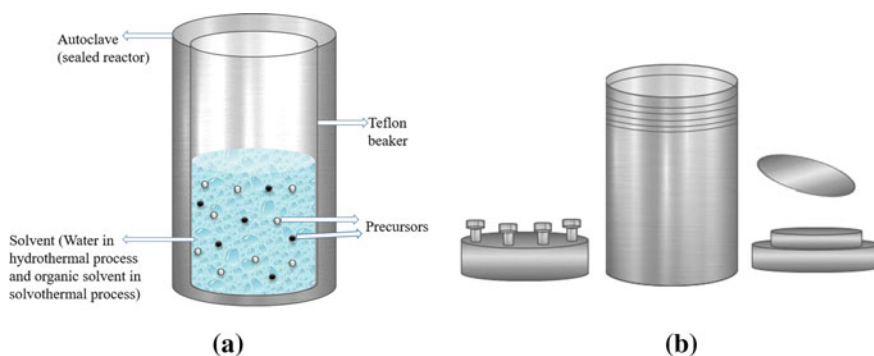


**Fig. 2 a** A diagrammatical representation of hydrothermal/solvothermal synthesis **b** A diagrammatical representation of an autoclave in nanomaterials research laboratory (NRL), DTU, India

## 1.2 Sonochemical Method

This is a method which neither requires high temperature and pressure nor long reaction times. In this process, the precursors are mixed and put together in solution form and then the sonochemical treatment is given. It involves passing ultrasonic waves through the solution using an ultrasonicator as shown in Fig. 3. In this way, the hotspots are generated

which can achieve very high pressure and temperature. The hotspots are the places where the reaction takes place at sufficiently high temperature and pressure conditions and the products are formed [9]. It is a powerful tool for synthesis or modification of nanomaterials where even a little variation in the reaction conditions can lead us to the change in morphologies and compositions of the product formed.

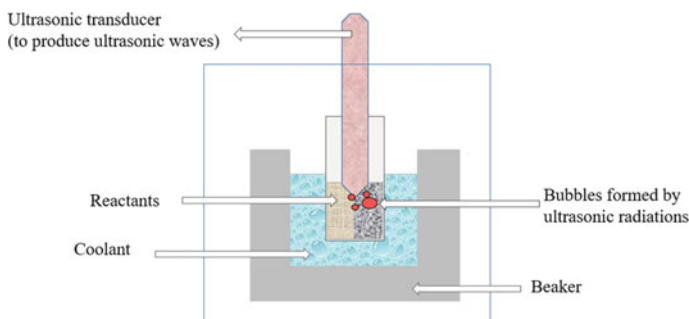


**Fig. 3** A diagrammatical representation of the sonochemical method

### 1.3 Chemical Vapour Deposition (CVD)

It is a vacuum deposition method that involves a chemical reaction inside a vacuum chamber. It is used for the production of various materials like alloys, carbides, oxides, nanoparticles, etc. Layers of materials are deposited on a solid surface called substrate below atmospheric pressure, i.e. vacuum. There are many types of CVD's namely, Thermal CVD, Metal–Organic CVD (MOCVD), Plasma Enhanced CVD (PECVD),

Atomic Layer CVD (ALCVD), etc. [10, 11]. Amongst these CVD variants, Double Zone Thermal CVD and PECVD are present in our Lab at DTU whose diagrammatical images are as shown in Fig. 4a, b, respectively. The technical details and working of the above two instruments are reported in detail in our previous work, '*Double Zone Thermal CVD and Plasma Enhanced CVD Systems for Deposition of Films/Coatings with Eminent Conformal Coverage*'. This bottom-up approach involves the deposition of one or more stable solid films on a substrate at high temperatures by a suitable chemical reaction as shown in Fig. 5.

### 1.4 Sol–Gel Method

The Sol–Gel method or Chemical Solution Deposition Method is a low-temperature, nanomaterial synthesis process in which solid materials are produced from small molecules. It is a bottom-up approach for material synthesis whose working principle is shown in Fig. 6. The sol–gel method, as is evident from the name, involves two materials, i.e. 'sols' (solid particles suspended in liquid) and 'gels' (porous network of particles having liquid between the pores). First, sols are formed inside a liquid which are then connected after some process to form a network of gels. The liquid then gets

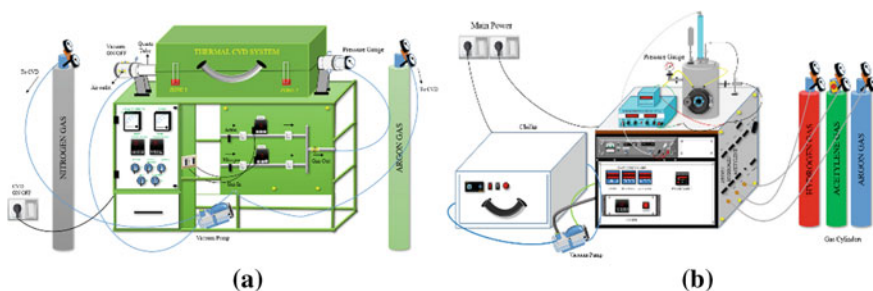


**Fig. 4** **a** Labeled diagram of Double Zone Thermal CVD at NRL, DTU, Delhi, India. **b** Labeled diagram of PECVD in NRL, DTU, Delhi, India

evaporated and we are left with the powder or thin-film formation. This method requires less energy consumption leading to less pollution and is generally used to generate highly pure and well-contained ceramic materials [10, 12].

### 1.5 Chemical Exfoliation Method

It is a top-down nanomaterials synthesis process where the reduction of interlayer forces takes place followed by the formation of intercalated compounds and then exfoliation occurs by rapid heating and sonication. This synthesis mechanism (as shown in Fig. 7) is mainly done for graphene as the process produces a large amount of graphene at low temperatures [13]. Exfoliation is a phase transition, which takes place when there is a layer to solvent molecule charge transfer and a minimum mixing enthalpy at well-defined elevated temperatures.

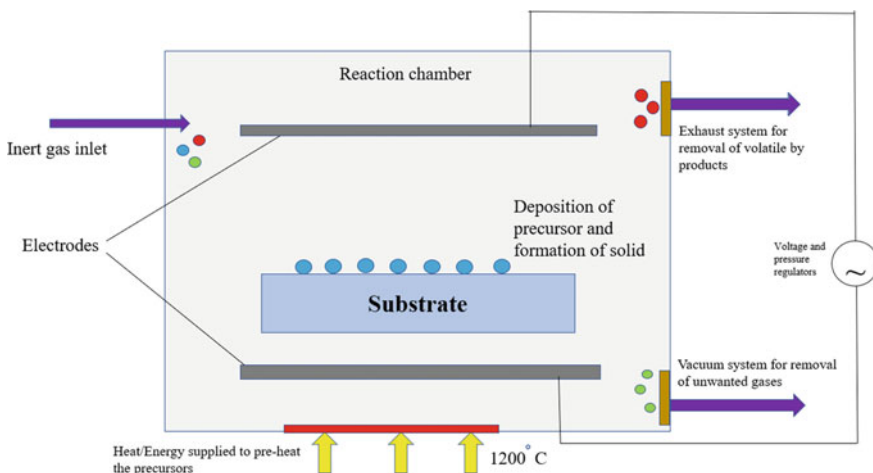


**Fig. 5** A diagrammatic representation of the working principle of the CVD process

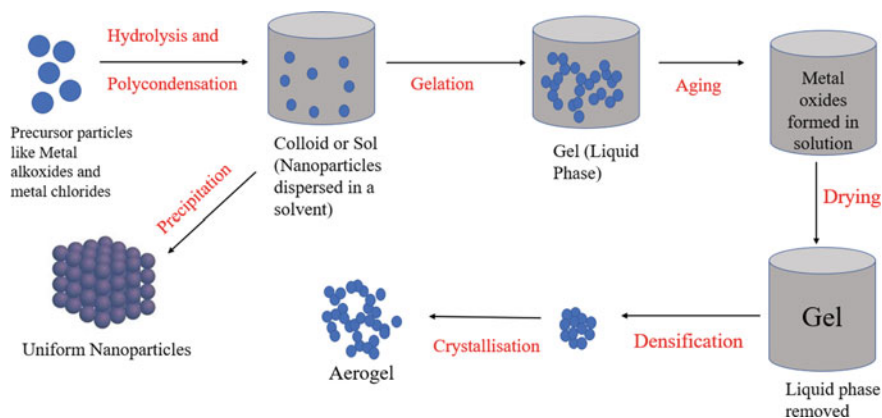


**Fig. 6** A diagrammatical representation of the working principle of the Sol-Gel process

## 2 Experimental

### 2.1 Chemicals and Materials

Tungsten Hexa-chloride ( $WCl_6$ ) and Thioacetamide or TAA ( $C_2H_5NS$ ) were purchased from Sigma Aldrich. Acetone was purchased from Rankem. Ethanol was purchased from Merck. We have used Milli-Q water, ( $18.2 M\Omega\text{ cm}$ ) as the solvent during our synthesis. All the chemicals used here had an analytical grading and were taken without any further purifications being done.

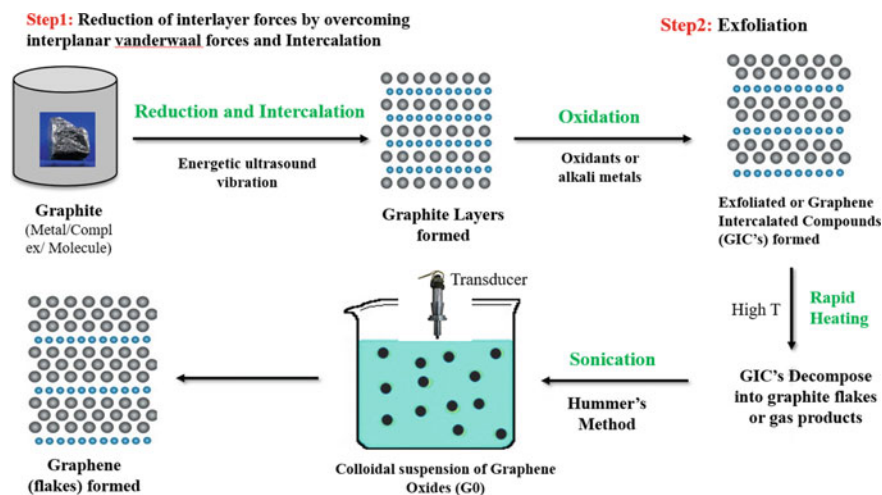


**Fig. 7** A diagrammatical representation of the working principle of the chemical exfoliation method



## 2.2 WS<sub>2</sub> Nanostructure Synthesis

WS<sub>2</sub> nanostructures were synthesized via the hydrothermal method and their phase was checked using XRD characterization. Figure 8 gives an outline of the hydrothermal process used for WS<sub>2</sub> nanomaterial synthesis in NRL lab, DTU, Delhi, India.

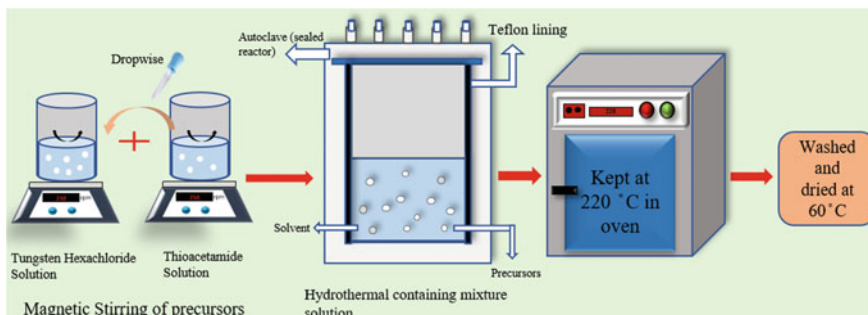


**Fig. 8** A diagrammatical representation of the general hydrothermal process used for sample preparation in NRL, DTU, Delhi, India

We first weighed the salts/precursors, i.e. Tungsten Hexa-chloride and TAA, and added them to two different beakers containing water as solvent. Beakers were then kept for magnetic stirring at room temperature (27–30 °C) with varied revolutions per second for 1 h for mixing of salts in water. Two different approaches were followed for the synthesis of WS<sub>2</sub> nanostructures. In one approach of synthesis, the TAA solution was added dropwise into WCl<sub>6</sub> solution after one hour while in the other approach, the WCl<sub>6</sub> solution was added into TAA solution. After this, the mixed solutions were kept for stirring for 1 h. The pH of the solutions was regulated and optimized to the values ranging from 6 to 8 which was initially 2 by adding liquor ammonia drop by drop. The solution mixtures were then transferred to Teflon lined autoclaves of different capacities and kept in the oven for 20–24 h at 220 °C. Then centrifugation and washing of samples was done using De-ionized water (DI) and ethanol, 3 times with each. Drying of samples was done at 60 °C in an oven for 24 h. Then the samples were sent for XRD analysis. We tried 5 reaction attempts to synthesize the materials at varied conditions. In the following Table 1, we have summarised all 5 reaction attempts and their physical optimization conditions.

After 24 h, samples were cooled down to room temperature. Then the samples were collected via centrifugation at 7,000 rpm for 7 min after washing with DI water and ethanol before drying at 60 °C for 24 h. We then collected the formed samples in Eppendorfs after crushing and named them 'S4' and 'S5', respectively.

## 3 Results and Discussions

In the first three attempts, no sample was obtained at the bottom of the Teflon as shown in Fig. 9a but in the 4th attempt, as shown in Fig. 9b and 5th attempt, as shown in

**Table 1** Reaction attempts summary for WS<sub>2</sub> synthesis

Sample	Precursor name	Amount (g)	DI water (mL)	Stirring conditions	pH
S1 (TAA into WCl <sub>6</sub> )	WCl <sub>6</sub>	0.522	30	stirred at 250 rpm, 30 °C	Initial: 2 Final: 6
	TAA	0.6	30	stirred until fully dissolved	
	TAA was added into WCl <sub>6</sub> and the mixture was stirred at 350 rpm at 30 °C				
	Solution mixture kept at 220 °C for 24 h in a 100 mL Teflon-lined autoclave				
S2 (WCl <sub>6</sub> into TAA)	WCl <sub>6</sub>	0.522	18	stirred at 350 rpm, 27 °C	Initial: 2 Final: 8
	TAA	1.000	17	stirred at 250 rpm, 27 °C	
	WCl <sub>6</sub> was added into TAA and the mixture was stirred at 350 rpm at 27 °C				
	Solution mixture kept at 220 °C for 24 h in a 50 mL Teflon-lined autoclave				
S3 (TAA into WCl <sub>6</sub> )	WCl <sub>6</sub>	1.044	18	stirred at 400 rpm, 27 °C	Initial: 2 Final: 8
	TAA	2.000	17	stirred at 250 rpm, 27 °C	
	TAA was added into WCl <sub>6</sub> and the mixture was stirred at 400 rpm at 27 °C				
	Solution mixture kept at 220 °C for 24 h in a 50 mL Teflon-lined autoclave				
S4 (TAA into WCl <sub>6</sub> )	WCl <sub>6</sub>	0.632	18	stirred at 400 rpm, 27 °C	Initial: 2 Final: 6
	TAA	1.211	17	stirred at 250 rpm, 27 °C	
	TAA was added into WCl <sub>6</sub> and the mixture was stirred at 400 rpm at 27 °C				
	Solution mixture kept at 220 °C for 20 h in a 50 mL Teflon-lined autoclave				
S5 (TAA into WCl <sub>6</sub> )	WCl <sub>6</sub>	1.566	17	stirred at 280 rpm, 27 °C	Initial: 2 Final: 6
	TAA	3.000	18	stirred at 400 rpm, 27 °C	
	TAA was added into WCl <sub>6</sub> and the mixture was stirred at 400 rpm at 27 °C				
	Solution mixture kept at 220 °C for 20 h in a 50 mL Teflon-lined autoclave				

Fig. 9c, an impressive amount of greyish coloured samples were formed. The suspected reason for failures is the manual or incomplete stirring of precursors due to unoptimized conditions. Here, we have included the XRD results of our 4th and 5th reaction attempts of the synthesis of WS<sub>2</sub> nanomaterial. The phases of the resultant nanomaterials obtained in the last 2 reactions are checked for the confirmation of WS<sub>2</sub> phase as can be interpreted from the preliminary XRD results.

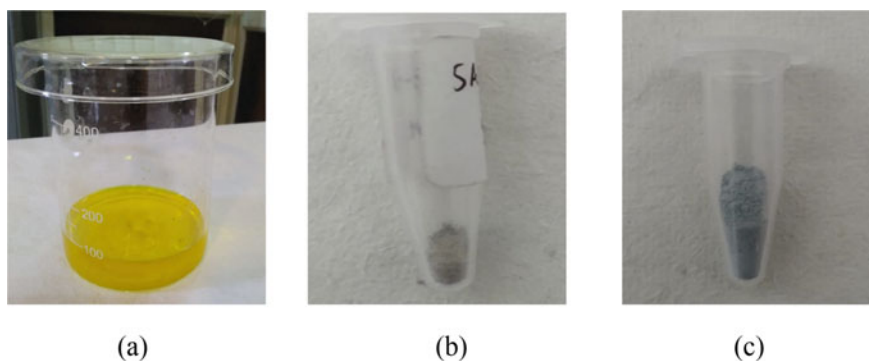


**Fig. 9** a No sample obtained in first three attempts b sample formed in the fourth attempt c sample formed in the fifth attempt

### 3.1 Characterization

XRD patterns were recorded using Bruker 8-D Advance System using CuK{alpha)  $\lambda = 1.54$  Angstrom at 40 kV voltage and 20 mA current with a scan rate of 1 °per minute to study the phase of the as-prepared samples. In our results, we present the diffraction patterns as recorded within the  $2\theta$  scanning range of  $-5$  to 90 degrees.

#### 3.1.1 XRD

XRD results of the prepared WS<sub>2</sub> sample numbers 4 (S4) and 5 (S5) are as shown in Fig. 10a, b. The crystal structure of these samples was interpreted using XRD spectra. In the XRD results of sample 4, diffraction peaks are obtained at  $2\theta$  angles of 15.05 °, 28.87 °, 32.12 °, 37.36 °, 46.20 °, 50.80 ° and 71.26 ° whereas, for sample 5, the diffraction peaks are more prominent and are obtained at  $2\theta$  angles of 8.81 °, 13.80 °, 15.29 °, 29.00 °, 29.63 °, 30.63 °, 31.12 °, 37.23 °, 53.43 ° and 64.89 °. The diffraction peaks corresponding to these samples were plotted and labelled and using OriginPro-2021 software.

## 4 Conclusions

There are many physical and chemical synthesis techniques for the preparation of nanoparticles namely hydrothermal, solvothermal, sonochemical, CVD, sol-gel and chemical exfoliation techniques. Some are top-down approaches while others are

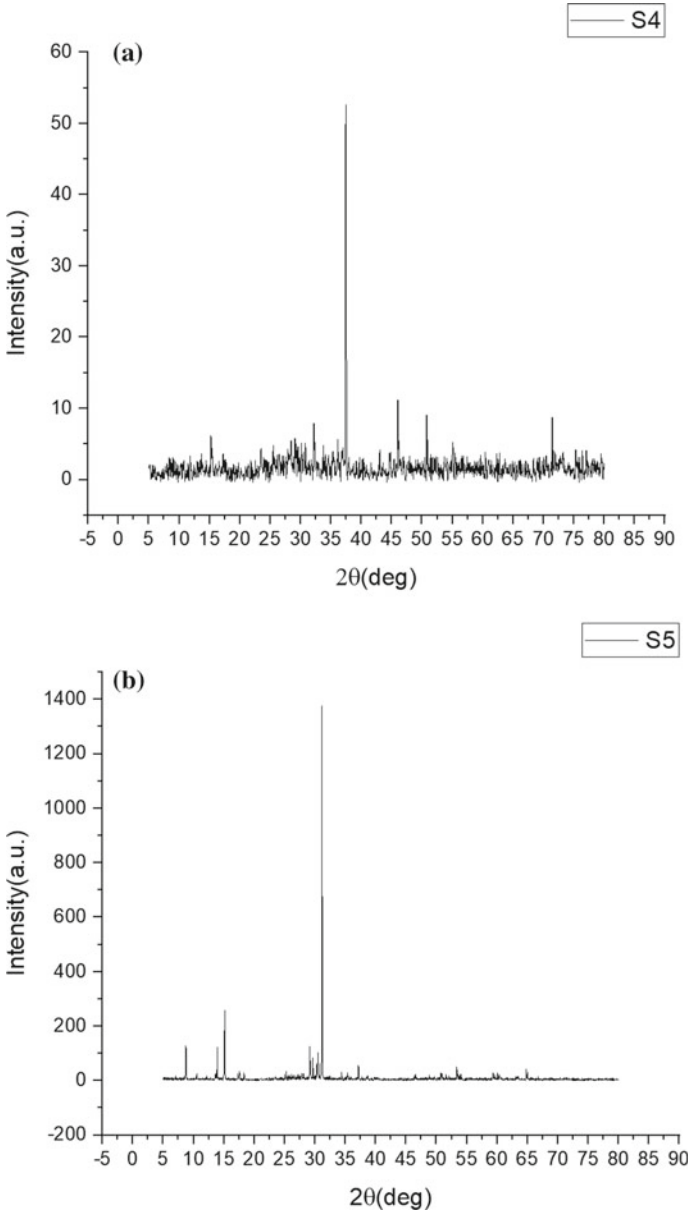


**Fig. 10** XRD of **a** sample 4 (S4), **b** sample 4 (S5)

bottom-up approaches. Both types of techniques have their advantages and disadvantages offering a variety of options to the users. Different types of nanomaterials like metal oxides, TMDs, etc. can be prepared by these approaches. Here, various attempts of preparation of WS<sub>2</sub> via facile hydrothermal method are reported with XRD results. In some of the materials, no sample was formed while in some other attempts greyish coloured powder was obtained after centrifugation and washing. This material can be used for a variety of applications in which solid lubrication is a famous one. The adhesion between sulphur layers is relatively weak which results in the sliding of layers over each other.

**Acknowledgements.** We are extremely grateful to Prof. Yogesh Singh, Vice-Chancellor, Delhi Technological University, Delhi, India for providing us the opportunity to work in this enchanting environment and gain experience in the field of research. Two of the authors, Anukool and Shreya also want to thank Mr. Sandeep Mishra for helping us in the characterization of our samples and our senior Ph.D. Scholars, Ms. Ritika Khatri and Mrs. Nikita Jain in the NRL lab, DTU, Delhi who guided and supported us at every possible step.

## References

1. Sahu K, Kar AK (2019) Morphological, optical, photocatalytic and electrochemical properties of hydrothermally grown ZnO nanoflowers with variation in hydrothermal temperature. *Mater Sci Semicond Process* 104:104648. <https://doi.org/10.1016/j.mssp.2019.104648>
2. Xu L, Cheng Y, Chen T, Mao R, Han Z (2021) The study on hydrothermal synthesis of ZrO<sub>2</sub> nanofl. *E3S Web Conf* 236:01038. <https://doi.org/10.1051/e3sconf/202123601038>
3. Zhao X et al (2021) Hexagonal WSe<sub>2</sub> nanoplates for large-scale continuous optoelectronic films. *ACS Appl Nano Mater*, p. acsanm.1c00521. <https://doi.org/10.1021/acsanm.1c00521>.
4. Eftekhari A (2017) Tungsten dichalcogenides (WS<sub>2</sub>, WSe<sub>2</sub>, and WTe<sub>2</sub>): materials chemistry and applications. *J Mater Chem A Royal Soc Chem* 5(35):18299–18325. <https://doi.org/10.1039/c7ta04268j>
5. Iqbal T, Fatima S, Bibi T, Zafar M (2021) Graphene and other two-dimensional materials in advance solar cells. 53:228. <https://doi.org/10.1007/s11082-021-02852-9>
6. Komarneni S, Noh YD, Kim JY, Kim SH, Katsuki H (2010) Solvothermal/hydrothermal synthesis of metal oxides and metal powders with and without microwaves. *Zeitschrift fur Naturforsch Sect B J Chem Sci* 65(8):1033–1037. <https://doi.org/10.1515/znb-2010-0809>
7. Vaquero F, Navarro RM, Fierro JLG (2017) Influence of the solvent on the structure, morphology and performance for H<sub>2</sub> evolution of CdS photocatalysts prepared by solvothermal method. *Appl Catal B Environ* 203:753–767. <https://doi.org/10.1016/j.apcatb.2016.10.073>
8. Lee JS, Choi SC (2005) Solvent effect on synthesis of indium tin oxide nano-powders by a solvothermal process. *J Eur Ceram Soc* 25(14):3307–3314. <https://doi.org/10.1016/j.jeurceramsoc.2004.08.022>
9. Lee GJ, Lee XY, Lyu C, Liu N, Andandan S, Wu JJ (2020) Sonochemical synthesis of copper-doped BiVO<sub>4</sub>/g-C<sub>3</sub>N<sub>4</sub> nanocomposite materials for photocatalytic degradation of bisphenol a under simulated sunlight irradiation. *Nanomaterials* 10(3):498. <https://doi.org/10.3390/nano10030498>
10. Jones AC, Hitchman ML (eds) (2009) Chemical vapour deposition—precursors, processes and applications. Royal Society of Chemistry, Cambridge
11. Choy KL (2003) Chemical vapour deposition of coatings. *Progress Mater Sci*, Elsevier Ltd., 48(2):57–170. [https://doi.org/10.1016/S0079-6425\(01\)00009-3](https://doi.org/10.1016/S0079-6425(01)00009-3)

12. Sebastián E, Murciano A, Madrigal R, De Aza PN, Velasquez P (2021) 3D CaP porous scaffolds with grooved surface topography obtained by the sol-gel method. *Ceram Int.* <https://doi.org/10.1016/j.ceramint.2021.04.158>
13. Cherubala BR, Kabuba J “Desulphurization of commercial diesel fuel using carbon-based metal oxide nanocomposites. <https://doi.org/10.21203/rs.3.rs-353427/v1>



# Design of GSM-Based Fire Detection System Using Microcontroller and Sensors

Aditya Rana, Tarun Kumar, and Nitin K. Puri<sup>(✉)</sup>

Department of Applied Physics, Nanomaterials Research Laboratory (NRL), Delhi  
Technological University, Bawana Road, Shahbad Daultapur, Rohini, Delhi 110042, India  
nitinkumarpuri@dtu.ac.in

## 1 Introduction

Fire is a catastrophe that claims thousands of lives every year. Millions of dollars are spent every year to make buildings and house complexes fireproof. The fire arises in four distinct stages. In the first, or developing stage, fuel, and oxygen burn together to cause the ignition of invisible gases in the form of pungent odour. In the second or growth stage, a developing flame is formed along with the detectable smoke which can be detected by smoke detectors. In the third or critical stage, when the critical temperature (or ignition temperature) of material is reached, sudden flames begin to form, and therefore their emitted thermal radiation (typically Infrared Radiation [IR]) can be sensed and detected using flame detectors. In the fourth or fully developed stage, energy in the form of heat is released and big flames arise leading to fire breakout; the temperature of the place rises rapidly causing maximum catastrophe to people and property, and then the use of thermal sensors becomes feasible and critical [1]. Fire suppression systems are the system that is capable of extinguishing, containing, dousing, or in some cases, entirely preventing fires from spreading or occurring in building premises. Fire suppression systems work on a variety of applications to make them fireproof, and as such, there are different types of suppression systems available for multifarious need of applications [2]. An ideal firefighting system can douse the fire with a motley of sensors including sensors and a fire extinguishing system. The most commonly used fire suppressing system is a good old fire extinguisher that douses fire using carbon dioxide, aerosols, and a mixture of other gases. However, in case of emergency, this becomes ineffective and we have to rely on an alternative and efficient method that smartly detects fire and suppresses it before any widespread property loss. The main goal of this paper is to design a system that indicates an area in which fire has occurred and alert the people on time. This system should also be connected to a fire suppressing system which will activate the water sprinkler if the fire is detected. This paper discusses the three main prospects of the system—the detection, monitoring, and controlling the system timely. For detection, various sensors and detectors are used such as heat sensors, smoke sensors, and flame detectors. The heat sensors will constantly gauge changes in temperature of surroundings whereas the smoke sensor will detect the presence of ignition particles in the building. The flame sensor will work on detecting the IR of the place and if the wavelength is around 4.34

microns, it will raise peak carbon dioxide emission. The microcontroller then constantly gauges for any change in the system and if any two of the above sensors are hit, it will raise alarm. Finally, the system will send the appropriate message to authorities about the exact location of the fire in the building in minimal time using GSM-based modem which is attached to the microcontroller. The main challenge of this work is to aptly connect to a fire suppressing system that will quickly smother fire for any further harm from the damage caused by fire. The result of this study will benefit the institution by timely alerting the authorities by means of having GSM-based fire detection system in case of emergency.

## **2 Literature Review**

As we developed our paper, we underwent numerous papers, journals, articles, and books on firefighting related to the title of our project. We believe that providing efficient and cost-effective methods of dousing fire will help organizations fireproof their buildings. We want to put in our technological acumen to be used in challenging work of public service. Hence, we underwent a great deal of work in the fire extinguishing system which we have briefly stated. We believe that all the materials that we have reviewed have been great for encompassing the necessary details for the overall development of this project.

### **2.1 Fixed Gas Fire Extinguishing System**

In a fixed gas fire extinguishing system, the fire is suppressed by cutting off the oxygen supply necessary for combustion to occur or by disrupting the thermo-chemical reactions critical for the development of fire to take place. Their main function is to rapidly douse a developing fire before it becomes hazardous and alert residents/authorities before catastrophic damage occurs by discharging the protected place with a suitable fire dousing chemical gas or extinguishing agent [3]. They usually incorporate carbon dioxide or a mixture of halide gases that will douse fire instantly.

### **2.2 Fixed Water-Fire Extinguishing Systems**

Water is considered an efficient and common source of extinguishing the fire as it is non-lethal and invariably abundant and easy to set up. Hence these suppression systems incorporate the cost-effective and readily available sources of water to sprinkle on blazing flames [4]. Initially, when water hits the combustible zone of material, it cools down its surface ignition temperature by absorbing a huge amount of heat through evaporation. Afterwards, there is a rapid decrease in the temperature of the combustible materials by the straight discharge of water droplets onto the burning material surface [4]. In this process, steam is released in the form of water which impedes oxygen for the ignition process that results in the further progress of the fire. This system consists of series of sprinklers, water sprays, and a water mist system to effectively douse the fire. The water is discharged through fixed pressurized hydrant systems comprising of distributed arrays of nozzles and sprinklers running overhead and are supplied to these nozzles from dedicated pumps.



### **2.3 Automatic Sprinkler Fire Suppressing Systems**

Automatic sprinklers were developed to control, confine, and extinguish fires in order to prevent the loss of life and minimize the loss of property. However, the existence of a sprinkler system should not cause apathy among building owners and occupants. Flammable products, gases, liquids, or the accumulation of combustibles and other sensitive materials (e.g. explosives and rocket-propellant fuels) require strict supervision and continuous prevention and control. Various types of sprinkler systems are used for different applications such as Wet-Pipe system, Dry-Pipe system, Deluge system, and Antifreeze system.

### **2.4 Foam Fire Extinguishing System**

Foam is a mixture of three components mainly: Water, air, and chemical foaming agent. Foam is first created by mixing an adequate quantity of foaming chemical with water to produce a foaming agent solution. This solution is then passed through an air chamber to introduce air bubbles. A properly chosen solution concentrate when mixed with water and passed through an aerating chamber will produce a foam suppression agent which can be sprayed using series of hydrants and nozzles. Foaming agents cover the burning material like a blanket and prevent the fire from coming in contact with oxygen and thus reduces fire progression. They are particularly useful in places where water is not an ideal source of suppression like aircraft hangars, inflammable liquid storage, electronic server rooms, etc.

### **2.5 Portable Fire Extinguishing System**

Portable fire extinguishers are handheld storage cylinders with water or foam as a fire suppressing agent. They are generally used as a first measure against the fire of limited scale. These are pressurized cans containing fire dousing agents when directed towards blazing flames. These types of extinguishers are generally selective and can be used against limited burning items such as wood, cloth, wires, and liquids. Hence, they must be used with a proper label or it will exacerbate the fire condition.

### **2.6 Fire Alarm Systems**

Essentially, all the fire alarm systems work on the same basic principle, i.e. if sensors detect any surge in combustible gases or potential increase in temperature beyond a threshold value, it will raise alarm and alert people. These systems typically include detection devices such as smoke, heat, or IR/UV flame detectors that digitally process fire outbreak to a central control panel which processes all the signals and immediately performs critical operations, such as sounding strobes and alarms, call for evacuation, removing power off machines, and discharging fire extinguishing system. It also supervises the data sending to the different auxiliary and messaging devices [5]. All the fire control systems are secured and fire-proofed to prevent circuit damage. Additionally, the control panels are also supplied with solar battery backup in case of a power cut during a fire. The fire alarm system can be further broken down into five categories [6]:—Conventional fire alarm systems, two-wire fire alarm system, analogue addressable fire alarm system, wireless fire alarm system, and aspirating smoke detection system.

### 3 Methodology of Project and Circuit Block Diagram

#### 3.1 Methodology

The methodology that we used during the development of the project starts from the project title selection and ends with a complete project submission. As the system contains both hardware and software, these designs are developed separately and integrated at last. As evident the project started for discussion of the title with the supervisor. After the topic has been selected, additional discussions were done to understand the concept of the project and work out key critical objectives of the proposal. After that proper brainstorming of the literature review has been done and adequate background of the project was studied in detail by referring to various sources such as journals, reference books, articles, and data sheets. Then the system for both software and hardware are designed independently and when completed are integrated. The system was then troubleshot for any defects and anomalies. Redesigning and troubleshooting processes will be carried out if the output obtained is not as expected. Finally, the project would be completed and finalized for presentation to the committee for verification.

#### 3.2 Process Model

The following process model (Fig. 1) was carried out for effective processing of thoughts and ideas for the successful completion of this project. The design methodology is explained in the flowchart in (Fig. 2):

- (1) **Requirement Planning:** At this phase, the members of this project discussed the exact requirements of the project both in terms of qualitative and quantitative analysis. The division of project details was discussed and what hardware and software components will be used.
- (2) **User Design:** In this phase, the requirements of the project were converted into workable designs. In this phase, we simultaneously worked on the hardware part and GSM user interface part.
- (3) **Construction:** The design has been built and advisors continued to review our design to make corrections and suggestions for improvements. The construction of circuit diagrams began to be designed and codes were embedded in C and Proteus Software. Various other sensors and microcontrollers were loaded to provide the desired output.
- (4) **Deployment:** The team delivered the finished application to the committee. The proponents were still under development for beta testing.

#### 3.3 Sources of Data and Information

To gather more information, we have also used Internet research on how such kinds of systems are designed by research studies related to our study. We have also gone through a lot of text and reference books in the library as well as online portals to understand our topic. In general, from the Internet and library, we have read more knowledgeable web links as well books. We also took reference from various books and articles on the Internet to keep yourself well versed with knowledge.

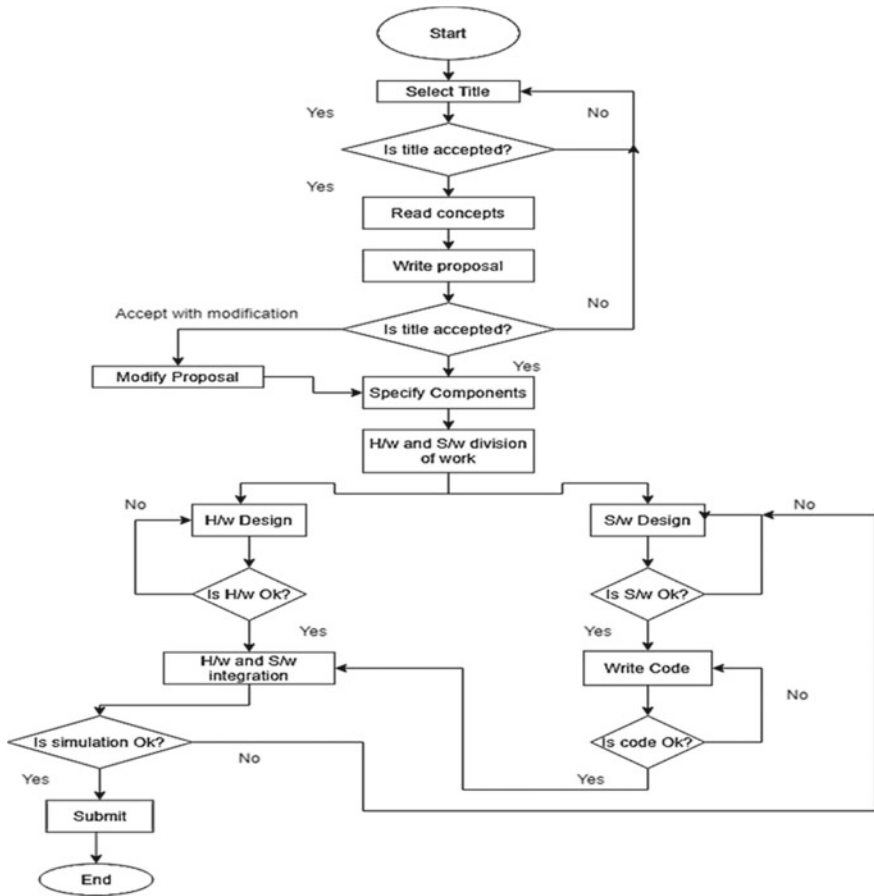


Fig. 1 Flowchart of the project design

### 3.4 System Block Diagram

The given Fig. 3 shows the block diagram of the project. The sensors are connected to the microcontroller PIC16F877A and will receive the data. The chip is connected to a relay system that will turn on the devices if sensors are high. The data will be displayed on the LCD screen and the message will be sent via the GSM module.

## 4 System Design

Fire detection systems are complex and require a series of actions to provide the desired result. As an example, the most institution needs to instal sensors and GSM modems to constantly gauge and monitor changes in ambience. They must be very connected with a central control panel to effectively monitor the place and control devices. In this section, various design modules have been discussed in detail.

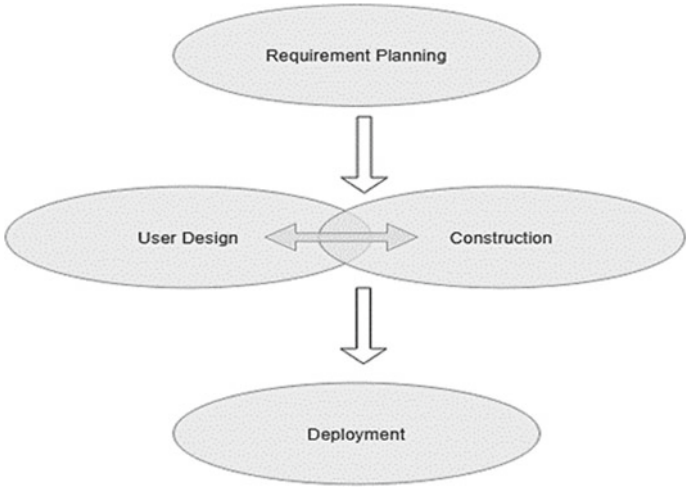


Fig. 2 Process model

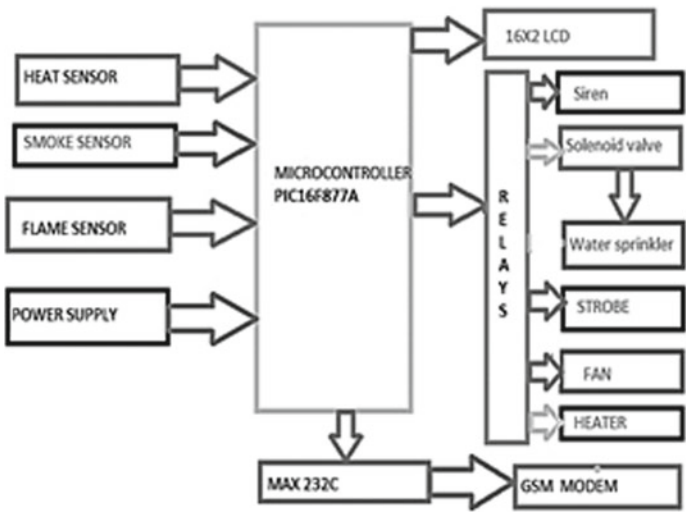


Fig. 3 Block diagram of the system with sensors and chip

## 4.1 Hardware Requirements

### 4.1.1 Smoke Detectors

A smoke detector is an electrical fire-protection device that automatically detects the presence of burning fumes, as a key indicator of fire, and alerts building occupants by sounding warning signs [7]. Smoke detectors work on the principle of buoyancy or forced airflow. A smoke detector invariably detects the emission of invisible fumes but detectable particles of combustion. A smoke detector is often considered a safe option

for early warning since incendiary flames always precedes after smoke in a fire. Smoke is released from the source of ignition and can travel rapidly through vapour fumes. As the smoke density rises, lighter particulate matter ignites from the combustible material which is detected by the sensor, and an alarm is activated indicating the presence of smoke particles within the controlled area. There are two types of smoke detectors that are used widely: photoelectric detector and ionization chamber. A photoelectric detector monitors the sudden scattering of the light wave when smoke enters the building or room, sounding the alarm. They respond at the early blazing phase before it breaks into flame usually in 15–40 min. Hence, we used photoelectric smoke detectors in this project due to their greater efficiency.

#### **4.1.2 Heat Detectors**

Thermal detectors or heat sensors respond to the sudden change in thermal emission produced from a fire. They accurately detect the rate of rising of heat energy and the detector is activated by normal means of conventional currents of heat air or combustion products or by radiation effects or both. They can be classified into two types—fixed temperature detector (i.e. trigger alarm if the temperature is beyond ambience point) and rate of rising (i.e. gives warning on the increasing rate of temperature) [8]. They both depend on the heat energy released from the surroundings to activate the sensor to trigger the alarm. The rate of rising can be detected either through bimetallic strip tube sensors or digital thermoelectric sensors [1]. The fixed temperature sensors trigger a warning when the surrounding temperature goes beyond a threshold safe limit. Since this activation takes some time before actual detection, thermal detectors are usually slower to respond to fire [1]. It is combined with an LM35 circuit sensor that sends signal which can be used to measure the rate of rising of heat proportional to the temperature (in °C).

#### **4.1.3 Flame Detectors**

Flame detection is yet another key indicator to detect fire in the place. It can be detected through thermal visualization of protected places by heat-sensing of thermal radiation or through the optical imaging techniques of thermal objects [9]. A flame detector detects and measures infrared (IR) radiation originating from hydro-carbon-based fires. They can detect fire by sensing a surge in IR radiation when the level goes beyond a threshold value (typically, 4.3  $\mu\text{m}$ , i.e. the peak of carbon dioxide emission). In this project, the IR flame detector has been incorporated for its low cost and high efficiency. It detects and responds to short wavelengths of very high temperature which is a characteristic of a flame. The radiation from flames is characterized by a flicker in the range of 5–30 Hz. Hot gases emit a certain thermal spectral pattern in the infrared region of wavelength typically around 4.4  $\mu\text{m}$ , which can be detected with a special type of thermal graphical device called a thermal imaging camera.

#### **4.1.4 LCD 16 × 2 Module**

The LCD displays data of status messages over 16 columns and 2 rows. The main function of the proposed LCD is to show the current temperature level report fire as

reported by the employed sensors and the exact location of a fire in the building. It has got 8 data pins to display data, 3 control pins for processing of data, and the rest 5 pins ground and supply voltage connections [10]. It is connected to the microcontroller from pin 33 to 40.

#### 4.1.5 GSM Modem

A GSM module or modem is a type of hardware wireless device that works over a subscription to a cellular operator. A GSM modem behaves just like a dial-up modem but with a serial, USB, or Bluetooth connection. It calls for a Subscriber Identity Module (SIM) similar to cellular phones to send and receive messages and perform data exchange with the network. In addition, GSM's also have unique International Mobile Equipment Identity (IMEI) numbers just like cellular phones [11]. A GSM modem can be paired with an external device such as LAN/Router or it can be connected to a PC Card. A GSM modem relies on TDMA to assign time slots to each user. GSM modems assist an extending set of AT instructions for sending and receiving cellular SMS messages. These extended AT instructions are described within the GSM standards. Because of its wide application in mobile communication, it provides messaging services in the range of 800–1920 MHz. Different AT and TTL commands received by the modem can be sent by the processor for a wide range of wireless networks to communicate with the GSM and GPRS network and data transmission [12].

#### 4.1.6 Microcontroller

**PIC16F877A** is a reliable and efficient easy-to-use CMOS FLASH-based 8-bit microcontroller chip device. It features 256 bytes of EEPROM data memory, 35 simple words instructions, interrupt capability with SSP and SPI, and self-programming module. The PIC microcontroller PIC16F877A is one of the most widely used, cost-effective, and time-efficient embedded processors in the chip industry. This microcontroller makes coding and programming easier on its chip owing to its fast read and write time cycles [13]. It takes all the data, processes it, and executes appropriate commands. It takes in data from the sensors and keeps on monitoring it. When any of the two sensors are high, it will send the message on the screen and simultaneously activates relays. It also sends the signal to MAX232C connected to the GSM modem.

## 4.2 Software Requirements

### 4.2.1 Proteus

Proteus is a virtual system modelling (VSM) and electronic circuit simulation software that is useful in designing circuit applications. It covers a comprehensive range of microcontroller models, wherein a circuit can be designed and tested as a prototype with all sorts of active and passive elements along with interactive simulation by the animated schematic. The schematic capture and simulator component is named ISIS, and a layout of the circuit can be designed using the application of the ARES suite [14]. Not only Proteus can simulate the interaction between the microcontroller and software running

but it also connects any analogue or digital electronics to the software. In this project, Proteus 8 software is used for simulation purposes.

### 5 Project Design and Simulation

In this section, the entire schematic of the circuit is shown in (Fig. 4) and the simulation in (Fig. 5). The sensors, relays, LCD, and GSM are connected to the microcontroller and the system is simulated. Once the simulation works correctly, the code is hard-wired into the microcontroller. All the components are connected in the project to the microcontroller via IDE and then hardcoded using C++ and Micro C language. Once the experimental simulation works correctly, it is employed for testing under various conditions for troubleshooting [15].

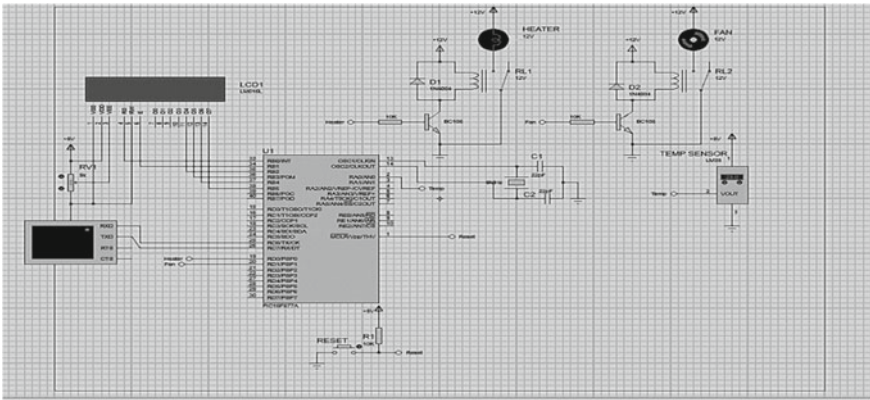


Fig. 4 Circuit design

### 6 Conclusion and Recommendations

The designed firefighting system can detect and deal with over-temperature, smoke, and flame. After successful deployment and testing of software, the system has shown positive and expected results as outlined in the proposal. The system is capable of sending the correct message via the GSM module to alert people and then displaying the status on an LCD. The microcontroller processes the sensor circuitry signals and it controls the indicator panel and circuit relays. A simulation of the system gave a satisfactory result as per expectations. The proposed paper demonstrates the outline structure of the system to detect and douse fire quickly with minimum delay. The availability of such a system is extremely preferred for the institutions for minimal damage in case a fire broke out. The system keeps on monitoring the ambience and gives feedback to the chip for processing. The proposed project leads to several recommendations concerning the wireless firefighting system problems in the evaluation of both source code and simulation. The following points give us a brief overview of some recommendations for improvements:



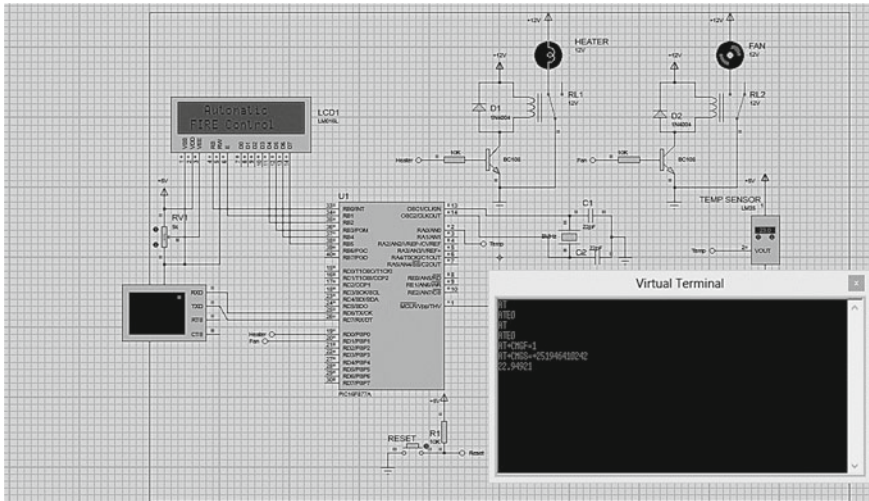


Fig. 5 Simulation

1. To use a database or website to record fire breakouts
2. To instal video cameras to get live footage and to turn on emergency lights when a fire breaks out (Table 1).



**Table 1** Pin description

Pin no	Description	Pin-name
1	Ground 0 V Voltage	GND
2	Supply Voltage 5 V	V <sub>cc</sub>
3	Display Adjustment	V <sub>EE</sub>
4	Selects CMD → low, DATA → high	REG select
5	READ and WRITE operations from register	RD/WR
6	Data to pins from high to low pulse	ENB
33	Eight data pins	DP0
34		DP1
35		DP2
36		DP3
37		DP4
38		DP5
39		DP6
40		DP7
15	LCD V <sub>cc</sub> (5 V)	LCD +
16	LCD ground (0 V)	LCD –

## References

1. Béla G (ed) (2003) Instrument engineers' handbook, Volume one: process measurement and analysis, vol 1., 5th edn CRC press, Chicago
2. Fire Suppression System (2021) [https://en.wikipedia.org/wiki/Fire\\_suppression\\_system](https://en.wikipedia.org/wiki/Fire_suppression_system). Last accessed 07 Apr 21
3. Fixed Gas Fire Extinguishing System (2021) <https://www.oshatrain.org/courses/mods/107m2.html>. Last accessed 7 Apr 21
4. Water Based Suppression System (2020) <https://www.janusfiresystems.com/products/water-based-suppression-systems>. Last accessed 8 Apr 21
5. Lataille J (2002) Fire protection engineering in building design. Elsevier, Chicago
6. Fire Alarm system (2021) <https://www.ifsecglobal.com/fire/a-guide-to-fire-alarm-system-types-2>. Last accessed 9 Apr 21
7. Smoke Detectors (2021) <https://www.ifsecglobal.com/smoke-detectors>. Last accessed 9 Apr 21
8. Heat Detector (2021) <https://www.sciencedirect.com/topics/engineering/heat-detector>. Last accessed 10 Apr 21
9. Nolan DP (2014) Handbook of fire and explosion protection engineering principles: for oil, gas, chemical and related facilities. 3rd edn, WA, UK
10. Monk S (2016) Programming arduino: getting started with sketches. 1st edn, McGraw-Hill Education
11. Sauter M (2010) From GSM to LTE: an introduction to mobile networks and mobile broadband, 1st edn. Wiley, UK

12. GSM modem (2020) [https://www.engineersgarage.com/article\\_page/gsm-gprs-module-all-you-need-to-know/](https://www.engineersgarage.com/article_page/gsm-gprs-module-all-you-need-to-know/). Last accessed 10 Apr 21
13. Wilmshurst T (2006) Designing embedded systems with PIC microcontrollers: principles and applications. 2nd edn, Newnes, UK
14. Bates MP (2013) Interfacing PIC microcontrollers: embedded design by interactive simulation. 2nd edn, Newnes
15. Thakur M (2016) Arduino projects vol-I: with proteus simulation files. Don't just read it, Try it, 1st edn



# Investigation of Thermal Battery Management Pack Using Liquid Cooling Systems in 3-D Li-Ion Battery Model

Vanshaj Mittal, Bhumika Mathur, Shivam Beniwal, and Amrish K. Panwar<sup>(✉)</sup>

Department of Applied Physics, Delhi Technological University, Main Bawana Road, New Delhi 110042, India  
amrish.phy@dtu.ac.in

## 1 Introduction

Recent fluctuation in crude oil prices and the widespread concern about the deteriorating environment and its impact on human health and social development have accelerated the efforts to develop more clean and sustainable energy resources. There is a high demand to utilize energy and to look for inexhaustible and clean fuel sources that can substitute petroleum products to empower the maintainable improvement of our economy and society. The lithium-ion battery is one of the solutions. It is the most attractive source of energy storage device to date because of the number of features that it provides, ranging from huge specific capacity to high voltage coupled with high-power; it shows the best performance [1].

In today's date, if you look around all the electronic devices such as small portable speakers, digital cameras, laptops, mobile phones, upcoming hybrid-electric vehicles, all of these things have one part in common, i.e., lithium-ion batteries. It is self-explanatory of the extensive use of these batteries. With such widespread application, it is expected for the battery to work for longer and longer hours. We know that battery performance is affected by the repeated charging or discharging process because the temperature of the battery pack rises steadily [2]. If a battery is used extensively and the battery pack temperature exceeds the optimal temperature range, the battery life degradation rate is accelerated. Under extreme temperature conditions, it can lead to thermal runaway [3].

For battery manufacturers across industries, they consider battery life as one of the most important factors during its development. Therefore, it is necessary to study thermal management systems to maintain battery temperature below the limiting value even in high-power consumption situations [4]. To solve this problem, we need to understand the heat dissipation/generation characteristics of the battery pack. Since numerical modeling and simulations are always preferable to prevent high costs and time usage, we have implemented them [5].

## 2 Cooling System in Battery Management

For various thermal batteries, such as lithium-ion, thermal management is a very crucial aspect of battery pack management [6]. The primary aim of a thermal management

system is to control the range of average temperature across the battery pack and maintain an ideal value [7].

There are 2 types of cooling systems, i.e.

1. Air-Based (Fans and heat sinks)
2. Liquid-Based (Cooling Fluid).

## 2.1 Air-Cooled Systems

Air-cooled systems offer the simplest thermal management system designs. It is mainly dependent on the surrounding air as a cooling medium. Further, it may only utilize the outside air without any other device or it could utilize already pre-conditioned air, and this is done with the help of devices such as a cooler/fan/evaporator to cool down air in or around the battery [8]. Air is not very effective in high-temperature conditions because of its low heat capacity [9].

## 2.2 Liquid-Based Systems

A liquid-based cooling system has direct contact between the coolant and the cells. Still, the use of liquid rather than air is supported by the properties of dielectric fluids, which help in easier heat flow in and around the battery material. Investigating the performance of liquid-based cooling systems is important because of the limitations of the air-based cooling systems. Liquid cooling could be further divided into two. “Firstly, direct cooling systems in which a battery is directly immersed in a fluid environment to regulate battery temperature. Non-conductive fluids like hydro-flouroether, mineral oil, de-ionized water, or silicon oil are required as they absorb more energy due to higher viscosity” [10].

Secondly, in-direct cooling systems are the ones in which there is a barrier between the battery and the fluid. Therefore, cooling plates show very low thermal efficiency because of the very high resistance of transferred heat. Even though cooling performance is good, in direct systems have found less practical applications because of the high weight and complex assembly and maintenance required [8].

# 3 Types of Coolant

## 3.1 Water/Glycol

We all know that water is one of the most abundant resources available on earth. Due to its high specific heat capacity, water is used as a cooling fluid in many fields like heavy machinery, car engines, and electrical items. “In Li-Ion batteries, water is not kept in direct link with the battery. It is done to prevent any kind of electrical short-circuit. Auxiliary devices such as jackets and tubes and cooling plates are included in increasing the battery pack’s complexity” [11].

Since water freezes at 0 °C, it is not suitable for coolant in winters/extremely cold conditions because serious defects could arise in the battery due to the expansion of the volume of frozen water. To prevent this, we mix ethylene glycol and water to bring down the freezing temperature. Usually, a mixture of 50/50 ethylene glycol/water is often used as non-toxic and does not corrode metal.

### 3.2 Mineral Oil

Mineral oil is also widely used as a coolant. It has an extensive application in electrical devices as a coolant because it is electrically non-conductive [12]. Oil is an insulator that does not catch fire. “The battery pack is often immersed in a coolant (oil) so that heat is transferred from the batteries to oil directly. This proves to be extremely effective for systems that are exhibited to super-high temperatures” [10]. Cooling occurs quickly because there is always a link between the battery and coolant. This is not the case with glycol/water. There is minimal thermal resistance in the case of oil, unlike an in direct system where there is a hindrance between the battery and liquid.

We also know that controlling for the flow rate, mineral oil has a better heat transfer efficiency compared to air due to high heat conduction and thin boundary layer [13]. “The most considerable drawback of oil-based cooling systems is that energy consumption is high controlling for the pumping rate. This is because of the high kinematic viscosity of mineral oil” [11].

### 3.3 Liquid Metal

Liquid metals have gained popularity in thermal systems because of their high thermal conductivity and low viscosity. Commercially used liquid metals are Gallium and its alloys [14]. Characterized by the property of high boiling point and low melting point, Gallium alloys tend to be in the liquid state. These features led to its widespread use in heat systems of computer chips [15].

“Since liquid metals are electrically conductive, they can be driven by electromagnetic forces. This provides an added benefit to using electromagnetic pumps, which better consider the life and maintenance of cooling systems” [16]. “This system has a very high cooling capacity, and it helps combat very strenuous conditions of the elevated-temperature environment, high-power draw, and battery defects” [10].

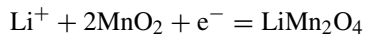
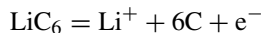
## 4 Simulation Model

### 4.1 Model Introduction

The existing lithium-ion battery model in COSMOL Inc. Multiphysics 5.6 is extended here by adding a battery pack and changing the coolants in the flow compartment. This thermal model is developed based on the 3-D thermal model described in [17].

A lithium manganese oxide (LiMn<sub>2</sub>O<sub>4</sub>) battery is chosen for this work. This is a simple model based upon battery and fuel cell physics (Fig. 1).

The chemical reaction taking place in the lithium-ion battery may be represented by



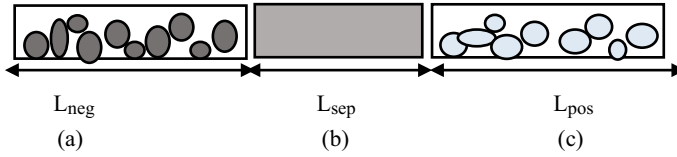


**Fig. 1** Visual representation of 1-D cell model created in COMSOL where the domains are **a** Negative porous Electrode (LixC6MCMB, 55  $\mu\text{m}$ ), **b** Separator (30  $\mu\text{m}$ ), **c** Positive Porous Electrode (LiyMn2O4, 55  $\mu\text{m}$ )

### 4.2 3-D Model Geometry

The battery pack (Flow Compartment) is designed around a cylindrical lithium-ion battery cell covered around a mandrel. The dimensions of the battery pack consist of a cuboidal pack containing the coolant. It includes the flow of the cooling fluid around the battery in a flow compartment—the fluid flow influences the heat transfer rate.

The geometry is as follows:

1. Active battery material domain (material: steel, height: 65 mm, radius:9 mm)
2. Mandrel (material: nylon isolator wound around battery cell, radius: 2 mm)
3. The cylindrical battery connector (material: steel, radius: 3 mm)
4. Flow compartment (Fig. 2).

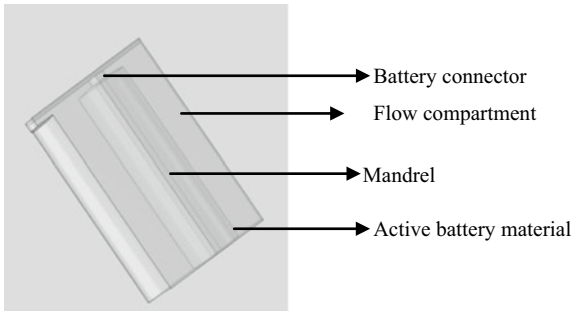
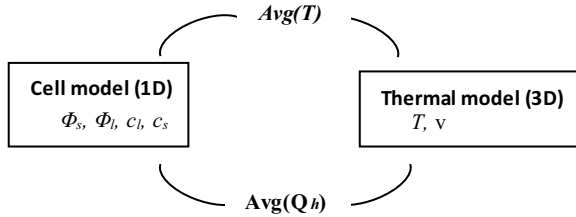


**Fig. 2** 3-D model geometry built-in COMSOL around the battery pack and connector

A 3-D 18,650 lithium-ion battery is modeled in an air-cooled cylindrical system. 1-D cell model was used to develop battery chemistry, and a 3-D model is used to study temperature. The average temperature and the generated heat source are used to couple the two models.



We have replicated a 1-D model into a 3-D thermal model. It is a co-dependent model where we calculate the average heat generation from the 1-D model by providing the average temperature basis of the 3-D model. The scaled heat source is obtained by multiplying the volumetric heat source from the 1-D Li-ion battery model by two factors. The first factor is the fraction of the total 1-D model in which heat is generated.

$$(L_{neg} + L_{sep} + L_{pos}) / (L_{batt})$$

$$\frac{((r_{batt} - d_{can})^2 - r_{mandrel}^2)(h_{batt} - 2d_{can})}{(r_{batt}^2 - r_{mandrel}^2)h_{batt}}$$

$$\frac{\text{Total Volume} - \text{Volume of Mandrel and Outer Can}}{\text{Volume of battery material}(\text{Cell Vol} - \text{Mandrel Vol})}$$

The second factor is the fraction of the total 3-D cylindrical cell geometry in which heat is generated:

Combining the equations we get;

$$Q_{h,3D} = Q_{h,1D} \frac{L_{neg} + L_{sep} + L_{pos}}{L_{batt}} \frac{(r_{batt} - d_{can})^2 - r_{mandrel}^2}{(r_{batt}^2 - r_{mandrel}^2)} \frac{(h_{batt} - 2d_{can})}{h_{batt}}$$

The battery is housed in a battery pack that consists of a battery matrix. Due to the spiral winding of the battery cell layers, the thermal conductivity of the active battery material is anisotropic. To account for the orthotropic thermal conductivity of the active material, a cylindrical coordinate structure is added to the model.

## 5 Result and Discussion

In this section, the simulation results have been discussed, and the temperature change across the battery pack for different types of coolants has been analyzed at an extremely high C-Rate since the batteries may have to undergo very harsh conditions.

Following are the initial conditions that were kept during our simulation. Inlet boundary temperature and battery initial temperature was instilled to be at room temperature, i.e., 298.15 K. Inlet velocity was kept at 0.1 m/s outlet pressure was maintained to be 1 atm. On the battery walls, no-slip conditions are applied.

From the simulation results, it is found that maximum heat is generated inside the battery can, and the heat decreases as we move toward the connector. It could be analyzed

that after adding coolants, temperature variation across the battery pack was uniform. In contrast, when there was no liquid coolant, we observed skewed heat distribution in the flow compartment of the battery pack.

While studying the temperature in 3-D model graphics, it was found that different coolants showed different temperature ranges in and around the battery. The heat generated in the battery pack when different coolants are added in the flow compartment is lower in comparison to when the coolants are absent. In Fig. 3 it could be seen that for liquid metal (Gallium), mineral oil, glycol/water, air maximum temperatures are 298.3599 K, 299.505 K, 299.571 K, and 311.2802 K, respectively. The graph comparing the temperature range across the battery pack for different coolants shows that liquid metal (Gallium) shows the least temperature spike.

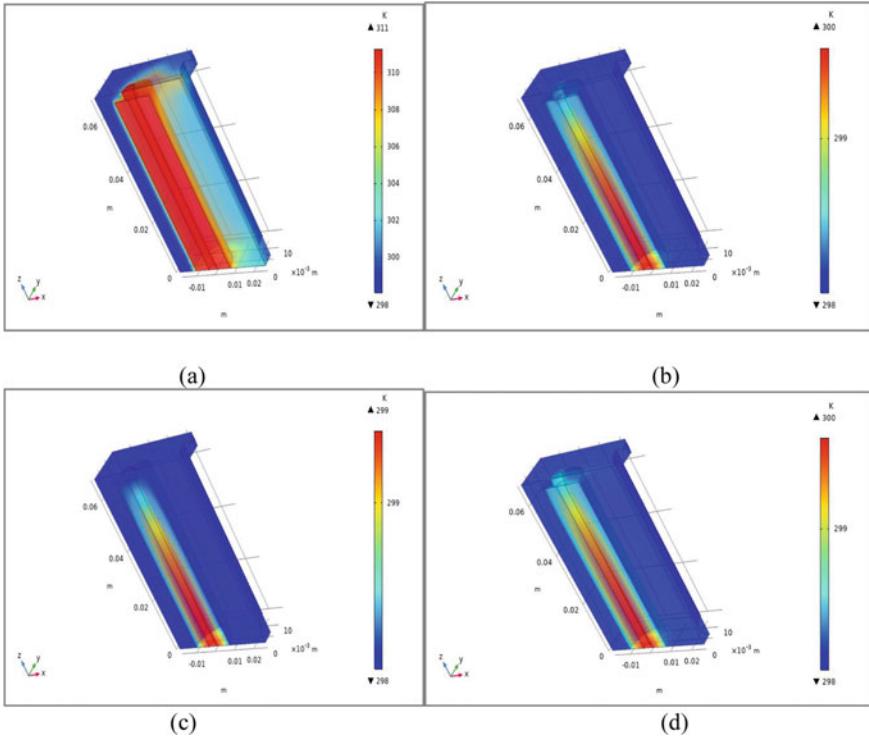


**Fig. 3** Simulation results for heat flow generation in battery packs by different coolants **a** Without coolant (Air), **b** With mineral oil, **c** With liquid metal (Gallium), **d** With water/glycol

Figure 4 shows the change of difference in battery temperature ( $T$ ) and inlet temperature ( $T_i$ ) was studied as well. According to this graph, the maximum change in temperature of the system is 3 K. For the first charge cycle, the temperature difference of the battery is increasing. For the first discharge cycle, the temperature is initially decreasing and is later rising sharply toward the end of the discharge cycle. Similarly,



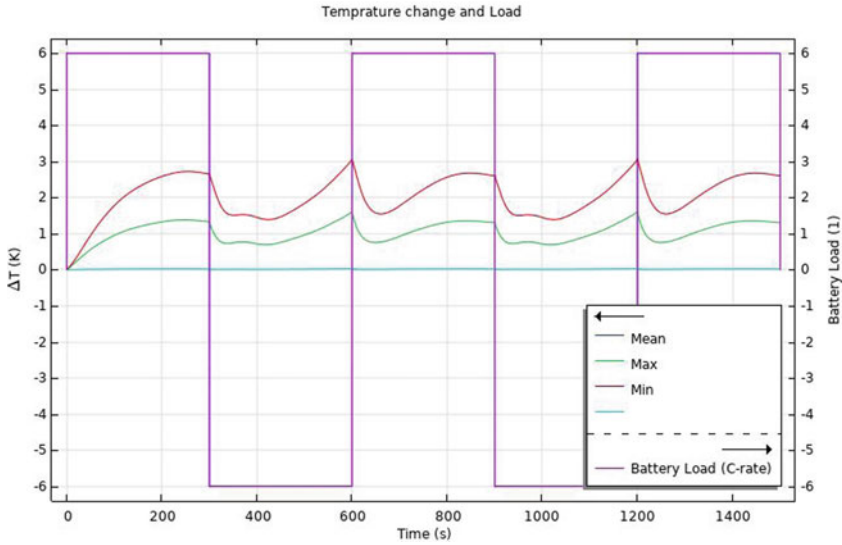


**Fig. 4** Temperature versus time graph, showing the change in temperature with respect to the load cycle

we can see a sharp decrease in the temperature for the subsequent charge cycles initially and again a steep ascend in the temperature values.

In Table 1, the material properties of all the coolants are mentioned. The high specific capacity and low kinematic viscosity of water/glycol mixture compared to air help it absorb a large amount of heat, improving the pumping efficiency in the battery pack. At the same time, mineral oil, being nonflammable and having a kinematic viscosity between water and air, makes it more efficient than air. We see that the heat transfer is more efficient due to the much higher thermal conductivity of the liquid metal. A very high kinematic viscosity of liquid metal makes mechanical pumping difficult, and hence electromagnetic pumps are used with liquid metals as coolants.

**Table 1** Material properties of all the coolants as compared to air

Properties	Air	Liquid metal (Gallium)	Water/glycol	Mineral oil
Density(kg/m <sup>3</sup> )	1.225	6093	1069	924.1
Specific heat capacity (J/(kg-K))	1006	409.9	3323	1900
Thermal conductivity (W/(m-K))	0.0242	29.28	0.3892	0.13
Kinematic viscosity (m <sup>2</sup> /s)	$1.46 \times 10^{-5}$	$1.89 \times 10^{-3}$	$2.58 \times 10^{-6}$	$5.60 \times 10^{-5}$

The common observation in Fig. 5 of pressure in the lithium-ion battery pack is that the active battery material surface facing the inlet edge is withstanding the maximum pressure. When the temperature of the battery increases, the pressure on the walls increases, making the battery expand and prone to explosion. We can observe in the graphs that compared to air, mineral oil has the least pressure in the battery pack, with a maximum pressure of 50.8 Pa, followed by water/glycol and liquid metal with 123.12 Pa and 396 Pa, respectively.

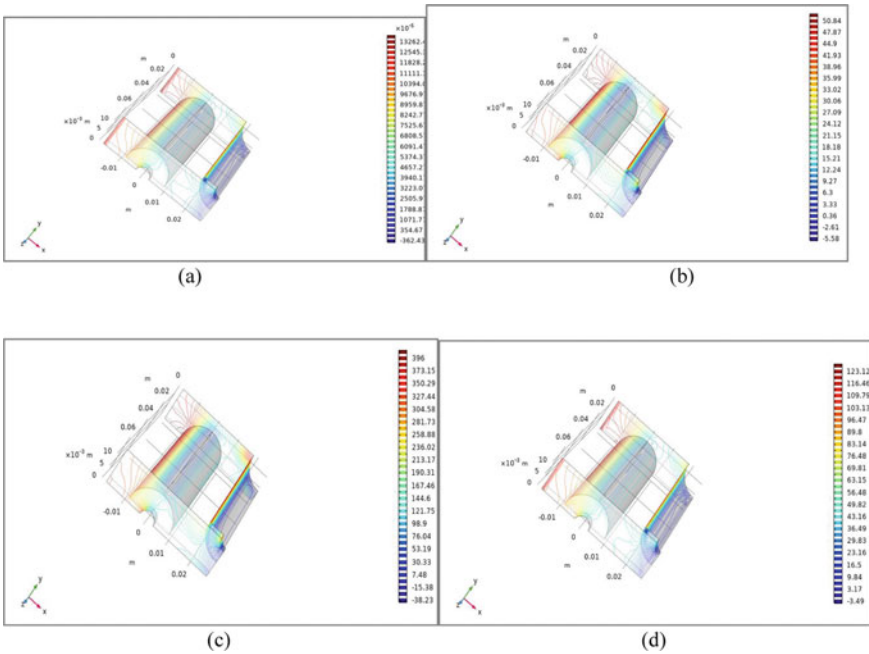


**Fig. 5** Simulation results for pressure variation in battery packs by different coolants **a** without coolant (air), **b** with mineral oil, **c** with liquid metal (gallium), **d** with water/glycol

## 6 Conclusion

This article successfully reviews the effect of different liquid coolants in direct cooling mechanisms that can be used to regulate the temperature in a battery flow compartment at a high C-Rate. Different coolants were tested and compared based on material properties like thermal conductivity/kinematic viscosity. Gallium (liquid metal) turns out to be the best-suited option to maintain temperature levels but is expensive and even the pressure tends to remain high. According to our research based on the simulation model, mineral oil should be a more preferable choice because active battery material can be directly immersed in the coolant avoiding additional costs, unlike water/glycol mixture. Finally, we conclude our research with findings that prove liquid cooling systems to be of great use in times of high-power draw as they did not let the change of battery temperature exceed more than 3 K and regulate pressure inside the flow compartment.

## References

1. Nanoscale Horiz (2016) Advanced cathode materials for lithium-ion batteries using nanoarchitectonics 1:423–444
2. Lu R, Yang A, Xue Y, Xu L, Zhu C (2010) Analysis of the key factors affecting the energy efficiency of batteries in electric vehicle. *World Electr. Veh. J.* 4:9–13. <https://doi.org/10.3390/wevj4010009>
3. Khateeb SA, Farid MM, Selman JR, Al-Hallaj S (2004) Design and simulation of a lithium-ion battery with a phase change material thermal management system for an electric scooter. *J Power Sources* 128(2). <https://doi.org/10.1016/j.jpowsour.2003.09.070>
4. Zhu C, Li X, Song L, Xiang L (2013) Development of a theoretically based thermal model for lithium ion battery pack. *J Power Sources* 223. <https://doi.org/10.1016/j.jpowsour.2012.09.035>.
5. Zhu C, Li X, Song L, Xiang L (2013) “Development of a theoretically based thermal model for lithium ion battery pack.” *J Power Sources* 223:155–164
6. Pistoia G (2009) Chapter 5—Vehicle applications: traction and control systems. *Battery operated devices and systems*, Elsevier, pp 321–378, <https://doi.org/10.1016/B978-0-444-53214-5.00005-4>.
7. Wang Q, Ping P, Zhao X, Chu G, Sun J, Chen C (2012) “Thermal runaway caused fire and explosion of lithium ion battery”. *J Power Sources* 208:210–224. <https://doi.org/10.1016/j.jpowsour.2012.02.038>.
8. Huber C, Kuhn R Thermal management of batteries for electric vehicles. Institute for Electrical Energy Storage Technology, Munich, Germany. 2TUM CREATE Ltd, Singapore (*Advances in Battery Technologies for Electric Vehicles*. <https://doi.org/10.1016/B978-1-78242-377-5.00013-3>)
9. Brotz F et al (2007) Kühlung von Hochleistungsbatterien für Hybridfahrzeuge. *ATZ Automobiltechnische Zeitschrift* 109(2):1156–1162
10. Experimental and simulation study of liquid coolant battery thermal management system for electric vehicles: A review Omer Kalaf1 | Davut Solyali2 | Mohammed Asmael1 | Qasim Zeeshan1 | Babak Safaei1 | Alyaseh Askir3 <https://doi.org/10.1002/er.6268>
11. Deng YW, Feng CL, E JQ, et al (2018) Effects of different coolants and cooling strategies on the cooling performance of the power lithium ion battery system: a review. *Appl Therm Eng* 142:10–29
12. A Novel Design for Lithium ion Battery Cooling using Mineral Oil Conference Paper · December 2016. <https://doi.org/10.14257/astl.2016.141.34>
13. Pesaran AA (2001) Battery thermal management in EVs and HEVs: issues and solutions. *Battery Man* 43(5):34–49
14. Liu J, Zhou Y-X. A computer chip cooling method which uses low melting point metal and its alloys as the cooling fluid. China Patent; 2002 [2131419].
15. Yang X-H, Tan S-C, Liu J (2016) Thermal management of Li-ion battery with liquid metal. *Energy Convers Manage* 117:577–585. <https://doi.org/10.1016/j.enconman.2016.03.054>
16. Miner A, Ghoshal U (2004) Cooling of high-power-density microdevices using liquid metal coolants. *Appl Phys Lett* 85:506. <https://doi.org/10.1063/1.1772862>
17. Inc., C (2020) COMSOL. Retrieved from <http://www.comsol.com/products/multiphysics/>



# Short-Term Electricity Demand Forecast Using Deep RNN and Stacked LSTM

Surbhi Singh and Madan Mohan Tripathi<sup>(✉)</sup>

Electrical Engineering Department, Delhi Technological University, Delhi, India  
mmtripathi@dce.ac.in

## 1 Introduction

In this reformist era of innovation, where knowledge of historical data is key in improving the future prospects of outcomes in any domain of industry, energy sector is no exemption. Load forecasting, be it long-term or short-term, is one of the important and pioneering areas of research, as predicting the probable electricity consumption not only helps to create a balance between the electricity demand and supply but also helps power plants in better load scheduling, thus preventing excessive production of electricity. Predicted results are also vital in the contingency planning, strategizing, and economic load dispatch. The electricity demand is changing with time; hence, the supply needs to be adaptable to this dynamic behavior.

An inaccurate prediction of demand not only results in financial losses to stake holders [1], but as the power generating stations use the forecasted values in assigning the power sources for the upcoming hours, inaccuracy in predictions would fail the planned structure. Also, power grids need to know ahead of time the transmission necessities to appoint assets. Crisis handling, load shedding, management methodologies, and strategic commercialization are totally impacted by load estimates. Hence, forecasting error should be corrected in order to avoid increased electricity production as well as transmission costs.

In the past decade, researchers have attempted to investigate the depth of forecasting in the energy sector and have come up with observations and solutions, with which a load predictive structure can be optimized [2]. Our pursuit of literature survey brought about the accompanying papers that zeroed in on exhaustive study concerning the strategies, models, and a few techniques utilized in electric demand forecasting along with relevant evaluation metrics which should be used for better understanding of the models' performance [3].

There are numerous studies to demonstrate that cutting-edge AI-based forecast strategies are clearing route for better and more accurate outcomes. There are conventional and unconventional approaches to short-term load forecasting. The former uses regression methodologies, smoothing procedures, and statistical investigations such as ARIMA models, and the latter employs AI-based and machine learning methods such as fuzzy inference systems, neural networks (NNs), neuro-fuzzy systems, support vector machines (SVMs), and their hybrid models. Popularly used of these are NNs [4].

Although both statistical and AI-based methodologies have been put to use, the latter provides better results as demand forecasting deals with nonlinearity, and these methodologies provide better results [5]. Random forest, bagging, and M5P which are regression tree-based machine learning algorithms are also utilized to effectively perform short-term load forecasting. The helpfulness of these techniques has been verified through broad tests utilizing genuine load data from the Australian power market where M5P gave desirable results [6]. Short-term load forecasting is used for adjusting power supply for generation, transmission, distribution expansion, and revenue analysis [7].

In one of the studies, where time series load forecasting of Kuwait dataset using neural networks and ARIMA was done and weather data such as temperature measures, humidity measure, oil price data, population, residence count, average salary, number of passengers, rate at which currency was earned, and economic factors were utilized as features, neural networks proved to perform better than ARIMA [8]. Another study shows that the artificial neural network model beats the regular methodology with 5% error as opposed to 15% error by using conventional methods [9]. Support vector regression has also proven to perform better while predicting when features like weather, calendar, and holiday data are utilized [10]. Past investigations suggest that prerequisite for any methodology, be it classical or AI-based particularly deep learning techniques, is adequate historical load data for training. This will improve the testing accuracy as well as the precision suggesting that the difference between actual and forecasted values is less, and the model is able to generalize well. It is also beneficial if multivariate models are built where features incorporated can be consumer behavior, commodity price of other sources such as petroleum, oil, appliances measurements, and weather features, in order to enhance accuracy [11]. Recent studies show that deep neural network techniques like LSTM and RNN outperform the classical methodologies used in electricity load forecasting [12].

## 2 Data Collection and Processing

Data was obtained from Kaggle extracted from PJM energy market for the distribution done by Dominion Energy Inc., which supplies electricity in Virginia, North Carolina, and South Carolina.

The data comprises per day hourly electricity demand in megawatts from May 2005 to August 2018. Hence for a day, there were 24 records depicting hourly electricity demand, with 116189 data points in total.

Normalization of data is done to bring each data point on a similar scale so that each element is similarly significant. As done in this paper, the original dataset had power consumption on the scale of 5000–22500 MW, and then the same dataset is normalized to be in the range of 0 and 1. The normalization strategies affect execution of a model at a fundamental level in prediction problems utilizing neural networks, resulting in better accuracy [14].

In this paper, min–max normalization is used. This technique changes data points from a reach  $[\text{Min}_T, \text{Max}_T]$  to a reach  $[\text{Min}_N, \text{Max}_N]$  dependent on the greatest estimation ( $\text{Max}_T$ ) also, on the least estimation ( $\text{Min}_T$ ) of the original dataset. Subsequently for each feature variable, the least value of that feature in consideration gets changed

into a 0, the greatest data point gets changed into 1, and each and every other value gets changed into a decimal somewhere in the range of 0 and 1. Mathematically, it is represented by Eq. 1.

$$N_i = \text{Min}_N + \frac{T_i - \text{Min}_T}{\text{Max}_T - \text{Min}_T} \times (\text{Max}_N - \text{Min}_N) \quad (1)$$

where  $N_i$  is the normalized value.

Further, the preprocessed dataset is categorized as training data and testing data. The training split is the sample of the dataset on which the model gets trained or learns the patterns to determine how is the feature matrix influencing the target matrix. Testing split is used to test how accurately a model has learnt the patterns and to assess model performance for an unseen sample. Hence, the testing dataset is never mixed with training dataset. Since the model needs large set of examples to get trained, so in this paper 80% of dataset is reserved for training and 20% for testing, which makes 92,951 records for training and rest 23,218 records for testing.

### 3 Algorithms Used in Forecasting

This section introduces the architecture of vanilla recurrent neural network and the fundamental LSTM unit.

#### 3.1 Basic Recurrent Neural Network

RNNs are artificial neural networks, where data goes in loops from one layer to another with the goal that the condition of the model is affected by its past states. When feed-forward neural networks can be considered as stateless, recurrent neural network is a speculation of feedforward neural network that has memory permitting the model to store data about its past calculations. Due to its dynamic temporal behavior, RNNs are found good in applications such as language modeling, speech recognition, and in reinforcement learning. The advantage of using the feedback is to improve the learning capacity to give better outcomes. In a recurrent neural network, the decision made by the recurrent network at some time stride denoted by  $t$  will be influenced by the choice made at the time stride denoted by  $t-1$ . Hence, the RNN unit will have two input values, the present time step input  $x_t$  and the preceding hidden state which is depicted by ' $h_{t-1}$ ', (output from the past state). This can be represented mathematically by Eq. 2.

$$h_t = f(W \times x_t + U \times h_{t-1}) \quad (2)$$

where  $f(\cdot) =$  activation function.

#### 3.2 Long Short-Term Memory Network

RNN can be difficult to model if it is required to hold information for a longer time due to the vanishing and exploding gradient which is a problem; hence, as a solution to this

problem, LSTM network is used [15]. Long short-term memory (LSTM) networks are a special case of RNN that have been found to have the ability to get familiar with the long-term dependencies [16]. The structure of LSTM network comprises special units or gates which control as to when an information should enter the memory, when the information be returned, and when it is to be forgotten. Firstly, the forget gate informs which information is to be considered and which is to be discarded using current input value depicted by  $X(t)$  and prior hidden state depicted by  $h(t - 1)$  and the sigmoid function, which gives values which are within 0 and 1 signifying absolutely keep it and absolutely forget it, respectively. The same is represented mathematically by Eq. 3.

$$f_t = \sigma(W_f \times (h_{t-1}, x_t) + b_f) \quad (3)$$

where  $\sigma(\cdot)$  = sigmoid function.

Then, the current state  $X(t)$  and past state  $h(t-1)$  are delivered to the second sigmoid function resulting a value of 0 and 1. A vector ( $C'(t)$ ) with values within  $-1$  and  $1$  is created when the information from the previous stage is passed via the function 'tanh'. The activation function gives the output values which are to be point-by-point multiplied. Multiplication of the preceding cell state  $C(t-1)$  is done with forget vector  $f(t)$ , and in case of 0, the values get dropped in the cell state. Next, a new cell state  $C(t)$  is updated after point-to-point addition. Finally, the output gate decides the value of the next hidden state. The same is presented through Eqs. 4–8:

$$i_t = \sigma(W_i \times (h_{t-1}, x_t) + b_i) \quad (4)$$

$$C'_t = \tanh(W_c \times (h_{t-1}, x_t) + b_c) \quad (5)$$

$$C_t = f_t \times C_{t-1} + i_t \times C'_t \quad (6)$$

$$O_t = \sigma(W_o \times (h_{t-1}, x_t) + b_o) \quad (7)$$

$$C'_t = \tanh(W_c \times (h_{t-1}, x_t) + b_c) \quad (8)$$

The success of the neural networks in varied challenging prediction problems is credited to their depth, such as layering LSTM hidden layers increases the depth of the model and all the more accurately depicting a deep learning technique [17]. Hence in this paper, use of multiple layers both in RNN and LSTM models has been done in order to gauge the changes occurring on the accuracy of predictions.

## 4 Simulation

Predictive analysis and modeling were done in Jupyter Notebook using Python and its Keras module. For each model, the sequence length/look back value used was 20; hence, previous 20 records were used to predict the 21st data value.

For the RNN model, three layers of simple RNN networks were used on top of each other, where each layer had 40 hidden nodes. The activation function used was ‘tanh’. After each RNN layer, dropout layer was added to avoid overfitting.

For the LSTM Model 1, three layers of LSTM network were used with each layer comprising 40 hidden nodes and ‘tanh’ as the activation function. The dropout layer with rate as 0.15.

The LSTM model 2 was hyper tuned by increasing the hidden units in the first LSTM layer to 60 hidden nodes, while the remaining two layers maintained 40 hidden units. The activation function used in this model was ‘tanh’, and the three dropout layers after each LSTM layer had 0.15 as rate depicting the fraction of input units to drop.

## 5 Results and Discussion

Mean squared error (MSE) is the loss, and we are trying to reduce it at each epoch while training. Ten epochs were used to train each model for obtaining decreased loss with every epoch. (Tables 1, 2 and 3).

**Table 1** Training pattern for RNN model

EPOCH	LOSS (MSE)
1/10	0.2358
2/10	0.0485
3/10	0.0201
4/10	0.0123
5/10	0.0091
6/10	0.0071
7/10	0.0059
8/10	0.0050
9/10	0.0044
10/10	0.0039

As observed from the above tables, LSTM model 2 has tried to obtain the minimum loss of 0.0018. Models are fit after training, and their performance can be assessed graphically from Figs. 1, 2 and 3, which plot the two-week predictions and from Figs. 4 and 5 which show single day hourly forecasts for each LSTM models.

In order to evaluate the models’ performance, R2 score along with RMSE and MAPE were calculated for all the three algorithms for a comparative investigation. The R2 score was obtained using Eqs. 9, 10 and 11, RMSE was calculated using Eq. 12, and the MAPE was calculated using 13.

$$R2SCORE = 1 - \frac{SSE}{SST} \quad (9)$$



**Table 2** Training pattern for LSTM model 1

EPOCH	LOSS (MSE)
1/10	0.0502
2/10	0.0121
3/10	0.0105
4/10	0.0055
5/10	0.0042
6/10	0.0071
7/10	0.0033
8/10	0.0023
9/10	0.0021
10/10	0.0019

$$SSE = \sum (T_i - F_i)^2 \quad (10)$$

$$SST = \sum (T_i - \bar{F})^2 \quad (11)$$

$$RMSE = \sqrt{\frac{\sum_{i=1}^N (F_i - T_i)^2}{N}} \quad (12)$$

$$MAPE = \frac{1}{N} \sum_{i=1}^N \left| \frac{T_i - F_i}{T_i} \right| \quad (13)$$

**Table 3** Training pattern for LSTM model 2

EPOCH	LOSS (MSE)
1/10	0.0546
2/10	0.0123
3/10	0.0114
4/10	0.0090
5/10	0.0048
6/10	0.0039
7/10	0.0031
8/10	0.0023
9/10	0.0021
10/10	0.0018

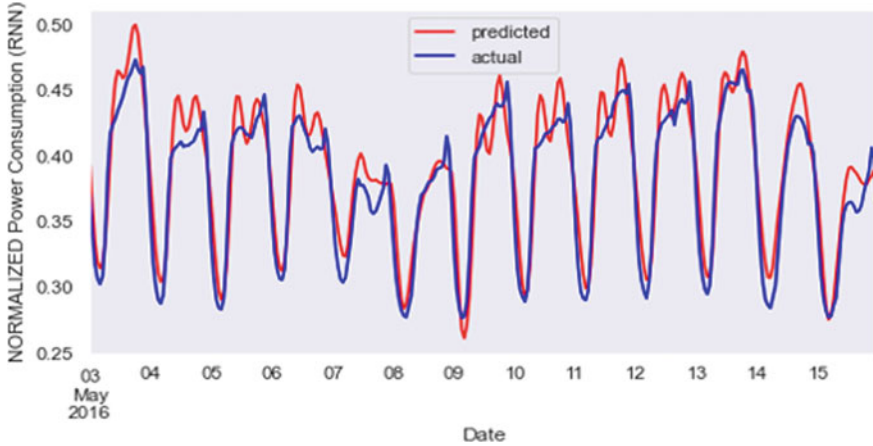


Fig. 1 Two weeks of prediction for simple RNN model

where  $F_i$  signifies the forecasted value,  $T_i$  depicts the actual value for the  $i$ th instance,  $\bar{F}$  depicts the mean of the forecasted values, and  $N$  depicts the total number of instances (Table 4).

As evident from the above metrics, the hyper tuned LSTM model, i.e., the LSTM model 2, where we increased number of hidden nodes, performed well as compared to the LSTM model 1 and the layered RNN model, as the R2 score for LSTM model 2 is closest to 1. The RMSE and MAPE values of LSTM model 2 were also impressive in comparison with the other two. Also, the LSTM model 1 did not show much improvement than the layered simple RNN model as can be seen from the evaluation metrics. This can be also be visualized by the plots below.

As observed from the plots above, for the LSTM model 2 (Fig. 8), a more number of error values lie between 0 and 0.07; hence, the mean error is significantly decreased

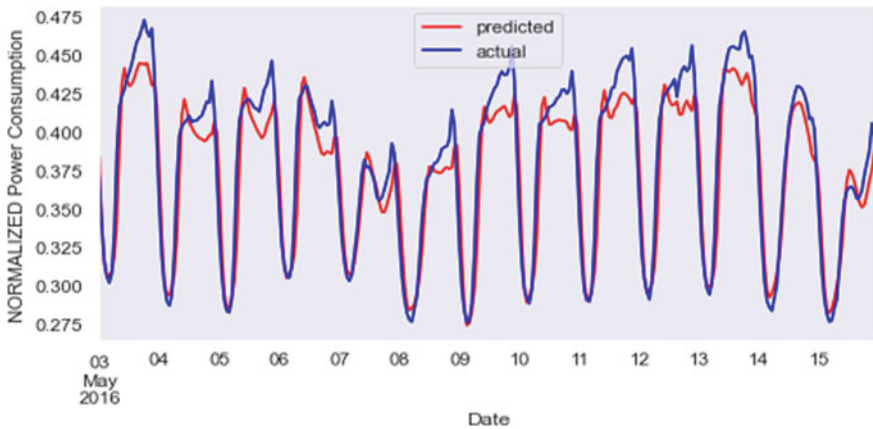
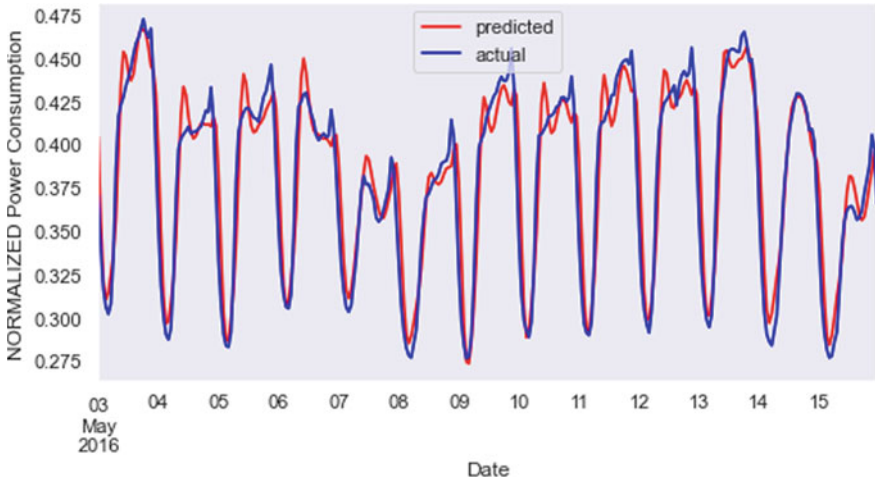


Fig. 2 Two weeks of prediction for LSTM model 1



**Fig. 3** Two weeks of prediction for LSTM model 2

as compared to first two models where a more number of relative error values lie within 0.02 and 0.08, leading to a greater mean value of relative error (Figs. 6 and 7).

## 6 Inference

The proposed paper sets the objective to investigate the effectiveness of deep learning algorithms, namely layered RNN and stacked LSTM network, for short-term electricity demand forecasting and shows a comparative investigation. It was observed that by incrementing the number of hidden nodes of the first layer of stacked LSTM model, R2 score improved to 0.973, and RMSE improved to 0.019.

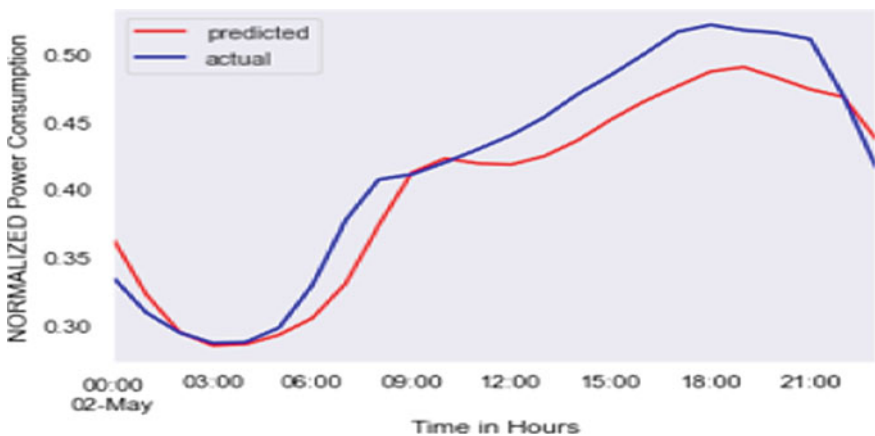


**Fig. 4** Single day hourly forecast by LSTM model 1

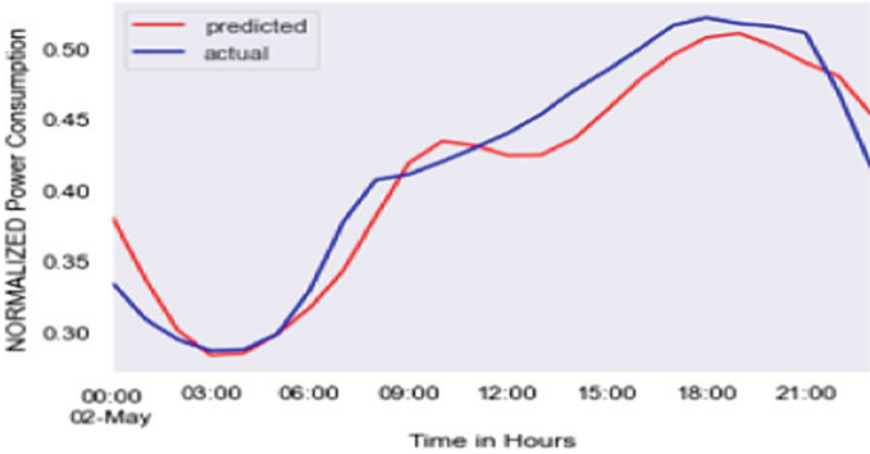


**Fig. 5** Single day hourly forecast by LSTM model 2

**Table 4** Evaluation metrics for the applied algorithms

Models	R2 score	RMSE	MAPE (%)
RNN model	0.959	0.02446	4.249
LSTM model 1	0.953	0.02614	4.05
LSTM model 2	0.973	0.01996	3.29

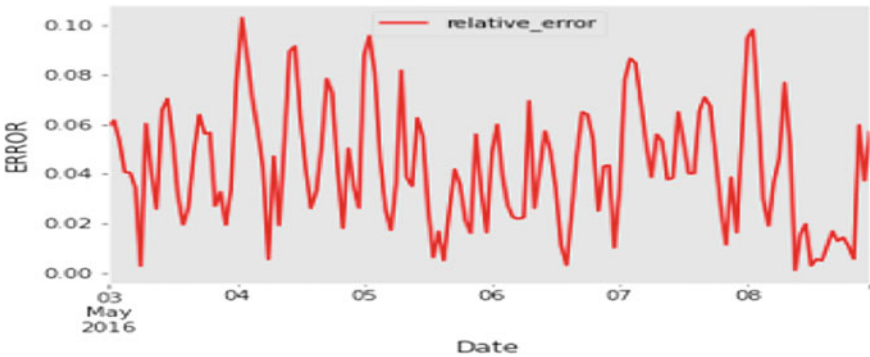


**Fig. 6** Plot of relative error for RNN model predictions

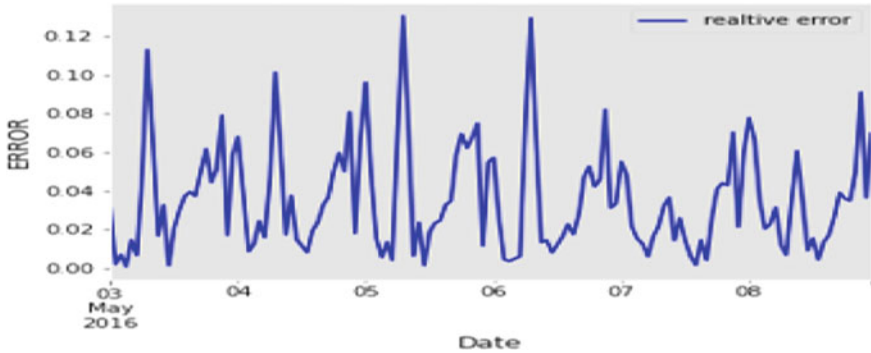


Fig. 7 Plot of relative error for LSTM model 1 predictions

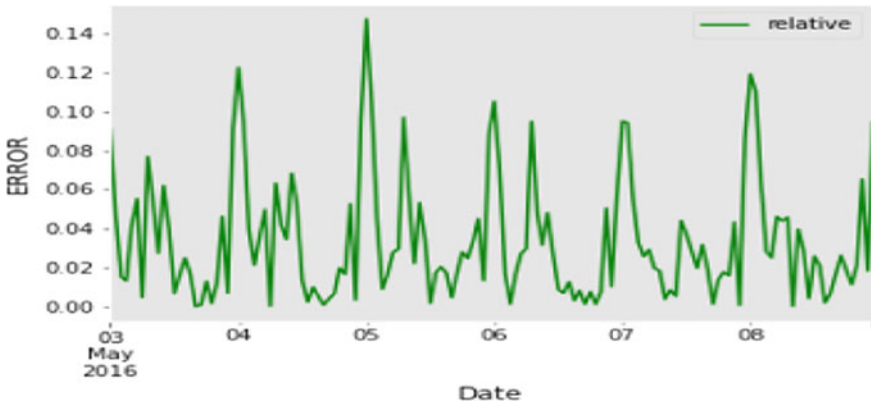


Fig. 8 Plot of relative error for LSTM model 2 predictions

It was evident from the results that no significant improvement in accuracy was observed in simple stacked LSTM model, i.e., LSTM model 1 as compared to the layered RNN model.

Hence, LSTM model being an improved variant of RNN can handle long-term dependencies and is expected to perform well. But if in some cases it does not happen, then increasing the number for hidden nodes in a stacked LSTM model can lead to an accurate prediction.

## References

1. Zhou K et al “A review of electric load classification in smart grid environment”. *Renew Sustain Energy Rev* 201 24:103–110
2. Hammad et al (2020) Methods and models for electric load forecasting: a comprehensive review. *Logistics Sustain Transport* 11:51–76
3. González-Briones et al (2019) “Machine learning models for electricity consumption forecasting: a review”. In 2nd international conference on computer app and IS, Saudi Arabia, pp 1–6

4. Tzafestas S, Tzafestas E (2001) Computational intelligence techniques for short term electric load forecasting. *J Intell Robot Syst* 31:7–68
5. Rahman S, Hazim O (1993) A generalized knowledge based short term load forecasting technique. *IEEE Trans Power Syst* 8(2):508–514
6. Srivastava AK (2020) “Short term load forecasting using regression trees, random forest, bagging and MSP”. *Int J Adv Trends Comput Sci Engg*, pp 1898–1902
7. Parlos G et al (1996) Development of an intelligent long term electric load forecasting system. *Proceedings of international conference on intelligent system application to power systems, USA*, pp 288–292
8. Zakarya S, Abbas H, Belal M (2017) “Long-term deep learning load forecasting based on social and economic factors in the Kuwait region”. *J Theor Appl Inf Tech*, pp 1524–1535
9. Luthuli QW, Folly KA (2016) “Short term load forecasting using artificial intelligence”. *IEEE PES power Africa, Zambia*, pp 129–133
10. Dahl M et al (2018) Improving short term heat load forecasts with calendar and holiday data. *Energies* 11:1678–1682
11. Quilumba F et al (2015) Using smart meter data to improve the accuracy of intraday load forecasting considering customer behaviour similarities. *IEEE Trans Smart Grid* 6:911–918
12. Weicong K et al (2018) Short term residential load forecasting based on LSTM recurrent neural network. *IEEE Trans Smart Grid* 33:1087–1088
13. Lee KY, Cha YT, Park JH (1992) Short term load forecasting using an artificial neural network. *IEEE Trans Power syst* 7(1):124–132
14. Jayalakshmi T, Santhakumaran A (2011) Statistical normalization and back propagation for classification. *Int J Comput Theory Eng* 3(1):1793–1801
15. Hochreiter S, Schmidhuber J (1997) Long short-term memory. *Neural Comp* 9(8):1735–1780
16. Bengio Y, Simard P, Frasconi P (1994) Learning long term dependencies with gradient descent is difficult. *IEEE Trans Neural Netw* 5(2):157–166
17. Hermans M, Schrauwen B (2013) “Advances in neural information processing systems”. Curran Associates Inc., vol 26, NIPS



# CFD Analysis to Enhance the Heat Transfer Coefficient in Micro-Channels

Sauraj Kumar Sharma, Shrikant Vidya<sup>(✉)</sup>, and K. S. Srikanth

Department of Mechanical Engineering, Galgotias University, Greater Noida Uttar Pradesh,,  
India

skvrsm@gmail.com

## 1 Introduction

Many domestic and industrial applications use heat transfer devices for recovery and conversion of heat. Since last five decades, the efforts for increase in heat transfer rate and cost and material saving are being attempted. Enrichment in heat transfer is referred to the process of improvement in heat deposition or removal from a surface. The techniques used to enhance the heat transfer can be as simple as the changes in fluid velocity in the channel or as complicated as the new geometries or inserts in the geometries. The enrichment in the heat transfer rate is of great interest due to its applications. The thermal power plants, boiling, condensation, sensible heating or cooling of milk, solar collector, cooling of electronics devices and machines use heat transfer techniques and improve performance. Improvement in effectiveness, low cost, simple installation, and reliability is heat transfer techniques that result in cost, material, and energy saving.

The techniques used to advance the heat transfer must improve the heat transfer coefficient and reduce the heat transfer zone in a new strategy for the same output. These techniques reduce the thermal resistance. The thermal resistance is reduced by creating turbulence or enlarging the heat transfer surface area. These enhancement techniques are classified into two categories, i.e., active and passive [1]. In the active category, external power, fluid movement, vibrations are involved that may result in higher cost. In the passive category, modifications in heat transfer surface are involved. The passive category's key feature is to reduce the boundary layer next to the surface. The boundary layer is the primary confrontation to heat transfer. The performance of the enhancement techniques is analyzed by the thermal performance factor (TPF). TPF is a ratio of the variation in the heat transfer rate to variation in friction factor. The channels are classified into three categories according to their hydraulic diameters, i.e., conventional, mini and micro-channel. Many researchers have provided the different range for this classification. Kandlikar et al. [2] differentiated this as conventional channel  $> 3$  mm, mini (3 mm - 200  $\mu$ m) and micro-channel ( $< 200$   $\mu$ m). G L Morini [3] suggested that channels having characteristics dimensions between 1 mm and 1  $\mu$ m are micro-channels. Fan et al. [4] suggested the micro-channels as 1–100  $\mu$ m. Khan et al. [5] suggested that the channels of the hydraulic diameter less than 1 mm are micro-channels. The latter classification is used for analysis in this paper. Heat transfer through mini and micro-channels is used in many applications as cooling of electronics equipment, compact heat exchangers, etc.

Tuckerman and Pease [6] used micro-channel for heat transfer to solve the high heat flux problem in the electronics industry in 1981. Today, micro-channel heat transfer has been well studied and established. Compactness is a significant consideration in numerous applications where space is a constraint. The enrichment in heat transfer through single-phase flow is being used in many applications and also being researched for better effectiveness. The heat transfer through conventional tube needs to be evaluated and verified to use that technique in mini and micro-channels. The researchers are trying to get the same output using single-phase flow in micro-channels to compete with the results of two-phase flow. The main objective of most of the analysis is to optimize the dimensions and boost the heat transfer rate. The overall thermal resistance is minimized to enhance the heat transfer rate. CFD analysis is done to get the accurate description of changes in the geometry or fluid in micro-channel. Wesberg et al. [7] analyzed the micro-channels for fully developed flow numerically for two-dimensional model. Fedorov and Viskanta [8] analyzed the micro-channels for fully developed flow numerically for three-dimensional model.

## 2 Problem Statement and Geometrical Dimensions

The current numerical investigation has been performed in a three-dimensional rectangular micro-channel with the length  $L = 15$  mm, height  $h = 1.1$  mm, and width  $w = 3.7$  mm. In this rectangular micro-channel, ribs are introduced to enhance heat transfer as shown in Fig. 1. Based on the dimensions of ribs, five sets of micro-channel have been designed for comparison as shown in Fig. 2. In all the micro-channel, ribs are starting after 2 mm from the inlet (rib length = 13 mm). Height of ribs in each configuration is same (rib height = 1 mm). Only, the width and number of ribs are varied in different configurations. Wall thickness of micro-channel is 0.1 mm. The study is performed for water as cooling fluid and copper as micro-channel material. As the micro-channels are used to extract heat from the heated surface, so a continual heat flux boundary condition is applied at bottommost wall of micro-channel. The study is performed for heat flux variation of 100–500 kW/m<sup>2</sup>. The inlet temperature of cooling fluid is  $T_{in} = 19.3$  °C. The mass flow rate is taken as  $Q = 8.26$  cc/sec. The micro-channel sizes and values of  $Q$  and  $qw''$  are selected on the base of the extreme temperature of the water in the computational province. The maximum temperature of the water in the computational province would not surpass 373 K, so that the fluid remains in single phase only. The influence of variations of the fluid properties on fluid friction is examined for a better empathetic of frictional micro-flow features.

## 3 Governing Equation

The water in the micro-channel has been considered to remain in liquid form (single phase) throughout the micro-channel. First heat is transferred through conduction in copper (solid) section then through convective heat transfer in water. To simulate solid–liquid interface, conjugate technique is executed. The steady-state simulation has been accomplished for single-phase flow in commercially available software Ansys Fluent. Numerical simulations have been performed assuming these assumptions:



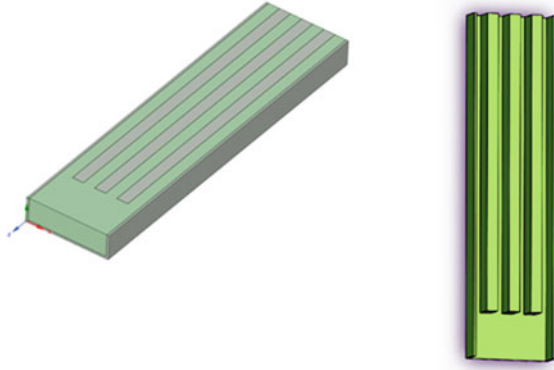


**Fig. 1** Computational domain

- (1) Steady and laminar flow.
- (2) Incompressible fluid.
- (3) Copper substrate holds constant thermal conductivity.
- (4) Outer walls are insulated.

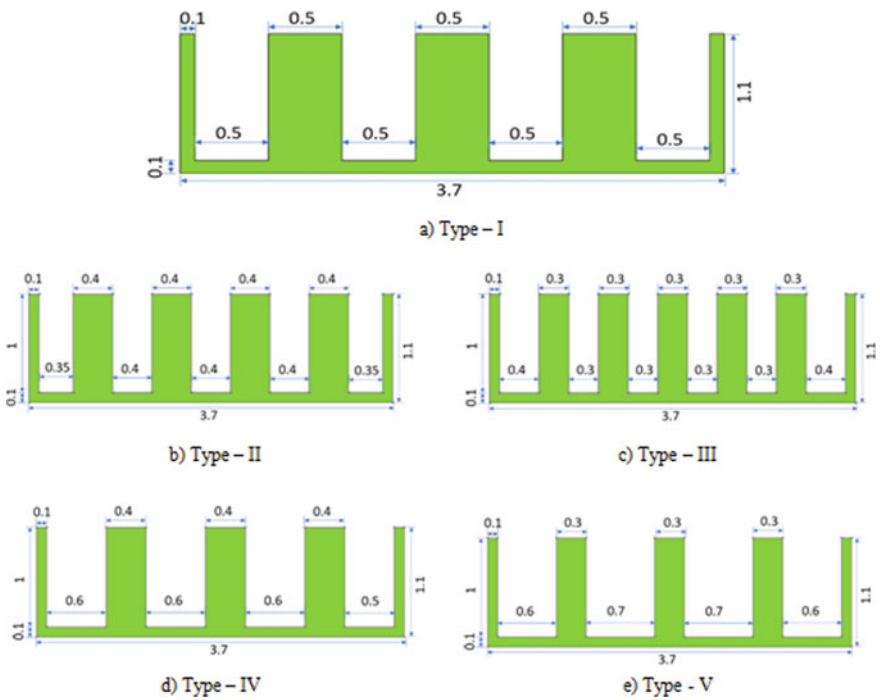


**Fig. 2** Configurations of micro-channel

The governing conservation equations (mass, momentum, and energy) are used by the software using finite volume method (FVM) for solid and liquid section.

Continuity equation

$$\frac{\partial(\rho u_j)}{\partial x_j} = 0$$

Momentum equation

$$\frac{\partial(\rho u_i u_j)}{\partial x_j} + \frac{\partial \rho}{\partial x_j} = \frac{\partial}{\partial x_j} \left[ u \left( \frac{\partial u_i}{\partial x_j} + \frac{\partial u_i}{\partial x_i} \right) \right] + \frac{\partial}{\partial x_j} \left[ u_t \left( \frac{\partial u_i}{\partial x_j} + \frac{\partial u_i}{\partial x_i} \right) \right]$$

Energy equation

$$\frac{\partial(\rho u_i T)}{\partial x_j} - \frac{\partial}{\partial x_j} \left[ (\Gamma + \Gamma_t) \frac{\partial T}{\partial x_j} \right] = 0$$

where

$\Gamma_t = \mu_t/Pr$  is the turbulent thermal diffusivity,  $\Gamma = \mu/Pr$  is the molecular thermal diffusivity,  $\mu$  and  $\mu_t$  is the viscosity ( $\text{Ns/m}^2$ ) and thermal viscosity, respectively,  $Pr$  is the Prandtl number  $\rho$  is the density,  $P$  is the pressure (Pa),  $u$  is the velocity (m/s), and  $T$  is the temperature (K).

Two significant properties of water, i.e., viscosity and density are varied with respect to temperature to confirm more exact outcomes. Both properties have been varied as per the following quadratic equations:

$$\begin{aligned} \rho_t &= 758.1214 + 1.8761T - 3.604 * 10^{-3}T^2 \\ u_t &= 0.02143 - 1.195 * 10^{-4}T + 1.699 * 10^{-7}T^2 \end{aligned}$$

## 4 Boundary Conditions and the Methodology

Constant heat flux boundary condition is functioned at the bottommost wall for heat input. All the remaining walls have adiabatic boundary condition; no heat transfer will take place from these walls. At inlet of the micro-channel velocity, inlet boundary condition is applied with uniform velocity = 0.129 m/s and inlet temperature = 303.15 K. At outlet of the micro-channel pressure outlet boundary condition is applied. As the flow in the micro-channel is laminar, laminar viscous model is used. At the walls of the micro-channel, no-slip condition was implemented. Momentum and energy equations have been discretized using second-order upwind scheme. SIMPLEC algorithm is applied to resolve the couple pressure-velocity coupling heat conduction and convection. To perform numerical analysis, the computational domain has to be discretized. In discretization, the computational body is divided into smaller elements called cells. The software will then solve the governing equations for each and every cell. Classically, the lesser the mesh size, the more exact the solution, as the geometries are well sampled

across the physical provinces. The trade-off is that the greater the accuracy, the higher the simulations develop and thus solving times are increased. So, to find the optimum mesh grid, independence is performed. The final mesh of the computational domain consists of non-uniform tetrahedral and hexahedral cells.

## 5 Results and Discussion

To validate our numerical setup, outcomes are compared with the results of Prajapati [9]. Graph is plotted between lower wall temperature and heat flux given as input as shown in Fig. 3.

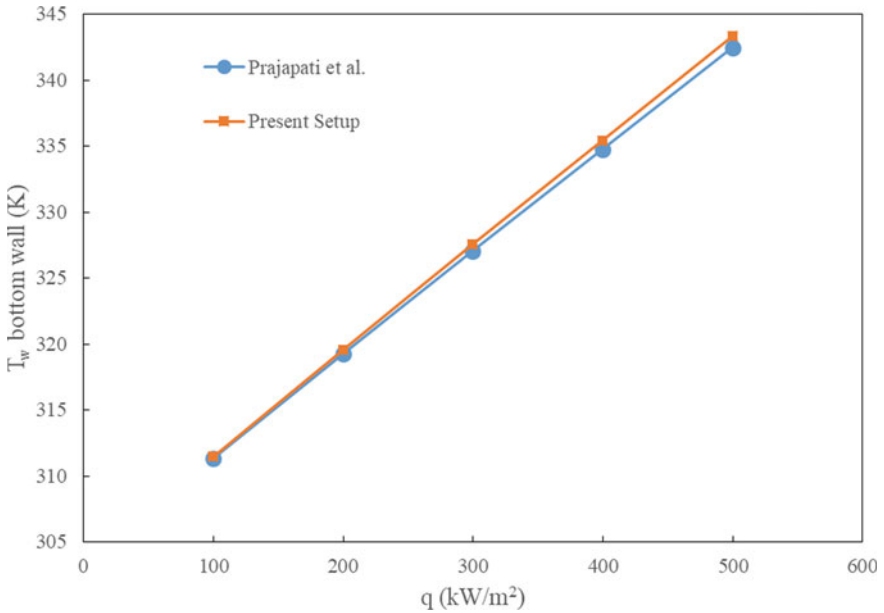


**Fig. 3** Validation graph

It is clear from the graph that the results of current numerical setup are very close to the results of Prajapati [9]. Numerical simulations have been carried out for Reynolds number 200 with varying heat flux at bottom wall from 100 kW/m<sup>2</sup> to 500 kW/m<sup>2</sup> for all five configurations. Figure 4 displays the graph of bottom wall temperature ( $T_w$ ) versus heat flux ( $q$ ) at the bottom wall for all five type of configuration of micro-channel.  $T_w$  is the area-weighted average temperature of the bottommost wall. For all the configuration of micro-channel, the bottom wall temperature is increased linearly with the increase in the heat flux. It is obvious that the bottom wall temperature will increase with the increase in heat input. The slope for type—III is minimum because this configuration has the capacity to dissolve extra heat at higher heat fluxes and able to control the increasing rate of bottommost wall temperature. The opposite is true for type—V that is why it has maximum slope. The bottom wall temperature for type—III is minimum because it has

maximum contact surface area with the fluid. From the graph, it is concluded that by increasing the number of fins, heat extraction can be increased and by decreasing width of fin by keeping number of fins constant heat extraction is reduced. Graph of outlet fluid temperature versus heat flux at bottom wall is shown in Fig. 5. The configuration which is extracting less heat from the bottom wall will allow the rise of temperature of the bottom wall which in turn also increase the fluid outlet temperature. The temperature for type—I, IV, and V is quite same and more than the type—II and type—III at all heat flux.

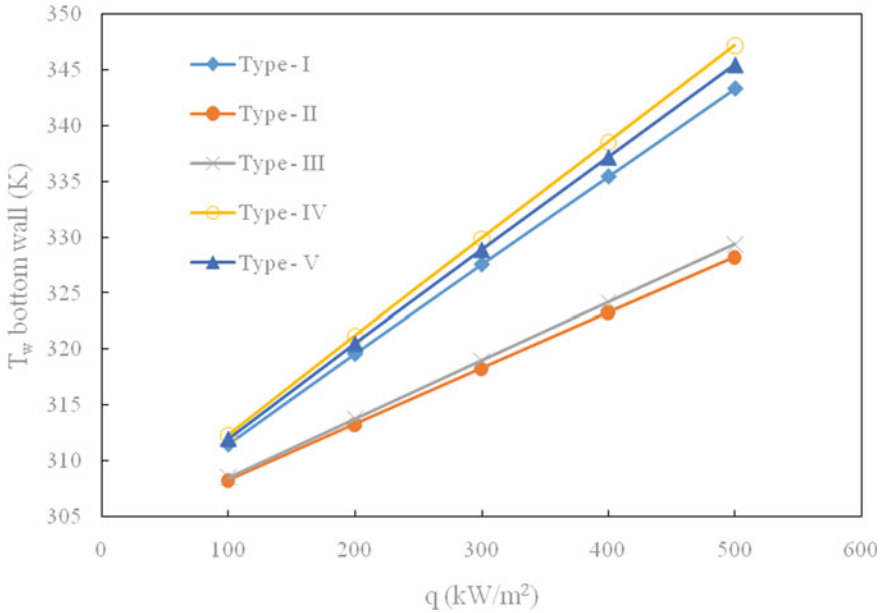


**Fig. 4** Graph of bottom wall temperature versus heat flux for five types of micro-channel

Graph of pressure drop versus heat flux at bottom wall is shown in Fig. 6 for all configuration. A similar trend is shown in all configurations; pressure drop is decreasing with the increasing heat flux. Pressure drop is maximum for type—III because the number of fins is more, and more fins mean more restrictions to the flow. In type—III, the contact surface area is also more, so more friction losses. In type—V, there is minimum restriction to the flow, so there is less pressure drop. Figure 7 demonstrates the contour of temperature of bottom wall for all configurations at Reynolds number 200 and heat flux  $500 \text{ kW/m}^2$ . It can be seen from the contour that at inlet region of plate the temperature is slightly higher than the region of plate where fins are starting. This is because fins are conducting heat from bottom plate more rapidly than fluid extracting heat by convection. In the outlet region, temperature is maximum because till this region water also get heated up and unable to extract heat.

Figure 8 shows the contour of pressure at a plane placed at a height  $0.5 \text{ mm}$  at Reynolds number 200 and heat flux  $500 \text{ kW/m}^2$ . The flow path of water is in upward

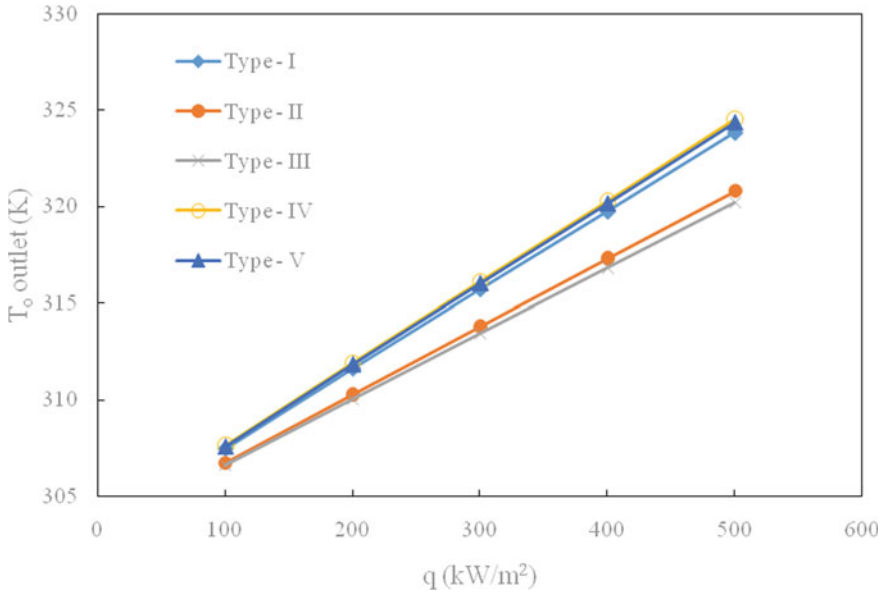


**Fig. 5** Graph of outlet temperature versus heat flux for five types of micro-channel

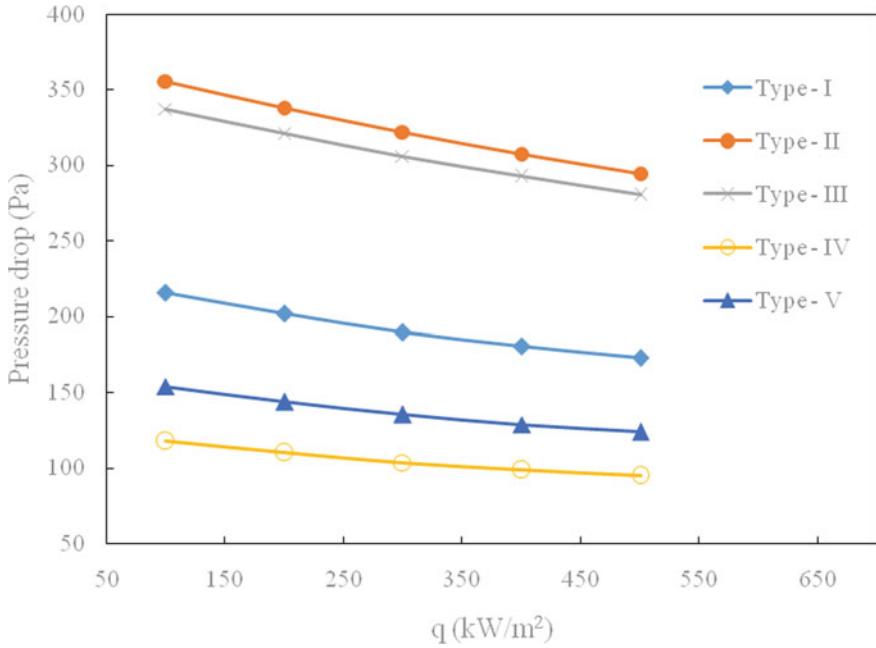


**Fig. 6** Graph of pressure drop versus heat flux for five types of micro-channel

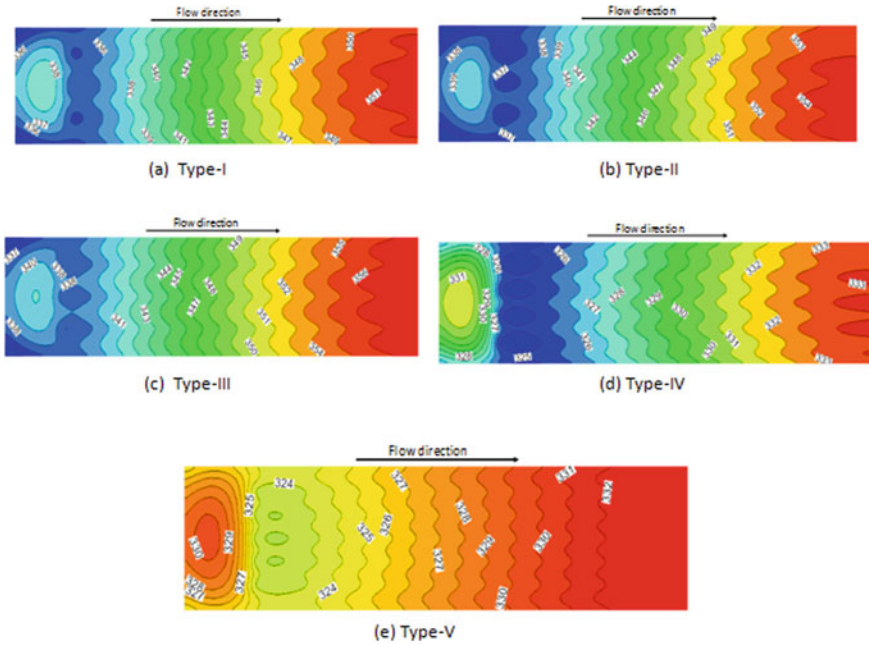


Fig. 7 Temperature of bottom wall of micro-channel

direction. All pressure contours are showing similar trends with only the variation in the magnitude of pressure. All pressure contours are showing abrupt drop in pressure at a distance of 2 mm from the inlet because the water at that place is incoming in the conduits which is fairly confined as related to inlet section.

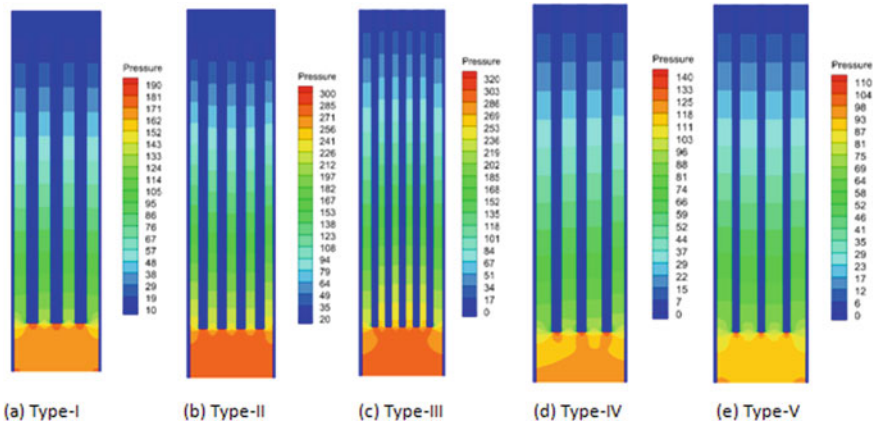


Fig. 8 Pressure contours

## 6 Conclusion

In the current work, the thermal performance of five configuration of micro-channel with fins is investigated numerically. The simulation has been carried out in 3D computational geometry by solving RANS equation. Following conclusions are drawn from the present work:

- By increasing the number of fins increases the heat extraction from the sink and by keeping the number of fins constant and reducing the width decreases the heat extraction.
- Pressure drop is increased if the number of fins is increased, and pressure drop is decreased if the width of fin is reduced by keeping the number of fins constant.

## References

1. Steinke ME, Kandlikar SG (2004) "Single-phase heat transfer enhancement techniques in microchannel and minichannel flows." In Proceedings second international conference. Microchannels Minichannels, pp 141–148. <https://doi.org/10.1115/icmm2004-2328>
2. Kandlikar SG, Grande WJ (2003) Evolution of microchannel flow passages-thermohydraulic performance and fabrication technology. *Heat Transf Eng* 24(1):3–17. <https://doi.org/10.1080/01457630304040>
3. Morini GL (2004) Single-phase convective heat transfer in microchannels: a review of experimental results. *Int J Therm Sci* 43(7):631–651. <https://doi.org/10.1016/j.ijthermalsci.2004.01.003>
4. Fan Y, Luo L (2008) Recent applications of advances in microchannel heat exchangers and multi-scale design optimization. *Heat Transf Eng* 29(5):461–474. <https://doi.org/10.1080/01457630701850968>
5. Khan MG, Fartaj A (2011) "A review on microchannel heat exchangers and potential applications." *Int J Energy Res* 35(7):553–582, Wiley. <https://doi.org/10.1002/er.1720>
6. Tuckerman DB, Pease RFW (1981) "High-performance heat sinking for VLSI." *IEEE Electron Device Lett* 2(5):126–129. <https://doi.org/10.1109/EDL.1981.25367>.
7. Weisberg A, Bau HH, Zemel JN (1992) Analysis of microchannels for integrated cooling. *Int J Heat Mass Transf* 35(10):2465–2474. [https://doi.org/10.1016/0017-9310\(92\)90089-B](https://doi.org/10.1016/0017-9310(92)90089-B)
8. Fedorov AG, Viskanta R (2000) Three-dimensional conjugate heat transfer in the microchannel heat sink for electronic packaging. *Int J Heat Mass Transf* 43(3):399–415. [https://doi.org/10.1016/S0017-9310\(99\)00151-9](https://doi.org/10.1016/S0017-9310(99)00151-9)
9. Prajapati YK (2019) Influence of fin height on heat transfer and fluid flow characteristics of rectangular microchannel heat sink. *Int J Heat Mass Transf* 137:1041–1052. <https://doi.org/10.1016/j.ijheatmasstransfer.2019.04.012>
10. Wang L, Chen Y, Wang C, Wang Q (2011) Fatigue life analysis of aluminum wheels by simulation of rotary fatigue test. *Strojniški Vestnik—J Mech Eng* 57(1):31–39.
11. Schijve J (2001) Fatigue as a phenomenon in the material. In: Schijve J. (eds) *Fatigue of structures and materials*. Springer, Dordrecht. ISBN: 978-0-306-48396-7, pp 7–44



# Optimization of Design Parameters for a Quadcopter Using Taguchi Design Methodology

Siddharth Sharma, Pratham Khurana<sup>✉</sup>, Manan Sharma, and Aditya Kumar

Netaji Subhas University of Technology, Dwarka Sector-3, Dwarka, Delhi 110078, India  
prathamkhurana57@gmail.com

## 1 Introduction

Robust design methodology was proposed by Genichi Taguchi in order to achieve significant quality improvement in products and processes [1]. Various quality engineering concepts including quality loss function, orthogonal arrays, and signal-to-noise ratios laid the foundation for the current formulation and employment of this methodology in various industrial processes across a diverse range of industries [2]. Collectively known as Taguchi's design of experiments (DOE), this concept is used for various optimization problems to obtain an optimal design which is inherently robust [3]. Owing to its wide applicability, Taguchi's methods have been implemented across industries for optimization of chemical processes [4], quality improvement of sustainable agricultural processes [5], optimization of parameters for manufacturing parts in foundry [6], optimizing the process parameters in stir casting [7], improving the surface roughness by optimizing the various machining parameters, [8] and process parameters in lathe facing operation [9]. It has also been used to study the interaction of different factors in submerged arc welding [10], for modeling and optimizing the process parameters for sustainable and eco-friendly machining of stainless steel [11] and even to analyze the service quality performance for improving customer satisfaction [12]. An integral component of Taguchi's optimization method is an orthogonal array, which is based on the mathematical concepts of factorial designs and difference sets [13]. Depending upon the number of control and noise factors, levels of each factor and number of experiments runs required, a suitable orthogonal array is chosen. For instance, one can choose an L9 orthogonal array to study four parameters being varied at three levels [14], whereas an L25 array can be used to analyze six factors with five levels each [15].

Commercial drones have experienced a considerable rise in their demands and hence their development [16]. According to McKinsey & Company, commercial drones have found their applications in entertainment and advertising, data management services, and especially for delivery services [17]. Even though drones in case of delivery services are still being used on a relatively smaller scale, this industry is expected to grow exponentially in the next few years [18]. Drones have also been used as post-disaster relief distribution vehicles [19]. Nowadays, quadrotors are easily accessible owing to their reduced costs and miniaturization, but robust design considerations for commercial



drones have been a major problem as it is a complicated procedure [20]. There are other design and manufacturing challenges when fabricating a drone, and therefore, various parameters should be considered in the design phase to overcome these [21]. Apart from this, calculation of the maximum take-off weight for a given drone is another critical problem [22]. A study has developed thrust and torque measurement apparatus for quadrotor drones [23], and some complex triphibian drones have also been conceptually designed [24]. Robust design methodology has been previously applied to a quadrotor drone which was focused on the structural parameters and used a Monte Carlo simulation [25]. Thrust is the main operational parameter of a drone that defines its flight characteristics and performance, and the minimum value of thrust for a drone should ideally be twice its weight [26]. Obtaining the maximum possible and optimal value for thrust will result in smooth, efficient, and reliable performance of the drone.

In this paper, Taguchi's method has been applied for quadrotor drone optimization by studying the effects of variation in its parameters simultaneously.

## 2 Research Methodology and Key Elements

Unmanned aerial vehicles or drones have been employed in a diverse range of industries owing to the availability of drones of various sizes and weights. In this paper, a quadrotor drone has been discussed. Even though the demand for drones has increased exponentially in the past few years, there are still several design challenges that scientists and engineers face till date when it comes to their fabrication. A number of trade-offs need to be taken care of to get best performance from our multi-rotor depending on the mission the drone is to be employed for. For instance, higher thrust is required for heavy lift drones, whereas more flight time is required for surveillance drones. Since this optimization of design and structural parameters is quite cumbersome, a well-structured approach should be implemented in the design phase so that the drone reaches its best efficiency.

Genichi Taguchi's method for optimization has been applied to serve the purpose. The Taguchi method is a statistical method to improve the quality of manufactured products by determining the 'cause and effect' relationship between design/operational factors and performance [4]. The entire Taguchi methodology is based on the concept that

*quality and robustness of a product should be controlled during the design stage. Emphasis should be placed on designing quality into products and processes instead of inspection of a product after it has been manufactured.* [3]

Apart from the design factors, some robust design experiments may even include signal and noise factors, as shown in Fig. 1.

The Taguchi method makes use of '**orthogonal arrays**' to conduct a '**design of experiments**.' Orthogonal arrays reduce the design problem into the best set of 'well-balanced (minimum)' experiments. An L25 orthogonal array has been used in our paper. We have selected L25 as our choice of orthogonal array since it was the most suitable array for our conditions and ensured the best possible interaction between the design parameters and the required response.

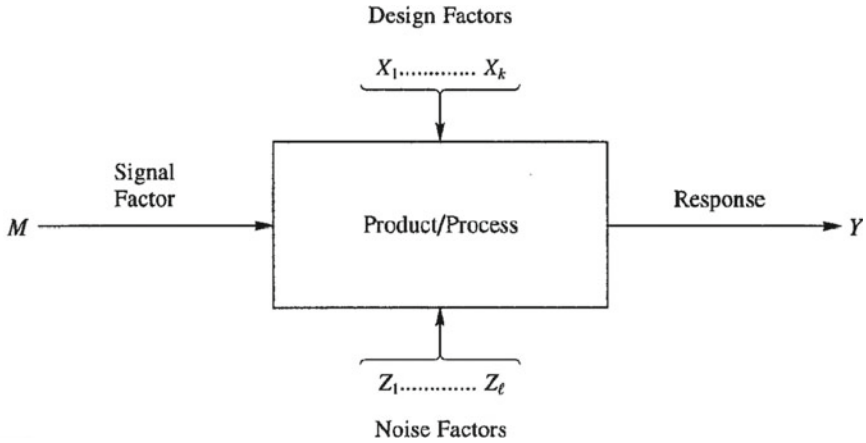


**Fig. 1** Interaction of design, signal, noise factors, and response in a process

Then, the optimal value for the design parameters is determined by calculating the ‘**signal-to-noise**’ ratio for each experiment in the orthogonal array. Signal-to-noise ratios (S/N) are log functions of the desired output that serve as the basic objective for optimization, and the optimality of each different solution can be checked with respect to the optimal ratio. S/N ratios are used to measure the quality and relative optimality of a solution, in a simple and additive manner [12].

There are three different types of S/N ratios. These are as follows:

1. Larger-the-better—This case is used when we have to maximize the optimal factors and reduce the effect of noise. It is represented as

$$N = -10 * \log_{10}[\text{mean of sum of squares of reciprocal of measured data}] \quad (1)$$

2. Smaller-the-better—This S/N ratio is chosen when we need to minimize undesirable characteristics and noise factors, the ideal value for which is zero.

$$N = -10 * \log_{10}[\text{mean of sum of squares of measured data}] \quad (2)$$

3. Nominal-the-best—This S/N ratio is used in a scenario where the optimal or the most desired output has a defined and specified value. The S/N ratio in this case is defined as

$$N = -10 * \log_{10}[(\text{square of mean})/\text{variance}] \quad (3)$$

Analysis of variance, or ANOVA, is then applied to evaluate the percentage contribution of each operational or design parameters on the desired output and assess the statistical significance of the design/operational factors and their effects in terms of p value (1). ANOVA compares the variance of a factor to the resulting variance of the output, and higher the variance of the output, higher is the effect the factor has on the output [8].

### 3 Case Study: Taguchi Optimization of a Quadrotor

Before applying the Taguchi method for optimization on our drone, it is crucial to first choose our objective function and to identify the factors which need to be analyzed to achieve the desired optimization. In our study, we have used a quadrotor drone or simply, a quadrotor. For this drone, the power can be given by the following equation derived by [27]:

$$\text{Power, } P = \text{Propeller Constant} * \text{rpm}^{\text{power factor}} \quad (4)$$

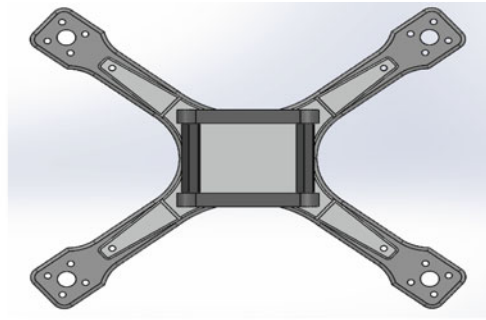
$$\text{Thrust} = \text{Power}/\text{Velocity} \quad (5)$$

Combining Eqs. (4) and (5),

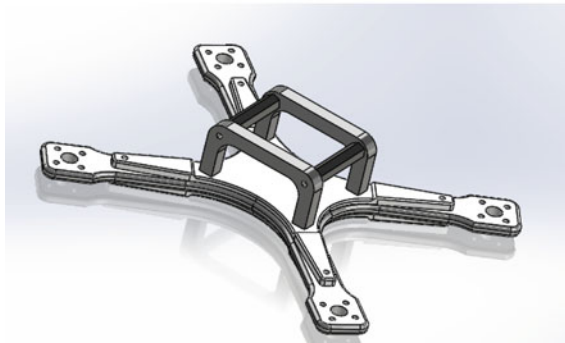
$$\text{Thrust} = \left( \text{Propeller Constant} * \text{rpm}^{\text{power factor}} \right) / \text{Velocity} \quad (6)$$

The propeller constant is the ratio of the pitch of the blade to the diameter length of a propeller of N blades. Further, power factor is defined as the ratio of operation power in kilowatts (kW) to apparent total power in kilovolt-amperes (kVA). For our study, we have taken the value of the power factor as 3.15, since this value returns the most significant result when analyzing its statistical plot [27]. Based on Eq. 6, our objective function is to maximize the thrust for our quadrotor drone and the necessary factors to be examined are pitch, diameter, RPM, and velocity (refer Appendix B.). The next step is to determine the number of levels of these factors so that the best interaction between our design parameters is ensured. The selection of an appropriate orthogonal array is also dependent on the number of factors and the number of levels of each of these. We have developed a CAD model for our quadrotor according to the dimensions specified in [28]. Based on the CAD model of our quadrotor, which is shown in Fig. 2, we have chosen five values for each of the four factors, while keeping in mind the dimensions of our drone and also considering the feasibility of these chosen values. Hence, for our four above-mentioned factors, we have considered five levels for each factor (Table 1). The values of RPM were taken in kilo-rev/min, i.e., 24 means 24,000 rev/min for RPM value. Further, we have chosen an L25 as the most appropriate orthogonal array to study the relationship between our factors and the responses. The L25 array has been shown in Table 2. This was generated using Minitab 19.

After generating the required L25 array, the same is to be analyzed. Using Minitab 19, we analyzed the array using Taguchi design of experiments. For signal-to-noise ratios, 'Larger-the-Better' was selected for the responses. The plots obtained from this experiment will give us the best combination of the factors in order to maximize our objective function, i.e., the thrust for our drone. We also used Minitab to examine the results obtained from ANOVA. The results from ANOVA depicted the most significant factors for the drone and percentage contribution of each of the factors in the resultant thrust.



(a) Top view of CAD model of the quadrotor



(b) Isometric view of CAD model of the quadrotor

**Fig. 2** **a** Top view of CAD model of the quadrotor and **b** isometric view of CAD model of the quadrotor

## 4 Result

### 4.1 Taguchi Analysis: Thrust Versus Velocity, Pitch, Diameter, and RPM

The delta statistic is given by the difference between the highest and the lowest average for each factor, and then, the ranks are assigned to these factors accordingly. From Table 3, it can be clearly seen that the parameter RPM is having the most significant effect on thrust because as compared to the other parameters and it has the highest max-min

**Table 1** Factor information

Factor	Type	Levels	Values
Velocity (m/s)	Fixed	5	12, 15, 18, 21, and 24
Pitch (mm)	Fixed	5	4, 5, 6, 7, and 8
Diameter (mm)	Fixed	5	81, 90, 100, 110, and 120
RPM (kilo-rev/min)	Fixed	5	20, 21, 24, 25, and 27

**Table 2** L25 orthogonal array

S. No.	Velocity	Pitch	Diameter	RPM	Thrust	S/N ratio
1	12	4	81	20	51.599	34.2528
2	12	5	90	21	67.692	36.6107
3	12	6	100	24	111.336	40.9327
4	12	7	110	25	134.287	42.5607
5	12	8	120	27	179.276	45.0705
6	15	4	90	24	65.977	36.3878
7	15	5	100	25	84.409	38.5278
8	15	6	110	27	117.345	41.3893
9	15	7	120	20	48.761	33.7614
10	15	8	81	21	96.273	39.6701
11	18	4	100	27	71.711	37.1117
12	18	5	110	20	31.663	30.0110
13	18	6	120	21	40.615	32.1738
14	18	7	81	24	106.907	40.5801
15	18	8	90	25	125.051	41.9417
16	21	4	110	21	25.319	28.0688
17	21	5	120	24	44.181	32.9047
18	21	6	81	25	89.322	39.0192
19	21	7	90	27	119.518	41.5486
20	21	8	100	20	47.766	33.5823
21	24	4	120	25	35.170	30.9236
22	24	5	81	27	82.998	38.3814
23	24	6	90	20	34.829	30.8388
24	24	7	100	21	42.646	32.5976
25	24	8	110	24	67.476	36.5830

value (8.21). It can also be seen from Fig. 4 that the maximum values of mean S/N ratio of velocity is at level 1 (12), pitch is at level 5 (8), diameter is at level 1 (81), and RPM is at level 5 (27). Hence, the optimal design parameters are velocity at 12 m/s, pitch at 8 mm, diameter at 81 mm, and RPM at 27,000 rpm. Using Equation 6, the value of thrust obtained at these levels of the design parameters is 265.59 N. We can also observe the main effect plot for means for all the parameters shown in Fig. 3 (Table 4).

**Table 3** Response table for signal-to-noise ratio (larger is better)

Level	Velocity	Pitch	Diameter	RPM
1	39.89	33.35	38.38	32.49
2	37.95	35.29	37.47	33.82
3	36.36	36.87	36.55	37.48
4	35.02	38.21	35.72	38.59
5	33.86	39.37	34.97	40.70
Delta	6.02	6.02	3.41	8.21
Rank	3	2	4	1

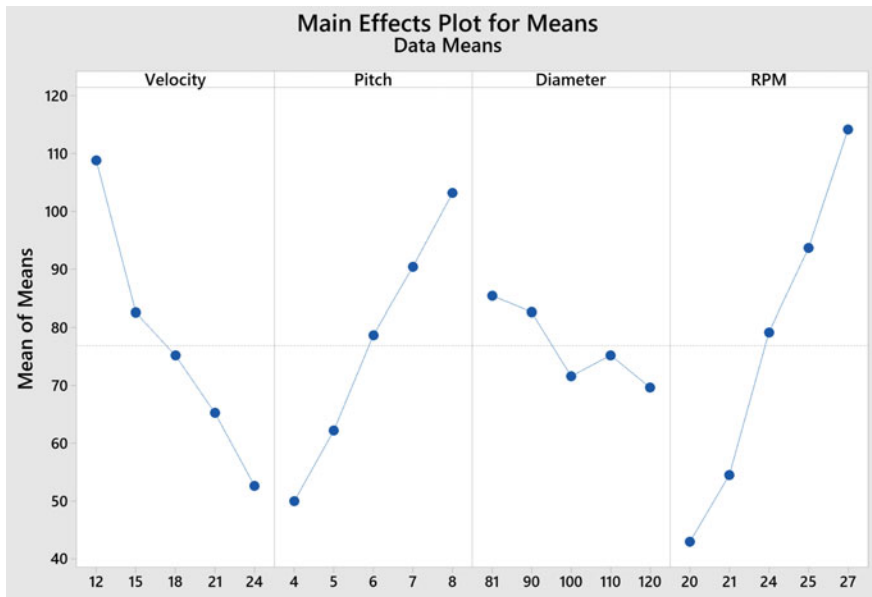


**Fig. 3** Main effects plot for means

We can see from Table 2 that the maximum S/N ratio is 45.07 for experiment 5 (refer Appendix A.). However, after the application of Taguchi design for optimization, we

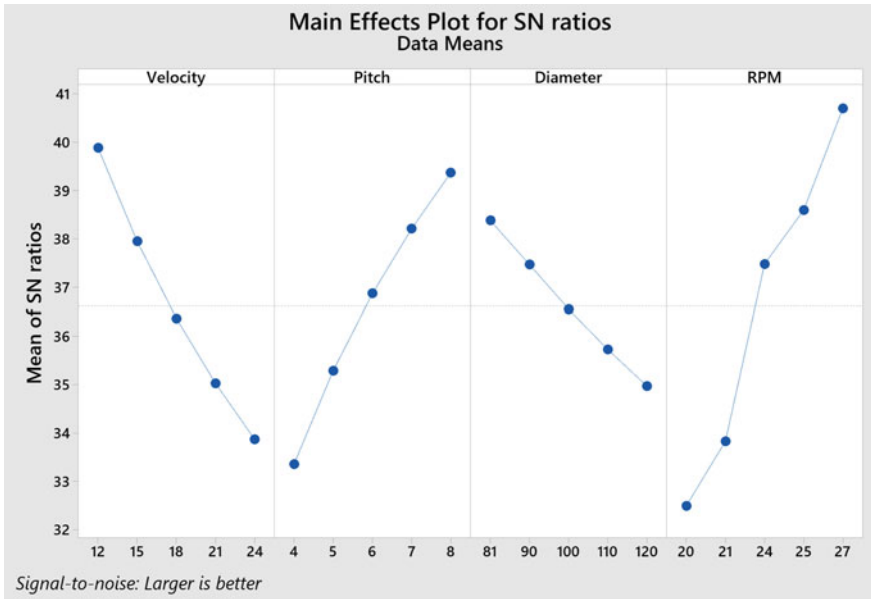


Fig. 4 Main effects plot for S/N ratios

obtained an optimum S/N ratio of 48.48 (using Eq. 7, refer Appendix C.).

$$n_{opt} = n_m + \sum_{i=1}^a (n_i - n_m) \tag{7}$$

As a result, a significant improvement of 7.57% on the S/N ratio was obtained in our proposed model.

Table 4 Response table for means

Level	Velocity	Pitch	Diameter	RPM
1	108.84	49.96	85.42	42.92
2	82.55	62.19	82.61	54.51
3	75.19	78.69	71.57	79.18
4	65.22	90.42	75.22	93.65
5	52.62	103.17	69.60	114.17
Delta	56.21	53.21	15.82	71.25
Rank	2	3	4	1

## 4.2 ANOVA

The results obtained from ANOVA of thrust are summarized in Table 5. It can be observed that for thrust RPM is the most significant parameter as it has the lowest  $p$  value (0.00006), followed by pitch with a  $p$  value of 0.00050 and then velocity with its  $p$  value (0.00054). The diameter is the least significant parameter with a  $p$  value of 0.21650. For the output thrust, the percentage contribution of RPM is 45.45%, pitch is 24.82%, velocity is 24.30%, and diameter is 2.59%. The R-squared and adjusted R-squared values for thrust are summarized in Table 6.

**Table 5** Analysis of variance: thrust versus velocity, pitch, diameter, and RPM

Source	DF	Adj SS	Adj MS	$F$ value	$P$ value	% Contribution
Velocity	4	8903.2	2225.8	17.18	0.00054	24.30
Pitch	4	9092.9	2273.2	17.54	0.00050	24.82
Diameter	4	948.5	237.1	1.83	0.21650	2.59
RPM	4	16,652.3	4163.1	32.12	0.00006	45.45
Error	8	1036.7	129.6			
Total	24	36,633.7				

**Table 6** Model summary

S	R-sq	R-sq (adj)	R-sq (pred)
11.3838	97.17%	91.51%	72.36%

## 5 Conclusion

Despite significant technology advancements in the drones designing and development industry, optimizing the design parameters for the best performance still remains a constant problem. In this paper, we proposed Taguchi optimization of a quadrotor in order to obtain the best combination of the design parameters for our drone. The research work done and presented in this paper can be concluded as follows:

- For this problem, L25 orthogonal array was used since this array ensured the best interaction between our input variables and the required response.
- The process parameters were pitch, diameter, RPM, and velocity, while the response variable was thrust. A higher value for thrust was desirable for our quadrotor, since they require a thrust of more than twice their own weight.
- “Larger-the-Better” was applied to the signal-to-noise ratios. After analyzing these values, the best combination of design parameters for the highest value of thrust was obtained. This optimal combination was velocity at 12 m/s, pitch at 8 mm, diameter at 81 mm, and RPM at 27,000 rpm, and the resultant thrust was obtained as 265.59 N.



- Later, ANOVA was also applied to our model to understand the most significant input parameters and their percentage contribution to the resultant thrust was computed. RPM was found to be the most significant parameter with a percentage contribution of 45.45%.

Even though we have analyzed a quadrotor in this paper, this methodology can be extended to other types of drones as well. The design parameters in those cases would vary depending on the purpose of that particular drone and the objective function which needs to be optimized. Taguchi optimization of drones would be useful for future drones since it would ensure the most feasible combination of process parameters for an optimal response, depending upon the constraints the desired objective function is subjected to.

## Appendix

### A. Calculation of S/N Ratio (larger-the-better)

$$n = -10 * \log_{10}[\text{mean of sum of squares of reciprocal of measured data}]$$

For experiment-1 in Table 2, measured values of thrust = 51.599 N

$$n_1 = -10 * \log_{10} \left[ \frac{1}{51.599^2} \right] = 34.2528 \text{ dB}$$

Similarly, other S/N ratios in Table 2 were calculated.

### B. Calculation of thrust for a given set of values for velocity, pitch, diameter, and RPM

For experiment-2 in Table 2, pitch = 5 mm<sup>2</sup>; diameter = 90 mm; propeller constant = pitch/diameter = 5/90 = 0.0556; RPM = 21 kilo-rev/min; power factor = 3.15; velocity = 12 m/s

$$\text{Power, } P = 0.0556 * 21^{3.15} = 812.30 \text{ W}$$

$$\text{Thrust} = \frac{812.30}{12} = 67.692 \text{ N}$$

Similarly, other values thrust were calculated in Table 2.

### C. Calculation of optimum S/N Ratio

$n_m = 36.62$  dB; (refer Table 3 for values of  $n_i$ )

$$n_{\text{opt}} = 36.62 + \sum_{i=1}^4 (n_i - 36.62)$$

$$n_{\text{opt}} = 36.62 + (39.89 - 36.62) + (39.37 - 36.62) \\ + (38.38 - 36.62) + (40.70 - 36.62) = 48.48 \text{ dB}$$

#### D. Calculation of percentage contribution of input parameters on the response

For RPM, the Adj SS = 16,652.3; and total Adj SS = 36,633.7 (Table 5)

$$\text{Percentage contribution of RPM to Thrust} = \left[ \frac{1 - 5523}{36533} \right] \times 100 = 45.45\%$$

Similarly, percentage contributions of all the input parameters for thrust were calculated.

## References

1. Steinberg DM (1996) 7 Robust design: experiments for improving quality. *Handbook Statist* 13:199–240
2. Rao S, Samant P, Kadampatta A, Shenoy R (2013) An overview of Taguchi method: evolution, concept and interdisciplinary applications. *Int J Sci Eng Res* 4(10):621–626
3. Ku KUJ, Rao SS, Chen L (1998) Taguchi-aided search method for design optimization of engineering systems. *Eng Optim* 30(1):1–23
4. Patyal VS, Modgil S, Maddulety K (2013) Application of Taguchi method of experimental design for chemical process optimisation: a case study. *Asia-Pac J Manage Res Innov* 9(3):231–238
5. Titu AM, Sandu AV, Pop AB, Titu S, Ciungu TC (2018) The Taguchi method application to improve the quality of a sustainable process. In: *IOP conference series: materials science and engineering*, vol 374, no 1. IOP Publishing, p 012054
6. Modi VK, Desai DA (2018) Review of Taguchi method, design of experiment (DOE) & analysis of variance (ANOVA) for quality improvements through optimization in foundry. *Int J Emerg Technol Innov Res* 5(1):184–194
7. Madhoo G, Shilpa M (2017) Optimization of process parameters of stir casting technique using orthogonal arrays. *Int J Adv Res Methodol Eng Technol* 1(2)
8. Pragajibhai DH, Nalwaya S, Singh P, Jain R (2018) Optimization of machining parameters on surface roughness by Taguchi approach. *Int J Res Sci Innov (IJRSI)* 5:349–351
9. Athreya S, Venkatesh YD (2012) Application of Taguchi method for optimization of process parameters in improving the surface roughness of lathe facing operation. *Int Refereed J Eng Sci* 1(3):13–19
10. Maheshwari S (2017) Study the effect of SiO<sub>2</sub> based flux on dilution in submerged Arc welding. In: *IOP conference series: materials science and engineering*, vol 225, no 1. IOP Publishing, p 012158
11. Sivaiah P, Chakradhar D (2019) Modeling and optimization of sustainable manufacturing process in machining of 17–4 PH stainless steel. *Measurement* 134:142–152
12. Ho LH, Feng SY, Yen TM (2014) A new methodology for customer satisfaction analysis: Taguchi's signal-to-noise ratio approach. *J Serv Sci Manage* 2014
13. Kacker RN, Lagergren ES, Filliben JJ (1991) Taguchi's orthogonal arrays are classical designs of experiments. *J Res Nat Inst Stand Technol* 96(5):577
14. Dar A, Anuradha N (2018) Use of orthogonal arrays and design of experiment via Taguchi L9 method in probability of default. *Accounting* 4(3):113–122
15. Shaligram NS, Singh SK, Singhal RS, Szakacs G, Pandey A (2008) Compactin production in solid-state fermentation using orthogonal array method by *P. brevicompactum*. *Biochem Eng J* 41(3):295–300

16. Gonzalez-Aguilera D, Rodriguez-Gonzalvez P (2017) Drones—an open access journal. *Drones* 1(1):1
17. Lee J (2017) Optimization of a modular drone delivery system. In: 2017 annual IEEE international systems conference (SysCon). IEEE, pp 1–8
18. Cohn P, Green A, Langstaff M, Roller M (2017) Commercial drones are here: the future of unmanned aerial systems. McKinsey & Company
19. Shavarani SM (2019) Multi-level facility location-allocation problem for post-disaster humanitarian relief distribution. *J Humanitarian Logistics Supply Chain Manage*
20. Benevides JR, Inoue RS, Paiva MA, Terra MH (2019) ROS-Based robust and recursive optimal control of commercial quadrotors. In: 2019 IEEE 15th international conference on automation science and engineering (CASE). IEEE, pp 998–1003
21. Hassanalian M, Abdelkefi A (2017) Classifications, applications, and design challenges of drones: a review. *Prog Aerosp Sci* 91:99–131
22. Putra HM, Fikri MR, Riananda DP, Nugraha G, Baidhowi ML, Syah RA (2020) Propulsion selection method using motor thrust table for optimum flight in multirotor aircraft. In: AIP conference proceedings, vol 2226, no 1. AIP Publishing LLC, p 060008
23. Rahnamai K (2016) Quadrotor drones thrust measurement apparatus. In: 2016 IEEE aerospace conference. IEEE, pp 1–6
24. Sharma P (2018) Conceptual design and non-linear analysis of Triphibian drone. *Procedia Comput Sci* 133:448–455
25. Coulombe C, Gamache JF, Mohebbi A, Chouinard U, Achiche, S (2017) Applying robust design methodology to a quadrotor drone. In: DS 87-4 proceedings of the 21st international conference on engineering design (ICED 17) Vol 4: design methods and tools, vancouver, Canada, 21–25 Aug 2017, pp 395–404
26. Semion AA (2018) A method for realization of nonlinear state-dependent coefficients regulators based on microcontroller memory. In: 2018 Moscow workshop on electronic and networking technologies (MWENT). IEEE, pp 1–5
27. Shen CH, Albert FYC, Ang CK, Teck DJ, Chan KP (2017) Theoretical development and study of takeoff constraint thrust equation for a drone. In: 2017 IEEE 15th student conference on research and development (SCOREd). IEEE, pp 18–22
28. Parandha SM, Li Z (2018) Design and analysis of 3D printed quadrotor Frame. *Int Adv Res J Sci Eng Technol* 5(4)



# Comparative Analysis of Different Dye-Sensitizer and Their Impact on a Solar Cell by Using SCAPS-1D Simulator

Sushmita Kumari<sup>(✉)</sup> and Cherry Bhargava

School of Electronics and Electrical Engineering, Lovely Professional University, Phagwara,  
Punjab 144411, India  
sushmpct@gmail.com

## 1 Introduction

An important application of solar energy is the solar cell. For solar energy conversion, various technologies have been used, among them, dye-sensitized solar cell is an alternative technique. Due to low fabrication cost of dye sensitizes solar cell researchers are more working on this cell.

Dye sensitized solar cell's design developed in this paper is composed of  $\text{TiO}_2$  layer, which is working as an electron carrier and as an electron generator organic dyes layer is working. The electrolyte solution donates the electron, and this helps it to recover its original states. To get a better efficient solar cell, the organic dye layer which is working as a photo sensitizer should have characteristics concerning the available light spectrum. Different sensitizers have different light absorption capabilities, and hence, every dye has different efficiency and cost. This paper based on these calculations tried to show the best efficient dye [1]. Generally, the five main components of dye-sensitized solar cell are—electrolyte, photo-anode, a counter electrode, oxide layer, and the photo sensitizer. In this work, the main focus has been given toward the improvement of the photo-sensitizer dye to get the best efficient and stable result by using DSSC technology [2]. In this study, three dyes—N719 + Z907 dye, strawberry dye, DPI-T dye have been used and short-circuit current ( $I_{sc}$ ), open-circuit voltage ( $V_{oc}$ ), fill-factor, and efficiency have been calculated with the help of SCAPS-1D software. These results in terms of data and terms of the graph have been shown below [3].

### 1.1 Design of DSSC

Here, in the diagram, different layers of dye-sensitized solar cells have been shown, each of the components had depicted very clearly to understand the exact simulation and the variations done in many of the layers by using the SCAPS (Fig. 1).

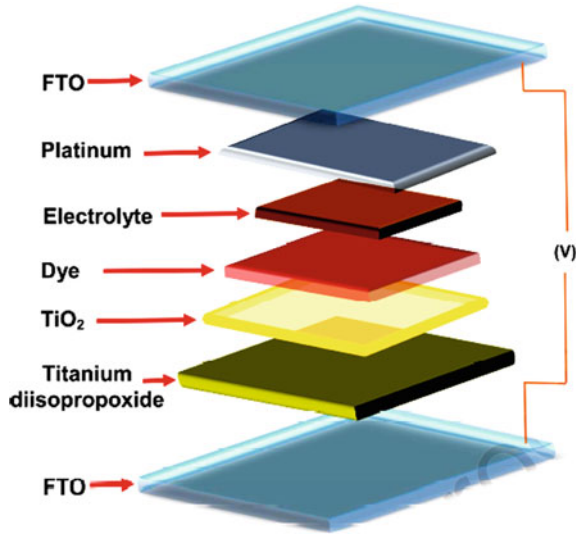


Fig. 1 Structure of dye-sensitized solar cell

### 1.2 Device Structures of N719+Z907 Dye, Strawberry Dye and DPI-T Dye

The solar cell structure is FTO/TiO<sub>2</sub>/ N719+Z907 dye/strawberry dye/DPI-T dye /Spiro-OMETAD, which is used for simulation of dye-sensitized solar cell. In this design, fluorine-doped tin oxide (FTO) works as an oxide layer, TiO<sub>2</sub> as a buffer layer, and all the dyes like N719+Z907 dye/strawberry dye/DPI-T dye as an absorber layer (Fig. 2).



Fig. 2 The device structure of DSSC when using different dyes in SCAPS-1D

### 1.3 Improvement in Dye Sensitizers

The dye or sensitizer plays an important role in absorbing the energy from the sunlight. To get a better efficient dye sensitizer, the design of DSSC should be effective. The used dye should be strong to the surface of TiO<sub>2</sub>, to be sure efficient electron injection into the conduction band of TiO<sub>2</sub>. Then, for efficient charge injection, the conduction

band should be lower to LUMO (lowest unoccupied molecular orbital [1]. For efficient regeneration of the oxidized dye, the whole transport layer must be higher than the highest occupied molecular orbital (HOMO) [4].

#### 1.4 Software Used for Simulation

##### SCAPS-1D

Solar cell capacitance simulator (SCAPS) is a one-dimensional application solar cell that is used as simulator tools. In SCAPS-1D, seven semiconductor layers can be added, and as an output efficiency, fill factor, short-circuit current, open-circuit voltage, I-V curve, C-V, C-F, and Q-E curve can be calculated [5]. As an input here, inserted parameters that can vary are—bandgap, thickness, dielectric permittivity, electron affinity, electron mobility, hole mobility, acceptor density, and donor density can be used. The calculation can be done in light as well as in dark. The main equations used behind this software are—current density equation, Poisson equation, and continuity equation [6] (Fig. 3).

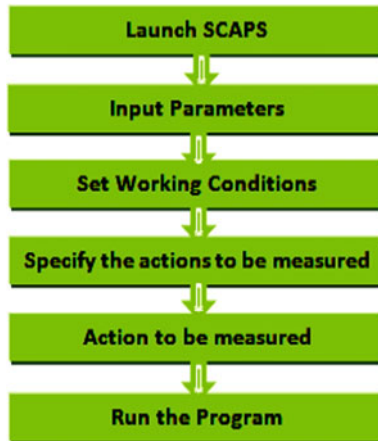


**Fig. 3** Steps followed to do the calculation with SCAPS-1D

##### Automeris

To extract the numerical data from the image of data visualization, a semi-automatic tool WebPlotDigitizer makes the process easier. It can be used for charts, ternary, maps, etc.

##### Origin lab

It is a GUI software in which at the front end, the spreadsheet appears. For scientific graphing and data analysis, origin is used. In origin, one can plot a 2D or 3D graph. Data analysis is possible in origin is statistics, curve fitting, and signals processing. Data can be in various forms like Excel, NI, SPC, ASCII text, etc. It can transfer graphs to any image format like JPEG, EPS, GIF, etc.

## 2 Simulation by Using SCAPS-1D

As an input of SCAPS, parameters like  $L(\mu\text{m})$ —thickness,  $E_g(\text{eV})$ —bandgap,  $\chi(\text{eV})$ —dielectric permittivity,  $\mu_e$ —electron mobility,  $\mu_p$ —hole mobility,  $N_d$ —donor density, and  $N_a$ —acceptor density have been taken from the different review papers and all in the summarized way shown through the table in tabulated format (Table 1).

**Table 1** SCAPS-1D input parameters are listed below in this table [7, 8]

Parameters	TiO <sub>2</sub> layer	FTO Layer	N719+Z907-dye layer	Strawberry-dye layer	DPI-dyes layer	Spiro OMETAD Layer
$L(\mu\text{m})$	3.000	0.300	0.020	0.010	0.020	0.150
$E_g(\text{eV})$	3.200	3.500	3.200	2.370	2.370	3.060
$\chi(\text{eV})$	3.900	4.000	3.900	3.900	3.900	2.050
$\epsilon_r$	9.000	9.000	30.000	30.000	30.000	3.000
$M_e$ ( $\text{cm}^2/\text{Vs}$ )	$2.000 \times 10$	$2.000 \times 10$	5.000	5.000	5.000	$2.000 \times 10^{-4}$
$M_p$ ( $\text{cm}^2/\text{Vs}$ )	$1.000 \times 10$	$1.000 \times 10$	5.000	5.000	5.000	$2.000 \times 10^{-4}$
$N_d$ ( $1/\text{cm}^3$ )	$1.000 \times 10^{15}$	$1.000 \times 10^{19}$	0.000	0.000	0.000	0.000
$N_a$ ( $1/\text{cm}^3$ )	0.000	0.000	$1.000 \times 10^{17}$	$1.000 \times 10^{17}$	$1.000 \times 10^{17}$	$1.000 \times 10^{18}$

### 2.1 Absorption Coefficient Graph of Dyes like—N719+Z907, Strawberry, DPI-T Dyes

Dye sensitizer plays an important role in the improvement of photo-absorption efficiency of the cell. For the excitation of electrons in the conduction band, the absorption of the material should be good. The absorption coefficient mainly depends upon the material used and the wavelength of the particular incident light. Here, in the graph by the calculation of the absorption coefficient of these dyes, it can be seen that the maximum efficient dye is DPI-T, it has a sharp high curve [9] (Fig. 4).

### 2.2 EQE-Curve of N719+Z907, Strawberry, and DPI-T Dyes

The carrier collected by the solar cell to the photon incident on the solar surface is defined as the quantum efficiency of the solar cell. The wavelength has a value above 350 nm that is only considered for the quantum efficiency calculation; below this wavelength, the power received is very low, which is not so useful in terms of proper outcome [10]. Through the shown curve, it can be seen that the wavelength N719+Z907 of dye has higher and stable as compared to other dyes [11] (Fig. 5).

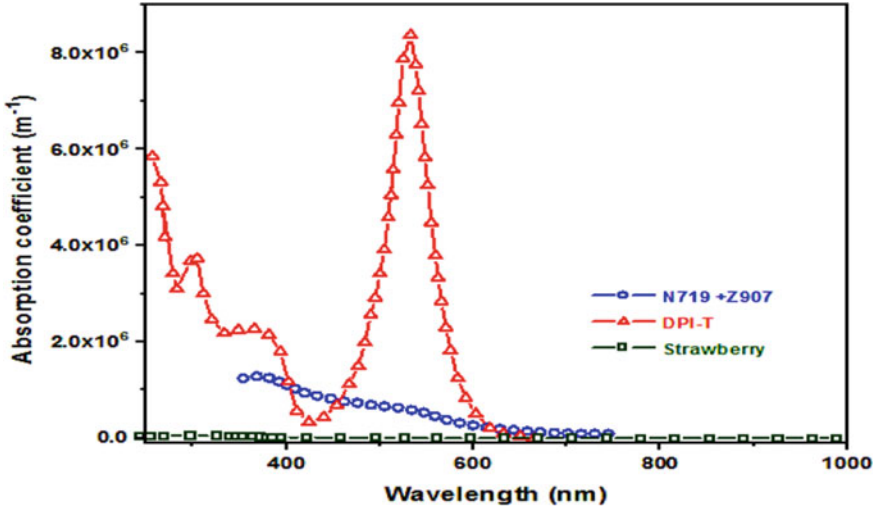


Fig. 4 The curve depicts the absorption coefficient of dyes

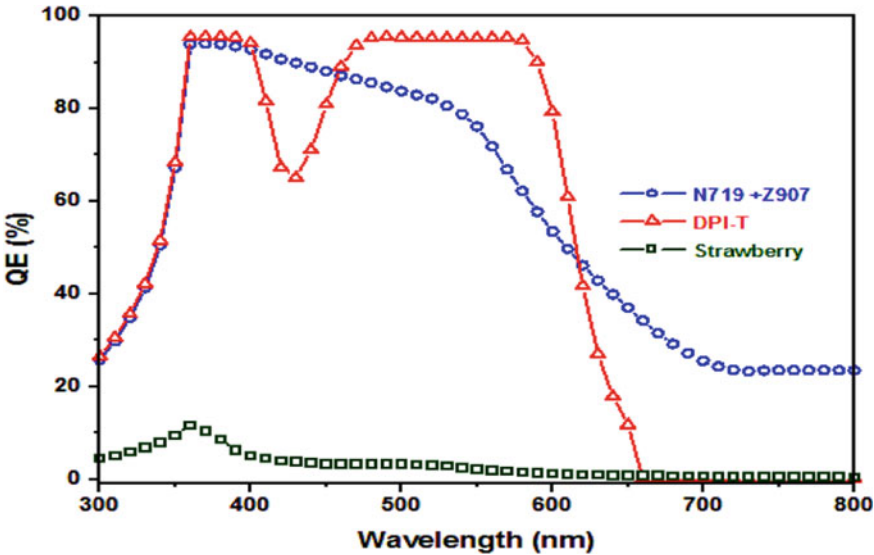


Fig. 5 The EQE curve of different dyes used in dye-sensitized solar cells

### 2.3 J-V-Curve of N719+Z907, Strawberry, and DPI-T Dyes

Voltage–current curve plays an important role when the overall performance of the device is going to calculate. J-V curve is based on the values of short-circuit current and open-circuit voltage, especially at the point where these two values can be obtained maximum [12]. The value of all three dyes has been shown through the graph (Fig. 6).



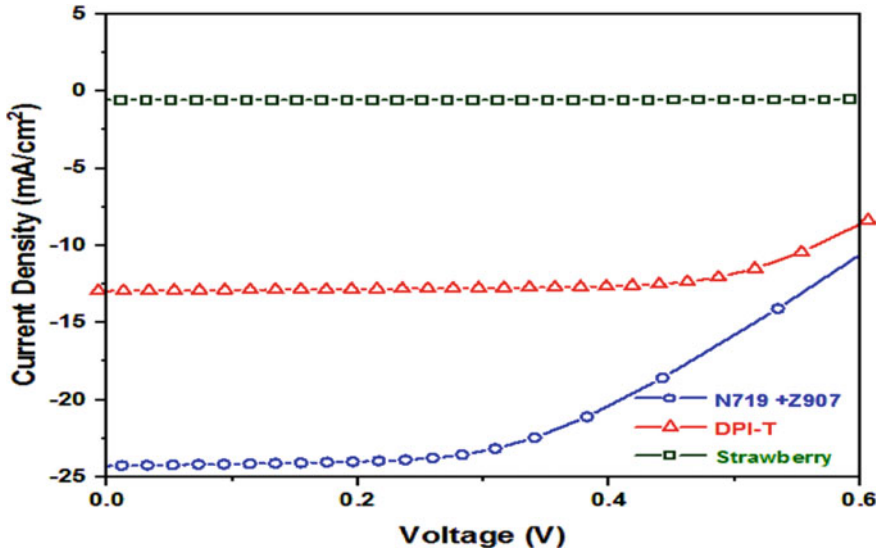


Fig. 6 J-V curve of dye-sensitized solar cell by using dyes

### 3 Results and Discussion

When the J-V-curve calculation has been done then various semiconductor parameters have been received as an output of this curve, such as open-circuit voltage, short circuit current, fill-factor, and efficiency of the cell. For the comparison of all three dyes, N719+Z907 dye, strawberry dye, and DPI-T dye have been done, and these are tabulated in the form of a table. Table 2 shows the expected value of these parameters from the different literature reviews, and Table 3 shows the received outcome from the design work done here in this paper. By seeing Table 3, it can be seen that the N719+Z907 dye can give maximum efficiency.

#### *Expected Outcomes*

**Table 2** Semiconductor parameters of different dyes from a literature review [12–14]

Parameters	Voc(V)	Jsc (mA/cm <sup>2</sup> )	FF	$\eta$ (%)
N719+Z907 dye	0.655	4.132	0.422	2.287
strawberry dye	–	–	–	0.013
DPI-T dye	0.58	3.18	0.69	1.28

#### *Obtained Outcomes*

**Table 3** Semiconductor parameters of solar cell received by using SCAPS-1D

Parameters	Voc (V)	Jsc (mA/cm <sup>2</sup> )	FF	η (%)
N719+Z907 dye	0.793	24.25	42.71	8.23
strawberry dye	0.677	566.22	79.52	0.30
DPI-T dye	0.7757	12.93	59.14	5.93

### 3.1 Effect on Temperature

Here, in this design of dye-sensitized solar cell, variation of temperature gives an important impact. The range [290–340 K] taken here for variation and the calculation of the based parameters have been shown through the different tables. In the result, it has been shown that after a certain rise of temperature, the efficiency starts decreasing, so for a stable result, only a particular variation is allowed. If there is variation in temperature of the cell, it can impact other associated parameters as well, such as concentration, electron–hole mobility, and the bandgap of the semiconductor material [15].

#### N719+Z907 dye

While using N719+Z907 dye, the best suitable temperature that can give the best output is 300 K, the obtained efficiency is 8.55%. If the temperature keeps rising, then the received output will be less (Table 4).

**Table 4** Temperature variations from 290 to 340 K and their effect on the different parameters while using the N719+Z907 dye

Temperature (K)	Voc (V)	Jsc (mA/cm <sup>2</sup> )	FF (%)	η (%)
290	0.7933	24.280607	42.71	8.23
300	0.7943	24.248115	42.70	8.55
310	0.7889	24.288199	42.26	8.10
320	0.7668	24.323246	40.99	7.65
330	0.7445	24.354185	39.69	7.20
340	0.7220	24.381803	38.52	6.78

#### Strawberry dye

For this dye, the suitable temperature is shown through the table, and the graphs are 300 K, the received maximum efficiency is 0.32%, which is better as compared to expected outputs from the available literature papers (Table 5).

**Table 5** Temperature variations from 290 to 340 K and their effect on the different parameters while using the strawberry dye

Temperature (K)	Voc(V)	Jsc (mA/cm <sup>2</sup> )	FF (%)	$\eta$ (%)
290	0.6772	566.221104E-3	79.52	0.30
300	0.6981	564.404472E-3	80.18	0.32
310	0.6718	566.682843E-3	79.45	0.30
320	0.6456	568.984010E-3	78.75	0.29
330	0.6192	571.126414E-3	77.72	0.27
340	0.5925	573.018065E-3	76.94	0.26

### DPI-T dye

For this dye, the most suitable temperature that should be used is 300 K; before and after this temperature, the value of the efficiency decreases. The same has been shown through the table (Table 6).

**Table 6** Temperature variations from 290 to 340 K and their effect on the different parameters while using the DPI-T dye

Temperature (K)	Voc (V)	Jsc (mA/cm <sup>2</sup> )	FF (%)	$\eta$ (%)
290	0.7757	12.935655	59.14	5.93
300	0.7938	12.908306	60.01	6.15
310	0.7712	12.942084	58.80	5.87
320	0.7484	12.971949	57.50	5.58
330	0.7254	12.998701	56.34	5.31
340	0.7021	13.022951	55.15	5.04

### 3.2 Effect of Thickness

Here, only the variation in the thickness of the TiO<sub>2</sub> layer shows the impact on the other constant parameter values. Variation in voltage and current can be seen and as well as fill factor and in the efficiency. Fill factors work opposite to the current and voltage. Efficiency has proportional relation with the thickness if thickness increases, the efficiency will also be increased, but at some certain point, then again it starts falling. All three dyes have been taken and the range of thickness taken for variation is 2–6  $\mu\text{m}$  [16].

#### N719+Z907 dye

The maximum efficiency can be gained at the thickness of 6  $\mu\text{m}$  by using this dye, the same has been shown through the table (Table 7).

**Table 7** Thickness variation of TiO<sub>2</sub> layer for the dye N719 + Z907

TiO <sub>2</sub> thickness(μm)	Voc (V)	Jsc (mA/cm <sup>2</sup> )	FF (%)	η (%)
2	0.7867	19.402893	49.50	7.56
3	0.7933	24.280607	42.71	8.23
4	0.7967	27.139557	39.24	8.48
5	0.7983	28.545235	37.48	8.54
6	0.7988	28.916658	37.00	8.55

### Strawberry dye

The maximum efficiency can be received at 6 μm thickness of TiO<sub>2</sub> layer (Table 8).

**Table 8** Thickness variation of TiO<sub>2</sub> layer for the dye Strawberry

TiO <sub>2</sub> thickness (m)	Voc (V)	Jsc (mA/cm <sup>2</sup> )	FF (%)	η (%)
2 μm	0.6772	566.220653E-3	79.52	0.30
3 μm	0.6688	412.596816E-3	80.34	0.22
4 μm	0.6825	696.538993E-3	78.85	0.37
5 μm	0.6860	799.825626E-3	78.15	0.43
6 μm	0.6882	876.875550E-3	77.55	0.47

### DPI-T dye

By using this dye, maximum efficiency can be received at 6 μm thickness of TiO<sub>2</sub> layer (Table 9).

**Table 9** Thickness variation of TiO<sub>2</sub> layer for the DPI-T dye

TiO <sub>2</sub> thickness (μm)	Voc (V)	Jsc (mA/cm <sup>2</sup> )	FF (%)	η (%)
2	0.7757	12.935655	59.14	5.93
3	0.7751	12.602592	60.13	5.87
4	0.7748	12.524736	59.37	5.76
5	0.7728	11.692478	60.24	5.44
6	0.7701	10.639539	61.65	5.05

## 4 Conclusion

This work explained the performance of the DSSC by using different dyes—N719+Z907, Strawberry, and DPI-T. As per the data obtained from the calculation by using the SCAPS-1D software and the Origin-lab software, the received efficiency of all three dyes are N719+Z907 (8.23%), strawberry (0.30%), and DPI-T (5.93%). Other parameters like fill-factors of dyes are N719+Z907 (42.71) strawberry (79.52), and DPI-T (59.14), Voc (V) of the dyes are N719 + Z907 (0.793) strawberry (0.677), and DPI-T (0.7757), and the current density of the dyes are N719+Z907 (24.25) strawberry (566.22), and DPI-T (12.93). By seeing all the parameters value, it can be seen that the N719+Z907 is the most efficient dye, and it can give better result in terms of making the efficient solar cell, so this can be used for fabrication of solar cell at the low cost with good efficiency. The efficiency of dyes can vary on the basis of the variation in the thickness and variation of the temperature in TiO<sub>2</sub> layer, as per the experimental result, 300 K is the stable temperature to obtain maximum efficiency, and the thickness will be varied as per the dye used for strawberry efficient thickness is 6 μm, for N719+Z907 dye it is 6 μm and for DPI-T the suitable thickness of TiO<sub>2</sub> layer should be 2 μm.

## References

1. Sathyajothi S, Jayavel R, Dhanemozhi ACJMTP (2017) The fabrication of natural dye sensitized solar cell (DSSC) based on TiO<sub>2</sub> using henna and beetroot dye extracts. 4(2):668–676
2. Faraz SM, Mazhar M, Shah W, Noor H, Awan ZH, Sayyad MHJPBCM (2021) Comparative study of impedance spectroscopy and photovoltaic properties of metallic and natural dye based dye sensitized solar cells. 602:412567
3. Prabavathy N, Shalini S, Balasundaraprabhu R, Velauthapillai D, Prasanna S, Muthukumarasamy NJJOER (2017) Enhancement in the photostability of natural dyes for dye-sensitized solar cell (DSSC) applications: a review. 41(10):1372–1396
4. Ghosh NN, Habib M, Pramanik A, Sarkar P, Pal SJNJOC (2019) Molecular engineering of anchoring groups for designing efficient triazatruxene-based organic dye-sensitized solar cells. 43(17):6480–6491
5. Azizi T, Toujeni H, Karoui MB, Gharbi R (2019) A comprehensive device modeling of solid state dye sensitized solar cell with SCAPS-1D. In: 2019 19th International conference on sciences and techniques of automatic control and computer engineering (STA). IEEE, pp 336–340
6. Das N, Paul R, Design and optimisation of lead free perovskite/silicon tandem solar cell using SCAPS-1D software
7. Vinutha K, Kumar KN, Tejas M, Kumar BJ, Kumar DS, Mahesh HJJIR (2016) Natural dye sensitized solar cells using anthocyanin pigment of strawberry as sensitizers. 2:1011
8. Ali AK, Bakr NA, Jassim SMJJOPM (2016) Technology, Fabrication of dye sensitized solar cell and efficiency enhancement by using N719 and Z907 dyes mixture. 2(3):20–24
9. Ayalew WA, Ayele DW (2016) Dye-sensitized solar cells using natural dye as light-harvesting materials extracted from *Acanthus sennii* chiovenda flower and *Euphorbia cotinifolia* leaf. J Sci Adv Mater Devices 1(4):488–494
10. Wu ZS et al (2020) New organic dyes with varied arylamine donors as effective co-sensitizers for ruthenium complex N719 in dye sensitized solar cells. J Power Sources. 451
11. Dematage N, Premalal E, Konno AJIJES (2014) Employment of CuI on Sb<sub>2</sub>S<sub>3</sub> extremely thin absorber solar cell: N719 molecules as a dual role of a recombination blocking agent and an efficient hole shuttle. 9:1729–1737

12. Vougioukalakis GC, Stergiopoulos T, Kontos AG, Pefkianakis EK, Papadopoulos K, Falaras PJDT (2013) Novel Ru (II) sensitizers bearing an unsymmetrical pyridine-quinoline hybrid ligand with extended  $\pi$ -conjugation: synthesis and application in dye-sensitized solar cells. *J Phys Chem C* 117(18):6582–6591
13. Sugathan V, John E, Sudhakar KJR, Reviews SE (2015) Recent improvements in dye sensitized solar cells: a review. *J Phys Chem C* 119:54–64
14. Kumara N, Lim A, Lim CM, Petra MI, Ekanayake PJR, Reviews SE (2017) Recent progress and utilization of natural pigments in dye sensitized solar cells: a review. *J Phys Chem C* 121:301–317
15. Berginc M, Opara Krašovec U, Jankovec M, Topič M (2007) The effect of temperature on the performance of dye-sensitized solar cells based on a propyl-methyl-imidazolium iodide electrolyte. *Sol Energy Mater Sol Cells* 91(9):821–828
16. Raga SR, Fabregat-Santiago F (2013) Temperature effects in dye-sensitized solar cells. *Phys Chem Chem Phys* 15(7):2328–2336



# Numerical Analysis of Low GWP Blends of R290 as an Alternative to R410A

Subham Mukhopadhyay, Hardik Gupta<sup>✉</sup>, Ajay Kumar, and Akhilesh Arora

Department of Mechanical Engineering, Delhi Technological University, New Delhi, India  
hardikgupta\_2k17me101@dtu.ac.in

## 1 Introduction

### 1.1 Refrigerant

In 1834, Jacob Perkins demonstrated the first refrigeration system that utilizes vapor compression refrigeration cycle. Overall, system consists of compression device, evaporator, condenser, expansion device and was using volatile fluid in a closed cycle which absorbs heat results in cooling and freezing that volatile fluid is termed as 'Refrigerant' [1]. Later on as researchers worked on their toes to discover different technologies introduced as alternatives to VCR like absorption and thermoelectric. But, we cannot run away from the fact that VCR is still dominating over other refrigeration technologies.

Refrigerant is a principal component of a vapor compression refrigeration system. It absorbs heat and remove it at a higher temperature and a higher pressure, generally via state change. Different substances can be used as refrigerants in a vapor compression refrigeration cycle, including those that naturally occur in the nature so-called natural refrigerants as well as fabricated substances (so-called synthetic refrigerants) [2].

### 1.2 Impact of Refrigerants on Environment

From ozone layer depletion to global warming, refrigerants have adverse effect on environment [3]. Replacement to any refrigerant that improves overall efficiency is likely to have more adverse impact than benefit based on net global warming impacts. So, along with looking for refrigerants that accomplish the efficiency, safe fluids that imply low global warming impact in vapor compression systems should be used as an alternative to present refrigerants.

Ng et al. [4] found in his paper an alternative of R410. Authors analyzed performance of two refrigerant mixtures R32/R1234ze and R32/R600a with low GWP 628 and 561, respectively. It was found that the two refrigerant mixtures on analysis show similar thermodynamic properties and COP is also close to R410 when used in air-cooled split air-conditioning system.

Tian et al. [5] in his paper, the refrigerant mixture R32/R290 (68%/32% by weight) has been investigated as the drop-in replacement for R410A in household air conditioners. The GWP of the mixture is 460. Theoretical and experimental investigations have been conducted on the performance of the air conditioners working with both R32/R290

and R410A. The results show R32/R290 blend with a mixing ratio of 68%/32% by weight is able to act as the drop-in replacement for R410A in household air conditioners. But increased flammability and condenser pressure are issues need to be investigated further.

In today's life, refrigerants have become an important part of the ecosystem for heating and cooling systems used by industries for refrigeration, human for comfort. And from human comfort, we mean ACs and refrigerators, and when we talk about air conditioner, we cannot forget about R410A refrigerant. It is widely used refrigerant in air conditioning, it has zero ODP that is why introduced as replacement of R22 as greener choice. Use and manufacturing of refrigerants are regulated under Montreal Protocol [6] and Kyoto Protocol. R410A consist of R125 and R32 in 1:1 ratio by mass having GWP of 2088. Overall, it has good efficiency. But due to its high GWP, it has been criticized by researchers around the world [7].

Reports show that demand for the air conditioning increasing by 20% YOY. This increase in demand will finally follow up to increase use of R410 refrigerants, which will badly impact our environment in the long run. So following this, we have to think of some alternatives for R410A with lower GWP to reduce overall impact on environment [8].

### 1.3 Alternatives to R410A with Lower GWP

Various companies such as Honeywell [9] introduced alternatives for R410 listed in Table 2 although development on additional mixtures is still ongoing on. Among the recently analyzed mixtures are, for instance, 9 alternatives to R410A, which have been estimated to be non-flammable or mild inflammable as ASHRAE [1] classified them under A2. A mixture of R32, R125 and R131I (49, 11.5 and 39.5% in composition, by mass, respectively) known as R466A that is a proposed non-flammable substitute to R410A. The R131I component, an iodine compound primarily used as a fire suppressant, contributes to reduced flammability of the mixture and a resulting GWP below 750. Thus, the proposed mixture is the lowest GWP non-flammable alternative to R410A, although its properties remain to be known in detail [10] (Table 1).

**Table 1** Already existing alternative refrigerants to R410A with lower GWP [11]

Refrigerant mixture	Composition	GWP
R466A	R32, R125, R131I (CF3I) (49,11.5,39.5)	733
R470A	R744, R32, R125, R1234ze(E), R227ea(10, 17, 19, 7, 44, 3)	909
R447B	R32, R125, R1234ze(E) (68, 8, 24)	741
R452B	R32, R125, R1234yf (67, 7, 26)	698
R454B	R32, R1234yf (68.9, 31.1)	466
R459 A	R32, R1234yf, R1234ze (68, 26, 6)	460

*Note* The GWP values used in this paper are taken from [12]



**Table 2** Composition of mixtures used, for GWP [7]

Components	R32	R125	R290	R227ea	GWP
GWP	675	3450	3	2900	
Mixture 1	30%	8%	60%	2%	579
Mixture 2	20%	5%	70%	5%	455
Mixture 3	45%	3%	50%	2%	467
Mixture 4	50%	2%	45%	3%	495

## 2 Working Methodology

- The main components of the refrigeration mixture are propane (R290) and R32 both these form about 90% of the mixture; rest of the two components are R125, R227ea forms only 10% of the mixture.
- **R32**: Also called difluoromethane use up to 20% less refrigerant than R410A equivalents making them more efficient which means lower carbon emissions and lower energy costs, thus helping in increasing the COP [13].
- **R125**: Also called pentafluoroethane is one of the major contributors of the high GWP of R410A and hence as an alternative should be kept as low as possible [14].
- **R290**: Also called propane has excellent thermodynamic and environmental properties.
- **R227ea**: Also called 1,1,1,2,3,3,3-heptafluoropropane is an excellent flammability-suppressing refrigerant [15].
- Four mixtures with different compositions of these components were studied to investigate parameters such as coefficient of performance (COP), refrigeration effect and power consumed.
- The properties of these mixtures were evaluated using REFPROP (NIST reference fluid thermodynamic and transport properties database) which is developed by NIST [16]. **LJ5 Lemmon and Jacobsen Model** [17] was used as a mixing rule with **Beta** and **Gamma** values equal to 1.
- To calculate a particular state point, **specific state points** with a particular composition were determined using the **Calculate** option from the menu and the data for two properties were provided to get rest of the information about that state point.
- VCRS cycle [18] was used and all the four state points were determined using the REFPROP software (Fig. 1).

### State Points are described below:

1. Evaporator Exit
2. Compressor Exit
3. Condenser Exit
4. Evaporator Entry.

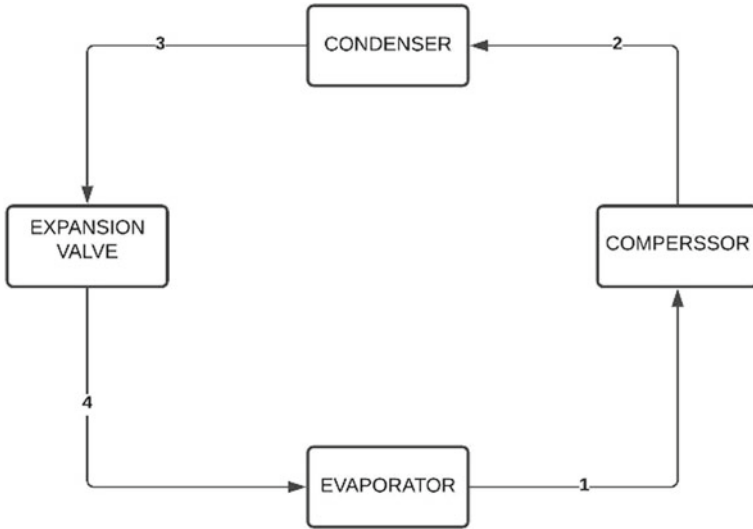


**Fig. 1** Block diagram representing various stages of a VCRS cycle made using LucidApp

**GWP calculations:**

GWP is a very important aspect of a refrigerant which the engineers consider while looking for new mixtures and substances as a substitute to the existing ones. It is a relative term and measures how much energy will be absorbed by emission of 1 ton of a gas as compared to that absorbed by 1-ton emission of CO<sub>2</sub>.

To calculate the GWP of four mixtures that are selected for this study, following formula is used, which is simply the weighted average of GWPs of individual components. [19]

$$GWP_{mixture} = \left( \sum GWP_{component} * Mass\% \text{ in mixture} \right) / 100$$

Thus, from the above equations, the GWP of the various samples can be calculated as follows:

**Pressure of Evaporator and Condenser:**

The standard evaporator and condenser pressure taken are 410.67 kPa and 2265.70 kPa.

**Steps:**

1. In order to calculate thermodynamic properties of every state point (1–4) of the above VCRS cycle, REFPROP was used.
2. For state 1, pressure is selected to be 410 kPa as mentioned above. The quality is taken to be equal to 1; now, rest of the properties as calculated by the REFPROP software.
3. For state 2, the entropy is equal to that of state 1, and the pressure of state 2 is equal to the pressure of state 3 which is taken as 2265.7 kPa; and the result of the properties are determined by the software.

4. For step 3, the pressure is equal to the pressure in state 2, and the air quality is 0 at this stage.
5. Similarly, for state 4, the pressure is equal to that in state 1, and the enthalpy is equal to the enthalpy of state 3.
6. The above steps are calculated for rest of the 3 mixtures, and the data is then processed to get desirable information.

### Plotting log P Versus T graph

In order to plot this graph, the saturation states at 50 different temperatures were determined using the REFPROP's saturation table property. The range was taken from 295 to 345 K. Once the data was collected for each mixture, it was then copied to the MS Excel, log P values were calculated using the excel formula, and the log p versus T graph was plotted.

## 3 Results and Discussion

### • Power per unit mass flow rate:

From the above graph, it can be concluded that the power per unit mass flow rate of the compressor is maximum in the case of the second mixture (20% R32/5% R125/5% R227ea/70% R290), indicating that as the amount of propane has a devastating effect for the power input of the compressor and hence the amount of propane has to be optimized so as to have a minimum power input to the compressor. However, it can also be seen that as the amount of propane is reduced and the amount of R32 is increased, there is a decrease in the power input indicating that R32 also have to be optimized to be maximum, and the power input of the compressor is dependent on both R290 and R32. However, the addition of R125 and R227ea has minimum effect on the power input of the compressor, and these are added just to decrease the flammability of the refrigerant (Fig. 2).

It can further be seen that the amount of R290 has disastrous effect on the power input as compared to R410A as the power input increases, indicating that more power would be required by the compressor, which is a negative sign.

### • Refrigeration effect per unit mass flow rate:

It can be seen from the above graph that the refrigeration effect is highest in the mixture 2 indicating that large amounts of R290 contribute to the increase in the refrigeration effect. However, due to the same reason, the refrigeration effect is minimum in case of mixture of 4 as it has minimum amount of R290 and maximum amount of R32, indicating that R32 also decreases the refrigeration effect. Hence, it can be concluded that the amount of propane increases the refrigeration effect. However, it can also be noted that although the amount of propane is high in case of sample 1 (almost 60%), the refrigeration effect is low due to the reason that in such a case the amount of R125 is

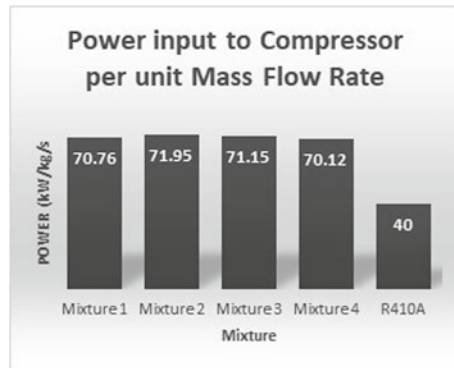


Fig. 2 Power input of compressor per unit mass flow rate of various compositions

highest (almost 8%), indicating that an increase in the amount of R125 deteriorates the refrigeration effect and so it has to be kept minimum with maximizing R290 (Fig. 3).

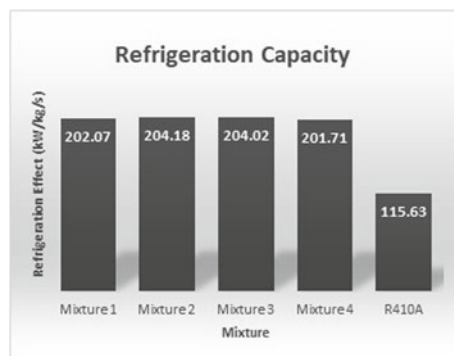


Fig. 3 Refrigeration effect per unit mass flow rate of various compositions

It can further be concluded that the amount of R290 also increases the refrigeration effect as compared to the R410A, which indicates that the cooling capacity increases which is a positive sign.

● **Coefficient of Performance of various composition:**

It can be seen that the COP is highest in case of sample 4 as the amount of R32 is highest and amount of propane (R290) is lowest, indicating that although R290 increases the refrigeration effect, but it has minimal effect on the COP as it also increases the power input of the compressor. It can also be seen that in case of mixture 2, the COP is minimum due to the reason that it has the largest amount of R290 (almost 70%) thus confirming the above. Also, it can further be concluded that the amount of R227ea does not have much effect on COP of the refrigerator. Also, the amount of R125 also has no significant

contribution in the COP, and so, it can be concluded that R32 and R290 are the major contributors in the COP of the system. However, it should be noted that there is a sudden drop in the COP of the system due to addition of R290, but this drop is insignificant when compared to the drop in the GWP indicating that R290 is a healthy alternative to R125 in the R410A mixture (Fig. 4).

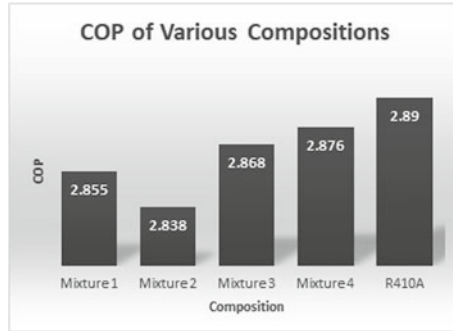


Fig. 4 Coefficient of performance of various compositions

- **GWP of various mixtures:**

From the above graph, it can be observed that the GWP is highest in case of mixture 1 where the R125 is maximum as 8% and is lowest in case of mixture 2 where the R290 is maximum. Thus, it can be inferred that R125 majorly deteriorates the GWP and has to be replaced with a suitable alternative. Also, R290 has the lowest GWP and hence adding more quantity of this would result in lower GWP, but it would also deteriorate the COP. Hence, an optimum mixture of R290 has to be used that has minimum effect on COP and maximum effect on GWP. It can also be seen that all the 4 mixtures have a lower GWP than R410A, so a successful combination has been created that is environmental friendly. This drop in GWP is much greater than the drop in COP, and hence, it can be concluded that COP can be compromised for the GWP in this case. Thus, from this, we can conclude that mixture 4 is the best mixture as it has a significant reduction in the GWP, and the COP reduction is also significantly small (Fig. 5).

- **Log P versus T graph for various compositions:**

From the above graph, it can be seen that a straight line has been obtained for all the 4 mixtures which indicates that the model that we have used to calculate the COP and the various performance characteristics are correct and the model is validated. It can further be seen that mixture 4 has a higher operating pressure as compared to other mixtures, indicating the amount of R290 also has effect on the operating pressure and hence on increasing the R290 composition, the operating pressure reduces. Thus,, mixture 2 with maximum R290 has minimum operating pressure among the 4 mixtures (Fig. 6).

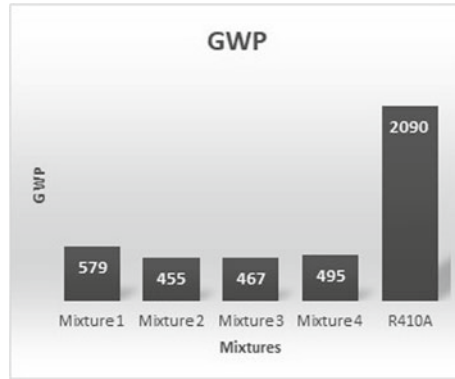


Fig. 5 Global warming potential (GWP) of various mixtures

### 4 Conclusion

Thus, the following can be concluded from above results:

- Addition of R290 lowers the GWP of the refrigerant drastically.
- But addition of R290 also reduces the COP of the system.
- R125 is the major pollutant of GWP and needs to be kept as low as possible and replaced with R290.
- R32 increases the refrigeration effect and also lowers the power input of compressor; hence, it should be kept as high as possible.
- The best mixture is obtained in mixture 4 with the composition being R32/R125/R290/R227ea(50/2/45/3) with the GWP being 495 which is a 76.315% decrease while the COP is 8.01% decrease, indicating that COP in such case can be compromised for the reduction in GWP.

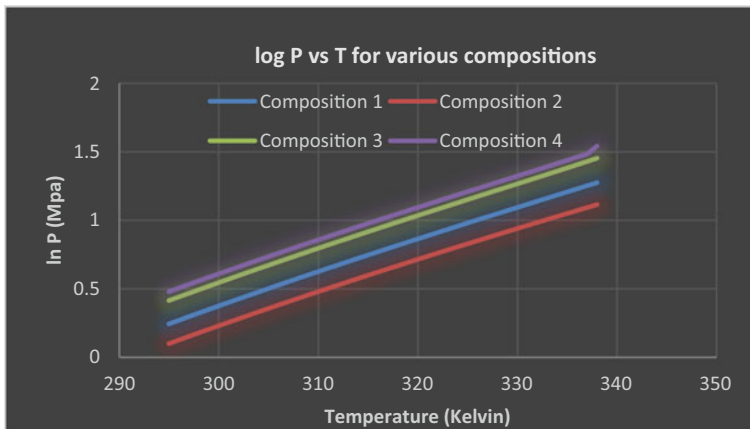


Fig. 6 log P versus log T of various compositions

## References

1. American society of heating, refrigerating and air-conditioning engineers, Inc., ANSI/ASHRAE standard 34-2016. Designation and safety classification of refrigerants. Atlanta, GA, 2016
2. Calm JM (2008) The next generation of refrigerants—historical review, considerations, and outlook. *Int J Refrig* 31:1123–1133
3. Benhadid-Dib S, Benzaoui A (2012) Refrigerants and their environmental impact Substitution of hydro chlorofluorocarbon HCFC and HFC hydro fluorocarbon. Search for an adequate refrigerant. *Energy Procedia* 1
4. Ng WB, Kamar HM, Kamsah N, Wang F-J (2019)
5. Tian Q, Cai D, Ren L, Tang W, Xie Y, He G, Liu F (2015) An experimental investigation of refrigerant mixture R32/R290 as drop-in replacement for HFC410A in household air conditioners. *Int J Refrig* 57:216–228
6. United Nations Treaty Collection. Chapter XXVII 2.a Montreal protocol on substances that deplete the ozone layer. [treaties.un.org](http://treaties.un.org).
7. Shrestha SS, Vineyard EA, Mumpower K (2016) Performance of R-410A alternative refrigerants in a reciprocating compressor designed for air conditioning applications. United States.
8. Coulomb D, Dopont JL, Morlet V. (2017) The impact of the refrigeration sector on climate change-35. Informatory note *Refrig Technol*
9. Honeywell (2018) Honeywell refrigerants roadmap
10. Uddin K, Arakaki S, Saha BB (2020) Thermodynamic analysis of low-GWP blends to replace R410A for residential building air conditioning applications
11. BITZER refrigerant report (2020)
12. IPCC (2007) Climate Change 2007: synthesis report. Contribution of working groups I, II and III to the fourth assessment report of the intergovernmental panel on climate change
13. Difluoromethane—Compound Summary. The PubChem Project. USA: National Center of Biotechnological Information
14. Tiwari AC, Barode SK, Performance analysis of vapour compression refrigeration systems using hydro fluorocarbon refrigerants. Department of Mechanical Engineering, University Institute of Technology, RGPV, Bhopal, 462024, India
15. Lemmon EW, Span R (2016) Thermodynamic properties of R-227ea, R-365mfc, R-115, and R131i. *J Chem Eng Data*. <https://doi.org/10.1021/acs.jced.5b00684>
16. NIST standard reference database (2013) NIST reference fluid thermodynamic and transport properties—REFPROP, version 10 (standard reference data program. National Institute of Standards and Technology. Website For REFPROP software <https://www.nist.gov/srd/refprop>
17. Lemmon EW (1996) A generalized model for the prediction of the thermodynamic properties of mixtures including vapor-liquid equilibrium. ProQuest Dissertations Publishing, 9701140. University of Idaho
18. Jones WP (2001) CEng, FInstE, FCIBSE, MASHRAE air conditioning engineering (5th edn), pp 241–278
19. Agarwal RS, Clark E, Ozonaction fact sheet—refrigerant blends: calculating global warming potentials



# Mortality Assessment Due to Fine-PM Exposure During 2019 Stubble Burning Season in Punjab, Haryana, and Delhi Using WHO AirQ+ model

Raghav Sharma, Vasu Singla, Aman Kaushik, and Lovleen Gupta<sup>(✉)</sup>

Department of Environmental Engineering, Delhi Technological University, Bawana Road,  
Delhi 110042, India  
lgupta@dce.ac.in

## 1 Introduction

Globally, proliferating populations, rapid urbanization, and industrialization have aggravated air quality through emissions from manufacturing, transportation, electricity generation, waste incineration, and a plethora of anthropogenic processes. The gravity of increasing air pollution can be realized from the lasting implications of spiked concentrations of gaseous and particulate pollutants on human health. Several studies have comprehensively discussed the respiratory and cardiovascular health impacts of air pollution [1–6]. The State of Global Air, 2020 estimates that air pollution was the fourth-largest cause of early deaths in 2019, with 6.67 million deaths attributable. The adverse effects of air pollution are more pronounced in heavily populated developing nations. South Asia recorded the highest population-weighted annual average  $PM_{2.5}$  concentrations, about eight times the WHO guideline of  $10 \mu\text{g}/\text{m}^3$ . Globally, India witnessed the highest population-weighted annual average  $PM_{2.5}$  concentration at  $83.2 \mu\text{g}/\text{m}^3$ , leading to about 980,000  $PM_{2.5}$ -attributable deaths [7]. The Indo-Gangetic Plains (IGP) are one of the heaviest polluted regions of the world due to myriad anthropogenic sources and high population density. The  $PM_{2.5}$  concentrations of IGP peaks during October–November due to widespread stubble burning (SB), primarily in the agriculture-intensive states of Punjab and Haryana, due to temperature inversion and low mixing height from declining temperatures post-monsoon. The widespread crop-residue burning in NW India is a major contributor to the exacerbated air quality of the IGP, as stubble burning pollutants are transported downwind to Delhi and Uttar Pradesh.

According to NASA Earth Observatory, the visible infrared imaging radiometer suite (VIIRS) sensor on the Suomi NPP satellite detected 87,000 fire incidents across Northern India, 80% of which were detected in Punjab [8]. The ISB of paddy stubble is a source of air pollutants and greenhouse gases like carbon monoxide (CO), oxides of nitrogen ( $NO_x$ ), particulate matter ( $PM_{10}$  and  $PM_{2.5}$ ), ammonia ( $NH_3$ ), polycyclic aromatic hydrocarbons (PAH), black carbon (BC), carbon dioxide ( $CO_2$ ), and methane ( $CH_4$ ) [9, 10]. The SB practice is prevalent during the months of October and November, which is accompanied by precarious haze episodes throughout the IGP. [11] mentions a large fraction of light-absorbing carbonaceous-type aerosols during haze events of November



2016, which confirms the SB practice as a major influencing factor for haze episodes. During this period, several Indian cities record maximum Air Quality Index (AQI). In November 2019, AQI in urban centers like Delhi, Ghaziabad, and Greater Noida reached potentially detrimental peaks of 487, 493, and 480, respectively, signifying severe air quality [12]. Furthermore, daily  $PM_{2.5}$  in New Delhi peaked in October–November when SB was active in IGP [13]. Beig et al. [14] utilized the SAFAR chemical transport model to determine that biomass burning contribution to Delhi's  $PM_{2.5}$  pollution in October–November peaked at 58%.

Several studies have mentioned the adverse health impacts of air pollutants emitted from ISB of agricultural residue [15–17]. Inhalation of  $PM_{2.5}$  may trigger mild symptoms like shortness of breath, chest pain, wheezing, and coughing. Exposure to fine PM may lead to an increased risk of hospital admissions, emergency room visits, worsened chronic respiratory and cardiovascular disorders, diminished lung capacity, and premature fatality [18, 19]. Although various air pollution-health impact studies with different objectives have been conducted for the major cities situated in IGP [20, 21], this study's objective is to assess the excess mortalities that would occur due to long-term exposure to elevated PM concentrations in October–November in Punjab, Haryana, and Delhi.

## 2 Methods and Tools

### 2.1 Study Locations

New Delhi (28.7041° N, 77.1025° E) was the world's most polluted capital city for the third year straight in 2020 [22]. The projected population of Delhi in 2019 was 29.596 million [23]. During the months of October and November in 2020, stubble burning contribution to Delhi's pollution peaked at 40% [24].

Haryana (29.0588° N, 76.0856° E) and Punjab (31.1471° N, 75.3412° E) are the two states which are responsible for most the stubble burning happening in India. Stubble burning is done in the months of October and November after the harvesting of the paddy crop. The projected population of Haryana and Punjab in 2019 is 28.70 million [25] and 30.46 million, respectively [26].

The Central Ambient Air Quality Monitoring Stations (CAAQMS) of Central Pollution Control Board (CPCB) [27] present in the study locations were used to obtain daily  $PM_{2.5}$  data (24-h) which was averaged over the seasonal and annual time periods to obtain mean  $PM_{2.5}$  concentrations over the two time resolutions. However, only the stations with consistent  $PM_{2.5}$  data were used to estimate mortalities at the district level. In several districts, appropriate monitoring systems with valid  $PM_{2.5}$  data were absent. The monitoring stations used to obtain  $PM_{2.5}$  data have been delineated in Table S1 of supplementary text.

### 2.2 Tools and Techniques

In the current study, Ri-MAP approach (risk of mortality/morbidity caused by air pollution) is adopted to estimate the excess numbers of deaths. Here, the attributable proportion (AP) concept is employed via AirQ+—v2.0 software, which is an open-source tool

distributed by the WHO Regional Office for Europe used for air quality impact assessment in this study. In this study, associated health risk due to exposure to PM<sub>2.5</sub> over long-term (annual and seasonal) is predicted by the model. The fraction of the health impact in a given population due to exposure to an air pollutant, assuming a proven causal relationship between exposure and health effect and no significant conflicting results in this interaction, is known as the attributable population (AP). It is calculated using the below equation:

$$AP = \frac{\sum [RR(c) - 1 \times P(c)]}{\sum [RR(c) \times P(c)]}$$

where RR(c) and P(c) denote the changed relative risk and the proportion of the target population for a specific health outcome in exposure category ‘c.’ RR is calculated as follows:

$$RR(c) = \frac{(C - T)}{10 \times (RR - 1) + 1}$$

where ‘C’ is the pollutant’s ambient air concentration, T is the pollutant’s WHO threshold level (10 ug/m<sup>3</sup>), and RR is the relative risk of the chosen health result. The rate of the health endpoint (IE) due to the exposure can be calculated using the baseline incidence (BI) of the health endpoint. Finally, the IE can be utilized to obtain the total number of cases in the study area using the equation:

$$IE = BI \times AP, NE = IE \times N$$

where N is the total population of the study area.

The mortalities assessment is based on long-term exposure (one year or seasonal) to air pollutants (Table 1).

**Table 1** WHO-specified and adopted values of baseline incidence and relative risk

Health endpoint	Pollutant	BI	RR	Reference
Total mortality	PM <sub>2.5</sub>	1013		[30]
Respiratory mortality	PM <sub>2.5</sub>	147	1.12824	[31]
Cardiovascular mortality	PM <sub>2.5</sub>	325	1.01502	[31]

The mean PM<sub>2.5</sub> concentration in a district is calculated by taking an average of all the monitoring stations selected, located within the district.

**2.3 Method Description**

In this study, AirQ+ model’s impact assessment function was employed to calculate the ENAC of total mortality (TM), cardiovascular mortality (CM), and respiratory mortality

(RM) from long-term exposure to  $PM_{2.5}$ . Here, district-level annual mean  $PM_{2.5}$  concentrations, India-specific BI values for TM, CM, and RM, and district-wise population at risk were used to estimate mortalities associated with long-term (one<sub>year</sub>) exposure to fine PM concentrations in year 'y' ( $TM_{an}$ ,  $CM_{an}$ , and  $RM_{an}$ ). Although, AirQ+ software enables the health risk assessment from exposure to  $PM_{10}$ ,  $PM_{2.5}$ ,  $NO_2$ , BC, and  $O_3$  due to both long and short-term exposure, the central focus of this study the proportion of annual mortalities caused due to fine PM during SB season.  $PM_{10}$  mean concentrations were avoided since they cannot be used in AirQ+ to evaluate attributable mortalities.  $NO_2$  on the other hand is not a major SB pollutant when compared to fine PM. Although  $NO_2$  is released during SB, the emissions are insignificant so as to cause a considerable increase in  $NO_2$  concentrations when compared to the already soaring  $NO_2$  emissions from vehicles. BC is also a major SB pollutant, but CAAQMS of CPCB in the study districts do not monitor BC concentrations.

In order to realize the objective of discerning the TM, CM, and RM attributable to SB season we utilized mean  $PM_{2.5}$  concentration during the SB period of October 23–November 15 ( $PM_{2.5\ sb}$ ), signifying the time-period for maximum satellite-detected active fire events during the harvesting season [30].

$$ENAC_{TM,CM,RM} = f(PM_{2.5\ sb}, BI_{TM,CM,RM}, \text{population at-risk})$$

However, these ENAC values would represent the mortalities that would occur due to annual exposure to  $PM_{2.5\ sb}$ . It was assumed that mortalities vary linearly with long-term exposure duration, considering that the AirQ+ Glossary permits the use of both seasonal and annual mean pollutant concentrations in long-term calculation. Hence, the long-term mortalities attributable specifically to the 23-day SB period ( $TM_{sb}$ ,  $CM_{sb}$ ,  $RM_{sb}$ ) would be

$$TM_{sb}, CM_{sb}, RM_{sb} = ENAC_{TM,CM,RM} \times \frac{23}{365}$$

The percentage of  $TM_{an}$  attributable to the SB season ( $TM_{sb}\%$ ) were calculated as follows.  $TM_{sb}\%$  was used as a metric to compare the influence of the SB season on total annual mortalities attributable to  $PM_{2.5}$  concentrations in a district.

$$TM_{sb}\% = \frac{TM_{sb}}{TM_{an}} \times 100$$

### 3 Results and Discussion

#### 3.1 Punjab

The ENAC of total mortality, respiratory mortality, and cardiovascular mortality from exposure to annual average  $PM_{2.5}$  concentration in 2019 ( $TM_{an}$ ,  $RM_{an}$ , and  $CM_{an}$ ) was the greatest in Ludhiana, followed by Jalandhar, and Amritsar. The lowest ENAC of  $TM_{an}$ ,  $RM_{an}$ , and  $CM_{an}$  was recorded in Rupnagar. For ENACP of  $TM_{an}$ ,  $RM_{an}$ , and  $CM_{an}$ , the leading district was Fatehgarh Sahib, followed by Jalandhar, and Ludhiana. The lowest ENACP of  $TM_{an}$ ,  $RM_{an}$ , and  $CM_{an}$  was observed in Amritsar.

The highest ENAC of total mortalities, respiratory mortalities, and cardiovascular mortalities associated with long-term (LT) exposure to seasonal PM<sub>2.5</sub> concentrations during the SB period in 2019 (TM<sub>sb</sub>, RM<sub>sb</sub>, and CM<sub>sb</sub>) were recorded in Ludhiana, followed by Amritsar and Jalandhar. The ENAC of TM<sub>sb</sub>, RM<sub>sb</sub>, and CM<sub>sb</sub> were the lowest in Rupnagar. In terms of ENACP of TM<sub>sb</sub>, RM<sub>sb</sub>, and CM<sub>sb</sub>, the leading district was Patiala, followed by Amritsar and Fatehgarh. The lowest ENACP of TM<sub>sb</sub>, RM<sub>sb</sub>, and CM<sub>sb</sub> was recorded in Rupnagar (25). The mean ENACP of TM<sub>sb</sub>, RM<sub>sb</sub>, and CM<sub>sb</sub> in Punjab for 2019 were 28, 6.4, and 3, respectively. District-wise ENAC of seasonal and annual mortalities has been presented in Table 2. District-wise ENACP of TM<sub>sb</sub>, RM<sub>sb</sub>, and CM<sub>sb</sub> in Punjab for 2019 have been presented in Fig. 1.

**Table 2** District-wise annual and seasonal ENAC of TM, CM, and RM in Punjab

District	TM <sub>an</sub>	TM <sub>sb</sub>	TM <sub>sb</sub> %	CM <sub>an</sub>	CM <sub>sb</sub>	RM <sub>an</sub>	RM <sub>sb</sub>
Amritsar	2529	346	13.68	825	77	356	37
Bathinda	1455	165	11.34	347	40	141	19
Fatehgarh	1693	191	11.28	470	43	203	21
Jalandhar	2223	289	13	718	65	311	31
Ludhiana	3246	438	13.49	1192	103	458	39
Patiala	1701	286	16.81	594	62	252	30
Rupnagar	854	75	8.78	224	18	97	9
Total	13,701	1,790	13	4,370	408	1,818	186

Patiala district recorded the highest percentage of TM<sub>an</sub> attributable to SB season (16.79%). Bathinda district recorded the highest percentage of CM<sub>an</sub> and RM<sub>an</sub> attributable to SB season in 2019 (11.59% and 13.41%). Minimum influence of SB season on TM<sub>an</sub> and CM<sub>an</sub> was observed in Rupnagar (8.82%, 8.24%). Ludhiana recorded the least percentage of RM<sub>an</sub> attributable to SB season. Mean contribution of TM<sub>sb</sub> to TM<sub>an</sub> across the seven study districts in Punjab was 12.64%. For CM and RM, mean contribution of SB season to CM<sub>an</sub> and RM<sub>an</sub> across the study districts was 9.50% and 10.50%, respectively. In 2019, percentage of annual mortalities attributable to the SB season was 13.04%, 9.33%, and 10.23% for TM, CM, and RM, respectively.

### 3.2 Delhi

The ENAC of total mortality, respiratory mortality, and cardiovascular mortality from exposure to annual average PM<sub>2.5</sub> concentration in 2019 (TM<sub>an</sub>, RM<sub>an</sub>, and CM<sub>an</sub>) was the greatest in North West district, followed by West, and South Delhi districts. The lowest ENAC of TM<sub>an</sub>, RM<sub>an</sub>, and CM<sub>an</sub> was recorded in New Delhi district. For ENACP of TM<sub>an</sub>, RM<sub>an</sub>, and CM<sub>an</sub>, the leading district was North West, followed by West, and East Delhi districts. The lowest ENACP of TM<sub>an</sub>, RM<sub>an</sub>, and CM<sub>an</sub> was observed in South West district.

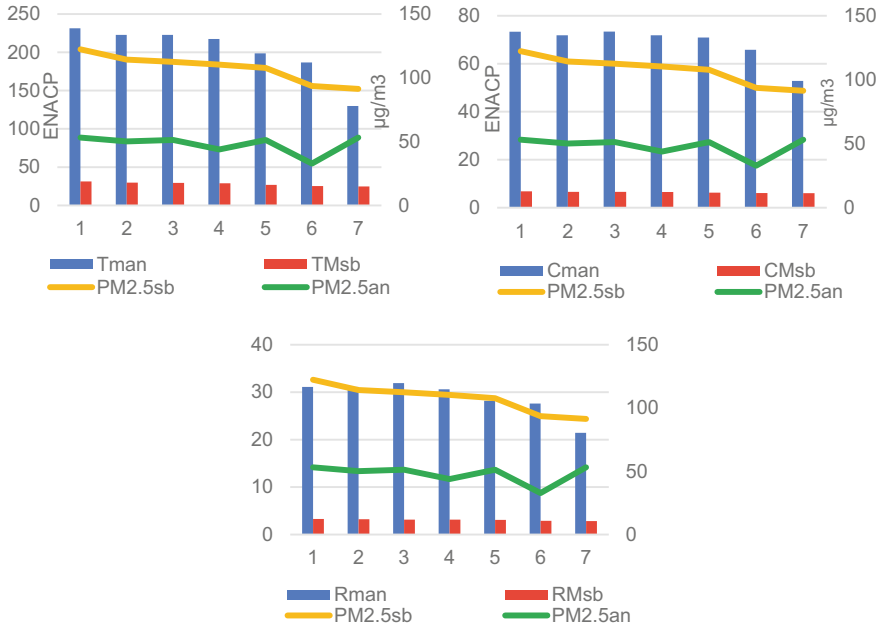


**Fig. 1** District-wise annual and seasonal ENACP of TM, CM, and RM in Punjab, 2019. (1: Patiala, 2: Amritsar, 3: Fatehgarh Sahib, 4: Jalandhar, 5: Ludhiana, 6: Bathinda, 7: Rupnagar)

The highest ENAC of total mortalities, respiratory mortalities, and cardiovascular mortalities associated with long-term (LT) exposure to seasonal PM<sub>2.5</sub> concentrations during the SB period in 2019 (TM<sub>sb</sub>, RM<sub>sb</sub>, and CM<sub>sb</sub>) were recorded in North West, followed by South and West Delhi districts. The ENAC of TM<sub>sb</sub>, RM<sub>sb</sub>, and CM<sub>sb</sub> were the lowest in New Delhi. In terms of ENACP of TM<sub>sb</sub>, RM<sub>sb</sub>, and CM<sub>sb</sub>, the leading district was New Delhi, followed by North West and West. The lowest ENACP of TM<sub>sb</sub>, RM<sub>sb</sub>, and CM<sub>sb</sub> was recorded in South West Delhi (44, 4, and 8, respectively). The mean ENACP of TM<sub>sb</sub>, RM<sub>sb</sub>, and CM<sub>sb</sub> in Delhi for 2019 were 49, 4.5, and 8.6, respectively. District-wise ENAC of seasonal and annual mortalities has been presented in Table 3. District-wise ENACP of TM<sub>sb</sub>, RM<sub>sb</sub>, and CM<sub>sb</sub> in Delhi for 2019 have been presented in Fig. 2.

New Delhi district recorded the highest percentage of TM<sub>an</sub> attributable to SB season (12.3%). It also recorded the highest percentage of CM<sub>an</sub> and RM<sub>an</sub> attributable to SB season in 2019 (8.95% and 9.95%). Minimum influence of SB season on TM<sub>an</sub>, CM<sub>an</sub>, and RM<sub>an</sub> was observed in East Delhi (9.85%, 7.89% and 8.47%, respectively). Mean contribution of TM<sub>sb</sub> to TM<sub>an</sub> across the nine study districts in Delhi was 10.68%. For CM and RM, mean contribution of SB season to CM<sub>an</sub> and RM<sub>an</sub> across the study districts was 8.34% and 9.08%, respectively. In 2019, the SB season’s contribution to annual mortalities in Delhi was 10.68%, 8.26%, and 8.96% for TM, CM, and RM, respectively.

**Table 3** District-wise annual and seasonal ENAC of TM, CM, and RM in Delhi

District	TM <sub>an</sub>	TM <sub>sb</sub>	TM <sub>sb</sub> %	CM <sub>an</sub>	CM <sub>sb</sub>	RM <sub>an</sub>	RM <sub>sb</sub>
North West	9660	1001	10.36	2091	171	1016	90
North	2112	234	11.08	482	41	231	21
North East	5242	546	10.42	1208	98	576	51
East	4257	420	9.87	950	75	457	39
New Delhi	326	40	12.27	76	7	36	4
Central	1309	146	11.15	308	26	146	13
West	6413	696	10.85	1422	119	696	63
South West	5033	538	10.69	1198	98	566	50
South	6320	721	11.41	1464	125	697	65
Total	40,672	4342	10.68	9199	760	4421	396

### 3.3 Haryana

The ENAC of total mortality from exposure to annual average PM<sub>2.5</sub> concentration in 2019 (TM<sub>an</sub>) was the greatest in Faridabad, followed by Gurugram and Rohtak. The lowest ENAC of TM<sub>an</sub> was recorded in Panchkula. The ENAC of respiratory mortality

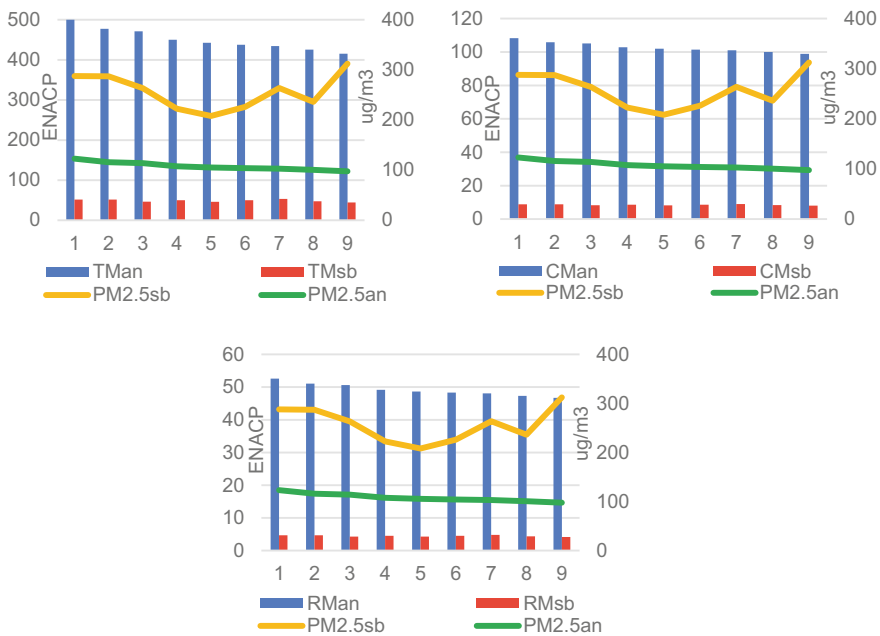


**Fig. 2** District-wise annual and seasonal ENAC of TM, CM, and RM in Delhi (1: North West, 2: West, 3: East, 4: North, 5: North East, 6: South, 7: New Delhi, 8: Central, 9: South West)

and cardiovascular from exposure to annual average  $PM_{2.5}$  concentration in 2019 ( $RM_{an}$  and  $CM_{an}$ ) was the greatest in Faridabad, followed by Gurugram and Panchkula. The lowest ENAC of  $RM_{an}$  and  $CM_{an}$  was recorded in Rohtak. District-wise ENAC of  $TM_{an}$ ,  $RM_{an}$ , and  $CM_{an}$  have been presented in Table 4. For ENACP of  $TM_{an}$ ,  $RM_{an}$ , and  $CM_{an}$ , the leading district was Faridabad followed by Gurugram and Rohtak. The lowest ENAC of  $TM_{an}$ ,  $RM_{an}$ , and  $CM_{an}$  per 100,000 people was observed in Panchkula.

**Table 4** District-wise annual and seasonal ENAC of TM, CM, and RM in Haryana, 2019

District	$TM_{an}$	$TM_{sb}$	$TM_{sb}\%$	$CM_{an}$	$CM_{sb}$	$RM_{an}$	$RM_{sb}$
Faridabad	6773	772	11.40	1603	101	759	71
Panchkula	625	65	10.40	216	14	92	8
Gurugram	1679	198	11.79	406	26	191	18
Rohtak	630	78	12.38	163	10	75	7
Total	9707	1113	11.47	2388	151	1117	104

The highest ENAC of total mortalities associated with long-term (LT) exposure to seasonal  $PM_{2.5}$  concentrations during the SB period in 2019 ( $TM_{sb}$ ) were recorded in Faridabad, followed by Gurgaon, and Rohtak. The ENAC of  $TM_{sb}$  were the lowest in Panchkula. The highest ENAC of respiratory mortalities and cardiovascular mortalities associated with long-term (LT) exposure to seasonal  $PM_{2.5}$  concentrations during the SB period in 2019 ( $RM_{sb}$ , and  $CM_{sb}$ ) were recorded in Faridabad, followed by Gurgaon and Panchkula. The ENAC of  $RM_{sb}$ , and  $CM_{sb}$  were the lowest in Rohtak. In terms of ENAC of  $TM_{sb}$ ,  $RM_{sb}$ , and  $CM_{sb}$  per 100,000 people, the leading district was Faridabad, followed by Gurugram and Rohtak. District-wise annual and seasonal ENACP in Haryana has been presented in Fig. 3. The lowest ENACP of  $TM_{sb}$ ,  $RM_{sb}$ , and  $CM_{sb}$  was recorded in Panchkula.

Rohtak district recorded the highest percentage of  $TM_{an}$ ,  $CM_{an}$ , and  $RM_{an}$  mortalities attributable to SB season (12.30%, 8.78%, and 9.73%). Minimum influence of SB season on  $TM_{an}$ ,  $CM_{an}$ , and  $RM_{an}$  was observed in Panchkula (10.36%, 8.20%, and 8.76%). Mean contribution of  $TM_{sb}$  to  $TM_{an}$  across the four study districts in Haryana was 11.47%. For CM and RM, mean contribution of SB season to  $CM_{an}$  and  $RM_{an}$  across the study districts was 8.53% and 9.35%, respectively.

In 2019, the SB season's contribution to annual mortalities was 11.47%, 6.32%, and 9.31% for TM, CM, and RM, respectively.

## 4 Conclusion

This study has attempted to discern the health endpoints such as total mortality, cardiovascular mortality, and respiratory mortality attributable to  $PM_{2.5}$  exposure in 2019 at the district-level in Punjab, Haryana, and Delhi. While health endpoints have been calculated for long-term (annual) exposure, the central focus is to investigate the mortalities attributable to aggravated  $PM_{2.5}$  concentrations during the SB season. A total of

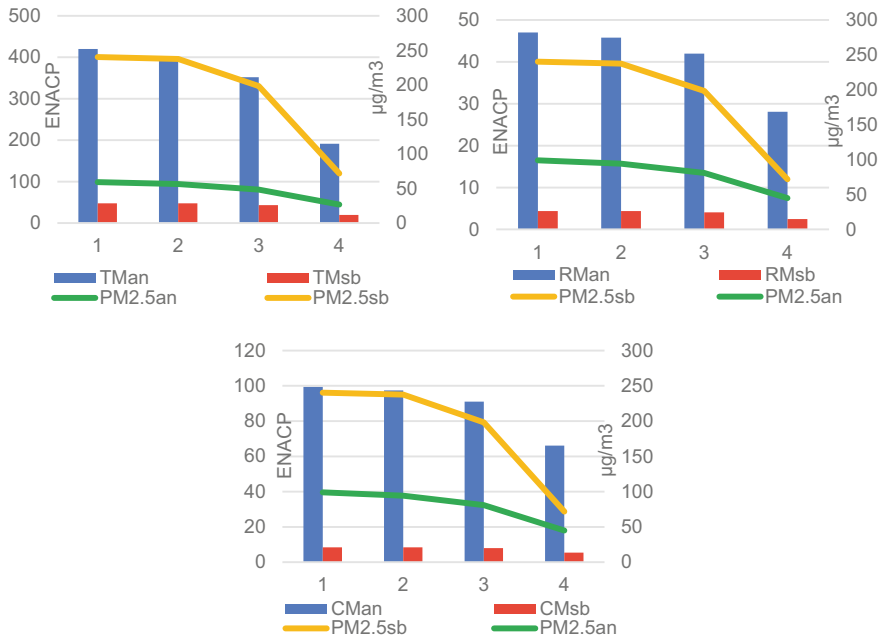


**Fig. 3** District-wise ENACP of TM, CM, and RM due to annual exposure and SB season (1: Faridabad, 2: Gurugram, 3: Rohtak, 4: Panchkula)

1790, 408, and 186 cases of TM, CM, and RM, respectively, were attributable to the SB seasons in 2019 in the seven study districts of Punjab. The total  $TM_{sb}$ ,  $CM_{sb}$ , and  $RM_{sb}$  in Delhi were 4342, 760, and 396, respectively. The total  $TM_{sb}$ ,  $CM_{sb}$ , and  $RM_{sb}$  in the four study districts of Haryana were estimated to be 1113, 151, and 104, respectively.

In 2019, Punjab recorded the highest  $TM_{sb}$  % (13%), followed by Haryana (11.47%) and Delhi (10.68%). The average ENACP of  $TM_{sb}$  across the study districts in 2019 was the greatest in Delhi (49), followed by Haryana (39) and Punjab (28). Moreover, since the average district population and  $PM_{2.5}$  concentration of Delhi is much greater than Punjab and Haryana due to an enhanced degree of urbanization and economic activity, the ENAC of  $TM_{sb}$  are also the greatest in Delhi. Districts with higher ENACP are characterized by higher  $PM_{2.5}$  levels, while higher ENAC is characterized by a larger population. It is evident from this study that SB activity exacerbates the health risk in populous locations with already high base levels of  $PM_{2.5}$  like Delhi, Faridabad, Gurugram, and Jalandhar, thereby causing an acute stress on fine PM-related mortalities. Such studies that quantify the impact of unsustainable practices like SB on human health can prove to be an eye-opener and call-to-action for policymakers. A holistic analysis of the lives lost solely due to elevated fine PM during the SB season proves to be a much more compelling tool to draw the attention of policy formulators toward forming a systemic policy for tackling this public health peril. Furthermore, a focused approach on singling out the cause-effect relationship between poor air quality and a high risk of mortality, apart from sensitizing concerned authorities, helps prepare healthcare institutions for tackling cases related to air pollution.



## References

1. Pope CA, Dockery DW, Schwartz J (1995) Review of epidemiological evidence of health effects of particulate air pollution. *Inhalation Toxicol* 7(1) (1995)
2. Héroux ME, Anderson HR, Atkinson R, Brunekreef B, Cohen A, Forastiere F et al (2015) Quantifying the health impacts of ambient air pollutants: recommendations of a WHO/Europe project. *Int J Publ Health* 60(5)
3. Kampa M, Castanas E (2008) Human health effects of air pollution. *Environ Pollution* 151(2)
4. Cohen AJ, Brauer M, Burnett R, Anderson HR, Frostad J, Estep K et al (2017) Estimates and 25-year trends of the global burden of disease attributable to ambient air pollution: an analysis of data from the Global Burden of Diseases Study 2015. *The Lancet* 389(10082)
5. Lelieveld J, Evans JS, Fnais M, Giannadaki D, Pozzer A (2015) The contribution of outdoor air pollution sources to premature mortality on a global scale. *Nature*, 525(7569)
6. Manisalidis I, Stavropoulou E, Stavropoulos A, Bezirtzoglou E (2020) Environmental and Health Impacts of air pollution: a review. *Front Public Health* 8
7. Health Effects Institute (2020) State of Global Air 2020. Boston, MA
8. NASA Earth Observatory. A Busy Season for Crop Fires in Northwestern India. [https://eoimages.gsfc.nasa.gov/images/imagerecords/147000/147547/seasonalburning\\_tmo\\_2020313\\_lrg.jpg](https://eoimages.gsfc.nasa.gov/images/imagerecords/147000/147547/seasonalburning_tmo_2020313_lrg.jpg). Last accessed 21 Mar 2021
9. Singh J, Singhal N., Singhal S, Sharma M, Agarwal S, Arora S (2018) Environmental implications of rice and wheat stubble burning in North-Western States of India. *Adv Health Environ Safety* 47–55
10. Awasthi A, Agarwal R, Mittal SK, Singh N, Singh, K, Gupta PK(2011) Study of size and mass distribution of particulate matter due to crop residue burning with seasonal variation in rural area of Punjab, India. *J Environ Monit* 13(4)
11. Kanawade VP, Srivastava AK, Ram K, Asmi E, Vakkari V, Soni VK et al (2020) What caused severe air pollution episode of November 2016 in New Delhi? *Atmos Environ* 222
12. Abdurrahman MI, Chaki S, Saini G (2020) Stubble burning: effects on health & environment, regulations and management practices. *Environ Adv* 2
13. Bray, CD., Battye, WH., Aneja, VP. The role of biomass burning agricultural emissions in the Indo-Gangetic Plains on the air quality in New Delhi, India. *Atmos Environ* 218
14. Beig G, Sahu SK, Singh V, Tikle S, Sobhana SB, Gargeva P et al (2020) Objective evaluation of stubble emission of North India and quantifying its impact on air quality of Delhi. *Sci Total Environ* 709
15. Agarwal R, Awasthi A, Singh N, Mittal SK, Gupta PK (2013) Epidemiological study on healthy subjects affected by agriculture crop-residue burning episodes and its relation with their pulmonary function tests. *Int J Environ Health Res* 23(4)
16. Singh J (2018) Paddy and wheat stubble blazing in Haryana and Punjab states of India: a menace for environmental health. *Environ Qual Manage* 28(2)
17. Kumar P, Kumar S, Joshi L (2015) Socioeconomic and environmental implications of agricultural residue burning. Springer, Nature
18. Kim KH, Kabir E, Kabir S (2015) A review on the human health impact of airborne particulate matter. *Environ Int* 74
19. Pope CA., Dockery, DW (2006) Health effects of fine particulate air pollution: lines that connect. *J Air Waste Manage Assoc* 56(6)
20. Kumar A, Mishra RK (2018) Human health risk assessment of major air pollutants at transport corridors of Delhi, India. *J Transport Health* 10
21. Manojkumar N, Srimuruganandam B (2021) Health effects of particulate matter in major Indian cities. *Int J Environ Health Res* 31(3)

22. IQ Air. World's Most Polluted Cities 2020. <https://www.iqair.com/world-most-polluted-cities>. Last accessed 21 Mar 2021
23. India Population 2020. Population of Delhi – 2020, <https://indiapopulation2020.in/population-of-delhi-2020.html>. last accessed 20 Mar 2021
24. At 40 per cent, stubble burning contribution in Delhi's pollution soars to season's high. The Economic Times. 1 Nov 2020
25. India Population 2020. Population of Punjab—2020. <https://indiapopulation2020.in/population-of-punjab-2020.html>. Last accessed 20 Mar 2021
26. Government of Punjab. Know Punjab. <https://punjab.gov.in/know-punjab/>. Last accessed 20 Mar 2021
27. Central Pollution Control Board. Central Control Room for Air Pollution—All India. <https://app.cpcbcr.com/ccr/#/caaqm-dashboard-all/caaqm-landing/caaqm-comparison-data>, last accessed 1/3/2021
28. Maji KJ, Dikshit AK (2016) Deshpande, A. Human health risk assessment due to air pollution in 10 urban cities in Maharashtra, India. *Cogent Environmental Sci* 2(1)
29. Aggarwal P, Jain S (2015) Impact of air pollutants from surface transport sources on human health: a modeling and epidemiological approach. *Environ Int* 83
30. Chhabra A, Sehgal VK, Dhakar R, Jain N, Verma R (2019) Monitoring of active fire events due to paddy residue burning in Indo-Gangetic plains using thermal remote sensing. *ISPRS Int Arch Photogrammetry Remote Sens Spat Inf Sci*. XLII-3/W6



# Design and Analysis of Spur Gear, Helical Gear, and Bevel Gear by Using ANSYS

Anuj Kumar Singh<sup>(✉)</sup>, Swapnil Kumar, Brahma Nand Agrawal,  
and Pawan Kumar Singh Nain

Department of Mechanical Engineering, Galgotias University, Greater Noida, India  
anujkumaretah751@gmail.com

## 1 Introduction

Gears are the mechanical component used to transmit power to the system. It is a rotating element having a cut tooth known as teeth, these teeth mesh with another gear teeth to transmit power and torque. Gears are used in a variety of machines, some are small as a wristwatch to heavy machines like automobile, the aerospace industry, marine, and many more. Spur gears are the basic type of gear in which teeth are external as well as internal, teeth are made parallel to an axis of the wheel. Some of the other types of gears are helical, worm, bevel, etc. Gear's use can be found in many types of machinery. Gears are used as the main component to transmit power in many types of machinery. Due to its compact size and a high degree of reliability, gears are a major choice of designer is present. Furthermore, enhancement in gear design is a major demand of industry because of its wide range of uses and to development of more lightweight and high-performance gears. In advancement in material science and newly developed materials in recent years, like composite material, alloy, etc., are used in gears to increase their performance. Although gears are simple but designing gear is a more complex and complicated task, which is done by engineers. The vibration and noise produced by the gear affects the transmission of power [1, 2]. For several years, several measures are adopted to minimize these effects and strengthen the service lifetime of gears like heat treatment or adjusting microgeometry. The main aim of design improvement is to increase the life of components. Fatigue occurs in components which fail the machine and can sometimes be led to an accident. Fatigue is generally understood as the breaking of material due to constant cyclic or continuous loads. The fatigue starts when there are some impurities in the structure of manufacturing defects or near fillet sections, and initial a small crack is developed will eventually become bigger and bigger over time [3, 4]. There is much reason for a gear failure like low-strength material used in gears, crack generation in fillet region, impurities during gear making, etc. All these features ultimately lead to gear failure. Bending stress and deformation cause the structural failure in root part [5]. Selecting material for gear is important to increase its fatigue life [6–8]. Aluminum alloys show weight reduction of approx. 55–67% as compared to other materials [9]. The selected material must have high-strength and high-fatigue life. With proper cutters, wear in gears can be reduced [10, 11]. Composite material which provides high strength and less weight is sometime also used for gear manufacturing [12].

For many years, gears are being studied by the designer to understand the precision and to reduce the error in power transmission. ISO, DIN, and AGMA are some of the standards followed in the industry to develop gears. These standards are made by taking special care in factor of safety that is why they provide high safety toward any accident. ANSYS is the most widely used software in industries for analysis, but there is many software that can be used. ANSYS can do finite element analysis over gear teeth, but one can also view results in each neighborhood of gear [13, 14].

The aim of this paper to design and analysis of the spur gear, bevel gear, and helical gear in solid works and compares the results using different methods in ANSYS.

## 2 Different Types of Gears

The three gears used in this paper for comparative study are spur gear, helical gear, and bevel gear. There are many more types of gear, some are discussed below.

### 2.1 Spur Gear

The simple type of gear is spur gear. The design of spur gear is consisting of a disk with project radially. The teeth of spur gear are not straight, but the edge of the teeth is straight and parallel to the axis rotation. These gears are mostly fitted with parallel shaft and not created axial thrust by the tooth loads. These gears are not battering work in high speed but excellent work in moderate speed. Direct metal laser is used to make gears with complex design with excellent surface finish [15]. This gear is divided into two main categories such as internal and external gear. Internal gears have teeth cut inside of the body, while the external gear has teeth cut on the outside that is the circumference of the body. In these types of gears, amplitude of stiffness of gear mesh and coefficient of friction are non-linear [16].

### 2.2 Bevel Gear

The axis of the two gear is intersecting at 90, and the tooth-bearing face of the gear is conical shaped is known as bevel gear. The tooth of bevel gear rea different type like a spiral, straight or Zerol. A straight tooth bevel gear is parallel to the generator of the cone. The gear is resembling spur gear and only conical rather than cylindrical. Spiral gear in this type of gear of teeth is spiral. In this gear, the teeth are spiral but not angled.

### 2.3 Worm Gear

The gear is an arrangement form of the screw and is similar in appearance to spur gear. The gear design using worm and worm wheel is considerably smaller than one made from plane spur gears and has the driver axes 90° to each other. The different types of gear used in the worm gear. First non-throated worm gear or groove and single toothed worm gear.

### 3 Methodology

Finite element analysis can successfully be used to determine the loads in composite materials as well as in general materials [17, 18]. It is a numerical method to analyze mechanical parts which are under load that do not vary with time. It is used to solve the majority of engineering problems because of its flexibility and diversity and many techniques provided by it to customize the problem parameter and results. It calculates an approximate result which is quite satisfactory. As an exact solution cannot be achieved by the mathematical equation and need the experimental result, this method is nearly accurate to analyze material under static load. One can view results at a specific position, draw the graph, visualize animation, and many more in the finite element analysis.

#### 3.1 Parameters

Module—6m gear teeth—30 pinion teeth—15

Pressure angle—20° (spur and helical gears) and 45 (bevel gears).

#### 3.2 Material Property

High-strength structural steel has the ability to work under a high-dynamic load. So, the material is selected as structural steel [19].

##### Material properties:

Structural steel

Coefficient of thermal expansion:  $1.2201e-005 \text{ C}^{-1}$

Density of material:  $7.85001e-006 \text{ kg mm}^{-3}$

Specific heat:  $4.3399e+005 \text{ m J kg}^{-1} \text{ C}^{-1}$

Compressive yield strength: 250 MPa

Thermal conductivity:  $6.05021e-002 \text{ W mm}^{-1} \text{ C}^{-1}$

Tensile ultimate strength: 460 MPa

Resistivity:  $1.69857e-004 \text{ } \Omega \text{ mm}$

#### 3.3 Meshing

Meshing is the property of ANSYS to divide the element into smaller sections or regions. More the division in the model high will be accuracy. ANSYS provides many different techniques to mesh the model. Each has its area of application. Since the gear has teeth in it and the body of gear has many curvatures in it, therefore, proximity and curvature type of meshing are done in this paper. This type of method does not mesh the face properly, but the curvature region is highly meshed. Since the stress develops at the teeth and area near it. So, the curvatures present in the teeth need to be meshed properly to

obtain accurate results, and the mesh at the middle can be ignored. The meshed model of spur gear is shown below to show how proximity and curvature function meshes the model (Fig. 1).

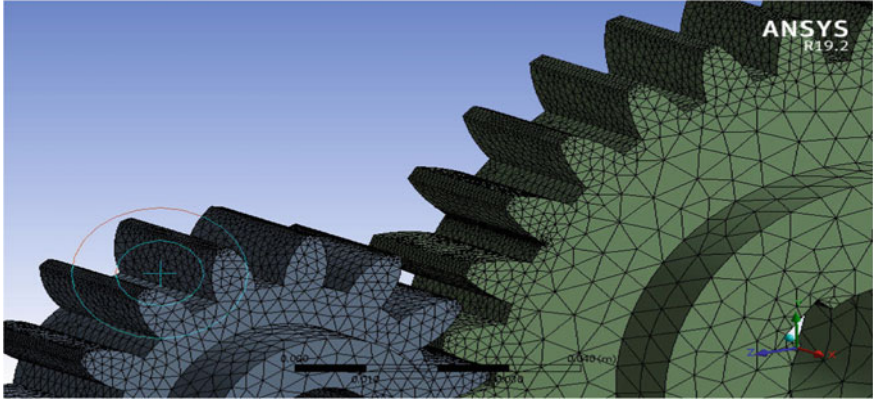


**Fig. 1** Meshed spur gear

### 3.4 Analysis Parameters

The moment of 1715 Nm is applied at the center of bigger gear, and frictionless supports are given at the center of two gears to stop the motion in the x direction. Similarly, frictionless supports are given at the face of gears to limit the movement of gears in the z direction (Table 1).

**Table 1** Analysis parameters

Loads/support	Frictionless support1	Frictionless support2	Moment
State	Fully defined		
Suppressed	No	No	No
Defined by		Component	
Magnitude		1715 N m (ramped)	
Direction		Z axis	

## 4 Results and Discussion

In this section, both analyzes have been done for comparative study among three gears as explain in earlier Sect. 2. The various results are in the form of graphs as follows:

- **Spur gears**
- **Helical gear**
- **Bevel gear.**

From the results obtained, it can be seen that the deformation occurred at the contact region that is the teeth area and the center of the face shows minimum deformation which is right because the main work of transferring power is done by the teeth. From Fig. 2, the max deformation is at the tip of teeth that is 0.00026358 m in spur gears. While the minimum is at the center. In the case of helical gears, the max deformation is less than the spur gears which is at the teeth 0.000030062 m, and same as the spur gear, the center area has the least deformation as seen in Fig. 5. From Fig. 8, it is cleared that the deformation in bevel gears is highest among the three that is 0.0013472 m. The values of deformations obtained are given below (Figs. 3, 4, 6, 7, 9 and 10):

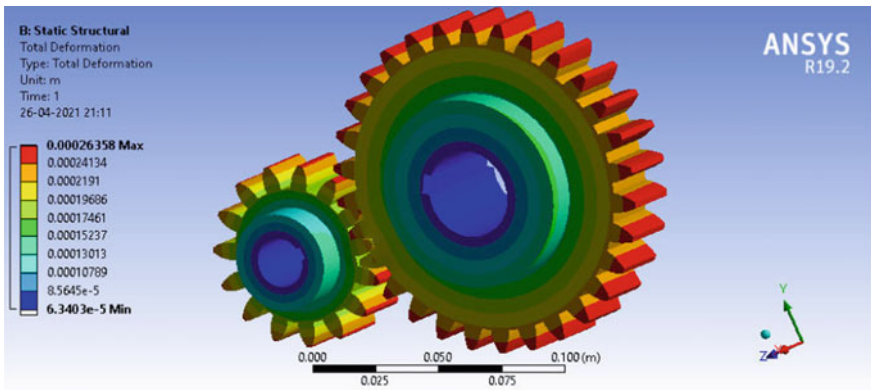


**Fig. 2** Total deformation in spur gear

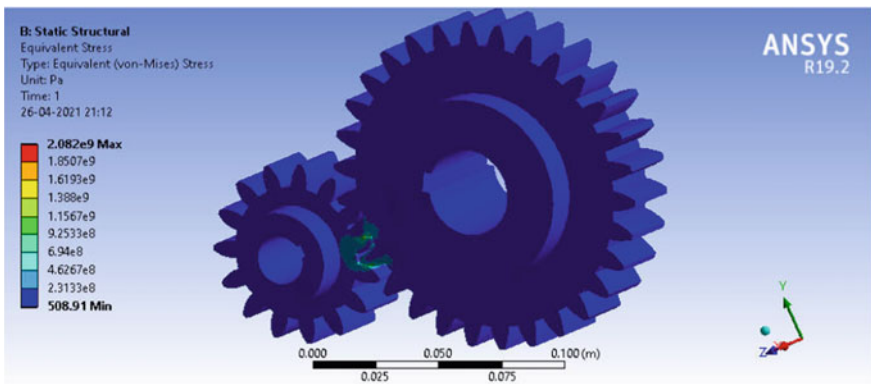


**Fig. 3** Stress distribution of spur gear

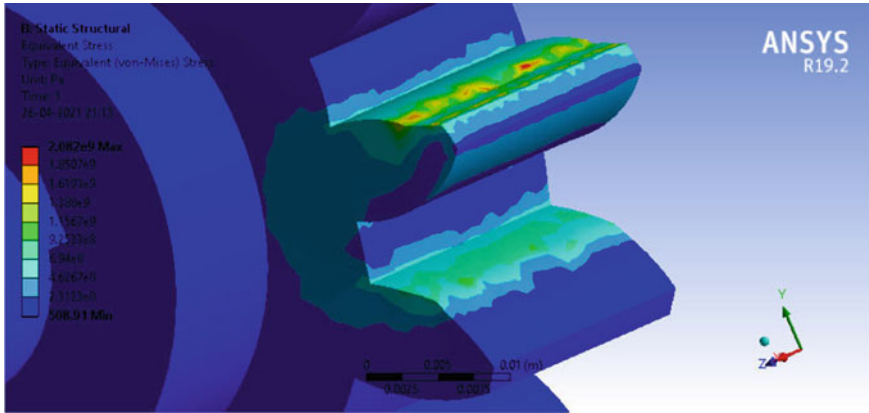


Fig. 4 Stress distribution of spur gear

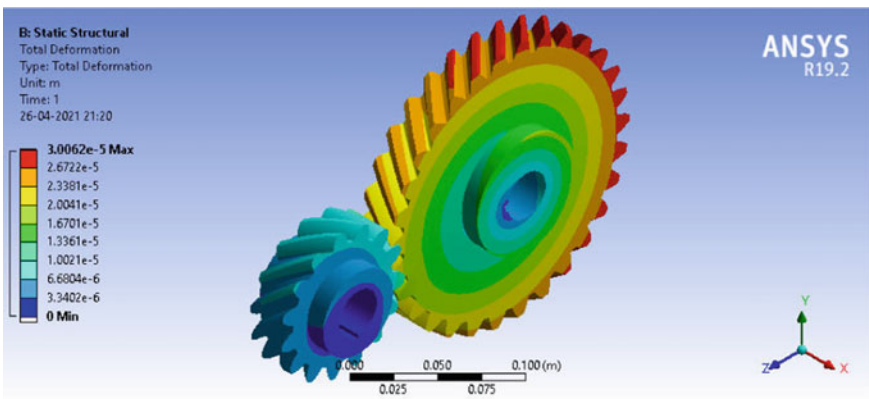


Fig. 5 Total deformation in helical gears

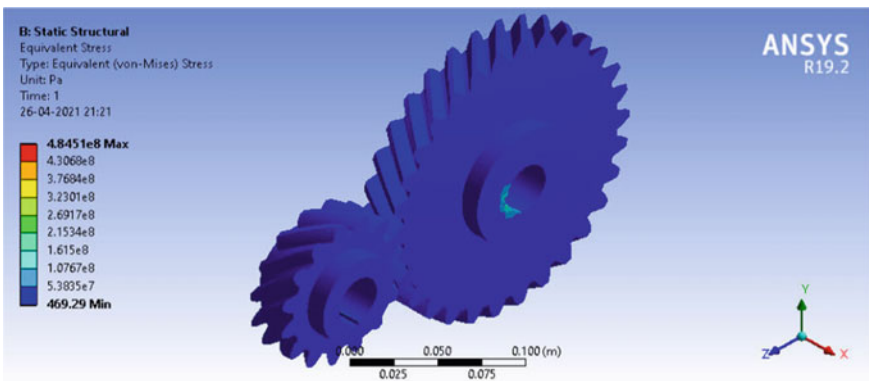


Fig. 6 Stress distribution of helical gears



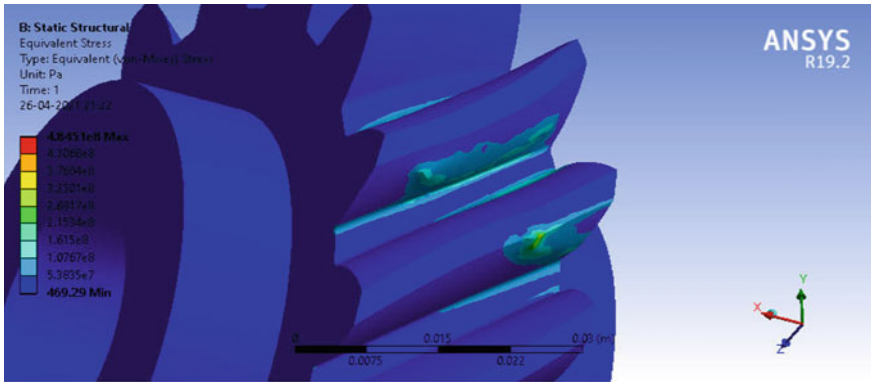


Fig. 7 Stress distribution of helical gears

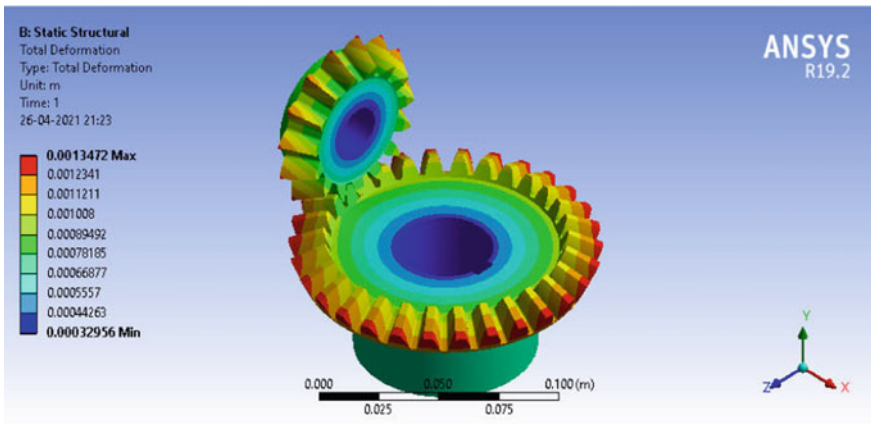


Fig. 8 Total deformation in bevel gears

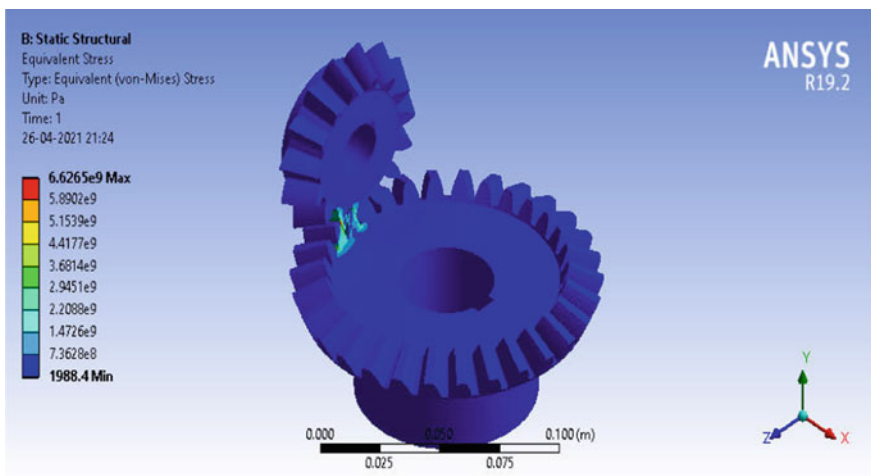
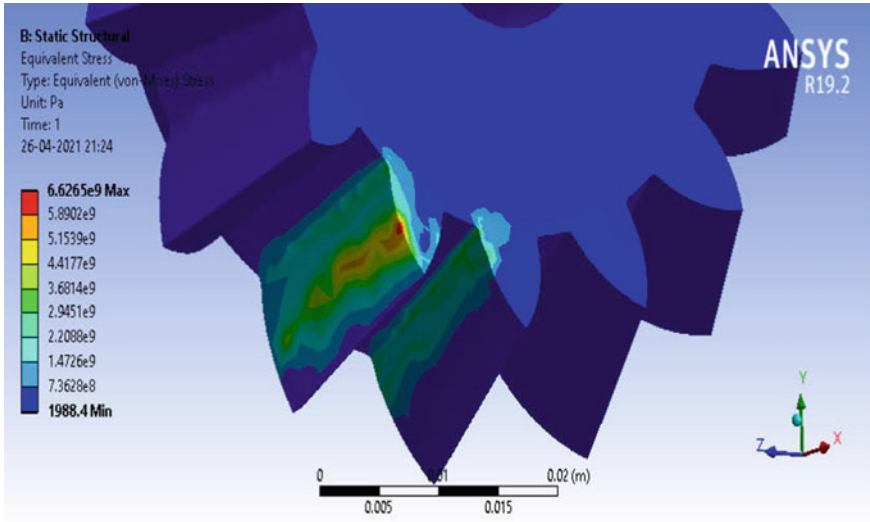


Fig. 9 Stress distribution in bevel gears



**Fig. 10** Stress distribution in bevel gears

1. Spur gear: 0.000063403–0.00026358 m
2. Helical gear: 0–0.000030062 m
3. Bevel gear: 0.00032956–0.0013472 m

It is clear from Fig. 3, the stress developed in spur gears in the contact region is maximum. Figure 4 shows the magnified view of the contact region, and the stress value is calculated as  $2.082e+9$  Pa in spur pinion teeth. From Fig. 6, a small amount of stress developed at the center approx.  $5.3857e+7$  to  $1.675e+8$  in helical gears. Figure 7 shows that the contact region experiences the stress of  $4.851e8$  Pa maximum at some small point of helical pinion teeth, but the major portion of the contact region has the stress of approx.  $5.385e7$  to  $1.615e8$  Pa. The bevel pinion teeth have experienced the stress of  $6.6265e9$  Pa as maximum, and the major portion has developed the stress of approx.  $7.3628e8$  Pa to  $2.2088e9$  Pa (Figs. 9 and 10) which is very close to spur gear stress value. The stress values are shown below:

1. Spur gears: (508.91– $2.082e9$ ) Pa
2. Helical gears: (469.29– $4.851e8$ ) Pa
3. Bevel gears: (1988.4– $6.265e9$ ) Pa.

## 5 Conclusion

This paper has been compared the results of three different gears under similar conditions. The model is prepared through Solidworks and exported to ANSYS for further analysis. Solid works assembly feature is used to mate the gear and pinion before sending to the ANSYS. From the results, conclusions are as follows:

- It is clear that minimum deformation is experienced by the helical gears of value 0.00030062 m, however, the maximum deformation occurs in case of bevel gears that are of 0.0013472 m.
- The bevel gears show the maximum formation of stress near teeth with 2.2088e9 Pa which is nearly the same as in spur gears.
- The helical gears show the least stress formation among all three gears. So, helical gears performed better in both the analyzes.

## References

1. Wang C (2021) Multi-objective optimal design of modification for helical gear. *Mech Syst Signal Process* 157:107762. ISSN 0888-3270
2. Brethee K, Zhen D, Gu F, Ball A (2017) Helical gear wear monitoring: modelling and experimental validation. *Mech Mach Theory*. 117:210–229. <https://doi.org/10.1016/j.mechmachtheory.2017.07.012>
3. Patil SS, Patil S, Sunil Kumar S, Saviraj AS (2018) A review on influence of various technological processes on mechanical properties of aluminum alloys. *IOP Conf Ser Mater Sci Eng* 376(1). <https://doi.org/10.1088/1757-899X/376/1/012043>
4. Schijve J (2003) Fatigue of structures and materials in the 20th century and the state of the art. *Int J Fatigue* 25(8):679–702. [https://doi.org/10.1016/S0142-1123\(03\)00051-3](https://doi.org/10.1016/S0142-1123(03)00051-3)
5. Chavadaki S, Nithin Kumar KC, Rajesh MN (2021) Finite element analysis of spur gear to find out the optimum root radius. *Mater Today Proc*. ISSN 2214-7853. <https://doi.org/10.1016/j.matpr.2021.01.422>. <https://www.sciencedirect.com/>
6. Raptis KG, Savaidis AA (2018) Science direct experimental investigation of spur gear strength using photoelasticity thermo-mechanical modeling of a high pressure turbine blade of an airplane gas turbine engine. *Procedia Struct Integr* 10:33–40. <https://doi.org/10.1016/j.prostr.2018.09.006>
7. Ghosh S, Ghosh R, Barman R (2017) Design and manufacturing of spur gear tooth : a new approach towards composites. *June*. <https://doi.org/10.21817/ijet/2017/v9i3/170903510>
8. Patil MNU, Chaphalkar SP, Chaudhari GL (2017) Stress analysis of spur gear by using different materials : a review. *(June):355–363*
9. Kumar A (2020) Modal analysis of helical gear train using ansys. 604–607
10. Zheng F, Zhang J, Yao L, Tan R (2021) Investigation on the wear of spur gears generated by modified cutter 9(2):288–300
11. Kalay OC, Doğan O, Yılmaz TG, Yüce C, Karpat F (2021) A comparative experimental study on the impact strength of standard and asymmetric involute spur gears. *Meas J Int Meas Confed* 172:108950. <https://doi.org/10.1016/j.measurement.2020.108950>
12. Aziz E (2001) An intelligent system for spur gear design and analysis. *March 2015*. <https://doi.org/10.1115/DETC2001/DAC-21037>
13. Santhosh J, Salia K, Iyasu J, Fanta W (2021). Spur gear mesh analysis under explicit dynamic speed conditions. 2:15–25
14. Apparao D, Jagannadha Raju MV (2020) Design and analysis of spur gear manufactured by DMLS process. *Mater Today Proc*. <https://doi.org/10.1016/j.matpr.2020.07.078>
15. ZZhao Z, Han H, Wang P, Ma H, Zhang S, Yang Y (2020) An improved model for meshing characteristics analysis of spur gears considering fractal surface contact and friction. *Mech Mach Theory* 158:104219. <https://doi.org/10.1016/j.mechmachtheory.2020.104219>

16. Zhao Z, Han H, Wang P, Ma H, Zhang Z, Yang Y (2021) An improved model for meshing characteristics analysis of spur gears considering fractal surface contact and friction. *Mech Mach Theory* 158:104219. ISS (Online). Available: <https://www.sciencedirect.com/science/article/pii/S0094114X20304365>
17. Singh V, Chauhan S, Kumar A (2012) Finite element analysis of a spur gear tooth using analysis and stress reduction by stress relief hole. *Int J Emerg Trends Eng Dev* 6:491–495
18. Balogh G (2017) Design and analysis of composite spur gears using finite element method design and analysis of composite spur gears using finite element method. <https://doi.org/10.1088/1757-899X/263/6/062048>
19. Bannykh OA, Sorokin AM, Bannykh IO, Lukin EI (2018) Structure and mechanical properties of high-strength structural steels. *Russ Metall* 2018(6):528–532. <https://doi.org/10.1134/S0036029518060046>



# Detection of Counterfeit Drugs in Medical Supply Chain Using Blockchain Technology

Abhinav Sanghi, Aayush, and Ashutosh Katakwar<sup>(✉)</sup>

Department of Mathematics and Computing, Delhi Technological University, New Delhi, India  
ashutoshkatakwar.26@gmail.com

## 1 Introduction

A Blockchain in simpler terms can be stated as: It is a linked list of blocks where each block is linked with the previous block by the means of a cryptographic hash. An individual block contains the transaction data, a timestamp (which denotes when that block was created), hash of the previous block, and preferably a nonce value (it can be thought of as, the miner is already given a part of a hash, and the miner has to find out the remaining hash corresponding to that block. Whosoever is able to find that first his/her block gets added to the chain and they receive a reward for that). The use of blockchain has increased over the years and is still increasing especially in the industrial fields. The only reason for this is the increased security of the confidential transactions.

The advantage of a distributed ledger is it removes the chances of a single point of failure. So as a result even if a very important node fails in the network, then still, we can retrieve the current set of transaction records or any other information from some other node that has the copy of the ledger. So if any transaction happens within the network, may it be addition of blocks or anything, then that information will be stored on all the ledgers, and hence in some way, this also guarantees the consistency of the data. By the term “distributed,” we mean that there are various subsystems involved in building, and this entire network and those subsystems run certain computerized programs in order to maintain the working of this entire network. Before adding any data in the original chain, it is necessary to have certain checkpoints so that the data that are going to be added are authentic/genuine. These checkpoints are achieved with the help of consensus. It means that any data that are going to be added have been verified initially by certain nodes, and after this checking, only then, they are going to be added. It is achieved by assigning some special roles to certain nodes in the network. A node in this system can be defined as a separate body that checks whether any data added are valid or not, or it may check whether a person who wants to enter this system is authentic or not, and it does many more roles. The joining/linking for the traditional case is done with the help of memory addresses but in the case of blockchain, memory address linking is not a very good way to achieve security over that data. Therefore, we use cryptographic hashes instead of memory addresses. We form a link between blocks using cryptographic hash, and the data integrity is maintained with the help of cryptographic mechanisms. The cryptographic hashes are generated on the basis of certain parameters such as data and

previous hash, and there are various algorithms having different mechanisms to generate the hash. Some of those algorithms are SHA-256, SHA-1, SHA-2, MD5, and many more. So, blockchain is a kind of a data structure that is maintained in a distributed manner, and the data are copied over certain nodes in the network with the main objective to maintain the integrity/consistency of the data. Till now, no one is able to tamper the data inside the blockchain. It has been achieved only because of the security mechanisms behind the entire network and the data integrity that it maintains. So what is the need of a blockchain? So let us explain this with the help of a practical example: Everyone usually maintains a note or a log of events. So for example, any search engine maintains a history section which tells which page we have visited recently. These matters are kept in something known as an event log. These logs are very important in case of some major mishappenings in the network. The most visible problem in case of keeping these logs is that it can suffer with data tampering. So a person or a malicious program designed by a person can extremely affect its performance by deleting some important information or by adding some useless information and many such things. So later on, when you check it, then possibly you are going to process some wrong information. So, the above limitation of a log system is overcome by blockchain. Blockchain is designed in such a way that it makes data tampering almost impossible. Blockchain has the property of immutability. The immutable property of a blockchain makes it free from any kind of tampering by any malicious party or a malicious program.

So with the help of this technology, we can store the same type of data as we stored in the events log but with much greater data integrity and security. All these data/informations that exist within the network are kept in an immutable ledger. So this is the basic mechanism behind blockchain. In this manner, data tampering is made almost impossible. Even till now, there is no possible case/news which is related to tampering of data in the blockchain. Blockchain was initially known because of the discovery of bitcoin. The idea behind all these can be summarized as: It is a paperless currency which can be exchanged for goods and services. Transactional data between any two parties are stored in blockchain without the control of any centralized agency. People usually know about blockchain by the means of bitcoin. But as we go deeper in our topic, we are going to see that cryptocurrency is only prevailing in the market because of the blockchain, and it is not the other way around. In the absence of which may be there could not be any concept of cryptocurrencies. You may have also heard a lot of news regarding many organizations or companies shifting their majority of confidential transactions on blockchain. For instance, the UAE Government has taken an advanced initiative by transferring approximately half of their daily transactions to blockchain. This will help the country to become the first country to be fully or maximally operated by blockchain. Many other countries are following the same path. The time is near when every government realizes the importance of this technology and similarly adopts certain strategies in order to develop their country. At current times, the majority of countries are facing the issue of black money and corruption. May be with the help of this technology, these issues can be removed to some extent.

## 2 Background

### 2.1 Problems in Current Pharmaceutical Industry

The current **supply chain** system in this industry is obsolete, and also it does not provide clear visibility over various points in this supply chain (manufacturers, wholesalers, etc.). According to a WHO report [1], around 10.5% of the pharmaceutical drugs in the markets of low- or middle-income countries are fake. Hence, there is a need to develop a strong model to overcome the issue of counterfeiting drugs. Also, because of their system being outdated, they are in no position to tackle the problems or threats posed by the hackers. If we talk about human health, then fake and false drugs can insert a heavy impact. These fake medicines reduce the immunity strength of the human body. So, this is the serious issue and also the main concern of the government because it can impact humans in a direct way. Now, the main question arises, which drugs are called counterfeit? So, this was answered by the World Health Organization (WHO). So, to answer this particular thing, World Health Organization clearly mentioned that all drugs that are intentionally and unethically mislabeled. They further clarified that these fake medicines are also original but they generally did not pass the quality procedure and requirements.

Several research has been conducted in this area. McGhin et al. [2] addressed the future research side of the medical sector. Kumar et al. [3] highlighted various challenges of blockchain for healthcare such as scalability restrictions, high development cost, standardization challenges, cultural resistance, and regulatory uncertainty. International Criminal Police Organization carried a raid in 2009 and seized about 2 crores counterfeit pills, sachets, etc. This raid is mainly performed Asian countries including China. Many outlets were closed due to this and about 3 dozen people were arrested. The main drugs that are collected from them are of antimalarial, birth prevention, etc. Michael Deats is associated with WHO in the vigilance and safety department. He mentioned that if in market, the products are insufficient, then the empty space will be occupied by counterfeit versions. According to WHO, Internet is the main key to appear in the market, and in the market, pharmaceuticals are considered as an opportunity for fakes. For the region of southeast Asia, a warning has been issued in 2016, when drugs used in vaccination and for hepatitis are found to be fake. This warning comes with various hidden indications. The main point that it highlights that this business of fake drugs is widely spread in Asian regions and it needs to be addressed on the urgent basis by the Government of respective country. According to World Custom Organization, the areas where the sea transport is in widely used is the epicenter of these fake drugs business. This include countries like Thailand, Myanmar, etc., So, now, a main thing comes into consideration that this type of business is greatly affected by the locations. If we talk about Asia, then India and China are the countries which constitute over 260 crore population. So, in short, these two countries require medicines in a large numbers, and hence, large numbers of medicines are also manufactured to meet the demands. So, due to this, the fake/counterfeit drugs are present in large numbers because it can be mixed with the original drugs in a very smooth manner. Half the deaths from this opioid crisis within the North American country were from the Dolophine hydrochloride analgesic, factory-made in China. The medicines that are being manufactured in Asia have a direct impact on the population of different countries in the world. Not solely, this, however,

a much bigger drawback is that as a result of this technique the production, distribution, and consumption of counterfeit medication has increased. Pretend drug producers generally use the brand of authentic producers and since of that the patient is unable to make your mind up about the genuineness of the medicine. Counterfeiting is completed everywhere the globe, however, principally in developing countries where there is a bottom check on the whole system of drug production. Associate degree calculable 10–30% of medicines oversubscribed in developing countries are counterfeit. Same is the case with medical instrumentation. Globally, around 8–10 p.c of all medical devices are of faux origin. These fake equipment devices damage patient rights, damage complete, and thus company's image and cause loss to original equipment manufacturers. It may also offer the user/doctor with the incorrect diagnosis of a patient's condition. For the bar of production of pretend medication associated with degreed medical devices, industries would like an economical and secured approach that is obtainable by a blockchain.

## **2.2 Impact of Counterfeit Medicines**

These drugs have many impacts on pharma companies along with the humans. Basically, these fake drugs reduce the profit for the manufacturing company. Also this can cause serious issues in human health, and they can also be sick or it can affect the human skin also. There are various examples that show the impact of counterfeit drugs. If we talk about Asia, people of Pakistan were affected in 2011. About 300 people died due to fake heart medicines. In some country, about 100 people died by taking throat curing medicines. We can see that throat curing medicines are very general in normal routine. So, it can have a large effect also. So, in short, these counterfeit drugs are very dangerous for humans. Medicines are used for curing disease but unfortunately, these fake drugs always invite some more problems rather than curing the existing ones. In Europe, there are directives for medicines which are given by the European Government. These types of initiatives should also be implemented in other regions of the world especially in Asia. In Europe, it is officially implemented in 2019 which says that every medicine that is sold in Europe should have 2 main key features. One is the 2D barcode which is also called as unique identifier, and another one is a type of seal. So, if this seal found to be broken, then that particular medicine cannot be sold anywhere in Europe.

## **2.3 Purpose of Using Blockchain**

So, from above discussion, it is evident that this drug supply chain management is lacking at various points. So, now if we want to improve this old system, then we can take help of blockchain technology which enables to track all the history of drugs from its origin to customer point. It allows the manufacturers to have a clear view on the journey of the product. And from the client side, the client can see whether the product is from a legitimate manufacturer and is the product tampered or not. Every time the ownership of the product changes, the transaction can be saved in a blockchain to create a permanent history of a product. So if anything goes wrong, then it will be easy to trace back and find the point of error.



### 2.3.1 What Traceability Will Help in Achieving?

Once a drug/medical device is produced by a manufacturer, it is registered on the blockchain, and then on every stage of transfer of that drug/medical device from one level to another, it is authenticated by tracking methods. As its ownership changes across its journey, all of this information is stored on the chain and hence tracing an error becomes easy. So, because of blockchain, the manufacturer can see the various steps involved between the points of generation to the customer point.

### 2.3.2 Security and Seclusion?

We need to ensure that only the legitimate users in the supply chain are able to push data on the blockchain, and therefore, in this proposed system, we will be using a permissioned blockchain. So as blockchain basically contains a common ledger between various participants of the network, therefore, the single point of failure disadvantage in a centralized system is overcome. Any new transaction is replicated to all the nodes, and the ledger of each node is updated. This is how security is maintained.

## 3 Methodology

As described earlier, we will be using permissioned blockchain, therefore, participating parties require permission before performing any of the functions such as adding and auditing on the blockchain. Private blockchains provide us with an extra layer of security, and also since, we are going to store data related to the healthcare industry, so security is of utmost concern. Now, suppose if one entity in the blockchain wants to purchase the drugs from some other entity, then every physical transfer of the drugs from one level to another will be accompanied with a digital data (referred as transaction) related to that transfer being stored on the blockchain. Now, if A wants to check whether the drug is genuine or not, then he/she will first query the drug's id and see the journey of that drug. If there is no information regarding that entity, then it has to be a fake drug or fake medical device. Below are the images for the smart contract architecture and the flow of transaction execution (Figs. 1 and 2).

### 3.1 Flow of the Implementation

The following are the partners that are involved in medical supply chain:

- Logistic service providers
- Drug distributors
- Pharmacy shops or hospitals
- Medical patient
- Drug manufacturers.

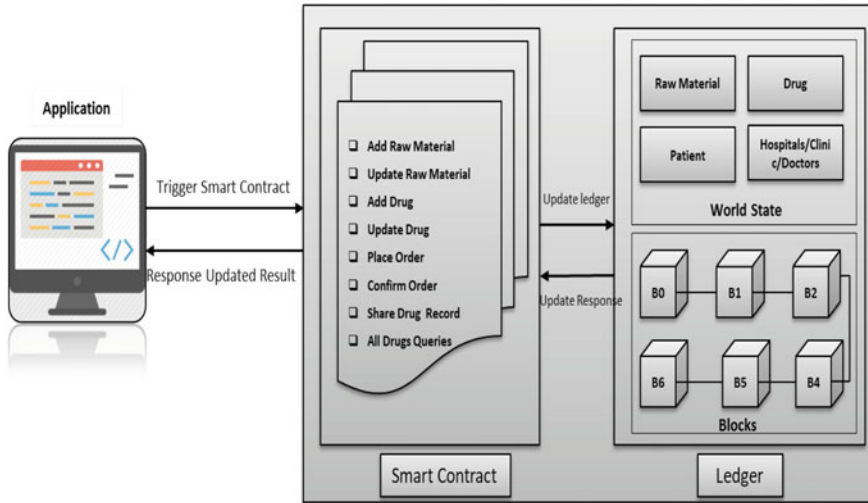


Fig. 1 Smart contract architecture

**Step 1: Generation of QR code and adding on to the medicine during the manufacturing process**

During the manufacturing stage, addition of the generated code on all medicines. Important information is contained in QR code like:

- Time stamp
- Name of item

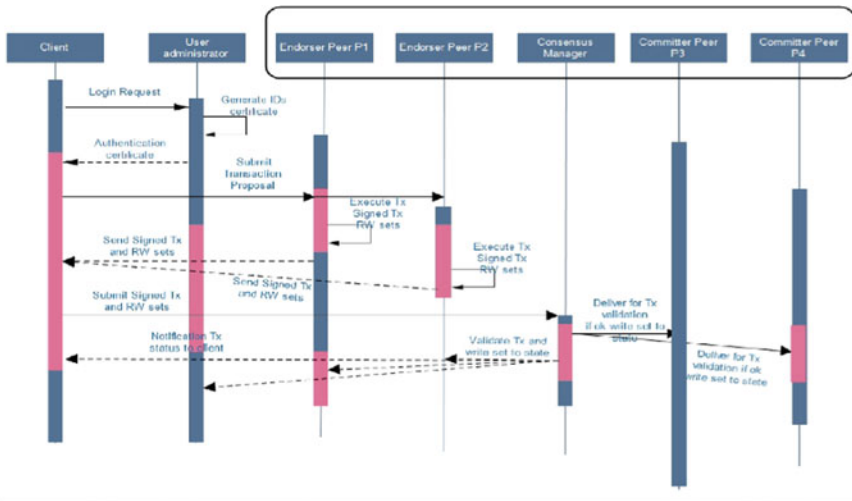


Fig. 2 Transaction execution procedure

- Location
- Expiry date and manufacturing.

Producer adds data which gets put away on the blockchain, which gives straightforwardness to the gracefully chain and partners. IoT-empowered vehicles with temperature sensors can be utilized to transport the medications to the wholesalers to empower cold-chain delivering. The drugs moved by the IoT-empowered vehicles can likewise send the ongoing area to the blockchain, permitting the public authority organizations and partners to follow drug conveyance helpfully.

The continuous area to the blockchain can likewise be moved through IoT-empowered vehicles, which can permit the partners and government organizations to follow medications' conveyance helpfully.

### **Step 2: Hospitals/pharmacists receive the medicine through wholesaler**

Wholesalers can confirm the cause of prescriptions subsequent to gathering them from the coordination specialist organizations, by the help of hash id that are stored in blockchain.

Gotten prescriptions are approved by the wholesalers and verify the exchanges. After that it is successfully appended to the blockchain.

The brilliant agreements get set off by the marked exchanges to send the medications to the emergency clinics/drug specialists.

### **Step 3: Drugs are received, and the source is verified by the pharmacists**

In any case if producer tries to offer counterfeit drugs with an assigned id to medical specialist or patients, at that point, all things considered the exchange would be viewed as invalid because of the bogus data added about the medication.

Any unapproved individual without a legitimate private key cannot finish an exchange in the medication flexibly chain environment.

In this way, drug specialists can discover oddities promptly inside the exchanges.

The exchange among them and the merchant is added to the blockchain once the drug specialist approves the got medications, guaranteeing the legitimate arrangement.

### **Step 4: When patients buy the medicine, they can verify its originating place by scanning the QR code**

Patients can check the QR code appended to the medication's bundling through their portable application and can guarantee if the medication they are purchasing is protected or not. They can know its source and quality norms.

Data are gotten from the blockchain utilizing the hash id connected to the QR code for the patient's entrance. Connected to the medication's id puts away on the blockchain, patients can likewise give criticism or appraisals for the medications they purchase.

It would be simple for others to choose if the particular medication is powerful or not with the assistance of rating added by the patient. Exchanges information of the drug flexibly chain kept up by the blockchain is permanent, agreement driven, and straightforward. This blockchain-based arrangement can help move the administration model of the medication flexibly bind from guideline to observation net.

### 3.2 In What Form the Data are Going to be Stored on Blockchain and How?

We are going to store the textual data on the chain. Once a drug has been manufactured, it will be assigned a unique id (cryptographic hash), and it will be registered on the chain. The hash generated will depend on various factors such as the medicine name, its chemical composition, the producer, its expiry date, and few more. To add an extra layer of security for every particular type of drug, a unique code can be assigned (binary code or alphanumeric code) and that code can also be taken into account to generate the hash for a particular block. A block contains data such as the name of the entity performing the transaction (such as manufacturer and distributor), date, time, the unique hash generated for that particular drug, and most importantly the previous block's hash. Now, suppose if the client wants to check the authenticity of the drug, then all he/she has to do is copy the code on that medicine and paste it on the application, and on the backend, it searches for the block related to that particular drug, and if found, then the client is shown the history of that drug, or if not found, then that drug is fake.

## 4 Conclusion

In this paper, we proposed a use case of blockchain technology in the healthcare sector. Serious health issues, including deaths, may occur if the users consume counterfeit drugs. Several counterfeit drugs have been detected in the market of developing countries. We addressed the issues in current pharmaceutical supply chain management, and explained how blockchain can be used to add traceability and visibility to drug supply and overcome the issue of counterfeiting. The proposed model aims to track the movement of drugs from the industry to the patient while keeping the patient's private data secret. In the last, we explained the stepwise working of the proposed method. This model can further be used for medical equipment such as oximeters and thermometers. This model can be implemented either by hyper-ledger fabric or Ethereum depending on the requirements.

## References

1. The impact of counterfeit drugs in south and south-east Asia, Available: <https://www.europeanpharmaceuticalreview.com/article/92194/the-impact-of-counterfeit-drugs-in-south-and-south-east-asia/>
2. McGhin T, Choo KR, Liu CZ, He D (2019) Blockchain in healthcare applications: research challenges and opportunities. *J Netw Comput Appl* 135:62–75
3. Kumar T, Ramani V, Ahmad I, Braeken A, Harjula E, Ylianttila M (2018) Blockchain utilization in healthcare: key requirements and challenges. In: *IEEE 20th international conference on e-health networking, applications and services*, pp 1–7. Czech Republic
4. Hasan et al (2020) A blockchain-based approach for the creation of digital twins. *IEEE Access* 8:34113–34126
5. Lin C, He D, Kumar N, Huang X, Vijayakumar P, Choo KR (2020) HomeChain: a blockchain-based secure mutual authentication system for smart homes. *IEEE Internet Things J* 7(2):818–829
6. Zhang C et al (2020) BSFP: Blockchain-enabled smart parking with fairness, reliability and privacy protection. *IEEE Trans Veh Technol* 69(6):6578–6591

7. Liu X, Sun SX, Huang G (2020) decentralized services computing paradigm for blockchain-based data governance: programmability, interoperability, and intelligence. *IEEE Trans Serv Comput* 13(2):343–355
8. Seven S, Yao G, Soran A, Onen A, Muyeen SM (2020) Peer-to-Peer energy trading in virtual power plant based on blockchain smart contracts. *IEEE Access* 8:175713–175726
9. Jaiman V, Urovi V (2020) A consent model for blockchain-based health data sharing platforms. *IEEE Access* 8:143734–143745
10. Guo H, Li W, Nejad M, Shen CC (2020) Proof-of-event recording system for autonomous vehicles: a blockchain-based solution. *IEEE Access* 8:182776–182786
11. Yang X, Yi X, Nepal S, Kelarev A, Han F (2020) Blockchain voting: publicly verifiable online voting protocol without trusted tallying authorities. *Future Gener Comput Syst* 112:859–874
12. Yuan Y, Wang F (2016) Towards blockchain-based intelligent transportation systems. In: *IEEE 19th international conference on intelligent transportation systems*, pp 2663–2668, Brazil
13. Mengelkamp E, Notheisen B, Beer C, Dauer D, Weinhardt C (2018) A blockchain-based smart grid: towards sustainable local energy markets. *Comput Sci Res Dev* 33:207–214
14. Turkanovic M, Holbl M, Kosic K, Hericko M, Kamisalic A (2018) EduCTX: a blockchain-based higher education, credit platform. *IEEE Access* 6:5112–5127
15. Kishigami J, Fujimura S, Watanabe H, Nakadaira A Akutsu A (2015) The Blockchain-Based digital content distribution system, In: *IEEE Fifth international conference on big data and cloud computing*, pp 187–190, China
16. Mettler M (2016) Blockchain technology in healthcare: the revolution starts here. In: *IEEE 18th international conference on e-health networking, applications and services*, pp 1–3, Germany
17. Agbo CC, Mahmoud QH, Eklund JM (2019) Blockchain technology in healthcare: a systematic review. *Healthcare* 7(2). Article no. 56
18. Siyal AA et al (2019) Applications of blockchain technology in medicine and healthcare: challenges and future perspectives. *Cryptography* 3(1), Article no. 3
19. Esposito C, Santis A, Tortora G, Chang H, Choo KR (2018) Blockchain: a panacea for healthcare cloud-based data security and privacy? *IEEE Cloud Comput* 5
20. Gordon WJ, Catalini C (2018) Blockchain technology for healthcare: facilitating the transition to patient-driven interoperability. *Comput Struct Biotechnol J* 16:224–230



# Recognizing Energy Wasting Households Using Data Mining and Incorporating the Cybersecurity Concept

Rahul Balout<sup>(✉)</sup>, Aaroahi Kumari, and Mayank Panchal

Department of Electronics and Communication Engineering, Delhi Technological University,  
Delhi 1100042, India

rahulbalout\_2k17ec135@dtu.ac.in

## 1 Introduction

Most of the times, the government aims to provide subsidies to customers to motivate them to reduce their consumption of electricity. But certain times, for example, considering the current situation of COVID-19, the government runs out of funds and goes in a financial debt instead. All of us have witnessed the situation of India when we were hit by the second wave of the deadly disease across our entire nation. While a lot of states were still able to manage the condition, Delhi specifically recorded a peak in the number of patients each day. Also, the worst part was the lack of availability of the oxygen cylinders. Had the government not provided with free electricity, there would have been a chance of having funds for the health sector as well. To help this scenario, instead of going up for heavy financial losses, the government can instead go for technology to determine the people who are using electricity effectively and those who are not. For those who tend to come out as good customers, they could be awarded with some benefits. While others could be charged some fine to help them not repeat energy wastage again. This way the nation would seek three advantages: sustainable development, financial sustainability, and development in technology. In our research, we have used the dataset for 50 residential apartments in Delhi and grouped the people into good and bad customers using unsupervised K-means clustering technique from machine learning. We give our dataset to our machine and allow it to display patterns between our features using clusters. The main method used is the K-means clustering algorithm, however, we have also included the use of 6 classification algorithms (logistic regression, decision tree, Gaussian Naive Bayes, K-nearest neighbor (KNN), support vector machine (SVM), random forest) to see which classification algorithm actually fits best for our dataset. We all know that data are the new oil. In this world, wherein everybody's data are displayed on the Internet, it is highly crucial to safeguard the data using cybersecurity techniques. We aim to provide our people, whose data we have considered in our dataset, the sense of security and thus to further secure our data we use AES encryption and decryption techniques.

## 2 Literature Review

Energy consumption is a major problem around the world which is being worked upon by a lot of researchers. The energy consumption in residential buildings around the world is increasing day by day with the increase in the expectations of people to live a luxurious lifestyle. Researchers around the world are also trying to research on energy consumption of residential buildings. Working with the quantity of datasets depends on the users. Certain times the user aims to go for a dataset containing high number of features stored in a data warehouse. Considering the fact that the researchers went in for a dataset of 370 clients from the university from the year 2011 to 2014 [1], other times the users may choose to go in for a comparatively lower range of features for their dataset. For example, researchers from Russia went in for the dataset for 288 people instead [2]. A major loss of data occurs due to missing or not a number (Nan) values. To overcome this problem, mean and mode are used for the prediction of missing data. Nan values are usually found in large datasets. The dataset from Chubu University faced the same scenario [1].

While researchers from Japan tried to work out on the dataset of Chubu University and came to a conclusion that it was possible to determine the electricity consumed using base consumption, involvement of certain human activities and air conditioning [1], researchers from UK realized that the major areas of energy wastage during peak hours arised due to activities involving cooking/eating, screen time, and laundry [3]. The accuracy prediction varies with the knowledge of researchers. Some found Loess Kalman, bagging (a technique majorly used in natural language processing), SVR, RF to be highly useful for accuracy prediction [2], while some simply went up for formula-based methodology to predict the accuracy of their model [1]:

$$\text{Accuracy} = \frac{Ap}{Tp} * 100\% \quad (1)$$

where  $Ap$  is the number of accurately classified patterns and  $Tp$  is the total number of patterns.

Discussing about the major languages used for machine learning, some find it easier to deal with R language while others prefer Python over it. Use of R has been seen by researchers from UK, wherein they focused on finding the numbers of clusters using NbClust package in R [3].

Many researchers have tried to rank residential buildings using clustering techniques on the basis of climate, characteristics of buildings, like the type and the area of a building, the heating and the cooling services provided in a building, and the behavior of the occupant residing in a building [4]. Estimation of the power consumption of electrical appliances is given a priority by some researchers [5]. However, some aim to predict the energy consumption of the whole residence instead, which is further on based on the historical data of energy consumption where taking the previous year data of residents is given importance [6]. Based on that data, the predictions for the energy consumption of residential buildings are carried out.

The combination of software and hardware can produce brilliant results when it comes to conducting a research. Using sensors to detect the occupancy and the movement of occupants inside, a residence was done in Lyon for two houses. This helps the

researchers to record the dynamic behavior of occupants in a house. Methods like cluster analysis, CPA, and ARM were further used to observe the patterns of energy wastage in the residences [7]. While our aim was focused in including the software world to learn about the hidden patterns from our dataset, the hardware was kept aside to ensure the security of our data. We made sure that we collected the data for not just two but hundred households instead. We further on clustered our data into 5 clusters using the elbow method and predicted the accuracy using other algorithms to finally come to a conclusion as to which algorithm comes out to be the best for our database. Securing the files using modern tools of cybersecurity like AES encryption and decryption was carried out using.

### 3 Methodology

In this paper, we classify residential apartments on the basis of their electricity consumption. We collect data using Google forms and store it in a spreadsheet. We then load it in our Colab file and work upon it. Using k-means clustering, it is an easy task in Colab, Kaggle, or Jupyter Notebook. The libraries used are simple, and so are the formulas. However, computing the same using pen and paper can be a long process. This is the power of machine learning we get to witness using real-time analysis of the projects.

We further normalize data using normalization techniques. Also, we try to find the correlation between the features using heatmap from seaborn library Matplotlib works great too, but seaborn definitely provides better visualization than matplotlib library. We can easily see even the histograms alongside our plot using seaborn.

Checking out Nan values is highly crucial. Though we know that the data we have collected does not really contain any missing values, we still check it using our code to make sure no Nan values exist for our dataset.

Using the features of our data: the bill, the energy consumed, and the number of occupants in the family, we let our machine produce and recognize patterns on the basis of our dataset. Using sklearn library, we import k-means elbow method to find out the number of clusters that can be formed out of our dataset. We arrive at a conclusion of formation of 5 clusters. Our clusters clearly help us to indicate the customers who are wasting energy and the others who are not.

After applying k-means clustering algorithm to divide the apartments into categories, we use 6 classification techniques to classify our apartments. Using these classification techniques, we create different models which we apply on our dataset. Using this model, predict in which category does any new incoming apartment entry belongs to. We measure the accuracy of each model in order to identify which model fits best to our dataset and helps us to classify apartments more accurately. The techniques which we use are as follows:

- Logistic regression
- Decision tree
- Gaussian Naive Bayes
- K-nearest neighbor
- Support vector machine



- Random forest.

We split our apartments dataset into train and test datasets in the ratio 75:25 (train:test). We use train dataset to train our model. Then, we use our test dataset to calculate the accuracy of our model by predicting the category of an apartment of test dataset and then comparing the predicted category with the actual category of the apartment. Like this we calculate the accuracy of all the models which we make using all the different techniques listed above and find the best suited model for our dataset.

Now to protect the privacy of the people in residential apartments, i.e., to protect the data in our dataset which contain some personal data of the people, we use AES encryption technique to encrypt our data in case our server got hacked and our data get leaked.

In AES algorithm, we input a message string and a key which are of 128 bits in size. Then, our message goes through 10 rounds of transformations. Each round have 4 type of transformations through which our message string passes through. Key has to play an important role in this 10 rounds. At the end of 10th group of transformation rounds, we get our encrypted data which we store in our database. At the time of usage of dataset, we decrypt our data and use it. We code AES algorithm in VHDL language using ISE software and we run this algorithm on a FPGA board of Xilinx. We are using Xilinx FPGA board Nexus a7. We used universal asynchronous receiver/transmitter (UART) protocol to input 128 bit of message and key and get output to/from FPGA board.

### 3.1 K-Means Clustering

K-Means is partitioning-based algorithm [8]. The aim is finding a fixed number of partitions which minimize the measure of squared Euclidean distances between cluster centroids and artifacts. Suppose  $\{X = x_i \parallel i = 1,2, \dots, n\}$  is a dataset where  $n$  defines number of objects,  $k$  defines number of clusters, and  $m_j$  defines centroid of cluster  $c_j$  where  $j = 1, 2, \dots, k$ . Algorithm then uses the Euclidean distance formula as shown in Eq. (2), in order to calculate distance between a centroid and a data object [9].

$$\begin{aligned} \text{Euclidean Distance}(X, Y) &= ((X_1 - Y_1)^2 + (X_2 - Y_2)^2 \\ &+ \dots + (X_{N-1} - Y_{N-1})^2 + (X_N - Y_N)^2)^{1/2} \end{aligned} \tag{2}$$

where  $X$  is first data point,  $Y$  is second data point,  $N$  is number of characteristics/attributes. Now, the first object is assigned to a cluster whose center is closest to the first object. Then, the cluster’s centroid/center changes as the center of mass of all the objects in that cluster, then the new center is used for distance calculation between cluster and new object. This process goes on till all the objects in the data space is clustered [10, 11].

### 3.2 Logistic Regression

It is a classification algorithm which uses supervised learning in estimating likelihood of chosen variable. Generally, logistic regression is called binary logistic regression in

which we have 2 classes only, but it can also be used in a scenario where we have more than 2 classes. A logistic regression model predicts the probability of a target variable belonging to a particular class/category. It is one of the basic classification algorithms and is used to solve many classification problems like finding where an e-mail is spam or not, where a person has cancer or not, etc.

### 3.3 Decision Tree

A decision tree is an algorithm in which input space of the dataset get divided into regions which mutually exclusive. Each of these regions has name, value, and/or action which is assigned to that region which defines its data points. As decision tree is transparent in nature, so one can know how the decision are taken just by following the tree structure [12]. Decision tree has a structure of a tree which consists of internal and external nodes which in-turn are connected by branches. Internal node is the decision-making unit of the tree which tests a decision function in order to decide the child node it should visit next. On the other hand, there are no child node associated with external node rather a mark or an attribute is associated with external node which tells about the data due to which that node is visited. On the other hand, two steps are need in a large number of other decision tree construction algorithms. First, a massive decision tree is cultivated, then in second step, we pruned the tree in order to reduce its size and data overfitting.

The classification tree is a pruned decision tree that is used for classification purposes [13]. In order to build a decision tree, we have to measure the entropy and knowledge gain [12].

### 3.4 Gaussian Naive Bayes

Gaussian Naive Bayes is a technique that uses the Bayesian theorem to classify inputs with a high dimensionality. Based on the input, the Bayesian classifier will calculate the most likely output. It is also possible to update the probabilistic classifier by adding new raw data at runtime [14]. With the given class variable, Gaussian Naive Bayes classifier assumption is that there is no bearing on the presence (or absence) of any other feature with the presence (or absence) of a specific feature of a class. For example, a fruit could be called an apple if it is round in shape and red in color. All of this properties are considered by Gaussian Naive Bayes classifier to independently contribute to the likelihood that the given fruit is an apple even if there is any dependency or presence of any other class feature.

### 3.5 K-Nearest Neighbors

In KNN classification algorithm, a unknown data point is classified on the basis of its closest neighbor class which is defined. In KNN algorithm, based on the value of k which tells the how many nearest neighbors should be considered to define a sample data point's class, the distance between the unknown data point and known data points is calculated using some chosen attributes of the data points. Then, the k number of closest known data points are used to classify the unknown data point according to the class which is in majority in those k known data points.

### 3.6 Support Vector Machines

Algorithmically, separating boundaries is build by support vector machines between datasets by solving a constrained quadratic optimization problem. With help of various kernel functions, various degrees of non-linearity and versatility can be used in the model [15]. In recent years, a lot of research attention is attracted by help vector machines as they can be derived from advanced statistical ideas and limits on the generalization error can be determined for them [16].

### 3.7 Random Forest

Random forest is supervised learning algorithm. It is majorly used in classification problems. Like a huge number of tree make up a forest like that in random forest algorithm, it make a number of decision trees from the given dataset and make prediction based on each tree, and at the end, it votes for the best solution out of all. It is a better approach then a single decision tree as it averages the result which minimize the overfitting problem.

### 3.8 Advanced Encryption Standard

AES algorithm is based on an iterative approach. It is based on two common techniques for encrypting and decrypting, i.e., data substitution and permutation network (SPN). In AES algorithm, the message string (plaintext) is 128 bits (16 bytes) long in size. AES converts every message string into a  $4 \times 4$  matrix and then work with that matrix. The number of transformation rounds through which the message passes is determined by the key size. In AES algorithm, there are three different key sizes to encrypt and decrypt data, i.e., 128 bits, 192 bits, or 256 bits. Number of rounds is based on the key size; for example, 10 rounds for 128 bit keys, 12 rounds for 192 bit keys, and 14 rounds for 256 bit keys [17]. In our paper, we have use key size of 128 bits hence 10 rounds. Each round includes the following four steps as illustrated in Fig. 1.

- Substitute bytes transformation
- Shift rows transformation
- Mix columns transformation
- Add round key transformation.

### 3.9 Classifier Accuracy

There are some criteria that can be used to test the efficiency of classifiers, such as accuracy, precision, and recall, which are discussed further below [12].

**Accuracy** of a classifier is given by the percentage of correctly classified data points by total data points.

$$\text{Accuracy} = \frac{(tp + tm)}{\text{Total Samples}} \quad (3)$$

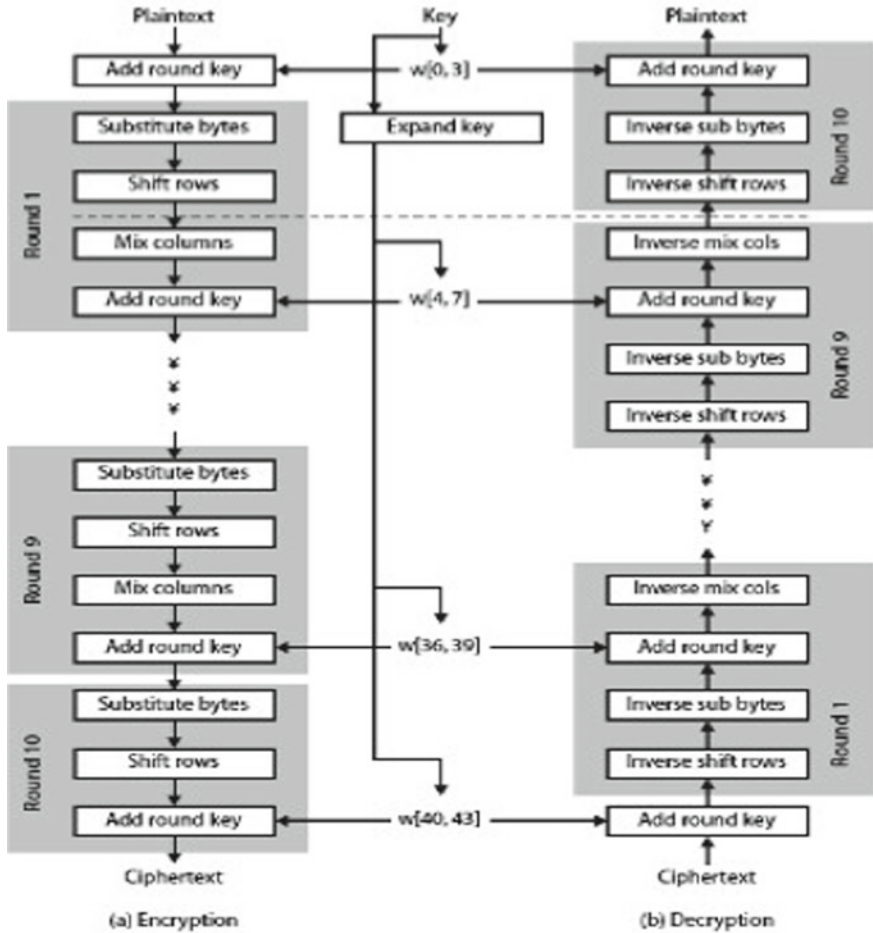


Fig. 1 Basic structure of AES

**Precision:** It is the proportion of predicted positive which is actual positive. The formula is defined as

$$\text{Precision} = \frac{tp}{(tp + fp)} \tag{4}$$

**Recall:** It is proportion of actual positives which are predicted positive. The formula is defined as

$$\text{Recall} = \frac{tp}{(tp + fn)} \tag{5}$$

where  $p$  is the number of positive data points,  $n$  is the number of negative data points,  $tp$  is the number of correctly classified true positives data points,  $tn$  is the number of

correctly classified true negatives data points,  $fp$  is the number of incorrectly labeled false positives data points and  $fn$  is the number of incorrectly labeled false negative data points.

**F-Measure:** It is combination of both precision and recall that is why it aggregates the above measure. The formula is defined as

$$Fmeasure = \frac{(2+Pr+Re)}{(Pr+Re)} \tag{6}$$

where Pr is precision and Re is recall.

## 4 Result

Every real-time analysis problem requires the analysis of data and its exploration. We use EDA or exploratory data analysis for the same. Using seaborn, we are able to see how the features of our dataset are related to each other.

To check the distribution of a particular feature in our dataset, we use dist plot. We check the distribution for occupants and see most of the occupants lie between 4 and 5 (Fig. 2), for the last electricity bill, it lies between 500 and 2000 (Fig. 3), and the units consumed lie between 650 and 800 units(Fig. 4).

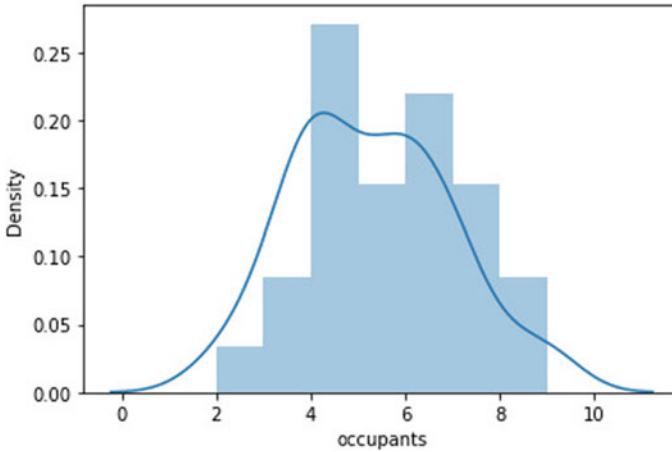


**Fig. 2** Distribution of occupants

To visualize the count of the features, we use countplot. Here, again, we are able to display the plots for occupants (Fig. 5), last electricity bill (Fig. 6), and the units consumed (Fig. 7) using countplot.

Finding the correlation between our features actually helps in feature selection. If our features are correlated to an extent of 90%, we can even skip one of the feature. In our code, we find the correlation between our features using `df.corr()` function first, where `df` is our dataset. Table 1 shows the correlation between occupants, last electricity

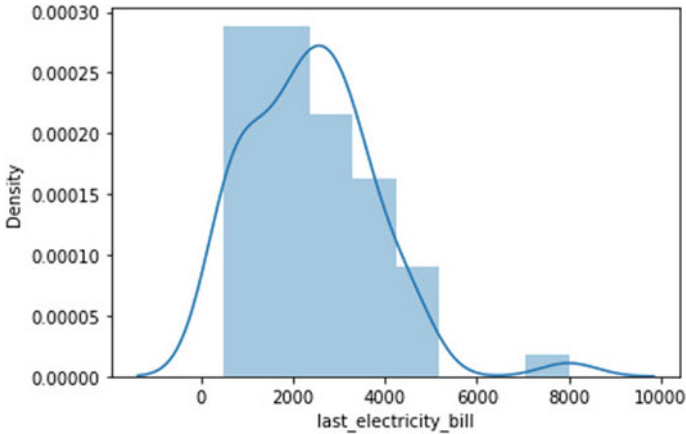


**Fig. 3** Distribution of last electricity bill

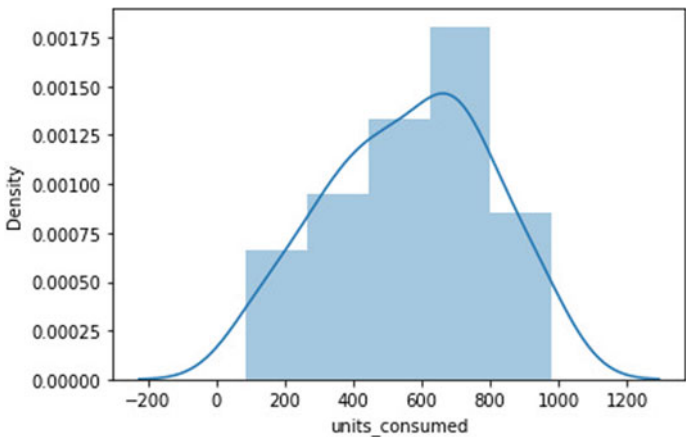


**Fig. 4** Distribution of units consumed

bill, and the units consumed. Since all three of them are related to each other in positive values, it shows that as one feature increases, the other does the same. We then create a visualization of our table using heatmap. The features that relate the most are colored lightly as shown in Fig. 8.

Moving forward to joinplot, it is mainly used for bivariate analysis. Using this, we can clearly see that most of the people consume units between 300 and 800 while the bill majorly lies between Rs. 2000–3500.

We have used both hexagonal and regression form as shown in Figs. 9 and 10, respectively, to visualize the same features: units consumed and the bill produced for the same.

What if we want to visualize more than two features at the same time? We end up using pairplot for the same as shown in Fig. 11. The nine figures show how each of the

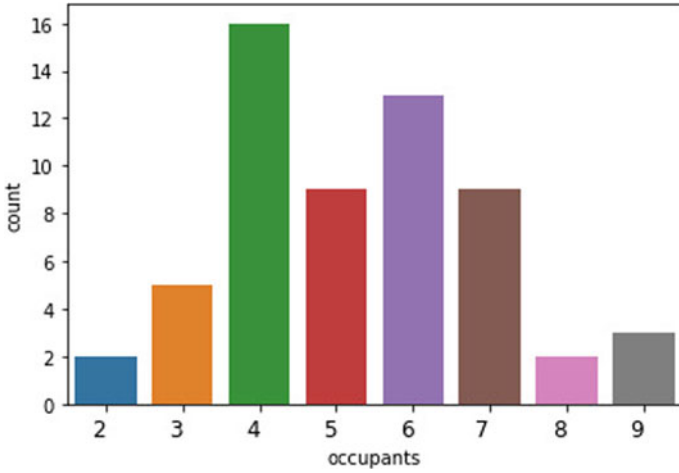


Fig. 5 Countplot of occupants

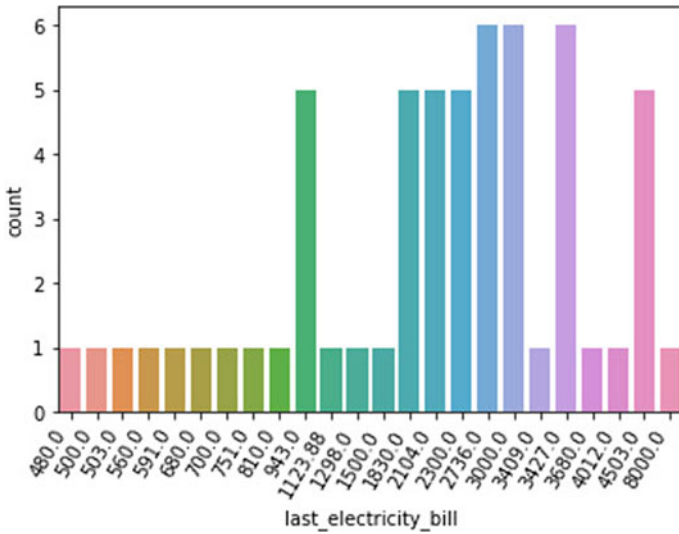


Fig. 6 Countplot of last electricity bill

feature is related to the other feature. The features considered here are again occupants, last electricity bill, and the units consumed.

After visualizing our data, we move on to clustering it using the elbow method. We derive 5 clusters and group our data under 5 labels: average, good, best, bad, and worst. We can see in Fig. 12 that one cluster falling into the worst category. This person has his bill of approximately 8000 bucks while even the occupants in his residence are less compared to people with almost the same number of occupants having bill way less than

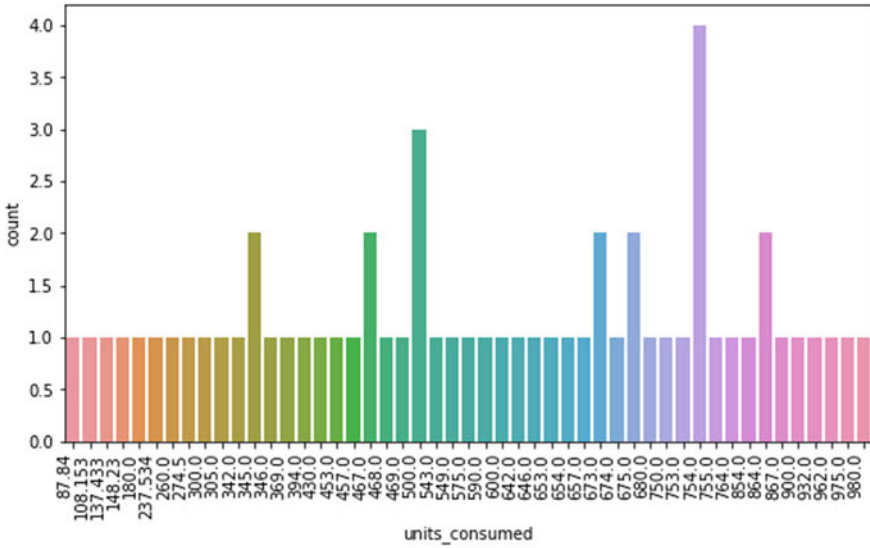


Fig. 7 Countplot of units consumed

Table 1 Correlation table

	Occupants	Last electricity bill	Units consumed
Occupants	1.000000	0.302240	0.226957
Last electricity bill	0.302240	1.000000	0.367386
Units consumed	0.226957	0.367386	1.000000

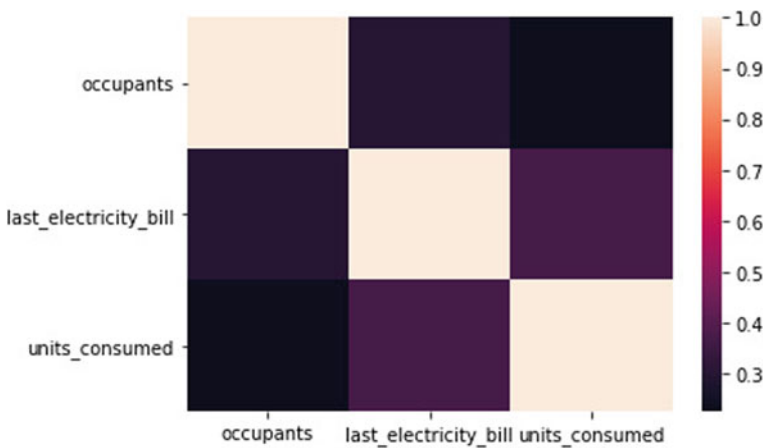
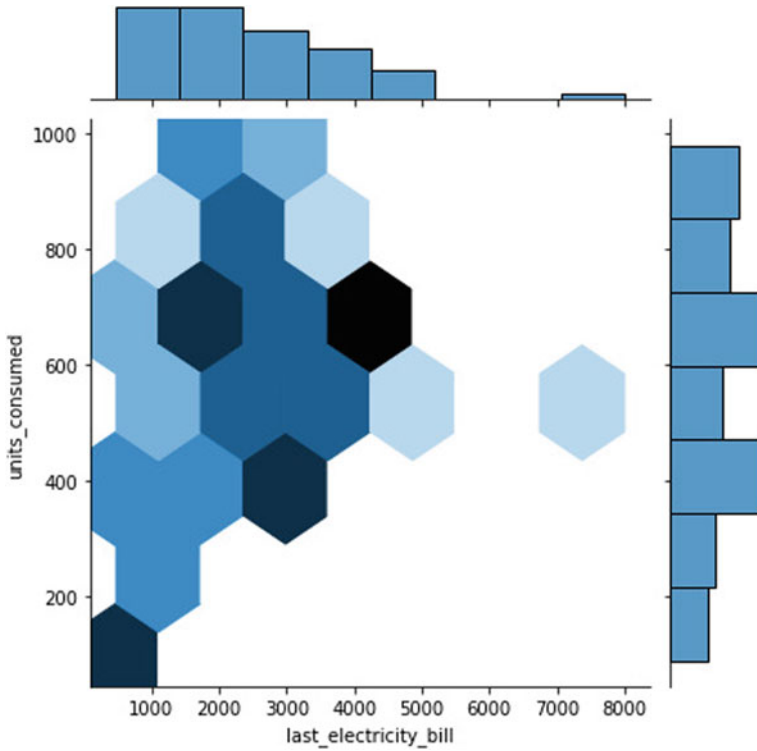


Fig. 8 Correlation heatmap





**Fig. 9** Hexagonal Jointplot

his bill. This shows abnormal pattern in using energy that clearly indicates that he is wasting electricity.

Further on we fit our 6 machine learning algorithms model onto our dataset. Table 2 shows value of accuracy, precision, recall, and F-measure value obtained from all models. We compare all 6 machine learning algorithms model using Table 2 [18].

As far as security of data is concerned, we apply AES encryption algorithm. For instance, suppose or message is “0123456789abcdeffedcba9876543210” and our key is “0f1571c947d9e8590cb7add6af7f6798,” then after applying the AES algorithm, we get our encrypted data as “ff0b844a0853bf7c6934ab4364148fb9” as shown in the Fig. 13.

## 5 Conclusion

We finally come to the conclusion that K neighbors classifier model fits on our database the best as the accuracy, precision, recall, and F-measure value we obtain from it is the highest among all. We are thus able to see that if we further on expand our dataset for a sample of a large population, we had be easily able to spot the customers that would show abnormal usage of electricity consumption and group them into the bad cluster using k-means clustering algorithm. We can then fit the data into K neighbors classifier

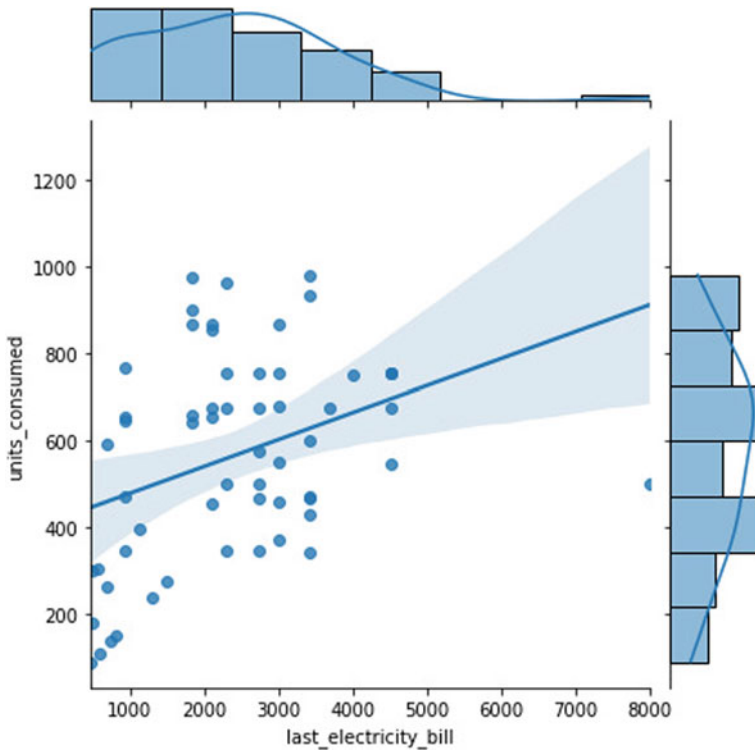


Fig. 10 Regression jointplot

model if we wish to train and test it as well. And we were successful in protecting the personal data of residents with the help of AES algorithm.

This shows how technology can help us determine people who are wasting electricity easily just by using machine learning algorithms. Machine learning and artificial intelligence deal with data easily. Data as we all know are the new oil and working with it using techniques of data science reveals the wonders of technology.

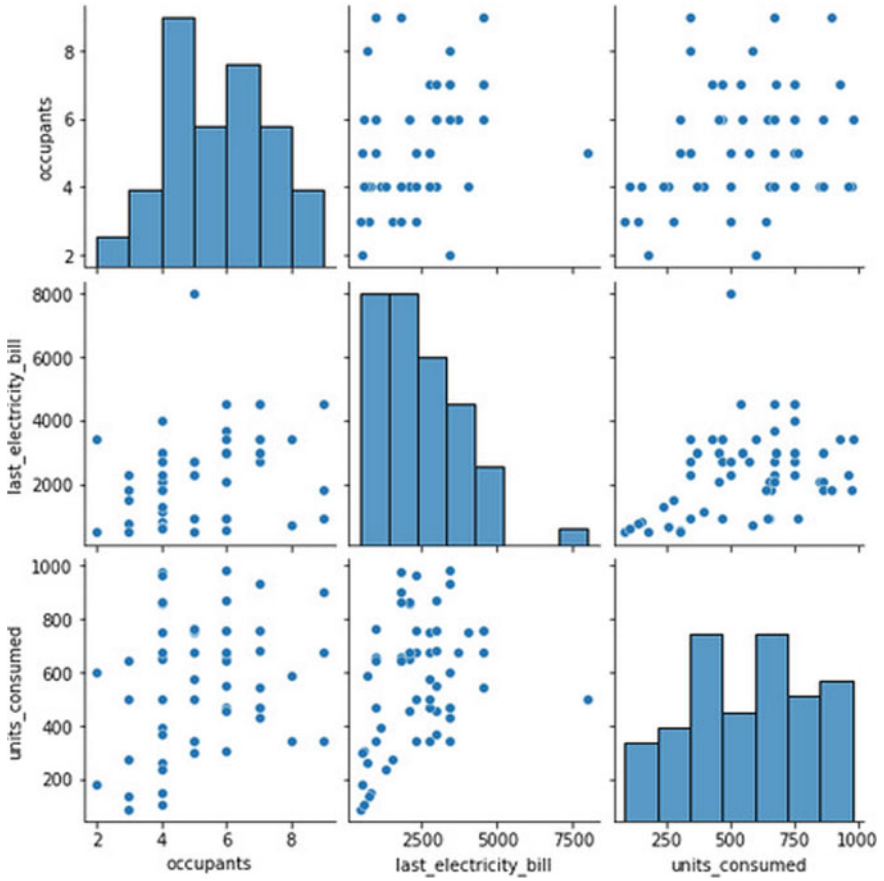


Fig. 11 Pairplot

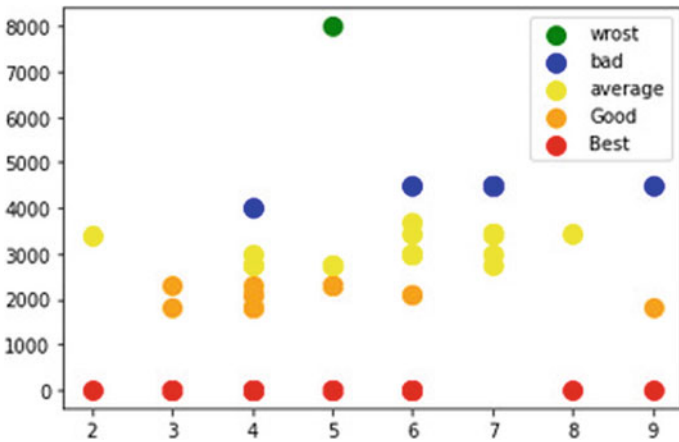
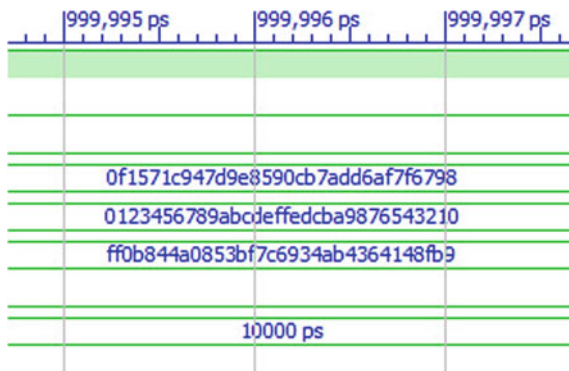


Fig. 12 Cluster plot

**Table 2** Performance of classification algorithms

Classifiers	Accuracy (%)	Precision (%)	Recall (%)	F-measure (%)
Logistic regression	80	76.667	80	76
Decision tree	93	95	93.333	92.698
Gaussian naive bayes	93	95	93.333	92.698
K neighbors classifier	100	100	100	100
Support vector machines	93	95	93.333	92.698
Random forest	93	95	93.333	92.698



**Fig. 13** AES algorithm output

## References

1. Nepal B, Yamaha M, Sahashi H, Yokoe A (2019) Analysis of building electricity use pattern using k-means clustering algorithm by determination of better initial centroids and number of clusters. *Energies* 12:2451. <https://doi.org/10.3390/en12122451>
2. Eugene Yu Shchetinin Cluster-based energy consumption forecasting insmart grids IOP Conf. Series: Journal of Physics: Conf. Series1205 (2019) 012051
3. Satre-Meloy A, Diakonova M, Grünewald P (2019) Cluster analysis and prediction of residential peak demand profiles using occupant activity data. 0306–2619/ © 2019 The Authors. Published by Elsevier Ltd.
4. Ashouri M, Haghighat F, Fung BCM, Yoshino H (2018) Development of a ranking procedure for energy performance evaluation of buildings based on occupant behavior. <https://doi.org/10.1016/j.enbuild.2018.11.0500378-7788> © 2018 Elsevier B.V. All rights reserved
5. Murata H, Onoda T, Estimation of power consumption for household electric appliances. In: Proceedings of the 9th international conference on neural information processing (ICONIP'OZ) , Vol 5. Published by IEEE.
6. Cai H, Shen S, Lin Q, Li Q, Xiao H (2019) Predicting the energy consumption of residential buildings for regional electricity supply-side and demand-side management. Digital Object Identifier <https://doi.org/10.1109/ACCESS.2019.2901257> Published by IEEE

7. Li J, Panchabikesan K, Yu Z (“Jerry”), Haghghat F, El Mankibi M, Corgier D (2019) Systematic data mining-based framework to discover potential energy waste patterns in residential buildings <https://doi.org/10.1016/j.enbuild.2019.07.0320378-7788/> © 2019 Elsevier B.V. Allrightsreserved
8. Singh S, Gill DS, Comparative study of different data mining techniques: a review, [www.ijltemas.in](http://www.ijltemas.in). IJLTEMAS II(IV). ISSN 2278–2540
9. Han J, Kamber M (2012). Data mining: concepts and techniques, 3rd.edn. Morgan Kaufmann Publishers, Boston
10. Chen H, Liu C, Research and application of cluster analysis algorithm. In: 2013 2nd International conference on measurement, information and control 978-1-4799-1392-3/13/\$31.00 m013. IEEE
11. Setyaningsih S (2012) Using cluster analysis study to examine the successful performance entrepreneur in Indonesia. In: International conference on small and medium enterprises development 2212–5671 © 2012 The Authors. Published by Elsevier Ltd.
12. Han J, Kamber M (2006) Data mining concepts and techniques. Elsevier Inc., 2nd edn. ISBN no. 978-81-312-0535-8
13. Decision tree at [http://chemeng.utoronto.ca/~datamining/dmc/decision\\\_tree/htm](http://chemeng.utoronto.ca/~datamining/dmc/decision\_tree/htm)
14. Navies bayes at [http://chem-eng.utoronto.ca/~datamining/dmc/naive\\\_bayesian.htm](http://chem-eng.utoronto.ca/~datamining/dmc/naive\_bayesian.htm)
15. Cristianini N, Shawe-Taylor J (2000) An introduction to support vector machines and other kernel-based learning methods. Cambridge University Press, Cambridge
16. Schölkopf B, Smola A (2002) Learning with kernels: support vector machines, regularization, optimization, and beyond. MIT Press, Cambridge, MA
17. Abdullah AM, Advanced encryption standard (AES) algorithm to encrypt and decrypt data
18. Brohi SN, Pillai TR, Kaur S, Kaur H, Sukumaran S, Asirvatham D (2019) Accuracy comparison of machine learning algorithms for predictive analytics in higher education. In: International conference for emerging technologies in computing (iCETiC 2019) proceedings published by SpringerLink



# Design, Development, and Manufacturing of Cost-Effective Face Shields for COVID-19

Mohan Aditya Pabolu<sup>1</sup> , Venkata Nori<sup>1</sup> ,  
and Jayaprakash Sharma Panchagnula<sup>2</sup>  

<sup>1</sup> Department of Mechanical Engineering, SRM University-Andhra Pradesh, Amaravati 522502, India

<sup>2</sup> Department of Mechanical Engineering, Birla Institute of Technology and Science, Pilani 333031, India

[pj.sharma@pilani.bits-pilani.ac.in](mailto:pj.sharma@pilani.bits-pilani.ac.in)

## 1 Introduction

Coronavirus disease 2019 or COVID-19 is declared as a global pandemic by the World Health Organization (WHO) and is posing a great challenge to mankind. It is a highly contagious disease caused by severe acute respiratory syndrome coronavirus 2 (SARS-CoV-2) that effects the respiratory system, which causes mild to severe symptoms, sometimes even leading to death [1]. The COVID-19 virus most likely spreads via contact or respiratory droplets or through airborne aerosols or from contaminated surfaces (fomite) [2]. The droplets that are released into the air when an infected person coughs, sneezes, talks, or sings are called as respiratory droplets and are  $>5\text{--}10\ \mu\text{m}$  in diameter. Whereas aerosols are responsible for airborne transmission of COVID-19 virus are  $<5\ \mu\text{m}$  in diameter and are most likely generated in the hospital environment during medical procedures that generate aerosols. Further research is being carried out to see if aerosols are generated in scenarios other than medical procedures, such as in indoors with poor ventilation [2]. These respiratory droplets or aerosols carrying SARS-CoV-2 can enter humans through the mucous membranes on the face (eyes, nose, and mouth) and propagate to the lungs. At an individual level, WHO recommends avoiding touching eyes, nose, and mouth in addition to physical distancing, good hand, and respiratory hygiene to not only prevent getting infected but also to prevent spreading of COVID-19 [3]. Face masks, goggles, and face shield are key components of the personal protection equipment (PPE) kit [4] that are needed to protect the COVID-19 frontline workers that include primary health caregivers, sanitation workers, law and order enforcement authorities, essential services personnel, and the good samaritans who spread awareness, feed the hungry, etc. However, COVID-19 is creating enormous stress on the healthcare systems of countries. It can be attributed to two reasons—one due to increasing case-loads and the other due to shortage of PPE kits arising out of disrupted supply chains [5]. In some countries, restrictions were imposed on the usage of surgical grade face masks by the general public to enable supply and availability of critical PPE equipment to COVID-19 frontline workers.

Face shields as a PPE gear are regularly used in hospitals, research, and industrial organizations. It contains a band that goes around the forehead and a sheet (also known as visor generally made out of plastic) that is transparent, scratch, impact, and moisture resistant is secured to the band generally made out of plastic, covers the whole face. In medical facilities, a face shield is generally used to protect mucous membranes in the nose, mouth, and eyes. During the COVID pandemic, its utility is even more enhanced and is generally used along with other PPE gear such as face masks and goggles by medical personnel, for example, interventional radiologists [6], oral, and maxillofacial surgeons [7] and those who perform aerosol generating procedures [8, 9], etc. In these times when surgical disposal face masks are in shortage, face shields not only provide an additional layer of protection by covering entire faces including masks but also extend the life of masks in the process. Several innovative solutions were provided to design and develop face shields with readily available materials and simple manufacturing techniques to meet the demand [9–15]. One such study converted arthroplasty helmets to serve as PPE [10]. Many industrial firms [16–20] have pitched in to meet the increasing demand, while research institutions [11–15] and independent makers and designers [21, 22], including the National Institute of Health, USA (NIH) 3D print exchange [23], have come forward and shared freely COVID-19-related face shield designs in the public domain. These face shields can be manufactured using injection molding, 3D printing, waterjet, and laser cutting. For example, Dow chemical company [18] has shared a face shield design with detailed drawings, material specifications, and the manufacturing procedure. Martin Culpepper and his team at MIT developed a low-cost mass manufacturing for disposable face shields using die cutting process [12]. The face shield is designed as a single piece and shipped as flat sheets that can be quickly folded into a 3D face shield. In India, Anatomiz3D [20] developed a cost-effective 3D printed face shield. Many studies have been published that use these open-source designs as a starting point and modified it based on the requirements and feedback [6–8]. Very few studies have offered protection to the ears as most of the designs catered to the medical personnel who wear caps that go cover the ears. Most of the face shields either focused on disposable face shields or used materials that cannot be easily disinfected and hence must be disposed [24]. Disposable face masks and face shields (like any other single use plastics) are creating a new environmental issue contributing to the already existing plastic waste in the environment [25]. To mitigate this environmental concern, more efforts must be put in to develop either reusable or biodegradable face shields. This assumes significance especially when studies propose the use of PPE (such as face shields) by the public to slow down the spread of COVID-19 [26].

In this article, two types of face shields using different manufacturing techniques are proposed. One with an additive manufacturing process commonly known as 3D printing (denoted by FS1) and the other with conventional material removal operation, i.e., milling operation (denoted by FS2). The headband material in FS1 is poly lactic acid (PLA) while in FS2, corrugated cardboard is used. FS1 can be treated with regular medical grade disinfectants whereas FS2 can be disinfected in an ultraviolet (UVC) germicidal chamber. Both prototypes are reusable, cost-effective, lightweight, comfortable, and easy to wear. The unique feature of FS2 is that it is biodegradable. These face shields were the outcome of rapid response efforts anticipating supply shortages, during March 2020, the

early days of COVID-19 in India. These face shields were widely reported in regional and national newspapers [27, 28]. The design methodology and the manufacturing techniques for realizing both the face shields are elaborated in the subsequent sections.

## 2 Methodology

### 2.1 Realization of FS1

Additive manufacturing (AM) commonly referred as 3D printing is a layer-by-layer manufacturing approach with less lead time [29]. AM uses a three dimensional (3D) virtual computer-aided design (CAD) model to manufacture the physical component. This process starts with designing a 3D CAD model. This CAD model is sliced into two dimensional (2D) layers using a slicing software, and then, each layer is deposited at a time with the intended material. The various steps involved in AM process are modeling, object orientation, slicing, deposition, and post-processing (in sequence) [30]. Some of the major advantages of AM processes are less material wastage, design flexibility, and shorter lead time. AM is only dependent on the design and is not influenced by machine limitations. In this way, AM provides a high degree of design freedom. The stereolithography file (\*.stl) is the de facto file used to convey geometric data from the CAD file to AM machine. With the advancement in the technology and research toward new material deposition, currently, almost all of the engineering materials (both metals and non-metals) are used in various AM applications. Some of the famous materials used in AM applications are polymers, glass, clay, concrete, iron, aluminum. AM is suitable even for difficult to machine materials such as nickel and titanium-based super alloys. On the other hand, as per American Society for Testing and Materials-F42 (ASTM-F42), AM is classified into seven types [31]. Those are material extrusion, material jetting, binder jetting, powder bed fusion, sheet lamination, vat polymerization, and directed energy deposition techniques, respectively. Each technique will differ depending on the material and machine technology used. Among above-mentioned techniques, material extrusion-based fused deposition modeling (FDM) is used in the current study. In the FDM process, a continuous thermoplastic filament is fed into a print head from a large spool. The print head is surrounded by a band heater where the solid plastic filament melts and transforms into a semi-solid state which then gets extruded through the nozzle. The movement of the print head is controlled by a computer to define the print geometry. In general, the head realizes one layer or in other words, one slice horizontally at a time. Upon successful completion of the layer, the head moves vertically by a small distance equal to the layer thickness. This process continues until the object is completed. The speed of the extruder head, stop, and start of the deposition is also controlled by the same computer. The universally available dimensions of the filament and the nozzle diameters are 1.75 mm and 0.4 mm, respectively. The same are used in the present study.

The sequence of steps followed to realize the cost-effective face shield through AM technique is described. The first step is to design a CAD model using modeling software. The next immediate step is to convert the CAD model into machine understandable language (G code generation) and then finally realizing the component using a 3D printer. The model and make of 3D printer are Ender 3 Pro and Creality, respectively, and the slicing software used is Ultimaker Cura 4.5. Once the parts are completely printed, a



175 microns thick, highly transparent scratch-resistant, and anti-fog sheet are attached to the rounded projections on the printed part (headband). The physical realization of a face shield through 3D printing technology is explained in Fig. 1. The initial dimensions of the realized face shield using AM process are 3 mm thick, 10 mm in height, and the end to end linear distance is 150 mm, and an elastic string of 3 mm diameter is used for securing it to the head. It has been observed that the time taken to complete one face shield headband in 3D printing operating is 49 min. After successful realization of the face shield, fifteen (15) copies of the same have been distributed to policemen and doctors for collecting feedback on various aspects of design and user comfort. Based on the feedback, the face shield design has been modified and the thickness of the elastic band increased to one inch (25.4 mm) to improve overall usefulness and user comfort. The modified dimensions of the face shield are as follows: 2.5 mm thick, 15 mm in height, and the end to end linear distance is 165 mm. It has been observed that the time taken to complete one modified face shield headband in 3D printing is 54 min. It is to be noted that all the parameters such as the speed of linear motion while deposition and ideal movements, material deposition rate, layer thickness, and infill percentage are identical for both the headbands. Figure 2 illustrates the differences between the initial and the modified face shield. Though the lead time is less in AM processes, the manufacturing time is slightly higher than the conventional manufacturing processes. Not only to minimize the manufacturing time but also to mass produce the same, the modified face shield designs are stacked vertically (one over the other), so that the multiple copies can be printed without human intervention [7]. It is to be noted that the manufacturing of FS1 through AM process is cost effective (INR 20 or USD 0.27). Figure 3 depicts the stacking of face shield CAD models with a 0.5 mm gap between them. Of course, by the virtue of 3D printing technology, the process generates a support material in the gap between the models and it can be easily removed. The dimensions of the printer allowed for printing a maximum of twenty (20) face shield headbands at a time.

Another method of mass production of face shield headband in a very short span is injection molding process. In this process, a combination of punch and die creates the cavity of the product to be manufactured. The molten material enters into the cavity and occupies the shape of the cavity. The major drawback with the injection molding system is the manufacturing of die and punch that requires longer lead time and expensive. However, the cost of the mass production through injection molding becomes comparable to that when produced by AM.

## 2.2 Realization of FS2

To manufacture the face shield using conventional machining operation, a computer numerically controlled (CNC) with G code generation computer-aided manufacturing (CAM) software is used. The input and the output for this software are a CAD draft to be manufactured and NC tool for the uploaded CAD draft for cutter, respectively. As discussed previously, a face shield consists of two major components (headband and a transparent shield). A 3 ply corrugated cardboard is used in making the headband for FS2. The schematic diagram of a 3 ply corrugated cardboard is illustrated in Fig. 4. Owing to the numerous advantages such as biodegradability, eco-friendliness, lightweight nature,

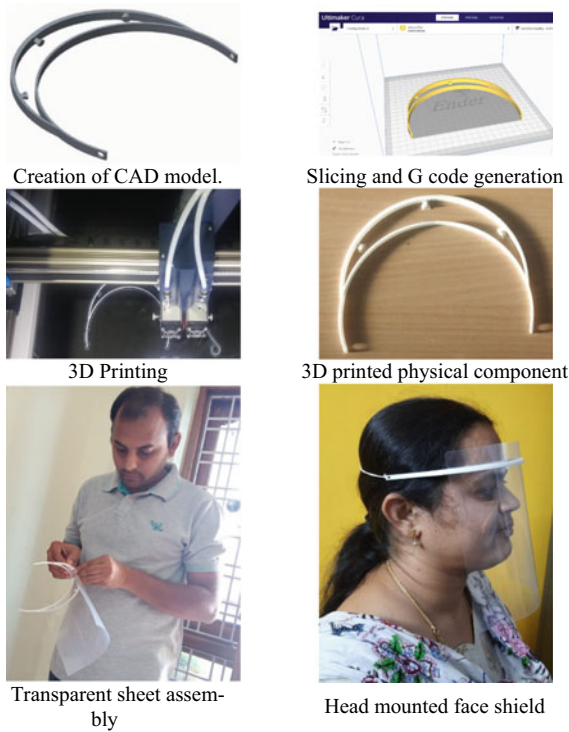


**Fig. 1** Various steps involved in realization of face shield using AM process

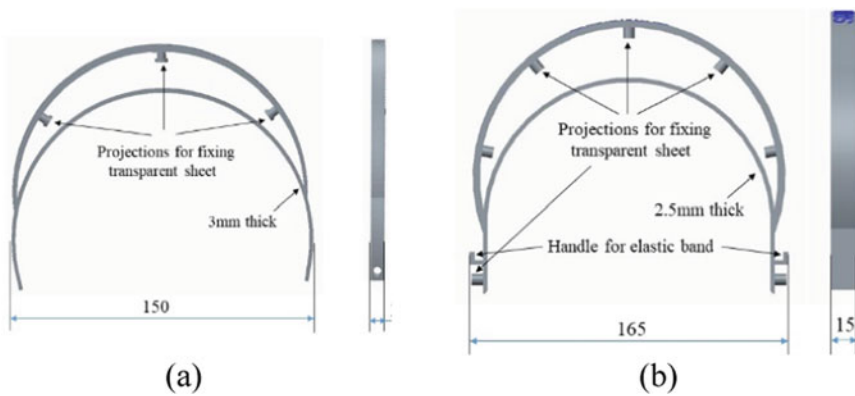


**Fig. 2** Face shield designs: **a** before modification, **b** modified model based on feedback (all dimensions in mm)

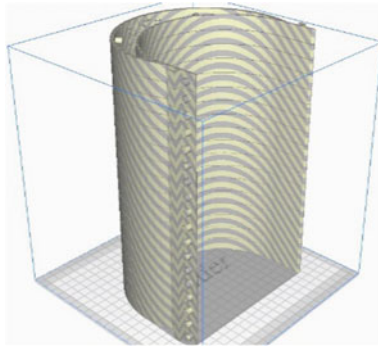


**Fig. 3** Stacking of face shields for mass production in 3D printing technology

and water resistance property, cardboard has been identified to be a suitable candidate for the face shield. A 3 ply corrugated cardboard is made of virgin kraft paper that has superior strength and strong fiber bonding and thus used in various engineering applications. Cardboard also has very high-tear resistance and bursting strength. The mechanical bursting strength of a 3 ply corrugated cardboard used in the current study is  $16 \text{ kg/cm}^2$  with E type flute profile and its grams per square meter (GSM) value is 590. The various dimensions of the headband and the transparent shield for tool path generation are depicted in Figs. 5 and 6, respectively.

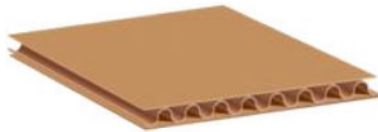


**Fig. 4** Schematic representation of 3 ply corrugated cardboard [32]

Like the previous face shield, a transparent protective sheet of  $175 \mu\text{m}$  thick is used, and an elastic band is attached to the headband. The uniqueness of the present headband is that it has several flake like structures at the contact area of the forehead. These structures provide a soft and comfortable feel to the user that enables the user to wear the face shield even for a long time without much strain. Another unique feature of the current design of the face shield is that it holds the transparent protective shield one inch (25.4 mm) away from the forehead that helps in air circulation and frees the temples of any pressure caused by the headband supports. This feature enables the face shield to handle variations in head circumference too. For the physical realization of the face shield, the below-mentioned CAD model in Figs. 5 and 6 is given as input to the CNC digital cutter (milling machine). Figure 7 illustrates the two-step manufacturing of face shield using CNC milling machine. The CNC digital cutter (milling machine) cuts the 3 ply corrugated cardboard (for headband) and the transparent sheet as per the given input dimensions.

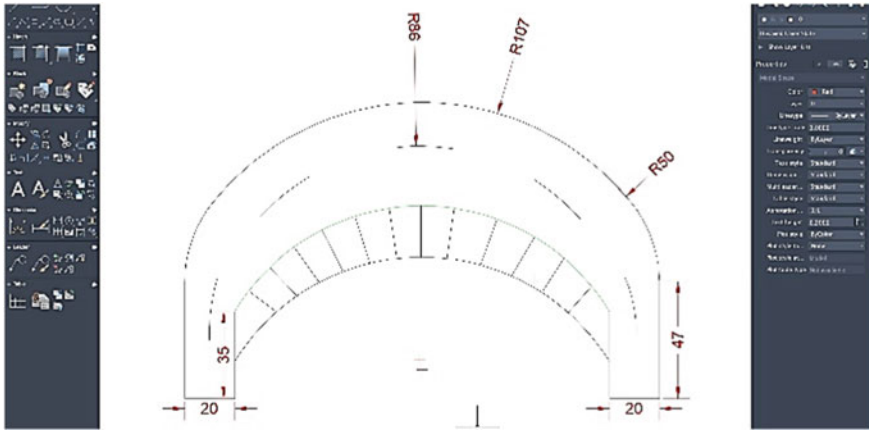


Fig. 5 Computer-aided draft of head band top view (all dimensions in mm)

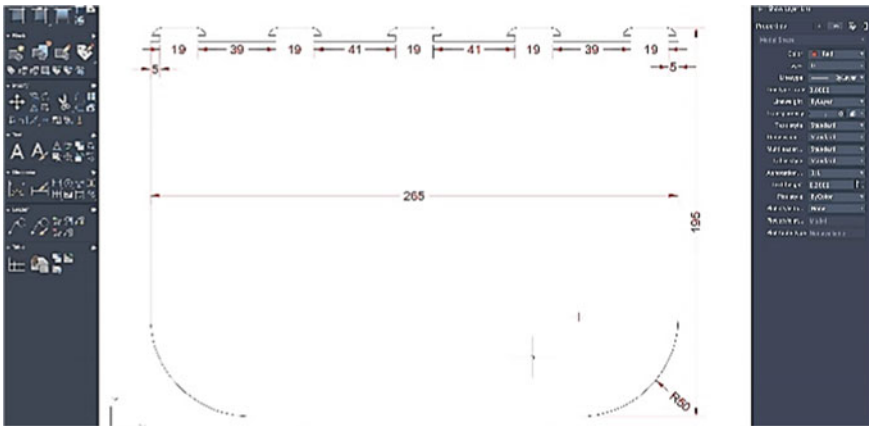
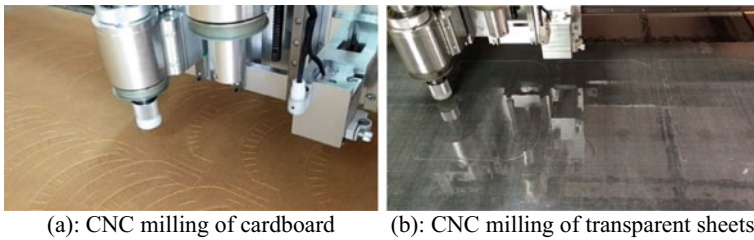


Fig. 6 Computer-aided draft of transparent shield for cutting path generation—front view (all dimensions in mm)



(a): CNC milling of cardboard (b): CNC milling of transparent sheets

Fig. 7 Two-step manufacturing of face shield: a CNC milling of cardboard, b CNC milling of transparent sheets

The transparent protective shield is attached to the headband using a slot type mechanism provided on the headband. This helps in disassembly and either the transparent shield or the headband can be removed easily for disinfection purpose. The CAD model, final assembled face shield, and frontal view of a student with face shield are shown in Fig. 8. The entire process of manufacturing and assembly took 3 min to complete. Fifty (50) face shields were freely distributed to the frontline workers such as policemen, doctors, and high officials in the government and all of them gave very good feedback.

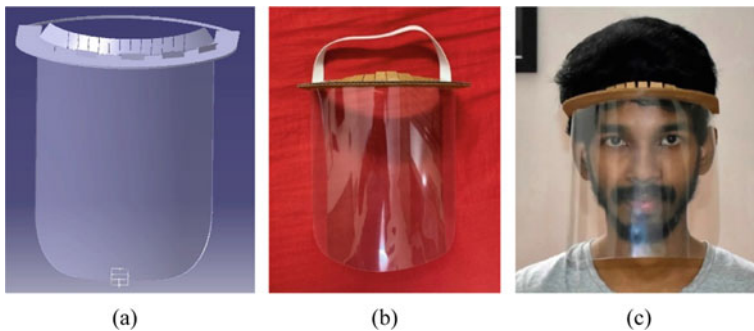


**Fig. 8** a CAD model, b assembled face shield, c student with face shield

### 3 Conclusions

COVID-19 is a highly contagious respiratory disease, and the whole world is struggling to find a solution. With global supply chains severely affected and the ever increasing COVID-19 cases, the healthcare systems around the world are facing a severe shortage of PPE kits. Many universities, industries, research communities, and hobbyists have shown tremendous ingenuity and supported the frontline workers by sharing designs in the public domain and helped set-up alternative supply chains to enable manufacturing of PPE locally. The two face shields, such as FS1 and FS2, presented in the paper were developed on war footing during the 1st week of March 2020, the early days of COVID-19 in India. The following conclusions can be drawn based on the current study.

- Face shield FS1, which is realized using AM process protects the ears too in addition to the facial region (that includes the mucous membranes).
- Face shield FS2 that is realized through conventional machining operation uses a biodegradable 3 ply corrugated cardboard making it eco-friendly, recyclable, light in weight, and water resistant.
- Both face shields received very good feedback from frontline workers.
- Mass-producing face shields at low costs (INR 20 or USD 0.27) is proposed

In the current situation, face shields are invaluable in not only offering additional protection to the COVID-19 frontline workers but also have the potential to prevent spread of COVID-19 in communities (especially with high-population density) when used with recommended cloth masks [26, 32].

## References

1. Lai C, Shih T, Ko W, Tang H, Hsueh P (2020) Severe acute respiratory syndrome coronavirus 2 (SARS-Cov-2) and coronavirus disease-2019 (COVID-19): the epidemic and the challenges. *Int J Antimicrob Agents* 55(3):105924
2. Transmission of SARS-CoV-2: implications for infection prevention precautions, scientific brief, 9 July 2020, Webpage. <https://www.who.int/publications/i/item/modes-of-transmission-of-virus-causing-covid-19-implications-for-ipc-precaution-recommendations>. Last accessed 01 Aug 2020
3. World Health Organization Webpage. <https://www.who.int/emergencies/diseases/novel-coronavirus-2019/advice-for-public>. Last accessed 15 Aug 2020
4. Cook T (2020) Personal Protective equipment during the coronavirus disease (COVID) 2019 pandemic—a narrative review. *Anaesthesia*. <https://doi.org/10.1111/anae.15071>
5. Volkin S (2020) How has COVID-19 impacted supply chains around the world? The Hub, April (2020). HUB Webpage. <https://hub.jhu.edu/2020/04/06/goker-aydin-global-supply-chain/>. Last accessed 01 Aug 2020
6. Sapoval M, Gaultier AL, Del Giudice C, Pellerin O, Kassir-Chikhani N, Lemarteleur V, Fouquet V, Tapie L, Morenton P, Tavitian B, Attal JP (2020) 3D-printed face protective shield in interventional radiology: evaluation of an immediate solution in the era of COVID-19 pandemic. *Diagn Interv Imaging* 101(6):413–415
7. Dina A, Nam N, Steven MR, Shelly A (2020) 3D printing of face shields during COVID-19 pandemic: a technical note. *J Oral Maxillofac Surg* 78(8):1275–1278
8. Mostaghimi A, Antonini MJ, Plana D, Anderson P, Beller B, Boyer E, Fannin A, Freake J, Oakley R, Sinha M, Smith L, Van C, Yang H, Sorger P, LeBoeuf N, Yu S (2020) Regulatory and safety considerations in deploying a locally fabricated, reusable face shield in a hospital responding to the COVID-19 pandemic. *Med*
9. Alborz S, Evripides GL, Edward E, Alexander JGL (2020) Exploration of alternative supply chains and distributed manufacturing in response to COVID-19; a case study of medical face shields. *Mater Des* 192:108749–108751
10. Erickson MM, Richardson ES, Hernandez NM, Bobbert DW, Gall K, Fearis P (2020) Helmet modification to PPE With 3D printing during the COVID-19 pandemic at duke university medical center: a novel technique. *J Arthroplasty* 35(7S):S23–S27
11. University of Washington Webpage. <https://www.washington.edu/news/2020/04/13/uws-3d-printed-covid-19-face-shields-from-innovation-to-delivery/>. Accessed 5 Aug 2020
12. MIT Webpage. <http://news.mit.edu/2020/face-shield-ppe-manufacture-covid-19-0331>. Last accessed 01 Aug 2020
13. Georgia Tech Webpage. <https://news.gatech.edu/2020/03/23/do-it-yourself-medical-devices-and-protective-gear-fuel-battle-against-covid-19>. Last accessed 01 Aug 2020
14. UW Makersspace Webpage. <https://making.engr.wisc.edu/shield/>. Last accessed 01 Aug 2020
15. 3D4Care Webpage. <http://3d4care.org/>. Last accessed 01 Aug 2020
16. Statt N (2020) 3D printers are on the front lines of the COVID-19 pandemic. *The Verge*, 25 May 2020. *Theverge* Webpage. <https://www.theverge.com/2020/5/25/21264243/face-shields-diyppe-3d-printing-coronavirus-covid-makerresponse>. Last accessed 01 Aug 2020
17. The Packaging Portal Webpage. <https://www.thepackagingportal.com/industry-news/leicester-company-launches-disposable-and-recyclable-cardboard-face-shield/>. Last accessed 01 Aug 2020
18. Corporate Dow Webpage. <https://corporate.dow.com/documents/ehs/768-370-01-face-shield-design.pdf>. Last accessed 01 Aug 2020
19. Prusa Research. Prusa face shields: Webpage. <https://www.prusaprinters.org/social/16-prusa-research/collections/17041>. Last accessed 01 Aug 2020

20. Anatomiz3d Webpage. <https://anatomiz3d.com/>. Last accessed 01 Aug 2020
21. Covidmakerresponse Webpage. <http://covidmakerresponse.com/>. Last accessed 21 July 2020
22. Open Face Webpage. <https://open-face-website.now.sh/>. Last accessed 21 July 2021
23. NIH Webpage. <https://3dprint.nih.gov/>. Last accessed 21 July 2021
24. Khan MM, Parab SR (2020) Safety guidelines for sterility of face shields during COVID 19 Pandemic. Indian J Otolaryngol Head Neck Surg 1–2. Advance online publication (2020). Webpage, <https://doi.org/10.1007/s12070-020-01865-2>
25. Fadare OO, Okoffo ED (2020) Covid-19 face masks: a potential source of microplastic fibers in the environment. Sci Total Environ 737:140279
26. Perencevich EN, Diekema DJ, Edmond MB (2020) Moving personal protective equipment into the community: face shields and containment of COVID-19. JAMA 323(22):2252–2253
27. Business Standard News Paper Webpage. [https://www.business-standard.com/article/pti-stories/varsity-professor-in-ap-designs-face-shield-that-will-help-cover-vital-parts-of-the-face-120050101024\\_1.html](https://www.business-standard.com/article/pti-stories/varsity-professor-in-ap-designs-face-shield-that-will-help-cover-vital-parts-of-the-face-120050101024_1.html). Last accessed 01 Aug 2020
28. Yourstory Webpage. <https://yourstory.com/socialstory/2020/05/srm-engineering-student-face-shield-coronavirus>. Last accessed 01 Aug 2020
29. Sebastian H, Lars P, Jens E (2016) Additive manufacturing and high speed machining-cost comparison of short lead time manufacturing methods. In: 26th CIRP design conference. <https://doi.org/10.1016/j.procir.2016.05.049>
30. Wang Y, Blache R, Xu X (2017) Selection of additive manufacturing processes. Rapid Prototyping J 23(2):434–447
31. Hybrid Manufacturing Webpage. [https://www.additivemanufacturing.media/cdn/cms/7\\_families\\_print\\_version.pdf](https://www.additivemanufacturing.media/cdn/cms/7_families_print_version.pdf). Last accessed 01 Aug 2020
32. Trident Webpage. <https://www.tridentpbi.in/products/corrugated-box> last accessed 2020/08/01.-cardboard-cartons. Last accessed 01 Aug 2020